IGARSS'96

1996 International Geoscience and Remote Sensing Symposium

IEEE

University of Nebraska Lincoln

NASA

NOAA

OFFICE OF NAVAL RESEARCH 50th Anniversary

U.R.S.I.

Remote Sensing for a Sustainable Future

Volume IV

Burnham Yates Conference Center
Lincoln, Nebraska USA
27-31 May 1996

IEEE Catalog Number 96CH35875
Library of Congress Number: 95-80706

DISTRIBUTION STATEMENT A
Approved for public release;
Distribution Unlimited

IGARSS'96

1996 International Geoscience and Remote Sensing Symposium

Remote Sensing for a Sustainable Future

Volume IV

DTIC QUALITY INSPECTED 2

19970520 018

IEEE Catalog Number 96CH35875
Library of Congress Number: 95-80706

Editor: Tammy I. Stein
Editorial Assistant: Jennetta Brunk
Production: IEEE Publications

Copyright and Reprint Permission: Abstracting is permitted with credit to the source. Libraries are permitted to photocopy beyond the limit of U.S. copyright law for private use of patrons those articles in this volume that carry a code at the bottom of the first page, provided the per-copy fee indicated in the code is paid through Copyright Clearance Center, 222 Rosewood Drive, Danvers, MA 01923. For other copying, reprint or reproduction permission, write to the IEEE Copyrights Manager, IEEE Service Center, 445 Hoes Lane, P.O. Box 1331, Piscataway NJ 08855-1331. All rights reserved. Copyright @1996 by the Institute of Electrical and Electronics Engineers, Inc.

IEEE Catalog Number 96CH35875
ISBN 0-7803-3068-4 (softbound edition)
ISBN 0-7803-3069-2 (casebound edition)
ISBN 0-7803-3070-6 (microfiche edition)
Library of Congress Number 95-80706

Additional copies of the IGARSS'96 Digest are available from the following source:

Institute of Electrical and Electronics Engineers, Inc.
Single Copy Sales
445 Hoes Lane
PO Box 1331
Picataway NJ 08855-1331

IGARSS'96 SPONSORS

IEEE

IEEE Geoscience and Remote Sensing Society

University of Nebraska Lincoln

University of Nebraska, Lincoln

NASA

National Aeronautics and Space Administration (NASA)

NATIONAL OCEANIC AND ATMOSPHERIC ADMINISTRATION
NOAA
25 YEARS OF SCIENCE & SERVICE
U.S. DEPARTMENT OF COMMERCE

National Oceanic & Atmospheric Administration (NOAA)

ONR . . . Investing in the Future
OFFICE OF NAVAL RESEARCH
50th Anniversary
1946 - 1996

Office of Naval Research (ONR)

IGARSS'96 TECHNICAL SPONSOR



U.S. National Committee
Union Radioscientifique Internationale

IGARSS'96 COOPERATIVE SPONSORS

Canon/Modern Methods Inc.

Center for Advanced Land Management Information Technologies, UNL

Center for Communication and Information Science, UNL

Center for Electro-Optics, UNL

Center for Laser Analytical Studies of Trace Gas Dynamics, UNL

Centurion International, Inc.

College of Engineering and Technology, UNL

Department of Electrical Engineering, UNL

ERDAS, Inc.

High Plains Climate Center, UNL

Li-Cor, Inc.

U.S. Geological Survey EROS Data Center

IGARSS'96 ORGANIZING COMMITTEE

Ram Narayanan
General Chairman

Robert McIntosh
Technical Program Co-Chairman

Calvin Swift
Technical Program Co-Chairman

Barbara Emil
Finance Chairman

James Merchant
Publications Chairman

Steve Reichenbach
CD ROM Chairman

Jim Lacy
WWW Chairman

Tammy Stein
Director of Conferences and Information Services, GRSS

LOCAL HOST COMMITTEE

Dennis Alexander
Mark Anderson
Ezekiel Bahar
Blaine Blad
John Boye
Mark Cockson
Natale Ianno
Robert Maher
Robert Palmer
Donald Rundquist
Karen St. Germain
Khalid Sayood
Tracy Soukup
Elizabeth Walter-Shea
Jon Welles

Dennis Alexander, University of Nebraska-Lincoln
Werner Alpers, University of Hamburg
Mark Anderson, University of Nebraska-Lincoln
Ghassem Asrar, NASA Headquarters
Kultegin Aydin, Penn State University
Ezekiel Bahar, University of Nebraska-Lincoln
Ronald Birk, Sverdup Technology Inc.
Andrew Blanchard, University of Missouri-Columbia
Dan Cress, Sandia National Laboratories
John Curlander, Vexcel Corporation
John Curtis, US Army WES
Don Deering, NASA Goddar Space Flight Center
Craig Dobson, University of Michigan
Fernando Echavarria, University of Nebraska-Lincoln
Edwin Engman, NASA Goddard Space Flight Center
Stephen Frasier, University of Massachusetts
Prasad Gogineni, University of Kansas
Richard Gomez, US Army TEC
Bill Grant, NASA Langley
Martti Hallikainen, Helsinki University of Technology
Jim Irons, NASA Goddard Space Flight Center
Akira Ishimaru, University of Washington
Thomas Jackson, USDA Hydrology Lab
James Kalshoven, NASA Goddard Space Flight Center
Timothy Kane, Pennsylvania State University
Roger Kassebaum, Millard North High School-Omaha
Wolfgang Keydel, Institut fur Hochfrequenztechnik
Nahid Khazenie, NASA Goddard Space Flight Center
Roger Lang, George Washington University
Ellsworth LeDrew, University of Waterloo
Fuk Li, Jet Propulsion Laboratory
Charles Luther, Office of Naval Research
Harlan McKim, US Army CRREL
David McLaughlin, Northeastern University
James Mead, University of Massachusetts
Nasir Memon, Northern Illinois University
James Merchant, University of Nebraska-Lincoln
David Meyer, EROS Data Center
Wooil Moon, University of Manitoba
Richard Moore, University of Kansas
Ram Narayanan, University of Lincoln-Nebraska
Eni Njoku, Jet Propulsion Laboratory
Robert Palmer, University of Nebraska-Lincoln
William Plant, University of Washington
Jeff Plaut, Jet Propulsion Laboratory
Paul Racette, NASA Goddard Space Flight Center
John Reagan, University of Arizona
Steven Reichenbach, University of Nebraska-Lincoln
Jack Rinker, US Army TEC
Christopher Ruf, Pennsylvania State University
Donald Rundquist, University of Nebraska-Lincoln
Khalid Sayood, University of Nebraska-Lincoln
Thomas Schmugge, USDA/ARS Hydrology Laboratory
Khalid Siddiqui, SUNY College at Fredonia
Alois Sieber, Joint Research Centre-Ispra
Karen St. Germain, University of Nebraska-Lincoln
Mikio Takagi, University of Tokyo
Jim Tilton, NASA Goddard Space Flight Center
Dennis Trizna, Naval Research Labs
Leung Tsang, University of Washington
Fawwaz Ulaby, University of Michigan
Bruce Wallace, Army Research Laboratory
Elizabeth Walter-Shea, University of Nebraska-Lincoln
JoBea Way, Jet Propulsion Laboratory
Edward Westwater, NOAA/ERL/WPL
Simon Yueh, Jet Propulsion Laboratory



IGARSS'96

1996 International Geoscience and Remote Sensing Symposium

Table of Contents

INTERACTIVE AREA 1 -- Atmosphere

1. Dual-Frequency Three-Dimensional Images of Clouds 1
Firda, J.M., S.M. Sekelsky and R.E. McIntosh

2. Preliminary Backscatter Lidar Measurements of Atmospheric Boundary Layer and Cirrus Clouds in Buenos Aires 34.6 S / 58.5 W 4
Lavorato, M.B., G.J. Fochesatto , E.J. Quel and P.H. Flamant

3. Improvement of a Standard Doppler Dealiasin Technique for Weather Radars Operating in Heavy Clutter Environment 7
Giuli, D., L. Facheris, F. Frattura and L. Baldini

4. Time-Frequency Analysis of Backscattered Lidar Signal to Study Atmosphere Dynamics 10
Molinaro, F., H. Bencherif, M. Bessafi and J. Leveau

5. Estimating RCS of the Sea Surface Perturbed by Rain for Rainfall Rate Retrieval 13
Capolino, F., D. Giuli , L. Facheris and F. Sottili

6. Assessment of Multiple Scattering Effects on Aerosol Retrievals from AVHRR NA
Ignatov, A., L. Stowe and R. Singh

7. Dielectric Constants for Melting Hydrometeors as Derived from a Numerical Method 16
Meneghini, R., and L. Liao

8. Analysis and Modeling of Atmospheric Transport of Water Vapor and Other Trace Constituents NA
Johnson, D.R.

9. Second Order Microwave Radiative Transfer Equation Solution with SSM/I Data NA
Souffez, S.H., and J.R. Givri

10. Adaptive Optical Aerosol Model of the Earth's Atmosphere NA
Smokty, O., and N. Kobjakova

11. Monitoring of Clouds Moisture for Problems of Increase Precipitation Artificially NA
Ruzhentsev, N.V., Yu.A. Kuzmenko and V.P. Bakhanov

12. Optical Remote Sounding of Aerosol Formations on the Base of Numerical Simulation of the Scattering Radiation 19
Belyaev, B.I., L.V. Katkovsky, V.P. Kabashnikov and V.P. Nekrasov

13. Investigation of the Anisotropy of the Atmospheric Turbulence Spectrum in the Low Frequency Range 22
Lukin, V.

14. Benguela Upwelling System: Satellite and Shipborne Data Analysis NA
Kazmin, A.S.

INTERACTIVE AREA 1 -- SAR Processing and Applications

15. A Simulation-Based Validation of Some Improvements in Automatic Stereo-Radargrammetry 25
Nocera, L., S. Dupont and M. Berthod

16. Detection and Localization of Lost Objects by SAR Technique 28
Dionisio, C.

NA -- Not available at time of printing.

17. REX -- An Automated Road Extraction Algorithm for SAR Imagery NA
Bergen, Z.D., D. Kaiser and R.E. Carande

18. Automated Matching Experiments With Different Kinds of SAR Imagery 31
Gelautz, M., G. Jakob, G. Paar, S. Hensley and F. Leberl

19. Detecting Man-Made Features in SAR Imagery 34
Carlotto, M.J.

20. Texture Analysis by Universal Multifractal Features in a Polarimetric SAR Image 37
Martinez, P., D. Schertzer and K. Pham

21. Reading CEOS-SAR Tapes: A New General Reader and a Proposed New Standard 40
Pierce, L.

22. RADARSAT Processing at ASF 43
Leung, K., M. Chen, J. Shimada and A. Chu

23. Radar Speckle: Noise or Information? 48
Xia, Z.G., and Y. Sheng

24. SAR and One-Bit Coding: New Ideas 51
Franceschetti, G., M. Tesauro and S. Wall

25. Preserving Exponentials in Synthetic Aperture Radar Data 54
Pepin, M.P., and J.J. Sacchini

26. Improved Multiple Look Technique 57
Yeo, T.S., W.L. Lay, Y.H. Lu, W.E. Ng, I. Lim and C.B. Zhang

27. Partially Correlated K-Distribution for Multi-Look Polarimetric SAR Imagery 60
Yu, Y., A. Torre and S. Huan

28. Speckle Reduction and Enhancement of SAR Images in the Wavelet Domain 63
Sveinsson, J.R., and J.A. Benediktsson

29. Adaptive Filtering Algorithms for SAR Speckle Reduction 67
Lu, Y.H., S.Y. Tan, T.S. Yeo, W.E. Ng, I. Lim and C.B. Zhang,

INTERACTIVE AREA 2 -- Marine/Ocean

1. Multispectral and Multisatellite Data for Investigation of Black Sea Upper Layer Processes NA
Stanichny, S.V., and D.M. Solov'ev

2. A Software Package for the Quality Assessment of the Low Bit Rate Mediterranean Scatterometer and Altimeter Products:ERS-1.WSC.DWP and ERS-1.ALT.MPR NA
Bartoloni, A., C. Celani, C. D'Amelio, G. Milillo and R. Viggian

3. Estimation of Adjacent Effects Over the Coastal Zone by Polarization Measurements NA
Kusaka, T., S. Sado and Y. Kawata

4. An Eolian and Marine Phenomena Characterization in Dune Sectors by Image Processing 70
Delignon, Y., L. Moreau and P. Clabau

5. Retrieval of Arctic Surface Conditions and Cloud Properties from AVHRR Data: A Time Series for the Beaufort Sea 73
Meier, W., J. Maslanik, J. Key and C. Fowler

6. Sensitivity Study of the Aerosol Size Parameter Derived from AVHRR's Channels 1 and 2 Over Oceans NA
Ignatov, A.

7. Evaluation of Remote Sensing Algorithms for the Retrieval of Optically-Active Components in Turbid Natural Waters 76
Kutser, T., A. Blanco and H. Arst

8. Comparison of Sea Traffics in Tokyo and Osaka Bays With JERS-1/OPS Data 79
Takasaki, K., T. Sugimura and S. Tanaka

9. NASA Scatterometer Near-Real-Time, Value Added Products for Meso/Synoptic-Scale Marine Forecasting 82
Spencer, M.W.

10. Wavelet Analysis of AVHRR Images for Feature Tracking 85
Liu, A.K., W.Y. Tseng and S.Y.S. Chang

11. Flourescence as a Potential Indicator of Coral Health 88
Holden, H., D. Peddle and E. LeDrew

12. Satellite Synthetic Aperture Radar, CODAR, and In Situ Measurements of Oceanic Features in Monterey Bay NA
Fernandez, D.M.

13. Variability of Rossby Wave Propagation in the North Atlantic from TOPEX/POSEIDON Altimetry 91
Cipollini, P., D. Cromwell and G.D. Quartly

14. Chlorophyll Retrieval from CZCS: Influence of Atmospheric Aerosols 94
Moldenhauer, O., M.L. Steyn-Ross and D.A. Steyn-Ross

15. A Global Sea Level Variability Study From Almost a Decade of Altimetry 97
Naeije, M.C., and R. Scharroo

16. Variability and Frontogenesis in the Large-Scale Oceanic Frontal Zones Derived from the Global Satellite Measurements NA
Kazmin, A.S.

17. Vertical Distribution of PAR and Diffuse Attenuation Coefficient Modeling and In Situ Measurements 100
Volynsky, V.A., A.I. Sud'bin and J. Marra

18. Determination of Optical Properties of Ocean Upper Layers by Reflectance Spectra Measurements NA
Parishikov, S.V., M.E. Lee and O.V. Martynov

19. Oil Spills Detection in the Sea Using ALMAZ-1 SAR NA
Ivanov, A.Yu., V.V. Zaitsev, O.V. Ivlev and V.Yu. Raizer

20. Detection of Convective Instability in Atmospheric Boundary Layer Over the Ocean by Airborne Ku- Band Real Aperture Radar 103
Mityagina, M.I., Y.A. Kravtsov, V.G. Pungin, K.D. Sabinin and V.V. Yakovlev

21. Analyzing the Discharge Regime of a Large Tropical River Through Remote Sensing, Ground-Based Climatic Data, and Modeling 106
Schloss, A.L., C.L. Vorosmarty, C.J. Willmott and B.J. Choudhury

INTERACTIVE AREA 3 -- Sea Ice

1. Using Temporal Information in an Automated Classification of Summer, Marginal Ice Zone Imagery 109
Haverkamp, D., and C. Tsatsoulis

2. Texture Representation of SAR Sea Ice Imagery Using Multi-Displacement Co-Occurrence Matrices 112
Soh, L.K., and C. Tsatsoulis

3. Phase Correction for Coherent Noise Reduction in Short-Range Radar Measurements 115
Beaven, S.G., S.P. Gogineni and P. Kanagaratnam

4. In-Situ Measurement of the Complex Dielectric Constant of Sea Ice From 1 to 10 GHz 118
Nassar, E., R. Lee, K. Jezek and J. Young

5. Nearshore Ice Surface Roughness Surveys on Lake Superior 121
Pilant, D.

6. Error Characteristics of the SIRF Resolution Enhancement Algorithm 124
Early, D.S., and D.G. Long

7. The Quantification of Sea Ice Melt Features from Low Level Aerial Photographs 127
Derksen, C.P., J.M. Piwowar and E.F. LeDrew

8. Electromagnetic Waves Scattering From Sea Ice with Inhomogeneous Dielectric Permittivity Profile NA
Timchenko, A.I., and A.O. Perov

9. Investigation of the Fast Troposphere Parameters Variations by Using Method of the Radioacoustic Sounding NA
Rapoport, V.O., N.I. Belova, V.V. Chugurin, Y.G. Fedoseev, Y.A. Sazonov and V.A. Zinichev

10. Applications of the Remote Sensing for Experimental Study of the Boundary Layer's Dynamics in the Coastal Zone of the Black Sea NA
Kontar, E.A., A.I. Ginzburg and M.M. Domanov

11. Modelling Inter-Annual Snow Variability in Eastern Canada NA
Lewis, J.E., and L. Lee

12. Mapping Snow Properties for Spatially Distributed Snow Hydrological Modeling in Mountainous Areas Using Passive Microwave Remote Sensing Data 130
Wilson, L.L., L. Tsang and J.N. Hwang

13. Snow Classification from SSM/I Data over Varied Terrain Using an Artificial Neural Network Classifier 133
Sun, C., C.M.U. Neale, J.J. McDonnell and H.D. Cheng

14. Snow Mapping with SIR-C Mulpolarization SAR in Tienshan Mountain 136
Li, Z., and J. Shi

15. Recent Progress in Development of the Moderate Resolution Imaging Spectroradiometer Snow Cover Algorithm and Project 139
Riggs, G., D.K. Hall and V.V. Salomonson

16. Relation Between Radiative and Microphysical Properties of Snow: New Efficient Approach NA
Zege, E.P., and A.A. Kokhanovsky

17. Variations in Radar Backscatter Across the Great Ice Sheets 142
Noltimier, K.F., and K.C. Jezek

18. Geophysical Data Management System 145
Baggeroer, P.A., K.C. Jezek and D.G. Hart

19. Ice Sheet Margin Detection Using ERS-1 Synthetic Aperture Radar 148
Sohn, H.G., and K.C. Jezek

INTERACTIVE AREA 3 -- Soil

20. Microwave Effective Permittivity Model of Frozen Soil and Applications to Passive Remote Sensing NA
Tikhonov, V.V.

21. Flood Monitoring in Norway Using ERS-1 SAR Images 151
Weydahl, D.J.

22. Relating Microwave Satellite Radiometer Observations to Land Surface Parameters: A Physical Approach 154
Karam, M.A., and A. Stogryn

23. Analysis of ERS-1 SAR Data to Study Soil Moisture Content in Rocky Soils 157
Sano, E.E., A.R. Huete, D. Troufleau, M.S. Moran and A. Vidal

24. Determining Water Stress in Potato Fields Using Infrared Thermometry NA
Peterson, J.R., J.M. Giarrusso and M.C. MacDonald

25. An Automated Overland Flow Model Based Upon Remote Sensing and GIS 160
Leu, C.H.

26. Analysis for Soil Moisture and Land Cover Studies ERS-1 and JERS-1 SAR Data 163
Rao, Y.S., P.V.N. Rao, L. Venkataratnam and K.S. Rao

27. Spatio-Temporal Dynamics of Soil Moisture in Tallgrass Prairie Using ERS-1 SAR Image Time Series: First Year Results 166
Henebry, G.M., and A.K. Knapp

28. Mapping Methane Emission from Arctic Tundra Using Satellite Data, a Digital Elevation Model, and Discriminant Functions Based on Field Data 169
Shippert, M.M.

INTERACTIVE AREA 4 -- Crustal Movements/Vegetation

1. Neogene-Quaternary Kinematics of the Northern Mediterranean Microplates NA
Yutsis, V.V., and V.N. Vadkovsky

2. Water Content Influence on Scattering Properties of Vegetation Cover 172
Roenko, A.N., Yu.F. Vasilyev, B.D. Zamaraev and V.L. Kostina

3. Experimental Study of Fire Risk by Means of Passive Microwave and Infrared Remote Sensing Methods 175
Liberman, B., A. Grankov, A. Milshin, S. Golovachev and V. Vishniakov

4. Investigation and Cataloguezation of Backscattering Characteristics of Different Earth Covers in Millimeter Wave Band 178
Vasilyev, Yu.F., B.D. Zamaraev, V.L. Kostina and A.N. Roenko

5. Classification Using Multi-Source Data Using and Predictive Ability Measure 180
Chong, C.C., and J.C. Jia

6. Center Pivot Irrigation System Analysis Using Airborne Remotely Sensed Imagery: A Commercial Remote Sensing Case Study 183
MacDonald, M.C.

7. The Sensitivity of a Land Surface Parameterization Scheme to the Choice of Remotely-Sensed Landcover Data Sets 186
Oleson, K.W., K.L. Driese, J.A. Maslanik, W.J. Emery and W.A. Reiners

8. Using the Wavelet Method for a Multispectral Remote Sensing Study of Plant Community Spatial Processes in Broad Range of Spatial Scales 189
Mikheev, P.V., S.S. Kheeroug, G.Y. Yakin and J. S. Todhunter

9. A Multi-Parameter Land Data Set for Regional Modeling 192
Thames, P., J. Maslanik, K. Oleson and W. Emery

10. Coincident Diurnal and Spatial Variations in Dielectric Constant Properties as Measured Along a Vertical Gradient in Stems of Norway Spruce NA
McDonald, K., R. Zimmermann and E.D. Schulze

11. Spatio-Temporal Land Cover Dynamics in the Pantanal Assessed Using Lacunarity Analysis on an ERS-1 SAR Image Time Series 195
Henebry, G.M., and H.J.H. Kux

12. Accuracy Analysis and Validation of Global 1 Km Land Cover Data Sets 198
Scepan, J., J.E. Estes and W.J. Starmer

13. Potential of SIR-C Data to Study Vegetation Over Gujarat Test Site, India 201
Rao, K.S., Y.S. Rao, L. Venkataratnam and P.V.N. Rao

14. Intercomparison of Several BRDF Models for the Compositing of Spaceborne POLDER Data over Land Surfaces 204
Hautecoeur, O. and M. Leroy

15. Monitoring Arid and Semi-Arid Regions with ERS-1 Wind Scatterometer Data NA
Frison, P.L. and E. Mougin

16. Estimation of Seasonal Dynamics of Pasture and Crop Productivity in Kazakhstan Using NOAA/AVHRR Data 209
Gitelson, A., F. Kogan, E. Zakarin and L. Lebed

17. The Reflectance of Pleurozium Schreberi as a Function of Water Status and Its Implications on Understory Reflectance Variations for BOREAS Sites 212
Fernandes, R., H.P. White, D.R. Peddle, J.R. Miller and L.E. Band

18. Mapping Species Rich Boreal Wetlands Using Compact Airborne Spectrographic Imager (CASI) NA
Jelinski, D.E., J.R. Miller, R. Steinauer, S. Narumalani and J. Freemantle

19. Seasonal NDVI Trajectories to Response to Disturbance: Toward a Spectral-Temporal Mixing Model for Tallgrass Prairie 215
Goodin, D.G., and G.M. Henebry

20. Analysis of the Canadian Boreal Forest Using Enhanced Resolution ERS-1 Scatterometer Imagery 218
Wilson, C.J., III, and D.G. Long

21. Comparison of Interferomertic SAR and Radar Profiling in Forest Mapping NA
Axelsson, S.R.J.

22. Land Cover Change Dynamics of a Himalayan Watershed Utilizing Indian Remote Sensing Satellite (IRS) Data 221
Krishna, A.P.

23. Classification of Cover Types in the Lower Delta of the Parana River Using a Multitemporal Approach NA
Karszenbaum, H., P. Kandus, L.A. Frulla and D.A. Gagliardini

24. Remote Sensing of Crop Responses to Ozone and Carbon Dioxide Treatments 224
Leblanc, E., C.S.T. Daughtry and C.L. Mulchi

25. Radar Profiling for Forest Inventory NA
Axelsson, S.R.J., M. Eriksson and S. Hallidin

26. Examination of Multi-Temporal ERS-1 Radar over the Rainwater Basin 227
Keithley, C., and M. Roberts

27. Application of Remote Sensing Measurements for Research an dService of Agriculture in Bulgaria NA
Kazandjiev, V.

28. A Comparison of NDVI and Spectral Mixture Analysis for Estimating Biophysical Properties in Boreal Forest Terrain 230
Peddle, D.R., F.G. Hall and E.F. LeDrew

29. Global Landcover Classification Training and Validation Issues and Requirements 233
Muchoney, D., J. Borak and A. Strahler

30. An Automatic Road Extraction Method Using a Map-Guided Approach Combined with Neural Networks for Cartographic Database Validation Purposes 236
Fiset, R., F. Cavayas, M.C. Mouchot, B. Solaiman and R. Desjardins

31. Plant Condition Remote Monitoring Technique 239
Fotedar, L.K., and K. Krishen

INTERACTIVE AREA 4 -- Geophysical Modelling

32. Feature Selection Using Decision Trees -- An Application for the MODIS Land Cover Algorithm 243
Borak, J.S., and A.H. Strahler

33. Regional Land Cover Characterization Using Multiple Sources of Intermediate-Scale Data 246
Vogelmann, J.E., S. Howard and T. Sohl

34. Multisensor Studies Using Landsat TM, SPOT and ERS-1 in Monitoring of Vegetation Damage in Nikel (Russia) and Varanger (Norway) NA
Lauknes, I. and H. Tommervik

35. Calibration and Classification of SIR-C SAR Data in Moderate Slope Areas 248
Holecz, F., T.R. Michel and M. Keller

36. A New Quick-Look Optical SAR Processor with Digital Input/Output 251
Litovechenko, K., P. Lemaire and C. Barbier

37. The Modeling of Forested Areas for Real and Synthetic Aperture Imaging Radar Simulation 254
Stuopis, P.A., J.M. Henson, R.E. Davis and K. Hall

38. Use of Geometrical SAR Simulation for Visibility Prediction: Application to Mission Planning and Urban Study 257
Gouinaud, C., and I. Pons

39. Modelling of Microwave Backscatter Using a Tree-Growth Model for Boreal Forests Within the NOPEX Test Site 260
Woodhouse, I.H., and D.H. Hoekman

INTERACTIVE AREA 4 *continued* -- Geophysical Modelling

40. Modeling Wetland Vegetation Using Polarimetric SAR 263
Slatton, K.C., M.M Crawford, J.C. Gibeaut and R.O. Gutierrez

41. Rain Pattern Detection by Means of Packet Wavelets 266
Marazzi, A., P. Gamba and R. Ranzi

INTERACTIVE AREA 5 -- Missions and Programs

1. The Development of the Seawinds Scatterometer Electronics Subsystem (SES) 269
Boller, B.D., R.D. Crowley, M.C. Smith and R.S. Roeder

2. Phase B and Breadboard Results for the TOPEX POSEIDON FOLLOW-ON Mission 273
Rey, L., N. Suinot, P. Oudart and G. Carayon

3. Science Data Collection with Polarimetric SAR 276
Dall, J., K. Woelders and S.N. Madsen

4. Spaceborne Rain Radar Mission and Instrument Analysis 279
Vincent, N., J. Chenebault, N. Suinot and P.L. Mancini

5. SIR-C/X-SAR Campaign on Ruegan Island, Germany - First Results 282
Prietzsch, C., and A. Bachem

6. The Indian Remote Sensing (IRS) Mission NA
Yang, J.

INTERACTIVE AREA 5 -- Electromagnetic Problems

7. Phase Fluctuations for Waves of Different Spatial Frequencies and Their Use in Determination of Inhomogeneous Dielectric Permittivity Profile NA
Timchenko, A.I.

8. Volume Scattering Function of Light for a Mixture of Polydisperse Small Particles with Various Optical Properties 285
Haltrin, V.I., A.D.Weidemann and W.E. McBride III

9. Simulation of RAR Reflectivity Maps of the Sea Surface for Remote Sensing Applications 290
Corsini, G., G. Manara and A. Monorchio

10. A Simplified Hybrid Model for Radiation Under Discontinuous Canopies 293
Li, X., W. Ni, C. Woodcock and A. Strahler

11. Estimation of Some Characteristics of Ocean Waters Using Optical Data (Case I) 296
Volynsky, V.A., J. Marra and C. Knudson

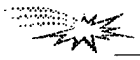
12. The Synthesis of Optimal Structure of Radar Using Polarization Adaptation 299
Loutin, E.A., A.I. Kozlov and A.I. Logvin

13. A Method and Algorithm of Computing Apparent Optical Properties of Coastal Sea Waters 305
Haltrin, V.I., and A.D. Weidemann

14. Scene Understanding from SAR Images 310
Datcu, M.

15. Microwave Specific Attenuation by Lossy Raindrops of Spheroidal Shapes: An Exact Formulation NA
Li, L.W., T.S. Yeo, P.S. Kooi and M.S. Leong

16. Theoretical Research on New Concepts for the Remote Sensing of Hydrometeors 315
Martin-Neira, M., J. Bara, A. Capms, F. Torres, I. Corbella and O. Gasparini



INTERACTIVE AREA 6 -- Educational Initiatives

1. Helping Students and Teachers Make Sense of Remote Sensing Via the Internet NA
Croft, S.K., and R.J. Myers

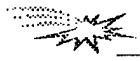
2 "Winds of Change" A Multi-Media Tool to Aid Teachers in Teaching Global Climate 321
Yanow, G., A. Sohus and B. Payne

3 From Surfer to Scientist: Designing a Canadian Remote Sensing Service for the Internet Audience 324
Langham, C.W., A.M. Botman and T.T. Alfoldi

4 Earth System Science Education Using Remote Imagery and Environmental Data Access NA
Fortner, R.W.

5 Using Weather Satellite Images in the Classroom of the Future NA
Keck, C.L.

6 The Use of Technology Driven Investigations in Geoscience and Remote Sensing Education: Findings from an Evaluation of the JASON Project NA
Coan, S.M., and C.J. Moon



INTERACTIVE AREA 7 -- SAR Interferometry

1. Linear Structures in SAR Coherence Data 330
Hellwich, O., and C. Streck

2. Detection and Velocity Estimation of Moving Objects in a Sequence of Single-Look SAR Images 333
Kirscht, M.

3. A Discrete Minimization Approach to Phase Unwrapping NA
Bartoloni, A., C. D'Amelio, A., Mariani, G. Milillo and M. Mochi

4. Comparison of Multigrid and Wavelet Techniques for InSAR Phase Unwrapping NA
Datcu, M.

5. Comparative Analysis of Phase Unwrapping Methods Using Self-Affine (Fractal) Models 336
Valero, J.L., and I. Cumming

6. A Workstation for Spaceborne Interferometric SAR Data 339
van der Kooij, M.W.A., B. Armour, J. Ehrismann, H. Schwichow and S. Sato

7. A Comparison of Phase to Height Conversion Methods for SAR Interferometry 342
Small, D., P. Pasquali and S. Fuglistaler

INTERACTIVE AREA 7 *continued* -- SAR Interferometry

8. Along-Track SAR Interferometry for Motion Compensation NA
Pasquali, P., B. Fritsch and D. Nuesch

9. SAR Interferometry: A Multigrid Markovian Approach for Phase Unwrapping with a Discontinuity Model 345
Labrousse, D., S. Dupont and M. Berthod

10. Echoes Covariance Modelling for SAR Along-Track Interferometry 347
Lombardo, P.

11. On the Survey of Volcanic Sites: The SIR-C/X-SAR Interferometry 350
Coltelli, M., G. Fornaro, G. Franceschetti, R. Lanari, M. Migliaccio, J.R. Moreira, K.P. Papathanassiou, G. Puglisi, D. Riccio and M. Schwabisch

12. DEM Generation by Repeat-Pass SAR Interferometry NA
Herland, E.A.

INTERACTIVE AREA 8 -- Techniques and Instrumentation

1. Atmospheric Induced Errors on Interferometric DEM Generation 353
Kenyi, L.W., and H. Raggam

2. Wavelet Projection Pursuit for Feature Extraction and Cloud Detection in AVIRIS 356
Bachmann, C.M., E.E. Clothiaux and D.Q. Luong

3. Atmospherical Correction of Satellite and Aircraft Spectral Image Without Calibration NA
Zege, E.P., I.L. Katsev and A.S. Prikhach

4. Absolute in Flight Calibration of Airborne Multichannel MM-Wave Imaging Radiometer 360
Cherny, I.V., A.A. Pankin and S.Y. Pantzov

5. Analysis of Map Speckle Suppression Algorithm 363
Zaitsev, V.V., and V.V. Zaitsev

6. Space "MSU-E" and "MSU-SK" Scanner Images Using for Evaluation of Antropogenic Pollution of Snow Cover NA
Mironov, V.L., S.A. Komarov, A.V. Yevtyushkin, I.N. Dubina, V.N. Yushakov and T.V. Baikalova

7. Laboratory and In-Flight Spectrometer Calibration Technique in Visible and Near Infrared Spectral Ranges 366
Belyaev, B.I., L.V. Katkovsky and V.P. Nekrasov

8. An Attempt to Differentiate Specific Absorption Characteristics by Solving Inverse Problem NA
Volynsky, V.A.

9. Secondary Processing Algorithm for Two-Frequency Aircraft Radiomapping System NA
Ruzhentsev, N.V., Yu.A. Kuzmenko and V.P. Churilov

10. Duct Detection over the Sea by TRANSIT Measurements 369
Gaikovich, K.P., A.N. Bogaturov, A.S. Gurvich, S.S. Kashkarov, S.N. Krivonozhkin, B.M. Shevtcov, V.K. Ivanov and V.D. Freylikher

11. The Abilities of Radioacoustical Sounding Method for Atmosphere Processes Diagnostic NA
Rapoport, V.O. and V.V. Tamoikin

12. An Investigation of the Textural Characteristic for Geological Purposes 372
Pasaribu, D.P.

13. Estimating Microwave Observation Depth in Bare Soil Through Multi-Frequency Scatterometry NA
Troch, P.A., F. Vandersteene and Z. Su

14. Validation of ERS-1/SAR Data to Map the Rio Amazonas Floodplain According to the Cartographic Accuracy Standards 374
Kux, H.J.H., and V. Barbosa da Silva

15. Detail-Preserving Segmentation of Polarimetric SAR Imagery 377
Andreadis, A., G. Benelli and A. Garzelli

16. Detection and Analysis of Ship Waves in ERS-1 SAR Imagery 380
Peng, C.Y., A.K. Liu and S.Y.S. Cheng

17. ROME: The Rosetta Microwave Experiment for the Investigation of the Cometary Nucleus 383
Fedele, G., G. Picardi and R. Seu

18. On the Use of Whitening Filter and Optimal Intensity Summation to Produce Multi-Look SAR Images 387
Bruniquel, J., A. Lopes, J.G. Planes, F. Cazaban and M. Deschaux-Beaume

19. Channel Design of the ADEOS-II/GLI (Global Imager) 390
Nakajima, T.Y., T. Nakajima and M. Nakajima

20. Atmospheric Effects on CO2 Differential Absorption Lidar Performance 393
Petrin, R.R., D.H. Nelson, J.R. Quagliano, M.J. Schmitt, C.R. Quick, R.K. Sander, J.J. Tiee and M. Whitehead

21. Improved Feature Classification by Means of a Polarimetric IR Imaging Sensor 396
Sadjadi, F., and C. Chun

22. A Comparison of Scintillation Crosswind Methods 399
Poggio, L., M. Furger and W.K. Graber

23. A Multi-Frequency, Dual-Polarization, Microwave Link for Rainfall Estimation 402
Rincon, R.F., S.W. Bidwell, A.R. Jameson and O.W. Thiele

24. Radiometric Normalization of Landsat/TM Images in Multitemporal Classification Procedures NA
Frulla, L., J. Milovich and H. Karszenbaum

25. Cost-Effective Parallel Processing for Remote Sensing Applications 405
Kim, H.J., and H.S. Kim

26. Design of a Geographic Information System Using OPS5 408
Menon, A.K., P. Jayaprakash and P.V. Usha

27. Multiresolution De-Speckle Based on Laplacian Pyramids 411
Alparone, L., B. Aiazzi, S. Baronti and C. Susini

28. Classification and Feature Extraction with Enhanced Statistics 414
Benediktsson, J.A., K. Arnason, A. Hjartarson and D. Landgrebe

29. Modeling and Simulation of Real Aperture Radar Images NA
Menegasssi Menchik, M.T., and D. Fernandez

30. A Rain Profiling Algorithm for the TRMM Precipitation Radar NA
Iguchi, T., T. Kozu, R. Meneghini and K. Okamoto

31. Application of Radar Target Decomposition Technique for Flood Detection: Results from SIR-C Data NA
Hess, L.L., Y. Wang and J.M. Melack

32. Solar Irradiance Determination by Using ATSR-2 Data 417
Xue, Y., D.T. LLewellyn-Jones and S.P. Lawrence

33. Automatic Interaction Detector (Aid) Application on Image Classification NA
Ho, L.L. and J.A. Quintanilha

34. Comparison of Linear Least Squares Unmixing Methods and Gaussian Maximum Likelihood Classification 420
Fernandes, R., J. Miller and L.E. Band

35. Development and Test of a Raster Scanning Laser Altimeter for High Resolution Airborne Measurements of Topography 423
Rabine, D.L., J.L. Bufton and C.R. Vaugh

36. Optical Correction of Scene Fractions for Estimating Regional Scale Ocean Coral Abundance in Fiji 427
Peddle, D.R., E.P. LeDrew and H.M. Holden

37. Development of SAR Interferometry at I.I.T. Bombay, India 430
Sukhatme, J.S., V. Walavalkar, Y.S. Rao, G. Venkataraman, M.V. Khire and K.S. Rao

38. Improved Procedures for the Retrieval of Stratospheric Trace Gases from Spectra of a Ground-Based Millimeter Wave Radiometer 433
Kuntz, M.

39. A New 278 GHz Ground-Based Radiometer for Vertical Profile Sounding of C10 and 03 in the Upper Atmosphere 436
Hochschild, G., and R. Krupa

40. Polarimetric SAR Image Classification Based on Target Decomposition Theorem and Complex Wishart Distribution 439
Du, L.J., and J.S. Lee

41. Hydrometeors Investigation by Means of 3 Millimeter Coherent Radar 442
Kosov, A.S., V.D. Gromov, S.N. Maleev, S.S. Kiselev, D.P. Skulachev and I.A. Strukov

42. Vegetation Obscuration Effects on Mid-Infrared Laser Reflectance of Soil 445
Guenther, B.D., and R.M. Narayanan

43. Applying Principal Components Analysis to Image Time Series: Effects on Scene Segmentation and Spatial Structure 448
Henebry, G.M., and D.R. Rieck

44. D.A.T.E. -- Dip Algorithm Testing and Evaluating Workbench 451
Kerzner, M.G.

45. High Resolution VHF SAR Processing Using Synthetic Range Profiling 454
Lord, R.T., and M.R. Inggs

46. A Region-based Approach to the Estimation of Local Statistics in Adaptive Speckle Filters 457
Fjortoft, R., F. Lebon, F. Sery, A. Lopes, P. Marthon and E. Cubero-Castan

47. A Precision Processor for Radarsat NA
Hughes, W., I. Arnon, K.A. Gault, D. MacGregor, L. Mikulin, L. Lightstone and J. Princz

48. Reversible Inter-Frame Compression of Multispectral Images Based on a Previous-Closest-Neighbor Prediction 460
Aiazzi, B., P.S. Alba, L. Alparone, S. Baronti and P. Guarnieri

49. Color Correction of HSI Transformed Images Using Color Space Transformation NA
Hosomura, T., and K. Katou

50. Lossless Compression of Multispectoral Images Using Permutations 463
Arnavut, Z., and S. Narumalani

51. Algoritms to Compute the Top-of-the-Atmosphere ALBEDO for Clear-Sky Conditions from Multi-Angle Data NA
Borel, C.C., and S. A.W. Gerstl

52. Parametric Representation of Atmospheric Disturbances NA
Mukherjee, D.P., P. Pal and J. Das

53. Radar Altimeter Return Noise Signals Identification 466
Maotang, L., J. Jingshan, W. Jingli and Y. Zhiqiang

54. Range and Angle Error Correction Measure for the Low Elevation Angle in Remote Sensing Data Analysis 469
Choi, J.

55. Potential and Use of Radar Images for Characterization and Detection of Urban Areas 474
Gouinaud, C., F. Tupin and H. Maitre

56. Phase Preservation in SAR Processing: The Interferometric Offset Test 477
Rosich Tell, B., and H. Laur

57. The Automation of Radar Operation and Calibration of NASA/JPL Airborne Multi-Frequency Polarimetric and Interferometric Synthetic Aperture Radar System NA
Lou, Y., and Y. Kim

58. Robust Restoration of Microwave Brightness Contrasts from the DMSP SSM/I Data 481
Petrenko, B.Z.

59. Advanced Airplane Version of the HUT 93 GHz Imaging Radiometer 484
Kemppinen, M., T. Auer, I. Mononen and M. Hallikainen

60. Ingara Dual Pass Cross Track Interferometry NA
Stacy, N.J.S., and G.G. Nash

61. A Low Range-Sidelobe Pulse Compression Technique for Spaceborne Rain Radar 487
Sato, K., H. Hanado and H. Kumagai

62. Pulse Compression With - 65 dB Sidelobe Level for a Spaceborne Meteorological Radar 490
Vincent, N., J. Richard, N. Suinot, M. Yarwood and C. Mavrocordatos

63. A SAR Antenna Calibration Method 493
Stevens, D., P. Bird and G. Keyte

64. Inflight Vertical Antenna Patterns for SIR-C from Amazon Rain-Forest Observation 496
Fang, Y., and R.K. Moore

65. A Contribution to Imaging Radiometer Sampling and Integration Period Determination 499
Kemppinen, M.

66. Radarclinometry for ERS-1 Data Mapping 503
Paquerault, S., H. Maitre and J.M. Nicolas

67. Millimeter-Wave Backscatter Measurements in Support of Surface Navigation Applications 506
Snuttjer, B.R.J., and R.M. Narayanan

68. A Novel Design of Return Signal Simulator for Radar Altimeters 509
Wu, J., and L. Lin

69. Polarimetric Calibration of Bistatic Radars Using Active Calibrators NA
Hevizi, L.G., and D.J. McLauglin

70. Calibration of Airborne Multiparameter Precipitation Radar with an Active Radar Calibrator 512
Hanado, H., H. Kumagai, T. Iguchi, T. Kozu, K. Nakamura and H. Horie

71. On the Accurate Calibration of the Sea Winds Radar Antenna: A Cylindrical Near-Field Measurement Approach 515
Hussein, Z.A., and Y. Rahmat-Samii

72. Detection of Pollutants in Liquids by Laser Induced Breakdown Spectroscopy Technique 520
Arca, G., A. Ciucci, V. Palleschi, S. Rastelli and E. Tognoni

73. Review of Vicarious Calibration of the Visible and Near-Infrared Channels of the Advanced Very High Resolution Radiometer NA
Rao, C.R.N., and J. Chen

74. Contextual Dynamic Neural Networks Learning in Multispectral Images Classifications 523
Solaiman, B., M.C. Mouchot and A. Hillion

TPAM -- Land Cover Mapping: Models and Applications

1. The Use of AVHRR Data for Creation of a New Global Land Cover Product for IGBP/DIS — NA
Belward, A., and T.R. Loveland

2. From Leaf to Scene: A Scaling Problems in Remote Sensing of Vegetation — 526
Goel, N.S., and W. Qin

3. Global Land Cover Classes Compatible with Radiative Transer Theory — NA
Nemani, R., S. Running and R. Myneni

4. ART Neural Networks for Remote Sensing: Vegetation Classification from Landsat TM and Terrain Data — 529
Carpenter, G.A., M.N. Gjaja, S. Gopal and C.E. Woodcock

5. New Approaches to Classification in Remote Sensing Using Hybrid Decision Trees to Map Land Cover — 532
Brodley, C.E., M.A. Friedl and A.H. Strahler

6. Proportional Estimation of Land Cover Characteristics From Satellite Data — 535
DeFries, R., M. Hansen and J. Townshend

7. Fuzzy ARTMAP Classification of Global Land Cover From AVHRR Data Set — 538
Gopal, S., C.E. Woodcock and A.H. Strahler

8. Exploring the Interannual Variability of Vegetation Activity Using Multitemporal AVHRR NDVI Imagery — 541
Mora, F., and J.W. Merchant

9. Correction of Land-Cover Area Estimates from Low Spatial Resolution Remotely Sensed Data — 544
Moody, A.

10. Landsat Pathfinder Data Sets for Landscape Change Analysis — 547
Dwyer, J.L., K.L. Sayler and G.J. Zlystra

TPAA -- Radar Remote Sensing and Precipitation

1. Factors Affecting NEXRAD-Based Point Rainfall Rate Estimation in the Seattle Area — 551
Seliga, T.A., and C. Chen

2. Analysis of Dual-Wavelength Dual-Polarization Returns from Frozen Hydrometeors — 554
Meneghini, R., T. Iguchi and L. Liao

3. Polarimetric Method for Ice Water Content Determination — 557
Ryzhkov, A.V., and D.S. Zrnic

4. Simulation of Dual-Polarization Bistatic Scattering from Rain and Hail — 560
Aydin, K., and S.H. Park

5. Computational Study of Millimeter Wave Scattering form Bullet Rosette Type Ice Crystals — 563
Aydin, K., and T.M. Walsh

6. Multiparameter Radar Snowfall Estimation Using Neural Network Techniques — 566
Xiao, R., and V. Chandrasekar

TPAA *continued* -- Radar Remote Sensing and Precipitation

7. Probing Electric Fields Near Sprites and Jets Using Multiparameter Radar and Chaff 569
Seliga, T.A., J.D. Sahr and R. H. Holzworth

8. Weather Radars with Pulse Compression Using Complementary Codes: Simulation and Evaluation 574
Mudukutore, A., V. Chandrasekar and R.J. Keeler

TPCP -- Remote Sensing: Boreal Ecosystems

1. Mapping of Boreal Forest Biomass Using SAR 577
Ranson, K.J., G. Sun, B. Montgomery and R.H. Lang

2. Carbon Dynamics in Northern Forests Using SIR-C/X-SAR Imagery 580
Bergen, K.M., M.C. Dobson and L.E. Pierce

3. Winter and Spring Thaw as Observed with Imaging Radar at BOREAS NA
Way, J.B., R. Zimmermann, K. McDonald and E. Rignot

4. Land Applications of ERS-1 Wind Scatterometer in Boreal Forest Zone 583
Pullianinen, J., N. Walker, T. Manninen, M. Hallikainen and J. Grandell

5. Monitoring Boreal Ecosystems in Siberia with the ERS-1 Windscatterometer NA
Schmullius, C., V. Wismann and K. Boehnke

6. Changes in Water Flux, Xylem Sap Composition, and Dielectric Constant Along a Vertical Gradient in Stems of Norway Spruce NA
Zimmermann, R., K. McDonald and E.D. Schulze

7. Spatial and Temporal Variability of Surface Cover at BOREAS Using Reflectances from a Helicopter Platform 586
Loechel, S.E., C.L. Walthall, E. Brown de Coulston, J.M. Chen and B.L. Markham

8. Use of Compact Airborne Spectrographic Imager (CASI) Data and Separability Measures for Classifying Complex Wetland Vegetation NA
Shepherd, P.R., D.E. Jelinski and J.R. Miller

9. Modeling Solar Radiation Transmission in Boreal Conifer Forests 591
Ni, W., X. Li, C.E. Woodcock, R.J. Roujean, R. Davis and A. Strahler

10. The Impacts of Environmental Conditions on Microwave Radiometry of Vegetation: A Physical Approach 594
Karam, M.A.

TPED -- Remote Sensing Applications of Sea Surface Modelling

1. Optimization of a Composite Surface Model for the Radar Backscattering Cross Section of the Ocean Surface as Measured by Wind Scatterometers 597
Romeiser, R.

2. A Physically-Based Two-Scale Electomagnetic Model for Backscatter From Ocean-Like Surfaces 600
Elfouhaily, T., and B. Chapron

3. An Application of the Two-Scale Model from the Point of View of the Small Slope Approximation to Radar Observations from the Ocean 603
Skirta, E.A., and A.N. Keane

4. A Comparison of Wind Wave Spectra Used in Ocean Remote Sensing Modeling 606
Elfouhaily, T., and B. Chapron

5. Evolution of Surface Waves of Finite Amlitude in Field of Inhomogeneous Current 609
Bakhanov, V.V., O.N. Kemarskaya, V.P. Pozdnyakova, J.A. Okomel'kova and I.A. Shereshevsky

6. Study of the Second Order Approximation of the Velocity Bunching in SAR Imaging Process Using the Bispectrum 612
Le Caillec, J.M., R. Garello and B. Chapron

7. Bistatic Sea Clutter: Simulations and Measurements 615
Khenchaf, A., F. Daout, Y. Hurtaud and J. Saillard

8. Verification of Microwave Scattering Mechanisms Using Optical Polarimetric Imagery 618
Barter, J.D., and P.H.Y. Lee

9. Fetch and Wind Speed Dependence of SAR Azimuth Cutoff and Higher Order Statistics in a Mistral Wind Case 621
Kerbaol, V., B. Chapron, T. Elfouhaily and R. Garello

10. Combined Radar and Cross-Polarizational Radiometer System for Detection and Identification of Some Anomalous Formations Originated on Sea Surface Due to Changes of Long and Short Waves Characteristics 625
Arakelian, A.K., and A.K. Hambaryan

TPES -- Youth Enhancing Space: KidSat

1. KidSat: Youth Enhancing Space 628
Choi, M.Y, G. Nagatani, J.B. Way and E.J. Stork

2. The Education Element of the KidSat/Youth Enhancing Space Project 631
McGuire, J., B. Fisher, R. Kassebaum, D. Barstow, K. Rackley, P. Bixler, M.A. Jones and J. Hunt

3. The Space Element of the Youth Enhancing Space Project NA
Lane, J., A. Leach, S. Davis, A. Ramirez and J. Baker

4. Mission Operations in the Classroom NA
Rackley, K., P. Bixler and H. Haugen

5. Youth Enhancing Space: Data System Element NA
Kirchner, C., M. Minino, R. Kassebaum, J. Lawson and P. Andres

6. Exploration Results from Charleston NA
Cowen, R., K. Rackley and the Fifth Grade Students of Buist Academy

7. Exploration Results from San Diego NA
Austin, A., S. Akpa, R. Anderson, P. Bixler and R. Ebel

8. Exploration Results from Pasadena NA
Brammer, C., M.A. Jones and the Fifth Grade Students of Washington Accelerated

TPF -- Remote Sensing for the Arctic Climate System

1. Future Opportunities and Issues in Radar Remote Sensing of Earth's High Latitudes 634
Carsey, F., and C. Wales

2. Satellite Remote Sensing of Atmosphere and Ice over the Arctic Ocean: A Perspective NA
Rothrock, D.A.

3. Expected Errors in Satellite-derived Estimates of the High Latitude Surface Radiation Budget 636
Key, J.R., R.S. Stone and A.J. Schweiger

4. Multitemporal Analysis of Fast Sea Ice Albedo Using AVHRR Data 639
De Abreu, R.A., and E.F. LeDrew

5. Assessing Variability and Trends in Arctic Sea Ice Distribution Using the Satellite Data 642
Belchansky, G.I., I.N. Mordvintsev and D.C. Douglas

6. Image Time Series Analysis of Arctic Sea Ice 645
Piwowar, J.M., G.R.I. Wessel, and E.F. LeDrew

7. An Analysis of Odden Event Intra- and Inter-Annual Variability 648
Fischer, K.W., C.A. Russel, R.A. Shuchman and E.G. Josberger

8. Remote Sensing Data Availability from the Earth Observation System (EOS) via the Distributed Active Archive Center (DAAC) at NSIDC 651
Weaver, R.L., and V.J. Troisi

9. CIDAS Climatological Ice Data Archiving System NA
Chagnon, R.

10. The Radarsat Geophysical Processor System NA
Rothrock, D., H. Stern, and R. Kwok

TPP -- SAR Interferometry: Processing Algorithms and Systems

1. Algorithms for Calculation of Digital Surface Models from the Unwrapped Intereferometric Phase 656
Goblirsch, W., and P. Pasquali

2. Elevation Correction and Building Extraction from Interferometric SAR Imagery 659
Burkhart, G.R., Z. Bergen, R. Carande, W. Hensley, D. Bickel and J.R. Fellerhoff

3. Unbiased Estimation of the Coherence from Multi-Look SAR Data 662
Touzi, R., A. Lopes, J. Bruniquel and P. Vachon

4. Automated Rapid Mapping with Interferometric Synthetic Aperture Radar Data 665
Ngai, F.M., and R.E. Carande

5. Ultra-Wideband and Low-Frequency SAR Interferometry 668
Ulander, L.M.H., and P.O. Frolind

6. Medium Resolution Efficient Phase Preserving Focusing for Interferometery 671
Gatelli, F., A. Monti Guarnieri, C. Prati and F. Rocca

7. EMISAR Single Pass Topographic SAR Interferometer Modes 674
Madsen, S.N., N. Skou, K. Woelders and J. Granholm

8. Parametric Estimation of Time Varying Baselines in Airborne Interferometric SAR 677
Mohr, J.J., and S.N. Madsen

9. On the Baseline Decorrelation 680
Franceschetti, G., A. Iodice, M. Migliaccio and D. Riccio

TPT -- Daytime Operation of Lidar Systems

1. Micro Pulse Lidar Daytime Performance: Simulations and Observations 683
Reagan, J.A., A.E. Galbraith and J.D. Spinhirne

2. Daytime Raman Lidar Measurements of Atmospheric Water Vapor NA
Whiteman, D., S.H. Melfi, G. Schwemmer, R. Ferrare and K. Evans

3. Lidar Studies of the Atmosphere NA
Carswell, A.I.

4. Daytime Temperature Measurements with a Sodium-Vapor Dispersive Faraday Filter in Lidar Receiver NA
Chen, H., M.A. White, D.A. Krueger and C.Y. Che

5. Rayleigh Lidar Observations During Arctic Summer Conditions 686
Thayer, J.P., N.B. Nielsen, R.B. Kerr and J. Noto

6. Daytime Tropospheric Water Vapor Profile Measurements by Raman Lidar 691
Bisson, S.E., and J.E.M. Goldsmith

7. A Differential Absorption Lidar System for Day and Night Measurements of Tropospheric Ozone NA
Langford, A.O., amd M.H. Proffitt

8. Spatial Properties of the Atmospheric Boundary Layer as Observed by Lidar NA
Cooper, D.I., and W. Eichinger

9. High Spectral Resolution, Low-Coherence Technique for Daytime Doppler Wind Measurements with Lidar 694
Fischer, K.W.

10. Field Calibration and Sensitivity Analysis of Coherent Infrared Differential Absorption Lidars 697
Richter, P.I., I. Peczeli, S. Borocz, L. Gazdag, J. Leonelli and T. Dolash

TPV -- Image Segmentation

1. Task-Specific Segmentation of Remote Sensing Images 700
Xuan, J., and T. Adah

2. Hybrid Image Segmentation for Earth Remote Sensing Data Analysis 703
Tilton, J.C.

3. Unsupervised Statistical Segmentation of Multispectral SAR Image Using Generalized Mixture Estimation 706
Marzouki, A., Y. Delignon and W. Pieczynski

4. Segmentation of SAR Images by Means of Gabor Filters Working at Different Spatial Resolution 709
Baraldi, A., and F. Parmiggiani

5. Markov Random Field Based Image Segmentation with Adaptive Neighborhoods to the Detection of Fine Structures in SAR Data 714
Smits, P.C., S. Dellepiane and S.B. Serpico

TPV *continued* -- Image Segmentation

6. Unsupervised Multiresolution Segmentation of Textured Image and Its Interpretation Using Fully Polarimetric SAR Data — NA
Liu, G., S. Huang and A. Torre

7. SAR Image Segementation by Mathematical Morphology and Texture Analysis — 717
Ogor, B., V. Haese-Coat and J. Ronsin

TPZ -- Microwave Remote Sensing of Vegetation

1. Analysis of Polarimetric Radar Backscatter of Moss-Bedded Conifers in Boreal Forest — NA
Saatchi, S.S., and M. Moghaddam

2. Scattering from Cultural Grass Canopies: A Phase Coherent Model — 720
Stiles, J.M., and K. Sarabandi

3. Scattering from Cultural Grass Canopies: Measured and Modeled Data — 723
Stiles, J.M., K. Sarabandi and F.T. Ulaby

4. Forest Backscatter Modeling: Simulation Versus Discrete Random Media Approach — 726
Lang, R.H., and R. Landry

5. Wave Scattering and Scene Image of Trees Generated by Lindenmayer Systems — 728
Zhang, G., and L. Tsang

6. Extraction of Biomass from SAR Data: A Realistic Approach — NA
Amar, F., M.S. Dawson, A.K. Fung and M.T. Manry

7. Estimation of Moisture Content of Forest Canopy and Floor From SAR Data, Part I: Volume Scattering Case — 730
Moghaddam, M., and S. Saatchi

8. Estimation of Moisture Content of Forest Canopy from SAR Data — NA
Moghaddam, M., and S. Saatchi

9. Investigating Correlations Between Radar Data and Characteristics of Mangrove Forests — 733
Proisy, C., E. Mougin and F. Fromard

10. Monitoring Vegetation Features with Multi-Temporal SAR Data — 736
Amodeo, G., P. de Matthaeis, P. Ferrazzoli, S. Paloscia, P. Pampaloni, G. Schiavon, S. Sigismondi and D. Solimini

TEAM -- Microwave Sensor Calibration

1. RADARSAT Calibration Studies NA
Lukowski, T.I., R.K. Hawkins, C. Cloutier, L.D. Teany, J. Iisaka and T. Sakurai-Amano

2. Near-Field Effect of Extended Targets on Absolute Calibration of Microwave Sensors 739
Wu, J., and J. Jiang

3. Calibration of an Airborne W-Band Polarimeter Using Drizzle and a Trihedral Corner Reflector 743
Galloway, J., A. Pazmany and R. McIntosh

4. Calibration of Bistatic Polarimetric Scatterometers 746
Daout, F., A. Khenchaf and J. Saillard

5. Accurate Antenna Reflector Loss Measurements for Radiometer Calibration Budget 749
Skou, N.

TEF -- Volume Scattering I

1. Electromagnetic Scattering Based on Pair Distribution Functions Retrieved from Planar Snow Sections 754
Zurk, L.M., L. Tsang, J. Shi and R.E. Davis

2. Modeling of Electromagnetic Wave Scattering from Time-Varying Snowcover 757
Ding, K.H., Y.E. Yang, S.E. Shih, J.A. Kong and R.E. Davis

3. Pulsed Beam Scattering from a Layer of Discrete Random Medium: With Applications to Spaceborne Weather Radars 760
Kilic, O., and R.H. Lang

4. TM Wave Scattering by Multiple Two-Dimensional Scatterers Buried Under One-Dimensional Multi-Layered Media 763
Cui, T.J., and W. Wiesbeck

5. TE Wave Scattering by Multiple Two-Dimensional Scatterers Buried Under One-Dimensional Multi-Layered Media 766
Cui, T.J., and W. Wiesbeck

TEH -- Subsurface Sensing and Material Properties I

1. High Resolution Imaging Techniques in Step-Frequency Subsurface Radars NA
Martinez-Madrid, J.J., J.R. Casar Corredera and G. de Miguel-Vela

2. Numerical Simulation of Scattering from Objects Embedded in a Medium with Randomly Rough Boundary 772
Tjuatja, S., Z.J. Li, A.K. Fung and C. Terre

3. A High-Resolution Imaging of Small Objects for Subsurface Radar Data Processing 775
Sato, T., T. Wakayama, K. Takemura and I. Kimura

4. Ground-Penetrating Radar Antenna Modeling 778
Haung, Z., K. Demarest and R. Plumb

5. 3-D SAR Imaging of Targets Obscured by Dielectric Media NA
Fortuny, J., and A.J. Sieber

TEM -- Land Cover: Innovation Classification Methods I

1. A Hierarchial Fuzzy Clustering Algorithm Using Pyramid Linking Data and Land-Cover Classification Experiments 781
Naka, M., T. Miyazaki and Y. Iwata

2. Fractal Concept to the Classification of Crop and Forest Type in IRS Data 784
Jeyarani, K., and K. Jayaram Hebbar

3. A Comparison of Three Neural Network Classifiers for Remote Sensing Classification 787
Gopal, S., and M. Fischer

4. A Decision Tree Classifier Design for High-Dimensional Data with Limited Training Samples 790
Tadjudin, S., and D.A. Landgrebe

5. Classification Accuracy Improvement and Delineation of Mixed Pixels Using Hierarchical Image Classification 793
Ediriwickrema, D.J., and S. Khorram

TEP -- SAR Interferometry

1. High Resolution 3-D SAR via Multi-Baseline Interferometry 796
Homer, J., D. Longstaff and G. Callaghan

2. Interferometric Analysis of Multifrequency and Multipolarisation SAR Data 799
Papathanassiou, K.P., and J.R. Moreira

3. Fusing L, C, and X Band Interferometric Phase Images by Means of Kalman Filtering Techniques NA
Loffeld, O., R. Kraemer, A. Hein, L. Dutra, G. Fornaro, R. Lanari, M. Migliaccio, J.R. Moreira, K.P. Papathanassiou, D. Riccio and M. Schwabisch

4. Quality Assessment of InSAR-Derived DEMs Generated with ERS Tandem Data 802
Schwabisch, M., M. Matschke,W. Knopfle and A. Roth

5. Atmospheric Heterogeneity: Effects on Multi-Pass Space Borne SAR Interferometry NA
Rossi, M., H. Vadon and A. Arnaud

TES -- Ocean Winds and Waves I

1. Surface Winds in a Midlatitutde Storm Seen by Satellites and Numerical Models 805
Katsaros, K.B., S. Dickinson, A. Bentamy, Y. Quilfen, S.S. Atakturk and R.A. Brown

2. The Comparison Between Active and Passive Microwave Data for Geophysical Ocean Surface Parameters Retrieval NA
Givri, J.R., S.S. Souffez and K. Bourbigot

3. Microwave Backscatter from the Sea Surface at Grazing Incidence 808
Buckley, J.R., and R.S. Johnson

4. Doppler-Radar-Radiometer Method of Near Sea Surface Wind Speed, Long Waves Roughness Degree, Water and Air Temperatatures Determination 811
Arakelian, A.K., and A.K. Hambaryan

5. An Offset between Scatterometer Directional Anisotropy and Wind Direction across the Equatorial Pacific Ocean 814
Rufenach, C.L.

TET -- Educational Initiatives

1. The Role of Remote Sensing in Training Activity of Tuscany Region 817
Cuomo, S., D. Giuli and G. Federici

2. Development of a Remote Sensing Core Curriculum Submitted for the Sessions on Educational Initiatives in Geoscience and Remote Sensing 820
Estes, J.E., and T. Foresman

3. NASA/JPL's Imaging Radar Outreach Program 823
Freeman, A., E. O'Leary, B. Chapman and J. Trimble

4. What Kind of Images Do I Need? What Is the Delay to Obtain Them? NA
Houzelle, S., P. Bellemain, J. Amalric and P. Herry

5. Geoscience Field Trainings in Russian Universities NA
Yutsis, V.V., and V.T. Trofimov

WAAM -- Land Cover: Tropical Forests and Vegetation

1. Discrimination of Africa's Vegetation Using Reconstructed ERS-1 Imagery 827
Hardin, P.J., D.G. Long and Q.P. Remund

2. The JERS-1 Amazon Multi-Season Mapping Study (JAMMS) 830
Freeman, A., B. Chapman and M. Alves

3. Forest Classification by Means of Pattern Recognition Method Applied to Scatterometer Data 833
Dechambre, M., and M. Bourdeau

4. Use of Polarisation Synthesis for Deforestation Studies Based on SIR-C/XSAR Data Analysis 836
Soyris, J.C., T. Le Toan, N. Floury, L. Thomasson, C.C.Hsu and J.A. Kong

5. Can the ERS-1 Scatterometer Be Used to Forecast the Inundation Extent in the Pantanal Wetland? 839
Wismann, V.R., and K. Boehnke

6. Forest Mapping and Monitoring in French Guiana: From Deforestation Mapping to a GIS for a Future National Park NA
Vedel, S., and D. Girou

7. Use of ERS-1 SAR Data for Forest Monitoring in South Sumatra 842
Le Toan, T., F. Ribbes, T. Hahn, N. Floury and U.R. Wasrin

8. Tropical Forest Monitoring Using Data from the ERS-1 Wind Scatterometer 845
Woodhouse, I.H., and D.H. Hoekman

9. Mapping and Monitoring the Mangrove: First Regional Map of Mangrove Using Remote Sensing and Geographic Information Systems NA
Girou, D., S. Vedel and O. Laroussinie

10. A Comparison of Reconstructed Ku-Band Scatterometry, C-Band Scatteromentry, and SSM/I Imagery for Tropical Vegetation Classification 848
Hardin, P.J., D.G. Long, Q.P. Remund and D.R. Dawn

WAAA -- Sensors and Remote Methods for Detecting Environmental Contaminants

1. Advances in Fiber Optic Based Laser-Induced Flourescence Sensors for In Situ Measurement of Petroleum Hydrocarbons in Soils — NA
Lieberman, S.H., and D.S. Knowles

2. Determination of Contaminants in the Enviroment Using Instrumentation Based on Laser-Induced Breakdown Spectroscopy — NA
Cremers, D.A., and M.J. Ferris

3. Trace Detection of Environmental Contaminants by Laser Photogragmentation / Fragment Detection Spectrometry — 851
Sausa, R.C.

4. Detection of Environmental Contaminants by Time Resolved Laser Induced Breakdown Spectroscopy Technique — 854
Arca, G., A. Ciucci, V. Palleschi, S. Rastelli and E. Tognoni

5. Influences on Detectability of Heavy Metals in Soils by Laser-Induced Breakdown Spectroscopy — 857
Alexander, D.R., D.E. Poulain, M.S. Khlif and E.R. Cespedes

6. Development and Testing of Electrochemical Sensors for Rapid Detection of Explosive Contaminants in Soils — NA
Cespedes, E.R.

7. Commercialization of the Laser Spark Continuous Metal Emissions Montor — NA
French, N.B.

8. Measurements of the Radar Backscattering Over Different Oceanic Surface Films During the SIR-C/X-SAR Campaigns — 860
Gade, M., W. Alpers , M. Bao and H. Huehnerfuss

9. Airborne CASI Imaging Spectrometer Used in Monitoring of Vegetation Damage in the Pasvik Area — NA
Tommervik, H., I. Lauknes and B. Johansen

10. Preliminary Evaluation of a Millimeter-Wave System for Air Pollution Monitoring — 863
Nadimi, S.A., and J.W. Bredow

WACP -- Microwave Synthetic Aperture Interferometric Radiometry

1. Two-Dimensional Aperture Synthesis Radiometers in a Low Earth Orbit Mission and Instrument Analysis — 866
Kraft, U.R.

2. Integration of MIRAS Breadboard and Future Activities — 869
Martin-Neira, M. , J.M Goutoule, A. Knight, J. Claude, J. Bara, A. Camps, F. Torres, I. Corbella, A. Lannes, E. Anterrieu, V. Laursen and N. Skou

3. Design and Implementation of the MIRAS Digital Correlator — 872
Batz, O., U. Kraft,W. Lindemer and H. Reichel

4. Characteristics of the Baseline Off-Nadir Angle of Supersynthesis Radiometer — 875
Komiyama, K., and Y. Kato

5. Icestar: Next Major Advance in Sea Ice Remote Sensing — NA
Cavalieri, D.J., L.L. Thompson, D.M. Le Vine and J.A. Weinman

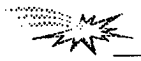
6. Calibration of Synthetic Aperture Radiometers in Space: Antenna Effects 878
Le Vine, D.M., and D.E. Weissman

7. RADSAR Synthetic Aperture Radiometer Test Results NA
Edelsohn, C.R.

8. Development of a 37GHz Synthetic Apeture Microwave Radiometer NA
Goodberlet, M.A., C.S. Ruf and C.T. Swift

9. Application of Sparse Phased Arrays to Millimeter-Wave Radiometry 881
Loveberg, J., S. Clark, D. Wilkner and B. Wallace

10. Radiometer System with Cross-Polarization and Correlation of the Channels of Observation 885
Arakelian, K.A., and A.K. Arakelian



WAED -- Remote Sensing of Littoral Submesoscale Processes I

1. Spatial Variations of Microwave Backscatter Magnitude and Angular Distribution: Response of the Short Waves to Wind and Surface Changes 888
Weissman, D.E., W.J. Plant, W.C. Keller and V. Hesany

2. Seagulls and SAR: Atmospheric Convection Effects in SAR Images over the Ocean 891
Vesecky, J.F., F.L. Ludwig, J.M. Daida, N. Chinchilla and G. Kimbreau

3. Evidence of a Land Breeze in an ERS-1 SAR Image of the New Jersey Coastline 893
Sikora, T.D., D.R. Thompson, G.S. Young and N.S. Winstead

4. Atmospheric Signatuares in SAR Imagery 896
Beal, R.C., D.R. Thompson, G.S. Young, H.N. Shire and T.D. Sikora

5. SAR Response to Spatially and Temporally Varying Wind Fields 899
Lyzenga, D.R.

6. Synthetic Aperture Radar Imagery of the Coastal Ocean Near Cape Hatteras, NC NA
Marmorino, G.O., D.R. Lyzenga, J.A.C. Kaiser and C.L. Trump

7. An End-To-End Simulation of Radar Signatures from the HI-RES 1 Rip Feature 902
Chubb, S.R., A.L. Cooper, R.W. Jansen and C.Y Shen

8. Low Grazing Angle Dual Polarized Doppler Radar Measurements of Oceanic Fronts 905
Allan, N., D.B. Trizna and D.J. McLaughlin

9. Effects of Wave Breaking on SAR Signatures Observed Near the Edge of the Gulf Stream 908
Lyzenga, D.R.

10. Issues Surrounding Surfactant Effects Upon Radar Imagery of Convergent Ocean Surface Flows with Application to the Hi-Res I Rip Feature 911
Cooper, A.L., S.R. Chubb and J.A.C. Kaiser

WAES -- Educational Initiatives I

1. Satellite Remote Sensing of the Environment: New Opportunities for the Educator NA
Winokur, R.S.

2. An Overview of Remote Sensing Education Projects Sponsored by the NASA Space Grant Program 914
Wersinger, J.M., and E. Ward

3. Mission to Planet Earth On-Line Earth Systems Science Course 917
Blurton, C., and S. McGee

4. Remote Sensing Data for Educational Purposes: The Policy of the European Space Agency and Its Achievements with the Meteosat Data NA
Le Ber, J.

5. Earth Observation Satellite Date and its Application to Environmental Education 920
Goto, A.

6. Applications of Satellite Imagery, Visualizations and Remote Sensing in Environmental/Science: An Earth Systems Science Approach 922
Moore, J.D.

7. Do We Really Understand What We See? Cognitive Issues in Remote-Sensing From the Perspective of a Scientist and an Educator 925
Barstow, D., and E. Frost

8. National Weather Service Portable Multimedia Presentations to Teachers and Students NA
Gird, R., and J. Von Ahn

9. Interdisciplinary Earth System Science and Earth Observations From the International Space Station: Partners in Education 929
Willis, K.J., D.L. Amsbury, C.D. McLaughlin and T. Miewald

10. Applied Environmental Problem-Solving Using Remote Sensing Technology: A Summer Practicum for Undergraduate Faculty NA
Panah, A.A.

WAF -- Sea Ice Remote Sensing (Models, Techniques and Applications) I

1. Global Sea Ice Monitoring from Microwave Satellites 932
Johannessen, O.M., M.W. Miles and E. Bjorgo

2. Sea Ice Identification Using Dual-Polarized Ku-Band Scatterometer Data 935
Yueh, S.H., R. Kowk, S.H. Lou and W.Y. Tsai

3. Temporal Mixture Analysis of SMMR Sea Ice Concentrations 938
Piwowar, J.M., D.R. Peddle and E.F. LeDrew

4. Polarimetric Backscattering at 23 cm Wavelength from Antarctic Lead Ice and Estimation of Ice Thickness 941
Winebrenner, D.P.

5. Characterization of Ice in the Chukchi Sea at the Start of the Growing Season Using Satellite SAR 944
Onstott, R.G.

6. Bistatic Microwave Investigations of Sea Ice-Like Media 947
May, G.C., J.W. Bredow, J. Juying, S.A. Nadimi and A.K. Fung

7. Validation of a Sea Ice Model Using Forward Simulation of ERS-1 SAR Data: A Case Study in the Beaufort Sea 950
Heinrichs, J., J. Maslanik and K. Steffen

8. The Influence of Cloud Cover on the Microwave Scattering Coefficient (σ°) of First-Year and Multiyear Sea Ice 953
Barber, D.G., and A. Thomas

9. Comparison of Aircraft and DMSP SSM/I Passive Microwave Measurements over the Bering Sea in April 1995 956
Cavalieri, D.J., D.K. Hall and J.R. Wang

10. Multi-Channel Algorithm Approach to Determining Melt for Arctic Sea Ice Using Passive Microwave Data 959
Anderson, M.R.

WAP -- SAR Interferometry and Geoscience Applications

1. Differential SAR Interferometry for Detection of Small Terrain Movements NA
Cavallo, A., D. Tarchi and A.J. Sieber

2. Satellite Radar Measurements of Land Subsidence 963
van Halsema, D., and M.W.A. van der Kooij

3. Flood Monitoring Using ERS-1 SAR Interferometry Coherence Maps 966
Geudtner, D., R. Winter and P.W. Vachon

4. Determination of Vegetation Height from SAR Interferometry: A Theoretical Study 969
Sarabandi, K.

5. Application of Interferometry to Studies of Glacier Dynamics 972
Mohr, J.J., and S.N. Madsen

6. Relating Forest Paramters to Interferometric Data 975
Floury, N., T. Le Toan and J.C. Souyris

7. Estimating Vegetation and Surface Topographic Parameters from Multibaseline Radar Interferometry 978
Treuhaft, R., M. Moghaddam, J. van Zyl and K. Sarabandi

8. On the Detection of Spatially Varying Current Fields at the Ocean Surface by Along-Track Interferometric Synthetic Aperture Radar 981
Romeiser, R., and D.R. Thompson

9. Study of Integration Time Effects on Coherent Radar Imagery of the Sea Surface 984
Moller, D., S. Frasier and R.E. McIntosh

10. Recent Earth Crust Movement of the Black Sea and Adjacent Areas: Application of Remote Sensing Data NA
Yutsis, V.V., V.G. Talitsky and A.F. Vasilevsky

WAT -- Lidar/Spectrometry

1. Daytime Performance Simulation of PN-Code Modulated Micro-Joule Lidar 987
Schoening, V.L., J.A. Reagan and P.A. Delaney

2. Application of Wideband Signals to Airborne Laser Bathymetry 990
Pillai, S.R., and A. Antoniou

3. Low Light-Level IR Detectors for Use in Lidar Systems 993
Mayer, T.S., and T.J. Kane

4. Scanning for a Satellite Radar Wind Sounder (RAWS) 996
Moore, R.K., B. Beh and S. Song

5. Feasibility Study of a Compact Low Cost Correlation LIDAR Using a Pseudo Noise Modulated Diode Laser and an APD in the Current Mode 999
Bundschuh, B.O., D. Schneider and M. Grindel

6. Remote Sensing Spectrometry of a Temperate Deciduous Forest -- A Modeling Approach 1002
Demarez, V., J.P. Gastellu-Etchegorry, F. Zagolski, E. Mougin, G. Marty, E. Dufrene and V. Le Dantec

7. A Revised Measurement Methodology for Spectral Optical Properties of Conifer Needles 1005
Middleton, E.E., S.S. Chan, M.A. Mesarch and E.A. Walter-Shea

8. Airborne Imaging Spectrometry in National Forest Inventory 1010
Makisara, K., and E. Tomppo

9. An Approach for Obtaining Best Estimates of Spectral Optical Depths and Calibration Intercepts from Solar Radiometer Data Corrupted by Temporal Variations 1014
Erxleben, W.H., and J.A. Reagan

10. Estimation of Abundances in Two-Component Mineral Mixtures Using Mid-Infrared Laser Reflectance Ratios 1017
Narayanan, R.M., K.K. Warner and R.F. Diffendal, Jr.

WAV -- Data Compression in Remote Sensing

1. Near Lossless Transform Coding of Multispectral Images 1020
Tescher, A.G., J.T. Reagan and J. A. Saghri

2. Progressive Model-Based VQ for Image Data Archival and Distribution 1023
Manohar, M., and J.C. Tilton

3. Effect of Compression on Physical Parameters Derived from Polar Ice Radiances 1026
St. Germain, K.M., and K. Sayood

4. Lossless Seismic Data Compression Using Adaptive Linear Prediction 1029
Mandyam, G., N. Magotra and W. McCoy

5. Performance of An Enhanced DCT Compression System for Space Applications 1032
Yeh, P.S., W.H. Miller and S. Hou

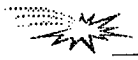
6. End-to-End System Consideration of the Galileo Image Compression System 1035
Cheung, K., K. Tong and M. Belongie

7. A Bounded Distortion Compression Scheme for Hyper-Spectral Image Data 1039
Memon, N.D.

8. Lossless Image Compression Based on a Generalized Recursive Interpolative DPCM 1042
Aiazzi, B., P.S. Alba, L. Alparone and S. Baronti

9. Image Sequence Compression Using Adaptive Wavelet Packet 1045
Sarita, S., and P. Nagabhushan

10. Using ATM Networks for Processing Global Earth Data 1048
Kess, B.L., P.R. Romig III, S.E. Reichenbach and A. Samal



WAZ -- Soil Moisture I

1. Applications of Passive Microwave Observations of Surface Soil Moisture 1051
Schmugge, T.

2. Spatial and Temporal Trends in Land Surface Moisture and Temperature Observable Using Data from the Nimbus-7 Microwave Radiometer 1054
Njoku, E.G., and B.W. Rague

3. Application of Microwave Remotely Sensed Surface Soil Moisture for Estimation of Sub-Surface Soil Hydraulic Properties 1058
Engman, E.T., N.M. Mattikalli, L.R. Ahuja and T.J. Jackson

4. Investigation of the Accuracy of Soil Moisture Inversion Using Microwave Data and Its Impact on Watershed Hydrological Modeling 1061
O'Neill, P.E., A.Y. Hsu, T.J. Jackson, E.F. Wood and M. Zion

5. Surface Soil Moisture Estimation with Radarsat: Early Results NA
Brisco, B., R.J. Brown and T.J. Pultz

6. SIR-C/X-SAR as a Bridge to Soil Moisture Estimation Using Current and Future Operational Satellite Radars 1064
Jackson, T.J., T.L. Li, E.F. Wood, A. Hsu, P.E. O'Neill and E.T. Engman

7. Backscattering over Bare Soils: Measurements and Simulations Using SIRC/XSAR and ERASME 1994 Data over Orgeval 1067
Zribi, M., Taconet, O., S. Le Hegarat-Mascle, D. Vidal-Madjar, C. Emblanch, C. Loumagne and M. Normand

8. Polarimetric Backscattering Measurements of Herbaceous Vegetation: A Sensitivity Study for Soil Moisture Retrieval 1070
Chiu, T.C., K. Sarabandi and F.T. Ulaby

9. Comparison of Spatial Statistics of SAR-Derived and In-SITU Soil Moisture Estimates 1073
Hirsave, P.P., R.M. Narayanan, B.T. Tracy , B.L. Gwilliam R.L. Bolus, T. Pangburn and H.A. McKim

10. Soil Moisture and Temperature Determination by Recursive Assimilation of Multifrequency Observations Using Simplified Models of Soil Heat and Moisture Flow and Emission 1076
Galantowicz, J.F., and D. Entekhabi

WPAM -- Land Cover: Radar for Forest Mapping

1. Radar Backscatter Components from Ponderosa Pine Forests 1077
Wang, Y., and F.W. Davis

2. The Applications of Space Born SAR on Forestry NA
Zeng, Q., J. Jiao, Z. Li and X. Che

3. The Suitability of Multifrequency, Multipolarimetric and Multitemporal Radar Data for Forest Monitoring 1080
Haas, A., and B. Forster

4. Sensitivity of Modeled C-Band from Loblolly Pine Forest Backscatter to Soil Surface Roughness and Moisture 1083
Wang, Y., J.L. Day and F.W. Davis

5. Multifrequency and Polarimetric Analysis of Forests with SIR-C/X-SAR Data 1086
Seifert, F.M., H. Kietzmann and M. Zink

6. Optimization of a Scanning Radar Altimeter for Forest Inventory: A Simulation Method 1089
Hyyppa, J., and M. Hallikainen

7. Temporal Stability of Northern Forest Biophysical Retrievals Using SIR-C/X-SAR 1092
Dobson, M.C., L.E. Pierce, K.M. Bergen and F.T. Ulaby

8. Regional Stability of an ERS/JERS-1 Classifier 1093
Kellndorfer, J.M., M.C. Dobson and F.T. Ulaby

9. Radar Modeling of Forest Spatial Structure 1096
Sun, G., and K.J. Ranson

10. Comparative Analysis of Forests Types Classification Methods Using SIR-C Multifrequency, Multipolarization and Repeated Orbits Interferometry Data NA
Zaitsev, V.V., and A.I. Zakharov

WPAA -- Weather Information Systems

1. Knowledge Based System for Weather Information Processing and Forecasting 1099
Siddiqui, K.J.

2. A Database Program to Archive and Analyze Current Weather Data 1102
Parkin, S.H. and J.P. Refling

3. Neural Network-Based Cloud Detection/Classification Using Textural and Spectral Features 1105
Azimi-Sadjadi, M.R., M.A. Shaikh, B. Tian , K.E. Eis and D. Reinke

4. An FFT-Based Algorithm for Computation of Gabor Transform with its Application to Cloud Detection/ Classification 1108
Tian, B., M.R. Azimi-Sadjadi, M.A. Shaikh and K.E. Eis

5. A Prototype Sea Ice Mapping System Using a Geographical Information System and Expert Knowledge 1111
Williams, R.N., and J. Hartnett

6. Campaign of Validation of Aerosol Optical Depth from Satellites in the Canary Islands Zone NA
Exposito, F.J., J.P. Diaz, M. Arbelo, J.C. Guerra and F. Herrera

7. A Split-Window Equation with Variable Coefficients to Obtain SST in Midlatitudes NA
Arbelo, M., V. Caselles, F.J. Exposito and F. Herrera

8. Pluviometry and Vegetation Monitoring in the Canary Island Zone Using the NOAA Advanced Very High Resolution Radiometer NA
Hernandez, P.A., M. Arbelo, F.J. Exposito and F. Herrera

9. Combined Use of Radar and Satellite Information for Precipitation Estimation in Hungary 1114
Csiszar, I., and J. Kerenyi

10. DSP Architecture for Dual Waveband Meteorological Data Processing NA
Malinovski, V.

WPCP -- Polarimetric Radiometry

1. The AEOLIS Program: Prospects for Future Low-Cost, Space-Borne Vector Wind Sensors 1117
Van Woert, M.L.

2. Polarimetric Scanning Radiometer for Airborne Microwave Imaging Studies 1120
Piepmeier, J.R., and A.J. Gasiewski

3. Ocean Surface Wind Direction Retrievals Using Microwave Polarimetric Radiometer Data 1123
Gaiserl, P.W., P. Chang and L. Li

4. Polarimetric Observation of Ocean Internal Waves by Microwave Radiometers During the Coastal Ocean Probing Experiment 1126
Irisov, V.G., and Yu.G. Trokhimovski

5. Broadband Phenomena in Oceanic Passive Wind Direction Signatures: The Sensitivity to Wave Asymmetry, Foam, and Atmospheric Profile 1129
Kunkee, D.B., and A.J. Gasiewski

6. A Numerical Study of Ocean Thermal Emission NA
Johnson, J.T., R.T. Shin, J.A. Kong, L. Tsang and K. Pak

7. A Comparison of Sea Emission Between Experimental Data and Model Predictions NA
Chen, K.S., S.J. Lai, A.K. Fung and S.Y. Yueh

8. Modelling of Wind Direction Signals in Polarimetric Sea Surface Brightness Temperatures 1132
Yueh, S.H., W.J. Wilson and F.K. Li

9. The Atmosphere Influence on Sea-Surface Polarized Microwave Emission 1135
Pospelov, M.N.

10. Oceanic Wind Vector Determination Using a Dual-Frequency Microwave Airborne Radiometer - Theory and Experiment 1138
Jacobson, M.D., W.J. Emery and E.R. Westwater

WPED -- SAR Applications for Oceanography

1. A PC-Based Remote Sensing System for Detection and Classification of Oceanic Fronts 1141
Askari, F., E. Malaret, D. Lyzenga, M. Collins, T. Donato, A. Skoelv, T. Jenserud and C. Brownsword

2. A Lightweight Spectrasat Concept for Global Ocean Wave Monitoring 1143
Beal, R.C., D.Y. Kusneirkeiwicz, J.L. MacArthur, F.M. Monaldo and S.F. Oden

WPED *continued* -- SAR Applications for Oceanography

3. Using the CCRS Along Track InSAR to Measure and Interpret Ocean Surface Currents 1146
Campbell, J.W.M., A.L. Gray, J.H. Clark, J. Gower and K.E. Mattar

4. Comparison of Wave Parameters Measured from the SIR-C On-Board Processor with WAM Predictions in the Southern Ocean 1149
Monaldo, F.M.

5. Estimation of Thermocline Depths From SAR Imagery and a Two Layer Density Model 1152
Porter, D.L., and D.R. Thompson

6. Validation of SAR Ocean Wave Measurements: ERS-1 and CV-580 Cross Spectra and CV-580 Along-Track InSAR 1155
Vachon, P.W., C. Bjerkelund, J. Buckley, J. Campbell, F.W. Dobson, A.L. Gray, H. Johnsen and R. Lalbeharry

7. Coast Watch - 95: ERS - 1/2 SAR Applications of Mesoscale Upper Ocean and Atmospheric Boundary Layer Process off the Coast of Norway 1158
Johannessen, O.M., J.A. Johannessen, A.D. Jenkins, K. Davidson, D.R. Lyzenga, R Shuchman, P. Samuel, H.A. Espedal, J. Knulst, E. Dano and M. Reistad

8. Evaluation of RADARSAT Synthetic Aperture Radar Data for Ocean Wave Measurements and Ship Detection NA
Olsen, R.B., P. Bugden, P. Hoyt, M.Henschel and M.R. Lewis

9. The Imaging of Submarine Sandwaves with Multi-Band SAR NA
Vogelzang, J.

10. Ocean Surface Slope Measurement Using Polarimetric SAR 1162
Lee, J.S. and D.L. Schuler

WPES -- Educational Initiatives II

1. Studying the Earth's Environment From Space - A Curriculum Workshop 1165
Alfultis, M.A.

2. NASA-NOAA Summer School for Earth Science - Processes of Global Change and Global Change Workshop for Teachers NA
Syvertson, M., S. Ride, D. McCleese and W. Mohling

3. Mission: Arkansas - Curriculum Enhancement and Dissemination of K-12 Science Mathematics Using Space Based Data and Geographic Information Systems NA
Hehr, L.H.

4. Constructing Earth System Science Learning Through Multidisciplinary Studies of Global Change 1166
Fortner, R.W., and V.J. Mayer

5. A CD-ROM Study Package on Current Forest Issues for Use in Secondary School Science Classes 1169
Hassol, S., and C.J. Tucker

6. Using Distributed Multimedia Systems to Enable Earth Systems Education in the Earth System Science Community NA
Keeler, M.,and F. Mahootian

7. Our Role in the Earth System: One K-12 School District's Science Education Initiative 1172
Lindgren, P.D.

8. Earth System Science Education: A Continuing Collaboration 1175
Johnson, D.R., M. Ruzek and M. Kalb

9. OMSI-NSF Young Scholars Research Participation Program, Oregon Museum of Science and Industry 1178
Gottfried, J.

10. Alaska SAR Facility Education Outreach 1181
Sandberg, D., and F. Carsey

WPF -- Research Progress Under the ONR Sea Ice Electromagnetics ARI

1. Observations of Sea Ice Physical Properties During the Sea Ice Electromagnetics Initiative 1184
Gow, A.J., and D.K. Perovich

2. Physical and Electrical Characteristics of Snow on Sea Ice: Implications for Forward Scattering Model Development 1187
Barber, D.G., S.D. Drobot and J. Iacozza

3. Sea Ice Polarimetric Backscatter Signatures at C Band 1190
Nghiem, S.V., R. Kwok, S.H. Yueh, J.A. Kong, A.J. Gow, D.K. Perovich, S. Martin and R. Drucker

4. Polarimetric Properties of Simulated Sea Ice with Special Focus on Property Retrieval and Important Scattering Processes 1193
Onstott, R.G.

5. Ultra-Wideband Radar Measurements of over Bare and Snow-Covered Saline Ice 1196
Gogineni, S.P., P. Kanagaratnam and K. Jezek

6. Microwave and Thermal Infrared Emission from Young Sea Ice and Pancake Ice 1199
Grenfell, T.C.

7. Modeling of Ice Thickness Effect and Its Application to Data Interpretation 1202
Fung, A.K, and R.G. Onstott

8. Electromagnetic Inversion of the Physical Properties of Sea Ice NA
Golden, K.M.

9. Inversion of Wideband Microwave Reflectivity to Estimate the Thickness of Arctic Lead-like Sea Ice 1205
Winebrenner, D.P., and J. Sylvester

10. Thickness Retrieval Using Time Series Electromagnetic Measurements of Laboratory Grown Saline Ice 1208
Shih, S.E., K.H. Ding, S.V. Nghiem, C.C. Hsu, J.A. Kong and A.K. Jordan

WPP -- SAR Processor Systems and Algorithms

1. ASF SAR Processing System Performance Overview NA
Jin, M., K. Leung, M. Chen and A. Chu

2. Vexcel Corporations' SAR Processing Ground Station: An Overview 1211
Compton, M., and R.E. Carande

3. Azimuth and Range Scaling for SAR and ScanSAR Processing 1214
Moreira, A., R. Scheiber and J. Mittermayer

WPP *continued* -- SAR Processor Systems and Algorithms

4. High Precision Processing of SIR-C ScanSAR Data 1217
Mittermayer, J., A. Moreira, G. Davidson, R. Bamler and Y.L. Desnos

5. A Comparison of the Range-Doppler and Chirp Scaling Algorithms with Reference to RADARSAT 1221
Hughes, W., K.A. Gault and J. Princz

6. Comparison of Medium Resolution Algorithms for Spacecraft On-Board SAR Image Generation 1224
Vidal, A., and J. Rosello

7. Registration SAR Images Using the Chrip Scaling Algorithm 1227
Fernandes, D., G. Waller and J. R. Moreira

8. Autofocus of Wide Azimuth Angle SAR Images by Contrast Optimisation 1230
Berizzi, F., G. Corsini, M. Diani and M. Veltroni

9. High Frequency Phase Errors in SAR Imagery and Implications for Autofocus 1233
Marechal, N.

10. Phase Errors Compensation in SAR Imaging 1241
Isernia, T., V. Pascazio, R. Pierri and G. Schirinzi

WPT -- Clouds, Aerosols and Boundary Layer

1. Cirrus Cloud Detection by Micro Pulse Lidar: Algorithm Development and Testing 1244
Galbraith, A.E., J.A. Reagan and J.D. Spinhirne

2. Cloud Masking with Satellite Infrared Images over Polar Oceans 1247
Schlueter, N., and T. Markus

3. Cloud Corrections for Satellite Images NA
Peltoniemi, J.I.

4. The Estimation of Aerosol Models by the Reflectance Analysis of the Airborne POLDER Data 1250
Yamazaki, A., K. Ueda, Y. Kawata and T. Kusaka

5. Particle Size Distributions and Extinction Determined by a Unique Bistatic Lidar Technique 1253
Stevens, T.D., and C.R. Philbrick

6. Remote Sensing of the Marine Atmospheric Boundary Layer and Oean Surface Winds: Observations from the LITE Correlative Flights 1257
Palm, S.P., G. Schwemmer, D. Vandemark, D. Hines and S.H. Melfi

7. Remote Measurement of Coastal Marine Atmospheric Boundary Layer (MABL) Features 1260
Jordan, M.S., C.H. Wash and K.L. Davidson

8. Estimation of the Ocean/Atmosphere Boundary Layer Height of Water Vapor from Space 1263
Ruf, C.S., and S.E. Beus

9. Rain Measurement with SIR-C/X-SAR 1266
Moore, R.K., A. Mogili, Y. Fang, B. Beh and A. Ahamad

10. Investigations of Atmospheric Boundary Layer by Using 5-Millimeter Radiometer NA
Kadygrov, E.N., and A.V. Troitsky

WPV -- Calibration and Correction Algorithms for Radiometric and Reflectance Measures

1. Artifact Correction and Absolute Radiometric Calibration Techniques Employed in the Landsat 7 Image Assessment System 1270
Boncyk, W.C., B.L. Markham, J.L. Barker and D.L. Helder

2. Landsat-7 Enhanced Thematic Mapper Plus In-Flight Radiometric Calibration 1273
Markham, B.L., J.L. Barkerm,W.C. Boncyk, E. Kaita and D.L. Helder

3. Short Term Calibration of Landsat TM: Recent Findings and Suggested Techniques 1276
Helder, D., W. Boncyk, J.L. Barker and B.L. Markham

4. Comparison of Scene-Dependent Radiometric Validation Methodologies for EOS-AM1 MODIS Level-1 Products NA
Barker, J.L., and S.G. Ungar

5. In-Flight Radiometric Calibration Plans for the Earth Observing System -- Multi-Angle Imaging Spectroradiometer 1279
Bruegge, C., R.Woodhouse, and D. Diner

6. Cross-Calibration of Two Small Footprint Sensors 1283
Gustafson-Bold, C.L., and K.J. Thome

7. Evaluation of The Aerosol Scattering Phase Function from PGAMS Observation of Sky Path Radiance 1286
Schiller, S., and J. Luvall

8. RADARSAT CALIBRATION: The Operational System and Initial Results 1290
Srivastava, S.K., T.I. Lukowski, R.K. Hawkins, C. Cloutier, L.D. Teany, N.W. Shepherd, R.B. Gray, A.P. Luscombe and R. Banik

9. Calibration Methods and Results for the Advanced Solid-State Array Spectroradiometer (ASAS) NA
Dabney, P.W., M.R. Tierney, J.R. Irons,W.M. Kovalick, M.C. Bur and C.A. Russell

10. Calibration of the AVHRR Thermal Infrared Channels: Determining the Temperature of the Internal Calibration Target 1293
Steyn-Ross, D.A., M.L. Steyn-Ross and S. Clift

WPZ -- Soil Moisture II

1. The Influence of Soil Moisture on Temporal CVV- and LHH- Signatures from Vegetated Fields - Summary of the DLR E-SAR Cleopatra Campaign NA
Schmullius, C., and J. Nithack

2. A Modified IEM Model for Scattering from Soil Surfaces with Application to Soil Moisture Sensing 1297
Fung, A.K., M.S. Dawson, K.S. Chen, A.Y. Hsu, E.T. Engman, P.O. O'Neill and J. Wang

3. Soil Moisture Retreival Using the Danish L- & C-Band Polarimetric SAR 1300
Ji, J., P. van der Keur, A. Thomsen and H. Skriver

4. Remote Sensing of Soil Moisture Using EMAC ESAR Data 1303
Su, Z., P.A. Troch and F.P. De Troch

5. Use of Polariztion Synthesis From Polarimetric SAR Data for Roughness Estimation over Bare Fields 1306
Mattia, F., J.C. Souyris, T. Le Toan, G. De Carolis, N. Floury, F. Posa and G. Pasquariello

6. Microwave Remote Sensing of Land Surfaces Soil Moisture at Global Hydrology and Climate Center 1309
Wu, S.T.S.

WPZ *continued* -- Soil Moisture II

7. Soil Hydraulic Characterization Derived from Landsat TM-5 Data 1312
Bresci, E., and I. Becchi

8. An Optical Reflectance Technique for Soil Moisture Measurement - Part I: Theory, Description and Application 1315
Belisle, W.R., A. Sharma and T.L. Coleman

9. Accuracy of Soil Moisture Determination by Means of Passive Microwave Remote Sensing Method: Modeling and Experiments 1320
Liberman, B., and A. Milshin

10. Microwave Dielectric Behavior of Wet Soils in Region of Transition Moisture 1323
Belyaeva, T.A., and Yu.M. Sosnovsky

WEAM -- Infrared and Optical Remote Sensing of the Ocean Surface

1. Ocean Skin Temperature Modulation by Swell Waves NA
G.A. Wick, Hesany and A.T. Jessup

2. Monitoring of the Sea Surface Thermal Patterns in a Marginal Sea Affected by an Ocean NA
Nakamura, S.

3. Sensitivity Analysis of a Coupled Optical Remote Sensing and Three Dimensional Hydrodynamic Model NA
Bostater, C., and T. McNally

4. Ocean Ripple Statistics Measured with a Scanning-Laser Glint Sensor 1328
Shaw, J.A., and J.H. Churnside

5. The Remote Technique of Sea Surface Waves by Optical Sensors 1331
Titov, V.I., and E.M. Zuykova

WEF -- Volume Scattering II

1. Radio Wave Propagation Along Mixed Paths Through Four-Layered Model of Rain Forest: A Closed Form Solution NA
Li, L.W., T.S. Yeo, P.S. Kooi and M.S. Leong

2. A Coherent Scattering Model for Forest Canopies Based on Monte Carlo Simulation of Fractal Generated Trees 1334
Lin, Y.C., and K. Sarabandi

3. A Numerically Derived Electromagnetic Scattering Model for Grass Grain Heads 1337
Siqueira, P., and K. Sarabandi

4. Electromagnetic Scattering by Multiple Three-Dimensional Scatteres Buried Under One-Dimensional Multi-Layered Media 1340
Cui, T.J., and W. Wiesbeck

5. Electromagnetic Wave Transmission in Randomly Distributed Inhomogeneous Spherical Particles NA
Osharin, A.M.

WEH -- Subsurface Sensing and Material Properties II

1. Wave Reflection From a Target Immersed into Disordered Medium — NA
Kanzieper, E., and V. Freilikher

2. The Modified Rayleigh-Gans Approach and Scattering Waves — 1343
Yildirim, O.

3. An Inverse Algorithm for Integral Equation Formaultion of Dielectric Loaded Cavities — 1346
Sabet, K.F., K. Sarabandi, J.G. Yook and L.P.B. Katehi

4. Method for Retrieval of Media Structural Parameters from Frequency Dependence of Transmission Coefficient — NA
Boyarskii, D.A.

5. Application of SIR-C L/C/X-Band Radar Data for Mineral Exploration Experiment in Hwanggangni Mining District, Korea — NA
Jiang, W.W., C.S. So, Y. Yamaguchi, W.M. Moon and S.K. Choi

WEM -- Remote Sensing Missions and Programs

1. Early Images from the RADARSAT Synthetic Aperture Radar — 1352
Luscombe, A.P., R. Gray, N. Shepherd, S. Srivastava, D. Meier and W. Jeffries

2. The Development of the ENVISAT-1 Advanced Synthetic Aperture Radar — 1355
Mancini, P., J.L. Suchall, Y.L. Desnos, R. Torres, J. Guijarro and G. Graf

3. Processing and Validation of the ERS-1 Radar Altimeter Data at the Italian PAF — NA
Celani, C., A. Bartoloni, G. Milillo and F. Nirchio

4. An Alaska SAR Overview in the RADARSAT Era — 1358
Cuddy, D., and K. Leung

5. Cassini Radar Investigation of Titan — NA
Wall, S., C. Elachi and L. Roth

WEP -- Active and Passive Remote Sensing of Precipitation

1. Validation and Ground Truth for TRMM Precipitation Radar Using the MU Radar — 1361
Sato, T., T. Teraoka and I. Kimura

2. Preliminary Results of Ground-Based Rain Measurements with a Dual-Frequency Multiparameter Radar-Radiometer — 1364
Horie, H., R. Meneghini and T. Iguchi

3. Active and Passive Microwave for Rainfall Monitoring — 1367
Nativi, S., L. Baldini, D. Giuli and P. Mazetti

4. Study of Potential of a Profile-Based Algorithm for Precipitation Retreival from MIMR — NA
Panegrossi, G., S. Dietrich, F.S. Marzano and A. Mugnai

5. Investigation of Multifrequency Multipolarisation Radar Signatures of Rain Cells, Derived From SIR-C/X-SAR Data — 1370
Melsheimer, C., W. Alpers and M. Bao

WESF -- Land Cover: Innovative Classification Methods II

1. Mathematical Morphology, Urban Change, Image-Oriented Geographic Information Systems 1373
Maupin, P., and B. Solaiman

2. Fuzzy Classification Techniques for Urban Area Recognition 1376
Console, E., and M.C. Mouchot

3. Robust Mixed Pixel Classification Using the Hypothesis Testing Hough Transform 1379
Bosdogianni, P., M. Petrou and J. Kittler

4. Improving Automated Land Cover Mapping by Identifying and Eliminating Mislabeled Observations from Training Data 1382
Brodley, C.E., and M.A. Friedl

5. An Automatic Technique for Detecting Land-Cover Transitions NA
Serpico, S.B., L. Bruzzone, F. Roli and M.A. Gomarasca

WES -- Ocean Waves and Winds II

1. A Not Pointwise Approach to the Wind Field Retrieval from Scatterometer Data NA
Bartoloni, A., C. D'Amelio and G. Milillo

2. X-Band Coherent Measurements of Ocean Backscatter from an Airship NA
Hesany, V., W.J. Plant, W.C. Keller and K. Hayes

3. Observations of the Ocean Surface Using an Aircraft Radar Altimeter, Scatteromenter and ROWS 1385
Vandemark, D., D. Hines, B. Chapron, J. Carswell and W. Donnelly

4. Dependence of Altimeter Returns on Wind Stress and Wave Age 1389
Elfouhaily, T., B. Chapron, V. Kerbaol, J. Gourrion, J. Tournadre, K. Katsaros and D. Vandemark

5. Correcting SeaWinds Scatterometer Measurements for Atmospheric Attenuation 1392
Moore, R.K., N. Kambhammettu and S. Song

WET -- Remote Sensing of Surface Waters

1. Spectrometry of Turbidity in Surface Water 1395
Han, L.

2. Validation of an Optical Remote Sensing Model Using Reflectance Signatures Collected From an Airborne Sensor NA
Bostater, C., W. Ma, T. McNally, M. Keller and M. Gimond

3. Quantitative Remote Estimation of Algal Density, Pigment Concentrations and Non-organic Suspended Matter in Aquatic Environments, Principles and Techniques NA
Gitelson, A.A., Y.Z. Yacobi and S. Plotnizky

4. SeaWiFS and MERIS: A Comparison of Their Performance for the Estimation of Optically Active Components in Ocean Water 1398
Cipollini, P., and G. Corsini

5. A Numerical Study of the Composite Surface Model for Ocean Scattering 1401
Johnson, J.T., R.T. Shin, J.A. Kong, L. Tsang and K. Pak

6. Algorithm Requirements for Operational Use of Airborne Remote Sensing in Inland Water Management NA
Dekker, A.G., H.J. Hoogenboom and M. Rijkeboer

THAAM -- Retrieval of Ecosystem Parameters from BRDF Data and Models

1. Kilometer-Scale Global Albedo from MODIS 1405
Wanner, W., A.H. Strahler, B. Zhang and P. Lewis

2. The Influence of Directional Sampling on Bidirectional Reflectance and Albedo Retrieval Using Kernel-Driven Models 1408
Wanner, W., P. Lewis and J.L. Rougean

3. Semiempirical Modelling of Bidirectional Utilizing the MODIS BRDF/Albedo Algorithm Models 1411
White, H.P., J.R. Miller, R. Soffer and W. Wanner

4. Analytic Forms of Bidirectional Reflectance Functions for Earth Radiation Budget Studies 1414
Manalo-Smith, N., and G.L. Smith

5. The Use of Bidirectional Reflectance to Estimate Broadband Hemispherical Albedo Over Tasmania 1417
Russell, M., and M. Nunez

6. A Technique for Combining Geometrical and Spectral BRDF Information for Retrieval of Plant Canopy Characteristics Uing AVHRR Optical Data NA
Braswell, B.H., J.L. Privette and D.S. Schimel

7. Estimating Hemispherical Reflectance and Selected Biophysical Parameters for Boreal Forest Canopies Using Spectral Bidirectional Reflectance Data Acquired by ASAS NA
Russell, C.A., J.R. Irons and P.W. Dabney

8. An Integrated Approach to Estimating LAI Using Multitemporal and Multidirectional Remote Sensing Measurements 1420
Qi, J., and M.S. Moran

9. Comparison of Vegetation Index Compositing Scenarios: BRDF Versus Maximum VI Approaches 1423
van Leeuwen, W.J.D., A.R. Huete, S. Jia and C.L. Walthall

10. Retrieval of Canopy Structural Parameters from Multi-Angle Observations Using an Artificial Neural Network 1426
Abuelgasim, A.A., S. Gopal and A.H. Strahler

THAAA -- Microwave/Millimeter-Wave Atmospheric Absorption and Scattering Models

1. Observations and Modelling of Radiometric Signatures of Storms in the Frequency Range of 90-220 GHz 1429
Wang, J.R., C. Kummerow, P. Racette, W. Olson and J. Zhan

2. Atmoshperic Water-Vapor Microwave Absorption - A Review of Models and Measurements NA
Rosenkranz, P.W.

3. Model Based Retrievals of Water Vapor Profiles from Microwave Radiances NA
Wilheit, T.T., C.B. Blankenship and S.L. Moore

4. Observed and Theoretical Millimeter Wave Emission in the Tropics 1432
Snider, J.B., and D.A. Hazen

5. Atmospheric Microwave Absorption Parameter Estimation Near 22 GHz 1435
Cruz Pol, S.L., C.S. Ruf and SJ. Keihm

6. Atmospheric Water Vapor and the Total GPS Signal Delay NA
Gutman, S.I., D.E. Wolfe and R.B. Chadwick

7. Recent Advances in Satellite Sounding at the U.K. Meteorological Office 1438
Barwell, B.R.

8. Wind Speed and Total Integrated Water Vapor Measurements Over the Ocean Using the Special Sensor Microwave/Imager (SSM/I) NA
Manning, W.

9. Influence of Scattering in the Absorbing Line Structure in Two-Phase Media 1441
German, M.L., V.P. Nekrasov and E.F. Nogotov

10. Atmospheric Effects Due to Different Particle Shapes on Propagation 1444
Yildirim, O.

THACP -- Microwave Remote Sensing of Ocean Surface Winds I

1. JPL Wind Radiometer Measurements NA
Wilson, W.J., and S.H. Yueh

2. Surface and Airborne Radiometric Observations During the Coastal Ocean Probing Experiment: An Overview 1450
Westwater, E.R., V.G. Irisov, L.S. Fedor and Yu.G. Trokhimovski

3. Surface Wind Measurements by Radiometer- Polarimeters in Frame of Russia Airspace Programs 1454
Kravtsov, Yu.A., A.V. Kuzmin, M.N. Pospelov and A.I. Smirnov

4. Observation of the Ocean Brightness Temperature Anisotrophy During the Coastal Ocean Probing Experiment 1457
Irisov, V.G., and Yu.G. Trokhimovski

5. High Altitude Aircraft Mapping of Near Surface Ocean Winds 1460
Hood, R.E., and R.W. Spencer

6. Performance Analysis for the Sea Winds Scatterometer 1463
Long, D.G., and M.W. Spencer

7. Remote Sensing of the Near Surface-Ocean Wind Vector Under Low-Wind Conditions Using Scatterometry 1466
Carswell, J., W. Donnelly and R. McIntosh

8. Ku-Band Ocean Backscatter Functions for Surface Wind Retrieval 1469
Nghiem, S.V., F.K. Li and G. Neumann

9. Scatterometer Measurements of Ocean Surface Stress Magnitude and Direction from Aircraft During SWADE and from ERS-1 1472
Weissman, D.E.

10. Statistics of Radar Backscatter from Wind Waves 1475
Long, D.G., R. Reed and D.V. Arnold

THAED -- Remote Sensing of Littoral Submesoscale Processes II

1. An Analysis of Drainage Flow Exit Jets Over the Chesapeake Bay as Seen in an ERS-1 SAR Image NA
Winstead, N.S., G.S. Young, D.R. Thompson and H.N. Shirer

2. Study of Katabatic Wind Fields by Using ERS-1 Synthetic Aperture Radar Imagery of the Ocean Surface 1478
Alpers, W., U. Pahl, G. Gross and D. Etling

3. A Coupled Wind — Internal Wave System 1481
Smirnov, A.V.

4. A Large-Scale Evaluation of Features for Automatic Detection of Oil Spills in ERS SAR Images 1484
Schistad Solberg, A.H., and R. Solberg

5. Ocean Features Evaluation from RADARSAT SAR Imagery NA
Staples, G.C.

6. Meteorological Explanation of a Sea Surface Roughness Streak Imaged by ERS-1 SAR Near Block Island, New York NA
Winstead, N.S., H.N. Shirer, T.D. Sikora and R.C. Beal

7. Internal Waves in the Strait of Messina Observed by the ERS1/2 Synthetic Aperture Radar 1487
Brandt, P., A. Rubino and W. Alpers

8. Studies of Rainfall Footprints on the Sea Conducted by Spaceborne SAR "Almaz" and Shipborne Microwave Radiometers 1490
Bulatov, M.G., M.D. Raev and E.I. Skvortsov

9. The Microwave Radar Signal Doppler Spectrum and the Problem of Ocean Surface Slicks Detection 1493
Kanevsky, M.B., and V.Y. Karaev

10. The Remote Sensing of the Ocean Surface in the Frontal Zone 1495
Lavrenov, I.

THAES -- Educational Initiatives III

1. The Weather Visualizer: A Java Tool for Interactive Learning 1498
Hall, S.E., M.K. Ramamurthy, R.B. Wilhelmson, J. Plutchak, D. Wojtowicz and M. Sridhar

2. Lessons Learned From Using GIS/RS as an Integrative Tool for Interdisciplinary Learing and Teaching in a Senior-Level Capstone Course on Global Change at Westminster College of Salt Lake City 1501
Ford, R.E., and J. Hipple

3. Classroom Applications of Marine and Environmental Remote Sensing Data 1504
Alfultis, M.A., and M.R. Hicks

4. A Model for Environmental Earth Science Module Design 1506
Meyers, R.J., J.A. Botti and K.D. Gonzalez

5. Remote Sensing and Inner City Youth: A Pilot Collaboration of the Aspen Global Change Institute's Ground Truth Studies and the 4-H After School Programs 1509
Katzenberger, J.

6. The Arctic Observatory: An Educational Tool for Intercomparison Studies and Time-Series Analysis Using Five Arctic Parameters on CD-Rom NA
Keeler, M., and F. Mahootian

7. Texas Space Grant Consortium: Educational Opportunites in Earth Science and Remote Sensing 1512
Neuenschwander, A.

THAF -- Sea Ice Remote Sensing (Models, Techniques and Applications) II

1. The SIMMS'93 SAR Polarimetry Experiment: Combined Surface and Airborne Radar Measurements for Winter Sea Ice 1515
Livingstone, C.E., D.G. Barber, F. Spring and W. Liu

2. Ice Roughness Classification and ERS SAR Imagery of Arctic Sea Ice: Evaluation of Feature-Extraction Algorithms by Genetic Programming 1520
Daida, J.M., R.G. Onstott, T.F. Bersano-Begey, S.J. Ross and J.F. Vesecky

3. A Microwave Technique for Mapping Ice Temperature in the Arctic Seasonal Ice Zone 1523
St. Germain, K.M., and D.J. Cavalieri

4. A Neural Network Sea Ice Edge Classifier for the NASA Scatterometer 1526
Alhumaidi, S.M., W.L. Jones, J.D. Park, S. Ferguson and M.H. Thursby

5. Fusion of Satellite SAR and SSM/I Data for Thin Sea Ice Concentration NA
Beaven, S.G.

6. Comparison of Open Water and Thin Ice Areas Derived from Satellite Passive Microwave Data with Aircraft Measurements and Satellite Infrared Data in the Bering Sea 1529
Markus, T., and D.J. Cavalieri

7. Lake Superior Ice Concentration Using SSM/I NA
Pilant, D.

8. Measuring Sea Ice Floe Size During Summer with ERS SAR Imagery NA
Holt, B., and S. Martin

9. Separating Ice-Water Composites and Computing Floe Size Distributions 1532
Soh, L.K., D. Haverkamp and C. Tsatsoulis

THAH -- Emerging Technologies and Techniques

1. Laser Diode Based New Generation Lidars 1535
Reagan, J.A., H. Liu and J.F. McCalmont

2. Antartic Miniature Lidar 1538
Rall, J.A.R., and J.B. Abshire

3. Fulfilling the Promise of Imaging Spectrometry: Underappreciated Aspects of Sensor Performance Which Affect Data Utility NA
Chrien, T.G., M.L. Eastwood, R.O. Green, C.M. Sarture and G.H. Bearman

4. Use of FT-IR and UV Spectrometers for Monitoring Multiple Pollutants in the Lower Troposphere 1541
Gibbs, D.P., and B. Krenek

5. Multimeter Wave Imaging Technology 1544
Huguenin, G.R.

6. Synthetic Aperture Radiometers for Microwave Remote Sensing from Space 1547
Le Vine, D.M., and C.T. Swift

7. Capabilities and Recent Results From the ER-2 Doppler Radar (EDOP) 1550
Bidwell, S.W., G.M. Heymsfield and I.J. Caylor

8. Millimeter-wave Radars for Remotely Sensing Clouds and Precipitation 1553
Mead, J.B., A.L. Pazmany, S.M. Sekelsky, R. Bambha and R.E. McIntosh

9. Airborne SAR Interferometry: Potential and Future Applications NA
Moreira, J.

10. Satellite SAR Interferometry: Present Status and Future Technologies NA
Guarnieri, A. M., C. Prati and F. Rocca

THAP -- SAR Speckle and Classification

1. Polarimetric Image Classification Using Optimal Decomposition of Radar Polarization Signatures 1556
Dong, Y., B. Forster and C. Ticehurst

2. A Comprehensive Evaluation of Filters for Radar Speckle Suppression 1559
Sheng, Y., and Z.G. Xia

3. SIR-C Polarimetric Image Segmentation by Neural Network 1562
Sergi, R., G. Satalino, B. Solaiman and G. Pasquariello

4. Determining the Number of Classes for Segmentation in SAR Sea Ice Imagery 1565
Soh, L.K., and C. Tsatsoulis

5. A Multi-Temporal Classifier for SIR-C/X-SAR Imagery 1568
Bergen, K.M., L.E. Pierce, M.c. Dobson and F.T. Ulaby

6. Study on Target Detection Using Multi-Look Polarimetric SAR Data NA
Xiong, H., G. Liu and S. Huang

7. Optimal Multi-look Polarimetric Speckle Reduction and Its Effects on Terrain Classification 1571
Liu, G., S. Huang, A. Torre and F. Rubertone

8. Polarimetric Signature Preservation in SAR Speckle Filtering 1574
Lee, J.S., G. De Grandi, M.R. Grunes and E. Nezry

9. Reduction of Multiplicative Noise in SAR Imaging by Wiener Filtering 1577
Pascazio, V., and G. Schirinzi

10. Statistical Characterization of the Phase Process in Interferometric SAR Images 1580
Di Bisceglie, M., and C. Galdi

THAV -- Image Processing: Restoration Problems

1. Aerosol Properties From Blurring Effect in Remotely Sensed Images 1584
Leone, A., B. Bulgarelli, M. Garello and G. Perona

2. Deriving the Anisotropic Atmospheric Point Spread Function of ASAS Off-Nadir Images and Removal of the Adjacency Effect by Inverse Filtering 1587
Hu, B., X. Li and A.H. Strahler

3. Quantitative Evaluation of Edge Preserving Noise-Smoothing Filter 1590
Pasaribu, D.P.

THAV *continued* -- Image Processing: Restoration Problems

4. A Constructive Deconvolution Procedure of Bandpass Signals by Homomorphic Analysis 1592
Marenco, A.L., and V.K. Madisetti

5. Cubic Covolution for One-Pass Restoration and Resampling 1597
Reichenbach, S.F., and K. Haake

THAV -- Image Processing: Registration and Resampling

6. Quantitative Aspects of the Radiometric Normalization of Multi-Temporal Satellite Scenes in the Creation of Large Area Image Mosaics NA
Guindon, B.

7. Landsat Thematic Mapper Band-to-Band Registration 1600
Barker, J.L., and J.C. Seiferth

8. Digital Resampling for Image Processing and Fusion of SSM/I Data 1603
Pellegrini, P.F., E. Piazza and A. Nervi

9. Spatial Resolution Enhancement of SSM/I Data: Vegetation Studies of the Amazon Basin 1606
Long, D.G., D.R. Daum and P.J. Hardin

10. Automated Image Registration for Change Detection from Landsat Thematic Mapper Imagery 1609
Dai, X., S. Khorram and H. Cheshire

THAZ -- The World's Airborne SAR Facilities I: Conventional Frequencies & Respective Applications

1. NASA/JPL Airborne Three-Frequency Polarimetric/Interferometric SAR System 1612
Kim, Y., Y. Lou, J. van Zyl, L. Maldonado, T. Miller, T. Sato and W. Skotnicki

2. Hughes Integrated Synthetic Aperture Radar 1615
Bayma, R.W.

3. Ingara: An Integrated Airborne Imaging Radar System 1618
Stacey, N.J.S., M.P. Burgess, M.R. Muller and R. Smith

4. The Canadian Airborne R&D SAR Facility: The CCRS C/X SAR 1621
Livingstone, C.E., A.L. Gray, P.W. Vachon, M. Lalonde, R.K. Hawkins, T.I. Lukowski, K. Mattar and J.W. Campbell

5. The DLR Airborne SAR Project E-SAR 1624
Horn, R.

6. EMISAR: C- and L-Band Polarimetric and Interferometric SAR 1629
Lintz Christensen, E., J. Dall, N. Skou, K. Woelders, J. Granhohm and S.N. Madsen

7. First Results and Status of the PHARUS Phased Array Airborne SAR 1633
Greidanus, H., P. Hoogeboom, P. Koomen, P. Snoeij and H. Pouwels

8. Development of NASDA Airborne Synthetic Aperture Radar (NASAR-1) 1636
Shimada, M., H. Oaku and M. Yamanashi

9. The NEC Interferometric SAR System "NEC-SAR" 1639
Nagata, H., H. Shinohara, M. Murata, M. Miyawaki, H. Nagata, H. Shinme, M. Sugawara, H. Totuka, Y. Ohura and H. Nohmi

THPAM -- BRDF Model Development, Validation and Inversion II

1. Angular Signatures, and a Space-Borne Measurement Concept 1642
Gerstl, S.A.W.

2. Estimation of Leaf Size from Hotspot Observation 1645
Qin, W., N.S. Goel and B. Wang

3. Multiple Scattering Approximations and Coherent Backscattering Theory for Soil Bidirectional Reflectance 1648
Liang, S.

4. A Four-Level Bidirectional Reflectance Model Based on Canopy Architecture and its Inverstion 1651
Chen, J.M., and S.G. Leblanc

5. Validation of a BRDF Model for Boreal Forest 1654
North, P.R., S.E. Plummer and D.W. Deering and M. Leroy

6. Assessing Canopy Biomass and Vigor by Model-Inversion of Bidirectional Reflectances: Problems and Prospects 1657
Brakke, T.W., J. Otterman, J.R. Irons and F.G. Hall

7. Retrieval of Forest Biophysical Parameters from Remote Sensing Images with the DART Model 1660
Pinel, V., J.P. Gastellu-Etchegorry and V. Demarez

8. Extracting Sub-Pixel Vegetation Endmember Bidirectional Reflectance for Canopy Model Inversion Using NOAA AVHRR Satellite 1663
Asner, G.P., J.L. Privette, C.A. Wessman and C.A. Bateson

9. Estimation of Bidirectional Reflectance Distribution Function from Land Surfaces Using Airborne POLDER Data 1666
Takemata, K., T. Yonekura, M. Asae and Y. Kawata

10. Validation of Kernel-Driven Semiempirical BRDF Models for Application to MODIS MISR Data 1669
Hu, B., W. Wanner, X., Li and A.H. Strahler

THPAA -- Passive Remote Sensing of the Environment

1. A Scanning 60 GHz Radiometer to Measure Air-Sea Temperature Difference: Recent Results During Cope 1672
Trokhimovski, Yu.G., E.R. Westwater, V.G. Irisov and V.Ye. Leuskiy

2. Measurements of Integrated Water Vapor and Cloud Liquid from Microwave Radiometers at the DOE ARM Cloud and Radiation Testbed in the U.S. Southern Great Plains 1675
Liljegren, J.C., and B.M. Lesht

3. Performance Evaluation of a Spinning Flat Reflector for Millimeter-Wave Radiometry 1678
Jacobson, M.D., and W.M. Nunnelee

4. Observations of Water Vapor and Cloud Liquid from an Airborne Dual-Frequency Radiometer During VORTEX'95 1681
Fedor, L.S., E.R. Westwater and M.J. Falls

5. Applications of Kalman Filtering to Derive Water Vapor Profiles from Raman Lidar and Microwave Radiometers 1685
Han, Y., E.R. Westwater and R.A. Ferrare

6. Application of Neural Nets to Rain Rate Retrieval from Simulated Multichannel Passive Microwave Imagery 1688
Gasiewski, A.J., G.A. Showman and G.M. Skofronick

7. Prediction of Water Vapor Scale Height from Integrated Water Vapor Measurements 1692
Boback, J.P., and C.S. Ruf

8. Feasibility of a New Ground-Based Microwave Measurement Method for the Atmospheric Water Vapor 1695
Hashimoto, S., N. Yamashita and T. Mikami

9. Determination of Humidity Profiles from Measurements of Up Going Radiation at Wavelengths 0.3 and 1.35 cm 1698
Markina, N.N., and A.P. Naumov

10. Recovering of Atmospheric Water Vapor and Liquid Water Contents by Multifrequency Radiometer: Experiments and Modeling 1701
Perfiliev, Y.P.

THPCP -- Microwave Remote Sensing of Ocean Surface Winds II

1. A Simple Model for Deriving Ocean Surface Wind Direction from the DMSP Special Sensor Microwave Imager (SSM/I) 1704
Boucher, D.J., B.H. Thomas, D.N. Ricci and A.M. Kishi

2. Ocean Surface Wind Speed and Direction Retrievals from the SSM/I 1707
Li, L., and P. Chang

3. Assessing the Ocean Surface Vector Wind Signal in SSM/I Data Using Neural Networks 1710
Bates, J.J., and K.C. McColl

4. The Effects of Tropospheric Water Vapor and Cloud Liquid Water on Ocean Surface Wind Vector Retrievals Using Polarimetric Radiometers NA
Gaiserl, P.W., and P. Chang

5. Surface Winds from the SSM/I Using Neural Networks 1712
Krasnopolsky, V.M., L.C. Breaker and W.H. Gemmill

6. Development of a Statistical Method for Eliminating Improbable Wind Aliases in Scatterometer Wind Retrieval 1715
Oliphant, T.E., and D.G. Long

7. Advanced Techniques for Improving Wind Direction Ambiguity Removal in Scatterometry 1718
Huddleston, J.N., R.D. West, S.H. Yueh and W.Y. Tsai

8. Geophysical Modeling Error in Wind Scatterometry 1721
Johnson, P.E., D.G. Long and T.E. Oliphant

9. Cramer-Rao Bound for Wind Estimation from Scatterometer Measurements 1724
Oliphant, T.E., and D.G. Long

10. Atmospheric Effects on the Wind Retrieval Performance of Satellite Radiometers 1727
West, R.D., and S.H. Yueh

THPED -- Remote Sensing of the Space/Time Characteristics of Water Surfaces

1. Laboratory Studies on Frequency-Wavenumber Spectrum of Short Wind Waves — NA
Hara, T., E.J. Bock and M. Donelan

2. Nonlinearities and Reverse Travelling Energy Observed in Wavenumber-Frequency Spectra of X-Band Ocean Backscatter — 1730
Frasier, S., and R. McIntosh

3. In Situ Measurements of Small Scale Wind-Waves and Their Moduation by Ocean Currents and Atmospheric Forcing — NA
Bock, E.J., T. Hara and J.B. Edson

4. Observed Space-Time Structure of Radar Backscatter from the Ocean Surface — 1733
Hesany, V., W.J. Plant, W.C. Keller and K. Hayes

5. Surface Wave Dispersion Observed With Airborne Spotlight Imaging Systems — NA
Dugan, J.

6. Optical, Radar and In Situ Measurements of Internal Wave Dispersion — 1736
Gotwols, B.L., E. Aarholt, R.D. Chapman and R.E. Sterner II

7. The Coastal Ocean Probing Experiment: Further Studies of Air-Sea Interactions with Remote and In-Situ Sensors — 1739
Kropfli, R.A. and S.F. Clifford

8. The Estimation of Ocean Current From ω-k Analysis of Radar Data — 1742
Lamont-Smith, T.

9. High Resolution Polarimetric Radar Scattering Measurements of Low Grazing Angle Sea Clutter — 1745
Twarog, E.M., D.J. McLaughlin and N. Allan

10. Simultaneous CODAR and OSCR Measurements of Ocean Surface Currents in Monterey Bay — 1749
Fernandez, D.M., and J.D. Paduan

THPES -- Land Cover: Multitemporal Analysis and Change Detection

1. A Comparative Analysis of ERS-1/SAR and Landsat/TM Multitemporarl Scenes for Land Use Studies in Sao Paulo State, Brazil — NA
Damiao, D.P., and H.J.H. Kux

2. A Multitemporal Land-Cover Change Analysis Tool Using Change Vector and Principal Components Analysis — 1753
Parra, G.A., M.C. Mouchot and C. Roux

3. Assessing Inter-Annual Variability for the Central Grassland Region of the US Using the 1990 Seasonal Land Cover Classification — NA
Stretch, L., B. Reed and D. Ojima

4. Land-Cover Dynamics in Eastern Amazonia, 10 Years of Change as Viewed by Landsat TM — NA
Roberts, D.A., G. Batista, J. Pereira and B. Nelson

5. Monitoring Land Cover of the Desert Fringes of the Eastern Nile Delta, Egypt — 1756
El-Khattib, H.M., N.M. El-Mowilhi and F. Hawela

6. Temporally Invariant Classifiers and the Classification of Floristics — NA
Fitzgerald, R.W.

THPES *continued* -- Land Cover: Multitemporal Analysis and Change Detection

7. Retrieval of Forest Parameters from Multitemporal Spaceborne SAR Data 1759
Kurvonen, L., J. Pulliainen, M. Hallikainen and P. Mikkela

8. Monitoring of the Change of Vegetative Conditions Using Multitemporal SAR Data 1763
Suga, Y., S. Takeuchi and H. Tsu

9. C- and L-Band Multi-Temporal Polarimetric Signatures of Crops 1766
Skriver, H., F. Nielsen and A. Thomsen

10. Characterization of Oklahoma Reservoir Wetlands for Preliminary Change Detection Mapping Using IRS-1B Satellite Imagery 1769
Mahlke, J.

THPF -- Microwave Remote Sensing of the Antarctic

1. RADARSAT Antarctica Mapping System: System Overview 1772
Norikane, L., B. Wilson and K. Jezek

2. RADARSAT: The Antarctic Mapping Project 1775
Jezek, K.C., J. Curlander, L. Norikane, F. Carsey, J.P. Crawford, C. Wales and J. Muller

3. The McMurdo Ground Station (MGS): Ready for SAR Acquisition 1777
Wales, C.

4. Calibration of Data from the Antarctic Mapping Mission 1780
Williams, J.

5. A Robust Threshold Retracking Algorithm for Extracting Ice-Sheet Surface Elevations from Satellite Radar Altimeters 1783
Davis, C.H.

6. Individual Weather Correction for Antarctic Sea-Ice Concentration from SSM/I 1788
Thomas, C.H., and G.C. Heygster

7. The Effect of the Grounded Tabular Icebergs in Front of Berkner Island on the Weddell Sea Ice Drift as Seen from Satellite Passive Microwave Sensors 1791
Markus, T.

8. Mueller Matrix Associated with Diffuse Scattering from Two-Dimensional Random Rough Surfaces -- Full Wave Analysis 1794
Lee, B.S., and E. Bahar

THPH -- Optical Remote Sensing Instrumentation and Techniques

1. Development and Present Configuration of the NASA GSFC/WFF Helicopter-Based Remote Sensing System 1797
Walthall, C.L., D.L. Williams, B.L. Markham, J.E. Kalshoven and R.F. Nelson

2. System Requirments for Active Optical Search and Rescue 1800
Field, C.T., and P.S. Millar

3. Shortwave Infrared Spectral Reflectance of Plant Litter and Soils 1803
Nagler, P.L., C.S.T. Daughtry and S.N. Goward

4. Using Laser Echo Recovery and a Scannable Field-of-View Telescope to Determine Vegetation Structure and Sub-Canopy Topography Over Wide Swaths 1806
Blari, J.B., D.J. Harding and D.B. Coyle

5. An Active Optical Remote Sensing System for Vegetation Index Determination 1809
Kalshoven, J.E., and D.P. Rosten

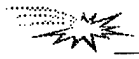
6. Effects of Excitation Wavelength on the Chlorophyll Flourescence Ratio F685/F730 nm 1812
Corp, L.A., J.E. McMurtrey, E.W. Chappelle, M.S. Kim and C.S.T. Daughtry

7. An Improved Aircraft Underflight Instrument for the Derivation of Band Gains in Satellite Sensors 1816
Abel, P., and B. Subramanya

8. Radiometric Corrections of Visible/Infrared Satellite Data Over Terrestrial Environments: Angular, Atmospheric and Topographic Effects 1823
Moreno, J.F.

9. Comparison of Lidar Water Vapor Measurements Using Raman Scatter at 266 nm and 532 nm 1826
Harris, R., F. Balsiger and C.R. Philbrick

10. Computer Modeling of Adaptive Optics and Sites for Telescopes Design 1830
Lukin, V.P.



THPP -- SAR Applications and Signal Processing

1. Mapping Geologic Structure on Barrier Islands Using Polarimetric SAR NA
Slatton, K.C., M.M. Crawford, J.C. Gibeaut and R.O. Gutierrez

2. Integration of SIR-C/X-SAR and Landsat TM Data for Geologic Mapping and Resource Exploration 1833
Wever, T., and M. Frei

3. Retrieval of Man-Made Structures in Siberia with INSAR Techniques Using ERS SAR Data 1836
Streck, C., and O. Hellwich

4. Angular Dependence of SAR Backscatter Around Mt. Taranaki, New Zealand 1839
Pairman, D., and S. Belliss and S. McNeill

5. Edge Detection in Speckled SAR Images Using the Continuous Wavelet Transform 1842
Chabert, M., J.Y. Tourneret and G. Mesnager

6. Heterogeneity in SAR Images NA
Mueller, H.J

7. Intersystem Normalization of Multifrequency Radar Imagery for Discrimination of Unvegetated Lava Surfaces NA
Kaupp, V.H., J.F. Hug, W.P. Waite, H.C. MacDonald and C.M. Ting

8. Removing RF Interferences from P-Band Ariplane SAR Data 1845
Cazzaniga, G., and A. Monti Guarnieri

THPV -- Methods of Data Analysis

1. Hybrid Consensus Theoretic Classification 1848
Benediktsson, J.A., J.R. Sveinsson and P.H. Swain

2. A Framework for Multi-Date Multi-Sensor Image Interpretation 1851
Murni, A., A.K. Jain and J. Rais

3. Optimal Projection Selection for Projection Pursuit in High Dimensional Feature Reduction NA
Velipasaoglu, E.O., and O.K. Ersoy

4. Automated Training Sample Labeling Using Laboratory Spectra 1855
Hsieh, P., and D.A. Landgrebe

5. Modified Divisive Clustering Useful for Quantitative Analysis of Remotely Sensed Data 1858
Prakash, H.N.S., S.R. Kumar, P. Nagabhushan and K.C. Gowda

6. Surface Information Retrieval From Optical/Microwave Data: Potentials and Limits of Synergistic Approaches 1861
Moreno, J.F., and S.S. Saatchi

7. Sensor Data Simulations Using Monte-Carlo and Neural Network Methods 1864
Kiang, R.K.

8. Model-Based Technique for Super Resolution and Enhanced Target Characterization Using a Step-Frequency Radar: A Simulation Study 1867
Chakrabarti, S., P. Kanagaratnam and P. Gogineni

9. Contextual Simulation of Landscape Based on Remotely Sensed Data 1870
Jung, M.,THPF: Microwave Remote Sensing of the Antarctic and M.M. Crawford

10. Intelligent Fusion and Analysis of AIRSAR Data for SEIDAM 1873
Bhogal, A.S., D.G. Goodenough, D. Charlebois, H. Barclay, S. Matwin and O. Niemann

THPZ -- The World's Airborne SAR Facilities II: Extraordinary Frequencies and Special Applications

1. Multi-Channel SAR with Phased Array: The Experimental Airborne System AER-II NA
Ender, J.H.C.

2. The German DO-SAR Sytem Abstract NA
Fritsch, B.

3. The Experimental Airborne VHF SAR Sensor CARABAS: A Status Report 1877
Gustavsson, A., L.M.H. Ulander, L.E. Anderson, P.O. Frolind, H. Hellsten, T. Jonsson, B. Larsson and G. Stenstrom

4. A H igh Resolution, Four-Band SAR Testbed with Real-Time Image Formation 1881
Walker, B., G. Sander, M. Thompson, B. Burns, R. Fellerhoff and D. Dubbert

5. The Lincoln Laboratory Millimeter-Wave Synthetic Aperture Radar NA
Murphy, T.J., and J.C. Henry

6. ONERA Airborne SAR Facilities NA
Boutry, J.M.

7. The Army Research Laboratory Ultra Wideband BoomSAR
Ressler, M.A. 1886

8. Status of the SASAR System 1889
Inggs, M.

9. Overview of the P-3 UWB SAR System NA
Sheen, D.R., and T.B. Lewis

10. YSAR: A Compact, Low-Cost Synthetic Aperture Radar 1892
Thompson, D.G., D.V. Arnold, D.G. Long, G.F. Miner and T. Karlinsey

FAAM -- Land Cover Characterization Using BRDF Models and Data

1. Nadir and Bidirectional Surface Measurements of Arctic Tundra: Site Differentiation and Vegetation Phenology Early in the Growing Season 1897
Vierling, L.A., D.W. Deering and T.F. Eck

2. Analysis of Airborne POLDER Data on Boreal Forest Covers 1901
Bicheron, P., M. Leroy and O. Hautecoeur

3. Variability of BRDF with Land Cover Type for the West Central HAPEX-Sahel Super Site 1904
Brown de Colstoun, E.C., C.L. Walthall, A.T. Cialella, E.R. Vermotel, R.N. Halthore and J.R. Irons

4. Use of BRDF Models to Normalize Angular Reflectances to NADIR for Temporal Compositing Schemes NA
Jia, S., A.R. Huete and W.J.D. van Leeuwen

5. Detection and Correction of the Bidirectional Effects in AVHRR Measurements Over Northern Regions NA
Li, Z., J. Cihlar, X. Zheng and L. Moreau

6. Conifer Shoot Bidirectional Scattering: Methodology and Preliminary Results 1908
Walter-Shea, E.A., M.A. Mesarch and L. Chen

7. Assymmetry in the Diurnal Variation of Surface Albedo 1911
Mayor, S., W.L. Smith, Jr., L. Nguyen, T.A. Alberta, P. Minnis, C.H. Whitlock and G.L. Schuster

FAAA -- Active Remote Sensing of the Lower Atmosphere

1. Retrieval of Boundary-Layer Turbulence Using Spaced-Antenna Wind Profilers 1914
Holloway, C.L., R.J. Doviak, S.A. Cohn and R.J. Lataitis

2. A Buoy-Mounted Wind Profiler for Remote Measurement of Ocean Winds 1917
Mead, J.B., P.M. Langlois and R.E. McIntosh

3. Frequency Domain Interferometry in the Planetary Boundary Layer: First Results 1920
Corner, B.R., R.D. Palmer and R.M. Narayanan

4. A Digital Beamforming Radar Profiler for Imaging Turbulence in the Atmospheric Boundary Layer 1923
Mead, J.B., G. Hopcraft, B. Pollard, R.E. McIntosh

5. Preliminary Results From the Arecibo 430 MHz Spatial Interferometry System 1926
Howell, P.B., R.D. Palmer, R.M. Narayanan, M.F. Larsen and J.Y.N. Cho

6. Measurements of Vertical Velocities and Divergence in the Atmosphere Using the MU Radar in Japan 1929
Ren, Y., R.D. Palmer, S. Fukao, M. Yamamoto and T. Nakamura

FAAA *continued* -- Active Remote Sensing of the Lower Atmosphere

7. Structure of the Atmosphere in an Urban Planetary Boundary Layer from Lidar and Radiosonde Observations — NA
Eichinger, W., and D. Cooper

8. Volume Imaging Lidar Observations of the Convective Boundary Layer — NA
Eloranta, E., and A. Piironen

9. Low-level Jet Detection in Snow with a Noncoherent Weather Radar — NA
Melnikov, V.M., and A.V. Ryzhkov

FACP -- Subsubsurface Electromagnetic Sensing at Deeper Depths

1. Radar Sounding of Glaciers in Greenland — 1932
Allen, C., B.P. Wolhletz and S. Gogineni

2. Sensing of Gradient Electromagnetic Fields from Subsurface Conducting Targets — 1935
Cress, D.H., and L.C. Bartel

3. Modeling the Electromagnetic Detection of Buried Cylindrical Conductors — 1938
Moses, R.W., R.E. Kelly and J.M. Mack

4. Marine Sediment Mapping with Airborne Electromagnetics — NA
Mozley, E.C., and J. Reynaud

5. Electromagnetic Modeling of Subsurface 3D Structures — 1941
Newman, G.A., and D.L. Alumbaugh

6. Demonstration of the Lasi High-Resolution Electromagnetic Sounding System at the Nevada Test Site — NA
Sternberg, B.K., and M.M. Poulton

7. Statistical Law of Surface Impedance Distribution — 1945
Bashkuev, Yu.B., V.B. Haptanov and L.H. Angarkhaeva

8. The Prediction Map of Geoelectric Sections of Australia, New Zealand and New Guinea — 1947
Bashkuev, Yu.B., V.R. Advokatov and L.H. Angarkhaeva

9. The Influence of Ground Stratification Upon a Field of Magnetic Loop — 1950
Dmitriev, W.V.

FAED -- Remote Sensing of Littoral Submesoscale Processes III

1. Frontal Signatures in Radar Imagery — NA
Vogelzang, J., K.G. Ruddick and J.B. Moens

2. Detection and Location of Internal Waves in Ocean SAR Images by Means of Wavelet Decomposition Analysis — 1953
Rodenas, J.A., and R. Carello

3. Imaging the Multiscale Structure of Atmospheric Turbulence Using Satellite-Based Synthetic Aperture Radar (SAR) — NA
Mourad, P.D.

4. Spectral Analysis of Non-Stationary Ocean SAR Images Using the Wigner-Ville Transform — 1956
Grassin, S., R. Garello and M. Prevosto

5. Results of Airborne Backscatter Measurements During the Surface Wave Dynamics Experiment 1959
Nghiem, S.V., F.K. Li G. Neumann and S.H. Lou

6. Quantitative Analysis of Radar Signatures of Underwater Bottom Topography According to a Bragg-Based Composite Surface Model 1962
Romeiser, R.

7. Near Nadir Microwave Specular Returns From the Sea Surface -- Measurements of Winds From Breeze to Hurricane 1965
Wu, J.

8. Spectral Variations of Sea Surface Emission at MM-Wave Frequencies Under Influence of Synoptical Oceanic Eddies 1968
Cherny, I.V., and V.P. Nakonechny

9. Examination of Sea Surface by Airborne Microwave Radar and Radiometers in Joint US/Russia Internal Waves Remote Sensing Experiment NA
Kuzmin, A.V., M.I. Mityagina and V.V. Yakovlev

10. Surface Wave Observation in the Gulf Stream Area Using ALMAZ-1 SAR 1971
Grodsky, S.A., V.N. Kudryavtsev, A.Y. Ivanov, V.A. Zaitsev and D.M. Solov'ev

FAES -- Land Cover: Agricultural

1. Land Cover Mapping in the Eastern Slopes of the Andes Using ERS-1 and Landsat Data NA
Echavarria, F.R., and C. Keithley

2. A Multisensoral Approach for Landuse Classifications and Grassland Monitoring Based on the Possibility Theory 1974
Stolz, R., and W. Mauser

3. Spectral Angle Mapper Classification and Vegetation Indices Analysis for Winter Cover Monitoring Using JERS-1 OPS Data 1977
Kim, C., and S. Cho

4. Comparison of Classification Techniques for Agricultural Crops Using Temporal Multiparameter Airborne DLR E-SAR Images NA
Schmullius, C., S. Erasmi and P. Hurlemann

5. SIR-C Polarimetric Backscatter Features of Agricultural Land Cover Types Early and Late During the Growing Season 1980
Davidson, M.W.J., R. Steingießer, W. Kuhbauch, F. Vescoui and F. Tano

6. Use of ERS-1 SAR Data for Field Rice Mapping and Rice Crop Parameters Retrieval 1983
Ribbes, F., and T. Le Toan

7. Textural Processing of Multi-Polarization SAR for Agricultural Crop Classification 1986
Treitz, P.M., O.R. Filho, P.J. Howarth and E.D. Soulis

8. Early Diagnostic of Disease Erisiphe Graminis with Using Remote Sensing Measurements NA
Kazandjiev, V.

9. Study on Auto-Extraction of Winter Wheat Planting Area from TM Image Based on Pattern Recognition Technology 1989
Yang, X., N. Wang and P. Qin

10. Spring Wheat Yield Prediction for Western Canada Using Weekly NOAA AVHRR Composites 1992
Hochheim, K.P., D.G. Barber and P.R. Bullock

FAF -- Microwave Remote Sensing of Snow

1. Snow and Ice Observations During the European Multi-Sensor Airborne Campaign in 1995 — 1995
Noll, J., M. Wooding and E. Attema

2. Overview of EMAC-95 Snow and Ice Airborne Campaign in Finland — 1998
Hallikainen, M., P. Ahola, K. Rautiainen, J. Pihlflyckt, T. Tirri, M. Makynen, J. Lahtinen, H. Servomaa, P. Makkonen, J. Grandell, M. Kemppinen, M. Nikulainen, H. Taskinen, S. Tauriainen and M. Roschier

3. First Results From EMAC '95 Snow Experiment in Norway — NA
Guneriussen, T., R. Solberg, K. Sand, J. Noll and D. Weydal

4. Estimation of Snow Water Equivalence Using SIR-C/X-SAR — 2002
Shi, J., and J. Dozier

5. Estimation of Snow Water Equivalent Using Passive Microwave Radiation Data — 2005
Tait, A.

6. Microwave Remote Sensing of Snow: Modeling and Measurements — NA
Hallikainen, M., J. Grandell, T. Pyhalahti and V. Jaaskelainen

7. Scattering and Emission from Dry Snow in the Range 35-120 GHz — 2008
Tjuatja, S., A.K. Fung and J.C. Comiso

8. Multi-Frequency FMCW Radar Profile of Snow Cover — NA
Koh, G., and N.E. Yankielun

9. Observations of Snow Crystal Shape in Cold Snowpacks Using Scanning Electron Microscopy — 2011
Foster, J.L., D.K. Hall, A.T.C. Chang, A. Rango, W. Wergin and E. Erbie

10. Dramatic Decrease in Radar Cross Section over Greenland Observed by the ERS-1 Scatterometer Between 1991 and 1995 — 2014
Wismann, V.R., and K. Boehnke

FAH -- UWB and Ground Penetration Radar

1. An Ultrawideband Imaging Radar for Sea Surface Studies — 2017
Sletten, M.A., and D.B. Trizna

2. Development of a Low Cost SFCW Ground Penetrating Radar — 2020
Langman, A., S.P. Dimaio B.E. Burns and M.R. Inggs

3. A Range Algorithm for Ground Penetrating Radar — 2023
Caffey, T.W.H.

4. Results of a Remote Sensing Experiment Using a Low Frequency Ultra-Wideband SAR to Investigate the Phenomenology of Landmines — 2027
Sturgess, K., L. Happ, J. Kurtz and M. Collins

5. Processing the Ground Penetrating Radar Data Using Its Correlation Property — NA
Jen, L., J. Li and M.X. Wang

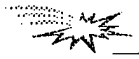
6. Signal Processing Aspects of Polarimetric Random Noise Radar Data for Shallow Subsurface Imaging — 2030
Xu, Y., P.D. Hoffmeyer, R.M. Narayanan and J.O. Curtis

7. An Interferomic Techniques for Synthetic Aperture Ground-Penetrating Radar 2033
Leuschen, C., N. Goodman, C. Allen and R. Plumb

8. Subsurface Imaging Using Ground-Penetrating Radar Measurements 2036
Goodman, N., C. Leuschen, R. Plumb and C. Allen

9. Multi-Layer Detection Tracking for Monostatic Ground Penetrating Radar 2038
Rampa, V., and U. Spagnolini

10. Analysis of Response of the Electromagnetic Induction for Detecting of Buried Objects 2041
Zhu, K.



FAP -- SAR Interferometry Processing Algorithms

1. Region Growing Algorithm for InSAR Phase Unwrapping 2044
Xu, W., and I. Cumming

2. A Comparison of Phase Unwrapping Techniques NA
Collins, J.D., G. Sessenrath and N. Marechal

3. A Theoretical Analysis on the Robust Phase Unwrapping Algorithms for SAR Interferometry 2047
Fornaro, G., G. Franceschetti, R. Lanari and E. Sansosti

4. SAR Interferometry: A Multigrid Markdown Approach to Phase Unwrapping with a Discontinuity Model NA
Labrousse, D., and M. Berthod

5. A Multiresolution Approach to Improve Phase Unwrapping 2050
Davidson, G.W., and R. Bamler

6. Maximum Entropy Solution for Interferometric SAR Phase Unwrapping 2054
Datcu, M.

7. Consistent 2-D Phase Unwrapping Guided by a Quality Map 2057
Flynn, T.J.

8. Absolute Phase Determination in SAR Interferometry 2060
Chiaradia, M.T., L. Guerriero, G. Pasquariello, A. Refice and N. Veneziani

9. Determination of Absolute Interferometric Phase Using the Beam-Amplitude Ratio Technique 2063
Bickel, D.L., and W.H. Hensley



FAV -- Method of Data Analysis

1. Multisource Data Integration Using Neural Networks: Optimal Selection of Net Variables for Lithologic Classification 2068
Yang, G., M.J. Collins and P. Gong

2. Multisensor Data Analysis Based on Neural Networks NA
Blonda, P., G. Pasquariello, V. la Forgia, A. Bennardo, G. Stalino, R. Sergi and R. Loizzo

3. A Completely Fuzzy Classification Chain for Multispectral Remote Sensing Images 2071
Gamba, P., A. Marazzi, A. Mecocci and P. Savazzi

4. A Raster-Based Fuzzy Expert System for Forestry Evolution 2074
Saint-Joan, D., and J. Desachy

FAV *continued* -- Method of Data Analysis

5. Evolving Feature-Extraction Algorithms: Adapting Genetic Programming for Image Analysis in Geoscience and Remote Sensing 2077
Daida, J.M., T.F. Bersano-Begey, S.J. Ross and J.F. Vesecky

6. Radar Imaging of Three-Dimensional Targets in the Laboratory 2080
Bertrand, J., and P. Bertrand

7. Use of Confocal Techniques in the Generation of Three Dimensional Images Using Conventional SAR NA
Byrd, M., A.J. Blanchard and B. Krenek

8. Reconstrucion of Complex Dielectric Profiles via Quadratic Models 2083
Pierri, R., T. Isernia, V. Pascazio and A. Tamlourrino

9. Topographic Measurements Using Polarimetric SAR Data 2086
Schuler, D.L., J.S. Lee and G. De Grandi

10. A New Method for Extracting Topographic Information From a Single Multispectral Image 2089
Carlotto, M.J.

FAZ -- Surface Temperatures: Observations and Applications

1. Thermal Emission from Rough Terrain: Anisotropy and Its Possible Consequences on Satellite Image Interpretation 2092
Jamsa, S.

2. Validation of Land-Surface Temperature Retrieval from Space 2095
Wan, Z., W. Snyder and Yulin Zhang

3. Model Simulations of the Effect of the Atmosphere on the Remote Sensing of Earth Surface Parameters with the Advanced Very High Resolution Radiometer NA
Rao, C.R.N., and N. Zhang

4. Land Surface Temperature Retrieval From AVHRR: Influene of Surface Emissivity and Atmospheric Water Vapor 2098
Steyn-Ross, M.L., and D.A. Steyn-Ross

5. TIR Observations in FIFE From Field, Aircraft and Satellite Platforms 2101
Schmugge, T.J., and G.M. Schmidt

6. A Simple Method for Estimating Surface Energy Fluxes and Air Temperatures From Satellite Observations 2104
Anderson, M.C., J.M. Norman, G.R. Diak and W.P. Kustas

7. Unmixing of Satellite Thermal Images: Simulation and Application to TM/Landsat Data 2107
Zhukov, B., D. Oertel, F. Lehmann and P. Strobl

8. SSM/I-Based Surface Temperature Retrieval Method for Boreal Forest Zone 2110
Pullianinen, J., J. Grandell and M. Hallikainen

9. Analyzing Thermal Properties of Forests Using Multitemporal Space Borne Thermal Data NA
Lohi, A., and Y. Awaya

10. Visualisation of Urban Surface Temperatures Derived from Satellite Images 2113
Nichol, J.

FPAM -- Rough Surface Scattering Effects on Remote Sensing of Terrain

1. A Further Study of the IEM Surface Scattering Model 2116
Fung, A.K., and C.Y. Hsieh

2. On the Use of the Quasi Specular Model for Surface Parameter Estimation 2119
Marchand, R., and G.S. Brown

3. Electromagnetic Scattering from Slightly Rough Surfaces with Inhomogeneous Dielectric Profile 2122
Sarabandi, K., and T. Chiu

4. Electromagnetic Wave Scattering From Real-Life Rough Surface Profiles and Profiles Based on Averaged Spectrum 2125
Pak, K., L. Tsang, R. Weeks, J.C. Shi and H. Rott

5. Analytical, Experimental, and Numerical Studies of Angular Memory Signatures of Waves Scattered from One-Dimensional Rough Surfaces 2128
Kuga, Y., C.T.C. Le and A. Ishimaru

6. The SIR-C/X-SAR Experiment: The Sensitivity of Microwave Backscattering to Surface Roughness of Bare Soils 2131
Coppo, P., G. Macelloni, P. Pampaloni, S. Paloscia and S. Sigismondi

7. Using SIR-C SAR and Cloude's Decomposition for the Determination of Soil Moisture in Vegetated Areas 2134
Chadwick, D.J., and J.R. Wang

8. Interferometric Technique of Determining the Average Height Profile of Rough Surfaces 2137
Ishimaru, A., C.T.C. Le, Y. Kuga, J.H. Yea, K. Pak and T.K. Chan

9. Detection of a Target in a Inhomogeneous Medium Using Angular Correlation Function 2140
Chan, T.K., Y. Kuga and A. Ishimaru

10. Numerical Study of Detection of a Buried Object Under a Single Random Rough Surface with Angular Correlation Function 2143
Tsang, L., G. Zhang and K. Pak

FPAA: Earth Radiation Budget

1. Remote Sensing of Land Surface Temperature: The Directional Viewing Effect 2146
Smith, J.A., N. Chauhan and J. Ballard

2. A Simulation of Topographic Solar Radiative Forcing over a Mountainous Region Using Geostationary Satellite Data 2149
Loechel, S., R.O. Dubayah, J. Barnett, C. Gautier and M. Landsfeld

3. Modeling Area-Averaged Fluxes over Partially Vegetated Land Surfaces Using Aircraft and In-Situ Thermal Data 2152
Friedl, M.A.

4. A One-Dimensional Hydrology/Radiobrightness Model for Freezing/Thawing Bare Soils 2155
Liou, Y.A., and A.W. England

5. On the New Long-Wave Radiation Determination from Satellite Data 2158
Xue, Y., S.P. Lawrence and D.T. Llewellyn-Jones

FPAA *continued* -- Satellite Measurements

6. Landsat 7 System Design Overview 2160
Andary, J., P. Spidaliere, S. Jurczyk and T. Arvidson

7. Landsat 7 and Beyond 2161
Irons, J.R., D.L. Williams and B.L. Markham

8. Reducing the Effects of Space-Varying Wavelength-Dependent Scattering in Multispectral Imagery 2164
Carlotto, M.J.

9. RADARSAT for Landuse Monitoring: Early Results NA
Brown, R.J., T.J. Pultz, B.G. Brisco, Y. Crevier and L. Tighe

FPCP -- Surface Scattering

1. An Exact Technique for Calculating Low Grazing Angle Backscatter from Rough Surfaces NA
Kasilingam, D.

2. Fractal Analysis of Bidimensional Profiles and Application to Electromagnetic Scattering of Soils 2167
Rouvier, S., P. Borderies, I. Chenerie, J.C. Souyris, T. Le Toan and N. Floury

3. Like and Cross Polarized Cross Sections for Two Dimensional Random Rough Surfaces: Bistatic Single and Double Scatter 2170
El-Shenawee, M., and E. Bahar

4. A Knowledge-Based Inversion of Physical BRDF Model and Three Examples 2173
Li, X., and A. Strahler

5. Scattering Cross Sections of Composite Rough Surfaces New Unified Full Wave Solutions 2177
Bahar, E., and Y. Zhang

6. Scatter Cross Sections for Two-Dimensional Random Rough Surfaces-Full Wave Analysis 2180
Bahar, E., and B.S. Lee

7. The Measured Polarized Bidirectional Reflectance Distribution Function of a Spectralon Calibration Target 2183
Betty, C.L., A.K. Fung and J. Irons

8. Energy Conservation in Soil Surface Scattering in the Optical Region 2186
Li, Z., A.K. Fung, S. Tjuatja, C. Betty and J. Irons

9. Optical Versus Radar Roughness in Agricultural Tillage 2189
Colpitts, B.G.

10. The Soil Surface Reflectivity in the Partial Coherent Microwaves at the Frequencies 300 and 900 MHz 2192
Bobrov, P.P., and I.M. Schetkin

FPED -- Laboratory Studies of Ocean Surface Scattering

1. Laboratory Investigations of the Hydrodynamics and Radar Backscattering Properties of Breaking Waves 2195
Meadows, G., E.B. Dano, D.R. Lyzenga, H. VanSumeren, R. Onstott and D.E. Lund

2. Doppler Characteristics and Angular Dependence of Radar Backscatter From Laboratory Breaking Waves 2198
Dano, E.B., D.R. Lyzenga and G. Meadows

3. Dependence of Polarimetric Doppler Spectra on Breaking-Wave Energy 2201
Lee, P.H.Y., J.D. Barter, K.L. Beach, B.M. Lake, H. Rungaldier, J.C. Shelton, H.R. Thompson, Jr., and R. Yee

4. Laboratory Study of the Fine Structure of Breaking Waves for Scatterometry Applications 2204
Rozenberg, A., W.K. Melville and M. Ritter

5. Small Grazing Angle Radar Scattering from a Breaking Water Wave: Demonstration of Brewster Angle Damping 2207
West, J.C., J.M. Sturm and M.A. Sletten

6. Dominant Wave Effects in Wavetank Measurement of Microwave Doppler Spectra 2210
Plant, W.J., V. Hesany, W.C. Keller and M.A. Donelan

7. Comparison of Experimental and Theoretical Ocean Wavenumber Spectra for Gravity-Capillary and Capillary Waves NA
Keller, M.R., and B.L. Gotwols

8. Depolarization in Microwave Scatterometry 2213
Lee, P.H.Y., J.D. Barter, K.L. Beach, B.M. Lake, H. Rungaldier, J.C. Shelton, H.R. Thompson, Jr., and R. Yee

9. Influences of Wind Bursting on Radar Return 2216
Savtchenko, A., S. Tang and J. Wu

10. Measuring Small-Scale Water Surface Waves: Nonlinear Interpolation and Integration Techniques for Slope-Image Data 2219
Daida, J.M., R.R. Bertram, D.R. Lyzenga, C. Wolf, D.T. Walker, S.A. Stanhope, G.A. Meadows, J.F. Vesecky and D.E. Lund

FPES -- Spatial Decision Support Systems: Cost/Benefit Analysis

1. Remote Sensing: Economic Viability Environmental Monitoring 2222
Macauley, M.K., and T.J. Brennan

2. Ecosystem Management: A Decision Support GIS Approach 2225
Ji, W.

3. Dawn of a New Era: The Image Information Age 2228
Jordan, III, L.E.

4. Non Point Source Pollution 2231
Subra, W., and J. Waters

5. A Genetic Approach to Ecosystem Modeling: Do the Benefits Warrant the Costs? NA
Morain, S., and A. Budge

6. Cost-Effective Environmental Consulting Using Geographic Information Systems and Remote Sensing 2234
Gibas-Tracy, D.R.

FPES *continued* -- Spatial Decision Support Systems: Cost/Benefit Analysis

7. Land Surface Remote Sensing and Geographical Information Systems for Water Quality Modeling 2237
Mattikalli, N.M., and E.T. Engman

8. Satellite Remote Sensing and Geographic Information System for Monitoring Morphodynamics of the Active Yellow River Delta, China 2240
Yang, X., M.C.J. Damen, R. van Zuidam, A. van Gelder, J.H. van den Berg and G. Chen

9. Remote Sensing and Core Data Needed to Support Planning and Policy Decision Making 2242
Foresman, T.W., J.E. Estes, J.J. Garegnani and D.L. Porter

FPF -- Snow, Glaciers and Permafrost

1. Analysis of Snow Cover in Alaska Using Aircraft Microwave Data (April 1995) 2246
Hall, D.K., J.L. Foster, A.T.C. Chang, D.J. Cavalier, J.R. Wang and C.S. Benson

2. Estimation of Snow Surface Albedo Using Landsat Thematic Mapper 2249
Shi, J., T.H. Painter and J. Dozier

3. Estimating Alpine Snow Cover with Unsupervised Spectral Unmixing 2252
Rosenthal, W.

4. Airborne and Spaceborne SAR Interferometry: Application to the Athabasca Glacier and Area 2255
Vachon, P.W., D. Geudtner, L. Gray, K. Mattar, M. Brugman, I. Cumming, and J.L. Valero

5. Effects of System Errors on Combined MM/IR Neural Network Inversion of Surface Snow Properties 2258
Jackson, S.R., and R.M. Narayanan

6. Machine-Based Snow Line Determination and the Identification of Ice Sheet Features in Visible and SAR Imagery 2261
Lin, I.I., and W.G. Rees

7. Thawing of Soils in Siberia Observed by the ERS-1 Scatterometer Between 1992 and 1995 2264
Boehnke, K., and V.R. Wismann

8. Passive Microwave Freeze/Thaw Classification for Wet Tundra Regions 2267
Kim, E.J., and A.W. England

9. Freeze / Thaw Classification for Prairie Soils Using SSM/I Radiobrightnesses 2270
Judge, J., J.F. Galantowicz, A.W. England and P. Dahl

FPH -- Advanced Sensors

1. Integrating Global Positioning Systems with Satellite Remote Sensing: Avoiding Major Pitfalls 2273
Leavitt, B.C., and S.L. Payton

2. Remote Sensing with Hyperspectral Imagery Using DASI -- An Imaging Interferometer 2276
Hammer, P.D., D.L. Peterson, W.H. Smith, S.E. Dunagan, L.F. Johnson, A.W. Strawa, J. Zott and G. Langford

3. Multi-Mission Radar Altimeter: Concept and Performance 2279
Jensen, J.R., and R.K. Raney

4. Backscatter Characteristics of Buried Targets Measured Using an Ultrawideband Polarimetric Random Noise Radar 2282
Hoffmeyer, P.D., Y. Xu, R.M. Narayanan and J.O. Curtis

5. Airborne 14-Channel Microwave Radiometer HUTRAD 2285
Hallikainen, M., M. Kemppinen, K. Rautiainen and J. Pihlflyckt

6. Experimental Investigation of Diffraction Gratings for Millimeter/Submillimeter-Wave Instruments 2288
Nadimi, S.A., J.W. Bredow and G.C. May

7. Ground Segment for ERS-2 GOME Sensor at the German D-PAF 2291
Balzer, W.

8. Dual Polarized L-Band Microstrip Patch Array for the AIRSAR/TOPSAR System 2294
Rostan, F., W. Wiesbeck and J.J. van Zyl

9. Self-adapting Sensor for Atmospheric Electricity Measuring 2297
Yanovsky, F.J.

10. Spectrometry From Airborne Platforms: Examples and Analysis of the Italian Research Council (CNR) MIVIS Campaigns Over Different Test Sites NA
Bianchi, R., R.M. Cavalli and S. Pignatti



FPP -- Land Cover: Inventory and Monitoring

1. Integration of Multispectral Land Ecological Data for Characterizing Montane Meadow Communities in the Greater Yellowstone Ecosystem 2300
Jakubauskas, M.E., D. Debinski and K. Kindscher

2. Case-Based Reasoning and Software Agents for Intelligent Forest Information Management 2303
Charlebois, D., D.G. Goodenough, A.S. Bhogal and S. Matwin

3. The Suitability of Future High-Resolution Satellite Imagery for Forest Inventory 2307
Solberg, R., A.H. Schistad Solberg, H. Koren and K. Aas

4. Applications of Multi-Frequency, Multi-Polarization and Multi-Incident Angle SAR Systems in Urban Land Use and Land Cover Mapping 2310
Xia, Z.G.

5. Variations in Land Cover Areas Estimated from Remotely Sensed Data 2315
Yang, W., and J.W. Merchant

6. Recent Experiences in Mapping Land Cover From AVHRR Data: People's Republic of China Test Sites 2318
Qiu, Z., L. Yang and T.R. Loveland

7. Validating Global Landcover Classification Pattern Using Spatial Resoluton -- Independent Landscape Metrics 2321
Frohn, R.C., and J.E. Estes

8. Using Geoinformation System and Space Imagery to Monitor Environmetal Changes in the Aral Sea Ecological Disaster Area 2324
Glushko, E.V., A.V. Ptichnokov and V.S. Tikunov

9. Limitations for Multispectral Classification of Temperate Forests -- Scaling Problems of Groundtruth and Satellite Data 2326
Kellenberger, T.W., and K.I. Itten

FPV -- SAR Geocoding and Orthorectification

1. Practical SAR Orthorectification 2329
Pierce, L., J. Kellndorfer, F. Ulaby and L. Norikane

2. Optimization of the Tie-Pointing Procedure for the Terrain Correction of SAR Data 2332
Roth, A., W. Knoepfle and M. Matschke

3. Applicability of Automatic Tie-Pointing for Geocoding and Mosaicking of Overlapping SAR Images NA
Raggam, H., A. Bauer and W. Hummelbrunner

4. Geocoding and Classification of ERS/JERS-1 Composites 2335
Kellndorfer, J.M., M.C. Dobson and F.T. Ulaby

5. Experiences In Multi-Sensoral SAR Geocoding 2338
Roth, A., D. Kosmann, M. Matschke, B. Mueshen and H. John

6. Design, Performance and Technology Aspects in Relation to a Next Generation High Resolution Spaceborne SAR Instrument 2341
Bottger, H., C.Heer and J.J. Wilson

7. Development of a High-Resolution Ground-Based Synthetic Aperture Radar 2344
Morrison, K., and J.C. Bennett

8. Integrated Design of Synthetic Aperture Radars for Unmanned Aircraft 2347
Vesecky, J.F., and J.M. Cornwall

9. ER-2 IFSAR Digital Terrain Matrix Collection System 2349
Malliot, H.A.

FPZ -- Vegetation Properties

1. Novel Algorithms for Remote Sensing of Chlorophyll Content in Higher Plant Leaves 2355
Gitelson, A.A., M.N. Merzlyak and Y. Grits

2. Chlorophyll Flourescence Measurements of Several Plant Species Compared with MNDVI-Images in Air Pollution Affected Sites in Varanger, Northern Norway NA
Tommervik, H.

3. An Approach for Mapping Light-Use Efficiency on Regional Scales Using Satellite Observations 2358
Norman, J.M., M.C. Anderson and G.R. Diak

4. Detecting Spatial and Temporal Patterns of Aboveground Production in a Tallgrass Prairie Using Remotely Sensed Data 2361
Su, H., J.M. Briggs, A.K. Knapp, J.M. Blair and J.R. Krummell

5. Assimilation of Shortwave Remote Sensing Observations Within an Agrometeorological Model -- Crop Production Estimation 2366
Moulin, S., A. Fischer and G. Dedieu

6. Mapping Field Crop Evapotranspiration Using Airborne Multispectral Imagery 2369
Ahmed, R.H., and C.M.U. Neale

7. Effects of Shadows on Vegetation Indices 2372
Huemmrich, K.F.

8. Multisensor Estimation of Vegetation Characteristics 2375
Zhang, J., R.M. Narayanan, B.T. Tracy, B.L. Gwilliam, R.L. Bolus, T. Pangburn and H.L. McKim

9. Subpixel Spatio Temporal Pattern Analysis of Remote Sensing Observations for Predicting Grassland Ecological and Biophysical Parameters 2377
Csillag, F., A. Davidson , S. Mitchell, B. Wylie, D. Wedin, H. Peat and M. Kertesz

10. Retrieval of Crop Biomass in 1989 by Using ANN MODEL of 1988 2380
Jin, Y.Q.



IGARSS'96

1996 International Geoscience and Remote Sensing Symposium

Technical Papers

Nadir and Bidirectional Surface Measurements of Arctic Tundra: Site Differentiation and Vegetation Phenology Early in the Growing Season

Lee A. Vierling
Department of Environmental, Population, and Organismic Biology, University of Colorado
Boulder, CO 80309-0334
tel: (303) 492-5130, FAX: (303) 492-5070, email: leev@hypatia.colorado.edu

Donald W. Deering
Biospheric Sciences Branch, NASA/Goddard Space Flight Center
Mail Code 923, Greenbelt, MD 20771. email: ddeering@ltpmail.gsfc.nasa.gov

Thomas F. Eck
Hughes/STX, NASA/Goddard Space Flight Center
Mail Code 923, Greenbelt, MD 20771. email: teck@ltpmail.gsfc.nasa.gov

Abstract -- Ground-based nadir and bidirectional radiometric measurements were collected on the North Slope of Alaska in early June to determine their utility in differentiating arctic tundra vegetation community types and examining differences in vegetation community structure and phenology. Three common arctic vegetation types were sampled: lowland wet sedge, tussock tundra essentially devoid of woody vegetation, and tussock tundra with dwarf woody shrub vegetation. Nadir measurements alone allowed spectral differentiation between the wet sedge site and the two tussock tundra sites, but did not allow clear discrimination between the two tussock tundra sites. Bidirectional reflectance measurements, however, permitted good discrimination between the two tussock tundra sites. This outcome is largely due to the fact that normalized difference vegetation index (NDVI) values derived from measurements taken at large view zenith angles were sensitive to the woody plant foliage that extends above the hummocky tussock tundra surface early in the growing season.

INTRODUCTION

Arctic latitudes are expected to undergo pronounced warming with continued increases of global atmospheric greenhouse gases [1]. Such warming will likely influence arctic ecosystems because permafrost, the dominant control on tundra ecosystem processes, is highly sensitive to temperature fluctuation [1, 2]. Shifts in arctic tundra ecosystem processes are likely to be expressed through changing vegetation phenology and species composition. For example, Chapin et al. [2] report that increases in deciduous shrub cover have accompanied arctic warming over the last decade.

Remote sensing may provide a viable means for estimating and monitoring large-scale shifts in tundra species composition [3]. Several investigators have recently conducted ecological remote sensing studies at arctic latitudes [4-12]. Of these studies, only Whiting et al. [12] considered and incorporated bidirectional reflectance measurements of the tundra canopy. However, no previous study characterizes the bidirectional reflectance of arctic tundra in detail.

Here, we report field bidirectional measurements of arctic tundra collected on the North Slope of Alaska. We specifically address the following research questions: 1) How may bidirectional reflectance measurements aid in differentiating arctic tundra vegetation community types in northern Alaska?, and 2) What aspects of arctic tundra vegetation structure and phenology are revealed in the early growing season when supplementing nadir views with multiple-view radiometric measurements?

SITE DESCRIPTION

Radiometric characteristics of arctic tundra were measured at three sites on Alaska's North Slope between June 5-13, 1995. The three sites are situated roughly on a north-south transect along the Dalton Highway and represent three different types of tundra vegetation. The northernmost site (69°38'N, 148°40'W, elev. 96 m) is located in a wet coastal lowland zone dominated by sedges. The second site (69°25'N, 148°42'W, elev. 332 m) lies on the northern flank of the Brooks Range foothills and is comprised of tussock tundra vegetation that is essentially devoid of woody deciduous shrub vegetation. At this site, sedges dominate the tussocks while evergreen species and mosses comprise the majority of the inter-tussock areas. Similar tussock tundra occurs at the third, southernmost site (69°11'N, 148°50'W, elev. 529 m), but the landscape at this site also contains a significant cover of low-growing woody deciduous shrub species.

The phenological state of the vegetation differed among sites at the time of field sampling. At the wet sedge site, the vegetation was highly senescent with virtually no photosynthetically active tissue contained in the canopy. The two tussock tundra canopies both contained a mix of standing dead (mostly sedges) and green vegetation (*Sphagnum* moss and evergreen shrubs), with the woody tussock tundra site exhibiting additional greenness due to emergent deciduous shrub foliage. Due to time and resource limitations, we did not conduct comprehensive biomass harvests to quantify the biomass fractions (green and senescent) at each site.

0-7803-3068-4/96$5.00©1996 IEEE

INSTRUMENTATION AND METHODS

Two field radiometers served as the primary instrumentation in this study. The first was the Portable Apparatus for Rapid Acquisition of Bidirectional Observations of the Land and Atmosphere (PARABOLA), a unique three-channel radiometer capable of measuring radiance over almost the complete (4π) sphere [13]. The PARABOLA's three channels reside in the red (650-670 nm), near infrared (810-840 nm), and shortwave infrared (1620-1690 nm) spectral regions, respectively. The second primary instrument was the Personal Spectrometer II (PS-II; Analytical Spectral Devices, Boulder, CO), a commercially available diode-array field spectroradiometer capable of rapidly gathering contiguous, narrowband (4 nm) spectral data ranging from 350-1050 nm.

A flat, near-horizontal (slope <5°) sampling area was selected for measurements at each site. A tripod/boom platform supported the PARABOLA during sampling, allowing data acquisitions from ~4.0 m above the tundra surface. Before and after each set of data acquisitions, the PARABOLA was leveled at ~0.3 m above a painted, calibrated barium sulfate reference panel to gather spectral incident radiance data.

Nadir spectra were acquired at each site by walking line transects with the PS-II spectrometer and sampling at points spaced 3 m apart from a height of ~1.4 m. Reference spectra of the same barium sulfate panel used with the PARABOLA were taken before and after each transect plot sample sequence.

We attempted to acquire PARABOLA and PS-II readings at solar zenith angles (Θ_ss) of 48°, 60°, and 75° for each site. NDVI values for the three sample sites were calculated according to Θ_s using both radiance and reflectance [NDVI=(NIR-RED)/(NIR+RED)]. PS-II NDVIs were calculated after averaging the radiometric values that corresponded to the bandwidths of the PARABOLA red and near-infrared channels to allow robust comparisons between the NDVIs derived from each instrument.

RESULTS AND DISCUSSION

The average nadir spectrum of the wet sedge site is easily differentiable from those of the two tussock tundra sites upon visual analysis (Fig.1). The spectral difference between the two tussock tundra sites, however, is not readily apparent. Statistical analysis reveals that, in all but the red region, the mean spectra of the two tussock tundra sites spectra fall within 1 standard deviation (σ) of each other. Calculated NDVI values similarly depict the site phenological differences (Table 1). The wet sedge NDVI value was considerably lower than those of the tussock sites. However, while the mean NDVI of the woody tussock tundra site was higher than that of the non-woody tussock site, the ranges ($\pm 1\sigma$) of the tussock site NDVIs exhibited significant overlap at nadir. Hence, the tussock tundra sites are not clearly differentiable using nadir measurements.

PARABOLA measurements, like the nadir PS-II spectra, show that the highly senesced wet sedge site possesses a significantly lower NDVI than the two tussock tundra sites over the full range of view angles (from 75° forwardscatter to 75° backscatter) in the solar principal plane. This relationship is seen regardless of Θ_S (Fig. 2). The NDVI values calculated from PARABOLA data for the two tussock tundra sites, however, reveal trends that are impossible to discern using nadir measurements alone. At large view zenith angles in both the forwardscatter and backscatter directions, the NDVI values of the two tussock tundra sites diverge considerably.

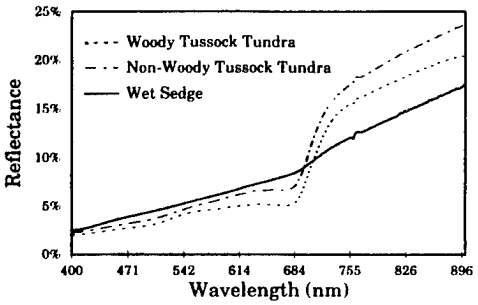


Fig. 1. Average nadir PS-II spectra of three vegetation types at θs=61°-66°.

Table 1. Nadir NDVI values derived from PS-II reflectance measurements for three tundra vegetation types sampled at θs=61°-66°.

site	θs	n (# of plots)	NDVI (mean)	NDVI (σ)
wet sedge	66°	20	0.31	0.03
non-woody tussock	62°	24	0.51	0.06
woody tussock	61°	12	0.56	0.04

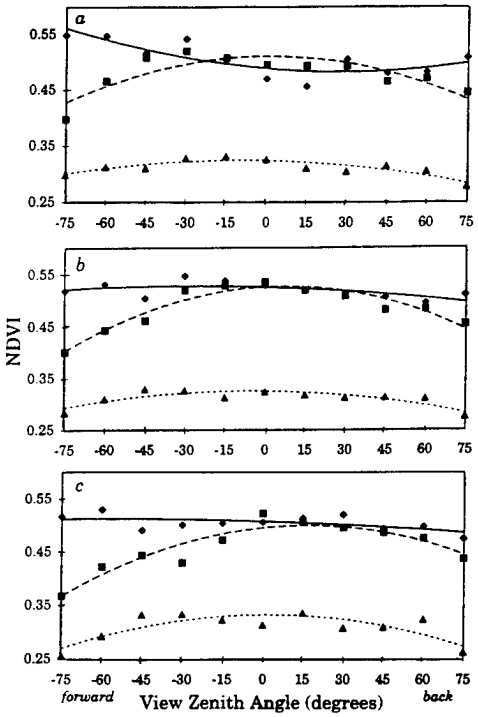


Fig. 2. NDVI values at three study sites with varying view zenith angle in the solar principal plane, derived from PARABOLA reflectance measurements. *a.* Θ_S=47.3°-52.5°, *b.* Θ_S=58.5°-61.2° (values for wet sedge site represented as Θ_S="60.0°" by averaging values from measurements at Θ_S=55.3° and 64.7°), *c.* Θ_S=69.1°-75.0°. In each graph, the wet sedge site is depicted with triangles (finely dashed line), the non-woody tussock tundra with squares (coarsely dashed line), and the woody tussock tundra with diamonds (solid line). All curves represent second order polynomial fits to the data.

The sensitivity of the reflectance signal at high view angles to differences in shrub cover is likely due to the structure of tussock tundra vegetation. In the early spring, woody deciduous shrub stems extend above the hummocky surface of sedge-dominated tussocks. Thus, although the new deciduous shrub leaves are very small, with increasing view zenith angles they comprise a larger proportion of the green vegetation canopy early in the growing season because: 1) they are well-illuminated by the sun at large Θ_S, and 2) the other major component of the signal at large view angles, the tops of the sedge tussocks, are still dominated by standing dead biomass during initial woody deciduous shrub leaf flush. In contrast, at and near nadir the small deciduous shrub leaves comprise a much smaller fraction of the green biomass because the inter-tussock regions contain large amounts of green *Sphagnum* moss and evergreen species. As a result, NDVI at large view zenith angles early in the growing season may be more indicative of deciduous woody shrub biomass than overall canopy greenness.

CONCLUSIONS

From the results of this study, we conclude that early in the growing season on the North Slope of Alaska: 1) nadir-viewing radiometric measurements allowed spectral differentiation between a highly senesced wet sedge site and two tussock tundra sites with differing amounts of woody deciduous shrub cover, 2) bidirectional reflectance measurements provided the information necessary to differentiate all three sites due to a divergence of the NDVI at large view zenith angles between the two tussock tundra sites, and 3) bidirectional reflectance data is probably more sensitive to the amount of deciduous shrub cover than absolute green biomass in tussock tundra due to the hummocky structure of the vegetation. Thus, bidirectional reflectance measurements of arctic tundra may reveal small increases in deciduous shrub biomass that are expected to accompany shifts in arctic climate.

ACKNOWLEDGMENTS

We thank B. Banerjee and S. Ahmad for data processing assistance. We extend special thanks to Dr. Si-Chee Tsay, who supported the field aspect of this study under the auspices of the NASA/ARMCAS project. L.A.V. was supported by the NASA Graduate Student Summer Program in the Earth System Sciences through the Universities Space Research Association.

REFERENCES

[1] Maxwell, B., "Arctic climate: potential for change under global warming," in Arctic Ecosystems in a Changing Climate. F. S. Chapin III, R. L. Jeffries, J. F. Reynolds, G. R. Shaver, and J. Svoboda, Eds. San Diego, Academic Press, 1992, pp. 11-34.

[2] Chapin, F.S., III, G.R. Shaver, A.E. Giblin, K.J. Nadelhoffer, and J.A. Laundre, "Responses of arctic tundra to experimental and observed changes in climate," Ecology vol. 76, no. 3, pp. 694-711, 1995.

[3] Walker, D.A. and M.D. Walker, "History and pattern of disturbance in Alaskan arctic terrestrial ecosystems: a hierarchical approach to analysing landscape change," J. Appl. Ecology vol. 28, pp. 244-276, 1991.

[4] Hansen, B.U., "Monitoring natural vegetation in southern Greenland using NOAA AVHRR and field measurements," Arctic vol. 44, supplement 1, pp. 94-101, 1991.

[5] Hope, A.S., J.B. Fleming, G. Vourlitis, D.A. Stow, W.C. Oechel, and T. Hack, (1995), "Relating CO_2 fluxes to spectral vegetation indices in tundra landscapes: importance of footprint definition," Polar Record vol. 31, no. 177, pp. 245-250, 1995.

[6] Hope, A.S., J.S. Kimball, and D.A. Stow, "The relationship between tussock tundra spectral reflectance properties and biomass and vegetation composition," Int. J. Remote Sens. vol. 14, no. 10, pp. 1861-1874, 1993.

[7] Markon, C.J., M.D. Fleming, and E.F. Binnian, "Characteristics of vegetation phenology over the Alaskan landscape using AVHRR time-series data," Polar Record vol. 31, no. 177, pp. 179-190, 1995.

[8] Shippert, M.M., D.A. Walker, N.A. Auerbach, and B.E. Lewis, "Biomass and leaf-area index maps derived from SPOT images for Toolik Lake and Imnavait Creek areas, Alaska," Polar Record vol. 31, no. 177, pp. 147-154, 1995.

[9] Stow, D.A., A.S. Hope, and T.H. George, "Reflectance characteristics of arctic tundra vegetation from airborne radiometry," Int. J. Remote Sens. vol. 14, no. 6, pp. 1239-1244, 1993.

[10] Tømmervik, H., B.E. Johansen, and J.P. Pedersen, "Monitoring the effects of air pollution on terrestrial ecosystems in Varanger (Norway) and Nikel-Pechenga (Russia) using remote sensing," The Science of the Total Environment vol. 160/161, pp. 753-767, 1995.

[11] Walker, D.A., N.A. Auerbach, and M.M. Shippert, "NDVI biomass, and landscape evolution of glaciated terrain in northern Alaska," Polar Record vol. 31, no. 177, pp. 169-178, 1995.

[12] Whiting, G., D.S. Bartlett, S. Fan, P.S. Bakwin, and S.C. Wofsy, "Biosphere/atmosphere CO_2 exchange in tundra ecosystems: community characteristics with multispectral surface reflectance," J. Geophys. Res. vol. 97(D15), pp. 16,671-16,680, 1992.

[13] Deering, D.W. and P. Leone, "A sphere-scanning radiometer for rapid directional measurements of sky and ground radiance," Remote Sens. Environ. vol. 19, pp. 1-24, 1986.

Analysis of airborne POLDER data on boreal forest covers

P. Bicheron, M. Leroy, and O. Hautecoeur
Centre d'Etudes Spatiales de la BIOsphère (CESBIO)
18 av E. Belin, 31055 Toulouse Cedex, France

ABSTRACT

POLDER (POLarization and Directionality of the Earth's Reflectance) airborne measurements were obtained during the BOREAS experiment. In a first approach, a BRDF model is tested against POLDER data acquired over the Old Aspen site, and its biophysical parameters (LAI, f_{IPAR}) compared to local observations. A second approach consists in mapping parameters retrieved by inversion of a semi-empirical model on data acquired at 100 m resolution on a region 5km wide surrounding the Young Jack Pine site. This demonstrates the ability of airborne POLDER experiment to retrieve the angular signature on every point of an extended region.

INTRODUCTION

Natural vegetation ecosystems constitute complex surfaces that are distinctly non lambertian reflectors [1]. The spaceborne POLDER instrument, which will be launched in 1996, has an optical concept which allows to measure the reflectance of a given surface under different directions [2]. In this perspective, an airborne version of the instrument has been built and tested during several campaigns [3]-[4].

This paper presents an analysis of the measurements of surface directional signature acquired with airborne POLDER during the BOREAS experiment. Two goals are pursued here. First, a POLDER data set is used in the inversion of an analytic BRDF model, a priori suitable to the inversion of spaceborne POLDER data in order to extract biophysical parameters such as the leaf area index LAI, or the fraction of intercepted PAR, f_{IPAR}. Second, we show that it is possible to perform an analysis of the angular signature on a large number of surface grid points, which is a large improvement relative to the limited set of targets processed previously, and which will permit in the future to test inversion and classifications procedures over extended areas.

DATA ACQUISITION AND PROCESSING

The POLDER instrument concept [2] images bidimensional pictures of the ground on a CCD matrix (288 lines x 384 colums) through a wide field of view optics. A given pixel thus may be observed with different viewing angles in consecutives images acquired during the sensor overflight. The airborne version [3] has an angular coverage of +/-42° in the crosstrack direction and +/-51° in the along track direction. The ground pixel size is proportional to the instrument altitude (typically 5500 m). It is 6 x 6 m^2 for an altitude of 1km. During operation, a rotating filter wheel that carries spectral filters and polarizers allows measurements in several spectral bands: 443 nm (with three directions of polarization), 550nm, 670nm, 864nm (three directions of polarization) and 910nm. The bandwidth is 10nm to 20nm depending on the band. A sequence of 9 images, corresponding to the 9 positions of the filter wheel, is performed within 3 seconds. The sequences are repeated every 10 seconds.

During part of the BOREAS experiment, the POLDER instrument was installed on the C-130 aircraft operated by NASA Ames Research Center and flew over « tower sites » of the South Sub Area in both IFC-1 and IFC-2 campaigns. Each target was overflown several times, each times at a different heading, so that multiple images could be collected in the principal, perpendicular, and oblique planes. For each image acquisition, POLDER recorded the aircraft position and attitude parameters provided by the data system on board the C-130. This gives the approximate position of a given pixel for all the POLDER images. However, the uncertainty in the navigation system is larger than the pixel size. A visual inspection, coupled with the use of a topographic map for a precise location, allows the determination of the pixel corresponding to the target. This permits to extract a measurement of reflectance spatially averaged on a 5 x 5 pixels (165 m) window around each « tower site ». A correction for atmospheric effects is made with the 6S code [5], using a subartic atmospheric model and a continental aerosol model, with as input aerosol optical thickness data from the BORIS data base [6]-[7], interpolated to provide values at 550 nm. Fig. 1 displays the BRDF measured on the Old Aspen « tower site » the 26th May 1994.

BRDF MODEL INVERSION

Many radiative transfer models have been developed to describe the reflection of optical radiation from vegetation canopies. Our goal is to prepare BRDF inversion techniques to be applied on spaceborne POLDER data. The BRDF model to be tested must be physical, but also simple and analytic to be tractable. We have chosen to test the Kuusk's model [8] which satisfies these critera, and is one of the only models describing both the directional and spectral variations of canopy reflectances. This model expresses the canopy reflectance as a function of wavelength, illumination and viewing angles, leaf area index LAI, chlorophyll concentration C_{ab}, mean leaf inclination θ_m, ratio of leaf size to canopy height l*, parameters describing the spectral

0-7803-3068-4/96$5.00©1996 IEEE

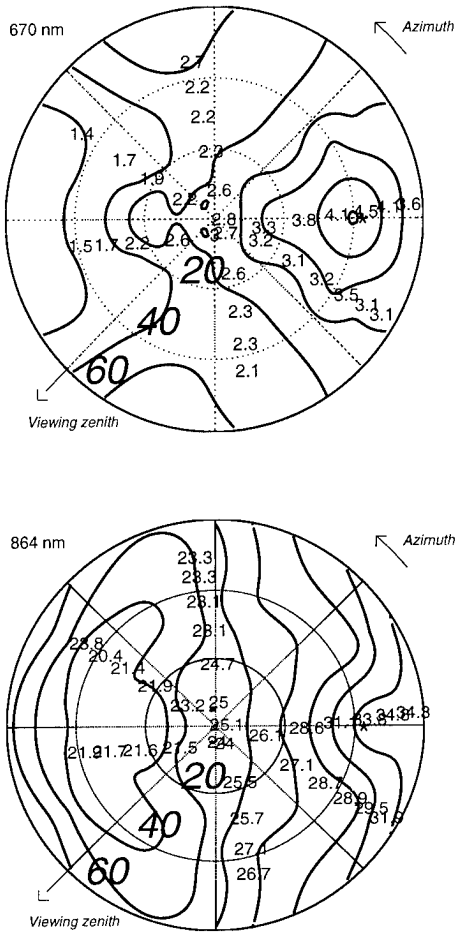


Figure 1. BRDF of Old Aspen (May 26, 1994)

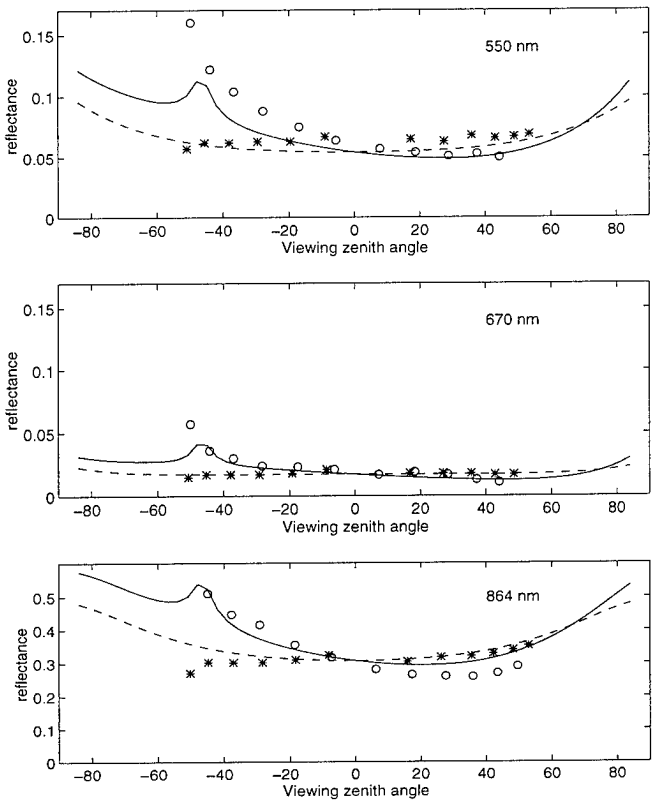


Figure 2. Reflectance measured by POLDER in the principal plane (o) and perpendicular planes (*) compared with Kuusk's model calculations. The solid lines and the dashed lines stand respectively for the principal plane and the perpendicular plane of the model. The parameter values are in Tab. 1.

reflectance of underlying soil, and structural and optical parameters of leaves [8].

The inversion procedure consisted to determine simultaneously some of the biophysical parameters, LAI, C_{ab}, θ_m, l^*, through an adjustment of the model against spectral and directional POLDER measurements. The inverted datasets were those acquired at 550, 670 and 864 nm over Old Aspen at 2 dates, May 26 and May 31, 1994, gathered to obtain significant variation of sun zenith angles. The parameter retrieval was obtained by minimizing the merit function [9] defined by:

$$\varepsilon^2 = \frac{1}{n}\sum_{j=1}^{n}(\rho_{j\,\mathrm{mod}} - \rho_{jmea})^2$$

where ρ_{jmea} is the directional reflectance for a given wavelength and view and sun geometry, $\rho_{j\,\mathrm{mod}}$ is the model estimate for the same wavelength and geometry, and n is the number of reflectance samples. The other model parameters are kept fixed to some reasonable value.

This minimization was solved using a modified Simplex method. Fig. 2 shows the comparison between measurements and model, whose retrieved parameters are summarized in Tab. 1. The LAI, the chlorophyll concentration C_{ab}, and f_{IPAR} are restituted with accuracies less than 5%, 23% and 4% respectively.

The results seem to be promising, considering that Kuusk's model is not the most appropriate to describe boreal forest covers. One should point out, however, that preliminary results of inversion acquired over other sites are not as satisfactory as those reported here.

Parameters	POLDER+ model	Ground truth from BORIS database
LAI	1.97	2.06 (Chen RSS-07)
C_{ab}	33.25	40.8 (Plummer RSS-04)
θ_m	57.1	no
l^*	0.035	no
f_{IPAR}	0.766	0.735 (RichTE-23)

Table 1. Comparison of retrieved and measured parameters for Old Aspen site . The rms error ε was 0.036.

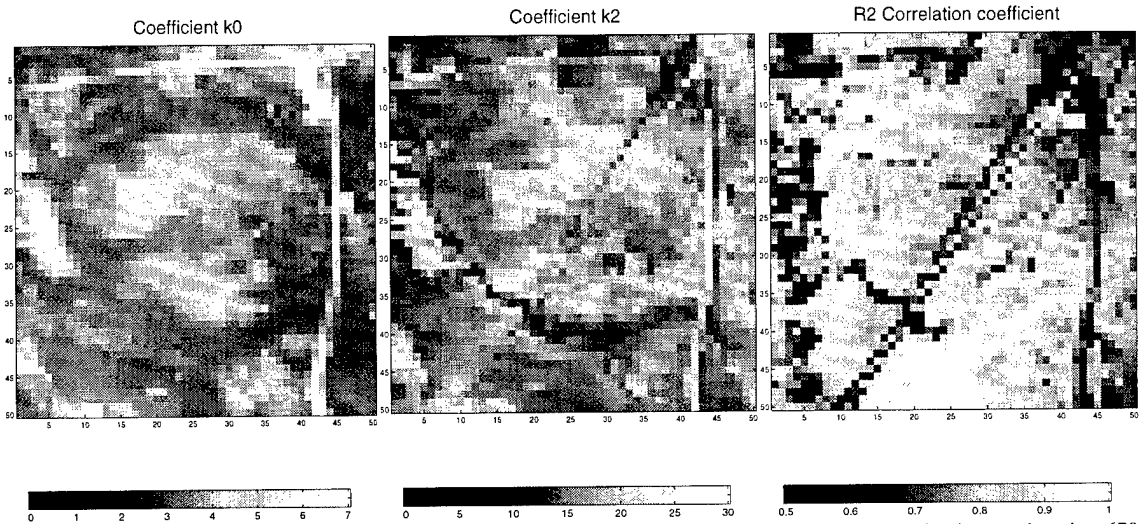


Figure 3. Retrieved parameters k_0 and k_2 (%), and squared correlation coefficient, using the model of Roujean for the wavelength at 670 nm.

SPATIAL EXTENSION OF ANGULAR SIGNATURE

The first part of the study focused on measurements on a well defined target. We also processed the airborne POLDER data to obtain, on a squared region of size 5km surrounding the « tower site » Young Jack Pine on July 21, a complete directional signature on every pixel of this region. Geometric registration between the 50 images or so of the data set was achieved using ground control points techniques. The space resolution was degraded from 33 m to 100 m to limit the effects of residual misregistration (of the order of 1 pixel). We then inverted the simple 3-parameters semi-empirical model of Roujean et al. [10] $\rho = k_0 + k_1 f_1 + k_2 f_2$, where f_1 and f_2 are functions of the sun and view angles only, over the directional reflectance measurements non corrected from atmospheric effects for all the 100 x 100 m^2 pixels independently and for the wavelengths 550nm, 670nm, and 864nm. The results at 670 nm are displayed in Fig. 3. The different structures (limits of parcells, rivers, and road) are clearly visible on the k_0 and k_2 plots of Fig. 3. The correlation between model and measurements is satisfactory. The noticeable oblique track of lower correlation appears on pixels characterized by the presence of directional measurements in the hot spot, of high magnitude [11], and not well accounted for by the model of Roujean et al.

CONCLUSIONS

The inversion of Kuusk's model with POLDER data acquired during the BOREAS experiment has been found to be successful, in one example, to retrieve LAI and f_{IPAR} with good accuracy. Other preliminary results, not described here, tend to show that the retrieval of these parameters on other sites and at other dates is indeed possible, but with an accuracy much less than that shown here. More work is needed to assess the potential of this inversion method in the context of airborne or spaceborne POLDER experiments. We have also shown that the POLDER concept actually permits to measure the directional signature on an extended area. This complements other similar results acquired over cultures [4]. We will use this potentiality in the future to assess whether the directional signature can be useful, in addition to the spectral signature, to discriminate surface types in boreal forests classifications.

REFERENCES

[1] D.W. Deering , Directional radiance measurements: callenges in the sampling of landscapes, *Physical Measurements and Signatures in Remote Sensing (Proceedings)* Val d'Isère (France), 17-21 Jan 1994, pp 561-567, 1994.

[2] P.Y. Deschamps et al., POLDER mission: Instrument characteristics and scientific objectives , *IEEE Trans. Geosc. Rem. Sens.*, 32, pp 598-615, 1994.

[3] J.L. Deuzé, F.M. Bréon, P.Y. Deschamps, M. Herman, A. Podaire, J.L. Roujean, Analysis of the POLDER airborne instrument observations over land surfaces, *Rem. Sens. Enviro.*, 44, pp 151-168, 1993.

[4] M. Leroy, F.M. Bréon, Surface reflectance angular signatures from airborne POLDER data , *Rem. Sens. Enviro.*, in press .

[5] E. Vermote, D. Tanré, J.L. Deuzé, J.J. Morcrette, Second simulation of the satellite signal in the solar spectrum: an overview , *IEEE Trans. Geosc. Rem. Sens.*, unpublished.

[6] R.C. Wrigley et al., Aerosol optical depth determination for BOREAS, *American Geophysical Union Fall Meeting (Abstract)*, San Fransisco, CA, EOS, 75, 5-9 Dec 1994, pp 133.

[7] B.L. Markham, R.N. Halthbore, B.N. Holben, Aerosol optical properties over North Central Canada during BOREAS, *IGARSS'95 (Proceedings)* , Florence (Italy).

[8] A. Kuusk, A multispectral canopy reflectance, *Rem. Sen. Enviro.*, 50, pp 75-82, 1994.

[9] N.S. Goel, D.E. Strebel, Inversion of vegetation canopy reflectance models for estimating agronomic variables. I. Problem definition and initials results using the Suits's model , *Rem. Sen. Enviro.*, 13, pp 487-507, 1983.

[10] J.L Roujean, M. Leroy, P.Y. Deschamps, A bidirectional reflectance model of the Earth surface for the correction of remote sensing data , *J. Geophys. Res.*, 97, pp 20455-20468, 1993.

[11] Bréon F.M. Vanderbilt V., Leroy M., Bicheron P., Walthall C.L., Kalshoven J.E, Evidence of hot-spot signature from airborne POLDER measurements, unpublished.

Variability of BRDF with Land Cover Type for the West Central HAPEX-Sahel Super Site

Eric C. Brown de Colstoun[1], Charles L. Walthall[2], Alice T. Cialella[3], Eric R. Vermote[1], Rangasayi N. Halthore[3] and James R. Irons[4]

[1] Laboratory for Global Remote Sensing Studies, Department of Geography, 2181 Lefrak Hall, University of Maryland, College Park, MD 20742 USA Tel.: (301) 405-3043 Fax: (301) 314-9299 e-mail: ebrownde@geog.umd.edu.
[2] Remote Sensing and Modeling Laboratory, USDA Agricultural Research Service, Beltsville, MD 20705 USA.
[3] Brookhaven National Laboratory, Department of Applied Science, Upton, NY 11973-5000 USA.
[4] Biospheric Sciences Branch, Code 923, NASA/Goddard Space Flight Center, Greenbelt, MD 20771 USA.

Abstract -- The issue of Bidirectional Reflectance Distribution Function (BRDF) spatial variability on the landscape and its linkages to surface characteristics has received little attention. Data sets such as those collected by the Advanced Solid-State Array Spectroradiometer (ASAS), an airborne imaging spectroradiometer with along-track pointability, are ideal for such investigations. ASAS data collected during the Hydrologic and Atmospheric Pilot Experiment (HAPEX-Sahel) near Niamey, Niger were analyzed to address spatial variability with land cover type, the effects of scale on the directional reflectance trends, and how well a simple BRDF model accounted for the principal plane reflectance trends. A hypothesis was also tested that critical elements of the BRDF of the land cover types, as captured by the terms of a simple model, could be scaled up to the BRDF of the full scene using a linear mixture model.

INTRODUCTION

Several recent studies have noted a linkage between Bidirectional Reflectance Distribution Functions (BRDF) and land cover as measured by satellite systems at coarse spatial resolution (e.g. [1]). Although there also exists a substantial body of local plot-level BRDF data [2], it is as yet unclear what the contribution of multiple landscape components is to the BRDF observed by current or future satellite remote sensing systems at coarse spatial scales. In many cases the bidirectional signal is considered as "noise" and attempts are made to remove or attenuate it. However, this signal is both spectrally and temporally variable, and appears to be related to the structural attributes of terrestrial surfaces such as leaf area index, leaf angle distribution, and soil brightness and roughness [2,3,4,5]. Thus, it is reasonable to expect that the additional information contained in the bidirectional signal should be useful in improving either global classification schemes or biophysical parameter retrieval from satellite remote sensing systems.

In this study, we have used aircraft bidirectional data at full spatial resolution and "degraded" to satellite resolution to examine the variability of the BRDF with landscape components of the West Central Super Site (WCSS) of the Hydrologic and Atmospheric Pilot Experiment (HAPEX-Sahel) [6] near Niamey, Niger. Specific objectives were to: 1) examine the variability of principal plane reflectance trends as a function of land cover, 2) assess the performance of a simple empirical model in describing these trends, and 3) determine if the BRDF of lower spatial resolution imagery could be described by a linear function of the higher resolution BRDFs.

DATA AND METHODS

The Advanced Solid-State Array Spectroradiometer (ASAS) [7] was used to collect airborne multidirectional, multispectral data in the solar principal plane over the HAPEX WCSS from an altitude of approximately 4750 m above ground level on September 3, 1992. The solar zenith angle at the time of measurement was 36° and the ground-measured aerosol optical thickness at 550 nm was 0.237. For HAPEX, ASAS provided spectral data for 62 spectral bands centered from 420 nm to 1037 nm and for 10 view zenith angles (70, 60, 45, 30, and 15 degrees forward along track, nadir, and 15, 30, 45, and 55 degrees aft). Because several spectral bands were significantly affected by instrument noise, only data for 33 spectral bands, from approximately 505 nm to 841 nm, were used. Imagery for 7 out of the 10 view zenith angles was available for this data set. The nadir spatial resolution was approximately 3.2 by 3 meters covering 1.5 by 1.1 Km for the full image.

The ASAS off-nadir imagery were co-registered to within one pixel to the nadir imagery through the use of ground control points and a nearest neighbor resampling routine. Principal component analysis of the nadir spectral data was performed to reduce the spectral information from the 33 useable bands to 10 principle components channels which were used in an unsupervised classification. Six distinct land

0-7803-3068-4/96$5.00©1996 IEEE

cover classes were identified on the classified imagery as old age fallow/bushland, intermediate age fallow, young age fallow/grassland, bare laterite/continental terminal deposits, bare dark soil/sparse millet and bare sandy soil/sparse millet. The classes represented approximately 12, 29, 19, 5, 13 and 23 percent, respectively, of the whole image.

Mean and standard deviations for spectral digital counts were extracted from each view angle image for the 33 spectral bands, for each land cover class, and for the entire image. Radiometric resolution factors which were supplied with the data were used to calculate at-sensor radiance values in $W/m^2/\mu m/sr$. The radiances were input to the 6S radiative transfer model [8] with a tropical standard atmosphere, a continental aerosol model, and the ground-measured aerosol optical thickness to obtain atmospherically corrected at-ground bidirectional factors. A simple empirical BRDF model [5] was then fitted to the signatures for each cover type and the coefficients were retained for analysis. This model describes the Bidirectional Reflectance Factor (BRF) at a particular view direction as:

$$BRF = a\theta_v^2 + b\theta_v\cos(\phi_v) + c \qquad (1)$$

where θ_v is the view zenith angle in radians, ϕ_v is the relative view azimuth angle and a, b, c are coefficients derived through least-squares regression analysis. Briefly, the a coefficient describes the general curvature of the BRDF, b provides a linear dependence on view zenith which interacts with the first term to fit more variable surface shapes, and c is the minimum reflectance for the particular BRDF [4,5].

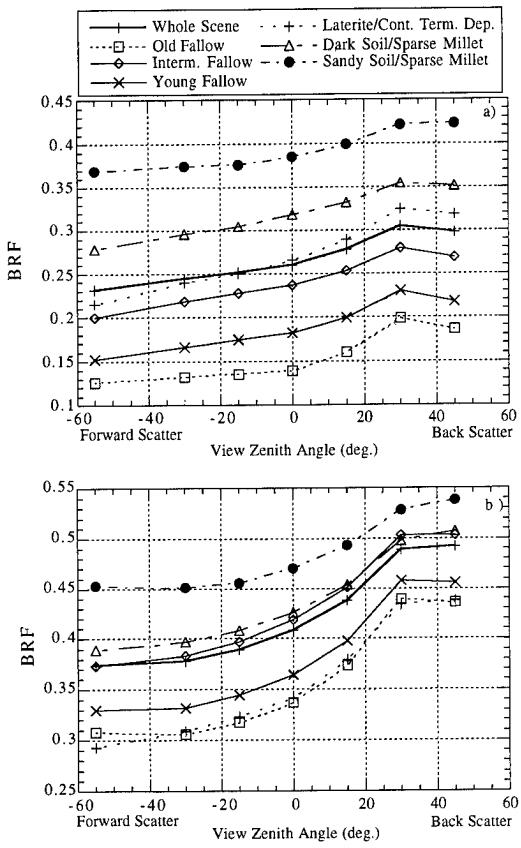


Fig. 1) ASAS Bidirectional Reflectance Factors (BRF) as a function of view zenith angle at: a) 676 nm and b) 800 nm.

RESULTS AND DISCUSSION

Fig. 1a and 1b show the BRFs for each of the land cover classes and for the whole image as a function of view zenith angle for ASAS spectral bands 27 (676 nm) and 39 (800 nm). The trends here are consistent with results seen in other soil-dominated canopies at similar illumination angles: strong back scattering peak values decreasing to minimum values in the extreme forward scatter direction [2]. These trends are mainly associated with viewing a greater proportion of shadows as the view zenith angle moves towards the forward scattering direction [2]. Also, the BRFs for each cover type are distributed about those for the whole scene, indicating that the full scene BRFs may be a combination of the sub-scene BRFs. A cursory examination of these plots also reveals that the curvatures for the BRFs are greater in the near-infrared (NIR) than in the visible wavelengths.

After application of eq. (1) to the curves for each spectral band, we have a quantitative way of describing this curvature, shown in Fig. 2a-2c. In general, the performance of the model in fitting and describing the trends associated with each of the BRDF distributions was very good, with a minimum r^2 value of 0.87 for the old fallow class at 697 nm. The a coefficients of the model, describing the general curvature of the BRDF, increased from negative values at 505 nm, meaning a convex curvature, to greater positive values, with concave curvatures, in the near-infrared (Fig. 2a). The a values for the old fallow class were the greatest for almost all the spectral bands, indicating an influence of the denser vegetation cover present for this class, a trend also seen in [4]. The bare sandy soil/sparse millet class also had large values of this coefficient in the visible but not as great in the near-infrared as the old fallow or young fallow classes. The a coefficients for the other classes generally showed little change over the visible or near-infrared wavelengths but were more variable in the NIR portion of the spectrum.

The b coefficients increased almost linearly with wavelength for all classes, indicating that the difference between the backscattering peak and the minimum value in the forward direction was greater in the NIR than in the

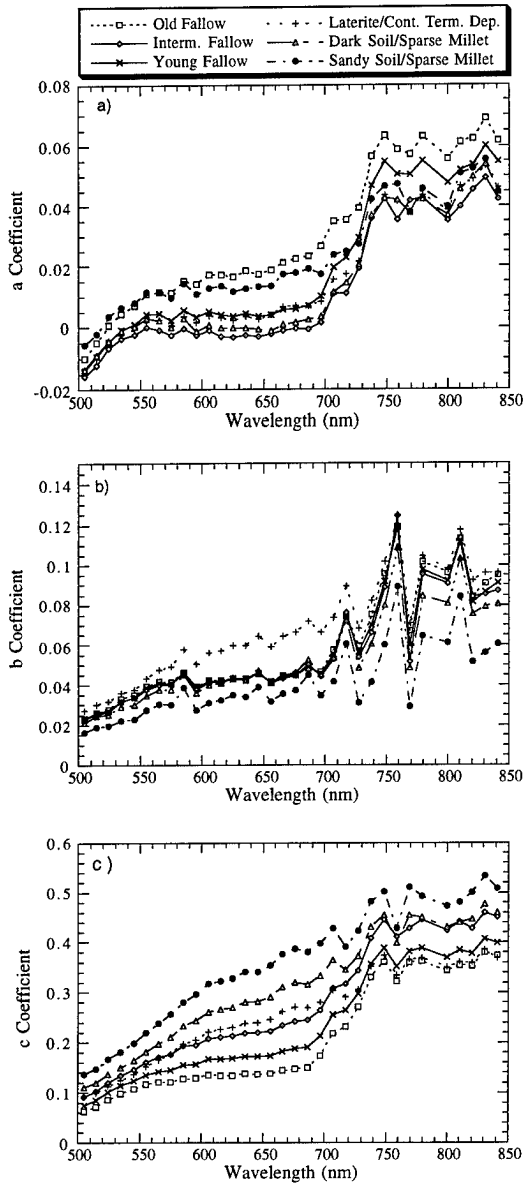


Fig. 2a,b,c) The three coefficients of eq. (1) vs. wavelength.

visible (Fig. 2b). The bare laterite/continental terminal deposits class was found to have the most "extreme" BRDF. The bare sandy soil /sparse millet class had the smallest b values for all wavelengths, presumably because of the strong multiple scattering by the soil particles and the large overall reflectance values at all view zenith angles. A more thorough analysis of this coefficient is currently ongoing.

Fig. 2c shows the minimum reflectances for each distribution (c coefficient) which were found for all classes

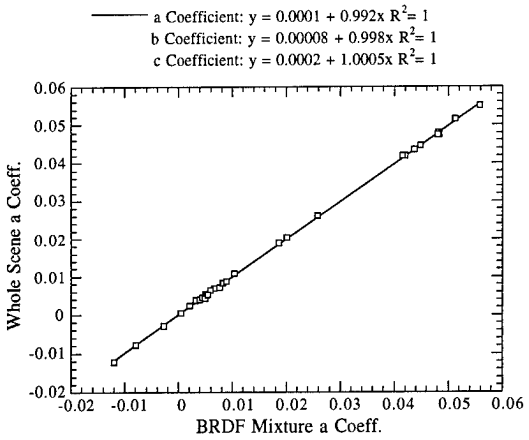


Fig. 3) The a coefficient for the whole scene vs. The a coefficient for a linear mixture model of subscene a coefficients. Also included are linear regression equations for all three coefficients.

and for this 36 degree illumination angle to be typically at 30 or 55 degrees in the forward scattering direction. These curves also show the strong effect of soil background materials for the reflectance factors of each of the land cover classes represented here, even for the more vegetated fallow classes.

Finally, we compared the coefficients for the whole scene with a linear mixture model of the coefficients for the land cover classes such that:

$$W = \sum_{i=1}^{6} p_i k_i \qquad (2)$$

where W is the a, b or c coefficient for the whole scene, p_i is the area percentage of each cover class (i) and K_i is the a, b or c coefficient for each cover class. These show very strong agreement for all three coefficients (Fig. 3), suggesting that bidirectional signals at the coarse scale are a mixture of those at the finer scale, and that this relationship is nearly perfectly linear.

CONCLUSIONS

The results from this analysis indicate that: 1) the bidirectional signal of different land cover types is variable both spectrally and spatially, 2) these signals are well described by a simple empirical model, 3) the signal for the whole scene, as described by the coefficients from the simple

model, appear to be a mixture of the signals for each of the land cover classes, as described by the same coefficients. However, a more rigorous test of the mixture model approach using two independent data sets such as ASAS at two altitudes over a target is required.

ACKNOWLEDGMENTS

The authors wish to thank Phil Dabney, Bill Kovalick, Mike Bur, the C-130 crew, M. Spanner and the Hapex Information System. This study was funded by NASA grant NAGW-3193.

REFERENCES

[1] A. Wu, Z. Li, and J. Cihlar, "Effects of land cover type and greenness on advanced very high resolution radiometer bidirectional reflectances: analysis and removal," J. Geophys. Res., vol. 100, pp. 9179-9192, May 1995.

[2] D. S. Kimes et al., "Directional reflectance factor distributions for cover types of northern africa," Rem. Sens. Environ., 18, pp. 1-19, 1985.

[3] E. C. Brown de Colstoun, C. L. Walthall, C. A. Russell, and J. R. Irons, "Estimating the fraction of absorbed photosynthetically active radiation (fAPAR) at FIFE with airborne bidirectional spectral reflectance data," J. Geophys. Res., vol. 100, pp. 25523-25535, December 1995.

[4] C. L. Walthall, "A study of reflectance anisotropy and canopy structure using a simple empirical model," Rem. Sens. Environ., in press.

[5] C. L. Walthall, J. M. Norman, J. M. Welles, G. Campbell, and B. L. Blad, "Simple equation to approximate the bidirectional reflectance from vegetative canopies and bare soil surfaces," Appl. Opt., 14, pp. 383-387, February 1985.

[6] S. D. Prince et al., "Geographical, biological and remote sensing aspects of the hydrologic atmospheric pilot experiment in the sahel (HAPEX-Sahel)," Rem. Sens. Environ., 51, pp. 215-234, 1995.

[7] J. R. Irons, K. J. Ranson, D. L. Williams, R. R. Irish, and F. G. Huegel, "An off-nadir-pointing imaging spectroradiometer for terrestrial ecosystem studies," IEEE Trans. Geosci. Remote Sens., 29, pp. 66-74, 1991.

[8] E. R. Vermote, D. Tanré, J. L. Deuzé, M. Herman, and J. J. Morcrette, "Second simulation of the satellite signal in the solar spectrum: an overview," IEEE Trans. Geosci. Remote Sens., in press.

Conifer Shoot Bidirectional Scattering: Methodology and Preliminary Results

Elizabeth A. Walter-Shea, Mark A. Mesarch and Liqiang Chen
Department of Agricultural Meteorology, University of Nebraska
246 L.W. Chase Hall, Lincoln, NE 68583-0728
voice: 402-472-1553/ FAX: 402-472-6614/ agme012@unlvm.unl.edu

Abstract -- Biophysical models describing radiant energy partitioning at the surface are dependent on our knowledge of the distribution of radiation on canopy elements and resulting interactions (i.e., reflectance, transmittance and absorptance) as well as on the existing state of coupled physiological parameters (such as stomatal conductance and photosynthesis). However, research on optical properties of coniferous forest canopy elements, particularly at the conifer shoot level, has been limited. The objective of this paper is to describe the methodology developed in the investigation of scattering from boreal forest conifer shoots and to present preliminary results using the methodology. An automated goniometer system and procedure were developed for characterizing the bidirectional scattering of conifer shoots. The system includes a computer-controlled goniometer, an SE-590 spectroradiometer, projected area device, sample stand, reference panel and artificial light source. Preliminary results of conifer shoot scattering indicate backscattering and forward scattering features specific to illumination-view-shoot geometries. The methodology presented offers an automated and fairly simple means of characterizing the bidirectional scattering from canopy elements where numerous measures are required. Such measurements are important in advancing our understanding regarding the dynamics of shoot-level absorptance of solar energy for physiological processes and interpreting remotely-sensed canopy reflectance in radiative transfer parameterization.

INTRODUCTION

Biophysical models describing radiant energy partitioning at the surface are dependent on our knowledge of the distribution of radiation on canopy elements and resulting interactions as well as on the existing state of coupled physiological parameters. Photosynthetically active radiation (PAR) is the source of energy for the fixation of carbon dioxide via photosynthesis; thus it is essential to understand the absorptance of PAR by canopy elements within a stand to understand canopy fluxes of CO_2 and water vapor. In addition, physiological processes are affected by absorptance of near-infrared (NIR) and longer wavelengths, i.e., the canopy element radiation balance. The heterogeneous structure of coniferous stands contributes to the difficulty in modeling coniferous canopy processes in a realistic yet simple manner [1, 2]. Refinement of existing three-dimensional radiation transfer models is needed to account for the complex architecture and the interaction of radiation with canopy elements displayed within these vegetation-filled objects, *e.g.*, needle, twig, shoot and branch radiation scattering and absorption. However, research on optical properties of coniferous forest canopy elements, particularly at the conifer shoot level, has been limited (*e.g.*, [3, 4]). This may be due to the difficulties in collecting data, the expense in making measurements within and above forest canopies, and past research emphasis on agricultural crops [3].

Leaves, needles and bark are canopy elements which are important in scattering radiation in boreal forest vegetation [5]. Needle and bark properties can vary considerably depending on age and height in the canopy; elements deep in the canopy may be covered with algae and fungi and shade-induced effects on shoot development may exist [5, 6]. In the NIR portion of the electromagnetic spectrum little radiation is absorbed so that scattering by canopy elements will be significant. In contrast, needles absorb a large portion of PAR [3, 7]. Conifer needles absorb more PAR than deciduous leaves; twigs, especially current year's growth, also absorb PAR [3]. Differences in the magnitude of reflectance between conifer shoots and individual needles, particularly in the NIR and especially in older shoots, have been reported [4]. The difference was attributed to the contribution of the more mature branch bark in the older branches.

Materials presented are only a part of a larger investigation in the Boreal Ecosystem-Atmospheres Study (BOREAS) [8] on the coupling between radiation and gas exchange of canopy elements in a boreal forest; characterization of radiation interaction with conifer shoots through measurement and modelling is required. To achieve this an automated goniometer system was developed for characterizing the bidirectional scattering of conifer shoots. The system includes a computer-controlled goniometer, an SE-590 spectrometer (Spectron Engineering, Denver, CO), sample stand, reference panel, light source and projected area device. The objective of this paper is to describe the methodology developed and to present preliminary results using the methodology.

METHODS

Radiative scattering from conifer shoots was characterized using the bidirectional reflectance factor (BRF). Conifer shoots were oriented in an azimuth relative to the light source azimuth,

0-7803-3068-4/96$5.00©1996 IEEE

designated as ϕ_{shoot}. Illumination, view and shoot orientation are represented as direction $(\theta_i,\phi_i;\theta_r,\phi_r;\phi_{shoot})$ where θ is the zenith angle, ϕ is the azimuth angle, 'i' indicates illumination direction and 'r' indicates the reflected direction . Thus, the BRF for a particular illumination-view-shoot geometry is defined as:

$$BRF(\theta_i,\phi_i;\theta_r,\phi_r;\phi_{shoot}) = \frac{\Phi_r(\theta_i,\phi_i;\theta_r,\phi_r;\phi_{shoot})}{\Phi_{r,id}(\theta_i,\phi_i;\theta_r,\phi_r;\phi_{shoot})} \quad (1)$$

i.e., the ratio of the reflected (scattered) flux $[\Phi_r(\theta_i,\phi_i;\theta_r,\phi_r;\phi_{shoot})]$ from the shoot to the reflected flux from an ideal Lambertian surface $[\Phi_{r,id}(\theta_i,\phi_i;\theta_r,\phi_r;\phi_{shoot})]$ [9]. Output from the SE-590 is proportional to the scattered radiant flux. The scattered flux from an ideal Lambertian surface $[\Phi_{r,id}(\theta_i,0;\theta_r,\phi_r;\phi_{shoot})]$ was estimated from a nadir-viewed calibrated Spectralon reference panel (Labsphere, Inc., North Sutton, NH) illuminated under the same conditions as the sample $[\Phi_{r,ref}(\theta_i,0;0,\phi_r;\phi_{shoot})]$. Nadir-viewed fluxes from the reference panel were corrected for the horizontal projected area of the sample [i.e., projected area in the direction of the light source ($A_{\theta i,\phi shoot}$) divided by $\cos\theta_i$] and for view angle ($\cos\theta_r$) to represent the reflected flux from an ideal Lambertian surface:

$$\Phi_{r,id}(\theta_i,0;\theta_r,\phi_r;\phi_{shoot}) = \frac{A_{\theta i,\phi shoot}}{A_{ref}\cdot\cos\theta_i}$$

$$\cdot\,\Phi_{r,ref}(\theta_i,0;0,\phi_r;\phi_{shoot})\cdot\cos\theta_r\cdot CF(\theta_i). \quad (2)$$

A_{ref} is the area of the spot size as "seen" from the SE590 in the nadir position, $\cos\theta_r$ corrects the flux for that in the scattered direction, and $CF(\theta_i)$ is the calibration factor for the reference panel. The target was illuminated by a light source with an output within the 400 - 900 nm range from a quartzline projection lamp characterized with a 2° divergent beam and irradiance variation of 5% along the minor axis and 12% along the major axis of the illuminated spot.

The projected area of the sample was estimated using an imaging camera with the shoot sample suspended by nylon monofilament line within a sample ring positioned over a light table. The sample ring was rotated and tilted so that the sample was projected in the same direction toward the imaging camera as it was toward the light source for scattered flux measurements (yielding projected area, $A_{\theta i,\phi shoot}$). Once the projected area for each illumination and shoot orientation condition was measured for a particular shoot, the sample ring was removed from the imaging system with the shoot sample still in place and then mounted under the goniometer for scattered flux measurements. The cut end of the sample was kept in a water-filled vial at all times to reduce moisture loss from the sample.

Bidirectional scattering of shoots was measured using an SE-590 spectrometer with a 6° field of view mounted on the automated goniometer yielding a 3.75cm diameter target spot. A constant distance of 36.5cm was maintained between the sample and sensor at all view angles. Shoot segment length was limited to 2.5cm to maintain the shoot sample within the SE-590 spot size at all view angles and to maximize the sample area within the spot size. Samples were mounted horizontally in a sample ring at various azimuthal orientations (ϕ_{shoot}) relative to the illumination azimuth so as to capture variations due to sample-light geometry. Scattered radiant flux from the shoot was measured at selected view zenith and azimuth angles and illumination angles.

RESULTS

Scattering from conifer shoots can be complex as indicated from bidirectional reflectance factors from jack pine (*Pinus banksiana*) shoots. Preliminary results indicate view direction had a much greater effect on scattering than did illumination angle (Fig. 1). Shoot orientation relative to the light source altered the sunlit and shaded portions of conifer shoot in the direction of the sensor so that ϕ_{shoot} had a similar effect on scattering from conifer shoots as did view angle (Fig. 2). Backscattering and forward scattering features varied for particular shoot-view geometries (data not shown).

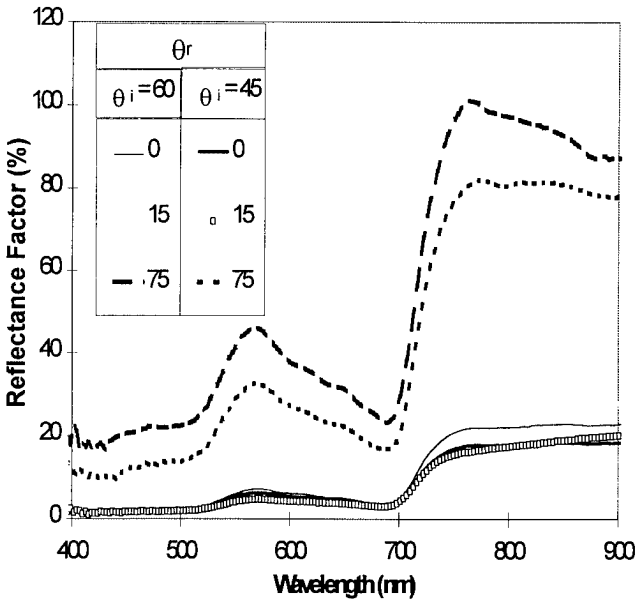


Fig. 1. Spectral bidirectional reflectance factors for a jack pine (*Pinus banksiana*) shoot oriented with the shoot tip directed away from the illumination azimuth (ϕ_{shoot} = 0°) and illuminated at zenith angles (θ_is) of 45° and 60° viewed at azimuth angles (ϕ_r) of 20°.

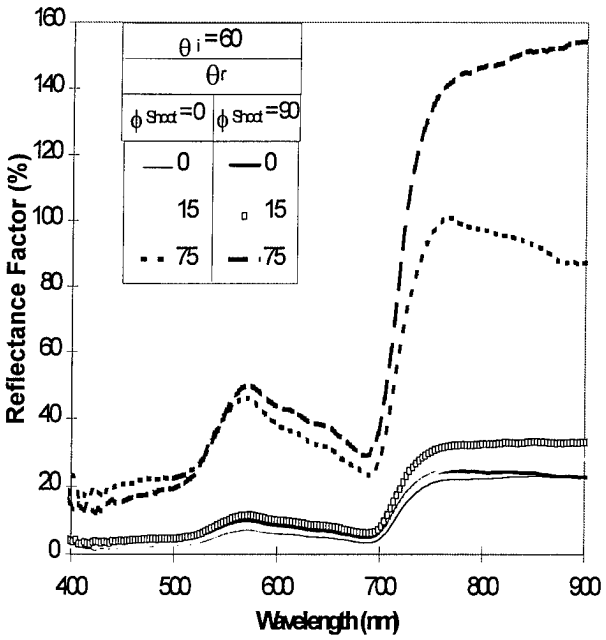


Fig. 2. Spectral bidirectional reflectance factors for a jack pine (*Pinus banksiana*) shoot illuminated at zenith angle (θ_i) of 60° and oriented with the shoot tip directed away from the illumination azimuth (ϕ_{shoot} = 0°) and oriented with the shoot axis perpendicular to the illumination azimuth (ϕ_{shoot} = 90°). Shoot was viewed at an azimuth (ϕ_r) of 20°.

DISCUSSION

The methodology presented offers an automated and fairly simple means of characterizing the bidirectional scattering from canopy elements where numerous measures are required. Such measurements are important in advancing our understanding regarding the dynamics of shoot-level absorptance of solar energy for physiological processes and interpreting remotely-sensed canopy reflectance in radiative transfer parameterization. Our overall goal is to analyze and synthesize field data through the use of mathematical models of conifer shoot radiative properties and gas exchange. The measurements of shoot scattering will enable us to test models of shoot radiative scattering and absorption in a step toward accomplishing our overall goal.

ACKNOWLEDGMENTS

We acknowledge the support by NOAA's Office of Climate and Global Change Program of our BOREAS research through grant NA36GP0281. We also thank J. Wurm (Li-Cor, Inc., Lincoln, NE) for assistance in the design of the light source.

REFERENCES

[1] D.L. Peterson and S.W. Running, "Applications in forest science and management," in *Theory and Applications of Optical Remote Sensing*, G. Asrar, Ed. New York: John Wiley & Sons, 1989, pp. 429-473.

[2] P. Oker-Blom, J. Lappi, and H. Smolander, "Radiation regime and photosynthesis of coniferous stands," in *Photon-Vegetation Interactions*, R.B. Myneni and J. Ross, Eds. New York: Springer-Verlag, 1991, pp. 469-499.

[3] D.L. Williams, "A comparison of spectral reflectance properties at the needle, branch, and canopy level for selected conifer species," *Remote Sens. Environ.*, vol. 35, pp. 79-93, 1991.

[4] B.N. Rock, D.L. Williams, D.M. Moss, G.N. Lauten, and M. Kim, "High-spectral resolution field and laboratory optical reflectance measurements of red spruce and eastern hemlock needles and branches," *Remote Sens. Environ.*, vol. 47, pp. 176-189, 1994.

[5] J.M. Norman and P.G. Jarvis, "Photosynthesis in Sitka spruce [*Picea sitchensis* (Bong,) Carr.] V. Radiation penetration theory and a test case," *J. Appl. Ecol.*, vol. 12(3), pp. 839-878, 1974.

[6] W.K. Smith and G.A. Carter, "Shoot structural effects on needle temperatures and photosynthesis in conifers," *Amer. J. of Bot.*, vol. 75, pp. 496-500, 1988.

[7] C.S.T. Daughtry, L.L. Biehl, and K.J. Ranson, "A new technique to measure the spectral properties of conifer needles," *Remote Sens. Environ.*, vol. 27, pp. 81-91, 1989.

[8] P. Sellers *et al.*, "The Boreal Ecosystem-Atmosphere Study (BOREAS): An overview and early results from the 1994 field year," *Bull. Amer. Meteorol. Soc.*, vol. 76, pp. 1549-1577, 1995.

[9] F.E. Nicodemus, J.C. Richmond, J.J. Hsia, I.W. Ginsberg, and T. Limperis, *Geometrical considerations and Nomenclature for Reflectance*, NBS Monograph 160, U.S. Government Printing Office, Washington, D.C., 1977.

Asymmetry in the Diurnal Variation of Surface Albedo

S. Mayor, W. L. Smith, Jr., L. Nguyen, T. A. Alberta
Analytical Services and Materials, Inc.
One Enterprise Parkway, Suite 300
Hampton, VA 23666

P. Minnis, C. H. Whitlock, G. L. Schuster
MS 420, NASA Langley Research Center
Hampton, VA 23681-0001

S. Mayor: phone, 804-827-4640; fax, 804-827-8659, s.mayor@larc.nasa.gov
P. Minnis: phone, 804-864-5671; fax, 804-864-7996, p.minnis@larc.nasa.gov

Remote sensing of surface properties and estimation of clear-sky and surface albedo generally assumes that the albedo depends only on the solar zenith angle. The effects of dew, frost, and precipitation as well as evaporation and wind can lead to some systematic diurnal variability resulting in an asymmetric diurnal cycle of albedo. This paper examines the symmetry of both surface-observed albedos and top-of-the-atmosphere (TOA) albedos derived from satellite data. Broadband and visible surface albedos were measured at the Department of Energy Atmospheric Radiation Measurement (ARM) Program Southern Great Plains Central Facility, at some fields near the ARM site, and over a coniferous forest in eastern Virginia. Surface and wind conditions are available for most cases. GOES-8 satellite radiance data are converted to broadband albedo using bidirectional reflectance functions and an empirical narrowband-to-broadband relationship. The initial results indicate that surface moisture has a significant effect and can change the albedo in the afternoon by 20% relative to its morning counterpart. Such effects may need to be incorporated in mesoscale and even large-scale models of atmospheric processes.

INTRODUCTION

Remote sensing of surface properties and estimation of clear-sky and surface albedo generally assume that the albedo depends only on the solar zenith angle (SZA). This assumption results in an albedo variation symmetrical about local noon. Both regular and irregular changes in the surface state can negate this assumption. The effects of dew, frost, and precipitation as well as evaporation and wind can lead to some systematic diurnal variability resulting in an asymmetric diurnal cycle of albedo. A combination of satellite and surface albedo measurements are used here to examine asymmetry in the diurnal cycle of clear-sky albedo.

DATA

Geostationary Operational Environmental Satellite (GOES) visible radiance data taken over a 0.3° grid centered on the Atmospheric Radiation Measurement (ARM) Program Southern Great Plains Central Facility (SCF) were converted to visible narrowband and shortwave broadband albedos on a half-hourly basis. GOES-7 and GOES-8 were used for April 1994 and October 1995, respectively. Only data for completely clear days were considered. Visible albedos were determined by correcting for reflectance anisotropy using the models of Minnis and Harrison [1]. These were converted to broadband albedos using the approach of Minnis et al. [2].

Surface albedos were measured over the SCF using the ARM broadband flux PSP radiometers on a 60-m tower in a wheat field. Other surfaces such as pasture and bare soil are also in the field of view of the downlooking radiometer. During October 1995, albedo measurements were also taken over four different surfaces near the SCF including bare soil, pasture, and newly planted wheat. April 1994 was a relatively wet period, while October 1995 was dry. Vegetation conditions changed between the two seasons. Half-hourly averages were computed from the surface albedo measurements taken over the SCF area. Meteorological conditions were monitored at the ARM SCF. An additional surface albedo data set was taken using a broadband PSP on a 100-m tower over a mixed coniferous-deciduous forest over eastern Virginia during 1995.

RESULTS

Surface albedo data were only available from 2 clear days during April 1994. On April 17, the afternoon albedos were greater than all of the corresponding morning albedos (Fig. 1). A similar variation was observed on April 15, 1994. The average afternoon-morning difference is on the order of 8% for both days. The complete diurnal cycle was not available for these 2 days. However, data were available for April 16 and 26 which were also mostly clear. The mean afternoon-morning difference in clear-sky albedo was slightly less than 2%. The winds were light ($v < 5$ mps) for all of the days. During the month, the ground was often observed to be wet with many puddles after nighttime rains. It did not rain between April 15 and April 17. Dew was noted for the mornings of April 16 and 26.

Many more clear days occurred during October 1995. Clear-sky albedos were observed October 12, 14, 15, 18, 20, 23, and 28. Relative humidity at dawn varied from 88% on October 12 to 46% on October 20. Mean daytime wind speed ranged from 2.5 mps on October 14 to 15 mps on October 23. The half-hourly surface albedos averaged for the SCF and adjacent radiometers are shown in Figs. 2 and 3 for October 23 and 28, respectively. The mean wind speed varied from

0-7803-3068-4/96$5.00©1996 IEEE

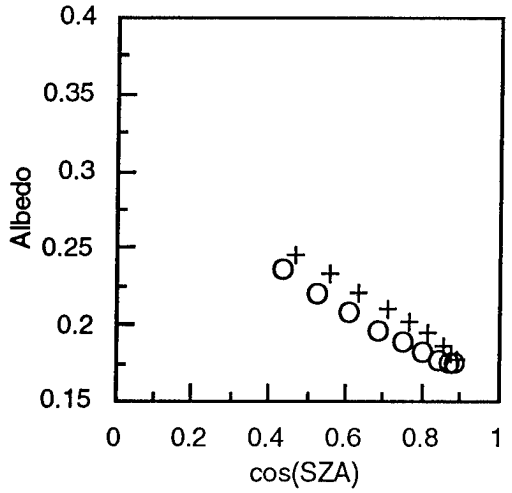


Fig. 1. Comparison of PM (+) and AM (O) broadband surface albedos over the ARM SCF on April 17, 1994.

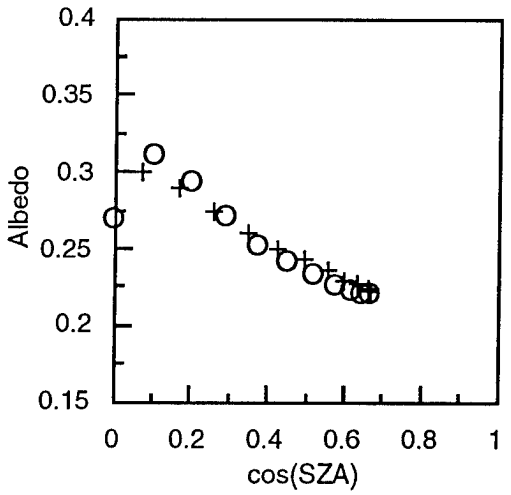


Fig. 2. Comparison of PM (+) and AM (O) broadband surface albedos over the ARM SCF on October 23, 1995.

10-19 mps during the 23rd compared to 1-4 mps on the 28th. The relative humidity (RH) was 48% and 57% at dawn on the 23rd and 28th, respectively. The albedos during the morning and afternoon are almost identical for the same SZA in Fig. 2. On the 28th (Fig. 3), the morning albedos are greater than those observed during the afternoon. The diurnal change in surface albedo during the remaining clear October days was similar to that of the 28th. The SCF radiometers gave results much like the averages for the 5 sites together suggesting that diurnal changes occurred independently of the surface type.

Figs. 4 and 5 show the GOES estimates of top-of-the-atmosphere broadband albedo for the same two days over the SCF area. The diurnal changes in clear-sky albedo during the 23rd and 28th are very similar to their surface-observed counterparts. Diurnal changes in clear-sky albedo during the other days are comparable to those seen on October 28 indicating consistency between the surface and satellite measurements. The GOES narrowband visible albedos revealed even greater morning-afternoon differences.

Together, the satellite and surface measurements provide evidence that the surface albedos are not symmetrical about local noon in many cases over the prairie and pasture of the southern Great Plains.

Data taken over the forest in Virginia also show a morning-to-afternoon asymmetry in surface albedo. The greatest observed change was seen during November 22, 1995 (Fig. 6). In this case, the deciduous trees were leafless, exposing some of the forest floor to direct solar illumination. A similar behavior was seen during other seasons over the forest, but to a lesser degree.

DISCUSSION

Different diurnal changes were observed over the SCF during April 1994 and October 1995. From the present data set, it is difficult to conclude why the afternoon albedos were greater than those in morning during April and less during October. Knowledge of the vegetation state is required.

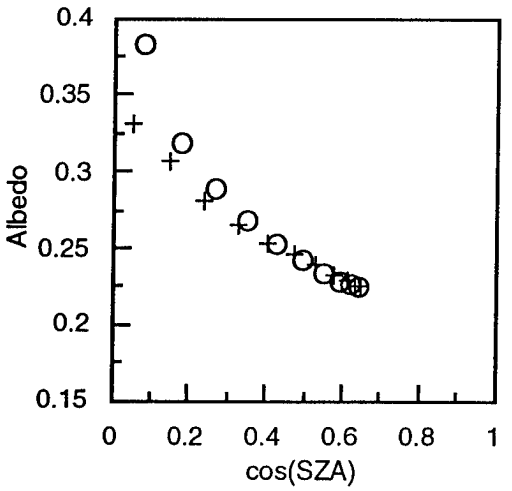


Fig. 3. Comparison of PM (+) and AM (O) broadband surface albedos over the ARM SCF on October 28, 1995.

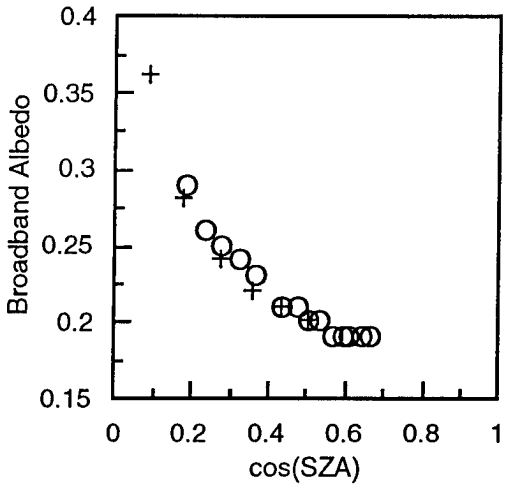


Fig. 4. Comparison of PM (+) and AM (O) broadband TOA albedos over the ARM SCF on October 23, 1995.

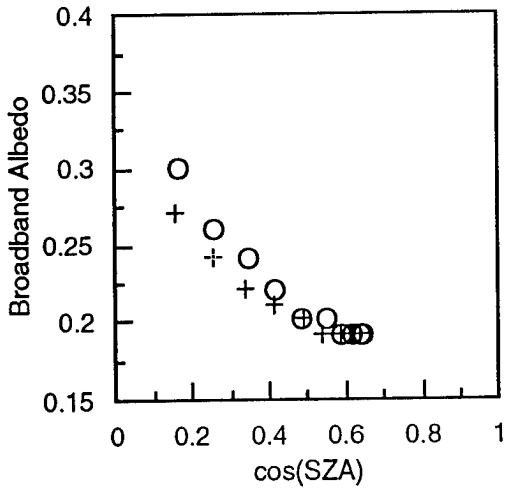


Fig. 5. Comparison of PM (+) and AM (O) broadband TOA albedos over the ARM SCF on October 28, 1995.

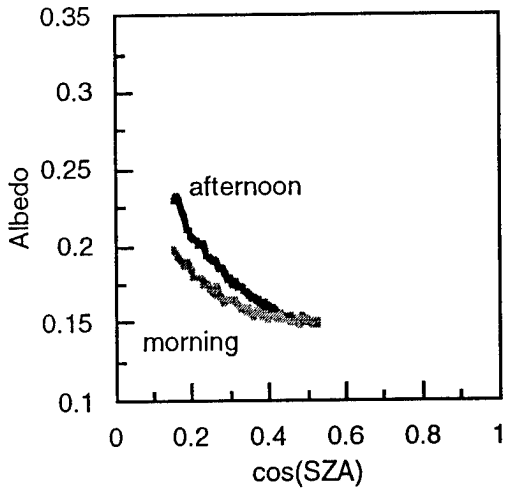


Fig. 6. Comparison of PM and AM broadband surface albedos over eastern Virginia on November 22, 1995.

There are obvious differences in soil moisture because of the relatively frequent April rains. Perhaps, the ground was moistened by the formation of dew during the night. Solar heating would dry the soil during the day raising the afternoon albedo. This type of effect would require some exposed soil in the surface radiometer field of view. The smaller change observed in the satellite data may indicate that the surface observations may only represent a small portion of the area. More measurements will be required to understand these observations

During October, drying occurred progressively during the month. In light winds, overnight radiative cooling will tend to produce dew on many exposed surfaces depending on the relative humidity and winds. Dew on most vegetation should increase the albedo because of the water droplet scattering. After the dew is evaporated by midmorning, the albedo should be nearly symmetrical for the times remaining around local noon.

To test this hypothesis, a measure of the diurnal change is introduced. The morning albedos are fit with a cubic polynomial. This fit is used to interpolate the morning albedos to the solar zenith angles of the afternoon observations. The average of the differences between the interpolated morning and observed afternoon albedos quantifies the diurnal change. Only data taken for SZA less than 85° are used. For October 28th, this mean difference is 4.2% compared to 0% on the 23rd. The greatest difference was 7.5% on October 15. These seven relative diurnal albedo differences were correlated with the mean daytime wind speed and dawn RH. The squared linear regression coefficients are 0.59 and 0.50, respectively. The correlation with wind speed is negative, indicating less diurnal change with increasing wind speed. Using these quantities as an indication of the probability of dew suggests that the observed changes in albedo over the course of the day are likely to be a result of the occurrence of dew on the vegetation overnight.

CONCLUDING REMARKS

These results are limited to a relatively small data set. However, at least during October, they are consistent with intuitive and physical theory about the effects of dew on albedo. During the early morning, the surface albedo can be 20 to 30% greater than the corresponding afternoon albedo. If measurements are taken during the early morning from a satellite such as the NOAA polar orbiter, the clear-sky albedo may be significantly overestimated for the remainder of the day. Thus, effects due to diurnal surface moisture variability should be considered in the remote sensing of clear-sky albedo. Additional measurements should be examined to determine how such changes vary with surface type and season.

ACKNOWLEDGMENTS

Research supported by Department of Energy, Inter Agency Transfer agreement (ITF# 2142216AQ1) through Pacific North-West Labs and by DOE ARM UAV program.

REFERENCES

[1] P. Minnis and E.F. Harrison, "Diurnal variability of regional cloud and clear-sky radiative parameters derived from GOES data; Part III: November 1978 radiative parameters," J. Climate and Appl. Meteorol., Vol. 23, pp. 1032-1052, July 1984.

[2] P. Minnis, W.L. Smith, Jr., D.P. Garber, J.K. Ayers, and D.R. Doelling, "Cloud properties derived from GOES-7 for the Spring 1994 ARM Intensive Observing Period using version 1.0.0 of the ARM satellite data analysis program," NASA RP 1366, 59 pp., August 1995.

RETRIEVAL OF BOUNDARY-LAYER TURBULENCE USING SPACED-ANTENNA WIND PROFILERS

C. L. Holloway, Institute for Telecommunication Sciences/NTIA
325 Broadway, Boulder, CO 80303, USA
(303) 497-6184, email: holloway@its.bldrdoc.gov
R. J. Doviak, NSSL/NOAA, Norman, OK, USA
S. A. Cohn, ATD/NCAR, Boulder, CO, USA
R. J. Lataitis, ETL/NOAA, Boulder, CO, USA

Abstract – In this paper, we present an algorithm for estimating turbulence (or wind variability) in the lower boundary layer for use with spaced-antenna systems.

INTRODUCTION

Using scattering theory [1], we derived analytical expressions for the diffraction pattern of scatter from refractive index irregularities having prescribed statistical properties (i.e., described by space-time correlation or spectral functions), and related these to the parameters of the radar as well as those of the advecting flow. Our approach expands on the earlier work by Liu et al. [2].

We showed [1] that under certain simplifying conditions (i.e., scatter from horizontally isotropic refractive index irregularities advected by uniform and/or turbulent flow), many of the diffraction pattern properties are known in terms of radar and atmospheric parameters. Formulas for the cross-correlation and cross-spectrum of signals in receiving antennas reduce to simple analytic forms. This simplifies considerably the estimation of wind profiles.

These simple analytic expressions have allowed us to develop both time-domain and frequency-domain algorithms to determine unbiased wind estimates [3,4]. By extending this work, we have developed an algorithm to estimate turbulence. In this paper we introduce this algorithm and show the calculation of turbulence using data from the National Center for Atmospheric Research's (NCAR) unique 915-MHz spaced-antenna (SA) wind profiler.

THEORY

In Doviak et al. [1] it was demonstrated that the magnitude of the normalized auto- and cross-correlation functions of signals in SA systems for receiving antenna separations less than the transmitter's antenna beamwidth are given by:

$$|c_{11}(\tau)| = \exp\left[-a_h^2\tau^2\left(v_{ox}^2+v_{oy}^2\right)-2(k_o\sigma_t\tau)^2\right] + \frac{N}{S}\delta(\tau) \tag{1}$$

$$|c_{12}(\tau)| = \exp\left[-a_h^2\left(v_{ox}\tau-\frac{\Delta x}{2}\right)^2-(a_h v_{oy}\tau)^2-2(k_o\sigma_t\tau)^2\right] \tag{2}$$

where τ is the time lag, S is the signal power, and N is the receiver's noise power. Because receiver noises are uncorrelated, there is no noise term in $c_{12}(\tau)$. $\delta(\tau)$ is the Dirac delta function, $k_o = 2\pi/\lambda$ is the radar wave number, Δx is the separation of the two receiving antennas, σ_t is the rms wind variability of each wind component if turbulence is isotropic, a_h is an antenna constant, and v_{ox} and v_{oy} are the horizontal wind components.

By completing the square in the exponent of (2), $|c_{12}|$ can be expressed as:

$$|c_{12}(\tau)| = \exp\left[-\eta - \frac{(\tau-\tau_p)^2}{2\tau_c^2}\right], \tag{3}$$

where

$$\eta = \left(\frac{a_h\Delta x}{2}\right)^2\left[\frac{v_s^2}{v_{ox}^2+v_s^2}\right] \tag{4}$$

is a loss factor that determines the lowering of the peak of $|c_{12}(\tau)|$ due to turbulence and the wind component (v_{oy}) across the baseline,

$$\tau_c = \frac{1}{2a_h\left(v_{ox}^2+v_s^2\right)} \tag{5}$$

0-7803-3068-4/96$5.00©1996 IEEE

is the square root of the second central moment of $|c_{12}(\tau)|$ (or $|c_{11}(\tau)|$), and finally

$$\tau_p = \frac{v_{ox}\Delta x}{2\left[v_{ox}^2 + v_s^2\right]} \tag{6}$$

is the time delay to the peak of $|c_{12}(\tau)|$. The effect of both the wind perpendicular to the antenna baseline v_{oy} and turbulence σ_t decorrelates the cross-correlation functions through the decorrelation parameter v_s given by:

$$v_s^2 = v_{oy}^2 + 2\left(\frac{k_o\sigma_t}{a_h}\right)^2 . \tag{7}$$

The effect of the vertical wind on the lowering of the cross-correlation is typically small and has been omitted.

η, τ_c, and τ_p can be expressed in terms of three unknowns [see (4)-(6)]: the baseline wind v_{ox}, the decorrelation parameter v_s, and the radar parameter a_h. These three equations allow us to solve for v_{ox} and v_s:

$$v_{ox} = \frac{\Delta x \tau_p}{4\eta\tau_c^2 + 2\tau_p^2} \qquad v_s^2 = \frac{4\eta\tau_c^2\Delta x^2}{4\left(4\eta\tau_c^2 + 2\tau_p^2\right)^2} \tag{8}$$

Notice that v_{ox} and v_s are functions of the three parameters, η, τ_c, and τ_p which completely define $c_{12}(\tau)$. Once τ_p, τ_c, and η are determined, v_{ox} can be obtained. In [3], a technique for fitting Gaussian functions to data is presented for determining these three parameters. There are various alternative methods that can be developed with the use of equation (3) for estimating v_{ox} in the presence of turbulence. Four different methods are presented in [3] and [4].

Equation (7) can be rearranged to give the following expression for turbulence:

$$\sigma_t = \frac{a_h}{k_o}\sqrt{\frac{v_s^2 - v_{oy}^2}{2}} \tag{9}$$

Once v_s and v_{oy} are estimated (v_{oy} can be estimated using another pair of receivers), turbulence σ_t can be obtained.

IMPLEMENTATION

NCAR has developed a unique UHF 915-MHz wind profiling radar that can operate interlaced in the Doppler beam swinging (DBS) and spaced-antenna modes. Modifications allow this radar to be used as a spaced-receiver system, with the full (four panel) antenna used to transmit and each single panel simultaneously receiving backscattered energy in four independent receiver channels [5] (Figure 1). Using time series of received signals from each receiver, we made a first attempt to implement the algorithm to estimate turbulence.

A detailed discussion of the implementation of this algorithm is found in [3]. Once the parameters τ_p, τ_c and η were determined from the radar data, v_s was estimated from (8). Given v_s and v_{oy} for any one of the six baselines from the four antennas in the NCAR system, σ_t was estimated from (9). Figure 2 shows results for σ_t from five of the baselines. The data for these results was collected on June 16, 1993 at 20:10:43 UT time from a 20-second sounding in Lamont, Oklahoma. Results from these five baselines are tightly grouped, illustrating the consistency of the four-antenna system.

Figure 3 shows an average of six different estimates of σ_t taken within a 1-hour period (20:00:00-21:00:00 UT). These results illustrate that the turbulence in the boundary layer for this date and time is about 0.5-0.8 m s^{-1}. While we have no independent measurements of σ_t to compare to our results, they are consistent with the 0.4-1 m s^{-1} values for a convective boundary layer reported in [6].

SUMMARY

We used analytic expressions, presented in [1], to derive an algorithm for estimating turbulence profiles from the auto- and cross-correlation of signals in spaced receivers. This algorithm has been implemented and preliminary results are encouraging when compared to those reported in [6].

Acknowledgments. This work was partially supported by the Atmospheric Technology Division of the National Center for Atmospheric Research, and the Atmospheric Radiation Measurement (ARM) program of the Department of Energy (DOE).

REFERENCES

[1] R. J. Doviak, R. J. Lataitis, and C. L. Holloway, "Cross correlations and cross spectra for spaced antenna wind profilers 1. Theoretical analysis," *Radio Sci., 31*(1), 157-180, 1996.

[2] C. H. Liu, J. Rottger, C. J. Pan, and S. J. Franke, "A model for spaced antenna observational mode for MST radars," *Radio Sci., 25*, 551-563, 1990.

[3] C. L. Holloway, R. J. Doviak, S. A. Cohn, and R. J. Lataitis, "Cross correlations and cross spectra for spaced antenna wind profilers 2. Algorithms to estimate wind and turbulence," in review for *Radio Sci.*, 1996.

[4] C. L. Holloway, R. J. Doviak, S. A. Cohn, and R. J. Lataitis, "Algorithms to retrieve wind from spaced-antenna wind profilers," *27th Conference on Radar Meteorology* (Oct. 9-13, 1995), Vail, CO.

[5] S. A. Cohn, J. K. Smith, C. Martin, C. L. Holloway, and J. S. Van Baelen, "Wind measurements with the NCAR UHF spaced antenna profiler: New algorithms implementation," *27th Conference on Radar Meteorology* (Oct. 9-13, 1995), Vail, CO.

[6] W. T. Pennell, and M. A. LeMore, "An experimental study of turbulence structure in the fair-weather trade wind boundary layer," *J. Atmospheric Sciences, 31*(7), 1308-1323, 1974.

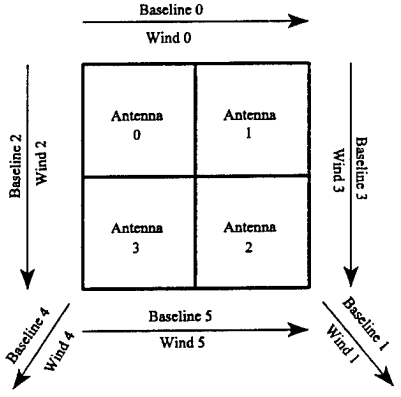


Figure 1: Antenna panel configuration of NCAR's system.

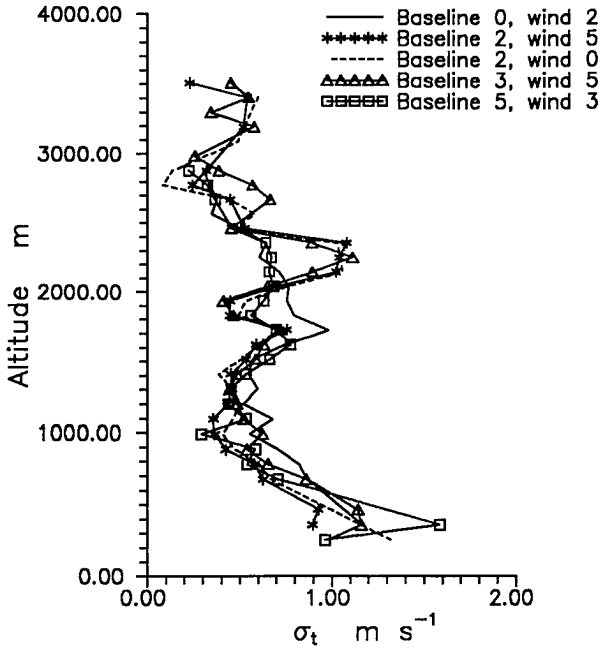


Figure 2: Estimations of σ_t as a function of altitude. These results are for five different baseline and wind components.

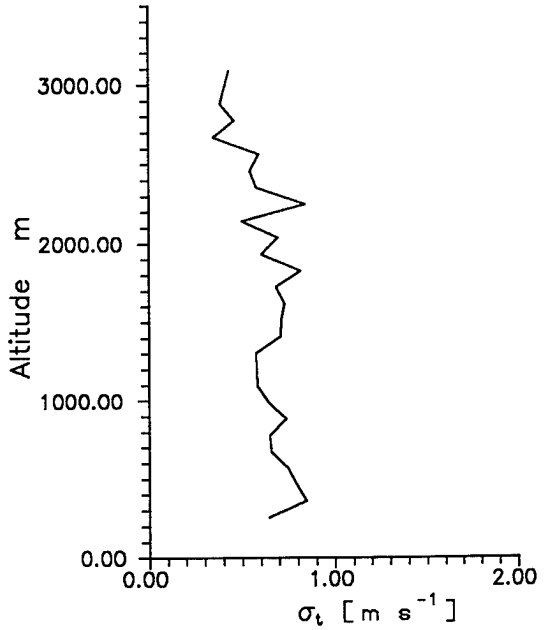


Figure 3: Averaged σ_t for six different estimates of σ_t taken within a 1-hour period.

A Buoy-Mounted Wind Profiler for Remote Measurement of Ocean Winds

James B. Mead, Philip M. Langlois, Robert E. McIntosh
Quadrant Engineering Inc.
107 Sunderland Rd.
Amherst, MA 01002
Phone: (413) 549-4402 FAX: (413) 549-5203
email:j.mead@ieee.org

Abstract – Quadrant Engineering has recently developed a compact, low power, marine boundary layer radar wind profiler (MBL Profiler) suitable for installation on a small boat or on a buoy. The MBL-Profiler utilizes high-efficiency radar and data acquisition componentry to minimize power consumption, with the radar and data system requiring approximately 60 W for full power operation. Additional power of about 15 W will be required to operate a low power PC and telemetry system. If used intermittently, (30 minute consensus wind estimate, every 2 hours), the system will draw less than 20 W average power, making it suitable for battery-powered operation. Motion compensation is achieved entirely in software. During data acquisition we constantly monitor the position of the antenna by storing the output of two tilt sensors and a compass. This is sufficient information to provide an accurate estimate of average wind speed and direction.

Overview of the MBL-Profiler

During the past fifteen years, small, UHF radar wind profilers have been developed to remotely sense winds in the atmospheric boundary layer (0 to approximately 2 km altitude)[1],[2]. Boundary layer profilers are compact (1 m x 1 m antennas), required only modest transmitter power (2-20 W average), and can detect winds at altitudes from 100 m to 5 km. Until now, these systems have been operated primarily from fixed land-based locations, or from stabilized platforms aboard ships [3]. The National Science Foundation recently funded Quadrant Engineering to develop a low-power, compact radar wind profiler using software motion compensation that is suitable for operation from a buoy or small fishing vessel.

The MBL Profiler consists of a 150 W peak-power solid-state radar, a 6' x 6' microstrip antenna, a radar controller/data acquisition/digital integrator card, a motion detection monitor, and a PC controller. A photograph of the system mounted on a 20 foot fishing vessel is shown in Figure 1. The radar transmitter/receiver box is mounted directly beneath the antenna to minimize transmission line loss. The remainder of the radar is mounted in a standard 19" rack, the bulk of which is occupied by the computer, monitor and keyboard.

This work was supported by the National Science Foundation, SBIR award no. 9223593.

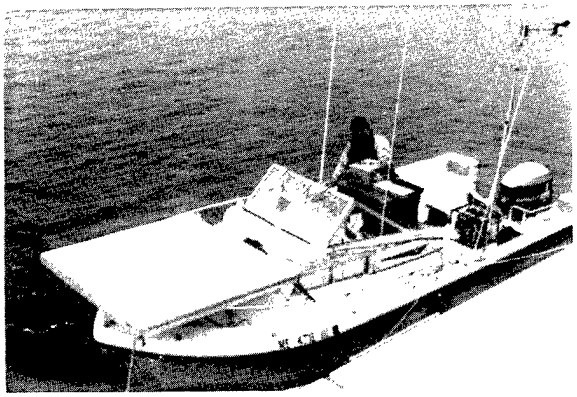


Fig. 1. Photos of MBL-Profiler mounted on 20' fishing vessel.

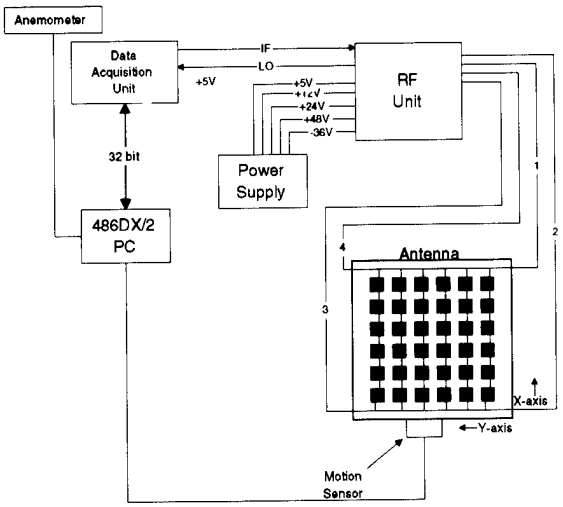


Fig. 2. System-level block diagram of the MBL Profiler.

A block diagram showing the major subsystems of the MBL-Profiler is presented in Figure 2. The system consists of the radar transceiver, a four-beam microstrip antenna, data acquisition/processor electronics, power supply, and a host computer. All of the digital electronics necessary to control the radar and acquire data are located on a single four-layer printed circuit board. Two Programmable Logic Arrays (PLAs) include all of the

0-7803-3068-4/96$5.00©1996 IEEE

TABLE I
MBL-PROFILER SYSTEM PARAMETERS

parameter	specification
nominal operating frequency	915 MHz
wavelength	.328 m
peak transmit power	150 W
average transmit power	6 W
pulse duration	.6-1.7 μ s
pulse repetition frequency	40 KHz
antenna effective area	1.3 m^2
antenna beamwidth	11-14°
antenna elevation angle	15°
antenna azimuth angles	NE, SE, SW, NW

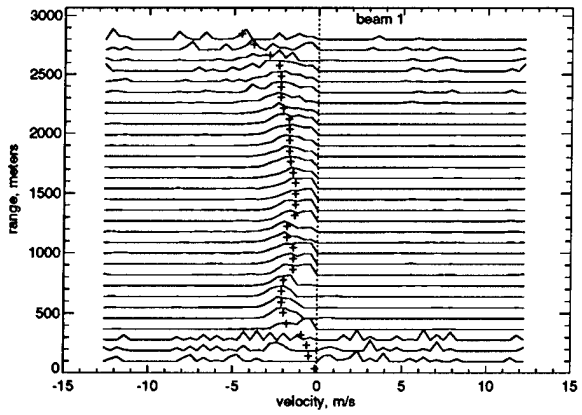


Fig. 3. Waterfall plot of the Doppler velocity spectrum for each range gate. Negative velocities are directed away from antenna.

TTL logic necessary to generate the radar control signals, such as pulse repetition frequency, pulse length, range gate spacing, number of gates, coherent average length, etc. This board also contains a digital integrator circuit, that samples the radar complex (I/Q) output with an 8-bit ADC, then sums these digital words using a ring-adder. This provides coherent signal integration in blocks of 16, 32,48, up to a maximum of 128 radar pulses.

Signal Processing

The coherent averages formed by the hardware integrator are transferred to PC memory via a National instruments ATDIO-32F DMA-transfer card. A 486-66 MHz PC programmed in C++ sorts the data, removes DC offsets, and computes 16, 32, 64 or 128 point FFTs in real-time. The FFTs are converted to power spectra, which are averaged for approximately 30 s before being stored for later analysis. The spectral means at each height are combined for all four beams to estimate wind velocity as a function of height. Like conventional land-based wind profilers, the MBL-profiler depends on relative motion between the desired atmospheric signal and stationary clutter to aid in signal tracking. The primary clutter source when operating at sea is ocean surface backscatter from antenna sidelobes, which exhibits zero mean frequency shift when averaging over long time periods (several minutes).

Motion compensation is necessary to account for antenna tilting and rotation. The MBL-profiler utilizes two inclinometers and a compass to determine the orientation of the antenna in world coordinates. Once the antenna position is known, the position of the four antenna beams in world coordinates can be determined. Knowing the average position of the antenna beams during the radar integration time is the only information necessary to extract the mean wind field.

Typical Clear Air Data – A waterfall plot showing the power spectrum of a 100 second average of data from antenna beam 1 is shown in Figure 3. The +'s represent the best estimate of the spectral mean computed using a centroid tracker. In the absence of adequate clear-air signal-to-noise or signal-to-clutter, the spectral mean can be estimated and marked by hand, as was done for gates 1-4. The first "+" sign, shown near zero altitude, is the projection of the surface wind velocity into the radar beam direction. For the ocean data presented below, the surface winds were measured by an anemometer mounted on the boat approximately 3 meters above the water surface.

RESULTS OF PRELIMINARY OCEAN TESTS OF THE MBL-PROFILER

On September 7, 1995, we installed the MBL-Profiler on a twenty-foot fishing boat and headed to a location approximately 1 mile beyond the mouth of the Merrimack River in Newburyport, MA. Figure 4 shows a typical Doppler spectra waterfall plot representing a sixteen minute consensus average, beginning at 10:40 am, Sept. 7. The solid vertical contour represents the CLASS-derived horizontal wind speed projected into beam 1 (the balloon data was gathered roughly 50 minutes after the radar data was collected. Ideally, the vertical line should coincide with the mean value of the Doppler spectra, as indicated by the "+" signs. The atmospheric conditions at the time this data was gathered gave good radar return to altitudes of 1200 m, so we have truncated the waterfall plots to 1500 m. The range of x-tilt angles was -18.8° to 2.6°, y-tilt angles, -15.5° to 16.0°, and headings, 72.8° to 142.7°.

Based on these data, we computed horizontal wind speed and wind direction, as a function of height, as shown in Figures 5 and 6. The wind speed and direction at zero range corresponds to anemometer measurements made on the boat. The dotted line represents CLASS-derived horizontal wind speed and direction. Vertical winds were not available from the balloon data, although

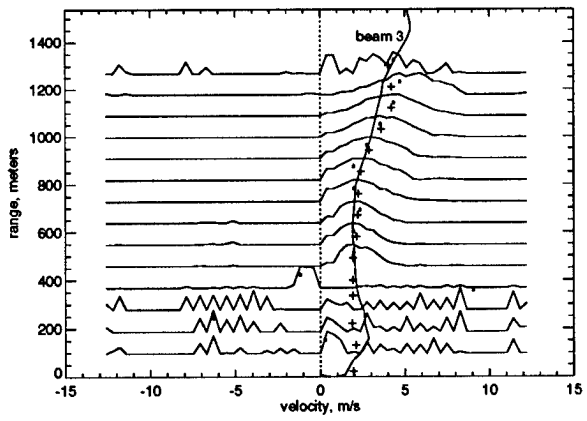


Fig. 4. Doppler spectra for beam 3, Sept. 7, 1995, 10:40-10:56 am. Beam 3 is directed SW; Wind is from the Southwest. Projection of CLASS-winds into the radar beams is shown by vertical line.

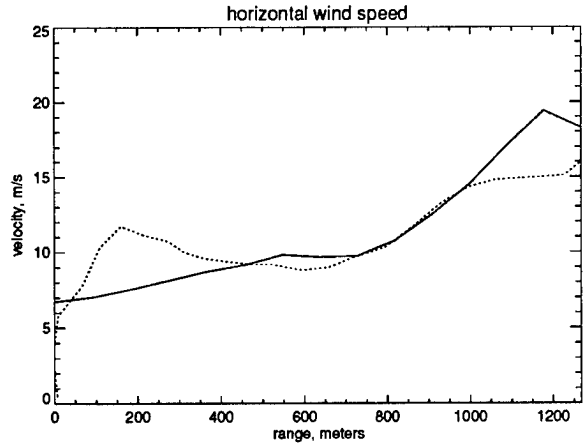


Fig. 5. Horizontal velocity measured by MBL-Profiler, Sept. 7, 1995, 10:40-10:56 am. Dotted lines represent CLASS data.

the radar-derived vertical winds varied between $\pm .6ms^{-1}$.

Discussion and Future Plans

The data presented above demonstrates that the MBL-Profiler can measure horizontal wind speed and direction from a moving ocean platform, to altitudes in excess of 1 km. While the accuracy of these measurements has not been demonstrated conclusively, the preliminary data gathered above shows reasonable agreement with radiosonde-derived winds.

The MBL-Profiler is currently being operated by the University of Massachusetts Microwave Remote Sensing Laboratory in support of the ARO-sponsored Turbulent Eddy Profiler program.

BIBLIOGRAPHY

1. Ecklund, W.L., D.A. Carter, B.B. Balsley, "A UHF Wind Profiler for the Boundary Layer: Brief Description and Initial Results", *J. Atmos. Ocean Tech.*, v. 5, n. 3, 432–441, 1988.

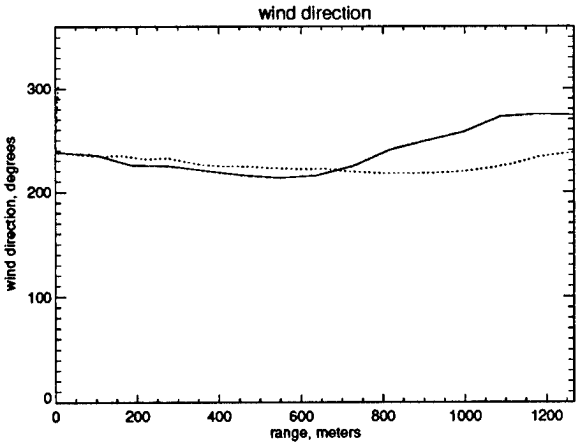


Fig. 6. Wind direction measured by MBL-Profiler, Sept. 7, 1995, 10:40-10:56 am. Dotted lines represent CLASS data.

2. Balsley, B.B., "Design Considerations for Coherent Radar Systems for Probing the Troposphere, Stratosphere, and Mesosphere", *Preprints, 18th Conference on Radar Meteorology (Atlanta)*, AMS, Boston, 387–390, 1978.
3. D.A. Carter, W.L. Ecklund, K.S. Gage, M. Spowart, H.L. Cole, E.F. Chamberlain, W.F. Dabberdt, J. Wilson, "First Test of a Shipboard Wind Profiler", *Bulletin American Meteo. Soc.*, 73(10), Oct. 1992, 1587-1592.

Frequency Domain Interferometry in the Planetary Boundary Layer: First Results

B. R. Corner, R. D. Palmer, and R. M. Narayanan
Dept. of Elec. Engr. and Center for Electro-Optics
216N WSEC, Univ. of Nebraska-Lincoln, Lincoln, NE 68588-0511
Tel: 402-472-6849, Fax: 402-472-4732, Email: bpalmer@unlinfo.unl.edu

Introduction

A 915 MHz boundary layer radar (BLR) is currently being used with frequency domain interferometry (FDI) and a Radio Acoustic Sounding System (RASS) to study the nocturnal jet. FDI is a technique by which the range resolution of an existing radar can be increased by using a pair of alternating transmitter frequencies. It is hoped that by using FDI, turbulent layers that exist at the shear regions of the nocturnal jet can be resolved within the resolution volume of the radar. The RASS is used to estimate the virtual temperature profile of the atmosphere from the local speed of sound. Using FDI and RASS will provide greater detail and hopefully an understanding of jet formation. Nocturnal jets are a low-level wind maximum that are common in the Great Plains region of the United States. Wind speeds in the jet can occasionally reach velocities in excess of 25 ms^{-1}. The jet occurs at an altitude of approximately 500 m and normally forms during the night in calm surface wind and clear sky conditions. The jet can generate severe turbulence and wind shear which can be hazardous to unsuspecting aircraft.

FDI Implementation

As previously mentioned, FDI is a radar technique which uses two closely spaced alternating frequencies to improve the altitude resolution of a radar [1]. The phase difference from the received signals is used to track the relative position of any scattering layer contained within the resolution volume [2]. The frequency difference (Δf) of the transmitted signal is chosen such that a maximum phase difference of 2π or less is obtained over the resolution volume as shown in Fig. 1. Ambiguity will result if the frequency difference is greater than 2π. Choosing the frequency difference as $\Delta f = 1/\tau$, where τ is the pulse width of the radar, gives a phase range of exactly $\pm\pi$. This allows the phase range to cover exactly one resolution volume. Any position change in a scattering layer causes its phase to change accordingly. The absolute position of the layer in the volume can then be determined from the initial transmitted phase of the system. In addition to the layer's position, the width of the layer can be obtained by an analysis of the coherence of the signal.

FDI will only work if a single layer is present within the resolution volume. If multiple layers exist, the FDI technique will provide only an average layer location and not improve the overall resolution. FDI data were analyzed by calculating the normalized cross-spectrum

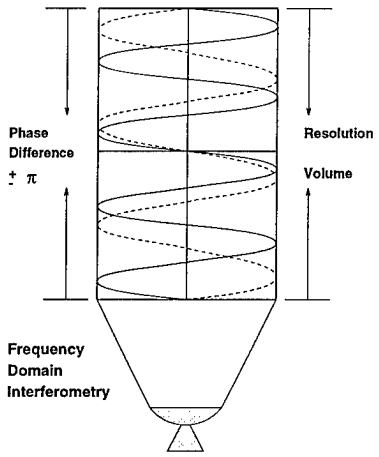


Fig. 1. A depiction of wave propagation using FDI in one resolution volume of the radar.

$$S(f_1, f_2) = \frac{\langle V_1 V_2^* \rangle}{(\langle |V_1|^2 \rangle \langle |V_2|^2 \rangle)^{1/2}} \quad (1)$$

as given by *Kudeki and Stitt* [1]. V_1 and V_2 are the Fourier transforms of the signals from the two frequencies, and $\langle \cdot \rangle$ represents the expected value operator. The magnitude and phase of $S(f_1, f_2)$ are given by

$$|S(f_1, f_2)| = e^{-2\Delta k^2 \sigma_r^2} \quad (2)$$

$$\phi_{12}^{FDI} = 2\Delta k \bar{r} \quad (3)$$

where Δk is the difference in the wavenumbers between the two frequencies, i.e., $\Delta k = 2\pi\Delta f/c$ and c is the speed of light. The magnitude of the normalized cross-spectrum (coherence) is used to find the thickness of the layer $2\sigma_r$ while the phase determines the relative position $\bar{r}$ of the layer in the resolution volume.

The hardware implementation of FDI used with the 915 MHz BLR is shown in Fig. 2. The BLR's 60 MHz IF oscillator is supplied to a DSB modulator as well as an appropriate Δf from a frequency synthesizer. A pre-pulse timing signal input to a flip-flop regulates a SPDT switch

0-7803-3068-4/96$5.00©1996 IEEE

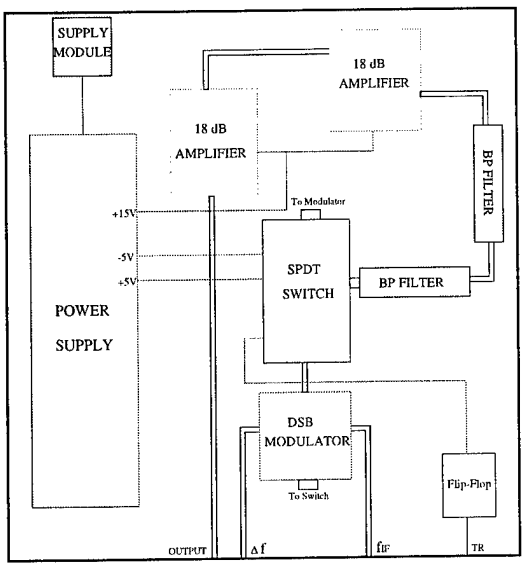


Fig. 2. Block diagram of the FDI hardware showing all the major components.

on the output of the modulator. Before each new pulse, switching occurs and results in an alternating frequency on the switch's output. This signal is then bandpass filtered and amplified before returning to the radar. Preliminary results have been obtained using the FDI system and soon FDI measurements of the nocturnal jet will be attempted.

Nocturnal Jet

Nocturnal jet formation is caused by a combination of several meteorological and geographical properties. The basics of its formation was developed by *Blackadar* [3]. At sunset, the planetary boundary layer (PBL) near the surface stabilizes as convective activity subsides. The lowest level of the atmosphere is cooled radiationally while the temperature in the remainder of the PBL remains essentially unchanged. This leads to a temperature inversion between the lower or Ekman layer and the upper inertial boundary layer. The frictional stress in the inertial layer is reduced and the wind speed increases to compensate with the existing pressure gradient [4].

As the night progresses, the Ekman layer becomes thinner as radiational cooling suppresses any buoyant mixing [5]. Kinetic energy dissipation to the surface is largely confined to this layer and becomes independent of the now growing inertial layer above. This effectively decouples the layers from each other frictionally as turbulent mixing is no longer significant in either layer. The scale of the winds in the inertial layer, without the effects of friction, become that of large-scale inertial motion. The inertial oscillations are slow to develop and may take several hours before influencing the jet. The jet tends to reach a maximum supergeostrophic velocity when the length of the night is greater than half the inertial period [6]. Since the inertial period is given by $2\pi/f$ (where f is the Coriolis parameter), the strength of the jet is not only a function of latitude, but also the time of year. Because of these conditions, the strongest nocturnal jets normally occur in the late fall to early spring months in the Great Plains. During this time the longer nights and decreased daytime convection provide ideal environmental factors for development.

Although the two-layer model provides a good explanation of jet development, numerous other factors play into its formation. First, clear skies are needed to allow radiational cooling and inertial motions to begin. Winds near the surface must also be light to prevent any turbulent mixing that would interfere with the formation of a temperature inversion between the layers. Frontal passages and cyclonic activity that produce turbulence and instability disrupt the majority of the conditions necessary to develop a nocturnal jet. Radiosonde observations have shown that jets do not exist during the time of a frontal or cyclonic disturbance [6]. During the daytime, convective heating and turbulent mixing causes the Ekman layer to fill the entire PBL. The convection also acts to evenly distribute momentum in the layer and eliminates any inertial flow. This process breaks down and rapidly dissipates any jet within a few hours after sunrise. The lapse rates in the daytime layer are basically adiabatic and the conditions at the top of Ekman layer are generally in geostrophic balance [5].

Preliminary Results

Although FDI measurements of the nocturnal jet have not yet been attempted, the BLR has been used to observe the jet on numerous occasions. Fig. 3 shows a wind magnitude plot while Fig. 4 shows a wind direction plot of the jet from October 7, 1993. A nocturnal jet is prevalent near a height of 500 m for much of the night and has winds of 28 ms^{-1}at its maximum intensity. The white rectangles in the plot indicate areas of missing or bad data. Surface winds at the time of the jet were light southerly. After 0800 LT the jet breaks down as turbulence created by solar heating occurs. The following day a frontal system brought thunderstorms and severe weather to the area and no jet occurred that night.

Another example of the jet occurred on June 6, 1995. In Fig. 5 the jet can be seen again at an altitude of 500 m with maximum winds of 17 ms^{-1}. Although not as strong as the jet of October 7, rain showers and clouds the preceding evening may have hindered some development. Surface winds were light south-southeasterly and the sky was clear during the night. Sunrise occurred just before 0600 LT and can be seen that the jet breaks down immediately thereafter. It is interesting to note that in the late

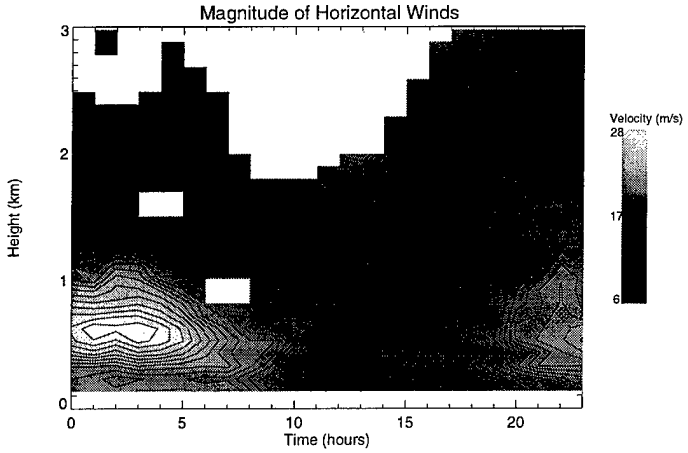


Fig. 3. Wind magnitude plot from October 7, 1993 showing the nocturnal jet.

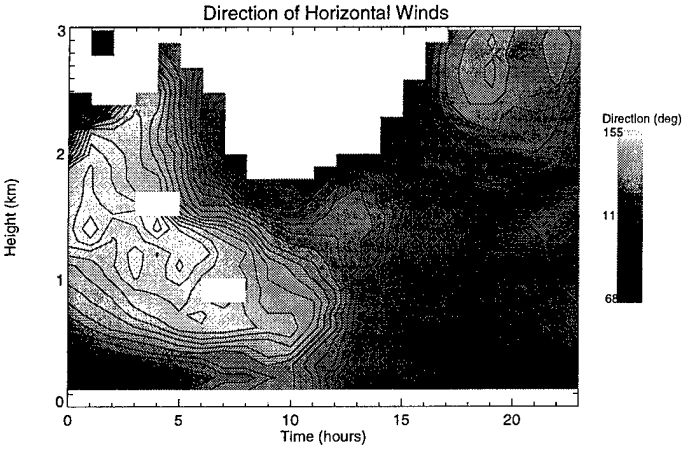


Fig. 4. Wind direction plot from October 7, 1993. The jet's wind direction is primarily from the southeast.

evening hours the jet begins to reform. During the night of June 7, however, a cold front brought thunderstorms and the reformed jet dissipated. For several days following June 7, low clouds, drizzle, and fog occurred and no jet was observed by the BLR.

Acknowledgments

BRC, RDP, and RMN were supported by the Division of Atmospheric Sciences of the National Science Foundation through grant ATM 94-02021.

References

[1] Kudeki, E. and G. R. Stitt, Frequency domain interferometry: A high-resolution radar technique for studies of atmospheric turbulence, *Geophys. Res. Lett.*, *14*(3), 198-201, 1987.

[2] Fukao, S. and R. D. Palmer, Spatial and frequency domain interferometry using the MU radar: A tutorial and recent developments, *J. Geomag. Geoelec.*, *43*, 645–666, 1991.

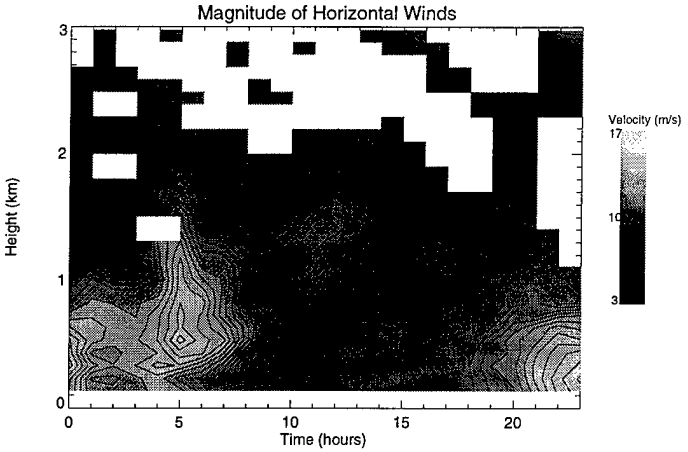


Fig. 5. Wind magnitude plot from June 6, 1995. The jet is prominent near 500 m during the night and reforms again the subsequent evening.

[3] Blackadar, A.K., Boundary layer wind maxima and their significance for the growth of nocturnal inversions, *Bull Amer. Meteor Soc., 38,* 283-290, 1957.

[4] McNider, R. T., and R. A. Pielke, Diurnal boundary-layer development over sloping terrain, *J. Atmos. Sci., 38,* 2198-2212, 1981.

[5] Hoxit, L. R., Diurnal variations in planetary boundary-layer winds over land, *B-L Meteor., 8,* 21-38, 1975.

[6] Thorpe, A. J., and T. H. Guymer, The nocturnal jet, *Quart J. Atmos. Sci., 32,* 2288-2308, 1977.

A Digital Beamforming Radar Profiler for Imaging Turbulence in the Atmospheric Boundary Layer

James B. Mead, Geoffrey Hopcraft, Brian Pollard, Robert E. McIntosh
Microwave Remote Sensing Laboratory
Knowles Engineering Building
University of Massachusetts
Amherst, MA 01003
Phone: (413) 545-2463 FAX: (413) 545-4652 email: mead@alex.ecs.umass.edu

Abstract – Digital beamforming techiques with adaptive processing have been used for several decades in high performance radar systems to track targets in the presence of jamming. With the availability of inexpensive microwave and digital componentry, these techniques are now practical for non-military applications. We have recently developed a 915 MHz digital beamforming radar system, termed the Turbulent Eddy Profiler, designed to resolve atmospheric C_n^2 fluctuations over a three-dimensional volume containing several thousand pixels, with each pixel approximately 30 m on a side. These scales are comparable with Large Eddy Simulations (LES) allowing a comparison of radar-derived structure statistics with those generated by LES.

INTRODUCTION

Boundary layer radar wind profilers have proven very effective in providing continuous monitoring of winds [1]-[2]. However, the spatial distribution and dynamics of atmospheric turbulence—the primary scattering mechanism for radar wind profilers—are less well understood, in large measure because instrumentation has not been available to image clear air turbulence in multiple dimensions. The development of four-dimensional atmospheric imaging techniques can play a major role in validating the output of advanced computer models. Codes such as LES are now being used to model local fluctuations in C_n^2 [3]—fluctuations which are proportional to the volume reflectivity measured by clear-air radars. These computer models suggest that isocontours of constant C_n^2 are coupled to isocontours of constant temperature and momentum flux which in turn are aligned with the mean wind vector.

The Turbulent Eddy Profiler (TEP) was designed to provide fine-scale imagery of the local index of refraction structure function parameter, C_n^2. TEP's 90 element array provides a focused beamwidth of 3.5°, yielding 30x30x30 cubic meter pixels at an altitude of 500 meters. TEP generates approximately 50 beams within its 25° field of view, yielding 2500 pixels between 100 meters and 1600 meters altitude. Noncoherently averaged spectra are computed for each pixel up to ten times per minute.

This work was supported by the US Army Research Office under Contract DAAL03-92-G-0110.

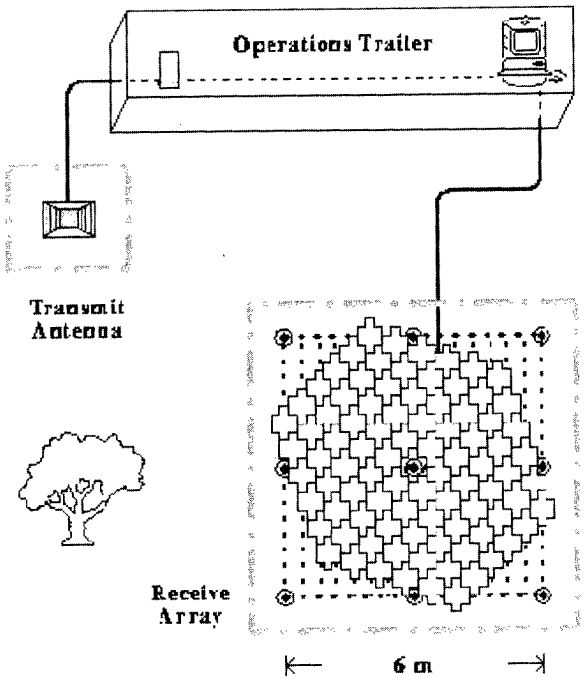


Fig. 1. Site plan of TEP.

A site plan for TEP is shown in Figure 1. A 48' long trailer houses the transmitter, data system, and host computer and can be used to transport the entire TEP system to a remote site. TEP's receiver array consists of 90 separate microstrip antennas, each backed by a low-noise receiver, digital integrator, and control and storage electronics. A corrugated horn transmit antenna, fed by a 25 kW peak-power transmitter, illuminates a 25 degree wide conical volume above the receiver array. Coherently integrated I and Q data from each receiver is processed using a software beamforming algorithm to produce focused beams of 3.5 degree width, resulting in approximately 50 beams from the full array. Table I lists the system parameters necessary to compute sensitivity and resolution.

DETAILED DESCRIPTION OF SIGNAL PROCESSING.

Signal processing with TEP involves a combination

TABLE I
TEP SYSTEM PARAMETERS

nominal operating frequency	915 MHz
wavelength	.328 m
transmit power, peak	25 kW
pulse duration	200 nS
average power	200 W
pulse repetition frequency	40 KHz
antenna effective area	.3 m^2
field of view	25°
array beamwidth	3.5°
receiver noise figure	1.0 dB, typical
FFT length	64 point
coherent average length	400 point

of digital beamforming techniques along with the spectral processing used by most conventional wind profilers. Data flow for the system is shown diagramatically in figure 2. Each of TEP's 90 receivers is backed by a digitizer/coherent integrator which forms separate 400 point coherent averages of I and Q for each range gate. Six separate PC-based data systems store the coherently averaged data to 8 mm tape.

Digital beamforming involves correcting the complex voltage at each element for phase and magnitude errors, then summing the voltage from each element with a phase offset that is determined by the location of the focal point of the array, i.e., the pixel location. This phase correction varies linearly across the face of the array provided that the array is focused beyond the antenna's far field (220 meters for TEP). Focusing to closer distances requires a parabolic phase correction. The irregular layout of the array makes it awkward to apply fast transform techniques, like the FFT, to compute the far-field pattern. Thus, the array response is computed independently for all pixels in the field of view.

Digital beamforming is performed 100 times per second using the 400 point sum of I and Q for each range gate of each antenna. The output of the digital beamforming algorithm is a coherent voltage for each pixel. After removing DC offsets the power spectrum of this data stream is computed for each pixel. A number of these spectra are averaged noncoherently to smooth the frequency-domain response. These spectra are then processed to remove clutter and any spurious signals before extracting spectral mean, spectral width and peak power. Two-dimensional or volumetric images of any of these data products may then be generated with new images produced as often as ten times per minute.

RESULTS OF ENGINEERING TESTS

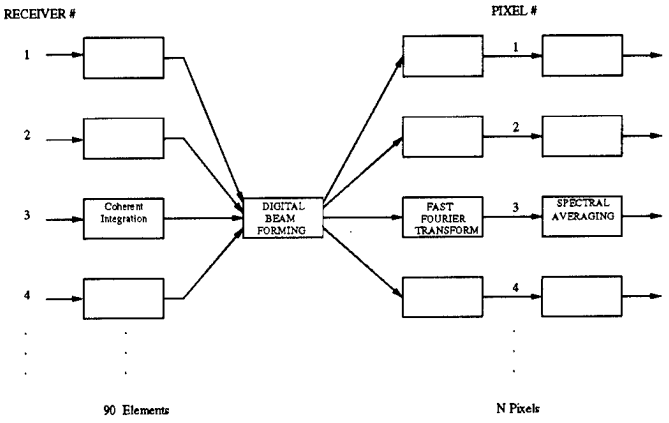


Fig. 2. Signal flow diagram showing coherent averaging, digital beamforming, and spectral processing.

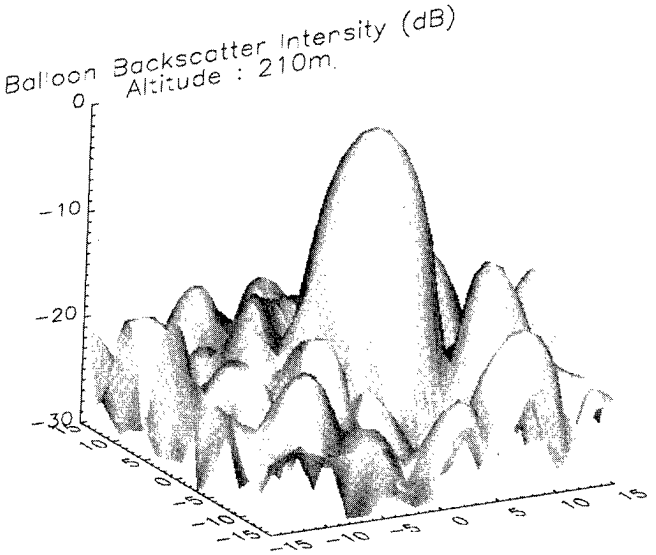


Fig. 3. Response of 37 element array to a crossed-dipole at an altitude of 210 m.

Since November, we have been operating a 37 element digital beamforming array to perform engineering tests of the system. On November 21, we launched a crossed-dipole over the array at an altitude of 200 m which we used to calibrate the array and test the ability of TEP to focus on a point target. Figure 3 shows the azimuthal amplitude response of the array to the crossed-dipole, which exhibited peak sidelobes of 12 dB. The ideal peak sidelobe level for this array is approximately 15 dB.

In early December we gathered data during a light snowfall, which provided an opportunity to test our ability to focus the array using the statistical properties of precipitation through a technique pioneered by Attia and Steinberg [4]. Figure 4 compares the Doppler spectra for snowfall received from a single element to the spectrum from the full array focused using the clutter calibration scheme. Focusing the array sharpens the spectrum by a

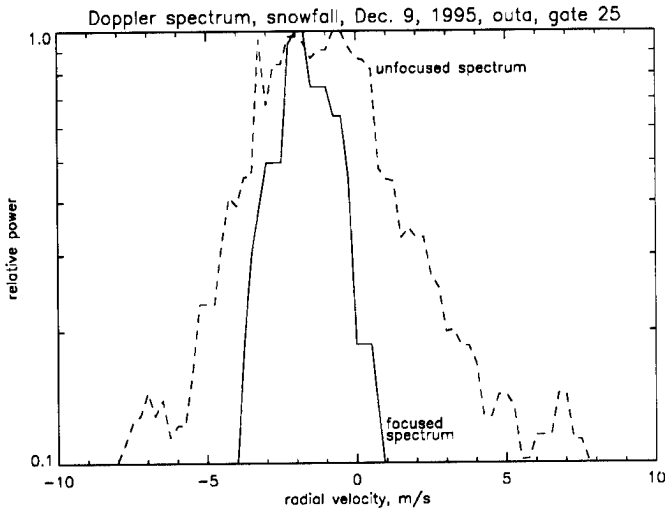


Fig. 4. Comparison of Doppler spectrum of the 37 element array to that of a single element.

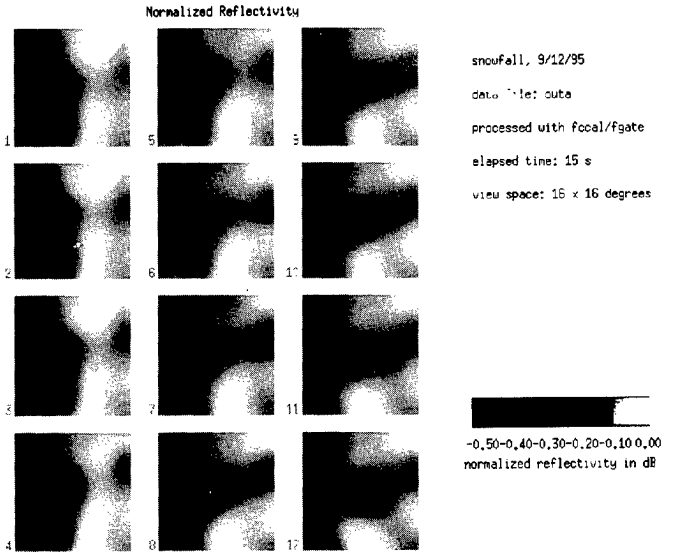


Fig. 5. Sequential series of twelve normalized reflectivity images of snowfall.

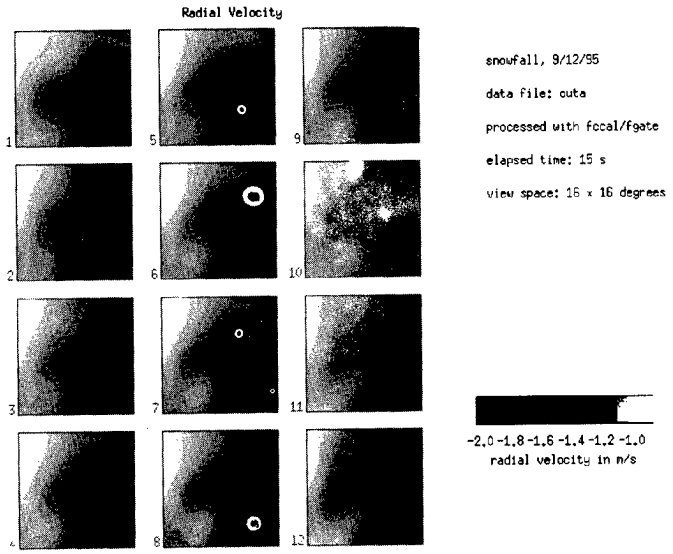


Fig. 6. Sequential series of twelve radial velocity images of snowfall.

factor roughly proportional to the ratio of the beamwidth of a single element to that of the full array, as long as the spectral width is dominated by horizontal motions of the scatterers. In the limit of very narrow array beamwidths, random motions of the scatterers will determine the spectal width.

The imaging capability of the full array is shown in Figures 5 and 6, where a series of two-dimensional reflectivity and radial velocity images are shown, each image representing variations over a horizontal slice through the imaging volume. The data are presented in the azimuthal plane with each axis displaying $\pm 8°$ off boresite averaged over three range gates between 90 and 150 m. The total elapsed time is 12 s.

In Figure 5, the snow exhibits a very narrow range of reflectivity values; thus, a large number of samples (500) were averaged to smooth the data. The two regions of high reflectivity in these images are likely to be regions of slightly higher snow density or contain larger particles than the surrounding snow volume. On average, the radial velocity images shows a velocity gradient pointing from right to left. The mean horizontal velocity was computed to be 3.6 ms^{-1} by removing the average vertical velocity of the snowfall of approximately 1.5 ms^{-1} and noting that the residual radial velocity varied $\pm$ .5 ms^{-1} over $\pm$ 8°.

Further information on TEP can be found on the TEP web-page at http://acadia.ecs.umass.edu/html/tep.html.

BIBLIOGRAPHY

1. W.L. Ecklund, D.A. Carter, B.B. Balsley, "A UHF Wind Profiler for the Boundary Layer: Brief Description and Initial Results", *J. Atmos. Ocean Tech.*, v. 5, n. 3, 432–441, 1988.
2. B.B. Balsley, "Design Considerations for Coherent Radar Systems for Probing the Troposphere, Stratosphere, and Mesosphere", *Preprints, 18th Conference on Radar Meteorology (Atlanta)*, AMS, Boston, 387–390, 1978.
3. L. J. Peltier and J. C. Wyngaard, 1995: "Structure-function parameters in the convective boundary layer from large-eddy simulation",*J. Atmos. Sci.*, **52**, 3641–3660.
4. E.H. Attia and B. D. Steinberg, "Self-Cohering Large Antenna Arrays Using the Spatial Correlation Properties of Radar Clutter," *IEEE Trans. Ant. Propagation*, 37, Jan. 1989, p. 30-38.

Preliminary Results From the Arecibo 430 MHz Spatial Interferometry System

P. B. Howell, R. D. Palmer, and R. M. Narayanan
Dept. of Elec. Engr. and Center for Electro-Optics
216N WSEC, Univ. of Nebraska-Lincoln, Lincoln, NE 68588-0511
Tel: 402-472-6849, Fax: 402-472-4732, Email: bpalmer@unlinfo.unl.edu

M. F. Larsen
Dept. of Physics, Clemson University, Clemson, SC 29634

J. Y. N. Cho
Arecibo Observatory, Arecibo, PR 00613-0995

Introduction

The 430 MHz radar system of the Arecibo Observatory (AO) possesses one of the largest power-aperture products in the world. The aperture is effectively 200-300 m and the peak power is approximately 2.5 MW. Designed originally for ionospheric and radio astronomy purposes, the AO is built into a natural bowl in the Puerto Rican terrain and is operated by the National Astronomy and Ionosphere Center. The feed system is directed downward, toward the dish, and then reflected into the atmosphere. As a result, the platform which houses the feed systems must be very stable. The structure is suspended by a network of steel cables strung from large concrete towers. In total, the feed platform weighs approximately 600 tons and cannot be moved rapidly. This results in an enormous amount of wasted time during the steering of the beam, which can take up to 30 min. Doppler beam swinging (DBS) techniques have been attempted with the system but adequate temporal resolution is difficult to obtain. The DBS technique determines the wind velocity by obtaining the Doppler shift of the scattered signal from several beam directions, which are converted into radial velocity estimates. Subsequently, the radial velocity estimate can be used to derive the overall wind field. DBS techniques have been attempted with the AO system but adequate temporal resolution is difficult to obtain because of the slow beam steering. Multi-receiver techniques, which use only a single beam direction, can alleviate the temporal resolution concern since no beam steering is needed. In a collaborative effort between the University of Nebraska, Clemson University, and Cornell University, a spatial interferometric (SI) system, i.e., multi-receiver, has been built and will be installed at the AO. Preliminary tests have been performed in 1995 with final installation planned for the spring of 1996. The results of the tests will be discussed in this paper.

Technical Description

The fundamental idea behind SI is to transmit with a beam width large enough to encompass the observation volume and receive using spatially separated antennas. Typically, three antenna arrays on two baselines are implemented. In most cases the magnitudes of the receive echos on each antenna array are similar due to the small antenna array separation distance D compared to the distance to the range volume. The phase is affected by the spatial separation of the receive antennas. The phase difference between two antennas is given by $\phi_{12} = \phi_1 - \phi_2 = kD\sin\delta$. Where ϕ_{12} is the phase differential, k is the wave number and δ is the angle from zenith. Some basic assumptions are made in that the winds are assumed to be uniform throughout the transmit beam and since the beam width is a few degrees, this assumption is valid. With this assumption, it can be seen that the scatterer location will range from half the radar beam width in one direction to half the radar beamwidth in the opposite. Theses maximum ranges will correspond to non-aliased phase values of $\pm\pi$. The distance D can be calculated from the known beamwidth and the desired phase range. Scatterers at these maximum ranges will have opposite Doppler shifts. Therefore, cross spectral analysis inherently Doppler sorts scatterers from different locations in the beam. The horizontal velocities can be obtained from linear variations in the cross spectral phase. As shown in Fig. 1 the location of the scatterer is known by observing the phase difference of the receive echos on the respective channels. It is clear that, in the mono-static case, a scatterer located at zenith will have a phase path differential of zero. This follows the discussion of *Larsen et al.*, [1] in which it was shown that if the scatterers are moving horizontally through the sampling volume with a uniform speed and the direction of the wind is parallel to a baseline, the radial velocity will vary from $-v_h sin\delta$ to $+v_h sin\delta$ where v_h is the actual horizontal wind speed. The fundamentals for this are based on works by *Wood-*

0-7803-3068-4/96$5.00©1996 IEEE

man and *Briggs*, see [2] and [3]. Further work was done by *Larsen* and *Röttger*, see [4] and references therein.

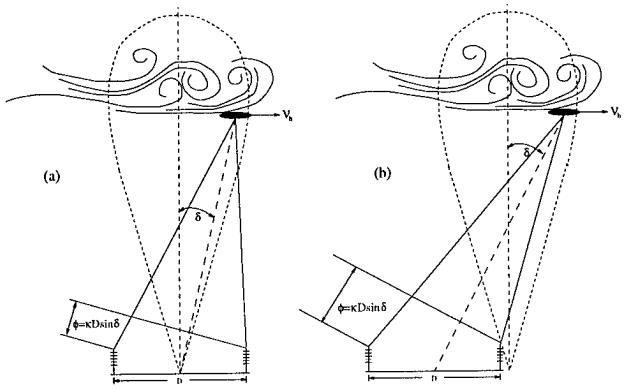


Fig. 1. A two dimensional mono-static (a) and bistatic (b) radars are shown. The turbulent scatterer can be located by the phase path difference to the receive antennas. It is clear that a scatterer located at zenith ($\delta = 0$), in the mono-static case, will have a phase difference of zero. In the bistatic case the phase difference of a scatterer at zenith will not be zero.

The Arecibo SI system is a bistatic radar which results in geometries shown in Fig. 1. The transmitter from the AO is used and the three receive antenna arrays are located approximately 327 m from the centerline of the dish. Each array consists of 4 Yagi antennas and is constructed on the corners of a 5 m equilateral triangle. The 70 cm Yagi arrays have a beamwidth of approximately 8° . Pre-amplification is done with a Mirage mast mount KP-2 pre-amplifier with two gain settings. The signal is cabled to the optical laboratory with RG-9 cable where it is connected to the pre-amplifier control units which provide power to the pre-amplifiers. The control units are cabled to the three channel receiver. The receiver is a three channel super-heterodyne system, with four sets of signal inputs, the 430 MHz RF inputs, the 30 MHz local oscillator (LO), the 5 MHz timing signal that synchronizes the internal 400 MHz PLO and the IPP pulse, a digital timing pulse that triggers data acquisition. Fig. 2 shows a block diagram of the system just described. The flow of the block diagram is from upper left to lower right. After pre-amplification, the first stage is a 430 MHz band pass filter with a passband of 10 MHz. After filtering, the signal is mixed with a 400 MHz CW produced by the PLO which uses a synchronization signal of 5 MHz. The result is filtered by a 30 MHz bandpass filter with a BW of 1.5 MHz. The signal is then amplified and attenuated to produce the signal levels required by the in-phase (I) and quadrature (Q) detectors. At this point the RF signal is approximately 30 MHz plus some small Doppler shift. The LO is a 30 MHz CW which the I/Q detector uses to mix the signal down to baseband and produce the I and Q component of the signal. Now there are three channels of I and Q signals that need to be sampled. This system has one A/D board which samples 2 signals simultaneously, therefore, the three channels must be multiplexed to the A/D board. A timing pulse from the transmitter drives the digital logic that, in turn, controls the multiplexers. Each channels I and Q signals are multiplexed, amplified and routed out of the receiver to the PC which houses the Datel PC-430f2 Analog to Digital data acquisition board. Some signal processing is done before the data is stored on disk.

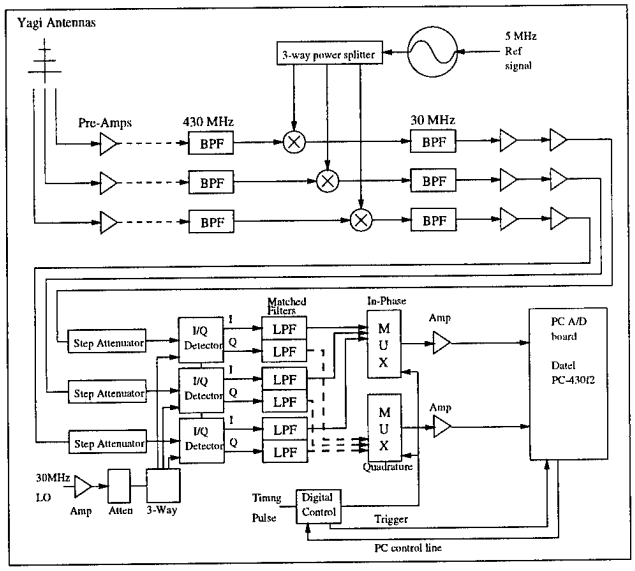


Fig. 2. The block diagram of the Arecibo SI three channel receiver. The receiver is configured in a super-heterodyne fashion. The in-phase and quadrature components from each channel are multiplexed to a 2-input, 12 bit A/D board.

Preliminary Results

The results described in this paper were obtained from data taken in a series of experiments conducted from August 22 to August 26 1995. The focus will be on data taken the morning of August 26, 0230-0630 LT. The conditions were cloudy with occasional precipitation. Due to the multiplexing of the receive channels, the data on the 2nd and 3rd channel were interpolated to the 1st channel. Since the atmosphere is relatively stationary between inter-pulse periods (1 ms) this is valid. The radial velocities $v_r^{(i)}$ were obtained by finding the first moment of the auto-spectra. The in-beam incident angles were obtained from the cross correlation function at zero lag. In a method similar to imaging Doppler interferometry (IDI) with three receivers, see [5], the three components of the wind field were solved in a least square sense from the

over-determined set of equations

$$\begin{pmatrix} x_1 & y_1 & z_1 \\ x_2 & y_2 & z_2 \\ \vdots & \vdots & \vdots \\ x_n & y_n & z_n \end{pmatrix} \begin{pmatrix} u \\ v \\ w \end{pmatrix} = \begin{pmatrix} v_r^{(1)} \\ v_r^{(2)} \\ \vdots \\ v_r^{(n)} \end{pmatrix} \quad (1)$$

where $x_i = \sin\delta_i \sin\theta_i$, $y_i = \sin\delta_i \cos\theta_i$, and $z_i = \cos\delta_i$. Angles denoted by δ_i and θ_i represent the zenith and azimuth angles of scatterer i, respectively, and are obtained by combining phase measurements from two baselines, typically the baselines with the largest cross-spectral amplitude. Fig. 3 show an example of the cross spectra between channels one and two. The data for this plot were taken at 0306 LT and the conditions were cloudy to partly cloudy. The spectral peaks show an associated non-random phase variation. The plotting range is a subset of the sampled range gates. Below 3 km, ground clutter was a problem and above 10 km the SNR was low. Further signal processing is underway and the effect of the bistatic geometries on the data is still being analyzed. Final installation of the SI system is scheduled for April 1996.

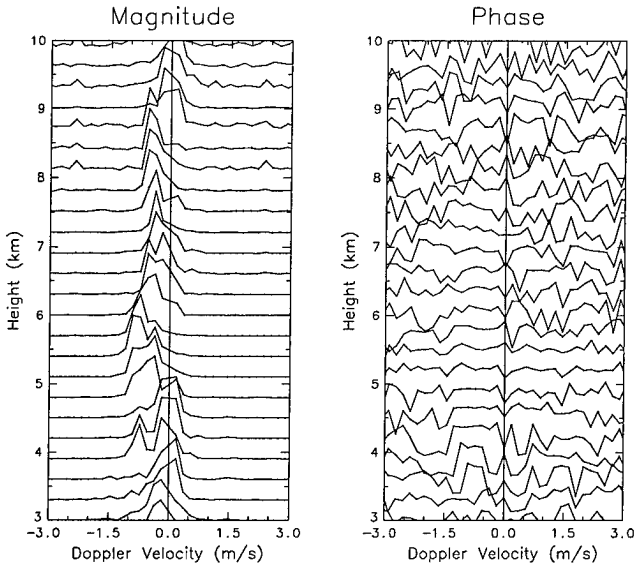


Fig. 3. Cross spectra taken at 0306 LT, with the transmit beam fixed vertically.

Acknowledgments

PBH, RDP and RMN were supported by the Division of Atmospheric Sciences of the National Science Foundation through grant ATM 94-02021. MFL was supported by the Division of Atmospheric Sciences of the National Science Foundation through grant ATM 92-01996. Special thanks to Bob Zimmerman, RF Engineer at the Arecibo Observatory for his advice, assistance and friendship. Thanks to Raul Garcia and Jose Cruz, technicians at the Arecibo Observatory. The Arecibo Observatory is the principal research facility of the National Astronomy and Ionosphere Center (NAIC), and is operated by Cornell University under a cooperative agreement with the National Science Foundation.

References

[1] Larsen, M. F., R. D. Palmer, S. Fukao, R. F. Woodman, M. Yamamoto, T. Tsuda and S. Kato, An analysis technique for deriving vector winds and in-beam incidence angles from interferometer measurements, *J. Atmos. Ocean Tech.*, *9*(1), 3–14, 1992.

[2] Woodman, R.F., Inclination of the geomagnetic field measured by an incoherent scatter radar technique,*J. Geophys. Tes.*, *76*, 178-184, 1971.

[3] Briggs, B., Radar observations of atmospheric winds and turbulence: a comparison of techniques, *J. Atmos. Terr. Phys.*, *42*, 823–833, 1980.

[4] Larsen, M.F., and Röttger,J.,The spaced antenna technique for radar wind profiling,*J. Atmos.Ocean tech.*, 6,920-938, 1989.

[5] Franke, P.M., D. Thorsen, M.Champion, S.J.Franke and E. Kudeki, Comparison of time and frequency domain techniques for wind velocity estimation using multiple-receiver MF radar data, *Geophys. Res. Lett.*, *17*(12), 2193-2196, 1990.

Measurements of Vertical Velocities and Divergence in the Atmosphere Using the MU Radar in Japan

Y. Ren and R. D. Palmer
Dept. of Elec. Engr. and Center for Electro-Optics
216N WSEC, Univ. of Nebraska-Lincoln, Lincoln, NE 68588-0511,
Tel: 402-472-6849, Fax: 402-472-4732, Email: bpalmer@unlinfo.unl.edu

S. Fukao, M. Yamamoto and T. Nakamura
the Radio Atmospheric Science Center, Kyoto University, Uji, Kyoto 611 JAPAN

Introduction

The accuracy of vertical velocity estimates obtained by Doppler radars is an important area of research. Many factors affect the estimates including beamwidth and wind field inhomogeneities. Typically, the radial velocity obtained from a vertically directed beam is assumed to represent the vertical velocity. By using two zenith angles, the extended velocity-azimuth display (EVAD) method can be used to account of divergence in the wind field, which must be present with a vertical velocity gradient [1]. A unique experimental configuration using 17 beam directions has been implemented with the Middle and Upper (MU) Atmosphere radar in the summer of 1995. The EVAD technique was used to provide realistic estimates of vertical wind and divergence over the observation period and over a height range of 6-16 km. A comparison of vertical velocity estimates obtained from the vertical beam and the EVAD technique will be presented for a case study of a typhoon passage in July, 1995. In addition, wind field divergence measurements will be provided.

Experimental Configuration

Our experiment for measuring vertical velocities and divergence was conducted on July 23-24, 1995, from 0900-0900 LT, using the MU radar located in Shigaraki, Japan [2,3]. The MU radar is a monostatic pulsed Doppler radar operating at 46.5 MHz with an active phased-array antenna 103 m in diameter. Its peak output power is 1 MW. The one-way 3-dB beam width is 3.6° .

The MU radar was operated in two modes during the observation period: the troposphere mode which observes a height region of 0.5-10 km, and the stratosphere mode which covers a height region of 6.0-16 km. The troposphere mode was used from 1700 to 1820 LT on July 23, and the stratosphere mode was used for other time periods. Seventeen beam directions were used, which were azimuthal scans with zenith angles of 9° and 20° . The exact beam positions are shown in Figure 1. The range resolution was set to 150 m. The beam directions were switched every inter-pulse period, which was set to 400 μs, in a cyclic manner. The received echo was sampled, then transferred into Doppler spectra using a 128-point FFT after coherent integration of 16 times in each beam direction.

Before the EVAD analysis was performed, the radial wind velocity and the echo power were estimated by fitting a Gaussian curve to the observed Doppler spectrum at each range gate. The signal-to-noise ratio (SNR) was directly determined by using the vertically pointing antenna beam.

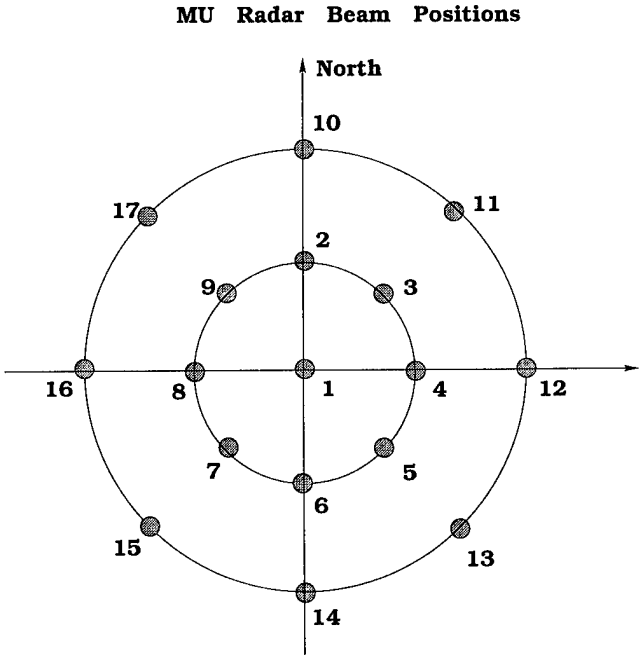


Fig. 1. Beam configuration used for the EVAD experiment with the MU radar.

Extended Velocity Azimuth Display

We consider a standard Cartesian coordinate system with the radar placed at the origin, with vertical axis z directed upward and axes x and y directed towards east

0-7803-3068-4/96$5.00©1996 IEEE

and north, respectively. The components of the wind vector along the x, y and z directions are denoted u (zonal), v (meridional) and w (vertical), respectively. Assuming a constant wind field, the radial velocity measured by the radar is given by the following expression.

$$v_r(\alpha,\beta) = u\sin\alpha\sin\beta + v\sin\alpha\cos\beta + w\cos\alpha \quad (1)$$

where α and β are the zenith and azimuth angles, respectively. Conversion of (1) into rectangular coordinates results in the following form of the radial velocity equation.

$$v_r(x,y,z) = \frac{ux+vy+wz}{\sqrt{x^2+y^2+z^2}} \quad (2)$$

where x, y, z is the location of the center of the resolution volume.

A uniform wind field in three dimensions is affected by kinematic properties (divergence, deformation, etc.) [4]. In our experiment, we focus our study on the effects of wind field gradients on the radial velocity equation. Since radar measurements are usually taken at a constant height, we ignore the gradients effect on the vertical direction. The horizontal wind components can be expanded to include gradients in the zonal and meridional directions using the following equations.

$$u = u_o + \frac{\partial u}{\partial x}x + \frac{\partial u}{\partial y}y \quad (3)$$

$$v = v_o + \frac{\partial v}{\partial x}x + \frac{\partial v}{\partial y}y \quad (4)$$

Where u_o and v_o denote the values at the center of the beam. Substituting these gradient equations into (2) and grouping terms, we arrive at the following standard equation [4].

$$\begin{aligned} v_r(x,y,z) &= \frac{1}{r}(u_o x + v_o y + wz) \\ &+\frac{1}{2r}\left(\frac{\partial u}{\partial x}+\frac{\partial v}{\partial y}\right)(x^2+y^2) \\ &+\frac{1}{r}\left(\frac{\partial u}{\partial y}+\frac{\partial v}{\partial x}\right)(xy) \\ &+\frac{1}{2r}\left(\frac{\partial u}{\partial x}-\frac{\partial v}{\partial y}\right)(x^2-y^2) \end{aligned} \quad (5)$$

where $r = \sqrt{x^2+y^2+z^2}$. This grouping of wind field gradients results in four distinct components. The first component is the constant wind field term. The second term represents the horizontal divergence $\nabla\cdot v_h$. The third and forth terms are the shearing and stretching deformation, respectively.

The technique of analyzing velocity fields using the VAD sampling scheme involves measurement of line-of-sight velocities at a fixed off-vertical angle around 360° of azimuth [5]. The EVAD method requires VAD measurements at two or more zenith angles. In our experiment, by using two zenith angles, the EVAD technique is used to provide realistic estimates of vertical wind and divergence over the observation period. The horizontal wind vector is represented by v_h, and the vertical-velocity component is w. The radial velocities measured around the azimuth circle will lie on a sinusoidal curve. The amplitude of the sinusoid fitted to the measured radial velocity will yield the horizontal wind speed, and the phase of the sinusoid will yield the wind direction. The magnitude of the vertical velocity can be obtained from the DC offset of the fitted curve C. Typically, the vertical velocity is non-zero and varies with height. In such a case, the divergence of the horizontal wind will also be nonzero. On the assumption of a linear variation in the wind field, C_i is given by the following expression [*Wilson and Miller*, 1972; *Doviak and Zrnić*, 1993] in the horizontal plane, where i corresponds to the two different zenith angles.

$$C_1 = \left[w + \frac{z}{2}\tan^2\alpha_1(\nabla\cdot v_h)\right]\cos\alpha_1 \quad (6)$$

$$C_2 = \left[w + \frac{z}{2}\tan^2\alpha_2(\nabla\cdot v_h)\right]\cos\alpha_2 \quad (7)$$

where α_1 and α_2 are the two zenith angles, at the same observation height.

Solving for divergence $\nabla\cdot v_h$ and w, we arrive at the following equations.

$$\nabla\cdot v_h = \frac{2}{z}\left[\frac{C_1\cos\alpha_2 - C_2\cos\alpha_1}{\cos\alpha_1\cos\alpha_2\cdot(\tan^2\alpha_1-\tan^2\alpha_2)}\right] \quad (8)$$

$$w = \left[\frac{-C_1\cos\alpha_2\tan^2\alpha_2 + C_2\cos\alpha_1\tan^2\alpha_1}{\cos\alpha_1\cos\alpha_2\cdot(\tan^2\alpha_1-\tan^2\alpha_2)}\right] \quad (9)$$

Preliminary Results

During the experimental period, a typhoon center passed within 500 km of the MU radar site at an approximate time of 2100 LT on July 23, 1995. Figure 2 shows a time-height cross section of the SNR, zonal and meridional wind components, where the subscript 1 corresponds to the 9° zenith angle. The SNR decreased with altitude but shows a distinct layering in the lower stratosphere. Zonal wind is relatively weak in the troposphere and increases with height, as is expected. A reversal in the zonal wind is also observed, which is consistent with the passage of the subtropical cyclone. The approximate passage time was 2100 LT, which corresponds to the zonal wind reversal at an altitude of 12-15 km. A consistent northward direction is observed in the meridional component of the horizontal wind and should be expected from the known direction of the typhoon path.

Using the EVAD technique, the divergence and vertical velocity were estimated and are shown in Figure 3.

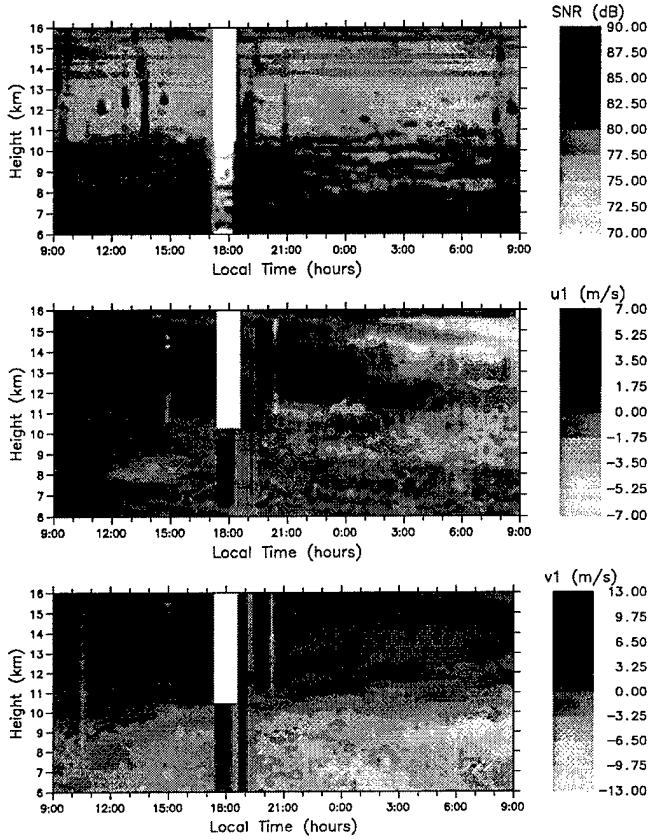


Fig. 2. Contour plots of SNR, zonal and meridional wind. Each profile in the contours correspond to a 6-min average.

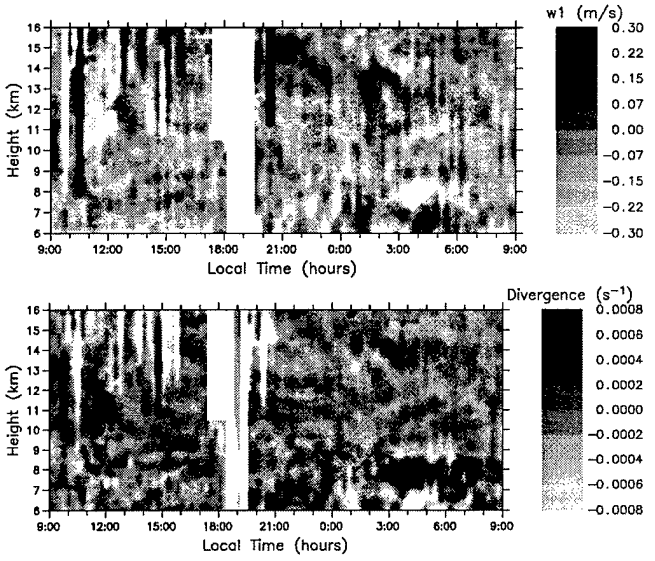


Fig. 3. Vertical velocity and divergence estimates obtained by using the EVAD technique for the 24-hour duration of the experiment.

As one should expect, a clear correlation can be observed between divergence and any vertical gradients in the vertical velocity. From the continuity equation, we know that sharp gradients in vertical velocity should correspond to increased divergence or convergence, depending on the sign of the gradient. Future work will involve the refinement of the vertical velocity measurements and study of divergence characteristics around a typhoon center.

Acknowledgments

YR and RDP were supported by the Division of Atmospheric Sciences of the National Science Foundation through grant ATM 94-02021. The MU radar belongs to and is operated by the Radio Atmospheric Science Center of Kyoto University.

References

[1] Srivastava, R. C., T. J. Matejka, and T. J. Lorello, Doppler radar study of the trailing anvil region associated with a squall line. *J. Atmos. Sci.*, *43*, 356-377, 1986.

[2] Fukao, S., T. Sato, T. Tsuda, S. Kato, K. Wakasugi and T. Makihira, The MU radar with an active phased array, 1, Antenna and power amplifiers, *Radio Sci.*, *20*(6), 1155–1168, 1985.

[3] Fukao, S., T. Tsuda, T. Sato, S. Kato, K. Wakasugi and T. Makihira, The MU radar with an active phased array, 2, In-house equipment, *Radio Sci.*, *20*(6), 1169–1176, 1985.

[4] Doviak, R., and D. Zrnić, Doppler Radar and Weather Observations, *Academic Press*, 2nd edition, 1993.

[5] Wilson, D. A., and L. J. Miller, Atmospheric motion by Doppler radar, *Remote Sensing of the Troposphere*, Chapter 13, *V. E. Derr, Ed.*, U.S. Department of Commerce, NOAA, (13)1–(13)34, 1972.

Radar Sounding of Glaciers in Greenland

C. Allen, B. Wohletz, and S. Gogineni
The University of Kansas, Radar Systems and Remote Sensing Laboratory
2291 Irving Hill Drive
Lawrence, KS 66045 USA
TEL: (913) 864-3017, FAX: (913) 864-7789, E-mail: callen@eecs.ukans.edu

Abstract—We have developed a coherent radar depth sounder operating at 150 MHz. The system is designed to operate as an unfocused SAR and obtains the sensitivity required to sound glacial ice through signal processing even though peak transmit power is about 200 W. We installed this system on a NASA P-3 aircraft and collected radar data on several flights over Greenland glaciers during the summer of 1995. The radar data were collected in conjunction with laser elevation measurements performed by NASA Wallops and are tagged with Global Positioning System (GPS) information. We collected data over the Humboldt, Jacobshavn and Petermann glaciers. To the best of our knowledge the radar data over these glaciers are the first ever obtained [1]. We applied a homomorphic deconvolution technique to remove multiple echoes of surface and ice-bottom interface. We have been able to identify the grounding line from the radar data. In this paper we provide a brief system description and experimental results along with geophysical interpretation of radar data. We also discuss the theory and present results of the homomorphic deconvolution procedure.

INTRODUCTION

The Greenland and Antarctic ice sheets together contain about 90% of the world's fresh water. The Greenland ice sheet, near equilibrium with its environment now, reached its maximum size about 15,000 years ago and has since retreated to its present size. By monitoring the mass balance of the ice sheets we can gain a better understanding of the effects of global warming on the ice sheets. The mass balance is determined by the annual precipitation, ablation, drainage at the edges, and iceberg calving. The volume of ice discharged into the sea by outlet glaciers is an important part of the total mass balance equation. To assess the ice flux in an outlet glacier, its thickness profile is needed as well as its flow rate. (Other techniques including spaceborne radar imaging have been shown to provide information on glacier flow rates [2].) While both radio echo sounding and seismic techniques have been used previously to measure the thickness of ice sheets with good agreement, radio echo sounding achieves much better range resolution and allows continuous recording of ice thickness data while seismic methods do not.

While many parts of the Antarctic and Greenland ice sheets have been successfully depth sounded, there have not been many successful radio-echo-sounding measurements made on outlet glaciers. Radio echo sounding of outlet glaciers is difficult because of absorption due to warm ice, scattering from water, or impurities in the ice, and because of reflections from nearby valley sides.

During the summer of 1995, we performed airborne radar echo soundings of several glaciers in Greenland. From our data we can determine glacier thickness, the location of the grounding line, and the ice thickness at the calving front. These soundings are the first successful radar sounding data collected from these glaciers [1].

SYSTEM DESCRIPTION

The radar depth sounder we used in this study is a modified and improved version of the Coherent Antarctic Radar Depth Sounder (CARDS) designed and build by the Radar Systems and Remote Sensing Laboratory (RSL) at The University of Kansas [3]. Modifications made to the original CARDS include an improved sensitivity time control (STC), a reduction in the noise level, improved isolation between the transmitter and the receiver, improved surface acoustic wave (SAW), and a new antenna structure resulting in less turbulence. This system was operated from a NASA P-3 aircraft that was also equipped with precision laser altimeter systems and Global Positioning System (GPS) receivers. Consequently, the radar data are tagged with precise GPS location information, providing accurate registration of sounding data with sensor position and an independent measurement of the ice surface elevation.

Our airborne, coherent radar system operates at a center frequency of 150 MHz. Operating at a pulse repetition frequency (PRF) of 9800 Hz, the transmitter generates a pulse that is frequency modulated (chirped) over a bandwidth of 17 MHz with a duration of 1.6 μs and a peak power of 200 W. The receiver, protected during transmit events by a blanking switch, compresses the received signal in a weighted SAW compressor resulting in a compressed pulse length of 60 ns and a depth resolution of 5 m in ice (n = 1.78). The received signal is next downconverted to baseband via coherent detection providing in-phase and quadrature (I and Q) analog outputs that are digitized in pairs with two 8-bit A/D converters at a rate of 18.75 megasamples/sec (MSPS). Coherent integration is then performed by summing complex data vectors from 256 consecutive transmit-receive periods. The data are then

0-7803-3068-4/96$5.00©1996 IEEE

detected by computing the power in each record ($I^2 + Q^2$) and then integrated further (incoherent integration) by summing four consecutive detected signals. The data are finally displayed to the user and are also recorded (along with position and time data provided by the on-board GPS receiver) at a rate of about 9 kbytes/sec on a removable hard disk.

Separate transmit and receive antennas are mounted beneath the left and right wings, with each antenna being a four-element, half-dipole array. The theoretical two-way, half-power beamwidth of this antenna configuration is about 18° in the plane normal to the flight path and about 66° in the plane parallel to the flight path. The coherent integration serves as a low-pass filter on the data and is equivalent to reducing the along-track antenna beamwidth from about 66° to 7° at the nominal velocity.

We believe the pulse compression, coherent processing and the bistatic antenna arrangement are the features that permitted this system to succeed in sounding these glaciers.

EXPERIMENT DESCRIPTION

In May 1995, an overflight of the Petermann glacier was flown principally along its flow line. This flight line is continuous, extending from the Greenland ice sheet to the ocean. Fig. 1 shows the flight line flown over the Petermann glacier. During data acquisition, the aircraft altitude was approximately 500 m above local terrain and the air speed was about 130 m/s.

DATA PROCESSING

When the data were analyzed, in addition to observing echoes from the surface of the ice and from the ice-rock interface at the bottom of the glacier, we sometimes observed numerous replicas of these echoes from the strongly scattering surfaces, that the range between these multiple echoes was relatively constant, and that this range corresponded to the altitude of the aircraft above the ice surface. We concluded that these artifacts resulted from a multipath phenomenon involving reflections from the ice surface and the underside of the aircraft.

To remove these artifacts without removing other real features in the data, we applied homomorphic deconvolution, wherein a signal composed of the convolution of two signals can be converted to a signal space where the two signals are now summed. In our case, we have a record of data that can be represented by the convolution of our pulse (and its delayed image) with a series of impulses corresponding with the reflection characteristics of the ice and bedrock. Oppenheim and Schmidt [4] developed much of the theory behind homomorphic deconvolution. Essentially, by transforming our data first to the frequency domain (transforming convolutional processes into multiplicative

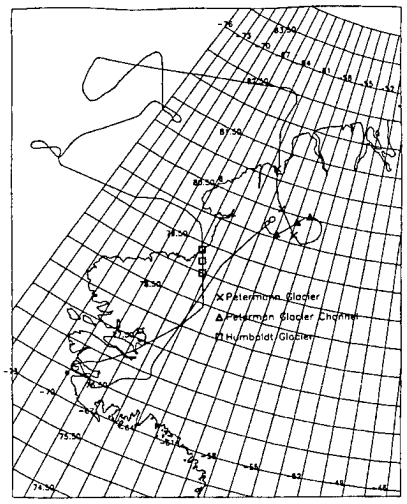


Fig. 1 Flight lines over the Petermann glacier.

ones) and then taking the complex logarithm of this frequency domain data (transforming multiplicative processes into additive ones), we are able to subtract the multiple reflection components without adversely affecting the remainder of the data. Returning to the original time domain of our data requires an undoing of the sequence just described (i.e., performing a complex exponential and then transformation from the frequency domain to the time domain via Fourier transform).

To separate successfully the multiple reflections from the desired data, the time-domain data must be either a minimal-phase or a maximal-phase sequence; however our data were neither, it was a mixed-phase sequence. Therefore we converted it into a minimal-phase sequence by multiplying our data sequence by an exponential weighting prior to applying the deconvolution process [5]. Removal of this exponential weighting is then required following the completion of the deconvolution.

RESULTS

Fig. 2 (top) shows the radio echogram from the Petermann glacier prior to homomorphic deconvolution. In the left half of this echogram, the return from the surface and the bottom are clearly identifiable. Also seen is a multiple echo resulting from a multipath between the ice surface and the aircraft. The distance between the true return from the ice surface and its multiple echo is approximately 60 pixels, and, while each pixel corresponds to 4.49 meters in ice, in air each pixel corresponds to 8 meters so that the separation between the true and multiple echoes is about 480 meters, which corresponds to the nominal aircraft altitude of 500 meters. In the right half of this echogram we see numerous multiple echoes again arising from the ice surface-aircraft multipath, except here we are also seeing multiples of the bottom return as it is also a relatively strong echo at the shallower depths.

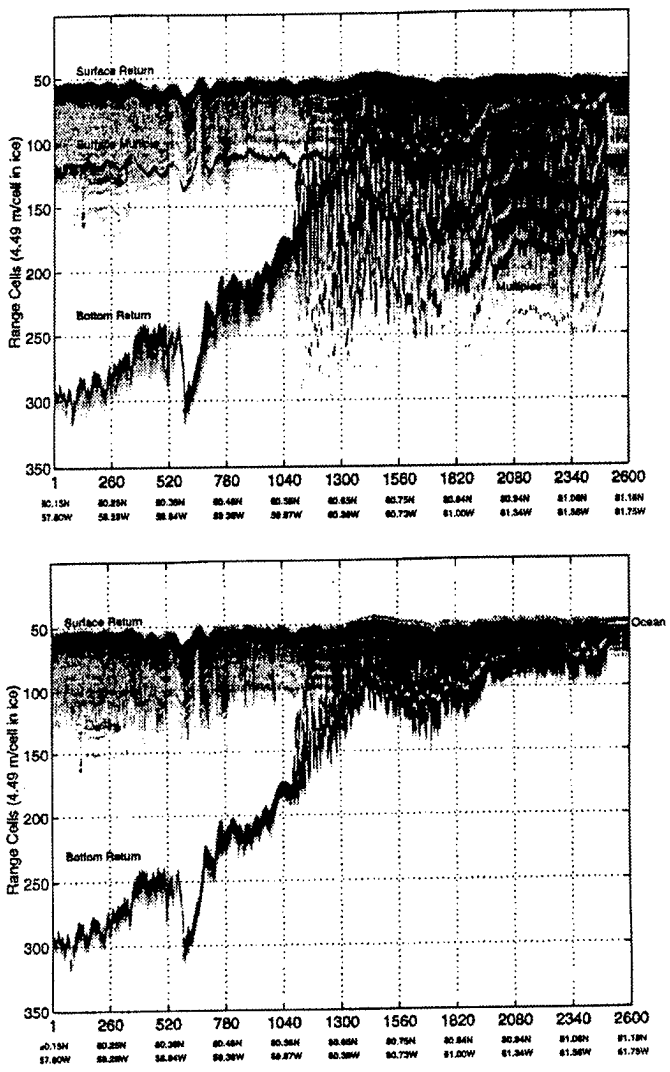


Fig. 2 Radio echogram of the Petermann glacier before (above) and after homomorphic deconvolution (below).

The distance between these multiple echoes is again approximately 60 pixels, supporting the ice-aircraft multipath hypothesis. Unambiguous determination of the ice thickness from these data is difficult at best.

In the lower part of Fig. 2 we see the effects of the homomorphic deconvolution. The multiple echo from the surface in the left half is removed and the numerous echoes in the right half are also removed, making the determination of the ice thickness possible by finding the distance between the surface return and the bottom return. The ice thickness of the Petermann glacier is presented in Fig. 3. In this plot we see a rapidly decreasing thickness as we approach the ocean, except for the valley at around 80.40N/58.60W. We believe the grounding line (where the glacier begins to float) may lie between points 80.59N/59.88W and 80.65N/60.39W as it appears that the glacier begins to experience bottom crevassing. The glacier thins rapidly immediately beyond the

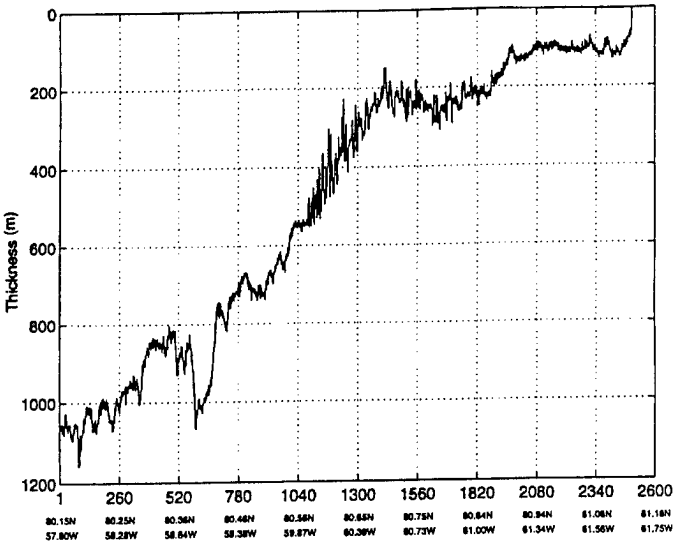


Fig. 3 Ice thickness of Petermann glacier.

grounding line but then it reaches a relatively constant thickness and at the calving front we see a thickness of 60 m.

CONCLUSIONS

We have developed a coherent depth sounder that is capable of measuring the thickness of outlet glaciers. Multiple echoes arise from the ice surface-airplane multipath. By applying homomorphic deconvolution we were able to remove these multiple returns, enabling us to measure the thickness of the Petermann glacier from the Greenland ice sheet continuously to its calving front at the ocean. We have also detected evidence of the grounding line.

REFERENCES

[1] Weidick, A. "Jacobshavn Isbrae During the Climatic Optimum," *Rapp. Gronlands Geolol. Unders.*, vol. 155, pp. 67-72, 1992.

[2] Joughlin, I., R. Kwok, M. Fahnestock, S. Gogineni, C. Allen, "Interferometrically Derived Topography, Velocity, and Ice-Flux Estimates for the Petermann Glacier," *EOS, Transactions, American Geophysical Union*, 1995 Fall Meeting, v. 76(46), p. F184, December 1995.

[3] Raju, G., W. Xin, and R. K. Moore, "Design, Development, Field Observations, and Preliminary Results of the Coherent Antarctic Radar Depth Sounder (CARDS) of the University of Kansas, U.S.A.," *Journal of Glaciology*, v. 36(123), pp. 247-254, 1990.

[4] Oppenheim, A. V. and R. W. Schafer, "Homomorphic Analysis of Speech," *IEEE Transactions on Audio and Electroacousatics*, AU-16(2), 1968.

[5] Schafer, R. W., "Echo Removal by Discrete Generalized Linear Filtering," Research Laboratory of Massachusetts Institute of Technology, Technical Report 466, 1969.

Sensing of Gradient Electromagnetic Fields from Subsurface Conducting Targets

Daniel H. Cress* and Lewis C. Bartel
Sandia National Laboratories
P. O. Box 5800, Albuquerque, NM, 87185-0860
Ph:(505) 844-7182
Fax:(505) 844-5290
Email: dhcress@sandia.gov
*-Corresponding Author: Dan Cress

Abstract --Electromagnetic techniques are presented for the problem of remotely locating buried conductors at depths on the order of 10 meters or more. The frequency ranges used vary from 5 Khz to 100 Khz. The subsurface is excited by bistatic or near-monostatic geometries. The sources for excitation include horizontal magnetic dipole (HMD), vertical magnetic dipole (VMD), and horizontal electric dipole (HED). Results emphasize the gradient receiver response of the field induced by the presence of the subsurface conductors. The gradient response is defined here to be the response of two opposing polarity (subtracting) magnetic dipole antennas displaced on the order of 5 meters from one another. Results are presented for a wire 10 meter beneath the surface.

INTRODUCTION

The objective of the work presented here is to evaluate several techniques for detecting man-made subsurface anomalies at depths from as shallow as several meters to depths of tens of meters using electromagnetic techniques. These depths are beyond the range of operation of conventional ground penetrating radars having frequencies in the 100 Mhz region or above in reasonably conducting soils (greater than 10 mhos/meter). The electromagnetic frequencies addressed here are from one to hundreds of kilohertz. The man-made anomalies are assumed to contain conductors that are considerably better than the surrounding soil. The man-made anomalies are assumed to have dimensions, at least in one dimension, on the order of the depth to the anomalies.

The work described here presents results from preliminary tests to detect a single wire conductor placed in a 20 centimeter diameter horizontal bore hole. A single wire was selected to provide an analytical target for which amplitude and phase responses of the instrumentation could be easily understood and evaluated. The borehole length projected to the surface was approximately 130 meters long. The depth of the borehole in the central section where detection tests were conducted was approximately 9 meters. Additional details are presented in the section titled **Data Collection.**

PROBLEM DESCRIPTION

Electromagnetic induction techniques in the frequency range of interest have been shown to be effective for characterizing ore bodies hundreds of meters beneath the surface. They are also effective for environmental characterization at shallow depths, generally less than five meters. This work is directed at the "in between" region from 5 to 50 meters or so. Because of the need for compact survey equipment, the transmitters and receivers in the frequency ranges from 1-100khz tend to be magnetic dipoles with air or ferrite cores rather than E-field antennas. Stand-off, ground-based transmitters may be used in either an E-field (grounded wire on the surface) or a large current loop configuration.

The dominant problems in the hardware development are: (1) suppressing the direct (primary) signal coupling between the transmitter and receiver, (2) suppressing the coupling among the transmitter-host (terrain)-receiver responses, and (3) maintaining or enhancing localized target response. Suppression of direct and host-response coupling can be addressed through hardware or through processing. Processing suppression of the direct and host responses requires adequate dynamic range to recover a target response that is generally much lower than the host or direct responses. Suppression through processing also requires that a number of geometrically distributed receiver measurements be made with sufficient geometric positioning and orientation accuracy to allow subtraction of

0-7803-3068-4/96$5.00©1996 IEEE

the direct and host fields while maintaining error margins in the processed data significantly less than the response to the target. Use of instrumentation for suppression depends on subtraction of receiver elements strategically located and electronically balanced in a manner that compensates for the direct and host coupling. For the following discussion, suppression of the host response is based on the assumption that the terrain response is horizontally invariant (for example: horizontally layered half-space).

INSTRUMENTATION

In order to suppress the primary and host responses, Sandia National Laboratories has collaborated with Raton Technology Research to apply a magnetic dipole gradiometer configuration to the problem of detecting subsurface conductors. Figure 1 presents the concept where the primary field is assumed to be coming, from a standoff location. The gradiometer consists of two magnetic dipole receivers separated by 5 meters. The gradiometer response is accomplished in analog fashion by simply using reversed sense windings on the two receivers.

The system response is based on coherent mixing of the transmitter command signal with the gradiometer receiver. The receiver signal is mixed down to an IF frequency 16KHz. The signal generator operates with a 16 Mhz clock that is divided down by 1024 to the nominal 16 Khz signal for the synchronous detector. The output of the synchronous detector is low-pass filtered at 200 Hz, then digitized and digitally averaged before recording. The averaging time is selectable and dependent on the speed of data acquisition and the expected target size. The averaging time for the tests presented here was on the order of one second. The transmitter and receiver are tuned to 5 pre-selected frequencies. The general frequency range of operation is from 5khz to 100khz. The numbers of turns in the transmitter and receivers are adjusted for improved impedance matching. Both a magnetic dipole transmitter and an electric field transmitter were used during the tests (Figure 2). The magnetic dipole transmitter moment is approximately 5 ampere turn-square meters at a frequency of 5 Khz. It decreased significantly with increasing frequency. However, the decrease was not characterized for these tests. The selected receiver turns on the 2.5 centimeter diameter by 30 centimeter long ferrite core vary from 122 turns at 5khz down to 24 turns at 100khz. The grounded electric dipole was laid on the surface and driven with a nominal current of 0.5 amperes.

DATA COLLECTION

The target was a 14 gauge wire in a 20 centimeter diameter horizontal borehole at a nominal depth of 10 meters and having a projected length on the surface of 130 meters. The layout (not to scale) is shown in Figure 2. The borehole sloped upward to the surface at each end with the upward slope from depth beginning at approximately 30 meters from each end. The tests were conducted on a transect at the center of the wire as shown in Figure 2 , identified by "gradiometer transect".

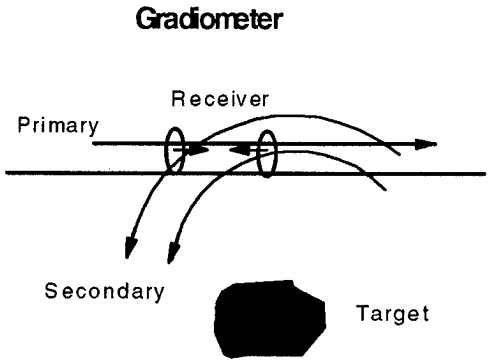
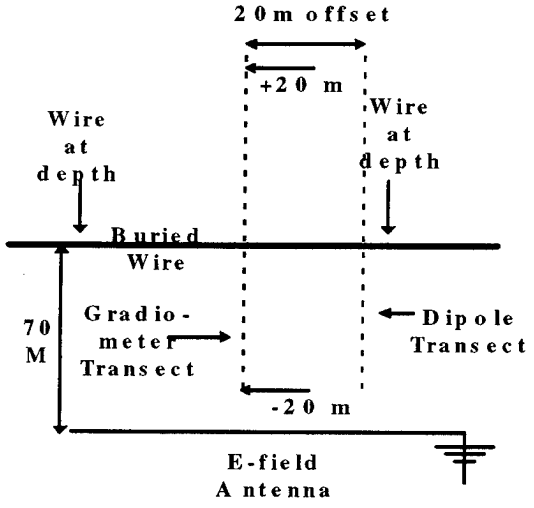


Figure 1. Gradiometer Concept

Two transmitter configurations were used. The first consisted of placement of a horizontal magnetic dipole(HMD) transmitter placed at 20 meter offset from the "gradiometer transect" on the line denoted by "dipole transect" in Figure 2. The second configuration was use of a 70 meter offset parallel E-field transmitter (parallel to the buried wire) as shown in Figure 2.

Figure 2. Test Layout

HMD Transmitter Tests. The HMD transmitter was aligned



with the dipole transect line. Data were acquired at fixed intervals of 5 meters from -15m to +20m where the

negative and positive directions are noted in Figure 2 by the ±20m markers.

RESULTS

Results are presented for the two configurations: (1) HMD with gradiometer receiver, and (2) E-field antenna with gradiometer receiver. The averaged magnitude of the gradiometer response for symmetric placement of the HMD dipole transmitter offset 20 meters is presented in Figure 3 for the 100kHz case. The magnitude is specified in units of nanovolts at the input. However, the true gain was not validated with the antennas incorporated into the system. The relative amplitudes should be accurate, however. The gradiometer was a 5m-separated HMD configuration with the gradiometer dipoles oriented parallel to the gradiometer transect. The HMD transmitter on the dipole transect was moved simultaneously with the gradiometer receiver in a symmetrical positioning so that the distance from both gradiometer receivers were the same. Said differently, the HMD transmitter on the dipole transect was on the perpendicular bisector of the line segment defined by the gradiometer receivers. In this configuration, the primary coupled wave should always be canceled provided the gradiometers receivers are matched. The gradiometer is configured to cancel localized host response that is horizontally invariant on scales on the order of several times the length of the gradiometer. The average response agrees well with the expected response to a line source by the gradiometer. The magnitude of the gradient of the cylindrical spreading of the line source can be expected to increase as the gradient approaches the line source. Similarly, the gradient response to any current in the buried wire also vanishes. Therefore one expects a null directly over the wire. Figure 3 suggests that the wire is probably located at the approximate two meter location rather than at the zero.

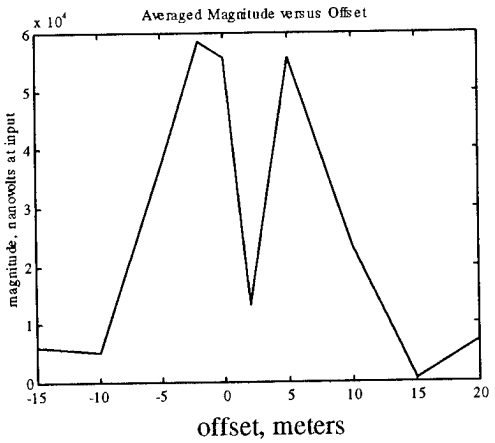


Figure 3. Magnitude over buried wire for the symmetric Tx-Rx configuration

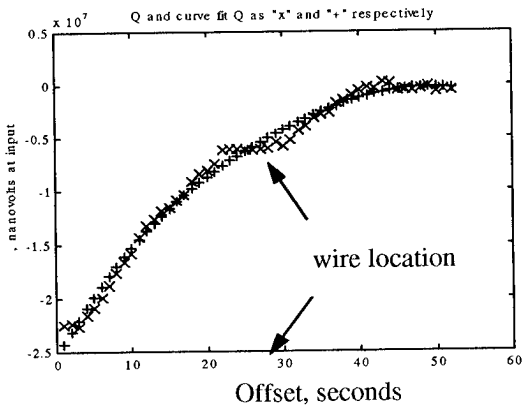


Figure 4. Curve fit, E-field Tx, Q, walking over wire.

Horizontal Electric Dipole. Results for the quadrature measurements of the horizontal electric dipole are presented in Figure 4 for continuous measurements while walking across the wire. The smooth line is the result of a second order polynomial fit. The electric dipole transmitter is parallel and 70 meters removed from the buried wire. The trends in the in-phase (I) and quadrature responses (Q) were subtracted using the polynomial fit to both raw I and Q. The residual I and Q are presented in Figure 5. The wire is located between the maximum excursions where the magnitude would be a minimum. Also note that the residual Q (+) indicates significant phase change on the values above 28 seconds relative to below 28 meters.

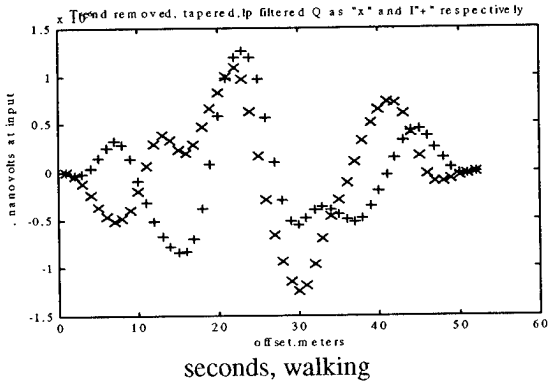


Figure 5: I and Q residuals after removing data trends. Wire at about 28 seconds.

. REFERENCES

Stolarczyk,L.G., "Radio Imaging in Seam Waveguides," Geotechnical and Environmental Geophysics, " Volume 3, Investigations in Geophysics, 5(3), pp.187-209,1991

Modeling the Electromagnetic Detection of Buried Cylindrical Conductors[+]

R. W. Moses,[*] R. E. Kelly,[^] and J. M. Mack[#]
Los Alamos National Laboratory
Los Alamos, NM 87545
mail stop - MS-B216,[*] MS-D410,[^] and MS-D434[#]
telephone - 505-667-5622,[*] 505-667-6492,[^] and 505-667-3416[#]
fax - 505-665-5926,[*] 505-667-7684,[^] and 505-665-3644[#]
email - rmoses@lanl.gov,[*] bkelly@lanl.gov,[^] and jmmack@lanl.gov[#]

Abstract -- The remote detection of buried structures and tunnels is important to the mining, construction, and defense industries. It is often desirable to identify underground power lines, pipe lines, and utility tunnels which have distinctive electromagnetic cross sections. A computational model for the electromagnetic detection of buried conducting cylinders is described in this paper. The source of electromagnetic radiation is either current injection into the soil or a surface based magnetic dipole with possible extensions to airborne platforms. A frequency range of 5 - 100kHz is considered. The target conductor is a cylinder buried directly in the soil or placed inside an insulating pipe. The receiver is a magnetic gradiometer held 1m above the ground, separate from the transmitter. Typically, data are taken in ten point scans above and normal to the buried conductor. Cases where the target conductor is grounded at both ends, one end, or not at all are modeled. The scattered field and field gradient are computed at or above ground level and compared in magnitude and phase with the transmitted signal. Calculated results are compared with experimental tests. Essential factors affecting detection performance are frequency, dynamic range of reception, and proper data processing.

INTRODUCTION

The central issues in the detection of underground structures and tunnels are attenuation, scattering, and clutter. Commonly applied techniques, such as electromagnetic, dc magnetic, seismic and gravitational, are impacted to varying degrees by these three factors. Only electromagnetic scattering (EMS) techniques are considered here.

Local conditions cause the electrical conductivity of soils to vary from place to place by several orders of magnitude, leading to significant variations in radiation skin depth, $\delta = \sqrt{2/(\mu\sigma\omega)}$, where σ is the electrical conductivity of the soil and ω is the angular frequency of the wave, $\omega = 2\pi\nu$. At low frequencies, an oscillatory plane wave attenuates by one factor of e for each skin depth it travels. If the target were a buried conducting sphere, the total scattering cross section would be approximately proportional to k^4a^6 where the radius of the sphere is a, the wave number in earth is k, and it is assumed that $ka << 1$. One may reduce attenuation by reducing the operating frequency, but the corresponding reductions in cross section will eventually overcome the improvements in attenuation.

In addition to attenuation by the soil and electromagnetic scattering by the target, the phenomenon of geologic noise or "clutter" is a major factor in underground detection. When natural variations in σ and dielectric constant, κ, introduce signal fluctuations comparable to the target scattering, accurate detection is impaired.

The work in this paper combines two realities inherent to the applications and physics of underground detection technology. First, many of the "targets" typical of underground detection applications are in long tunnels: pipelines, power lines, communications, and transportation. Second, cross sections for long conductors parallel to incident wave polarization are significantly greater than for smaller objects such as storage bunkers and containers.

PHYSICS MODELING

The physics issues described above are well known, [1]-[3]. The objective of this work is to combine the physics representations of the transmitter, target scattering, and receiver into one computational model capable of predicting system performance. The modeling has been done with *Mathematica* in MKS units.

The systems concepts in this paper are largely drawn from the work of Dr. L. Stolarczyk of Raton Technology Research (RTR) in Raton, NM [4]. The base case is illustrated in Fig. 1. In this example, the wave transmission is current injection into the ground by means of an ac power supply connected to ground points approximately 100m apart. An alternative transmitter used by L. Stolarczyk and collaborators at RTR and Sandia National Laboratory, Albuquerque (SNLA) is a horizontal

[+]Work supported under the auspices of the USDOD

0-7803-3068-4/96$5.00©1996 IEEE

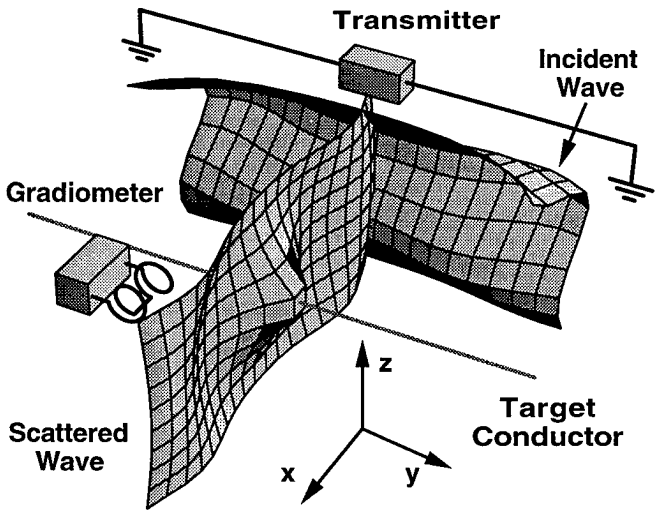


Fig. 1. Conceptualization of current injection, field propagation and gradiometer reception.

ferrite loop antenna. The far fields of the current injection and the horizontal magnetic dipole are similar.

The subterranean electric field for an infinitely long wire on the surface is derived in [2] and [3]. An approximation for a grounded wire of finite length was derived and incorporated into the present model to compute both **E** and **B** at and above the target conductor. The transmitter to target separation, R, is assumed to be long compared to the skin depth of the earth, δ, but short compared to the wavelength in air, λ_a. These assumptions enable one to treat the vertical and horizontal dependencies of the fields as separable.

The target is taken to be a conducting wire or pipe of radius a inside an insulated tunnel of radius b. The conductor may be grounded at both ends, one end or neither end. It is also possible to have the conductor be a part of the tunnel wall and in contact with the ground along its length.

The **E** field of the transmitter drives a current in a target conductor of finite length. This was computed using a Green's function technique presented by Hill [5], and it was checked against an independent Fourier expansion model.

The choice of a magnetic gradiometer for the receiver is drawn from experience at RTR. For a bistatic configuration where the transmitter and receiver are located separately, the gradient of the scattered field, $\partial \mathbf{B}_{sc}/\partial x$, is expected to be distinguished from the background better than the profile of $\mathbf{B}_{sc}$ itself.

RESULTS

Buried wire tests A series of tests was carried out by SNLA, RTR, and LANL at SNLA during 1995. The target was a #14 gauge wire drawn through a 4" diameter plastic pipe. The pipe was ~100m long and the central 50m were buried to a depth of ~10m. Various transmitter configurations were used including current injection from a 100m line parallel to the target and 100m away from it. Also a horizontal ferrite loop antenna was placed directly over one end of the buried wire. The Sandia tests showed a distinct horizontal magnetic gradient as the gradiometer was taken across the buried grounded wire. These results are illustrated in Fig. 2 where the transmitter was a ferrite loop antenna operating at 100kHz and moved across the wire in tandem with the receiver to reduce transmitter interference.

To model the buried wire experiments, the characteristics of the earth were assumed to be $\kappa = 10$ and $\sigma = 0.03$mho/m. The results computed using the model described above are shown in Fig. 2. Both sets of results are shown with arbitrary normalization. The shapes of the gradiometric amplitudes are similar except the two peaks of amplitude are more widely separated for the computation than in the experimental results. Perhaps the actual dielectric constant and conductivity of the soil were somewhat different from the values used in the computation, causing the different scales of the gradiometric results. When the wire is not grounded, the computations predict the driven current to be reduced by a factor of ~80. The reduction is ~20 if only one end is grounded. The experimental tests of open ended conductors were inconclusive.

Yucca Mountain tests A series of tests by SNLA, RTR, and LANL is underway at the Yucca Mountain site in Nevada. In this case, a 3.6m diameter tunnel ~ 40m under ground is being surveyed. A variety of transmitter configurations are planned: ranging from a rectangular loop, 100m×200m, placed to the side of the tunnel to horizontal magnetic dipoles at various positions around the tunnel. The operating frequencies are $\nu = 5$, 10, 30, 60, and 100kHz.

The model presented above has been used to predict

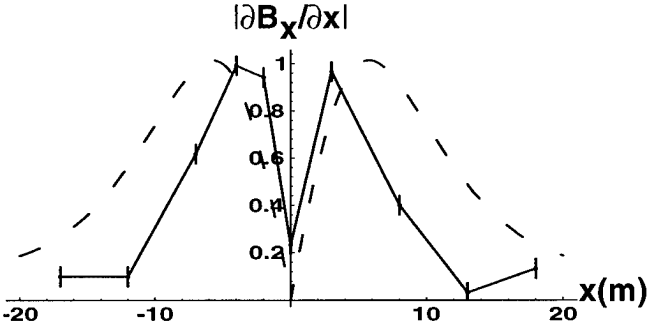


Fig. 2. Experimental (solid) and theoretical (dashed) normalized values of horizontal magnetic field gradient for the SNLA tests at 100kHz over a grounded wire 10m deep.

the gradiometric signals to be expected when a large rectangular loop, carrying 1Amp, is placed with its nearest edge 200m away from the center line of the tunnel. The soil parameters are taken to be $\kappa = 12$ and $\sigma = 0.002$mho/m. The computed gradients of the horizontal and vertical magnetic field are plotted as functions of horizontal position in Figs. 3a and 3b respectively for a 3.6m diameter tunnel with conducting reinforcement. In segments of the tunnel which are not reinforced with metal walls, scattering is from railroad tracks and parallel cabling along the tunnel. Estimating these as equivalent to a conducting cylinder 20cm in diameter gives the gradient of horizontal field shown in Fig 3c.

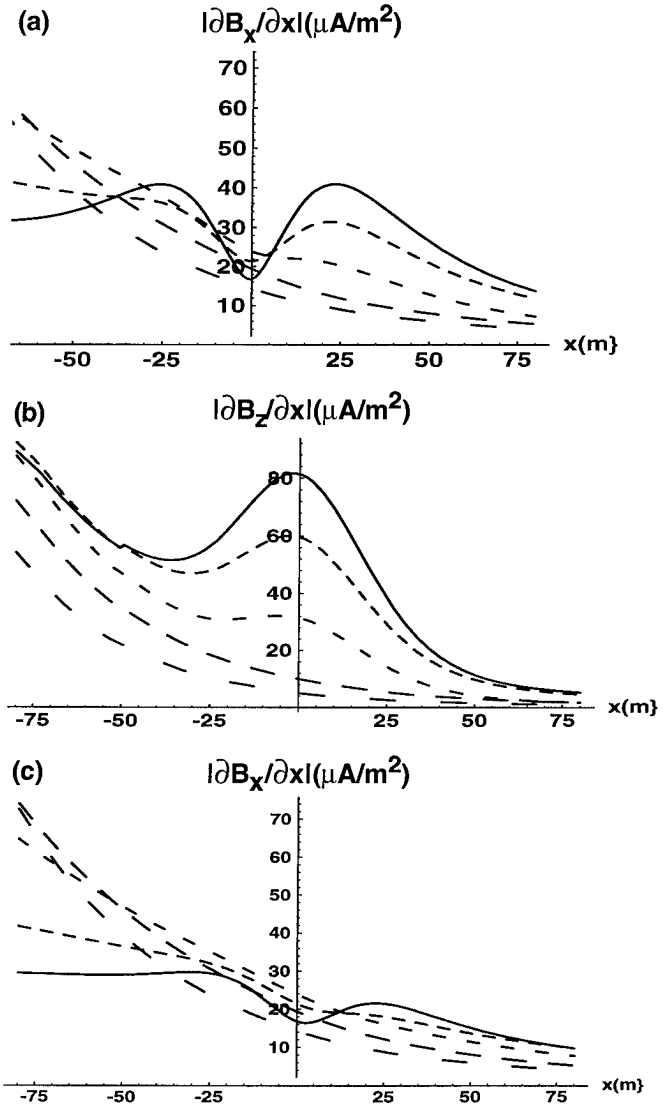


Fig. 3. Computed magnetic field gradient for the Yucca Mountain tests at 5, 10, 30, 60, and 100kHz. (solid-short dashing-long dashing respectively) over a 3.6m diameter tunnel ~40m deep at $x = 0$; showing (a) horizontal field gradient and (b) vertical field gradient for a conducting walled tunnel, and (c) horizontal field gradient for an open tunnel containing small conductors.

Although there is a scattered signal present for all five frequencies, the characteristic inflection points are well defined for the lowest of the frequencies. The large tunnel with insulated walls scatters three to four times more in amplitude than the 20cm diameter conductor in an insulated tunnel. Experimental results will be available for comparison soon.

The present results indicate that even when operating with field gradients, the transmitter signals may mask out the scattered signals. By accurately modeling the transmitter fields, fully recording the amplitude and phase of the received signal, and assuring an adequate dynamic range of the receiver, it should be possible to extract conductor locations using image analysis techniques.

CONCLUSIONS

The performance of sub-surface detection is enhanced by adapting the wavelength and orientation of the probing radiation to the configuration of the underground structure and to the soil characteristics. Experimental-theoretical agreement has been achieved in the shape of the scattered signal for a wire buried at 10m depth in tests at SNLA. Theoretical predictions indicate that a tunnel at the Yucca Mountain facility should be locatable by examination of gradiometric data versus position for frequencies in the 5-30kHz range. Assuming the dynamic range of the receiver is sufficient, data processing may reveal the tunnel location with higher frequencies.

ACKNOWLEDGMENTS

The authors greatly appreciate L. Stolarczyk and Y. M. Wong of RTR, and D. Cress and L. Bartel of SNLA for their consultation and sharing of data in this research.

REFERENCES

[1] M. N. Nabighian, Editor, *Electromagnetic Methods in Applied Geophysics*, Society of Exploration Geophysicists, Tulsa, OK (1988).

[2] M. L. Burrows, *ELF Communications Antennas*, IEE Electromagnetic Wave Series 5, Peter Peregrinus Ltd., Stevenage, England (1978).

[3] J. R. Wait, *Electromagnetic Wave Theory*, Harper & Row, New York (1985).

[4] K. D. Mahrer and D. F. List, "Radio Frequency Electromagnetic Tunnel Delineation at the Otay Mesa Site," *Geophys.*, Vol. **60**, p. 413-422 (1995).

[5] D. H. Hill, "Magnetic Dipole Excitation of an Insulated Conductor of Finite Length," *IEEE Trans. Geosci. Remote Sensing*, Vol. **28**, p. 289-294, (1990).

ELECTROMAGNETIC MODELING OF SUBSURFACE 3D STRUCTURES

Gregory A. Newman and David L. Alumbaugh
Sandia National Laboratories
P.O. Box 5800, Albuquerque NM 87185-0750
Tel: (505) 844-8158; Fax:(505) 844-7354
Email: ganewma@sandia.gov

ABSTRACT

A 3D frequency domain electromagnetic numerical solution has been implemented for sensing buried structures in a lossy earth. Because some structures contain metal, it is necessary to treat them as very good conductors residing in a complicated lossy earth background. To model these scenarios and to avoid excessive gridding in the numerical solution, we assume the structures to be perfectly conducting, which forces the total electric field to zero within the conductor. This is accomplished by enforcing internal boundary conditions on the numerical grid.

The numerical solution is based on a vector Helmholtz equation for the scattered electric fields, which is approximated using finite differences on a staggered grid. After finite differencing, a complex-symmetric matrix system of equations is assembled and preconditioned using Jocobi scaling before it is iteratively solved using the quasi-minimum residual (qmr) or bi-conjugate gradient (bicg) methods. For frequencies approaching the static limit (< 10 kHz), the scheme incorporates a static-divergence correction to accelerate solution convergence. This is accomplished by enforcing the divergence of the scattering current within the earth as well as the divergence of the scattered electric field in the air.

INTRODUCTION

An important application of electromagnetic (EM) sensing involves detecting buried manmade structures. Because these structures often include metal in their fabrication as well as electrical wiring, they can sometimes be modeled as highly conducting bodies and wires in a lossy earth. Sheet models have been useful to model such cases, [1], but are limited in their complexity and the complexity of the earth background that can be incorporated in the model. To overcome these limitations, finite element and difference solutions to the EM field can be implemented. However because of the highly conductive nature of the above mentioned structures it appears that excessive gridding is needed. Still, this problem can be avoided if we treat the structures as perfectly conducting, and in effect replace them with an internal boundary condition that enforces zero electric field.

In this paper we demonstrate how this idea can be implemented using an iterative solution to the vector Helmholtz equation based on finite difference approximations. In addition we will show how this solution can be accelerated at low frequencies by incorporating a static-divergence correction which enforces auxiliary divergence conditions on the fields. Fast low frequency simulations are important because some targets can be buried at depths where lower frequencies are required for their detection.

THEORETICAL FORMULATION

The Vector Helmholtz Equation

Assuming a time harmonic dependence of $e^{i\omega t}$ where $i = \sqrt{-1}$ the vector Helmholtz equation for the scattered electric field given by [2] is written here as

$$\nabla\times\frac{\mu_p}{\mu}\nabla\times\mathbf{E_s}+i\omega\mu_p(\sigma+i\omega\varepsilon)\mathbf{E_s}= \tag{1}$$
$$-i\omega\mu_p\left[(\sigma-\sigma_p)+i\omega(\varepsilon-\varepsilon_p)\right]\mathbf{F_p}-i\omega\mu_p\nabla\times\left[\left(\frac{\mu-\mu_p}{\mu}\right)\mathbf{H_p}\right].$$

In this expression the electrical conductivity, magnetic permeability and dielectric permittivity are denoted by σ, μ and ε, respectively, where the subscripts "p" and "s" designates background, or primary values, and scattered values respectively. Given this definition of primary and scattered fields, the total electric and magnetic fields are determined from $\mathbf{E_t} = \mathbf{E_p}+\mathbf{E_s}$ and $\mathbf{H_t} = \mathbf{H_p}+\mathbf{H_s}$. In addition note that $[(\sigma-\sigma_p) + i\omega(\varepsilon-\varepsilon_p)]\mathbf{E_p}$ and $[(\mu-\mu_p)]\mathbf{H_p}$ can be thought of as equivalent source vectors of the background medium. The primary fields and background values found in these source vectors can be that of a whole space, a layered half-space, or some previously run model for which results were saved to be incorporated as a primary field. For all examples presented here the primary field is assumed to arise from impressed dipole sources in a whole space background. When equation (1) is approximated with finite differences on a staggered grid a sparse linear system results in which the matrix is complex symmetric. This system can be efficiently solved iteratively using Krylov sub-space methods, including the quasi minimum residual (qmr) and bi-conjugate gradient (bicg) solvers. The reader is referred to [2] and [3] for details on how these solvers are implemented.

The Static-Divergence Correction

As has been demonstrated by [4], a staggered grid is a natural grid to use in the numerical solution since it implicitly enforces the auxiliary divergence conditions on the

0-7803-3068-4/96$5.00©1996 IEEE

fields. With a scattered electric field formulation the critical condition is

$$\nabla\cdot\{(\sigma+i\omega\varepsilon)\mathbf{E_s}\}=-\nabla\cdot\left\{\left[\left(\sigma-\sigma_p\right)+i\omega\left(\varepsilon-\varepsilon_p\right)\right]\mathbf{E_p}\right\}. \quad (2)$$

Even with the benefits of a staggered grid we have observed that the time needed to solve for the fields greatly increase with falling frequency as one approaches the static limit. The reason can be traced to the fact that the numerical solution poorly approximates equation (2). To overcome this difficulty a correction can be implemented following a procedure developed by [4] for a total field formulation. Here we will modify the procedure for the scattered fields such that equation (2) is enforced periodically during the iterative solution. To accomplish this let us define an *error* where,

$$error=-\nabla\cdot\{(\sigma+i\omega\varepsilon)\mathbf{E_s}\} \quad (3)$$
$$-\nabla\cdot\left\{\left[\left(\sigma-\sigma_p\right)+i\omega\left(\varepsilon-\varepsilon_p\right)\right]\mathbf{E_p}\right\}.$$

Ideally the *error* should be zero, but because of precision problems it is not, particularly as frequency approaches the static limit. Next we define a scalar potential, ϕ, such that

$$error=\nabla\cdot\{(\sigma+i\omega\varepsilon)\nabla\phi\}. \quad (4)$$

Difficulties still arise with this equation when air is present in the model because it cannot support electric currents in the static limit. To overcome this difficulty, we redefine equation (4) in the air to read

$$error'=\nabla\cdot\nabla\phi. \quad (5)$$

When the sources are buried in the earth we need to enforce the condition that total electric field is divergence free in the air, thus

$$error'=-\nabla\cdot\mathbf{E_s}-\nabla\cdot\mathbf{E_p}. \quad (6)$$

On the other hand if the sources are in the air we force the scattered electric field to be divergence free, hence

$$error'=-\nabla\cdot\mathbf{E_s}. \quad (7)$$

To enforce equation (2) and the divergence conditions on the electric field in the air we solve equations (4) and (5) for the potential on the staggered grid using a finite difference approximation. The corrected version of the scattered electric field is then given by

$$\mathbf{E_s}'=\mathbf{E_s}+\nabla\phi. \quad (8)$$

Solution to equations (4) and (5) take much less time than solving equation (1) does. To obtain the potential solution we assemble the scalar equations into a single system, precondition it with simple Jocobi scaling and solve it using a bi-conjugate gradient algorithm for non-symmetric matrices. This correction procedure is alternated with a series of qmr or bicg iterations on the vector Helmholtz equation. At each correction step the scalar equations only need to be solved very approximately to dramatically improve the convergence of the Helmholtz equation at low frequency as in Figure 1.

The number of sub iterations operating on the Helmholtz system is critical for effective acceleration of the solution when using the static-divergence correction. If too few sub iterations are specified there is a possibility that the solution will never converge to an acceptable error level. To overcome this difficulty an adaptive scheme has been implemented, which will continue to double the number of sub iterations if the error has not been reduced by a factor of two from the previous set of sub iterations. This procedure is continued until convergence to a given error level is achieved or a maximum number of iterations (including all sub iterations) has been attained.

Simulations Involving Very Good Conductors

To model very good conductors and to avoid excessive gridding in the numerical solution, we assume the structures to be perfectly conducting. Large-scale good conductors can be treated with this approach as well as wire conductors since wires can easily be accommodated in a staggered grid.

With a perfectly conducting boundary condition, the total electric field is forced to zero within the conductor as well as on its surface. Instead of explicitly enforcing this condition, we have designed it implicitly on internal portions of the grid due to ease of implementation. At or inside a very good conducting region, equation (1) can be written as

$$\nabla\times\frac{\mu_p}{\mu}\nabla\times\mathbf{E_s}+i\omega\mu_p\sigma_{large}\mathbf{E_s}=-i\omega\mu_p\sigma_{large}\mathbf{E_p} \quad (9)$$

where conductivity property dominates over the dielectric and magnetic permeability properties of the medium. Because the medium is highly conducting the following inequality is also true;

$$\left|\nabla\times\frac{\mu_p}{\mu}\nabla\times\mathbf{E_s}\right|<<\left|\omega\mu_p\sigma_{large}\mathbf{E_s}\right|. \quad (10)$$

Considering equation (10) with equation (9) numerically yields

$$(\sigma_{large})\mathbf{E_s} = -(\sigma_{large})\mathbf{E_p} \qquad (11)$$

or effectively $\mathbf{E_s} = -\mathbf{E_p}$. Thus $\mathbf{E_t} = 0$ which is the condition required in and on a perfect conductor.

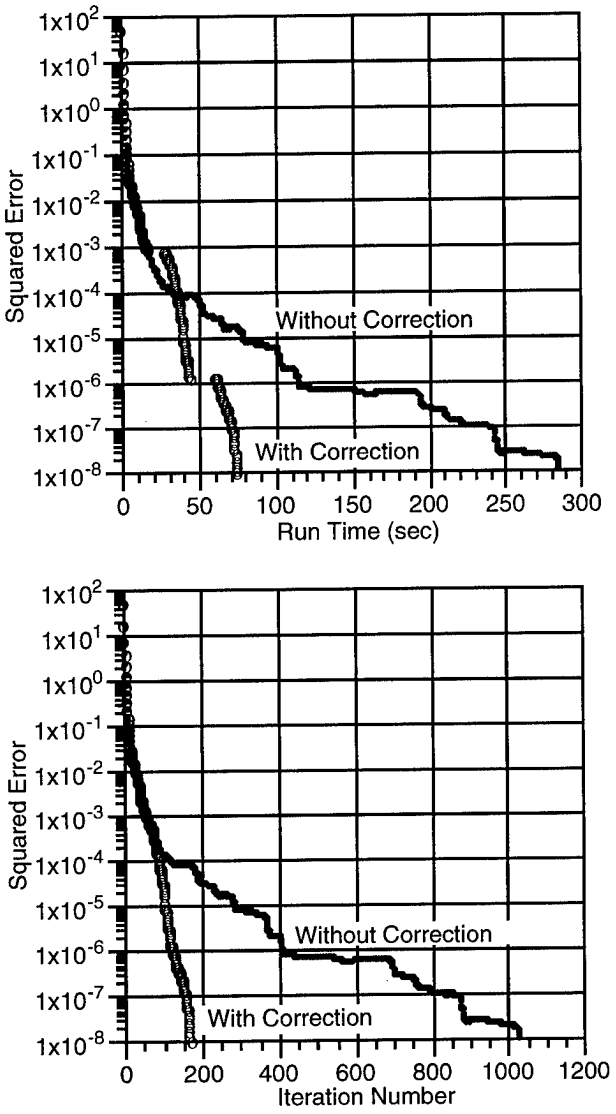


Fig. 1. Comparison between solution run times and number of iterations needed to achieve convergence with and without the static-divergence accelerator. The model consists of 96 338 cells and simulates a 100 Ωm half space with a vertical dipole magnetic source positioned 20 m above the surface and operating at a frequency of 90 Hz. The numerical solution is assumed to have converged when a squared error level of 10^{-8} is attained. Time gaps in the corrected version of the solution correspond to the times needed to make the static-divergence correction. Sixty sub iterations were used with the corrected version.

Through numerical experiments we have determined that σ_{large} assigned a numerical value of about 10^{+8} appears to work best. Larger values introduce numerical instability. Figure 2 shows an excellent check on the technique for a perfectly conducting layer. In Figure 3 we show a check against a highly conducting sheet model, and although the comparison is not as good as that of the layered model, the shapes of the curves agree quite well. We believe that discrepency between the two solutions occurs due to discretization problems with the sheet model. The reasons for this belief are 1) with increasing discretization of the sheet the comparison continues to improve, and 2) the excellent check against the layered model. Note, we could not disretize the sheet model beyond 1600 cells due to computer memory limitations.

While this technique works well for detecting buried structures from the surface or from the air it is not ideal for computing fields in the shadow zones of very good conductors. This limitation is caused by subtractive cancellation between the scattered and primary fields. For problems of this sort a total field solution would appear to work best. We are now in the progress of implementing such a solution which could be of great use in mapping the lateral extent of highly conducting ore bodies with crosswell configurations.

CONCLUDING REMARKS

We have demonstrated several extensions to the solution published by [2] on 3D wideband EM modeling. The inclusion of a static divergence condition has been demonstrated to cause significant speed up in solution run times at low frequencies, and a novel technique, which is implicit in nature yet simple to implement, for simulating responses of perfectly conducting bodies has been demonstrated.

REFERENCES

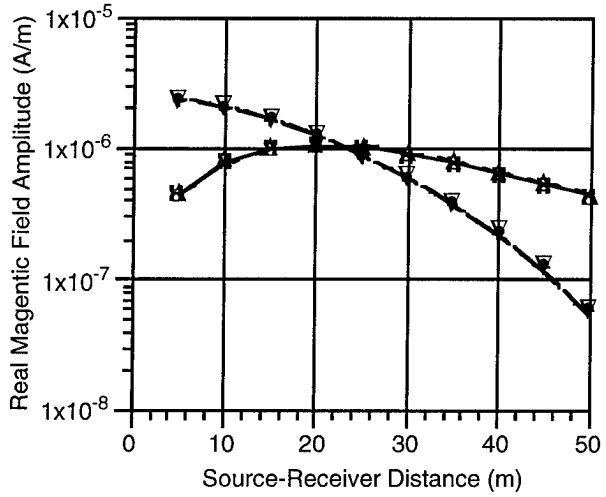
[1] Weidelt P., 1981, Dipole induction in a thin plate with host medium and overburden: Research Project NTS **83**, no. 89727, Federal Inst. for Earth Sciences and Raw Materials, Hannover Germany.

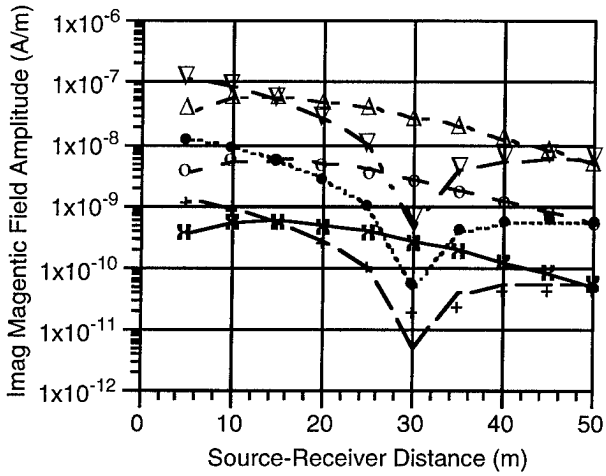
[2] Alumbaugh D. L., Newman G. A., Prevost L. and Shadid J. N., 1996, Three-dimensional wideband electromagnetic modeling on massively parallel computers: Radio Science, **31**, 1-23.

[3] Newman G. A. and Alumbaugh D. L., 1995, Frequency-domain modelling of airborne electromagnetic responses using staggered finite differences: Geophysical Prospecting, **43**, 1021-1042.

[4] Smith, T. J., 1992, Conservative modeling of 3D electromagnetic fields: International Association of Geomagnetism and Aeronomy, 11th Workshop on

Electromagnetic Induction in the Earth, Wellington, New Zealand, Meeting Abstracts.





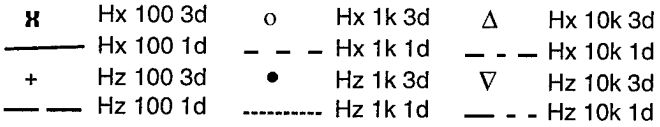
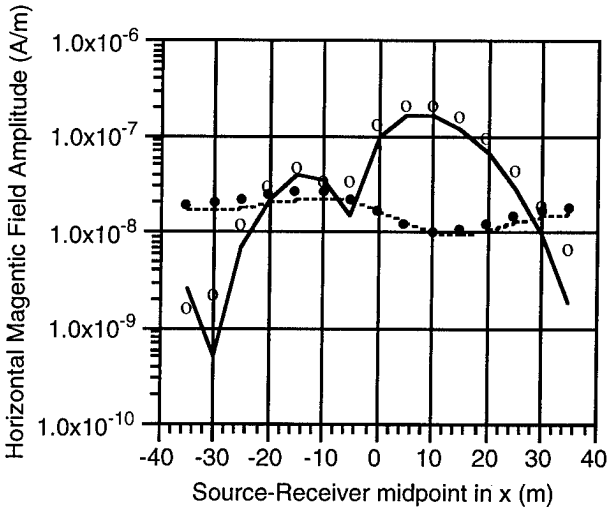
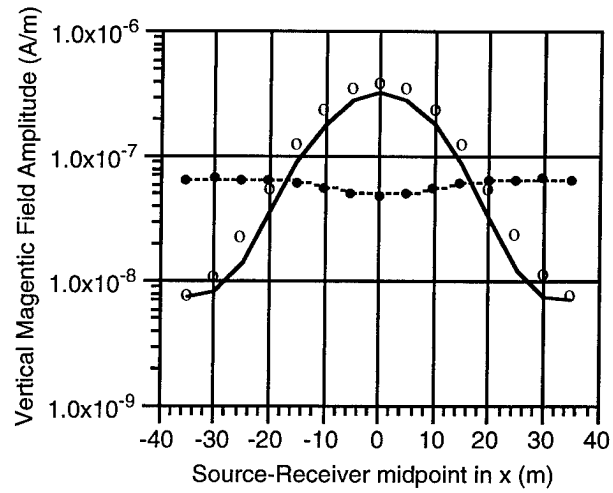


Fig. 2. Check on the perfectly conducting boundary condition implemented implicitly on the internal portions of the finite difference mesh. The model consists of a 10 m thick perfectly conducting layer buried 10 m deep in a 100 Ωm half-space. Checks we carried out for three different frequencies 100, 1 000 and 10 000 Hz, where a vertical magnetic dipole transmitter is deployed 10 m above the surface and magnetic fields computed horizontally away from the source point. Symbols depict the 3D solution with the free space response removed, which uses 381 217 cells and lines the results from a semi-analytic 1D Hankel transform solution of Ki Ha Lee.





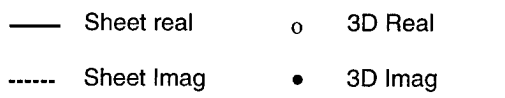


Fig. 3. Check of the perfectly conducting boundary condition against the sheet model of Weidelt [1]. The model consists of a 20 m by 40m sheet buried at 15 m depth in a 100 Ωm half-space. The conductance of the sheet is $1x10^{10}$ S and a frequency of 1 000 Hz is employed. The calculations simulate measurements of the vertical and horizontal magnetic fields at a distance of 10 from a VMD source. Fifteen source positions were employed in the x direction from -40m to +30m. Symbols depict the 3D solution with the free space response removed, which uses 381 217 cells and lines the sheet results. At x=0 the discrepency between the real parts of the two solutions is about 24%.

Statistical Law of Surface Impedance Distribution

Yu.B. Bashkuev, V.B. Haptanov, and L.H. Angarkhaeva
Buryat Institute of Natural Sciences Siberian Department of Russian Academy of Sciences
6 Sakhyanova str., Ulan-Ude, 670042, Russia
Tel: +7 301 22 31210, Fax: +7 301 22 32841, E-mail: root@bien.buriatia.su

The surface impedance of underlying medium is the generally accepted electrodynamic characteristic of boundary conditions in the problems of excitation and propagation of radiowaves. The normalized surface impedance of the multilayered geoelectric section is defined as [1]:

$$\delta = \delta_1 \frac{1 - R_{12}\exp(-i2k_{1z}h_1)}{1 + R_{12}\exp(-i2k_{1z}h_1)}, \qquad (1)$$

where $R_{j(j+1)} = (\delta_j\alpha_{j+1} - \delta_{j+1}\alpha_{j+1})/(\delta_j\alpha_{j+1} + \delta_{j+1}\alpha_{j+1})$ is the reflection factor at the boundary between j-th and $j+1$-th layers; $\alpha_j = 1 \pm R_{j(j+1)}\exp(-i2k_{jz}h_j)$; $k_{jz} = k_0\sqrt{\varepsilon_{jc} - \sin^2\theta}$; $k_0 = 2\pi/\lambda$; $\delta_j = \sqrt{\varepsilon_{jc} - \sin^2\theta}/\varepsilon_{jc}$; $R_{n(n+1)} = 0$, $\lambda_n = 1$ when $j = n$; $\varepsilon_{jc} = \varepsilon_j + i60\lambda\sigma_j$ is the relative complex dielectric permeability; h_j is the thickness of j-th layer; θ is the angle of incidence of plane vertically polarized wave on the "air-earth" interface (time dependence is $\exp(-i\omega t)$).

Two-layered media of the types "insulator on conductor" and "conductor on insulator" with the strongly contrasted variables $\rho_j = 1/\sigma_j$, ε_j allow to change the values of impedance from highly-inductive to highly-capacitive ($-90° \leqslant \varphi_\delta \leqslant +90°$) . Low-highly-inductive ($-45° \leqslant \varphi_\delta \leqslant -72°40'$) and highly-highly-inductive ($-90° < \varphi_\delta < -72°40'$) subareas are distinguished, in addition in the latter subarea there are "critical" phases of impedance: $\varphi_{2cr} = -80°$ and $\varphi_{3cr} = -83°30'$ [2]. All these cases are realized only for $|\varepsilon_{1c}| < |\varepsilon_{2c}|$. In the class of natural stratified media the example of highly-inductive structure is two-layered "ice-sea water" medium occupying considerable spaces of the Global ocean in winter and in near-polar regions. Antarctic shelf glaciers of 100-350 m thickness and of hundreds of thousands square kilometres space give highly-highly-inductive values of impedance in the ELF-VLF ranges. The values of φ_δ reach $-89°$ and they are practically limiting values for natural stratified media. Electric characteristics of investigated regions are typical for continental crust. Surface impedance belongs to inductive area and it varies within the wide limits from minimal for salines to maximal for granitoids and glacial shields.

Probability model of geoelectric section (GES) is more full corresponds more full to nature of object under investigation - stratified underlying medium. Hereat resistivities ρ_j (conductivities) and thicknesses h_j of layers of mountain rocks' one-type complex are regarded as random variables with determinate distribution laws [3]. The statistical model construction aim was consisted in the selection of approximating distribution, which is means of generalized convolute presentation of the δ measured data. There are several different approaches to basis of the δ distribution statistical models under conditions of rocks' natural bedding. It is worthwhile to find the statistical model either by method of statistical tests (Monte-Carlo method) or by a selection of approximating distribution, for example, from Pearson distributions' family: normal, lognormal, gamma, beta, Weibull, Erlang. Physical-statistical approach to the selection of the δ distribution type is founded on distribution laws of the resistivity and thickness of mountain rock layer, obtaining on the basis of physical preconditions of their formation [4]. As a rule, resistivities ρ_j and thicknesses h_j of layers are lognormal variables (sometimes h_j is normal variable), as far as mountain rocks' formation is the result of even action of great number of random factors, and variables ρ_j, h_j, $|\delta|$, Re δ are limited on the one side, i.e. always they are more than zero [4]. So, geoelectric conditions on the real GES allow to suggest the hypothesis about lognormal distribution of $|\delta|$, Re δ, Im δ and normal distribution of φ_δ. Normal law for φ_δ follows from the determination $\delta = |\delta|e^{i\varphi_\delta}$, according to which $\ln\delta = \ln|\delta| + i\varphi_\delta$. The hypothesis leads to results, which agree well with measured data. To test the hypothesis about distribution law of impedance of mountain rocks' one-type complex let us consider the δ measured results on granitoids in ELF (80 Hz) and VLF-LF (15-50 kHz) ranges.

Selection totality of δ for granitoids satisfies homogeneity condition and it does not include data of measurements near by boundaries with other rocks. The histogram on statistical series of φ_δ for frequency 80 Hz and normal theoretical distribution are given on Fig.1. The test of hypothesis about lognormal distribution of $|\delta|$, Re δ, Im δ and about normal one of φ_δ has shown that selective data do not contradict to accepted hypotheses about distribution functions. Positively asymmetrical histograms of distribution of $|\delta|$, Re δ, Im δ and shown on Fig.2 cumulates testify this fact. The selection of distributions was carried out on the basis of selective estimations of asymmetry and excess, in turn based also on selective estimations of moments [5]. The comparison of data for ELF and VLF-LF ranges obtained for mountain rocks' one-type complex (granitoids) has shown that the action of different natural factors and frequency change cause statistical models parameters change with the preserva-

0-7803-3068-4/96$5.00©1996 IEEE

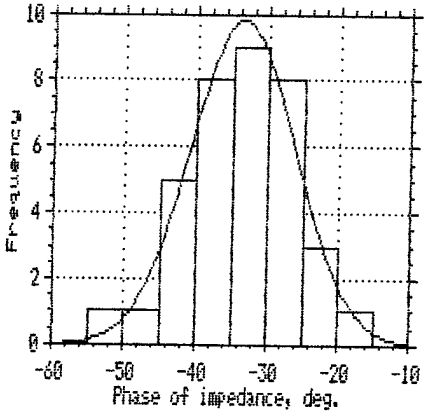


Fig.1 The histogram of φ_δ for frequency 80 Hz and normal theoretical distribution.

tion of lognormal distribution law for $|\delta|$, Re δ, Im δ and normal one for φ_δ. Asymmetry property of statistical distribntions of Re δ and Im δ points to nonlinearity of correlative dependence between them. When use logarithmic scales lg(Re δ) and lg(-Im δ) regression line becomes near to straight line. In the case the regression equation for granitoids is: lg(-Im δ)=-0,187+lg(Re δ).

In conditions of linearity of regression equation selective estimation of correlation coefficient r=0,85±0,13. The test of hypothesis about availability correlative connection of two-dimensional lognormal variable was shown that calculated value of t-parameter [5] $t=r/\sqrt{1-r^2}\sqrt{n-2}$=9,37 is more than table value of Student's critery 2.03 at selection volume n=36 and significance λ=0.05. That witnesses about statistically significant correlative connection between lg(Re δ) and lg(-Im δ). The regression equation allows to restore value of Re δ on value of Im δ measuring in aerovariant of radioelectromagnetic profiling method for widespreaded in Euroasia granitoid massives.

CONCLUSIONS

It is established that many-parameters integral electrodynamic characteristic of the stratified natural medium - surface impedance of mountain rocks' one-type complex - corresponds to lognormal distribution law for $|\delta|$, Re δ, Im δ and normal distribution law for φ_δ. It is shown that the action of different natural factors and frequency change cause statistical models parameters change with the law of distribution preserved. Validity and trustworthiness of conclusions have been confirmed by good quantitative coincidance of calculate-theoretical results with statistical data of measurements on different natural stratified media.

REFERENCES

[1] Ch.Ts. Tsydypov, V.D. Tsydenov, and Yu.B. Bashkuev, Issledovanie Elektricheskih Svoistv Podstilaiushei Sredy, Novosibirsk: Nauka, 1979, p. 176.

[2] G.I. Makarov, and V.V. Novikov, "Rasprostranenie elektromagnitnyh Voln v Plosko-Sloistoj Srede," Teoriya Rasprostraneniya Voln v Neodnoronnyh i Nelinejnyh Sredah, Moscow: IRE RAN, 1979, pp. 188-259.

[3] A.A. Ahmetishin, V.M. Kalinin, and V.S. Yakupov, "Geoelektricheskoe Stroenie Territorii YuTPK (Veroyatnostnaya Model)," Nizkochastotny Volnovod "Zemlya-Ionosphera", Alma-Ata: Gylym, 1991, pp. 86-87.

[4] K.S. Turitsin, "Osnovnoj Statisticheskij Zakon Raspredelenija Phisicheskih Svojstv Gornyh Porod," in Geophisicheskie Issledovanija pri Reshenii Geologicheskih Zadach v Vostochnoi Sibiri, vol. 3, Moscow: Nedra, 1964, p. 210.

[5] A.B. Kajdan, and O.I. Guskov, Matematicheskie metody v geologii, Moscow: Nedra, 1990, p. 251.

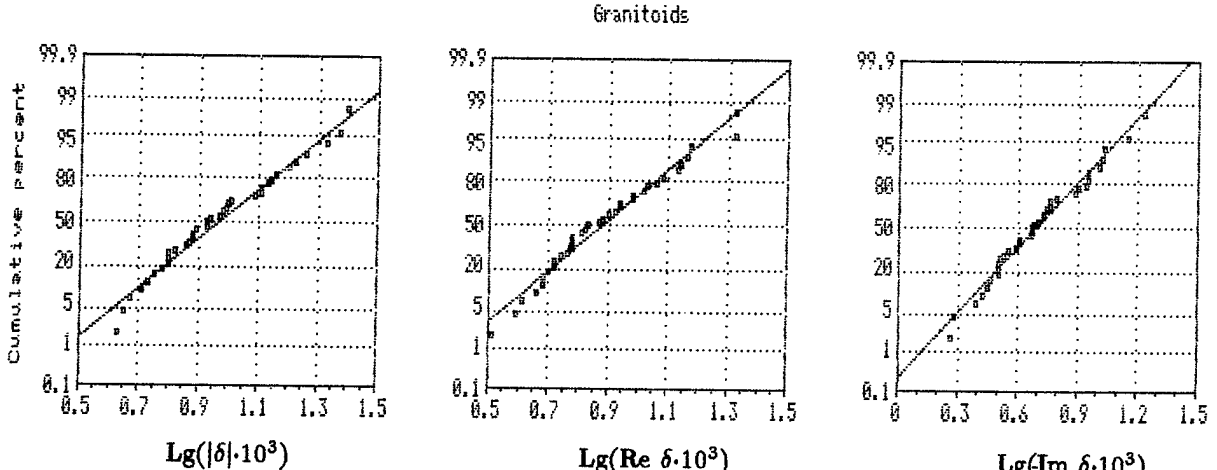


Fig.2 Cumulative distributions and least square regression lines for sets of $|\delta|$, Re δ and Im δ.

The Prediction Map of Geoelectric Sections of Australia, New Zealand and New Guinea

Yu.B. Bashkuev, V.B. Advokatov, and L.H. Angarkhaeva
Buryat Institute of Natural Sciences Siberian Department of Russian Academy of Sciences
6 Sakhyanova str., Ulan-Ude, 670042, Russia
Tel: +7 301 22 31210, Fax: +7 301 22 32841, E-mail: root@bien.buriatia.su

The prediction of characteristics of excitation and propagation of radiowaves in low frequency radiorange area is realized with the regard for electric properties of underlying medium, as a rule. Operational effectiveness of different telecommunication systems depends considerably on good knowledge of electric characteristics of underlying medium and it's time and space variations. Considering it, the background electric characteristics of large areas are of the great interest for practice because they let the researchers make the exact calculations of electromagnetic fields [1,2]. Electric properties of stratified underlying medium in low frequency area of radiorange are regulary changed in space and depend on a type of geoelectric structure (depression, massif, fault zone) and belonging to this or that complex of crystal and sedimentary rocks. The method of prediction of stratified medium electric properties of uninvestigated territories is based on the classification of geoelectric structures and on quantitative results of diagnostics of territories-analogues (key-areas). It permits to make an goal-directed quest for areas with predetermined electric characteristics.

The R.Morgan-E.Maxwell's conductivity map of the globe [3] doesn't often satisfy the needs of practice, because it is composed on homogeneous underlying medium model. There are considerable differences with measured results in some regions, hereat electric boundaries of the map don't coincide with real electric and geological boundaries. Therefore a creation of new prediction map of geoelectric sections of world's continents has been necessary.

In 1971-1995 our Institute worked out the basis of radiophysical diagnostics of electric state of the stratified underlying medium in the low frequency area of radiorange. With the help of ground and remote (from plane's board) methods of radioimpedance sounding and profiling the general and regional regularities of space-time and frequency variation of Euroasia stratified underlying medium geoelectric characteristics have been established [4]. Electric characteristics of investigated regions are typical for continental crust. Surface impedance belongs to inductive area and it varies within the wide limits from minimal for salines to maximal for granitoids and glacial shields. On the basis of objective classification of geoelectric structures of the Earth's crust and the interpretation algorithms of the radioimpedance sounding data the new effective method of physical-statistics prediction of the geoelectric sections of stratified natural media basic types are developed.

The methodology of geoelectric prediction is based on the following propositions:

1. There exists a regular connection between resistivity (conductivity) and lithological, hydrogeological, frozen ground parameters of mountain rocks, its composition and the peculiarities of the spatial varyability of geoelectric section (GES).
2. The resistivity of the certain type of mountain rock is a lognormal value.
3. The contours of the areas with similar electric properties coincide with the geological boundaries, the thickness of mountain rocks is sustained.
4. Prediction is carried out on the geological maps of basic mountain rocks and quaternary deposits with consideration for available resistivity sounding and boring data.
5. GES within the limits of skin-layer for VLF range (f=10 kHz) in the general case is presented as 2- or 4-layered.
6. In the areas with relatively simple geological structure the prediction of GES with the accuracy, sufficient for practice, is necessary to carry out basing on the key-areas study (territories-analogues) with the following prognostic spreading of the characteristics on allied in geological respect territories.

By composing the prediction map of GES parameters we mean the determination of the area distribution of different types of GES, the evaluation of resistivity ρ_j and thickness h_j of separate certain layers of the section on the whole scale of the map basing on limited quantity of the initial information. The problem is to determine the GES type (for instance $\rho_1 > \rho_2$ or $\rho_1 < \rho_2$) of the homogeneous area and its boundaries and statistic evaluation of ρ_j and h_j parameters.

The information on GES maps is described as codes, determining resistivity ρ_j and thickness h_j of the layers on the logarithmically-equal scale. The logarithm of the discretization step of ρ_j and h_j is equal to 0,333. The median values of ρ_j, h_j are calculated according to step number N by the following formula:

$$\rho_j = 10^{0,333(N-0,5)} \text{ Ohm.m}, \quad N = 0 \div 15;$$
$$h_j = 10^{0,333(N-3,5)} \text{ m}, \quad N = 1 \div 15.$$

0-7803-3068-4/96$5.00©1996 IEEE

The dielectric permeability ε_j of layers according to the experimental data is equal to $\varepsilon_j = 10$.

The Australia, New Zealand and New Guinea GES mapping has been carried out on a little scale because of the experimental data limits. Under creating the map published works' materials on electric and radioimpedance sounding of Australia and New Zealand territories were used [5-8]. As the geological and topographical basis we used "The geological map of the Continents", scale 1:15000000.

Explanatory note closed to the prediction map of GES of Australia, New Zealand and New Guinea on 8,8 million square kilometres area contains:
- tables of the 19 founded geoelectric structures and frequency dependences of surface impedance in the 10-1000 kHz range;
- qualitative estimation of truth of the composed map;
- review of utilized materials about electric properties of upper part of Earth's crust of the investigated territories.

On the Fig.1 the fragment of the prediction map of GES of Australia is presented. On this fragment the area distribution of geoelectric sections is reflected.

According to Morgan-Maxwell's map [3] Australia has 3 gradations of conductivity. The general background of Western and Northern Australia is 10^{-3} S/m, Southern and Eastern Australia - 10^{-2} S/m. New Zealand characterizes by 2 gradations 10^{-2} S/m; 10^{-3} S/m), the general background of it's territory is 10^{-2} S/m. New Guinea has 2 gradations too (10^{-2}; $3 \cdot 10^{-3}$ S/m), the general background of it's territory is 10^{-2} S/m.

The normalized surface impedance of the n-layered medium is presented as $\delta^{(n)} = \delta_1 \cdot Q^{(n)}$, which is suitable to be computer calculated [1]. Here δ_1 is homogeneous medium's surface impedance with the first layer parameters; $Q^{(n)} = F(f, \rho_j, \varepsilon_j, h_j)$ is a correcting factor taking into account lower earth's layers. On the Fig.2 the frequency dependences of the impedance modulus $|\delta|$ and phase φ_δ° are given for more spreading types of GES of Australia.

Analysis of the modulus $|\delta|$ and phase φ_δ° of impedance on GES map shows the considerable limits of its variations. So, at f=10 kHz the values of $|\delta|$ are changed from 0,0026 up 0,027, φ_δ° - from -34° up to -51°; and at f=1000 kHz the values of $|\delta|$ vary from 0,019 up to 0,18, φ_δ° - from -26° up to -50°.

The maps of GES help us to determine an radiofield attenuation function W in wide radiowave range with regard for relief and forest. The values of W for model of impedance multisectional radiopath are calculated on the basis of the numerical solution of Hufford's integral equation [2]. The prediction mistake of field attenuation is $\pm(15 \div 30)\%$.

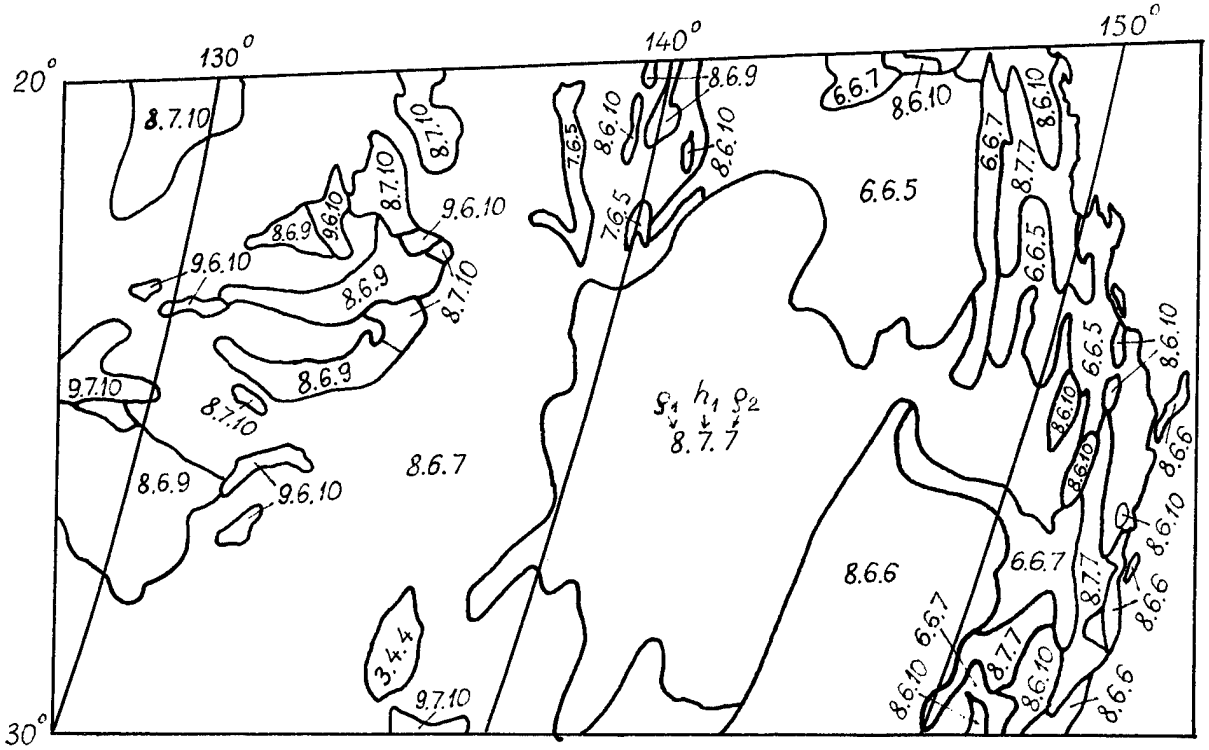


Fig.1 The fragment of the prediction map of GES of Australia.

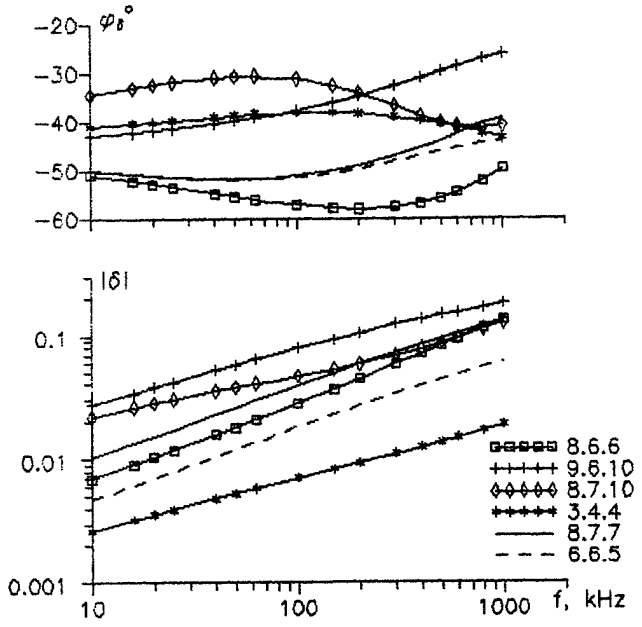


Fig.2 The frequency dependences of $|\delta|$ and φ_δ for typical GES of Australia.

Prediction maps of GES are composed for a dry season. The conditions in upper layer of GES are changed in a year cycle, also there are the change of temperature distribution character and rock's structure, humidity, saline composition and phase state of water in rock. The mapping territories belong to the equatorial and the subtropic areas basically, for which an unregular distribution of precipitations in a year is typical. The variation of electric condition of GES for these areas is conditioned mainly by mass-exchange (moisture-ion-transfer). The stratified medium model with properties and structure varying according to climatic conditions [9] allows to take into account season changes of impedance of boundary surface and neararthly radiofield.

CONCLUSIONS

The method of physical-statistics prediction of GES of stratified natural medium basic types has been developed. It takes into account physical processes in medium of different space-time scale. The methodology of small and large-scale geoelectric mapping has been grounded and elaborated in details. The prediction maps of GES of Australia, New Zealand and New Guinea have been compiled. In order to precise maps it is necessary to test the prediction by direct measurements of surface impedance.

REFERENCES

[1] Ch.Ts. Tsydypov, V.D. Tsydenov, and Yu.B. Bashkuev, Issledovanie Elektricheskih Svoistv Podstilaiushei Sredy, Novosibirsk: Nauka, 1979, p. 176.

[2] V.S. Dorzhiev, V.R. Advokatov, and B.B. Bodiev, Geoelektricheskie Razrezy Iuga Sibiri i Mongolii, Moscow: Nauka, 1987, p. 94.

[3] R. Morgan, and E. Maxwell, Omega Navigation System Conductivity Map, Office of Naval Research, Washington, D.C., Deco Electronics, 1965, Dec., p. 105.

[4] Yu.B. Bashkuev, V.S. Dorzhiev, and L.H. Angarkhaeva, "Geoelectric Sections Map of Euroasia," Internat. Symp. on Electromagnetic Environments and Consequences, Bordeaux, 1994, pp. THp-08-05-09-01.

[5] D.V. Thiel, "Surface-Impedance Changes in the Vicinity of an Abrupt Lateral Boundary at the Earth's Surface," IEEE Trans. Geosci. Remote Sensing, vol. 28, no. 4, pp. 500-502, July 1990.

[6] D.V. Thiel, "A Preliminary Assessment of Glacial Ice Profiling Using VLF Surface-Impedance Measurememts," Journal of Glaciology, vol. 32, no. 112, 1986, pp. 376-382.

[7] H.M. Bibby, "Electrical Resistivity Mapping in the Central Volcanic Region of New Zealand," New Zealand Journal of Geology and Geophysics, vol. 31, 1988, pp. 259-274.

[8] S.C. Constabl, "Resistivity Studies over the Flinders Conductivity Anomaly, South Australia," Geophys. J. Roy. Astron. Soc., 83, no. 3, 1985, pp. 75-86.

[9] Yu.B. Bashkuev, V.R. Advokatov, and V.S. Dorzhiev, "Season Variation of the Electrical Properties of Stratified Ground in Central Asia," 1989 Int. Symp. on EMC, Nagoya, vol. 2, pp. 895-900, Sept. 1989.

The influence of ground stratification upon a field of magnetic loop.

W.V.Dmitriev
Omsk State Pedagogical University,
14, Tukhachevsky Embankment, Omsk, 644099, Russia
Tel.: 7 381-2-24-37-95 Fax: 7 381-2-23-12-20
E-Mail: fis@lvt.ospi.omsk.su

Abstract -- In work the influence of inclined ground stratification upon a near field of loop is studied. The results is: a) inclined stratification causes the change of coupling coefficient of two perpendicular loops; b) coupling coefficient is a function of azimuthal angle; c) by using azimuthal dependence of coupling coefficient it's possible to retrieve some characteristics of ground layers.

INTRODUCTION

At some applications (underground sensing, antennas technics ets.) it is necessary to know the ground stratification. Stratification include the dates about order, depth, grade angle of layers and their dielectric properties - relative dielectric constant and conductivity. In this paper the influence of inclined ground stratification upon a near field of magnetic loop is studied. The main purpose is to investigate the resources of solution of inverse problem, i.e. the resources of

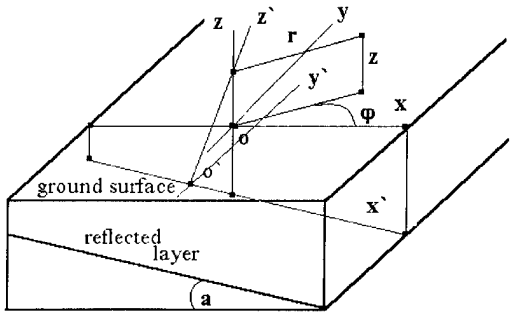


Fig. 1

determination of ground stratification using knowledge about near field of magnetic loop.

In papers of previous authors influence of ground stratification on near field of antennas always was examined[1,2]. However they investigated the case when ground layers parallel ground surface. At first in this paper the method of calculation of near magnetic field of loop and coupling coefficient of two perpendicular loops in case inclined ground layer is proposed. At second some theoretical results is discussed.

1.THEORY

0-7803-3068-4/96$5.00©1996 IEEE

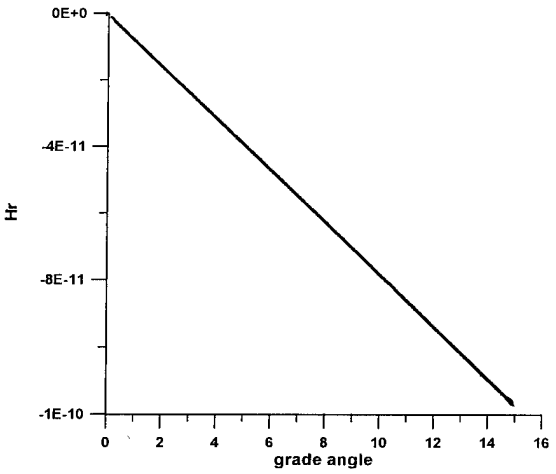


Fig.2 a

At Fig.1 the geometry of task is shown. In work the polar coordinates (ρ, φ, z) is used mainly.

Strong determination of field of antennas at or above ground surface is difficult problem and is based on Sommerfeld's results [3]. It's necessary to calculate Sommerfeld's integral.Commonly it needs numerical methods. At some cases this task assumes simplification. The near field of magnetic loop is the quasi-static field. It may be determined by using image theory [2].

The calculation of near field of magnetic loop above stratified ground with grade layers is based on Bannister's expressions [2]. At first our task is reduced to cause when ground layers parallel ground surface. To do it we pass on new X'Y'Z' coordinates see Fig.1. In that cause the horizontal magnetic dipole (HMD) in XYZ coordinates is reduced to HMD' and vertical magnetic dipole (VMD') in X'Y'Z' coordinates. Than we calculate the magnetic field in new coordinates and pass on old coordinates XYZ or (ρ, φ, z).

2. SINGLE LOOP FIELD

By using described in part 1 methods we have calculated values of all components (Hρ - radial, Hφ - azimuthal and Hz - z axis) near field single magnetic antenna as a function of azimuthal angle - φ and grade angle of reflected layer - α. As a result we have investigated the dependencies of Hρ, Hφ and Hz from φ and α. Main attention has directed to influence of grade angle to radial and azimuthal components of field. On Fig.2 shown

dependencies of Hρ, Hφ and Hz from grade angle. Components of magnetic field (Fig.2) were calculated with next parameters of task: ρ = 2 m, height loop at surface = 1 m, GMD = 1, soil conductivity = 0.01, GMD is oriented down to slope i.e. GMD angle = 0°, φ = 270° (see Fig.1). At next that case mark as 0-270 case.

Basing on results of calculation we make the Table 1. It show the change tendencies of field components with increasing grade angle. The Tab.1 includes the results for GND and azimuthal angle = 0,90,180,270° only. From Tab.1 ones see that grade angle change has more powerful an influence upon magnetic field when GMD is oriented up or down to slope (GMD angle = 0°, 180°). The tendencies for GMD angle = 0 ° and 90 ° practically is inverse at tendencies for GMD angle = 180 ° and 270 ° . That result is physically evident. It may be indicator of calculation rightness.

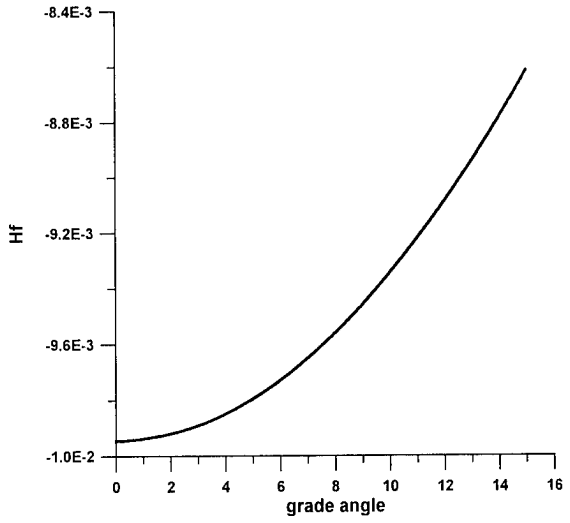


Fig.2 c

The cases 0-90, 0-270 (Fig.2), 180-90 and 180-270 for Hρ and Hz is most interesting. The cases 90-90, 90-270 (Fig.2), 270-90 and 270-270 for Hφ is most interesting. In that cases corresponding field components is absent for nought grade angle. It show that nonzero corresponding field components is indicator of inclination of reflected (water-bearing) layer of soil.

3. COUPLING COEFFICIENT OF TWO LOOPS

In previous part of that work we show that near field of magnetic loop demonstrate strong dependence from grade angle of reflected soil layer. Consequently the value of field components may used for investigation of ground stratigraphy. However measurements of real value of near magnetic field of antenna is difficult experimental task.

Experimental difficulties may be reduced by using two loops simultaneously. In that case we may to measure by using numerous difference

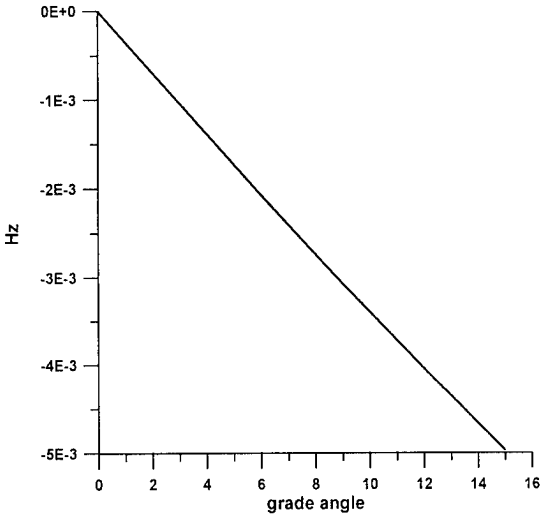


Fig.2 b

methods or by relative measurements. Experience show that it is easy.

We know 6 main variants of mutual configurations of two loops.For example we consider one of there - Fig.3. The signal at second antenna is defined of Hφ. In case on nought grade angle of reflected layer it is independent from

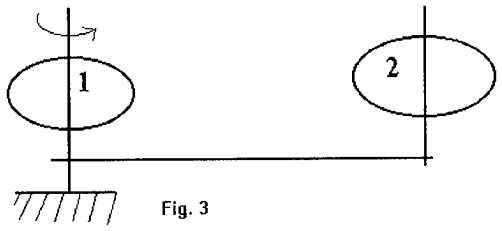


Fig. 3

azimuthal angle. Hence the coupling coefficient is independent too. In case on nonzero of grade angle Hφ is changed at φ = 0 ° and 180 ° (Tab.1). It cause changes of signal at second antenna. Hence the coupling coefficient become dependenced from azimuthal angle - Fig.4. By using that dependencies we may to determine grade angle and slope direction.

4. CONCLUSIONS

As a result we see that:
a) inclined stratification causes the change of coupling coefficient of two perpendicular loops;
b) by using azimuthal dependence of coupling coefficient of two loops it's possible to retrieve grade angle and slope direction of reflected (water-bearing) layer of soil;
c) next step must be the multilayered and rough surface model.

ACKNOWLEDGMENTS

I thanks Maslennikov N.M. for purpose of task.

Table 1

Hρ	Hφ	Hz	case
incr. H>0	0	incr. H>0	0-0
decr. 0	decr. H<0	decr. 0	0-90
incr. H<0	0	decr. H<0	0-180
decr. 0	incr. h<0	decr. 0	0-270
0	const<0	0	90-0
const>0	incr. 0	decr. H>0	90-90
0	const>0	0	90-180
const<0	incr. 0	incr. H<0	90-270
decr. H<0	0	decr. H<0	180-0
incr. 0	incr. H<0	incr. 0	180-90
decr. H>0	0	incr. H>0	180-180
incr. 0	decr. H>0	incr. 0	180-270
0	const>0	0	270-0
const<0	decr. 0	incr. H<0	270-90
0	const<0	0	270-180
const>0	decr. 0	decr. H>0	270-270

REFERENCES

[1] P.R.Bannister,"Summary of image theory expressions for the quasi-static fields of antennas at or above the earth's surface," Proc.IEEE, V.67, pp.1001-1008, July,

[2] J.R.Wait, "Electromagnetic waves in stratified media." NY: Pergamon, 1970, ch.2.

[3] A.Sommerfeld,"On the propagation of waves in wireless telegraphy," Ann.Phys, V.81, pp.1135-1153, 1926

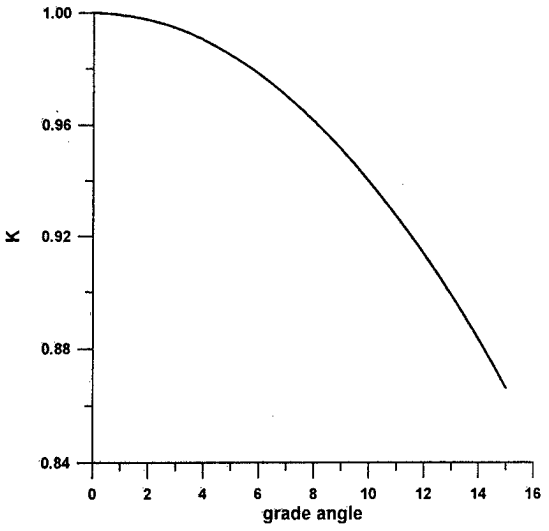


Fig.4

Detection and Location of Internal Waves in Ocean SAR Images by means of Wavelet Decomposition Analysis

Josep A. Rodenas, René Garello
Télécom Bretagne, Dept. ITI, BP 832
29285 Brest Cedex, France
e-mail: rodenas, garello@gti.enst-bretagne.fr

Abstract - This paper presents the construction of an appropriate wavelet basis based on a soliton analytical model, to detect and localize these nonlinear signatures in SAR images. A local statistics filter, to suppress the speckle noise produced in the process of forming the images, is applied so as to obtain noiseless SAR images profiles. The structure of arbitrary wavelet basis derived from the generalized B-spline wavelets is studied in order to obtain a more optimal decomposition. Comparisons are made for wavelet decompositions based on several families of compactly supported wavelets.

INTRODUCTION

The manifestation of internal wave packets in ocean SAR images has always been of considerable interest to oceanographers. If, as seems likely, the greytone patterns of the ocean SAR images can be confirmed to correspond to trough and crest patterns of internal waves, then a great deal can be learnt about internal waves from satellite data. Internal waves become visible on radar images because they are associated with variable surface currents which modify the surface roughness pattern. The radar is a surface roughness sensor: the higher the roughness, the higher is the radar return and the brighter is the image intensity.

Our goal is to identify and locate these signature patterns (nonlinear waves) within an arbitrary data sequence (ocean SAR image profile). For periodic signals, Fourier analysis lends itself to accurate and efficient identification algorithms. However, for localized (and thus nonperiodic) signals hidden in a much larger sequence, Fourier analysis falls far short of solving the detection problem. Wavelet analysis, on the other hand, offers a much more natural approach to such problems. It allows to decompose a signal onto a set of basis functions of subspace having some determined properties so as to be able to localize signal irregularities (i.e. abrupt variations or high frequencies) in time.

The Discrete Wavelet Transform (DWT) has been recognized as a natural wavelet transform for discrete-time signals. The transformation is inherently localized in both time and frequency, and as such is a valuable tool when analyzing nonperiodic data. The DWT decomposes a signal into a series of orthogonal wavelet subspaces. This decomposition preserves energy relationships between the subspaces, and the DWT can even be designed so as to be orthogonal within each individual subspace. We then seek to optimize the structure of the DWT by the construction of arbitrary wavelet basis that are ideally suited for the detection of a given signature waveform.

OCEAN SAR IMAGES FILTERING

Radar images of the Strait of Gibraltar have been obtained by Synthetic Aperture Radar (SAR) aboard the First European Remote Sensing Satellite ERS-1, which was launched on July 17, 1991 [1]. In theory, SAR systems can achieve along-track resolution independent of range, a very attractive characteristic for space imagery. However, SAR generates images by coherent processing of the scattered signals and consequently, they are highly susceptible to speckling effects. It is well known that, in theory, speckle obeys a negative exponential distribution, and therefore, is multiplicative in the sense that its standard deviation is equal to its mean. To filter speckle from SAR images requires a precisely defined statistical properties, such as correlation between neighboring pixels, and its probability distribution.

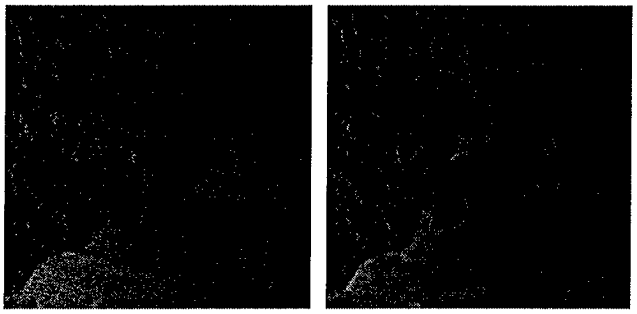
A smoothing algorithm, Lee's filter [2], based on local statistics, is applied to an ERS-1 SAR image from the Strait of Gibraltar with the result of effectively removing speckles while retaining subtle details. The Lee's method consists of making a linear estimation of the pixel, using the Least Mean Square (LMS) criterion, according to the observed value. From Fig. 1, we can observe that regions are better defined and fine details are easier recognized in the filtered image. Spikes produced by the speckle noise are eliminated since the standard deviation of the multiplicative noise is reduced. Thus, speckle reduction should be carried out in the image before getting ocean SAR images profiles.

NONLINEAR WAVES IN SAR IMAGES

The Strait of Gibraltar connects the Atlantic Ocean with the Mediterranean Sea. The water body in the Strait of Gibraltar and its approaches consists of a deep layer of saltier Mediterranean water and an upper layer of less dense Atlantic water [1]. Internal waves are primarily generated in the Strait by the interaction of the tidal current with prominent underwater bottom features. Internal waves become visible on radar images because they are associated with variable surface currents which modify the surface roughness patterns via current-wave interaction.

The ERS-1 SAR image depicted in Fig. 1 shows roughness patterns associated with a soliton-like internal wave inside the Strait of Gibraltar which was generated during the previous tidal cycle. Solitons are referred to as internal waves because they propagate beneath the sea surface in a medium whose density varies as a function of depth [3]. Based on an empirical oceanographic analysis (Korteweg and de Vries equation [4]), an approximation to analytically model the

0-7803-3068-4/96$5.00©1996 IEEE



(a) (b)

Fig. 1 ERS-1 SAR image from the Strait of Gibraltar from September 13, 1993, acquired with nominal resolution of 12.5 m x 12.5 m. Image size: 1000 x 1000 pixels (image resolution has been divided by 8). (a) Original image. (b) Image after speckle reduction.

behavior of solitons in the ocean surface can be defined by the following dimensionless equation:

$$u(x,t)=\frac{4}{3}A\operatorname{sech}^2\left[\sqrt{A}\left(x-\frac{(3-2A)}{3}t\right)\right] \quad (1)$$

where x is the horizontal displacement down the channel and of time t, and A is a constant that depends on the soliton trains amplitudes. Fig. 2 illustrates a simulation of the approximated analytical model of a soliton wave signature.

WAVELET ANALYSIS CONSTRUCTION

The idea of the Wavelet analysis, is in some, but not all, ways similar to the Fourier analysis. It provides a natural tool for time-frequency signal analysis. Given an input function, we wish to expand that function in terms of some orthonormal (ON) basis functions ϕ. The wavelet basis functions are all dilations and translates of a single function called the mother wavelet ψ. The wavelet $\psi_{j,k}$ is obtained from the mother wavelet by shrinking by a factor of 2^j and translating by $2^{-j}k$, to obtain:

$$\psi_{j,k}(x)=2^{j/2}\psi(2^j x-k) \quad (2)$$

If the ON wavelet is compactly supported, then finite-power signals can also be localized in time and scale, thus facilitating the study of the time-scale behavior of nonperiodic and nonstationary signals. The compactly supported wavelets satisfy several well documented properties, including the fact that the basis functions are relatively isolated in both time and frequency [5]. For the scope of this work, we are interested in constructing a wavelet basis best suited to the detection process.

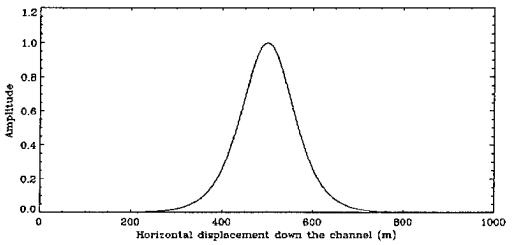


Fig. 2 Soliton wave simulation from the analytical model.

One of the basic methods for constructing wavelets involves the use of cardinal B-splines functions. When we talk about cardinal B-splines, we mean "polynomial spline functions" with equally spaced simple knots. The construction of the cardinal B-splines is carried out as proposed by Chui [6].

A fundamental result of the interpolation theory states that any function residing in π_m, the space of polynomials of order m, can be generated using the corresponding B-spline of order m. Therefore, the basis function β^m is the central B-spline of order m that can be generated by repeated convolution of spline of order 0:

$$\beta^m(x)=\beta^{m-1}*\beta^0(x)=\underbrace{\beta^0*\beta^0*\cdots*\beta^0}_{m+1\text{times}}(x) \quad (3)$$

where $\beta^0(x)$ is the characteristic function in the interval [0,1).

The scaling and wavelet functions can be generated by the two-scale sequences $\{p_{m,k}\}$ and $\{q_{m,k}\}$ as follows:

$$\phi_m(x)=\sum_k p_{m,k}\phi(2x-k)\,,\ \psi_m(x)=\sum_k q_{m,k}\phi(2x-k) \quad (4)$$

Once the cardinal B-spline wavelet has been constructed, we can create an entire class of wavelets which generate the same signal subspace by taking an invertible linear combination of the original wavelet. In our case, we would like this new wavelet $\tilde{\psi}(x)$ to resemble the detection signature as closely as possible at a given resolution level [7]. This new wavelet must also satisfy a two-scale relation, and so we redefine not the wavelet itself but the two-scale relation which generates it. This can be done by

$$\{\tilde{q}_{m,k}\}=\{\tilde{s}_k\}*\{q_{m,k}\} \quad (5)$$

The new wavelet at a given resolution level j is given by

$$\tilde{\psi}(2^j x)\big|_{2^j x=k}=\{\tilde{s}_k\}_{\uparrow 2^{-j}}*\psi(2^j x)\big|_{2^j x=k} \quad (6)$$

Let j=-1 (finer resolution level) be the resolution level at which we want to approximate the signature waveform. Then, expressed in matrix form (6) becomes

$$\Psi_k^{-1}\tilde{S}_k=\tilde{\Psi}_k^{-1} \quad (7)$$

where $\tilde{\psi}_k^{-1}$ are the samples of the soliton analytical model at the integers, ψ_k^{-1} are the convolution matrix elements, and $\tilde{S}_k$ are the nonzero coefficients from the upsampling. By using the Moore-Penrose pseudoinverse of Ψ_k^{-1}, (7) can be solved for S_k, and the resulting $\{\tilde{q}_{m,k}\}$ can be obtained.

The new wavelet is guaranteed to satisfy the properties of the wavelet transform and should make an ideal detector for soliton signatures in SAR images. Fig. 3 shows the scaling and wavelet functions for the new wavelet basis. Note that the low frequency components of the soliton analytical model have been removed prior to constructing the new wavelet.

The DWT algorithm is based on the multiresolution approximation method proposed by Mallat [8], and it is a special case of a two channel subband coder using the conjugate quadrature filters [9] as shown by (4), where the

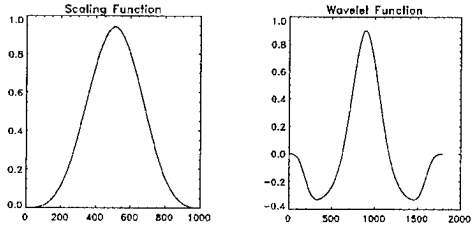


Fig. 3 New constructed wavelet basis.

two-scale sequences, $\{p_{m,k}\}$ and $\{q_{m,k}\}$, are the lowpass and highpass analysis filters, respectively. It provides a systematic mechanism for analyzing data at different scales. Hight frequency events (j near 0) are treated with relatively small translation steps, so they get the fine resolution they require, while low frequency events (j<<0) get larger time windows needed to encompass them. For the detection problem, we are only interested in the higher resolution level energies since it provides us with the enough information to detect and locate the soliton signatures.

In order to detect the presence of soliton waves, the ocean SAR image profile from Fig. 4 has been transformed using well known families of compactly supported wavelet bases. The resulting higher level DWT decompositions can be seen in Fig. 5. From the magnitudes of the decompositions, we can see that the new wavelet gives a better detection and location of the soliton signatures in the SAR image profile (soliton waves energies are more pronounced against the background noise and a better detection of all soliton waves, which can be observed in the image, is obtained). The standard families of wavelets, since they do not resemble the soliton signature, do not give an optimal decomposition (their DWT resulting coefficients are not mazimized when a soliton signature is encountered in the SAR image profile).

CONCLUSIONS

It has been seen that wavelet methods give a flexible alternative to fourier methods in nonstationary signals analysis. Speckle reduction on SAR images is required before getting SAR images profiles. B-splines methods give most suitable wavelet basis for the detection of a given signature. Comparisons done on an ERS-1 SAR image profile confirm that a new wavelet based on the soliton analytical model

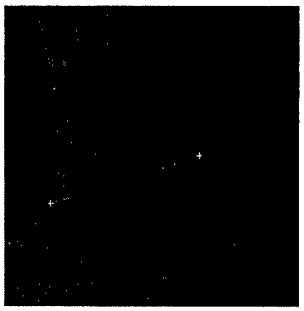


Fig. 4 Zoom in image of the soliton-like internal wave packet observed in the ERS-1 image from Fig. 1 (image with speckle reduction). Image size: 1000 x 1000 pixels. The crossing line shows the ocean SAR image profile chosen for the DWT decompositions.

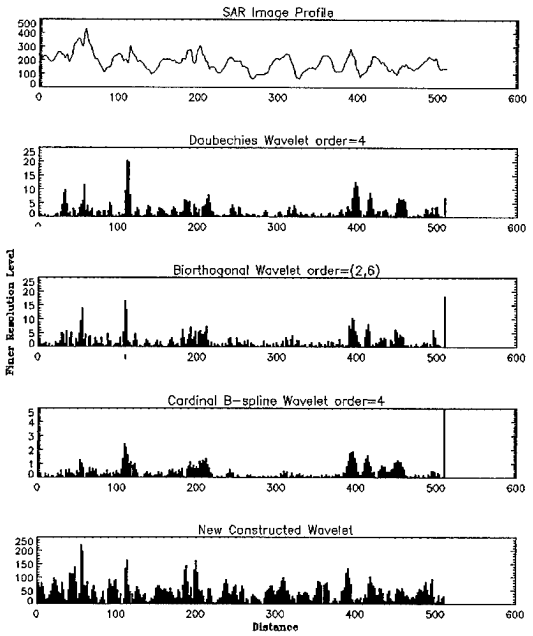


Fig. 5 Higher level DWT decompositions of the SAR image profile shown in Fig. 4 (from left-hand side point to right-hand side point). The original data is shown at the top, with the detail signals for the finer decomposition level for different wavelet basis displayed below.

gives a better detection performance than such well known families of compactly supported wavelets. Future work will show that using speckle reduction based on multiresolution filtering techniques gives better SAR images profiles to detect and locate nonlinear waves signatures and packets from ocean SAR images.

ACKNOWLEDGMENTS

This work was supported by the MAST-III (MORSE) Programme of EC, under the contract MAS3-CT95-0027. We thank Dr. W. Alpers, Hamburg University, for providing us with the ERS-1 SAR images from the Strait of Gibraltar.

REFERENCES

[1] W. Alpers and P.E. La Violette, "Tide-Generated Nonlinear Internal Wave Packets in the Strait of Gibraltar observed by the Synthetic Aperture Radar aboard the ERS-1 Satellite", Proceedings of the First ERS-1 Symposium, Cannes, France, Nov. 4-6, 1992, published by ESA Publications Division, ESA SP-359, March, 1993.

[2] J-S. Lee, "Speckle Analysis and Smoothing of Synthetic Aperture Radar Images", Computer Graphics and Image Processing, n. 17, pp. 24-31, 1981.

[3] A.R. Osbourne and T.L. Burch, "Internal Solitons in the Andaman Sea", Science, vol. 208, n. 4443, pp. 451-460, May 1980.

[4] P.G. Drazin and R.S. Johnson, "Solitons: An Introduction", Cambridge Texts in Applied Mathematics, Bristol, England, 1990.

[5] I. Daubechies, "Ten Lectures on Wavelets", Society for Industrial and Applied Mathematics, Philadelphia, PA, 1992.

[6] C.K. Chui, "An Introduction to Wavelets", Academic Press, San Diego, CA, 1992.

[7] M.A. Coffrey and D.M. Etter, "Wavelet Analysis in Soliton Detection", ICASSP 95, pp. 1109-1112, Detroit, May 1995.

[8] S. G. Mallat, "A Theory of Multiresolution Signal Decomposition: The Wavelet Representation", IEEE Trans. on Pattern Anal. Machine Intell., vol. 11, n. 7, pp. 674-693, July 1989.

[9] M. Vetterli and C. Herley, "Wavelet and Filter Banks: Theory and Design", IEEE Trans. on Signal Processing, vol. 40, pp. 2207-2232, 1992.

Spectral Analysis Of Non-Stationary Ocean SAR Images Using The Wigner-Ville Transform

S. Grassin, R. Garello
Télécom Bretagne Dept ITI BP 832
29285 BREST CEDEX, France

M. Prevosto, DITI, IFREMER, BP 70, 29280 Plouzané, France

Abstract – Physical events, such as swell or internal waves, have a strong signature on ocean SAR (Synthetic Aperture Radar) images. The spatial periodicity of these phenomena justifies the use of spectral analysis tools for their detection, localization and pertinent parameter estimation (wavelength, direction of propagation, energy, ...). However, these spectral phenomena are highly non-stationary, especially near the coast where the bathymetric conditions greatly influences the propagation. As the study of these variations are important near the coast, because of human activity, spectral analysis tools robust in non-stationary situations have to be considered. For that purpose, investigations were carried out to evaluate the efficiency of the Wigner-Ville distribution. This representation exhibits very good properties and has been quite extensively studied, even if the numerical implementation still presents some difficulties.

INTRODUCTION

The detection and estimation of periodical physical phenomena on the ocean surface, such as swell or internal waves, have been of interest for scientists for a long time. The imaging mechanism of the SAR (Synthetic Aperture Radar) permits to detect such phenomena. However, if all of them permits to estimate wavelength and direction of propagation, none of them allows a direct estimation of the energy parameters. In order to recover the wavelength and directional information, a good (in the sense of well adapted to this situation) spectral analysis tool has to be used, especially if we need these estimations for another applications (e.g., bathymetry recovery [1]). Furthermore the spectral high frequency cutoff, characteristic of the SAR imaging mechanism, may be linked to local changes in surface roughness allowing in turn a possible automatic detection of oil spills or floes. All these phenomena are interesting in highly non-stationary zones especially near the coast. For that reason, spectral analysis tools robust in non-stationary situations will be considered. A first set of parametric spectral estimation methods was developed [2] on very short spans of data (typically 32x32 pixels windows), but the choice of the parameter model (particularly the order) is rather difficult. Anyway, good results were obtained and some investigations were carried out on the use of a recursive solution to evaluate automatically the support of the parameters, as well as their values [3]. In this paper we will only consider benefits brought by a time-frequency representation. This type of spectral analysis, which combines together the notion of time and frequence seems well suited for its natural adaptability to the non-stationarity itself. Different time-frequency representations exist. Some decompose linearly the signal into time-frequency atoms. Wavelets, which are time-scale representation, belong to this class, assuming that the scale is related to the frequency. Such representation are of importance, especially in compression-decompression problems where the synthesis of the signal from the decomposition has to be done during decompression. As such properties are not of importance from a spectral analysis point of view, only time-frequency representation of the energy of the signal will be considered. Time-scale representation are avoided due to the difficulty to estimate the frequency of a phenomenon from a scalogramme. Among the infinity of possible time-frequency representations, the Wigner-Ville distribution was chosen. The reasons that motivated this choice were multiple. From a theoritical point of view, this representation owns a set of good properties which seemed well adapted to our purpose. From a practical point of view, the implementation of this representation, as well as the difficulties arising during its use, have been extensively studied in the litterature.

THE WIGNER-VILLE DISTRIBUTION

1 Definition

The Wigner-Ville Distribution (WVD) belongs to the general class of Cohen. This class regroups all the bilinear time-frequency representations of the signal which are covariantes with translations either in time or in frequency. The WVD lies at a particular place in that class. Firstly, all other distributions of the class can be expressed in function of it and secondly it is one of the distribution that has the best properties. As we are working with images, time will be replaced by two coordinates and the frequency will be two-dimensional. The Wigner-Ville distribution of a complex valued image $f(x,y)$ is by definition:

$$W_f(x,y,u,v) = \int f\Big(x+\frac{\alpha}{2},y+\frac{\beta}{2}\Big) f^*\Big(x-\frac{\alpha}{2},y-\frac{\beta}{2}\Big) \times \exp\Big(-2\pi i(u\alpha+v\beta)\Big)\, d\alpha\, d\beta. \quad (1)$$

When no integral limits are given, the limits are over all real values.

0-7803-3068-4/96$5.00©1996 IEEE

2 Properties

The properties of the Wigner-Ville distribution (WVD) have been extensively studied [4, 5]. The ones relevant to this paper are listed below. All the properties are identical for one or two dimentional signals.
Like all members of the class of Cohen (e.g. spectrogram, Choi-Williams, Page, Rihaczek distributions), the WVD is a bilinear form of the signal. For 1D complex valued signals, it means that the WVD of h (where $h = af + bg$, $f \,\&\, g$ being complex signals, and $a \,\&\, b$ being real constants), is given by:

$$W_h(x,u) = a^2\, W_f(x,u) + b^2\, W_g(x,u) + 2\Re\{W_{f,g}\} \quad (2)$$

where $W_{f,g}$ is the cross-term WVD of f and g, and is given by:

$$W_{f,g}(x,u) = \int f\Big(x+\frac{\alpha}{2}\Big)\, g^*\Big(x-\frac{\alpha}{2}\Big)\, \exp(-2\pi i u\alpha)\; d\alpha$$

or by the equivalent frequency definition.

3 Drawbacks of the bilinearity property

The WVD is recognised as a powerful tool for analysis of non-stationary signals. However, the bilinearity property is at the origin of some problems. If we consider f and g as pure frequencies components in (2), the Wigner-Ville time-frequency representation will be affected by spurious terms due to interferences between f and g. The mechanisms leading to these interferences, as well as their patterns on the time-frequency plane, have been extensively studied [6]. These interference terms are located directly inbetween and equidistant from the two terms in question. These terms contain no useful information and worstly can corrupt the true information. In order to suppress inference terms due to interactions between the positive frequency component and the equivalent negative component (in case of a real signal), the Wigner-Ville distribution will be performed on a 2D analytic signal of the image [7]. To eliminate these terms (and greatly reduce other interference terms which occur near the (u,v) origin), the concept of an analytic signal is introduced. An analytic signal is a modification of the original, but is more useful for the analysis of the WVD, because it removes the positive/negative pair interference terms whilst retaining all the information contained in the signal.

4 The discretization of the distribution

Several discretizations of the WVD have been proposed [4]. We retain the one proposed in [8] where the time-frequency plane is discretized both in time and in frequency. This leads to the Discrete Time and Frequency Wigner-Ville Distribution (DTFWVD). The definition of the DTFWVD for a 2D discrete complex valued signal of size $N_x \times N_y$ is:

$$W(n_1,n_2,m_1,m_2) = \frac{1}{4N_X N_Y} \times \sum_{l_1=0}^{N_X-1} \sum_{l_2=0}^{N_Y-1} f(l_1,l_2)\, f^*(n_1-l_1, n_2-l_2) \times \exp\Big(-i\pi\Big(\frac{m_1}{N_X}(2l_1-n_1) + \frac{m_2}{N_Y}(2l_2-n_2)\Big)\Big) \quad (3)$$

where it is assumed that f is $N_x N_y$-periodic. The WVD of the signal sampled in both domains, denoted by $\bar{f}$, expresses in function of the DTFWVD [8]:

$$W_{\bar{f}}(x,y,u,v) = \frac{1}{XY} \sum_{n_1,n_2,m_1,m_2} W(n_1,n_2,m_1,m_2)\, \delta\Big(x - n_1\frac{X}{2}\Big)\, \delta\Big(y - n_2\frac{Y}{2}\Big)\, \delta\Big(u - \frac{m_1}{2N_x X}\Big)\, \delta\Big(v - \frac{m_2}{2N_y Y}\Big) \quad (4)$$

This shows that the DWV of such a signal is sampled at twice the rate ($X/2$ and $Y/2$) in the spatial domain and that it is repeated in frequency with a period $1/2X$ and $1/2Y$ on respective axis. To avoid frequency aliasing, the image has to be sampled at twice the Nyquist rate (at least). As the signal has a finite spread, its bandwidth is theoritically infinite. Obviously, a trade has to be done in practice between both of them.

Pre-processings

In order to diminish the two types of aliasing, some preprocessings have to be done on the image. Firstly a sliding window is applied on the area where spectral estimation is wished in order to retain a finite number of values. The window is usually rectangular, but other types of window can be considered. The windowed image is centered: the DC component is removed and leads to more calibrated spectrum. This image is then interpolated to prevent frequency aliasing. A zero-padding operation is done in the Fourier domain. The size of the Discrete Fourier Transform (**DFT**) is doubled in each dimension and the three areas containing high frequencies are set to null. Performing the inverse DFT yields an interpolated image sampled at the quarter of the Shannon frequency. This last operation prevents only from frequency aliasing and another similar operation is necessary against spatial aliasing. A zero padding operation in the spatial domain suffices for that purpose. The drawback is that again the size of the image is doubled in each dimension. We have to notice that the order for which the operation are performed is significant as they are not commutative. The order we indicate justifies only on empirical studies. At last, an Hilbert Transform (**HT**) is done to limit the spectrum to an half plane in order to reduce interferences occuring between all possible pairs of auto-components laying each on one side. The HT cannot avoid frequency aliasing for 2D signals like it does for 1D signals, justifying in that way the interpolation stage in 2D case.

RESULTS

The Smoothed Pseudo Wigner-Ville Distribution (**SPWVD**) was applied on 16 small areas (32 × 32 pixels) of an ERS-1 image near the coast of Portugal (see fig. 1). This image is 512 pixels wide and has a heigth of 64 pixels (twice the size of the sliding window). The smoothing in the spatial domain is done with a 3 × 3 box window. Fig. 3 displays one of the local spectrum obtained. Graduations on frequency axis are normalized. There are nearly no frequency components after the quarter (0.25) of the Nyquist frequency (on both dimension) due to the interpolation stage. Half the plane, corresponding to negative X-frequencies, is null because the SPWVD was performed on an analytic version of the image (computed at each position of the sliding window).

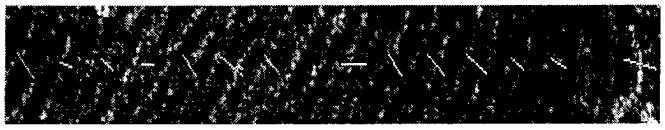


Figure 1: Evolution of the swell moving towards the coast (at the rigth of the image)

The same analysis was performed again with a 64 × 64 sliding window for comparison.

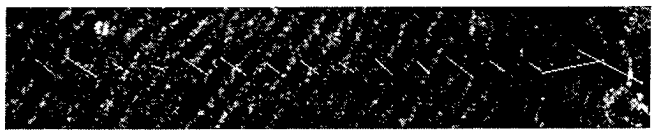


Figure 2: Spectral analysis with a 64 × 64 sliding window

CONCLUSION

We show in this paper one possible use of the Wigner-Ville Distribution as a powerful tool for spectral analysis of ocean surface in nonstationary situations. The main drawback with this distribution is the large amount of interferences terms. Some investigations about others bilinear time-frequency representations will be carried out in order to try to find a representation better suited.

ACKNOWLEDGMENT

The authors thanks M. Prevosto from IFREMER for providing the ERS-1 image.

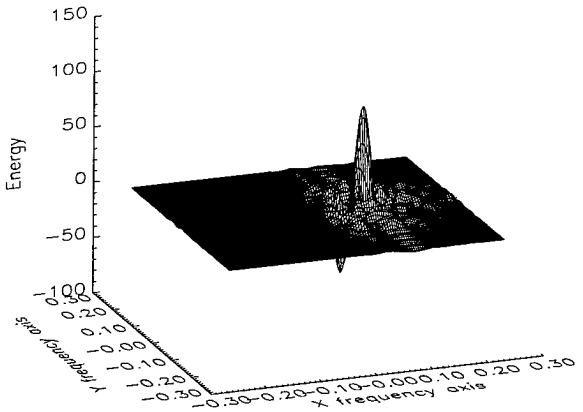


Figure 3: Smoothed Pseudo WVD of an ERS-1 image of the cost of Portugal

REFERENCES

[1] C. Guedes Soares, H.E. Krogstad, and M. Prevosto. Wavemod project: Probabilistic models for coastal site investigations. In IEEE, editor, *Proceedings of OCEANS 94*, volume 1, pages I–493–I–497, Brest, France, September 1994.

[2] R. Garello, C. Cariou, and J-M Boucher. Estimation spectrale paramétrique d'images SAR de la surface de la mer. *Télédétection et Gestion des Ressources*, vol. VII:pp. 271–279, 1991.

[3] L.F. Chaparro and M. Boudaoud. Two-dimensional linear prediction covariance method and its recursive solution. *IEEE Trans. on Systems, man, and cybernetics*, vol. SMC-17(4):pp. 617–621, July/August 1987.

[4] T. A. C. M. Claasen and W. F. G. Mecklenbräuker. The Wigner distribution. a tool for Time-Frequency signal analysis. *Philips J. Res.*, 35:217–250, 276–300, 372–383, 1980.

[5] Y. M. Zhu, F. Peyrin, and R. Goutte. Transformation de Wigner-Ville: Description d'un nouvel outil de traitement du signal et des images. *Annales des Télécommunications*, 42(3-4):105–118, 1987.

[6] P. Flandrin. *Temps-fréquence.* Traitement du signal. Editions HERMES, Paris, 1993.

[7] Y. M. Zhu, F. Peyrin, and R. Goutte. On the use of 2-D analytic signals for Wigner analysis of 2-D real signals. In *Int. Conf. Acoust., Speech, Signal Processing*, pages 1989–1992, Albuquerque, New Mexico, USA, April 1990. IEEE.

[8] F. Peyrin and R. Prost. A unified definition for the discrete-time, discrete frequency and discrete Time-Frequency Wigner distribution. *IEEE Trans. Acoust., Speech, Signal Processing*, 34:858–867, August 1986.

Results of Airborne Backscatter Measurements During the Surface Wave Dynamics Experiment

S. V. Nghiem, F. K. Li, G. Neumann, and S. H. Lou

Jet Propulsion Laboratory, MS 300-235
California Institute of Technology
4800 Oak Grove Drive, Pasadena, CA 91109, USA
Tel: 818-354-2982, Fax: 818-393-5285
E-mail: nghiem@malibu.jpl.nasa.gov

Abstract – Ocean backscatter data over a wide variety of oceanic and atmospheric conditions were obtained by the Jet Propulsion Laboratory NUSCAT K_u-band scatterometer during the Surface Wave Dynamics Experiment (SWADE) off the coast of Virginia. A sea surface temperature front at the Gulf-Stream boundary existed in the SWADE measurement area. Swells up to 6 m in significant wave height and a large range of wind speeds were encountered. Large differences in backscatter between cold and warm sides of the Gulf Stream were observed. Relations of backscatter with friction velocity are derived from the NUSCAT-SWADE data set. The increasing trend observed in the backscatter with younger wave age agrees with a rougher surface condition for a younger wave field. The results show that backscatter is more sensitive to friction velocity with smaller deviation factors compared to the backscatter functions of wave age. NUSCAT data indicate that the azimuth direction, at which the backscatter is maximum, is in between the wind direction and the dominant wave direction at light wind conditions. Excluding cases of large swells, there is no systematic trend between backscatter and significant wave height.

INTRODUCTION

The NASA Scatterometer (NSCAT) will be launched to measure backscatter at $K_u$band for ocean remote sensing [1]. Thus it is important to study the dependence of ocean backscatter on environmental conditions. In this paper, backscatter signatures at $K_u$band as functions of oceanic and atmospheric parameters are investigated with the NUSCAT-SWADE data base. NUSCAT is an airborne K_u-band scatterometer developed at the Jet Propulsion Laboratory. The scatterometer was mounted on the NASA Ames C130 aircraft on a gimbal with a full azimuth scanning capability. The range of incidence angles was from 0° to 60° for both vertical and horizontal polarizations. The scatterometer has a high signal-to-noise ratio and a large dynamic range to measure ocean backscatter for a wide range of air and sea conditions.

SWADE was carried out in an instrumented oceanic area off the coast of Virginia. During an intensive observation period (IOP) of SWADE in the winter of 1991, 30 hours of backscatter data were collected in 10 flights by NUSCAT. The Gulf Stream boundary was included in the area of the experiment. Sea surface temperatures across the boundary were different by as much as 10°C. Swells reached to 6 m in significant wave height (SWH). A wide range of wind speeds was encounted during the experiment. Various atmospheric and oceanic parameters were measured by an array of buoys deployed in the SWADE area. These measurements together with the backscatter data form the basis of the analysis in this paper. Backscatter signatures are investigated for the dependence on friction velocity, wave age, and SWH.

This work was performed under a contract with the National Aeronautics and Space Administration at the Jet Propulsion Laboratory, California Institute of Technology.

ACROSS THE GULF STREAM BOUNDARY

In a number of flights across the north wall of the Gulf Stream, NUSCAT was flown over the sea surface temperature front. These flights provide backscatter data to study the temperature effects.

In a NUSCAT flight on 28 February 1991, the boundary of the Gulf Stream was between Discus C buoy located on the warm side and Discus A on the cold side. NUSCAT data corresponding to this case were at vertical polarization and 30° incidence angle. The observed increase from the cold side to the warm side was about 5.5 dB at downwind, 5.2 dB at upwind, and 4.5 at crosswind. Accounting for the wind speed difference between the two sides of the sea surface temperature front, SASS-II geophysical model function [2], which relates backscatter to neutral wind at 19.5 m, gives only a 3-dB difference. Large differences in backscatter at $K_u$band were also observed for the horizontal polarization at various incidence angles in several other flights. These case studies indicate that ocean backscatter also depends on other atmospheric and oceanic parameters besides the neutral wind speed.

BACKSCATTER AND FRICTION VELOCITY

Radar returns from ocean surfaces are related to friction velocity, u_*, in both the Bragg and the sea-spike scattering components [3]. Liu and Large [4] used u_* derived from direct observations to show the correlation of backscatter with u_*. Li et al. [5] demonstrated the dependence of backscatter on u_* based on experimental measurements from the Frontal Air-Sea Interaction Experiment.

In this paper, we utilize the NUSCAT-SWADE data base to study the dependence of σ^0 on u_*. Friction velocity u_* used in this analysis is determined from buoy data

0-7803-3068-4/96$5.00©1996 IEEE

with the formulation by Large and Pond [6] for ocean momentum flux measurements. Fig. 1 presents backscatter as a function of friction velocity for the horizontal polarization and incidence angles from 10° to 60° in the upwind direction. NUSCAT data are represented by the symbols and the continuous curves are for linear fitting functions in the logarithmic domain. At the incidence angle of 10°, the backscatter is insensitive to the friction velocity. For larger incidence angles, the horizontal backscatter is sensitive to the friction velocity with stronger backscatter for larger u_*. Slopes of the linear curves in the logarithmic domain correspond to the positive exponents of u_*. Similar results are obtained for both horizontal and vertical directions in terms of upwind, downwind, and crosswind normalized radar cross sections.

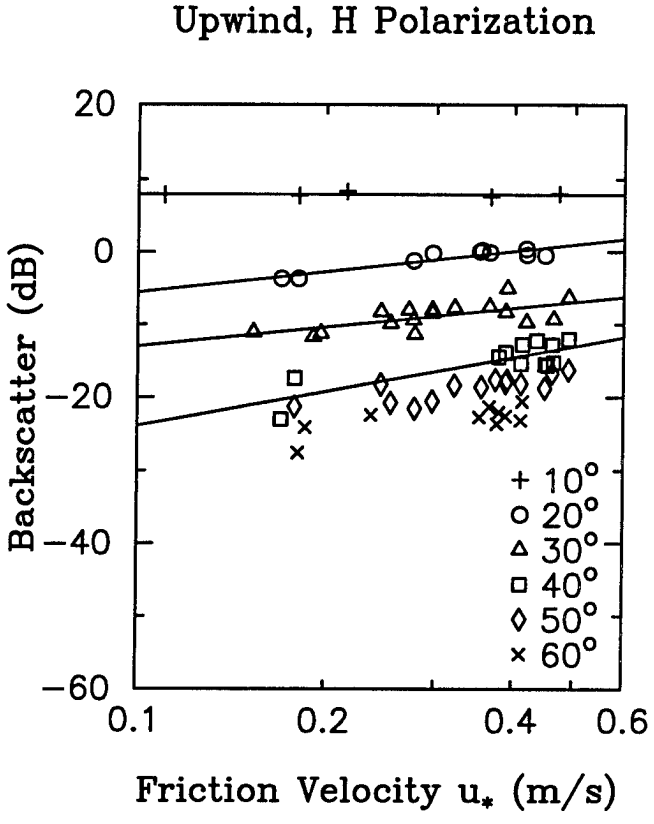


Figure 1. Horizontal backscatter versus friction velocity. The symbols denote NUSCAT data at different incidence angles and the continuous curves are for linear fitting functions.

BACKSCATTER AND WAVE AGE

Wave age is defined by the ratio of the dominant gravity wave phase speed over the friction velocity. Geernaert [7] showed smaller values of wave age correspond to larger drag coefficients and steeper wave slopes. Plenty of experimental evidences ([8] and more recently [9]) support the correlation of rougher sea surfaces for younger wave ages. Rougher surfaces give rise to larger backscatter for smaller wave ages. On the contrary, a smoother roughness has been suggested for younger wave ages [10].

Considering these differences, we use NUSCAT-SWADE data to investigate the trend between backscatter and wave age. Fig. 2 plots horizontal backscatter as a function of wave age for incidence angles from 10° to 60°. These results are for the case of upwind backscatter. As observed from Fig. 2, the data have a decreasing trend with wave age, characterized by the negative slopes of the linear fitting curves in the logarithmic domain. An exception is at 10° incidence angle where the backscatter is insensitive to the wave age. For downwind and crosswind directions and also for the vertical backscatter, the results show the decreasing trend with wave age. These observations of backscatter are consistent with a rougher sea surface condition for a smaller wave age.

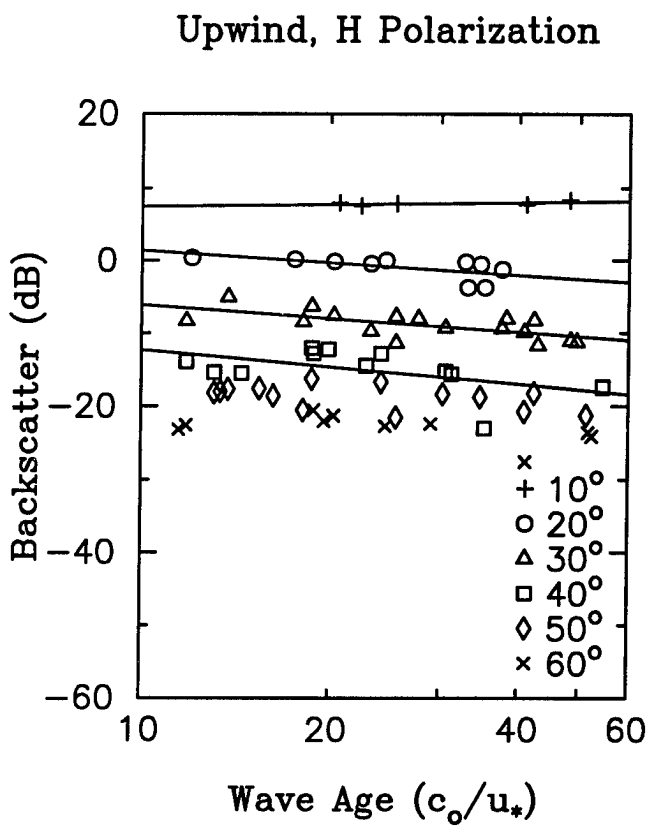


Figure 2. Horizontal backscatter versus wave age. The symbols denote NUSCAT data at different incidence angles and the continuous curves are for linear fitting functions.

BACKSCATTER AND WAVE HEIGHT

Swells with a large significant wave height have been shown to have a strong impact on ocean backscatter at light wind conditions but not at moderate winds [11]. Tower measurements also suggested that backscatter can be affected by long waves at lower wind speeds [12]. Another study concluded that effects of varying wave height on radar measurements is of little importance [13]. Thus in general, backscatter seems to have a weak dependence

on significant wave height.

Results from NUSCAT-SWADE indicated that the azimuth direction, at which the backscatter is maximum, is in between the wind direction and the dominant wave direction at light wind conditions. An examination of a direction wave spectrum at an intermediate wind speed shows that NUSCAT maximum direction aligned with high frequency wave components. Figure 3 presents upwind horizontal backscatter as a function of significant wave height excluding cases of swells with a larger wave height. No systematic correlation between the backscatter and the wave height is observed. Similar observations apply to vertical backscatter.

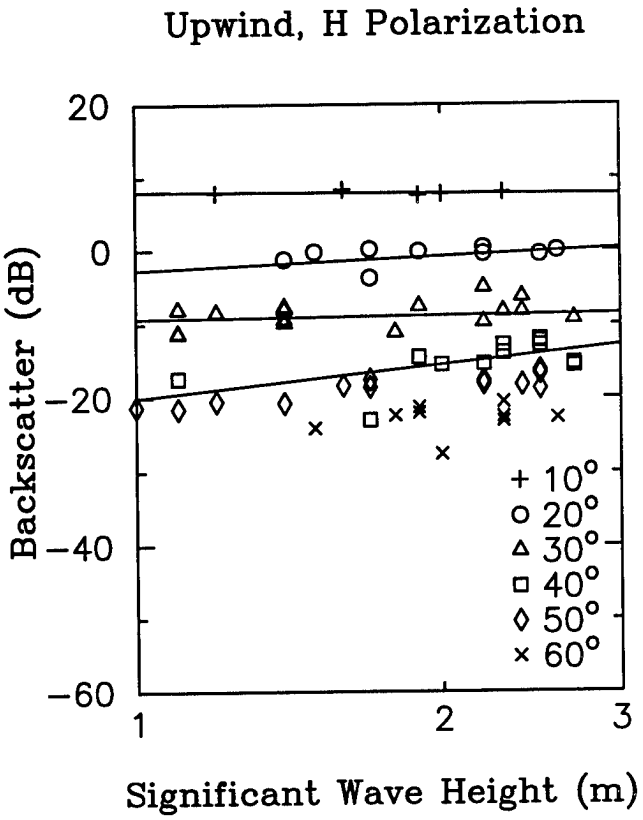


Figure 3. Horizontal backscatter versus significant wave height. The symbols denote NUSCAT data at different incidence angles and the continuous curves are for linear fitting functions.

SUMMARY

Ocean backscatter at $K_u$band was successfully measured by the Jet Propulsion Laboratory NUSCAT scatterometer during SWADE over a wide variety of atmospheric and oceanic conditions. Relations of backscatter with friction velocity have a positive trend with positive exponents of u_*. Results show the trend of increasing backscatter with younger wave age, which corresponds to a rougher surface for a younger wave field. No systematic trend between backscatter and significant wave height is observed.

ACKNOWLEDGMENTS

The authors thank Dr. J. D. Oberholtzer, Dr. K. Steele, and Dr. D. Wang for the buoy data.

REFERENCES

[1] F. M. Naderi, M. H. Freilich, and D. G. Long, "Spaceborne radar measurement of wind velocity over the ocean – an overview of the NSCAT scatterometer system," *Proceedings of the IEEE*, vol. 79, no. 6, pp. 850-866, 1991.

[2] F. J. Wentz, S. Peteherych, and L. A. Thomas, "A model function for ocean radar cross sections at 14.6 GHz," *J. Geophys. Res.*, vol. 89, no. C3, pp. 3689-3704, 1984.

[3] O. M. Phillips, "Radar returns from the sea surface – Bragg scattering and breaking waves," *J. Phys. Oceanogr.*, vol. 18, pp. 1065-1074, 1988.

[4] W. T. Liu and W. G. Large, "Determination of surface stress by Seasat-SASS: A case study with JASIN data," *J. Phys. Oceanogr.*, vol. 12, pp. 1603-1611, 1981.

[5] F. Li, W. Large, W. Shaw, E. J. Walsh, and K. Davidson, "Ocean radar backscatter relationship with near-surface winds: A case study during FASINEX," *J. Phys. Oceanogr.*, vol. 19, no. 3, pp. 342-353, 1989.

[6] W. G. Large and S. Pond, "Open ocean momentum flux measurements in moderate to strong wind," *J. Phys. Oceanogr.*, vol. 11, pp. 324-336, 1981.

[7] G. L. Geernaert, "Bulk parameterizations for the wind stress and heat fluxes," *Surface Wave and Fluxes*, G. L. Geernaert and W. J. Plant, eds., Vol. I, pp. 91-172, 1990.

[8] M. A. Donelan, F. W. Dobson, S. D. Smith, and R. J. Anderson, "On the dependence of sea-surface roughness on wave development," *J. Phys. Oceanogr.*, vol. 23, no. 9, pp. 2143-2149, 1993.

[9] B. A. Juszko, R. F. Madsen, and S. R. Waddell, "Wind stress from wave slopes using Phillips equilibrium-theory," *J. Phys. Oceanogr.*, vol. 25, no. 2, pp. 185-203, 1995.

[10] Y. Toba and M. Koga, "A parameter describing overall conditions of wave breaking, whitecapping, sea-spray production and wind stress," in *Oceanic Whitecaps*, Ed. by E. C. Monahan and G. Mac Niocaill, pp. 37-47, 1986.

[11] S. V. Nghiem, F. K. Li, S. H. Lou, G. Neumann, R. E. McIntosh, S. C. Carson, J. R. Carswell, E. J. Walsh, M. A. Donelan, W. M. Drennan, "Observations of ocean radar backscatter at Ku and C bands in the presence of large waves during the Surface Wave Dynamics Experiment," *IEEE Trans. Geosci. Remote Sens.*, vol. 33, no. 3, pp. 708-721, 1995.

[12] W. C. Keller and W. J. Plant, "Cross Sections and Modulation Transfer Functions at L and K_u Bands Measured During the Tower Ocean Wave And Radar Dependence Experiment," *J. Geophys. Res.*, vol. 95, no. C9, pp. 16277-16289, 1990.

[13] D. Ross and W. L. Jones, "On the relationship of radar backscatter to wind speed and fetch," *Boundary Layer Meteorol.*, vol. 13, pp. 151-163, 1978.

Quantitative Analysis of Radar Signatures of Underwater Bottom Topography According to a Bragg-Based Composite Surface Model

Roland Romeiser

University of Hamburg, Institute of Oceanography, Troplowitzstr. 7, 22529 Hamburg, Germany
Phone: +49 40 4123 5430 Fax: +49 40 4123 5713 E-Mail: romeiser@ifm.uni-hamburg.de

Abstract -- We have recently developed a calibrated composite surface model for the calculation of normalized radar backscattering cross sections (NRCS) of the ocean surface. Using an optimized parameterization of the waveheight spectrum, the measured dependence of the mean NRCS on radar parameters and on the wind speed vector is reproduced quite well. In this paper the sensitivity of the NRCS to intensity variations of different wave spectral components is analyzed, and theoretical radar signatures associated with spatial surface roughness variations over underwater bottom topography in tidal waters are investigated. The composite surface model yields comparable radar signatures at high (10 GHz, X band) and low (1 GHz, L band) radar frequencies. However, measured NRCS variations at high radar frequencies appear to be still underestimated in some cases. Possible reasons and further improvements of the theory are discussed.

INTRODUCTION

The fact that underwater bottom topographic features become, under certain environmental conditions, visible on radar images has attracted the interest of scientists for more than 20 years. The imaging mechanism is a two-step process: First, the spatial variations of the water depth lead to a modulation of the tidal flow. The resulting surface current gradients give then rise to a hydrodynamic modulation of the surface roughness which can be detected by radar.

According to a first model by W. Alpers and I. Hennings [1] the radar signatures of a given surface current feature should be most pronounced at low microwave frequencies, since the corresponding resonant Bragg scattering surface waves of wavelengths in the decimeter range experience the strongest hydrodynamic modulation. Experimental results show, on the other hand, that the radar signatures do not depend very much on the frequency.

This discrepancy can be solved by employing composite surface models which account not only for basic Bragg scattering but for the effect of the complete ocean wave spectrum on the normalized radar backscattering cross section (NRCS). However, most existing composite surface models have not been calibrated for a reproduction of measured absolute NRCS values. They are thus not perfectly suited for quantitative analyses. The few calibrated models, on the other hand, are quite complex or require very detailed sets of input parameters which are normally not known.

In another paper [2] we have presented a calibrated composite surface model which has been optimized for the computation of absolute NRCS values. Measured absolute NRCS values for a wide range of radar frequencies (1 GHz (L band) through 34 GHz (K_a band)), horizontal (HH) or vertical (VV) polarization, moderate incidence angles between approx. 30° and 60°, arbitrary azimuthal radar look directions with respect to the wind direction, and wind speeds up to 20 m/s can be reproduced quite well by the proposed model.

We now want to employ our model for a quantitative study regarding the radar signatures of underwater bottom topography in tidal waters. Assuming that given wave spectra will be converted correctly into NRCS values, it is possible to evaluate the performance of existing models for the spatially varying wave spectra over underwater bottom topography. In view of the available data, this is a promising approach, since dedicated in-situ wave measurements have not been carried out during most experimental campaigns.

COMPOSITE SURFACE MODEL

Details of the theory of the proposed composite surface model have been described elsewhere in this issue [2]. Here we want to mention only that the model is based on Bragg scattering theory and a Taylor expansion of the NRCS in the two-dimensional surface slope. It accounts not only for geometric effects but also for the hydrodynamic modulation of the Bragg waves by longer ocean waves which causes an upwind / downwind asymmetry of the NRCS. In the following, $\langle\sigma\rangle$ denotes the expectation value of the NRCS for a given set of radar parameters and a given ocean wave spectrum. It consists of the zeroth-order term $\sigma^{(0)}$ and an expectation value $\langle\sigma^{(2)}\rangle$ of a sum of second-order terms which depend on the mean square surface slopes parallel or normal to the azimuthal radar look direction or on the mean product of the two slope components.

Fig.1 shows the relative contribution of $\langle\sigma^{(2)}\rangle$ to $\langle\sigma\rangle$ as function of wind speed. The impact of $\langle\sigma^{(2)}\rangle$ is largest at high radar frequencies, HH polarization, and an upwind pointing antenna. In addition, its relative contribution increases clearly with wind speed.

This work has been supported by the European Community, Grant Nos. MAST-0040-C and MAS2-CT94-0104, by the Deutsche Agentur für Raumfahrtangelegenheiten, Grant Nos. 50 QS 9014 and 50 QS 9016, and by the Deutsche Forschungsgemeinschaft, Grant No. Al 88/2.

0-7803-3068-4/96$5.00©1996 IEEE

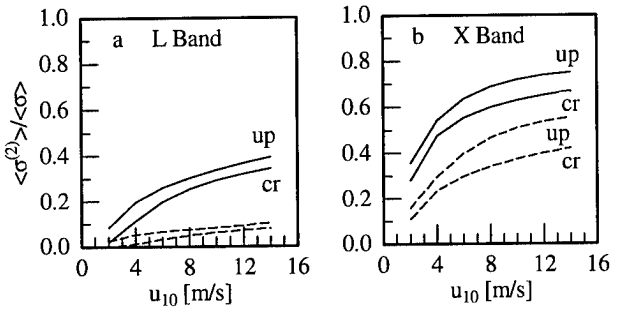


Figure 1: Relative contribution of the second-order terms to $\langle\sigma\rangle$ as function of wind speed u_{10} for upwind and crosswind pointing radar antennas. Incidence angle is 45°, wind speed is 10 m/s. Solid lines: HH, dashed: VV polarization; a) L band (1 GHz), b) X band (10 GHz).

Figs. 2 and 3 show the composition of $\langle\sigma^{(2)}\rangle$ as function of wavenumber and wave direction, respectively. Fig.2 shows the growth of the integrated quantity $\langle\sigma^{(2)}\rangle$ when integrating over wavenumber, normalized by the total integral which is obtained when the integration has arrived at the upper integration limit $k = 1/6\ k_B$ (where k_B is the Bragg wavenumber). These diagrams can be used for an estimation of the effect of roughness variations at different wavelengths on $\langle\sigma\rangle$. For example, intensity variations at wavenumbers greater than 1 rad/m will affect a portion of about 35 percent of $\langle\sigma^{(2)}\rangle$ for L band, VV, upwind, while almost 90 percent of $\langle\sigma^{(2)}\rangle$ for X band, VV, crosswind, will vary with the intensity of these waves. An interesting fact is that $\langle\sigma^{(2)}\rangle$ is affected more strongly by long waves in case of an upwind pointing antenna than in the crosswind case.

The directional composition of the second-order terms is shown in Fig.3. Here the integration is carried out from the direction opposite to the azimuthal radar look direction ($\Delta\phi = 180°$) through the radar look direction. For an upwind looking antenna, the largest portion of the second-order terms is associated with waves traveling parallel to the wind direction. Also in case of a crosswind pointing antenna the second-order terms are dominated by waves traveling along and against the radar look direction, although the maximum slopes occur in the direction normal to this direction. This shows that the effect of "parallel" slopes is generally stronger than the effect of "normal" slopes.

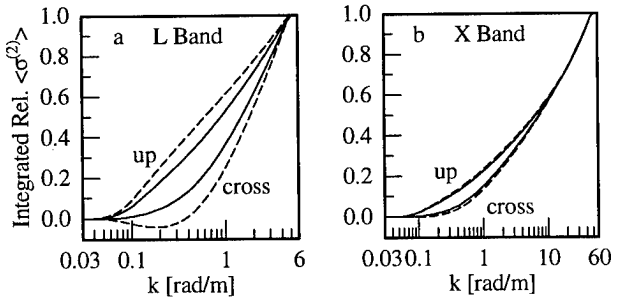


Figure 2: Growth of the second-order terms of $\langle\sigma\rangle$ when integrating over wavenumber; same conditions as in Fig.1.

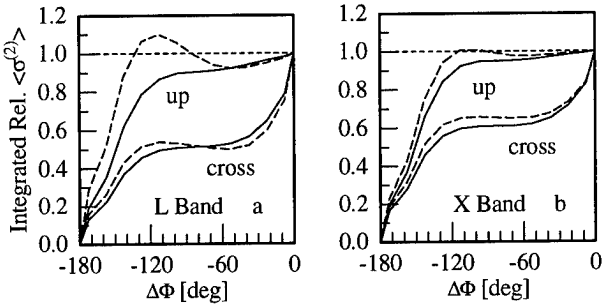


Figure 3: Same as Fig.2, but growth when integrating over wave direction; $\Delta\phi$=0 corresponds to the radar look direction.

WAVE–CURRENT INTERACTION MODEL

If the current flow over underwater bottom topography is laminar, free of vertical current shear, and quasi-stationary, the relationship between the horizontal current and the water depth is given by a simple continuity equation. We do not want to discuss flow modeling aspects in more detail within the framework of this work.

Models for the wave–current interaction are normally based on the equations of weak hydrodynamic interaction theory. The evolution of the energy of a wave packet is described by the action balance equation

$$\frac{dN}{dt} = \left(\frac{\partial}{\partial t} + \frac{d\underline{x}}{dt}\frac{\partial}{\partial \underline{x}} + \frac{d\underline{k}}{dt}\frac{\partial}{\partial \underline{k}}\right)N = Q(\underline{k},\underline{x},t)\,, \tag{1}$$

where $N = \Psi\rho\omega_0/k$ is the action spectral density of the wave packet and Q is a source function. The evolution of position and wavenumber with time is determined by the two ray equations

$$\frac{d\underline{x}}{dt} = \frac{\partial\omega}{\partial\underline{k}} = \underline{c}_g(\underline{k}) + \underline{U}(\underline{x})\,, \tag{2}$$

$$\frac{d\underline{k}}{dt} = -\frac{\partial\omega}{\partial\underline{x}} = -\left(\underline{k}\frac{\partial}{\partial\underline{x}}\right)\underline{U}\,. \tag{3}$$

Here $\underline{c}_g = \partial\omega_0/\partial\underline{k}$ denotes the group velocity of the wave packet and $\omega = \omega_0 + \underline{kU}$ its apparent (Doppler shifted) frequency in the moving medium, while ω_0 is the intrinsic frequency. Furthermore, Ψ is the waveheight spectrum, ρ is the density of seawater, and $\underline{U}$ is the surface current.

Spatial variations of the action spectrum can be computed by integrating (1) along ray paths given by (2), (3). The crucial element of the integration is the source function Q which represents the combined effect of wind input, nonlinear wave–wave interaction, and dissipation that forces a disturbed wave spectrum to relax towards an equilibrium state. Different parameterizations of Q can be found in the literature. The simplest source function is the linearized one:

$$Q = -\mu(N - N_0)\,, \tag{4}$$

where μ is the so-called relaxation rate, and N_0 is the equilibrium action spectrum.

Several authors have used a form of Q which includes terms up to second order in $(N–N_0)$. It reads

$$Q = -\mu\left((N-N_0)+\frac{(N-N_0)^2}{N_0}\right) = \mu N\left(1-\frac{N}{N_0}\right). \quad (5)$$

The relaxation rates proposed by various authors differ by up to one order of magnitude. A parameterization which has been used quite often in the literature is the one according to [3]. We use this parameterization for our test calculations. For the directional variation of μ we adopt the spreading function of the equilibrium waveheight spectrum as developed in [2]. As an option, the wind speed that enters into Q can be corrected for the local surface current. From the physical point of view, this correction should be applied, but it has been neglected by most other authors.

Some authors have tried to develop source functions which are more closely related to the original terms for the general case. For example, Yu.G. Trokhimovski [4] proposed an expression of the form

$$Q = \alpha\omega_0 N\left(N\frac{k^5}{\rho\omega_0}\right)^n\left(1-\left(\frac{N}{N_0}\right)^n\right), \quad (6)$$

where α and n are functions of wavenumber.

Other approaches account for the effect of a feedback mechanism between the modulated surface roughness and the friction velocity ([5], [6]). Also the generation of additional small-scale roughness like parasitic waves in the crest region of steep decimeter or meter waves [7] or the formation of surface films in regions of convergent surface currents [8] may contribute to the modulation mechanism.

MODEL RESULTS

A well investigated test area for model calculations is situated 30 km off the Dutch coast, 20 km northwest of Measuring Platform Noordwijk (MPN), where many experiments have been carried out since the late 1960s. We have tried to simulate signatures of a sandwave feature which is well visible on a P band synthetic aperture radar image and on two X band real aperture radar images. The P band image was obtained at 0.44 GHz, VV, and an incidence angle of approx. 35°. The wind speed was 4 m/s. The X band images were obtained at two different times corresponding to opposing current directions and thus reversed signatures, at 9.4 GHz, HH, and an incidence angle of approx. 65°; the wind speed was about 8 m/s.

We have computed the spatially varying wave spectra for the three scenarios by using five different source functions:

- The linear source function (4) with wind correction;
- the quadratic source function (5) without wind correction;
- the quadratic source function with wind correction;
- the quadratic source function with wind correction and using a relaxation rate reduced by a factor of 1/10;
- and the source function (6) with wind correction;

where the model runs using the quadratic source function without wind correction were carried out in order to get an impression of the relevance of the wind correction.

In case of the P band image, a measured dark signature, corresponding to a divergent surface current, was found to be well reproduced when using the quadratic source function. The wind correction turned out to be not very important.

Also in case of the X band images, the dark signature was reproduced satisfactorily. Here the quadratic source function with a reduced relaxation rate led to best results. Again, the effect of the wind correction was not very significant. The bright signature in the other image, on the other hand, was underestimated with all source functions by a factor of at least 2. Also Trokhimovski's source function, which was developed in order to explain large modulations, did not perform as well as expected.

We conclude from these results and from some further analyses that weak hydrodynamic interaction theory alone cannot explain all observed signatures of underwater bottom topography. Additional modulation effects as discussed in [5], [6], [7], and [8] should be taken into account. Dedicated in-situ measurements should be carried out in order to get more insight into details of the modulation mechanism.

REFERENCES

[1] W. Alpers and I. Hennings, "A theory of the imaging mechanism of underwater bottom topography by real and synthetic aperture radar," J. Geophys. Res., vol. 89, 1984, pp. 10,529-10,546.

[2] R. Romeiser, "Optimization of a composite surface model for the radar backscattering cross section of the ocean surface as measured by wind scatterometers," Proc. IGARSS '96, Lincoln, NE, 1996.

[3] W.J. Plant, "A relationship between wind stress and wave slope," J. Geophys. Res., vol. 87, 1982, pp. 1,961-1,967.

[4] Yu.G. Trokhimovski, "The gravity capillary waves modulation in internal waves current field," Rep. Pr-1855, Russian Academy of Science, Space Research Institute, Moscow, 1993.

[5] R. Romeiser, A. Schmidt, and W. Alpers, "A three-scale composite surface model for the ocean wave–radar modulation transfer function," J. Geophys. Res., vol. 99, 1994, pp. 9,785-9801.

[6] V.N. Kudryavtsev, C. Mastenbroek, and V.K. Makin, "The interaction of long and short waves. Modulation of the evolution of short waves via the atmospheric boundary layer," unpublished.

[7] D.R. Thompson and R.F. Gasparovic, "Intensity modulation in SAR images of internal waves," Nature, vol. 320, 1986, pp. 345-348.

[8] S.A. Ermakov and E.N. Pelinovski, "Variations of the spectrum of wind ripples on coastal waters under the action of internal waves," Dyn. Atmos. Oceans, vol. 8, 1984, pp. 95-100.

Near Nadir Microwave Specular Returns from the Sea Surface - Measurements of Winds from Breeze to Hurricane

Jin Wu
Institute of Hydraulic and Ocean Engineering
National Cheng Kung University
Tainan, Taiwan, Republic of China

and

Air-Sea Interaction Laboratory
Graduate College of Marine Studies, University of Delaware
Lewes, Delaware 19958

Abstract -- Wind velocity over the sea surface is the most important parameter governing atmospheric and oceanic systems. Two satellite-borne sensors: scatterometer and altimeter have been developed. The former has been specifically designated for mapping sea-surface winds, but the latter which can also detect the surface elevation has attracted a great deal of attention lately. The scatterometer, operated on the basis of Bragg scattering from ocean ripples, are found to be operative at only intermediate winds with speeds between 4 and 10 m/s; it is quite incentive at both low and high winds. Low wind speeds, however, prevail over the world's oceans, while measurements over stormy conditions are most needed as in situ instruments often fail.

The remote sensing of sea-surface winds with an altimeter is based on specular reflections from the surface roughness. At low and intermediate winds, the altimeter return is shown to be inversely proportional with the mean-square slope contributed mainly by ocean ripples, having their lengths longer than the radar wavelength. An algorithm is justifiably constructed, and is tuned with reported buoy-measured winds. This algorithm is most sensitive at low winds. At high winds, the sea-surface roughness produced by breaking waves starts to influence the altimeter return. Reported data obtained under hurricanes are used to show that additional altimeter returns at various wind speeds are consistent with the results of sea-surface whitecap coverages. With these understandings of backscattering mechanisms at different wind regions, a continuous function is proposed to determine the sea-surface winds, from breeze to hurricane, from the altimeter returns.

MICROWAVE REFLECTION FROM OCEAN RIPPLES

Reflection from Wind-Roughened Sea

The backscattering of radiation at nadir is primarily specular reflections from the sea-surface roughness; the latter at low winds consists of wind-generated ripples. Specular-point models offer the following normalized radar cross section for a nadir-looking altimeter [1]

$$\sigma_{or}(0°) = |R(0°)|^2/\overline{s_r^2}, \tag{1}$$

where σ_{or} is the specular return from ripples, $|R(0°)|^2 = -2.1$ dB is the Fresnel reflection coefficient of the sea surface at normal incidence, and s_r^2 is the mean-square slope of ripples distributed over the radar illuminated area. Only those ripples having their length longer than the radar wavelength, however, can contribute to altimeter returns [2].

Cox and Munk [3] determined slopes of the sea surface from sun glitter on the sea surface; mean-square slopes were obtained under various wind velocities. The mean-square slope can be related to the directional wavenumber spectrum $\psi(\boldsymbol{k})$ of ocean waves through [4]

$$\overline{s^2} = \int k^2 \psi(\boldsymbol{k}) \mathrm{d}k, \quad \psi(\boldsymbol{k}) = (B/\pi)k^{-4},$$
$$\overline{s^2} = B \ell n (k_c/k_o) = B \ell n [(U_{10}^2/g)k_c], \tag{2}$$

in which k and $\boldsymbol{k}$ are wavenumber scalar and vector, respectively; B is the spectral coefficient of the gravity range; $k_o = g/U_{10}^2$ represents the wavenumber at the spectral peak, with g being the gravitational acceleration and U_{10} the wind velocity at 10 m above the mean sea surface, and k_c is the cutoff wavenumber. Following the general trend shown in (2), mean-square slopes measured by Cox and Munk in the gravity range, with their wavenumber smaller than 3.6 rad cm^{-1}, were shown by Wu [4] to be

$$\overline{s^2} = (0.90 + 1.20\ ln\ U_{10})\ x\ 10^{-2}, \tag{3}$$

where U_{10} is in m s^{-1}.

The X-band radar was used for the GEOSAT altimeter; it has a wavenumber of about 2.9 rad cm^{-1}, differing only slightly from the cutoff wavelength for the mean-square slope shown in (3). An analytical algorithm was then obtained [5], by substituting (3) into (1).

0-7803-3068-4/96$5.00©1996 IEEE

Validation of Altimeter Sea-Returns

Since the altimeter was not fully calibrated, the calculated return was then compared with buoy winds compiled by Dobson et al. [6]. The latter consist of 121 coincident GEOSAT and buoy observations with separations being less than 50 km spatially and 30 min temporally. For the best match, the calculated return was shifted downward by 2.1 dB; the latter is reasonable to accommodate the calibration requirement [7]. The altimeter return for wind speeds above 2.4 m s^{-1} was verified to follow

$$\sigma_{or} = \{|R(0°)|^2 - 10 \log \overline{s_r^2}\} - 2.1 = \\ - 4.2 - 10 \log (0.009 + 0.012 \ell n U_{10}), \quad (4)$$

in which σ_{or} is in dB. The above expression, the so-called analytical altimeter wind algorithm, is shown as a continuous curve in Fig. 1a.

For higher wind speeds, the variation of σ_o with U_{10} becomes gradual, as ocean ripples providing altimeter returns tend to approach a state of saturation as the wind speed increases [8, 9]. Furthermore, the increase of mean-square slopes at higher winds was shown to come mainly from the capillary region [9]; these waves are too short to produce altimeter returns.

ALTIMETER RETURNS UNDER HIGH WINDS

Reported Results

The variation with the wind speed of altimeter returns from ocean ripples alone becomes insensitive at high winds. Recently, Young [10] assembled data over tropical cyclones during the GEOSAT mission; only those with the satellite ground track passing through the eye of a storm were selected. On the basis of these data, the altimeter returns under hurricane winds were suggested by Young as

$$\sigma_{om} = 11.25 - 0.15625 \, U_{10}, \quad (5)$$

which is shown as a solid line in Fig. 1a.

Under a continuous influence of the wind, waves grow and eventually become unstable locally; the waves then break to dissipate excessive energy provided by the wind [11]. Large breaking ocean waves are always accompanied by whitecaps. In an equilibrium state, the energy lost through wave breaking must be balanced by the energy gained from the wind. Consequently, the percentage of sea surface covered by breaking waves under this state can be related to the energy flux from the wind; a power law of the whitecap coverage increasing with the wind velocity was then deduced [12], on the basis of reported oceanic data

$$W = 2 \, U_{10}^{3.75}, \quad (6)$$

in which W is the sea-surface whitecap coverage in ppm.

Altimeter Algorithm

Young [10] attempted to relate altimeter returns at high winds to the mean-square slope of ocean ripples generated directly by the wind. I, on the other hand, attribute additional altimeter returns at high winds to large-scale breaking waves, which become more intensive at higher wind velocities. Roughnesses produced by breaking waves were demonstrated to be effective at producing radar returns [13]. These roughnesses are clearly not generated directly by the wind stress, and therefore should not be expected to obey the upper limit of the mean-square slope discussed by Young. These roughnesses can hardly reach a saturated state, as there are more breaking waves at higher wind velocities, as shown in (6). In summary, I suggest that the altimeter returns collected under hurricanes were actually from roughnesses produced by breaking waves, and provide evidence of this mechanism by interpreting these returns in terms of whitecap results.

A gap is seen iin Fig. 1a between the curve representing (4) and the straight line given by (5). If the straight line is translated upward, a tangent point with the curve is found to be located at 9.32 m s^{-1}, and the upward movement of (5) to reach this point is 0.469 dB. With this shift, the algorithm proposed by Young is adjusted to

$$\sigma_o = 11.719 - 0.15625 \, U_{10}. \quad (7)$$

In other words, the combination of (4) and (7) is proposed to represent altimeter sea returns for the entire wind-speed region from breeze to hurricane. The portion of algorithm represented by (4) and the curve in Fig. 1a for $U_{10} < 9.32$ m s^{-1} have been well validated by not only winds measured by a network of buoys [6], but also from SEASAT [14]. This portion of the curve is, therefore, sufficiently reliable to warrant the upward shift of (5); the magnitude of the shift, 0.469 dB, is also acceptable in view of either the instrument calibration error or the data scatter.

Roughnesses produced by breaking waves contribute negligibly to the altimeter returns for wind speeds below 9.32 m s^{-1}, at which the whitecap coverage is less than 1%. Above this wind speed, (4) is suggested to still represent the contribution of ripples, as it was derived by extending the mean-square slope measured at wind speeds below 7 m s^{-1} to high winds. In accordance with (1) and (4), the returns measured by Young [10] contributed by roughnesses produced by both ripples and breaking waves can be written as

$$\sigma_o = -4.2 - 10 \log (\overline{s_r^2} + \overline{s_b^2}), \quad (8)$$

in which $\overline{s_b^2}$ is the mean-square slope associated with roughnesses produced by breaking waves. Consequently, this component of the mean-square slope can be obtained from the above expression with σ_o from (7) and $\overline{s_r^2}$ from (3); the results are shown in Fig. 1b. The mean-square slope from ocean ripples, $\overline{s_r^2}$, is also diagramed in Fig. 1b; it is greater than that from breaking waves up to the wind speed of about 39.5 m s^{-1}.

Following this line of reasoning, the difference between the radar cross section measured by Young [10] and (7), $\Delta\sigma = |\sigma_{om} - \sigma_{o\alpha}|$, is suggested to be the additional altimeter return introduced by breaking waves.

Assuming that the roughnesses produced by breaking waves at all wind velocities act similarly in producing microwave specular returns, the total influence of these roughnesses is simply proportional with the whitecap coverage. Consequently, the radar return from breaking waves should, and have been verified to, vary linearly with the sea-surface whitecap coverage; its variation with the wind velocity should have the same power as that of whitecaps as indicated in (6).

CONCLUDING REMARKS

The sea-surface roughness, which produces specular reflections of impinging microwaves, mainly consists of ocean ripples at low and intermediate winds. Roughnesses produced by breaking waves start to influence the altimeter returns at high wind speeds, say beyond 10 m s^{-1}. Their influence is consistent with the results of sea-surface whitecap coverages. With this understanding of the backscattering mechanism, the wind speed of hurricanes can be monitored confidently from space. Such measurements are much more convenient and accurate than those performed in-situ over the stormy sea.

ACKNOWLEDGMENT

I am very grateful for the support of this work provided under the Ocean Science Educators Award, Office of Naval Research, and National Science Council.

REFERENCES

[1] D. E. Barrick, "Wind dependence of quasi-specular microwave sea scatter," IEEE Trans. Antennas Propagat., Vol. AP-22, pp. 135-136, 1974.

[2] G. S. Brown, "Backscattering from a Gaussian-distributed perfectly conducting rough surface," IEEE Trans. Antennas Propagat., Vol. AP-26, pp. 472-482, 1978.

[3] C. S. Cox, and W. H. Munk, ""Measurement of the roughness of the sea surface from photographs of the sun's glitter," J. Opt. Soc. Am., Vol. 44, pp. 838-850, 1954.

[4] Jin Wu, "Mean-square slopes of the wind-disturbed water surface--Their magnitude, directionality, and composition," Radio Sci., Vol. 25, pp. 37-48, 1990a.

[5] Jin Wu, "Near nadir microwave specular returns from the sea surface--Altimeter algorithms for wind and wind stress," J. Atmos. Oceanic Tech., Vol. 9, pp. 659-667, 1992.

[6] E. Dobson, F. Monaldo, J. Goldhirsh, and J. Wilkerson, "Validation of Geosat altimeter-derived wind speeds and significant wave heights using buoy data," J. Geophys. Res., Vol. 92, pp. 10719-10731, 1987.

[7] L. B. Wetzel, "Sea clutter," Rep. 9244, Naval Research Laboratory, Washington, D. C., 1990.

[8] M. L. Banner, I. S. F. Jones, and J. C. Trinder, "Wavenumber spectra of short gravity waves," J. Fluid Mech., Vol. 198, pp. 321-344, 1989.

[9] Jin Wu, "Radar sea returns--Ocean-ripple spectrum and breaking-wave influence," J. Phys. Oceanogr., Vol. 20, pp. 1985-1993, 1990b.

[10] I. R. Young, "An estimate of the GEOSAT altimeter wind speed algorithm at high wind speeds," J. Geophys. Res., Vol. 98, pp. 20275-20285, 1993.

[11] P. A. Hwang, Delun Xu, and Jin Wu, "Breaking of wind-generated waves: Measurements and characteristics, J. Fluid Mech., Vol. 202, pp. 177-200, 1989.

[12] Jin Wu, "Oceanic whitecaps and sea state," J. Phys. Oceanogr., Vol. 9, pp. 1064-1068, 1979.

[13] M. L. Banner, and E. H. Fooks, "On the microwave reflectivity of small-scale breaking waves," Proc. Roy. Soc. London Ser. A, Vol. 399, pp. 93-109, 1985.

[14] D. L. Witter, and D. B. Chelton, "A Geosat altimeter wind speed algorithm and a method for altimeter wind speed algorithm development," J. Geophys. Res., Vol 96, pp. 8853-8860, 1991.

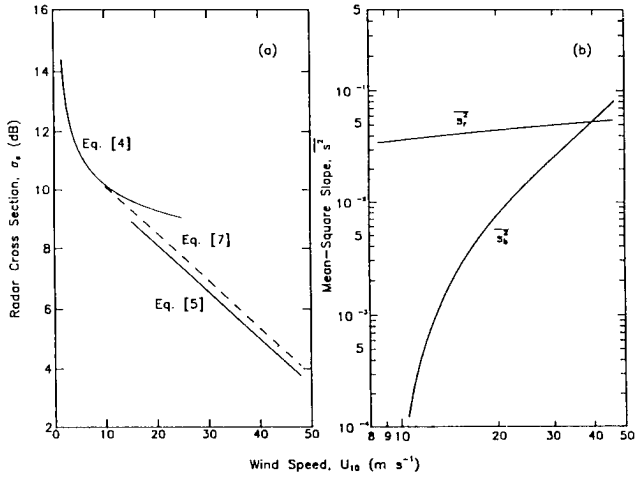


Figure 1 - MATCHING OF LOW AND HIGH WIND ALGORITHMS AND MEAN-SQUARE SLOPES CONTRIBUTED BY RIPPLES $\overline{s_r^2}$ AND BREAKING WAVES. $\overline{s_b^2}$.

Spectral Variations of Sea Surface Emission at MM-Wave Frequencies Under Influence of Synoptical Oceanic Eddies

I.V.Cherny and V.P.Nakonechny

Center for Program Studies, Russian Space Agency,
Profsoyusnaya, 84/32, Moscow, 117810, Russia,
Fax: 7-(095)-420-2275, Email: solom@febes.msk.su

Abstract - The experimental results of airborne multispectral mm-wave imaging observations of two coupled oceanic eddies of opposite sign - cyclone and unticyclone in Kuroshio region, are discussed.

INTRODUCTION

Recent studies show that many of the deep oceanic processes give rise to variations of sea surface microwave emission [1]. The sea surface brightness temperature can be changed by means of current influence onto the surface, for example, due to internal oceanic waves, or intensive hydro-physical finestructure of water medium, for example, frontal oceanic zones, synoptical rings, "relic rain" [1-3]. The latter processes are accompanied by spectral variations of brightness temperature at mm-wave frequencies. It is important to defer these microwave variations from those, caused by the surface and atmospheric factors such as wind stress, sea surface temperature, humidity and cloud liquid water.

Below we discus the experimental results of airborne observations of oceanic eddies at frequencies of 22, 37, 48 and 75 GHz. In the last-two are non-typical remote sensing frequencies. The correlation between brightness temperatures of two different frequencies is used to analyze the upwelling radiation of ocean-atmosphere system under influence of oceanic eddies and meteorological parameters of atmosphere. Various combinations of frequencies are investigated for both experimental and theoretical microwave data.

DESCRIPTION OF EXPERIMENT

The joint experiment on studying the Pacific subarctic frontal zone along the 149°E meridian from 34 to 45°N was carried out by research vessel "Academician Lavrentev" and research aircraft TU-134 on October 1990. The pattern of experiment is shown in Fig. 1. Airborne microwave mapping of the ocean surface was carried out by means of multispectral mm-wave imaging technique [4], on October 18, 20 and 21. The aircraft flight height was equal to 10 km. Multi-spectral microwave images of this region at frequencies of 22, 37 and 48 GHz (vertical polarization) and 75 GHz (horizontal polarization), obtained on October 20, are shown in Fig. 2. At the same time, the research vessel made the hydrological section along 149°E meridian. The depth distribution of water temperature of the upper ocean layer (0-300 m) is shown in Fig.3.

The unique oceanic phenomenon has been detected during this mission. This is a synoptical Kuroshio ring, consisting of two coupled oceanic eddies of opposite sign - cyclone and anticyclone (Rossby Soliton) [5]. Anticyclonic eddy was disposed near the surface, but cyclonic eddy was disposed at the depth more than 150 m (Fig. 3). It is significant that both eddies are clearly seen at microwave images (Fig. 2) and in addition the brightness temperature contrast due to the deep eddy much more than one, caused by the near surface eddy.

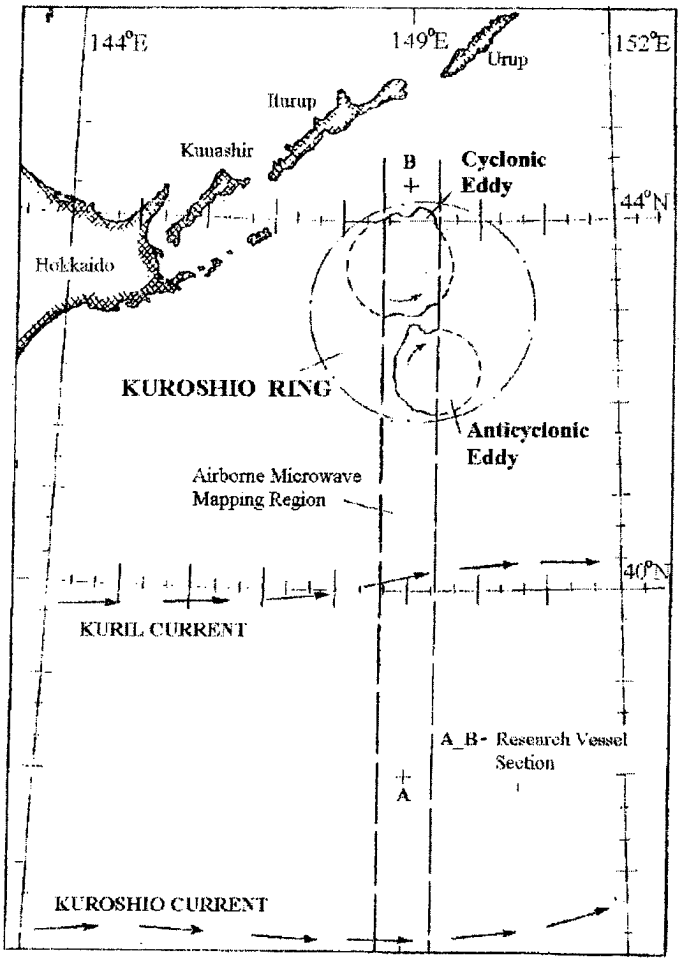


Figure 1. Pattern of experiment on joint studying of Kuroshio ring by aircraft and research vessel. The size and position of anticyclonic and cyclonic eddies are shown according to aircraft microwave data.

0-7803-3068-4/96$5.00©1996 IEEE

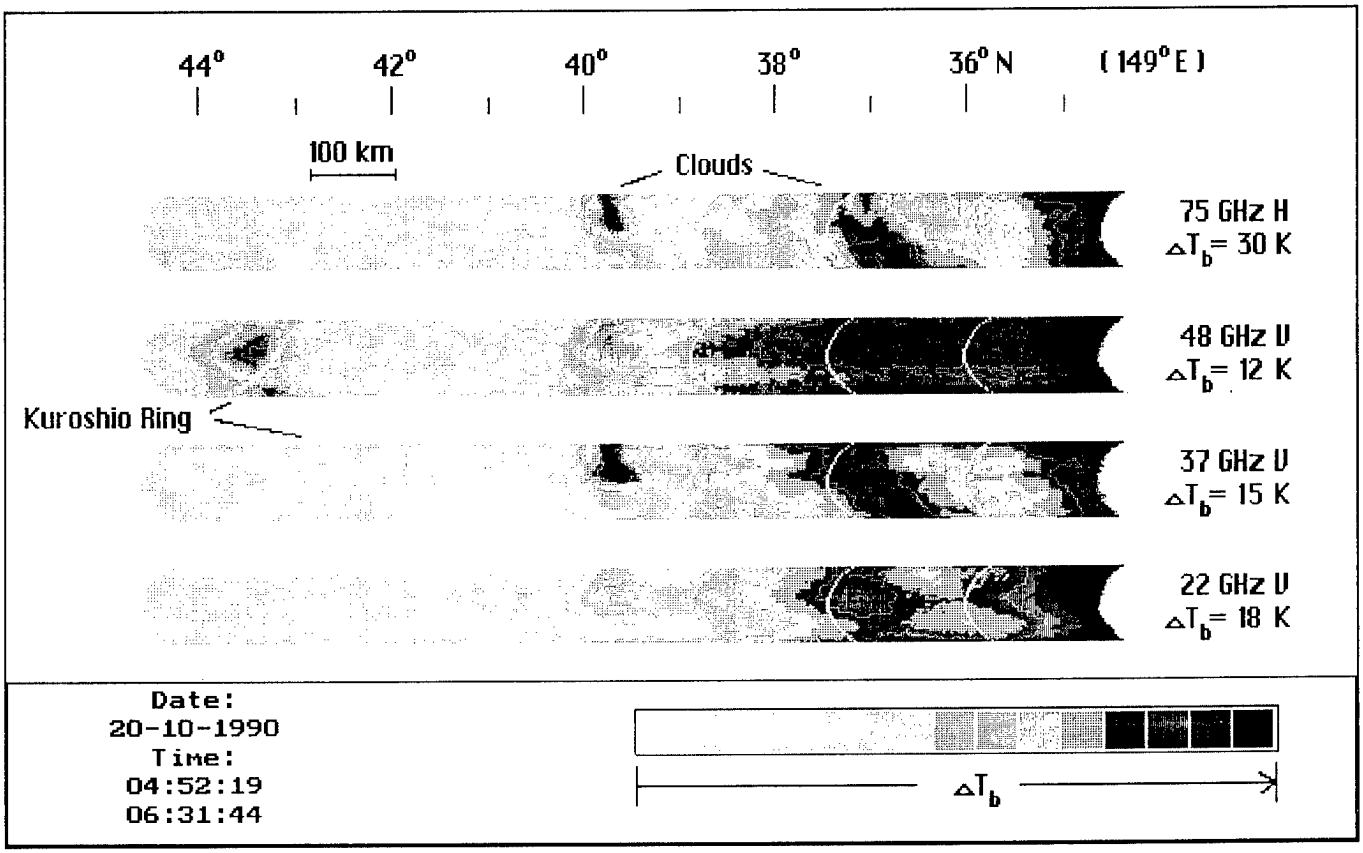


Figure 2. Multispectral microwave images of ocean surface along 149E meridian on October 20, 1990, by research aircraft TU-134. Kuroshio ring is seen at frequencies of 37 and 48 GHz only.

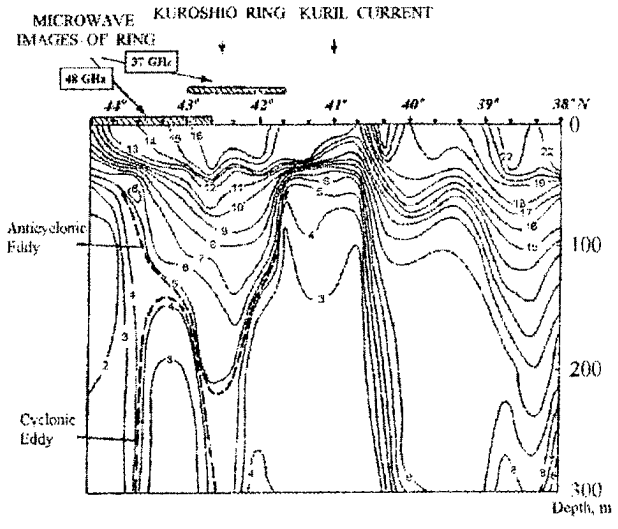


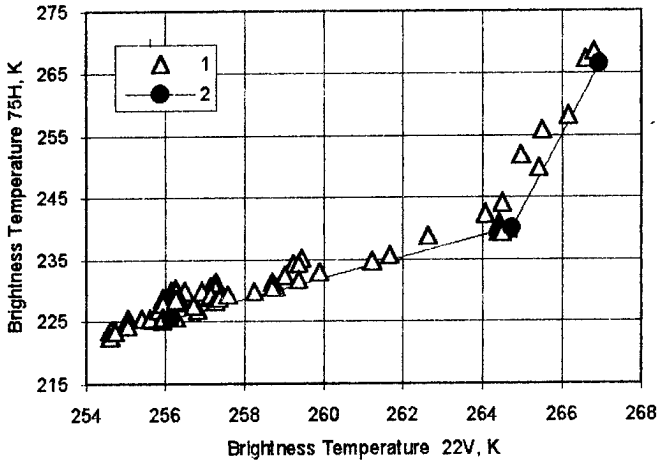
Figure 3. South-north temperature (in degrees Celsius) section along 149E meridian between October 16 and 18, 1990, by r/v "Academician Lavrentev". Microwave images of Kuroshio ring at frequencies of 37 and 48 GHz coincide with the position of anticyclonic and cyclonic eddies respectively.

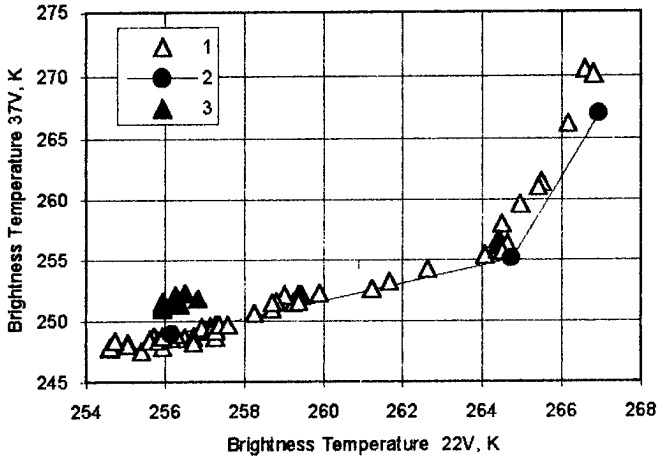
RESULTS AND DISCUSSION

The regression diagrams are used (see Fig.4) to analyze the brightness temperature variations in the region of Kuroshio ring shown in Fig. 2. Brightness temperature variations are due to both oceanic processes and variable meteorological parameters of atmosphere. Theoretical brightness temperature data (three points), based on in-situ shipboard measurements (see table 1), are also presented in Fig. 4. The calculations were made for viewing angle of 75° and flight height -10 km, using model described in [6].

A high correlation is demonstrated between brightness temperature variations for two channels combination of 22 and 75 GHz (Fig.4). In this case, the meteorological variables - humidity, cloud liquid water content, air and water surface temperature are mainly responsible for brightness temperature changes. The experimental and theoretical data are in a good agreement.

The similar high correlated relationship between brightness temperature variations also takes place in diagrams for both frequencies combination of 22 and 37 GHz, and 22 and 48GHz.





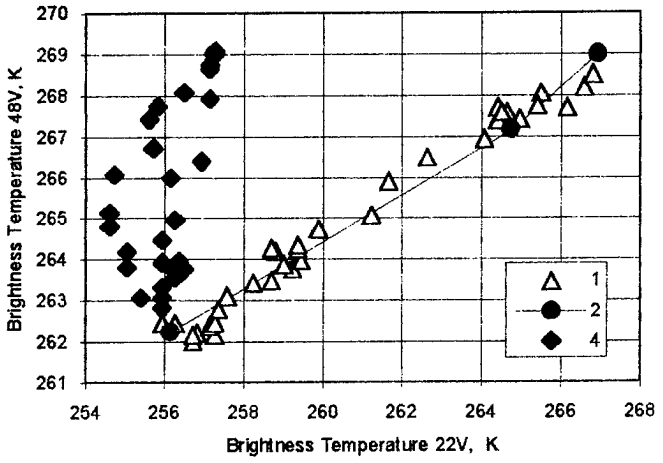


Figure 4. Regression between brightness temperature variations in the region of Kuroshio ring at frequencies of 22 GHz and 37, 48, 75 GHz according to Fig.2:
1 - brightness temperature variations due to meteoparameters;
2 - theoretical data;
3 - brightness temperature variations, due to anticyclonic eddy;
4 - brightness temperature variations, due to cyclonic addy.

Table 1.Meteorological parameters used for brightness temperature calculation.

parameter	point 1	point 2	point 3
sea surface temperature, °C	16	19	19
wind speed, m/s	10	11	11
temperature of air, °C	14.5	18	18
absolute humidity, g/m³	9.6	12.3	12.3
cloud liquid water, kg/m²	-	-	0.4

At the same time, there is absolutely non-correlation between brightness temperature variations due to oceanic eddies. This situation corresponds to the cyclonic eddy, when frequency of 48 GHz is used, and to unticyclonic eddy, when frequency of 37 GHz is used. The brightness temperature contrast at frequency of 48 GHz due to cyclonic eddy reaches 6-7 K and to be comparable with one caused by clouds system at that frequency.

On the other hand, as follows from regression diagrams, this spectral effect in upwelling microwave emission of ocean-atmosphere system can not be related to the atmosphere meteorological variables, as well as, sea surface temperature and wind stress. It is just the result of influence of the deep oceanic processes onto the surface, in particular, caused by synoptical eddies. It should be noted, this influence is most pronounced in channel of 48 GHz, which is non-typical remote sensing frequency. Therefore, to study appropriate class of oceanic processes, as mentioned above, it should be carried out the remote sensing of ocean surface in wide rang of mm-wave frequencies with sufficiently high spectral resolution.

REFERENCES

[1] V.Yu.Raizer and I.V.Cherny, Microwave Diagnostics of Ocean Surface, Gidrometeoizdat, Saint-Petersburg, 232p.,1994.

[2] G.Ya.Gus'kov, S.S.Moiseev and I.V.Cherny, Secondary Instabilities in the Ocean-Atmosphere System and Microwave Diagnostics of Natural Calamities, Preprint IKI RAN (Space Research Institute), N1762, Moscow, 34p.,1991.

[3] I.V.Cherny, The "Relic rain" Effect on Sea Surface Microwave Emission, Proceedings of IGARSS'92 Symposium, Houston, Texas, IEEE 92CH3041-1, Vol.I, pp.254-256, 1992.

[4] I.V.Cherny, A.M.Alesin, N.N.Gorobetz, V.P.Nakonechny, S.Yu.Pantzov, A.I.Zabishny, Advanced Airborne Multi-Spectral mm-Wave Imaging Technique for Ocean and Atmosphere Studies. Proceedings of CO-MEAS'95 Symposium, Atlanta, Georgia, April, 1995.

[5] V.M.Kamenkovich, M.N. Koshlyakov, and A.S. Monin, Synoptic Eddies in the Ocean, Gidrometeoizdat, Leningrad, 512p., 1987.

[6] I.V.Cherny, A.A.Pankin, S.Yu.Pantzov, Absolute in Flight Calibration of Airborne Multichannel MM-Wave Imaging Radiometer, Proceedings of IGARSS'96 Symposium, Lincoln, Nebraska, May, 1996.

Surface Wave Observation in the Gulf Stream Area Using ALMAZ-1 SAR

S.A.Grodsky[1], V.N.Kudryavtsev[1], A.Yu.Ivanov[2], V.V.Zaitsev[2], and D.M.Solov'ev[1]
1. Marine Hydrophysical Institute, Ukrainian Academy of Science, Kapitanskaya St.2, Sevastopol, 335000, Ukraine, e-mail: odmi@mhi2.sebastopol.ua, phone: +380-692-522118
2. NPO Mashinostroenia, Center ALMAZ, Gagarin St.33, Reutov, Moscow Region, 143952, Russia, e-mail: NPO@mashstroy.msk.su, phone: +7-095-307 9194, fax: +7-095-302 2001

Abstract -- Wave reflection by fair current was observed with ALMAZ SAR in the Gulf Stream frontal zone. Two-dimensional (2D) wave spectra calculated from radar image reveal substantial variability of wave directionality on different sides of the Gulf Stream. Wave spectra are analyzed in terms of wave kinematics. Model calculations are performed with surface current field reconstructed using the data of quasi-synchronous measurements from R/V AKADEMIK VERNADSKY.

INTRODUCTION

Wave-current interaction in the areas of non-uniform currents may cause substantial spatial variability of wave energy. Theoretical analysis predicts (see e.g.[1]) the most interesting effects: waves reflection by fair current, and wave-guide like behavior of the trapped waves. Trapped waves concentration within a jet may produce a hazard for shipping [2]. Experimental investigation of these phenomena is difficult because the data on wave parameters over a large area is needed.

Wave behavior on currents was investigated in a number of spaceborne Synthetic Aperture Radar (SAR) missions [3,4,5]. Unfortunately, these data were not supported by surface current measurements. Special observations of waves and current in the Gulf Stream area were performed by shipborne radar [6]. This paper presents data collected by Soviet ALMAZ-1 S-band SAR over the Gulf Stream frontal zone during the OKEAN-I Experiment. Spaceborne observations were supported by *in-situ* measurements from board of R/V AKADEMIK VERNADSKY.

RESULTS

Observation was carried out on August, 28, 1991 under westerly wind of W=10m/s. Fig.1 presents the scheme of the experiment which depicts NOAA sea surface temperature (Tw) map with ALMAZ-1 image overlaid. The Gulf Stream thermal interface is viewed in Fig.1 as a contrast line separating shelf waters (Tw=24° C, dark) and more warm Gulf Stream waters (Tw=28-29° C, light). Its position correlates well with area of surface current maximum. Radar

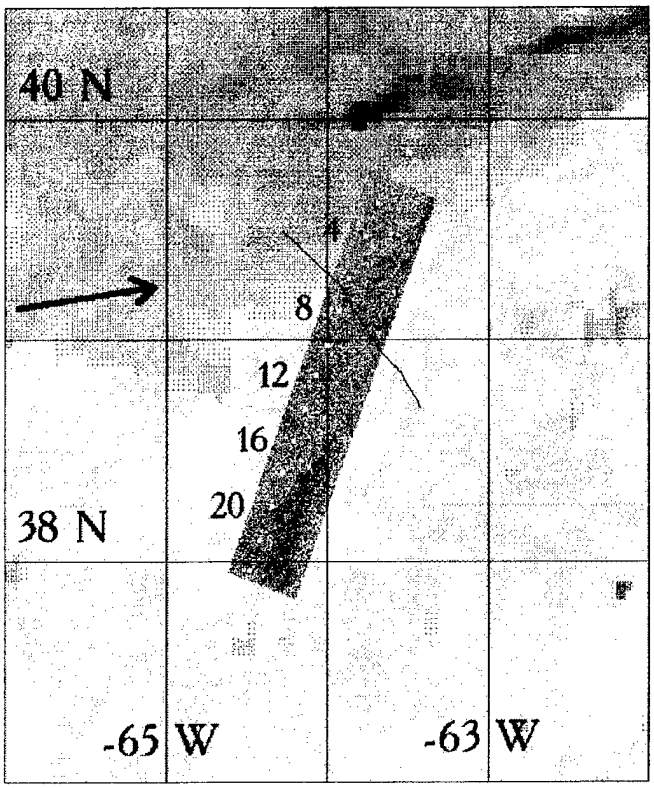


Figure 1. The scheme of the experiment Aug. 28, 1991. Presented are NOAA AVHRR sea surface temperature map (8:00 GMT, APT), ALMAZ image (12:16 GMT, Rev.#2396), and VERNADSKY run #16. White circles and digits mark locations and numbering of 2D radar spectra .The arrow shows wind direction.

image occupies both northern and southern sides of the Gulf Stream that allows investigation of wave variability induced by wave-current interaction.

Fig.2 presents a selection of 2D radar spectra to illustrate the main observed features of cross-current variability. The vertical axis in Fig.2 is directed to the north, the horizontal one - to the east. Spectra numbering corresponds to the numbers of radar images in Fig.1. The 180° uncertainty in wave direction has been eliminated from radar spectra using visual observations from the ship. Each spectrum was

This investigation was supported by the Fisheries Committe of Russia and the Grant UD9000 from the International Science Foundation.

0-7803-3068-4/96$5.00©1996 IEEE

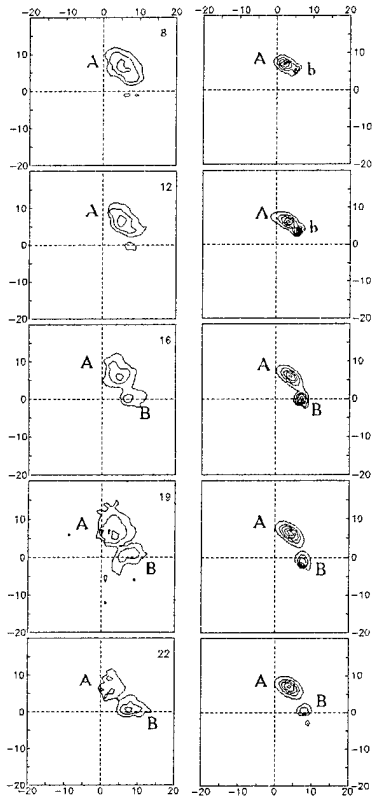


Figure 2. Selection of 2D wavenumber spectra. Left column presents radar spectra, right column shows model ones. Discreteness in wave number is 0.005 rad/m. Isolines are drawn in 20% of each spectrum maximum.

obtained through averaging over 9*9 km area and has 98 degrees of freedom.

The main characteristic of the data obtained is the apparent decrease of the spectrum angular width from the southern side of the current (the lower part of Fig.2) to the northern side. One can distinguish two local maxima A and B in radar spectra. On the Gulf Stream northern side the radar spectra have in general a one-peak structure (system A, see points 8-12). In the southern Gulf Stream side, the radar spectra have a wider angular width. In these spectra one may distinguish the local maximum corresponding to the system A and another local maximum (system B) in which the wave number vector deviates clockwise from that of system A. Both wave systems have wavelength of 150m. The dimensionless frequency of the spectral peak equals W/c_p =0.65 where $c_p = (g/k_p)^{0.5}$ is phase speed, i.e. these waves are swell.

Wave spectra partitioning described above is supported by wave rays calculation. Wave packet kinematics is described by the geometrical optics equations [7]:

$$d\boldsymbol{k}/dt = -\partial\Omega/\partial\boldsymbol{x} \qquad d\boldsymbol{x}/dt = \partial\Omega/\partial\boldsymbol{k} \qquad (1)$$

where $\boldsymbol{k}(t)$ is the wave number vector of the wave group, $\boldsymbol{x}(t)$ its location, $\Omega = \omega(k) + \boldsymbol{kU}$, $\omega(k) = (gk)^{0.5}$, $\boldsymbol{U}$ - is surface current. Surface current field was constructed using the measured cross current profile and thermal front configuration (see Fig.1). It was assumed that in any section normal to the temperature front the velocity profile corresponds to measured one and the current direction coincides with the front one. Fig.3 (top) shows wave rays calculations corresponding to homogenous wave field south off the jet with wave number corresponding to that of system A. Wave rays are the lines mapped out by $\boldsymbol{x}$. It is clear that

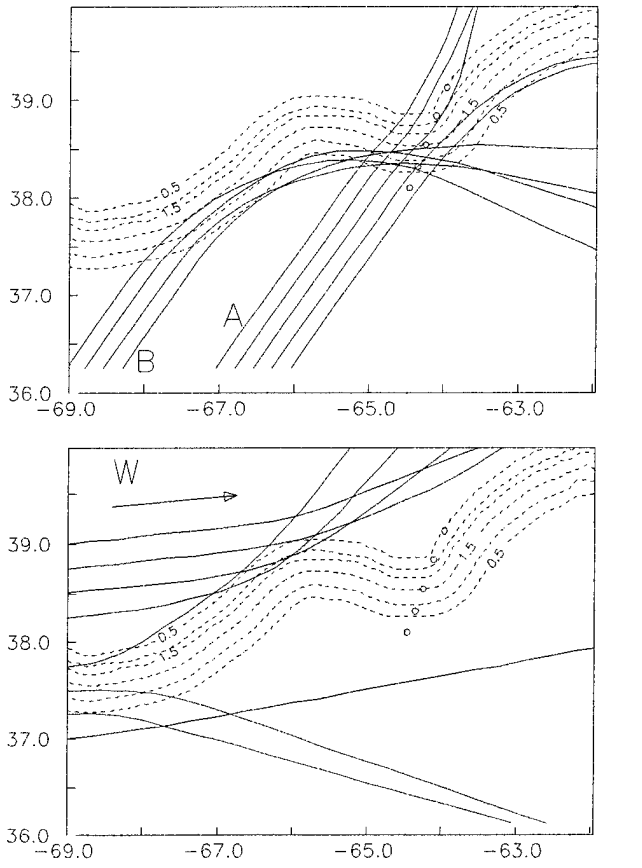


Figure 3. Reconstructed surface current field. The digits mark speed isolines in m/s. The top panel presents the wave trajectories calculated for wave systems A and B. The bottom panel shows the wave rays of wind wave system. The arrow marks wind direction. The open circles present the locations of radar image frames used to calculated 2D spectra presented in Fig.2

observed wave spectra (see Fig.2) can be explained by wave reflection from the Gulf Stream southern side. Wave reflection takes place west off the observed area where incidence angle of waves approaching the current is larger due to thermal front curving. Shear current influences uniform incident wave field significantly. The regions of focused wave rays are very likely to be seen locally as a dramatic increase in wave energy.

Fig.3 (bottom) presents also the wave rays for wind generated wave system. The area covered by radar image is located within "wave shadow" area produced by wave reflection. It explains the absence of wind wave maximum in radar spectra (Fig.2).

The character of wave rays field leads to the appropriate peculiarities in model wave spectra (see Fig.2). To calculate them we used simplified wave action equation with zero right hand side. It may be done as the observed waves are swell. The wave action equation in adiabatic approximation takes the form

$$dN/dt=0 \qquad (2)$$

where $N(\boldsymbol{k})=S(\boldsymbol{k})/\omega$ is the wave action, $S(\boldsymbol{k})$ is the wave number spectrum. Equation (2) describes the wave action variation along $\boldsymbol{k}(t)$ and $\boldsymbol{x}(t)$ curves being the solution of Equation 1. To initialize the calculations the background wave action spectrum (south off jet) was defined as 2D Gaussian function with wave number and angular width equal $0.1k_p$ and 10^o respectively.

Fig.2 presents the results of spectra calculations. Model spectra reflect quantitatively the main peculiarities of the observed wave field. On the southern side of the Gulf Stream model spectra posses two local maxima corresponding to observed wave systems *A* and *B*. The waves of system *B* do not penetrate on the northern side of the Gulf Stream that leads to a decrease in spectrum angular width.

RESUME

The effects of wave reflection by fair current was analyzed using the data from ALMAZ SAR. The same phenomenon was observed in [6] by shipborne radar under similar wave and wind conditions.

It is shown that complex wave field observed in the Gulf Stream frontal zone is a superposition of two wave systems: transmitting waves and reflected waves. It may be formed by a homogeneous wave field interacting with fair shear current.

Wave energy concentration in vicinity of current boundaries may produce a hazard for shipping due to both wave enhancement and substantial increase of spectrum angular width.

REFERENCES

[1] K.E. Kenyon., "Wave refraction in ocean currents", Deep-Sea Res.,18, 1971, pp.1023-1034.

[2] Ye.Sh.Gutshabash, and I.V.Lavrenov, "Swell transformation in the cape Agulhas current", Izv.Acad.Sci. USSR Atmos.Oceanic Phys.,Engl. Transl., 22(6), 1986, pp.494-497.

[3] R.C. Beal., T.W. Gerling, D.E. Irvine et al, "Spatial variations of ocean wave directional spectra from SEASAT SAR", J. Geophys. Res., 91(C2), 1986, pp.2433-2449.

[4] D.E.Irvine, "Extreme waves in the Agulhas a case study of wave-current interactions", Johns Hopkins APL Tech. Dig., 8(1), 1987, pp.100-106.

[5] T.P.Barnett., F. Kelley, and B. Holt, "Estimation of the two-dimensional ocean current shear field with a Synthetic aperture radar", J. Geophys. Res, 94(C11), 1989, pp.16.087-16.095.

[6] V.N.Kudryavtsev, S.A.Grodsky, V.A.Dulov, and A.N.Bolshakov, "Observations of wind waves in the Gulf Stream frontal zone", J.Ge .ph.Res., vol.100, C10, 1995, pp.20,715-20,728.

[7] G.B.Whitham, "A note on group velocity", J.Fluid Mech., 9, 1960, pp.347-352.

A Multisensoral Approach for Landuse Classifications and Grassland Monitoring Based on the Possibility Theory

Roswitha Stolz, Wolfram Mauser
Institute of Geography, Department of Geography and Geographical Remote Sensing
University of Munich
Luisenstr.37, D-80333 Munich
ph.:++49-89-5203-333, fax:++49-89-5203-321
e-mail:w.mauser@iggf.geo.uni-muenchen.de

Abstract — Accurate landuse classifications derived from remote sensing data are of great importance as input data for hydrological models. However, during the vegetation period often the problem occur that different landuses show similar spectral signatures. The investigations were carried out in the Bavarian alpine foreland, an area characterized by a complex landscape. In this area misclassifications mainly occur between grassland and cereals. To solve this problems a method was developed to incorporate ancillary geo-information in a maximum-likelihood classification procedure using an approach based on the possibility theory.

INTRODUCTION AND BACKGROUND

The landcover strongly influences the evaporation and is therefore an important element of the hydrological cycle. Particularily for calculating the runoff of a catchment using hydrological models, most accurate landcover data is of importance to model the evaporation. Due to this background highly differenced determination of landuse data of large areas is of need. Various publications proved remote sensing systems, especially such using MIR, suitable to provide the necessary landcover information. Since, the acquisition time has to be during the main vegetation period, to be able to distinguish between the different crops, as well as between arable land and different forms of grassland, the problem occurs that grassland and crops show similar spectral signatures. The use of multitemporal data increases the accuracy, but often not to the necessary extent. Another problem is, that the presently available operational optical sensor systems often acquire only one cloud free image per vegetation period in the investigated testsite. Therefore the aim of this work is to develope a method to combine only one remote sensing image with ancillary data to derive an accurate landuse classification suitable for hydrological modelling.
A further problem is the estimation of the water requirement of agricultural used areas from remote sensing data. For grains and corn methods are already developed to estimate the development of the plants from remote sensing data and according to a growth development model the water consumption can be estimated [3]. For grassland this estimation is much more difficult. Due to the fact that the growing height of meadows can not be derived from optical data, some preliminary investigations were done to check the capability of ERS-SAR data for this topic. Especially due to its weather independency the ERS could have the capacity to derive the different landuse structure and growth conditions of grassland.

TEST SITE

The testsite corresponds to the catchment of the Ammer river, which is located in the Bavarian alpine foreland. It covers an area of about 1250km. The terrain ranges in altitude from 500m in the basin of Lake Ammersee to 1700m at the alpine foothills. Due to this location the area shows a high climatic and geomorphological heterogeinity. It is characterized by intensive agricultural landuse. The landuse structure changes from the north to the south, due to a climatic and altitudinal gradient.

METHODOLOGY

In classifying LANDSAT-TM data the problem often occurs that during the vegetation period different landuse show similar spectral signatures. This problem runs through the complete vegetation period. For example, using the broad spectral bands of the TM, the spectral differences within grassland are higher than the differences between grassland and cereals or other crops. This is also true for rocks, open soil and developed areas. To solve these problems a method is developed to incorporate existing geographical knowledge into the classification process.
The Maximum Likelihood classifier (ML) is used as the basic algorithm in this possibility based approach, in which geographical knowledge and remote sensing data are used to produce a highly accurate landuse classification for a complex landscape. Growing conditions of plants are strongly based on climatic and soil consitions. However, the problem is that no sharp borders existing in nature. Growing conditions cannot be described in discrete numbers or with "Yes" or "No", but with linguistic predicates such as "often", "sometimes" etc. Applying possibility theory, these imprecise predicates are represented by fuzzy subsets and are quantified by possibilty and necessity numbers. The possibility theory is already used in different approaches e.g. artificial intelligence, because it is well suited to deal with uncertain knowledge. A fuzzy subset contains so called membership functions which define the grade of membership of an event (1 means it is "principally"possible, 0 means it is "never" possible).

0-7803-3068-4/96$5.00©1996 IEEE

However, the problem appears that ancillary data in common do not meet the condition of multivariate Gaussian distribution, as it is necessary for a ML classification. This can be solved by not including the ancillary data itself to the ML procedure, but the grades of membership of each class.
The expert knowledge is now used to define the influencing environmental conditions, the so called geofactors, in a testsite, as well as to define the grades of membership different landuse classes appear according to the geographical conditions. E.g. agricultural statistics as well as agronomic literature show as a general rule that the elevation of 800m is the limit for wheat production in the Bavarian alpine forelands. Nevertheless already below this 800m limit wheat production is reduced, as well as it is still possible to grow wheat at very favourable locations above 800 m. A closer look at the agricultural statistics shows that wheat production starts to decline at about 650m and that above 950m definitely no wheat can grow. Using this information, a spline function is chosen to connect the two critical elevations and to define a membership function, which is shown in *Fig.1.* For each landuse class and each geofactor a set of membership functions has to be set up to define the necessity numbers. A necessity number evaluates the degree of certainty of an event. If no rule or membership function can be defined, the membership grade of a class is set to "principally". For each class we now have an information source of the geofactors and the spectral information. If we want to combine these information sources, to define the most possible class a pixel belongs to, the rules of information fusion for the possibilty theory has to be considered. The fusion rules are described in literature [1,2,4,5].

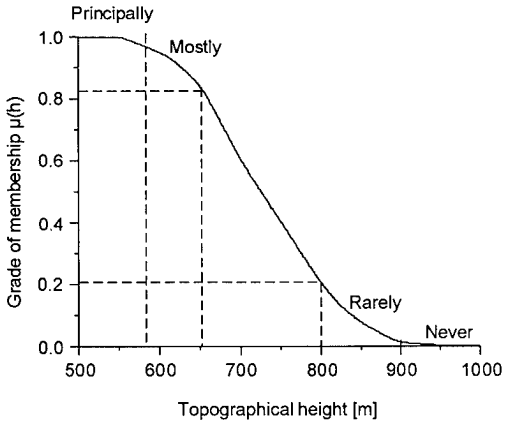


Fig. 1: The membership function of wheat displaying the dependency of the possibility of occurance vs. elevation.

The following classification procedure was implemented within the frame of the Institute for Geography 's image processing and GIS software:

1 in a first run the ML probabilities for the remote sensing data are calculated for each class using predefined training sites
2 The possibility measures of the defined classes for the remote sensing data were calculated by normalizing the probability measures
3 Applying a set of rules and membership functions the necessity/possibility measures for the predefined classes are deduced from the chosen geofactors.
4 Using the fusion rules (fuzzy operators) the possibility measures for each pixel are combined and the pixel is now assigned to the class showing the highest possibility.

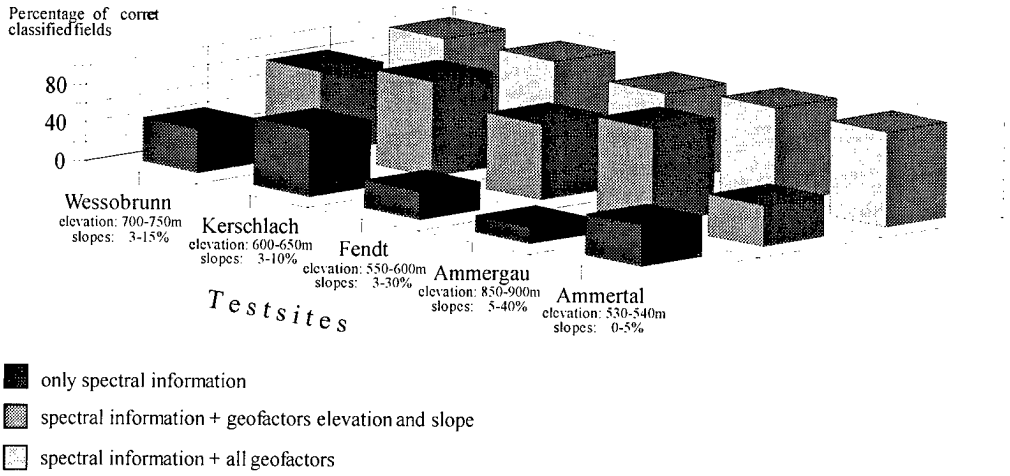
EVALUATION

The method was tested on a LANDSAT TM image of May 28 1992. A preprocessing has to be done. Since the testsite is partly located in rugged terrain, besides a reflection calibration an illumination compensation has to be carried out as well. No pixel displacement according to the height differences occurs, because the image section used is located at the scene nadir.
The distribution of landuse within any given region is determined by a set of environmental factors and plant physiology, which can be summarized as geographical context, and the human impact. In the testsite the influencing environmental factors (geofactors) are the topographical height, the slope, climate (precipitation, temperature, wind) and soil-physical properties. To determine these geofactors a GIS was established consisting of a terrain model and the Bavarian Agricultural Masterplan (ALP). Both data sources are available in digital format and form the full set of information necessary. All data layers were corregistered on the same resolution and a pixel size of 30m x 30m.
For the subsequent ML classification 45 training sites for 14 different classes, 8 of them agricultural landuse, were defined. Due to the season the different cereals had to be summarized to the groups spring- and summer-active cereals, because the different summer- /spring cereals do not show any differencies in their spectral signature and membership grades.
To evaluate the classification accuracy, the results were compared with ground truth data. For this purpose a digital ground truth map is available. To consider to what extent the possibility based integration of ancillary data increases the classification accuracy three classification proceedures were carried out:

1 Only the TM image was classified using the spectral information of the 6 reflective bands
2 Classification of the spectral information of the remote sensing data set, combined with the geofactors elevation and slope, derived from the digital terrain model.
3 Classification of the remote sensing data combined with all geofactors (elevation, slope and the geofactor soil-potentials, which is derived from the ALP.)

When only using TM-data misclassifications appear especially in the southern part of the testsite, at higher elevations, at steeper slopes and in the fen areas, where grassland is classified as cereals. This is due to the different plant communities, phenologies and landuse patterns. The integration of the geofactors topographical height and slope significantly improves the classification accuracies of grassland in areas above 700m without eliminating the scattered arable fields. But there still remain misclassifications in the intensively used agricultural parts of valleys. The additional consideration of the

Tab. 1: Comparision of the results of the different classification procedures for five selected control sites on a field basis



geofactor "soil-potentials" improves the classification accuracies decisively in these areas. To quantify the degree of improvement, randomly selected fields were analysed. The result is shown *in Tab.1.*

GRASSLAND MONITORING

If the evaporation of an area should be modelled, the knowledge about the exact landcover is only one factor. Besides the type of the vegetation cover and its spatial distribution, biomass and the biomass developement is of great importance. In the testsite grassland is the major agricultural landuse. Whereas for corn and cereals work already was done to determine the biomass using optical remote sensing data, the biomass of grassland cannot be determined using optical data. In this work a preliminary attempt should be shown, to determine the biomass of meadows from ERS-SAR data. The data used were acquired during the vegetation period 1992 and 1993. The investigations were carried out in the northern part of the testsite which corresponds to the flat valley of the Ammer river. This has the advantage that no radiometric distortions due to the relief occur. The data used are single-look-complex (SLC). They were calibrated and speckle filtered using an adaptive filter approach. This has two advantages. On one hand it reduces the noise caused by speckle and on the other hand it shifts the data distribution from a Rayleigh to a Gaussian distribution. Finally the SAR image was superimposed to the digital ground truth map, to derive the field boundaries. Using the field boundaries as a segment information, the mean backscatter value for each meadow can be calculated. During an intensive field campaign plant parameters, such as growth height, wet and dry biomass were measured for different meadows. The mean value of the fieldwise derived backscatter coefficient was now statistically compared to the measured plant parameters derived. As displayed in *Fig. 2* the backscatter coefficient shows a high correlation with the mean plant height of the meadows. Using this statistically relation, a "height distribution map" for the investigated area can be derived from the ERS-SLC radar data.

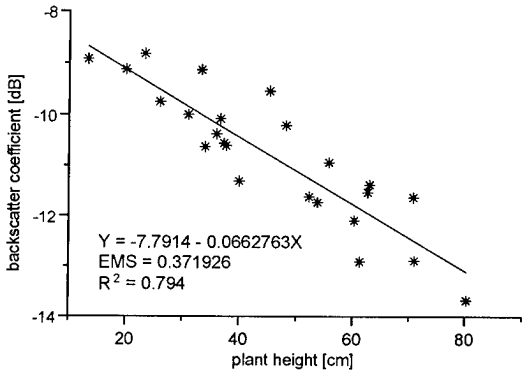


Fig. 2: Statistical comparison between the backscatter coefficient of ERS-SAR data and the mean plant height of meadows derived from five meadows during the years 1992 and 1993 (after: A.Demircan, unpublished ERS-1 research report).

REFERENCES

[1] L. Roux, J. Desachy, "Satellite Image Classification Based on Multisource Information Fusion with possibility theory", Proc. of IGARSS'94, Pasadena, pp. 885-887

[2] I. Leiss et al., "Improving Landuse Classification in Rugged Terrain Using Radiometric Correction and a Possibility Based Classification Approach", Proc. of IGARSS'95, Florence, pp. 1924-1926

[3] C. Conese, F..Maselli et al., " Statistical Integration of Ancillary Data into an Advanced Maximum Likelihood Classifier", Proc. Of ISPRS Symposium vol.30, part 3/1, Munich 1994

[4] Teubner Taschenbuch der Mathematik, vol.II, 1995

[5] F. Wang, "Integrating GIS's and Remote Sensing Image Analysis by Unifying Knowledge Representation Schemes. IEEE Trans.on Geoscience and R.S. 29 (4):656-664

[6] R. Schadt, J. Kellndorfer, W. Mauser, "Comparision of ERS-1 SLC and Landsat TM data for monitoring grassland and detecting changes in agricultural areas, Proc. 2.ERS-1 Symposium, Hamburg,1993,vol.1,p.75-78

Spectral Angle Mapper Classification and Vegetation indices Analysis for Winter Cover Monitoring Using JERS-1 OPS Data

Choen Kim[1] and Seonghoon Cho[2]
[1] Department of Forest Resources, Kookmin University, Seoul 136-702, KOREA
(t) +82.2.910.4813 (f) +82.2.910.4809 email : choenkim@kmu.kookmin.ac.kr
[2] Department of Forest Resources, University of Idaho, Moscow, ID 83844-1133
(t) +1.208.885.5612 (f) +1.208.885.6564 email : cho0000@novell.uidho.edu

Abstract -- Low solar elevations cause strong shadow effects in mountainous terrain. In order to examine the effect of bidirectional reflection on the reflected radiance response of the JERS-1 OPS bands, the NDVI and TVI were analyzed for differential shading. These geometric illumination conditions hinder accurate land use classification. This paper shows how the effects of differential shading on the classification of vegetation could be reduced through the use of the Spectral Angle Mapper(SAM) algorithm. This method proved better than layered classification logic or rule-based expert systems and fuzzy classification with nonparametric priors. The spectral angle mapper classification method produced seven land cover classes in the lower Nakdong River region : forest, urban, winter agricultural area, reed vegetation, barren(rock & sands), river(freshwater) and sea (salt water), and an unclassified category which indicated shadow areas in the mountainous forests.

INTRODUCTION

Until recently, the incorporation of ancillary data and fuzzy logic have been used for improving the classification accuracy of remotely sensed data. However, these methods are applied only to the specific information extraction, require a more complex hierarchical process than conventional supervised classification method, and are more expensive[1]-[3].

The Spectral Angle Mapper(SAM) method allows single-step matching of pixel spectra to reference spectra in n-dimensional spectral space. The effects of shadow on the final classification image can essentially be eliminated using this technique.

Moreover, this method can also be applied to discrimination of vegetated surfaces which reflect incident solar radiation anisotropically.

NASDA(National Space Development Agency) of Japan provided the JERS-1 OPS data, whose ownership belong to MITI(Ministry of International Trade and Industry)/NASDA. This work was financially supported by the Korea Science and Engineering Foundation under Contract KOSEF 941-1300-008-1 with the Kookmin University.

These considerations led to the initiation of a research project to determine if multispectral data acquired by the Japanese Earth Resource Satellite-1 Optical Sensor (JERS-1 OPS) could be used for classifying land-use and vegetative cover type in the lower Nakdong River region. It is anticipated that JERS-1 OPS data will provide information on regional land cover changes for environmental and ecological monitoring.

The objectives of this paper are :

1) To develop a winter land cover classification using the Visible and Near-Infrared (VNIR) bands of JERS-1 OPS.
2) To analyze the vegetation indices (NDVI and TVI) for geometric illumination conditions influenced by topography (slope, aspect and elevation) and shadows (solar elevation and azimuth angle).
3) To assess the accuracy of the SAM classification in comparison with the maximum likelihood method.

STUDY AREA AND DATA

The study area includes the western part of Pusan, and is situated at approximately 35° 12' North latitude, 128° 52' East longitude. It is approximately 8027 hectares in size. Within the area, the test sites which comprise the homogeneous forest canopies of mountainous Morundai (A) and the homogeneous hanging reeds near Shinho village (B) were specially selected for analysis of the bidirectional effects.

The dominant overstory tree species in site A is pine (*Pinus tunbergii* Parl.), and the understory trees are oaks (*Quercus acutissima* Carruth, *Quercus aliena* Bl. and *Quercus dentata* Thunb.). Site B is a typically flat region of reed vegetation (*Phragmites communis* Trim.) in the Nakdong River estuary , and is well-known as winter habitat for migratory birds. The area is divided into a steep mountain portion, a delta pain portion and a river and coastal sea portion. The last portion has the characteristics of upstream tidal currents and dispersion of the Nakdong River water.

JERS-1 OPS data for the study area were obtained on 26 December 1992, 11 : 23 A.M. with a solar elevation of 28.9° and a sun azimuth of 160.8°. The system correction which

0-7803-3068-4/96$5.00©1996 IEEE

has performed by RESTEC (Remote Sensing Technology Center) of Japan was made up to BSQ Level 2. The OPS VNIR sub-system has two bands in the visible region (band 1 : 0.52 - 0.60μm, band 2 : 0.63-0.69μm), and two bands in the near infrared region (band 3,4 : 0.76 - 0.86μm), including one for stereoscopic view (forward looking) with a ground resolution of 18.3m x 24.2m.

METHODOLOGY

A total of 137 sample polygons of mountainous forest were selected within the study area image for four different aspects : N(316° - 45°), E(46° - 135°), S(136° - 225°), W(226° - 315°). The digital numbers of three bands (green, red and near infrared) were measured for each of these polygons. In order to minimize the heterogeneity of the samples and to explore bidirectional effects on different canopy types resulting from vegetation and topography the normalized difference vegetation index (NDVI) and the transformed vegetation index (TVI) were investigated.

In this study the NDVI was calculated as (OPS 3 - OPS 2) / (OPS 3 + OPS 2) and the TVI was calculated as $[(\text{OPS 3} - \text{OPS 2}) / (\text{OPS 3} + \text{OPS 2}) + 0.5]^{1/2}$, where OPS 2 and OPS 3 are the DN values in OPS band 2 and 3 , respectively.

For most vegetated surfaces with variation in reflectance directionality the obtained vegetation indices were unable to discriminate the detailed classes for land cover when the change rates of vegetation indices against for different aspects were larger than the change rates of reflectance values for different aspects caused by the effect of shadows due to steep slopes and low solar elevation. The maximum-likelihood classification algorithm was also unable to classifying the mountainous areas accurately.

During the course of this study we found that the effects of shadows on the classification of TM images could be reduced through the SAM algorithm. The SAM algorithm determines the spectral signature similarity between the representative spectral mean DN values calculated from the training field pixels and the spectral DN values derived from each pixel in the image through the spectral angle differences (angluar distance in radians) between their vector directions in n-dimensional (band) space. A more detailed mathematical description of the algorithm, concepts and applications of the program are described in [7]-[9].

The OPS VNIR data were processed and analyzed using Environment for Visualizing Image (ENVI) software on a Sun sparc 10/51 workstation.

RESULTS AND DISCUSSION

The weighted mean values of the spectral digital numbers and vegetation indices for four slope orientations obtained through 137 sample polygons are given in Table 1. In the mountainous forests at a sun elevation of 28.9° and a sun azimuth of 160.8°, the spectral reflectance(DN) values decrease in the order of south, east, west and north. But the magnitude order of NDVI is neither consistent with that of TVI nor of the DNs, and the change rates of NDVI values for different directions are larger than those of TVI values.

These phenomena can be explained by the heterogeneity of the samples and the variation of bidirectional effects. Table 2 presents the variation of vegetation indices due to bidirectional effects in the homogeneous forest canopy structure of the mountainous site A when compared to the vegetation indices of reeds vegetation on the flat site B. Since the both VI values of site B are similar for all four reflected directions these normalized relationship methods can be used as a winter cover monitoring parameter on flat terrain, regardless of illumination under low sun elevation condition.

Due to the strong illumination variation in mountain area with steep slopes the obtained vegetation indices were also stratified by aspect against the four reflective directions. For water surfaces the VNIR data acquired by an off-nadir optical system with a Charge Coupled Device(CCD) are relatively insensitive to illumination effects.

Therefore, the spectral reflectance responses and derived vegetation indices could be used to estimate the quality of water, monitor the water pollution sources, and the turbid water induced by tide in Nakdong River estuary. With the limitation of flat water surfaces the supervised classification method using a maximum likelihood decision rule provided the best display of the location and movement of both freshwater and salt water. Because the classified pixels have

Table 1 : Weighted mean values of the spectral DN and VI influenced by bidirectional effects

Direction	Digital Number			Vegetation Index	
	Green	Red	IR	NDVI	TVI
North	47.9	39.7	50.9	0.107	0.776
South	60.0	60.4	79.4	0.173	0.797
East	55.7	52.4	73.5	0.156	0.808
West	51.0	45.7	53.1	0.058	0.744

Table 2 : Vegetation indices of four different directions in testsite A (mountainous forest) and in testsite B (flat reeds vegetation).

Direction	Site A (Morundai)		Site B (near Shinho)	
	NDVI	TVI	NDVI	TVI
North	0.049	0.741	-0.099	0.633
South	0.374	0.935	-0.101	0.631
East	0.291	0.889	-0.107	0.627
West	-0.211	0.538	-0.102	0.631

the highest probability, the resulting classes are sufficiently accurate for the mapping of the diffusion Nakdong River water into the coastal sea, and also its influences on the adjacent coastal environments.

Finally, a major advantage of SAM algorithm is that it is available for discriminating the given seven classes within shaded polygons by using as an additional parameter the measure of maximum acceptable angle between spectra vectors, because the decision rule of spectral angle depends only on the direction of the spectra, not their length[8]. The site-specific accuracy assessment that compared and ground truth data with a GIS supporting verification the results of SAM classification are presented in Table 3.

The identification of shadow areas(mainly termed unclassified) was accomplished through visual interpretation, and could be exactly displayed on the processed images.

CONCLUSION

1. The SAM method produced a more accurate land cover classification of areas with steep slopes, various aspects and low solar angles than conventional classification methods.
2. The spectral digital numbers and vegetation indices of mountainous forest areas were higher for aspects facing the sun than for aspects away from sun under low sun elevation condition.
3. The supervised classification of water surface was useful for monitoring changing water properties in esturaine and coastal areas.

Table 3 : Comparison of the SAM classification with GIS supported in-situ analysis in percentage of the classified of the classified pixels.

Class	N. of Pixels	Cover %	N. of Re.Sample	Cover %
Unclassified	111039	9.08	-	-
Forest	378379	18.87	39	28.06
Urban	81991	6.70	10	7.19
W.Agricul.	232493	19.01	16	11.51
Vinylhouse	-	-	8	5.75
Barren	6046	0.49	-	-
Reed Vegetation	54168	4.43	5	3.60
River	69881	5.71	5	3.60
Sand dune	-	-	1	0.72
Coast sea	436588	35.70	55	39.57
Total	1222940	100	139	100

REFERENCES

[1] Y. Wang and D. L. Civco. "Post-classification of misclassified pixels by evidential reasoning : A GIS approach for improving classification accuracy of remote sensing data," XVII ISPRS Congress, Washington D. C. Commission VII, vol. 2, pp. 80-86. August 1992.

[2] J. R. Jensen. Introductory Digital Image Processing : A remote sensing perspective, 2nd ed. Upper Saddle River, NJ : Prentice Hall. pp 240-247. 1996.

[3] F. Maselli, C. Conese, T. D. Filippis and S. Norcini. "Estimation of forest parameters through fuzzy classification of TM data," IEEE Trans. Geosci. Remote Sensing, vol. 33, pp 77-83. 1995.

[4] D. S. Kimes. "Dynamics of directional reflectance factor distribution for vegetation canopies," Appl. Opt., vol. 22, pp 1364-1372. 1983.

[5] S. Durrieu. "Correction of topographic effects affecting for stands by modeling consequences of variation in roof canopy structure on radiometry for high resolution satellite images," Proc. of IGARSS'95 Symposium, Firenze, pp. 315-319. 1995.

[6] N. P. Hanan, E.C. Brown de Colstoun and S. D. Prince. "Estimation of canopy photosynthetically active radiation (PAR) interaction using bidirectional aircraft reflectance measurements of the HAPEX-sahel bush-fallow subsite," Proc. of IGARSS'95 Symposium, Firenze, pp. 1299-1301. 1995.

[7] Center for the Study of Earth from Space, SIPS User's guide. The Spectral Image Processing System, vol. 1.1. University of Colorado : Boulder. 1992.

[8] Research Systems, Inc., ENVI Version 2.0 Tutorial. October 1995 ed., pp. 41-47.

[9] R. H. Yuhas and A. F. H. Goetz. 1993. "Comparision of airborne (AVIRIS) and spaceborne (TM) imagery data for discriminating among semi-arid landscape endmembers," Proc. of Ninth Thematic Conference on Geologic Remote Sensing, Pasadena. pp. 503-511. February 1993.

SIR-C Polarimetric Backscatter Features of Agricultural Land Cover Types Early During the Growing Season

M. J. W. Davidson[1], R. Steingießer[1],W. Kühbauch[1], F. Vescovi[2] and F. Tano[2]

[1]Institut für Pflanzenbau, Katzenburgweg 5
University of Bonn, D-53115, Bonn, Germany
T: (49-228) 732871, F: (49-228) 732870, Email: ulp107@ibm.rhrz.uni-bonn.de

[2]Istituto di Agronomia, Via Celoria 2
Università degli Studi di Milano, I-20133, Milan, Italy

Abstract -- This study focuses on the polarimetric radar backscatter responses observed for different agricultural land cover types early during the growing season, in two well-separated test sites. These were Oltrepo Pavese in northern Italy and Oberpfaffenhofen in southern Germany. Results show that L-band was better at discriminating between agricultural land cover types than C-band. However effects due to soil roughness and those due to vegetation in the fields were difficult to separate using only backscatter amplitude information. Polarimetric information expressed through the HH-VV correlation coefficients and as polarimetric signatures however, provided additional information on the backscatter mechanisms for various land cover types and allowed for the separation of vegetation and soil effects.

Introduction

The polarimetric backscatter characteristics for agricultural land cover types are of interest because they provide clues on the interactions mechanisms between emitted electro-magnetic waves and the vegetation and soil layers within the fields. Differences in backscatter as a function of transmit-receive polarisations and wavelength provide information on the structure of the vegetation canopy, and serve as the basis for the mapping of crop and land use types as well as crop status over large areas.

A number of recently published studies have dealt with the polarimetric backscatter characteristics for agricultural fields as a function of crop type and crop status late during the growing season, when crops such as potatoes, corn and sugarbeet have well defined structural features. However little has been published on the polarimetric features of agricultural fields very early during the growing season.

Table 1: Main agroclimatological characteristics of the German and Italian test sites investigated during the April 1994 shuttle mission.

Test Site	Oberpfaffenhofen	Oltrepo Pavese
Latitude	48 °	45 °
Height	529 m	147 m
Climate	humid	humid
Avg.temp	8 °C	13 °C
Avg. rainfall	922 mm	997 mm
Growing Season	160 days	230 days
Main crops	wheat, barley	wheat, rice, corn
N° test fields	11	6

Ground Truth and Image Data Processing

In this study we make use of two full-polarimetric images, at L- and C-band, acquired by the SIR-C instrument over our test sites in northern Italy (Oltrepo Pavese) and southern Germany (Oberpfaffenhofen) during the April 1994 SIR-C/X-SAR shuttle mission. Both images were acquired with roughly the same incidence angle - 23° and 27° respectively. During the mission a detailed map of crop types found in both areas was compiled and digitised. Furthermore within each test site a number of fields containing winter barley were selected and parameters such as biomass, dry mass, leaf area index and soil humidity and roughness were determined for these fields simultaneously to shuttle passes over the test site. The longer growing season in Italy meant that similar crops, e.g. winter cereals, were more developed in Italy than in Germany. Table 1 summarises some of the main parameters for each test site. The main land cover types in Oberpfaffenhofen were barley, wheat, rapeseed, seedbed (smooth) and ploughed (rough) bare soil fields. In Oltrepo Pavese the main agricultural categories were winter cereals (mostly wheat with some barley), seedbed and ploughed fields as well as poplar tree nurseries.

Using the digital crop maps it was possible to extract an average complex scattering matrix $\overline{S}$ for each field. These were then further averaged to yield a single scattering matrix for each crop type.

Assuming reciprocity between HV and VH polarisations and no average correlation between cross-polarisation and like-polarisation channels for natural targets [1], the information on the backscatter phases and amplitudes for any target can then be described using only four variables: the backscattered power at HH, VV and HV polarisations (σ_{HH}, σ_{VV}, σ_{HV}) and the complex correlation coefficient between HH and VV polarisations ρ. The extra information due to the recording of the relative phases between polarisations is therefore embedded in a single complex number ρ. The average backscatter characteristics for all important crop types in both test sites are summarised in Table 2.

Amplitude Features

In both test sites the dynamic range in backscatter amplitudes between various land cover types was much higher in L band than in C band. Thus L band amplitude images are more suitable for mapping different land cover types at this early

0-7803-3068-4/96$5.00©1996 IEEE

Table 2: Backscatter characteristics for the main crop types (minimum of 15 fields) found in each test site. All backscatter amplitudes are in dB. The phase of the HH-VV correlation coefficient is given in degrees. δ represents the dynamic range in backscatter coefficients for each parameter.

Oberpfaffenhofen										
	C Band (5 cm)					L band (23 cm)				
Land Cover	σ_{HH}	σ_{HH}	σ_{HV}	$\lvert\rho\rvert$	ϕ_ρ	σ_{HH}	σ_{VV}	σ_{HV}	$\lvert\rho\rvert$	ϕ_ρ
Barley	-5.6	-6.8	-15.5	0.68	18.5	-17.1	-16.7	-27.5	0.61	12.9
Wheat	-2.7	-3.2	-13.7	0.80	15.9	-13.1	-11.3	-26.2	0.86	5.9
Seedbed	-4.5	-4.7	-18.0	0.88	12.8	-18.1	-17.2	-29.7	0.76	2.4
Ploughed	-3.7	-4.4	-15.3	0.82	8.6	-9.4	-8.4	-21.8	0.87	5.1
Rapeseed	-5.0	-5.6	-13.4	0.67	8.4	-9.4	-10.8	-20.2	0.61	3.7
δ	2.9	3.6	4.6	0.21	10.1	8.7	8.8	7.3	0.25	10.5
Oltrepo Pavese										
Cereals	-11.2	-12.4	-18.9	0.41	15.8	-17.3	-18.0	-28.9	0.46	26.0
Seedbed	-11.5	-11.1	-22.3	0.79	5.6	-19.4	-18.9	-30.6	0.74	11.6
Ploughed	-9.4	-9.1	-18.9	0.73	5.6	-14.3	-13.9	-25.7	0.79	11.8
Poplar Trees	-7.6	-7.7	-12.8	0.28	4.9	-7.1	-8.8	-14.7	0.12	58.1
δ	3.9	4.7	3.4	0.51	10.9	12.3	10.1	15.9	0.67	46.5

stage during the growing season than C band images. The standard deviations in the backscatter means (i.e.: the within category variance) are of the order of 2 dB for classes, meaning that a number of land cover types are indistinguishable or barely distinguishable if only backscatter amplitudes are considered. In general seedbed and ploughed fields can be well distinguished one from another with L band. However roughness-like effects caused by higher within-field vegetation levels, such as for rapeseed fields in Oberpfaffenhofen and winter cereal fields in Oltrepo Pavese, are difficult to distinguish from those due to rough soil conditions. The observed differences in backscatter between barley and wheat fields in Oberpfaffenhofen were found to be due to different soil preparation techniques in that area for these two crops. These leave the soil texture beneath winter wheat in a rougher state than in barley fields. Thus the L band co-polar backscatter amplitudes observed for winter wheat are actually responding to an intermediate soil roughness category lying between that of barley (and seedbed) and ploughed fields. While there is less contrast between land cover types in C band images than in L band images, C-HV images appear to be useful for separating the smooth seedbed surfaces from other categories.

In general however backscatter amplitudes for similar categories do not translate well from one test site to the next. This is likely due to the different agronomic conditions and agricultural management practices associated with each test sites as well as the north-south gradient in development stages for identical crop types such as winter cereals.

Polarimetric features

Added information on land cover type as well as the interaction mechanisms between radar waves and agricultural categories can be found in the HH-VV correlation coefficient. In this case, as was noted in a previous study by Matthaeis et al. [2], the HH-VV correlation coefficients appears to provide a way to distinguish between three basic scattering mechanisms that can take place within the agricultural fields

1. surface scattering from the soil strata (seedbed, ploughed, wheat). Models such as the small-perturbation model predict relatively high values. Here HH-VV correlation magnitudes $\lvert\rho\rvert$ lie between 0.7 and 0.9.
2. surface scattering along with volume scattering within the vegetation canopy (barley, rapeseed, winter cereals in Oltrepo Pavese). These have lower $\lvert\rho\rvert$ values ranging from 0.4 to 0.7 depending the amount of vegetation present within the field.
3. volume scattering (poplar). These have relatively low $\lvert\rho\rvert$ values, less than 0.2 in this case.

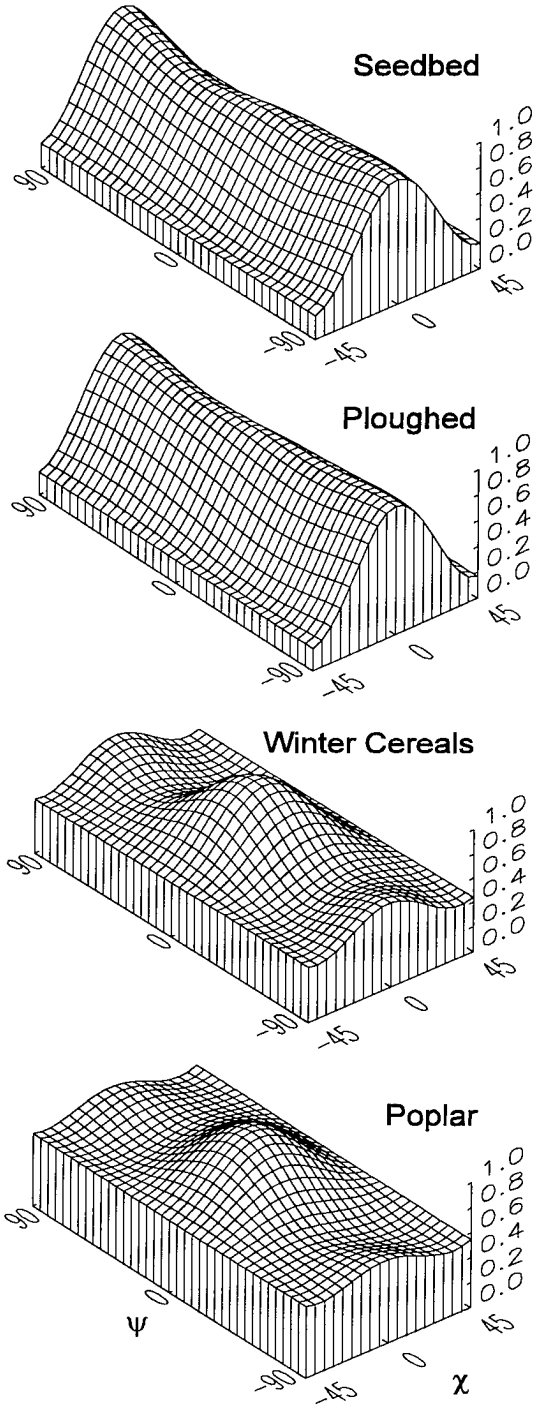
This grouping into backscatter classes appears to hold both test sites. The phase of the HH-VV correlation coefficient on the other hand is only significant for poplar trees, where a double-bounce scattering mechanism can take place between the tree trunks and the soil. These fields have an average ϕ of 58°.

Another unique aspect to polarimetric radar is that a knowledge of the scattering matrix $\overline{S}$ of a target, in this case a particular agricultural land cover type, makes it possible to synthesise backscatter values for all possible transmit-receive polarisation configurations. These are usually plotted as response surfaces with the transmit and receive polarisation states defined by their ellipticity and orientation angles [3].

The L-band co-polar signatures for Oltrepo Pavese winter cereal, seedbed, ploughed and poplar fields (see Fig. 1) also help identify the main backscattering mechanisms and provided additional information on the backscatter amplitudes as a function of polarisation.

Both bare soil categories exhibit remarkably similar signatures although their backscatter magnitudes often differ by up to 9 dB. The returns from both types of bare soil fields are highly polarised due to the surface scattering interaction with the incoming radar waves. This is seen in the large variations in backscatter magnitude as a function of polarisation. The returns from bare soil fields can be

Fig. 1: Co-polar polarimetric signatures representing the synthesised backscatter response from Oltrepo Pavese seedbed, ploughed and cereal agricultural land cover types.



minimised by using circular polarisations ($\chi = \pm 45$) for instance. Also both soil categories have VV returns ($\chi = 0, \psi = \pm 90$) which are slightly higher than HH returns ($\chi = 0, \psi = 0$), as predicted by the small perturbation model.

The signatures for winter cereal fields and poplar trees however are quite different and are characterised by fairly large unpolarised components. This is evident by the smaller range between maximum and minimum backscatter values at all polarisations. This pedestal (i.e. minimum backscatter level at all polarisations) is typical of multiple scattering within vegetation causing the incident signal to lose it's polarisation. It is also caused by inhomogeneities in the backscattering mechanisms within a single land cover type [4], so that through the pixel averaging process no dominant scattering mechanism emerges and the computed response as a function of polarisation remains relatively flat.

Other difference between bare soil and vegetation signatures is the change in HH/VV ratio as a function of above ground biomass. This is especially evident in the winter cereals signature, where the higher interaction coefficient of HH signals with above-ground vegetation lead to a remarkable peak in backscatter at HH polarisation ($\chi = 0, \psi = 0$). Barley fields in Oberpfaffenhofen had much smaller peaks at this polarisation due to the lower biomass levels within the fields there.

Conclusions

This study has shown that L band images show a higher contrast between agricultural land cover types early during the growing season in both test sites than C band images. However backscatter amplitudes for similar agricultural categories do not translate well from due to different agronomic conditions within each test site.

However polarimetric information expressed through the HH-VV correlation coefficient and as well as polarimetric signatures can be used to classify various land cover types in both test sites by their interaction mechanism with incoming radar waves. Also evident in the polarimetric signatures of bare soil fields was the high degree of polarisation and HH/VV ratios less than one. Fields containing vegetation exhibited higher unpolarised components due to multiple scattering in the vegetation canopy and HH/VV ratios greater than 1.

Acknowledgements

This study was made possible through a grant from the German Space Agency, DARA.

References

[1] M. Borgeaud, S.V. Nghiem, R.T. Shin and J.A. Kong, "Theoretical models for polarimetric remote sensing of earth terrain", Journal of Electromagnetic Waves and Applications, vol. 3, 1987, pp. 67-86.

[2] P. de Matthaeis, G. Schiavon and D. Solimini, "Effect of scattering mechanisms on polarimetric features of crops and trees", Int. J. Remote Sensing, vol. 15, no. 14, 1994, pp. 2917-2930.

[3] J. van Zyl, H. Zebker and C. Elachi, "Imaging radar polarisation signatures: theory and observation", Radio Science, vol. 22,no. 4,1987, pp. 529-543.

[4] D. Evans, T. Farr, J. van Zyl and H. Zebker, "Radar Polarimetry: Analysis Tools and Applications", IEEE Transactions on Geoscience and Remote Sensing, vol. 26, no. 6, 1988, pp. 774-789.

Use of ERS-1 SAR data for ricefield mapping and rice crop parameters retrieval

Florence Ribbes, Thuy Le Toan
CESBIO - CNES/CNRS/Université Paul Sabatier, Toulouse, France
bpi 2801, 18 Avenue Edouard Belin, 31055 Toulouse Cedex
Tél : (33) 61 55 85 12 Fax : (33) 61 55 85 00
E-mail : ribbes@cesbio.cnes.fr

ABSTRACT

The objective of the paper is to assess the use of ERS-1 SAR data for identification of rice growing areas and monitoring of rice growth. The approach includes an examination of experimental results obtained at two geographical locations where rice growth conditions are different : short cycle tropical rice in Indonesia and long cycle temperate rice in Japan. The experimental data show a comparable temporal increase of the radar backscatter at both sites. An algorithm has been developed for rice field mapping and for retrieving of rice crop parameters.

1- INTRODUCTION

Since the launch of the European ERS-1 satellite, a number of pilot projects undertaken in Japan [1], in Thailand [2] and in Indonesia [3], showed the usefulness of radar satellite data for rice monitoring. These studies underlined also the need to further investigate the capabilities of SAR data for operational rice monitoring at a diversity or rice growing regions.

The objective of this paper is to make a synthesis of experimental observations at 2 different geographic locations and to interpret the results in order to develop a robust algorithm for mapping rice growing areas and retrieving of rice crop parameters.

2 - EXPERIMENTAL RESULTS

2-1 The experimental data

The experimental data have been provided by projects conducted in the past 3 years to investigate the use of ERS-1 SAR data for rice monitoring. The first data set comes from the SARI project (Satellite Assessment of Rice in Indonesia) which has been conducted in 1994 in Indonesia at the Semarang test-site [4]. The second data set is provided by a rice crop monitoring experiment carried out in 1992 and 1993 at the Akita test-site in Japan [1].

2-2 Ground data synthesis

The ground data collected at the two sites have been compared. Different rice parameters have been analysed as a function of the plant age (number of days after sowing).

Fig. 1 presents the temporal variation of the plant height. The general increasing trend is observed for the two data sets until the end of the reproductive stage, then remains stable (0.90 - 1m for both data sets). More dispersion in the data points are observed at

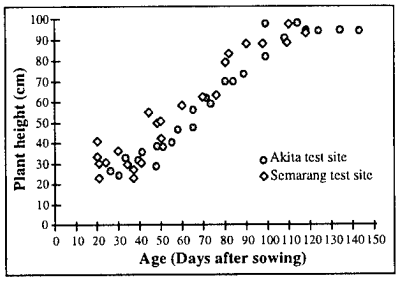


Fig. 1 : Temporal variation of the plant height

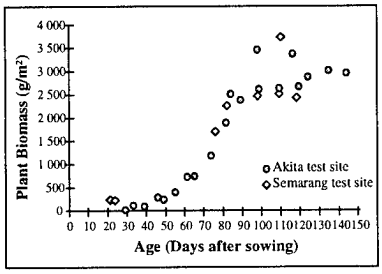


Fig. 2 : Temporal varaition of the plant biomass

Semarang, where sampled field have been selected within a large agricultural region, compared to the Akita data set measured at an experimental site. The data dispersion is due to various causes including the sampling procedure, the within field variability, the uncertainty related to the estimated plant age when transplanting, and the inter-field variability due to rice variety and cultural practices.

The plant fresh weight (or biomass) (fig. 2) shows also an increase until the reproductive phase. The maximum biomass values present some dispersion due to rice variety and cultural practices and also to climatic conditions.

2-3 Analysis of ERS-1 data

The ERS-1 satellite provides SAR images at C band, VV polarisation and 23° incident angle. The data are 3 looked PRI images with pixel sizes of 12.5 m in azimuth and range directions.

The backscattering coefficient σ° have been extracted from test fields. For the two data sets, the uncertainty associated to σ° for a given field can be estimated to be ± 1 dB. σ° increases as a function of rice parameters (plant age, height and biomass) (fig. 3 to 5) until the reproductive phase is reached for both data sets.

0-7803-3068-4/96$5.00©1996 IEEE

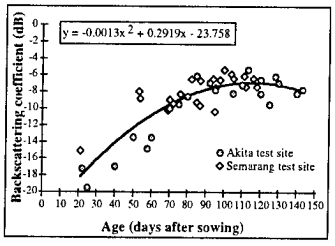


Fig. 3 : Temporal variation the radar backscatter

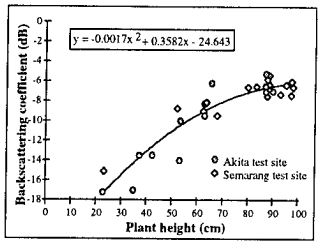


Fig. 4 : Variation of the σ° with the Plant height

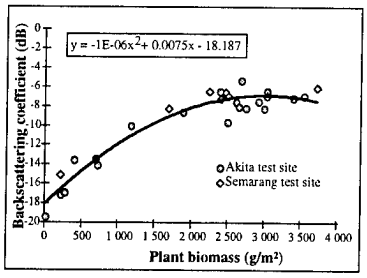


Fig. 5 :Variation of the σ° with the Plant biomass

At the beginning of the cycle, flooded fields provide very low backscatter (-15 to -20 dB). At the end of the reproductive phase, σ° values reach -8 dB to -6 dB and remain stable. Fig. 3 shows a large dispersion between the 2 data sets at the first part of the cycle. This can be explained by the duration of the vegetative phase - thus the plant development - which differs from one site to the other. The dispersion is reduced when σ° is expressed as a function of the plant height (fig. 4) and the two data sets appear to follow the same law when expressed in terms of biomass (fig. 5). These observations have been interpreted by a theoretical model which indicates that the dominant backscattering interaction mechanism is the multiple vegetation-water scattering [3]. This scattering component increases as a function of the plant above water biomass.

2-4 Spatial variation of the radar backscatter

Due to the strong temporal variation of the σ° of rice fields during the vegetative stage, a shift in the crop calendar of different fields can produce a large variation in their radar backscatter. A delay of 6-8 weeks between early and late transplanting dates is relatively common in regions such as the flood-plains in Java, whereas at higher latitude, a 2 week delay is usual.

Using the experimental curve of the σ° *vs.* age, it is possible to simulate the radar responses of early crop and late crop present in a given site. Fig. 6 presents the simulated rice crop succession at the Semarang test-site for fields transplanted mid November (solid line) and that of fields transplanted early January (dashed line).

At the first 3 ERS-1 acquisition dates, the early crops are at the end of the cycle corresponding to a σ° that does not vary. Meantime, the late crops have a σ° that can increase as much as 6 dB between January 23 and February 16. Between the 16/02/94 and the 06/03/94, the early crops have been harvested and thus their backscattering coefficient drops whereas it goes on increasing for the late crops.

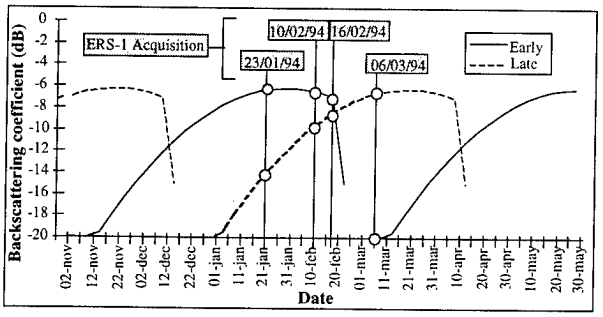


Fig. 6 : Rice crop succession simulation

Considering one cycle, it is possible to determine, from the experimental curve of the σ° *vs.* age (fig. 3), the σ° variation of a given field between 2 ERS standard acquisitions (35 days). Knowing the crop calendar of a given region, it is possible to determine the optimum ERS acquisition dates in order to have a maximum of temporal variation of σ°, which can be used to characterise rice fields.

4 - RICE FIELD MAPPING

The above observations show that rice fields can present a large variation in their temporal and spatial radar responses. The standard classification methods, based on given spectral responses of cover types at a given time will not be appropriate.

One possibility is to use the temporal curves of the radar backscatter as classifier. However, with the ERS-1 (and ERS-2) multi-disciplinary cycle (every 35 days) only few data points could be acquired during a rice crop cycle (maximum 3). An alternative is to use the temporal change between any pairs of data acquired during the crop cycle or between the end of one cycle and the beginning of the following cycle.

An algorithm was developed, based on the use of the backscatter temporal change. The mapping results which will be presented concern the Semarang test-site. First, speckle filtering was applied on the different ERS-1 scenes, followed by the computation of a temporal change index which is the ratio between the mean backscatter intensity related to the surfaces of interest. A segmentation based on thresholding the change index image will provide a rice/non rice map.

Filtering : The filters to be selected must reduce the speckle effect significantly, while providing relatively less damage in the spatial resolution and preserving fine structure. The filter used is a multi temporal filter [5].

Temporal Change Index : Differencing and ratioing are well-known techniques for change detection. Ratioing of the multidate radar intensities is shown to be better adapted to the statistical characteristics of SAR data. However, the ratio is very sensitive to the speckle noise. For instance, to detect changes in radar intensity less than 1 dB with a confident interval better than 80 %, the effective number of looks (ENL) must be > 128 [6]. For rice fields, where expected change is of 3 dB and more, the speckle reduction can be less drastical (ENL=64 for a confident interval of 90 %).

Fig. 12 and 13 show respectively an example of ratioed image and the resulting rice/non rice segmentation.

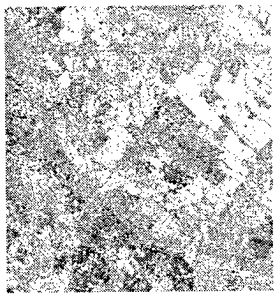


Fig. 12 : Change Index image



Fig. 13 : □ Rice/■ Non rice mask

Rice/Non rice Segmentation : The principle is to threshold the ratio image to identify pixels that change by more than ± x dB. Selecting threshold values depends on the nature and magnitude of the expected changes. For rice fields, a general threshold can be determined if optimum SAR data acquisition is guaranteed. Otherwise, the threshold must be optimised given the data acquisition and local crop calendar constraints. At the Semarang test-site and for the available SAR data, a threshold of 3 dB has been used. A binary image is then obtained (fig. 13).

5 - RICE GROWTH MONITORING

Using the inversion of the relation between the σ° and the rice height or biomass it was possible to realise a map of the rice fields at different heights and different levels of biomass. A segmentation is realised on the height images so as to separate the rice fields that still are at the vegetative stage and the rice fields at the end of the cycle (reproductive stage). The beginning of the reproductive cycle appears when the plant is around 80 cm height. Fig. 16 shows the results obtained : in white and grey rice fields respectively smaller (vegetative stage) and higher (reproductive stage) than 80 cm.



Fig. 16a : 23/01/94

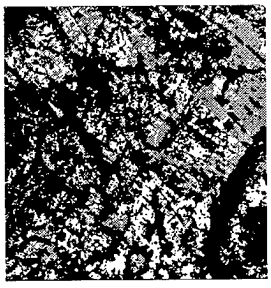


Fig. 16b : 10/02/94



Fig. 16c : 16/02/94



Fig. 16d : 06/03/94

Fig.16 : Maps of Height classes (■ < 80 cm □ > 80 cm)

The result permits to follow the evolution of the different rice fields (late and early) which have distinct growing cycles. Similar maps have been realised for the biomass classes.

The results concerning rice growing areas are currently evaluated. Nevertheless, the results already show good agreement with existing SPOT image of May 1994 particularly concerning the early rice fields that are again at the end of the cycle in May and thus are well detected on the SPOT image. Even the thin details such as the field boundary are well preserved in the SAR results.

6. CONCLUSIONS

In conclusion, the major aim of the study was to assess the use of ERS-1 data for the identification of rice growing areas and the monitoring of rice growth. The approach includes a comparison and synthesis of experimental results obtained at two geographical sites where rice growth conditions are different, an interpretation of the experimental data and a development of methods for mapping rice fields and mapping rice growth parameters.

The study will be further completed by a validation of the results on the site. Furthermore, additional study has to be conducted to evaluate the effect of weather condition (wind), the small size of fields, the topography (terrace rice), the cultural practices (direct sowing rice on non flooded soil). Anyway, the results appear already promising and applications using ERS and RADARSAT data can be foreseen.

ACKNOWLEDGMENT

The SARI project is a ERS-1 ESA pilot funded by the CNES under contract n°94/CNES/0381. We thank SCOT CONSEIL (France) and BPPT and MOA (Indonesia) for data acquisition.

REFERENCES

[1] T. Kurosu, M. Fujita and K. Chiba, 1995. "Monitoring of rice crop growth from space with ERS-1 C-band SAR". Submitted to IEEE. Trans. on Geoscience and Remote Sensing.

[2] J. Aschbacher, A. Pongsrihadulchai, S. Karnchanasutham, C. Rodprom, D. R. Paudyal and T. Le Toan, 1995. "Assessment of ERS-1 data for rice crop mapping and monitoring". Proc. IGARSS'95, Florence.

[3] T. Le Toan, F. Ribbes, N. Floury, L. Wang, J.A Kong, T. Kurosu and M. Fujita, 1996. "Rice crop monitoring using ERS-1 data : experiment and modelling", unpublished.

[4] SCOT CONSEIL and CESBIO, 1995. « Satellite assessment for rice in Indonesia ». SARI Project, Phase 1B, Final Report, n° 94/CNES/0381, 101 p.

[5] J. Bruniquel and A. Lopes, 1994. « Analysis and enhancement of multi-temporal SAR data », SPIE/EUROPTO Symp., Rome, vol. 2315, pp. 342-353.

[6] E.J.M. Rignot and J.J. Van Zyl, 1993. "Change detection techniques for ERS-1 SAR data". IEEE Transactions on Geoscience and Remote sensing, Vol. 31, N° 4, pp. 896-906.

Textural Processing of Multi-Polarization SAR for Agricultural Crop Classification

Paul M. Treitz[1], Otto Rotunno Filho[2], Philip J. Howarth[3] and Eric D. Soulis[4]

[1] Department of Geography, York University, North York, Ontario, Canada M3J 1P3
Phone: (416) 736-2100 x22436; Facsimile: (416) 736-5988: Email: treitz@yorku.ca

[2] Universidade Federal do Rio de Janeiro - COPPE, Programa de Engenharia Civil - Laboratorio de Hidrologia
Centro de Tecnologia - Bloco B, Caixa Postal 68506, Ilha do Fundao - Rio de Janeiro - RJ - 21945-970 Brasil
Facsimile: 011 55 21 290 6626; Email: OTTO@hydra.hidro.ufrj.br

[3] Earth-Observations Laboratory, Institute for Space and Terrestrial Science
Department of Geography, University of Waterloo, Waterloo, Ontario, Canada N2L 3G1
Phone: (519) 885-1211 x3404; Facsimile: (519) 888-6768; Email: howarth@wateol.uwaterloo.ca

[4] Department of Civil Engineering, University of Waterloo, Waterloo, Ontario, Canada N2L 3G1
Phone: (519) 885-1211 x2175; Facsimile: (519) 888-6197; Email: ric@sunburn.uwaterloo.ca

Abstract—In this study, three techniques for generating texture statistics are examined: the Gray-Level Co-occurrence Matrix (GLCM), the Gray-Level Difference Vector (GLDV) and the Neighboring Gray-Level Dependence Matrix (NGLDM). The objective of these statistical approaches is to translate visual texture properties into quantitative descriptors in a manner that they can be used to discriminate relevant land features using additional image processing techniques. These second-order statistical methods are used to generate texture features from C-HH and C-HV airborne synthetic aperture radar (SAR) data collected on July 10, 1990 over an agricultural area in southern Ontario Canada. Texture features generated from the GLCM, GLDV and NGLDM are classified individually using a *k*-Nearest Neighbor (*k*-NN) supervised classifier. The greatest classification improvement ($\approx$ 20%) was observed with the mean and correlation texture features derived from the GLCM. However, the selection of a specific second-order statistical technique may not be critical, since similar classification improvements were observed for the GLCM, GLDV and NGLDM statistical techniques. The results reported here highlight the importance of texture processing to methods of classifying agricultural crops using SAR data.

INTRODUCTION

Tonal values in a synthetic aperture radar (SAR) image represent point measurements of the backscattering coefficient and are related to the radar wavelength and the elements within the scene that are interacting with the signal over a single pixel area. Texture, or the intrinsic spatial variability of SAR tone is recognized as an important interpretive tool for discriminating different land-cover and land-use types. A texture field within a SAR image is described as homogeneous if the spatial arrangement of pixel values are more homogeneous (as a unit) within than between texture fields [1]. In response to the need for extracting information based on the spatial arrangement of digital image data, numerous texture algorithms have been developed based on structural approaches, Fourier power spectra, first-order statistics, second-order statistics, texture spectrum and spectral texture pattern matching. In studies comparing statistical texture measures, second-order gray-level co-occurrence statistical techniques tended to be superior to other statistical methods for capturing the textural content of an image [1]. Second-order statistical approaches [2], [3], [4] make use of gray-level probability density functions, which are generally computed as the conditional joint probability of pairs of pixel gray levels in a local area of the image.

It has been demonstrated that texture transforms have a role in SAR analysis of land cover and land use, and in agriculture by improving crop separability. However, optimal textural processing for inclusion in an overall image processing strategy for agricultural crop classification and mapping has not been clearly defined. In this study, the Gray-Level Co-occurrence Matrix (GLCM), Gray-Level Difference Vector (GLDV) and Neighboring Gray-Level Dependence Matrix (NGLDM) statistical methods are used to generate texture features from C-HH and C-HV airborne SAR data. The comparison of the GLCM, GLDV and NGLDM techniques is based on the discrimination of seven agricultural crop types from individual texture features.

STUDY AREA AND DATA DESCRIPTION

Airborne C-Band (5.3 GHz) SAR data with HH and HV polarizations were collected on July 10, 1990 for an agricultural area in Oxford County in southern Ontario Canada. The major crops in the area are alfalfa, corn, soybeans, pasture and winter wheat. The incidence angles for the SAR data ranged from 45 to 76 degrees. The study site, however, fell within approximately 10 degrees of the incidence-angle range. As a result, backscatter variation within this range was assumed to be indicative of surface variation, rather than of incidence-angle effects. Data were collected in 7 looks, in a slant range presentation with 6m spatial resolution.

0-7803-3068-4/96$5.00©1996 IEEE

METHODOLOGY

Texture Processing

The GLCM is a two-dimensional array that provides the conditional joint probabilities of all pairwise combinations of pixels within a defined computation window [2]. The co-occurrence of gray values represents the probability of any two pairs of gray values occurring at a user-defined interpixel sampling distance (δ) and orientation (α). The texture statistics generated from the GLCM represent a single spatial measure of the image texture. These statistics are characterized as point estimates since each statistic provides a single measure of the distribution of gray-level pairs within the GLCM. Texture features (angular second moment, correlation and mean) based on GLCMs were generated by defining the following three input parameters: (i) window size for which the co-occurrence matrix was generated; (ii) interpixel sampling distance; and (iii) direction for pixel co-occurrence within the sampling window [5]. For this analysis, a window size of 13x13, an interpixel sampling distance of 1 (δ =1), and an orientation of 0° (α=0°) were used to generate the GLCM.

The GLDV is derived from the GLCM and tabulates the occurrence of reference to neighbor pixel absolute differences [3], [5]. Element 0 of the GLDV is the number of times the difference is 0 (i.e., the neighbor pixel value equals the reference pixel value), element 1 the number of times the absolute difference is 1 (i.e., the reference minus neighbor pixel value is (- 1 or +1), and so forth. The GLDV is derived from the GLCM by adding the matrix elements in lines parallel to the main diagonal. The texture of an image is related to the distance of the co-occurrence matrix elements to the diagonal elements (elements (1,1), (2,2), ... (n,n)). Here, the amount of dispersion that the matrix elements had about the diagonal were measured using the angular second moment and mean texture statistics.

The NGLDM method [4] is similar to the GLCM but entries have no directional dependence and there are fewer columns in the matrix. Each entry within the matrix is computed using a square sliding window which tracks across each row of pixels contained in the image, evaluating the gray level relationship between the center pixel and its adjacent neighbors. The large number emphasis (LNE) texture feature based on the NGLDM was generated using software developed at the University of Waterloo [6]. The texture features characterize and quantify the entry distribution within the dependence matrix, referred to as the Q-matrix. For computing the NGLDM there are two user-defined parameters; the gray-level interval or similarity range (α), and the displacement distance from the center pixel (β). Each entry of the matrix for a class Q(k,s) is generated by counting the number of occurrences in which the difference in gray level between each pixel in the class with gray tone k and s of its neighbors is equal to or less than α at a specified β. For this analysis, large number emphasis texture features were generated for α= 24 and 32 and β=1 for all cases.

Classification and Sampling Design

A stratified random sampling scheme was used to acquire 400 calibration and 400 validation pixels for seven agriculture classes (wheat, soybean, corn - parallel/perpendicular, forest, alfalfa and pasture). SAR data for corn was differentiated based on the predominant row orientation with respect to the SAR signal. A *k*-NN classifier was used in this analysis [5]. Calibration pixels representing each of the seven agricultural classes were used to define the training-set feature vectors for each texture feature submitted to the *k*-NN classifier. Classification is performed by computing the Euclidean distance between the validation pixel's feature vector and each calibration sample's feature vector. The pixel values of a specified number of calibration pixels (*k*) in closest proximity to the sample are determined. The unclassified pixels are then assigned to the class that has the majority of the *k* values. Typical *k* values range from 1 to 10, with larger values necessary for noisy data or data with high dimensionality [5]. For this study, the SAR data demonstrated significant noise (i.e., speckle), but were of low dimensionality (i.e., 1 feature). Therefore, a *k* value of 5 was selected for analysis. The Kappa coefficient ($\hat{K}$) was calculated for the validation accuracies of each classification. The Kappa coefficient is a measure of agreement between the ground sample classes and those derived through classification of remote sensing data. This measure accounts for all elements of the confusion matrix and excludes the agreement that occurs by chance.

RESULTS

Summaries of the validation accuracy assessments for the various trials are presented in Tables I and II for the C-HH and C-HV data respectively. Since the purpose was to compare the information content of tone and texture features directly, it is not unexpected that validation accuracies for single feature tone and texture features were very low. A single feature provides limited discriminant capabilities. The results are also a function of a very specific set of crop classes. Based on contingency table analyses, there appears to be no justification for separating corn fields based on row direction. At the stage of development for corn in mid-July (height <1m), row direction does not have a significant impact on radar backscatter. Similarly, grouping alfalfa and pasture into a single class would be logical based on the high level of confusion between these two classes. The two classes discriminated most readily are wheat and alfalfa, a result of a combination of contrasting tones and textures.

Validation accuracies for texture features were, on average, 10-20% higher than those of tone alone (Tables I and II). Specifically, the mean and correlation statistics derived from the GLCM provided the highest classification accuracies, a 20% improvement over tone alone. Finally, there was not a large difference in validation accuracies between C-HH and C-HV polarizations (Tables I and II).

Table I
Classification Accuracies (%) of Validation Data for C-HH Tone and Texture Features

Feature	Wheat	Soybean	Corn (//)	Corn (⊥)	Forest	Alfalfa	Pasture	Mean (%)	Kappa ($\hat{K}$)(%)
Tone	57.00	35.75	10.50	7.00	11.25	38.00	4.25	23.39	10.63
GLCM									
Angular Second Moment	57.00	46.25	21.25	9.00	4.50	64.75	33.00	33.68	22.63
Mean	51.25	37.25	33.00	20.50	33.50	64.00	50.00	41.36	31.58
Correlation	55.50	44.00	34.00	23.25	17.75	58.00	50.75	40.46	30.54
GLDV									
Angular Second Moment	48.50	38.25	23.00	16.25	9.50	62.00	43.00	34.36	23.42
Mean	55.00	50.50	30.00	8.00	5.50	72.50	28.50	35.71	25.00
NGLDM									
LNE (α=24)	46.25	44.50	27.75	11.50	15.50	60.25	38.25	34.86	24.00
LNE (α=32	40.00	45.00	29.75	13.00	21.25	76.25	29.25	36.36	25.00

Table II
Classification Accuracies (%) of Validation Data for C-HV Tone and Texture Features

Feature	Wheat	Soybean	Corn (//)	Corn (⊥)	Forest	Alfalfa	Pasture	Mean (%)	Kappa ($\hat{K}$)(%)
Tone	66.92	25.31	17.26	8.08	2.82	14.21	5.51	19.86	6.64
GLCM									
Angular Second Moment	53.88	29.57	36.29	12.12	44.37	49.13	15.79	34.58	23.73
Mean	62.16	33.58	31.73	23.99	23.00	58.10	27.32	37.03	26.56
Correlation	54.14	38.10	34.01	26.77	24.41	50.37	27.82	36.43	25.89
GLDV									
Angular Second Moment	50.13	30.33	31.73	19.70	29.11	55.61	16.29		22.19
Mean	54.39	33.08	29.19	14.14	25.82	54.61	20.05	33.04	21.91
NGLDM									
LNE (α=24)	53.63	29.82	41.12	16.16	42.96	55.61	18.05	36.85	26.37
LNE (α=32	50.88	31.83	34.01	18.69	44.60	52.12	11.53	34.93	24.12

CONCLUSION

Although single features (tone or texture) do not provide sufficient information for agricultural crop classification, it is clear that texture processing improves classification accuracy over tonal data alone. The mean and correlation texture features derived from the GLCM provided the highest classification results. Results indicate that although texture features provide improved classification accuracy, the differences between the various texture features tested are generally small. Texture features derived from multi-polarimetric SAR data and integrated with optical data should provide sufficient discriminatory power when subjected to appropriate classification algorithms for identifying agricultural crops and crop conditions.

ACKNOWLEDGMENTS

This research was funded through a Center of Excellence Grant from the Province of Ontario to the Institute for Space and Terrestrial Science. Additional support was provided by NSERC Grant OGP 0043957 awarded to Dr. Soulis.

REFERENCES

[1] D.G. Barber, M.E. Shokr, R.A. Fernandes, E.D. Soulis, D.G. Flett, and E.F. LeDrew, "Comparison of second-order classifiers for SAR sea ice discrimination," Photogramm. Eng. and Rem. Sens., vol. 59, no. 9, pp. 1397-1408, 1993.

[2] R.M. Haralick, K. Shanmugam, and I. Dinstein, "Textural features for image classification," IEEE Trans. on Sys., Man, and Cyber., vol. 3, no. 6, pp. 610-621, 1973.

[3] J.J. Gerbrands, "Inleiding in de digitale beeldverwerking," Technical University Delft, The Netherlands, 1991.

[4] C. Sun, and W.G. Wee, "Neighboring gray level dependence matrix for texture classification," Comp. Vision, Graphics and Image Proc., vol. 23, pp. 341-352, 1983.

[5] PCI Inc., EASI/PACE Image Analysis System Manual Version 6.0: PCI Inc., Toronto, Ontario, Canada, 1996.

[6] O.C. Rotunno, P.M. Treitz, E.D. Soulis, P.J. Howarth, and N. Kouwen, "Texture processing of synthetic aperture radar data using second-order spatial statistics," Computers and Geosciences, (in press).

Study on Auto-extraction of Winter Wheat Planting Area from TM Image Based on Pattern Recognition Technology

Xiaohuan Yang Naibin Wang Ping Qin
Commission for Integrated Survey of Natural Resources, Chinese Academy of Sciences
P.O. Box 9717, Beijing 100101
Tele: 86-10-4917351 Ext. 3309 Fax: 86-10-4914230

Abstract--This work is a part of Yield Estimation of Main Crops by Remote Sensing Technology and it has made import progress.

Quick and precise extraction of planting area is a key problem in the research of estimation of crops yield by remote sensing technology. The focus of this paper is on extracting pure wheat land and intercropping wheat land automatically based on the selected proper TM information source on which multi-dimension greenness map was built and characteristics and development of winter wheat and pattern recognition technology. The deviation between the wheat planting area got from computer interpretation and manual interpretation respectively is small and meet the requirement of practice.

BACKGROUND

This paper is one of the achievements in scientific research on the project Main Crops Yield Estimation by Remote Sensing in Important Food Area, which was a key scientific project in the period of national eighth five-year plan in China (from 1990 to 1995). In the last four years, we forecasted the yield of three kinds of crop, winter wheat in North China, corn in Song-liao plain (in Northeast China), rice in Jianghan plain and Taihu Lake plain. Whole working area is $1.04 * 10^8$ hectare. The precision of estimation is respectively more than 95% (winter wheat) and 85% (corn and rice). A experiment running system has been built in CISNAR.

Quick and precise extraction of planting area is a key problem in the research of estimation of crops yield by remote sensing technology. China has a varied topography, broken massif and complicated cropping system, it is very difficult to know well the planting area of crop by conventional statistic method. So the government can't grasp exact total output, in other words, success or failure in Main Crops Yield Estimation by Remote Sensing is up to whether crop planting area can be extracted precisely or not.

0-7803-3068-4/96$5.00©1996 IEEE

This paper only expounds some problems relate to winter wheat yield estimation by remote sensing.

SELECTION OF TM INFORMATION SOURCE

To select proper TM information source is the guarantee of improving the precision of pattern recognition, especially for extracting single crop planting area. In North China, the growth period of winter wheat is September to June next year. From the middle of November to the middle of April next year, vegetation is almost withered except winter wheat, conifer and a few vegetables. In this time, winter wheat can be extracted more easily from TM image with the aid of GIS.

THEORETICAL BASIS OF PATTERN RECOGNITION

Early in 1977, Richardson and Wiegand studied vegetation recognition and put forward a new concept: "soil spectrum line". The research result shows as figure 1.

Fig. 1 indicates: vegetation points are above the soil line, but water points are below the soil line. If expressed with difference greenness,

vegetation point: $g_1(x)=IR-R>0$

water point: $g_2(x)=IR-R<0$

soil line: $IR=KR+b$

In fact, soil points are distributed in the around of a line, so

$g_1(x)=IR-R>\varepsilon$ (where ε is a small positive number)

From the view of classification, the soil line equation can be regarded as discriminant of water and vegetation, the value of g(x) is the value of discriminant.

$$g(x) = IR-R-b \geq \varepsilon$$

Obviously, the relation of vegetation, soil and water is:

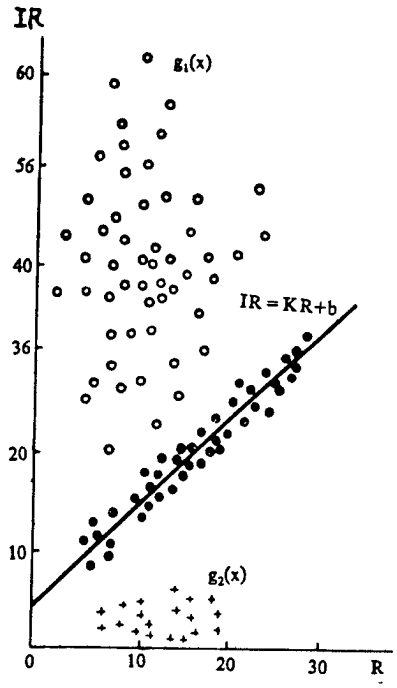


Fig 1 Soil Line

$$g_1(x) > g(x) > g_2(x) \qquad (1)$$

Each point the value is greater than g(x) is vegetation.

CONSTRUCTION OF 3-DIMENSION GREENNESS MAP

Fig. 2 is a 3-dimension map that consists of IR, R and G, where G is greenness, which value is the difference of IR and R.

In order to get quantitative information, suppose some planes parallel to IR-O-R break up the 3D map of IR-R-G. The height is G_i, which is the value of classification function, it is to say, G_i is the threshold value of vegetation and non-vegetation. Counting the pixel number and deducting the pixel numbers of conifer and vegetables with the aid of GIS, winter wheat planting area can be obtained easily.

CALCULATION OF THE THRESHOLD

Calculate value of differentiate functions as follow:

$$G_1 = IR_{11} - R_{12} + b_1 \quad (\text{wheat land})$$

$$G_2 = IR_{12} - R_{22} + b_2 \quad (\text{non-wheat land}) \qquad (2)$$

Change (2) to standard equation (3):

$$g_1(x) = a_{11}x_{11} - a_{12}x_{12} + c_1 b_1$$

$$g_2(x) = a_{21}x_{21} - a_{22}x_{22} + c_2 b_2 \qquad (3)$$

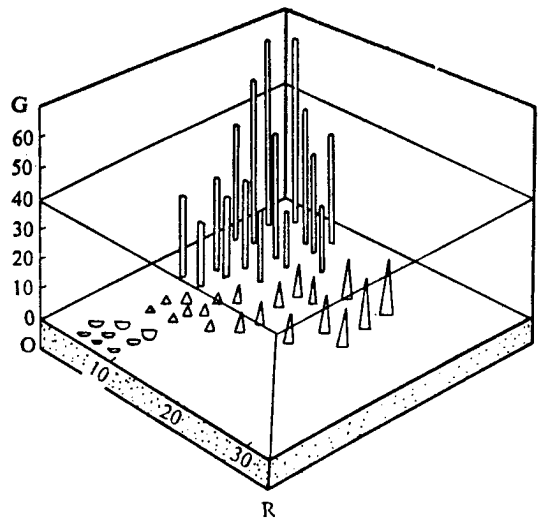


Fig. 2 3-D space that consists of IR, R and G

where:

x_{11}, x_{12}, x_{21} and x_{22} are not equal each other.

Suppose $b_1 = b_2 > 0$, $a_{11} = a_{12} = a_{21} = a_{22} = c_1 = c_2 = 1$, calculate $g_1(x)$ and $g_2(x)$ according to (3).

If $g_1(x) > g_2(x)$, suppose a[0,1]

$$a_{11}' = a_{11} - ax_{11} \quad a_{21}' = a_{21} + ax_{21}$$

$$a_{12}' = a_{12} - ax_{12} \quad a_{22}' = a_{22} + ax_{22}$$

$$c_1' = c_1 - a \qquad c_2' = c_2 + a$$

Replace the coefficients above into (3), and then calculate $g_1(x)$ and $g_2(x)$.

If $g_1(x) < g_2(x)$, suppose $a' = a/2$

$$a_{11}'' = a_{11}' + a'x_{11} \quad a_{21}'' = a_{21}' - a'x_{21}$$

$$a_{12}'' = a_{12}' + a'x_{12} \quad a_{22}'' = a_{22}' - a'x_{22}$$

$$c_1'' = c_1' + a' \qquad c_2'' = c_2' - a'$$

Calculate $g_1(x)$ and $g_2(x)$ again by replacing the coefficients above into (3).

Calculate $g_1(x)$ and $g_2(x)$ and so on and so forth until $g_1(x) \approx g_2(x) = G$. It is G that is the threshold value between wheat land and non-wheat land.

CONCLUSION

A experiment was done in Yucheng county, Shandong province, where G = 4. The meaning is that the pixel IR minus R is equal to or greater than 4 is wheat land, other pixels are non-wheat land.

The result shows as in table 1.

Table 1 Winter Wheat Planting Area Obtained by Two Methods (unit: hectare)

method	wheat land	real area	precision
manual interpretation	32507	32560.2	99.84%
computer interpretation	32316.7	32560.2	99.25%

Table 1 indicates: the deviation between the wheat planting area got from computer interpretation and manual interpretation respectively is small and meet the requirement of practice.

REFERENCES

[1] James, M. H: Remote sensor comparison for crop area estimation, 1989.

[2] Huete, A. R: Soil spectral effects on 4-space vegetation discrimination. Remote Sensing of Environment, 1984.

[3] Richard, C. C: Comparison of Landsat MSS, Nimbus-7 CZCS, and NOAA-7 AVHRR features for land-use analysis, Remote Sensing of Environment, 1984.

Spring Wheat Yield Prediction for Western Canada Using Weekly NOAA AVHRR Composites

Klaus P. Hochheim[1], David G. Barber[1] and Paul R. Bullock[2]

1 Centre for Earth Observation Science, Department of Geography,
University of Manitoba, Winnipeg, Manitoba, Canada, R3T 2N2.
Ph. (204) 474-7376. Fax (204) 275-8281, hocheim@cc.umanitoba.ca
2 The Canadian Wheat Board, 423 Main Street, P.O. Box 816,
Winnipeg, Canada.

ABSTRACT -- The growing and marketing of wheat and other small grains is a major national and international industry. Accurate methods of acquiring crop condition information in a timely manner is critical within the global grain marketing environment. Any technique that helps reduce uncertainties with respect to marketing decisions is therefore important. This paper reviews the use of maximum value NDVI composites (MVCs) to predict spring wheat yield for Western Canada. Results show that cumulative NDVI estimates provide a reproducible and reliable means of generating early season yield estimates for Western Canada. Results for 1991 and 1992 growing season show that early season NDVI yield estimates are within 5% of official yields estimates released 3 months following harvest.

INTRODUCTION

Organizations as such as the Canadian Wheat Board (CWB) have recently adopted the use of weekly maximum value AVHRR NDVI composite data as a supplementary tool for generating pre-harvest spring wheat yield estimates for Western Canada [1]. This data has been available since 1987 and is generated at the Manitoba Remote Sensing Centre (MRSC) in cooperation with the Canada Centre for Remote Sensing (CCRS).

Previous work has shown that seasonal vegetation indices (VIs) are highly related to percent cover, leaf area index (LAI), and green biomass. LAI and biomass are an expression of a variety of environmental factors such as soil moisture conditions, soil fertility, planting date and planting density. The magnitude and duration of the seasonal time series of VI's is considered an indicator of potential yield [2] [3].

Early adoption of NOAA data as a semi-quantitative tool for yield estimation was hindered by AVHRR data calibration problems, residual cloud contamination in MVCs and the difficulty of generating meaningful regression relationships between NDVI and yields on regional scales. This work deals primarily with the latter problem, that is, generating regression relationships over a large physically and spectrally heterogeneous area given a limited data set, 1987-92. NDVI data from 1993 -1995 is not included at this time due to outstanding data calibration issues.

METHODS

Prior to the extraction of NDVI statistics per Crop Reporting District (CD) (N=48) a number of preprocessing functions were conducted to address data quality. These included the substitution of prelaunch calibration coefficients with piecewise linear coefficients proposed by [4] and designing a rigorous cloud masking scheme to minimize the inclusion of cloud contaminated pixels [1]. Since CDs were going to be integrated regionally over a number of years, variations in crop phenology over time and space had to be accounted for. A method was adopted where the median value of seven highest NDVI values per CR per year provided the bench mark to align seasonal NDVI profiles. The method assumes that peak NDVI values occur around the heading stage of wheat. Median values were assigned to Julian Week (JW) 29 (mid July), a period typically associated with maximum NDVI values in Western Canada.

To establish relationships between NDVI and yield, physical and spectral variations between CD's had to be considered. Seasonal plots of NDVI for 1989 and 1990 for the province of Saskatchewan serve to demonstrate the variability of NDVI independent of yield (Fig. 1).

From subsequent analysis it became apparent that a stratification scheme based on soil moisture regime and percent summer-fallow would have to be adopted to define physical and spectral homogeneous areas.

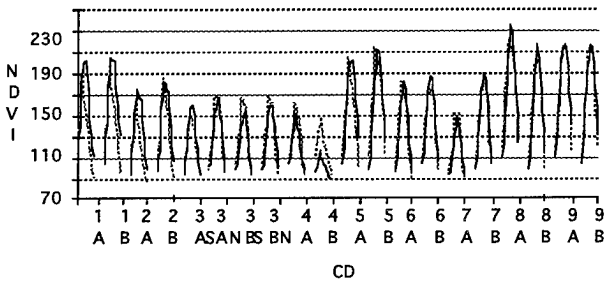


Fig. 1. Seasonal NDVI curves for Saskatchewan CDs, 1989 & 1990.

0-7803-3068-4/96$5.00©1996 IEEE

RESULTS AND DISCUSSION

Prior to adopting a regression scheme to predict spring wheat yields for the 1991 and 1992 , CDs were aggregated into "homogeneous" or "uniform" regions. As part of the process toward defining uniform regions, maximum three week mean NDVIs computed from 1989-91 data were regressed with percent summerfallow (Fig.2). Based on these results percent summerfallow was shown to be a significant factor affecting NDVI. Summerfallow was adopted as an initial

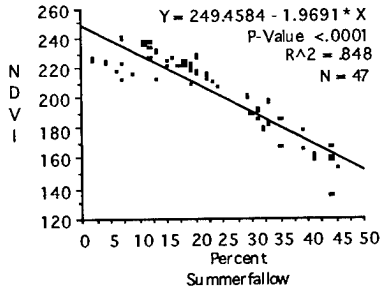


Fig 2. Linear regression relating maximum three week average NDVIs and percent summerfallow.

stratification variable based on its percentile distribution (Table 1). CDs in the 75th and 90th percentile (F34 and F43) were further stratified to take into account variations in soil moisture regimes (or soil type, D. Brown Chernozems and Brown Chernozems respectively).

Table 1. CD stratification scheme for Western Canada.

Percentile	10	25	50	75	90	>90
% Fallow per CD ID.	≤ 7 (F7)	>7 -13 (F13)	>13 - 20 (F20)	>20 - 34 (F34)	>34 - 43 (F43)	>43 (F50)
Soil Moisture Regime	Sub-humid	Sub-humid	Sub-humid	Semi-arid / Sub-arid	Semi-arid / Sub-arid	Sub-arid

A number of NDVI estimators were used to predict wheat yield potential. One week means (1WK) and three week running means (3WK) over JWs 25-32; cumulative NDVIs from (JW) 22 (C22) and JW 25 (C25) (Fig.3); and sum of the 7 highest NDVI values (M7) followed by the integration of three additional weeks (i.e. M7+1,...+3) (Fig. 4).

Yield estimates were computed per "uniform area" for 1991, using NDVI data from 1987-1990, and for 1992 using NDVI data from 1987-1991. The performance of the NDVI estimators varied based on the integration period. A percentile plot of yield ranges for each NDVI estimator showed that NDVIs integrated using M7+1 to M7+3 and C22-29 to C22-32 provided the most consistent yield estimates over time (<0.1 t/ha) followed closely by the C25

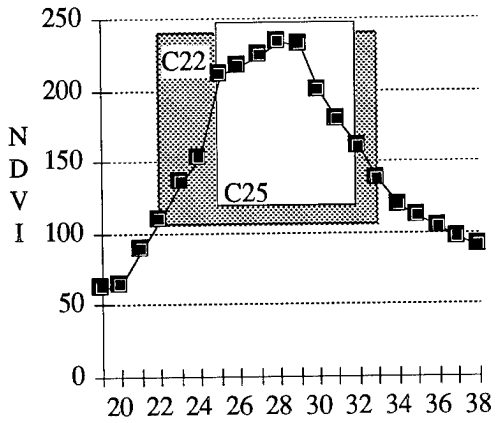


Fig. 3. NDVI integration periods starting JW 22 (C22) and integration periods starting JW 25 (C25).

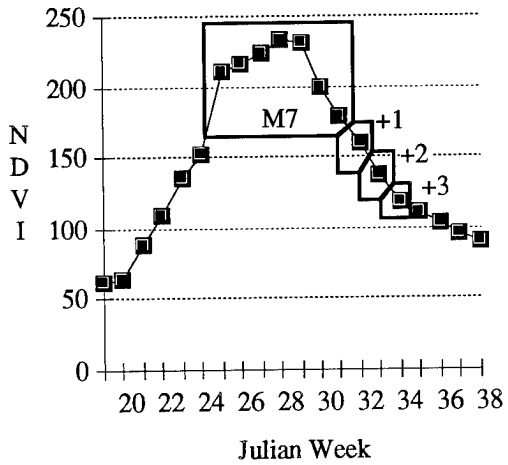


Fig.4 . NDVI estimator M7+1 to M7+3.

estimator (Fig. 5). This result is significance to users of such data as the results are repeatable and tend to improved over the integration period; this is not so for the 1WK or 3WK means.

Yield estimates for 1991 and 1992 are presented for M7 and C22 NDVI estimators only (Figs. 6 & 7). NDVI yields per CD per "uniform area" were aggregated to a provincial estimates for each of the prairie provinces, Alberta (AB), Saskatchewan (SK), and Manitoba (MB); and to a Western Canada estimate (W. CDN).

Results for 1991 indicate that the M7 estimator predicted 99-103% of the official yield estimate and 104 - 106% of the official yield estimate using C22 (Fig. 6). The MB results are notable in that the NDVI yield estimates were much higher than the official estimate. The over estimation was a result of a heat stress event during heading period which significantly reduced the expected yield.

For 1992 NDVI yield estimates for W.CDN were within

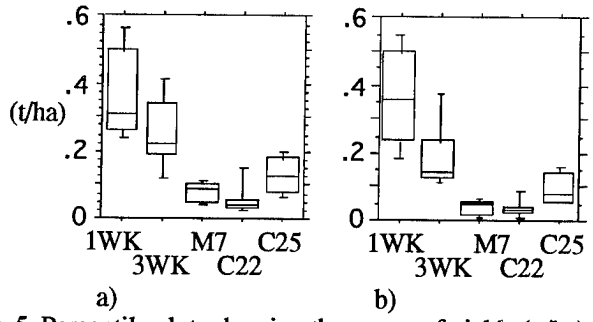


Fig. 5. Percentile plots showing the range of yields (t/ha) per NDVI estimator a over the prediction period for a) 1991 and b) 1992.

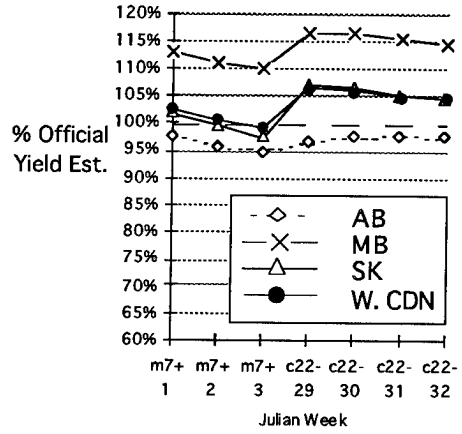


Fig. 6. NDVI spring wheat yields for Western Canada and the prairie provinces, 1991.

95-97% of the official estimate. NDVIs were uncharacteristically low for SK and MB despite excellent growing conditions. The underestimation is mainly attributed to the persistence of cloud cover in 1992 Atmospheric aerosols from Mount Pinatubo may have compounded the

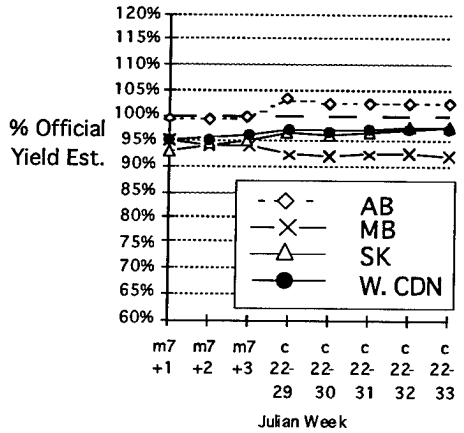


Fig. 7. NDVI spring wheat yields for Western Canada and the prairie provinces, 1992.

effects of cloud cover but this remains speculative as the aerosols (largely SO_2) were concentrated between 20°S and 30° N latitude [5].

The results show that NDVI can be used as a supplemental tool to predict spring wheat yield potential for Western Canada and other major wheat growing regions of the world. It is recommended that cumulative NDVI estimators be used due to improved precision over the prediction period.

Results also highlight ongoing concerns for users of optical data, primarily the need for timely and accurate calibration coefficients for the AVHRR data and ongoing concerns regarding cloud contamination especially given a weekly NDVI compositing period. NDVI yield estimates for MB in 1991 highlighted another concern for users of optical data, in that stress events following peak "greenness" are largely undetectable thus leading to over estimations of yield. Additional stress indices generated from climatological data following maximum seasonal NDVI would be useful in adjusting NDVI yield estimates.

LITERATURE CITED

[1] Hochheim, K.P. 1995. Western Canada Spring Wheat Yield Estimation using Weekly AVHRR NDVI Composite Data. *Masters Thesis*, University of Manitoba, Canada. pp. 224.

[2] Rudorff, B. F. T. and G. T. Batista (1990). Spectral response of wheat and its relationship to agronomic variables in the tropical region. *Remote Sensing of Environment*.. 31:53 - 63.

[3] Tucker, C. J., B.N. Holben, J. H. Elgin, Jr., and J. E. McMurtrey III (1980). Relationship of spectral data to grain yield variation. *Photogrammetric Engineering and Remote Sensing*. vol. 46, no. 5, pp. 657 - 666.

[4] Teillet, P.M. and B.N. Holben 1994. Towards operational radiometric calibration of NOAA AVHRR Imagery in the visible and near-infrared channels. *Canadian Journal of Remote Sensing*. vol. 20, no.1, pp. 10.

[5] Stowe, L.L., R.M. Carey and P.P. Pellegrino 1992. Monitoring the mount pinatubo aerosol layer with NOAA-11 AVHRR data. *Geophysical Research Letters*, vol. 19, no. 2, pp. 159-162.

SNOW AND ICE OBSERVATIONS DURING THE EUROPEAN MULTI-SENSOR AIRBORNE CAMPAIGN IN 1995

J. Noll[1], Mike Wooding[2], and E. Attema[1]
[1]European Space Agency, ESTEC–XEP,
P.O. Box 299, NL 2200 AG Noordwijk
Tel: +31-71-565-5158, Email: josef@xe.estec.esa.nl
[2] Remote Sensing Applications Consultants
Mansfield Park, Medstead, Alton-Hants GU345PZ, UK

Abstract:

The European Multi-sensor Airborne Campaign (EMAC-94/95) was initiated to provide support for future satellite remote sensing programmes and their users. In 1995 the programme concentrated on snow and ice experiments in northern Europe. The paper gives an overview of the active and passive remote sensing instruments involved in the campaign. It highlights the objectives of the boreal land snow test sites (Finland, Sweden), the alpine like land ice and snow test site (Norway) and the sea ice test site (Finland) and presents first results. Further information can be found at `http://www.jw.estec.esa.nl:8080/emac/EMAC.html` .

1. Introduction

The basic motivation for the EMAC-94/95 campaign is to support ESA's Earth Observation programmes. Data evaluation from the participating SAR sensors will help in preparation for ENVISAT's ASAR and for a future multi-frequency SAR. Data obtained from passive microwave sensors are of relevance for current and future meteorological spaceborne sensors such as the METOP instruments AMSU-A and MHS and advanced passive microwave radiometers such as MIMR.

EMAC-95 concentrated on multi-temporal/multi-frequency observations over snow and ice targets. Four test sites in Finland, Sweden and Norway have been selected (Fig. 1) and were visited in the March to July time-frame.

2. Microwave Sensors

Active instruments participating in the campaign were the Danish EMISAR, operating in full-polarimetric L- or C-band mode, and the German ESAR with dual polarized measurements in P-, L-, C- or X-band. The EMISAR operated on-board a Gulfstream G-3 at a nominal altitude of 12000 m co-



Figure 1: EMAC-95 test sites

vering an area of 9 × 9 km with a resolution of 2 × 2 m. The ESAR was mounted on a Do-228, operating at an altitude of 3.3 km and covering 6 × 6 km with a resolution of 4 × 4 m.

Participating passive microwave radiometers were the Finish HUT radiometer and the MARSS and DEIMOS radiometers from the UK Met Office. The HUT radiometer was mounted on a Short SC7 Skyvan with a nominal operation altitude of 400 m, covering the MIMR frequencies 6.8, 10.65, 18.7, 24, 35 and 94 GHz. The UK Met Office uses a C130 aircraft at an altitude from 150 to 1500 m mainly for atmospheric research. The aircraft is equipped with in-situ sensors for meteorological and cloud micro-physics measurements. Two microwave radiometers scan along the

0-7803-3068-4/96$5.00©1996 IEEE

aircraft track, MARSS at 89 and 157 GHz from zenith to nadir and DEIMOS at 23.8 and 50.3 GHz from nadir to 40 degrees.

The airborne data sets are complemented by satellite observations from ERS-1, JERS-1, Landsat and DMSP with SSM/I and SSM/T2 data.

3. Test Sites and Objectives

Observations of **sea ice** were performed in the Gulf of Bothnia (Fig. 2), in order to discriminate ice types and open water with SAR, to derive ice concentration and other ice characteristics from microwave radiometer data and evaluate the combined use of active and passive sensors. The sea ice test sites were visited several times by all sensors.

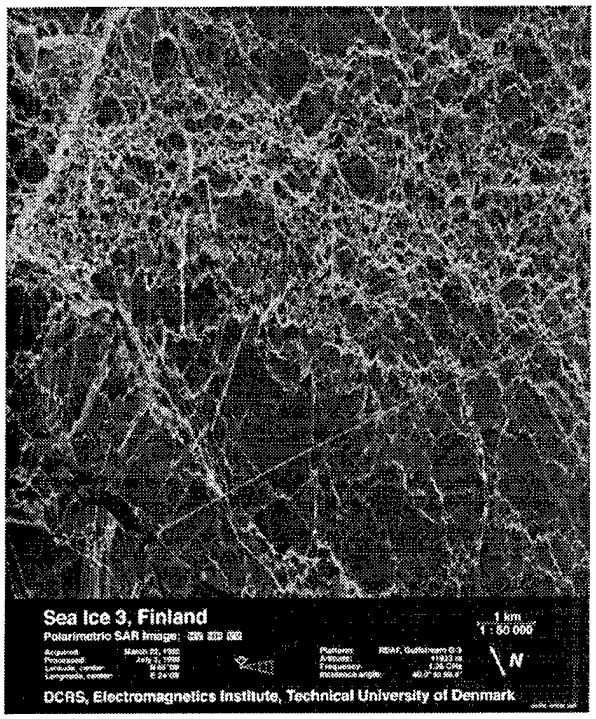


Figure 2: Finland sea ice (region 3), 23Mar95, L-band

The **snow test site in Finland** included four scenes, covering bare soils and different types of vegetation, ranging from agricultural fields to boreal forests (Fig. 4). The **main objectives of snow monitoring** were the determination of water equivalent, the monitoring of snow melt, and the determination of snow extent. The four scenes were intensively monitored by the HUT radiometer during four flights in the March to May time frame, accompanied by ESAR observations in early April and EMISAR observations in March and May.

The **Uppsala test site in Sweden** includes two

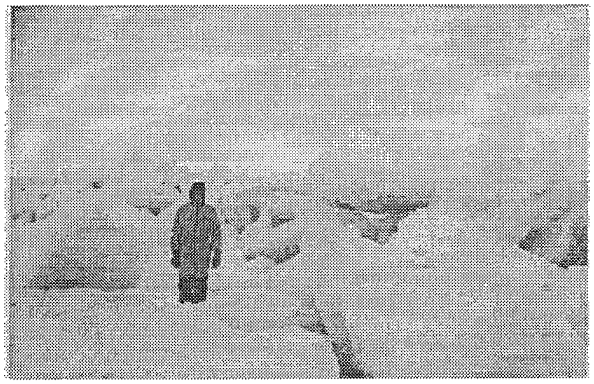


Figure 3: 'Ground truth' on the sea ice (region 3)

scenes with forest and agricultural usage and is a regular revisited NOPEX site (Fig. 5). The EMISAR observed the test sites during the NOPEX CFE-2 field campaign in July 1995.

The **Okstindan test site in Norway** consists of a glacier scene 'Okstindan' (Fig. 6) and an alpine forest scene 'Kongsfjellet' (Fig. 7) with strong relief variation and alpine like snow conditions and glacier characteristics. The 'Okstindan' site was observed in order to map and monitor glaciers, including surface elevation and topography. The test sites were monitored from the EMISAR at L- and C-band on 22/23 March, 2/3 May and 5/6 July 1995.

The multi-polarization images presented here give an indication of the variety of the different test sites. Data collected during EMAC-95 are of high quality and will be used for the definition of spaceborne sensor characteristics and for advanced integrated surface and atmosphere parameter retrieval algorithms.

Acknowledgments

The authors would like to thank all 17 groups representing 34 laboratories for their proposals. We hope that the results of the selected test sites will be useful for all of them. Special thanks applies to those who either operated the aircrafts or collected the 'ground truth'.

References

[1] Hallikainen, M., E. Attema, and M. Wooding, 1995, "EMAC-95 Snow and Ice airborne campaign", Proc. IGARSS'95, Florence, 1811-1813

[2] Attema, E., and M. Wooding, 1995, "EMAC Experimenters Handbook, Programme for 1995", ESA ESTEC



Figure 4: Finland snow (region 2), 22Mar95, C-band

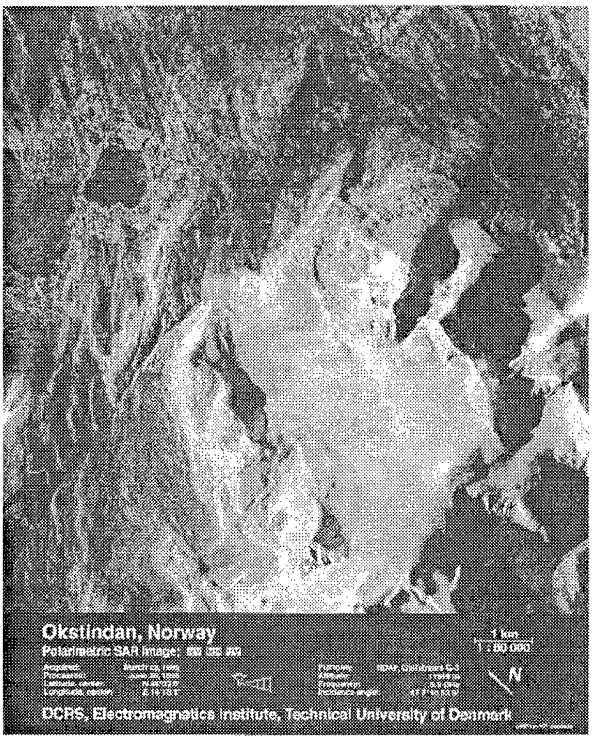


Figure 6: Okstindan glacier on 23Mar95 at C-band

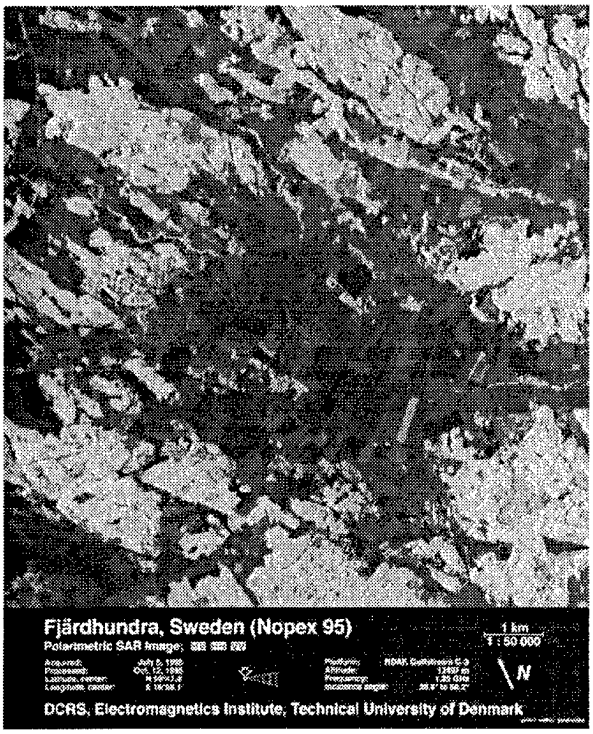


Figure 5: Fjärdhundra (NOPEX), 5Jul95, L-band

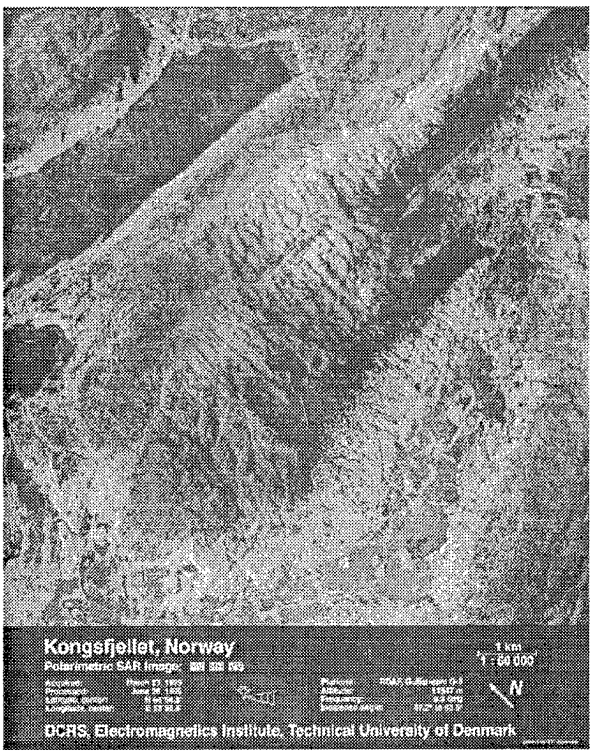


Figure 7: Kongsfjellet on 23Mar95 at C-band

Overview of EMAC-95 Snow and Ice Airborne Campaign in Finland

Martti Hallikainen, Pekka Ahola, Kimmo Rautiainen, Jörgen Pihlflyckt, Tomi Tirri, Marko Mäkynen,
Janne Lahtinen, Henri Servomaa, Petri Makkonen, Jochen Grandell, Martti Kemppinen,
Mikko Nikulainen, Hannu Taskinen, Simo Tauriainen, Markku Roschier
Laboratory of Space Technology, Helsinki University of Technology
Otakaari 5 A, 02150 Espoo, Finland
Telephone +358-0-451 2371, Fax +358-0-451 2898, E-mail Hallikainen@ava.hut.fi

Abstract -- The 1995 European Multisensor Airborne Campaign (EMAC-95) on Snow and Ice was funded by European Space Agency (ESA) and national authorities. The main test sites were in Finland (sea ice, snow in boreal areas) and Norway (land ice, snow in mountainous areas). The airborne instruments included two microwave radiometer systems (Helsinki University of Technology HUTRAD) and UK Meteorological Office system) and two SAR sensors (ESAR from DLR (Germany) and EMISAR from Technical University of Denmark). This paper summarizes the activities in the Finnish test sites. Results from the HUT microwave radiometer measurements in the Campaign are given.

CAMPAIGN GOALS AND TOPICS

EMAC-94/95 is a collaborative programme of European Space Agency and European Union, providing support for the preparation of future satellite remote sensing programs and their users [1]. The main motivation of EMAC-95 Snow and Ice activities is to improve the quality of snow and ice information derived from satellite data [2]

For snow in boreal areas, the planned main topics in EMAC-95 were: Determination of snow extent and snow water equivalent, including the effect of forest canopies; monitoring of snow melt.

For sea ice, the planned main topics were: Classification of ice types and open water in various weather conditions.

TEST SITES

The base for airborne operations was the city of Oulu in northern Finland. The test sites of EMAC-95 Snow and Ice activities were located as follows:

- Snow: Liminka - Kuusamo (4 test sites)
- Sea ice: Gulf of Bothnia, Finland (4 test sites)

The location of the two flight lines is depicted in Figure 1. Each flight line is about 150 km long with four intensive study areas, each of size 9 km by 9 km, for both sea ice and snow. Along the snow test line, the depth of snow increases towards northeast. The four sea ice test sites provide different ice types for airborne measurements.

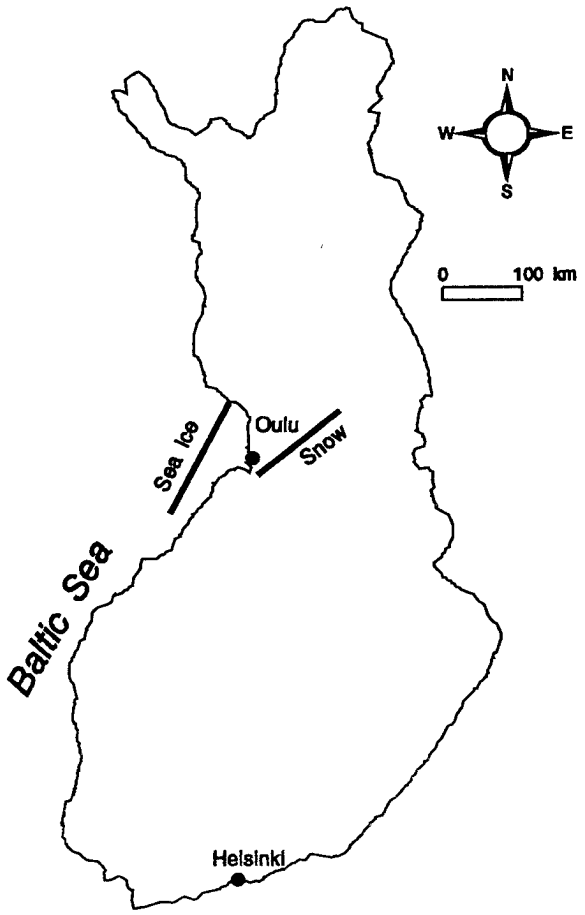


Figure 1. Location of test sites in Finland.

0-7803-3068-4/96$5.00©1996 IEEE

AIRBORNE SENSORS

The characteristics of the airborne instruments used in EMAC-95 Snow and Ice activities were discussed in a previous paper [3]. The characteristics of the HUT radiometer system HUTRAD are close to those of the ESA near-future MIMR instrument, Table 1. After EMAC-95, the HUTRAD system has been upgraded and its present characteristics are given in another IGARSS'96 paper [4].

Table 1. Characteristics of HUTRAD during EMAC-95.

Parameter	HUTRAD capability
Frequency	6.8, 10.65, 18.7, 24, 35, 93, 94 GHz
Profiling channels	6.8, 10.65, 18.7, 24, 35, 94 GHz
Imaging channels	93 GHz
Polarization	V + H: 6.8, 10.65, 18.7, 93, 94 GHz V: 24, 35 GHz
Antenna beamwidth	2° to 5°, depending on frequecy
Viewing	To rear of aircraft
Incidence angle	50°
Additional equipment	Video camera
Platform	Shorts SC7 Skyvan

AIRBORNE AND GROUND-BASED DATA SETS

Measurements were conducted from late March through late May, 1995 in order to collect time series of microwave signatures of snow and ice under various development phases and weather conditions. Availability of airborne sensors is depicted in Table 2.

Two corner reflectors were provided in each test site for SAR image localization. Surface measurements were carried out in the Finnish test sites by teams from national institutes. Finnish Environment Agency measured the depth and water equivalent of snow for the four snow test sites and took photographs of snow grains during dry snow conditions. Helsinki University of Technology measured the snow wetness and density. Finnish Forest Research Institute provided information on forest canopies. Table 3 shows the ground truth measurements for snow test sites.

Table 2. Snow and Ice flight program.

Sensor	Snow test sites	Sea ice test sites
HUTRAD	22 March 4-5 April 2-3 May 24 May	22 March 4-5 April 2-3 May 24 May
UKMO	27 March - 9 April	27 March - 9 April
ESAR	4-6 April	4-6 April
EMISAR	21-22 March 2-3 May	21-22 March 2-3 May

Table 3. Ground truth parameters along the center line of the four snow test sites. Length of each test site is 9 km. Test site 1 denotes the southernmost site.

Parameter	Observation
Snow extent	Skyvan video image
Snow depth	Every 100 meters
Snow water equivalent	Every 1000 meters
Snow density profile	Every 1000 meters
Snow wetness profile	Every 1000 meters
Snow temperature	Data logger in test sites 2 and 3
Snow stratigraphy	Selected locations
Snow grain size	Selected locations
Forest canopy data	FFRI data base and field work
Weather data	Test sites 1, 3 and 4 Regular data from Met. Office

Finnish Institute for Marine Research carried out ice ground truth measurements on March 31- April 6 in test sites 2, 3 and 4 (the southernmost test site is denoted number 1) using R/V Aranda as the base for operations. The data included ice extent, ice salinity, ice thickness, crystal structure, air bubbles and ice temperature. The surface roughness was measured by the Chalmers University of Technology team in test sites 3 and 4. Helsinki University of Technology was responsible for the measurements for other campaign dates, and used a helicopter from Oulu. The HUT ice data included ice salinity, thickness and density. HUT also conducted snow measurements in sea ice test sites, including snow depth, density and wetness. Due to varying ice and weather conditions, ground truth measurements in sea ice test sites

were not as systematic as in snow test sites and were limited to selected locations.

The southernmost sea ice test site was always free of ice, so it was used as an open water reference. The northernmost sea ice test site was fast ice, whereas the other two test sites had varying ice conditions. The average snow depth in the snow test sites was higher than the 30-year average and varied from 20 to 110 cm for dry snow. On 24 May, the snow test sites were free of snow, providing a bare ground-reference.

Five automatic weather stations were used to collect weather data in snow test sites 1, 3 and 4, and in sea ice test sites 3 and 4. The data included air temperature, wind speed and direction, and relative humidity. In sea ice test site 3 the weather station could be used only in March, due to drifting ice. During March 31 - April 6 the R/V Aranda weather stations collected weather data. Additional data is available from four coastal weather stations of the Finnish Meteorological Institute.

A data report of Finnish EMAC-95 airborne and ground-based results is under preparation [5]

EXPERIMENTAL RESULTS

Snow measurements

An example of the results for snow test sites is given in Figure 2. Brightness temperatures at 6.8/10.65 and 18.7 GHz, vertical and horizontal polarization, are shown for a portion of test site 2, consisting of agricultural areas and coniferous forest. The farmland area in Figure 2 is limited to the central portion and has low brightness temperatures for dry snow and snow-free terrain. The brightness temperature is higher for forested areas than for farmland. The distance between consecutive samples is 30 meters.

Sea ice measurements

One of our data analysis capabilities is demonstrated in Figure 3, showing a video image of the target and the measured brightness temperatures along the flight line (center line). Figure 3 shows the experimental values at 10.65 and 18.7 GHz, vertical and horizontal polarization. The capability of microwave radiometry to discriminate sea ice from open water is obvious.

ACKNOWLEDGMENTS

Airborne data collection with the HUTRAD radiometer system was funded by European Space Agency. Technology Development Centre funded modification of our radiometer system for accommodation aboard our Skyvan aircraft and, additionally, campaign organization and ground truth activities.

REFERENCES

1. Evert Attema, Mike Wooding, "EMAC Experimenters Handbook, Programme for 1995", ESA ESTEC, 1995.

2. Martti Hallikainen (editor), "ESA EMAC-94/95 Snow and Ice Thematic Group proposal", September 1993.

3. Martti Hallikainen, Evert Attema, Mike Wooding, "EMAC-95 Snow and Ice airborne campaign", Proc. IGARSS'95, pp. 1811-1813, 10-14 July 1995, Florence, Italy.

4. Martti Hallikainen, Martti Kemppinen, Kimmo Rautiainen, Jörgen Pihlflyckt, Janne Lahtinen, Tomi Tirri, Ilkka Mononen, Tuomo Auer, "Airborne 14-channel microwave radiometer HUTRAD", IGARSS'96, 27-31 May 1996, Lincoln, Nebraska, USA.

5. Martti Hallikainen et al., "Data report of EMAC'95 in Finland", unpublished

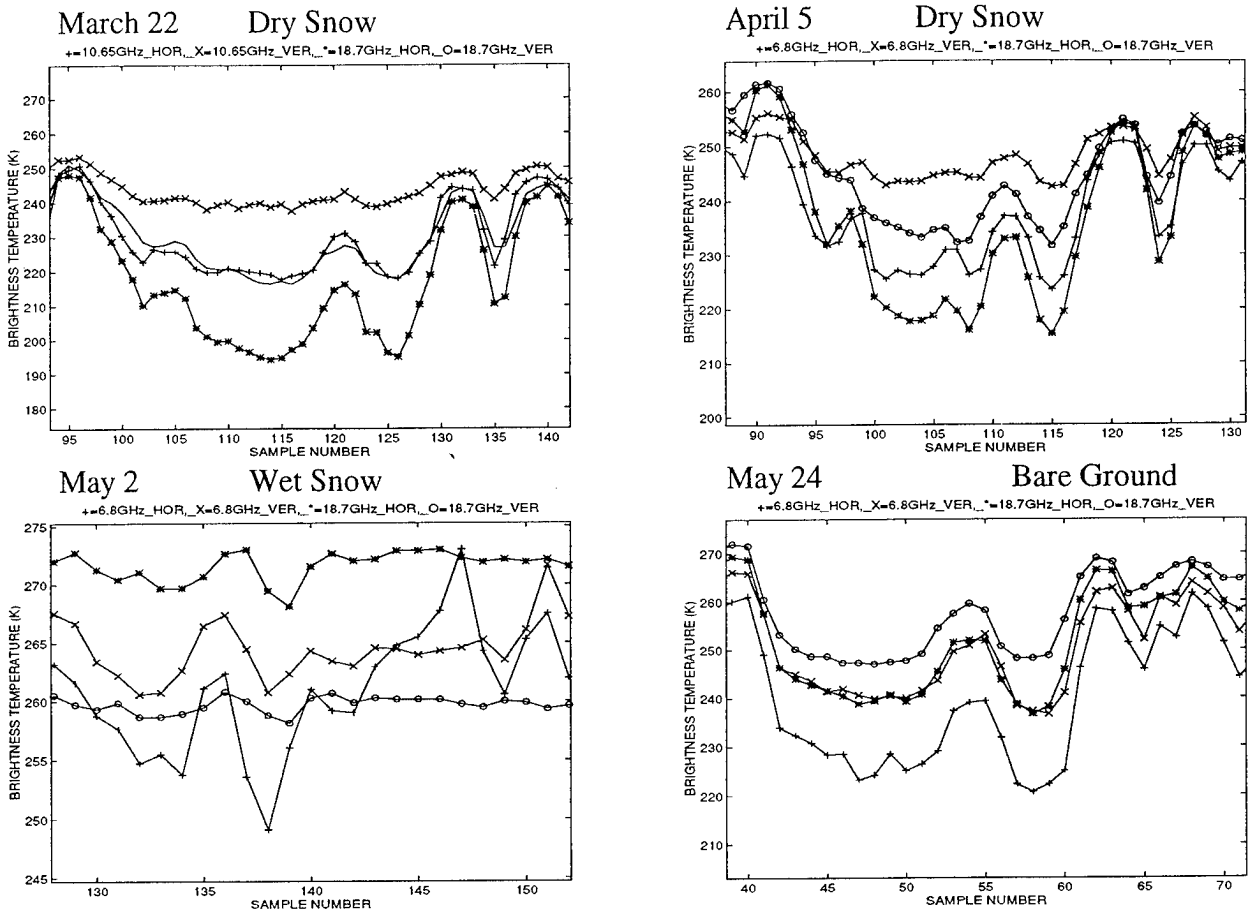


Figure 2. Experimental brightness temperatures at 18.7 and 6.8/10.65 GHz for farmland and forest. See text for details. Symbols: + 6.8/10.65 GHz H-pol., **X** 6.8/10.65 GHz V-pol, * 18.7 GHz H-pol, **0** 18.7 GHz V-pol

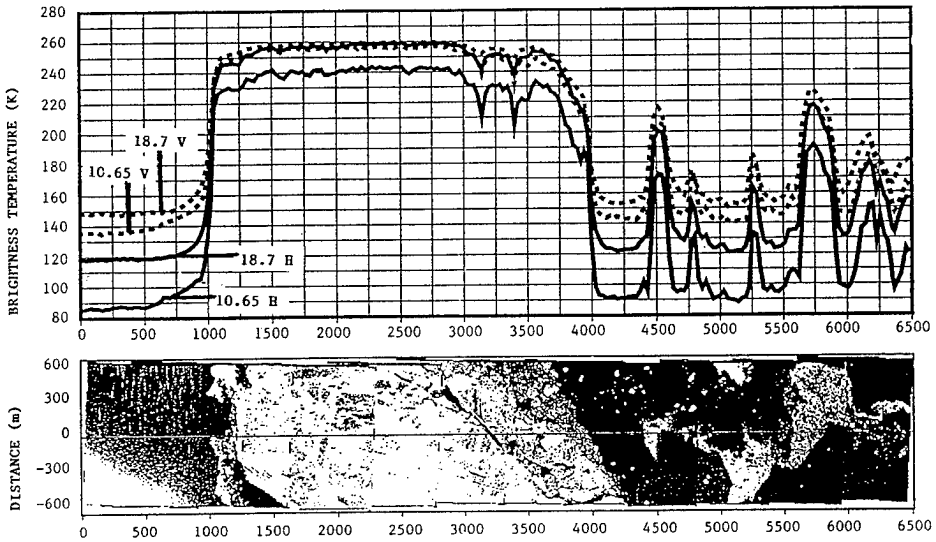


Figure 3. Video image of sea ice test site 3 on May 3 and measured brightness temperatures at 10.65 and 18.7 GHz, vertical and horizontal polarization, along the center line of the test site. Total distance is 6500 m and swath is 1200 m.

Estimation of Snow Water Equivalence Using SIR-C/X-SAR

*Jiancheng Shi and Jeff Dozier**

Institute For Computational Earth System Science (ICESS)
**School of Environmental Science and Management*
University of California, Santa Barbara, CA 93106, U.S.A
Tel:805-893-2309, Fax:805-893-2578, E-mail:shi@icess.ucsb.edu

ABSTRACT - In hydrological investigations, modeling and forecasting of snow melt runoff requires information about snowpack properties and their spatial variability. This study demonstrates the capabilities of the SIR-C/X-SAR, a multi-frequency and multi-polarization Spaceborne Synthetic Aperture Radar (SAR), on deriving snow water equivalence. In contrast to a single-polarization SAR, this study shows that SIR-C/X-SAR has the capabilities to estimate snow water equivalence when snow is dry.

INTRODUCTION

The study of snow has become an important area of research in the natural sciences, particularly in hydrology and climatology. Active microwave sensors are highly sensitive to the most snowpack parameters interested by hydrologists. They are not affected by weather, day-night capability, and have a spatial resolution compatible with the topographic variation in alpine regions. Furthermore, Space-shuttle image radar - C and X-band synthetic aperture radar (SIR-C/X-SAR) with three frequencies L-band at 1.25 GHz (wavelength 24 cm), C-band at 5.3 GHz (wavelength 5.6 cm), and X-band at 9.6 GHz (wavelength 3.1 cm) and with multi-polarization: polarimetry at L-band and C-band, and VV polarization at X-band provide much more information per pixel than single-polarization data [1][2].

Backscattering measurements from dry snow are affected by three sets of parameters:

- Sensor parameters which include frequency, polarization, and viewing geometry,
- Snow pack parameters which include snow density, depth, particle size, size variation, stickiness, stratification, and snow pack temperature,
- Under ground parameters which include dielectric and roughness parameters.

The relationships between the backscattering and snow water equivalence can be either positive or negative depending on above three parameters [3]. In order to estimate snow water equivalence, we need to separate the backscattering signals of snow volume from background. In this study, we demonstrate the principles and techniques of estimating snow water equivalence using the SIR-C/X-SAR imagery obtained during its first mission in April, 1994 over one of our test site - Mammoth Mt., California.

The Mammoth Mt., One of our test site for SIR-C/X-SAR investigations of alpine snow properties, is located at $37^{o}25'$N and $118^{o}45'$W on the eastern slope the Sierra Nevada. During SIR-C/X-SAR first mission in April, 1994, there were ten data-takes over this test site and we carried out an intensive field campaign to obtain snow properties for verification of the inversion models. Those ground measurements included both snowpack vertical profiles (temperature, density, wetness, gain size and size distribution) and snow survey (depth, wetness, and surface roughness) for each data-take. For radiometric and polarimetric calibration, we deployed triangle corner reflectors. For terrain correction of SAR image data, we used the Shuttle ephemeris information and digital elevation model (DEM) to generate the local incidence angle and the calibration factor maps for each data-take.

ESTIMATION OF SNOW DENSITY

Snow density has also great influence on radar backscattering. At high frequency such as C- or X-band , backscattering contribution from snow-pack with a same gain size is inversely related to snow density. This is because snowpack is a dense media where the coherent scattering properties result in the near-field effect when the wavelength is larger than the distance between scatters. Otherwise, the volume scattering albedo increases as the scatter size or size variation increases because Raleigh scattering theory explains that the scattering coefficient is proportional to the third power of the scatter radii for a given volume fraction. The studies [4][5] also showed that volume scattering albedo is directly correlated to particle size variation, since large particles play a more important role than smaller ones in the Raleigh scattering region even though large particles only constitute a very small fraction of the scatters.

At long wave length (L-band with 24 cm wave length) snow particle size has little effect on the backscattering signals from a dry snow cover. The scattering mechanism can be considered as a homogeneous dielectric layer (snow pack) over a rough surface. Figure 1 shows a numerical simulation of HH backscattering coefficients at L-band for comparison of a bare surface without and with dry snow cover. The solid

0-7803-3068-4/96$5.00©1996 IEEE

and dotted lines represent the backscatterings with and without snow cover. The same ground dielectric and roughness parameters were used in the simulation. We can see that the backscattering is much higher for snow covered condition, especially at large incidence angle. This is because when radar signal passes through a dry snowpack, there are several changes playing important roles in comparison to the interaction with a bare surface. First, it will result in a change of wave propagation constant because snowpack is a dense media. In other words, depending on snow density the wave length will shifted shorter so that the snow-ground interface becomes rougher. Secondly, it will also cause a change in incidence angle according to Snell's law. Thirdly, the dielectric contrast at snow-ground interface will be different with even the same ground without snow cover. The first factor is especially important at low frequency, such as L-band. At high frequency, however, the first factor becomes less important since the surface backscattering at snow-ground interface become independent of frequency according to Geometric Optics Model [6].

Based on the scattering mechanisms described above, we have developed a physical based inversion model for estimation of snow density and ground dielectric and surface roughness parameters using L-band co-polarization measurements. This algorithm includes four set of equations based on the simulated backscattering for most bare surface condition by IEM model:

$$\begin{aligned} &10\log 10(\sqrt{\sigma_t^{vv}}/T_{vv}+\sqrt{\sigma_t^{hh}}/T_{hh})=a_d(\theta_r)+b_d(\theta_r)\\ &\times 10\log 10\left(\sqrt{\sigma_t^{vv}\sigma_t^{hh}}/T_{vv}T_{hh}\right)+c_d(\theta_i)\\ &\times 10\log 10(\sigma_t^{vv}/T_{vv}^2+\sigma_t^{hh}/T_{hh}^2) \end{aligned} \quad (1)$$

$$\begin{aligned} &10\log_{10}\left[\frac{|\alpha_{vv}|^2+|\alpha_{hh}|^2}{\sigma_s^{vv}+\sigma_s^{hh}}\right]=a_{vh}(\theta_r)\\ &+b_{vh}(\theta_r)10\log_{10}\left[\frac{|\alpha_{vv}||\alpha_{hh}|}{\sqrt{\sigma_s^{vv}\sigma_s^{hh}}}\right] \end{aligned} \quad (2)$$

$$\sigma_s^{vv}=|\alpha_{vv}|^2\left[\frac{S_R}{a_{vv}(\theta_r)+b_{vv}(\theta_r)S_R}\right] \quad (3)$$

$$\frac{\sigma_s^{hh}}{\sigma_s^{vv}}=\frac{|\alpha_{hh}|^2}{|\alpha_{vv}|^2}\exp\left[a_r(\theta_r)+ks(b_r(\theta_r)+c_r(\theta_r)W)\right] \quad (4)$$

Where σ_t^{pp} and σ_{st}^{pp} are the total backscattering and the under ground surface backscattering coefficients. pp indicates polarization. α_{pp} is same as the small perturbation model and only depend on the incidence angle and dielectric contrast. T_{pp} is the power transmittivity at air-snow interface. $S_R=(ks)^2W$ is the under ground surface roughness parameter. W is the Fourier transform of the power spectrum of the surface correlation function. *a, b, c* are the coefficients that depend only on the incidence angle, differ in each equation above, and are derived from nonlinear regression analyses.

In (1), there is only one unknown - snow density since both refractive angle and transmittivity are only dependent on snow density. With estimated snow density from (1), we can estimate under ground dielectric constant using (2). Furthermore, (3) and (4) can be used to solve simultaneously for the surface roughness parameters, rms. height and surface power spectrum. Figure 2 shows an estimated snow density map obtained from the data-take 67.1 on April 13, 1994 The brightness is proportion to snow density.

ESTIMATION OF SNOW DEPTH

With estimated snow density, under ground dielectric and roughness parameters from L-band measurements, we can calculate the surface backscattering components at C-band and X-band. The inverse algorithm for estimation of snow depth and equivalent particle size, based on the first-order backscattering model, can be written as:

$$\sigma_t^{pp}=\sigma_v^{pp}+T_{pp}^2\sigma_s^{pp}\exp(-x) \quad (5)$$

Where $x=2\kappa_e d/\cos(\theta_r)$, d is snow depth and κ_e is snow volume extinction coefficient. σ_v^{pp} is the backscattering component from snow pack and can be written as

$$\begin{aligned} \sigma_v^{vv}&=0.75T_{vv}^2\omega\cos(\theta_r)[(1-\exp(-x))(1+R_{vv}^2\exp(-x))\\ &+2xR_{vv}^2\exp(-x)(\sin^2(\theta_r)-\cos^2(\theta_r))^2] \end{aligned} \quad (6)$$

$$\begin{aligned} \sigma_v^{hh}&=0.75T_{hh}^2\omega\cos(\theta_r)[(1-\exp(-x))(1+R_{hh}^2\exp(-x))\\ &+2xR_{pp}^2\exp(-x)] \end{aligned} \quad (7)$$

Where ω is volume scattering albedo. R_{pp} is reflectivity of snow-ground interface and can be calculated from refractive angle and dielectric contrast. In (6) and (7), there are only two unknowns - snow equivalent particle size and snow depth. With C-band VV, HH, and X-band VV backscattering measurements, we can solve snow depth and particle size simultaneously using two measurements. Figure 3 shows the estimated snow depth and equivalent particle size maps obtained from the data-take 67.1 on April 13, 1994 from top to bottom. The brightness is proportion to the depth and particle size, respectively.

CONCLUSION

SIR-C/X-SAR, a multi-frequency and polarization SAR system, has capabilty to estimate snow water equivalence. In this study, we derived an algorithm to measure snow water equivalence and tested on several SIR-C/X-SAR imagery. The results indicated that a multi-frequency and polarization SAR system is required for mornitoring spacial and temporal varibilities of snow water equivalence for hydrological and climatology studies.

REFERENCES

[1] van Zyl, J. J., H. A. Zebker, C. Elachi. Imaging radar polarization signatures: Theory and observation, *Radio Science,* 22(4):529-543, 1987.

[2] Evans, D. L., T. G. Farr, J. J. van Zyl, and H. A. Zebker. Radar polarimetry: Analysis tools and applications, *IEEE Trans. Geosci. Remote Sens.,* 26(6):774-789, 1988.

[3] Shi, J., J. Dozier and H. Rott, Modeling and observation of polarimetric SAR response to dry snow, in *Proceedings of IGARSS'93,* IEEE Catalog Number:93CH3294-6, vol. III, pp. 1042-1045, 1993.

[4] Tsang, L., Dense media radiative transfer theory for dense discrete random media with particles of multiple sizes and permittivities, in *Progress in Electromagnetic Research,* PIER 6, ch. 5, pp. 181- 225, 1992.

[5] Shi, J., R. E. Davis, and J. Dozier, Sterological determination of dry snow parameters for discrete-scatter microwave modeling, *Annals of Glaciology,* vol. 17, pp. 295-299, 1993.

[6] Ulaby, F. T., R. K. Moore, and A. K. Fung, in *Microwave Remote Sensing: Active and Passive,* vol. 2, Addison-Wesley, Reading MA, 1982.

Figure 1. *Comparison of the L-band HH backscattering coefficients for with and without snow cover .*

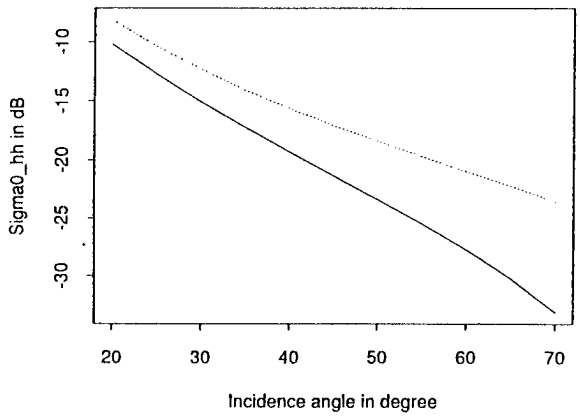


Figure 2. *SIR-C's L-band derived snow density map. Black regions are non-snow covered regions. The snow density value is proportion to image brightness.*

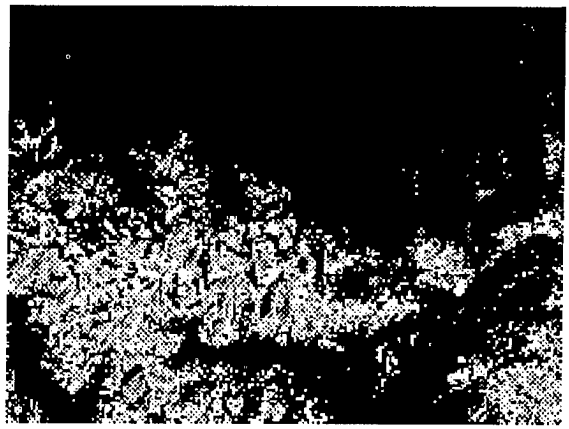
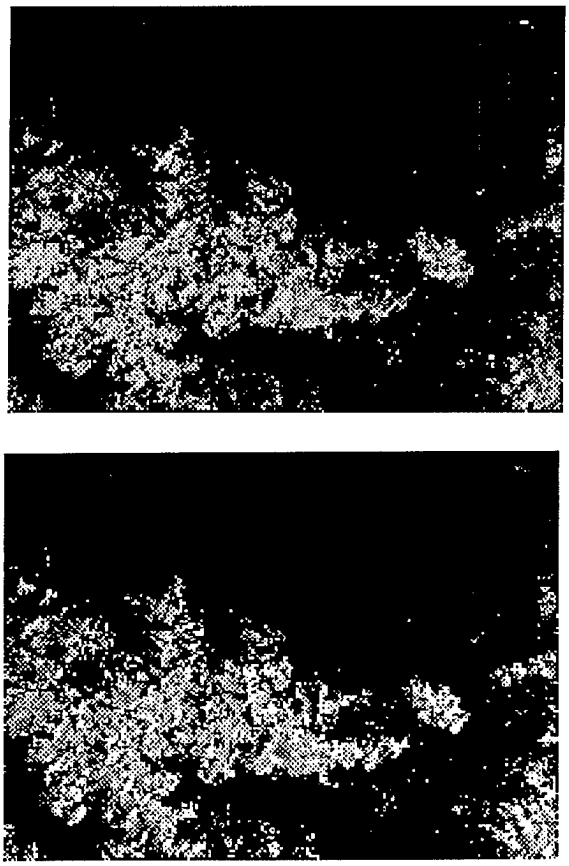


Figure 3. *SIR-C's C-band and X-SAR derived snow depth and particle size maps from top to bottom. Black regions are non-snow covered regions. The snow depth and particle size values are proportion to image brightness*



Estimation of snow water equivalent using passive microwave radiation data

Andrew Tait
CIRES/University of Colorado
CB 449, Boulder, CO 80309
Ph: (303) 4926115, Fax: (303) 4922468, E-mail: tait@nsidc2.colorado.edu

ABSTRACT

The principal objective of this study was to analyze, through regression modelling, the degree to which passive microwave radiation can be used to interpret snow water equivalent. The methodology reflects the importance of isolating phenomena other than snow water equivalent which may influence the microwave signal. These factors include: snow wetness; depth hoar; complex mountainous terrain; dense forest cover; and atmospheric precipitable water. It is shown that for a non-forested, non-mountainous terrain, the snow water equivalent of a pack with no depth hoar and no melting snow can be estimated with 95 percent confidence within plus or minus 44 mm. This error doubles when there is depth hoar present, and the relationship between snow water equivalent and brightness temperature reverses, as the scattering is greatest in shallow snowpacks with large depth hoar crystals. Significant results are obtained for melting snow conditions, despite theory indicating the contrary, by using only the night-time satellite passes. Dense forest cover impacts the microwave signal but appears not to completely mask the influence of the underlying snowpack. Lastly, it is difficult to collect ground data in regions of complex mountainous terrain which accurately represent snow conditions over a large area. However, some information can be obtained using high elevation SNOTEL sites from the Rocky Mountains.

Keywords: Passive microwave radiation, snow water equivalent, regression models.

INTRODUCTION

It is estimated that about three quarters of the world's terrestrial water reserves, used mainly for municipal and agricultural purposes, are locked in snow and ice. A detailed knowledge of the volume of potential water present in snowpacks is therefore vital. In addition, the climatic role of snow cover is extensive. Snow cover and depth are often indicators of the type and frequency of weather systems incident upon a region, and long-term records of these snowpack variables are often used to study the climate and climatic change of a region. Also, there is evidence that snow cover itself modifies regional weather and climate.

Several large areas of the globe, such as Siberia and Canada, contain sizable gaps in the spatial coverage of climate stations. Also, methods of snow measurement often vary considerably between, and sometimes within countries. Such disparities in data collection may be highly problematic for large-scale climatological or hydrological analyses. For these reasons, remotely sensed snowpack estimates, calculated at standard spatial and temporal resolutions over the entire globe, are an important data resource.

PASSIVE MICROWAVE-DERIVED SNOW DATA

There has been considerable research regarding the microwave signatures of snow, and the applicability of satellite remote sensors for estimating snow properties[4]. Results show that although ideally there is a distinct relationship between snow water equivalent and microwave brightness temperature, interpretation is often severely hampered by local variability.

Interpretation difficulties arise because physical characteristics of the snowpack affect the amount of radiative scattering and hence the intensity of the emitted microwave radiation. The principal impacting characteristics are snow wetness and grain size, which often vary according to geographic location, time of day, and season. In addition, variables such as the land cover, especially the presence of dense forest cover and highly variable mountainous terrain, may also influence the snow cover and/or the recorded brightness temperature. Therefore, in order to understand and interpret the complex signatures of snow, proper characterization of the snowpack and ground surface is required.

Also, high frequency radiation (greater than around 30 GHz) may be affected by the presence of atmospheric water vapor and clouds[1]. Studies over ocean have shown that microwave radiation can be used to estimate atmospheric precipitable water and water vapor.

The principal objective of this study was to analyze the degree to which passive microwave radiation can be used to interpret snow water equivalent. The methodology of this study reflects the importance of isolating, and then incorporating as much of the variability in the microwave

0-7803-3068-4/96$5.00©1996 IEEE

signal as possible caused by phenomena other than snow water equivalent. These include: snow wetness; presence of depth hoar; dense forest cover; complex mountainous terrain; and atmospheric precipitable water.

RESULTS AND DISCUSSION

The globe was divided into four highly simplistic regions based on physiographic characteristics :

- **Region 1)** Non-complex terrain with no dense forest cover;
- **Region 2)** Non-complex terrain with dense forest cover;
- **Region 3)** Complex terrain with no dense forest cover;
- **Region 4)** Complex terrain with dense forest cover.

In addition to the above physiographic classification, the analysis was further sub-divided according to the state of the snowpack. When liquid water is present the snowpack acts more as an emitting medium in the microwave wavelengths, whereas it acts as a scatterer when the snow is dry. Wet snow, therefore, often results in an underestimation of the water equivalent of snow. A reasonable indicator of the presence of wet snow is a daily surface air temperature greater than 0°C [5]. Using this cutoff, presence or absence of wet snow was computed.

Large faceted depth hoar crystals may increase scattering of microwave radiation to a point where snow water equivalent and snow depth estimates are grossly exaggerated. The large crystals are the result of a positive temperature gradient greater than around 10°C/m existing from the ground-snow interface to the snow-air interface. Once depth hoar crystals are present, they remain for the rest of the snow season.

In order to estimate the location of depth hoar snow, two assumptions were made. Firstly, the temperature at the ground-snow interface was assumed to be near 0°C. Secondly, the presence of depth hoar was assumed to be generally found in regions where the snowpack has a depth of one meter or less. This is a gross assumption as no information was available regarding the depth of snow in each pixel. However, it is considered a reasonable starting point and was changed slightly during the model optimization scheme. Using modelled surface temperature data (from NOAA/CDC), a depth hoar criterion was derived given the following conditions:

1) Surface air temperature is less than -10°C (this value is derived from the 10°C/m temperature gradient stipulation, assuming snow depths of less than around 1 m);
2) The average temperature of the previous ten days is less than -10°C (this sets the condition that there has been an extended cold period, enough to produce large depth hoar crystals);
3) Once the above two conditions have been met, the region is considered to have depth hoar snow for the remainder of the snow season.

It must be noted that the above methods of identifying wet snow and depth hoar are extremely simplified and use modelled temperature data. Some concern exists regarding the quality of the NMC modelled surface temperature data in areas such as Alaska, which have a low density of climate station coverage. However, as a first approximation, and as input to a snow water equivalent algorithm which previously had no such distinctions, the methodology is warranted. Further development of these approximations may serve to improve the accuracy of the model.

The physiographic regions 1 through 4 were each sub-classified according to the following criteria, resulting in sixteen separate categories :

- **Snow State 1)** No depth hoar or melting snow present;
- **Snow State 2)** No depth hoar, but melting snow present;
- **Snow State 3)** Depth hoar, but no melting snow present;
- **Snow State 4)** Both depth hoar and melting snow present.

The method of analysis performed on each of the sixteen categories was one of regression modelling of snow water equivalent against brightness temperature. Atmospheric precipitable water was also inputed as an independent variable. A stepwise model is used to identify the combination of variables which best accounts for the variance in the snow data. Brightness temperature data from the SSM/I (Special Scanner Microwave Imager) instrument are available for both ascending and descending orbits. Only the ascending orbital data were used, however, as these data were recorded in the morning (DMSP F8) when there was little or no solar heating, reducing some of the problems associated with snow melt. The 19, 37, and 85 GHz channels, both horizontal and vertical polarizations, were experimented with as independent variables in the regression analyses.

The results of the regression analysis for the first category, representing the simplest snow and surface conditions obtained through the regionalization process (i.e. non-forested non-mountainous terrain, with no melting snow and no depth hoar), are shown in Figure 1. The 95% confidence interval associated with the best-fit regression line is plus or minus 44 mm. Interestingly, of all the combinations of brightness temperature variables experimented with, 19_H - 37_H (H = Horizontal Polarization) produced the smallest confidence interval. This is the same combination of channels and polarization used by Chang[2], as well as several other investigators. The slope of the line is 3.1 mm/K, which is similar to the Chang value of 4.8 mm/K.

The optimum combination of microwave channels

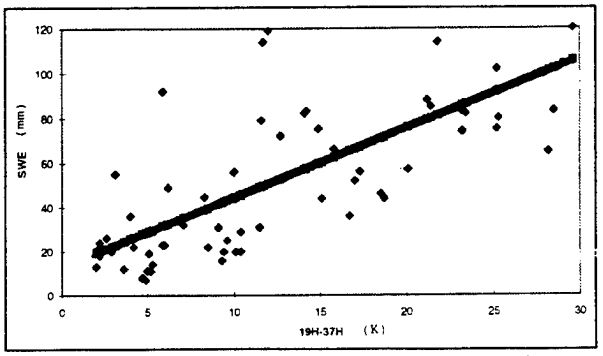


Figure 1 : Best-fit regression line for category 1.

and polarizations varies depending upon the type of snow and surface conditions. So too does the associated regression 95% confidence limits. When depth hoar is modelled, the error value doubles. It is concluded that further parameterization of depth hoar snow is required before this error can be reduced. The depth hoar categories need to be sub-classified according to the depth of snow and the relative depth of the layer of depth hoar crystals. This may be accomplished by including both surface air temperature data and accumulated precipitation data in the depth hoar regionalization scheme. Also, some work has been performed using AVHRR data to estimate mean snow grain size[3].

Division of the data according to a threshold air temperature for melting snow resulted in statistically significant, and different models of snow water equivalent for both melting and non-melting snow. This is surprising as theory suggests that in the presence of liquid water, the dry snow - brightness temperature relationship dissolves due to absorption and re-emission of the radiation. Because a significant relationship was derived for melting snow conditions, it is suggested that the scattering properties of the snowpack are dominant. This conclusion is only valid if the liquid water has re-frozen and thenceforth acts as a scatterer rather than an emitter. This is likely the case as the brightness temperature data were chosen such that only the morning passes (ascending orbits for DMSP F8) were used.

Both an underestimation and an overestimation of snow water equivalent is present in the forest cover categories. It is argued that this is likely the result of different tree densities, yet further investigation is still required. It is suggested that this physiognomic variable should be incorporated into future analyses.

There are three main factors which serve to inflate the 95% confidence interval in areas of complex mountainous terrain. Firstly, there is a limit of around 250 mm beyond which microwave radiation no longer accurately models snow water equivalent. This is due to a finite penetration depth for microwave radiation equal to approximately 10 to 100 times the wavelength. Secondly, not all climate station locations are representative of the average snow conditions of the SSM/I pixel which encompasses that site. This factor is reduced somewhat by using only high elevation locations, but the error is not totally eliminated. Lastly, inclusion of slope and aspect data as terrain-type discriminators may reduce the variability associated with varying incidence angle.

CONCLUSIONS

The statistical significance of this product together with the inclusion of an error statistic, result in a marked improvement upon the experimental data set originating from the work of Chang[2]. The previous model used a single equation to estimate snow water equivalent for all terrain types and for all snow conditions. It has been shown in this study that different models are required for different regional categories, and in almost all cases significant results can be generated. Because the errors associated with some of the category models are very large, however, especially in regions of complex terrain and depth hoar snow, interpretation of these passive microwave-derived snow data must always include an analysis of the associated regression confidence intervals. In this way, a level of confidence can be gained which is vital if the data are to be used in future studies.

REFERENCES

[1] Chang, A.T.C and T.T Wilheit, "Remote sensing of atmospheric water vapor, liquid water, and wind speed at the ocean surface by passive microwave techniques from the Nimbus 5 satellite". Radio Science, 14(5), pp 793-802, 1979.

[2] Chang, A.T.C; J.L Foster and D.K Hall, "Nimbus-7 SMMR derived global snow cover parameters". Annals of Glaciology, 9, pp 39-44, 1987.

[3] Dozier, J.; S.R Schneider; and D.F McGinnis, "Effect of grain size and snowpack water equivalence on visible and near-infrared satellite observations of snow". Water Resources Research, 17(4), pp 1213-1221, 1981.

[4] Foster, J.L; D.K Hall; A.T.C Chang and A. Rango, "An overview of passive microwave snow research and results". Reviews of Geophysics and Space Physics, Vol. 22(2), pp 195-208, 1984.

[5] Tait, A.B and R.L Armstrong, "Validation of SMMR satellite-derived snow depth with ground-based measurements. International Journal of Remote Sensing. In Press, 1995.

Scattering and Emission From Dry Snow in the Range 35–140 GHz

Saibun Tjuatja[1], Adrian K. Fung[1], and Josefino C. Comiso[2]

[1]Wave Scattering Research Center, Department of Electrical Engineering
University of Texas at Arlington, Box 19016, Arlington, TX 76019, U.S.A.

[2]Laboratory for Oceans, Code 971
NASA Goddard Space Flight Center, Greenbelt, MD 20771, U.S.A.

Phone: (817) 273-3974 Fax: (817) 273-3443 Email: eetjuatj@utacnvx.uta.edu

Abstract – Scattering and emission models for an irregular layer of dense inhomogeneous medium is developed and applied in the analysis of dry snow scattering and emission in the range 35-140 GHz. The models are developed based on the matrix doubling formulation, and accounts for full incoherent multiple scattering inside the snow layer. The effects of close spacing and first order coherent interactions between scatterers inside the snow layer are included in the model via a dense medium phase matrix. The dense medium phase matrix is derived using the extended concept of three-dimensional antenna array theory which accommodate randomly located scatterers. The final expression for the dense medium phase matrix differs from the conventional (sparse medium) one in two major aspects in that there is an amplitude and a phase correction.The rough interfaces of the air-snow and snow-ground (or snow-ice) boundaries are modeled using the IEM rough surface model. Emission model predictions agree well with field measurements reported in the literature. Backscattering calculations from the theory are compared with measurements from field measurements of dry snowpack. Predictions from such a theory agree well with the measured data.

INTRODUCTION

In the past few decades, much investigation has been done on both the theoretical and the experimental aspects of electromagnetic wave propagation and scattering in a random medium consisting of a distribution of scatterers. These studies are useful for many applications such as in microwave remote sensing of snow and sea ice. Many previous studies on modeling have assumed that the scatterers are in the far field of one another, leading to the use of independent scattering approximation. However, this approximation breaks down when the scatterers are correlated with one another. The far-field approximation is thus not applicable in an electrically dense medium where there is more than one scatterer within the distance of a wavelength.

In this study, scattering and emission models for an electrically dense medium are developed. Dense medium effects, such as multiple incoherent scattering, close spacing, and first order coherent interaction effects, are accounted for in the model via the modified dense medium phase matrix. The dense medium phase matrix is incorporated into the modified radiative transfer formulation to study radar backscatter and emission from dry snow layers at 35–140 GHz. The set of radiative transfer equations are solved using the matrix doubling technique [1,2]. Descriptions of the model and the dense medium phase matrix are given in the following section. Calculation results are provided in the subsequent section.

SCATTERING AND EMISSION MODELS FOR A SNOW LAYER

The model geometry is shown in Fig. 1 where the lower half space is either sea ice or soil. Note that the snow layer is an electrically dense inhomogeneous medium. The modified radiative transfer equation is solved within the inhomogeneous layers subject to the boundary conditions at the upper, and lower randomly rough boundaries. As opposed to the conventional far field phase matrix, the dense medium phase matrix which accounts for close spacing between scatterers and first-order coherent interaction is utilized in the model. The elements of the phase matrix are also functionally dependent on the size of scatterer, dielectric properties of scatterer, background medium, frequency, polarization states, and volume fraction of the scatterers. The formulation of the dense medium phase matrix is given in the following subsection. To account for the rough interface scattering effects, the IEM surface scattering model [2] is integrated into the snow layer scattering and emission models via the generalized boundary relation. In addition to the effects of boundary roughness, the generalized boundary relation also accounts for the coupling effects between an inhomogeneous layer and its rough boundaries. Detailed formulation of the generalized boundary relation is given in [2]. Thus, the snow layer scattering and emission models account for volume scattering, surface scattering by the interfaces, and surface-volume interactions simultaneously.

Dense Medium Phase Matrix

The phase matrix for dense medium is given by [3]

$$\bar{P} = \langle|\Psi|^2\rangle_n \bar{S} = \langle|\Psi|^2\rangle_n \begin{bmatrix} S_{VV} & S_{VH} \\ S_{HV} & S_{HH} \end{bmatrix} = \begin{bmatrix} P_{VV} & P_{VH} \\ P_{HV} & P_{HH} \end{bmatrix} \quad (1)$$

where $\langle|\Psi|^2\rangle_n$ is the dense medium phase correction factor needed to account for the first order coherent interaction between scatterers. The phase correction factor $\langle|\Psi|^2\rangle_n$ is given by

0-7803-3068-4/96$5.00©1996 IEEE

$$\langle|\Psi|^2\rangle_n = \frac{1-e^{-k_{si}^2\sigma^2}}{d^3} + \frac{e^{-k_{si}^2\sigma^2}}{d^3}\sum_{q=1}^{\infty}\frac{(k_{si}^2\sigma^2)^q}{q!}\cdot \left[\left(\sqrt{\frac{\pi}{q}}\left(\frac{l}{d}\right)\right)^3 \exp\left(\frac{-k_{si}^2\sigma^2}{4q}\right) - a(k_x)a(k_y)a(k_z)\right] \quad (2)$$

where $k_{si} = |\vec{k}_s - \vec{k}_i| = |\hat{x}k_x + \hat{y}k_y + \hat{z}k_z|$; $\vec{k}_s$ and $\vec{k}_i$ are the propagation vectors in the scattered and the incident directions respectively; σ is the standard deviation of the scatterer position deviation from its deterministic position in the three-dimensional scatterer array; d is the mean distance between scatterers; and l is the correlation length of one scatterer position deviation from its deterministic position to the other scatterer position deviation in the array; and

$$a(k_r) = \sqrt{\frac{\pi}{q}}\left(\frac{l}{d}\right)\exp\left(\frac{-k_r^2 l^2}{4q}\right)\mathrm{Re}\left\{\mathrm{erf}\left(\frac{(qd/l) + jk_r l}{2\sqrt{q}}\right)\right\}. \quad (3)$$

σ, l, and d are determined by the physical properties of the inhomogeneous medium, such as scatterer size and volume fraction. The average distance between scatterers is related to the scatterer volume fraction v_f and scatterer radius a by

$$d = a\left(\frac{4\pi}{3v_f}\right)^{1/3}. \quad (4)$$

In (1), $\bar{S}$ is the phase matrix of a single scatterer which includes amplitude correction due to close spacing of scatterers in a dense medium. Detailed derivation of $\bar{S}$ is provided in [2].

MODEL ANALYSIS

Backscattering From a Dry Snow Layer

The comparisons between model calculations and field measurements from dry snowpack given in Ulaby et al. [4] at 95 GHz and 140 GHz are provided in Fig. 2 and Fig. 3 respectively. Due to metamorphism, ice particles near the top of a natural snow layer are usually smaller than those near the bottom [5]. Moreover, penetration depth will change with frequency. Thus, a higher effective size is chosen for the 95 GHz case (a = 0.24 mm) compared to those at 140 GHz (a = 0.22 mm). Since natural ice particles in the snow layer are irregular in shape and different in size, and are randomly oriented as well, σ, the standard deviation of the variations from mean position, should be large. In this case, it is chosen as σ = 0.55d for the 95 GHz case and 0.50d for 140 GHz since at longer wavelength of 95 GHz, the wave is expected to see more variations in size. The correlation length l of snow samples has been reported in the literature [6] and is found to be within 0.05 mm (for fine snow grain sample) and 0.3 mm (for coarse snow grain sample). In the model predictions, l is chosen to be 0.12 mm for ice particles of radius 0.24 mm, and 0.11 mm for particles of radius 0.22 mm. The permittivity of ice particle is estimated from Appendix E of Ulaby et al. [7].

Emission From Snow Covered Sea Ice

The physical parameters given in [8] are used in the emission calculations. The snow layer thickness is 8 cm; average snow grain radius is 0.5 mm; and snow layer volume fraction is 30%. The electrical parameters for snow and sea ice were determined using the formulas and tables provided in Appendix F of [7]. Fig. 4 shows the emissivity of sea ice with dry snow cover at 10, 37, and 90 GHz. Note that model predictions show a higher emissivity (brightness temperature) of the snow-covered sea ice at 37 GHz than at 10 GHz. The emissivity decreases as frequency increases from 37 GHz to 90 GHz. This frequency behavior have also been observed in field experiments. As snow volumetric water content decreases, the total emissivity decreases due to an increase in snow albedo. Also, The separation between V and H polarizations decreases as snow volumetric water content decreases. Fig. 5 shows the emissivity of the snow covered sea ice with the snow cover grain size (radius) of 1.0 mm. As snow grain size increases from 0.5 mm to 1 mm, the snow layer albedo increase, resulting a decrease in the total emissivity. Note that the variation of snow parameters affects the emissivity more at higher frequencies.

SUMMARY

Scattering and emission models for a snow layer which accounts for dense medium effects have been developed using the extended concept of three-dimensional antenna array theory which accommodate randomly located scatterers. Emission model predictions agree well with field measurements reported in [8]. Backscattering calculations from the theory are compared with measurements from field measurements of dry snowpack. Predictions from such a theory agree well with the measured data.

ACKNOWLEDGEMENTS

This work is supported by the Office of Naval Research under ONR Grant N00014-90-J-1329. The computing resources are provided by NASA Goddard Space Flight Center.

REFERENCES

[1] S.Tjuatja, A.K.Fung, and M.Dawson, "An Analysis of Scattering and Emission from Sea Ice," *Remote Sensing Review*, Vol. 7, pp. 83-106, 1993.

[2] A.K.Fung, *Microwave Scattering And Emission Models And Their Applications*, Artech House, MA, 1994.

[3] H.T.Chuah, S.Tjuatja, A.K.Fung, and J.W.Bredow, "The

Volume Scattering Coefficient of A Discrete Random Medium," Submitted for publication.

[4] Ulaby, F.T.,Haddock, T.F.,Austin, R.T., and Kuga, Y., "Millimeter-wave radar scattering from snow: Comparison of theory with experimental observation," *Radio Science*, vol. 26, pp. 343-351, 1991.

[5] Stiles, W.H., and Ulaby, F.T., "The active and passive microwave response to snow parameters: Part 1 - wetness," *J. Geophysics. Res.*, vol. 85, pp. 1037-1044, 1980.

[6] Vallese, F., and Kong, J.A. "Correlation function studies for snow and ice," *J. Appl. Phys.*, vol. 52, pp. 4921-4925, 1981.

[7] F.T.Ulaby, R.K.Moore, and A.K.Fung, *Microwave Remote Sensing*, Vol. 3, Artech House, Norwood, MA, 1986.

[8] T.C.Grenfell, J.C.Comiso, M.A.Lange, H.Eicken, M.R.Wensnahan, "Passive microwave observations of the Weddell Sea during austral winter and early spring," *J. Geophy. Res.*,Vol. 99, No. C5, pp. 9995-10010, May 15, 1994.

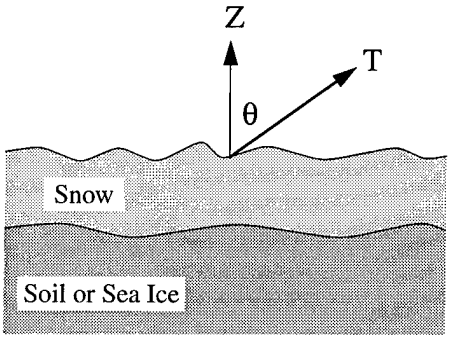


Figure 1. Geometry of the snow layer model.

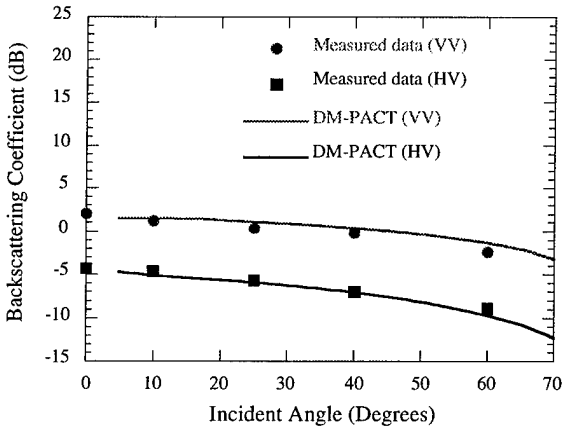


Figure 2. Backscattering from dry snow layer over soil at 95 GHz.

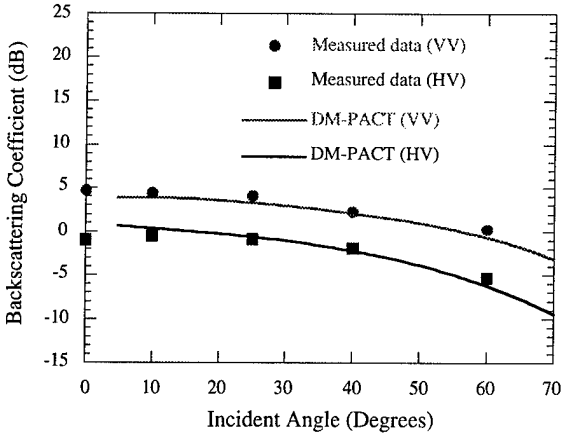


Figure 3. Backscattering from dry snow layer over soil at 140 GHz.

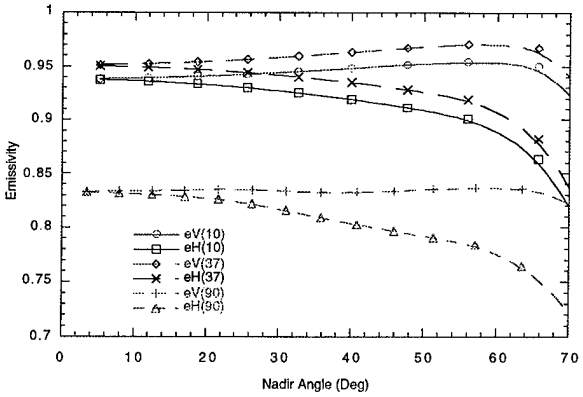


Figure 4. Emissivity of the snow-covered sea ice with dry snow cover.

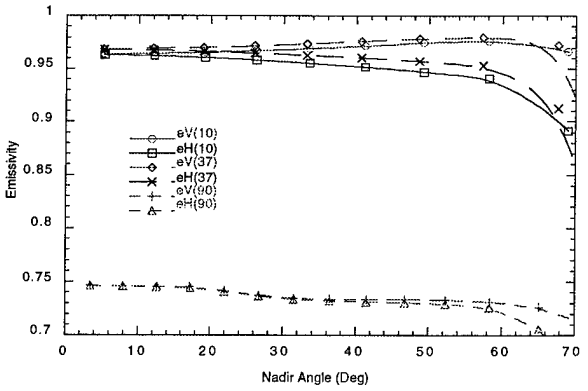


Figure 5. Emissivity of the snow-covered sea ice with snow grain size (radius) of 1.0 mm.

Observations of Snow Crystal Shape in Cold Snowpacks Using Scanning Electron Microscopy

J.L. Foster, D.K. Hall and A.T.C. Chang
NASA Goddard Space Flight Center, Code 974
Hydrological Sciences Branch
Laboratory for Hydrological Sciences
Greenbelt, MD
phone: 301-286-7096, fax: 301-286-1758
e-mail: jfoster@glacier.gsfc.nasa.gov

A. Rango, W.Wergin and E. Erbe
U.S. Department of Agriculture, Hydrology Laboratory
Agricultural Research Service
Beltsville, MD

INTRODUCTION AND BACKGROUND

Microwave emission from a layer of snow over a ground medium consists of contributions from the snow itself and from the underlying ground. Both contributions are governed by the transmission and reflection properties of the air-snow and snow-ground boundaries and by the absorption/emission and scattering properties of the snow layer. Presently, a number of microwave algorithms are available to evaluate and retrieve snow cover and snow depth for specific regions and specific seasonal conditions. These algorithms have been derived from research using a combination of microwave sensors on-board sattelites, aircraft and trucks, as well as in-situ field studies. However, most of the attention in algorithm development has been directed towards the effects of snow crystal size in scattering microwave energy, but crystal size alone does not account for all of the scattering or energy redistribution. Relatively little effort has been given to the role that crystal shape plays in this regard.

The goal of this study is to determine how both the shape and size of snow crystals affects the response of microwave radiation emanating from below and within the snowpack, and to use this information to produce more reliable snow cover and snow depth algorithms.

The lack of precise information about snow crystal size and shape is compensated for by using an average size and an assumed shape in the radiative transfer equations used to calculate energy transfer through the snowpack. If the crystals differ significantly from the averages and assumptions, then poor snow water equivalent (SWE) values will result. A better understanding of the physics of snow and how microwave energy interacts with snow crystals is needed to make the snow/microwave algorithms more reliable.

A cryosystem has been developed [1] to preserve snow crystals collected in the field so that they can be imaged using low-temperature scanning electron microscopy (SEM). This technique uses liquid nitrogen as a coolant and special pre-cooled dewars to store and transport the snow crystal samples. The undisturbed crystals can then be studied in a laboratory setting.

The use of SEM to gather information on snow grain size, shape and bonding will be valuable for improving radiative transfer models, which are used to calculate the microwave response, and thus, for refining algorithms used to derive snow cover and depth.

STUDY AREA AND EXPERIMENT SET-UP

In the microwave region, wet and dry snow snow behave very differently. The emphasis of this study is on dry snow conditions. This is why the study areas selected are located either in high elevation or high latitude areas, or were sampled during the snow accumulation period. Snow crystal samples have been collected and examined on the North Slope of Alaska, in the Rocky Mountains of Colorado and Wyoming, and in the Appalachian Mountains of West Virginia. Samples from Alaska were collected in April of 1995, and samples from West Virginia, Wyoming and Colorado were collected in March of 1996. A feature of cold, dry snowpacks is the rapid formation of depth hoar crystals when temperature gradients exceed 10° C/m [2]. Depth hoar crystals are typically very large (> 1 mm in diameter), loosely bonded, multifaceted, and often hollow (Fig. 1). These large, irregularly shaped grains are very effective scatters of microwave radiation in the 35-95 GHz range, and hence their presence may result in microwave brightness temperatures (TB) that are anomalously low.

0-7803-3068-4/96$5.00©1996 IEEE

A steep, negative temperature gradient occurs in the snowpack of the Arctic Coastal Plain [3]. Even though the winter air temperatures can be lower than -45° C, snow/soil interface temperatures will be much higher due to the insulating properties of the snow. For example, in interior Alaska, there can be a 40° C difference in temperature between the snow/air and snow/soil interfaces because continuous heat flux from the soil maintains the soil/snow interface temperatures between -3 and -5° C [4]. Pressure gradients, associated with the temperature gradients, cause water vapor to diffuse from areas of higher to areas of lower pressure and from warmer to colder parts of a snowpack. As vapor diffuses onto the snow crystals they increase in size in a direction opposite to that of the vapor pressure gradient. In general, the larger the gradient, the larger the crystal. The snow crystals grow in size from the bottom of the snowpack (soil/snow interface) towards the top of the pack (snow/air interface). Although temperature differences between the soil/snow and snow/air interfaces in Alaska are higher than in the contiguous states, gradients can still be sufficiently high to produce large depth hoar crystals.

Snow samples from each of the study areas were collected from snow pits. A specially fabricated snow sample holder was covered with a thin layer of methyl cellulose solution (Tissue Tek) and placed near the snow pit wall. Snow crystal samples from a selected layer of the snowpack were gently dislodged from the pit wall and collected on the surface of the sample holder (Fig. 2). After obtaining a visible accumulation of snow crystals in this manner, the holder was plunged into a styrofoam resevoir containing liquid nitrogen (LN2) at -196° C and transferred to a square profile, brass tube for low temperature storage during shipping. Once filled with sample holders, the brass tubes are placed in dry shipping dewars at liquid nitrogen temperatures and shipped to Beltsville, Maryland [U.S. Department of Agriculture (USDA) SEM laboratory] for analysis. The Alaskan samples were in transit to Beltsville, for seven days, but the dewars maintained a temperature of -196° C, and the samples generally appeared to be undisturbed upon observation (for more information on this technique see [5]).

RESULTS AND DISCUSSION

Because the winter 1996 data have not been analyzed as of this writing, these results pertain only to the data collected in Alaska. Referring again to Fig. 1, these crystals are typical of the hollow, angular nature of depth hoar observed in Alaska. They were collected at the base of the snowpack on the North Slope of Alaska. Crystals sampled from the mid layer of this snowpack, though smaller in size, also portray this intricate design.

Depth hoar crystals may vary in size and shape, not only from one area to another within the same region, but also from one season to another, and are vastly different from the spherical-shaped, constant-sized crystals assumed in the Chang et al. (1987) snow/microwave algorithm [6]. Table 1 shows the shape versus size distribution of the snow crystals sampled for the Alaska study.

A question that needs to be addressed is, how much of a difference do the large, multifaceted depth hoar crystals make compared to the same-sized spherical crystals in assessing the SWE of a given area? Reference [7] shows the effects of shape on extinction efficiency, which can be used as a measure of the effectiveness of different shaped scatterers (Fig. 2). Here, extinction efficiency is the extinction cross section divided by the physical (particle size) cross section.

This figure shows that the form of the curves for the sphere and the cylinder are similar, but that for a cylinder the curve is shifted to the left compared to that of the sphere. Therefore, based on this result, it appears that the extinction response for a cylinder is somewhat higher, though not significantly different from that of a sphere if the size parameter is less than about 6. So it may be that different shapes do not play an important role in the degree to which microwave energy is scattered.

Another question that needs to be more thoroughly investigated is, how effective are aggregates of snow crystals (clusters or chains of crystals which can be over 10 mm in diameter) in scattering microwave energy? The scattering cross section and the number of facets is greatly increased for clusters compared to individual crystals. It is known that large crystals (> 1 mm in diameter) are very effective scatterers of microwave radiation, but the behavior of clusters, in terms of their extinction efficiency, is poorly known.

FUTURE PLANS

To test whether or not the above modeling result is valid, field experiments will be conducted to look at the microwave response of different sized and shaped snow crystals. A portable (hand-held) radiometer will be used for this purpose. This work, scheduled for the winter of 1996 in Wyoming, is contingent on the availability of a calibrated radiometer. In addition, a laboratory experiment is planned, for a cold room environment, to look at the microwave response of various depth hoar crystals having approximately the same size.

The effects of crystal size on microwave response will be compared to the effects found for snow crystal shape. If the shape is demonstrated to contribute to microwave response, then a shape model (models) will be developed and employed to better account for the transfer of radiation from the ground through the snowpack to the microwave sensor.

REFERENCES

1. Wergin, W.P., A.Rango and E.F. Erbe, "Observations of snow crystals using low-temperature scanning electron microscopy", Scanning, Vol. 17, 41-49, 1995.

2. Armstrong, R., A.T.C. Chang, A. Rango and E. Josberger, "Snow depths and grain size relationships with relevance for passive microwave studies". Annals of Glaciology, Vol.17, 171-176, 1993.

3. Hall, D.K.,"Influence of depth hoar on microwave emission from snow in northern Alaska". Cold Regions and Science Technology, Vol. 13, 225-231, 1987.

4. Trabant, D. and C.S. Benson, " Field Experiments on the development of depth hoar". Geological Society of America Memoir, No. 135, 309-322, 1972.

5. Rango, A. W.P. Wergin and E. F. Erbe, "Snow crystal imaging using scanning electron microscopy, Part II - metamorphosed snow". Hydrological Sciences Journal (in press).

6. Chang, A.T.C., J.L. Foster and D.K.Hall, "Nimbus-7 SMMR derived global snow cover parameters". Annals of Glaciology, Vol. 9, 39-44, 1987.

7. Kerker, M., The Scattering of Light. Academic Press, New York, NY, 27-307 pp, 1969.

TABLE 1

SIZE VS SHAPE OF SNOW CRYSTALS IN ALASKA

shape	size (in diameter) < 1 mm	1 -5 mm	> 5 mm
hollow/angular (bottom layer)		x	x
irregular (throughout)	/	x	
rounded (top layer)	x	/	

x = often observed
/ = sometimes observed



Figure 1. SEM image of depth hoar crystals.

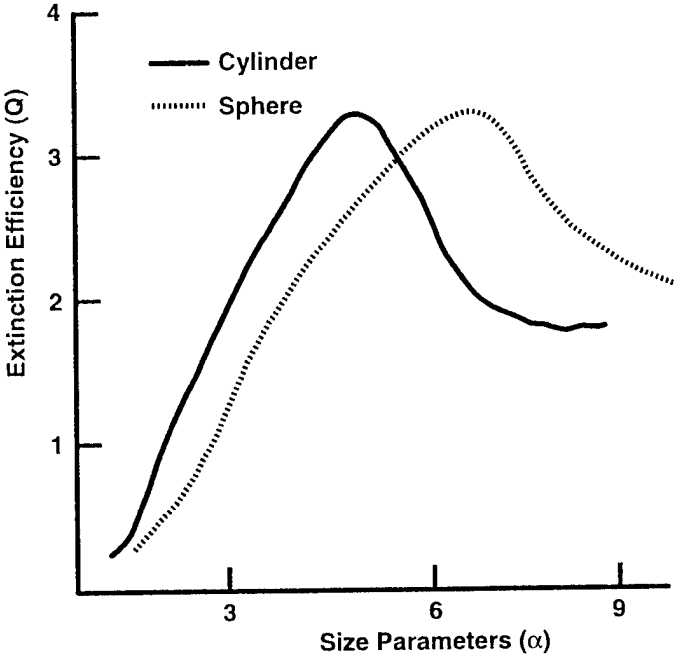


Figure 2. Extinction efficiency for cylindrical and spherical particles.

Dramatic Decrease in Radar Cross Section over Greenland Observed by the ERS-1 Scatterometer Between 1991 and 1995

Volkmar R. Wismann and Kai Boehnke

Institute for Applied Remote Sensing, Bahnhofstrasse 54, 22880 Wedel, Germany,
T : +49 (0)4103 13922; F : +49 (0)4103 7469; E : 100412.1731@compuserve.com

ABSTRACT

Radar backscatter measurements obtained over Greenland by the ERS-1 scatterometer between August 1991 and November 1995are investigated. The different snow and ice facies can be identified on NRCS maps by their different radar cross section. In the wet snow zones summer melting leads to a strong short-term decrease in NRCS of several dB in the months June to August (summer-dip). Here, a general trend of an increasing summer dip was observed from summer 1992 to summer 1995. In the Southwest part of Greenland for large areas of the percolation zone a significant trend of decreasing radar cross section of the order of 0.5 dB per year was observed, even when data of the summer-dip months were not considered. The largest gradients in radar backscatter are found at altitudes between 1500 m and 2500 m where the snow and ice cover persists during the entire year.

INTRODUCTION

In July, 1991, the European Space Agency (ESA) launched the First European Remote Sensing Satellite ERS-1 carrying a C-band (5.3 GHz) wind scatterometer for global wind measurements over the ocean. This sensor operates at vertical polarization (VV), its three antennae are looking 45 degrees forwards, sideways, and 45 degrees backwards with respect to the satellite flight direction, the incidence angle ranges from 18 to 57 degrees, the illuminated swath is 500 km wide, and the along-track and cross-track spatial resolution is 50 km. The normalized radar cross section (NRCS) measurements are independent of cloud coverage and illumination by the sun and provide a global coverage within 3 to 4 days.

Greenland is covered by polar snow and ice. Summer melting is pervasive over a considerable portion of Greenland unlike Antarctica where most summer temperatures are well below melting. Therefore, the Greenland snow and ice sheet is expected to respond immediately to global warming. The surface of Greenland can be divided into four characteristic zones : (1) dry snow (central Greenland), (2) the percolation zone, (3) the soaked zone (wet snow), and (4) the ablation zone (ice facies) [1]. These facies result from different diagenesis of the snow and ice cover which depends on the amount of accumulation and melt and therefore, on the local climate. Any change in the local climate will result in a shift of the borders between these zones. Due to the very gentle slope of the ice shield a slight change in climate will result in a large lateral shift of these borders. Therefore, monitoring these borders may provide information on climate change.

RADAR BACKSCATTER DATA

In this investigation the NRCS measurements obtained between August, 1991, and November, 1995, are analysed. Until March, 1995, the full data set distributed on CD-ROM by CERSAT, the French Processing and Archiving Facility (F-PAF) was available and for the period April to November, 1995, Fast Delivery Copy (FDC) products were used. For the first analysis, monthly averaged NRCS values for two incidence angle ranges (18°-30° and 40°-57°) were computed on a grid with a resolution of 0.5° in latitude and 1° in longitude which corresponds roughly to the instrument resolution of 50 by 50 km. For the detailed analysis, the NRCS data were re-sampled to the same grid, then, for three day intervals, an average radar cross section (NRCS-40) is computed for each grid point by linear regression between the measured NRCS and their respective incidence angles. NRCS-40 is the value of this regression line at an incidence angle of 40°. On one hand, this accounts for variations of the mean NRCS due to sampling and orbital characteristics when averaging at high or low incidence angles only. On the other hand, variations of the mean NRCS are eliminated which are attributed to changes in the slope of the NRCS with respect to the incidence angle when the contributions of volume and surface scattering are changing in space and time.

The capability of discriminating different snow and ice facies by radar remote sensing was shown for the C-band SAR of ERS-1 [2], for the K_u-band Seasat-A scatterometer and the C-band ERS-1 scatterometer [3,4]. Fig. 1 depicts a NRCS map of Greenland for incidence angles between 40 and 57 degrees for July 1993. The superimposed topography (500 metre contour lines) originates from the TerrainBase Global DTM [5]. The dry snow zone in the centre of Greenland with low radar cross section is surrounded by the percolation zone having the highest NRCS. Further to the coast the wet snow zone and the ablation zone have again lower radar cross section. Despite of the coarse resolution of the scatterometer a lot of details are resolved when comparing this map to a mosaic of Greenland produced from ERS-1 SAR imagery (see Fig. 2 of [3]). It is worth pointing out a feature which

This research was funded by the European Space Agency within the Earth Observation Preparatory Programme (EOPP) under ESTEC contract 11103/94/NL/CN.

0-7803-3068-4/96$5.00©1996 IEEE

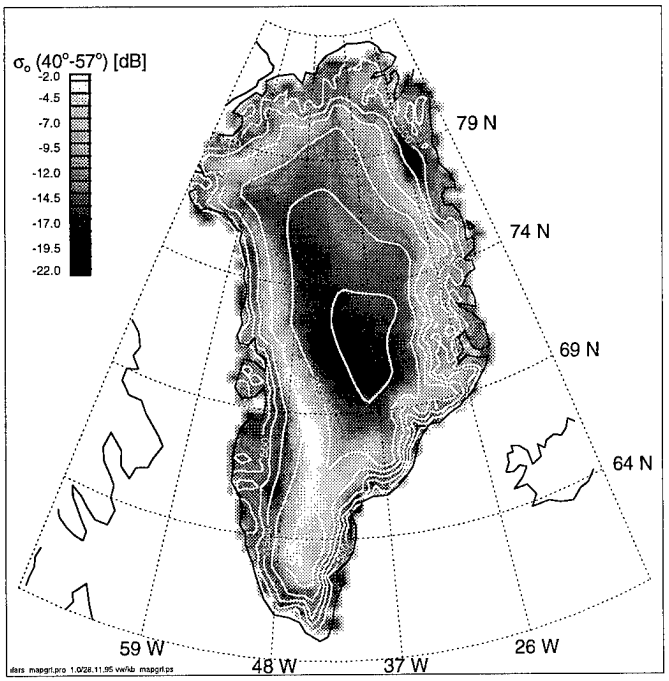


Fig. 1 : NRCS map of Greenland. Data for incidence angles between 40 and 57 degrees and July 1993. Superimposed are 500m contour lines of the topography.

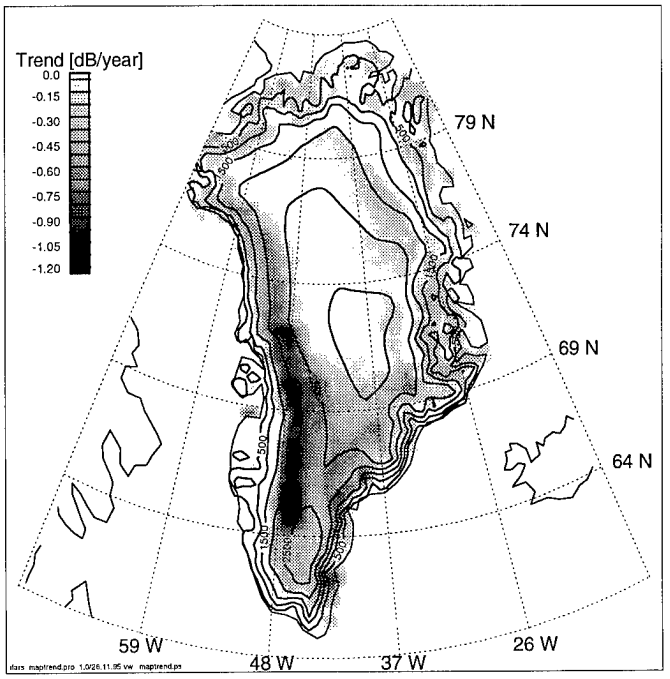


Fig. 2 : Map of the trend of the radar backscatter at incidence angles between 40 and 57 degrees for the period April 1992 to August 1995.

was detectable only in July 1993, namely the dark patch at approximately 78°N; 26°W having extremely low NRCS. This is very likely due to very wet snow caused by untypical weather conditions in this area in July 1993 [6].

NRCS TRENDS

The evaluation of the time series of the scatterometer measurements yields striking results. Fig. 2 depicts the trend of the NRCS measurements in the incidence angle range 40°-57° for the period between April 1992 and August 1995. At each grid point the trend was estimated by a linear regression through the entire NRCS time series for the respective grid point. As a result Fig. 2 shows large areas where the NRCS decreases significantly by up to 1 dB per year. When comparing Fig. 2 to Fig. 1, it is obvious that the changes in NRCS take place exactly at the borders between the different snow and ice facies. Here we have to differentiate between, first, the trend at the border between the dry snow and percolation zone and, second, the trend at the border between the percolation and wet snow zone.

Fig. 3 depicts a typical time series of the NRCS-40 values for a location at the border between the dry snow and the percolation zone. The radar cross section decreases nearly linearly from August 1991 to July 1995, while a very sudden jump in NRCS is encountered in August 1995. The long term decrease in radar cross section can be attributed to a shift of the border between the dry snow zone and the percolation zone towards the West. Fig. 4 depicts NRCS-40 transects from 49°W to 39°W along the latitude of 70°N for three different dates, i.e., August 1991 (solid line), July 1995 (dotted line), and November 1995 (dashed line). The dry snow zone is located in the East having a low radar cross section of -17 dB while the percolation zones is in the West having a high radar cross section of -1 dB. The curves for August 1991 and July 1995 are parallel but separated by nearly 1 degree in longitude. This indicates that the dry snow extended further West in 1995 than in 1991. The shape of the NRCS-40 curve for November 1995 is slightly different from the curve in July 1995, but it seems that the border has moved towards the East, back to the location of August 1991. So far, we have no explanation for the abrupt change in radar backscatter encountered in August 1995. An instrumental failure can be excluded since this jump in radar cross section could be observed only at the border between the dry snow and percolation zone. In addition, these results are confirmed by ERS-1 SAR imagery of the same area which have been acquired at the respective dates.

A completely different behaviour in radar backscatter can be found at the border between the percolation and wet snow zone. Again a typical example of a time series of NRCS-40 for a location at this border is shown in Fig. 5. In the months June to August summer melting and, therefore, increasing wetness of the snow leads to a strong short-term decrease of several dB in radar cross section (summer dip) due to enhanced absorption of the microwaves in the wet snow. Here, a general trend of an increasing summer dip was observed from summer 1992 to summer 1995.

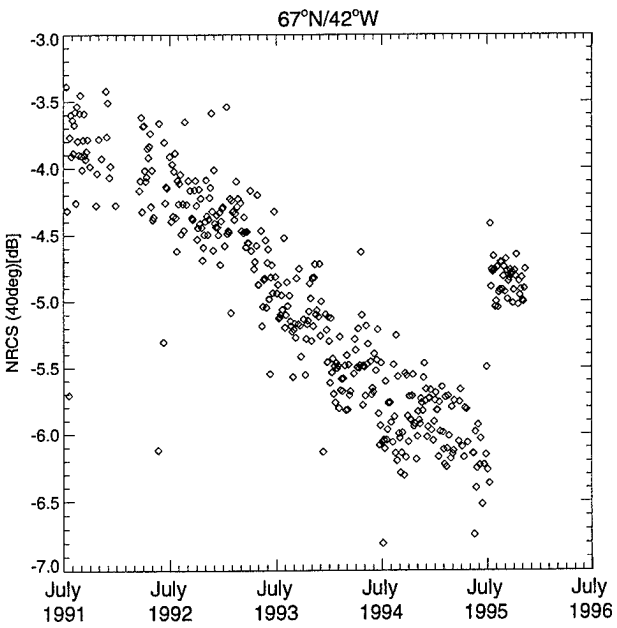


Fig. 3 : Time series of NRCS-40 at 67°N; 42°W, 3 day mean values.

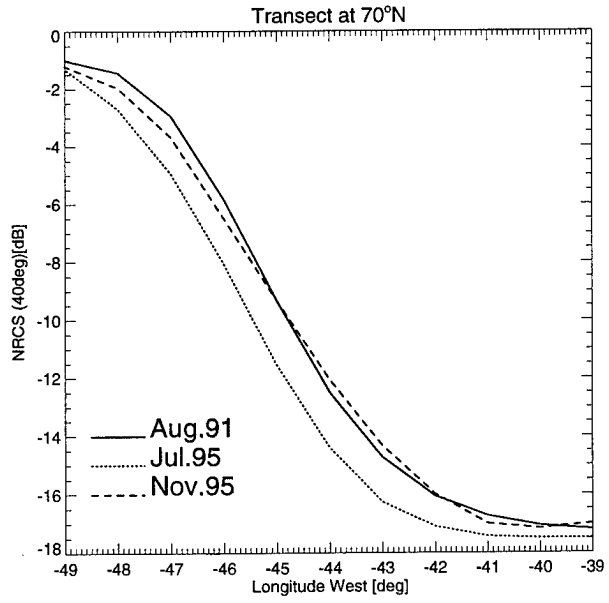


Fig. 4 : Transect of NRCS-40 at 70°N for three dates, August 1991, July 1995, and November 1995.

The question whether these trends in the radar backscatter behaviour are expressions of the interannual variability of the local climate in Greenland or indications of global change must remain unanswered from this data set. A continuation of the monitoring of the Greenland ice shield will be done using the scatterometer aboard the ERS-2 satellite and will

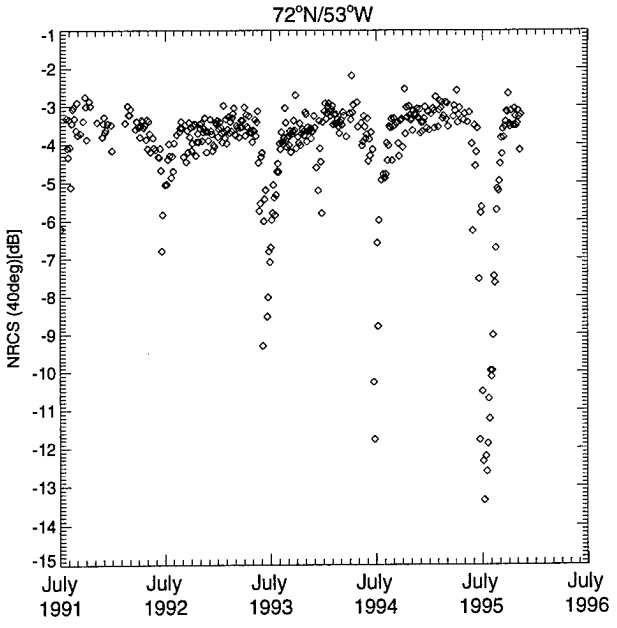


Fig. 5 : Time series of NRCS-40 at 72°N; 53°W, 3 day mean values.

hopefully continue with NSCAT aboard the Japanese ADEOS and ASCAT aboard the European METOP satellites.

REFERENCES

[1] Benson, C. S., Stratigraphic studies in the snow and firn of the Greenland ice sheet, SIPRE Res. Rep. 70, 1962.

[2] Fahnstock, M. R., Bindschadler, R. Kwok, and K. Jezek, Greenland ice sheet surface properties and ice dynamics from ERS-1 SAR imagery, Science, Vol. 262, 1530-1534, 1993.

[3] Long, D. G., and M. R. Drinkwater, Greenland ice-sheet surface properties observed by the Seasat-A scatterometer at enhanced resolution, J. of Glaciology, Vol. 40, No. 135, 213-230, 1994a.

[4] Long, D. G., and M. R. Drinkwater, Comparison of enhanced resolution images of Greenland from ERS-1 and Seasat scatterometer, Proceedings of the International Geoscience and Remote Sensing Symposium, IGARSS´94, California Institute of Technology, Pasadena, California, USA 8-12 August, 2382-2384, 1994b.

[5] Lee, W. R. III, and D. Hastings, TerrainBase Global DTM Version 1.0 (on CD-ROM), National Geophysical Data Center and World Data Center-A for Solid Earth Geophysics, Boulder, Colorado, USA, April, 1995.

[6] Konzelmann, T. and R. J. Braithwaite, Variations of ablation, albedo and energy balance at the margin of the Greenland ice sheet, Kronprins Christian Land, eastern north Greenland, J. of Glaciology, Vol. 41, No. 137, 174-182, 1995.

An Ultrawideband Imaging Radar for Sea Surface Studies

Mark A. Sletten, Dennis B. Trizna
Naval Research Laboratory
Code 7255, 4555 Overlook Ave. SW, Washington DC 20375
voice (202) 404-7971; fax (202)767-3303; mslette@seascat.nrl.navy.mil

Abstract - An ultrawideband imaging radar for the study of the surface disturbances caused by submerged mines is described. The system uses an extremely short pulse (0.2 ns, 40% bandwidth) for range resolution and time-domain beamforming for azimuthal imaging. The system also employs a "pulse pair" algorithm for the estimation of surface velocity.

INTRODUCTION

The Remote Sensing Division of the Naval Research Laboratory is involved in the ONR-sponsored Mine Surface Effects (MISE) program. The objective of this program is to determine the feasibility of using radar systems to detect the surface effects associated with flow around shallow, moored mines. Preliminary numerical simulations of the flow around a submerged mine have indicated that the backscattered power and Doppler manifestations of these disturbances should be observable by properly designed radar systems.

However, the sub-meter scale size of the predicted surface features dictates that high resolution radar systems are necessary to image these disturbances. This paper describes an ultrawideband radar system designed to image the fine structure of these signatures. Ultra-high resolution (3 cm) in the range direction is achieved via a short, (nominally) X-band pulse, while azimuthal resolution on the order of 1 m is achieved through time-delay beamforming using an eight element receive antenna array. Imaging in the Doppler domain is also possible, since each antenna element is sampled by a pair of cascaded sampling heads which are scanned in range. This arrangement allows the use of a "pulse pair" algorithm for velocity estimation. The hardware comprising this system and its associated signal processing are described in the sections below.

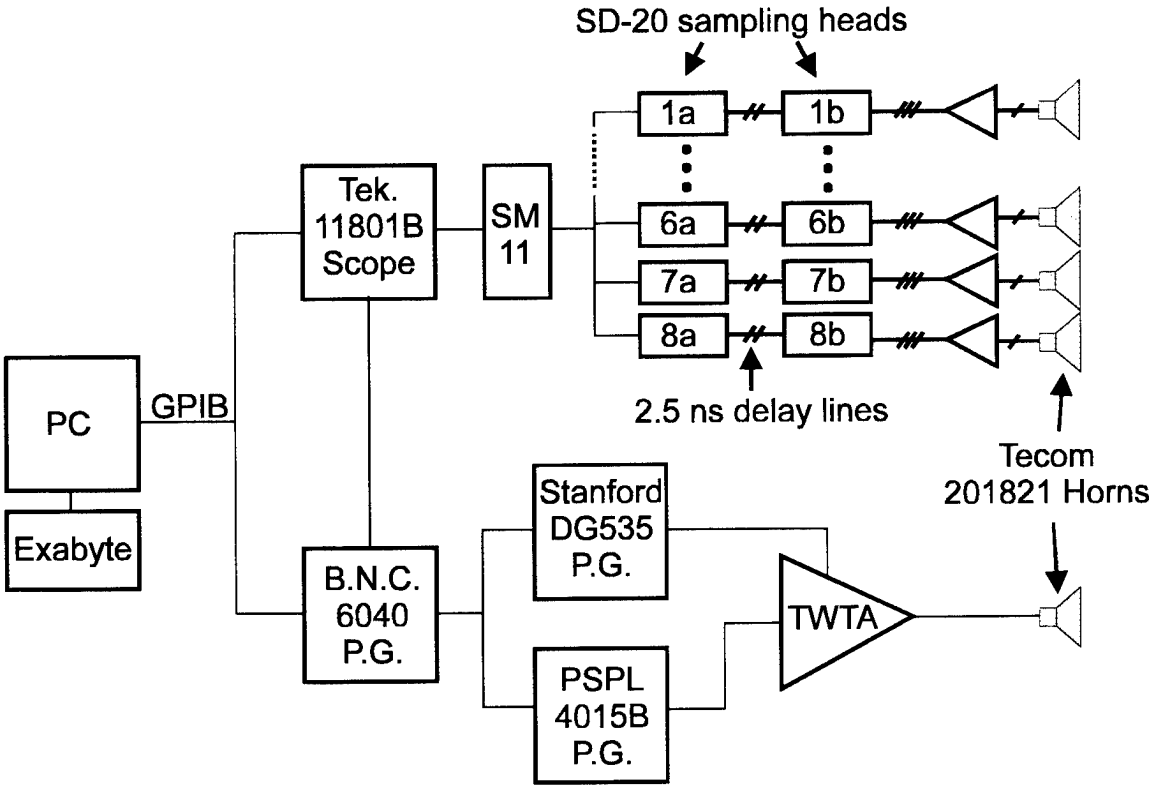


Figure 1. Block diagram of the ultrawideband imaging radar system

0-7803-3068-4/96$5.00©1996 IEEE

HARDWARE DESCRIPTION

Fig. 1 contains a block diagram of the radar system. The transmitter, receive antenna array, and data acquisition system are described in the following paragraphs.

Transmitter

The transmitter is formed by three pulse generators and a traveling wave tube amplifier (TWTA). A Berkeley Nucleonics Corporation (BNC) Model 6040 Pulse Generator with a 201E 150 ps rise-time module is used as a master trigger source. The BNC pulse is used to trigger a Picosecond Pulse Labs (PSPL) Model 4015B Pulse Generator to produce a 15 ps rise time, 9 v step. This fast step excites a Logimetrics Model A750/XU-704A TWTA, generating a 10 GHz pulse with a 3-dB bandwidth of 4 GHz and a peak power of approximately 1 kw. As shown in Fig. 2, this pulse consists of approximately two 10 GHz oscillations for a 3-dB pulse width of 0.2 ns and a corresponding range resolution of 3 cm. This technique for generating short pulses has been used previously at NRL [1], [2]. An additional pulse generator (Stanford, Model DG535) is used to generate a gating signal for the TWTA. A dual-polarized, Tecom Model 201821 horn (1.8-18 GHz) is used as a transmit antenna. At 10 GHz, the beamwidth of the Tecom horn is approximately 10 degrees.

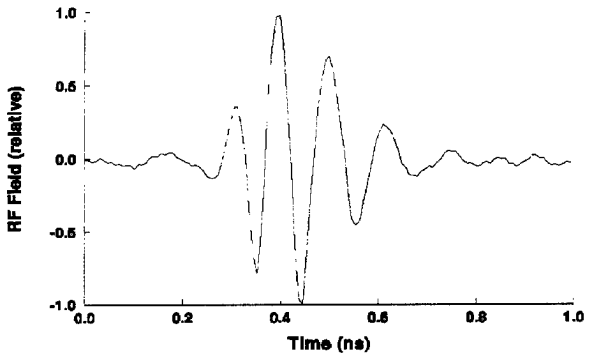


Figure 2. Output pulse produced by step excitation of the TWTA

Receive Antenna Array

An eight element, ultrawideband horn array is used for azimuthal imaging. The antenna consists of eight Tecom Model 201821 horns arranged in a linear array with a center to center spacing of 25 cm. (This is the minimum element spacing for a linear array of these horns, given their lateral dimensions.) The Tecom horns were selected on the basis of their excellent short-pulse response and commercial availability. The 3-dB beamwidth of the array is approximately 1 degree, providing azimuthal resolution of about 1 m at the proposed operating range of 70 m. As with the transmit antenna, the array can be polarized either horizontally or vertically. Image formation is accomplished by time-domain processing of the signals from the antenna elements, each of which is sampled by a pair of cascaded sampling heads.

Data Acquisition System

The core of the radar system consists of a Tektronix 11801B Sampling Oscilloscope with an SM-11 Multichannel Expansion Unit. A total of sixteen SD-20 sampling heads are housed in the SM-11 to allow sampling of the outputs from each of the eight antenna elements comprising the receive array. At each head, the microwave echo (such as the pulse seen in Fig. 2) is sampled directly using equivalent time sampling. No down-shifting to intermediate or video frequencies is performed. A pair of cascaded heads is used for each element to allow the use of pulse-pair (covariance) algorithms for Doppler estimation. The pair is scanned simultaneously in range during the process of equivalent time sampling, and thus the second head in each pair revisits the range location sampled by the first after a time interval determined by the sample rate and the sample spacing. At a 100 kHz sample rate and a sample spacing of 10 ps, the 2.5 ns delay lines joining the two heads in a pair produces a revisit time of 2.5 ms. Samples are initially stored in memory buffers within each head. Full buffers are off-loaded to an Exabyte tape via a GPIB interface controlled by the PC.

SIGNAL PROCESSING

Time Delay Beamforming

In narrowband phased array systems, beamforming is normally accomplished by performing a Fourier Transform of the signals received from the individual antenna elements. In the present system, however, imaging in the azimuthal dimension is performed in the time domain, simply by "steering" the array beam during post-processing via time delays applied to the sampled waveforms. Let the waveforms collected by the first bank of sampling heads (1a, 2a, 3a, ..., 8a) be given by $e_n^a(t), n = 1,2,3,...,8$. An image can be generated by first forming the coherent sum of the individual waveforms with time delays appropriate for the particular azimuthal angle θ of interest,

$$E^a(t,\theta) = \sum_{n=1}^{8} e_n^a\left(t - (4 - n + \tfrac{1}{2})\frac{d}{c}\sin\theta\right) \quad (1)$$

where d is the spacing between antenna elements and c is the speed of light. The Hilbert Transform $H(f(t))$ provides a convenient means by which a power envelope image can be obtained from (1). (Note that the waveforms formed by (1) contain oscillations at the 10 GHz center frequency of the transmitted pulse). Let

$$\hat{E}^a(t,\theta) = E^a(t,\theta) + jH\left(E^a(t,\theta)\right). \quad (2)$$

A power envelope image can be formed by taking the amplitude of the complex image, $\left|\hat{E}^a(t,\theta)\right|$, defined by (2). Finally, transformation from time t to the polar (spatial) coordinate r can be accomplished by the simple radar relationship between time and range, $t = 2r/c$, allowing formation of the backscattered power image $\left|\hat{E}^a(r,\theta)\right|$.

Doppler Processing

The Hilbert Transform also provides a means by which velocity images can be obtained. Recalling the 2.5 ms delay between images formed by the "a" and "b" banks of sampling heads, a phase image can be defined by coherent averaging of the phase difference between the "a" and "b" images:

$$\phi(r,\theta) = \arg\left(\sum_p \hat{E}_p{}^a(r,\theta)\cdot\hat{E}_p{}^b(r,\theta)^*\right) \quad (3)$$

where "$*$" denotes complex conjugate, and the subscript p refers to a particular pair of "a" and "b" images used in the coherent summation. A velocity image can then be obtained as

$$v_r(r,\theta) = \left(\frac{\lambda\cdot\phi(r,\theta)}{4\pi\tau}\right) \quad (4)$$

where λ is the electromagnetic wavelength (nominally 3 cm for this radar system) and τ is the time delay between the "a" and "b" pulse pairs (2.5 ms). This is a covariance estimate of the mean of the Doppler spectrum [3] and is similar to the estimate used with the FOPAIR ocean imaging radar system [4].

SUMMARY

This paper describes an ultrawideband radar system under development for the imaging of the surface disturbances caused by submerged mines. The system uses transient excitation of a TWTA to form a 0.2 ns, (nominally) X-band pulse which results in a range resolution of approximately 3 cm. Azimuthal imaging is accomplished through individual sampling of the eight elements in a horn antenna array and subsequent beamforming in post-processing. Doppler velocity images of the surface are also available through the use of two banks of cascaded sampling heads and a pulse-pair velocity estimation algorithm.

REFERENCES

[1] M. A. Sletten, D. B. Trizna, and J. P. Hansen, "Ultrawideband Radar Observations of Multipath Propagation Over the Sea Surface", *IEEE Trans. Antennas and Propagat.*, Vol 44, no. 5, May, 1996.

[2] J. P. Hansen, "Experimental Measurement of Sea Clutter Using an Ultrawideband X-band Radar with Variable Resolution", *Ultrawideband Radar*, Ivan J. LaHaie, editor, Proc. SPIE 1631, pp 182-193 (1992).

[3] K.S. Miller and M. M. Rochwarger, "A Covariance Approach to Spectral Moment Estimation", *IEEE Trans. Info. Theory*, vol. IT-18, no.5, September, 1972.

[4] S.J. Frasier, Y. Liu, D. Moller, R. E. McIntosh, and C. Long, "Directional Ocean Wave Measurements in a Coastal Setting Using a Focused Array Imaging Radar", *IEEE Trans. Geosci. Remote Sense.*, vol. 33, no.2, March, 1995.

Development of a Low Cost SFCW Ground Penetrating Radar

Alan Langman, Simon P. Dimaio, Brian E. Burns and **Michael R. Inggs**
Radar Remote Sensing Group, Dept of Electrical Engineering, University of Cape Town
Private Bag, Rondebosch 7700, South Africa
Tel: +27 21 650 4019 Fax: +27 21 650 3465
Email: alangman@eleceng.uct.ac.za

Abstract—Due to their system complexity and high component cost, stepped frequency continuous wave radars have not been popular in the Ground Penetrating Radar industry. However, over the last decade the cost of RF technologies has decreased considerably, making it more feasible to make SFCW GPR's.

This paper discussed the implementation and development of a low cost SFCW GPR using digital radio technology, a homodyne single channel receiver and a digital signal processor. The radar operates over a bandwidth from 490MHz to 780MHz and is capable of taking a single depth profile measurement using 256 frequency steps in less than 0.5 seconds.

The results of field trials are also presented.

INTRODUCTION

The purpose of Subsurface Radar is to detect or locate objects or features buried beneath the Earth's surface. It is an electromagnetic technique which has found a number of important applications over the past twenty years.

The Ground Penetrating Radar field has seen the development of two distinct techniques, namely *Pulse or Impulse Radar* and *Stepped Frequency Continuous Wave (SFCW) Radar.* While the latter technique has been investigated since 1972, it is Pulse Radar which has dominated the GPR industry. This was due to the high cost and complexity of SFCW GPR. Over the last decade the cost of RF technologies (fast switching synthesizers) has decreased considerably, making it more feasible to develop SFCW GPR. In addition the availability of fast, low cost digital signal processors has contributed to the growing interest in this implementation of a subsurface radar.

In this paper we describe the design and development of a low cost stepped frequency continuous wave ground penetrating radar (SFCW GPR). The radar has been implemented using digital radio technology, a single channel homodyne receiver and a digital signal processor. The radar is then interfaced to a laptop for data storage and display.

The paper begins by reviewing the basic principles of a SFCW GPR system. It then continues to describe its hardware implementation. Finally results of the radar are presented and conclusions are drawn.

BASIC PRINCIPLES OF STEP FREQUENCY RADAR

The theory of a stepped frequency continuous wave (SFCW) subsurface radar is generally well documented, and the reader is referred to the many papers for theoretical details [1,2]. This section serves only to provide an overview of the principles of SFCW radar.

The SFCW radar obtains the distance to a target by measuring the coherent target reflections over a number of stepped frequencies (N) within the given bandwidth (B). This raw frequency data is then sent through a Discrete Fourier Transform (DFT) to yield the scattering from individual targets. It can be shown that the range resolution, ΔR (DFT bin size), for a SFCW radar utilising N steps of Δf in a medium with velocity v is

$$\Delta R = \frac{v}{2N\Delta f} \tag{1}$$

The range measured will be unambiguous as long as the target distance does not exceed $R_{\max}$, where

$$R_{\max} = \left(\frac{N}{2} - 1\right)\Delta R \tag{2}$$

It is important to note that $R_{\max}$ in Equation 2 is the unambiguous range for a single channel homodyne receiver [3].

SYSTEM OVERVIEW

The system block diagram for the SFCW radar is given in Figure 1

The radar consists of five major sub-systems:

- The *transceiver:* This is responsible for generating the transmitted waveforms and receiving the reflected waveforms.
- The *antennas:* They couple the energy from the transcei into and out of the subsurface media.
- The *DSP or Digital Signal Processor*: This system transforms the raw spatial frequency data into spatial data.

0-7803-3068-4/96$5.00©1996 IEEE

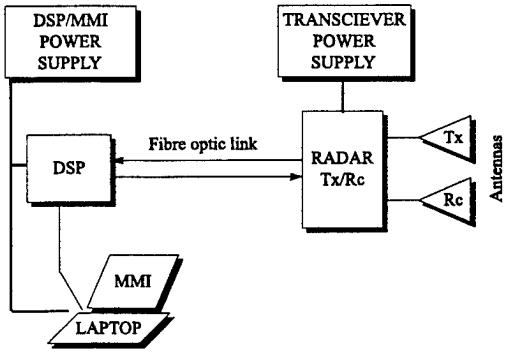


Figure 1: Block diagram of the developed SFCW GPR

- The *MMI or Man-Machine interface*: The MMI contains the software to set up the DSP and store and displays the subsurface images.
- Battery power supplies.

The transceiver is connected to the DSP/MMI via a fibre optic serial interface. This isolates the transceiver, hence reducing the Radio Frequency Interference (RFI). The complete component cost for the system (excluding the MMI and antennas) is under $200.

HARDWARE IMPLEMENTATION

This section discusses the modules of the radar in more detail.

The block diagram of the transceiver subsystem is shown in Figure 2

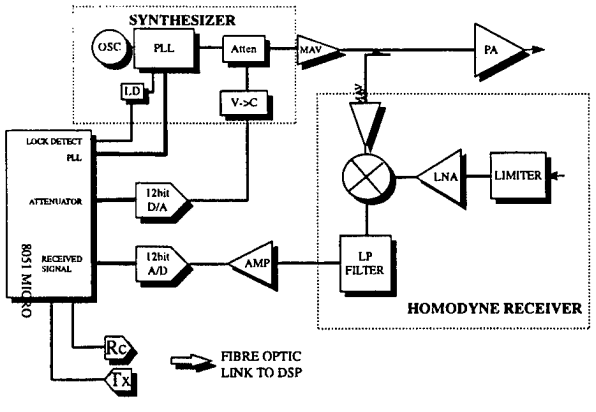


Figure 2: Block diagram of the radar transceiver

The transceiver is made up of a synthesizer and a homodyne receiver. These are controlled by an 8051 microcontroller which communicates with the DSP via a RS232 fibre optic link.

The transmitter was implemented using cellular phone synthesizer technology. It consists of a synthesizer chip, wideband oscillator, reference oscillator and a system microcontroller. The synthesizer has the following specifications

Frequency band	$490MHz$ - $780MHz$
Minimum step size	$25kHz$
Lock time	$<$ 1.6ms

A small packet protocol exists between the DSP and the controller to enable the DSP to control the synthesizer. The output of the PLL is fed through a programmable attenuator which is controlled by the microcontroller. This is to insure that signal amplitude out of the transmitter is kept constant with frequency and that the gain variation of the local oscillator signal does not vary by more than a 1 dB.

The receiver is a simple homodyne receiver with a single coherent output. It has a calculated noise figure of less than $4.1dB$. The maximum input signal for the receiver is $-10dBm$ and the noise floor ($1kHz$ receiver bandwidth) is less than $-100dBm$. This provides an effective receiver dynamic range of $90dB$ allowing for a 14 bit A/D to be used.

The DSP has two major functions:

- **Radar controller:** It scans through the N transmit frequencies and then digitizes and stores the received data. After processing it downloads the data to the MMI for storage and display.
- **Processor:** It processes the raw data by transforming from the spatial frequency domain to the time domain using windowing and the Fast Fourier Transform (FFT).

The DSP module comprises of a TMS320C50 evaluation board from Texas Instruments and a communication interface board. The latter interfaces to the DSP evaluation board to allow for two asynchronous serial links to be available for communication to the radar transceiver and the MMI. Both these serial links use a fibre optic transmission media.

The MMI is a Microsoft Windows^{TM} software package that has three major functions:

- **Data input:** Provides a user friendly enviroment for the entry of radar and processing parameters.
- **Display:** The radar image is displayed on the screen as the radar is moved over the ground surface.
- **Data storage:** The data is saved to disk in a binary format along with the radar parameters, processing parameters and scan information. The data can then be retrieved and viewed with the MMI software at a later stage. Data can also be exported to MATLAB^{TM} and IDL^{TM}.

The radar is powered by two 12V / 4.2Ah Lead Acid batteries: a separate battery for the transceiver and the DSP. These voltages are then translated to the radar system voltages using DC/DC convertors.

The antennas used are cavity backed archimedes spiral antennas. Their polarization is circular, with each radiating surface transmitting an orthogonal polarization.

Before viewing the data it is necessary to perform gain compensation on each depth profile to remove the effects of geometric spreading of the electric field and the losses in the media. Trace subtraction is also performed on the image to enhance hyperbolic features in the image

RESULTS

In this section two sets of results are presented. The first is shown in Figure 3. In order to demonstrate that the radar functioned, a radar image was generated by moving the system towards a wall in a large laboratory. The reflections from the wall are clearly visible in Figure 3.

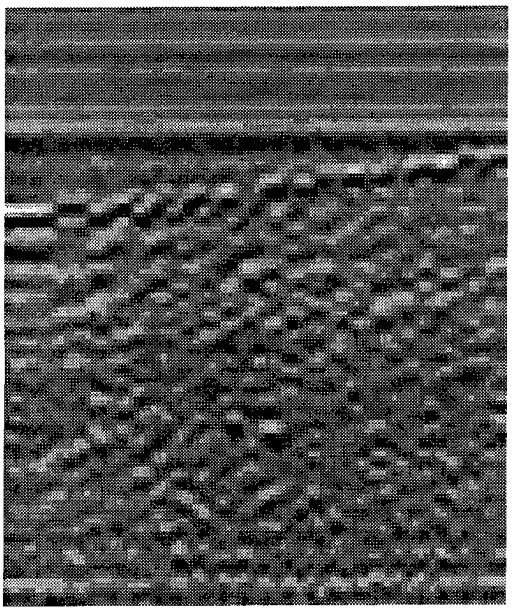


Figure 3: Radar image of antennas moving towards a wall

For the second result, a 10m scan was performed over a roadbed, to detect a storm drain and a water pipe. Figure 4 shows the resultant radar image. The large lighter region on the right of the image is where the radar crossed over the storm drain. Slightly down and to the left is the response from a water pipe.

CONCLUSIONS

A low cost SFCW GPR has been constructed and tested yielding promising results. It uses standard components

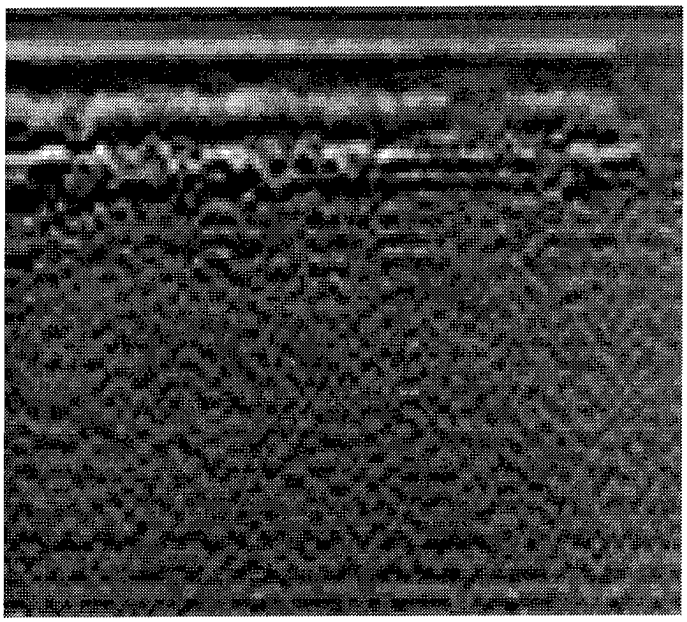


Figure 4: GPR image of a Roadbed

which are available at low cost due to their volume production in the digital radio industry. This has totally revolutionized the prospects for development of SFCW GPR.

Work has started in the development of more complex SFCW GPR's for mine detection, operating over a $2GHz$ bandwidth. The new system will have a faster measurement time and a wider dynamic range.

REFERENCES

[1] Alois P. Freundorfer and Keigo Iizuka, "Detection of Nonmetallic Buried Objects by a Step Frequency Radar", In *Proceedings of the IEEE*, vol. 71, pp. 277–279, February 1983.

[2] Lloyd A. Robinson, William B. Weir and Leo Young, "Location and Recognition of Discontinuities in Dielectric Media Using Synthetic RF Pulses", In *Proceedings of the IEEE*, vol. 62, no. 1, January 1972.

[3] Alan Langman, "A SFCW Polarimetric GPR for Landmine Detection", PHD Thesis, UCT, December 1996.

A Range Algorithm for Ground Penetrating Radar

Thurlow W. H. Caffey
Sandia National Laboratories◊
P. O. Box 87185
Albuquerque, NM 87185-0705
Tel 505-844-4217 / Fax 505-844-0240 / twcaffe@sandia.gov

Abstract — A range-to-target algorithm for application to targets which exhibit a crude hyperbolic wiggle trace is described. The current practice is to use the apex time of the hyperbolic response together with an estimate of the propagation velocity to furnish the range. This new algorithm minimizes a difference function over a velocity search interval to provide the range. Examples for a variety of media, targets, range, and operating frequency are given for both simulated data and actual field data provided by others. Generally, the range is within 5% of the true value when known, or is consistent with values furnished by others.

ASSUMPTIONS

Several assumptions are required for the development of the algorithm: The transmitter is not modulated during the pulse interval; the media between the radar and the target is homogeneous and isotropic; the round-trip travel time is measured during a linear traverse past the target; and the transmitting and receiving antennas of the GPR are appropriately separated.

THE TRAVERSE

Suppose that the radar is translated in uniform increments along its own axis and approaches, illuminates, and passes-by a discrete target as shown in Fig. 1. If the maximum radius of curvature of the target is much less than the minimum range, the slant range is given by

$$R_i = 0.5 v t_i \ , \tag{1}$$

where v is the velocity, t_i is the round trip time, and R_i is the slant range from the midpoint of the antenna separation distance $2s$ at the i-th traverse position z_i. The minimum time is denoted by t_o and the corresponding traverse position is denoted by z_o. The minimum range is given by

$$\rho = 0.5 v t_o \ . \tag{2}$$

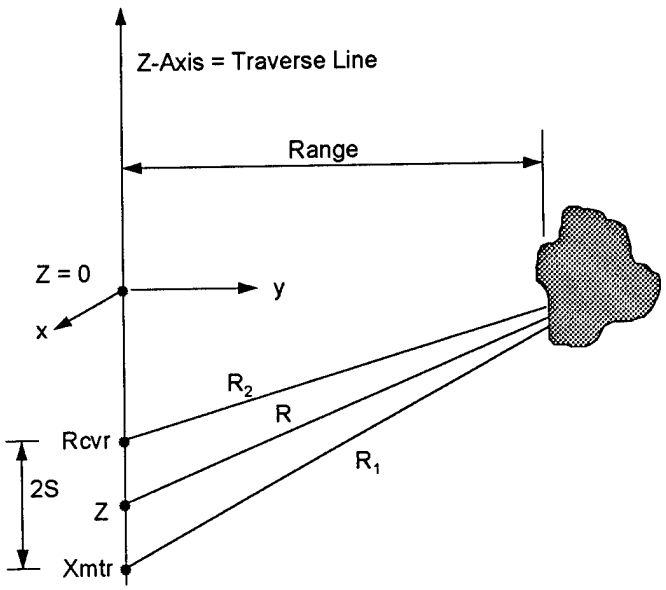


Figure 1. Traverse Geometry

The slant range from the midpoint can also be written as

$$R_i = \sqrt{\rho^2 + z_i^2} \ . \tag{3}$$

The form of the trace generated with the traverse is obtained by equating (1) and (3), and using (2) to get

$$\frac{t_i^2}{t_o^2} - \frac{z_i^2}{\rho^2} = 1 \ , \tag{4}$$

which is the standard form for an hyperbola centered at $(z_i, t_i) = (0,0)$.

From Fig. 1 it is simple to write the expression for the round-trip path length $R_{rt,i}$ in terms of R_i, namely

$$R_{rt,i} = R_i \left\{ \sqrt{1 + \frac{\eta^2 + 2\eta\Gamma_i}{1+\Gamma_i^2}} + \sqrt{1 + \frac{\eta^2 - 2\eta\Gamma_i}{1+\Gamma_i^2}} \right\}, \tag{5}$$

◊ This work was supported by the United States Department of Energy under Contract DE-AC04-94AL85000.

0-7803-3068-4/96$5.00©1996 IEEE

where $\eta = s/\rho$ is the normalized separation distance, and $\Gamma_i = |z_i|/\rho$ is the normalized traverse distance. We see from Fig. 2 that the error in using $2R_i$ for the round-trip path length is greatest when $z_i = 0$, and that the separation distance should be made as small as possible.

ALGORITHM DEVELOPMENT

The key idea in the algorithm consists in minimizing the difference between the propagation form for range, (1), and the Pythagorean form, (3), which is called the *difference function:*

$$DF = \left| \sqrt{z_i^2 + \left(v_j t_o / 2\right)^2} - v_j t_i / 2 \right|, \qquad (6)$$

where the v_j are trial values of velocity, $j = 1, 2 \ldots j_{\max}$. The difference function is zero when $t_i = t_o$. I assume that, when the mean difference function is minimized over the set of trial velocities $\{v_j\}$, the velocity at the minimum will provide the range which is most consistent with the data.

The difference function may be set to zero and solved directly for as many trial velocities as there are data points. Often, the velocities thus found imply combinations of relative dielectric constant, *RDC*, and conductivity which are very different from any reasonable estimates of what the electrical soil parameters could be. These so-called direct solution velocities are not used in the algorithm.

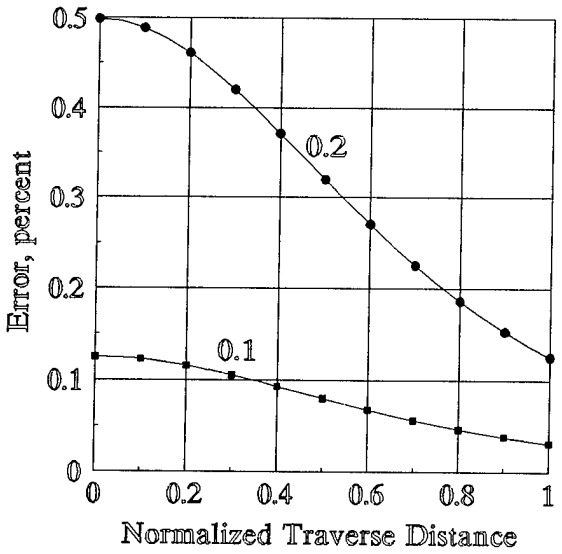


Figure 2. Midpoint error for $\eta = 0.1, 0.2$

Constraints

The range-to-target algorithm is a numerical solution process and must be constrained to avoid instability, unwarranted precision, and results that are physically impossible. Because the difference method may require a large amount of computation and is subject to round-off errors, the (t_i, z_i)-data are read-in as double-precision numbers, and the computations are performed in double precision.

Stability: One problem arises from the limited precision of the time measurement itself. The several values of t_i in the vicinity of the apex of the hyperbola often have the same value, and the question arises as to which of these t_i-values should be designated as t_o. If the number of such values is odd, the middle value is chosen as t_o; if the number is even, the mean value of the two z_i in the center is inserted as z_o together with a corresponding t_o. The z_i are subsequently recalculated so that only $z_o = 0$, and all other t_i equal to t_o are excluded from use in (6). This also increases the minimum values of the Γ_i and reduces the midpoint approximation error as shown in Fig. 2.

Precision: The uncertainty associated with each (z_i, t_i)-pair, namely Δz and Δt, can be used to estimate the relative error in the difference function, and to control the number of significant figures or *NSF* retained in the subtraction. The error in the trial velocities, which are computed values, is neglected.

The NSF to retain in the difference function is given by the characteristic of the common logarithm of the reciprocal of the relative error. If the NSF is one or more, only one or more significant figures are retained in the difference function; if the NSF is less than one, the difference function is not accumulated into the mean value. Consequently, it may turn out that the process of minimization may fail for lack of adequate precision.

Velocity interval: The difference function requires the use of trial velocities, and I assume that it usually possible to make an estimate of the lower and upper limits of each of the electrical parameters. These are used to compute lower and upper bounds of the wavelength which, in turn, are used to provide bounds for the trial velocities. Alternatively, of course, the search could be conducted directly in terms of wavelength rather than velocity.

EXAMPLES

Several examples are given below which demonstrate the usefulness of the algorithm in several different combinations of soils and targets. The first three examples use simulated data based on the return from a sphere [1], and the remaining six examples use field data taken by others on commercial equipment. The velocity search increment was 0.1% of the velocity interval in each example.

Air Example: The target is a 1m OD conductive sphere centered 50m from the traverse line. The transmitter and receiver are separated by 0.5m. The target RDC is also that of air, but the conductivity is 10mS/m. At a frequency of 100MHz the minimum round-trip time to the target surface is 330.2ns. The traverse extends ±0.85m in 0.1m intervals and provides extreme times of 330.3ns. Using just the extreme time on each side, 3 points in all, the estimated range is 49.49m which is very close to the minimum range-to-target distance of 49.5m.

An Air Cavity in Granite: The Boulder Creek granite formation near Raymond, Colorado has been extensively measured *in situ* at frequencies up to 25MHz [2]. At 12.5MHz the RDC is 7.8 and the conductivity is 1.8 mS/m which provide a wavelength of 8.47m and a velocity of 0.106 m/ns. A 1.6m-OD spherical cavity is centered 33m away. The transmitter & receiver are separated by 0.5m, and the traverse increment is 0.1m. Using data points between ± 3.25m provides a range of 32.3m which is close to the minimum distance of 32.2m.

A Saline Cavity in Granite: This is the same as the previous example except that the target is changed to a 0.5m OD saline sphere centered at 9.64m. The target RDC is 81 and the conductivity is 180mS/m. Using data points between ± 4.5m provides a range of 9.36m which is 3cm short of the minimum distance of 9.39m.

Pipes and Barrels in Sand: The January 1994 issue of *EKKO UPDATE*, a newsletter published by Sensors & Software, Inc., illustrated the responses from pipes and barrels buried at the University of Waterloo test site located at Canadian Forces Base Borden near Barrie, Ontario. Fig. 3 shows the wiggle traces corresponding to five targets. All targets were buried at a depth of 1.30m in a uniform sand overlying a water table which began at a depth of 4m. The trace for the vertical barrel, the 4th target, is rather flat on top and does not extend as far along the traverse as the other traces because there is very little return from the vertical sides. A spurious response is also present at about 12m along the traverse. The trace for the horizontal barrel shows a minimum round-trip time which is about 1ns greater than that of the other targets which suggests that the barrel is at a slightly greater depth. Sensors & Software, Inc. has kindly supplied the data which was acquired at 450MHz. The antenna separation of 0.25m made $\eta \approx 0.1$ so that the midpoint approximation error of Fig. 2 is very small. The results of using the algorithm, with media search limits of $5 \leq RDC \leq 10$, and $0.1ms/m \leq Conductivity \leq 1mS/m$, are shown below.

Target Description	Depth, meters	Velocity, m/ns
0.5m steel cylinder	1.29	0.134
0.16m OD plastic pipe	1.25	0.130
0.16m OD steel pipe	1.28	0.133
Vertical barrel, 180L	1.31	0.134
Horizontal barrel, 180L	1.33	0.128

The differences between the computed and implanted depths are less than 4% for the first four targets. The horizontal barrel is about 3cm deeper than intended.

Rebar Mesh in Concrete Slab on Grade: In the January 1995 issue of *EKKO UPDATE*, Sensors & Software described the measurements shown in Fig. 4, and graciously provided a copy of the actual data obtained at 1200MHz. The antennas were separated by 7.5cm which was one-half the mesh spacing and one-half of the nominal slab thickness. The return at 1.2m along the traverse was investigated with media search limits of $5 \leq RDC \leq 15$, and $0.01ms/m \leq$ Conductivity $\leq 10mS/m$. Times were only known to 2 significant figures, and the algorithm provided a depth of 11cm. This is consistent with both the traverse data and migrated image of Fig. 4 when using the algorithm velocity of 0.082m/ns and a minimum time of 2.7ns. The slab has not yet been bored to determine the actual depth of the mesh.

CONCLUSIONS

The results given here are encouraging because of the variety of media parameters, frequency, and hyperbolic quality, but further testing is desirable. The algorithm appears to be ready for stand-alone use, or for integration into software associated with existing GPRs. It is worth noting that the algorithm is also applicable to seismic surveys with constant-offset gather.

REFERENCES

[1] H. W. March, "The field of a magnetic dipole in the presence of a conducting sphere," Geophysics, vol. 18, #3, pp. 671-684, July 1953.

[2] R. N. Grubb, P. L. Orswell, and J. H. Taylor, "Borehole measurements of conductivity and dielectric constant in the 300 kHz to 25 MHz frequency range," Radio Science, vol. 11, #4, pp275-283, April 1976.

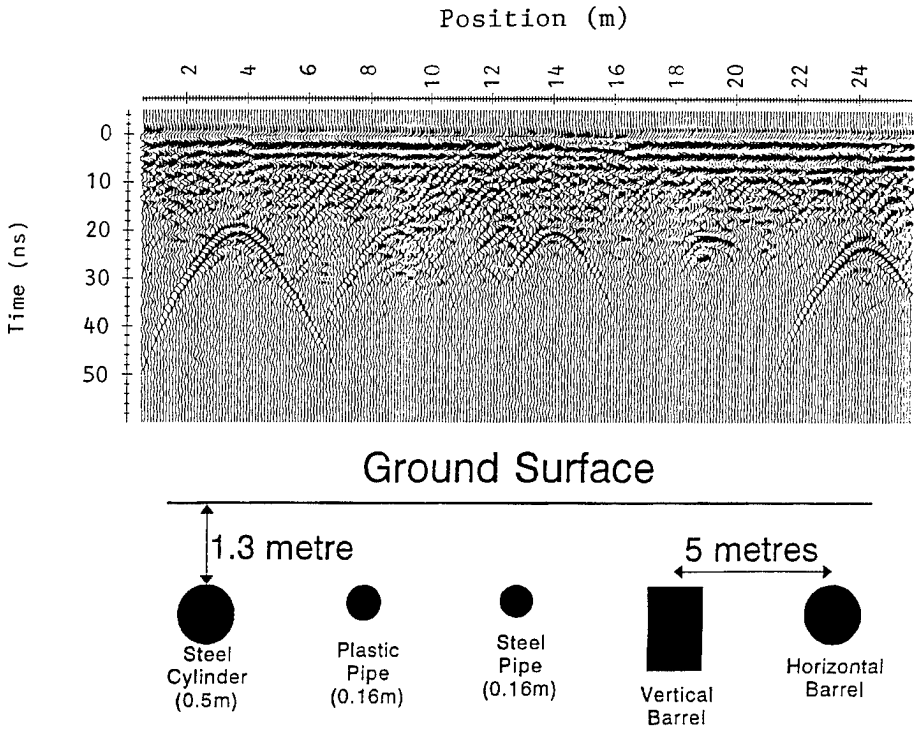


Figure 3. GPR returns at 450MHz at University of Waterloo GPR antenna test site

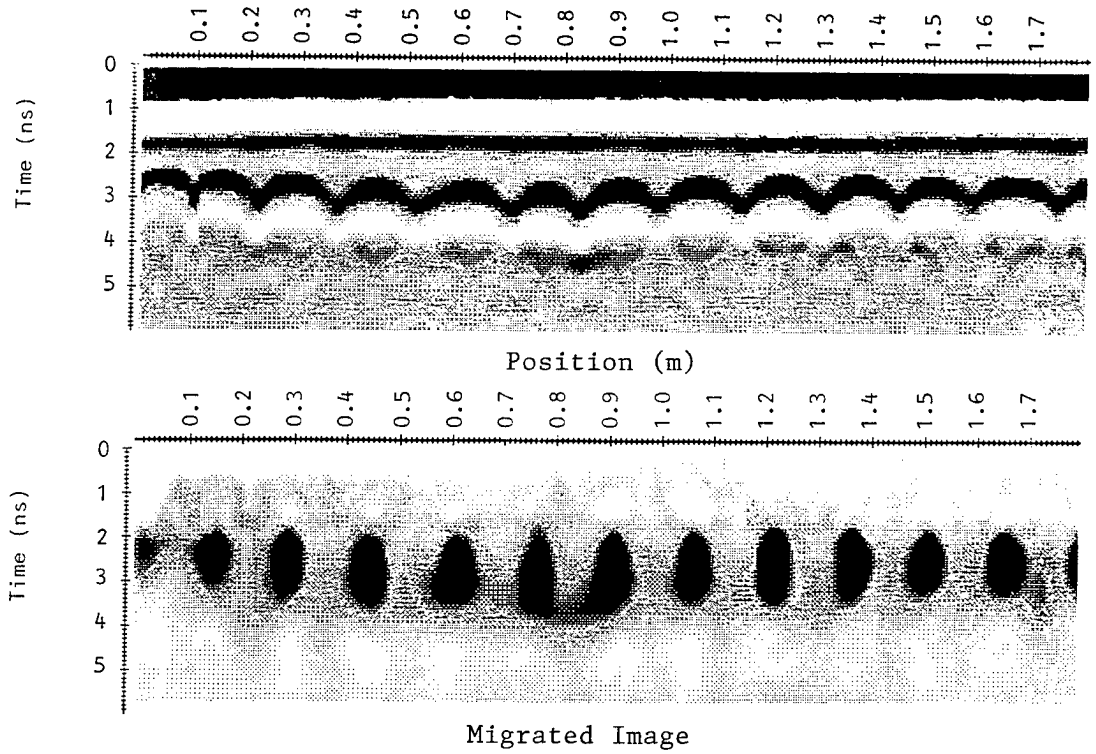


Figure 4. GPR returns at 1200MHz from rebar mesh in a concrete slab
15mm x 15mm square mesh of 3mm wire in ~ 15cm thick slab

Results of a Remote Sensing Experiment Using a Low Frequency Ultra-Wideband SAR to Investigate the Phenomenology of Landmines

Keith Sturgess[1]
Lynn Happ[1]
James Kurtz[2]
Mary Collins[3]

[1] Army Research Laboratory, 2800 Powder Mill Road, Adelphi, MD 20783
telephone: (301)394-2530, fax: (301)394-4690, email: lsturges@clark.net

[2] University of Florida, Electronics Communications Laboratory, PO Box 140245, Gainesville, FL 32614
telephone: (904)392-1705, fax: (904)392-7169, email: jlk@alpha.ecl.ufl.edu

[3] University of Florida, Soil and Water Science Department, PO Box 110290, Gainesville, FL 32611
telephone: 904-392-1951, fax: (904)392-7169, email: MEC@gnv.ifas.ufl.edu

ABSTRACT

The Army Research Laboratory (ARL) has developed a low frequency, ultra-wideband, (UWB) synthetic aperture radar (SAR) based on impulse technology to explore foliage penetration (FOPEN) and ground penetrating radar (GPR) phenomenology. The radar has a bandwidth of 1 GHz and center frequency of 550 MHz, and is mounted on a boom-lift that can operate at heights of 5 to 45 meters while moving at 1 kilometer per hour allowing the radar to operate in a strip-map SAR mode.

A GPR data collection was held at a prepared site at Yuma Proving Ground, Arizona using the ARL SAR in January 1996. A thorough geophysical characterization was conducted of the site using an EM-31, a GSSI SIR-3 with 150, 300, and 500 MHz antennas, as well as over 25 test pits. Data was collected with the boom-SAR at depression angles ranging from 10 to 45 degrees and aspect angles of up to 100 degrees. This paper will concentrate on an area of the site containing over 80 surface, flush, and 6 inch buried inert landmines, and covers target RCS vs. depression angle as well as the frequency dependence of the target scattering.

INTRODUCTION

Many organizations, both inside and outside the Department of Defense, have a need to detect and identify obscured and/or buried targets. Since it is well known that the skin depth of dielectric media increases for low-frequency electromagnetic energy, and that range resolution of a radar is a function of bandwidth, a low-frequency ultra-wideband (UWB) synthetic aperture radar (SAR) was chosen to investigate minefield detection at the Army Research Laboratory. This implementation, it was hoped, would give the best ground penetration while providing the highest possible resolution in both range and cross-range.

The ARL UWB SAR is a fully polarimetric radar that operates across a 1-GHz-wide band, from 60 MHz to 1 GHz. This bandwidth provided a measured range resolution of 6 inches, while the aperture length provides a nominal 1 foot cross-range resolution. The radar consists of several major subsystems that are modular in nature to allow for the evaluation of alternate approaches. Many of the subassemblies exist as standard 19-in. rack mount units or as VME-compatible printed circuit assemblies. Much of the system operation is controlled by software, allowing easy modifications or other future upgrades.

The transmitter, a gallium arsenide bulk avalanche semiconductor switch (GaAs BASS), generates a 2 ns-wide pulse with a 70-ps rise and 2 ns fall time at an amplitude of 10 kV into 50Ω. The spectral distribution of the received pulse shows a low-end roll-off largely attributed to the frequency response of the antenna, while the high-end roll-off is primarily driven by the bandwidth of the data-acquisition system.

Radar location is provided by a Geodimeter theodolite which updates at 2.5 Hz and provides location to within 15 mm. Including a linear predictive filter to provide location between measurement updates allows this position accuracy to be maintained as the boom SAR moves down a road. The SAR integration angle used is nominally 35 degrees.

Each of the transmit antennas (horizontal and vertical) is a linear 200Ω TEM horn — open sides with 200 ohms from the throat to the opening — that is 4.5 ft long, with an additional 1.5 ft of resistively loaded parallel plate section on the radiating end. The span of frequencies the radar covers requires a direct baseband receiver. The receivers are a pair

0-7803-3068-4/96$5.00©1996 IEEE

of Tektronix 8-bit 2 Gs/s (gigasamples per second) A/D converters capable of digitizing 4096 samples at approximately 1 kHz. These A/D converters also measure the time between the trigger and the A/D clock edges, which allows software to maintain system coherency.

The SAR collects data at positions located approximately every 10 cm along the road. There are 4096 range samples taken per pulse, covering a range swath of 300 m. Since movement of the boom is slow enough, 128 pulses are transmitted; 64 pulses for each polarization, and the received pulses are aligned and integrated to increase the effective power on target. The received data is pre-processed on a Sun-based SPARC 2-E chassis that operates multiple i860-based array processors for data interleaving, integration, and Radio Frequency Interference (RFI) extraction. Processed records are then stored to optical disc for focusing and image processing within a co-located data processing van.

The radar is located on top of a 150 foot boom capable of traveling along roads acquiring data while fully extended. The boom-SAR provides a unique scientific capability for high quality data collection in a number of ways. First, in a strip mapping mode, this testbed can collect better than 1 square kilometer per hour of high resolution data for phenomenological studies as well as limited site characterization. Second, because this boom has an articulated arm, data can also be collected in a relatively large 2-D aperture providing significant amounts of data for true 3-D image formation. Finally, it simulates a airborne imaging SAR allowing for component and algorithm testing and risk reduction while giving higher quality data than would be expected from a flying system.

TEST SITE CHARACTERIZATION

The site selected for this first ground penetration test of the boom-SAR was the Steel Crater test site within Yuma Proving Ground, Arizona. A rather extensive geophysical survey was conducted of this one square kilometer site using an EM-31, GSSI SIR-3 ground contact radar, and the collection of over 150 soil samples, prior to burying targets. Targets buried within the site include mines, 55 gallon drums, missile mock-ups, wires, pipes, arms caches, and tactical vehicles at depths from 0 to 2.0 meters.

Soil samples where taken to the Soil and Water Science Department at the University of Florida where chemical and electrical characterization was performed. The soils within the Steel Crater site are predominately Calcids, with some Argids or Cambids. Calcium carbonate percentages were typical less than 6%, though several layers at locations within the site had up to 30 percent $CaCO_3$. Moisture content throughout the site ranged from 0.02% to 4.72% by weight. The soils analyzed from the site generally had a high sand content (80 - 96%) and a low clay content (most less than 5%). The iron content of the site was uniformly low.[1]

At the mine site, the SIR-3 detected an increased moisture content layer at approximately 30 - 45 cm depth. Otherwise, the profiles showed little structure, and a relatively low loss. Laboratory analysis of soil samples taken from an area of the minefield indicate that the soil is a Typic Haplocalcid, meaning that the $CaCO_3$ percentage is less than 5% and the clay content is less than 3%. Electrical properties were measured over a frequency range from 100 MHz to 1 GHz using a swept frequency complex permittivity measurement device. Fig. 1 shows the real dielectric constant of the soil, and Fig. 2 shows the conductivity in mmhos/m as a function of frequency and depth. These measurements show the same increase in moisture content, increasing the conductivity and dielectric constant, as was seen in the SIR-3 data.

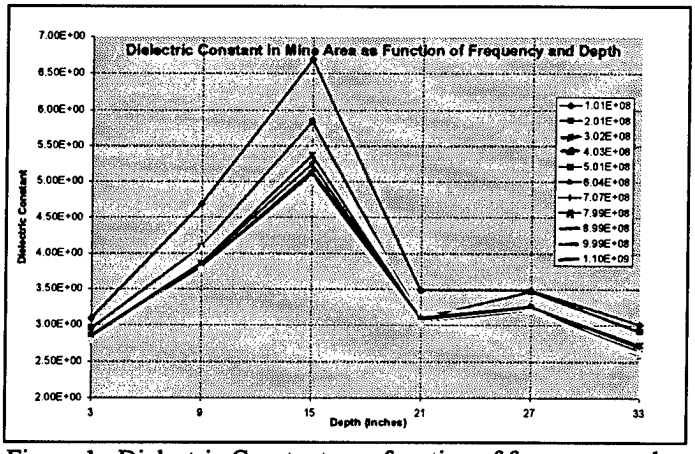


Figure 1. Dielectric Constant as a function of frequency and depth

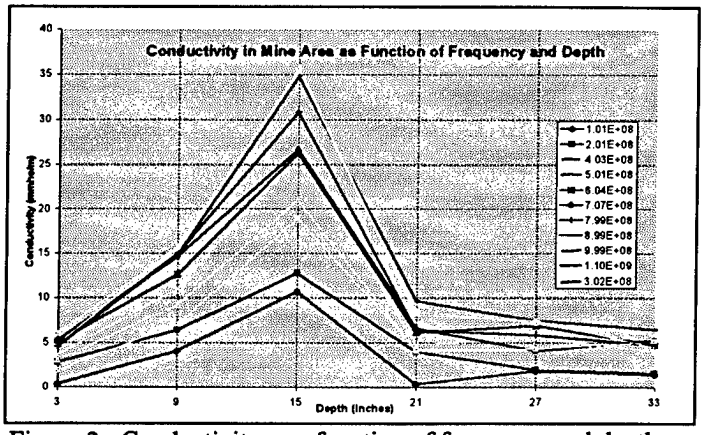


Figure 2. Conductivity as a function of frequency and depth

MINEFIELD RESULTS

The minefield consisted of 6 rows of anti-tank mines. The rows were 10 meters apart, and mines within a row were spaced 7 meters apart. The minefield consisted of 34 M20 metallic antitank mines buried flush with the surface, another 34 buried 6 inches deep, and 6 mines placed on the surface. The M20 mine is very nearly a cylindrical disc approximately 12 inches in diameter and 5 inches high. The minefield also contained 13 plastic anti-tank mines, 6 just below the surface and 7 buried 6 inches deep, of roughly the same shape and dimensions as the M20 mines.

During the data collection being presented, the boom-SAR traveled down a road parallel to and approximately 55 meters from the forward edge of the minefield. The radar was at a height of 45 meters giving a 39 degree depression angle to the forward row of mines and a 23 degree depression angle to the rear row of mines. Given the dielectric constant in fig. 1, the Brewster angle for this soil corresponds to a depression angle of approximately 27 degrees. To take advantage of the Brewster angle effect, data from the VV (vertical transmit, vertical receive) channel is being presented. The synthetic aperture used to focus the SAR image from which the data in figs. 3 and 4 are taken was 100 meters long, giving a cross range resolution of approximately 12 inches, while the full bandwidth gives a range resolution of 6 inches. The subbanded data has a range resolution of just under 1 meter.

In fig. 3 we present measured M20 mine RCS as a function of depression angle and depth of burial. The clutter data was obtained by making measurements of multiple non-target pixel RCS values, and clearly, there is a significant target to clutter ratio for the metal mines in this desert environment. The Method of Moments (MoM) model prediction is for a flat disc using HH polarized data, so one would expect there to be a slight increase in the RCS near the Brewster angle not shown on the predictive curves. The measured data does indeed show a slight increase in the RCS of the mines near the Brewster angle of 27 degrees. It must be pointed out that no data for the plastic mines is presented. The plastic mine's dielectric constant is between 3 and 4, giving very little contrast between it and the soil, leading to its RCS being at the clutter level.

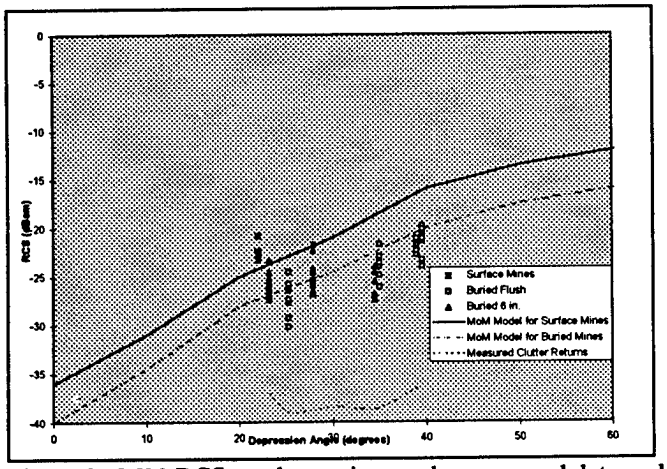


Figure 3. M20 RCS vs. depression angle: measured data and model predictions

Since the bandwidth of this system is so large, studies can be undertaken to select the optimum subband for specific targets. Fig. 4 shows the results of looking at the furthest row of 6 inch deep buried M20 mines at a low and high frequency subband. As might be expected, the relative response of the buried mines was stronger in the lower frequency band since it is not attenuated as much in the soil as the higher band. For the high band, many of the mines were at the clutter level and indistinguishable.

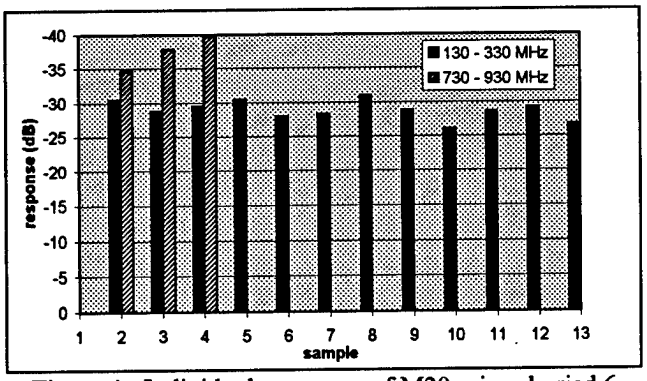


Figure 4. Individual responses of M20 mines buried 6 inches in subbands 130 - 330 MHz vs. 730 - 930 MHz

SUMMARY

Given the target to clutter ratio presented for the metallic anti-tank mine, it seems possible for a low-frequency UWB SAR to detect a minefield, if not individual mines from a stand-off platform. The remaining challenges are to develop target discrimination techniques[2], since contrast alone will lead to many false alarms in the data we have examined, and to develop methods to detect plastic landmines.

REFERENCES

[1] M. Collins, R. Kuehl, D. Heuberger, J. Kurtz, "Soil Properties at the Yuma Proving Grounds as Related to Ground Penetrating Radar," unpublished.

[2] K. Sturgess, M. Bennett, M. Ressler, T. Grosch, "Army Research Laboratory Ultra-Wideband Boom-SAR: System Overview and Minefield Detection and Recognition Results," Symposium for the Application of Geophysics to Engineering and Environmental Problems, pp. 582-588, 1995.

Signal Processing Aspects of Polarimetric Random Noise Radar Data for Shallow Subsurface Imaging

Yi Xu, Paul D. Hoffmeyer, Ram M. Narayanan, and John O. Curtis*

Department of Electrical Engineering and Center for Electro-Optics
University of Nebraska, Lincoln, NE 68588-0511, USA
T: 402.472.5141 F: 402.472.4732 EMail: eerdrmn@engvms.unl.edu

*U. S. Army Corps of Engineers, Waterways Experiment Station
Environmental Engineering Division
3909 Halls Ferry Road, Vicksburg, MS 39180-6199, USA
T: 601.634.2855 F: 601.634.2732 EMail: curtisj@ex1.wes.army.mil

Abstract—A novel polarimetric random noise radar system has been developed by the University of Nebraska for shallow subsurface probing applications. The radar system has been fabricated and tested, and its initial performance has been found to be quite satisfactory in detecting and locating buried objects. The system produces images of the co-polarized amplitude, cross-polarized amplitude, depolarization ratio, and polarization phase difference of the radar reflected signal as the antennas are scanned over the surface below which the objects are buried. Various signal processing algorithms are being explored to enhance target detection and clutter suppression. Since the radar system provides polarization phase differences between the orthogonal receive channels, algorithms based on Stokes matrix processing are being explored to detect and identify specific targets. One of the main advantages of Stokes matrix processing is in detecting long and slender cylindrical targets, which are not clearly detected in the conventional images. Furthermore, the optimal use of thresholding and smoothing operations to reduce and eliminate clutter is being examined. Examples of the preprocessed and post-processed images are presented.

INTRODUCTION

The use of radar techniques to detect, locate and identify buried shallow subsurface objects is of considerable interest in recent years [1]. The University of Nebraska has developed a polarimetric random noise radar system used mainly for detecting shallowly buried minelike objects. This novel Ground Penetrating Radar (GPR) system was designed, built and tested over the last two years. Simulation studies [2] and performance tests [3] on the system confirm its ability to respond to phase differences in the received signal, despite the fact that the probing waveform in random noise. This GPR system uses a wide bandwidth random noise signal operating within the 1-2 GHz frequency range. A block diagram of the system is shown in Fig. 1. High spatial resolution in the depth (range) dimension is achieved due to the wide bandwidth of the transmit signal. Complete details on backscatter data acquired by this system from various targets are provided in [4]. The radar system is operated and controlled by a PC and the data acquired is stored in the hard drive in the real time. From the raw data, the system produces four images corresponding to the co-polarized receive amplitude, cross-polarized received amplitude, depolarization ratio ,and polarimetric phase difference between the orthogonally polarized received signals. The polarimetric random noise radar system was used to gather data from a variety of buried targets from a specially designed sand box 3.5 m long and 1.5 m wide. Targets that were buried included metallic as well as non-metallic objects of different size and shapes that mimicked land mines as well as other objects. These objects were buried at different depths and with different relative orientations.

This paper describes two examples out of the entire data set collected that demonstrate the usefulness of Stokes matrix processing to enhance target detection. From the raw pre-processed images, we describe how the Stokes matrix images are computed. Simple image processing techniques, such as smoothing and thresholding algorithms are studied in order to enhance detection, and these results are also shown.

IMAGE ANALYSIS USING STOKES MATRIX FORMULATION

From the raw data collected by the radar system, we generate images based on the Stokes matrix formulation for facilitating the detection and recognition of targets using the polarimetric information on the buried target. The Stokes vector is a convenient method for representing the polarization state of an electromagnetic wave, and is denoted as $[S]$, given by

$$[S] = \begin{bmatrix} S_0 \\ S_1 \\ S_2 \\ S_3 \end{bmatrix} \tag{1}$$

The individual elements of the $[S]$ vector are defined as follows:

$$S_0 = |H|^2 + |V|^2 \tag{2}$$

$$S_1 = |H|^2 - |V|^2 \tag{3}$$

The partial support of this work by the U.S. Army Corps of Engineers, Waterways Experiment Station under Contract #DACA39-93-K-0031 is gratefully acknowledged.

0-7803-3068-4/96$5.00©1996 IEEE

$$S_2 = 2|H||V|\cos\theta_d \quad (4)$$

$$S_3 = 2|H||V|\sin\theta_d \quad (5)$$

In the above equations, θ_d is the polarimetric phase angle, i.e, the difference between the phase angle of the horizontally received signal and the vertically received signal. Also, $|H|$ and $|V|$ are the electric field amplitudes of the horizontally and vertically polarized received signals, whose squared values represent the co-polarized reflected power and cross-polarized reflected power respectively (assuming the transmit polarization is horizontal). We recognize S_0 as the total reflected power (sum of the co-polarized and cross-polarized reflected power). S_1 is recognized as the difference between the co-polarized and cross-polarized reflected power. S_2 is proportional to the cosine of the polarimetric phase angle, while S_3 is proportional to the sine of the polarimetric phase angle θ_d. Both S_2 and S_3 are weighted by the absolute electric field amplitudes of the reflected co-polarized and cross-polarized signals, as can be seen from their definitions. It is also to be noted that

$$S_0^2 = S_1^2 + S_2^2 + S_3^2 \quad (6)$$

The use of S_2 and S_3 is very helpful in detecting targets, since these parameters move in opposite directions, and thereby provides additional information about the reflected signal. When S_2 is high, S_3 is low, and vice versa. Thus, no matter what the polarimetric phase angle, the target image is bound to show up in either S_2 or S_3, or sometimes in both.

The above mentioned Stokes matrix images were generated, and combined with simple image processing operations to improve target detectability and clutter rejection. The smoothing filter is used for reduction of radar clutter and noise. It was found from the original raw data that high-frequency tonal variations were prevalent in regions without targets, and these grainy variations were attributed to the fact that the soil volume was inhomogeneous, and contained voids and rocks. The smoothing operation, when performed, results in low pass filtering and eliminates the high-frequency noise components. The thresholding operation is applied on the global scale to the entire smoothed image. It enhances image intensities above the mean intensity of the entire image, thereby enhancing target detectability, while simultaneously eliminating clutter, identified as low intensity areas, by setting these to zero digital number. As will be shown, these post-processing operations are successful in reducing clutter and enhancing target detectability. We emphasize here that currently, smoothing and thresholding operations have been investigated only for S_0 and S_1.

In the following figures, the four pre-processed images show the co-polarized received power (top), the cross-polarized received power (second from top), the depolarization ratio (second from bottom), and the polarimetric phase angle bottom). The four post-processed images show S_0 (top left), S_1 (bottom left), S_2 (top right), and S_3 (bottom right). The pre-processed image corresponding to two objects, one a round metal plate 23 cm in diameter and 2 cm thick, and the other a wooden plate of the same shape and dimensions, is shown in Fig. 2. The objects are buried in dry sand at 23 cm depth each, with a lateral separation of 32 cm. The Stokes matrix processed images are shown in Fig. 3. Both objects, especially the wooden plate (right object) is detectable in the S_1 image.

We also show images of polarization sensitive objects to demonstrate the capability of the system to utilize polarimetric features of the target in Fig. 4 and Fig. 5. In these figures, images were obtained for combinations of target orientation parallel to (Fig. 4) and perpendicular to (Fig. 5) the scan direction. The transmit polarization was parallel to the longitudinal axis of the object, which was a metal pipe 6 cm in diameter and 85 cm long. When the transmit polarization was perpendicular to the object axis, detection was not possible; hence, these images are not shown. From the processed images, we observe that a long slender object can be detected, no matter what its orientation is with respect to the scan direction, as long as the transmit polarization is parallel to the object orientation. This indicates that a dual-polarized transmitter, i.e, one that simultaneously or switchable transmits vertical and horizontal polarized signals can easily detect such an object.

CONCLUSIONS

From the experimental results obtained using the polarimetric random noise radar system, we find that it is capable of detecting shallowly buried objects. Application of the Stokes matrix image processing techniques provides a method for extracting the target polarimetric reflected properties for enhancing target detection and identification. Although the algorithm for image processing is relatively simple, it provides good results for enhancing target detectability. The experiments described in this paper were primarily performed with targets buried in dry sand, which is a low loss medium. Future study is needed to evaluate the radar system and its signal processing algorithms under more adverse conditions, such as wet clayey soil.

REFERENCES

[1] D.J.Daniels, D.J.Gunton, and H.F.Scott, "Introduction to subsurface radar," IEE Proceedings Part F, vol. 135, pp. 278-320, August 1988.

[2] R.M.Narayanan, Y.Xu, and D.W.Rhoades, "Simulation of a polarimetric random noise/spread spectrum radar for subsurface probing applications," Proc. IGARSS'94, Pasadena, CA, pp. 2494-2498, August 1994.

[3] R.M.Narayanan, Y.Xu, P.D.Hoffmeyer, and J.O.Curtis, "Design and performance of a polarimetric random noise radar for detection of shallow buried targets," Proc. SPIE Conf. on Detection Technologies for Mines and Minelike Targets, Orlando, FL, pp. 20-30, April 1995.

[4] P.D.Hoffmeyer, Y.Xu, R.M.Narayanan, and J.O.Curtis, "Backscatter characteristics of buried targets measured using an ultrawideband polarimetric random noise radar," Proc. IGARSS'96, Lincoln, NE, May 1996.

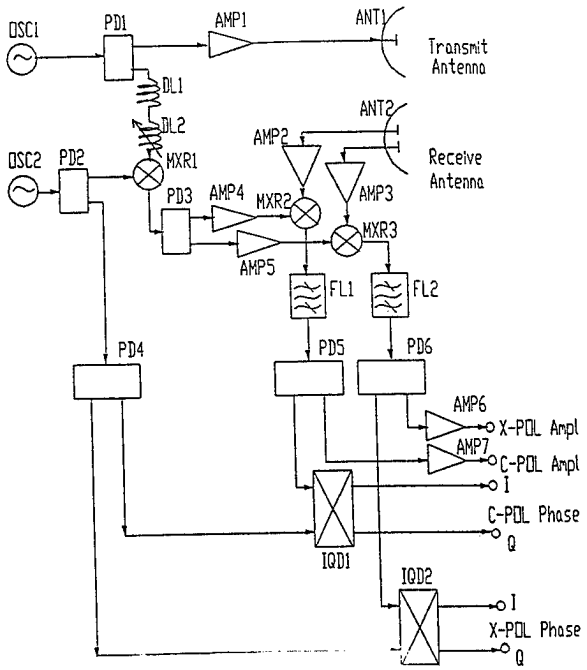


Figure 1: Block diagram of the polarimetric random noise radar system.

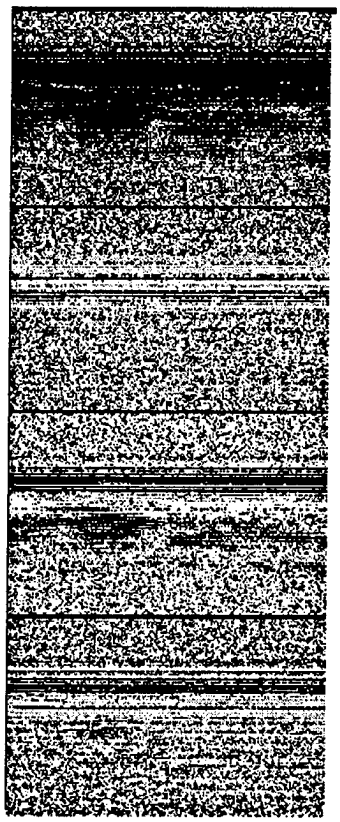


Figure 2: Pre-processed image of two buried objects.

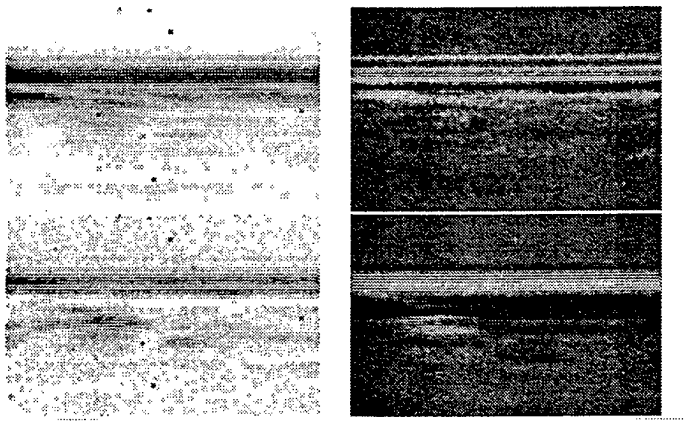


Figure 3: Post-processed image of two buried objects.

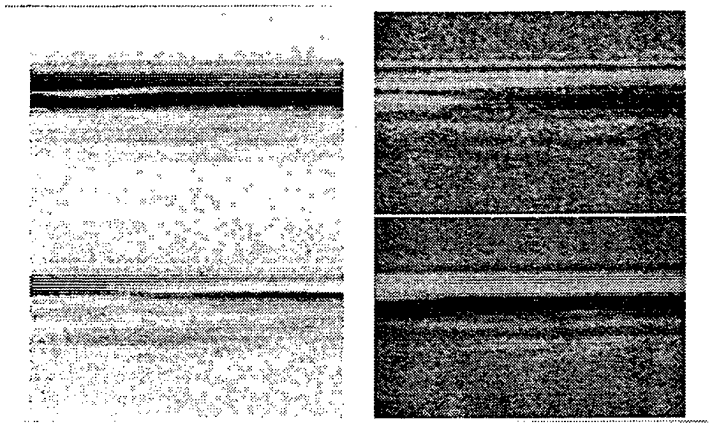


Figure 4: Post-processed image of slender pipe parallel to scan direction.

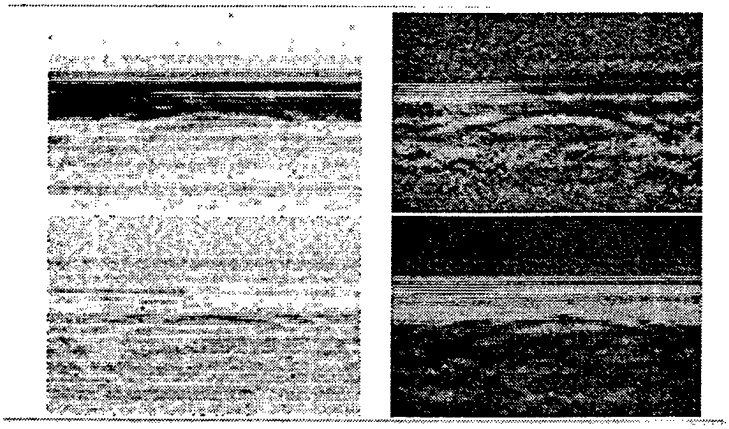


Figure 5: Post-processed image of slender pipe perpendicular to scan direction.

An Interferometric Technique for Synthetic Aperture Ground-Penetrating Radar

Carl Leuschen, Nathan Goodman, Chris Allen, Richard Plumb
The University of Kansas, Remote Sensing Laboratory
2291 Irving Hill Road, Lawrence, KS 66044
TEL: 913/864-3017 , FAX: 913/864-7789 , E-mail: callen@eecs.ukans.edu

Abstract--Many synthetic aperture radar (SAR) algorithms for ground-penetrating radar involve making measurements along a single path and using the collected data to form a two-dimensional image of the scattering object. In the calculation of these images, certain assumptions are made about the scattering objects; mainly, that the reflections are occurring directly below the antenna location, which is not always the case. By applying interferometric techniques to SAR-based images, it is possible to construct an image of the scattering object that contains all three dimensions rather than only two, eliminating the need for these assumptions. This paper proposes a method of combining radar interferometry with SAR-based ground-penetrating radar. The methodology used is to expand several two-dimensional images, each calculated from measurements collected along single paths, into a three-dimensional image of the scattering object through the use of radar interferometry. This process involves superimposing two complex two-dimensional images and using the information found in the phase differences of corresponding locations from each image to calculate the location of the object in the dimension not contained within the previous two-dimensional images. This method is tested using both computer-simulated data and also data collected from the measurements of objects buried in sand.

INTRODUCTION

Currently, most interferometric applications consist of topographic mapping from data collected either from aircraft or satellite. This paper uses the techniques developed for these applications and applies them to the case of subsurface imaging in which the reflections occur much closer to the radar antennas. The primary objective in the application of interferometry to ground-penetrating radar is to expand the two-dimensional images collected using SAR processing into three dimensions. Since two-dimensional images contain ambiguities concerning the exact scatterer locations in real space, the need for an image of subsurface reflections containing all of the dimensions is essential in obtaining an accurate idea of what lies beneath the surface.

Although this technique illustrates a method to image a subsurface area, a prior knowledge of the velocity profile of the ground is required to obtain the correct distances from the time responses. Also, as with many imaging techniques, the reflections are assumed to originate from point scatterers. Due to these two assumptions, the main scope of this technique is for homogeneous ground with localized scatterers.

DEVELOPMENT

Through the application of interferometry to two-dimensional synthetic aperture radar (SAR) images, the reflections of the scattering targets can be expressed with locations containing all three dimensions, eliminating any ambiguity found in the previous images. The process of interferometry involves examining the phase difference at corresponding locations of two two-dimensional SAR images in order to obtain information of the reflection's location in terms of the dimension not contained within the SAR images. The basic geometry for an interferometric application, as shown in Fig. 1, consists of two SAR images collected along a parallel path separated by a baseline, *B*. The goal is to generate an image in a vertical plane parallel to the SAR paths at a distance, *d*, from path 1.

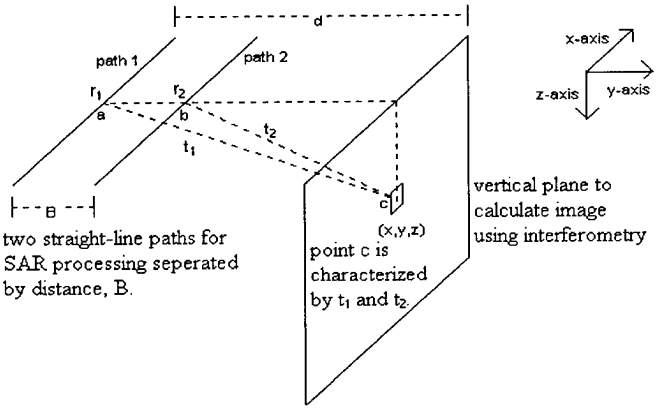


Fig. 1. The basic geometry for an interferometric application

0-7803-3068-4/96$5.00©1996 IEEE

To demonstrate how interferometry is used to calculate images in terms of all three dimensions, the response due to a single point scatterer will be considered first, and then the existence of multiple scatterers is assumed to produce similar results due to superposition. However, by applying superposition, all the coupling effects between scatterers is ignored. Before applying interferometry, the images are expected to contain resolution in range and also in the same dimension of the two paths as a result of SAR processing. The images will be calculated in three dimensions by using the information found in the phase differences at corresponding locations along the two SAR paths to expand the range dimension into a depth, z, at a specific distance, d, resulting in a two-dimensional image at a constant distance from path 1.

By considering two SAR images calculated from measurements collected along two parallel paths in the presence of a single scatterer, the time responses, r_1 and r_2, at corresponding locations along the path can be related by a time shift, t_s, due to the separation of the baseline, B. This time shift is represented in the frequency domain as a phase shift as shown by

$$r_1(t) = r_2(t - t_s) \tag{1}$$

$$R_1(f) = R_2(f)\exp(-j2\pi f t_s). \tag{2}$$

The relationship of the responses in the frequency domain provides the phase information, seen on the right-hand side of (2), as a direct result from the time shift in (1). Since this time shift is uniquely determined by the scatterer's location and also by the baseline, B, the phase information is used to determine the scatterer's depth for a given distance, d, from path 1.

By noticing that the scatterer's location is related to the time shift in (1), a response describing the relationship between r_1 and r_2 in terms of any time shift, τ, is expressed by the correlation of r_1 and r_2, which is shown in both the time domain (3) and the frequency domain (4).

$$r_{12}(\tau) = \sum_k r_1(t_k) r_2(t_k - \tau) \tag{3}$$

$$r_{12}(\tau) = \frac{1}{N}\sum_{i=1}^{N} R_1(f_i) R_2^*(f_i)\exp(j2\pi f_i \tau). \tag{4}$$

In (4), R^* represents the complex conjugate. Substituting the relationship of R_1 and R_2 for a single scatterer (2) into (4), r_{12} can be shown to have a peak value occurring at a time shift, t_s, which corresponds to the scatterer's location.

$$\begin{aligned} r_{12}(\tau) &= \sum_{i=1}^{N} R_2(f_i)\exp(-j2\pi f_i t_s) R_2^*(f_i)\exp(j2\pi f_i \tau) \\ &= \sum_{i=1}^{N} \left|R_2(f_i)\right|^2 \exp\left(j2\pi f_i(\tau - t_s)\right) \end{aligned}. \tag{5}$$

Since the correlation response of r_1 and r_2, (3) and (4), contains peak values at time shifts corresponding to the locations of scatterers, by normalizing this response between zero and one, the correlation can be used to show the tendency for a scatterer to exist at any location that is characterized by a specific time shift, τ.

$$c_{12}(\tau) = \frac{r_{12}(\tau)}{\sqrt{r_{11}(0) r_{22}(0)}}. \tag{6}$$

An image of a vertical plane occurring at a distance, d, is now formed by combining the contributions of the two individual responses, r_1 and r_2, along with the response of their normalized correlation, r_{12}. As shown in the Fig. 1, every point in the imaging area can be characterized by two times, (t_1,t_2), corresponding to the point's location relative to path 1 and path 2.

$$(x, y, z) \Rightarrow (t_1, t_2). \tag{7}$$

Finally, an approximation to a specific location is calculated by scaling the average of the two responses at their corresponding times, (t_1,t_2), by the value of the normalized correlation at the time shift, (t_1-t_2).

$$p(x, y, z) = c_{12}(t_1 - t_2)\frac{1}{2}\left\{r_1(t_1) + r_2(t_2)\right\}. \tag{8}$$

By using this technique, an area spanned by two parallel SAR images can be described in all three dimensions.

SIMULATION

To demonstrate how interferometry can be used to expand two two-dimensional SAR images into three dimensions, a simple test configuration was simulated on a computer. With respect to Fig. 1, the configuration consists of two SAR paths separated by a baseline of one meter with 16 measurements collected along each path. The configuration also consists of \

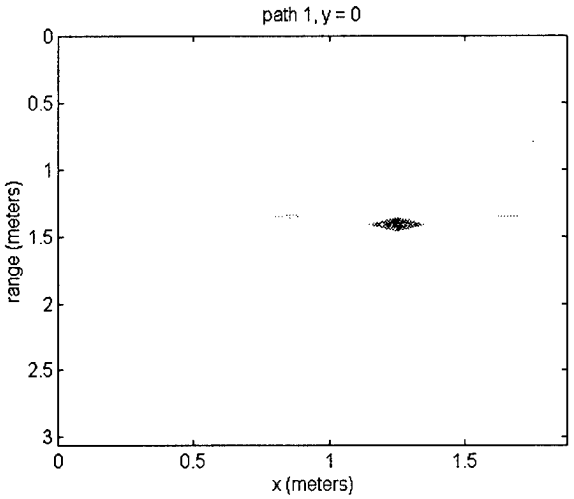


Fig. 2. SAR image along path 2

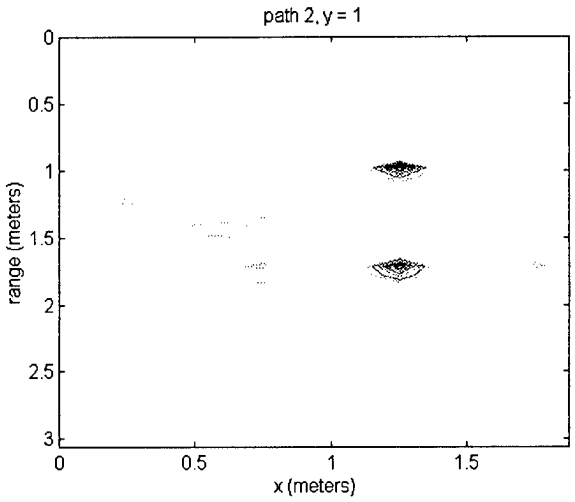


Fig. 3. SAR image along path 1

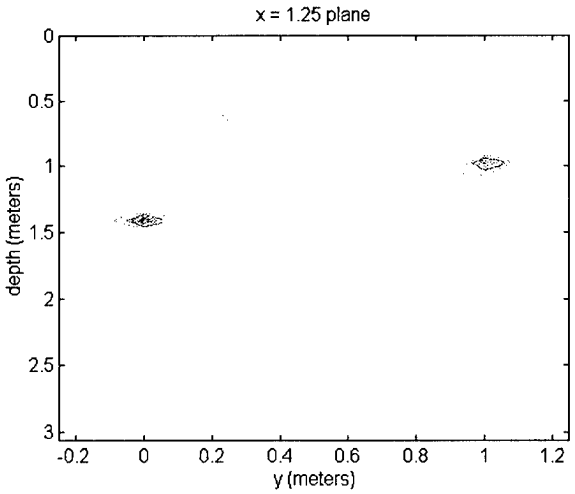


Fig. 4. Image calculated using interferometry

two scatterers located at coordinates (1.25,1,1) and (1.25,0,1.4142) such that the reflections appear at equal times from path 1. By using the difference between the two images calculated from measurements collected along the two paths, the single reflection occurring in image 1 is expanded into locations in three dimensions to describe scatterers located at two coordinates.

Fig. 2 and Fig. 3 are the SAR images calculated from the data simulated along two paths seperated by a distance of one meter. As expected there exists only one reflection in Fig. 2 since the scatterers were located equal distances from path 1. By applying interferometry to the two images, the locations of the two scatterers were separated into their correct positions as shown in Fig. 4.

DISCUSSION

In this paper, a technique has been presented in which two two-dimensional SAR-based images are used in order to obtain an image containing all three dimensions, eliminating any assumptions or requirements concerning the imaging area. This technique has been tested from data simulated on a computer using phase propagation. For further verification, this technique will be tested using real data collected from measurements of objects buried in sand, which also meets the assumption of homogeneous ground with localized scatters.

REFERENCES

[1] C. T. Allen, "Interferometric Synthetic Aperture Radar," *IEEE Geoscience and Remote Sensing Newsletter*, issue 96, pp. 6-13, September 1995.

[2] D. Massonnet and T. Rabaute, "Radar Interferometry: Limits and Potential," *IEEE Trans. on Geoscience and Remote Sensing*, vol. 31, no. 2, pp. 455-464, March 1993.

[3] A. Gunawardena and D. Longstaff, "A Matched Filter Based Synthetic Aperture Radar(SAR) Algorithm For Stepped Frequency Ground Penetrating Radar," *IEEE International Radar Conference*, pp. 239-243, 1995.

Subsurface Imaging using Ground-Penetrating Radar Measurements

Nathan Goodman, Carl Leuschen, Richard Plumb and Chris Allen
University of Kansas, Radar Systems and Remote Sensing Laboratory
2291 Irving Hill Road, Lawrence, KS 66045-2969 USA
TEL: 913/864-7735, FAX: 913/864-7789, E-mail: plumb@eecs.ukans.edu

Abstract – Much work has been done toward reconstructing the electrical parameters of an unknown buried object. Many methods, and accompanying results from simulations, have been presented. Most research in the area, however, has been in developing imaging algorithms that have been tested primarily through computer simulation. This paper presents a newly constructed facility for ground-penetrating radar experiments, as well as the proposed applications for such a facility. The test site consists of a sand-filled volume approximately 15 feet long, 13 feet wide, and 7 feet deep. The experimental setup consists of transmitters and receivers in several common configurations, such as the offset VRP, cross-borehole, and surface-to-surface configurations. The motivations for such an experimental site are presented, as well as the imaging algorithms intended for application. These algorithms include migration techniques, SAR processing, Born-iterative method, and diffraction tomography.

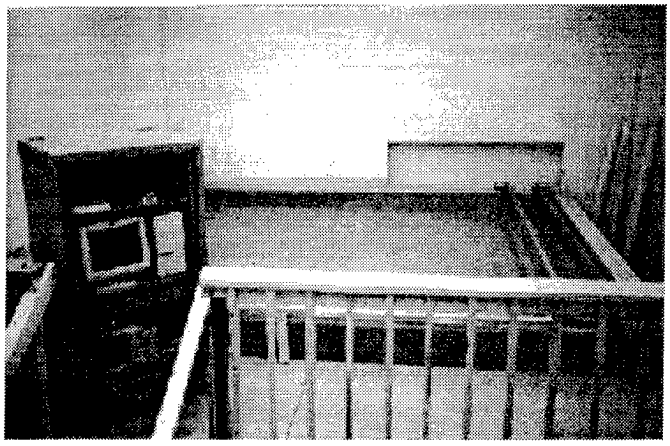
INTRODUCTION

Ground-penetrating radar has many applications ranging from detection of buried pipes to non-destructive probing for contaminants to mapping of the subsurface layers. Furthermore, the advantages of ground-penetrating radar over drilling and digging are tremendous. Ground-penetrating radar is less destructive and can provide more information than other methods of exploration. Ground-penetrating radar will also become less expensive and more powerful as technology and computing power progress. These reasons have sparked a growing interest in ground-penetrating radar algorithms that image the subsurface. However, very few of these algorithms have been applied outside the realm of computer simulation. It is this last fact that has motivated the ground-penetrating radar group at The University of Kansas in much of our recent work.

The lack of application of ground-penetrating radar in real field experiments has driven our current research toward developing techniques that can be successfully applied in the field. However, it is obvious that many difficulties would arise were the algorithms taken directly from the computer simulation environment to the field. For this reason a facility has been constructed that will allow for testing of many imaging approaches and algorithms in a controlled environment. Many common algorithms will be tested and compared. The results, computational power needed, ease of data acquisition, and other parameters will be investigated. The end result will be a thorough investigation of ground-penetrating radar subsurface imaging techniques, another step toward making ground-penetrating radar a more widely used method of subsurface exploration.

EXPERIMENTAL FACILITY

Work has just been completed on a fully automated test facility. A large concrete box was constructed with inner dimensions of 15 feet long by 13 feet wide by 7 feet deep. A platform provides easy access to the top of the box. The box is filled with sand providing a homogeneous background. Last, drains were included at the bottom of the box. These drains will be used in the future for experiments on imaging liquid contaminants and for providing an adjustable water table.



Experimental Facility and Test Equipment

Mounted on top of the box is a custom-designed gantry system. The system is constructed of extruded aluminum and spans the entire test area. Two independent gantries provide positioning for two antennas that can be placed at any two positions above the sand. Also, with another mechanical attachment, the antennas can be lowered into the sand, allowing for other ground-penetrating radar configurations that require the use of a borehole, such as the cross-borehole and offset VRP configurations. Last, one length of PVC pipe spans the entire box below the level of the sand. This opening allows a receiving antenna to be placed within the sand in order to verify our predictions of the fields radiated from more complicated antennas.

The gantry system is fully controllable with a personal computer. A 4-axis PC Servo-Motor Controller card was purchased and placed in a PC. The card drives four servo

0-7803-3068-4/96$5.00©1996 IEEE

amplifiers independently, with each amplifier driving a different axis. Each gantry can be placed at any position above the sand with the exception that the two cannot cross each other. This limitation will be easily overcome through electronic switching of the antennas through software. Each axis is equipped with an optical encoder, and the Servo-Motor Controller uses this information to generate and execute any programmed motion profile with excellent accuracy. The entire experiment can be programmed and left alone.

RADAR EQUIPMENT

Experiments will be performed with two different radar systems. The first uses a Hewlett Packard 8753D Vector Network Analyzer. The network analyzer measures the desired reflection or transmission parameter. The network analyzer is fully controllable via a National Instruments GPIB Interface Board and Labview software. Commands and data can be read from and written to the network analyzer using this board. The board also allows for control of two coaxial switches located at the antennas. The commands for the switches are sent to a Hewlett Packard switch driver that drives the control signals for both switches. The switches allow for the use of dual-polarized antennas. The second radar system is a Sensors and Software pulseEKKO 1000.

Two sets of antennas will be used. First, two Tecom dual circular sinuous antennas will be used. Their frequencies of operation are from 2 GHz to 18 GHz, and the coaxial switches will use both circular polarizations. A pair of loaded dipole antennas will also be used. Their frequencies of operation are from 450 MHz to 1350 MHz, and they are provided with the pulseEKKO 1000.

With the above equipment, the entire experiment can be preprogrammed and left alone to execute. The programming for the antenna-positioning system and the radar system is fully integrated using Labview. The result is an operational ground-penetrating radar system that is fully integrated in both hardware and software.

PROCESSING METHODS

Several post-processing techniques will be evaluated using the ground-penetrating radar test facility. Migration techniques, interferomic SAR, Born-iterative method, and diffraction tomography will all be applied, and the results compared.

The migration techniques include FK migration. In this method the time responses along a single path are collected. The two-dimensional Fourier transform of the time responses and of the position along the path puts the data into the FK domain where F is for frequency and K is for spatial frequency. The FK domain is filtered in order to focus the returns from a single point [1].

The SAR-processing methods include Interferomic SAR. Interferomic SAR applies the phase difference between two baseline traces in order to locate a scatterer in three dimensions, rather than only two as in conventional SAR processing [2].

The Born-iterative technique uses the Born approximation to linearize the scattering equation with respect to the object profile. Once an initial reconstruction of the object profile is obtained, it is used to solve the forward scattering problem. The inverse scattering problem is then solved again using the new information. A new object profile is obtained, and the iterations continue until the object profile converges [3], [4], [5].

Diffraction tomography is another technique that will be investigated. Diffraction tomography relates the two-dimensional Fourier transform of the scattered field within a plane to the three-dimensional Fourier transform of the object along a hemispherical arc. The object is illuminated with a plane wave that can be synthesized using stacking or other techniques [5], [6].

CONCLUSIONS

A new experimental facility for testing subsurface imaging algorithms has been presented and described, as well as the justification for such a site. The facility is fully automated and will allow for ease of data acquisition in a controlled manner. Plans for testing existing algorithms have been presented. Each algorithm will be implemented, and the results compared along with other factors such as computational and data acquisition requirements. Experiments are now underway and results are expected soon. A full investigation of the applicability of ground-penetrating radar imaging techniques will follow.

REFERENCES

[1] Stolt, R.H., "Migration by Fourier Transform," *Geophysics*, vol. 43, No. 1, pp. 23-48, 1978.

[2] Allen, C.T., "Interferometric Synthetic Aperture Radar," *IEEE Geosci. & Rem. Sen. Newsletter*, issue 96, pp. 6-13, Sept. 1995.

[3] Chew, W.C., *Waves and Fields in Inhomogeneous Media*, Van Nostrand Reinhold, New York, 1990.

[4] Moghaddam, M., and Chew, W.C., "Nonlinear Two-Dimensional Velocity Profile Inversion Using Time Domain Data," *IEEE Trans. On Geosci. & Rem. Sen.*, vol. 30, no. 1, pp. 147-156, 1992.

[5] Chaturvedi, P., "Electromagnetic imaging and classification of subsurface targets," Ph. D. Dissertation, University of Kansas, 1995.

[6] Devaney, A.J., "Geophysical Diffraction Tomography," *IEEE Trans. On Geosci. & Rem. Sen.*, vol. GE-22, no.1, pp. 3-13, January 1984.

Multi-layer detection/tracking for monostatic Ground Penetrating Radar

V. Rampa (*) and U. Spagnolini (**)
(*) C.S.T.S.-C.N.R., Politecnico di Milano
(**) D.E.I., Politecnico di Milano, Piazza L. da Vinci 32, I-20133, Milano, Italy
tel: +39-2-2399-3575, fax: +39-2-2399-3413, email: {rampa,spagnoli}@elet.polimi.it

Abstract—**In monostatic ground penetrating radar (GPR) the interfaces profile can be estimated from echoes amplitude and time of delay (TOD) using a layer stripping inversion algorithm. Our aim is to establish a reliable processing sequence for layer stripping inversion by estimating echoes TOD that keeps into account the layers lateral continuity, and by tracking the corresponding interfaces. Here we propose first an algorithm for multitarget tracking and then we describe the application of detection/tracking to 1ns pulse monostatic GPR. The system is used to estimate layer thicknesses of asphalt and concrete in pavement profiling. Detection/tracking shows a better recognition capability of the lateral continuity in near surface interfaces with respect to algorithms that employ only local detection of echoes.**

I. INTRODUCTION

In monostatic Ground Penetrating Radar (GPR) the ultimate goal is to obtain a profile of the near surface layers. This can be achieved with simple layer stripping inversion that exploits the relationships between amplitude and time of delay (TOD) of the echoes that belong to the same interfaces. The multi-layer detection/tracking algorithm presented in the first part was developed for tracking amplitudes and TOD's of multiple interfaces by applying iteratively a single-layer detection/tracking algorithm [3]. This research was motivated by the application discussed in the second part: a short range (within 0.8 m) radar system was mounted on a vehicle to estimate asphalt and concrete thicknesses in pavement profiling. In spite of its simplicity, the layer stripping inversion is a promising approach for this application to automatically process large amount of data (approximately 15-20 Mbytes/Km) in real time (vehicle speed is 50Km/h). The validation tests with core samples show thickness errors within 10%.

II. INTERFACE DETECTION AND TRACKING

A. Problem formulation

The signal $r(x_i,t)$, measured by the GPR system at space location $x_i = i\Delta x$, is assumed to be a superposition of L_i echoes that correspond to L_i interfaces (or targets):

$$r(x_i,t) = \sum_{l=1}^{L_i} a_l(x_i)\, s(t-\tau_l(x_i)) + w(x_i,t); \qquad (1)$$

where $s(t)$ is the transmitted pulse waveform having pulse-width T_s; $a_l(x_i)$ and $\tau_l(x_i)$ are the amplitude and the time of delay (TOD) respectively of the echo due to the *l-th* interface; $w(x_i,t)$ is the zero mean Gaussian noise assumed spatially and temporally uncorrelated with variance $E\left[w^2(x_i,t)\right] = \sigma^2$. Since amplitude is proportional to the reflection coefficient at the interface, it is $|a_l(x_i)| \leq 1$. The TOD's that correspond to the *l-th* interface are laterally continuous (when present) with $|\tau_l(x_i) - \tau_l(x_{i+1})| \leq T_s$; the number of interfaces L_i may change from one location to the adjacent one ($|L_{i+1} - L_i| \leq 1$) but it is bounded by the maximum number of interfaces L ($L_i \leq L$). According to model (1) these assumptions involve multiple interfaces (up to L) that may be laterally continuous or discontinuous. The purpose of this paper is to estimate the interface TOD's $\tau_l(x_i)$ and amplitude $a_l(x_i)$ from monostatic GPR observations $r(x_i,t)$ by assuming known the pulse shape $s(t)$.

The likelihood ratio test may be used in this case to discriminate between two alternative hypotheses $H_0(x_i)$ and $H_1(x_i)$ [5]. $H_1(x_i)$ denotes the presence of an echo within the observation window $T \gg T_s$ regardless of its TOD $\tau_l(x_i)$ while $H_0(x_i)$ indicates absence of echoes (i.e. $r(x_i,t) = w(x_i,t)$). The correlation filter (CF) is known to represent an optimum approach in the estimation of echo amplitude and TOD once the echo has been detected within T [4]. However, the detected echoes may be part of an interface or may be due to false alarms. This classification is performed herein by exploiting the lateral continuity of interfaces within a multitarget tracking approach.

B. Detection/tracking algorithm

For the tracking algorithm we assume only one interface: $L_i \leq L = 1$. For the *i-th* scan $\mathbf{r}_i = \{r(x_i,t)\}$, we can assume two hypotheses: $H_0(x_i)$ and $H_1(x_i)$ that denote absence or presence of the interface, respectively (interface subscript $l = 1$ is understood). Since echoes can have any of M TOD's in the time sampling bins, a sequence of $M+1$ disjoint sub-hypotheses $h_m(x_i)$ ($m = 0,1,...,M$) is thus defined as a partition of the whole hypotheses space. $h_m(x_i)$ with $m = 1,...,M$ corresponds to the hypothesis that echo is present at time delay $m\Delta t$; when echo is ab-

0-7803-3068-4/96$5.00©1996 IEEE

sent the hypothesis is denoted as $h_0(x_i)$ (or, equivalently, $H_0(x_i)$). On the other hands, hypothesis $H_1(x_i)$ is the union of all sub-hypotheses $h_1(x_i),...,h_M(x_i)$.

The a-posteriori pdf of the $M+1$ sub-hypotheses $p[h_m(x_i) \mid \mathbf{r}_i]$ allows the estimation of the echo TOD's by using the maximum a–posteriori (MAP) or the minimum mean square error (MMSE) criteria. The a–priori pdf will be estimated from neighboring scans after detecting and tracking those TOD's that are consistent with the lateral continuity of interface.

The a–posteriori pdf that is evaluated for interface tracking includes all the data up to the *i-th* scan: $p[h_m(x_i) \mid \mathbf{R}_i]$ where $\mathbf{R}_i = [\mathbf{r}_i, \mathbf{r}_{i-1}, \ldots, \mathbf{r}_1]$. From Bayes' theorem it follows that $\forall m$:

$$p\left[h_m\left(x_i\right)|\mathbf{R}_i\right] = A_i\, p\left[\mathbf{r}_i|h_m\left(x_i\right)\right]\, p\left[h_m\left(x_i\right)|\mathbf{R}_{i-1}\right]; \tag{2}$$

$p\left[h_m\left(x_i\right) \mid \mathbf{R}_{i-1}\right]$ and $p\left[h_m\left(x_i\right) \mid \mathbf{R}_i\right]$ denote the a-priori and the a-posteriori pdf that hypothesis $h_m\left(x_i\right)$ holds true in scan *i-th*; $p\left[\mathbf{r}_i \mid h_m\left(x_i\right)\right]$ is the conditional pdf that there is an echo with TOD $m\Delta t$ under the assumption that the observations $\mathbf{r}_i$ are independent of all the observations up to scan *(i-1)-th* (i.e., $p\left[\mathbf{r}_i \mid h_m\left(x_i\right), \mathbf{R}_{i-1}\right] = p\left[\mathbf{r}_i \mid h_m\left(x_i\right)\right]$); A_i is a normalization term. Interface detection should be carried out before interface tracking by evaluating the a-posteriori pdf of detection derived from the union of all tracking hypotheses $h_m\left(x_i\right)$ (with $1 \leq m \leq M$):

$$p^{(d)}\left[H_1\left(x_i\right)|\mathbf{R}_i\right] = \sum_{m=1}^{M} p\left[h_m\left(x_i\right)|\mathbf{R}_i\right] > \frac{1}{2}\,. \tag{3}$$

The a-posteriori pdf of tracking

$$p^{(t)}\left[h_m\left(x_i\right)|\mathbf{R}_i\right] = \frac{p\left[h_m\left(x_i\right)|\mathbf{R}_i\right]}{\sum_{m=1}^{M} p\left[h_m\left(x_i\right)|\mathbf{R}_i\right]}\,, \tag{4}$$

with $m = 1,\ldots,M$ is the probability that hypothesis $h_m\left(x_i\right)$ holds true conditioned to the assumption that an echo has been detected in scan *i-th* regardless of its TOD. Detection (3) and tracking pdf's (4) are evaluated separately but exploited sequentially. In other words, for each scan, the detection of the interface is based on pdf $p^{(d)}\left[H_1(x_i)|\mathbf{R}_i\right]$ and the estimation of interface TOD is based on pdf $p^{(t)}\left[h_m\left(x_i\right)|\mathbf{R}_i\right]$.

Once the a-posteriori pdf's are known for *i-th* scan, the MAP or MMSE estimate of the interface delay $\widehat{\tau}\left(x_i\right)$ is given by the maximum or the mean of the a-posteriori pdf (4) respectively. The conditional pdf $p\left[\mathbf{r}_i|h_m\left(x_i\right)\right]$ for $m \geq 1$ is evaluated by assuming known the waveform $s\left(t\right)$. Because of the normalization in the relationship between a-priori and a-posteriori pdf's (2), it is more convenient to evaluate the likelihood ratio function of the data samples that is (the time interval is long enough to contain the waveform without edge effects):

$$\frac{p\left[\mathbf{r}_i|h_m\left(x_i\right)\right]}{p\left[\mathbf{r}_i|h_0\left(x_i\right)\right]} = \exp\left\{-\frac{E_s - 2c(x_i,t_m)}{2\sigma^2}\right\}; \tag{5}$$

E_s is the energy of the pulse and $c(x_i,t_m) = \sum_{k=1}^{M} r(x_i,t_k)\; s(t_k - m\Delta t)$ denotes the correlation filter evaluated in $t_m = m\Delta t$.

C. Markov model for a-priori pdf computation

The lateral continuity of interfaces is exploited by relating the a-priori pdf of scan *i-th* to the a-posteriori pdf of scan *(i-1)-th*. This is obtained assuming a Markov model for the interface generation process. The a-priori pdfs for scan *i-th* are thus obtained from the a-posteriori pdf's for scan *(i-1)-th* by using different transition probabilities for detection and tracking:

$$\begin{aligned} &p^{(d)}\left[H_1(x_i)|\mathbf{R}_{i-1}\right] = \\ &\quad (1-q)\, p^{(d)}\left[H_1(x_{i-1})|\mathbf{R}_{i-1}\right] + q\, p^{(d)}\left[H_0(x_{i-1})|\mathbf{R}_{i-1}\right] \\ &p^{(t)}\left[h_m\left(x_i\right)|\mathbf{R}_{i-1}\right] = \textstyle\sum_{k=-n}^{n} b_k\, p^{(t)}\left[h_{m-k}\left(x_{i-1}\right)|\mathbf{R}_{i-1}\right]. \end{aligned} \tag{6}$$

The transition probability for detection q is proportional to the state-variation across neighboring scans (i.e., the probability to change from the state of interface absent $H_0(x_{i-1})$ to interface present $H_1(x_{i-1})$ or viceversa). The transition probabilities for tracking b_k have an odd symmetry with respect to b_0 and are normalized to one (i.e., $\sum_{k=-n}^{n} b_k = 1$). The choice of the shape of the transition probabilities b_k as well as the width n depends on the lateral continuity of interfaces according to the specific problems. In the application discussed in this paper we preferred a triangular shape $b_k = \left[1 - |k|/n\right]/n$ with n ranging from 2 to 10. A mirror boundary condition should be adopted to guarantee uniform stationary pdf [2]. During the initialization phase, the a-priori pdf of detection and tracking are assumed to be uniformly distributed. The a-priori pdf for the $M+1$ hypotheses $p\left[h_m\left(x_i\right) \mid \mathbf{R}_{i-1}\right]$ to be used in Bayes' formula (2) are thus derived from a-priori pdf's for detection (i.e., $p\left[h_0\left(x_i\right)|\mathbf{R}_{i-1}\right] = p^{(d)}\left[H_0(x_i)|\mathbf{R}_{i-1}\right]$) and tracking (i.e., $p\left[h_m\left(x_i\right)|\mathbf{R}_{i-1}\right] = p^{(d)}\left[H_1(x_i)|\mathbf{R}_{i-1}\right] p^{(t)}\left[h_m\left(x_i\right)|\mathbf{R}_{i-1}\right]$).

D. Multiple interface tracking

Tracking of echo TOD's are performed with MAP or MMSE criteria. However, the approach discussed so far is for detecting and tracking one interface only. In presence of more than one interface, the detection/tracking algorithm tracks the echo delay with the larger amplitude or better SNR. This tracking ambiguity could be avoided, in principle, by processing subsequences of time samples. In practice, errors are difficult to avoid when two interfaces

are close to each other (limits in TOD resolution) or when one interface splits into two interfaces (or two interfaces merge into one).

Tracking of multiple interfaces is performed here iteratively, and each iteration is limited to one interface only. Let $\widehat{\tau}_l(x_i)$ denote the estimated TOD for the *l-th* interface from data $r^{(l)}(x_i,t)$ (superscript denotes the *l-th* iteration), the echo amplitude estimate is: $\widehat{a}_l(x_i) = c(x_i,\widehat{\tau}_l(x_i))/E_s$. The *l-th* interface already tracked is removed from data to avoid multiple tracking of the same interface. The observed data to be used for *(l+1)-th* interface tracking is: $r^{(l+1)}(x_i,t) = r^{(l)}(x_i,t) - \widehat{a}_l(x_i)\, s(t-\widehat{\tau}_l(x_i))$ (note that $r^{(0)}(x_i,t) = r(x_i,t)$). Detection/tracking iterations are performed until the residual $r^{(l+1)}(x_i,t)$ achieves a reasonable level or by limiting $l \leq L$. Even if this approach can be considered sub–optimum, comparative analysis in [3] shows that it should be preferred to the global approach of multitarget tracking [1] mostly for its capability to handle tracking of interfaces that are closely spaced in their TOD's. Figure 1 shows a simulation of the multitarget tracking for two sinusoidal interfaces (SNR=5dB) where it has been assumed $L = 3$. After $l = 2$ the a-posteriori pdf of detection is mostly below threshold (i.e., $p^{(d)}\left[H_1(x_i)\,|\mathbf{R}_i^{(l>2)}\right] < 1/2$) which corresponds to the case when no more interfaces are to be tracked.

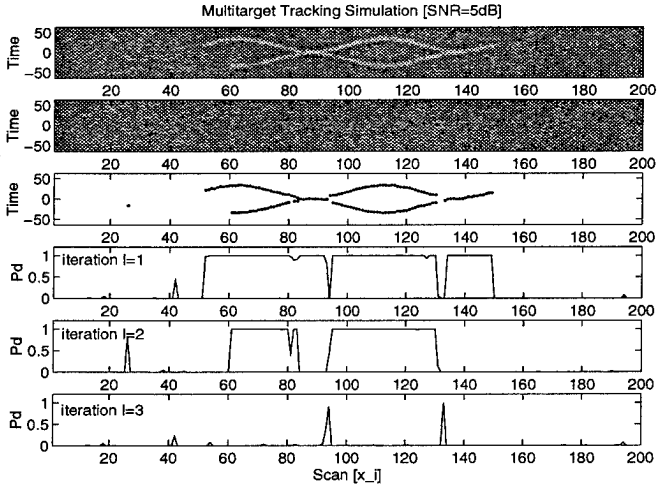


Fig. 1. Tracking of simulated data (from the top): data with SNR=5dB; residual after multitarget tracking $r^{(L)}(x_i,t)$; $p^{(d)}\left[H_1(x_i)\,|\mathbf{R}_i\right]$ during iterations ($L = 3$).

III. APPLICATION AND DISCUSSION

Since in pavement profiling with GPR the echo amplitude decreases with time (or depth) and medium properties vary randomly within the illuminated volume, the SNR of the echoes also decreases with depth. Even if the reliability of amplitude and TOD estimate that are used in layer stripping inversion is fair for deeper interfaces, layer thicknesses estimates are accurate enough for most practical purposes. Fig. 2 describes an example of monostatic radar data with pulse width 1ns (currently used for pavement profiling). The interfaces (within 8ns) of this multilayered structure of the asphalt are rather difficult to track. However, residual $r^{(L)}(x_i,t)$ after tracking $L = 6$ (potential) interfaces does not show any residual interface.

The pulse $s(t)$ is measured separately by placing a flat metal plate at a known distance from the antenna. Uncertainty in pulse shape and in SNR should be properly adapted in practice to multitarget tracking for pavement profiling. Additional aspects not covered here but that make the quantitative use of GPR possible, involve the accurate analysis of propagation effects and of radar calibration.

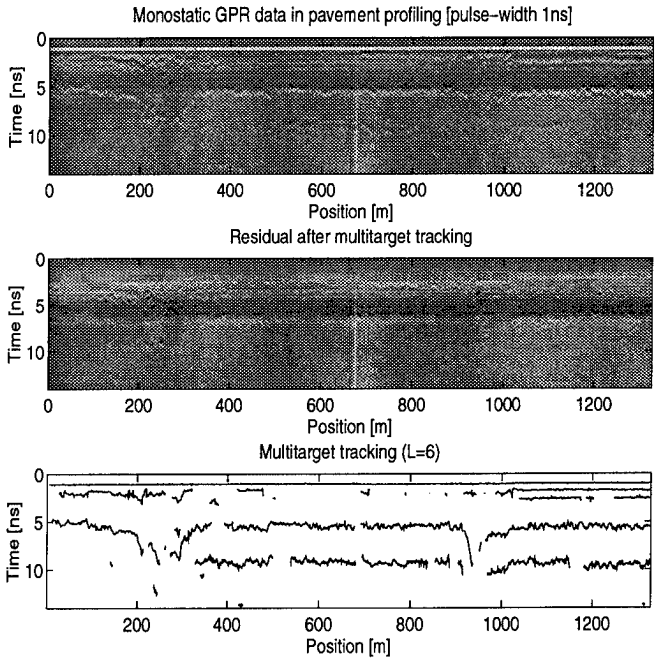


Fig. 2. Example of multitarget tracking for 1ns monostatic GPR (from the top): data and residual after multitarget tracking (not the same scale); tracked interfaces (L=6).

REFERENCES

[1] Bethel, R. E., Paras, G. J, "A PDF Multitarget Tracker", IEEE Transaction on Aerospace and Electronic Systems, Vol. AES-30, No. 2, 1994.

[2] Bethel, R. E., Rahikka , R., G., "An Optimum First-Order Time Delay Tracker", IEEE Transaction on Aerospace and Electronic Systems, Vol. AES-23, No. 6, 1987.

[3] Stagni, G., Toja, C., "Sviluppo di tecniche per la stima e l'inseguimento dei tempi di arrivo degli echi radar", Politecnico di Milano, Thesis as Dottore in Ing. Elettronica, 1995.

[4] Van Trees, H., L., "Detection, Estimation and Modulation Theory", Part I, John Wiley & Sons, 1968.

[5] Whale, A., D., "Detection of Signal in Noise", Academic Press, 1971.

ANALYSIS OF RESPONSE OF THE ELECTROMAGNETIC INDUCTION FOR DETECTING OF BURIED OBJECTS

KALIN ZHU

Tokai University,

Department of Aeronautics and astronautics,Graduate School of Engineering,

1117 Kitakaname, Hiratsuka-shi, Kanagawa, 259-12 JAPAN

(t)+81.463.581211. (f)+81.463.598292

Email:kalin@aurora.ms.u-tokai.ac.jp

ABSTRACT: The detecting technology of subsurface objects microwave method, e.g. synthetic aperture radar (SAR) are increasingly developing and reported in recent. But these prospecting system are met with some limitation in the aspect of both detecting depth and pattern recognition of buried objects (e.g.Diameter of a buried object-pipe),and it is difficult to recognize material properties of buried objects. In this paper,the low frequency electromagnetic technique is used. For detecting and location of a target-buried object, the analysis of the response of buried object in electromagnetic induction is taken. In an alternating electromagnetic field source, the response characteristic of the electromagnetic induction for the buried targets, which are conducting objects (pipes),are investigated. The principles of the Helmholtz reciprocity is applied to obtain the induction EMF in coils which are placed on the ground surface. Depending on the response characteristic of the object which containing different size and material of the buried metallic pipes. The position and depth of the target-buried object can be detected and located with help of a microcomputer. The experimental results made in a usual laboratory was shown.

I. INTRODUCTION

Recently, the detecting of subsurface objects technology are increasingly developing. With the microwave method of detection, e.g., by synthetic aperture radar (SAR). But it is difficult to increase testing depth of targets and recognition of target shape with a microwave method. The detection of subsurface objects which buried shallow place and the maximum depth of targets, e.g., gas pipes and steel plate is about 3 meters are reported [1].In this paper, the low frequency technology is used with an electromagnetic induction method (EMI) for detecting buried objects. The response characteristic of objects, including different shapes and depths of subsurface targets (Gas-pipe) are analyzed. The strength of response produced by a object is depended on its shape and size, and on its electrical properties as well as its position and orientation with respect to the detecting sensor coils. By the virtue of the response characteristic of a target object, the depth and size of a buried object can be detected with help of microcomputer.

The detecting experiment was made in a usual laboratory. The detector component of the system consists of two adjacent electromagnetic induction sensors, a pair of transmit and receiver coils which are built in around co-axial. In this experiment, the target object-pipe to be detected is excited by the alternating magnetic field produced by passing a series of current pulses through the transmit coil. The frequency of the current pulse is chosen such that eddy-currents field is induced in the target object-pipe. The secondary magnetic field will be created by the eddy-currents. The secondary field or anomalous field can be detected by the receiver coil. During each exciting current pulse, open the "window" to process the induction signals in the receiver coil for analyzing the response of electromagnetic induction in the presence of target object-pipe. Amplified signal in the receiver coil are processed in microcomputer. Depending on the response characteristic of the target-buried object which containing different size and material of the buried metallic pipes, The position and

0-7803-3068-4/96$5.00©1996 IEEE

depth of the target object is detected and located. In this paper, We discussed an approximate but analytic approach to provide a way for prediction of the major feature of the response profiles of buried target-pipe. The experimental results of detection (steel pipes) are illustrated at the end of this paper.

II. ANALYSIS

In this paper, the electromagnetic induction method is used. By virtue of the electromagnetic anomaly in the presence of a target-buried object, the analysis of the response characteristic is taken. we assume following points,

1). the soil conductivity is small (less than 1 S/m) in comparison to the buried target-object conductivity (is of order 10^7 S/m),test object is metallic pipe. So the soil effect is small. The detecting experiment was taken in free space.

2). the effect of finite length of target pipes are studied, because of the energy transmitted from transmitter coil is limited.

3). the detecting experiment was done in a usual lab, the low frequency is used as to avoid the effect of circumstance disturbance.

The analysis is based on the EM method [2],the transmitter and receiver are fixed relative positions, in the presence of a conducting and /or permeable object in the vicinity, that will appears the electromagnetic anomaly. Since the strength of the secondary field produced buried target-object will be proportional to the primary field intensity which is proportional to the electric current flowing in the transmitter, and since the additional emf induced in the receiver is proportional to the time rate of changes of in the secondary field.

From [2],we know the response of detecting system to buried objects is

$$\varepsilon^{(s)} / \varepsilon^{(p)} = k\, f(\alpha)$$

where $\varepsilon^{(s)}$ is the emf induction in the receiver by secondary magnetic field. $\varepsilon^{(p)}$ is the emf induction in the receiver by primary field. k is coupling coefficient which couples the receiver to the transmitter, and its value changes with the position of the detecting system but not with the frequency of the alternating current in the transmitter nor with the electrical properties of the buried target object. $f(\alpha)$ is the response function which is the complex function $X(\alpha)+iY(\alpha)$. It changes with the electrical properties of the buried target object and with the frequency of the alternating current in the transmitter. In other words, the position and size of the detecting system is fixed, only the electrical properties and size of buried target object affect response function. Depending on the response characteristic of the target-buried object which containing different size and material of the buried metallic pipes, the position and depth of the target object is detected and located.

III. EXPERIMENTAL RESULTS

The detecting experiment was carried out in the usual laboratory, and the relevant parameters of each of detecting system were:

1).**Transmitter:**

a).coil diameter: 27cm; 30 turns; inductance: 0.41 mH, b).current: rectangular pulse train, pulse width is 6 ms ON, $\doteqdot$ 1.4A, c). frequency: 80Hz.

2).**Receiver:**

a). coil diameter: 27cm; 100 turns; inductance: 4.9 mH, b). amplifier: gain is 1000.

3).**Detecting windows:** start time is before 20 μ s of falling edge of a transmitter pulse.

Test object are steel pipes which different diameter (Gas pipe: ϕ 21, ϕ 60mm) were detected as buried target objects, these test objects have same length 500mm and thickness 3mm. The transmitter and receiver is fixed at co-axial and distance between their centers is 20mm. The transmitter and receiver coils are placed over the test object. The depth is a distance between the receiver and the target object. The response profiles of the target gas-pipe in different depth (110mm, and 150mm) are illustrated in Fig.1-Fig.3. Depending on the different response (phase and strength),the buried object can be detected.

It was found that the size and depth of target object can be identified from the response profiles of object in electromagnetic induction method.

IV. CONCLUSION

In a usual laboratory, the response profile of different size and depth of target object are investigated in electromagnetic induction method. It shows the pos-

sibility of applying this analysis method and technology in detecting buried target object. Increasing detecting depth and detecting in the actual spot will be studied.

REFERENCES

[1] Ikuo Arai,Kouich Washio,Tsutomu Suzuki, "Synthetic aperture using pattern matching method for subsurface radar," TECHNICAL REPORT OF IEICE, SANE92-83 (1992-12), pp.37-41.

[2] F.S.Grant and G.F.West, "Interpretation Theory in Applied Geophysics", New York: McGraw-Hill,1965, pp.445-544.

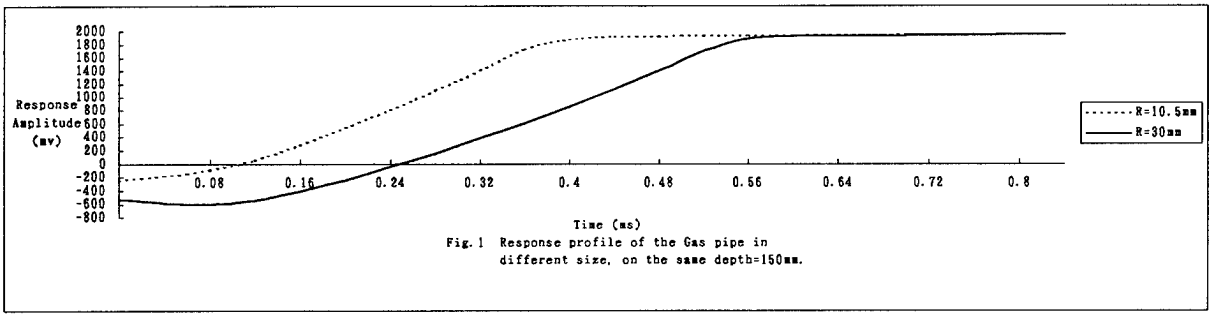


Fig. 1 Response profile of the Gas pipe in different size, on the same depth=150mm.

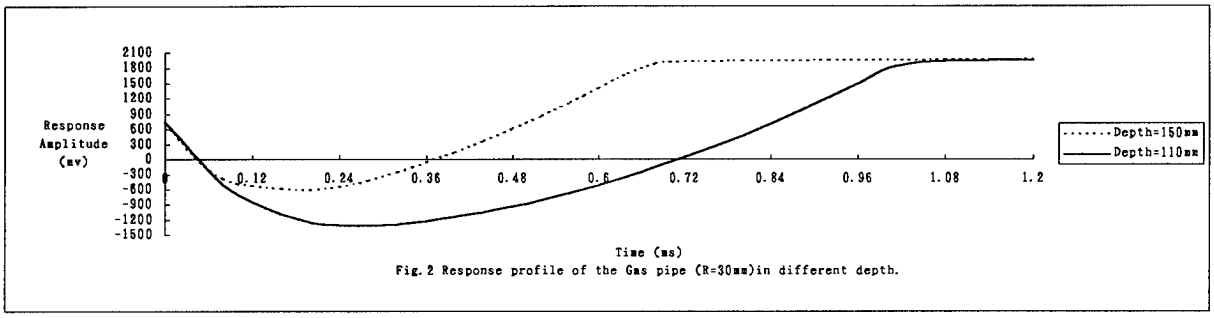


Fig. 2 Response profile of the Gas pipe (R=30mm)in different depth.

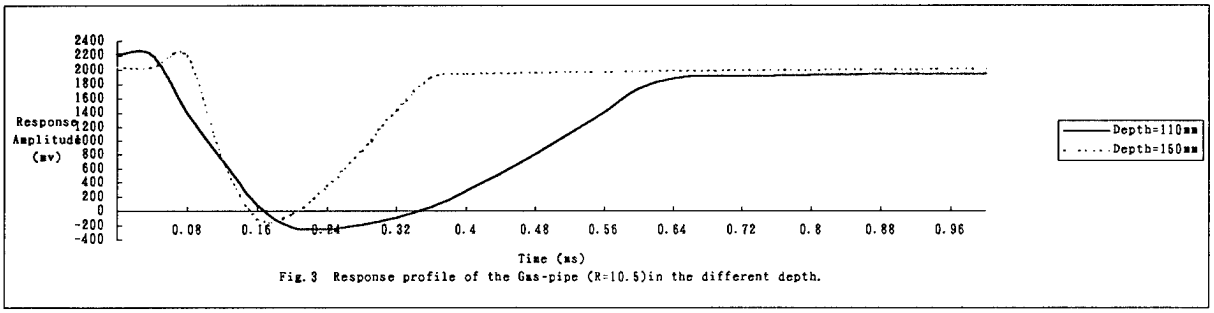


Fig. 3 Response profile of the Gas-pipe (R=10.5)in the different depth.

A Region Growing Algorithm for InSAR Phase Unwrapping

Wei Xu, Ian Cumming
Department of Electrical Engineering, University of British Columbia
2356 Main Mall, Vancouver, B.C. Canada V6T 1Z4
Tel: (604) 822-4162, Fax: (604) 822-5949, Email: weix@ee.ubc.ca

Abstract — In this paper, a region growing algorithm for InSAR Phase Unwrapping is presented. Initial experiments show that the region growing phase unwrapping algorithm can handle SAR interferograms which are more noisy than other unwrapping algorithms can handle. This algorithm also allows dense fringes caused by steep topography.

INTRODUCTION

A number of phase unwrapping algorithms for SAR interferogram have been proposed in recent years [1–4], However, none of them are very satisfactory when noisy and dense fringes occur.

BASIC CONCEPTS

The success of phase unwrapping depends upon the path chosen to perform the unwrapping, and choosing of the best path has been troublesome for many current algorithms. The region growing algorithm minimizes unwrapping errors by starting at pixels of high data quality, and proceeding along paths where unwrapping confidence is high. The algorithm is also able to correct unwrapping errors to a certain extent, and stop their propagation. Part of the basic concepts of this algorithm has been described in [5].

The unwrapping process can be considered as a state machine. At each step, the current state consists of some contiguous regions of unwrapped pixels. Surrounding each region, one pixel layer deep, is a ring of pixels which will be considered for unwrapping in the next step. Each pixel in the ring is called a growth pixel, as illustrated in Fig. 1, where each disc represents a pixel. The transparent discs represent pixels which have been unwrapped, and together they from an unwrapped region, shown dotted in Fig. 1. The gray and black discs represent pixels which have not yet been unwrapped. The gray discs represent the growth pixels. The black discs represent other pixels which will not be considered for unwrapping in the current iteration. The growth pixel marked "G" is the current pixel to be considered for unwrapping.

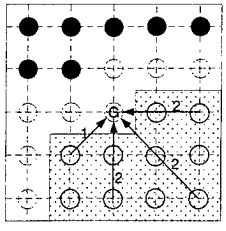


Figure 1 Growth pixel and its neighbours

How a Growth Pixel Is Unwrapped

Unwrapping of a growth pixel uses phase predictions. From each of the N_u unwrapped neighbour pixels of the growth pixel, an individual prediction of unwrapped phase value $\phi^p{}_k$ of the growth pixel is calculated based on the unwrapped phase or phase gradient along each line shown in Fig. 1. The subscript k is the prediction line number and the superscript p stands for prediction. The predictions are of 1st order or 0th order depending on the neighbour status. The composite prediction ϕ^p is a weighted average of these $\phi^p{}_k$:

$$\phi^p = \left(\sum_{k=1}^{N_u} w_k \phi_k^p\right) \Big/ \left(\sum_{k=1}^{N_u} w_k\right) \tag{1}$$

The weights w_k are given by the number of unwrapped pixels used in the prediction.

The phase prediction (1) is used to try to unwrap the growth pixel. The proposed unwrapped phase value ϕ_u at the growth pixel is computed as:

$$\phi_u = \phi_w + 2\pi m \tag{2}$$

where ϕ_w is the wrapped phase at the growth pixel, and the ambiguity number m is the integer closest to $(\phi^p - \phi_w)/(2\pi)$. As the unwrapping is based on the final prediction rather than any of its neighbours alone, a phase change larger than π between two adjacent pixels is then possible.

Control of Unwrapping Using Reliability Tests

The attempt at unwrapping the growth pixel is accepted only when a reliability test is passed. Let the measurement of reliability be r, and a tolerance threshold be t. The reliability test is passed when $r > t$. There may be various measurements of reliability. Three of them that have been used in our experiments are:

1.
$$r_p = 1 - d_p/(2\pi) > t_p \tag{3}$$
$$d_p = \left(\sum_{k=1}^{N_u} w_k |\phi_k^p - \phi^p|\right) \Big/ \left(\sum_{k=1}^{N_u} w_k\right). \tag{4}$$

2.
$$r_u = 1 - d_u/(2\pi) > t_u \tag{5}$$
$$d_u = |\phi_u - \phi^p| \tag{6}$$

3. r_c is the local coherence c of the interferogram [6]
$$r_c = c = \left|E\{a_m e^{j\phi_m} a_s e^{-j\phi_s}\}\right| / \sqrt{E\{a_m^2\}E\{a_s^2\}} \tag{7}$$
where (a_m, ϕ_m) and (a_s, ϕ_s) are the amplitude and phase of the master and slave SLC images, and $r_c > t_c$.

0-7803-3068-4/96$5.00©1996 IEEE

After running a number of experiments, it was found that the following combination of reliability tests worked the best: A fixed threshold test for measurement 1 and measurement 2 is added to the application of measurement 3, while t_c is gradually relaxed, and all of the three measurements must pass their respective tests.

The Process of Region Growing and Merging

Phase unwrapping is carried out concurrently but independently in a number of regions. Each region starts from a seed where reliability is high, as measured by the local coherence.

As each of the regions grows individually, two or more regions may develop an overlap area. As each growth pixel is processed in the current iteration, growth rings are established, as shown in Fig. 2. The gaps in the growth ring are pixels which have failed the reliability test. The regions before growing are dotted and the overlaps that occur in the growth rings are shaded in Fig. 2.

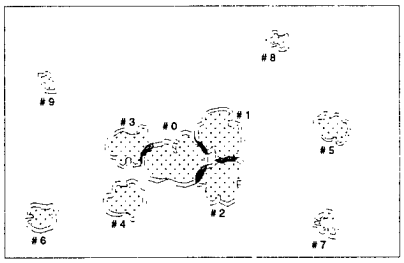


Figure 2 Regions, growth rings and overlaps

Suppose region i and region j have an overlap area of N pixels. The difference between the ambiguity number m_i for region i and the ambiguity number m_j for region j, caused by the different seed, is examined at each pixel k in the overlap area. Their average ambiguity number difference *dif* is then calculated:

$$dif = \frac{1}{N}\sum_{k=1}^{N}(m_j(k) - m_i(k)) \qquad (8)$$

and *dif* is then rounded off to its closest integer *adif*.

The reliability of this estimate is then checked by the following procedure. Suppose there are N_c pixels in the overlap area that agree with *adif*. The estimate of the difference between the ambiguity number for the two regions, *adif*, is considered as reliable as long as the following two threshold tests are passed:

$$N_c \geq t_{rn}, \qquad N_c/N \geq t_{rr} \qquad (9)$$

If the estimation of the difference between the ambiguity number for the two regions is reliable, the two regions are then be merged. Otherwise, the two regions are kept separate and the whole overlap area is cleared. An example of merged regions and cleared overlaps is shown in Fig. 3.

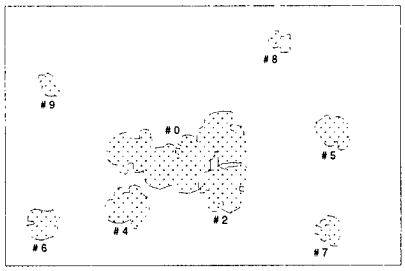


Figure 3 Merged regions and cleared overlaps

Whenever vacancies of region indices appear after region merging, additional regions can be started from newly-selected seeds.

PHASE UNWRAPPING EXPERIMENT

A portion of the phase image of an Sardegna ERS-1 interferogram is shown in Fig. 4, with the corresponding local coherence image shown in Fig. 5.

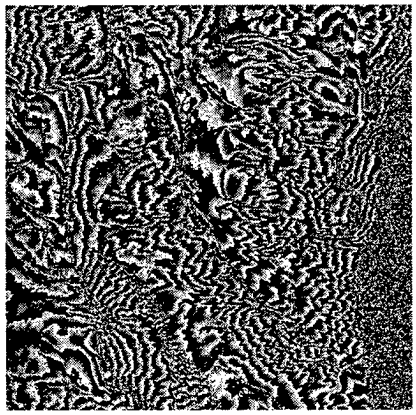


Figure 4 Phase of the interferogram, before unwrapping.



Figure 5 Coherence of the interferogram

This SAR interferogram is considered to be difficult to unwrap because of its many areas of low coherence caused by the local topography and vegetation. The distribution of the "residues" is shown in Fig. 6. This interferogram is too noisy for "residue linking" algorithms [1, 3] as they must correctly link the right pairs of "residues", which is difficult with such a high "residue" density [7]. The "edge detection" algorithm [2] faces the difficulty of detecting edges where edges join together and are fractured.

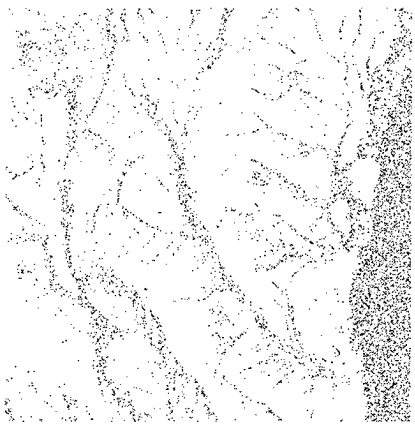


Figure 6 The "residues" distribution of the interferogram

The Sardegna interferogram was unwrapped using the region growing algorithm. A total of 255 initial seeds were selected based on regional diversity and highest coherence. Growth pixels were checked for unwrapping reliability using the thresholds: $t_p = 0.75$; $t_u = 0.75$; t_c starts from $200/256$ and is gradually relaxed to 0. Unwrapped regions are joined using the following reliability thresholds: $t_{rn} = 3$; $t_{rr} = 3/4$.

The unwrapped phase is shown in Fig. 7. The gray scale is reversed so that increasing heights as brighter. The displayed result is the region with index 0. The total number of pixels in this region is about 92% of the land area.



Figure 7 Unwrapped phase of the interferogram, region 0

CONCLUSIONS

We have developed a new phase unwrapping algorithm based on the following principles: using a prediction technique to estimate correct phase; using as much neighbourhood phase information as possible; applying a reliability check to the growth pixel unwrapping attempts; relaxing the reliability threshold gradually; carrying out unwrapping in regions which are allowed to grow with careful checking; merging and rearranging the growth regions properly.

With these principles, the region growing phase unwrapping algorithm can handle SAR interferograms which are more noisy than that other unwrapping algorithms can handle, as the Sardegna ERS-1 interferogram is commonly considered difficult for phase unwrapping. In addition, areas with steep topography where phase changes larger than π between two adjacent pixels are allowed by this algorithm.

ACKNOWLEDGMENT

The authors would like thank Dr. H. Lim and Mr. L. K. Kwoh of the Centre for Remote, Imaging and Sensing in the National University of Singapore for early discussions and encouragement. The authors would like thank Mr. M. Seymour and Mr. J. L. Valero of the Radar Remote Sensing Group in UBC for helpful discussions. The authors would like thank ESA for data, and NSERC, CCRS, MDA, BCASI, BCSC for research funding.

REFERENCES

[1] R. M. Goldstein, H. A. Zebker, and C. L. Werner, "Satellite Radar Interferometry: Two-dimensional Phase Unwrapping". Radio Science, Vol. 23 pp. 713-720, July-August 1988.

[2] Q. Lin, J. F. Vesecky, and H. A. Zebker, "Decorrelation in Interferometric Radar Echoes". IEEE Trans. Geosi. Remote Sens., Vol. 30 pp. 950-959, Sep. 1992.

[3] C. Prati, M. Giani, and N. Leuratti, "SAR Interferometry: A 2-D Phase Unwrapping Technique Based on Phase and Absolute Value Informations". Proceedings of IGARSS'90, pp. 2043–2046, Washington, D. C., USA, 1990.

[4] J. L. Valero, "A Survey of Phase Unwrapping Techniques, with Applications to SAR". Technical Report, Dept. of EE, UBC, Vancouver B. C., Canada V6T 1Z4, June 1995.

[5] H. Lim, W. Xu, and X. Huang, "Two New Practical Methods for Phase Unwrapping". Proceedings of IGARSS'95, pp. 196-198, Firenze, Italy, July 1995.

[6] H. A. Zebker, C. L. Werner, P. A. Rosen, and S. Hensley, "Accuracy of Topographic Maps Derived from ERS-1 Interferometric Radar". IEEE Trans. Geosi. Remote Sens., Vol. 32 pp. 823-836, July 1994.

[7] A. Sowter and H. D. Groof, "Co-registration and Phase Unwrapping Techniques". ERS-1 Fringe, 1st Workshop, Frascati, Italy, 1992.

A Theoretical Analysis on the Robust Phase Unwrapping Algorithms for SAR Interferometry

Gianfranco Fornaro[1], Giorgio Franceschetti[1,2], *IEEE Fellow*, Riccardo Lanari[2], *IEEE Member*, Eugenio Sansosti[2]

[1]Università di Napoli Federico II, *Dipartimento di Ingegneria Elettronica*,
Via Claudio 21, 80125 Napoli, Italy. ☎ (39)-81-7681111 fax+(39)-81-5934438 email: francesc@irece1.irece. na.cnr.it

[2]Consiglio Nazionale delle Ricerche, *Istituto di Ricerca per l'Elettromagnetismo e i Componenti Elettronici (I.R.E.C.E.)*,
Via Diocleziano 328, 80124 Napoli, Italy. ☎ (39)-81-5704945 fax +(39)-81-5705734 email: lanari@irece1.irece.na.cnr.it

Abstract -- Two-Dimensional phase unwrapping is a necessary step within the interferometric SAR topography generation procedure. We analyze two available robust phase unwrapping procedures, and demonstrate their theoretical equivalence. Differences between their implementation are also highlighted.

INTRODUCTION

SAR Interferometry (IFSAR) is an important tool for the evaluation of Digital Elevation Models (DEM). The IFSAR DEMs are computed by exploiting the phase difference between two complex SAR images of the same site [1-3]. Phase unwrapping (PhU) is a basic step of the IFSAR DEM generation technique allowing to retrieve the actual phase difference (*unwrapped* phase) starting from its restriction (*wrapped* phase) in to $(-\pi, \pi)$ interval. The PhU operation can be strongly unpaired by the presence of *critical areas.* These appear in case of undersampling phenomena (*layover*) or low signal-to-noise ratio [4].

Most of the 2-D PhU methods presented in literature make use of the gradient of the unwrapped phase computed from the corresponding wrapped values. One of the most used algorithm [5], designed for SAR applications, is based on local integration of the computed gradient along a path connecting the image pixels. However, this method does not adequately account for the 2-D nature of the problem: the result can be strongly affected by drastic error propagation phenomena if the integration path crosses the *critical areas* [5]. It is evident that a severe pre-processing step on the data is necessary to identify and exclude all the *critical areas.*

Most recently two very promising approaches have been proposed [6-10]; they are based on the global integration which accounts for the two-dimensional nature of the problem for the IFSAR case. The first approach [6-9] is based on a Least Square (LS) solution in the discrete domain; the second one [10] benefits of the first Green Identity (GI) and is formulated with respect to the continuos domain. The global nature of these two PhU algorithms makes them robust in terms of error propagation.

In this paper a theoretical analysis and comparison between these two PhU techniques is presented. To this end, the LS method has been reformulated in the continuos domain, leading to a minimization (with respect to the unknown *unwrapped* phase function) of a pertinent functional. The minimization is performed by applying variational theory.

The theoretical equivalence between the two algorithms is then demonstrated.

LEAST SQUARES ALGORITHMS REFORMULATED

Phase unwrapping algorithms include two basic steps [10]:

1. Estimation of the gradient of the unwrapped phase;
2. Integration of the estimated gradient.

Let us concentrate on the estimation of the unwrapped phase gradient $\nabla\varphi$. This is generally performed by computing the gradient of the wrapped phase $\nabla\varphi_m$ and "chopping away" the 2π amplitude spikes appearing along the discontinuity lines [10]. Alternative phase gradient estimation procedures are also presented in [11]. Unfortunately, the presence of *critical areas* affects the estimation [10-11]. If we refer to as $\mathbf{s}$ the estimated phase gradient, the unwrapped phase retrieval problem can be synthesized by the following equation:

$$\nabla\varphi = \mathbf{s}\,, \tag{1}$$

wherein, in general, $\mathbf{s}$ is a non conservative field.

A robust solution to (1), based on the Least Squares (LS) approach, is presented in [6-9], wherein the overall analysis is performed in the discrete domain. In order to theoretically compare the LS algorithm to the Green's identity based one we reformulate the LS approach in the continuos domain.

The solution of. (1) in the least-squares sense is represented by the function φ such that:

$$L[\varphi] = \|\nabla\varphi - \mathbf{s}\|^2 \rightarrow \min\,, \tag{2}$$

0-7803-3068-4/96$5.00©1996 IEEE

wherein $L[\cdot]$ is the functional to be minimized and $\|\|$ is the norm operator:

$$\|\nabla\varphi-\mathbf{s}\|^2=\langle\nabla\varphi-\mathbf{s},\nabla\varphi-\mathbf{s}\rangle = \iint_S dS\left[(\nabla\varphi-\mathbf{s})\cdot(\nabla\varphi-\mathbf{s})^*\right] \quad . \tag{3}$$

We enforce the requirement set in (2) by setting:

$$\delta L=2\iint_S dS[\nabla\varphi\cdot\nabla\delta\varphi-\mathbf{s}\cdot\nabla\delta\varphi]=0 \quad . \tag{4}$$

By applying the first Green's identity and the following relationship:

$$\mathbf{v}\cdot\nabla u=\nabla\cdot(\mathbf{v}u)-u\nabla\cdot\mathbf{v} \quad , \tag{5}$$

being $u=\delta\varphi$ and $\mathbf{v}=\mathbf{s}$, (4) transforms as follows:

$$-\iint_S dS\nabla^2\varphi\ \delta\varphi+\oint_C dc\frac{\partial\varphi}{\partial n}\delta\varphi - \iint_S dS\nabla\cdot(\mathbf{s}\delta\varphi)+\iint_S dS\,\mathbf{s}\cdot\nabla\delta\varphi=0 \, . \tag{6}$$

Further application of divergence theorem leads to:

$$\iint_S dS(\nabla\cdot\mathbf{s}-\nabla^2\varphi)\delta\varphi-\oint_C dc\left(\mathbf{s}\cdot\hat{\mathbf{n}}-\frac{\partial\varphi}{\partial n}\right)\delta\varphi=0 \, , \tag{7}$$

which is identically verified if:

$$\begin{cases}\nabla^2\varphi=\nabla\cdot\mathbf{s} & \text{in } S \quad (8a)\\ \dfrac{\partial\varphi}{\partial n}=\mathbf{s}\cdot\hat{\mathbf{n}} & \text{on } C \quad (8b)\end{cases}$$

We can state that a robust solution, in a Least Squares sense, to the 2D-PhU is the solution of the Poisson problem described in (8a) and (8b).

We now demonstrate that the obtained solution is equivalent, in discrete domain, to that proposed in literature [6-9]. Finite Differences approximation of the problem in (8a) and (8b) leads to the following set of equations:

$$\begin{aligned}&a_i(\varphi_{i+1,j}-\varphi_{i,j})-a_{i-1}(\varphi_{i,j}-\varphi_{i-1,j})+b_j(\varphi_{i,j+1}-\varphi_{i,j})\\ &-b_{j-1}(\varphi_{i,j}-\varphi_{i,j-1})=a_i s^x_{i,j}-a_{i-1}s^x_{i-1,j}+b_j s^y_{i,j}-b_{j-1}s^y_{i,j-1} \quad (9)\\ &\text{with } i=0,\ldots,N-1 \qquad j=0,\ldots,M-1\end{aligned}$$

wherein:

$$\begin{cases}a_i=1 & i=0,\ldots,N-2\\ a_{-1}=a_{N-1}=0\end{cases} \tag{10a}$$

and

$$\begin{cases}b_j=1 & j=0,\ldots,M-2\\ b_{-1}=b_{M-1}=0\end{cases} \tag{10b}$$

and the boundary condition (8b) has been properly included in the known term of (9). This set of equations is identical to the discrete Poisson problem with Neumann homogeneous boundary conditions presented in [7]. Note that in the literature it is usually stated that the LS method is equivalent (in the discrete domain) to the solution of a Poisson equation with homogeneous boundary condition [7-9], see (9) and (10),. A more precise statement is that the intrinsically inhomogeneous boundary condition have been absorbed in the source distribution by including boundary sources given by (8b), as it is clear by all the material presented in this section. In addition, this allows a substantial additional freedom which may be used in the implementation of the LS methods [9,12].

EQUIVALENCE BETWEEN GREEN'S FUNCTION AND LEAST SQUARES METHODS

Let us first summarize the method presented in [10] whose starting point is the first Green's identity in its 2-D form. With reference to a planar domain S bounded by the curve C, we have:

$$\iint_S dS\left[\varphi\nabla^2 g+\nabla\varphi\cdot\nabla g\right]=\oint_C dc\,\varphi\frac{\partial g}{\partial n} \quad , \tag{11}$$

wherein $\hat{\mathbf{n}}$ is the unit outward vector on C and g is a test function. We first replace, in (11), $\nabla\varphi$ by $\mathbf{s}$ computed from the measured wrapped values [10]

$$\iint_S dS\left[\varphi(\mathbf{r})\nabla^2 g(\mathbf{r}'-\mathbf{r})+\mathbf{s}(\mathbf{r})\cdot\nabla g(\mathbf{r}'-\mathbf{r})\right] = \oint_C dc\,\varphi(\mathbf{r}_C)\frac{\partial g(\mathbf{r}'-\mathbf{r}_C)}{\partial n} \quad , \tag{12}$$

wherein $\mathbf{r}$ and $\mathbf{r}'$ are the vector coordinate in S and $\mathbf{r}_C$ refers to the curve C. Then, we take g to be the Green's function for the unbounded domain:

$$\nabla^2 g(\mathbf{r})=\delta(\mathbf{r}) \quad , \tag{13}$$

and we get, from (12), the following solution for the PhU problem:

$$\varphi(\mathbf{r}')=-\iint_S dS\,\mathbf{s}(\mathbf{r})\cdot\nabla g(\mathbf{r}'-\mathbf{r}) + \oint_C dc\,\varphi(\mathbf{r}_C)\frac{\partial g(\mathbf{r}'-\mathbf{r}_C)}{\partial n} \quad , \qquad \mathbf{r}'\in S. \tag{14}$$

Equation (14) represent the key point of this robust PhU algorithm. It is a linear convolution, therefore Fast Fourier Transform (FFT) codes can be applied for its solution once that φ has estimated on C [10].

Let us now demonstrate that the solution of Poisson problem presented in the previous section is equivalent to the one obtained by Green's function method. We start from the following identity:

$$\iint_S dS\,\varphi(\mathbf{r})\nabla^2 g(\mathbf{r}'-\mathbf{r}) = \varphi(\mathbf{r}') \,, \tag{15}$$

wherein g is that of (13). By means of the second Green's identity, (15) is replaced by:

$$\begin{aligned}\iint_S dS\, g(\mathbf{r}'-\mathbf{r})\nabla^2\varphi(\mathbf{r}) + \oint_C dc\,\varphi(\mathbf{r}_C)\frac{\partial g}{\partial n}(\mathbf{r}'-\mathbf{r}_C) \\ - \oint_C dc\, g(\mathbf{r}'-\mathbf{r}_C)\frac{\partial\varphi}{\partial n}(\mathbf{r}_C) = \varphi(\mathbf{r}') \,.\end{aligned} \tag{16}$$

We consider φ to be the solution of the Poisson problem in (8a) and (8b). Accordingly:

$$\begin{aligned}\iint_S dS\, g(\mathbf{r}'-\mathbf{r})\nabla\cdot\mathbf{s}(\mathbf{r}) + \oint_C dc\,\varphi(\mathbf{r}_C)\frac{\partial g}{\partial n}(\mathbf{r}'-\mathbf{r}_C) \\ - \oint_C dc\, g(\mathbf{r}'-\mathbf{r}_C)\frac{\partial\varphi}{\partial n}(\mathbf{r}_C) = \varphi(\mathbf{r}') \,,\end{aligned} \tag{17}$$

which, taking into account also of (5), gives:

$$\begin{aligned}\iint_S dS\,\nabla\cdot\left[g(\mathbf{r}'-\mathbf{r})\mathbf{s}(\mathbf{r})\right] - \iint_S dS\,\nabla g(\mathbf{r}'-\mathbf{r})\cdot\mathbf{s}(\mathbf{r}) \\ + \oint_C dc\left[\varphi(\mathbf{r}_C)\frac{\partial g}{\partial n}(\mathbf{r}'-\mathbf{r}_C) - g(\mathbf{r}'-\mathbf{r}_C)\frac{\partial\varphi}{\partial n}(\mathbf{r}_C)\right] = \varphi(\mathbf{r}') \,.\end{aligned} \tag{18}$$

Use of the Gauss theorem in the first integral in (18) leads to:

$$\begin{aligned}\oint_C dc\, g(\mathbf{r}'-\mathbf{r})\mathbf{s}(\mathbf{r})\cdot\hat{\mathbf{n}} - \iint_S dS\,\nabla g(\mathbf{r}'-\mathbf{r})\cdot\mathbf{s}(\mathbf{r}) \\ + \oint_C dc\left[\varphi(\mathbf{r})\frac{\partial g}{\partial n}(\mathbf{r}'-\mathbf{r}) - g(\mathbf{r}'-\mathbf{r})\frac{\partial\varphi}{\partial n}(\mathbf{r})\right] = \varphi(\mathbf{r}') \,,\end{aligned} \tag{19}$$

which coincides with (14) when the boundary conditions (8b) are enforced. This demonstrates that the two methods, the LS and the GI, are equivalent from a theoretical point of view.

THE TWO METHODS IMPLEMENTATION

The numerical implementation of the LS and GI based methods has shown that the latter is more efficient, especially for large matrix, from the computational point of view. This id due to the possibility to separately estimate, as presented in [10,12], the unwrapped phase on the contour C, see (14), via a second kind Fredholm equation on C. This is an alternative feature of the GI method when *critical areas* inside the interferogram need to be excluded for improving the PhU results. In particular, the GI method, dealing with vectorial input data, can be used to estimate the unwrapped phase values on the additional boundaries of the resulting multi-connected domain. The result is a remarkable advantage with respect to the LS method which needs iteration on the overall domain.

REFERENCES

[1] L. C. Graham, "Synthetic interferometric radar for topographic mapping", Proc. IEEE, **62**, 763-768, (1974)

[2] H. A. Zebker and R. M. Goldstein, "Topographics mapping from interferometric synthetic aperture radar observations", J. Geophys. Res., **91**, 4993-4999, (1986)

[3] J. M. Martin, "Theory and design of interferometric synthetic aperture radars", IEE Proc. F, **139**, 147-159, (1992)

[4] R. M. Goldenstein, H. A. Zebker and C. L. Werner, "Satellite radar interferometry: two-dimensional phase unwrapping", Radio Sci. **23**, 713-720, (1988)

[5] Q. Lin, F. Vesecky and H.A. Zebker, "Comparison of elevation derived from INSAR data with DEM over large relief terrain", Int. J. Remote Sensing, **15**, 1775-1990, (1994)

[6] H. Takajo and T. Takahashi, "Noniterative methods for obtaining the exact solution for the normal equation in least-squares phase estimation from phase difference", J. Opt. Soc. Am. A **5**, 1818-1827, (1988)

[7] D. C. Ghiglia and L. A. Romero, "Direct phase estimation from phase difference using fast elliptic partial differential equation solvers", Opt. Lett. **14**, 1107-1109, (1989)

[8] D. C. Ghiglia and L. A. Romero, "Robust two-dimensional weighted and unweighted phase unwrapping that uses fast transform and iterative methods", J. Opt. Soc. Am. A **11**, 107-117, (1994)

[9] M. D. Pritt and J. S. Shipman, "Least-squares two dimensional phase unwrapping using FFT's", IEEE Trans. Geosci. Remote Sens. **32**, 706-708, (1994)

[10] G. Fornaro, G. Franceschetti and R. Lanari, "Interferometric SAR phase unwrapping using Green's formulation", IEEE Trans. Geosci. Remote Sens. *in print*

[11] U. Spagnolini "2-D phase unwrapping and instantaneous frequency estimation", IEEE Trans. Geosci. Remote Sens. **33**, 579-589, (1995)

[12] G. Fornaro, G. Franceschetti, R. Lanari and E. Sansosti, "Robust phase unwrapping techniques: a comparison", *submitted.*

A Multiresolution Approach to Improve Phase Unwrapping

Gordon W. Davidson and Richard Bamler
German Aerospace Research Establishment (DLR)
82234 Oberpfaffenhofen, Germany
Tel.: +49 8153 281326, Fax: +49 8153 281448 email: davidson@dfd.dlr.de

Abstract — A method is presented for robust phase unwrapping based on instantaneous frequency estimation at multiple resolutions. Estimation is done of the frequency difference between resolution levels, resulting in asymptotically zero bias in the aliasing error. The frequency for the highest resolution level is found by the sum of difference frequencies, and the final frequency estimates are input to a least squares phase reconstruction algorithm. A hierarchical algorithm for frequency estimation at all resolution levels, based on the correlation Doppler centroid estimator, is derived. Also, an adaptive multiresolution approach is presented, in which the highest resolution level required for a frequency estimate without aliasing and thus a smooth phase reconstruction, is determined at each point. The method is investigated by simulations, and results show successful phase unwrapping without slope bias, even in the presence of undersampling and low coherence.

INTRODUCTION

In the construction of a digital elevation model using SAR interferometry, the topography is related to the absolute phase of the interferogram, whereas the phase of each pixel of the interferogram is only known modulo 2π. The purpose of 2–D phase unwrapping is the calculation of the absolute phase by the integration of wrapped phase differences, or estimates of instantaneous frequency [1].

Phase unwrapping is made difficult by aliasing errors due to noise decorrelation and undersampling, which cause the measured phase gradient field to be nonconservative. Also, in the presence of a nonzero phase slope, the aliasing error due to noise alone has a nonzero mean, which causes a slope bias in least squares phase reconstruction [2,3,4]. This results in a coherence dependent underestimation of slopes which prevents reconstruction of the full height of the unwrapped phase. Branch–cut phase unwrapping algorithms seek to identify an integration path that avoids the nonconservative part of the field [5], although an error in branch–cut location can cause a phase unwrapping error that is propagated along the rest of the integration path.

Typically, interferogram smoothing or 'multi–looking' is used to improve the phase estimate of the interferogram at the expense of spatial resolution. However, the phase estimate is degraded by phase variation within the estimation window. If a coarse resolution unwrapped phase is available, for example from a DEM or another interferogram acquired with a larger wavelength [6] or smaller baseline, then the coarse phase can be subtracted from the phase of the interferogram by a complex multiply. The resulting interferogram can be unwrapped much more reliably, because of more accurate phase estimation by multilooking, and because the effect of aliasing is greatly reduced.

In this paper we present a method for phase reconstruction, without aliasing error even in the presence of local undersampling, by performing frequency estimation at multiple resolutions. The idea is to estimate instantaneous frequenices at a low resolution (large estimation window), and then use this estimate to reduce the phase variation of the next higher resolution by a complex multiply. This can be repeated for each next higher resolution until the resolution of indivual phase differences is reached. In this way, estimation is actually done of the difference in instantaneous frequency between resolution levels. Final frequency estimates at the highest resolution are then obtained by the sum of frequency differences. Thus, frequencies greater than 0.5 cycles per sample can be measured in areas of undersampling. Aliasing errors due to noise occur, but because of the smaller frequency being estimated, the error has asymptotically zero mean, thus avoiding the slope distortion in least squares phase reconstruction. Thus the full height of the topography is obtained.

In a refinement of the method, called adaptive multiresolution, the frequency differences are added for higher resolution levels only as long as aliasing errors in the frequency estimates do not occur, as detected by the curl of the measured phase gradient. In this way, the inherent resolution in the data, which depends on the amount noise, is found automatically, and a smooth reconstruction of unwrapped phase is obtained.

METHOD

Let the i'th pixel of an interferogram be

$$z_i = |z_i| e^{j\phi_i} \tag{1}$$

where ϕ_i is the interferometric phase. Since the wrapped phase differences for phase unwrapping are calculated in the range or azimuth directions, a one–dimensional representation is used here for simplicity. The wrapped phase difference between pixels i and i+1 can be calculated as

$$\arg[z_i^* z_{i+1}] \tag{2}$$

which can also be interpretted as an estimate of the instantaneous frequency (in radians per second) at i.

Instantaneous frequency estimation, for input to phase unwrapping, could be performed with one of several methods: For example, for the linear phase variation the maximum likelihood estimate is given by the peak of the magnitude of the FFT. For estimation over a larger window in the presence of nonlinear phase variation, however, it is desired to find an average frequency, or centroid of the spectrum. From the field of Doppler centroid estimation [7], such an estimate is

$$f = \arg[\sum z_i^* z_{i+1}] \tag{3}$$

0-7803-3068-4/96$5.00©1996 IEEE

where the summation is over the estimation window.

Using this estimation method, Fig. 1 shows a possible hierarchical algorithm for multiresolution frequency estimation, with accumulation of frequency differences to obtain the final measured frequencies at each point. The highest resolution level, n=0, is the array of products,

$$C_0(i) = z_i^* z_{i+1} \tag{4}$$

of length 2^N. For lower resolution levels from n=1 to n=N, the window size is 2^n, and level n is calculated from level n–1 by

$$C_n(i) = C_{n-1}(2i) + C_{n-1}(2i+1) \tag{5}$$

giving

$$C_n(i) = \sum_{k=i2^n}^{(i+1)2^n-1} z_k^* z_{k+1} \tag{6}$$

for i=0,...$2^{(N-n)}$–1. Each $C_n(i)$ corresponds to a sum of terms in equation (3) for the successively larger window sizes, and the frequency estimate for resolution level n would be

$$f_n(i) = \arg[C_n(i)] \tag{7}$$

However, to reduce the risk of aliasing at each level, the frequency difference between resolution levels is calculated, for levels from 0 to N–1, by

$$\delta_n(i) = \arg[C_n(i) C_{n+1}^*(i/2)] \tag{8}$$

and these frequency differences are then summed to get the final, highest resolution frequency, f_0, as shown in the Figure.

The approach in Fig. 1 results in nonoverlapping estimation windows. Nonoverlapping windows have the disadvantage that if one frequency difference estimate at a low resolution is aliased, although unlikely, it can affect a large area in the final, reconstructed frequency array. Also, in the adaptive method, if high resolutions in an area are not used because aliasing was detected, then the phase reconstruction will have a facetted appearance. Note that in general, each lower resolution level is calculated from the previous one by filtering and subsampling. A certain overlap in windows can thus be achieved by not subsampling for the first few (highest) resolution levels. That is, at these levels, a sliding window is used so that each window position affects only one point in the frequency array. A structure for the calculation of multi–level frequency estimates with overlapping windows is shown in Fig. 2. The first two levels are filtered without subsampling, and for these levels the filter kernel length is an odd number so that the kernel can be centered over a sample.

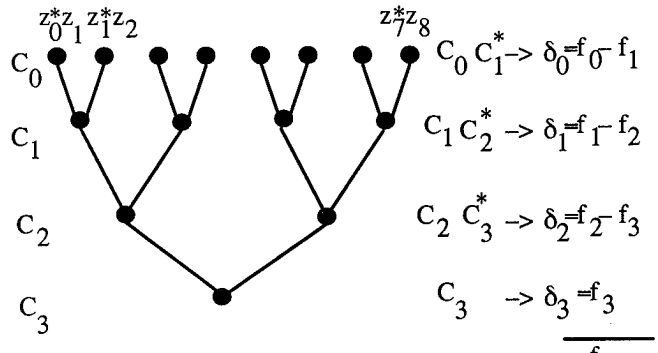


Figure 1. Multi–level frequency estimation, nonoverlapping windows.

In the multiresolution approach, a frequency estimate at a desired resolution level, m, is found by accumulating the frequency differences, starting at the lowest resolution (n=N), up to level m:

$$f_m = \sum_{n=m}^{n=N} \delta_n \tag{9}$$

Typically, the coherence varies across the interferogram, and in some areas the frequency should be estimated at a lower resolution than at others. In the adaptive multiresolution approach, the curl, or 'residues', of the 2–d frequency field is computed at each resolution level. At the point (i,k) in the n'th resolution level, let $f_n^i(i,k)$ and $f_n^k(i,k)$ be the frequency components in the i and k directions, and the curl, $r_n(i,k)$, is computed as

$$r_n(i,k) = f_n^i(i,k) + f_n^k(i+1,k) - f_n^i(i,k+1) - f_n^k(i,k) \tag{10}$$

At points where the magnitude of the curl exceeds a threshold, the frequency differences are only accumulated up to the lower resolution level. This means the difference frequency arrays must be stored, for both the range and azimuth directions, for each resolution level, so they can be later summed to the correct level. In the adaptive resolution method, the frequency at every point is estimated at the resolution level, or window size, for an accuracy that ensures a sufficiently conservative phase gradient field. The frequency estimates are then used in a least squares reconstruction to obtain a smoothed, unwrapped phase without slope distortion.

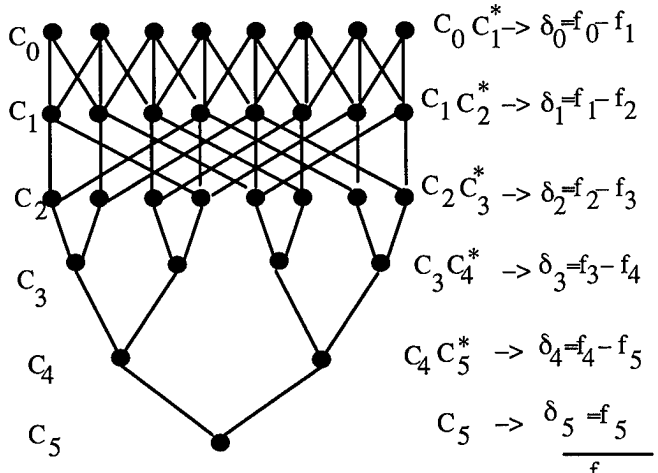


Figure 2. Multi–level frequency estimation, overlapping windows.

SIMULATIONS

An interferogram is generated from two simulated complex images, $z=s_1 s_2^*$, where

$$s_1 = xe^{j\phi} + n_1 \quad (11)$$

$$s_2 = x + n_2 \quad (12)$$

and where x is a complex gaussian signal, ϕ is the interferometric phase, and n_1 and n_2 are independent complex gaussian noises whose variance depends on the desired coherence. In all cases interferograms of 128 by 128 samples are simulated. The interferogram is then used in different methods of frequency estimation for least squares phase unwrapping: simple phase differences, multiresolution, and adaptive multiresolution. Figure 3a shows a wrapped noise–free interferometric phase, ϕ, which was used in the simulation, and Figures 3b to 3d show the results of phase unwrapping for a coherence of 0.8. The loss of fringes due to the slope loss when phase differences are used is visible in Figure 3b. Note that the loss of fringes is quite severe even for the good coherence of 0.8, which would not be masked in a weighted least squares algorithm. Figure 3c shows the results of multiresolution, in which the slope distortion has been avoided, although the result is noisy because of noise and aliasing errors at the high resolutions. Figure 3d shows the result of adaptive multiresolution, where the accumulation of aliased frequency estimates at finer resolutions has been avoided, obtaining a smooth result.

The slope distortion with least squares using phase differences is illustrated further in Figure 4. In this case the 2–d phase used in the simulation was constant in one direction, while in the other direction the phase had a specified shape such as a ramp or parabola. The graphs show plots of unwrapped phase averaged in the constant direction. Also, in this case the coherence varied in the direction of the phase variation, being 0.8 or 0.3, as shown. With phase differences, the loss of slope can be seen, especially over the low coherence area.

Finally, Figure 5 shows a noise–free phase surface used in a simulation, which contains an area in which phase differences greater than π, as shown, resulting in aliasing due to undersampling. Also some detail is added in the form of the small 'hill'. Figures 6 and 7 show least square reconstructions for a coherence of 0.6 and 0.3, respectively, a) using adaptive multiresolution, and b) with simple phase differences. For both values of coherence, the multiresolution approach retains the coarse phase variation without loss of overall phase height, whereas phase differences results in a severe distortion of the unwrapped phase. In the adaptive multiresolution method, with the 0.6 coherence the resolution was high enough to retain the detail, although it is flattened slightly, whereas the loss of resolution because of the smoothing required at 0.3 coherence can be seen in Figure 7a.

CONCLUSION

The multiresolution approach can obtain instantaneous frequency estimates without bias in the aliasing error, so that least squares phase unwrapping can obtain the full phase height in the reconstruction, even in the presence of local undersampling.

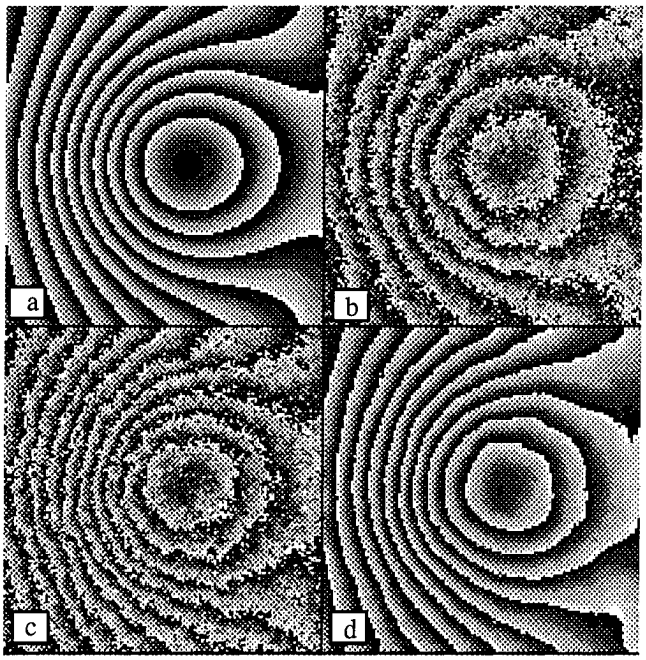


Figure 3. Results of least squares phase unwrapping from simulated interferogram, coherence=0.8, a) wrapped original noise free phase b) rewrapped reconstrcution from phase differences, c) rewrapped phase using multiresolution d) rewrapped phase using adaptive multiresolution.

The frequency estimation method allows the measure of an average frequency over a large window for low resolutions, and a hierarchical algorithm allows the frequencies at all resolution levels to be computed efficiently. However, in the case of a flat phase, for the same window size, it appeared from simulations that the variance of the frequency estimate is greater than the variance of the measure of phase differences using multilooking. Thus, the multiresolution approach can be used to obtain a unwrapped phase at a slightly coarser resolution, for reducing the phase variation of the interferogram. Then, an accurate, finer resolution unwrapped phase can be obtained by multilooking and unwrapping of the result.

Multiresolution frequency estimation has other applications: low resolution instantaneous frequency estimates could be obtained quickly, and used in spectral shift filtering, and the coarse unwrapped phase could be used in accurate coherence estimation.

REFERENCES

[1] U. Spagnolini, "2–D phase unwrapping and instantaneous frequency estimation," IEEE Trans. Geoscience and Remote Sensing, vol 33, pp. 579–589, 1995.

[2] H. Takajo and T. Takashi, " Least–squares phase estimation from the phase difference", J. Opt. Soc. Am. A, vol. 5, pp. 416–425, 1988.

[3] D. C. Ghiglia and L. A. Romero, "Robust two–dimensional weighted and unweighted phase unwrapping that uses fast transforms and iterative methods," J. Opt. Soc. Am. A, vol. 11, pp. 107–117, 1994.

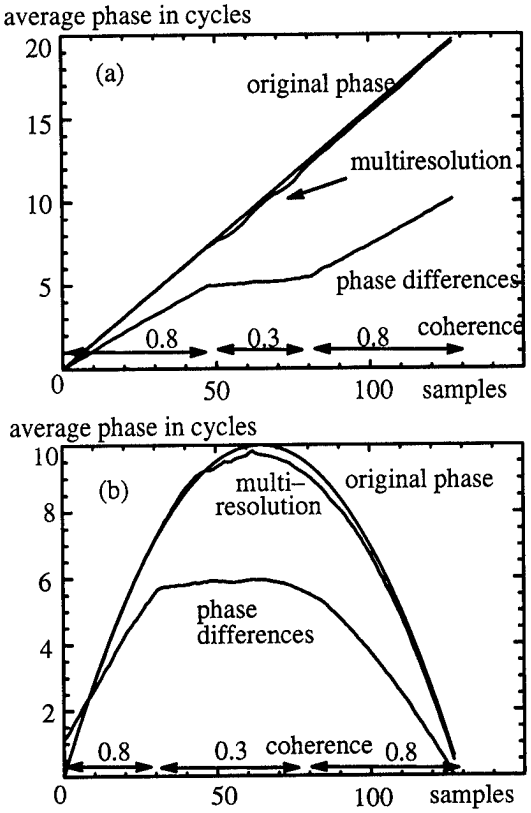


Figure 4. Unwrapped phases, averaged in orthogonal direction in which original phase is constant. Varying coherence.

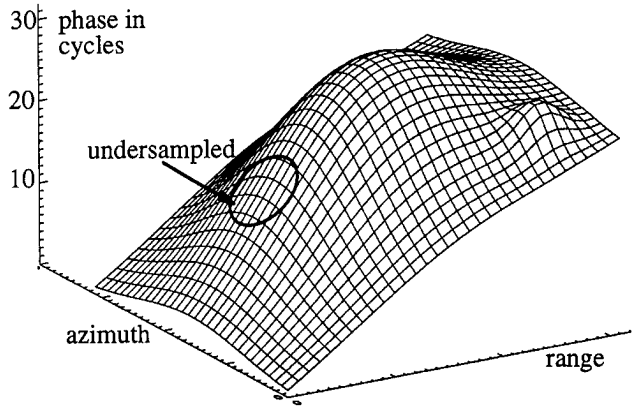


Figure 5. Original noise–free phase surface.

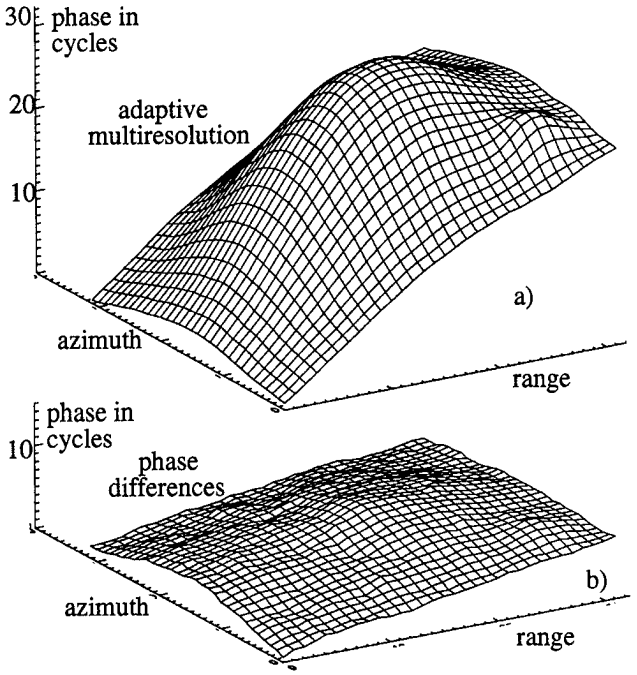


Figure 6. Unwrapped phase surfaces, least squares reconstruction with a) adaptive multiresolution, and b) simple phase differences. Coherence = 0.6.

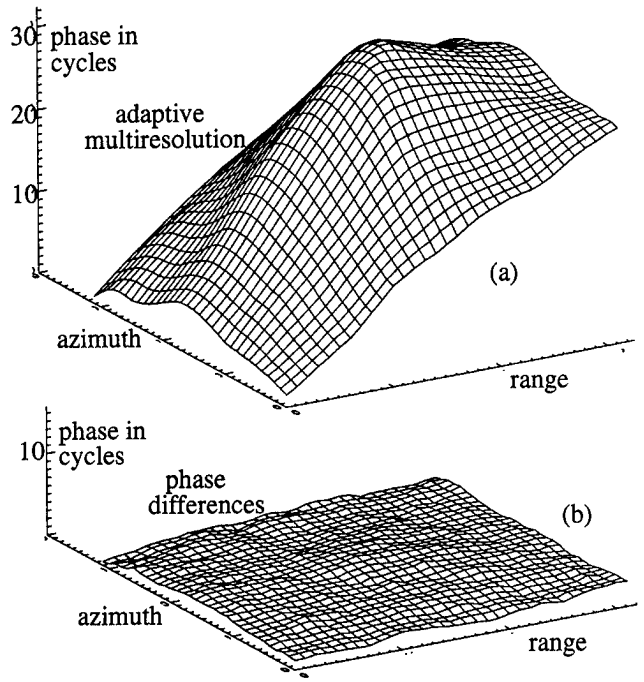


Figure 7. Unwrapped phase surfaces, least squares reconstruction with a) adaptive multiresolution, and b) simple phase differences. Coherence = 0.3.

[4] R. Bamler, N. Adam, G. W. Davidson, and D. Just, "Noise–induced slope distortion in 2–d phase unwrapping by linear estimators with application to SAR interferometry," submitted to IEEE Trans. Geoscience and Remote Sensing, Jan. 1996.

[5] R. M. Goldstein, H. A. Zebker, and C. L. Werner, "Satellite radar interferometry: two–dimensional phase unwrapping," Radio Science, vol. 23, pp. 713–720, 1988.

[6] R. Lanari *et al.*, "Generation of Digital Elevation Models by using SIR–C/X–SAR Multi–frequency Two–Pass Interferometery: the Etna Case Study," submitted to IEEE Trans. Geoscience and Remote Sensing, 1995.

[7] S. N. Madsen, "Estimating the Doppler centroid of SAR data," IEEE Trans. Aerosp. and Elec. Syst., vol. AES–25, pp.134–140, 1989.

Maximum Entropy Solution for Interferometric SAR Phase Unwrapping

Mihai Datcu

German Aerospace Research Establishment (DLR)
German Remote Sensing Data Center (DFD)
W–82234 Oberpfaffenhofen, Germany

Abstract

The high interest to derive digital terrain models from interferometric SAR (InSAR) data stimulated the research to optimally solve the phase unwrapping problem. Several solutions have been proposed. We hereby address the phase unwrapping stated as a ill–posed inverse problem and investigate the solutions based on the principle of maximum entropy.

1. Introduction

The principle of maximum entropy (ME) is a method of translating information into a probability assignment. The ME formalism provide a coherent tool for incorporating new information (in terms of constraints) into initial models. Inferring the data that satisfies the constraint set can be seen as solving an ill–posed inverse problem, with the entropy as regularizing functional.

For InSAR phase unwrapping problem the set of constraints encode the degree of roughness of the desired digital elevation model. In the ME assumption the maximum smoothness of the reconstructed phase is obtained.

The problem statement is: minimize an error measure between the observed and the simulated data, and maximize the entropy of the phase. The simulated data are iteratively obtained as function of the current phase estimate. The simulation is a forward model. The degree of refinement of the solution is given by the complexity and the amount of prior knowledge encapsulated in the forward model.

The pure ME principle does not consider the noise. In order to see how noise can be incorporated into the ME method, we consider the full Bayesian approach. Taking into account the noise the pure ME solution is modified, moving to a point where the entropy is higher. This solution corresponds to a smoother solution with a higher entropy than would be possible if the data were noiseless. The solution is obtained by imposing a supplemental *hard* constraint on the possible solutions. We use as a *hard* constraint the chi–squared statistic of error measure between the observed and the simulated data.

The presented solution for phase unwrapping has the advantage to fully consider the prior knowledge and to take into account in a systematic way the noise. The phase estimate is a maximum a posteriori (MAP).

2. Phase Unwrapping – problem statement

The Phase Unwrapping is the key step in recovering the terrain elevations from InSAR data. The problem is to find an estimate of the phase values Φ known the wrapped noisy phase observations Ψ.

$$\Psi_k = W\{\Phi_k + n_k\} \tag{1}$$

where **W** represents the *mod2π* wrapping operator, **n** is the observation noise and **k** is the spatial index for the samples of the data in a 2–dimensional grid **k**=(x,y). Several solutions have been proposed [2,6]. They, generally, aim at the minimization of:

$$\sum_k | \nabla \Phi_k - f_k |^2 \tag{2}$$

where f_k are the observations of the wrapped phase gradient.

3. Solutions as ill–posed inverse problem

The phase unwrapping is an ill–posed inverse problem, the solution is not unique and depends on the prior knowledge encapsulated in the constraints introduced for the regularization of the solution. Recently [4] solutions using quadratic regularization functionals and the Bayesian approach have been reported. Hereafter we introduce a solution for phase unwrapping in the light of the ME principle.

3.1 The Maximum Entropy regularization

The ME principle [3], was first introduced as a general methods of inference about unknown probability densities subject to a set of constraints.

0-7803-3068-4/96$5.00©1996 IEEE

In terms of the inference of the probability densities, suppose one has a system which has a set of states $S=\{s_i\}$, having the unknown probabilities $q(s_i)$. Additional information about the probabilities of the states is also available in term of constraints on the distribution $q(.)$: values of certain expectations, or other. These expectations constraint the space of the solutions to a certain domain (preferable convex), but usually there remains an infinte set of distributions that are not ruled out by the constraints. The principle of maximum entropy states that of all distributions $q(.)$ that satisfy the constraints, one should choose the one with the largest entropy

$$H(q) = -\sum_i q(s_i) log(q(s_i)) \tag{3}$$

In the case of phase unwrapping the set S is assigned to be the set of all possible unwrapped phase values and the distribution $q(.)$ is identified with $\Phi(k)$ (appropriately normalized). The ME solution will be understood as the most uniform solution.

The pure ME principle does not consider the noise. To consider the noise in our solution there are two approaches, to modify the ME solution taking into account the errors introduced by the noise or to state the full Bayesian solution.

In the first approach a misfit measure between the actual data and the simulated data is introduced. The measure can be the mean square error or the chi–squared statistic. The simulated data are obtained by modelling the forward problem, the W operator applied on an intermediate guess of the phase solution. The problem statement is: find the maximum of H and the minimum of the MSE:

$$MSE = \sum_k | \nabla\Phi_k - f_k |^2 \tag{4}$$

$$H(\Phi) = -\sum_k \Phi_k log(\Phi_k) \tag{5}$$

Formally the solution is found at the extremum of

$$Q = H - \lambda\, MSE \tag{6}$$

where λ is the Lagrange multiplier.

The solution is iterative:

$$\Phi^{i+1} = K\, exp\{-\lambda\, (\nabla f - \Delta\Phi^i)\} \tag{7}$$

K is a constant, i the iteration index, f^i the simulated data (the output of the forward model).

The exponent in relation (7) has the same expression as the Poisson equation which solve the unwrapping problem in least squares sense [2]. The ME principle forces this solution to its maximum smoothness. The parameter λ controls the degree of roughness–smoothness of the solution. In the paradoxal case of unconstrained least squares solution, the exponent is null, the ME forces the data to be constant, an uniform field.

3.2 The Bayesian solution

The ME solution does not take into account the noise, or in its modified form the noise is considered as a *hard* constraint.

The Bayesian inference gives the frame to specify the complete set of prior knowledge.

The interferogram generation can be written in operator formalism:

$$i = \mathcal{I} z + n \tag{8}$$

$$\Phi = \measuredangle z, \qquad f = \measuredangle i \tag{9}$$

where i represents the complex interferogram, $\mathcal{I}$ is the operator describing the interferogram formation, z the interferometric SAR images, and n the noise of system. The problem statement in this formalism is the inversion of equation (8) to find the InSAR phase Φ.
Considering the noise to be described by the probability distribution function p_σ, the likelihood of i is:

$$p_{i|z}(z) = p_o(\|\mathcal{I} z - i\|) \tag{10}$$

In [5] a Bayesian formalism is proposed for the phase unwrapping problem. The assumed model refers only the arguments of the complex data. In order to invert the wrapping operator W a relaxation of its action is introduced: only the differences of the field to be unwrapped are constrained to be integer multiples of 2π, the absolute values are allowed unrestricted. The phase noise is assumed Gaussian and the prior information for the phase field is Markovian, expressed by a Gibbs distribution. The unwrapped phase maximum a posteriori (MAP) estimate, is the solution of the extremum of equations (11–13).

$$p_{\Phi,\mu|\Psi}(\Phi, \mu) = K\, exp(-(\alpha + \beta)) \tag{11}$$

$$\alpha = \sum V(\Phi) \tag{12}$$

$$\beta = \gamma \sum (\Psi - \Phi + 2\pi\mu)^2 \tag{13}$$

where V is the potential function of the Gibbs model, μ is the modified wrapping/unwrapping variable, K a constant.
In the case of double pass InSAR the phase noise model is generally unknown. An alternative Bayesian solu-

tion can be formulated [1]. The noise is considered taking into account only its variance in the chi–squared data misfit measure (14).

$$\chi^2 = \sum_k \frac{|\nabla\Phi_k - f_k|^2}{\sigma^2} \qquad (14)$$

The regularization of the solution is done based on the ME principle (3,5) and the problem statement is: find extremum of the functional Q:

$$Q = H - \lambda\,\chi^2 \qquad (15)$$

Solving (15) does not explicitly include the unwrapping. There are three possible solutions: to add a new constrain for the phase discontinuity, to use the assumption that only the differences of the field to be unwrapped are constrained to be integer multiples of 2π, the absolute values are allowed unrestricted, or to apply the algorithm only for the regularization of the solution of one of the unwrapping methods.

4. Final remarks

In the classical approach, a set of observed data is given and it is used to decide wether some hypothesis is true. The classical approach embeds the observed data set in a *sample space*, an imaginary collection containing other data sets that one thinks might have been observed but were not. Then one introduces the probabilities that the data set would be observed if the hypothesis were true. This are called the sampling distribution and are interpreted as the frequency with which the data set would be observed in the long run if the measurement were made repeatedly with the hypothesis constantly true. The sampling distribution is the only probability distribution we are allowed to use, for that reason classical statistics is ofted called *sampling theory* and the merits of any method of analysis are to be judged by its sampling properties. By ignoring the prior information, classical approaches are able to deal only with a part of the real problem of inference. The pure ME approach utilizes our prior information and the reasoning format is almost the opposite. Instead of considering the class of all data sets consistent with a hypothesis, we consider the class of all hypotheses consistent with the one data set that was actually observed. Out of the class of the hypotheses consistent with our data we pick the one having the ME. However, ME fails to take noise into account, a factor that frequentist methods do deal with. So, they represent opposite reasoning formats: classical methods apply in cases where we have a sampling distribution (noise) of known properties but no prior information (constraints); while ME is for cases where we have known constrains but no noise. For the case when we have both noise and prior information, one must use the full Bayesian method, incorporating as limit cases both the classical approach and the ME method. The Bayesian analysis is performed, using *soft* constraints, i.e. the prior estimates. ME uses as prior information statements in the form of the *hard* constraints described in the previous subsection. So, if a statement referring to a probability distribution is testable (e.g. it specifies a mean value), then it cannot be used as a conditioning statement in Bayes' theorem. Similarly, a statement about an event (e.g. an observed frequency) can be used as a conditioning statement in applying Bayes' theorem, whereupon it yields a posterior distribution which may be contracted to a marginal distribution; but cannot be used as a constraint in applying the ME because it is not testable information. In order to incorporate the noise into the ME method, we consider the full Bayesian approach.

References:

[1] Burch S.F., Gull S.F., Skilling J., *Image Restoration by a Powerful Maximum Entropy Method*, Comp. Vis. Graph. and Imag. Processing, Vol. 23, pp. 113–128, 1983.

[2] Ghiglia D. C., Romero, L.A., *Direct phase estimation from phase differences using fast elliptic partial differential equation solver*, Optics Letters, vol.14, pp. 1107–1109, 1989.

[3] Jaynes E.T. , *On The Rationale of Maximum–Entropy Methods*, IEEE Proc., Vol. 70, No.9, pp. 939–952, 1982.

[4] Marroquin J.L., Rivera M., *Quadratic regularization functionals for phase unwrapping*, J. Opt. Soc. Am. A., Vol. 12, No. 11, pp. 2393–2400, 1995.

[5] Marroquin J.L., Tapia M., Rodriguez–Vera R. Servin, M., *Parallel algorithms for phase unwrapping based on Markov random field models*, J. Opt. Soc. Am. A., Vol. 12, No. 12, pp. 2578–2585, 1995.

[6] Pritt M., *Multigrid phase unwrapping for interferometric SAR*, Proc. IGARSS'95, Firenze, Italy, pp. 562–564, 1995.

Consistent 2-D Phase Unwrapping Guided by a Quality Map

Thomas J. Flynn
Sandia National Laboratories
P.O. Box 5800, MS 0572
Albuquerque, NM 87185-0572, USA
Voice: +1 505 844-0552 Fax: +1 505 844-7593 Email: tjflynn@sandia.gov

Abstract -- The problem of 2-D phase unwrapping arises when a spatially varying quantity is measured modulo some period. One needs to reconstruct a smooth unwrapped phase, consistent with the original data, by adding a multiple of the period to each sample. Smoothness typically cannot be enforced over all of the scene, due to noise and localized jumps. An unwrapping algorithm may form a mask within which phase discontinuities are allowed. In interferometry a quality map is available, indicating the reliability of the measurements. In this case, the mask should be contained as much as possible in areas of low quality. This paper presents an algorithm for phase unwrapping in which the mask design is guided by the quality map. The mask is grown from the residues (as defined by Goldstein et al.) into areas where the quality is below a threshold. A connected component of the mask stops growing when its residue charge becomes balanced. The threshold is raised as necessary to allow growth. This stage terminates when all components are balanced. The mask is then thinned by removing points that are not needed to cover the residues correctly. The unwrapped phase is found by simple 1-D unwrapping along paths that avoid the mask. We present an example solution found by the algorithm and discuss possible modifications.

INTRODUCTION

The problem of 2-D phase unwrapping arises when a spatially varying quantity is measured modulo some period. Such measurements can be thought of as phase angles, hence the term "phase unwrapping." The task is to make a reconstruction of the unwrapped phase, removing the periodicity of the measurement. It is assumed that the phase difference between adjacent pixels is almost always a small fraction of a cycle. Hence, along a typical path, the unwrapping can be done by wrapping the differences between successive samples (adding cycles as necessary to make the differences less than one-half cycle in magnitude) and accumulating. The resulting unwrapped phase is consistent with the original data (different at each pixel by an integer number of cycles). This method can fail due to regions in which the assumption of smoothness fails to hold. These can cause the unwrapped phase found at one pixel, starting out from another, to depend on the choice of path. Equivalently, the sum of wrapped phase differences around a closed path may be a nonzero number of cycles. The choice of path must be restricted to avoid this condition.

A systematic criterion for path restriction has been found by Goldstein et al. [1]. They observe that unwrap path dependency is caused by pointlike sources called "residues." A residue is a loop of four neighboring pixels for which the clockwise sum of wrapped phase differences around the loop is not zero, but plus or minus one cycle; the residue is said to have charge +1 or -1. The sum of wrapped phase differences around any closed path is equal, in cycles, to the sum of the charges of the enclosed residues. If all closed paths are constrained to enclose zero net residue charge, then the phase difference sum around any path is zero, and the unwrapped phase is defined uniquely. The constraint can be imposed by forming the residues into clusters, each with zero charge sum, and requiring that the path enclose either all or none of the residues in each cluster. If there is a mask of forbidden pixels such that the residues within each cluster are connected by mask pixels, then any path made up entirely of unmasked pixels is guaranteed to be suitable for unwrapping. (The edge of the image can serve as a residue charge source in this method: an unbalanced cluster is allowed if the mask connects it to the edge.) The problem of unwrapping is thus reduced to that of finding a good clustering of residues and a mask that enforces it.

The residues in each cluster should be as close together as possible, so that no long links are needed in the mask. The algorithm of [1] starts a cluster with a single residue, then adds nearby residues found by a local search. The cluster stops growing when it becomes balanced or reaches the edge. The growing process then starts again with another unpaired residue. The algorithm terminates when all residues are in clusters. There is no global search for the best set of clusters. Depending on the order in which the residues are accessed, a residue may be left without unclustered near neighbors, making a link to a faraway residue necessary. Such links can create erroneous jumps in the unwrapped phase. Recently developed algorithms [2,3] include an optimization stage that interchanges the residues among clusters to reduce the length of the links.

An interferogram is formed by complex correlation of neighborhoods of image pixels [4]. The phase of the correlation forms the data to be unwrapped, while its magnitude indicates the quality of the phase data, ranging

This work was supported by the U.S. Department of Energy under contract DE-AC04-94AL85000.

0-7803-3068-4/96$5.00©1996 IEEE

from 0 (poor) to 1 (perfect). This *quality map* can help to guide phase unwrapping: the mask should be confined as much as possible to pixels of low quality, as well as covering as few pixels as possible.

The least-error-path method, due to Roth [5], uses the quality map to choose unwrap paths directly. It assumes that a path that goes entirely through high-quality pixels is suitable for unwrapping. Regions of very high quality are seeded with initial unwrap values. An unwrap solution is then grown from each seed point by summing the wrapped phase differences, starting with the highest-quality pixels and working downward. The growing process leaves the image covered by smooth locally unwrapped patches. These are joined by successively locating the highest-quality pixel pair on the boundary between two patches, then adding cycles to minimize the unwrapped phase difference at that pair. The algorithm performs no explicit residue detection or matching, so it has no direct control on the location of discontinuities.

We now present an algorithm to compute an unwrapped phase solution, consistent with the data, in which the phase discontinuities are confined to an explicitly computed mask, chosen to lie as much as possible within regions of low quality. The algorithm can be thought of as the reverse of the least-error-path method: instead of growing unwrap paths through high-quality regions, one grows the mask through regions of low quality, starting from the residues. The algorithm keeps track of the residue charge of each connected component of the mask, terminating when all components are balanced. The unwrapped phase is then computed by path following, avoiding the mask.

IMPLEMENTATION

We are given, at each location (i,j), the phase $\phi_{ij} \in [0, 2\pi)$ and quality $\rho_{ij} \in [0, 1]$. Introducing the phase wrapping operator

$$W(\phi) \equiv ((\phi + \pi) \bmod 2\pi) - \pi, \quad (1)$$

the residue map is computed as follows:

$$r_{ij} = \frac{1}{2\pi}[W(\phi_{i+1,j} - \phi_{ij}) + W(\phi_{i+1,j+1} - \phi_{i+1,j}) - W(\phi_{i,j+1} - \phi_{ij}) - W(\phi_{i+1,j+1} - \phi_{i,j+1})]. \quad (2)$$

The r_{ij} can have value 0, +1 or -1. Locations where r_{ij} is nonzero are called positive or negative residues according to their sign.

The inputs to the mask-design algorithm are the residue map and the quality map. The phase data are used only to find the residues. The pixels adjoining residues are the seed points for the mask. To confine the mask to regions of low-quality data, an outer loop allows it to grow only into eligible pixels (seed points and pixels adjoining the mask) whose quality lies below a threshold. The threshold is initialized, then incremented when mask growth becomes impossible. The initial threshold and increment size are the only adjustable parameters in the algorithm. The loop terminates when all mask components have zero residue charge (so that further growth is unnecessary).

Within the outer loop, growing is done by an inner loop which makes repeated passes through the image, adding to the mask eligible pixels whose quality is below the threshold. Once a pixel is added, its neighbors become eligible. To reduce unnecessary growth, uncharged components are not extended. If a pixel adjoins several components, adding it to the mask merges them and combines their residue charges. The residue-charge table and component labels are updated to reflect the merger. To simplify recordkeeping, the newly merged component is not allowed to grow further until the next pass. A component that reaches the edge is marked as uncharged. The inner loop terminates when a pass through the image adds no pixels to the mask (so that further growth is impossible without raising the quality threshold). In summary, the mask-growing stage of the algorithm acts as follows:

```
Replace quality map with its 3x3 minimum
Compute residues
Declare pixels surrounding residues to be seed points
Initialize threshold
repeat
  repeat
    Declare all components unmerged
    for (each pixel in image)
      if (quality < threshold and pixel is not in mask
       and [pixel is a seed point
            or pixel adjoins a charged component]
       and pixel adjoins no merged component) then
        Add pixel to mask
        if (pixel adjoins several components)
          merge all adjoined components
        if (pixel's component adjoins edge)
          set charge to zero
      end
    end
  until (no pixels added)
  Increment threshold
until (all components are uncharged)
Add all neighbors of residues to mask
```

Mask growing typically puts many pixels in the mask that are not needed to cover the residues correctly. A thinning stage is used to remove them. This starts by identifying and labeling the connected components of *unmasked* pixels, then masking out all but the largest component. It then makes repeated passes through the mask, each time removing pixels that adjoin the unmasked region. A pixel is removed if: 1) it does not adjoin a residue; 2) its quality is above the initial

threshold used in growing; and 3) removing it does not change the connectivity of the mask. The connectivity is tested by examining the 3x3 neighborhood of the candidate pixel. Removal is forbidden if it would leave disconnected mask pixels within the neighborhood. The thinning stage ends when a pass finds no removable pixels.

With the mask prepared, the unwrapped phase is computed by path-following. In the absence of a reference point whose wrap count is known, we can start with an arbitrary point, giving it a wrap count of 0.

EXAMPLE

Figs. 1 and 2 display a portion of a synthetic-aperture radar interferogram computed from an ERS-1 image pair taken over Ft. Irwin, California. Fig. 1 contains the phase data, and Fig. 2 contains the quality map. Occurrences of layover appear as discontinuities in the phase data, with corresponding low regions in the quality map. The initial quality threshold was 32 (on a scale of 0 to 255) and the increment was 2. The mask is presented in Fig. 3. The algorithm has clearly succeeded in finding a mask that covers a small number of pixels and allows only localized discontinuities. The unwrapped phase is displayed in Fig. 4. It has been inverted, and a tilt has been removed, to make terrain features more visible. Some of the masked regions appear as jumps in the unwrapped phase.

CONCLUSIONS AND FUTURE WORK

We have presented an algorithm for phase unwrapping, for data that include a quality map. It works by growing a mask, preferentially through low-quality regions, so as to enforce a residue-balance condition, allowing unwrapping by path following in the unmasked region. The method is intended to find a small, compact mask, largely confined to low-quality regions. Computations on actual interferograms indicate that this goal is achieved in most cases.

The algorithm produces inappropriate results on some data sets. Its worst failures happen when groups of residues are not joined by low-quality paths, so that the growing stage connects them, not to each other, but to the edge. The thinning stage leaves bridges to the edge, across which the unwrapped phase makes erroneous jumps. This problem points out how the performance of the algorithm depends on the accuracy of the quality map. An alternative version of the algorithm, in which the mask is grown through regions where the wrapped phase differences are large, often works well in cases where the quality map is missing or inaccurate.

A more robust algorithm would make short connections as needed to achieve residue balance, overriding the quality threshold. This might be done by combining the mask-growing method with minimum-distance residue matching as in [2,3]. An initial stage of mask growing would form a small number of mask components, some of them charged. The distances between components would then be computed and a minimum-distance pairing found. Links enforcing this pairing would then be added to the mask.

ACKNOWLEDGMENTS

This work was helped by discussions with the author's colleagues Dennis Ghiglia, Paul Thompson, Daniel Wahl, Jack Jakowatz and Terry Calloway. The ERS-1 interferogram was prepared by Dick Shead.

REFERENCES

[1] R. Goldstein, H. Zebker and C. Werner, "Satellite radar interferometry: Two-dimensional phase unwrapping," Radio Science, vol. 23, pp. 713-720, July-August 1988.

[2] J. Buckland, J. Huntley and S. Turner, "Unwrapping noisy phase maps by use of a minimum-cost-matching algorithm," Applied Optics, vol. 34, pp. 5100-5108, 10 August 1995.

[3] J. Quiroga, A. Gonzalez-Cano, and E. Bernabeu, "Stable-marriages algorithm for preprocessing phase maps with discontinuity sources," Applied Optics, vol. 34, pp. 5029-5038, 10 August 1995.

[4] J. Hagberg, L. Ulander and J. Askne, "Repeat-pass SAR interferometry over forested terrain," IEEE Trans. Geosci. and Remote Sensing, v. 33, pp. 331-339, March 1995.

[5] M. Roth, "Phase unwrapping for interferometric SAR by the least-error path," unpublished.



Fig. 1: Phase data

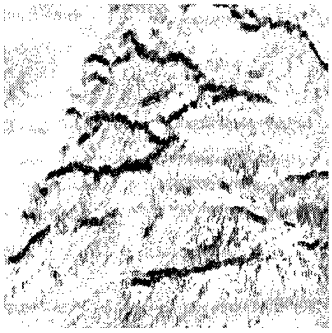


Fig. 2: Quality map

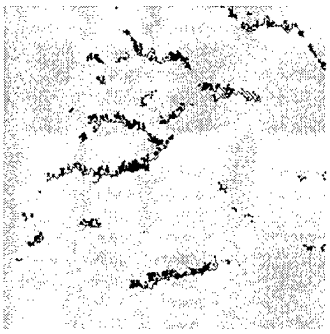


Fig. 3: Mask

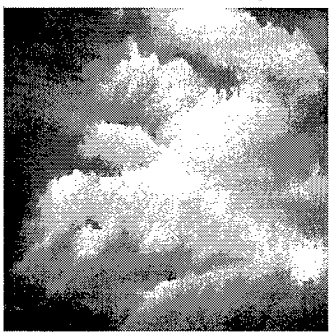


Fig. 4: Unwrapped phase

Absolute Phase Determination in SAR Interferometry

M.T. Chiaradia, L. Guerriero, G. Pasquariello(*), A. Refice, and N. Veneziani(*)

Dipartimento Interateneo di Fisica,
Via Amendola, 173 - 70126 Bari (Italy)
Telephone: +39 80 5443224 Facsimile: +39 80 5443224 E-mail: guerriero@ba.infn.it

(*) CNR - Istituto Elaborazione Segnali e Immagini
Via Amendola, 166/5 - 70126 Bari (Italy)
Telephone: +39 80 5481699 Facsimile: +39 80 5484311 E-mail: veneziani@iesi.ba.cnr.it

Abstract -- High resolution extended DEM can be obtained from interferometric SAR image pairs. In order to evaluate the elevation of a pixel with respect to a slant-range reference plane, its absolute interferometric phase is required and this is usually derived unwrapping a 2D interferometric fringe pattern. Different methods have been suggested for phase unwrapping, based on local or global approaches. In both cases, phase incostistencies (residues) in SAR interferograms due to noise and topography determine unwrapping errors which appear as discontinuities in the computed absolute phase field. In this paper, results are reported on our experiment addressed to improve the output of phase unwrapping techniques by means of a residue classification procedure, according to their origin. Working on both simulated and real phase fields, we have found some differences between the spatial configurations of phase fields around singular points due to noise or linear discontinuities. A practical method has been developed to solve some ambiguities in the phase unwrapping of real SAR interferograms, useful for the linear integration approach as well as for global methods.

INTRODUCTION

Interferometric synthetic aperture radar observations provide a mean for obtaining high-resolution digital topographic maps from amplitude and phase measurements of two complex radar images [1]. The phase is, however, known as principal value (wrapped phase). Absolute interferometric phase can be obtained by integrating phase differences or, equivalently, by adding properly chosen multiples of 2π shifts to the wrapped phase values [2]. Phase can be unwrapped by integrating the wrapped differences of principal values, when the sampled phase field satisfies the unwrapping continuity constraint. In the presence of phase aliasing, arising from insufficient spatial sampling of rapid phase slopes or from low SNR, the phase unwrapping becomes path-dependent and inconsistent results are obtained.

Different methodologies have been developed to prevent error propagation: in [3] the authors describe a method that identifies and avoids the residues so that the integration of the phase differences is performed along a path not interrupted by residue regions. To reduce the number of residues the images are low-pass filtered. In [4] a technique is proposed where ghost lines are identified and avoided by the integration path. An alternative approach [5] unwraps the phase by first detecting the fringe lines by means of edge enhancing, thinning and linking, then adding 2π whenever the path crosses a fringe line. All the previous methods are based on local approaches. An alternative way of integrating the phase derivatives is based on a least-squares method (global approach) [6, 7, 8]. In this case the solution is obtained by minimizing the differences between the discrete partial derivatives of the wrapped phase function and those of the unwrapped one. In this case, too, aliasing and noise tend to make phase unwrapping ambiguous. All the phase unwrapping methods reported involve a certain degree of smoothing of the phase image before the unwrapping step to reduce the number of detected residues. Global approaches perform also a further smoothing of the phase field, so that, in the presence of ambiguities in the wrapped phase, the result is altered with respect to the original wrapped phase by values which are not integer multiples of 2π. In this paper we introduce a phase unwrapping method which deals with residues in a local way. As it will be explained in the following section, couples of residues can originate in a limited and controlled number of local configurations of the principal phase values. By analizing and correcting each one with the appropriate series of corrections, we are able to obtain an unwrapped phase which is completely consistent with itself, that is it does not show evidence of inconsistencies spreading out of control on the entire image. More interestingly, experiments with simulated phase fields show that the reconstructed phase is identical to the original one except for isolated, pointlike differences of integral multiples of 2π. Thanks to its local nature, our approach can be used on interferograms containing an arbitrary large number of residues, the limiting factor being only the computational time. This reduces the necessity of image pre-filtering, improving the detail of the final image.

PHASE UNWRAPPING

In this paper we will deal with linear discontinuities, defined as curves on the imaged surface on which the absolute phase presents differences between adjacent pixels greater than π rad in magnitude. This fact does not necessarily imply that

0-7803-3068-4/96$5.00©1996 IEEE

the discontinuity is visible on the principal phase image: this depends on the particular phase values of the pixels affected by the discontinuity. One of the most common types of linear discontinuity is a shear line, that is a phase jump located on an open curve. It is noted that these absolute phase discontinuities are very different in nature from the wrapped phase discontinuities that constitute the interferometric fringes. Consequently, they are to be treated in a different way by the phase unwrapping algorithm: while fringes need to be integrated, that is their edges need to be "smoothed" by rising or lowering a whole part of the phase field of a multiple of 2π, "real" discontinuities *must* be conserved on the final unwrapped image, because they are not interferometrical artifacts but actual features of the surface. If we use a conventional unwrapping algorithm assuming that the principal phase field is everywhere consistent with the "unwrapping theorem" [2], an open fringe will always cause an inconsistency which will spread over the unwrapped image in a way depending on the particular algorithm adopted. On the open fringes, wrapping the differences of the wrapped phase values does not give the absolute phase differences. Instead, the real (not wrapped) differences between the wrapped phase values should be used and integrated, which would leave on the unwrapped image a discontinuity localized on the fringe, thus avoiding inconsistencies. We adopt a method which involves a fringe-following step previous to the unwrapping. Once two residues have been connected by a fringe line, all the phase differences relative to the fringe are marked so that their values are not wrapped. Later, the integration step can be performed, leaving the open fringes unmodified. All the previous considerations must be modified in order to take into account the effects of noise. Noise can alter in a random way some of the phase differences, giving origin to couples of adjacent residues of opposite sign. The most probable effect is the alteration of a locally isolated phase difference. This gives rise to a couple of residues of opposite sign located on adjacent pixels. With a lesser degree of probability, noise can also alter two or more adjacent phase differences, generating a couple of residues of opposite sign separated by more than one pixel. Figure 1 shows the four possible cases of first-order isolated residue couples generated by noise, and some of the most common second-order configurations with the residues located on diagonal-adjacent pixels. Actually, noise can also alter a phase difference across a "normal" fringe. The fringe in this case results interrupted by a couple of residues. In this case, an interrupted fringe will be erroneously recognized as a natural discontinuity, and will not be unwrapped, so we need to take into account this possibility. What we have to do is to couple the residues of opposite sign when they are located across a fringe, by increasing or lowering artificially the phase differences involved so as to "close" the fringe. In principle, all the possible configurations should be taken into account, but the complete problem is practically unsolvable, because it is very difficult to decide whether two residues are to be coupled to close a true fringe or to cancel an artificial one. However, we have realized that in the majority of cases, only the most probable configurations – that is the first- and second-order configurations previously showed – arise as a consequence of noise. The procedure can be then modified in order to account for this limited number of possibilities and "cure" them in a way which leaves unaltered the neighbouring pixel values. Our algorithm is thus basically divided into two parts: first, the residues forming couples one or two pixels apart – which are the majority – are cancelled by altering the proper phase differences involved; after this step, the residues remaining are mostly the ones due to actual linear discontinuities on the surface imaged, and can be coupled by the fringe following algorithm described before.

RESULTS AND DISCUSSION

The performance of the exposed method for phase unwrapping has been compared with the LMS approach. In order to give quantitative results, we have generated absolute phase fields corresponding to a known altimetric map, corrupted by noise. Fig. 2 shows the wrapped phase values corresponding to the simulated phase field with a percentage of residue points of more than 10%. The well-shaped solution of the mean-square algorithm hides a poor correspondence between the retrieved phase values and the expected ones. This situation is well depicted in Fig. 3, showing the distribution of phase differences. The errors produced by the local algorithm (upper plot) are confined to a few points, while LMS errors are distributed in a continuous way. Fig. 4a shows the interferogram produced using two ERS-1/ERS-2 Tandem images (ERS-1 orbit n. 21481, frame n. 2781, ERS-2 orbit n. 1808; August 24th and 25th, respectively), corresponding to a region near the city of Matera, in southern Italy. Fig. 4b shows the unwrapped phase field obtained using our local approach. In this case, in order to give a comparison with the LMS algorithm, in Fig. 5 we report the distribution of differences between the re-wrapping of the reconstructed absolute phase and the

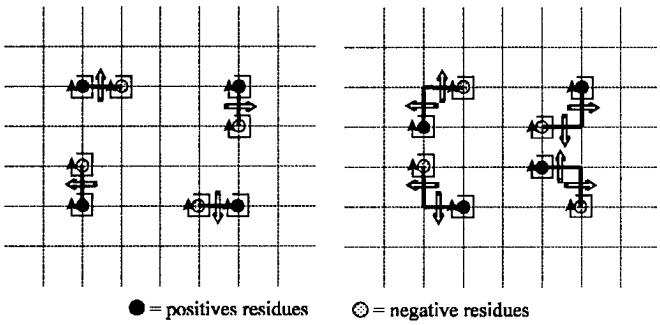


Figure 1. Left: first-order couples of residues generated by isolated phase differences out of the range $(-\pi, \pi)$. Right: some second-order configurations. The solid arrows represent the phase jumps greater than 2π in magnitude.

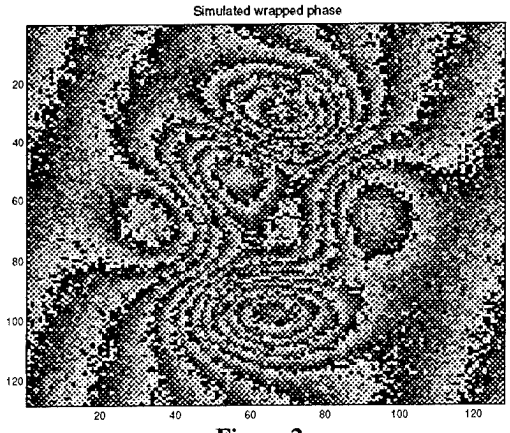


Figure 2

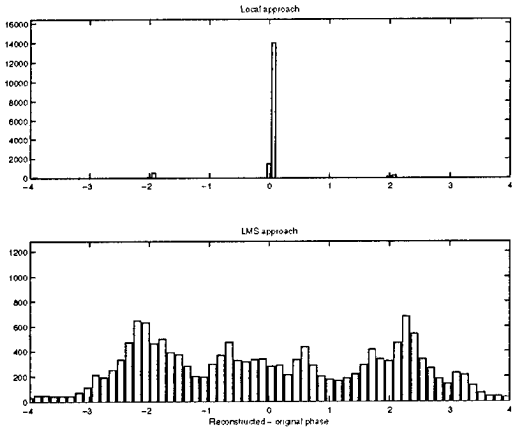


Figure 3: abscissae in π units.

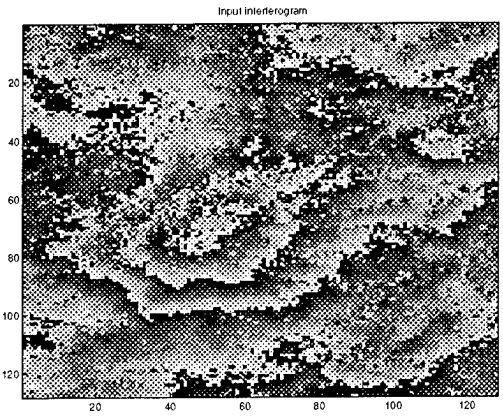


Figure 4a

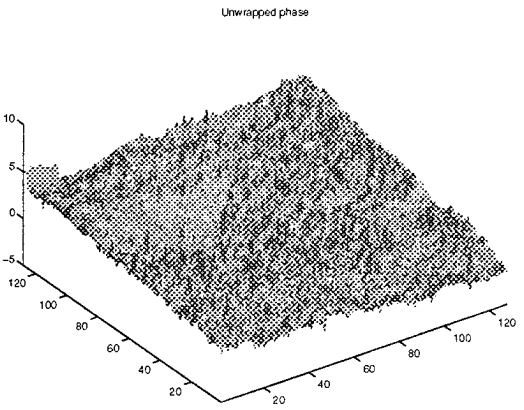


Figure 4b

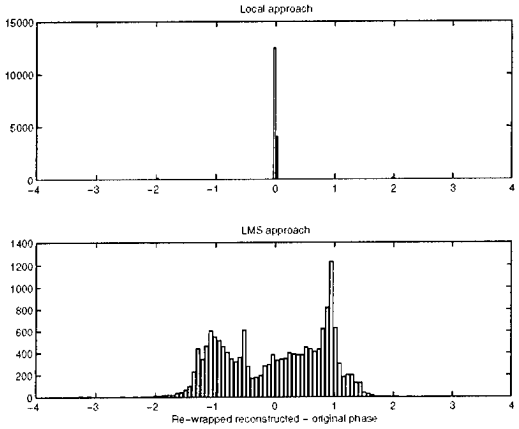


Figure 5: abscissae in π units.

original one. As in the simulated case, the local approach (upper plot) shows a better agreement than the LMS results.

REFERENCES

[1] H.A. ZEBKER, and R.A. GOLDSTEIN, "Topographic Mapping from Interferometric SAR Observations", *Journal of Geophysical Research*, 91(B5) 4993-4999, 1986.

[2] J. TRIBOLET, "A New Phase Unwrapping Algorithm", *IEEE Transactions on Acoustics, Speech, and Signal Processing*, Vol.25, No.2, April 1977.

[3] R.M. GOLDSTEIN, H.A. ZEBKER, and C.L. WERNER, "Satellite Radar Interferometry: Two-Dimensional Phase Unwrapping", *Radio Science*, Vol.23, No.4, July-August 1988.

[4] C. PRATI, F. ROCCA, A.M. GUARNIERI, E. DAMONTI, "Seismic Migration for SAR Focusing: Interferometrical Applications", *IEEE Transactions on Geoscience and Remote Sensing*, Vol.28, July 1990.

[5] Q. LIN, J.F. VESECKY, H.A. ZEBKER, "New Approaches in Interferometric SAR Data Processing", *IEEE Transactions on Geoscience and Remote Sensing*, Vol.30, May 1992.

[6] H. TAKAJO, T. TAKAHASHI, "Least-Squares Phase Estimation From the Phase Difference", *J. Opt. Soc. Am. A*, Vol.5, No.3, 1988.

[7] D.C. GHIGLIA, and L.A. ROMERO, "Robust two-dimensional weighted and unweighted phase unwrapping that uses fast transforms and iterative methods", *J. Opt. Soc. Am. A*, Vol.11, No.1, January 1994.

[8] U. SPAGNOLINI, "2-D Phase Unwrapping and Phase Aliasing", *Geophysics*, Vol.58, No.9, 1993.

Determination of Absolute Interferometric Phase using the Beam-Amplitude Ratio Technique

D. L. Bickel and W. H. Hensley
Sandia National Laboratories
Albuquerque, NM 87185-0537 USA
Telephone: 505-845-8112, Facsimile: 505-845-9888, Email: dlbicke@sandia.gov, whhensl@sandia.gov

ABSTRACT

Determination of the absolute phase difference (i.e., not modulo 2π) is a key problem in interferometric synthetic aperture radar (IFSAR) for topographic mapping. One way of solving this problem requires use of a technique different from the basic interferometry to resolve a "coarse" angle measurement that lies within the IFSAR ambiguity angle. The method investigated in this paper involves taking advantage of the difference in the amplitude ratio versus elevation angle that occurs when the elevation beams of the two IFSAR antennas are pointed in slightly different directions. The performance of the technique is a function of the angular separation of the two beams, the elevation beamwidth, and the symmetry of the two beam-amplitude patterns. The performance required of the technique is set by the ambiguity angle of the interferometer. This paper presents an analysis of the beam-amplitude ratio technique and shows experimental results.

INTRODUCTION

There continues to be growing interest in the area of height mapping using interferometric synthetic aperture radar (IFSAR). The ultimate goal of IFSAR is to provide an automatic way of producing elevation models in a true ground coordinate system or a WGS-84 coordinate system. This is accomplished in IFSAR by estimating an elevation angle relative to an antenna baseline-coordinate system, and then transforming to the desired ground or WGS coordinates. The elevation angle estimate is derived from the measurement of the interferometric phase.

One of the problems that must be overcome is determining the absolute ambiguity of the interferometric phase. This ambiguity comes from the fact that practical IFSAR systems do not adequately Nyquist sample the antenna elevation beamwidth. The consequence is that the elevation angle determined from the interferometric phase is unknown to some multiple of the spatial Nyquist frequency.

Two techniques have been proposed to address this issue in [1], and an overview of techniques is found in [2]. These methods can be thought of in two general categories. The first is to acquire additional Nyquist samples, such as multiple frequencies or baselines [3]. The second is to use non-phase information to aid the process. This could be tie-points, or it could be a range-stereo technique as proposed in [1,2].

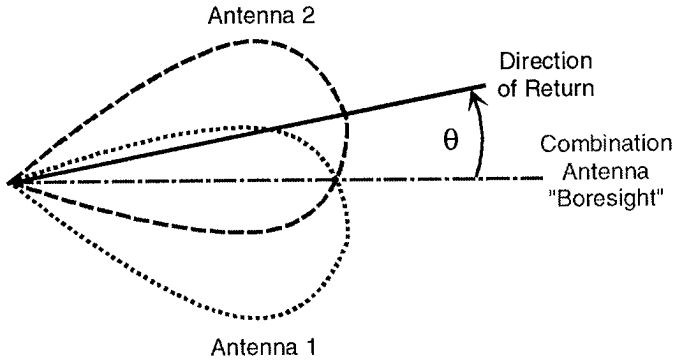
In this paper we describe another technique that falls into the second category. This technique proposes applying a different elevation squint to each of the IFSAR antennas, as with amplitude monopulse, and using the relative intensity information to unambiguously determine the antenna pointing. Tying the antenna pointing to the IFSAR angle allows us to determine the absolute ambiguity in the IFSAR elevation angle measurement.

In the following sections we will briefly discuss the theory of operation and calibration. Finally, a couple of examples are presented.

THEORY

Principle of Operation

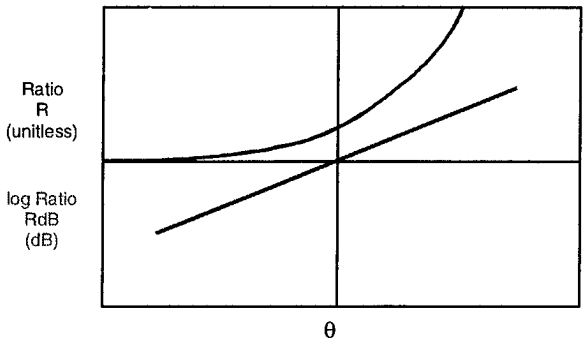
Figure 1 illustrates the fundamental operating principle of the beam-amplitude ratio technique. The idea is that the elevation angle to a target within the scene can be determined from ratio of the intensity between the two antennas. The angle measurement is not as sensitive as the angle determined from the interferometric phase. However, it only needs to be sensitive enough to determine the ambiguity.



(a) Polar Plot of Antenna Beam Patterns

Figure 1: Principle of Beam-Ratio Technique

0-7803-3068-4/96$5.00©1996 IEEE



(b) Ratio of Antenna Beam Amplitudes vs. Elevation Angle θ

Figure 1 (continued): Principle of Beam-Ratio Technique

As Figure 1 (a) shows, the peaks of the amplitude patterns of the two interferometer antennas are purposely mis-aligned in elevation. Figure 1 (b) shows that the ratio of the amplitude of a signal in channel 2 to its amplitude in channel 1 gives a measure of the angle of arrival of the signal. Also note that the log of the ratio is approximately linear.

Ignoring noise and assuming a Gaussian antenna pattern, we can follow the derivation of [4] and arrive at the following equation for the angle estimate:

$$\theta = \frac{R_{dB}(\theta) - \left(P_{2,dB} - P_{1,dB}\right)}{\eta} \qquad (1)$$

where:

θ - is the estimate of the elevation angle

$R_{dB}(\theta)$ - is the beam ratio in dB

$P_{2,dB}$ - is the 2-way peak power of antenna #2

$P_{1,dB}$ - is the 2-way peak power of antenna #1

η - is a scale factor

The scale factor, η, can be shown in this case to be:

$$\eta = -12.04 \cdot \left(\frac{\theta_0}{\theta_B^2}\right) \qquad (2)$$

where:

θ_0 - is angular separation between the two beams

θ_B - is half of the beamwidth of the one-way antenna pattern

Engineering Tradeoffs

Equation (2) indicates that it is desirable to separate the antenna beam pointing as far as possible. It is intuitive that there is a noise penalty paid by both the beam-ratio technique and the IFSAR due to the antenna separation that is not borne out in equation (2). The signal-to-noise (SNR) penalty that the beam-amplitude ratio technique has on the IFSAR height noise can be calculated using equation (22) from [5] and equations (25) and (31) from [6]. Figure 2 shows the IFSAR height noise increase due to the antenna separation for an example system configuration. The calculations in figure 2 are based on a system with a 15-dB SNR at the beam center, a pair of antennas with 15-degree elevation beamwidths, a 1700-m ground swath at a 45-degree incidence angle, and a short range (5 km). Note that at 3 degrees of beam separation there is only a 5 % height noise penalty. This corresponds to an increase of only 0.4 dB in the system noise floor, which is acceptable for many system applications. The 3 degree beam separation gives a separation ratio of 1/5 of the beamwidth. An offset of around 1/4 to 1/5 the beamwidth provides a good compromise between ratio sensitivity and system height noise.

The fact that the antennas are not aligned also leads to a reduction in the 3-dB beamwidth measured from the full two-antenna SNR. This is an important consideration when optimizing the design of an interferometer. Figure 3 shows the reduction of system beamwidth with beam separation for the case described above. Again, the penalty is small for a separation ratio of 1/5, and quickly becomes unacceptable as the separation approaches 1/2.

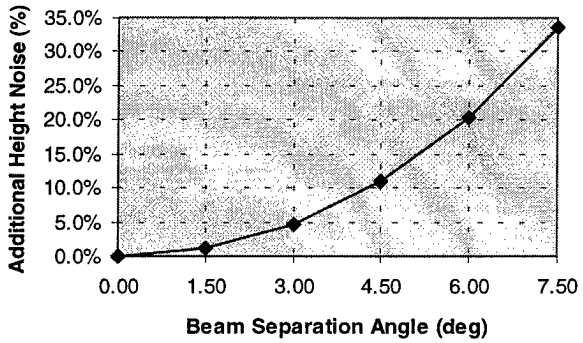


Figure 2: Additional Height Noise due to SNR Reduction from Beam Separation

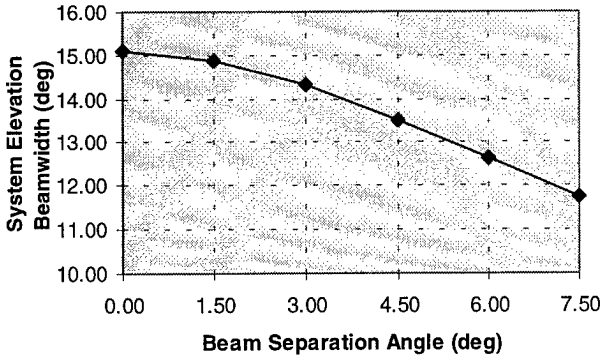


Figure 3: Reduction of System Beamwidth from Beam Separation

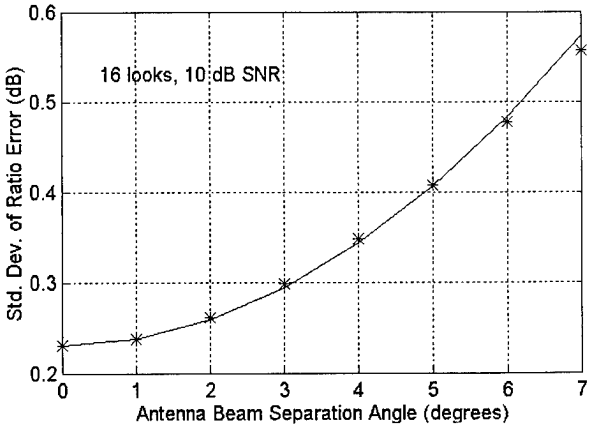


Figure 4: Effect of Beam Separation on Beam Ratio

Performance Analysis

Increasing the beam separation angle also increases the noise for "coarse" angle estimate from the beam-ratio. Simulations were run for the case of a Gaussian antenna pattern with a 3° beam separation and a 15° elevation beamwidth. Figure 3 shows the effect of SNR and the effect of number of looks on the error in the estimate of the beam ratio, $R_{dB}(\theta)$. Figure 4 shows the effect that the antenna beam separation angle has on the error in the beam ratio.

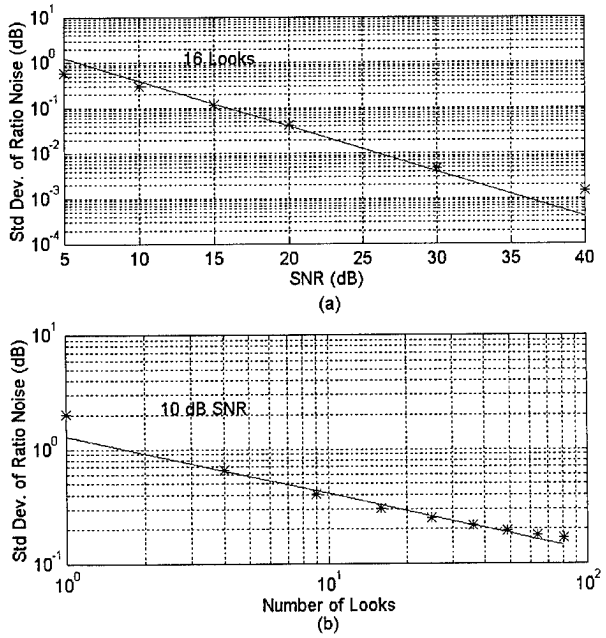


Figure 3: Effect of SNR and Number of Looks on Beam Ratio

The error in the angle estimate is found by dividing by the scale factor, η. The system design is based upon keeping the standard deviation of the angle error well below half of the IFSAR ambiguity angle. This is accomplished by a trade-off of number of looks, sufficient beam separation and height noise.

CALIBRATION

In order to determine the absolute ambiguity angle, we must be able to sufficiently calibrate the relative power between the two channels. Calibration error introduces an error into the term $\left(P_{2,dB} - P_{1,dB}\right)$ in equation (1). The accuracy with which we can calibrate the relative channel power influences how we set the scale factor; hence, ultimately how we set the antenna separation. This is a potentially more important influence on the choice of antenna separation than is the SNR consideration because we can always increase the number of looks in the SNR case.

EXAMPLES

In this section we give a couple of examples of applications of the beam-amplitude ratio technique. The first is an example from the Four Hills area southeast of Albuquerque, New Mexico. The second example is of the Washington Monument in Washington D. C.

Absolute Phase Determination

The Four Hills formation is a small range of mountains with terrain height changes sufficient to require an absolute-phase technique. For this example, the beam ratio was calculated for adjacent patches of the mountain terrain at a point where the number of ambiguities should have changed. Figure 5 shows that the third patch (aperture 26) has an ambiguity relative to the second patch (aperture 25) at the center of the scene (range bin number 1024). In Figure 6, the beam ratios for each patch are plotted versus the estimated angles from the respective unwrapped phases.

The patch with the ambiguity is shifted by an integer multiple of the ambiguity angle. From this figure we can see that the best fit is when the second patch is shifted by one ambiguity with respect to the first patch.

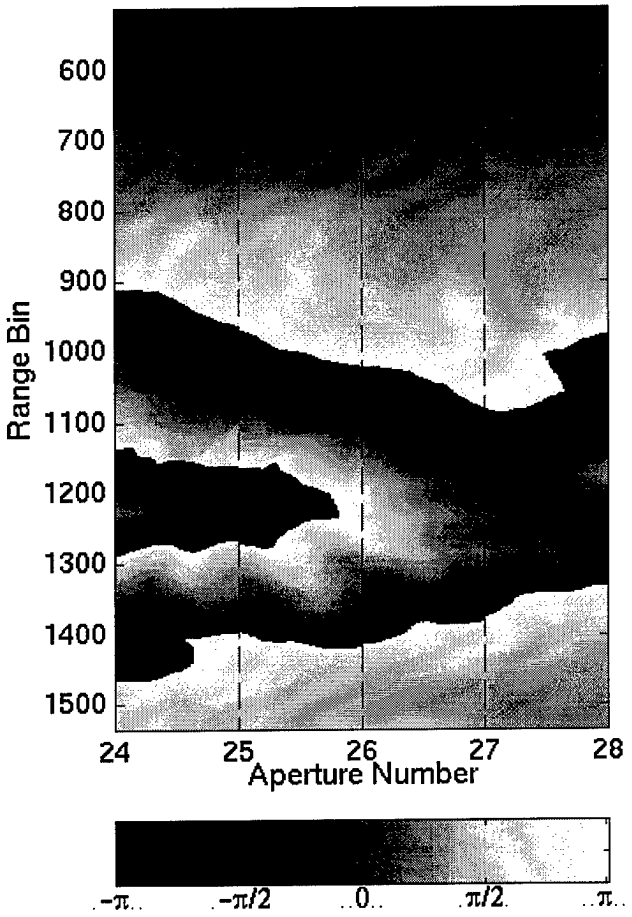


Figure 5: Phase Image showing 2π Ambiguity Change at Center Range Bin

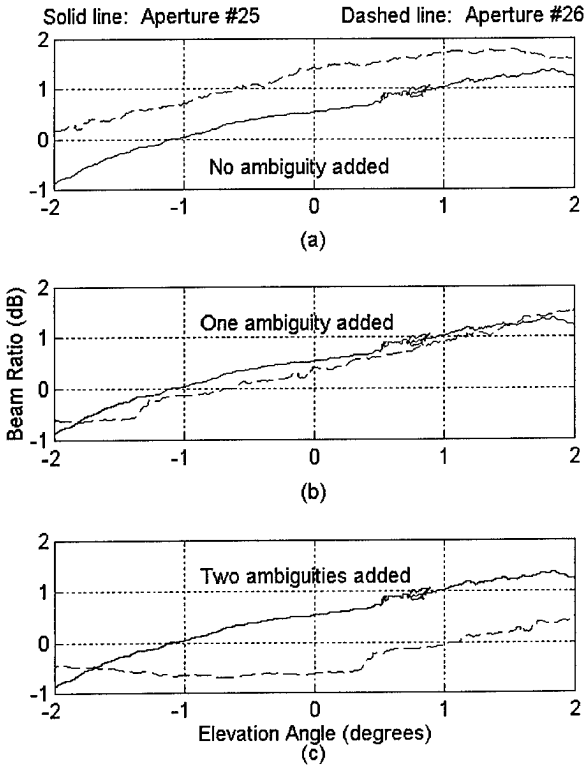


Figure 6: Example of beam-ratio for Mountain Terrain

Detection of Phase Unwrapping Error

The Washington Monument is an example of an entirely different application of the beam-ratio -- identifying a specific area within a scene that cannot be unwrapped using traditional path-following techniques. The beam-ratio technique can also be used for this more difficult and general problem if SNR and calibration issues are adequately addressed. Figure 7 illustrates this use of the technique.

Figure 7 (a) shows the height of the top of the Washington Monument estimated directly from the unwrapped phase difference. Because the top of the monument is less than π radians below the surrounding terrain in the phase image, there is no indication that a wrap has occurred. Figure 7 (b) shows the beam-ratio computed for the same scene, scaled as a number of 2-π ambiguities. In the Monument area, the ratio value shows that 1.75 ambiguities must be added back. The indicated value must be rounded, giving an actual phase to be added of 2•2π. Figure 7 (c) shows the estimated Monument height after the 4π phase ambiguity has been added. The measured value is about 520 feet, while the actual height is 555 feet from the base to the top.

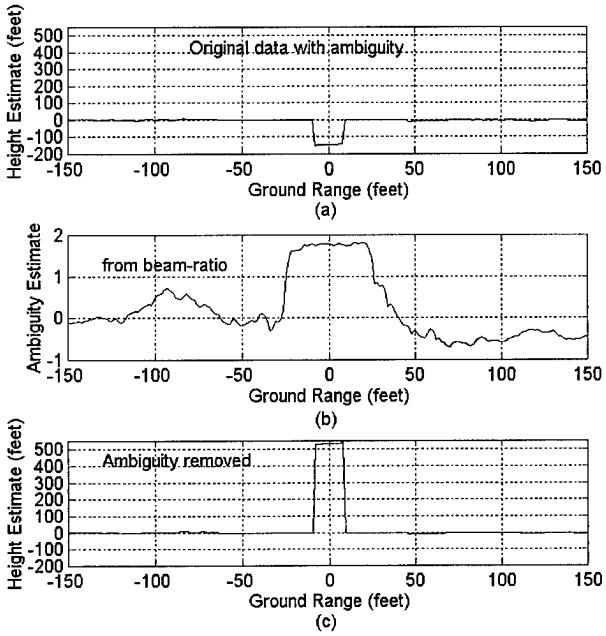


Figure 7: Use of the Beam-Ratio for Detecting Phase Unwrapping Error

CONCLUSIONS

The theory and examples show that the beam-amplitude ratio technique can be used as a method for determining the absolute ambiguity angle; hence, the absolute phase of the IFSAR system. The overall height noise penalty paid can be kept small. The key to successful ambiguity determination is the ability to measure and control the relative calibration between the two channels of the IFSAR system. The technique does not require the additional image formation processing of the multi-frequency approach or the extra hardware of the multi-baseline approach, and it avoids the computation-intensive correlation required for using range stereo.

In the case of a well-calibrated system with high SNR, the beam-ratio can also be used either to eliminate or seed the phase-unwrapping process. This will lead to much more robust system performance in areas with rapidly changing terrain.

ACKNOWLEDGMENTS

The beam-ratio technique is being developed for the Airborne Multi-sensor Pod System (AMPS) SAR for the Department of Energy. The authors wish to thank both the AMPS management and design staff for their assistance.

The examples in this paper were produced using an experimental capability on Sandia Laboratories' Twin Otter IFSAR. Thanks go to the flight test crew and the system developers for their assistance, and for answering all those questions!

This work was supported by the United States Department of Energy under Contract DE-AC04-94AL85000.

REFERENCES

[1] S. N. Madsen, "On absolute phase determination techniques in SAR interferometry", *Proceedings of the SPIE*, Orlando, Florida., 19-21 April, 1995, Vol. 2487, pp. 393-401.

[2] W. G. Carrara, R. S. Goodman, R. M. Majewski, section 9.3.5 of *Spotlight Synthetic Aperture Radar*, Artech House, 1995.

[3] C. V. Jakowatz, D. E. Wahl, and P. A. Thompson, "Ambiguity Resolution in SAR Interferometry by Use of Three Phase Centers", *Proceedings of S.P.I.E Aerosense Conference*, 8-12 April, 1996, Orlando, Florida.

[4] L. G. Bullock, G. R. Oeh, and J. J. Sparagna, "An Analysis of Wide-Band Microwave Monopulse Direction-Finding Techniques", *IEEE Trans. on Aerospace and Electronic Systems*, Vol. AES-7, No. 1, Jan., 1977, pp. 188-202.

[5] D. Just and R. Bamler, "Phase statistics of interferograms with applications to synthetic aperture radar", *Applied Optics*, Vol 33, No. 20, July 10, 1994, pp. 4361-4368.

[6] E. Rodriguez and J. M. Martin, "Theory and design of interferometric synthetic aperture radars", *IEE Proceedings-F*, Vol. 139, No. 2, April, 1992, pp. 147-159.

Multisource Data Integration with Neural Networks: Optimal Selection of Net Variables for Lithologic Classification.

Grace Yang
Department of Geology and Geophysics
University of Calgary
Calgary, AB, Canada T2N 1N4

Michael J. Collins
Department of Geomatics Engineering
University of Calgary
Calgary, AB, Canada T2N 1N4

Peng Gong
Department of Environmental Science, Policy and Management
University of California
Berkeley, CA, USA 94720-3114

ABSTRACT

Different types of images generated from gravity, magnetic, gamma ray spectrometry and remote sensing images such as Landsat Thematic Mapper, radar and SPOT are available in Melville Peninsula, N.W.T. to delineate geological patterns as an aid to geological field mapping in Arctic regions in Canada. Feedforward neural networks were trained to formulate mapping classifiers to predict the lithologic units.

Through the analysis of classification accuracy with increased number of iterations, we demonstrated that the optimal choice of input layers is the most sensitive factor in achieving better accuracy result. The classification accuracy may be maximized by choosing an optimal combination of input data layers. The complexity of the training task which includes the selection of the training samples, the number of training samples, are critical for a satisfactory classification. The classification accuracy is inversely proportional to the number of output classes. The overall average accuracy of classification gets better by increasing the number of iterations to a certain degree, however, at the expense of some individual classification accuracy.

The variance in the individual classification accuracy were found to be significant which has lead to some criterion on the selection of net variables. For lithologic mapping, the network should be structured in accordance with the importance of each individual class.

INTRODUCTION

Geologic lithology mapping traditionally is compiled based on field survey data. It is time-consuming and requires a great deal of manpower. In many remote areas, the lithology maps have not been completed. Efforts have, therefore, been made to aid the geological field mapping in Arctic regions in Canada. Although a relatively high accuracy of classification using neural network technique has been reported in some research work [1,2], the detailed operations of the neural network are not well understood in the classification application using multi-source data. One phenomenon often noted in applying neural networks to classification is large variations in the classification accuracy of individual classes. Questions such as which parameter or parameters are primarily responsible for these differences in accuracy (for example: learning rate, momentum rate, the number of hidden units, the number of training iterations, network stability achieved, and the input data sets) remain unanswered in the application of neural networks to the classification of multi-source data [1,3] In this paper, what we will present are the experimental results of feedforward back-propagation neural network approach to select optimal variables in lithological classification when multisource data are available.

MULTISOURCE DATA

The data set used in the study is part of a Digital Data Atlas in the Hall Lake Area, Melville Peninsula, Northwest Territories [4]. The images contain 512 x 512 pixels. They were provided and processed by the Geological Survey of Canada (GSC) and recorded in a digital format. They include seven channels of Landsat Thematic Mapper (TM), one channel of synthetic aperture radar (SAR), one channel of SPOT and different types of images generated from gravity, magnetic, and gamma ray spectrometry. The geologic outcrop map was provided by GSC and used as base map for training the network.

EXPERIMENTAL DESIGN

Several experiments are designed to gain insight into the network operation to examine the multiple dependencies of the accuracy on training parameters and net variables. All experiments carried out in these study are based on the following concerned parameters:

1. the number of layers in the network (or the number of hidden layers),

0-7803-3068-4/96$5.00©1996 IEEE

2. the number of input nodes which usually equals to the number of input data sets (or input channels,
3. the number of output nodes which usually equals to the number of classes to be classified,
4. the number of nodes in the hidden layer,
5. the size of the training samples,
6. the iteration number, and
7. the training coefficients such as momentum factor, and the learning rate.

In all the experiments, only three layers (i.e. a single hidden layer) were used.

The variables used in each experiment and their purpose are shown in table 1. In geological mapping, each rock unit (or class) represents meaningful information about the depositional environment. Even with a small population one particular class may be more important than others if it is an indicator of certain mineral deposits. Therefore more emphasis will be placed on the classification accuracy of the individual classes. The process of classification (i.e. with increase of iteration number) is also what we will focus on.

By changing the variables in each experiment, the accuracy results were obtained and compared.

RESULTS

Effect of selection of input data set: The experiments are conducted by changing the combination of input data set. The other parameters are fixed (momentum factor = 09., the learning rate = 0.01, and the number of hidden nodes is 30). We found that the number of input data layers is not the factor that produces higher classification accuracy. In fact, indiscriminately increasing the number of input data sets may produce less accurate results. More relevant input data is the key to aid the improvement in classification accuracy. The input data sets should contain information relevant to the rock lithology to significantly affect the classification accuracy.

Effect of number of output classes: To show how the number of output classes affects the accuracy results, the only variable of the network is the number of the output classes. We found that, in general, the average and overall classification accuracy decreases as the number of output classes increases. However it is not true for each individual class.

Effect of selection of training samples: In these experiments the only variable is the selection or the number (size) of training samples. The results show that the average and overall accuracy tend to get better with larger training samples. However, the accuracy of each individual class does not behave in the same fashion. That is the larger number of training samples does not guarantee a better individual classification accuracy.

Effect of number of hidden nodes: Two sets of variables were used in these experiments, the input data sets and the number of hidden nodes. We found that the optimal number of hidden nodes is dependent on the input data layers and the classification accuracy has a larger variation among various numbers of hidden nodes for the network with 15 input channels than the network with 10 channels (also true for 7 channels).

Effect of momentum factor and learning rate: These experiments indicated that the learning rate has similar performance as the momentum factor: the larger the learning rate, or the larger the momentum rate, the faster the network reaches its maximum classification accuracy. The variation among the various momentum rates is about 1least variation among all the experiments. The momentum rate affects the learning speed and the convergence rate. As the momentum factor increases, the number of iterations necessary to be less than the fixed error decreases. The relationship between the momentum factor and the iteration is approximately linear. The effect of learning rate is to change the slope but not the intercept.

CONCLUSION

From the experiments shown above, we reach the following conclusions:

1. The selection of input data sets has a significant effect on classification accuracy. The classification results are sensitive to the choice of input channels.
2. The classification accuracy is inversely proportional to the number of output classes.
3. The overall average accuracy of classification gets better by increasing the number of iterations to a certain degree, however, at the expense of some individual classification accuracy.
4. For lithologic classification, the network should be structured in accordance with the importance of each individual class.

ACKNOWLEDGEMENTS

We would like to acknowledge Dr. C.F. Chung from the Geological Survey of Canada for providing the data. Dr. P. Gong of the University of California at Berkeley provided valuable support and guidance in the initial stages of this study.

REFERENCES

[1] An, P. and Chang-Jo. F. Chung. 1994. Neural Network Approach for Geological Mapping: Technical Background and Case Study. *Canadian Journal of Remote Sensing*, Vol. 20, No. 3. pp. 293–301.

[2] Gong, P. Integrated Analysis of Spatial Data from Multiple Sources: using Evidential Reasoning and Artificial Neural Network Techniques for Geological Mapping. *Photogrammetric Engineering and Remote Sensing* (in press).

[3] Peddle, D.R., G.M. Foody, A. Zhang, S.E. Franklin, E.F. LeDrew. 1994. Multi-source Image Classification II: An Empirical comparison of Evidential Reasoning and Neural Network Approaches. *Canadian Journal. of Remote Sensing*, Vol. 20, No. 4, pp. 396-407.

[4] Schau, M., A.Rencz, L. Dredge, C.F. Chung and L. Chorlton 1993. Digital Data Atlas, Hall Lake Area, Melville Peninsula, Northwest Territories. Geological Survey of Canada, Open File 2786.

A Completely Fuzzy Classification Chain for Multispectral Remote Sensing Images

Paolo Gamba(*), Andrea Marazzi(*), Alessandro Mecocci(†) and Pietro Savazzi(*)
(*)Dipartimento di Elettronica, Università di Pavia, Via Ferrata, 1, I-27100 Pavia
Tel: +39-382-505923 Fax: +39-382-422583 E-mail: gamba@ipvmw2.unipv.it
(†)Facoltà di Ingegneria, Università di Siena, Via Roma, 77, I-53100, Siena

Abstract – In this work a new classification algorithm that uses FNP mixed with a pyramidal approach is proposed. The prototypes of each class are generated by means of FCM with a FNP initialization. The aim of the work is to improve the performances of the usual non parametric classifiers by extracting the maximum information from the training pixels and from the pixels to be classified. This is done by using both the high spatial-correlation between pixels and the confidence levels, given by the fuzzy algorithm. Results are presented that show the improvement obtained by applying the proposed method to multispectral image classification.

1. INTRODUCTION

The unsupervised classification of remote sensing images is a necessary procedure [1] in a world where huge amounts of data are continously obtained from earth monitoring sources (and satellite and airborne thematic mappers are only a part of them). And this fact is even more important, if we consider that only 10% of these data [2] is normally studied and classified.

In recent years many fuzzy algorithms for remote sensing image classification have been introduced [3], aiming to exploit fuzzy concepts to achieve a reliable recognition of different patterns in single or multispectral data ([4]-[6]) or for texture classification [7]. They have been introduced in many steps of the data interpretation procedure, from the the formation of prototypes and their confidence region for multidimensional data [8] to the learning algorithms for image recognition [9]. As for data classification, non parametric fuzzy algorithms have been proposed, like the Fuzzy K-Nearest Neighbours (FKNN) and the Fuzzy Nearest Prototype (FNP) methods [10], as well as clustering algorithms such as the Fuzzy C-Means (FCM) ([11]-[13]).

However, a lot of theoretical study has to be done to improve classification procedures that do not exploit enough the characteristics of remote sensing data. In particular, we must point out that none of the classification methods introduced and even succesfully applied in the above presented applications exploits the spatial correlation among neighbouring pixels, since they only focus on their spectral features.

In this paper we present a classification chain that uses FNP in a pyramidal environment followed by a new technique, the Fuzzy Spatial Nearest Neighbours (FSNN), that further improves the classification performance by considering the spatial neighbouring pixels and their characteristics. It enables a better discrimination among elements of spectrally similar classes, based on their spatial correlation.

Improvements has been obtained also in the class prototypes definition, where we achieved more reliable data by feeding the standard Fuzzy C-Means algorithm with the output of a previous Fuzzy Nearest Prototype step. The choice to rely on a FCM and FNP definition chain has proved to be very useful for a winning definition of the classification prototypes. In fact, the FCM output can be entered directly as prototypes for the successive steps of the classification procedure only if the training pixels form well distinguishable clusters in the features space. Therefore we applied the FNP procedure to the training pixels, assuming as starting points the average values. To avoid biasing effects, the maximum number of elements of each class has been defined, retaining only those with the highest relative membership.

The experimental results stress the advantages obtained by using, in all the classification steps, both the high spatial-correlation between pixels and the confidence levels given by the fuzzy algorithms. The procedure has been applied to 8-bands digital multispectral images, acquired by an Airborne Terrain Mapping (ATM) sensor.

2. THEORY

Given a set S, a fuzzy set [14] is characterized by a membership function or degree that associates to each element a real number between 0 (non-membership) and 1 (total membership). By considering the image pixels as belonging to fuzzy sets, each related to one of the classes that we want to classify, it is possible to take into account the intrinsic inexactness in the measures whose value define the pixel grey level. Usually, this process is called as featuring

0-7803-3068-4/96$5.00©1996 IEEE

a "fuzzy partition". Starting from a set of n multidimensional data x_k, that we want to subdivide in c classes, we aim to generate a fuzzy partition matrix $U = u_{ik}$ whose generic element u_{ik} represents the fuzzy membership degree of x_k related to the i-th class ($i = 1, \ldots, c$).

2.1. Pyramidal Fuzzy Nearest Prototype algorithm

To exploit the advantages of fuzzy techniques in a pyramidal environment [15], it was implemented a classification system based on the following processing steps:

1. the classification, by means of a comparison between precompiled land thematic maps and the multispectral image, of a part of the pixels (about 25%) whose 30% is used to train the classifier (training sets), and the remaining 70% to verify the results obtained (true sets);

2. the evaluation of the prototypes by means of both the FNP and FCM algorithms;

3. a pyramidal classification using the FNP technique and the creation of a thematic map;

4. the comparison of this map with true sets and the evaluation of the confusion matrices.

The choice of the joined application of the two fuzzy techniques introduced in step 2 relies on the fact that the FCM algorithm produces good class prototypes only if the training pixels are separated enough in the multidimensional feature space and if there is not too much difference in the number of the training elements of the classes. Therefore, it is necessary to define a choice criteria for the more representative training elements of each class. To reach this goal we applied the FNP procedure to the training pixels, but only after initializing it with the average values of the same pixels. To avoid biasing effects, it has been defined a maximum number of points for each class, by selecting those having the higher relative membership, and also greater than a given threshold. The pyramidal classification procedure is based on a 4 levels. To exploit the properties of a pyramidal classification procedure, it is necessary to have some suitable homogeneity criteria to decide if the square block of pixels of the considered pyramidal level we are interested in is entirely constituted by pixels with the same characteristics. To grant the homogeneity, the fuzzy classification algorithm has been defuzzyfied according to a threshold value: for each classified element the class with maximum fuzzy membership value is retrieved, and, if the value obtained is greater than a threshold chosen by the operator, the pixels in that block are considered as homogeneous and belonging to the environment characterized.

2.2. Fuzzy Spatial Nearest Neighbours (FSNN) algorithm

The FSNN starts from a partially classified image (i.e. a crisp set) or from a partial fuzzy partition of it. Let $x_k = (x_{k1}, x_{k2}, \ldots, x_{kp})$ be an unclassified pixel, in a p-dimensional feature space. We consider its L spatial nearest neighbors y_j

For each image element x, the FSNN computes the new fuzzy membership $u_i(x)$ to class i, according to the following formula

$$u_i(x_k) = \frac{\sum_{j=1}^{L} u_{ij} \left(\frac{1}{d(x_k, y_j)}\right)^{\frac{2}{(m-1)}}}{\sum_{j=1}^{L} \left(\frac{1}{d(x_k, y_j)}\right)^{\frac{2}{(m-1)}}} \qquad (1)$$

where u_{ij} is the fuzzy membership of y_j to the i-th class, $d(x_k, y_j)$ is the spectral distance between x_k and y_j, and m is a parameter that evaluates the degree of influence of the spatial proximity with respect to spectral distance. If, for some j, $d(x_k, y_j) = 0$, then $u_i(x_k) = u_{ij}$ $\forall i$ The spatial-neighbors approach produces a fuzzy membership that takes into account both the number of Spatial Nearest Neighbors occurrences of the pixels of a given class and their spectral resemblance. This choice allows to avoid false classification in the case of a pixel surrounded by a lot of spectrally different neighbors (like a terrain pixel surrounded by sea ones).

3. EXPERIMENTAL RESULTS

The proposed procedure has been applied to the classification of a multispectral (8 bands) image of the Orbetello lagoon. The resolution of each pixel is about 100 square meters. The classification obtained considers 11 different typologies, chosen by a comparison between the examined image and a regional thematic map, at a 1:25000 scale, relative to the Orbetello lagoon and part of the Monte Argentario. The performance of the fuzzy pyramidal classifier presented in this paper has been compared with the results of a bayesian classifier, using as prototypes of the classes the average values of the training elements. Tables 1 represents the correct classification percentages relative to the different classes, given by the two classifiers. The 10 selected class are: 1-copse wood, 2-conifers, 3-lagoon, 4-pasture, 5-sea, 6-roads, 7-urban ground, 8-beach, 9-orchard, 10-dry simple sowbelly.

4. CONCLUSIONS

We observe from Table 1 that our procedure performs better than the bayesian classifier in almost each class, and surely in the global correct classification percentage (98.46 vs. 92.48). Classes 6 and 7 apparently present a

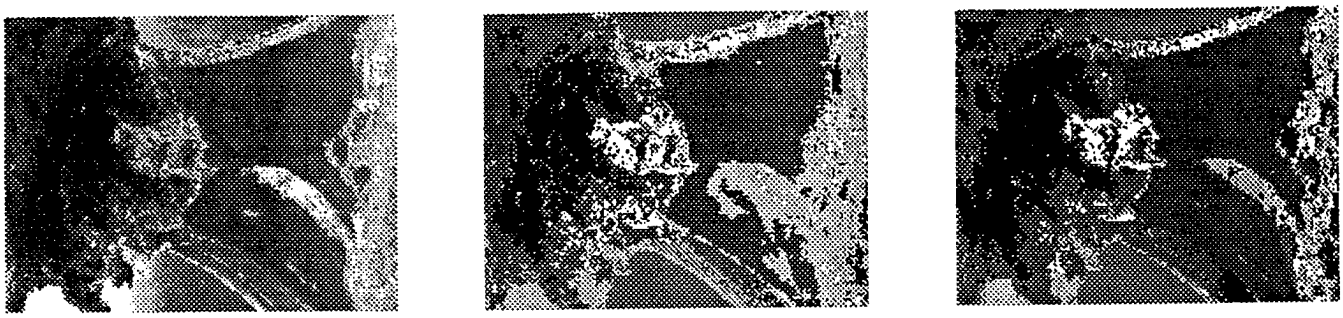


Figure 1: The Orbetello lagoon. From the left: the first band of the original image; the results of the bayesian classifier; our results.

Table 1: Classification percentages

Class	Bayesian	Fuzzy chain
1	88.5%	98.2%
2	69.8%	96.3%
3	93.2%	99.8%
4	59.6%	85.1%
5	98.7%	99.9%
6	85.6%	55.7%
7	98.4%	80.3%
8	77.2%	80.6%
9	97.9%	97.9%
10	66.5%	80.8%

worse classification, but this is due to a scarce mapping accuracy: in fact, the bayesian classifier assigns a greater number of pixels to these classes, but its map (as can be easily seen in fig. 1) is caharacterized by big errors. The problem is related to the estimate of the *a priori* probablities of each class, that is very difficult to achieve. With our approach, instead, the information carried by each pixel of the multispectral image is exploited, as well as its spectral and spatial neighbourhood's properties.

REFERENCES

[1] R.O. Duda and P.E. Hart, *Pattern classification and scene analysis*, Wiley Interscience, New York, 1973.

[2] J.G. Fabos, *Planning the total landscape: a guide to intelligent land use*, Boulder, CO, Westview Press Inc., 1979.

[3] J.C. Bezdek, *Pattern recognition with fuzzy objective function algorithm*, Plenum Press, New York, 1981.

[4] F.C. Hadipriono, J.G. Lyon, and T. Li W.H., "Expert opinion in satellite data interpretation", *Photogrammetric Eng. and Remote Sensing*, Vol.57, no. 1, pp. 75-78, Jan 1991.

[5] F. Wang, "Fuzzy supervised classification of remote sensing images", *IEEE Trans. on Geosci. Remote Sensing*, Vol.28, no. 2, pp. 194-201, March 1990.

[6] F. Wang, "Improving remote sensing image analysis through fuzzy information representation", *Photogrammetric Eng. and Remote Sensing*, Vol.56, no. 8, pp. 1163-1169, Aug. 1990.

[7] P. Kundu and B.B. Chaudhuri, "Fuzzy geometric feature-based texture classification", *Pattern Recognition Letters*, Vol.14, no. 10, pp. 825-832, Oct. 1993.

[8] W. Pedrycz, "Formation of prototypes and their confidence regions in classification and concept formation problems", *Pattern Recognition Letters*, Vol.12, no. 12, pp. 739-746., Dec. 1991.

[9] P. Pellegretti, F. Roli, S.B. Serpico, and G. Vernazza, "Supervised learning of descriptions for image recognition purposes", *IEEE Trans. on Pattern Anal. and Machine Intell.*, Vol.PAMI-16, no. 1, pp. 92-98, Jan. 1994.

[10] J.M. Keller, M.R. Gray and J.A. Givens jr., "A fuzzy K-nearest Neighbor algorithm", *IEEE Trans. Syst., Man, Cybern.*, Vol. SMC-15, No. 4, pp. 580-585, July/Aug. 1985.

[11] I. Gitman and M.D. Levine, "A fuzzy relative of the ISODATA process and its use in detecting compact well-separated clusters", *Journ. Cybernetics*, 1973.

[12] R.N. Dave, "Characterization and detection of noise in clustering", *Pattern Recognition Letters*, Vol.12, no. 11, pp. 657-664, Nov. 1991.

[13] J.C. Bezdek and P.F. Castelaz, "Prototype classification and feature selection with fuzzy sets", *IEEE Trans. on Syst., Man., Cybern.*, Vol. SMC-7,No. 2, pp. 87-92, Feb. 1977.

[14] L.A. Zadeh, "Fuzzy sets", *Inform. Control*, 1965.

[15] M.M. Trivedi and J.C. Bezdek , "Low level segmentation of aerial images with fuzzy clustering", *IEEE Trans. on Syst., Man., Cybern.*, Vol. SMC-16, No. 4, pp. 589-598, Apr. 1986.

A raster-based fuzzy expert system for forestry evolution

D. Saint-Joan and J. Desachy
IRIT -UPS, 118 route de Narbonne - 31062 Toulouse - France
Tel:(+33) 61 55 69 28 Fax:(+33) 61 55 62 58 - E-mail: stjoan@irit.fr

Abstract *GIS users are increasingly turning to decision spatial systems to assist them solving complex spatial problems which are not simply maps overlay. So, we have implemented the GEODES (GEOgraphic Decision Expert System) system that allows users to specify easily symbolic knowledge of a problem through a graphic user interface by using, on the one hand, data and knowledge spatial characteristics and, on the other hand, fuzzy knowledge. This problem specification and geographic data are used by the system to provide a problem solution map showing favorable and less favorable areas. GEODES can be used in many domains as geographic, ecology, agriculture, natural resources management, manufacturing ... It is a fuzzy expert system using raster data and managing principally several types of rules based on knowledge and data intersection and union. The inference engine uses fuzzy inferences with fuzzy sets trapezoïdal representations to decrease computional cost. There is a particular type of rule named gradual rule. Their structure is "If (More/Less) X is A Then (More/Less) Y is B". This rule can specify particular geographic knowledge as "more the altitude is low then more the forest can grow". We have implemented the system GEODES to modelise the evolution of the forest in a region of the south of France by using several maps. We have used spot maps and several data to obtain the forest map, the DEM and a map of fire frequency with reports of the agriculture ministry. By using these maps, we have made some experimentations with GEODES to modelise the forest evolution.*

INTRODUCTION

To improve GIS applications some new techniques appear and particularly expert system techniques [3]. However, current GIS applications are predominantly based on Boolean logic, a rigid two-valued mathematical system which gives no room for imprecision and uncertainty in information. Most systems use a cartographic algebra like maps overlay [1]. To improve such systems, we have developed the GEODES system. It is a fuzzy expert system using several kinds of rules and especially gradual rules which manage the concept of "graduality" of knowledge characterizing straight relations between gradual data in a rule.

0-7803-3068-4/96$5.00©1996 IEEE

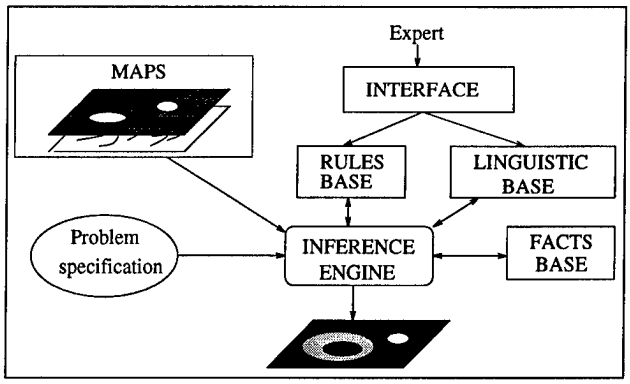


Figure 1: Architecture of the system.

SYSTEM ARCHITECTURE

Our system consists of three subsystems (figure 1):

- A geographic data subsystem for acquiring, modifying and displaying the raster maps.
- A knowledge acquisition subsystem for acquiring knowledge in the rules base and the linguistic base through an interface with a formal language using key words.
- An inference subsystem for computing the resulting map by using all the bases and the fuzzy inference engine.

KNOWLEDGE BASES

Fuzzy sets

The approach we suggest is based upon idea of fuzzy subsets introduced by Zadeh [5]. A fuzzy set in U or, equivalently a fuzzy subset of U, is characterized by a membership function $\mu_A : U \rightarrow [0,1]$ which associates for each element u of U a number $\mu_A(u)$ in the interval [0,1] ($\mu_A(u)$ represents the grade of membership of u in A). In our system, each membership function is represented by a trapezoïdal function with five parameters $A = (a, b, c, d, e)$ corresponding to the weighted interval in the figure 2 (e represents the uncertainty). In the figure 2, $\mu_A(x) = 0.6$ implies the element x does not characterize totally the linguistic expression represented by the fuzzy set A but with a degree of membership equals to 0.6.

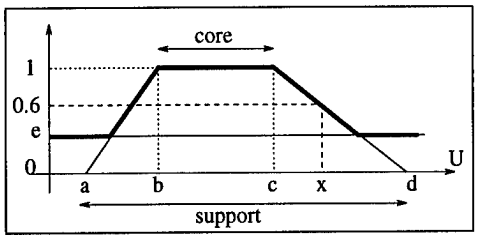


Figure 2: Definition of a fuzzy set.

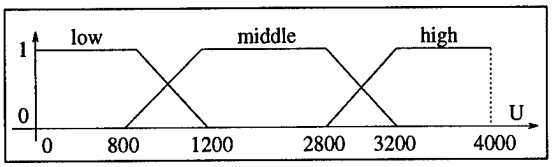


Figure 3: Definition of the linguistic variable Altitude.

Linguistic base

The linguistic base contains the description of each linguistic variable and their linguistic terms used in the production rules and the description of the universe on which they are defined. For example, the linguistic variable "Altitude" is defined in meters from 0 to 4000 and can take three linguistic terms: low, middle and high. Each linguistic terms is represented by a fuzzy set (figure 3).

Rules base

The rules base contains the expert knowledge in the form of production rules defined as :

IF <operator>
[More/Less]<Variable 1> is <Linguistic Term>
...
[More/Less]<Variable n> is <Linguistic Term>
THEN
[More/Less]<Variable> is <Linguistic Term>

We have defined three rule operators:
- *AND* : all the premises must be satisfied
- *OR* : just one premise must be satisfied
- *AVG* : the premises must be partly satisfied

The key word "More" and "Less" define gradual rules that represent the most general rule when two data are closely connected (so it is not necessary to provide all the possible rules). The expert has just to provide a gradual rule with judicious linguistic variables and terms with the two key words "More" and "Less".

Example: Generally the temperature decrease when the altitude increase. A gradual rule can formalize the relation "More the altitude is high then More the temperature is low".

INFERENCE ENGINE

Generalised modus ponens

In Boolean logic, with the rule "If X is A Then Y is B", the proposition X is A has to be observed to consider the proposition Y is B. In fuzzy logic, a proposition X is A' quite different of the rule premise X is A can be observed to provide a conclusion Y is B' quite different of the rule conclusion Y is B [2]. A simple fuzzy inference can be represented in a schematic form as:

Rule : IF X is A THEN Y is B
Fact : X is A'
Conclusion : Y is B'

The generalised modus ponens is based on the fuzzy implication of Brouwer-Gödel [2] which is implemented by a fast algorithm to reduce the computing time because the geographical data are 512×512 pixels maps. This rapid algorithm uses geometric properties of the supports and the cores of the fuzzy sets [4] (see figure 2). The generalised modus ponens is expressed with the following formula:

$$\forall u \in U,\ \forall v \in V \quad \mu_R(u,v) = \begin{cases} 1 \text{ if } \mu_A(u) \leq \mu_B(v) \\ \mu_B(v) \text{ otherwise} \end{cases}$$
$$\mu_{B'}(v) = \sup_{u \in U} \min(\mu_{A'}(u), \mu_R(u,v))$$

Gradual rule inference

The mechanism of our system consists to create the best rule with linguistic approximations among linguistic values of the linguistic variables of the rule. Assume A_1, A_2, A_3 (resp. B_1, B_2, B_3) three fuzzy sets representing the linguistic values of the linguistic variable X (resp. Y) in the universe U (resp. V). Assume the rule IF *more* X is A_1 THEN *less* Y is B_3 and the evidence X is A'. The mechanism is the following (figure 4):

- do the linguistic approximation of A' in U :A_3
- compute a fuzzy distance D between A_1 and A':
- add D or subtract D to B_3 to obtain a new fuzzy sets B_{dist}.
- do the linguistic approximation of B_{dist} in V:B_1
- apply the generalised modus ponens with the rule IF X is A_3 THEN Y is B_1 and the fact X is A'.

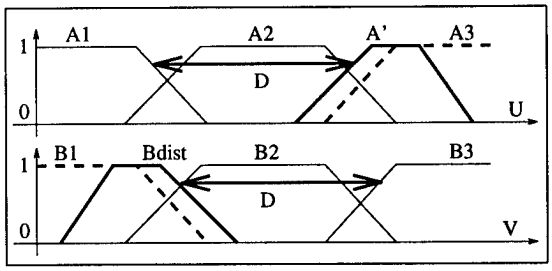
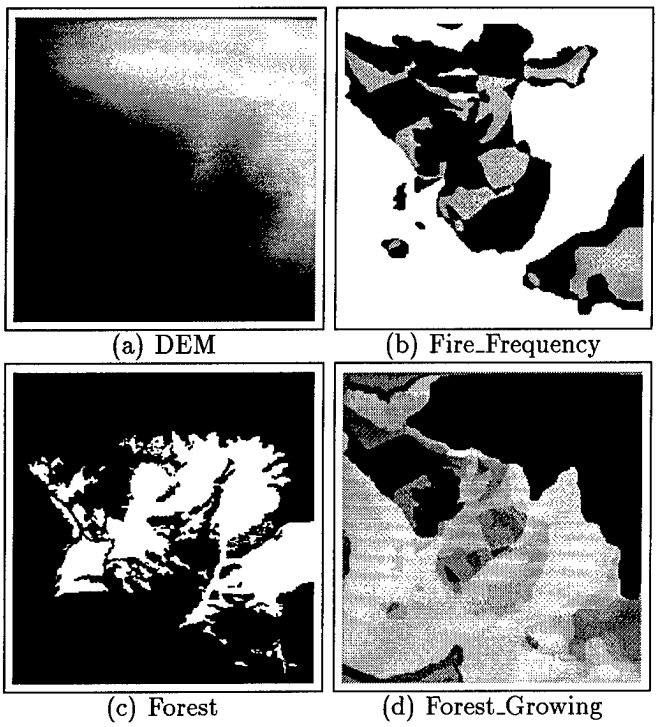


Figure 4: Principle of gradual rule inference.



(a) DEM (b) Fire_Frequency

(c) Forest (d) Forest_Growing

Figure 5: Data maps and result map.

EXPERIMENTAL RESULTS

Geographic data

The studied area is the "Soulane" in the Ariege mountains in the south of France. We have used only 3 maps :

- The DEM(figure 5(a)),
- A map of frequency of forest fires established with forest fire reports of the agriculture state department (figure 5(c)). This frequency is coded in 5 frequencies (from 0 to 4),
- The forest map obtained from a classification of a sequence of aerial photographies (figure 5(c)).

Expert knowledge

After different interviews with an expert, we have extracted the following knowledge to determine the best favorable areas for a forest evolution and more precisely for a forest extension:

- If the forest is in a frequently burnt areas, then there is no chance for an extension of the forest,
- Near the forest, there is a chance for an extension if the forest dynamic is big,
- The forest cannot grow above 1700 meters.

The figure 5(d) shows the final potentiality map (bright zones indicate areas where the forest can grow).

Production rules

The following rules represent the expert knowledge:

IF OR
  Distance (Fire_Frequency = 4) is little
  Distance (Fire_Frequency = 3) is very little
THEN Dynamic is big

IF OR
  Fire_Frequency = 2
  Fire_Frequency = 1
THEN Dynamic is middle

IF Fire_Frequency = 0
THEN Dynamic is little

IF MOY
  More Dynamic is big
  More Distance Forest is little
THEN More Forest_Growing is big

IF Altitude >1700
THEN Forest_Growing is impossible

CONCLUSION

The importance of fuzzy logic in the design of intelligent GIS is demonstrated in this paper. At the opposite of maps algebra systems based on Boolean logic, this system manages imprecise and uncertain information in an efficient manner:

- the fuzzy reasoning allows to solve some problems without critical choice and provides more information about a particular fact because fuzzy sets characterize it precisely.
- the gradual rules increase the solution accuracy.
- the easy specification or modification of a problem allows to an expert or an user to specify and solve any problem by using a formal language.

References

[1] J. K. Berry. Fundamental operation in computer-assisted map analysis. In *International journal of geographical information system*, volume 1, pages 119–136. 1987.

[2] A. Kandel. *Fuzzy expert systems.* CRC press, 1993.

[3] D. J. Maguire, M. F. Goodchild and D. Rhind. *Geographical information systems : Principles and applications*, volume 1. Longman, London, 1994.

[4] D. Saint-Joan and J. Desachy. A fuzzy expert system for geographical problems : An agricultural application. In *FUZZ-IEEE'95, Fourth IEEE International Conference on Fuzzy Systems*, volume 2, pages 469–476, 1995.

[5] L. A. Zadeh. Fuzzy sets. In Didier Dubois, Henri Prade and Ronald R. Yager, editor, *Readings in fuzzy sets for intelligent systems*, pages 27–65. Morgan Kaufman Publishers Inc, 1993.

Evolving Feature-Extraction Algorithms: Adapting Genetic Programming for Image Analysis in Geoscience and Remote Sensing

Jason M. Daida*, Tommaso F. Bersano-Begey*, Steven J. Ross*, and John F. Vesecky**

*The University of Michigan, Artificial Intelligence Laboratory and the Space Physics Research Laboratory
2455 Hayward Avenue, Ann Arbor, Michigan 48109-2143
(313) 747-4581 FAX (313) 764-5137 EMAIL: daida@eecs.umich.edu
**The University of Michigan, Department of Atmospheric, Oceanic and Space Sciences
2455 Hayward Avenue, Ann Arbor, Michigan 48109-2143

Abstract—This paper discusses a relatively new procedure in the computer-assisted design of pattern-extraction algorithms. The procedure involves the adaptation of genetic programming, a recent technique that has been used for automatic programming, for image processing and analysis. This paper summarizes several of the measures we have taken to develop two prototype systems that help a user to design pattern-extraction algorithms.

1. INTRODUCTION

The task of extracting patterns from remotely sensed imagery can be difficult, particularly if increasingly novel patterns need extraction or when using data from new imaging technologies. In such cases, off-the-shelf software—e.g., geographic image processing systems or image analysis software libraries—may be able to meet a part, but not all the specifications for a pattern-extraction problem at hand. To fulfill such specifications, the best software tool to use may end up being code that has been specifically designed for a particular problem.

To assist in the development of problem-specific pattern-extraction tools, there has existed a range of options from which one could choose. On one hand, one could choose to program such tools from scratch, usually in a high-level programming language. On the other hand, one could also program in an even higher-level macro-language (e.g., many geographic image processing systems or scientific visualization systems often feature a macro- or a scripting-language capability). In either case, success of custom-tailored, pattern-extraction tools resides not only in one's ability to design a procedure with which to extract patterns, but also in one's ability to program.

The overhead associated with programming can be substantial and often include such tasks as specifying software, programming, debugging, and testing, as well as contending with learning curves associated with new languages, new software libraries, or new programming tools. To reduce this overhead would be a desirable objective, since programming often represents only a means (albeit a time-consuming one) for delivering what is needed—namely, a tool for extracting a particular pattern.

In part to address this objective, previous work has included investigations of strong and weak methods in artificial intelligence. The terms "strong" and "weak" refer not to a measure of a method's performance, but to the amount of knowledge about a given problem that a method requires. An example of a "strong" method is an expert system, which consists of a substantial portion of code that is problem-specific and a smaller portion of code that is generic. An example of a weak method is a neural network, which consists of a substantial portion of code that is largely generic, and a smaller part that is problem-specific. Either of these methods can still involve a fair amount of programming, although one could argue that these methods can reduce programming overhead. (In particular, by making programs more adaptable, more robust, and more intelligent, less programming would be required on the part of a user.)

In the past several years, there have been new techniques in weak methods that show additional promise in reducing programming overhead. This paper describes one of these techniques and highlights how this particular technique can be used for creating problem-specific pattern-extraction algorithms for use with remotely sensed image data.

2. GENETIC PROGRAMMING

This paper specifically discusses our use of genetic programming, an unsupervised technique that generates computer code. Originally introduced in 1989 by Koza [5], genetic programming has since been applied in a variety of domains, ranging from molecular biology to robotics to economics. Genetic programming has been shown to solve a number of problems that have served as benchmarks for neural nets [4, 6]. It has also been shown to solve problems in which neural nets might not be the most appropriate technology to use (e.g., symbolic regression) [6].

Genetic programming does have several attributes that potentially justify its use with remotely sensed image data. First, it has been shown to work with imperfect or incomplete problem specifications, while still yielding reasonable solutions [2]. Second, it has been able to produce extremely robust classification code that yields accuracies that are comparable to that which has been obtained with manually produced algorithms [4]. Third, it has been able to work with linear or nonlinear problems with little or no changes to its core (generic) portion [6, 7]. Fourth, it has been shown to work with a wide range of data types, including multi-channel image data [2]. Fifth, it has been able to output several types of code ranging from macros (which would require some type of interpreter) [6] to assembler [9]. Sixth, it has been used to automatically produce code with features such as subroutines, registers, and iterative loops [8]. Seventh, it has been routinely used to manipulate both symbolic and numeric data [6, 7].

Basic genetic programming can be briefly described as follows. A genetic programming run starts with a set of

0-7803-3068-4/96$5.00©1996 IEEE

randomly created programs that have been generated from the components that a user has supplied. We presume that somewhere in this random collection of programs are the building blocks necessary for the desired solution. The trick, of course, is to sift through this random code in order to synthesize a desired solution from these building blocks. To implement this trick, genetic programming uses two operations that are modeled after biological processes: natural selection and genetic crossover. In this case, natural selection means that only the most fit individuals reproduce and have offspring. In terms of an operator, natural selection means that these random programs need to be ranked by performance. Ranking is accomplished by means of a fitness function, which has been specified by a user before a run. A fitness function is supplied as a subroutine that tests for how close a program comes to a known result given a known set of inputs. Reproduction and the bearing of offspring refer to the biological process of how offspring are the genetic composite of both parents—i.e., through genetic crossover. In terms of an operator, crossover means that a portion of code from one program is replaced with a portion of code from another program. The resulting composite program is analogous to an "offspring." Crossover occurs mostly among the fittest programs (the pairing of prospective parents is stochastic, but probabilities favor the fittest programs) and continues until a new population of offspring is attained. The operations corresponding to natural selection and crossover are then repeated for this new population. A genetic programming run continues for subsequent populations until a candidate program obtains the best score allowable under the user-supplied fitness function.

Detailed descriptions of genetic programming can be found in [6, 7].

3. PROBLEMS

In spite of its apparent advantages and benefits, genetic programming has only recently appeared in the geoscience and remote sensing literature. Part of this relatively late appearance can be traced to two difficulties. One difficulty involves computational overhead. In Section 2, we noted that basic genetic programming involves the creation and test of many individual candidate programs. A typical run in genetic program may involve the creation and test of several thousand of such candidate programs. For numerous problems previously addressed by genetic programming, testing of each candidate solution is relatively quick and inexpensive (e.g., each program uses several tens of kilobytes of memory and executes in under a minute). For problems involving remotely sensed imagery, candidate solutions could easily use major blocks of memory and minutes to hours of CPU time.

The other difficulty is that the canonical genetic programming system, which has been freely available for some time, is in LISP. (The code for the canonical genetic programming system can be obtained at ftp://ftp.io.com/pub/genetic-programming.) While LISP is arguably the most intuitive language for genetic programming to use, LISP has a few idiosyncrasies that can hinder processing remotely sensed imagery.

4. ADAPTATIONS

This section summarizes our experiences to date in adapting genetic programming for processing remotely sensed imagery [1, 2, 3]. Our particular experience involves the extraction of low-contrast ridge and rubble patterns in low-resolution ERS synthetic aperture radar images of arctic sea ice. (See [3] in this conference proceedings.) Our problem has been relatively typical of those that involve multiple channels of image data (in our case, several textural channels).

To solve our problem, we have implemented six adaptations to genetic programming. The first three have helped in reducing computation time (for a LISP version of our system) to several CPU hours on a Sun SPARCStation 20 workstation. A fourth adaptation has enabled the LISP version of our system to process megabyte images. A fifth adaptation has helped to further reduce computation time to tens of minutes. A sixth adaptation has been proven necessary when using our methods for directly processing images with genetic programming.

4.1 Preprocessing

We preprocessed as much of the data as was possible to reduce genetic programming run time. For our problem, this has meant that the texture measures were computed beforehand. In particular, our problem was one in which it was possible to use texture channels, where each channel represents a different filtered version of the image data to be processed. (Two of the channels we specified corresponded to layers in an image pyramid: mean images filtered with kernel sizes of 3×3 and 5×5, respectively. The other two channels corresponded to edge detection: a Laplacian image of kernel size 5×5 and a Laplacian, 5×5, of a mean, 3×3, image.) In a sense, what was left for genetic programming to do was to formulate an algorithm (a rule set) that governs how the data in each channel was to be combined with the others.

Note that a complete algorithm produced by genetic programming would then consist not only of a rule set, but would also include the subroutines implicit with each filtered channel. While this may seem obvious, there may be unintentional side effects if one simply converted the algorithm produced by genetic programming to a standalone application and then used a different software implementation to generate each filtered channel.

4.2 Test Points

We used test points in an image that have been manually interpreted to serve as programming benchmarks. Each candidate algorithm produced in genetic programming is executed with these test points to assess that algorithm's accuracy in extracting a desired pattern (i.e., in the context of a fitness function). The number of test points that need to be provided does not have to be large. For our problem, the best algorithm that we have obtained to process full-sized low-resolution ERS SAR data products was developed using only 53 test points.

Note that we used test points, rather than subimage patches, to serves as "training sets" for genetic programming. We have found that the use of subimage patches was too constraining, did not help, and has even hindered processing times. See [2].

4.3 Dynamic Fitness

Instead of requiring all candidate algorithms to use a fixed standard, we opted to use a sliding standard. By that we mean the number of test points needing to be solved at the outset of a genetic programming run are fewer than the number of test points needing to be solved towards the end of that run. We have found this technique to result in better quality algorithms than without this technique, when genetic programming needs to solve for the entire test point set at the outset. See [1, 2] for implementation details.

4.4 Chunking

LISP requires a fairly sizable amount of processing overhead, which negatively affects the size of an image that can be processed at any one time. As a workaround intended mostly for LISP systems, we chunked low-resolution ERS SAR image data into smaller subimages, processed the subimages, then integrated the processed subimages to obtained a whole derived data product. The nature of the operators that we used for genetic programming allowed for seamless integration of subimages.

Our first prototype was built around the canonical genetic programming kernel, which means that our prototype system was implemented in LISP.

4.5 C-Language Port

As well suited for LISP as genetic programming is, there have been several reasons that have prompted us to design our second prototype in C: larger array sizes, faster run times, broader user community, wider range of programming flavors and tools. We have developed our second prototype around a recently introduced C-language version of genetic programming. (The code for the C-language version of the genetic programming kernel is available at the following URL: http://isl.cps.msu.edu/GA/software/lil-gp/) Early tests have shown that our second prototype runs about an order of magnitude faster than our LISP version.

4.6 Scaffolding

More often times than not, in cases where custom-designed code is needed, one is not able to start with an exact specification of a pattern. There often exists an uncertainty on what does, indeed, constitute the desired pattern. This uncertainty can show up as inappropriately interpreted test points, or even as inappropriately chosen test points. Several iterations of trying and interpreting different test points are usually the norm.

For this and other reasons described in [1, 2], we have designed our system with the deliberate intent to involve the user. In a sense, we have designed our system so that genetic programming facilitates the testing of a user's hypotheses on what a desired pattern should be. The user learns about specifying a desired pattern in a consistent manner, while the computer assumes the role of a human programmer, who would logically extend a user's specification into code. This cooperative relationship has been referred in the education and technology literature as scaffolding.

5. CONCLUSIONS

This paper has highlighted some of the adaptations used to incorporate genetic programming in the design of algorithms that extract features from remotely sensed images. In particular, this paper has summarized six adaptations: preprocessing, test points, dynamic fitness, chunking (for LISP versions), C-language port, and scaffolding. Although many applications have employed genetic programming as an unsupervised method, we have integrated genetic programming as part of an interactive system that serves as a tool for computer-assisted algorithm design. The overall system has been developed to help a user to focus more on the problem at hand and less on programming detail.

Additional references on genetic programming include [6, 7]. One can also obtain information and software about genetic programming at the following URL addresses:

- http://www.cs.ucl.ac.uk/research/genprog/
- ftp://ftp.io.com/pub/genetic-programming

ACKNOWLEDGMENTS

This research has been partially funded with grants from the Office of Naval Research, the Naval Research Laboratory (Stennis) and the Space Physics Research Laboratory (U-M). We gratefully acknowledge the following individuals for their invaluable assistance: I. Kristo, S. Daida, J. Hommes, J. Koza, R. Onstott, R. Riolo, E. Soloway, and A. Wu.

BIBLIOGRAPHY

[1] Daida, J.M. T.F. Bersano-Begey, S.J. Ross, and J.F. Vesecky, "Computer-Assisted Design of Image Analysis Algorithms: Dynamic and Static Fitness Evaluations in a Scaffolded Environment," Submitted to *Genetic Programming '96.*

[2] Daida, J.M., J.D. Hommes, T.F. Bersano-Begey, S.J. Ross, and J.F. Vesecky, "Algorithm Discovery Using the Genetic Programming Paradigm: Extracting Low-Contrast Curvilinear Features from SAR Images of Arctic Ice," *Advances in Genetic Programming II,* P. Angeline and K. Kinnear, Jr., (ed.), Cambridge: The MIT Press, 1996. In Press.

[3] Daida, J.M. R.G. Onstott, T.F. Bersano-Begey, S.J. Ross, and J.F. Vesecky, "Ice Roughness Classification and ERS SAR Imagery of Arctic Sea Ice: Evaluation of Feature-Extraction Algorithms by Genetic Programming," *Proceedings of IGARSS '96,* IEEE Press. In Press.

[4] Francone, F.D., P. Nordin, B. Banzhaf, "Benchmarking the Real-World Generalization Capabilities of an Advanced, Compiling Genetic Programming System Using Sparse Data Sets," Submitted to *Genetic Programming '96.*

[5] Koza, J.R. "Hierarchical Genetic Algorithms Operating on Populations of Computer Programs," *Proceedings of the 11th International Joint Conference on Artificial Intelligence,* Volume 1., Morgan Kaufmann.

[6] Koza, J.R., *Genetic Programming: On the Programming of Computers by Means of Natural Selection,* Cambridge: The MIT Press, 1992.

[7] Koza, J.R., *Genetic Programming II: Automatic Discovery of Reusable Programs,* Cambridge: The MIT Press, 1994.

[8] Koza, J.R., D. Andre, "Evolution of Iteration in Genetic Programming," *Evolutionary Programming V: Proceedings of the Fifth Annual Conference on Evolutionary Programming,* Cambridge: The MIT Press. In Press.

[9] Nordin, P., "A Compiling Genetic Programming System that Directly Manipulate the Machine Code," *Advances in Genetic Programming,* K. Kinnear, Jr. (ed.), Cambridge: The MIT Press, pp. 311–331.

Radar imaging of three-dimensional targets in the laboratory.

J.Bertrand and P.Bertrand***

(*) LPTM, University Paris VII, F-75251 Paris Cedex 05, France,
e-mail:bertrand@ccr.jussieu.fr
(**) ONERA/DES, BP 72, F-92322 Chatillon, France,
e-mail:bertrand@onera.fr

Abstract. Radar imaging allows to localize the reflecting parts of a target by processing the values of its backscattering function. The technique is usually described in the two-dimensional case where the computed maps concern only the projections of the bright points on a plane. In fact, the development of a three-dimensional extension is necessarily complex since the question of the polarization diversity in the target response becomes unavoidable. The object of the paper is to show that a systematic formulation of the technique is however possible in that case.

INTRODUCTION

Coherent imaging through wavelet analysis has proved useful for the representation of radar targets in various situations where polarization effects are not analyzed [1]. It has allowed to introduce the notion of hyperimage which describes the targets in terms of bright points characterized simultaneously by their positions and scattering properties. Basically, the procedure is founded on the physical requirement that a consistent imaging technique must be independent of the reference system which is used in the description. In practice, a key role is given to the group of transformations relating all possible reference frames. In the special case of scattering on a two-dimensional static target [2], the relevant group was the similarity group of the plane. Hyperimages were thus functions of four parameters (space, frequency and direction of illumination) which were obtained by a wavelet analysis associated with that group.

The following developments show how this procedure can be generalized in order to associate hyperimages with three-dimensional polarimetric scattering data.

MONOSTATIC RESPONSE OF A THREE-DIMENSIONAL STATIC TARGET

Suppose that the outcome of a radar scattering experiment is given as a matrix depending on frequency and direction of illumination. The first task is to define precisely the reference system in which the scattering matrix is expressed.

The transmitted wave is characterized by an electric field vector with components $\widetilde{E}_T^i(\boldsymbol{k})$ in a cartesian coordinate system where $|\boldsymbol{k}| \equiv k$ is connected to the working frequency by $k = 2f/c$. Polar coordinates with origin at the scatterer are introduced so that:

$$\begin{aligned} k_x &= k \sin\theta \cos\phi \\ k_y &= k \sin\theta \sin\phi \\ k_z &= k \cos\theta \end{aligned} \tag{1}$$

These relations can also be written in terms of a unit vector $\boldsymbol{u}$ in the z-direction as:

$$\boldsymbol{k} = [W(\theta,\phi)]^{-1}\, k\, \boldsymbol{u} \tag{2}$$

where $\boldsymbol{u} \equiv (0,0,1)$ and $[W(\theta,\phi)]$ is the 3×3 matrix representing the action of a rotation ϕ about the z-axis followed by a rotation θ about the x-axis.

For the incident and reflected field, the following relation holds:

$$\boldsymbol{k}.\widetilde{\boldsymbol{E}}(\boldsymbol{k}) = 0 \tag{3}$$

A local frame of reference is chosen as usual to coincide with the standard vectors (e_r, e_θ, e_ϕ) of the spherical coordinate system [3, 4]. The components of the electric field vector $\boldsymbol{E}_T$ in the local frame are given in terms of $\widetilde{E}_T^i$ by the relation:

$$\boldsymbol{E}_T(k,\theta,\phi) \equiv [W(\theta,\phi)]\, \widetilde{\boldsymbol{E}}_T(k,\theta,\phi) \tag{4}$$

and such that $E_T^3 = 0$.

Since the transmitting and receiving antennas are supposed to be at the same place, the same local reference frame will be used for the received and transmitted fields. The received field in the local frame will be denoted by $\boldsymbol{E}_R$. With these conventions, the scattering matrix is defined by [4]:

$$\boldsymbol{E}_R \simeq \frac{e^{ikr}}{r}[S(\boldsymbol{k})]\, \boldsymbol{E}_T \tag{5}$$

where $[S]$ is a complex 2×2 matrix function of frequency and direction of observation through $\boldsymbol{k}$.

0-7803-3068-4/96$5.00©1996 IEEE

So far, a linear polarization basis has been used implicitly to describe the polarization of the waves. It will be useful to transform the fields to a circular polarization basis. This is performed by a unitary matrix U defined by [5]:

$$[U] = (1/\sqrt{2}) \begin{vmatrix} i & -1 \\ 1 & -i \end{vmatrix} \tag{6}$$

Explicitly, the transmitted field in the circular polarization basis is defined by:

$$\boldsymbol{F}_T \equiv [U]\, \boldsymbol{E}_T \tag{7}$$

Since the reflected field transforms by $[U^*]$, its circular polarization representation is defined by:

$$\boldsymbol{F}_R \equiv [U]^*\, \boldsymbol{E}_R \tag{8}$$

The scattering matrix in the circular polarization basis is obtained from (5), (7) and (8) and reads:

$$[S_c] = [U]^*\, [S]\, [U]^{-1} \tag{9}$$

DATA TRANSFORMATION IN A CHANGE OF REFERENCE SYSTEM

The group of transformations relating the different reference frames is the similarity group of Euclidean space. It consists of transformations $(a, \boldsymbol{b}, R)$ where $a > 0$ is a dilation, $\boldsymbol{b}$ is a vector representing a 3-translation and R is a rotation. The rotation is parameterized by classical Eulerian angles (β, α, γ), where α denotes a rotation about the x-axis, and acts on the cartesian components (1) as a 3×3 matrix $[R]$.

To write the effect of a change of reference system on the scattering matrix, we need to study first the transformation of the field components. For simplicity, only the rotation part of the transformations will be written. In a rotation R, the cartesian components of the transmitted electric field $\widetilde{E}^i_T(\boldsymbol{k}), i = 1, 2, 3$ transforms as:

$$\widetilde{E}^i_T(\boldsymbol{k}) \longrightarrow \widetilde{E}'^i_T(\boldsymbol{k}) \equiv [R]^i_j\, \widetilde{E}^j_T(aR^{-1}\boldsymbol{k}) \tag{10}$$

The application of transformation (4) to both sides of the above relation gives the transformation law of the field components in the local system:

$$E_T{}^i(k, \theta, \phi) \longrightarrow \tag{11}$$
$$E'_T{}^i(k, \theta, \phi) \equiv [W(\theta, \phi)]^i_j\, [R]^{i'}_{j'} ([W^{-1}(\theta', \phi')]^{j'}_j\, E^j_T(\boldsymbol{k}')$$

where

$$\boldsymbol{k}' \equiv aR^{-1}\boldsymbol{k} \equiv (k', \theta', \phi') \tag{12}$$

Since the field has only two components different from zero, the matrices $[W]$ and $[R]$ act in fact as 2×2 matrices. In addition, it must be stressed that the matrix $[\Omega]$ defined by

$$[\Omega] \equiv [W(\theta, \phi)]^i_{i'}\, [R]^{i'}_{j'} [W^{-1}(\theta', \phi')]^{j'}_j \tag{13}$$

represents simply a rotation of axis $\boldsymbol{k}$. The angle ω of this rotation, which depends on R and on the spherical coordinates (θ, ϕ) of $\boldsymbol{k}$ can be computed from (13) and is given by:

$$\tan\omega = \frac{\sin\alpha\, \sin(\phi + \beta)}{\sin\theta\cos\alpha + \sin\alpha\cos\theta\cos(\phi + \beta)} \tag{14}$$

Remark that angle ω does not depend on the γ part of rotation R. The components of the received field $\boldsymbol{E}_R$ transform in the same way:

$$E^i_R(k, \theta, \phi) \longrightarrow \tag{15}$$
$$E'^i_R(k, \theta, \phi) \equiv [W(\theta, \phi)]^i_{i'}\, [R]^{i'}_{j'} W^{-1}(\theta', \phi')]^{j'}_j\, E^j_R(\boldsymbol{k}')$$

Transformations (11) and (15) are representations of the rotation group that mix the components of the field vectors. It is thus essential to go over to the circular polarization basis in which the vector components will transform independently. Performing transformation (7) on $\boldsymbol{E}_T$, we deduce from (11) the transformation law of the components of $\boldsymbol{F}_T$:

$$\begin{vmatrix} F'^1_T(\boldsymbol{k}) \\ F'^2_T(\boldsymbol{k}) \end{vmatrix} = \begin{vmatrix} e^{-i\omega} & 0 \\ 0 & e^{i\omega} \end{vmatrix} \begin{vmatrix} F^1_T(aR^{-1}\boldsymbol{k}) \\ F^2_T(aR^{-1}\boldsymbol{k}) \end{vmatrix} \tag{16}$$

with ω given by (14). The transformed components of field $\boldsymbol{F}_R$ are obtained in the same way.

The transformation law of the scattering matrix $[S_c]$ in the circular polarization basis is then easily computed. The only point to be aware of is that each element of S_c has the physical dimension of a length and must transform accordingly under a dilation. Thus, a change of reference system characterized by $(a, \boldsymbol{b}, R)$ transforms matrix $[S_c]$ into a matrix $[S'_c]$ given by:

$$[S'_c(\boldsymbol{k})] = a\, e^{-2i\pi \boldsymbol{k}.\boldsymbol{b}}\, [\Omega]\, [S_c(a\, R^{-1}\boldsymbol{k})]\, [\Omega] \tag{17}$$

where the matrix Ω is equal to:

$$[\Omega] \equiv \begin{vmatrix} e^{-i\omega} & 0 \\ 0 & e^{i\omega} \end{vmatrix} \tag{18}$$

and ω is a function of (θ, ϕ) and R.

Thus, in such a polarization basis, each component of the scattering matrix is transformed independently. Moreover, only the diagonal elements are sensitive to the rotation of the local frame. Indeed, two cases of particular targets can be recalled. For the perfectly reflecting sphere, $[S_c]$ is given by

$$[S_c] = \begin{vmatrix} 0 & 1 \\ 1 & 0 \end{vmatrix} \tag{19}$$

and it is effectively unsensitive to rotations. For the dihedral corner,

$$[S_c] = \begin{vmatrix} -1 & 0 \\ 0 & 1 \end{vmatrix} \tag{20}$$

and this will be affected by rotations as it should.

INTRODUCTION OF THE NOTION OF HYPERIMAGE

In the present situation, what is meant by a hyperimage of $[S_c]$ has to be defined. In accordance with earlier works [1, 2], the image space parameters are taken as $(\boldsymbol{X}, \boldsymbol{K})$ and could partly characterize elementary reflectors constituting the target. The hyperimage corresponding to the scattering matrix will be a function $I(\boldsymbol{X}, \boldsymbol{K})$ transforming pointwise in a change of reference system, i.e. going to $I'(\boldsymbol{X}, \boldsymbol{K})$ such that:

$$I'(\boldsymbol{X}, \boldsymbol{K}) = I(a^{-1}\, R^{-1}\, (\boldsymbol{X} - \boldsymbol{b}), a\, R^{-1}\, \boldsymbol{K}) \qquad (21)$$

To go further it is necessary to perform a wavelet analysis associated with the group of changes of reference systems. However, there are some peculiarities to notice. First, it is a matrix $[S_c]$ that is to be analyzed and this is a new situation. In fact, it will not be a problem because, according to (17), each component of $[S_c]$ is transformed independently. The construction of one hyperimage for each element of the scattering matrix is thus possible. Secondly, a straightforward wavelet analysis is not well adapted here since it would give a function on the 7-parameter similarity group and not on space $(\boldsymbol{X}, \boldsymbol{K})$. In fact, a quotient of the group by the rotations around an axis has to be performed to obtain the relevant space of parameters. Only then will the wavelet analysis give a satisfactory answer as will now be sketched.

The scalar product on the space of scattering matrices is defined by:

$$([S_c^1], [S_c^2]) = \int_{\mathbf{R}^3} \mathrm{Tr}[S_c^1(\boldsymbol{k})][S_c^2(\boldsymbol{k})]^\dagger \frac{d\boldsymbol{k}}{k} \qquad (22)$$

where $\dagger$ stands for conjugate transpose. This scalar product is invariant by changes not only of reference system but also of polarization basis .

Let $\Phi(\boldsymbol{k})$ be a function that is axially symmetric and verifies $\int |\Phi(\boldsymbol{k})|^2 d\boldsymbol{k}/k = 1$. It will be used to construct the basic wavelet in the following way. Consider the matrices $[\Phi^{(q)}(\boldsymbol{k})]$, $q = 1..4$ whose elements are null except for one which is equal to $\Phi(\boldsymbol{k})$. These matrices are assigned to the point $\boldsymbol{X}_0 = 0, K_0 = 1, \widehat{\theta}_0 = \widehat{\phi}_0 = 0$ of image parameter space. They are tentatively interpreted as the scattering matrices of elementary reflectors of a given type located around $\boldsymbol{X}_0$ and with reflecting characteristics about $\boldsymbol{K}_0$. Applying a transformation $(a, \boldsymbol{b}, R(\beta, \alpha, \gamma))$ to $(\boldsymbol{X}_0, \boldsymbol{K}_0)$ leads to a point whose coordinates $(\boldsymbol{X}, \boldsymbol{K})$ are expressed in terms of the group parameters as:

$$\boldsymbol{X} = \boldsymbol{b}, \quad K = a^{-1}, \quad \widehat{\theta} = -\alpha, \quad \widehat{\phi} = -\beta \qquad (23)$$

With these definitions, the set of functions obtained from Φ by action of the similarity group forms a 4-fold family of wavelets labelled by the points $(\boldsymbol{X}, \boldsymbol{K})$. Each family corresponding to a given index (q) is separately stable by changes of reference systems. Thus it is possible to define four wavelet coefficients by:

$$C^{(q)}(\boldsymbol{X}, \boldsymbol{K}) = (S, \Phi^{(q)}_{\mathbf{X},\mathbf{K}}) \qquad (24)$$

where

$$\Phi^{(q)}_{\mathbf{X},\mathbf{K}}(\boldsymbol{k}) \equiv \frac{1}{K}\, e^{-2i\pi \boldsymbol{k}.\boldsymbol{X}}\, e^{-2i\zeta(q)\omega}\, \Phi(K^{-1}R^{-1}\boldsymbol{k}) \qquad (25)$$

with $\zeta(1) = -\zeta(4) = 1, \zeta(2) = \zeta(3) = 0$. Because of the axial rotation invariance of function Φ, only the (β, α) part of rotation R is effective and the wavelet coefficients are well defined. An isometry relation can be written in the form:

$$\int |C^{(q)}(\boldsymbol{X}, \boldsymbol{K})|^2 d\boldsymbol{X}\, d\boldsymbol{K} = \chi \int \mathrm{Tr}[S_c^{(q)}(\boldsymbol{k})][S_c^{(q)}(\boldsymbol{k})]^\dagger \frac{d\boldsymbol{k}}{k} \qquad (26)$$

where

$$\chi \equiv \int_{\mathbf{R}^3} |\Phi(\boldsymbol{k})|^2 \frac{d\boldsymbol{k}}{k^4} \qquad (27)$$

and $[S_c^{(q)}]$ is the component of the scattering matrix in the subspace of $[\Phi^{(q)}]$. If χ is finite, a reconstruction formula can be written for each elementary scattering matrix.

It is possible to extend the analysis by introducing new basic wavelets as linear combinations of the $[\Phi^{(q)}]$ in the following way:

$$[\Phi] \equiv \sum_{q=1}^{4} \lambda_q [\Phi^{(q)}] \qquad (28)$$

where λ_q are complex numbers such that $\sum_{q=1}^{4} |\lambda_q|^2 = 1$. By the linearity property of the wavelet transform, the corresponding coefficient C_λ is equal to $\sum \lambda_q C^{(q)}$. The corresponding hyperimage is:

$$I_\lambda(\boldsymbol{X}, \boldsymbol{K}) = \left| \sum_{q=1}^{4} \lambda_q C^{(q)} \right|^2 \qquad (29)$$

By varying the λ_q, it is possible to obtain images corresponding to various types of elementary targets.

REFERENCES

[1] J.Bertrand and P.Bertrand, Theoretical radar imaging: from images to hyperimages, Proc. IGARSS'95, Florence (Italy).

[2] J.Bertrand, P.Bertrand and J.P.Ovarlez, "Frequency-directivity scanning in laboratory radar imaging", Int. J. of Imaging Systems and Technology, Vol.5, 39-51 (1994).

[3] W-M. Boerner, Wei-Ling Yan and An-Qing Xi, "Basic Relations of Wideband Radar Polarimetry",Proc. of the First Los Alamos Symposium on Ultra Wide-Band Radar, 1990.

[4] *Radar Polarimetry for Geoscience Applications*, F.T. Ulaby and C.Elachi (Eds), Artech House, 1990.

[5] D.H.O. Bebbington, "Target Vectors-Spinorial concepts", Second International Workshop on Radar Polarimetry, IRESTE, Nantes(France), 1993.

Reconstruction of Complex Dielectric Profiles via Quadratic Models

Rocco Pierri[1], **Tommaso Isernia**[23], **Vito Pascazio** [4], **Antonello Tamburrino**[5]

[1]Dipartimento di Ingegneria dell'Informazione, Seconda Università di Napoli
via Roma, 29 - 81031 Aversa - Italy, ☎ +39-(0)81-5044035, fax +39-(0)81-5045804, E-mail: pierri@uxing2.sunap.unina.it
[2]Dipartimento di Ingegneria Elettronica, Università di Napoli *Federico II*, Italy
[3]Istituto di Ricerca per l'Elettromagnetismo e i Componenti Elettronici, Consiglio Nazionale delle Ricerche, Napoli, Italy
[4]Istituto di Teoria e Tecnica delle Onde Elettromagnetiche, Istituto Universitario Navale, Napoli
[5]Dipartimento di Ingegneria Industriale, Università di Cassino, Italy

INTRODUCTION

The electromagnetic inverse scattering problem deserves special attention in many branches of applied science, such as f.i. geoscience (detection of buried objects , oil prospection , Ground penetrating Radar (GPR) applications), non destructive testing or evaluation of materials, non invasive detection or monitoring in biomedical engineering, and many others. Besides theoretical uniqueness of a solution and limitations induced from measurement errors, the development of solution algorithms effectively capable to retrieve the unknown parameters in a reliable way should be addressed.

In order to discuss factors affecting accuracy and reliability of solution algorithms we refer in the following, by the sake of simplicity,to a two dimensional (2D) geometry. All results can be anyway extended to the 3D case. We consider an inhomogeneous object, whose compact support is Ω, imbedded in an homogeneous medium. The dielectric permittivity of the object is equal to $\varepsilon_b \varepsilon_r(\cdot)$, where ε_b is the one of the external medium and the magnetic permeability is everywhere equal to μ_0. Under these hypothesis, and when a TE polarized incident field is used, the equations describing the scattered field reduce to

$$\begin{cases} E_s(\boldsymbol{r}) = k^2 \int_\Omega G(\boldsymbol{r},\boldsymbol{r}')\chi(\boldsymbol{r}')E(\boldsymbol{r}')d\boldsymbol{r}', & \boldsymbol{r} \in \Gamma, \\ E(\boldsymbol{r}) = E_i(\boldsymbol{r}) + k^2 \int_\Omega G(\boldsymbol{r},\boldsymbol{r}')\chi(\boldsymbol{r}')E(\boldsymbol{r}')d\boldsymbol{r}', & \boldsymbol{r} \in \Omega, \end{cases} \quad (1)$$

where E, E_i and E_s are the total, the incident and the scattered fields, respectively, $k = \sqrt{\omega \varepsilon_b \varepsilon_0}$ and $G(\boldsymbol{r},\boldsymbol{r}') = -(j/4)H_0^{(2)}(k|\boldsymbol{r}-\boldsymbol{r}'|)$ are the wavenumber and the Green function in the external homogeneous medium at a prescribed frequency, respectively, $\chi(\cdot) = \varepsilon_r(\cdot)/\varepsilon_b - 1$ is the contrast function, with $\varepsilon_r(\cdot)$ being the relative complex permittivity of the object, and Γ is a curve external to the object.

The inverse scattering problem amounts to retrieve the unknown contrast function χ from the knowledge of the scattered fields E_s corresponding to a (collection of) known incident fields E_i.

Several methods to solve the inverse scattering problem have been developed. Methods based on first order Born approximation, and its derivations, belong to the class of linear methods. In this case the inverse problem reduce to a linear one where the unknown is the contrast function while the total electric field inside the object is assumed to be equal to the electric field as computed for permittivity equal to the background , say E_b.Linear methods have also been heuristically exploited in the so-called Born Iterative Method and its distorted version.

In a second class of methods, no approximation is made and, substituting second Eqn. (1) into the first one, i.e., eliminating the total electric field inside the object, a strongly non linear operator equation in the unknown contrast χ is obtained. This equation is solved either through a Newton-Kantorovich (NK) procedure , or through the minimization of a proper functional .

Due to the non linear nature of the operator to be inverted, the NK approach will converge to the seeked result only when started within a proper ball enclosing the solution. Minimization approaches, at least in principle, can take advantage from global optimization procedure, such as Simulated Annealing or genetic algorithms, but they can actually work only with a limited number of unknowns.

In order to overcome limitations related to the limited range of validity of linear approaches and/or to the local effectiveness of strongly non linear methods, it can be useful to consider approaches using a "manageable" degree of non-linearity.

The so called Quadratic Model [1] adopts an approximated model of the reality and it is based on the use of a first order expansion, with respect to the unknown profile, of the total electric field inside the object so that the overall scattering is approximated via a quadratic operator. This formulation allows to reconstruct a class of unknown profiles certainly larger than the one reconstructed by adopting the usual linear Born approximation. In particular, both higher and faster spatially varying profiles can be considered. As a matter of fact, the approach has been already successfully applied to 1-D and 2-D dielectric profiles reconstruction and to 2-D and simple 3-D reconstruction of conductivity profiles using eddy currents.

On the other hand, Bilinear approaches [2], which are indeed based on exact models (no approximation is involved) achieve a moderate degree of non linearity considering both the contrast and the electric field inside the object as unknowns of the problem. At the expenses of an enlargement of the set of the unknowns, the degree of non linearity reduces, so that a bilinear operator has to be inverted. Note the bilinear operator can be regarded as a quadratic one when introducing a single set of unknowns including both contrast and internal field functions.

Both the quadratic model and the bilinear model (1) can be seen as quadratic operators say to be inverted, so that all results in [3] apply. In particular the moderate degree of non-linearity allows to control the false solution presence as long an adequate ratio between the essential dimension of the space of data and number of unknowns is considered. In the following, some examples are reported in order to show

0-7803-3068-4/96$5.00©1996 IEEE

limitations of linearized methods as well as (extended) capabilities and of both the proposed methods.

THE QUADRATIC MODEL

In order to understand limitations of linear approximations and appreciate performances that can be obtained through a quadratic model, let us consider the problem of inverting the operator that maps an unknown conductivity profile (i. e., $\chi = \sigma / j\omega\varepsilon_0$, $\varepsilon_b = \varepsilon_0$) into the scattered electric field through respectively a first and a second order expansion. In both cases the expansion is made with respect to the unknown profile parameters around an "initial point" σ_0 which is herein taken equal to the background conductivity . In the following example the conducting domain is a cylinder whose section is a circular crown with inner radius $R_{in} = 16$ mm and outer radius $R_{es} = 16.5$ mm. The conductivity depends only upon ϑ. The incident field is produced by a couple of filamentary conductors, placed at $r = 16.8$mm, $\vartheta = \vartheta_e \pm 15°$, carrying opposite sinusoidal currents at $f = 10$kHz. The excitation system is sequentially placed around the cylinder axis, taking $N_e = 5$ series of measurements; $N_m = 7$ field sensors are symmetrically located around the cylinder at $R_m = 16.8$ mm. The background conductivity is $\sigma_0 = 10^4$ S/m.

In Fig. 1 is shown the real part of the Fourier coefficient of the second order approximations whereas in Fig. 2 is shown the difference between the first and second order expansions when the conductivity profile is $\sigma/\sigma_0 = \cos(60\vartheta)$. The exact field is not reported since it coincides with the second order approximation. It can be appreciated that while the linear approximation does not furnish any useful information, the second order approximation is able to describe the scattered field. This is due to the fact that the linear approximation amounts to consider $E = E_b$ in (1) so that when the profile is spatially faster varying than E_b the linear model gives a scattered field that is approximately zero. On the other hand, it can be seen that the second order approximation can give a good estimate of the scattered field on profiles which are "invisible" at the first order.

Coming to the inversion procedure, let us consider the unknown conductivity profile of Fig. 3. In this case the ratio between (essential) dimension of data and dimensions of the unknown is about 1.5, which suffices to guarantee robustness against false solutions problems.The approximation error in the direct problem is about 13% and 5% for the first and second order expansions, respectively.

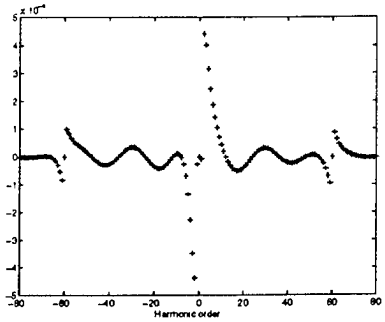


Figure 1. The real part of the Fourier coefficients of the second order approximated electrical field.

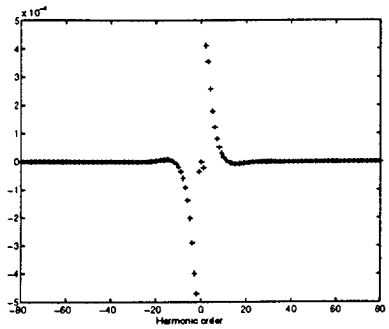


Figure 2. The real part of the Fourier coefficients of the difference between the second and first order approximated electrical field.

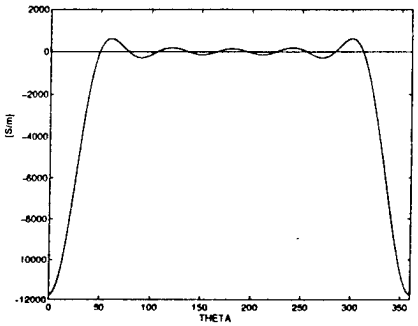


Figure 3 The unknown conductivity profile.

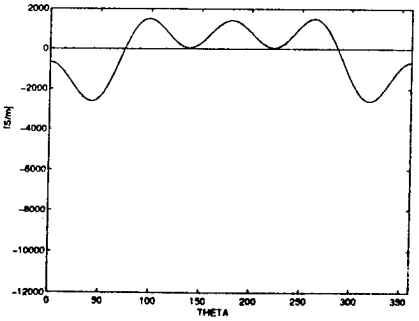
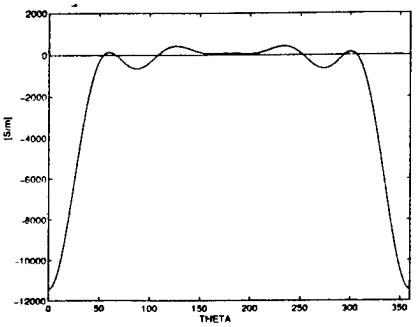


Fig.4. Reconstructed conductivity using the linear model



Fig; 5. Reconstructed conductivity using the quadratic model

In Fig. 4-5 are shown the results of the reconstruction of the unknown profile based on the linear and quadratic approximations, respectively. It can be noted that the linear method is unable to reconstruct the unknown contrast whereas the quadratic model allows to achieve a good estimate.

As a consequence of a better approximation of the direct problem, as long as one is capable to avoid the false solution

problem, as in the present case,the quadratic approximation allows to achieve more accurate reconstructions with respect to linear models.

THE BILINEAR APPROACH

In this Section we present results obtained by using the bilinear approach (1). To test its performances, we consider that the object whose contrast has to be reconstructed is positioned inside a square domain under investigation, and its shape is considered totally unknown. We illuminate the domain with plane waves at a fixed frequency, incident from a set of known angles. In correspondence of each incident fields the scattered field is measured on points positioned, and equi-angle spaced, on a circle having the same center of the square and a radius greater that the semi-diagonal of the square. The number of incident fields and of measurement points are chosen in accordance with the known results on the degrees of freedom of the scattered field. In the following, finite dimensional Fourier series have been assumed to represent the problem unknowns. This choice, besides taking into account in a natural fashion continuity properties of internal fields, allows one to deal with a number of unknowns coefficients considerably lower than the overall dimension of the grid used to solve the direct problem, so that, whenever a priori information allows it, or on the basis of blind hypothesis, one can reduce to a large extent the number of contrast unknowns with respect to common assumptions. Note, this circumstance is essential in order to deal with a problem having a number of unknowns not exceeding the number of independent data, i.e., the degrees of freedom of the scattered field.

The minimization, for all the following experiments, has been performed by using the Polak-Ribiere conjugate gradient method, and the background has been chosen as starting guess of the minimization.

Consider the complex profile of Fig. 6, where the side of the square under test is equal to $d = 2\lambda$, with $\lambda = 2\pi/k$ the background wavelength.

According to the dimension of the considered object, the number of independent measures we can do for each incident field is given by $N_M \cong 2\,k\,a$, a being the radius of the minimum circle enclosing the object; for scatterers whose dimensions are comparable with the wavelength, some additional independent measures, say ΔN, are available. Accordingly, we could collect a maximum of about 22 independent measures. As a consequence, by reciprocity argument, the total number of independent measures will be approximately given by $N_T \cong N_M^2/2 = 264$.

The reconstruction, started from the background, when 9×9 unknown parameters are searched for and $N_v \times N_M = 12\times22$ independent measures are collected, is presented in Fig. 7. Note that, in this case, also when we search for a number of unknowns less than the number of data, the non-linear nature of the inverse problem do not allow to reconstruct the unknown profile because of the presence of undesired local optima. The reconstruction, when 5×5 unknown parameters are searched for is presented in Fig. 8. Only in this last case, reducing the number of searched unknowns, it is possible to get a satisfactory reconstruction of the profile, thus confirming arguments in the previous Sections: false solutions can be avoided increasing as possible the ratio between the essential dimension of data and the number of the searched unknown parameters. As the number of degrees of freedom of the scattered field is anyway limited, this circumstance also affects the number of unknown parameters that can be reliably extracted.

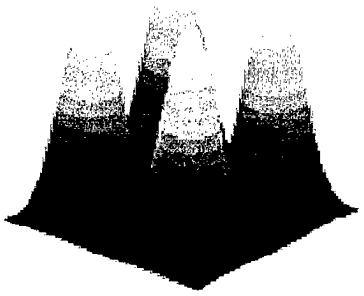


Figure 6: Ideal profile Maximum contrast 1.6



Figure 7: Reconstructed profile searching 9x9 unknowns

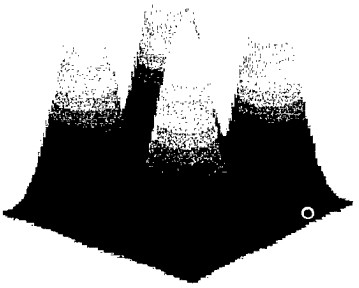


Figure 8: Reconstructed profile searching 5x5 unknowns

REFERENCES

[1] A. Brancaccio, V. Pascazio, R. Pierri, "A Quadratic Model for Inverse Profiling: the One Dimensional Case", *Jou. Electr. Waves Appl.*, **9**, 1995.

[2] R. E. Kleinman, P. M. van den Berg, "An Extended Modified Gradient Technique for Profile Inversion", *Radio Science*, **28**, no. 5, pp. 877-884, 1993.

[3] T. Isernia, G. Leone, R. Pierri, "Phase Retrieval of Radiated Fields", *Inverse Problems*, **11**, pp. 183-203, 1995.

TOPOGRAPHIC MEASUREMENTS USING POLARIMETRIC SAR DATA

D.L. Schuler and J.S. Lee
Remote Sensing Division, Code 7263
Naval Research Laboratory
Washington, DC 20375-5351 USA
Tel/Fax: + [1] (202) 767-8248/5599, E-mail: schuler@imsy1.nrl.navy.mil

G. De Grandi
European Union Commission Joint Research Center
Institute for Remote Sensing Applications
21020 Ispra(Va) Italy
Tel/Fax: + [39] (332) 789823/789073, E-mail: gianfranco.degrandi@jrc.it

Abstract - A technique using polarimetric SAR has been developed which is capable of directly sensing terrain surface slopes in the along-track (or azimuthal) direction. The method involves measuring the shift in orientation angle of the maximum in the polarimetric signature. The technique has measured slopes and derived elevations for both open and forested terrain. The method of polarization signature decomposition has been employed to identify components of the covariance matrix which produce the shift in the polarimetric peak position. Selected examples of terrain slope/elevation measurements made using both L- and P-band polarimetric SAR data will be given for heavily-forested areas near Freiburg, Germany and in northern California.

INTRODUCTION

Polarimetric synthetic aperture radar (SAR) measures the amplitude and phase terms of the complex scattering matrix. It has been used extensively for classification studies involving natural scenes and man-made targets. A method is introduced here which provides a means of remotely measuring topography using the same data. Studies have been carried out to determine the effects of resolved surface tilts on co-pol polarization signatures of terrain backscatter. Resolved azimuthal tilts produced significant displacements in the location of the co-pol orientation maximum of the signature parallel to the ellipticity (χ) axis. Similar shifts in the position of the maximum have been observed to occur for the cross-pol case.

This polarimetric SAR capability provides both a direct measure of terrain azimuthal slopes and a derived estimate of terrain elevations. Azimuthal direction terrain slope maps can be produced over wide areas without a priori knowledge about the terrain. Terrain elevations can be derived from the polarimetric SAR slope measurements by integrating the slope profiles in the azimuthal direction. To obtain absolute, rather than relative, elevation values, at least one elevation "tie-point" must be independently known somewhere along each slope profile being integrated. Two-dimensional topographic elevation and slope maps can then be constructed from sets of elevation profiles spaced throughout the range direction.

MEASUREMENT OF SLOPE DISTRIBUTIONS

Image analysis for both open and forested areas [1] showed that an azimuthal tilt δ of the terrain caused a proportional shift of the signature maximum from its flat terrain polarimetric orientation (ψ) by an angle $\Delta\psi$ that is almost equal to the slope δ. Fig. 1 shows a comparison of slope distributions measured by the new algorithm in an area parallel to the Breg River near Freiburg, Germany. The slope distributions obtained using the polarimetric technique agree well in mean and standard deviation with those derived from a stereo-photograph Digital Elevation Model (DEM) for the same area. Direct measurement of such distributions is an important application of the new technique.

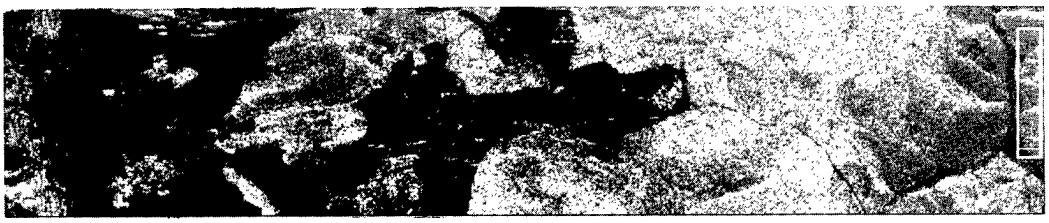
ORIGIN OF THE SIGNATURE SHIFT

It is important to identify the dominant electromagnetic scattering terms in the polarimetric covariance matrix which are causing the slope-induced shifts in orientation. Secondly, an explanation must be developed why these terms are significantly large when slopes are present. A technique known as signature decomposition has been used to determine which components of the covariance matrix are causing the shifts observed in open and forested terrain. The technique was applied to azimuthal profiles of NASA JPL/AIRSAR P-band backscatter data from the Freiburg/Black Forest study area.

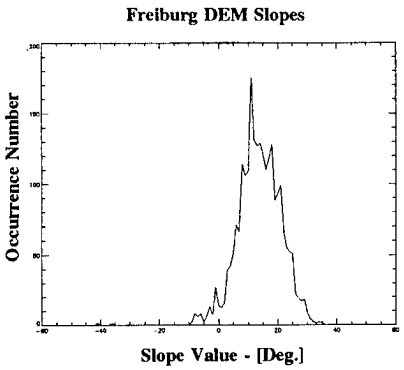
The following approach can be used to decompose the co-pol signature [2]. The polarization synthesis equation can be

Support for this research was provided by the Advanced Research Projects Agency (Dr. Mark E. Davis).

0-7803-3068-4/96$5.00©1996 IEEE



Freiburg P-band HH pol Image



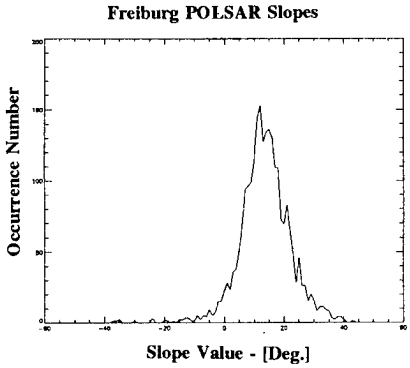


Fig. 1 a) P-band HH-pol image of the Black Forest study area and b) slope distributions for the area within the boxed area (upper-right corner of image).

written:

$$\begin{aligned}\sigma_0(S,\ \psi_r,\ \chi_r,\ \psi_t,\ \chi_t) &= |C_1|^2\sigma_{hhhh} \\ &+ |C_2|^2\sigma_{hvhv} + |C_3|^2\sigma_{vvvv} \\ &+ 2Re[C_1C^*_2]Re[\sigma_{hhhv}] - 2Im[C_1C^*_2]Im[\sigma_{hhhv}] \\ &+ 2Re[C_2C^*_3]Re[\sigma_{hvvv}] - 2Im[C_2C^*_3]Im[\sigma_{hvvv}] \\ &+ 2Re[C_1C^*_3]Re[\sigma_{hhvv}] - 2Im[C_1C^*_3]Im[\sigma_{hhvv}]\end{aligned} \quad (1)$$

where, S is the scatter matrix, σ_{ij} are the elements of the covariance matrix, (r,t) refer to receiver/transmitter, and C_i are functions which depend only on the orientation and ellipticity angles viz:

$$C_1 \equiv \frac{1}{2}(cos2\psi + cos2\chi + i\ sin2\psi sin2\chi) \quad (2)$$

$$C_2 \equiv sin2\psi - i\ cos2\psi sin2\chi \quad (3)$$

$$C_3 \equiv \frac{1}{2}(-cos2\psi + cos2\chi - i\ sin2\psi sin2\chi) \quad (4)$$

The real and imaginary values of the products $C_iC^*_j$ are called shape functions. The polarimetric signature is broken down into component shape functions weighted by covariance matrix elements. The advantage of this decomposition is that the impact of each of the covariance matrix elements may be analyzed separately. The shape functions associated with the power terms in the covariance matrix (e.g., σ_{hhhh}, σ_{vvvv}, and σ_{hvhv} all have maxima centered at orientation angles of 0° (or 90°). These terms, therefore, cannot account for shifts in the co-pol maxima; they only modulate the absolute value of the co-pol local maxima. Attention must be paid to the terms which describe the correlation between polarimetric channels (e.g., σ_{hhvv}, σ_{hhhv}, and σ_{hvvv}). Of these, the σ_{hhvv} has peaks in its real part at ±45° but they are symmetric with respect to 90° orientation and therefore cannot introduce a net shift of the co-pol maximum in one direction. The only terms which are relevant in an analysis of the azimuthal tilt modulation are the off-diagonal terms σ_{hhhv} and σ_{hvvv}. In particular, it will be shown that the $C_1C^*_2$ shape function plays the most important role in shifting the co-pol peak of forest signatures in response to the azimuthal tilt modulation. The shape factors have been described in [2]. In the Black Forest study area the peak is determined primarily by the σ_{hhhh} scattering term and the C_1^2 shape function. In the same area, the term that shifts the peak back and forth along the orientation axis is σ_{hhhv} weighted by the shape function $C_1C^*_2$.

To determine the major factors that give rise to the sensitivity of the co-pol peak position to azimuthal tilts, the decomposition has been applied to the Black Forest dataset. Two different examples taken from a azimuthal profile of 512 pixels over sloping terrain are given in Fig. 2(a-b). Each pixel is an average over 109m in the azimuthal direction and 132m in the range direction. When all of the component terms in Figs. 2(a-b) are compared to the total power curve it is evident that the magnitude and asymmetry of the $Re[\sigma_{hhhv}]$

term causes the major part of the total orientation shifts of 8° and 13.2°, respectively in the figures. The shifts caused just by the σ_{hhhv} term for the entire profile may be calculated and compared with those shifts obtained using a search algorithm for the signature maxima. Assuming that the dominating factor in the co-pol maximum shift is caused by a summation of the σ_{hhhv} and σ_{hhhh} terms then the synthesized power (normalized by σ_{hhhh}) can be written as

$$\sigma_o = 0.25(1 + cos2\psi)^2 + A(1 + cos2\psi)sin2\psi \quad (5)$$

where, A = Re[σ_{hhhv}]. The position of the co-pol maximum can be found by finding the roots of

$$2Acos2\psi(1 + cos2\psi) - (1 + cos2\psi)sin2\psi - 2Asin^2 2\psi = 0 \quad (6)$$

The co-pol maximum position has been computed using (6) and for the samples where the range of angle values are between 0° and 30°.

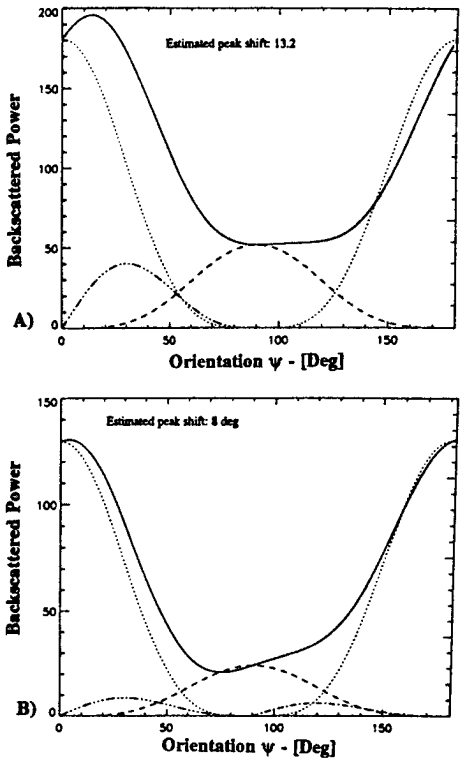


Fig.2: Signature decomposition of Black Forest backscatter for two different terrain slopes along an azimuthal profile. Total power: solid line, weighted components, σ_{hhhh}: dotted line, σ_{vvvv}: dashed line, Re[σ_{hhhv}]: dash dot dot dot line, and Re[σ_{hvvv}]: dash dot line.

In this range the synthesized power approximation using only the σ_{hhhh} and σ_{hhhv} terms gives a good estimation of the co-pol maximum position. The correlation between slope profiles using the approximation and the full search algorithm is 0.878.

The cross term σ_{hhhv} can be related to the azimuthal symmetry properties of forest scatterers. By symmetry we mean reflection symmetry about a horizontal plane. Intuitively an azimuth terrain tilt will introduce a distortion in the symmetry properties of distributed scatterers such as in a forest. The flat terrain symmetry properties might, for example, be dominated by the orientation of trunk or branch structure. It should be noted that scattering from the actual ground-plane is not a condition for the technique to work. The resolution cell symmetry is the important parameter and it is altered when an azimuthal slope is present. Therefore it can be inferred that the slope estimation algorithm will work well in all cases (open- or forested terrain) where the topography (in the azimuthal direction) modulates the symmetry properties of the resolution cell.

CONCLUSIONS

A new polarimetric SAR technique has been developed which is capable of measuring terrain slopes/elevations in the azimuthal direction over wide areas. Slope distributions generated by the technique agree well with co-registered slope ground-truth.

An explanation for the origin of the orientation shift has been developed. Slope-induced changes in Stokes matrix components related to symmetry within the resolution-cell cause the shifts. This concept has been supported by analysis using polarimetric SAR image data.

ACKNOWLEDGMENTS

We thank the NASA/JPL AIRSAR team for providing the polarimetric SAR data used in these studies. Thanks are also due to Drs. A.J. Sieber, J.P. Malingreau, and Mr. H. De Groof (JRC Ispra, Italy) for their help and support.

REFERENCES

[1] D.L. Schuler, J.S. Lee, and G. De Grandi, "Measurement of topography using polarimetric SAR images" IEEE Trans. Geoscience and Remote Sensing, 1996 (in press).

[2] G.G. Lemoine, "On polarimetric signatures", Proc. Geosci. Remote Sensing Symp. (IGARSS'92), Houston, TX, vol.II, 1992, pp. 913-915.

A NEW METHOD FOR EXTRACTING TOPOGRAPHIC INFORMATION FROM A SINGLE MULTISPECTRAL IMAGE

Mark J. Carlotto, PSR Corp., 1400 Key Blvd. Suite 700, Arlington VA 22209 (mjcarlotto@ma.psrw.com)

Abstract -- A new method for extracting the variation in brightness due to topography (topographic component) from multispectral imagery is described. A lookup table relates multispectral brightness values within a training area to the topographic component computed from elevation data for a given reflectance model. The lookup table can then be used to determine the topographic component directly from the imagery in areas where elevation data does not exist.

INTRODUCTION

Techniques which estimate topography from a single image (shape-from-shading, or photoclinometry) convert shading information into slope that is, in turn, integrated to form an elevation surface. If we assume that atmospheric effects have been removed, the brightness in a multispectral image at pixel (i,j) in band n is given by

$$b(i,j,n) = a(i,j,n)t(i,j) \tag{1}$$

where $a(i,j,n)$ is the spectral albedo and $t(i,j)$ is the brightness due to the topography (topographic component). It is usually assumed that the topographic component does not depend on wavelength. When the albedo of the surface is constant over the area brightness is related to slope by the reflectance map [1]. Except in limited situations (e.g., planetary surfaces, terrestrial deserts and snow), surfaces are covered by different materials so the albedo must also be treated as a variable. In a previous approach [2], multispectral imagery is clustered into regions with similar spectral properties using band ratios. Under certain conditions, the average value of a band over each region can be used as an estimate of the albedo of the region. The topographic component can then be estimated by dividing a band by its albedo. The performance of this approach depends critically on the clustering.

METHOD

We estimate the topographic component directly from multispectral imagery without clustering. It is assumed that surface reflectance function is known (or can be assumed), and that elevation data is available over a representative portion of the image (training area). Over the training area elevation data is coregistered to the image and used to compute a lookup table that can be used to estimate the topographic component directly from the multispectral image over areas where elevation data does not exist.

For a Lambertian surface the topographic component is

$$t(i,j) = \max\left\{ \frac{1 + p(i,j)p_0 + q(i,j)q_0}{\sqrt{\left[1 + p^2(i,j)q^2(i,j)\right]\left[1 + p_0^2 + q_0^2\right]}}, 0 \right\} \tag{2}$$

where p_0 and q_0 are the i- and j-gradients in the direction of the sun. The i- and j-gradients of the surface at (i,j) are

$$\begin{aligned} p(i,j) &= \left[e(i,j) - e(i-1,j)\right]/\Delta_i \\ q(i,j) &= \left[e(i,j) - e(i,j-1)\right]/\Delta_j \end{aligned} \tag{3}$$

where $e(i,j)$ is the elevation, and Δ_i and Δ_j are the sizes of an elevation cell (i.e., its resolution) in the i and j directions.

Instead of using elevation data, we seek an estimate of the topographic component as a function of the brightness values:

$$\hat{t}(i,j) = f\left[b(i,j,1),\ldots b(i,j,N)\right] = f\left[\mathbf{b}(i,j)\right] \tag{4}$$

Assume that a relationship exists between the brightness values and the topographic component. Let $\mathbf{b}_K = \left[b(1),\ldots b(N)\right]$ denote the k-th unique combination of the N brightness values within the training area. The joint probability distribution $p(t,\mathbf{b}_K)$ is proportional to the number of times the t-th value of the topographic component (Eq. 2) occurs together with the k-th combination of brightness values. The function that minimizes the mean-square error between the topographic component derived from the elevation (Eq. 2) and topographic component estimated from the brightness (Eq. 4) is given by the conditional expected value [3]

$$f\left[\mathbf{b}_k\right] = \frac{\sum_{(i,j)\in R_k} t(i,j)p\left(t(i,j),\mathbf{b}_k\right)}{p\left(\mathbf{b}_k\right)} \tag{5}$$

where $p\left(\mathbf{b}_k\right) = \sum_t p\left(t,\mathbf{b}_k\right)$ and R_k is the region in the image occupied by the k-th combination of brightness values, i.e., the (i,j) where $\mathbf{b}(i,j) = \mathbf{b}_k$.

The above function can readily be implemented as a lookup table. The topographic component for brightness value combinations not in the training area and thus not represented in the lookup table are interpolated to the nearest value in the table.

0-7803-3068-4/96$5.00©1996 IEEE

EXPERIMENTAL RESULTS

Our method has been evaluated using Landsat TM imagery and USGS digital elevation models (DEMs). In order to reduce the complexity of the algorithm and the size of the lookup table, we used the first three Landsat TM principal components. Figure 1a shows the first principal component over a study area that includes the eastern portion of Albuquerque, NM and the Sandia Mountains. The full image is 1361 x 1285 pixels. This area is particularly challenging for shape-from-shading due to the variety of land cover categories. The DEM was resampled to 25 meters and registered to the imagery (Figure 1b).

A 200 x 200 pixel training area extracted from near the center of the study area is shown in Figure 2a. Figure 2b is the topographic component computed from the DEM using a Lambertian reflectance map. Within the training area, 14,538 unique combinations of the three principal component values were found. Figure 2c is the topographic component estimated from the three principal component images by our method.

We then used the lookup table to estimate the topographic component from the Landsat imagery outside of the training area. Figure 3a shows the topographic component derived from the DEM over the full study area. Figure 3b is the topographic component estimated from the imagery using the lookup table derived over the training area. The full study area contained 133,213 unique combinations of the three Landsat TM principal component values. Thus within the study area only about 10% of the spectral diversity of the image is represented. Results over a 200 x 200 pixel area south-southeast of the training area are shown in Figure 4.

CONCLUSION

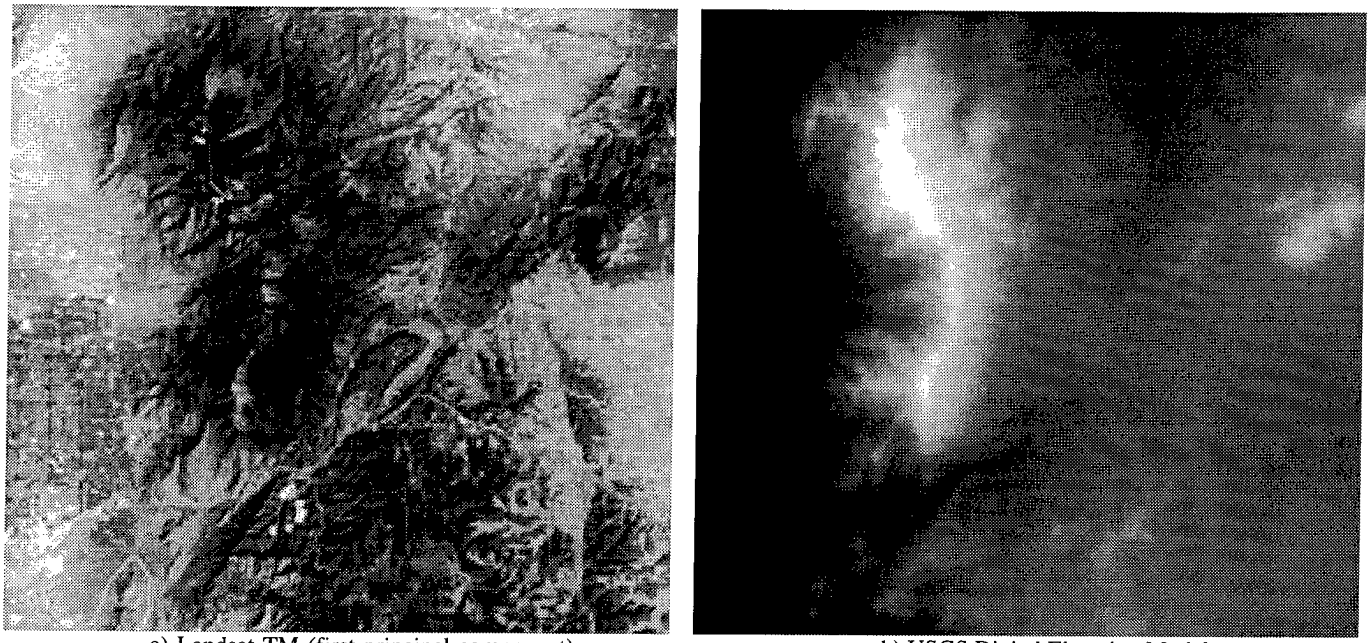
A new method for extracting topographic information from multispectral imagery has been described. Within the training area, the method is able to spatially enhance the topographic component, revealing subtle detail not visible in the lower resolution DEM. On average, the value of the topographic component computed from the imagery is about the same as that computed from the DEM. Outside of the training area the topographic component can be extracted from multispectral imagery over areas where elevation does not exist. However, the value of the topographic component computed from the imagery was lower on average than that computed from the DEM. We have found that this bias can be reduced by increasing the size of the training area. Better understanding the training requirements of the algorithm is an area of future work.

References

[1] B.K.P. Horn, "Understanding image intensities," *Artificial Intelligence*, Vol. 8, pp 201-231, 1977.

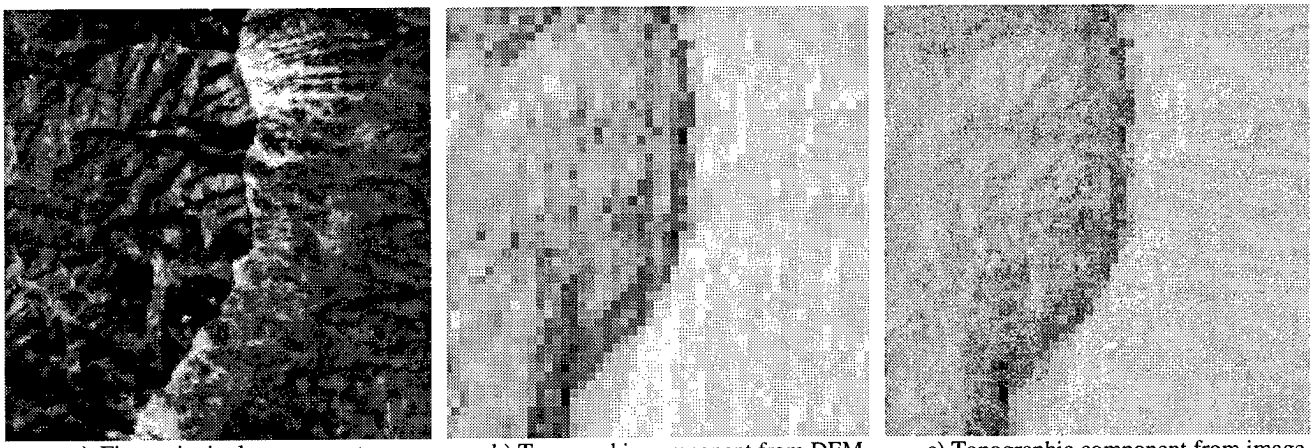
[2] P. Eliason, L. Soderblom and P. Chavez, "Extraction of topographic and spectral albedo information from multispectral images, *Photogrammetric Engineering and Remote Sensing*, Vol. 48, No. 11, pp 1571-1579, 1981.

[3] A. Papoulis, *Probability, Random Variables and Stochastic Processes,* McGraw-Hill, 1965.



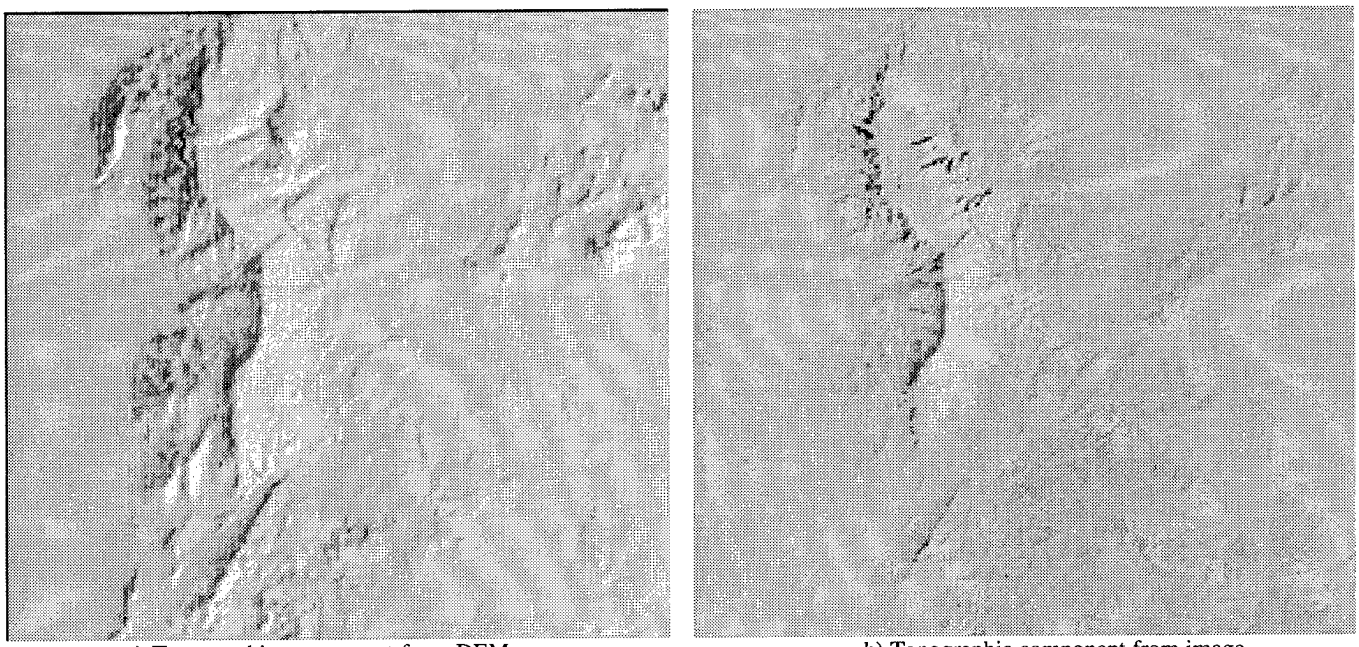
a) Landsat TM (first principal component) b) USGS Digital Elevation Model

Figure 1 Full study area -- Albuquerque and Sandia Mountains



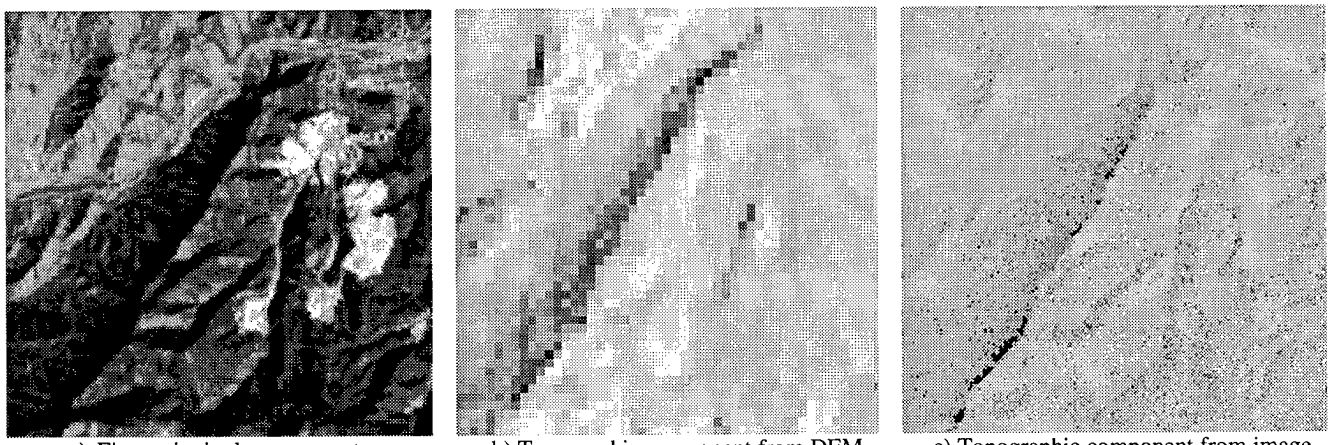
a) First principal component b) Topographic component from DEM c) Topographic component from image

Figure 2 Training area



a) Topographic component from DEM b) Topographic component from image

Figure 3 Results comparison over full study area



a) First principal component b) Topographic component from DEM c) Topographic component from image

Figure 4 Evaluation outside of training area

Thermal Emission from Rough Terrain: Anisotropy and Its Possible Consequences on Satellite Image Interpretation

Sauli Jamsa
Research Scientist, Finnish Geodetic Institute
Geodeetinrinne 2, FIN-02430 Masala, Finland
tel: +358-0-29555213, fax: +358-0-29555200
email: Sauli.Jamsa@fgi.fi

Abstract

The thermal emission from a rough terrain is generally not equal in all directions, due to variations in surface temperature. These variations can be caused by differing exposition to sunshine, wind, or moisture etc. In this paper we study the effects of a non-uniform surface temperature on the anisotropy of the surface's thermal emission, and the consequences it may have on the interpretation of satellite images. The temperature distributions here are hypothetical, i.e. not yet measured in nature, but the examples indicate that more information could be derived from satellite images than is currently being done. One could erroneously interpret two pixels of an image being of different types of terrain, when the differing signal is partly or entirely due to anistropic emission.

1 INTRODUCTION

Satellites carry two basic types of thermal imagers: conical and line scanners. A line scanner scans the ground in a linear motion across the track of the satellite, and thus produces a single image by adjusting the speed of its rotating mirror so that succeeding scans slightly overlap. A conical scanner rotates around a cone whose center axis points usually about 25 degrees forward from the nadir, and whose opening angle is twice this angle. Conical scanners form two distinct images of the ground: the first is formed by scans along the rear side of the cone (approximately, but not quite, like a line scanner), and the other by scans along the front side of the cone, at a larger angle from the nadir. The advantage of having two images is that the atmospheric attenuation of the signal can be more accurately estimated than from a single image alone.

There is, however, another advantage of conical scanners compared to linear scanners that has generally been overlooked. That is the detection of anisotropy in the radiation leaving the ground. A line scanner can only detect intensity differences in the vertical plane perpendicular to the track of the satellite (across track), but a conical scanner can in addition, due to its viewing geometry, detect intensity differences in the vertical plane that contains the track.

In Sect. 2 we give two examples of hypothetical, but quite plausible, temperature distributions on the surface of a non-planar terrain. In Sect. 3 we give the polar and azimuth angles of the radiation leaving the ground towards a line and conical scanner onboard a satellite, and Sect. 4 contains a description how the differences in the polar and azimuth angles, together with the non-uniform temperature, affects a satellite image. Finally, Sect. 5 contains conclusions and discussion, and suggestions for further study.

2 NON-UNIFORMITY OF SURFACE TEMPERATURE

It is a self-evident fact that if a terrain surface is not a smooth plane and the Sun heats it, there may be temperature variations across the surface, due to some parts having an aspect towards the Sun and others away from it, and shading. Here, we assume that the ground is at the freezing temperature $T_g = 273$ K, but that areas with aspect towards the Sun have melted, which allows their temperature to rise. The air temperature T_a is assumed to be 20 degrees above freezing, and the solar constant is $F_0 = 635$ W/m^2 at the site; the zenith angle of the Sun is assumed to be $\pi/4$.

The temperature of a facet on the surface is assumed to be given by

$$T = T' + 0.5 \max[(F_0/\sigma)^{1/4} \vec{n_0} \cdot \vec{n} - T', 0] \quad (1)$$

$$T' = T_g + 0.5\,(T_a - T_g) \max[\vec{n_0} \cdot \vec{n}, 0], \quad (2)$$

where σ is Stefan-Boltzmann constant, $\vec{n_0}$ is the unit vector towards the Sun, and $\vec{n}$ is the facet's unit normal. Eq.

0-7803-3068-4/96$5.00©1996 IEEE

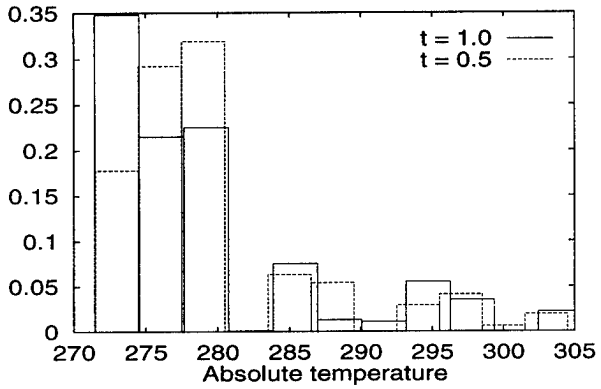


Figure 1: Predicted temperature distributions on a surface with Gaussian height statistics, that are used in deriving the IR intensity detected by line and conical scanners onboard a satellite. Dashed line: the standard deviation of the tangent of the surface normal's zenith angle is 0.5; solid line: it is 1.0. The ordinate gives the percentage of surface area, projected onto the horizontal plane, at the indicated temperature interval. The solar zenith angle is $\pi/4$, and in this case the distributions don't depend on the Sun's azimuth angle.

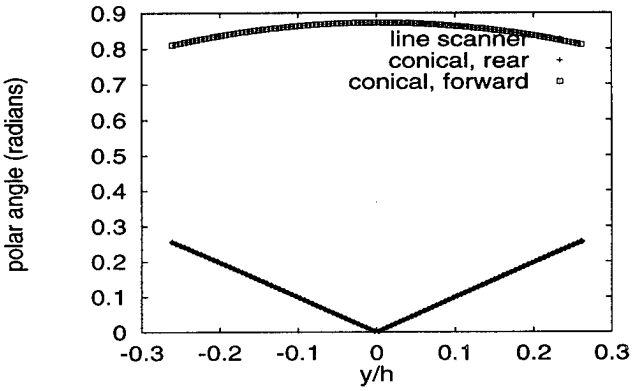


Figure 2: Polar angle of radiation leaving the ground at horizontal distance $\alpha = y/h$ from the satellite ground track, towards a line scanner, and towards a conical scanner with opening angle of 50 degrees during its rear and forward scans. The curve for the conical scanner's rear scan is nearly identical to that of the line scanner. The boxes represent the conical scanner's forward scan.

2 gives an estimation of the air heating contribution (note that the temperature of the frozen, shadowed facets cannot rise until they melt), and Eq. 1 gives that of the Solar contribution.

We give two examples of different non-planar terrains, both described with Gaussian height statistics. The height z probability of a surface point is [3]

$$n(z,\rho) = \exp(-z^2/2\rho^2)/(\sqrt{2\pi}\rho), \tag{3}$$

where ρ is the standard deviation of z, and the mean of z is chosen to be zero. It has been shown that, under certain assumptions about the autocorrelation of the surface heights, the inclination t (defined as the tangent of the zenith angle of the normal of a facet) also has Gaussian statistics. In these examples, we give values 0.5 and 1.0 to the standard deviation of t. Gaussian surface statistics are discussed more thoroughly in [3] and [2].

The temperature distributions in the two cases, resulting from Eqs. 1 and 2, are shown in Fig. 1.

3 VIEWING GEOMETRY OF SCANNERS

Let us set an xyz coordinate system on the ground such that the origin is below the satellite, x-axis pointing forward, y-axis to the left, and z-axis upward, and use the common notation for polar coordinates, $x = r\sin\theta\cos\phi$, $y = r\sin\theta\sin\phi$, $z = r\cos\theta$. Let the satellite altitude be h, and define $\alpha \equiv y/h$.

Then the vector $\vec{u}$ from the surface point that a conical scanner is viewing at time τ is

$$u_x = \frac{-h[\sin\gamma - \sin(\gamma\cos\omega\tau)]}{\cos\gamma + \tan\gamma\sin(\gamma\cos\omega\tau)} \tag{4}$$

$$u_y = \frac{\mp h\sqrt{\cos^2(\gamma\cos\omega\tau)/\cos^2\gamma - 1}}{\cos\gamma + \tan\gamma\sin(\gamma\cos\omega\tau)} \tag{5}$$

$$u_z = h, \tag{6}$$

where ω is the angular velocity of the scanner, and τ is the time, chosen to be zero when looking at the nadir.

The scanner phase $\varphi \equiv \omega\tau$ as a function of α is given by

$$\sin(\gamma\varphi) = \frac{\alpha^2\sin\gamma\cos^2\gamma \pm \sqrt{\sin^2\gamma - \alpha^2(\cos^4\gamma - \sin^4\gamma)}}{1 + \alpha^2\sin^2\gamma}, \tag{7}$$

where the upper (lower) sign corresponds to the rear (front) side scan of the cone. The polar and azimuth angles as a function of α are given, for $\gamma = 25$ degrees, in Figs. 2 and 3.

4 EFFECTS ON A SATELLITE IMAGE

In this example, we assume that the Sun's azimuth angle in our coordinate system as described in Sect. 3 is $\phi_0 = 3\pi/4$, i.e. it shines from the left hand side behind the

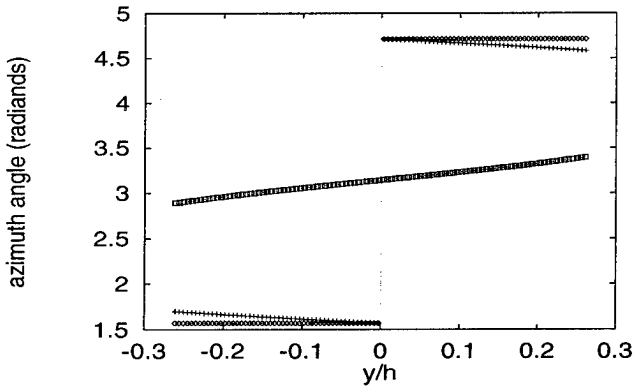


Figure 3: Same as in Fig. 2, but for azimuth angles instead of polar angles. The diamonds (lowest and highes curves) represent the line scanner, the plus signs the conical scanner's rear scan, and the boxes its forward scan.

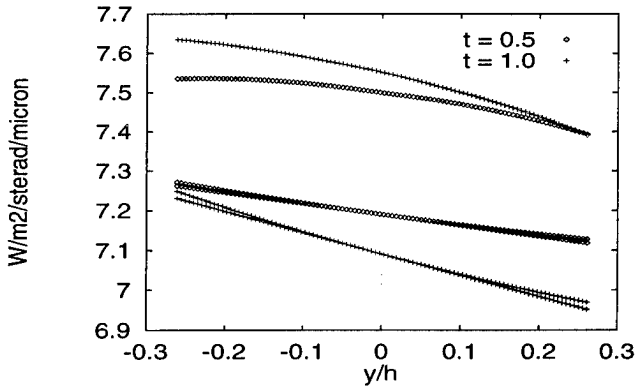


Figure 4: Infrared intensity leaving the ground towards a satellite as a function of $\alpha \equiv y/h$. The diamonds represent results for the temperature distribution with the standard deviation of inclination t equal to 0.5, and the plus signs represent those when it is 1.0. In both cases, there are three curves: the lowest (line scanner result) is almost identical with the conical scanner's rear scan result, but the third (conical scanner's forward scan) is quite distinct. The opening angle of the cone is 50 degrees.

satellite. The surface facets that have an aspect towards the Sun (i.e. the warmest) are best seen to the right forward of the satellite, and therefore the signal from there is the greatest. In Fig. 4 we give the IR intensity leaving the ground towards the detector as a function of α.

The plots in Fig. 4 represent the IR intensity leaving the ground, i.e. they correspond to the detector signal after correcting for the atmospheric attenuation. The attenuation is greater in the forward scan of the conical scanner, and so the detected intensity difference will be smaller than the difference at ground level. Nevertheless, if the signal after the correction shows such a systematical difference between the rear and forward scans, one could conclude that the IR emission of the terrain is anisotropic, and one possible cause for that is the topography, together with sunshine or other heat source.

5 CONCLUSIONS AND DISCUSSION

The temperature distribution resulting from the topography in this paper is hypothetical, but the calculated results show that they cause an observable effect on a satellite image. There is no doubt that nature can exhibit quite large temperature variarions in a small area, e.g. on deserts in the morning after a cold night when the Sun has started to warm it, but there are still a lot of shadows. For a discussion how the Sun and the atmosphere affect the surface temperature of the ground, see [1].

No attempt has been made to compare real satellite images obtained by the rear and forward scans of a conical scanner. Such images exist, e.g. from the ERS1 ATSR device, but they are commonly produced together, and the final product is a surface temperature map. This temperature is close to the average temperature of the pixel, but it would be interesting to compare the two images before they are merged, to see if one could estimate the non-uniformity of the temperature also.

ACKNOWLEDGMENTS

The author thanks Dr. Ian Main of the University of Edinburgh for extremely valuable comments during the preparation of the manuscript, and Dr. Mario Antonioletti of the Edinburgh Parallel Computing Centre for his help in preparing the figures.

References

[1] G.J.Zissis (Ed.), The Infrared and Electro-optical Systems Handbook Vol. 1: Sources of radiation, SPIE Optical Engineering Press, c1993

[2] S.Jämsä, J.I.Peltoniemi, K.Lumme, Thermal emission from a rough surface: ray optics approach, A&A 271, 319-325 (1993)

[3] K. Lumme, J. I. Peltoniemi, W. M. Irwine, Diffuse reflection from stochastically bounded, semi-infinite media, Transp. Theory & Stat. Phys. 19 (3-5), 317-332, (1991)

Validation of Land-Surface Temperature Retrieval from Space

Zhengming Wan, Will Snyder and Yulin Zhang
Institute for Computational Earth System Science
University of California, Santa Barbara, CA 93106, USA

Abstract — We developed an integrated field TIR (thermal infrared) measurement system and methodology for validating land-surface temperature (LST) algorithms prepared for generating the EOS (Earth Observing System) MODIS (Moderate Resolution Imaging Spectroradiometer) LST product. The system has been used for measurements of spectral TIR BRDF (bidirectional reflectance distribution function) / emissivity and surface temperature of terrestrial materials in laboratory and field campaigns. Our validation results indicate that it is possible to validate LST within 1 °K in favorable atmospheric and surface conditions.

INTRODUCTION

Land-surface temperature (LST) is one of the key parameters in the physics of land-surface processes on a regional as well as global scale, combining the results of all surface-atmosphere interactions and energy fluxes between the atmosphere and the ground. Therefore it is required for a wide variety of climatic, hydrological, ecological and biogeochemical studies. In order to understand the entire Earth system better on the global scale, the Earth Observing System (EOS) will provide surface kinetic temperatures at specified accuracies of 0.3 °K for oceans and 1 °K over land.

MODIS (Moderate Resolution Imaging Spectroradiometer) is an EOS instrument that will serve as the keystone [1] for global studies of atmosphere, land, and ocean processes. It scans ±55° from nadir in 36 bands, with bands 1-19 and band 26 in the visible and near infrared range, and the remaining bands in the thermal infrared from 3 to 15 μm. It will provide images of daylight reflection and day/night emission of the Earth every 1-2 days, with continuous duty cycle. It uses 12 bits for quantization in all bands. The thermal infrared bands have an IFOV (instantaneous field-of-view) of about 1 km at nadir. MODIS will view cold space and a full-aperture blackbody before and after viewing the Earth scene in order to achieve calibration accuracy of better than 1% absolute for thermal infrared bands. MODIS is particularly useful because of its global coverage, radiometric resolution and dynamic ranges, and accurate calibration in multiple thermal infrared bands designed for retrievals of SST, LST and atmospheric properties.

Two LST algorithms have been developed for retrieving LST from MODIS data. The generalized split-window LST algorithm [2, 3] will be used to retrieve LST for surfaces with relative stable emissivities that can be referred from land cover types and a knowledge base of surface emissivities. A new physical based day/night LST method [4] will be used to simultaneously retrieve surface band-averaged emissivities and daytime and nighttime temperatures from day-night pairs of MODIS thermal infrared data. We have developed an integrated field TIR measurement system and methodology for validating these LST algorithms. Several field campaigns have been conducted and more validation activities have been planned.

VALIDATION OF MODIS LST ALGORITHMS

Overall Approach The validation is a comparison between temperatures retrieved from in-situ measurements and those retrieved from airborne and satellite thermal infrared data. Test sites such as silt playas and inland lakes have been chosen because their in-situ surface temperatures can be measured more accurately. These areas primarily validate the atmospheric correction and emissivity-extraction portions of the MODIS LST algorithms. We also plan to make in-situ measurements of surface temperature for validation over a wider variety of land cover types. After MODIS's launch these same techniques will be applied to validate the MODIS LST product.

Sampling Requirements Spectral requirements: spectral emissivities of land covers need to be measured in order to validate band-averaged surface emissivities. Spatial requirements: product validation needs to be carried out for different land cover types and different latitudes. This sampling should include a range of surface temperatures and atmospheric conditions. The land cover types will include prototypes of the main groups such as desert, bare soil, crop-land, grassland, forests, water, snow and ice. For unstructured surfaces, the in-situ measurements can be made with transects large enough to represent the aerial pixel average. For structured surfaces, tower or high-standing measurements will be required. Ideal test sites are in flat areas with size larger than 3km by 3km covered with uniform or uniformly mixed surface materials so that the uncertainty in spatial sampling could be significantly reduced. Temporal requirements: For in-situ measurements the short-term changes in temperature (in scale of seconds) are difficult to quantify, so weather conditions for such measurements must be stable (constant wind speed). In each validation field campaign, in-situ measurements will be made at least for a half hour to ensure the overpass of airborne and/or satellite flights is covered. LST need to be monitored monthly or each season throughout the year.

0-7803-3068-4/96$5.00©1996 IEEE

The requirements for temporal sampling depend on latitude, and can be combined with the requirements for spatial sampling. In other words, we need a range of surface temperatures and atmospheric conditions. Angular requirements: The surface temperature algorithm should be validated over the range of MODIS look angles. Since there are more than one looks per day at high latitudes due to overlap and MAS (MODIS Airborne Simulator) views the Earth surface at different look angles, in-situ measurements should be made at multiple view angles at ground validation sites. For daytime measurements, a range of sun angles also must be incorporated for validation of the mid-infrared band processing and for validation of the mixed-temperature model with structured surfaces.

Measures of Success The metric for measures of success will be the difference between the surface temperature from in-situ measurement data and that retrieved from airborne or satellite data. Since there are errors in both the ground measurements and the aerial measurements, the success criterion will depend on the ground measurement accuracy as well as the accuracy of airborne and satellite data. All major components of the instrument used in ground measurements should be carefully calibrated. The success criterion will also depend on atmospheric and surface conditions. It is critical to have high quality ground measurements data with smooth temporal and spatial variations in order to reduce the uncertainties in temporal interpolation, spatial sampling, and geometric co-registration. Records of the atmospheric and surface weather conditions, analysis of temporal and spatial variations should be provided with the difference between LST values from in-situ measurements and those retrieved from airborne and satellite data for each field campaigns. The LST product will be considered valid when the standard deviation of LST differences is smaller than or around 1 °K and the uncertainties in instrument calibrations, temporal and spatial variations are well below 1 °K.

Instrumentation and Methodology Surface temperature measurements can be made with contact sensors, hand-held infrared thermometers as wideband radiometers, and infrared spectrometers. Transects will be made with infrared thermometers. The contact sensors are primarily for water surface temperature measurements. The spectrometers do not translate easily, but they can scan a range of angles to provide temporal and angular spectral surface radiance and atmospheric downwelling radiance (from a diffuse reflector). Temperature is recovered directly from the contact sensors. The downwelling radiance, instrument calibrations, and surface emissivity must be applied to compute the temperature from the non-contact sensors. Spectral directional-hemispherical emissivity can be measured with an integrating sphere facility which includes a Fourier transform infrared (FTIR) spectrometer and a 5-inch infragold integrating sphere. The spectrometer has sensitivity both in the mid and thermal infrared, covering all MODIS bands of interest for LST. This instrument is primarily used for emissivity measurements of samples such as ice, water, silt, sand, soil, leaf surface, etc. The surface roughness of these samples is limited to a few millimeters. Field measurements of BRDF (bidirectional reflectance distribution function) / emissivity are made with the SIBRE (Spectral Infrared Bidirectional Reflectance and Emissivity) instrument, which includes a hemispherical pointing system, FTIR spectrometer, a TIR source, and reference plates. The effect of surface temperature change due to the thermal source heating is carefully corrected [5]. Samples of approximately one square foot are measured with 187 source-sensor geometries. An abbreviated measurement set of 45 geometries is an alternative for materials whose BRDF shapes are reasonably well known. For each geometry, there are 1232 spectral samples from 3.3 to 14.5 microns. These can be integrated to provide band-averaged values for MODIS or MAS. The spot size viewed by the InSb/MCT sandwich detector is approximately 3cm diameter so materials with some small-scale surface structure can be examined. We also have a beam expander that gives a 10cm spot for more structured surfaces. We can recover angular spectral emissivity (but not BRDF) from absolute radiance measurements using a sun-shadow technique. Our goal for the sun-shadow method is to increase the spot size to an half meter so that band-averaged emissivities and radiometric temperature of structured surfaces such as vegetation canopy can be measured.

Some Validation Results We validated the sun-shadow method with measuring samples of soil, sands, grass and a black aluminum plate on the roof platform of our building at UCSB on January 19th and 26th, 1996. The solar beam is blocked for an half of the samples. The TIR spectrometer views the portions in sunshine and in shadow for two separate measurements and also views a diffuse reflecting gold plate in the same spots for providing information of the solar and atmospheric downwelling radiation. After calibrating the spectrometer with blackbody at three different temperatures, another two separate measurements are made. For each sample, we obtained two pairs of data for the sunshine and shadow portions and the diffuse reflecting gold plate. A band average procedure with the spectral response functions in 7 MODIS TIR bands (i.e., 20, 22, 23, 29, 31, 32, and 33) is used to achieve a high signal-to-noise ratio. Radiometric calibration is made with 3 blackbody temperatures, spectral emissivity of the blackbody surface and the front mirror, and the temperature of the front mirror. Then we use two methods to recover the surface temperature. In the conventional method, we use the spectral emissivity curves of samples measured with the integrating sphere system. In the sun-shadow method, we make non-linear χ^2 fit of the sun-

shadow data set for recovering surface temperatures in sunshine and in shadow, and the band-averaged emissivities. The LST values of samples of sand, soil, grass and black plate in sunshine and in shadow recovered by these two methods are shown in Fig. 1. Noted that the mark squares represent the first method. The standard deviations are 0.4 °K and 0.1 °K, and the maximum LST differences are 0.7 °K and 0.2 °K, for the LST difference in sunshine and in shadow, respectively.

We conducted a field campaign with the JPL (Jet Propulsion Laboratory) ASTER (Advanced Spaceborne Thermal Emission and Reflection Radiometer) team at a large flat silt playa site in Railroad Valley, Nevada, on August 3rd, 1995. MAS and TIMS (Thermal Imaging Multispectral Spectrometer) data, and field measurement data of surface spectral emissivity and temperature with TIR spectrometer and broadband radiometer were collected. Temporal and spatial analysis has been made. As shown in Table I, LST retrieved from MAS data using the generalized split-window LST algorithm at view angle (θ_v) 18.95 ° agrees with field measurement LST values within 1 °K. In this case, the LST accuracy is mainly limited by the uncertainty in its spatial variation. The MAS was calibrated with the new method [6].

CONCLUSION

We developed an integrated field TIR measurement system and methodology for validating MODIS LST algorithms. Our validation results indicate that it is possible to validate LST within 1 °K in favorable atmospheric and surface conditions.

Acknowledgments — This work was supported by EOS Program contract NAS5-31370 of the National Aeronautics and Space Administration.

REFERENCES

[1] V. Salomonson, W. Barnes, P. Maymon, H. Montgomery, and H. Ostrow, "MODIS: advanced facility instrument for studies of the Earth as a system," *IEEE Trans. Geosci. Remote Sens.*, vol. 27, no. 2, pp. 145-153, 1989.

[2] Z. Wan and J. Dozier, "Land-surface temperature measurement from space: physical principles and inverse modeling," *IEEE Trans. Geosci. Remote Sens.*, vol. 27, no. 3, pp. 268-278, 1989.

[3] Z. Wan and J. Dozier, "A generalized split-window algorithm for retrieving land-surface temperature measurement from space," *IEEE Trans. Geosci. Remote Sens.*, in press 1996.

[4] Z. Wan and Z.-L. Li, "A physical based algorithm for retrieving land-surface emissivity and temperature from EOS/MODIS data," *IEEE Trans. Geosci. Remote Sens.*, submitted 1996.

[5] W. Snyder and Z. Wan, "Surface temperature correction for active infrared reflectance measurements of natural materials," *Appl. Optics*, in press 1996.

[6] M. D. King, W. P. Menzel, P. S. Grant, J. S. Myers, G. T. Arnold, S. E. Platnick, L. E. Gumley, S. C. Tsay, C. C. Moeller, M. Fitzgerald, K. S. Brown, and F. G. Osterwisch, "Airborne scanning spectrometer for remote sensing of cloud, aerosol, water vapor and surface properties ," *J. Atmos. Ocean. Technol.*, submitted 1995.

Table I. Summary of LST values over the test site (38' 31.46'N, 115' 42.74'W) in Railroad Valley, NV during 1:22 and 1:30 PDT on 8/3/95.

size of area	mean (°K)	stdv (°K)	remarks
12 cm diameter	58.5		by radiometer
5 cm diameter	59.2		by spectrometer
1 MAS pixel	59.1		at θ_v 18.75 °
3 by 3 MAS pixels	58.9	0.48	
5 by 5 MAS pixels	58.8	0.67	
7 by 7 MAS pixels	58.9	0.76	
9 by 9 MAS pixels	59.0	0.81	
11 by 11 MAS pixels	58.9	0.82	
21 by 21 MAS pixels	58.9	1.21	

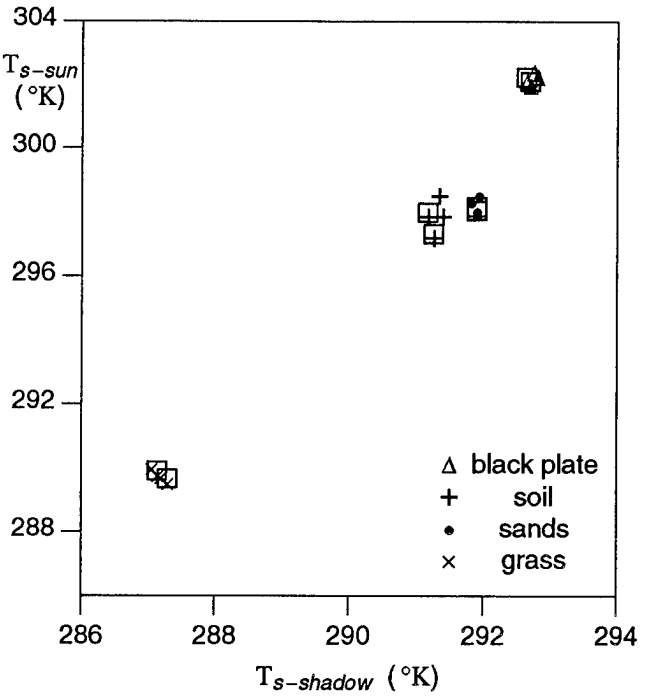


Fig. 1, LST values retrieved by using two methods.

Land Surface Temperature Retrieval from AVHRR: Influence of Surface Emissivity and Atmospheric Water Vapor

Moira L. Steyn–Ross and D. Alistair Steyn–Ross
Physics Department, University of Waikato
Hillcrest Road, Private Bag 3105, Hamilton, NEW ZEALAND
ph: +64-7-838-4026 / fax +64-7-838-4219 / email: asr@waikato.ac.nz

Abstract -- The retrieval of land surface temperatures (LSTs) from satellite infrared radiometry is a more challenging problem than the corresponding surface temperature retrieval over sea. This because of problems associated with defining the surface, large spatial variablity exhibited by LSTs, unknown surface emissivity, and variable atmospheric water vapor column.

We present a method which retrieves LSTs from AVHRR radiances sensed through atmospheres with large and strongly varying water vapor content. The method recognizes that the emissivities are unknown, but likely to lie within a narrow range which is close to, but less than, unity. We have applied this method to the satellite and *in-situ* data obtained from the 1989 FIFE (First International Satellite Land Surface Climatology Project (ISLSCP) Field Experiment) in Kansas. Results show our method outperforms standard fixed coefficient algorithms which over-simplify atmospheric effects.

INTRODUCTION

The thermal infrared channels of the advanced very high resolution radiometer, AVHRR, (channel 4: 10.8 μm; channel 5: 11.9 μm) have been used successfully to measure SST for well over a decade.

Many workers have examined the practicality of retrieving LSTs from AVHRR; see Prata [1] for a comprehensive review. In principle, given a pair of at-satellite radiances in channels 4 and 5, an LST algorithm must solve the equations of transfer for surface temperature. The two channels provide two equations but there are five unknowns: surface temperature, surface emissivities ε_4, ε_5 corresponding to channels 4 and 5, and the atmospheric contributions to the at-satellite radiances of channels 4 and 5. The atmospheric contribution can be estimated by initializing an atmospheric transmission model, such as LOWTRAN-7 [2], with local radiosondes or historical climatologies, thus reducing the number of unknowns to three: (ε_4, ε_5, T_S). LST retrieval follows with a specification of the emissivities. The LST retrieval scheme which we describe in the next section assumes that the emissivities are essentially spectrally independent, $\varepsilon_4 \approx \varepsilon_5 = \varepsilon_{req}$, with ε_{req} being a 'requested' emissivity estimate which may be less than or equal to unity, based on some knowledge of land type.

DYNAMIC WATER VAPOR METHOD

Our LST algorithm is a generalization of the dynamic water vapor (DWV) method of Steyn-Ross *et al.*, [3]: A regression-free approach to the problem of retrieving accurate SSTs in the presence of strongly varying water vapor. A first-guess water vapor profile is dynamically tuned until the SSTs predicted by the equations of transfer for channels 4 and 5 converge.

The need for water vapor tuning over land targets is indicated by the experiments of Bruegge *et al.* [4] who estimate that surface topography and vegetation induce variations in water column across the 15- by 15-km FIFE site of the order of 10 percent.

The generalization of DWV to land targets proceeds as follows: Assuming clear skies, azimuthal independence, and a Lambertian land surface, the monochromatic radiation $I_\nu(\theta)$ at wavenumber ν reaching the radiometer along a slant path of zenith angle θ is the sum of the surface radiation, the reflection of the sky radiance in the surface, and the upwards sky radiance [1]:

$$I_\nu(\theta) = \left[\varepsilon_\nu B_\nu(T_S) + (1-\varepsilon_\nu)L_\nu^{\downarrow}\right]\tau_\nu(\theta) + I_\nu^{\uparrow}(\theta) \qquad (1)$$

where $B_\nu(T_S)$ is the Planck function evaluated at wavenumber ν, surface temperature T_S; $\tau_\nu(\theta)$ is the transmittance along the slant path from surface to satellite; and $I_\nu^{\uparrow}(\theta)$ is the upwelling atmospheric radiance. The quantity $L_\nu^{\downarrow}$ is the downwelling sky radiance averaged over the upper hemisphere.

Assuming that the surface emissivity is constant over the channel i bandwidth, we can replace ε_ν by ε_i and solve (1) to give a pair of equations for emissivity as a function of surface temperature:

0-7803-3068-4/96$5.00©1996 IEEE

$$\varepsilon_4 = \frac{I_4 - I_4^{\uparrow} - \tau_4 L_4^{\downarrow}}{\tau_4 B_4(T_S) - \tau_4 L_4^{\downarrow}} \qquad \varepsilon_5 = \frac{I_5 - I_5^{\uparrow} - \tau_5 L_5^{\downarrow}}{\tau_5 B_5(T_S) - \tau_5 L_5^{\downarrow}} \quad (2)$$

where the individual terms in each numerator and denominator have been integrated over the channel response function. The integrations were replaced by summations whose frequency resolution is set to match that of LOWTRAN-7: $\Delta\nu = 5\ \mathrm{cm}^{-1}$.

Using (2), we plot ε_4 and ε_5 for a range of possible surface temperatures, and locate the temperature and emissivity coordinate (T_x, ε_x) at which the two curves intersect.. If $\varepsilon_x = \varepsilon_{\mathrm{req}}$, then the surface temperature has been retrieved: $T_S = T_x$.

If $\varepsilon_x \neq \varepsilon_{\mathrm{req}}$, the first-guess atmosphere is in error, so adjust the water vapor profile until ε_x and $\varepsilon_{\mathrm{req}}$ agree to within a tolerance band, e.g., $|\varepsilon_x - \varepsilon_{\mathrm{req}}| < 0.0005$.

RESULTS

Field and satellite data used in the validation were gathered in July and August, 1989 as part of FIFE [5]. The surface truth was obtained from infrared themometers (IRTs) located at eight AMS (automatic meteorological station) sites.

We checked, and where necessary corrected, the navigation of 11 NOAA-11 FIFE images using both the public-domain CIA World Database II and the "Digital Chart of the World in ASCII" [6]. The calibration of the thermal channels (conversion from raw channel 4, 5 count to radiance) follows the method described by Steyn-Ross *et al.* [7].

LOWTRAN was initialized with the radiosonde atmospheric soundings from Dodge City and Topeka archived on vol. 1 of the FIFE CD-ROM set.

We ran the DWV-LST algorithm at each of the 8 IRT sites identified in 11 images, for a total of 86 IRT/DWV-LST matchups (two matchups were discarded because of cloud contamination). Assuming the IRT point measurement T_S can be meaningfully compared with the AVHRR-scale LST-DWV retrieval T_x, we computed the bias ($T_x - T_S$) and the rms (standard deviation of this difference) errors for each matchup. The results are presented in Table 1 and Figure 1.

The day and night statistics are quite distinct. For the five night passes, the average bias error is small and positive, while for the six day passes, the bias and rms values are substantially larger. The larger rms error is consistent with the pronounced spatial variabilities expected in daytime surface temperatures. We believe that the large daytime bias in the DWV-LST retrieval arises from the non-representativeness of the IRT sampling of the FIFE region.

Table 1: Average Bias and RMS Errors (K) for DWV, Price, and BT4 Methods

	Night (5 passes)		Day (6 passes)	
Method	Bias	RMS	Bias	RMS
DWV	+0.39	1.11	+4.09	3.10
Price	+0.74	1.14	+6.13	3.13
BT4	-1.52	1.13	-3.32	3.46
No. of matchups	39		47	

The IRT sites were fenced off and therefore well vegetated compared with the surrounding prairie which is grazed and/or burned. Thus the IRT field of view will be predominantly of vegetation, while the AVHRR view (area ~1 km^2) will contain a much larger proportion of sparsely vegetated land.

If there is a vegetation-induced temperature bias, then we would expect the bias error to diminish with satellite scan angle, since at larger angles the satellite radiometer receives more radiation from the cooler canopy and less from the ground. Figure 2 shows the DWV-LST bias errors plotted as a function of scan angle for the 6 day and 5 night passes. The best-fit line through the day pass results seem to support the differentially-vegetated hypothesis. At night the temperatures are more homogeneous, the errors are smaller, and any vegetation effects are probably negligible.

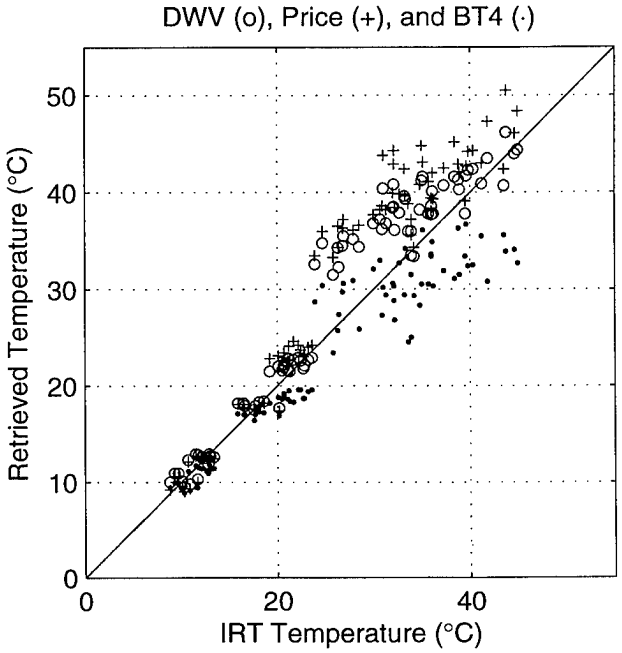


Figure 1. Comparison of retrieved surface temperatures with IRT ground measurements. (a) Circles are DWV-LST retrievals; plus-signs are Price predictions (3); dots are channel-4 brightness temperatures.

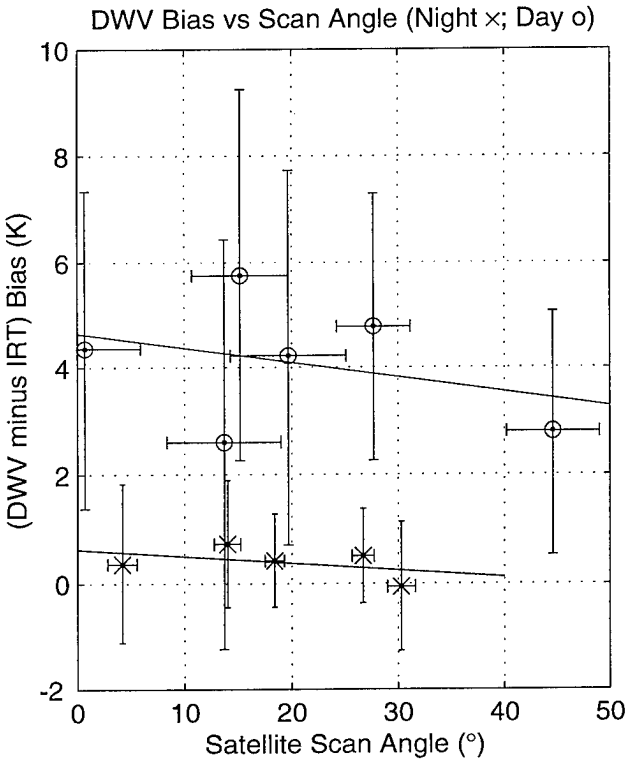


Figure 2. DWV-LST bias errors as a function of AVHRR scan angle for 5 night and 6 day passes. The decreasing trend with angle for the day passes is consistent with a vegetation-induced bias effect. Each vertical error-bar shows the standard deviation in the 8 DWV values for a given pass; the matching horizontal error-bar is the standard deviation in the 8 IRT measurements for that pass.

We compared the DWV-LST with a standard single-line, fixed-coefficient algorithm (Price [8]) which retrieves a surface temperature estimate from a linear combination of the at-satellite brightness temperatures in channels 4 and 5:

$$T_{\text{Price}} = \text{BT}_4 + 3.33(\text{BT}_4 - \text{BT}_5). \quad (3)$$

The comparative results for DWV, Price, and BT4 were shown in Table 1. All three methods have very similar rms values, but very distinct bias values. On average, BT_4 underestimates the IRT reading by 1.5 K at night, and by 3.3 K during the day, indicating that the atmospheric attenuation is not negligible. The fixed-coefficient method (3) is able to compensate partially for atmospheric effects, but not as successfully as DWV-LST. This is not surprising, since the DWV approach corrects for local variations in water vapor column, while the fixed-coefficient algorithm ignores local variability by applying a regression-fitted constant obtained from long-term and large-region averaging.

ACKNOWLEDGMENT

This research was supported in part by a grant from the New Zealand Lottery Science Research Committee.

REFERENCES

[1] Prata, A. J., Land surface temperatures derived from the AVHRR and ATSR, 1, Theory, *J. Geophys. Res.*, *98*, 16,689-16,702, 1993.

[2] Kneizys, F.X., *et al.*, Users guide to LOWTRAN-7, Optical/Infrared Technology Division, *Tech. Rep.*, *AFGL-TR-88-0177,* U. S. Air Force Geophys. Lab., Hanscom Air force Base, Mass., 1988.

[3] Steyn-Ross, M. L., D. A. Steyn-Ross, P. J. Smith, J. D. Shepherd, J. Reid, and P. Tildesley, Water vapor correction method for advanced very high resolution radiometer data, *J. Geophys. Res.*, *98*, C12, 22817-22826, 1993.

[4] Bruegge, Carol, J. E. Conel, R. O. Green, J. S. Margolis, R. G. Holm, and G. Toon, Water vapor column abundance retrievals during FIFE, *J. Geophys. Res.*, *17*, D97, 18,759-18,766, 1992.

[5] Strebel, D. E., D. R. Landis, K. F. Huemmrich, and B. W. Meeson, *Collected Data of the First ISLSCP Field Experiment*, vols 1 and 2, CD-ROM, NASA, 1994.

[6] Ph.D. Associates, *Digital Chart of the World in ASCII*, CD-ROM, Ph.D. Associates Inc., Toronto, Canada, 1994.

[7] Steyn-Ross, D. A., M. L Steyn-Ross, and S. Clift, Radiance calibrations for advanced very high resolution radiometer infrared channels, *J. Geophys. Res.*, *97*, 5551-5568, 1992.

[8] Price, J. C., Land surface temperature measurements from the split window channels of the NOAA 7 AVHRR, *J. Geophys. Res.*, *89*, 7231-7237, 1984.

TIR Observations in FIFE from Field, Aircraft and Satellite Platforms

T.J. Schmugge and G.M. Schmidt
USDA Hydrology Lab, Beltsville, MD 20705, USA,
Tel:301-504-8554, FAX:301-504-8931, email: schmugge@hydrolab.arsusda.gov
USA

ABSTRACT --Observations of the surface radiometric temperature by the AVHRR sensor on board the NOAA-9 satellite are presented. The satellite observations were corrected for atmospheric effects using a path radiance model (MODTRAN3) and radio soundings of the atmosphere. Problems with this approach include the non-simultaneity of the soundings with the overpass and errors involved in profile measurements. For the former, soundings before and after the overpass were interpolated to the time of the overpass. For the latter, the errors arise from the +/- 0.5C uncertainty in the dry and wet bulb temperatures which produces a +/- 14% relative uncertainty in the water vapor. To over come this the water vapor profiles were adjusted until the channel 4 and 5 temperature differences over a large reservoir were reduced to zero. This adjusted profiled was then used over the entire site. The results are compared to ground broadband temperature readings at about 10 sites and to aircraft results from the thermal channel of the NS001 sensor on the C-130 aircraft and found to be in good agreement considering the difference in footprint sizes.

INTRODUCTION

This study attempts to understand how well satellite observations of thermal infrared radiation from the land surface can be corrected for atmospheric effects. The satellite data are from the Advanced Very High Resolution Radiometer (AVHRR) sensor on the NOAA-9 satellite during the First ISLSCP Field Experiment (FIFE)[1] conducted in central Kansas during 1987 and 1989. The MODTRAN3 path radiance model[2] was used with radiosoundings launched during FIFE to calculate the atmospheric path radiance and transmission. The corrected temperatures were compared with ground and aircraft infrared measurements. The problems involved in doing the comparison are discussed. They include; the different spectral bandpasses for the radiometers, varying view angles for both the satellite and aircraft observations and differences in the times of the observations. The data used in this analysis were obtained off the FIFE CD-ROM[3].

MEASUREMENTS

The radiosoundings[4] of the atmosphere measured the dry- and wet-bulb temperatures along with the pressure as the balloon ascends. These are then used to calculate the vapor pressure. In general there were radiosoundings available before and after the times of the satellite or aircraft overpasses. The values of the atmospheric profiles were interpolated to the time of the overpasses. For input to MODTRAN, 34 levels were selected, this was done on the basis of equal amounts of water vapor in each level. The manufacturer's stated accuracy for the dry and wet bulb temperatures is ± 0.5°C which results in a ±14% uncertainty in water vapor amount. To compensate for this uncertainty the brightness temperatures for channels 4 and 5 were calculated for a few pixels centered on a reservoir north of the FIFE site. The water vapor profiles were adjusted to yield a zero temperature difference for these pixels. These adjusted profiles were then used to do the atmospheric corrections for the data over the entire site. This method is similar to that published by Gu et al.[5].

The AVHRR has two thermal channels in the 10 - 12 μm band, channel 4 (10.3 - 11.3 μm) and channel 5 (11.5 - 12.5 μm). The resolution for these channels is approximately 1 km at nadir degrading to about 1.7 km at 55°. The data in digital counts from the CD-ROM were converted to radiance using the calibration information given in the documentation for each image. The latitude and longitude for each pixel were provided in ancillary files for each image. This information was used to locate the ground sites in the AVHRR data. Because of the uncertainties in these location data, a 3 x 3 grid of pixels around the ground site was used to calculate the AVHRR response. with the center pixel being weighted more heavily.

The ground IRT measurements were performed at about 10 Automatic Meteorological Stations (AMS). These data were taken with a 8 - 14 μm bandpass radiometer mounted about 2 m above the ground and viewing the ground at about a 10° view angle and having a 0.5m field of view.

The aircraft data were acquired with the thermal channel of the NS001 sensor which has an 10.4 - 12.5 μm bandpass. The sensor was on the NASA C-130 aircraft and flew at an altitude of 15,000 ft (4500m). At this altitude the IFOV for the thermal channel is 12m. These data were also corrected for atmospheric effects using MODTRAN. A fourth data source was from the Modular Multichannel Radiometer (MMR) which was carried by a helicopter at a nominal altitude of 300 m yielding a footprint on the ground of approximately 5 m. The helicopter would hover over individual ground sites to acquire data for several minutes. We selected data for a site that was covered at about the same time as the NS001 coverage.

RESULTS

0-7803-3068-4/96$5.00©1996 IEEE

In figure 1 we present a comparison of the data from the four sources on June 4 1987 (day 155). The temporal variation of the ground data at site 4439 is presented from about 10 am (LDT) to 5 PM. This site is an upland burned grass site used for extensive flux measurements. The temperature range is from 302 K to 294 K at about 4:30PM. The NS001 and MMR data were acquired at about the same time, 1:30PM (2030 GMT), which is about 1 hour before the AVHRR overpass. The NS001 data is for a 1km square area around the site and the value shown is average and plus and minus one standard deviation. It should be noted that the NS001 data is about 6 K warmer than the ground measurements while the MMR result is about 3 K warmer. Both of these temperatures were corrected for atmospheric effects. The AVHRR pass was at 2:30 PM (LDT - 2130 GMT) and is about 5 or 6 K warmer than the ground measurements. It should be noted that all the remotely sensed measurements were made with sensors operating in the 10 - 12 μm band and are in reasonable agreement with each other. For example if the NS001 measurement is translated by the amount the ground measurements changed in time to the AVHRR time ($\Delta T \sim 2$ K) to the results are in good agreement. A possible explanation for the lower reading for the broader band ground radiometers is that they were seeing some bare soil which can have a lower emissivity in the 8 - 9 μm region. [6] However considering the limited amount of bare soil showing it is unlikely that this emissivity difference could be large enough to account for the 3 to 4K differences observed.

This approach was repeated for several additional days with AVHRR overpasses during 1987. A summary of the results is shown in figure 2 for 12 days in 1987 from June 4 (155) until 6 October (279). The AVHRR results for channel 5 obtained before (x's) and after (+'s) adjusting the profile are shown. The actual adjustment factors are shown at the top of the figure and except for three cases the adjustment factor was within the ±14% limits. We need to look further into the case when the factor was 2, day 279, when the moisture profile was very dry. The viewing angle is also indicated at the top of the graph showing that many of cases were acquired at the angular extreme of $\geq 50°$. The atmospheric water vapor amounts are indicated by the bars at the bottom of the figure in cm of H_2O. This the amount of water along the viewing path and thus can be large for the large angles. The AMS readings are shown as the black squares. It is seen that the AVHRR results track the AMS results very well but are consistently 5 or more degrees higher for this site. In most cases the temperature changes due to the profile adjustments are rather small, a degree or two. Also the differences between the channel 4 and channel 5 results are less than 0.5 K after the profile adjustment compared to more than 0.5 before the adjustment.

DISCUSSION

The results presented indicate the magnitude of the problem of evaluating the accuracy of surface temperature measurements made from spaceborne platforms. The corrected AVHRR brightness temperatures were consistently at least 5 K higher than those observed at this particular AMS site. These differences can be attributed to the different spatial resolutions of the two sensors and to their different bandpasses, we believe mostly the former because it is unrealistic to compare $1m^2$ brightness temperature with that for 10^6 m^2. This difference is observed at the other AMS sites also. We had hoped that the aircraft data would birdge this gap but were frustrated by the time difference. The profile adjustment process was seen to reduce the brightness temperature differences between the two channels indicating that this process is moving in the correct direction.

REFERENCES

[1] Sellers, P.J., F.G. Hall, G. Asrar, D.E. Strebel and R.E. Murphy, (1992) An Overview of the First International Satellite Land Surface Climatology (ISLSCP) Field Experiment (FIFE), J. Geophys. Res., 97, pp 18,345-18371.

[2] Kniezys, FX, Shettle, EP, Abreu, LW, Chetwynd, JH, Anderson, GP, Gallery, WO, Selby, JEA, & Clough SA (1988) User Guide to Lowtran 7, Air Force Geophysics Laboratory Report No AFGL-TR-88-0177, Hanscom AFB, Massachusetts 01731.

[3] Strebel, D.E.,D.R. Landis, K.F. Huemmrich and B.W. Meeson, 1994. "Collected Data of The First ISLSCP Field Experiment, Volumes 1,2, and 3". Published on CR-ROM by NASA.

[4] Sugita, M. And W. Brutsaert, 1990 Wind velocity Measurements in The Neutral Boundary Layer Above Hilly Prairie, .J. Geophys. Res., 95, pp 7617-7624.

[5] Gu, X.F., B. Seguin, J.F. Hanocq and J.P. Guinot, 1994. Evaluation and Comparison of Atmospheric Correction Methods for Thermal Data Measured by ERS1- ATSR, NOAA11-AVHRR, and Landsat5 - TM Sensors. Proc Sixth Intl. Symp. on Physical Measurements and Signatures in Remote Sensing, Val d'Isere, France, 17-21 January 1994.

[6] Schmugge, TJ, F Becker and Z-L Li, 1990, Spectral Emissivity Variations Observed in Airborne Surface Temperature Measurements, Rem Sens Environm, vol. 34, pp. 95-104.

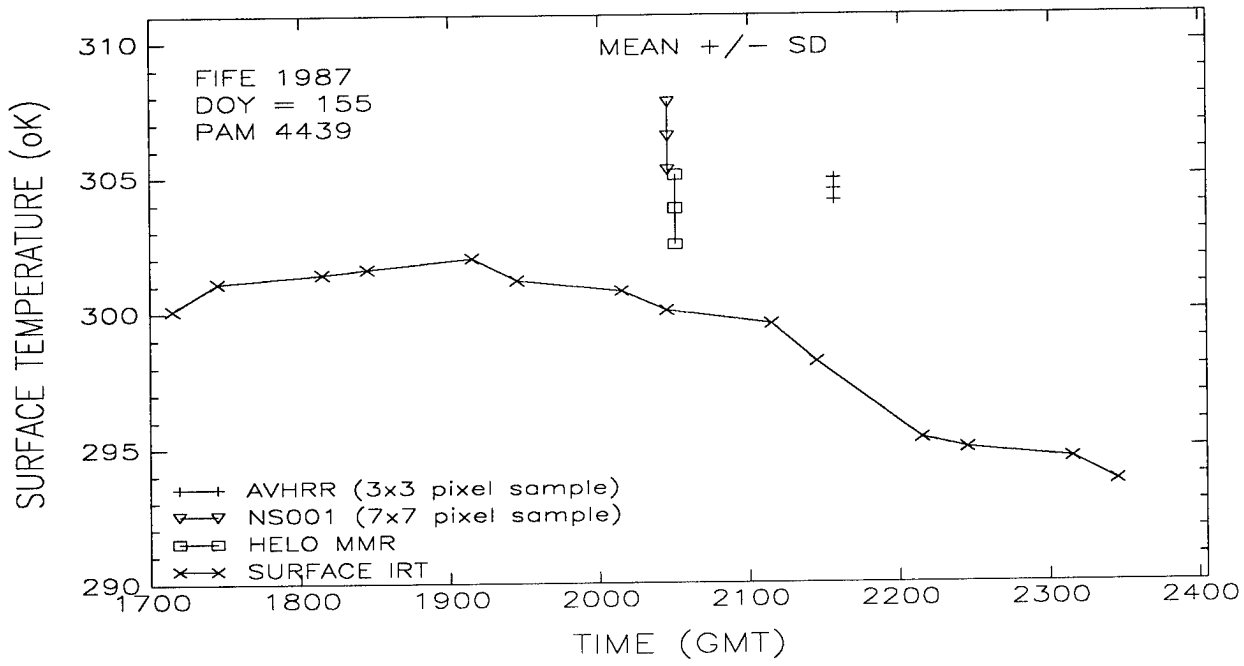


Figure 1. Comparison of surface brightness temperatures from AVHRR (channel 5), NS001 (channel 8), MMR, and IRT platforms.

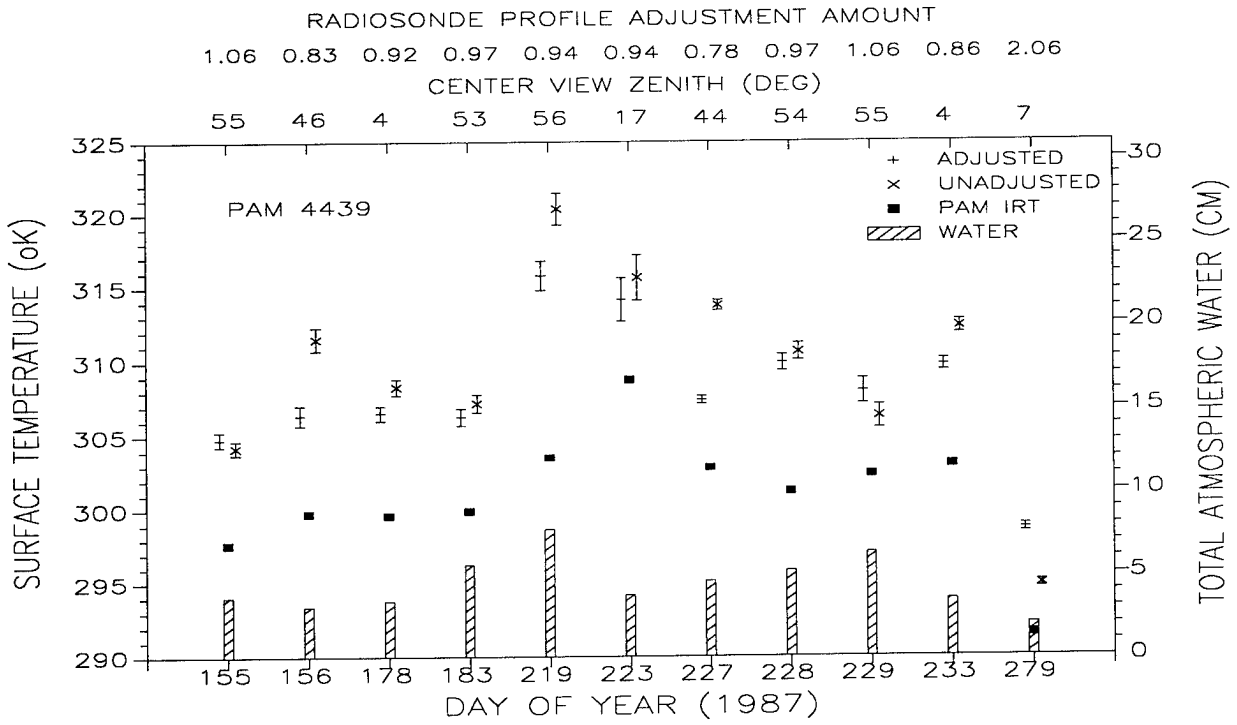


Figure 2. Comparison of AVHRR (channel 5) surface temperatures from adjusted and unadjusted radiosonde profiles.

A Simple Method for Estimating Surface Energy Fluxes and Air Temperatures from Satellite Observations

M.C. Anderson[1], J.M. Norman[1], G.R. Diak[1], W.P. Kustas[2]

[1]1525 Observatory Drive, University of Wisconsin
Madison, WI 53706 USA
T: (608) 262-0415 F: (608) 265-2595 EMAIL: anderson@bob.soils.wisc.edu
[2]USDA-ARS-Hydrology Lab, Building 007, BARC-West
Beltsville, MD 20705-2350 USA

ABSTRACT

We present an operational two-source (soil+vegetation) time-integrated model (TSTIM) for estimating energy fluxes from a vegetated surface given measurements of the time rate of change of radiometric surface temperature (T_{RAD}). This model requires ancillary measurements of wind speed, albedo, vegetation type and cover and initial atmospheric lapse rate. Unlike most algorithms for flux estimation proposed to date, however, this method does not require in situ measurements of air temperature. This is a significant benefit when T_{RAD} is acquired remotely and it is difficult to collocate surface and air temperature measurements. The dependence of apparent radiometric temperature on sensor view angle is taken into account, so off-nadir satellite measurements can be used to drive the model. When applied to surface data collected during the FIFE and Monsoon '90 field experiments, RMS deviations between measurements and model predictions were comparable to those achieved by models that do require air temperature as an input, and to measurement errors typical of standard micrometeorological methods for flux estimation.

INTRODUCTION

The flux of sensible heat from a surface is proportional to the temperature difference between the surface and the air, divided by the bulk aerodynamic resistance to heat transport between these levels. Thermal IR satellite imagery traces surface temperature variations and should therefore provide an effective means of mapping surface heat fluxes over large spatial scales. Several factors complicate the analysis, however: (1) Air temperature is strongly influenced by local surface characteristics, thus if air temperature measurements are not collocated with the IR image pixel, flux estimates can be significantly corrupted. (2) The heat fluxes from vegetated and non-vegetated surface components in the field of view are often coupled to the air through very different resistances. To accurately estimate the net flux from a composite system, the thermodynamic temperature and fractional spatial coverage of each individual component must be known. (3) Satellite measurements of surface temperature will typically be off-nadir, so the dependence of apparent surface temperature on sensor view angle must be accounted for in the model. (4) Atmospheric corrections are required to retrieve a true radiometric surface temperature from the brightness temperature observed at the satellite.

The model for surface flux estimation presented here addresses each of these difficulties. The two-source model (TSM) of [1] is used to estimate the individual temperatures of and fluxes from the soil and vegetation components in the scene (addressing problems 2 and 3). The need for air temperature measurements (problem 1) is eliminated by interfacing the TSM with a simple model of planetary boundary layer (PBL) development - the integrated sensible heat flux into the PBL over a specified period of time is related to the change in temperature in the layer. Because only time *changes* in temperature are used by this model, only time-dependent atmospheric corrections need be evaluated, reducing the impact of problem 4.

MODEL DESCRIPTION

The radiometric temperature of a vegetated surface is a composite of the individual thermodynamic temperatures of the soil (T_s) and vegetation canopy (T_c) lying within the sensor field of view, and can be expressed approximately as

$$T_{RAD} \approx f(\phi)T_c + [1-f(\phi)]T_s , \qquad (1)$$

where $f(\phi)$ is the fraction of the sensor field of view occupied by vegetation when viewed at a zenith angle ϕ. The soil and canopy temperatures also influence the net flux of sensible heat from the soil+vegetation system. Reference [1] shows that the net sensible heat flux (H) from a sparsely vegetated surface can be adequately represented by assuming that the fluxes from the soil (H_s) and vegetation (H_c) within the field of view are in parallel, so that

$$H = H_c + H_s . \qquad (2)$$

The component fluxes in (2) are driven by the temperature difference between the source and the air:

$$H_c = \rho c_p \frac{T_c - T_a}{R_a}, \quad H_s = \rho c_p \frac{T_s - T_a}{R_s + R_A} . \qquad (3)$$

The quantity R_a is the aerodynamic resistance to heat transport

0-7803-3068-4/96$5.00©1996 IEEE

between the canopy and the height at which the air temperature, T_a, is measured [2], and R_s is the additional resistance encountered by heat transported from the soil through the boundary layer immediately above the soil surface [3]. Both resistances depend on wind speed and surface roughness.

Combining (1)-(3) yields

$$T_{RAD} = T_a + f(\phi)\frac{H_c R_a}{\rho c_p} + [1-f(\phi)]\frac{(H-H_c)(R_a+R_s)}{\rho c_p} . \quad (4)$$

The canopy heat flux, H_c, can be estimated with a modified version of the Priestly-Taylor approximation [1]. The unknowns remaining in (4) are then H and T_a.

The TSTIM solves for these quantities using a simple model of planetary boundary layer development -- the rate at which air temperature evolves will depend on the rate at which sensible heat is supplied to the PBL. Currently, the TSTIM uses a simple slab model for the mixed layer, assuming all air within the layer is at a uniform potential temperature, θ_m. At the land surface, the mixed layer potential temperature and the air temperature are related by

$$\theta_m = T_a\left(\frac{100}{p}\right)^{R/c_p} \quad (5)$$

where p is the surface atmospheric pressure (in kPa) , and R/c_p = 0.286. Further we assume that the height of the boundary layer at time t_i can be approximated by the height z_i at which an adiabat at the current mixed layer potential temperature, $\theta_{m,i}$, intersects an early morning temperature sounding.

Reference [4] gives a simplified conservation equation describing the growth of a convective boundary layer over time:

$$\rho c_p (z_2\theta_{m,2} - z_1\theta_{m,1}) = \int_{t_1}^{t_2} H(t)dt + \rho c_p \int_{z_1}^{z_2} \theta_s(z)dz . \quad (6)$$

Here, $\theta_s(z)$ is the potential temperature profile above the mixed layer. During the time interval t_1 to t_2, the top of the mixed layer rises from height z_1 to z_2. The net growth is determined by the amount of energy supplied to the mixed layer during this time interval, introduced at the surface by the addition of sensible heat, and at the top of the PBL by warm air entrained from above the capping inversion as the boundary layer grows.

In the morning hours, shortly after sunrise until just before local noon, sensible heating increases approximately linearly with time. Good results have been obtained with the form [5]

$$H(t) = \frac{H_N}{T}t \quad (7)$$

where H_N is a scaling flux and T is a flux rise time (3 hours), and t is referenced to one hour past sunrise. Combining the integral of (7) with (5) and (6), and substituting $H_i T/t_i$ for H_N yields the following expression for the sensible heat flux at a time t_i during this linear phase:

$$H_i = \left(\frac{p}{100}\right)^{R/c_p} \frac{2\rho c_p t_i}{(t_2^2 - t_1^2)} [z_2 T_{a,2} - z_1 T_{a,1} - \int_{z_1}^{z_2} \theta_s(z)dz] \quad (8)$$

In the TSTIM, (8) is applied twice during the morning hours, at 1.5 and 5.5 hours past sunrise (times t_1 and t_2). Because z_1 and z_2 are determined by $\theta_{m,1}$ and $\theta_{m,2}$ under our assumptions, and $\theta_s(z)$ is given by the early morning sounding, the unknowns in (8) are H_1, H_2, $T_{a,1}$, and $T_{a,2}$. Thus, given measurements of radiometric surface temperature at times t_1 and t_2, (4) and (8) yield four equations which can be solved for these four unknowns. Given an independent estimate of the soil heat flux [6], the latent heat flux can be computed as a residual to the surface energy budget equation.

The ancillary surface data required by the TSTIM are wind speed, solar radiation, albedo, canopy height, LAI or fractional canopy cover, and approximate leaf size. In lieu of measured air temperatures, the TSTIM requires a description of PBL lapse rate structure in the early morning. Sensitivity tests suggest that the TSTIM is not significantly affected by errors in lapse rate on the order of a couple of degrees Kelvin per kilometer [6].

MODEL VALIDATION

The performance of the TSTIM was evaluated in comparison with surface flux observations collected during the First ISLSCP Field Experiment (FIFE), conducted in the Konza Prairie near Manhattan Kansas in May-October 1987 [7], and during the Monsoon '90 experiment, conducted in the Walnut Gulch watershed near Tombstone, Arizona in July-August 1990 [8]. Single-layer models typically have had difficulty accommodating both sparse and well-vegetated surfaces without resorting to empirical adjustments, so these databases provide a good test of the generality of the TSTIM.

Figs. 1a-b compare sensible and latent heat fluxes measured during the FIFE campaign with those predicted by the TSTIM at time t_2. The RMS deviations (RMSD) between measured and modeled H and LE (61 and 55 W m^{-2}, respectively) are comparable to those achieved by the TSM and to the expected error in the reference observations [1]. The degree of correlation between the predicted and measured air temperatures (Fig. 1c) is notable, with a coefficient of determination of 0.86. The 3 ^{0}C bias in estimated air temperatures may trace back to biases in the T_{RAD} measurements due to small-scale inhomogeneity in the landscape [6]. Fig. 1c and further sensitivity tests suggest that this bias, constant with time, is being absorbed into the computed air temperatures, leaving the true difference T_a - T_{RAD} intact. The time-independent component of atmospheric corrections to satellite-obtained T_{RAD} measurements should likewise be absorbed.

Figs 1d-e compare observed and modeled sensible and

latent heat fluxes from the Monsoon '90 campaign at sites 1 and 5. The TSTIM yields RMSD values for H and LE and G of 33 and 35 W m^{-2}, respectively; a slight improvement over the TSM [1]. The correlation between modeled and measured air temperatures for Monsoon '90 (Fig. 1f) is somewhat worse than that achieved in the FIFE simulations. The origin of the biases apparent in Fig. 1f is not clear, as special steps were taken in Monsoon '90 to assure that brightness temperature measurements were spatially representative. The discrepancies may be due to a combination of small individual errors, both in the measurements and in our description of the system.

CONCLUSIONS

The two-source time-integrated model for surface flux estimation from measurements of surface radiometric temperature presented here has been tested with data collected during the FIFE and Monsoon '90 experimental campaigns. The model performs well over both well- and sparsely-vegetated surfaces. The TSTIM is well-suited to remote applications because it does not rely on in situ air temperature measurements and it can accept radiometric observations at any sensor view angle. Time-independent biases in surface temperature measurements do not affect the flux estimates significantly, therefore the accuracy in atmospheric corrections to T_{RAD} required by the TSTIM is greatly reduced.

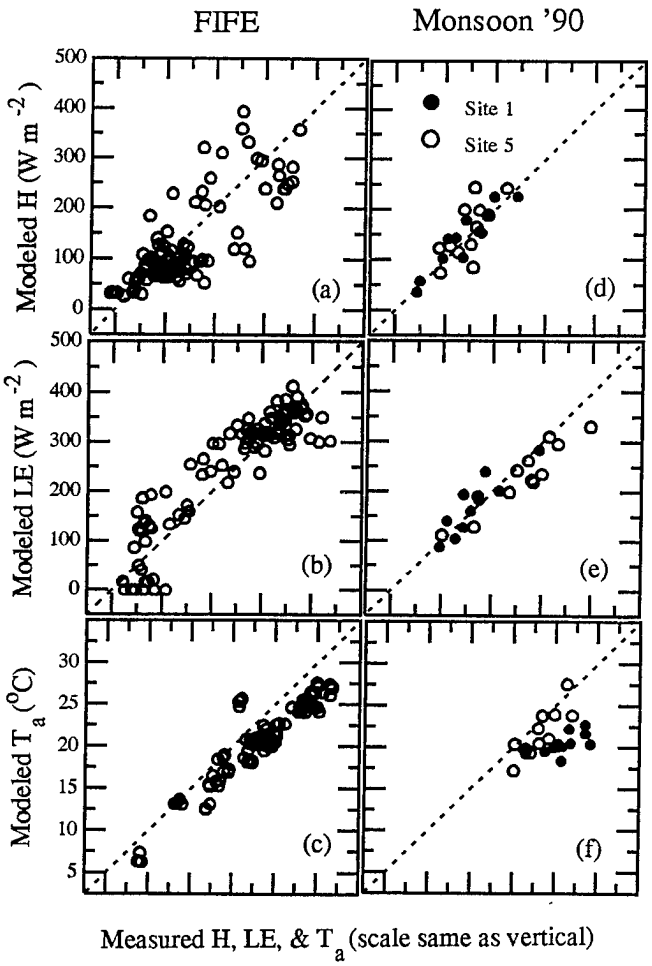


Figure 1. Modeled vs. measured sensible heat, latent heat and air temperature from FIFE and Monsoon '90.

ACKNOWLEDGMENTS

This research was supported by NASA Grant NAGW-4138, with the assistance of the University of Wisconsin Agricultural Experiment Station. Measurements collected by W.D. Nichols (USGS-Water Resources Division, Carson City Nevada), D.I. Stannard (USGS-Water Resources Division, Denver, Colorado) and J.H. Blanford (University of Arizona) during Monsoon '90 were essential for testing the model for this experimental site. Funding from NASA Interdisciplinary Research Program in Earth Sciences (NASA Reference Number IDP-88-086) and funds from the USDA-ARS Beltsville Area Office provided the necessary financial support to conduct this field study.

REFERENCES

[1] J.M.Norman, W. P. Kustas, and K.S. Humes, "A two-source approach for estimating soil and vegetation energy fluxes from observations of directional radiometric surface temperature", Agric. For. Meteorol., vol. 77, pp 263-293, 1995.

[2] W. Brutsaert, Evaporation into the Atmosphere: Theory, History and Applications, Hingham, MA: Reidel, 1982.

[3] T.J. Sauer, J.M. Norman, C.B. Tanner, and T.B. Wilson, "Measurement of heat and vapor transfer at the soil surface beneath a maize canopy using source plates", Agric. For. Meteorol., vol. 75, pp. 161-189, 1995.

[4] K.G. McNaugton and T.W. Spriggs, "A mixed-layer model for regional evaporation", Boundary-Layer Meteorol., vol. 34, pp. 243-262, 1986.

[5] H. Tennekes, "A model for the dynamics of the inversion above a convective boundary layer", J. Atmos. Sci., vol. 30, pp. 558-567, 1973.

[6] M.C. Anderson, J.M. Norman, G.R. Diak, W.P. Kustas, and J.R. Mecikalski, "A two-source time-integrated model for estimating surface fluxes from thermal satellite observations", unpublished.

[7] P.J. Sellers, F.G. Hall, G. Asrar, D.E. Strebel, and R.E. Murphy, R. E. "An overview of the First International Satellite Land Surface Climatology Project (ISLSCP) Field Experiment (FIFE)", J. Geophys. Res., vol. 97, pp. 18,345-18,371, 1992.

[8] W.P. Kustas and D.C. Goodrich, "Preface to Monsoon '90 experiment", Water Resour. Res., vol. 30, pp. 1211-1225, 1994.

Unmixing of Satellite Thermal Images: Simulation and Application to TM/Landsat Data

B.Zhukov[1], D.Oertel[2], F.Lehmann[2], and P.Strobl[3]

[1] Space Research Institute, Russian Academy of Sciences, Profsoyuznaya 84/32, 117810 Moscow, Russia, tel: +7-095-3332445, fax: +7-095-3301200

[2] Institute of Optoelectronics, German Aerospace Research Establishment (DLR), 82230 Weßling, Germany, tel: +49-08153-282786, fax: +49-08153-281349

[3] Institute of Geography, University of Munich, Luisenstr. 37, 80333 Munich, Germany, tel: +49-08153-281533, fax: +49-08153-281458

Abstract -- The Multi-Sensor Multi-Resolution Technique (MMT) was applied to unmix a lower resolution thermal TM image using higher resolution multispectral images obtained in the reflective TM channels. It allowed to reveal high-resolution features, which were smeared or not recognizable in the original thermal image. The MMT accuracy was tested on a simulated data set and proved to be 0.8 K for the mean error of class radiant temperature retrieval and 1.6 K for the pixel error of the low-pass corrected unmixed image when the optimal number of classes was selected.

INTRODUCTION

The spatial resolution of the thermal channels of satellite multispectral scanners TM (LANDSAT), MSU-SK (RESURS), ASTER and MODIS (EOS-AM1) is a factor of 3 to 6 lower than the resolution of their reflective channels. In this case high-resolution images obtained in the reflective channels can be used to unmix lower-resolution thermal images.

One approach to perform this cross-channel unmixing is based on assuming a linear correlation between the reflective and thermal channels [1].

A more adaptive and more general solution to the problem can be provided by the Multi-resolution Multi-sensor Technique (MMT) [2,3]. The MMT is based on using the data of higher resolution instruments (channels) for differentiating and mapping 'homogeneous' classes with a high spatial resolution and on retrieving the mean class signatures from the data of lower resolution instruments (channels). The MMT application to the problem of unmixing thermal images is discussed in this paper.

TECHNIQUE

The basic MMT algorithm, adapted to the problem of unmixing thermal images, includes the following steps [2,3]:

- (unsupervised) classification of high-resolution multispectral reflective images;
- definition of class contributions to the signal of each thermal pixel with accounting for both, the class proportions in thermal pixels and for the point spread function (PSF) of the thermal channel;
- retrieval of the mean class thermal radiance by the least-squares inversion of the linear mixture model;
- generation of the unmixed thermal image by assigning the retrieved mean class thermal radiances to corresponding high-resolution pixels of the classification map.

The basic MMT limitation is that it allows to unmix radiant temperatures of only those classes which can be recognized in reflective images. For this purpose, the radiances in the thermal and reflective bands do not need to be related by a linear correlation. It is required only that radiant temperature variations should be accompanied by any reflectivity variations (but not all reflectivity variations need to be accompanied by radiant temperature variations). The physical background for this requirement is: a) albedo variations in the visible spectral range is one of the principal factors controlling the surface temperature, and b) surface emissivity variations in the thermal infrared range are often accompanied by reflectivity variations in the reflective spectral range.

If objects with different radiant temperatures cannot be differentiated in the reflective channels, they will be integrated in a common class and only their average thermal radiance will be retrieved. This will lead to averaging the thermal radiance of such objects at the scale of the whole image. Even low-frequency radiant temperature variations may be lost, which can be recognized in the initial low-resolution thermal image, if they are not accompanied by reflectivity variations. One approach to deal with this problem is to process the image by small windows [4]. In the present paper we use a simpler approach which can be conventionally called 'low-pass correction'. It is based on merging high-resolution thermal radiance variations in the unmixed image (obtained by the basic MMT. algorithm) with low-resolution variations in the initial thermal image. This can be done by replacing the low-frequency component of the unmixed image, which is obtained by its low-pass filtering in accordance with the PSF of the thermal channel, by the initial low-resolution thermal image. In this way all the information about temperature variations, which is contained in the initial thermal image, is preserved in the low-pass-corrected unmixed image.

0-7803-3068-4/96$5.00©1996 IEEE

SIMULATION

The MMT accuracy was tested on a simulated image, which was generated from a mosaic of airborne DAEDALUS images of a part of the Ruegen island (Germany). The DAEDALUS images were obtained in the TM spectral bands with the resolution of 5 m. The TM image was simulated by degrading the resolution of the DAEDALUS image mosaic to the TM pixel size of 30 m in the six reflective channels and of 120 m in the thermal channel. The size of the simulated image was 512 × 512 reflective pixels.

Additionally, a random noise with the signal-to-noise ratio of SNR = 50 was added to each band of the simulated image to account for the instrument noise. The errors of inter-channel co-registration were simulated by a random 2-dimensional relative shift of the band images, the maximal shift being 0.5 of the reflective pixel size in each direction.

Classification of the simulated 6-band reflective image was performed with the iterative ISODATA clustering algorithm [5], with the number of spectral classes (clusters) N_{cl} varying from 2 to 256.

The MMT accuracy was estimated by comparing the results with the reference thermal image which was generated with the resolution of 30 m. Fig.1 shows the following parameters of the MMT accuracy: 1) the mean pixel error of the uncorrected unmixed image σ_{pix}, which was defined as its standard deviation from the reference image, 2) the mean pixel error of the low-pass corrected unmixed image σ_{pix}^{LP}, which was defined in the same way, 3) the mean error of retrieving the radiant temperatures of the classes $\overline{\Delta T_{cl}}$, and 4) the mean thermal inhomogeneity of the classes $\sigma_{in-class}$, which was defined as the standard deviation of within-class radiant temperature.

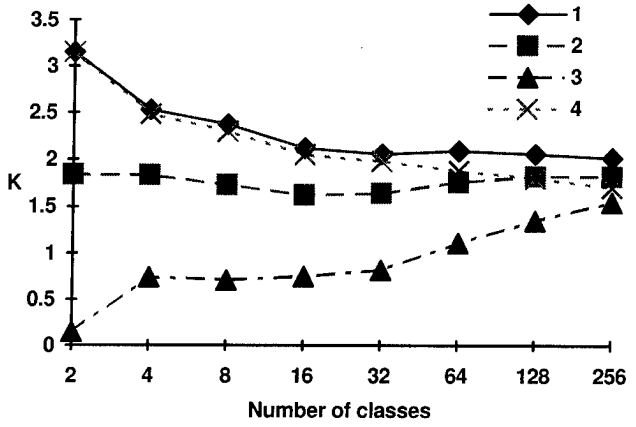


Figure 1. Parameters of the MMT radiant temperature retrieval accuracy as a function of the number of classes: 1 - σ_{pix}; 2 - σ_{pix}^{LP}; 3 - $\overline{\Delta T_{cl}}$; 4 - $\sigma_{in-class}$

The MMT provided a reasonable mean class radiant temperature retrieval accuracy of $\overline{\Delta T_{cl}} \leq 1$ K for the number of classes of $N_{cl} \leq 50$. The mean pixel accuracy of the uncorrected unmixed image is $\sigma_{pix} \sim 2$ K for $32 \leq N_{cl} \leq 256$. The thermal inhomogeneity of the classes $\sigma_{in-class}$ is the main component of this pixel error. The low-pass correction allowed to decrease the pixel error down to $\sigma_{pix}^{LP} =$ 1.6 K for N_{cl} = 16-32.

UNMIXING OF A TM/LANDSAT THERMAL IMAGE

The MMT was applied to process a TM/Landsat image of a part of Ruegen, which was different from the one covered by the simulated image but had a similar land cover type distribution and the same size of 512 × 512 reflective pixels. The PSF of the TM thermal channel was assumed to be constant within its geometric pixel size and to be zero outside it. Classification of the 6-band reflective image was performed with 32 classes, which had been found to be close to optimal for a similar scene during the simulations.

The sharpness of fields, of the coast line, and of the high-way with a bridge across the gulf are restored in the unmixed images (Fig.2c,d), though they are smeared in the original thermal image (Fig.2b). Even the smaller objects like small roads and ships near the bridge, which are not seen in the original thermal image, are revealed in the unmixed images.

Waters with various turbidity, which are well recognized in the reflective image (Fig.2a), in most cases do not show thermal differences (Fig.2c,d). One exception is the near-shore waters which have both a higher turbidity and a higher temperature.

The opposite effect can be illustrated by the general water temperature distribution with off-shore cooling as observed in the original thermal image (Fig.2b). Some features of this distribution are not reconstructed in the uncorrected unmixed image (Fig.2c), since they are not accompanied by turbidity variations. However, they are restored in the low-pass-corrected image (Fig.2d).

A significant correction of the temperature of some fields can also be noticed in the low-pass-corrected image.

REFERENCES

[1] R.Nishii, S.Kusanobu, and S.Tanaka, "Spatial resolution enhancement of low resolution thermal infrared image based on other high resolution band images", in Proc. IGARSS'95, vol. I, pp. 667-669.

[2] B.Zhukov and D.Oertel, "A technique for combined processing of the data of an imaging spectrometer and of a multispectral camera", in Proc. SPIE'95, vol. 2480, pp. 453-465.

[3] B.Zhukov and D.Oertel, "Multi-sensor multi-resolution technique and its simulation", Zeitschrift für Photogrammetrie und Fernerkundung, No.1, 1996, pp. 11-21.

[4] B.Zhukov, M.Berger, F.Lanzl, and H.Kaufmann, "A new technique for merging multispectral and panchromatic images revealing sub-pixel spectral variation", in Proc. IGARSS'95, vol. III, pp. 2154-2156.

[5] J.A.Richards, Remote Sensing Digital Image Analyses, Springer Verlag, Berlin, Heidelberg, 1986.

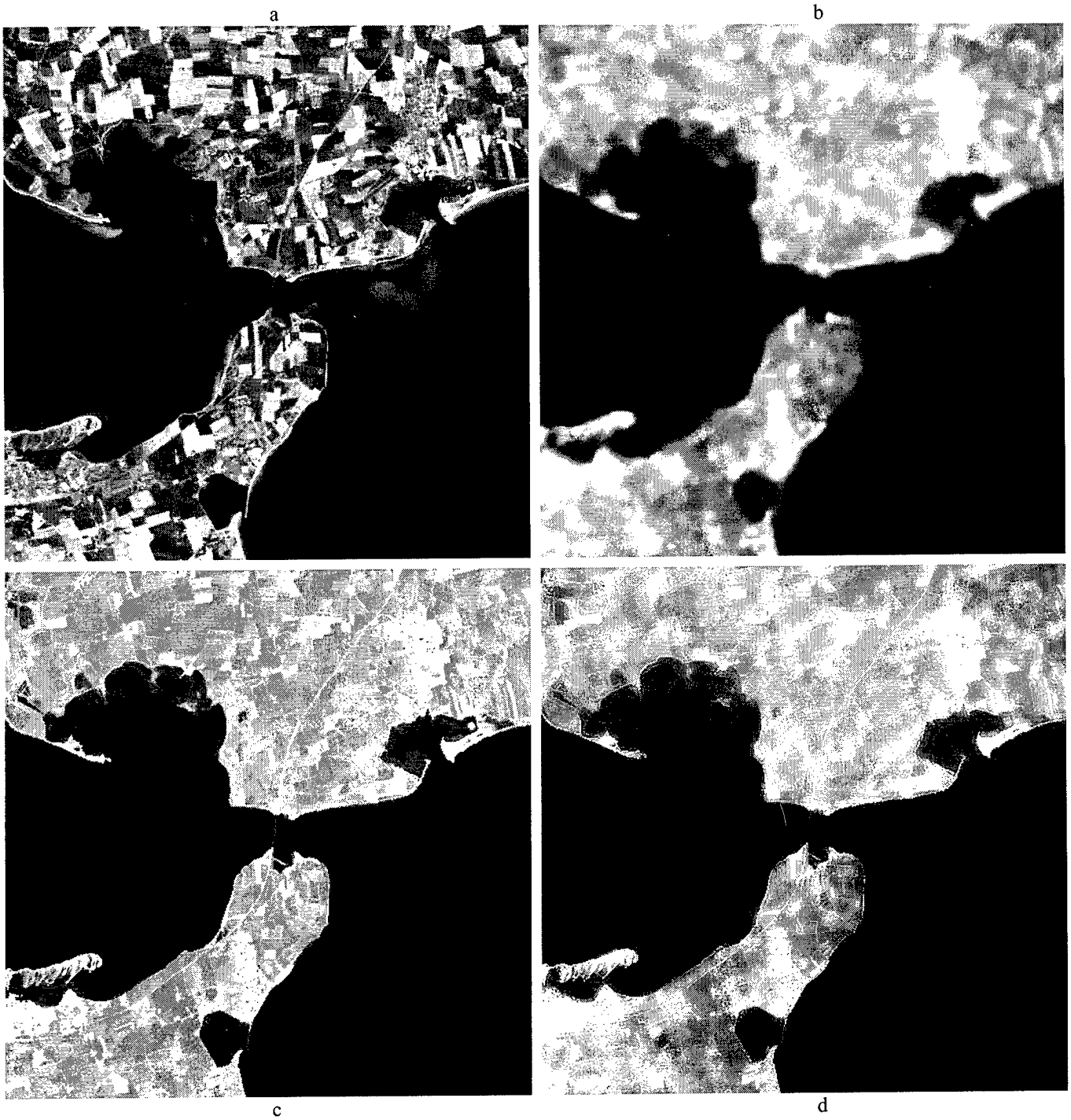


Figure 2. Unmixing of a TM thermal image of Ruegen: a - TM image in the 0.52-0.60 μm spectral band; b - TM thermal image; c -uncorrected unmixed thermal image ; d - low-pass-corrected unmixed thermal image

SSM/I-Based Surface Temperature Retrieval Methods for Boreal Forest Zone

Jouni Pulliainen, Jochen Grandell and Martti Hallikainen
Helsinki University of Technology, Laboratory of Space Technology
Otakaari 5A, 02150 Espoo, Finland
Fax: +358 0 460224, email: pulliainen@ava.hut.fi

Abstract -- Novel inversion methods for the retrieval of surface temperature (air temperature at ground level) in forested areas using space-borne multi-channel microwave radiometer data are presented and analyzed. The first technique is an inversion method based on the use of a semi-empirical emission model. The other methods discussed are empirical approaches: multiple linear regression and polarization difference formulas. The methods are evaluated in the case of Finnish boreal forests. The results show that for conifer dominated boreal forests the surface temperature can be estimated reliably from SSM/I measurements during snow-free conditions. The highest test site-wise correlation coefficients (r) between the ground-based reference values and the SSM/I-based estimates are above 0.97 and the corresponding unbiased rms errors are smaller than 1.3 °C.

INTRODUCTION

Boreal forests cover the circumpolar regions of Europe, Asia and North America forming the largest vegetation zone on the Earth. The test areas of this study are located in Finland, where boreal forests cover most of the country. The forests are relatively sparse and the dominant tree species are Scots pine and Norway spruce.

The developed and investigated temperature retrieval methods are based on the observation that for the SSM/I frequencies, the emissivities of forested areas in a given location are approximately constant during snow-free conditions (regardless of precipitation and soil moisture variations). The presence of snow cover changes the surface emissivity considerably. In Finland, the snow season prevails usually from mid-December to mid-April in the south, and from the end of October to mid-May in the north. The snow season sets the temporal limits to the use of the temperature retrieval algorithms.

STUDY SITES AND MATERIAL

The study material includes (1) daily SSM/I data interpolated into a fixed 25 km by 25 km grid for two test areas in Southern and Northern Finland, respectively (both sized 500 km by 500 km), (2) gridded land use characteristics (determined from a digital land use map), (3) daily air temperature and precipitation information from a set of weather stations and (4) bi-monthly snow cover extent and snow water equivalent information covering the area of Finland. Our SSM/I data set covers a 12-month period from July 1993 through June 1994.

The average relative forest cover in land areas of the test areas is 77 %. However, mixed pixels with inland lakes and agricultural areas are usual. The agricultural areas are mainly located in the southernmost part of the South Finland test area, while lake clusters are usual in all regions. The grid cell-wise reference data includes the distributions of different land use categories and soil types. The land use data also include information on the total forest stem volume. The average stem volume in forest areas is 96 m^3/ha in the South Finland test area (which corresponds to a total dry forest biomass of about 58 tons/ha), and 64 m^3/ha in the North Finland test area (38 tons/ha), respectively.

The main reference data employed is the daily mean air temperature at the height of 2 m measured at 15 weather stations scattered around the two test areas.

TEMPERATURE RETRIEVAL ALGORITHMS

The developed and tested temperature retrieval methods are (1) the semi-empirical model-based inversion approach, (2) the statistical multiple linear regression model, and (3) the empirical polarization difference method introduced in [1]. The SSM/I data used in the analyses were obtained from 48 grid cells that around the weather stations. Since the temperature retrieval methods fail to work for snow-covered ground, a set of 121 dates from July to September 1993 and from June 1994 was employed for the analysis.

Inversion method

The developed inversion method is a two-stage process that first estimates the average surface emissivity of a given location for each SSM/I channel using multi-temporal SSM/I data interpolated into that location. In the second stage, these emissivities are employed to determine the physical temperature.

The first stage of the algorithm estimates the surface emissivities and, additionally, the physical temperatures for a set of SSM/I measurements. The multi-temporal data set should cover a time period long enough so that the mean atmospheric conditions are valid on average. The algorithm is:

$$\text{Minimize} \quad \sum_{j=1}^{N} \sum_{i=1}^{7} [(T_b)_{i,j} - \; g_{i,j}(e_i, (T_{phys})_j, \hat{\gamma})]^2, \qquad (1)$$

where

$(T_b)_{i,j}$ = SSM/I-derived brightness temperature for channel i and observation j
N = 30, total number of multi-temporal observations
g = model for brightness temperature
e_i = surface emissivity at ith channel
$\hat{\gamma}$ = 0.0368, a constant that defines the mean atmospheric transmissivity.

The model g for the brightness temperature is:

0-7803-3068-4/96$5.00©1996 IEEE

$$g_{i,j} = e_i(T_{phys})_j t_i(\gamma_j) \quad (2)$$

$$+ \alpha_{\uparrow}(T_{phys})_j (1 - t_i(\gamma_j)) + \alpha_{\downarrow}(T_{phys})_j (1 - e_i) t_i(\gamma_j)(1 - t_i(\gamma_j)),$$

where $\alpha_{\uparrow}$ and $\alpha_{\downarrow}$ are atmospheric profile factors related to the atmospheric transmissivity t_i by a polynomial fit [2,3]. t_i is given by the statistical principal component model [3]:

$$t_i(\gamma) = \left[(t_P^0)_i + (t_P^1)_i \gamma\right]^{1.0681}, \quad (3)$$

where scalar variable $\gamma = \hat{\gamma} = 0.0368$. t_P^0 and t_P^1 are the zero-order and the first-order principal components of the atmospheric transmissivity for different SSM/I channels:

$$t_P^0 = (0.9211 \quad 0.9211 \quad 0.8326 \quad 0.8624 \quad 0.8624 \quad 0.6656 \quad 0.6656)^T \quad (4)$$

$$t_P^1 = (0.2069 \quad 0.2069 \quad 0.4642 \quad 0.2746 \quad 0.2746 \quad 0.8163 \quad 0.8163)^T$$

In (4), the first term refers to vertically polarized 19 GHz channel and the last term to the horizontally polarized 85.5 GHz channel.

Once the surface emissivities for a certain pixel have been determined, these values can be used for predicting the physical temperature for any measurement date. Now, the atmospheric parameter γ can be considered as a free parameter or a Gaussian random variable with a known mean value and a known standard deviation. In this case, the algorithm for estimating the physical temperature T_{phys} can be written as

Minimize

$$\sum_{i=1}^{7} \frac{1}{2\sigma_i^2}[(T_b)_i - g_i(e_i, (T_{phys}), \gamma)]^2 + \frac{1}{2\lambda^2}(\gamma - \hat{\gamma})^2, \quad (5)$$

where

σ_i = standard deviation of SSM/I-derived brightness temperature for channel i (assumed to be 2 K for 19, 22 and 37 GHz channels and 5 K for 85.5 GHz channels)

λ = standard deviation of γ (λ=0.05 used in this paper).

Multiple linear regression equations

The multiple linear regression equations were developed and tested by using the SSM/I data from all 48 test grid cells. A 60-day teaching data set was used to determine the regression coefficients for the algorithms. The algorithms were tested using (a) all measurement dates and (b) a test data set that excluded the teaching data.

The regression equation for temparature, T, in °C using SSM/I results and reference air temperature values covering the first 60 consecutive measurements from 48 test grid cells is

$$T = 0.2769 \cdot T_{b,19V} - 0.5101 \cdot T_{b,19H} + 0.9758 \cdot T_{b,22V}$$

$$+ 0.6959 \cdot T_{b,37V} - 0.4244 \cdot T_{b,37H} - 0.03812 \cdot T_{b,85V}$$

$$- 0.02716 \cdot T_{b,85H} - 243.4. \quad (6)$$

Multiple linear regression was also tested using channel subset regression equations. These tests indicate that almost as high performances can be obtained using only three channels as those employing all seven SSM/I channels. In this case, the regression equation for T (in C°) is

$$T = 0.8315 \cdot T_{b,19V} - 0.9173 \cdot T_{b,19H}$$

$$+ 1.022 \cdot T_{b,22V} - 240.0. \quad (7)$$

Polarization difference approach

An empirical algorithm for the retrieval of the physical temperature based on the employment of the polarization difference at 19 GHz was introduced in [1]:

$$T_{phys} = [kT_{b,19V} - (k-1)T_{b,19H}]/e_x. \quad (8)$$

The parameters k and e_x were determined here from a teaching data set covering 60 dates in order to compare the polarization difference algorithm directly with the results obtained using inversion approach and multiple regression formulas. The mean values obtained for the 48 test grid cells are: $k = 2.275$ and $e_x = 0.9432$.

COMPARISON OF RETRIEVAL ALGORITHMS

When multiple linear regression formulas are compared with the inversion approach, one should note that the regression methods have some drawbacks that do not appear in the case of the inversion method. First, regression formulas require teaching data over long periods. Second, they employ coefficients that do not have any physical background. Hence, the applicability of the method is restricted to conditions similar to those under which the algorithm was developed. Also the polarization difference approach requires the employment of two empirical coefficients. However, the algorithm has some physical background, which probably increases its feasibility.

The test results of inversion algorithm are shown in Fig.1. The retrieval errors for all data points are depicted in Fig.1a. These results show that the overall rms retrieval error is 2.25 °C. If the results for a single grid cell are investigated, the retrieval error is often significantly lower. This is shown in Fig.1b which depicts that for a single grid cell the retrieval error may be as small as 1.2 °C. The higher level of scatter evident in Fig.1a is mainly due to the varying retrieval bias between the different grid cells.

Table 1 presents a comparison of the three temperature retrieval approaches. The results were obtained using all 48 grid cells. Additionally, the test results for some individual pixels are presented. The comparison shows that the multiple linear regression equations and the empirical polarization difference equation gave better overall performance than the inversion method. However, in the case of individual pixels the inversion approach may give better performance. Especially, this is the case for heavily forested pixels. In Table 1, grid cells #111 and #131 represent heavily forested areas, while grid cell #249 represents a mixed pixel. The same feature is also illustrated in Fig.2 which shows a comparison of grid cell-wise performances between the polarization difference algorithm and the inversion approach. These results clearly indicate that the inversion algorithm provides better results in most cases (i.e. heavily forested grid cells). For mixed pixels the performance of polarization difference method is better.

Table 1. Comparison of four temperature retrieval formulas (using all measurement dates from July - September 1993 and June 1994). The overall and single grid cell-wise rms retrieval errors and coefficients of determination are shown.

Method	All Grid Cells (48 Pixels)		Examples of Single Grid Cell-Wise Results: Pixel North #111		Pixel North #131		Pixel South #249	
	rms (C°)	r^2	rms (C°)	r^2	rms (C°)	r^2	rms (C°)	r^2
Inversion Method (Eqs. (1) - (5))	2.25	0.83	1.37	0.94	1.25	0.95	2.11	0.87
7-Channel Multiple Regression (Eq. (6))	1.55	0.91	1.72	0.93	1.82	0.94	1.40	0.89
3-Channel Multiple Regression (Eq. (7))	1.58	0.90	1.67	0.93	1.75	0.93	1.52	0.88
Polarization Difference (Eq. (8))	1.98	0.85	2.19	0.90	2.39	0.88	2.00	0.80

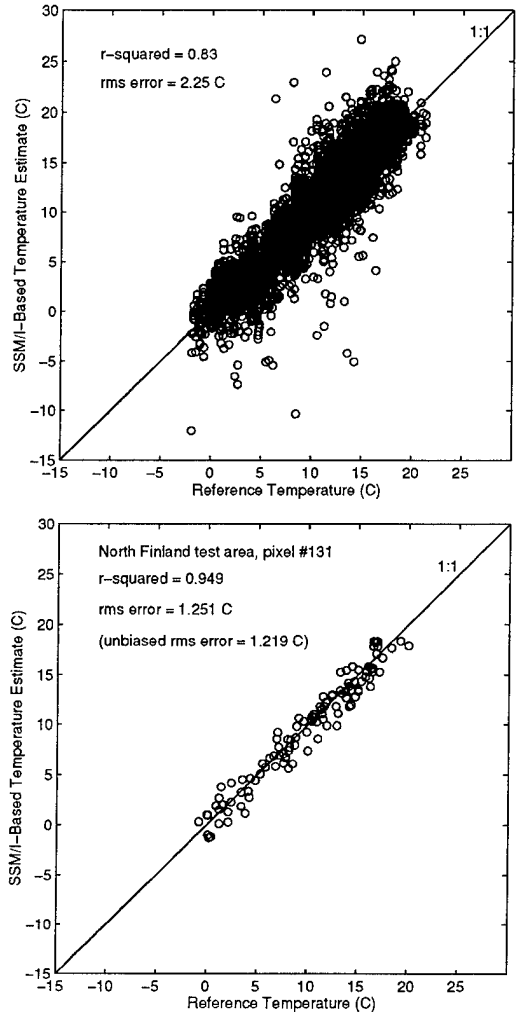


Figure 1. Inversion algorithm-based temperature retrieval results using SSM/I data from July to September 1993 and June 1994. The results are shown for: (a) All grid cells (5057 points), including the mean bias correction (6.03 °C) and (b) A single grid cell (pixel #131 of the North Finland test area).

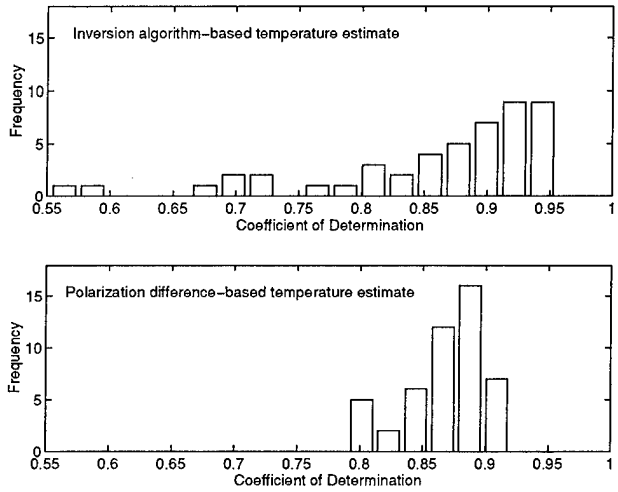


Figure 2. Behavior of pixel-wise coefficient of determination in cases of inversion and polarization difference methods.

CONCLUSIONS

Our results show that the physical temperature at the surface level can be retrieved with an accuracy of 1.2 to 2.5 °C using SSM/I data under snow-free conditions. This performance is the same or better than that reported for space-borne infrared instruments (NOAA AVHRR) [4,5]. Moreover, the use of microwave data is not affected by weather conditions.

REFERENCES

[1] D. Hiltbrunner, C. Mätzler and A. Wiesmann, "Monitoring land surfaces with combined DMSP-SSM/I and ERS-1 scatterometer data," *Proc. IGARSS'94 Symp.*, pp. 1945-1947, Pasadena, 1994.

[2] J. Aschbacher, "Land surface studies and atmospheric effects by satellite microwave radiometry," Ph.D. dissertation, Univ. of Insbruck, 1989.

[3] J. Pulliainen, J-P. Kärnä and M. Hallikainen, "Development of geophysical retrieval algorithms for the MIMR," *IEEE Trans. Geosci. Remote Sensing*, vol. 31, pp. 268-277, 1993.

[4] Y. Kerr, J. Lagouarde and J. Imbernon, "Accurate land surface temperature retrieval from AVHRR data with use of an improved split window algorithm," *Remote Sens. Environ.*, vol. 41, pp. 197-209, 1992.

[5] A. Vidal, "Atmospheric and emissivity correction of land surface temperature measured from satellite using ground measurements or satellite data," *Int. J. Remote Sensing*, vol. 12., pp. 2449-2460, 1991.

Visualisation of urban surface temperatures derived from satellite images

Janet Nichol
Division of Geography, Nanyang Technological University
469, Bukit Timah Rd, Singapore 259756
Fax: (65) 469-2427; email: nicholj@nievax.nie.ac.sg

Abstract - In recognition of the limited application of the satellite-based 'nadir' viewpoint for monitoring urban microclimate, a study was carried out to investigate the three-dimensional temperature relationships in high rise housing estates in Singapore. The data derived from this study are combined with LANDSAT TM thermal data to construct an automated 3-dimensional model of the high rise urban environment which can be varied according to sun angle and azimuth at the time of imaging and the viewing angle required by the user.

INTRODUCTION

The increasing spatial resolution of thermal satellite sensors has permitted observations of remotely sensed urban heat islands [1, 2] to include the detailed analysis of urban microclimate from pixel-derived surface temperature patterns [3, 4]. Daytime high resolution data are capableof revealing complex and discrete Surface Temperature patterns, since due to the heterogeneous nature of the urban environment, surface temperatures are discontinuous between structures and are influenced by building geometry.

Such a relationship provides an important input to urban design strategies for regulating the urban microclimate and can suggest the need for new or revised landscaping policies for mitigating the thermal effects of building geometry and high building mass. For this, a realistic means of portraying the detailed horizontal and vertical pattern and structure of heat generating surfaces within the urban canopy layer would be a useful input to urban design policies.

LIMITATIONS OF THE SATELLITE VIEWPOINT

Although a close relationship was established between Surface Temperature (**Ts**) and Air Temperature (**Ta**) for high rise housing estates in Singapore [4], a significant shortcoming of the use of satellite-derived data for microclimatic assessment concerns the limited satellite view of Ts, which does not represent the complete **active surface** (1) [1,3,5] and is only a proportion of the total, particularly in high rise urban developments. Vertical building sides, usually cooler than horizontal surfaces are unseen by the satellite's nadir viewing angle but may comprise a significant proportion of the active surface. Since the satellite views proportionally more of the active surface in low rise areas with shorter building sides, these areas would appear disproportionally hot relative to high rise areas due to more horizontal surfaces **'seen'** (2). The effect is also accentuated in tropical cities where high solar elevation means that horizontal 'seen' surfaces including roofs and tree canopies may be heated proportionally more than vertical surfaces. A study [4] using ground data collected at points in urban canyons in high rise housing estates in Singapore showed a strong relationship between **Ts** and **Ta** for both horizontal and vertical surfaces, both of which were significant at the 1% level. In spite of the fact that surfaces 'seen' by the satellite ie. horizontal surfaces including roofs, ground and tree canopies were more closely related to air temperature (r=0.7) than vertical ('unseen') surfaces (r=0.49), greater accuracy could be acheived if models of the complete surface were developed.

PLANNING OBJECTIVES FOR CLIMATE CONTROL

Planning objectives in a humid tropical city such as Singapore differ from those in temperate cities in that heat loads always need to be minimised. Considerations include the high sun angle year-round, causing faster heating of urban canyons, thus a need to minimise solar penetration to street level. Additionally, in the heating of vertical surfaces, east-west aspect is a dominant influence, operating on a diurnal time scale, to give east west building faces extreme surface temperatures in morning and evening respectively. In temperate cities in the other hand, the differential heating of north and south aspects has a greater overall effect.

OBJECTIVES OF THE STUDY

Specific objectives of the study are (i) to develop a methodology for estimation of the temperature of the complete urban surface in high rise housing estates in Singapore based on LANDSAT Thematic Mapper thermal data supplemented by ground-based surveys within the urban canopy layer. (ii) To construct an automated model for visualisation of the temperature of the complete urban surface which can be varied according to sun angle and azimuth at the time of imaging and the viewing angle required by the user.

THE STUDY AREA

The environment of Singapore's housing estates has been described elsewhere [3, 4] but two characteristics deserve emphasis. Firstly, the active-to-plan (seen) area ratio in a typical estate is 1.7/1; thus 67% of the surface 'seen' by the satellite is at ground level, the remainder being at tree

(1) The active surface comprises all surfaces both horizontal and vertical in the urban landscape where energy interactions with the atmosphere take place.

(2) The 'seen' surface is defined as that part of the active surface whose projection towards the satellite comprises the Instantaneous Field of View (IFOV).

The EOSAT Grants Program funded this research.

0-7803-3068-4/96$5.00©1996 IEEE

canopy (16%) and roof level (17%) (Table 1). Secondly, a common characteristic of Singapore's high rise estates is the predominantly east-west orientation of the long axis of housing blocks (Figure 1). This ensures minimal direct insolation of building faces and almost zero at the two equinoxes (Singapore is 1°12' North). At these times of year only the east and west-facing narrow ends of buildings, and floors of street canyons receive direct insolation (in morning and evening).

METHODS

A LANDSAT TM image of 24th May, 1989 was used for the study The local time of overpass at 10.40 am corresponded to a sun elevation of 51° and azimuth of 58°.

The pixel values of the thermal waveband were converted to Ts using Planck's law and emissivity correction [3]. The image pixels were then converted to vector polygon format and registered to a detailed building and street plan of Toa Payoh estate in ARCAD. The image was saved as a distinct drawing layer (TEMP) from the building and street plan (BUILD). The following procedures calculated and assigned the mean temperature of building polygons and building faces (Figure 2).

Step1. CLIP the image temperature polygons (TEMP) with the building outlines (BUILD) to give BLDTEMP

Step 2 Use STATISTICS on BLDTEMP to write the mean temperature for each building polygon to a record theme

Step 3 Use CLASS to classify the temperature values and allocate colours to each building class

In order to visualise the complete active surface, including both horizontal and vertical facets to it was necessary to construct surfaces as 3-D representations whose temperatures could be varied according to the effects of sun angle and azimuth at the time of imaging. Thus step 4:-

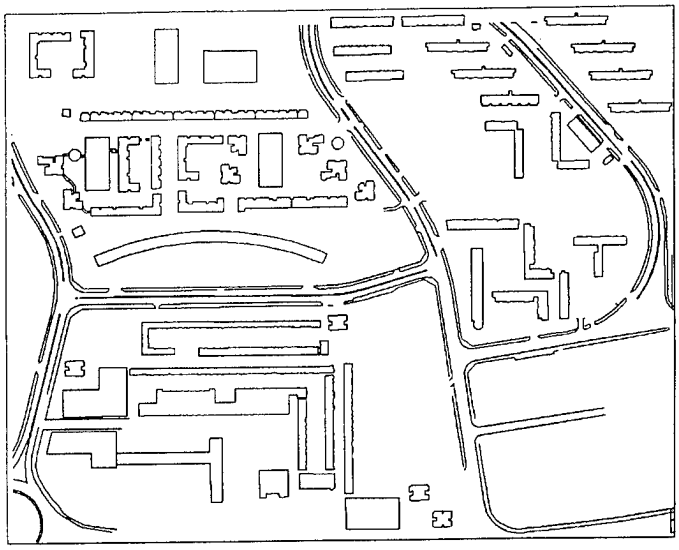


Figure 1. Building & street outlines

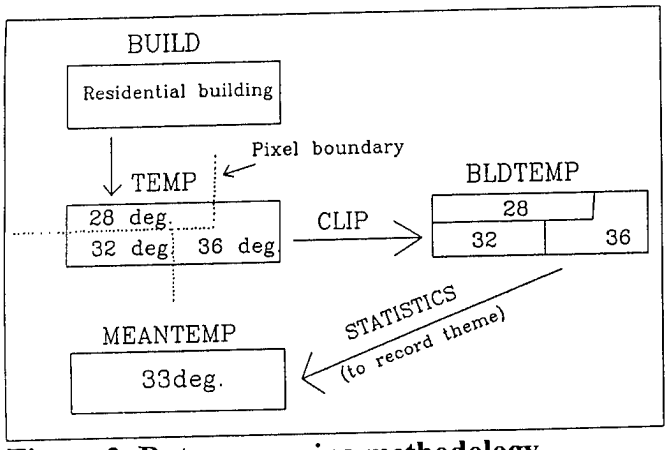


Figure 2. Data processing methodology

Step 4: Construction of the 3-D model

Extrude the building polygons as 3-dimensional wire frame models. Add solid 3-D faces as graphic primitives by layer, according to aspect (four aspects for walls and two for high and low roofs respectively).

Step 5 Temperature allocation to building facets

Temperatures were determined for the 3_D faces according values and relationships derived from a previous study which included detailed microclimatic observations of surface and air temperatures during daytime hours in differently oriented street canyons and at different elevations above street level in two of Singapore's high rise housing estates [4].

Accordingly, enhancement of the 3-D surface temperature model was carried out using the following relationships observed at the time of imaging (mid-morning)..

(i). Mean **Ts** for vertical surfaces was approximately 1°C cooler than that for horizontal surfaces.

(ii). **Ts** of the highest roof surfaces at 40m was slightly cooler (up to 0.5°C) than lower roofs and the ground.

(iii). Sunny walls were 1.5-2°C warmer than shady walls

(iv). All unshaded ground surfaces were warmer than all aspects of vertical surfaces, though shaded ground may be cooler than sunny walls.

Accordingly, temperatures of the vertical building faces were adjusted using selection by drawing layer or by AUTOCAD's FILTER function:- All vertical faces, selected by layer were allocated two classes cooler than the 2-D building polygon, except for sunny walls (selected by layer according to aspect) allocated one class cooler. Highest roofs are one class cooler than the corresponding ground surface.

DISCUSSION

Figures 3 and 4 show 3-D views of the model representing the temperature of the active surface, as seen from the south-east aspect, and satisfying the objectives of visualisation, ie. *the process of representing information synoptically for the*

purpose of recognising, communicating and interpreting pattern and structure [5].

Specifically, such data may achieve the following planning objectives:-

To illustrate the advantages of close spacing between buildings, thus ensuring that the inter-building space is not greater than the shadow length and maintaining shady canyons between blocks at most times during the day (A and B on Figure 3). This is particularly important due to the high sun angle in low latitude cities giving shorter shadow lengths.

The models indicate the location and morphological characteristics of extensive warm areas and can indicate the need for effective greening campaigns as well as to assess the effectiveness of existing vegetation. (Figure 4).

3-D visualisation can contribute to the understanding of the role of the type and spatial arrangement of different surface materials in urban areas, as well as indicate potential areas of energy interaction with the overlying boundary layer for modelling of heat and air pollution dispersal.

REFERENCES

[1] Balling, R.C., and S.W. Brazell, Photog. Eng. & Rem. Sensing, Vol. 54(9) 1988, pp.1289-1293.

[2] Roth, M., T.R. Oke, and W.J. Emery, , Int.J. Rem. Sen. Vol. 10(11), 1989, pp.1699-1720.

[3] Nichol, J.E., Phot. Engr. & Rem. Sensing, 60(10), 1994, pp.1225-1232..

[4] Nichol, J.E., J. Appl. Meteorol., 35(1), 1996, pp.135-146.

[5] Buttenfield, B. & W.A Mackaness, Visualisation in Geographical Information Systems: principles and applications, Maguire, D.J., Goodchild, M.F. and Rhind, DW., (eds.) Longman, 1991, pp. 427-455.

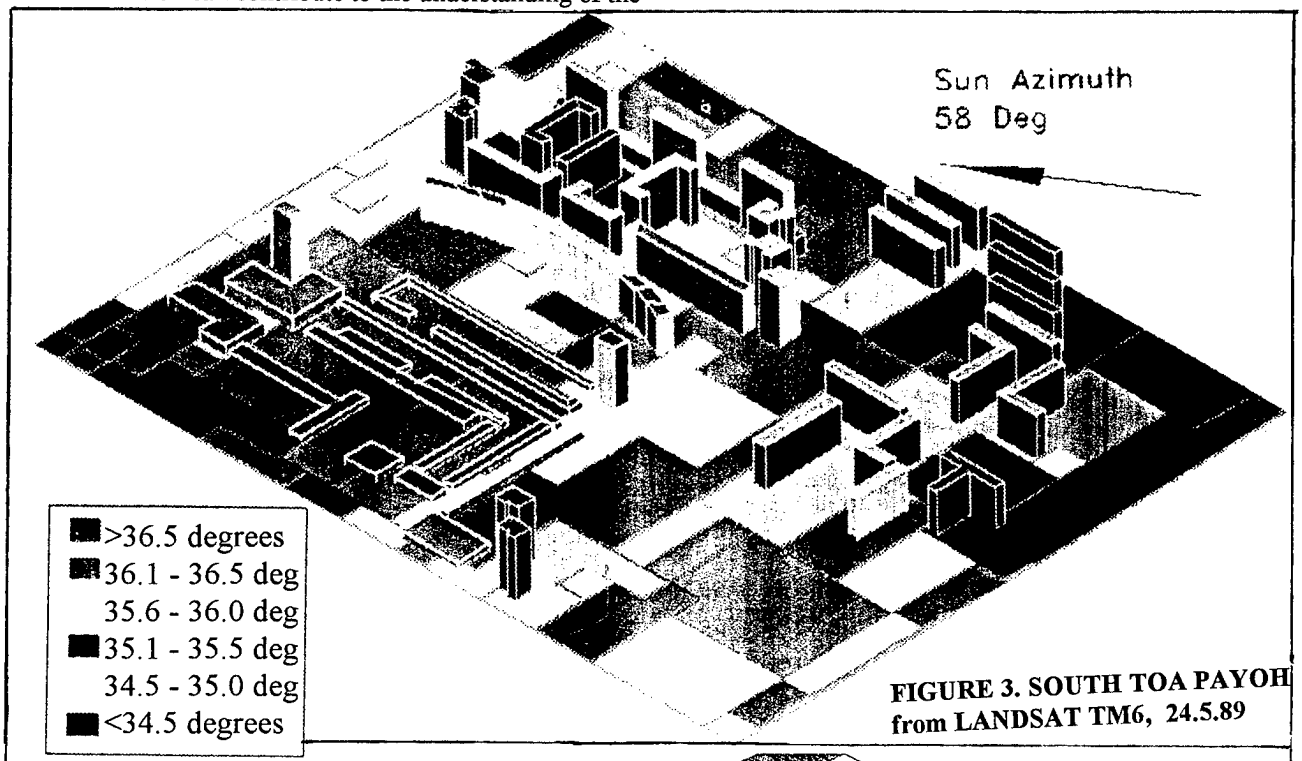


FIGURE 3. SOUTH TOA PAYOH from LANDSAT TM6, 24.5.89

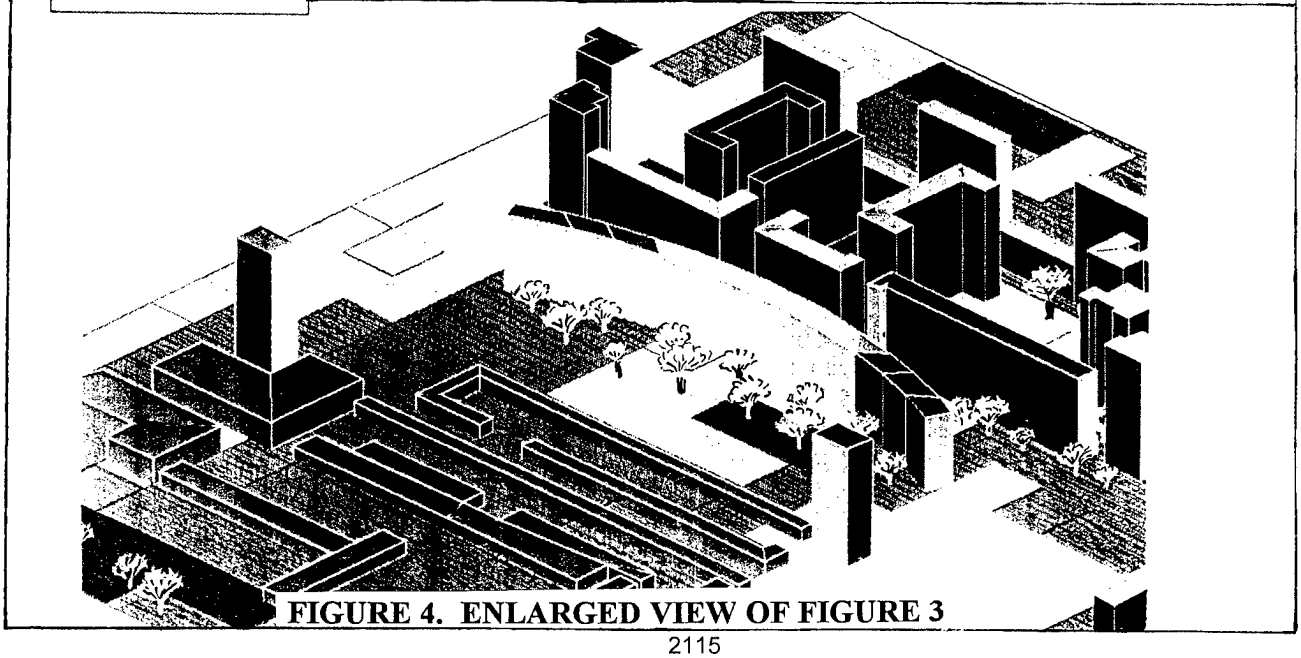


FIGURE 4. ENLARGED VIEW OF FIGURE 3

A Further Study of the IEM Surface Scattering Model

A.K. Fung and C.Y. Hsieh
[1]E.E. Dept.,Box 19016, University of Texas at Arlington, TX 76019
Tel: 817–273–3422, FAX 817-273-3443, eefung@uta.edu
Giuseppe Nesti and A. Sieber
IRSA/AT, JRC - Ispra, TP 720
Giuseppe.Nesti@jrc.it, tel: +39 332 78 592221020 Ispra (VA) - Italy,
Peter Coppo
Center for Microwave Remote Sensing (CeTeM)
Via Panciatichi 64
50127 Firenze (Italy)

Abstract -- The IEM surface scattering model was developed based on an approximate solution of a pair of integral equations governing the surface current. Among the assumptions leading to the approximation is the use of a simplified expression for the Green's function in spectral form. In particular, it was argued that the absolute value of the difference in the surface heights at two surface points appearing in the phase of the Green's function can be ignored. This argument was arrived at by noting that (i) if the two points are close together, the difference in heights should be small and (ii) if the two surface points are far apart, there should be a negligible amount of correlation between the two points and hence will not contribute significantly to the scattered power. Mathematically, there is no reason to make this assumption and it is also questionable whether the contribution from two surface points that are neither near or far can always be ignored. In this paper we want to remove this assumption by keeping this phase term and examine the difference in scattering calculations with and without it. It is found that in all cases considered the existing IEM model gives satisfactory predictions in single scattering. However, in multiple scattering calculations it is not possible to ignore this phase especially for surfaces with large roughness. An application of this model to scattering from known rough dielectric surfaces acquired at the EMSL of the JRC at Ispra is shown and good agreements are realized. Further application to a large slope surface that causes backscattering enhancement also gives good agreement with data.

INTRODUCTION

The approximate solution for the surface current used in the existing IEM surface scattering model [1] ignores a phase term in the Green's function which represents propagation of waves in the upward and downward directions. In single scattering calculation this is not an important issue because we only need the total equivalent current on the surface and we can correct for shadowing separately by multiplying the final average scattered power by a shadowing function, S.

In multiple scattering calculation the problem is much more complex. We need to separate the scattered field into upward propagating and downward propagating components (Figure 1). Let S represent an applicable shadowing function for a given randomly rough surface. Then, the fraction of the upward scattered field that leaves the surface is S and the fraction intercepted by the surface is (1-S). The fraction of the downward scattered field is obviously intercepted by the surface.Thus, these intercepted scattered waves represent the next round of incident field on the surface. Without

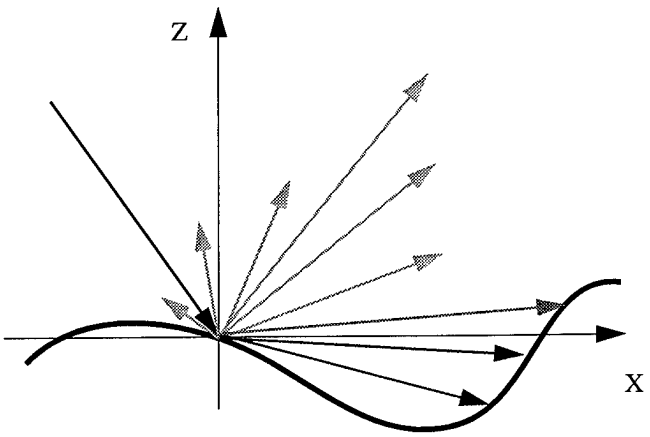


Figure 1 Geometry of the scattering problem

identifying the upward and downward scattered field it is not possible to assign the correct fraction and obtain the correct equivalent current for multiple scattering calculation.

THE MODIFIED ENSEMBLE AVERAGES

When the phase term of the Green's function with an absolute value sign is included, the major impact is on the evaluation of the ensemble averages. For example, a quantity to be averaged in the average power expression is

$$\langle \exp[jk_{sz}z + jk_z z' - jq|z - z'|] \rangle \quad (1)$$

where z and z' are the random variables representing the surface height at different locations on surface. Without the absolute value term the average is the standard characteristic

0-7803-3068-4/96$5.00©1996 IEEE

function for two variables. With the absolute value term present there is no known solution. Integration has to be carried out in two dimensions to find the average. A method to deal with this situation is to apply a transformation such as

$$z = (y_1 + y_2)/\sqrt{2}$$
$$z' = (y_1 - y_2)/(\sqrt{2}) \quad (2)$$

so that after transformation only one variable appears in the absolute sign yielding

$$\langle \exp\left[j\frac{k_{sz}(y_1+y_2)}{\sqrt{2}} + j\frac{k_z(y_1-y_2)}{\sqrt{2}} - j\sqrt{2}q|y_2| \right] \rangle \quad (3)$$

The reason for doing this is that the integration on y_2 can be broken into two integrals from $-\infty$ to 0 and then from 0 to ∞ leading to a closed form expression,

$$\langle \exp[jk_{sz}z + jk_z z' - jq|z-z'|] \rangle = \frac{1}{2}\exp\left[-\frac{\sigma^2(k_{sz}^2 + k_z^2)}{2} \right]$$
$$\left[e^{-\sigma^2(k_{sz}k_z - q^2 + qk_{sz} - qk_z)\rho - \sigma^2(q^2 - qk_{sz} + qk_z)} + \right.$$
$$\left. e^{-\sigma^2(k_{sz}k_z + -q^2 - qk_{sz} + qk_z)\rho - \sigma^2(q^2 + qk_{sz} - qk_z)} \right] \quad (4)$$

Using this technique it is possible to obtain closed form expressions for ensemble averages involving three- and four-variables as follows,

$$\langle \exp[jk_{sz}(z-z'') - jk_z(z''-z') - jq|z-z'|] \rangle$$
$$= \frac{1}{2}\left\{ \left[1 + erf\left(j\frac{\sigma a_1}{2\sqrt{1-\rho_1}} \right) \right] e^{-\sigma^2 p_1} \right\}$$
$$+ \left[1 + erf\left(j\frac{\sigma a_2}{2\sqrt{1-\rho_1}} \right) \right] e^{-\sigma^2 p_2} \quad (5)$$

where $a_1 = k_{sz} - k_z - 2q - k_{sz}\rho_1 + k_z\rho_1 + 2q\rho_1 - k_{sz}\rho_2$
$- k_z\rho_2 + k_{sz}\rho_3 + k_z\rho_3$

$a_2 = k_{sz} - k_z + 2q - k_{sz}\rho_1 + k_z\rho_1 - 2q\rho_1 - k_{sz}\rho_2$
$- k_z\rho_2 + k_{sz}\rho_3 + k_z\rho_3$

$p_1 = (k_{sz}^2 + k_{sz}k_z + k_z^2 - k_{sz}q + k_z q + q^2)$
$+ (k_{sz}k_z - q^2 + k_{sz}q - k_z q)\rho_1 - (k_{sz} - q)(k_{sz} + k_z)\rho_2$
$-(k_z + q)(k_{sz} + k_z)\rho_3$

$p_2 = (k_{sz}^2 + k_{sz}k_z + k_z^2 + q^2 + k_{sz}q - k_z q)$
$+ (k_{sz}k_z - q^2 - k_{sz}q + k_z q)\rho_1 - (k_{sz} + q)(k_{sz} + k_z)\rho_2$
$-(k_z - q)(k_{sz} + k_z)\rho_3$

In the above expressions ρ_i 's are the correlation functions at different spacings. Finally, the real part of the average of a four-variable expression is

$$\langle \exp[jk_{sz}(z-z'') + jk_z(z'-z''') - jq|z-z'| + jq'|z''-z'''|] \rangle$$
$$= \frac{1}{4}[r(q,q')c_1(q)c_2(q,q')c_3(q,q')]$$
$$[c_4(q,q')c_5(q,q')c_6(q,q')]$$
$$+ \frac{1}{4}[r(-q,q')c_1(-q)c_2(-q,q')c_3(-q,q')]$$
$$[c_4(-q,q')c_5(-q,q')c_6(-q,q')]$$
$$+ \frac{1}{4}[r(q,-q')c_1(q)c_2(q,-q')c_3(q,-q')]$$
$$[c_4(q,-q')c_5(q,-q')c_6(q,-q')]$$
$$+ \frac{1}{4}[r(-q,-q')c_1(-q)c_2(-q,-q')c_3(-q,-q')(-q,-q')]$$
$$[c_4(-q,-q')c_5(-q,-q')c_6(-q,-q')] \quad (6)$$

where

$$r(q,q') = \exp\left\{ (-\sigma^2)[k_{sz}^2 + k_z^2 + q^2 + q'^2 \right.$$
$$\left. -(k_{sz} - k_z)(q + q')] \right\}$$

$$c_1(q) = \exp[-\sigma^2(k_{sz} - q)(k_z + q)\rho_1]$$

$$c_2(q,q') = \exp[-\sigma^2(k_{sz} - q')(k_{sz} - q)\rho_2]$$

$$c_3(q,q') = \exp[-\sigma^2(k_{sz} - q)(k_z + q')\rho_3]$$

$$c_4(q,q') = \exp[-\sigma^2(k_{sz} - q')(k_z + q)\rho_4]$$

$$c_5(q,q') = \exp\left\{ -\sigma^2[(k_z + q)(k_z + q')]\rho_5 \right\}$$

$$c_6(q,q') = \exp\left\{ -\sigma^2[(k_{sz} - q')(k_z + q')]\rho_6 \right\}$$

APPLICATIONS OF MODIFIED IEM MODEL

The availability of the above ensemble averages allows the recognition of propagation directions and hence an appropriate correction with the shadowing function on the equivalent current term for multiple scattering calculation. That this is so is evidenced by the following application to laboratory measurements from known randomly rough surfaces where all surface parameters are known. We shall consider two cases in which surface slope and roughness are large so that multiple scattering is significant. Furthermore, backscattering enhancement which results from multiple surface scattering is present.

Case 1 is a dielectric surface prepared at JRC with backscattering and dielectric measurements taken at EMSL of JRC. It is a Gaussian correlated surface with rms height of 2.5 cm and a correlation length of 6 cm. Comparisons with like and cross backscattering measurements over a wide range of frequencies are shown in Figures 2 and 3.

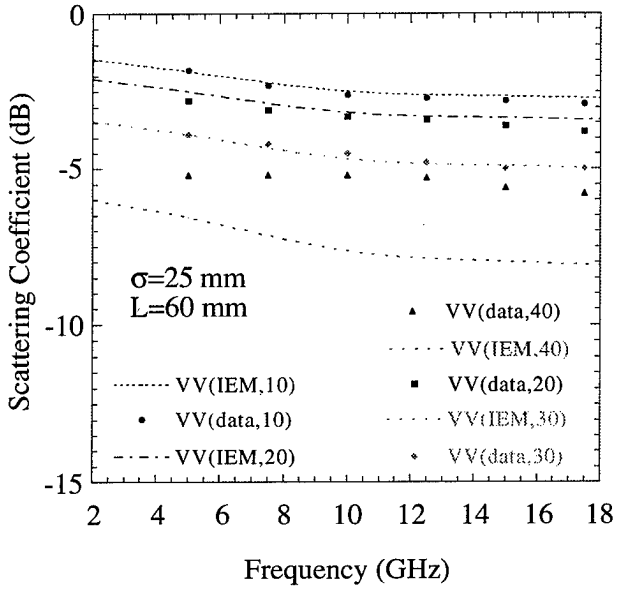


Figure 2 Comparison with like polarization data over 5 to 17GHz and 10 to 40 degrees.

In Figure 2 excellent agreement occurs for all frequency and angles up to 30 degrees. At 40 degrees theory is 1 to 2 dB lower than the data. It is possible that for dielectric surface there is an unknown dielectric profile which may account for this discrepancy at large angles.

In Figure 3 comparisons are made with cross polarized measurements over 5 to 17 GHz and an angular range from 10 to 50 degrees. Here, again the agreement is excellent except at 50 degrees where there may be a coupling problem because the like polarized return is very high.

Finally, in Figure 4 we show comparisons with bistatic cross polarized measurements from a perfectly conducting surface with known roughness showing backscattering enhancement. The theoretical model prediction by Ishimaru is also shown along with the data. It is evident that excellent agreement is obtained between our model predictions and the data. The backscattering enhancement peak is clear and occurs in exactly the same location as the data.

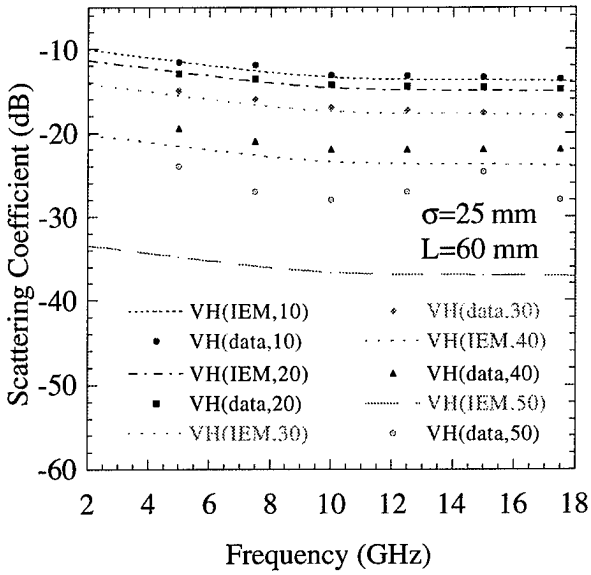


Figure 3 Comparison with cross polarization over 5 to 17GHz and 10 to 50 degrees.

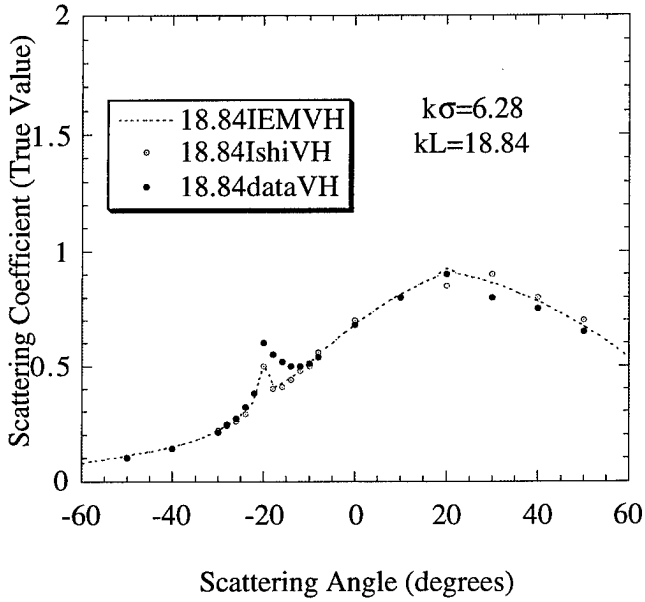


Figure 4 Comparisons with cross polarization bistatic data with backscattering enhancement.

Acknowledgment:This work was supported by NASA SIR-C data analysis program funded through the JPL.

REFERENCES

[1] Fung, A.K., *Microwave Scattering and Emission Models and Their Applications*, Artech House, Norwood, MA, 1994.

On The Use Of the Quasi Specular Model For Surface Parameter Estimation

Roger Marchand and Gary S. Brown
Bradley Department of Electrical Engineering
Virginia Polytechnic Institute and State University
Blacksburg, VA 24061-0111
EMAIL: RogerM@birch.ee.vt.edu / Randem@vtvm1.cc.vt.edu

Abstract -- The specular point or quasi specular model has seen extensive use in inversion algorithms to estimate surface roughness, i.e. the variance of surface slopes, and the reflection coefficient of randomly rough surfaces from backscattered fields [1-3]. In the quasi specular model, the mean scattering cross section per unit illuminated area of the rough surface is directly proportional the magnitude of the flat surface Fresnel reflection coefficient, R, and the probability density function (pdf) of the filtered surface slopes. i.e. for a one dimensional surface

$$\sigma^0_{backscattered}(\theta) = \pi \sec^3(0) pdf_{\nabla S}(\tan^{-1}(\theta))|R(0^o)|^2. \qquad (1)$$

In effect, the reflection coefficient influences the portion of the incident field scattered and the slope pdf determines the direction in which there is preferred scattering. The quasi specular model is developed from a high frequency approach in which the surface is assumed to be sufficiently rough in height that there is no coherent scattering but not so rough that multiple scattering is significant [4].

Despite the model's wide usage, no comprehensive quantitative study of the model's range of validity as an inversion tool has been performed. In this presentation, quantitative results of a numerical study on the use of the quasi specular model for parameter estimation in two dimensions (i.e. a one-dimensional surface) are presented.

The study shows how the accuracy of the quasi-specular model as an inversion tool varies over a wide range of parameters for Gaussian surfaces through the use of Monte Carlo simulation results where exact surface parameters are known. Of particular importance in the parameter estimation problem is the numerical noise present in any finite length Monte Carlo simulation and the angular region over which "data" is to be compared to the model. As with most problems of this nature, there are a number of tradeoffs and these will be explored.

GENERAL CHARACTERIZATION

In this section Method of Moment (MOM) simulations of the average normalized radar cross section (NRCS) are compared to the quasi specular model for Gaussian surfaces having both a Gaussian height pdf and a Gaussian correlation function. Such a surface can be characterized by two values: (1) the slope variance, σ_s^2, and (2) the height variance, σ_h^2.

Consider first Fig. 1 which compares the TE backscattered NRCS divided by the square of the magnitude in the reflection coefficient to the same quantity predicted by the quasi specular model. The NRCS has been divided by the reflection coefficient because the quasi specular model suggests that this quantity will be independent of the scattering material (i.e. the scattering will only be a function of the surface roughness). For a surface of the same height but with a slope variance of 0.1 (not shown here), there is only a very slight difference in the near nadir region between the scattering from a perfect electric conducting (PEC) material and an $\varepsilon = 2.0$ material. But in Fig. 1 where the slope variance is 0.2, there is a very noticeable difference between the PEC and the $\varepsilon = 2.0$ material. Near nadir, the scattering from the dielectric material remains much closer to the quasi specular model than for the PEC material. Because the surface roughness is exactly the same in both cases (in fact identical surface profiles where used), this suggests that multiple scattering is significantly contributing to the scattered field, see below.

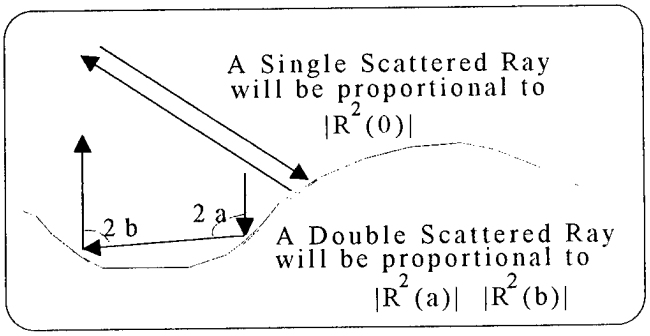


Fig. 2 plots the same data shown in Fig 1. except that it is given in dB (i.e. 10 $\text{Log}_{10}(\text{NRCS}/R^2(0))$. Taking the log of the data reveals that the quasi specular model underpredicts the backscattered cross section well away from nadir. In general, it has been observed that as the slope variance increases (or as the height decreases - see Fig. 4) the quasi specular model becomes increasingly inaccurate at large incident angles. This appears to be due to the effect of small scale structure.

0-7803-3068-4/96$5.00©1996 IEEE

INVERSION METHODS

Taking the ratio of the quasi specular backscattered cross section, (1), at any two angles yields an expression which is only a function of the distribution of the surface slopes. i.e.

$$\frac{\sigma^o_{bs}(\theta_1)}{\sigma^o_{bs}(\theta_2)} = \frac{\sec^3(\theta_1) P_{\nabla\zeta}(\tan(\theta_1))}{\sec^3(\theta_2) P_{\nabla\zeta}(\tan(\theta_2))}. \quad (2)$$

For a Gaussian pdf this two point equation can be easily manipulated to determine the variance of the surface slopes,

$$\sigma_s^2 = \frac{1}{2} \frac{\tan^2(\theta_2) - \tan^2(\theta_1)}{\ln(\frac{\sigma^o_{bs}(\theta_1)}{\sigma^o_{bs}(\theta_2)}) - 3\ln(\frac{\cos(\theta_2)}{\cos(\theta_1)})}. \quad (3)$$

In this numerical study, the NRCS is obtained from a Monte Carlo method of moments simulation. Unfortunately, this "simulated data" will have some unavoidable fluctuations arising from the finite number of samples available to form the average. To reduce the impact of this "realization noise", the average over many angle combinations can be taken. However, when the two angles are close together, the fluctuations can cause the slope of the NRCS to appear to increase (largely due to non zero angular correlation) and (3) will produce extreme outliers. As a results, some kind of windowing (which prevents the use of angles which are "close" together) or a more robust estimator of the "average" must be used.

Alternatively, the simulated data can be fit to the model using a minimization approach. In a minimization approach, a merit function is defined which describes the difference between the model and the data for a given set of model parameters. The set of model parameters which give the smallest value for the merit function (i.e. its minimum) are taken to be the values which best fit the model to the data. The maximum likelihood estimator for an exponential distribution is the least absolute deviate, (commonly referred to as the L1 norm)

$$f_{merit}(a_1, a_2..a_m) = \sum_{i=1}^{N} |data(x_i) - model(x_i, a_1, a_2..a_m)|. \quad (4)$$

INVERSION RESULTS

Fig. 3 compares the inversion results using the backscattered NRCS over 0 to 50 degrees obtained via: (1) a 15/85 average, i.e. the largest and smallest 15% of the values obtained using the two angle approach over all pairs of angles are ignored, (2) an 8° window, i.e. using the two angle approach over all pairs of angles more than 4° apart, (3) L1 minimization, and (4) minimization in dB, i.e. |10 log(data) - 10 Log(model)|. Here the scattering surface has height variance of 0.506 wavelengths squared and a slope variance of 0.2, and reflection coefficients of -1.0, -0.75, -0.5, and -0.2. These results are for the TE (or h) polarization. The error bars represent Gaussian confidence limits obtained by inverting 20 cross sections (each cross section being obtained by averaging the RCS from 200 surfaces with a length of 80 wavelengths).

The plot shows that the relative error, (5), is larger for the L1 minimization than for the other four approaches. This occurs because the NRCS decreases as a function of the backscattered angle, but the merit function defined by (4) weights each data point equally. Thus the L1 minimization will place most emphasis in the nadir region where the error is large due to multiple scattering. In effect the multiple scattering causes the NRCS to appear to decay faster than is predicted by the quasi specular model and therefore yields a low estimate for the slope. The minimization in dB approach on the other hand, emphasizes the region far from normal incidence. Because the quasi specular model underestimates the backscattering in this region, the minimization in dB approach increases the slope estimate to fit the curve in this region. Not surprisingly, the two angle approaches which treat every angle nearly equally estimate values between the two minimization approaches.

$$relative\ error \equiv \frac{Known\ Value - Estimated\ Value}{Known\ Value}. \quad (5)$$

As an example of the overall estimation trends, Figs 5 and 6 are included as representative samples. Fig. 5 plots the relative error in the reflection coefficient and Fig. 6 plots the relative error in the slope variance. Both are obtained for the same height variance as in Fig. 3, but for slope variances of 0.2, 0.3 and 0.4 in both the TE(h) and TM(v) cases using a 15/85 average.

[1] The use of a specular reflection model to study sea surfaces has been used by numerous authors as early as Cox and Monk in 1954 (J. Opt. Soc. Am. vol. 44, 838-850) to the present (See for example Jackson, F.C., Walton, W.T. and Hines, D.E., JGR Vol. 97, No. C7, July 15, 1992.)

[2] Tyler, Leonard G., Simpson, Richard A., Maurer, Michael J., and Holman, Edgar. "Scattering Properties of the Venusian Surface: Preliminary Results from Magellan," JGR Vol. 97, No. E8, August 25, 1992.

[3] Kim, Yunjin, Rodriguez, Ernesto and Saachi, Sasan, "Venus Surface Parameter Estimation Algorithm Using the Magellan Data," IEEE AP-S International Symposium, 1994.

[4] Brown, Gary S. "Quasi-Specular Scattering From the Air-Sea Interface, " Surface Waves and Fluxes, Vol. II eds. G. L. Geernaert and W. J. Plant, Kluwer Academic Publisher, printed in the Netherlands, 1990.

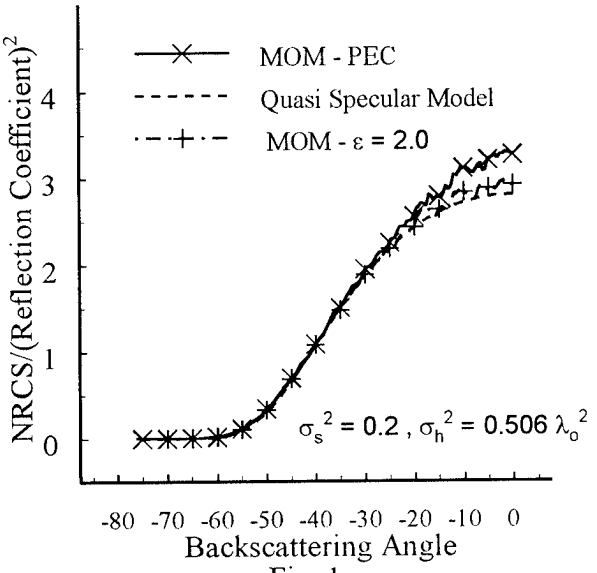


Fig. 1

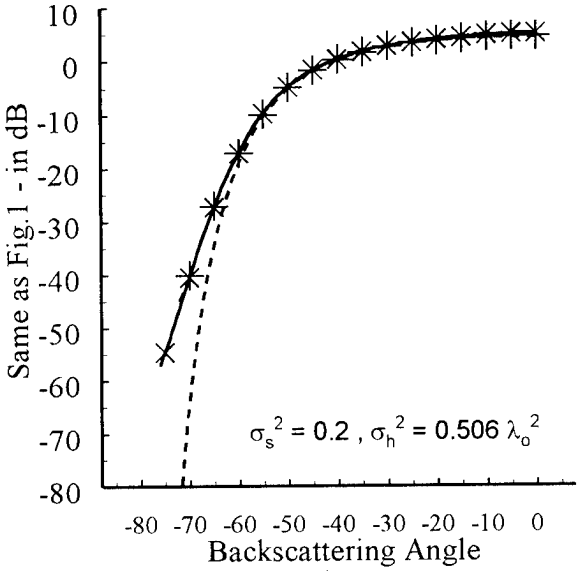


Fig. 2

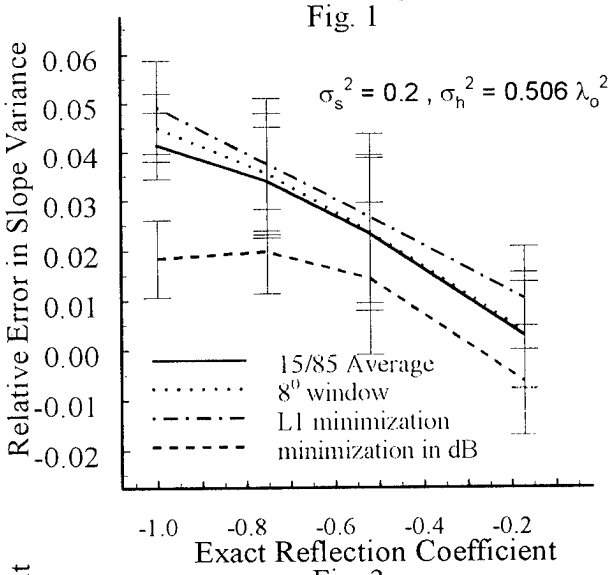


Fig. 3

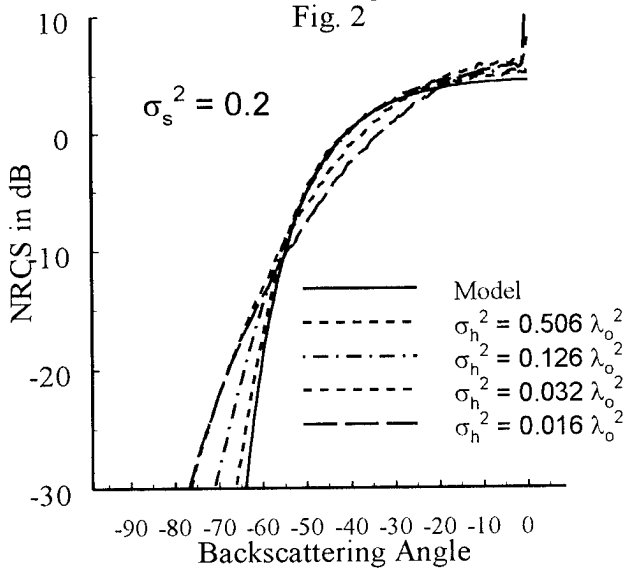


Fig. 4

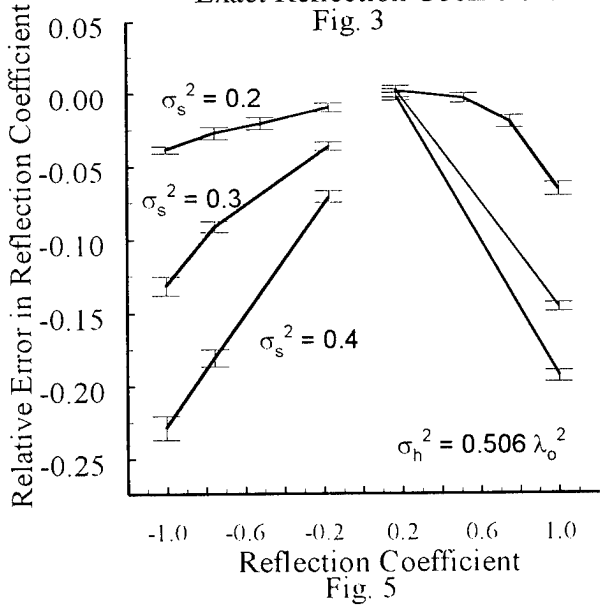


Fig. 5

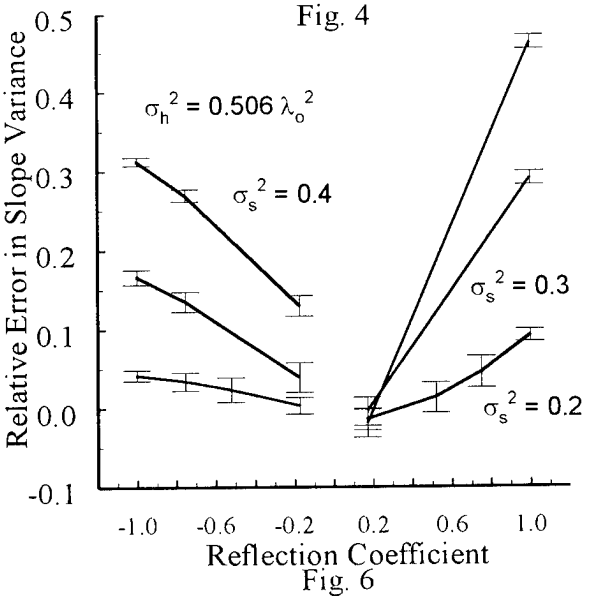


Fig. 6

Electromagnetic Scattering from Slightly Rough Surfaces with Inhomogeneous Dielectric Profile

Kamal Sarabandi and Tsenchieh Chiu
Radiation Laboratory
Department of Electrical Engineering and Computer Science
The University of Michigan, Ann Arbor, MI 48109-2122
Tel :(313) 936-1575
Email: saraband@eecs.umich.edu

Abstract – Remote sensing of soil moisture using microwave sensors require accurate and realistic scattering models for rough soil surfaces. In the past much effort has been devoted to the development of scattering models for either perfectly conducting or homogeneous rough surfaces. In practice, however, the permittivity of most soil surfaces is nonuniform, particularly in depth, for which analytical solution does not exist. The variations in the permittivity of a soil medium can easily be related to its soil moisture profile and soil type using the existing empirical models. In this paper analytical expressions for the bistatic scattering coefficients of soil surfaces with slightly rough interface and stratified permittivity profile are derived. The scattering formulation is based on a new approach where the perturbation expansion of the volumetric polarization current instead of the tangential fields is used to obtain the scattered field. Basically, the top rough layer is replaced with an equivalent polarization current and using the volumetric integral equation in conjunction with the dyadic Green's function of the remaining stratified half-space medium the scattering problem is formulated. All first-order scattering solutions and second-order scattering solutions for the cross-polarization fields are obtained. The theoretical results are compared with the backscatter measurements of rough surfaces with known dielectric profile and roughness statistics.

INTRODUCTION

Soil moisture, its temporal and spatial variations are influential parameters in both climatic and hydrologic models. Soil dielectric constant at microwave frequencies exhibits a strong dependence on the soil's moisture content. At L-band, for example, the real part of the dielectric constant ranges from 3 for dry soil to about 25 for saturated soil condition. This variation can result in a change on the order of 10 dB in the magnitude of the radar backscatter coefficient [1]. With the advent of synthetic aperture radar (SAR) and radar polarimetry, radar remote sensing of soil moisture has attained significant prominence in the past decade. SAR systems are capable of producing backscatter map of the terrain with high resolution from an airborne or space-borne platform. From the electromagnetic point of view, remote sensing of soil moisture, in the absence of vegetation cover, can be defined in terms of an inverse scattering problem where the dielectric constant and surface roughness statistics are to be determined from a set of backscatter measurements.

Problem of wave scattering from random rough surfaces has been the subject of ongoing research over the past fifty years because of its application in many areas of science and engineering. Generally speaking, the available electromagnetic scattering models can be categorized into three major groups: (1) analytical, (2) empirical, and (3) numerical. The analytical solution to the rough surface scattering apply in two limits so far as the surface roughness parameters are concerned. These limits correspond to extreme conditions where the roughness dimensions of the surface are either much smaller and much larger than the wavelength. For surfaces with small surface rms height and slope, small perturbation model (SPM) is the most commonly used formalism [2]. In this approach, the surface fields are expanded in terms of a power series of the small roughness parameter and then using either the Rayleigh hypothesis or the extended boundary condition, the expansion coefficients are obtained recursively. Scattering formulation based on SPM exist for two-dimensional dielectric and perfectly conducting rough surfaces up to second order. On the other hand, if the irregularities of the surface have relatively small slopes and large radii of curvature, the Kirchhoff approximation (KA) can be used. In this approach the surface fields at a given point are approximated by those of the local tangent plane. In the past two decades many attempts have been made to extend the validity region of SPM and KA. Among these, phase perturbation method (PPM) [3] and unified perturbation expansion (UPE) [4] for extending the low- and the integral equation method (IEM) [5] for extending the high-frequency techniques can be mentioned.

In this paper no attempt is made to extend the validity region of the existing methods, instead another practical aspect of the scattering problem is investigated. In most practical situations, the soil's moisture content as a function of depth is nonuniform in depth. The soil moisture profile is usually a complex function of soil type, temperature profile, surface evaporation and moisture content. For radar remote sensing of soil moisture, the effect of the inhomogeneity in the complex permittivity of the soil surface on its backscatter must be understood. For this purpose, analytical expressions for the bistatic scattering coefficients of a slightly rough surface with inhomogeneous dielectric profile are derived. Using the classical perturbation expansion of the electric field, a new volumetric integral equation approach is used to obtain the iterative scattering solutions. In what follows, the theoretical formulation for

0-7803-3068-4/96$5.00©1996 IEEE

the scattering problem is given. The theoretical solution will be compared with experimental backscatter measurements collected using the University of Michigan's bistatic indoor facilities.

THEORETICAL ANALYSIS

Consider an inhomogeneous half-space medium with a rough interface as shown in Fig. (1). It is assumed that the permittivity function is only a function of z given by $\epsilon(x,y,z) = \epsilon(z)$. Suppose a plane wave is illuminating the rough interface from the upper medium. It is further assumed that the surface height variation is small compared to the wavelength of the incident wave. To make the solution tractable, the permittivity of the top layer down to a depth of d is considered to be uniform where $-d < min\{\text{surface profile}\}$. Let us denote the surface height profile by function $z = \triangle f(x,y)$ which is a zero-mean stationary random process with a known autocorrelation function and $\triangle << \lambda_0$ is a small constant known as the perturbation parameter.

The scattered field $\mathbf{E}^s$ can be expressed in terms of the polarization current and is given by

$$\mathbf{E}^s = ik_0 Z_0 \int\limits_{V_{slab}} \bar{\bar{\mathbf{G}}}(\mathbf{r},\mathbf{r}') \cdot \mathbf{J}(\mathbf{r}')\, dv' \tag{1}$$

where $\bar{\bar{\mathbf{G}}}(\mathbf{r},\mathbf{r}')$ is the dyadic Green's function of the half-space inhomogeneous layer. The integral equation for the polarization current can be obtained

$$\frac{1}{\epsilon - 1}\mathbf{J}(\mathbf{r}) = -ik_0 Y_0(\mathbf{E}^i + \mathbf{E}^r) + k_0^2 \int\limits_{-\infty}^{\infty}\int\limits_{0}^{d+\triangle f(x',y')} \bar{\bar{\mathbf{G}}}(\mathbf{r},\mathbf{r}') \cdot \mathbf{J}(\mathbf{r}')\, dv', \tag{2}$$

where $\mathbf{E}^i$ and $\mathbf{E}^r$ are incident and reflected plane waves when the surface is smooth. (2) is solved up to first-order for the co-polarization fields and second-order for the cross-polarization fields. The first-order solutions for the elements of the scattering matrix are found to be

$$S_{hh}^{(1)} = \frac{1}{2\pi}\left(k_{1z}^i - k_z^i\right) k_z^i e^{-i(k_z^i + k_z^s)d} \cos(\phi_s - \phi_i) \cdot (1 + R_h^s) \cdot \left[\triangle \widetilde{f}(\bar{k}_\perp^s - \bar{k}_\perp^i)\right] \cdot C_{h1}(\bar{k}_\perp^s, d) \cdot C_{h1}(\bar{k}_\perp^i, d)\,,$$

$$S_{hv}^{(1)} = \frac{1}{2\pi}\frac{k_0(\epsilon-1)k_z^i k_{1z}^i}{k_{1z}^i + \epsilon k_z^i} e^{-i(k_z^i + k_z^s)d} \sin(\phi_s - \phi_i) \cdot \left[\triangle \widetilde{f}(\bar{k}_\perp^s - \bar{k}_\perp^i)\right] \cdot (1 + R_h^s) \cdot C_{h1}(\bar{k}_\perp^s, d) \cdot C_{v2}(\bar{k}_\perp^i, d)\,,$$

$$S_{vh}^{(1)} = \frac{1}{\pi}\frac{(k_z^i - k_{1z}^i)k_z^i k_{1z}^s}{k_{1z}^i + \epsilon k_z^i} e^{-i(k_z^i + k_z^s)d} \sin(\phi_s - \phi_i)\cos\theta_s \cdot \left[\triangle \widetilde{f}(\bar{k}_\perp^s - \bar{k}_\perp^i)\right] \cdot C_{v1}(\bar{k}_\perp^s, d) \cdot C_{h1}(\bar{k}_\perp^i, d)\,,$$

$$S_{vv}^{(1)} = \frac{1}{\pi}\frac{k_0(1-\epsilon)k_z^i}{k_{1z}^i + \epsilon k_z^i}\frac{k_{1z}^s \cos\theta_s}{k_{1z}^s + \epsilon k_z^s} e^{-i(k_z^i + k_z^s)d} \cdot \Big\{ C_{v1}(\bar{k}_\perp^s, d) \cdot k_{1z}^i \cos(\phi_s - \phi_i) \cdot C_{v1}(\bar{k}_\perp^i, d) - \frac{k_0^2 \epsilon}{k_{1z}^s} \sin\theta_i \sin\theta_s \cdot C_{v2}(\bar{k}_\perp^s, d) \cdot C_{v2}(\bar{k}_\perp^i, d) \Big\} \cdot \left[\triangle \widetilde{f}(\bar{k}_\perp^s - \bar{k}_\perp^i)\right]\,.$$

where

$$C_{h1}(\bar{k}_\perp, z) = \frac{(R_h - r_h)\, e^{ik_{1z}z} + (R_h r_h - 1)\, e^{-ik_{1z}z}}{R_h\,(R_h - r_h)\, e^{ik_{1z}z} + (R_h r_h - 1)\, e^{-ik_{1z}z}}\,,$$

$$C_{v1}(\bar{k}_\perp, z) = \frac{(r_v - R_v)\, e^{ik_{1z}z} + (R_v r_v - 1)\, e^{-ik_{1z}z}}{R_v\,(R_v - r_v)\, e^{ik_{1z}z} + (R_v r_v - 1)\, e^{-ik_{1z}z}}\,,$$

$$C_{v2}(\bar{k}_\perp, z) = \frac{(R_v - r_v)\, e^{ik_{1z}z} + (R_v r_v - 1)\, e^{-ik_{1z}z}}{R_v\,(R_v - r_v)\, e^{ik_{1z}z} + (R_v r_v - 1)\, e^{-ik_{1z}z}}\,.$$

The scattering coefficients can easily be obtained by noting that $\sigma_{ij}^0 = \lim_{A\to\infty} \frac{4\pi}{A}\left\langle |S_{ij}|^2 \right\rangle$, $i,j \in \{h,v\}$ and $\lim_{A\to\infty} \frac{1}{A}\left\langle \left|\triangle \widetilde{f}(\bar{k}_\perp^s - \bar{k}_\perp^i)\right|^2 \right\rangle = W(\bar{k}_\perp^s - \bar{k}_\perp^i)$ where $W(\bar{k}_\perp)$ is the power spectral density of the surface.

From the second-order solutions, the cross-polarized backscattering coefficient is given by

$$\sigma_{hv}^0 = \frac{1}{2\pi^3}\left|\frac{k_0(\epsilon-1)^2 k_z^i k_{1z}^i}{k_{1z}^i + \epsilon k_z^i} \cdot (1 + R_h^i) \cdot C_{h1}(k_z^i, d) \cdot C_{v2}(k_z^i, d)\right|^2 \cdot \int\limits_{-\infty}^{\infty} d\bar{k}_\perp \cdot W(\bar{k}_\perp - \bar{k}_\perp^i) W(\bar{k}_\perp + \bar{k}_\perp^i) \cdot \sin^2(\phi - \phi_i)\cos^2(\phi - \phi_i) \cdot \left|\frac{k_0^2}{k_z + k_{1z}} \cdot C_{h1}(k_z, d) - \frac{k_z k_{1z}}{k_{1z} + \epsilon k_z} \cdot C_{v2}(k_z, d)\right|^2.$$

These equations reduce to those reported in the literatures for a homogeneous surface by allowing $R_h = r_h$ and $R_v = r_v$.

EXPERIMENTS

The experiments were conducted using Bistatic Measurement Facility of Radiation Laboratory of the University of Michigan. The backscatter measurements were performed polarimetrically using an HP-8720 network-analyzer-based scatterometer. The center frequency and the bandwidth were chosen to be 9.25 GHz and 1.52 GHz respectively. The footprint size at a distance of about 2.7m was $0.27 \sec\theta_r\ m^2$. The effect of the distortion parameters of the radar system, such as the channel

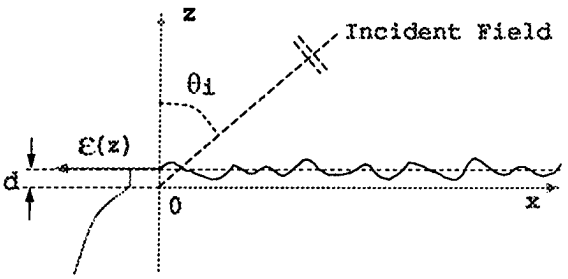


Figure 1: An inhomogeneous halfspace medium with a rough interface.

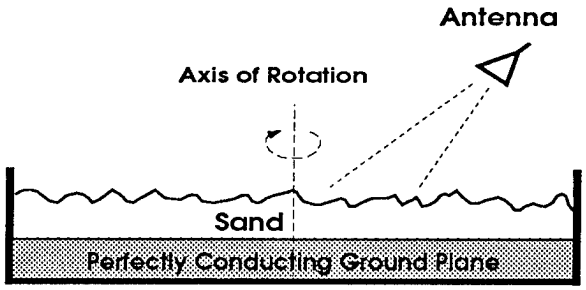


Figure 2: Sideview of the sandbox.

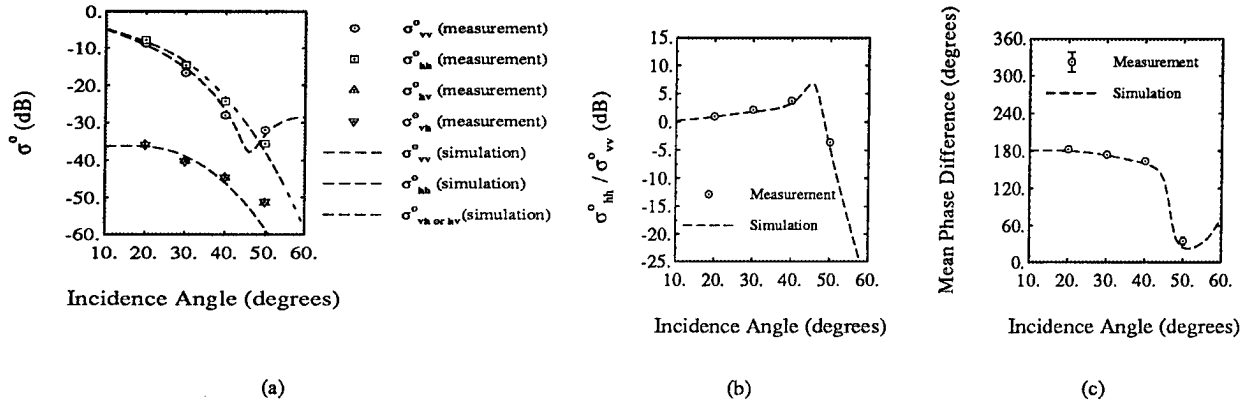


Figure 3: Measurement results: (a) σ^0, (b) $\sigma^0_{hh}/\sigma^0_{vv}$, and (c) mean co-polarization phase difference versus incidence angle.

imbalances and the antenna cross-talk factors, on the measured scattering matrices were removed by using the single target calibration technique (STCT). A 6 feet $\times$ 6 feet box was used to contained a fine uniform sand layer with relative permittivity $2.7 + i0.05$. The radius of the sand particle is less than 0.148 mm to minimized volume scattering. An aluminum plate was place at the bottom of the sandbox to create an inhomogeneous profile(see Fig. 2). In each angle, 100 measurements were collected by rotating the sandbox, and time-domain gating was applied to eliminate the effect of radar return from walls of the sandbox.

Rough templates were made to produce rough surfaces. Using these templates we were able to generate rough surfaces repeatedly while varying the sand layer thickness. The surface roughness was measured using a laser profiler to acquire the autocorrelation function. A rough surface with $ks = 0.122$ and $kl = 2.69$, which meet the validity conditions associated with the small perturbation method was created and measured. The measured autocorrelation closely resembles a exponential correlation function.

Fig. 3 compares the backscatter measurements for the inhomogeneous rough sand layer with thickness 3.5cm with those predicted by the theory. An excellent agreement is obtained.

REFERENCES

[1] Y. Oh, K. Sarabandi, and F.T. Ulaby, "An empirical model and an inversion technique for radar scattering from bare soil surfaces," *IEEE Trans. Geosci. Remote Sensing*, vol. 30, pp. 370-382, Mar. 1992.

[2] M. Nieto-Vesperinas, "Depolarization of electromagnetic waves scattered from slightly rough random surfaces: A study by means of the extinction theorem," *J. Opt. Soc. Am.*, 72(5), pp. 539-547, 1982.

[3] D. Winebrenner and A. Ishimaru "Investigation of a surface field phase perturbation technique for scattering from rough surfaces," *Radio Science*, vol. 20, no. 2, pp. 161-170, Mar-Apr, 1985.

[4] E. Rodriguez and Y. Kim "A unified perturbation expansion for surface scattering," *Radio Science*, vol. 27, no. 1, pp. 79-93, Jan-Feb, 1992.

[5] A.K. Fung, Z. Li, and K.S. Chen, "Backscattering from a randomly rough dielectric surface," *IEEE Trans. Geosci. Remote Sensing*, vol. 30, pp. 356-369, Mar. 1992.

Electromagnetic Wave Scattering from Real-life Rough Surface Profiles and Profiles Based on an Averaged Spectrum

Kyung Pak, Leung Tsang, Robin Weeks*, J.C. Shi**, and Helmut Rott***
Department of Electrical Engineering,
University of Washington, Box 352500, Seattle, WA 98195-2500
Telephone: (206)543-2159 Fax: (206)543-3842 E-mail: kyung@ee.washington.edu

* Department of Geology, University of Washington
** University of California, Sata Barbara
*** University of Innsbruck

Abstract

In this paper, we study the electromagnetic wave scattering from rough surface of three different kinds. The scattering cross section is calculated exactly for each profile and the average scattering cross sections are compared. In the first method, we use real-life measured profiles of a natural surface. The first method gives the correct scattering result or bench mark result. In the second method, we use the measured profiles to calculate the averaged spectrum. We then use the averaged spectrum to generate many profiles. In the third method, the averaged spectrum obtained from the second method is fitted with a power-law spectrum. The fitted spectrum is then used to generate profiles. We find that the third method can give results which can be as much as 6 dB different than the correct result. The second method generally give reasonable results within 2 to 3 dB of the first method solution. Examples used in this paper include soil, snow, and rock surfaces.

1. Introduction

In the past, electromagnetic wave scattering analysis and data matching from rough surfaces has been based on characterization of the rough surface by an averaged spatial spectrum or a correlation function [1]. This is because in real-life, one is often faced with a problem of estimating the average surface spectrum and height probability density function from a limited number of surface profile data. Investigators have suggested that many natural surface profiles can be well approximated by fitting its surface spectrum with a power-law [2] or a spectrum corresponding to an exponential correlation function. Thus, a best-fit spectrum (or a correlation function) has been used in scattering models. However, scattering solutions based on a best-fit surface spectrum (or a correlation function) has not been rigorously verified.

In this paper, electromagnetic wave scattering from three different types of random rough surfaces are studied. In the first method, we use a limited number of field-measured profiles of a natural surface to find an average scattering cross section. This is the bench mark result. In the second method, an average surface spectrum is found from the profiles of the first method and use it to generate profiles. Based on this average spectrum, many realizations of synthetic surfaces are numerically generated by the spectral method. Then, an average scattering cross section of the generated profiles is found. In the third method, which is the commonly adopted procedure, the average surface spectrum found in the second method is fitted with a power-law function. From the best-fit spectrum, many independent realizations of surfaces are numerically generated. Then, the average scattering cross section is calculated.

2. Formulation

The scattering examples are presented in terms of an average scattering coefficient $\hat{\sigma}(\theta_s)$

$$\hat{\sigma}(\theta_s) = \frac{1}{N_\beta} \sum_\beta \sigma(\theta_s)_\beta \tag{1}$$

where N_β is the total number of profiles and β is the realization index.

Rough Surface Types

The surfaces generated by methods one, two, and three shall be labeled as S_1, S_2, and S_3, respectively. In method one, we use a limited number of measured

0-7803-3068-4/96$5.00©1996 IEEE

profiles of soil, snow, and rock surfaces. The measured profiles are called S_1. Based on the measured profile $z = f_t(x_n)$, where t denotes true profiles, we compute the average bistatic scattering coefficient. The number of profiles used for rock, snow, and soil are 20, 35, and 14 respectively. The sampling rate is at least 10 points per incident wavelength.

Synthetic Surfaces In methods two and three, realizations of height profiles are generated from a specified spectral density $W(K_n)$. Using $W(K_n)$, we generate a realization of $F(K_n)$ by

$$F(K_n) = W_n \begin{cases} \frac{1}{\sqrt{2}}[N(0,1) + iN(0,1)], & n \neq 0, \frac{N}{2} \\ N(0,1) & n = 1, \frac{N}{2} \end{cases} \quad (2)$$

where $W_n = \sqrt{2\pi L W(K_n)}$, and $N(0,1)$ is a sequence of normally distributed random numbers in $[0,1]$ with zero mean and unity standard deviation and N is the total number of sampling points. From $F(K_n)$, the rough surface profile is given by

$$f(x) = \frac{1}{L} \sum_{n=-N/2}^{N/2-1} F(K_n) \exp(iK_n x) \quad (3)$$

Method 2: S_2 Surfaces We compute the spectral density from the true measured profiles $f_t(x_n)$

$$\hat{W}(K_n) = \frac{L}{2\pi NU} < |\sum_{n=0}^{N-1} f_t(x_n) g(x_n) \exp(-j2\pi n/L)|^2 > \quad (4)$$

where $g(x_n)$ is a space-domain window function, $<>$ is the ensemble average, U is a normalization constant, and $K_n = 2\pi n/L$. We then set $W(K_n) = \hat{W}(K_n)$.

Method 3: S_3 Surfaces This is a common procedure. The averaged power spectrum $\hat{W}(K)$ found in (4) is fitted with a function $W_p(K)$. We use a weighted least squares method to fit a calculated spectrum of (4) with a power-law spectrum. On a log-log scale

$$log(W(K)) = -\alpha log(|K|) + log(C) \quad (5)$$

where C and α are parameters to be determined. Then we let $W(K) = W_p(K)$ in (3) to generate independent realizations of synthetic surfaces.

3. Results and Discussion

In Figure 1 the power spectrums of S_2 and S_3 surfaces for rock, soil, and snow are illustrated on a log-log plot. It should be noted that in fitting the calculated power spectrum with a power-law, we have disregarded regions of non-linear behavior on a log-log plot. Since the power-law function blows up for $K = 0$, we have assigned $W(0) = 0$ in the surface generation. An alternate approach is to taper the power-law spectrum by an exponential function for small values of K_n [2]. However, we find that the alternative approach of an exponential tapering did not produce a noticeable difference in the scattering result.

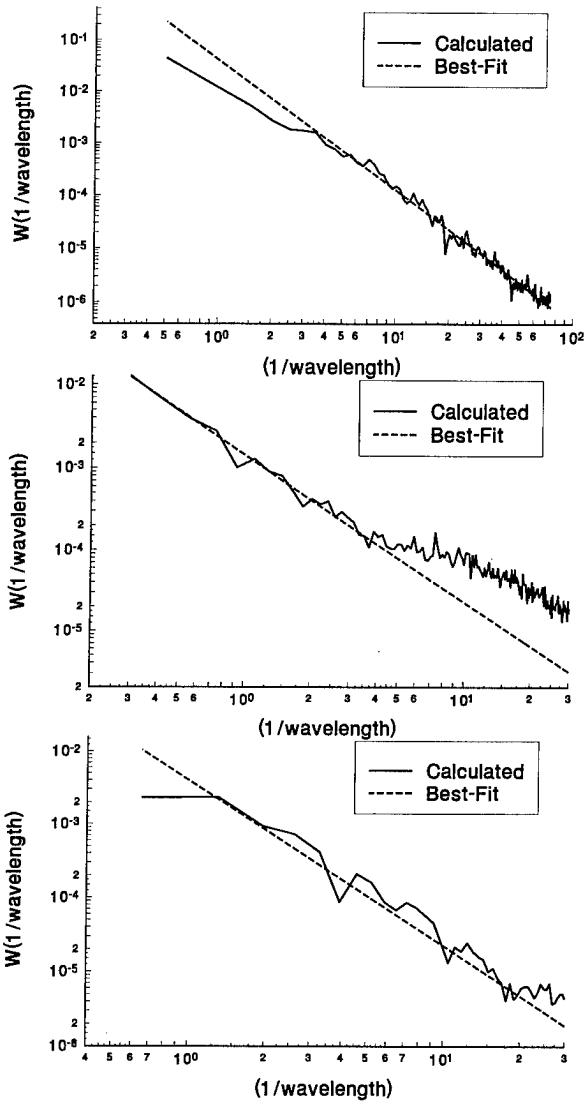


Figure 1: *Comparison of calculated average spectrum and a best-fit spectrum for (a) rock ($\alpha = 2.5$, $C = 10^{-1.4}$), (b) snow ($\alpha = 1.8$, $C = 10^{-2.85}$), and (c) soil ($\alpha = 2.25$, $C = 10^{-2.4}$).*

It can be seen from Figure 1(a) and 1(b) that the power-law gives a good fit for the cases of rock and soil surface spectrums. For a rock surface, a power-law fit over estimates the calculated spectrum for spatial frequencies lower than $3/\lambda$. Therefore, a rock surface generated with a fitted spectrum generates surfaces with larger RMS surface heights by 38 %. For a soil

surface spectrum, the agreement between the calculated spectrum and the best-fit spectrum is good over a wider range than the This is further evident in the RMS height comparison where the agreement is within 1%.

Next, bistatic scattering cross section from three types of surfaces of rocks, snow, and soil are presented in Figures 2(a), (b), and (c), respectively. The incident angle is fixed for all simulations at 45 degrees. All simulations in this paper satisfies the power conservation check to less than 1%. From Figures 2(a), (b), and (c), it is seen that the backscattering from the calculated spectrum (S_2 Surfaces) are within 1.1 dB of real-life surfaces (S_1) for all cases. In view of the fact the scattering coefficient is averaged over a limited number of S_1 surfaces, the agreement is about 2 to 3 dB. Also, note that due to limited number of real-life profiles the calculated power spectrum $\hat{W}(K_n)$ oscillate (Figure 1). However, the backscattering from S_2 surfaces all converge to within 1.1 dB of the correct results. For rocks the best-fit model scattering result is 5.6 dB above that of the real-life surface. For snow surfaces, the scattering solutions between the real-life and best-fit spectrum are 4 dB different. One encouraging result is that only a few profiles (14 to 20 profiles as shown numerically in this paper) are needed to achieve a reasonable convergence value for the averaged cross section.

4. References

[1] L. Tsang, J. A. Kong, and R. T. Shin, *Theory of Microwave Remote Sensing*, New York: Wiley-Interscience 1985.

[2] Austin, R., England, A. and Wakefield, G., "Special problems in the estimation of power-law spectra as applied to topographical modeling," *IEEE Transactions on Geoscience and Remote Sensing*, vol. 32, no. 4, pp. 928-939, July 1994.

[3] L. Tsang, C. H. Chan, K. Pak, H. Sangani, A. Ishimaru, and P. Phu, "Monte Carlo simulations of large-scale composite random rough surface scattering based on the banded matrix iterative approach," *J. Opt. Soc. Am. A*, vol. 11, pp. 691-696, 1994.

[4] K. Pak, L. Tsang, C. H. Chan, and J. Johnson, "Backscattering enhancement of vector electromagnetic waves from two-dimensional perfectly conducting random rough surfaces based on Monte Carlo simulations," *J. Opt. Soc. Am. A*, Vol. 12, No. 11, pp. 2491-2499, 1995.

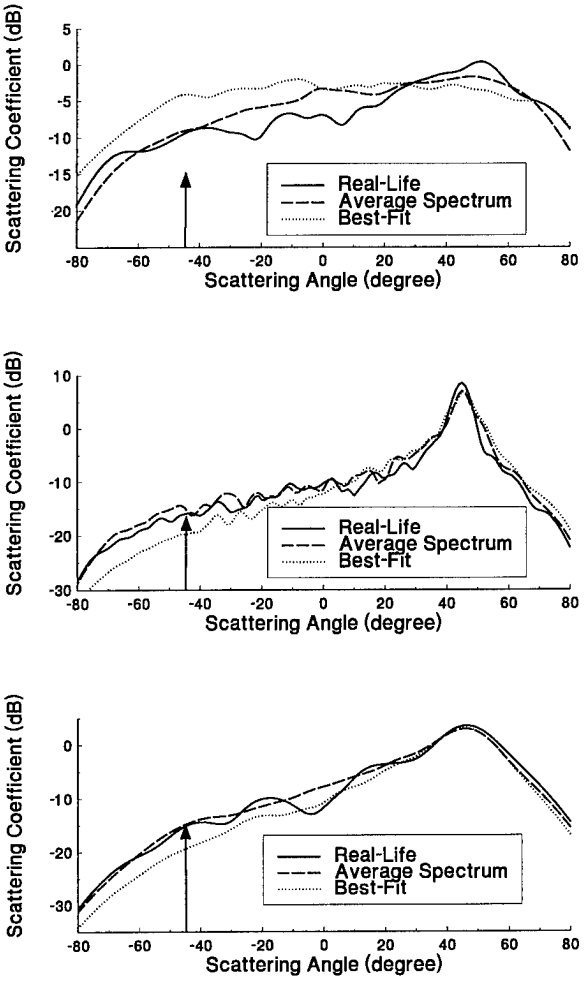


Figure 2: *Comparison of bistatic scattering coefficient from three types of surfaces: (a) rock, (b) snow, and (c) soil surfaces.*

TABLE I : Real-Life Surface Profile Data

	rock	snow	soil
# of samples	20	35	14
surface length (λ)	12.5	34.1332	9.6
number of points N	300	512	96
RMS height (λ)	0.4	0.156	0.1

Analytical, Experimental, and Numerical Studies of Angular Memory Signatures of Waves Scattered from 1-dimensional Rough Surfaces

Yasuo Kuga, Charlie T.C. Le, and Akira Ishimaru

Department of Electrical Engineering
University of Washington, Box 352500
Seattle, WA 98195-2500

Abstract - It is known that a change in the direction of an incident wave on a random medium is "remembered" by the scattered wave in the angular correlation characteristics. This "memory effect" is studied for rough surface scattering by means of theoretical (second-order Kirchhoff approximation (KA)), numerical (Monte Carlo simulations) and experimental (millimeter-wave range) approaches. The second-order KA has been found to be effective for wave scattering from very rough surfaces with large radii of curvature and high slopes (0.5 to 1.5). The results are presented in a form of memory signatures which clearly exhibit the important features of this effect.

INTRODUCTION

The correlation of scattered waves from random media and rough surfaces has attracted considerable interest in recent years [1]. In general, the scattered electromagnetic field is a function of position, angle, frequency, and polarization. Among these correlation functions, the frequency correlation which is related to the pulse broadening has been studied most extensively in the past. Recently, however, the angular correlation function has become an intense research subject after Feng et al.[1] predicted important correlation effects in the scattered wave as the incident wave changes its direction. This is called the "angular memory effect". This angular correlation function (ACF) is defined as

$$\Gamma(\theta_i',\theta_s';\theta_i,\theta_s) = < E_s(\theta_i,\theta_s)\, E_s^*(\theta_i',\theta_s')> \qquad (1)$$

where the angle brackets denote the ensemble average. As long as the difference in the transverse wave numbers is the same for the incident and the scattered wave, there will be a strong correlation for $\Gamma(\theta_i',\theta_s';\theta_i,\theta_s)$ indicating the memory effect. In this paper, we will present analytical, numerical and experimental studies of the ACF of electromagnetic (EM) waves scattered from 1-D rough surfaces. Our purpose is to compare the analytical and experimental results with the exact numerical simulations. This will give us an estimate of the applicable region of the theory. The analytical theory is based on the second-order KA which has been found to be effective for EM waves scattered from very rough surfaces with large radii of curvature and high slopes (0.5 to 1.5) [4]. Although the second-order KA is based on a number of approximations including the geometrical optics approximation and the approximate forms of the shadowing functions, excellent agreement with Monte Carlo simulations and millimeter-wave experiments was achieved. The results are presented in the form of memory signatures which clearly exhibit the important features of this effect.

THEORY

The second-order Kirchhoff approximation with angular and propagation shadowing functions has been developed to calculate the bistatic cross section of waves scattered from one-dimensional random rough surfaces [4]. Its extension to the case of angular correlation is shown in detail in Ref [5]. Figure 2 shows the ACF along the memory line as a function of θ_i' for the surface $(\sigma,l)=(1\lambda,1\lambda)$ at the same reference angles. The first-order term and the second-order ladder and cyclical terms are plotted separately to show their relative contributions to the total ACF. The following important features of the memory line can be deduced from these figures.

(i) The first-order scattering gives a strong correlation when the following condition is satisfied.

$$\sin\theta_s' - \sin\theta_s = \sin\theta_i' - \sin\theta_i \qquad (2)$$

This condition was previously named the "memory line", away from which the correlation decreases very rapidly. The angular width of the correlation is of the order of λ/L where L is the illumination distance. The details of the angular width will be shown in Fig.5.

(ii) Along the memory line, the ACF has two peaks when $\theta_s > -\theta_i$. One peak occurs at $(\theta_i', \theta_s') = (\theta_i, \theta_s)$ and the other peak at $(\theta_i', \theta_s') = (-\theta_s, -\theta_i)$, which are point A and B in Fig.1, respectively. The widths of the ACF at these peaks are of the order of λ/σ. The shape of the correlation is determined by the difference in the vertical wave numbers. When $\theta_s = -\theta_i$ (backscattering direction), these two peaks coalesce to one broad peak.

(iii) The second-order ladder term gives a sharp peak at $(\theta_i', \theta_s') = (\theta_i, \theta_s)$, which corresponds to point A in Fig.1. At point A, the two waves are traveling in the same direction and the ACF reduces to the autocorrelation of the incident wave. The cyclic term gives another sharp peak at (θ_i', θ_s')

0-7803-3068-4/96$5.00©1996 IEEE

$= (-\theta_i, -\theta_s)$, shown as point B in Fig.1. The widths of the ACF at these two peaks are of the order of λ/D where D is the propagation distance for the second-order scattering. In the backscattering case $\theta_i = \theta_i' = -\theta_s = -\theta_s'$, these two peaks coincide, which produces the enhanced backscattering for a very rough surface.

NUMERICAL SIMULATIONS

Numerical simulations of scattering from rough surfaces are based on the exact integral equation with an improved numerical method [3]. For each simulation run, the surface length was set at 50λ and discretized into 500 points. The number of surface realizations was 200. Numerical simulations with TE incident polarization were conducted for surfaces with parameters $(\sigma,l)=(1\lambda,1\lambda)$. Figure 3 shows the numerical simulations of the ACF of $(1\lambda,1\lambda)$ rough surfaces. The reference angles are $(\theta_i, \theta_s) = (20°, -40°)$. A narrow distinct memory line is clearly visible as well as two peaks corresponding to the autocorrelation and time-reversed path. The many parallel contour lines due to small correlation (less than 0.1) may be related to the long range correlation effect, but the value is close to the noise level of our numerical simulations.

MILLIMETER-WAVE EXPERIMENTS

The experimental system consists of a bistatic MMW system operating from 75 to 110 GHz. The experimental setup and calibration techniques were described in depth by [2]. The incident polarization was set to TE which was also used for numerical and analytical studies. In order to obtain an appreciable amount of angular correlation between the scattered fields, the choices of θ_i' and θ_s' must be such that (θ_i', θ_s') lies along the angular memory line on the $(\sin\theta_i', \sin\theta_s')$ plane for a given set of reference antenna directions (θ_i, θ_s) as shown in Fig.1. Outside the memory line, the correlation was found to be very small for all surfaces. The reference antenna configurations of $(\theta_i, \theta_s) = (20°, -40°)$ were considered. The measured correlation functions and the ACF of the scattering amplitude can be expressed as

$$< \frac{V_{r1}}{V_o} \frac{V_{r2}^*}{V_o^*} > \approx 2 \frac{\Delta\theta_r}{\cos\theta_s'} < f_1 f_2^* > \qquad (3)$$

where V_r/V_o is the measured S-parameter response, f_1 and f_2 are the scattering amplitudes, $\Delta\theta_r$ is the HPBW of the receiver and is roughly equal to 6° over 95--100 GHz, and θ_s' refers to the scattering angle at which the receiver is looking. Using Eq.(3), the absolute measurements of the ACF of scattering amplitudes can be obtained from the measured fields.

COMPARISON WITH NUMERICAL AND EXPERIMENTAL RESULTS

Figure 4 shows the ACF of $(\sigma,l)=(1\lambda,1\lambda)$ for $(\theta_i, \theta_s) = (20°, -40°)$. In this case the peaks due to the autocorrelation and reciprocity conditions are separated. Overall agreement between the numerical simulations and experiments is excellent. Figure 5 shows the width of the ACF for the $(1\lambda,3\lambda)$ surface. Data are obtained along the line perpendicular to the memory line in Fig.1 and passing through the autocorrelation point A. Numerical, experimental and analytical results all show a similar narrow peak at $\theta_i' = 20°$.

CONCLUSION

The angular memory effects for rough surface scattering are presented in the form of "memory signatures" which give the correlation of the scattered field as a function of $\sin\theta_s'$ and $\sin\theta_i'$ at a fixed θ_i and θ_s. Excellent agreement was obtained between experiments and numerical simulations. The second-order KA correctly shows the peaks at angles where the autocorrelation and reciprocity conditions are satisfied, but the width and value are less than that of the experiments and numerical simulations.

REFERENCES

[1] S. Feng, C. Kane, P.A. Lee and A.D. Stone, "Correlations and fluctuations of coherent wave transmission through disordered media", *Phys. Rev. Lett.*, 61, (7), 834-37, (1985).

[2] P. Phu, A. Ishimaru and Y. Kuga, "Co-polarized and cross-polarized enhanced backscattering from two-dimensional very rough surfaces at millimeter wave frequencies", *Radio Science*, 29, 1275-91, (1994).

[3] L. Tsang, C.H. Chan, K. Pak, and H. Sangani "Monte Carlo simulations of large-scale problems of random rough surface scattering and applications to grazing incidence with the BMIA/Canonical grid method", *IEEE Trans. Antenn. and Prop.*, Vol.43, No.8, 851-859, (1995)

[4] A. Ishimaru, C. Le, Y. Kuga, L. Ailes-Sengers and T.K. Chan, "Polarimetric scattering theory for high slope rough surfaces", *Progress in Electromagnetics Research*, in press, Elsevier Science Pub., Cambridge, Mass, (1996).

[5] C. Le, Y. Kuga and A. Ishimaru, "Angular correlation function based on the second-order Kirchhoff approximation and comparison with experiments", to appear, *J. Opt. Soc. Am. A*, (May, 1996).

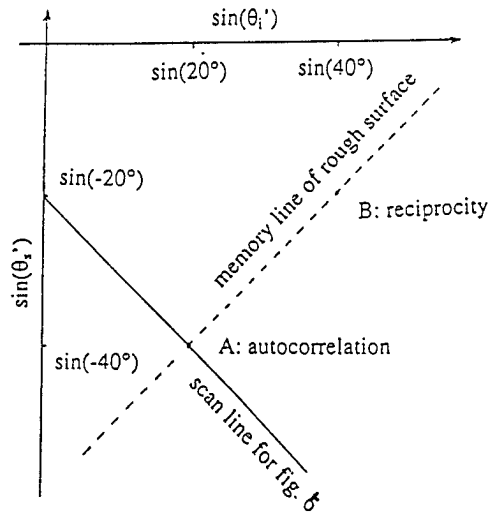


Fig.1: Memory line at $(\theta_i, \theta_s) = (20°, -40°)$; solid line is the angular scan used in Fig.5.

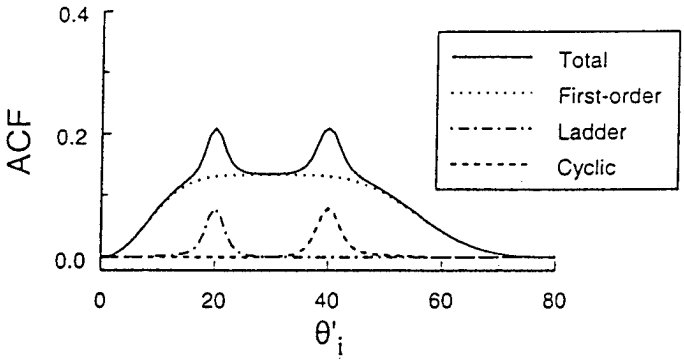


Fig.2: Theory: ACF along the memory line for $(\sigma,l)=(1\lambda,1\lambda)$ at $(\theta_i, \theta_s) = (20°, -40°)$.

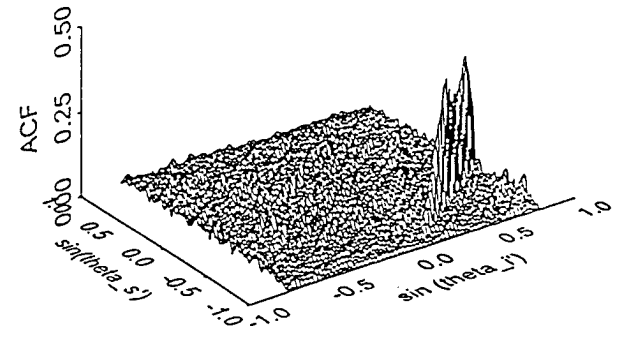


Fig.3: Numerical simulations for $(\sigma,l)=(1\lambda,1\lambda)$ at $(\theta_i, \theta_s) = (20°, -40°)$.

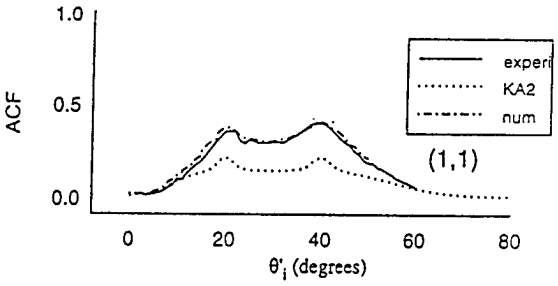


Fig.4: Comparisons between analytical, experimental and numerical results for $(\sigma,l)=(1\lambda,1\lambda)$ at $(\theta_i, \theta_s) = (20°, -40°)$.

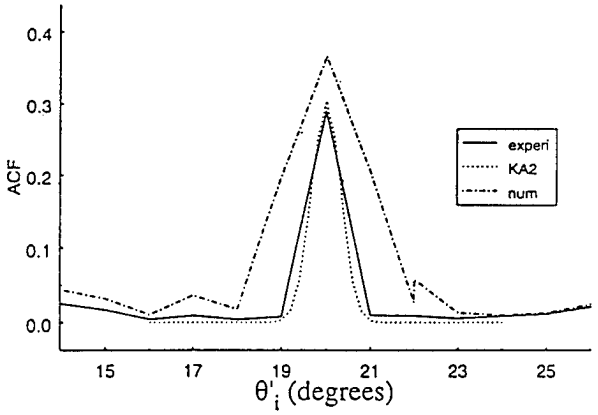


Fig.5: ACF along the line perpendicular to the memory line as shown in Fig.1. Comparison of ACF for $(\sigma,l)=(1\lambda,3\lambda)$ at $(\theta_i, \theta_s) = (20°, -40°)$.

The SIR-C /X-SAR experiment: the sensitivity of microwave backscattering to surface roughness of bare soils

P. Coppo[1], G. Macelloni [2], P. Pampaloni[2], S. Paloscia[2] and S. Sigismondi[3]

[1] CeTeM - Center for Microwave Remote Sensing - via Panciatichi 64, Firenze, Italy

[2] IROE- CNR - via Panciatichi 64, Firenze, Italy
Fax: 39 55 4235290 - E-Mail Microrad@iroe.fi.cnr.it

[3] Dept. of Earth Sciences - Univ. of Florence, Via La Pira 4 - 50122 Firenze

Abstract -- The relations between microwave backscattering and surface roughness parameters have been investigated using multifrequency polarimetric SAR data collected with SIR-C/X-SAR on Montespertoli test site (Italy). Three bare soils specifically worked with different scales of random roughness have been taken into consideration to study the effect of soil roughness and to validate surface scattering models.

INTRODUCTION

The potential of SAR data in detecting some significant land features has been pointed out in many experiments carried out with the NASA/JPL airborne multifrequency AIRSAR. A considerable amount of research has been carried out and is still underway in the framework of SIR-C/X-SAR Project in order to interpret polarimetric data and to correlate them to the most important geophysical parameters (soil moisture, surface roughness, vegetation cover and biomass) [1]. Although the detection of these parameters has been the subject of many investigations, carried out in past years with ground based and airborne sensors, only a very few preliminary investigations have been carried out using data collected with spaceborne sensors [2,3]. A major problem in retrieving the soil parameters is that each of them affects in a different way the radar backscattering and the separation of the effects requires the use of appropriate multifrequency polarimetric algorithms.

In this paper, the backscattering coefficient, measured at at L- and C- bands, at different incidence angles θ (35° and 50°), is represented as a function of surface parameters (height standard deviation and soil mositure content) and compared with the analytical solutions of the Integral Equation Model (IEM), based on the electromagnetic theory. This model seems to have validity conditions less restricitive than the standard anlytical solutions (i.e. Small Perturbation, Geometrical Optics and Physical Optics models) [4].

THE EXPERIMENT

The supersite of Montespertoli (Italy) was imaged several times at different incidence angles between 20° and 55° by the fully polarimetric P-, L- and C-bands AIRSAR during the MAC-Europe Campaign in summer 1991, L- and C-band SIR-C and the VV polarization X- band X-SAR during the two SIR-C/X-SAR missions in April and October 1994.

Most data were delivered already calibrated; however calibration was improved by means of trihedral corner reflectors deployed parallel to the flight lines.

The test site included an agricultural area, cultivated with vineyards, wheat, colza, sorghum, sunflower, alfalfa and corn, surrounded by forest covered hills. At the time of MAC'91 vegetation was generally well develped and weather was mostly dry, whereas during SIR-C/X-SAR surveys most agricultural fields were bare or covered with small vegetation. Since weather was mostly rainy both in April and October, the average gravimetric soil moisture was therefore rather high and generally higher than 20%. During these experiments three bare soils with different scales of random roughness had been specifically prepared to study the effect of soil roughness and to validate surface scattering models. Despite a small residual periodicity due to working practice, the correlation functions of these surfaces approximated an exponential distribution with a height standard deviation σ ranging between 1.0 cm and 3.5 cm and a correlation length between 4 cm and 10 cm. Only the roughness parameters measured on profiles parallel to the observation direction (which are in this case parallel to the rows) have been taken into account for the model analysis.

0-7803-3068-4/96$5.00©1996 IEEE

EXPERIMENTAL RESULTS AND COMPARISON WITH MODELS

It is known that the degree of roughness of a surface depends on the electromagnetic wavelength and presently the only analytical theoretical model that can be applied to a large range of frequencies is the one based on the Integral Equation Model (IEM) [4], which well reproduce the results of Small Perturbation Method (SPM) at low frequencies and Geometrical Optics (GO) or Physical Optics (PO) models at high frequencies. Moreover the validity conditions of IEM are less restricitve than those of the other models [4].

The comparison of experimental data with theory has been carried out considering direct relations between the backscattering coefficient (at L and C bands, HH polarization) at two different incidence angles (θ=35° and 45°) and the surface roughness and soil moisturre content. An exponential autocorrelation function has been used to fit the roughness data and the dielectric constant of soil has been simulated by using the polynomial fit of Hallikainen et al. [5] with a mean value of texture of 70% of sand and 30% of silt+clay.

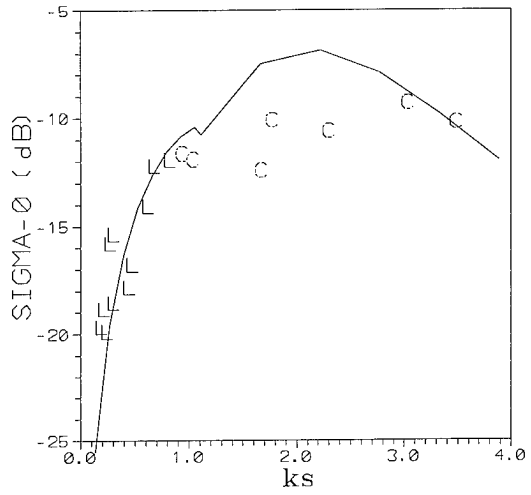


Figure 1 - σ° at L- (L) and C- (C) bands (HH pol., θ=45-50°) as a function of *ks*. Line represents the IEM model computed at θ=45°, l=6cm and SMC=20%

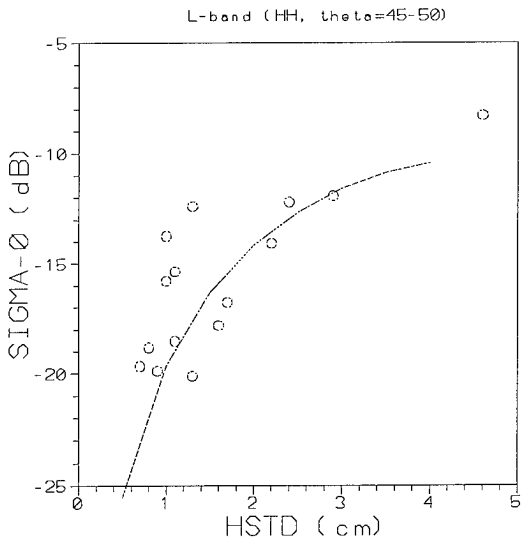


Figure 2 - σ° at L-band (HH pol., θ=45-50°) as a function of the height std of bare or scarcely vegetated soils. Line represents the IEM model computed at θ=45°, l=6cm and SMC=20%. Label refer to experimental data

Since the degree of roughness of a surface is defined in terms of electromagnetic wavelength, a typical parameter used to investigate the variations of the backscattering coefficient with roughness is the ratio between the height standard deviation *hstd* or *s* and the wavelength or the product of *s* with the wave number *k* (*ks*). In Fig. 1 the backscattering coefficient σ° at L and C bands (HH pol., θ= 45-50°), measured with AIRSAR in June-July1991 (θ=50°) and SIR-C in April 1994 (θ=45°), is shown as a function of *ks*. Data have been collected on bare (correlation length l between 4 and 10 cm) or scarcely vegetated soils (leaf area index, LAI <1), with a gravimetric soil moisture content ranging between 15 and 20%. A saturation effect is present at C-band, whereas at L-band σ° gradually increases as the soil roughness increases as well. This confirms that the same surfaces appear smooth or medium rough at L-band and rough at C-band. A value of *ks* =0.28 in the L-band data range can be considered a threshold value for separating smooth from rough soils, in accordance with the Fraunhofer criterium, applied for an incidence angle of 45°.

Simulations have been done with the IEM using θ=45°, soil moisture of 20% and a correlation length of 6 cm, which is the mean value of the measured ones. The model (continuous line) seems to reproduce quite

well the data at L-band, while at C-band it shows a maximum not present in the experimental data, due to the multiple roughness scales which are usually present in ploughed soils.

Fig. 2 represents σ°_{HH} (at θ=45° for SIR-C data and 50° for AIRSAR data) at L- band as a function of the height standard deviation (*hstd*, in cm) of bare or poorly vegetated fields (LAI < 1). We can see that at this frequency the sensitivity to soil roughness is rather high and that the effect of vegetation is negligible. Data have been compared with the IEM model (continuous line) using the same parameters of Fig.1.

The sensitivity of the radar signal to soil moisture has been confirmed in many experiments carried out over the past years, although the sensitivity is influenced by surface roughness and vegetation cover as well. These spurious effects are minimized for observations at small incidence angles. However, the quality of SAR images at incidence angle θ close to nadir is affected by a relatively poor spatial resolution which makes difficult the exact identification of field borders.

Figure 3 represents the L-band, σ°_{HH} at θ= 35° collected with AIRSAR in 1991 and SIR-C in April 1994, on a certain number of bare fields. The scattering of data appears at least partially related to surface roughness. By separating two classes of roughness with *hstd* ≤ 2 cm and *hstd* > 2 cm respectively, the spread of data decreases and the correlation coefficient, which is quite low (r^2 = 0.48) when the soils are considered all together, goes up to r^2 = 0.65 once the fields are separated in the two roughness categories. Lines represent the IEM model computed at θ=35° and correlation length l=6 cm for two different roughness conditions: *hstd*=1.5 cm (continuous line) and 3 cm (dashed line). It can be observed that also in this case the simulations performed using this model are quite in accordance with the experimental points.

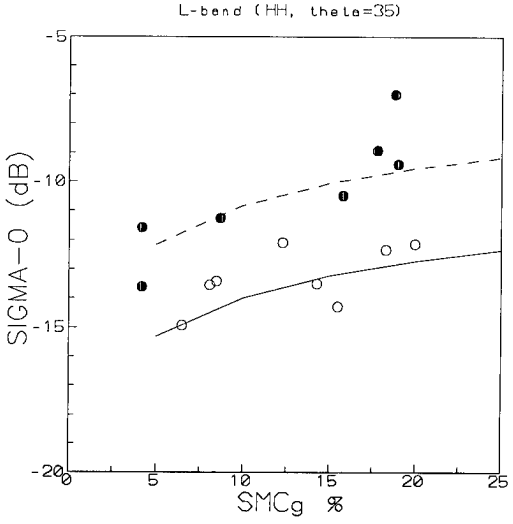


Figure 3 - Backscattering coefficient σ° at L-band (HH pol, θ=35°) as a function of gravimetric soil moisture (SMCg%). ● bare soils with hstd>2cm, O bare soils with hstd <2cm. Lines represent the IEM model computed for two different values of hstd: continuous line hstd=1.5cm, dashed line hstd=3cm and l=6cm.

SUMMARY

The effects of surface roughness on microwave scattering have been studied comparing experimental data, collected at L and C bands (HH pol.) during the MAC-Europe '91 and SIRC/XSAR campaigns on Montespertoli area, with the theoretical analytical solutions of the Integral Equation Model.

The backscattering coefficient shows variations with roughness, soil moisture and frequency according to theory. The results show the L-band seems to be the more suitable frequency to measure surface roughness of bare or scarcely vegetated soils

AKNOWLEDGMENTS

This work was partially supported by Italian Space Agency (ASI)

REFERENCES

[1] Evans D., Farr T., Van Zyl.J, and Zebker, H..,1988, Radar Polarimetry: Analysis Tools and Applications. *IEEE Trans. Geosci. Remote Sens.*, **26**, 774-789.

[2] Baronti S., F.Del Frate, P.Ferrazzoli, S.Paloscia, P.Pampaloni, G.Schiavon, 1995, "SAR polarimetric features of agricultural areas", *Int. Journal of Remote Sensing,* vol.16, n.14, pp.2639-2656

[3] Coppo P., G. Luzi, F.Del Frate, G.Schiavon, 1994, Microwave surface scattering from rough soils: A comparison between models and experimental data collected with airborne radar", Proc of PIERS'94, 11-15 July 1994, pp. 2P7/4.15, Noordwijk (NL)

[4] Fung A.K., 1994, "Microwave scattering and emission models ant their applications" Artech House Inc., Boston

[5] Hallikainen M.T., Ulaby F., Dobson M.C., El-Rayes M.A., Lin Ku Wu, 1985, "Microwave dielectric behavior of wet soils - Part I: Empirical models and experimental observations", IEEE Trans. Geosci. Remote Sensing, vol. GE-23, pp. 25-33

Using SIR-C SAR and Cloude's Decomposition for the Determination of Soil Moisture in Vegetated Areas

D. John Chadwick
Hughes STX Corporation
7701 Greenbelt Rd., Greenbelt, MD 20770 U.S.A.
phone: (301)441-4016/fax: (301)441-1853
chadwick@sensor.gsfc.nasa.gov

James R. Wang
Goddard Space Flight Center
Code 975, Greenbelt, MD 20771 U.S.A
phone: (301)286-8949/fax: (301) 286-1762
wang@sensor.gsfc.nasa.gov

Abstract -- Decomposition of SIR-C polarimetric SAR backscattering coefficients into odd (direct return, single-bounce) and even (dihedral, double-bounce) reflection mechanisms was performed on images of selected study areas of the Chickasha, Oklahoma hydrological supersite. The sensitivity of the direct and dihedral reflection strengths to field-measured volumetric soil moisture was evaluated, and the results show that the strength of the direct reflection component changes at a different rate than the dihedral component in response to soil moisture changes, thus the ratio of the two reflection mechanisms can be used to estimate soil moisture. This ratio changes at a constant rate with soil moisture for several different landcover types and bare soil. Soil moisture estimation using this method may be possible in areas with moderate to heavy vegetation, areas where previous soil moisture algorithms produced poor results.

INTRODUCTION

The relation between radar backscatter and soil moisture has been studied using spaceborne and airborne radars, as well as ground-based scatterometers [1-8]. Soil moisture increases the complex dielectric constant of the soil, which increases its reflectivity in synthetic aperture radar (SAR) imagery. Though a strong correlation exists, and soil moisture algorithms have been relatively successful in bare soil areas, the effects of surface roughness and vegetation cover have complicated the process of developing soil moisture algorithms for most landcover types. Long-wavelength SAR is capable of penetrating even relatively dense vegetation canopies to reach the soil, therefore robust soil moisture algorithms using polarimetric SAR may be possible in spite of the presence of vegetation.

DATA DESCRIPTION

The Little Washita watershed near Chickasha, Oklahoma is an extensively studied hydrology field site and the location of a Shuttle Imaging Radar-C (SIR-C) supersite. The watershed in the study area is largely characterized as agricultural, with additional areas of natural rangeland and small forested areas. SAR data was acquired on twenty passes over the study area during the April and October, 1994 shuttle missions. Imagery was acquired in C- and L- (6 and 23.5 cm wavelengths, respectively) bands, with horizontal and vertical transmit and receive polarizations (HH, HV, VV, VH). X-SAR, the German/Italian instrument also provided X-band (3 cm wavelength) imagery with VV polarization. The SIR-C/X-SAR mission was the first orbital test of a polarimetric SAR.

Volumetric soil moisture measurements were collected in twelve agricultural, rangeland, and bare-soil fields on most of the days during the two missions to coincide with shuttle overflight times. Field sizes ranged from approximately 0.5 km^2 to about 2 km^2, and the soil moisture sampling interval was approximately 100 m in each field. Samples were collected at 1 cm and 5 cm depths. Volumetric soil moistures were obtained by weighing the soil samples immediately after collection and after oven drying. Soil textures in the study fields ranged from clay loams, to silt loams, to sandy loams. Root mean square (RMS) roughness values ranged from about 0.5 to about 3.5 cm.

Backscatter varies with incidence angle, so SIR-C image pairs with similar incidence angles were selected for this study. Two image pairs were used: April 12 and 15 (both 42.3° incidence angles), and October 3 and 6 (41.4° and 40.5° incidence angles, respectively). Both images in each pair have different track angles, as the April 12 and October 3 images were acquired on ascending orbits (40.7° and 40.5° track angles, respectively), and April 15 and October 6 were acquired on descending orbits (138.2° and 139.2°). However, slopes are relatively low (< 2°), and backscatter from the fields in the image pairs is assumed to be azimuthally homogenous.

Rain was reported on 10-11 April, and field collected soil samples show a drying trend between the 12th and 15th. Overall soil moistures were much drier in October

0-7803-3068-4/96$5.00©1996 IEEE

than in April, but showers occurred on the evening of the 4th. Therefore, some of the fields were wetter on the 3rd than the 6th, and some were drier.

STUDY DESCRIPTION

For common surface materials, an incident radar signal interacting with the surface undergoes direct reflection (single-bounce), dihedral reflection (double), and volume scattering. The dihedral mechanism is initially a forward scatter (specular reflection), which may subsequently interact with vegetation or surface roughness. The return signal can be decomposed into the three components based on the phase. Cloude's decomposition [9,10] is used to determine the strengths of the reflection mechanisms. A single reflection results in a 180° phase difference between the HH and VV returns, whereas a double bounce results in a 0° phase difference. In this study, we will analyze the relation between volumetric soil moisture and its relation to the single and double reflection strengths.

RESULTS

Change in the ratio of single- to double-bounce return strengths (Δb) were plotted against change in average volumetric soil moisture (ΔMv) for each study field in the April (Fig. 1) and October (Fig. 2) L-band VV image pairs. A strong correlation is evident, and a linear regression for the April images is Mv= 0.35b, with an R^2 value of 0.6, and an F statistic value of 25.1 (critical value of 4.8, n=13). For fields in the October image pair, the linear equation is Mv =0.2b, the R^2 value is 0.6, and an F-statistic value of 17.9 (critical value of 6.61, n=6). Combined, the two datasets describe the equation Mv =0.34b, with an R^2 value of 0.75, and an F-statistic value of 75.8 (critical value of 4.4, n=19). Y-intercepts were fixed to the origin for all regressions. The slopes for the April and October regressions are slightly different, but soil moisture variation was very low between the two October images (points in lower-left corner of Fig. 3), and the regressions generated from the April data and the combined data (Fig. 3) are likely more reliable. These results suggest that the ratio of the strengths of the return signals from the vegetated and bare study fields is controlled by volumetric soil moisture. Moreover, the ratio changes with soil moisture at a constant rate for the six different land use types in this study.

Regressions were also performed for LHH, CHH, and CVV. LHH single- to double-bounce ratios show very little or no response to soil moisture. Both C-band co-polarized single- to double-bounce ratios are responsive to changes in soil moisture, though less so than the LVV. This is possibly due to attenuation by vegetation and less soil penetration of the shorter wavelength radar.

Because this technique relies on the presence of dihedral reflectors, soil moisture algorithms based on reflection ratios may be more reliable in moderate to heavily vegetated areas than previous algorithms that are reliable only for bare soil. The width and height of vertical stems likely have a strong influence on the dihedral mechanism, and different vegetation types and densities will have different bounce ratios for a given soil moisture. Although the ratios change at a constant rate with soil moisture for all the vegetation types in this study, the results also show a general decrease in the single- to double-bounce ratio as biomass increases (bare-soil fields have the highest ratios), suggesting a multivariate analysis is required to adjust for vegetation parameters. Row structure in agricultural areas will likely influence the bounce ratio as well, and these issues will be addressed as this study progresses.

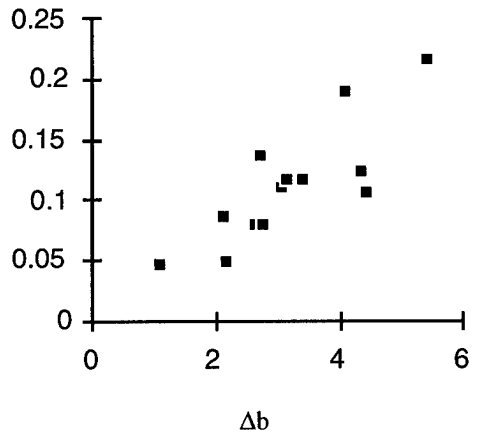


Fig. 1. Change in volumetric soil moisture (ΔMv) from April 12th to 15th vs. change in single- to double-bounce ratio (Δb).

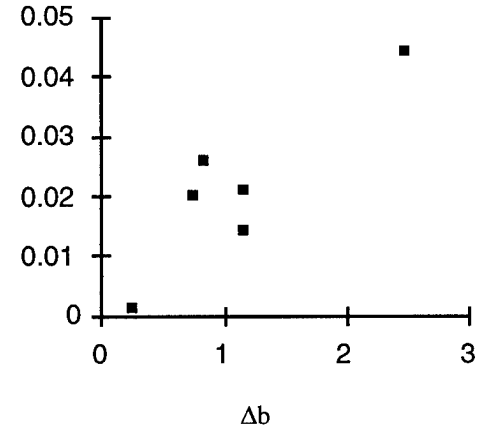


Fig. 2. Change in volumetric soil moisture (ΔMv) from October 3rd to 6th vs. change in single- to double-bounce ratio (Δb).

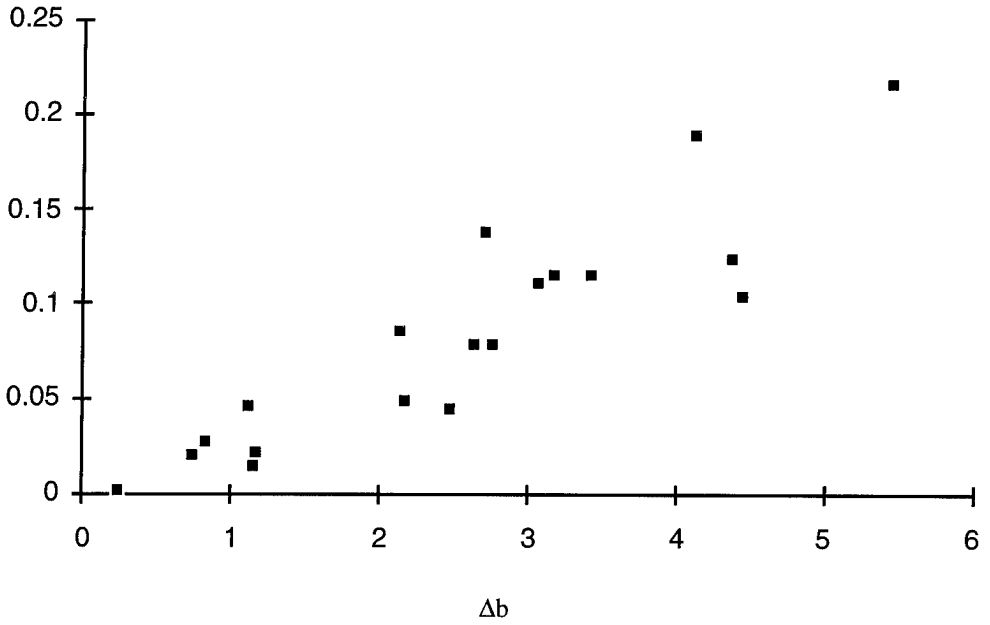


Fig. 3. Change in volumetric soil moisture (ΔMv) vs. change in single- to double-bounce ratio (Δb) for both the April 12 and 15, and October 3 and 6 image pairs.

ACKNOWLEDGMENTS

The authors wish to thank Ann Hsu for assistance with the image data, and we thank Peggy O'Neill, Ted Engman, Ann Hsu, and Chris Bell for consultations on the science aspects of this paper.

REFERENCES

[1] F.T. Ulaby, and P.P. Batlivala, "Optimum radar parameters for mapping soil moisture," IEEE Trans. Geosci. Remote Sensing, vol. 14, no. 2, pp. 81-93, 1976.

[2] F.T. Ulaby, G.A., and M.C. Dobson, "Microwave backscatter dependence on surface roughness, soil moisture, and soil texture: Part II-vegetation-covered soil," IEEE Trans. Geosci. Remote Sensing, vol. 17, no. 2, pp. 33-40, 1979.

[3] M.C. Dobson, F.T Ulaby, "Active microwave soil moisture research," IEEE Trans. Geosci. Remote Sensing, vol. 24, no. 1, pp.23-36, 1986.

[4] J.R. Wang, E.T. Engman, J.C Shiue, M. Rusek, and C Steinmeier, "The SIR-B observations of microwave dependence on soil moisture, surface roughness, and vegetation covers," IEEE Trans. Geosci. and Remote Sens., vol 24, no. 4, pp. 510-516, 1986.

[5] D.S. Lin, E.F. Wood, K. Bevin, and S. Saatchi, "Soil moisture estimation over grass-covered areas using AIRSAR," Int. J. Remote Sens., vol. 15, no. 11, pp. 2323-2343, 1994.

[6] E.T. Engman, and N. Chauhan, "Status of microwave soil moisture measurments with remote sensing,", Remote Sens. Environ., vol. 51, pp. 189-198, 1995.

[7] P.C. Dubois, J.J. Van Zyl, and E.T. Engman, "Measuring soil moisture with imaging radar," IEEE Trans. Geosci. and Remote Sens., vol. 33, no. 4, pp. 915-926, 1995.

[8] J.C. Shi, J.R. Wang, A. Hsu, P.E. O'Neill, and E.T Engman, "Estimation of bare surface soil moisture and surface roughness parameters using L-band SIR-C image data," unpublished..

[9] S. R. Cloude, "Uniqueness of target decomposition theorems in radar polarimetry," Direct and Inverse Methods in Radar Polarimetry, Kluwer Academic Publishers, pp. 267-296, 1992.

[10] J.J. van Zyl, "Application of Cloude's target decomposition theorem to polarimetric imaging radar data," Society of Photo Optical Instrumentation Engineers, vol. 1748, pp. 184-191, 1992.

INTERFEROMETRIC TECHNIQUE FOR DETERMINING THE AVERAGE HEIGHT PROFILE OF ROUGH SURFACES

Akira Ishimaru, Charles T. C. Le, Yasuo Kuga, Ji-Hae Yea, Kyung Pak, and Tsz-King Chan

Department of Electrical Engineering
University of Washington
Box 352500
Seattle, WA 98195-2500
Tel: (206)543-2169; Fax: (206)543-3842; E-mail: ishimaru@ee.washington.edu

Abstract A new angular correlation phenomenon called the "angular memory effect" (AME) is applied to interferometric SAR (InSAR). Two transmitters illuminate the surface and the scattered waves are observed at two receivers. The mutual coherence function (MCF) for the scattered waves shows that the phase is linearly related to the average topographic height. This is extended to the two-frequency MCF which shows the relationship between the pulse arrival times and the height profile. The theoretical results are confirmed by experiments and numerical simulations.

INTRODUCTION

In recent years, interferometric technique has been applied to Synthetic Aperture Radar (InSAR) for obtaining global topographic maps and other geophysical applications, and extensive theoretical and experimental studies have been reported [1, 2]. Recently, we have been involved in the study of the angular correlation of scattered waves from rough surfaces and have made detailed studies of the "memory effects" [3]. In this paper, we extend our previous study of the memory effect to include the slowly varying average height variations and the relationship with InSAR. Two transmitters at different angles θ_i and θ_i' illuminate the surface and the MCF for the corresponding scattered waves at two different angles θ_s and θ_s' are calculated (Fig. 1). The theory is based on the Kirchhoff approximation applicable to rough surfaces with large radii of curvature [3]. It is shown that the phase of the MCF is related to the average surface profile, and therefore, the height profile can be determined by the measurement of the correlation of the scattered waves. The MCF is expressed in the memory diagram which shows the correlation as a function of the second incident θ_i' and scattered θ_s' for given reference incident θ_i and scattered θ_s. This gives the general characteristics of the amplitude and the phase of the MCF, and clearly shows the effects of the locations of the antennas on the sensitivity of the correlation. Next we extend the theory to the two-frequency MCF and the time-domain response. It shows the relationship between the pulse arrival time and the surface height profile. Millimeter wave experiments and Monte-Carlo simulations are conducted and the results are compared with the theory.

THE MUTUAL COHERENCE FUNCTION

Using the first-order Kirchhoff approximation and the stationary phase approximation, we express the mutual coherence function between waves observed at the scattered angles θ_s, θ_s' due to waves incident at θ_i, θ_i' as

$$< \psi(\bar{K})\psi^*(\bar{K}') = FF'^* G_o G_o'^* < II'^* > \qquad (1)$$

where $F = -i[|\bar{K} - \bar{K}_i|^2/(K_z - K_{iz})]r$; $F' = -i[|\bar{K}' - \bar{K}_i'|^2/(K_z' - K_{iz}')]r'$; G_o and G_o' are the free-space Green's functions; and $< II'^* >= \int d\bar{x} \int d\bar{x}' \exp(-i\bar{v}\cdot\bar{x} - iv_z f - i\bar{v}'\cdot\bar{x}' - iv_z' f')$; $\bar{K}, \bar{K}_i$ are the propagation vectors; r is the reflection coefficient; the coordinates of the target are represented by $(\bar{x}, f(\bar{x}))$ where f denotes the height above a flat reference plane; $\bar{v} = (\bar{K} - \bar{K}_i)_{xy}$, $v_z = (\bar{K} - \bar{K}_i)_z$; the prime represents the corresponding variables for the second beams.

The surface height f is decomposed into two parts $f =< f_c > + f_r$, where $< f_c >$ denotes the slowly varying component representing the average topography height with slope $\bar{m} = \frac{\partial < f >}{\partial x}\hat{x} + \frac{\partial < f >}{\partial y}\hat{y}$, and f_r is the small fluctuating component having a Gaussian distribution with rms height σ and a Gaussian correlation function $C(x_d) = \exp(-x_d^2/l^2)$ where l is the correlation length. For the antenna patterns, we use Gaussian beam waves $|W|^2 = \exp(-x^2/L^2)$ with L being the illumination area . Following the approach

0-7803-3068-4/96$5.00©1996 IEEE

used in [3], we were able to obtain a closed form solution.

$$< II'^{*} >= F_1 F_2 \quad (2)$$

$$F_1 = (\frac{\pi l^2}{\nu_z \nu_z' \sigma^2}) \exp[-\frac{1}{2}(\nu_z - \nu_z')^2 \sigma^2] \exp[-\frac{|\nu_c + \bar{m}\nu_{zc}|^2 l^2}{4\nu_z \nu_z' \sigma^2}] \quad (3)$$

$$F_2 = (\pi L^2) \exp[-\frac{\nu_d^2 L^2}{4}] \exp[-i\nu_{zd} < f_c >] \quad (4)$$

where $D(x_d) = 2 < f_r^2 > (1 - C(x_d))$; $\bar{x}_c = (1/2)(\bar{x} + \bar{x}')$, $\bar{x}_d = (\bar{x} - \bar{x}')$, $\bar{v}_c = (1/2)(\bar{v} + \bar{v}')$, $\bar{v}_d = \bar{v} - \bar{v}'$, $v_{zc} = (1/2)(v_z + v_z')$, $v_{zd} = v_z - v_z'$.

The effects of the average topographic height are now visible. The degree of correlation depends on its slope $\bar{m}$ in Eq. (3). The average height $< f_c >$ produces a phase shift $\phi = \nu_{zd} < f_c >$ in Eq. (4).

THE TWO-FREQUENCY MCF

The MCF is applicable for continuous wave (CW). For pulse problems such as InSAR, we need the two-frequency MCF [4], which is the correlation (in the frequency domain) of two waves (already at different angles) at different frequencies. The Fourier transform of the two-frequency MCF then gives the ACF in the time domain. The correlation of the two scattered waves $E_s(t_1)$ and $E_s'(t_2)$ at two different times t_1 and t_2 can be written as [4]

$$< E_s(t_1) E_s'(t_2) >= \int\int d\omega_1 d\omega_2 \, U_i(\omega_1) U_i^*(\omega_2) \Gamma \exp(-i\omega_1 t_1 + i\omega_2 t_2) \quad (5)$$

where Γ is the two-frequency MCF given in the previous section; $U_i(\omega) = \int u_i(t) \exp(i\omega t)$ is the spectrum of the transmitted pulse $u_i(t)$ assumed to have a Gaussian profile $u_i(t) = A_o \exp(-i\omega_o t) \exp(-t^2/T_o^2)$. We now study the effects of the pulse arrival times on the interferometric phase $\phi = \nu_{zd} < f_c >$. So the two-frequency MCF is written as (ignoring other factors)

$$\Gamma = e^{-i\nu_{zd} < f_c >} e^{ik(R_1 + R_2) - ik'(R_1' + R_2')} \quad (6)$$

where R_1 and R_2 are the distances from the reference transmitter and receiver to the flat surface, and similarly for the primed variables. Eq. (5) can now be evaluated and the result is (ignoring other unimportant factors)

$$< E_s(t_1) E_s'(t_2) > \propto \exp[-i\omega_o(\gamma_d < f_c > /c + t_d - R_d/c)] \exp[-(\gamma_d < f_c > /c + t_d - R_d/c)^2/(2T_o^2)] \exp[-(\gamma_c < f_c > /c + t_c - R_c/c)^2] \quad (7)$$

where $\gamma_d = (\cos\theta + \cos\theta_i) - (\cos\theta' + \cos\theta_i')$, $\gamma_c = (1/2)[(\cos\theta + \cos\theta_i) + (\cos\theta' + \cos\theta_i')]$, $t_d = t_1 - t_2$, $t_c = (1/2)(t_1 + t_2)$, $R_d = (R_1 + R_2) - (R_1' + R_2')$, $R_c = (1/2)[(R_1 + R_2) - (R_1' + R_2')]$.

The first exponential term gives the total phase shift due to different observing angles ($\omega_o \gamma_d < f_c > /c$), different observing times ($\omega_o t_d$), and different ranges ($\omega_o R_d/c$). The second exponential term yields a small decrease in the correlation, in addition to the decorrelation in the previous section. The last exponential term provides the arrival time of the pulses (the peak of the exponential), which is on average R_c/c (average propagation path), minus $\gamma_c < f_c > /c$ (earlier time due to the average topographic height).

THE MILLIMETER-WAVE EXPERIMENT and MONTE-CARLO SIMULATION

To validate the predicted phase from the theory, we performed millimeter-wave scattering experiments (MMWE) at $\lambda = 3$ mm ($f = 100$ GHz). The experimental setups and procedures are well documented in [5]. The antennas were scanned along the memory line for high level of correlation [3], which implies higher accuracy in the phase measurement. For given reference and scanning angles, we raised the test surface in the vertical direction from zero to 17λ (5 cm). This simulates the average topography height. We also carried out Monte-Carlo simulation using the banded matrix iterative approach/canonical grid (BMIA/CAG) method [6]. Rough surfaces of different characteristics were used to study their effects on the interferometric phases, and to demonstrate the robustness of using the AME technique to get the phase of InSAR. Comparison between numerical and theoretical results at normal reference incident angles is shown in figure 2 for $(\sigma, l) = (0.25\lambda, 0.6\lambda)$ and $\theta_i' = 2.5^o$ and 5^o. For the MMWE, we chose rough surface with $(\sigma, l) = (0.25\lambda, 0.25\lambda)$ and measured the phase. Comparison between theoretical, numerical and experimental results are shown in figure 3. The uncertainty in the measured phase is also shown as error bars.

CONCLUSION

We have shown that the AME can be applied to InSAR for the retrieval of topographic height. The interferometric phase is *not* sensitive to the surface roughness, thus showing the robustness of the technique. Validation of the theory by performing MMWE and numerical simulation yields good agreement.

References

1. S.N. Madsen, H.A. Zebker, and J. Martin, "Topographic mapping using radar interferometry: processing techniques", *IEEE Trans. Geosci. Rem. Sens.*, **31**, 246-256, (1993)

2. E. Rodriguez and J. Martin, "Theory and design of interferometric synthetic aperture radars", *IEE Proceedings*, **139**, 147-159, (1992)

3. C. Le, Y. Kuga, and A. Ishimaru, "Angular correlation function based on the second-order Kirchhoff approximation and comparison with experiments", *J. Opt. Soc. Am. A*, accepted for publication, (1996).

4. A. Ishimaru, *Wave Propagation and Scattering in Random Media.* New York: Academic, (1978), pp. 96.

5. T-K Chan, Y. Kuga, and A. Ishimaru, "Angular memory effect of millimeter-wave scattering from two-dimensional conducting random rough surfaces", *Radio Science*, accepted for publication, (1996).

6. L. Tsang, C.H. Chan, K. Pak, and H. Sangani, "Monte-Carlo simulations of large-scale problems of random rough surface scattering and applications to grazing incidence with the BMIA/canonical grid method", *IEEE Trans. Antenn. Propa.*, **43**, 851-859, (1995).

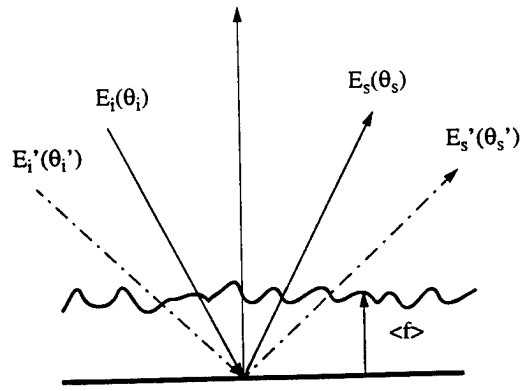


Figure 1: The scattering geometry.

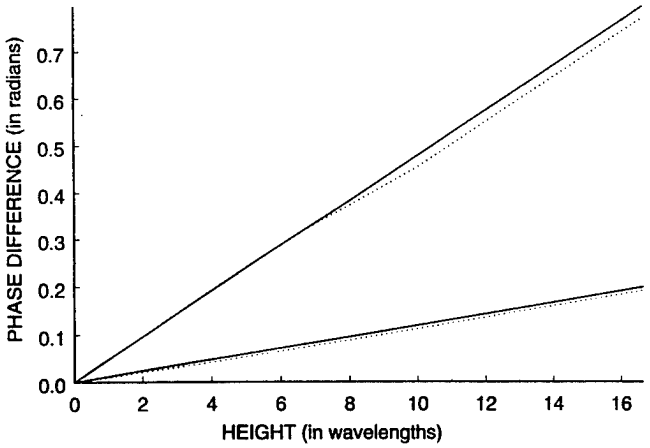


Figure 2: Interferometric phases: theoretical (solid), numerical (dashed). Reference angles $(\theta_i, \theta_s) = (0^o, 0^o)$. Upper curves $(\theta_i' = 5^o)$, lower curves $(\theta_i' = 2.5^o)$.

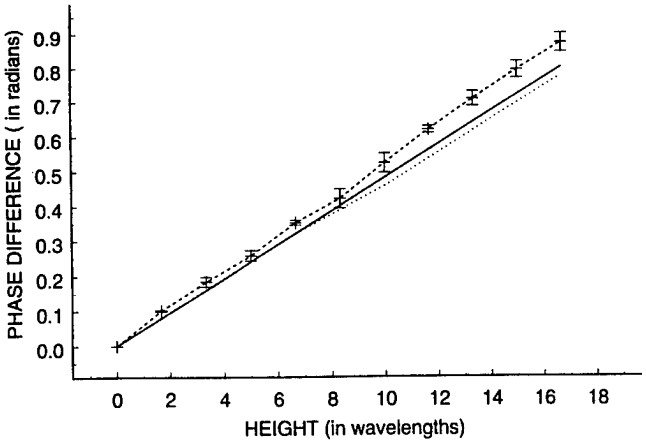


Figure 3: Interferometric phases: theoretical (solid), numerical (dashed), experimental (dashed-dotted). Reference angles $(\theta_i, \theta_s) = (0^o, 0^o)$; $\theta_i' = 5^o$.

Detection of a Target in a Homogeneous Medium Using Angular Correlation Function

Tsz-King Chan, Yasuo Kuga, and Akira Ishimaru

Department of Electrical Engineering
University of Washington
Box 352500
Seattle, WA 98195-2500

Abstract – A novel technique for detecting a target buried under a homogeneous medium is presented in this paper. This technique is based on a phenomenon known as the Angular Memory Effect, and involves measurement of the Angular Correlation Function (ACF) for scattered waves observed at antenna positions where the masking effect of the medium on the desirable target ACF return is minimized. Millimeter-wave experiments were conducted to demonstrate the effectiveness of this technique.

INTRODUCTION

Over the past several decades since the invention of radar, various radar applications have required extensive research on the detection of targets embedded in clutter and/or buried under ground/sea [1-4]. Among these applications are, for instance, the detection of a vehicle camouflaged by a thick tree canopy and removal of potentially active land/undersea mines buried in battlefields. While traditional approaches making use of radar cross-section measurement usually result in inconclusive decisions for the presence/absence of the target(s), modern advanced radars with polarimetric, transient, and bistatic features provide alternatives with mixed success [1-4].

In this paper, we propose a new technique based on ACF measurement for target detection in a homogeneous medium formed by very fine sand particles. We evaluated the effectiveness of this approach by performing millimeter-wave experiments on the ACF measurement for the detection of a long conducting cylinder (diameter $\approx 1\lambda$) oriented perpendicularly to the plane of incidence. The cylinder was buried at a depth of about 1λ below the sand medium which has a flat sand-air interface, as shown in Fig. 1. Our results indicate that by measuring the ACF corresponding to an appropriate set of incident and scattering angles, the masking effect of the medium on the desirable target ACF return can be minimized, thus allowing successful target detection.

ANGULAR MEMORY EFFECT

Recent studies showed that there is memory associated with the angular dependence of multiply scattered waves from random rough surfaces in response to a change in the direction of the incident wave [5-7]. This angular correlation phenomenon was known as the Angular Memory Effect and can be characterized by the ACF defined as [8-9]

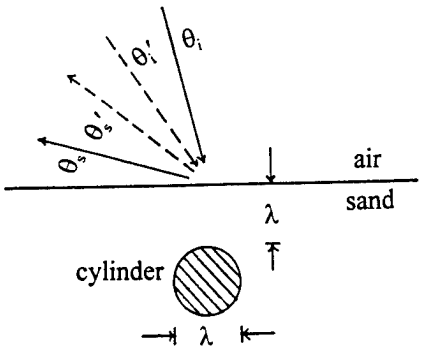


Fig. 1 Scattering geometry of the experimental setup

$$\Gamma(\theta_i,\theta_s;\theta_i',\theta_s') = \langle E_s(\theta_i,\theta_s)E_s^*(\theta_i',\theta_s')\rangle \qquad (1)$$

$\Gamma(..)$ represents the angular correlation between the reference scattered wave observed at θ_S due to an incidence at θ_i and the variable scattered wave observed at θ_S' due to an incidence at θ_i', with angle brackets denoting an ensemble averaging operation. In general, the ACF or rough surface is negligibly small because of the phase cancellation due to multiple scattering, but becomes significant when the difference in the transverse wave numbers is the same for the incident and scattered waves [9]. This condition can be stated as

$$k(\sin\theta_i' - \sin\theta_i) = k(\sin\theta_s' - \sin\theta_s) \qquad (2)$$

For a given pair of reference antenna positions (θ_i, θ_S), the ACF is therefore almost zero everywhere except along the line (the *angular memory line*) defined by (2) on the $\sin\theta_i'$–$\sin\theta_s'$ plane. The lateral width of this line is quite narrow and is on the order of λ/L [8-9], where L is the illumination width. In our experiments, λ/L is smaller than 1°, indicating rapid decorrelation away from the angular memory line. In the case of a perfectly reflective flat surface, the condition for strong

0-7803-3068-4/96$5.00©1996 IEEE

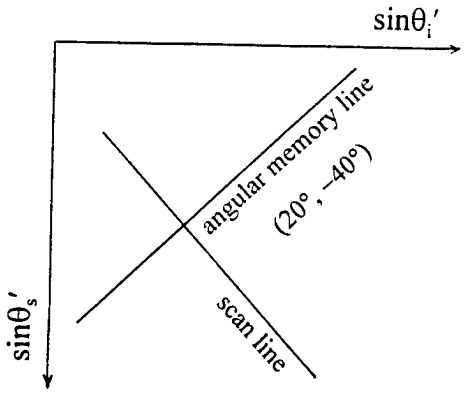


Fig. 2 The angular memory line and the scan line

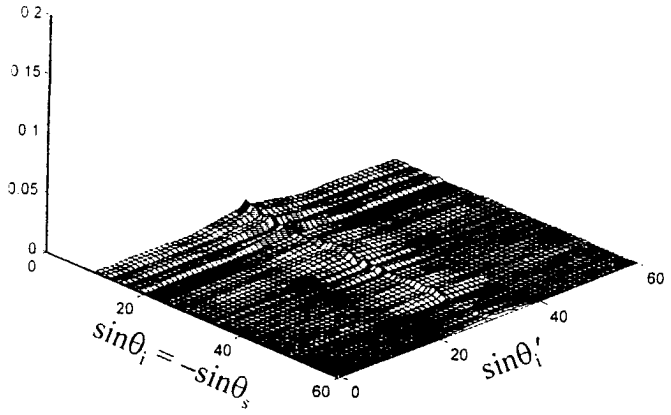


Fig. 3 Sand medium alone

angular correlation is similar to (2), but without the sine dependence.

Since rough surface ACF is most significant when measurement is made along the angular memory line, in order to minimize the masking effect of the medium on the desirable target ACF return in the combined scene (medium together with the target), measurement should be made along a line (the *scan line*) which is *perpendicular* to the angular memory line. In this study, this scan line was chosen to be a straight line intersecting perpendicularly with the angular memory line at the reference antenna positions ($\theta_i = 20°, \theta_s = -40°$). These two lines are shown in Fig. 2.

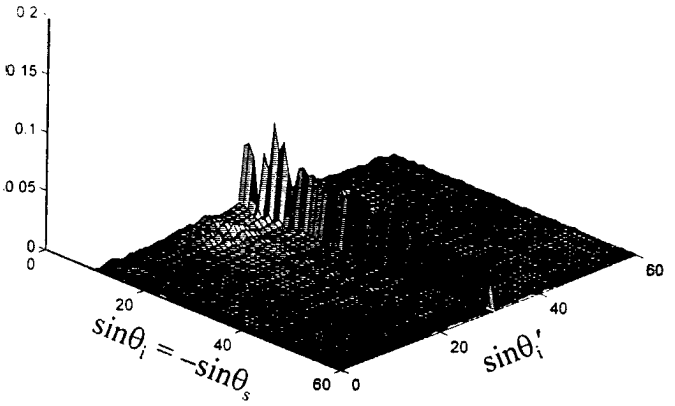


Fig. 4 Sand medium with a buried 3mm–cylinder

EXPERIMENTS AND RESULTS

Wideband millimeter-wave experiments were conducted to evaluate the effectiveness of this correlation technique for the detection of a target in a homogeneous medium. At 75–110 GHz, a long conducting cylinder (diameter $\approx 1\lambda$) was buried at a depth of about 1λ below a homogeneous medium formed by very fine sand particles with a flat sand-air interface. The size of the sand particles was chosen so that the dominance of surface scattering over volume scattering can be justifiably assumed. An ACF measurement based on one single spatial sample was then made along the scan line. Mechanical accuracy of the experimental setup was reinforced by using computer-controlled rotational stages and electronic devices with angular position feedback. The ensemble averaging operation in (1) was achieved using the available independent frequency samples over the frequency band of 80–105 GHz. Because of the large dynamic range of the energy content in ACF measurements, target visibility (or target-to-background contrast) can be enhanced by taking the Fourier transform on the raw ACF data. Only the magnitude of the complex transformed-ACF is presented in this paper.

Figures 3 and 4 illustrate respectively the magnitudes of the transformed-ACF without and with the presence of the

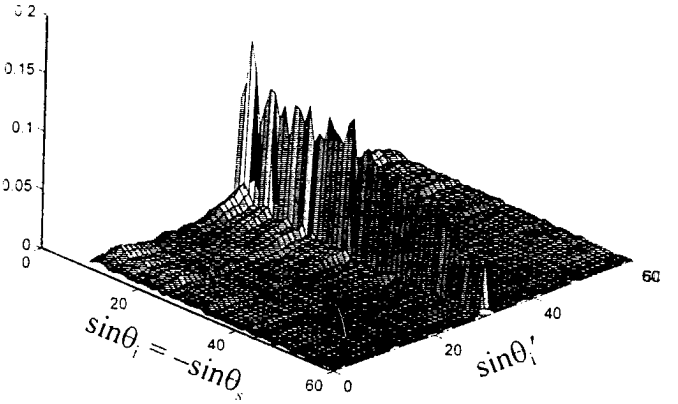


Fig. 5 Sand medium with a buried 12mm–cylinder

1λ–cylinder using TM incidence for ($\theta_i = 20°, \theta_s = -40°$) based on one single spatial sample. The results were plotted with reference antenna positions (θ_i, θ_s) equating variable antenna positions (θ_i', θ_s') for each (θ_i', θ_s') lying along the scan line. As evident from these figures, the difference in the height of the two central edges clearly reveals the presence of the cylinder. Intuitively, one may expect that larger targets should provide higher target visibility. This is confirmed in Fig. 5 for the case of a buried cylinder of diameter $\approx 4\lambda$.

CONCLUSION

A new approach for target detection based on the angular correlation (memory) effect is proposed. The experimental studies conducted with a conducting cylinder buried in a homogeneous sand medium demonstrate the effectiveness of this correlation technique. The fact that successful detection can be based on one single spatial sample makes this approach a competitive candidate to practical implementation of a target detection system. Proposed research based on this technique should focus on its potential applications in the detection of land/undersea mines or targets embedded in clutter.

REFERENCES

[1] *Radar Handbook*, 2nd Ed, Edited by M. Skolnik, McGraw-Hill, 1990.

[2] *Ultrawideband Radar*, Proceedings SPIE, Vol. 1631, Los Angeles, Jan. 1992.

[3] *Ultrawideband Radar*, Proceedings of the First Los Alamos Symposium, Ed. B. Noel, CRC Press, 1991.

[4] *Radar Polarimetry for Geoscience Applications*, edited by F. Ulaby and C. Elachi, Artech House, 1990.

[5] I. Freund, M. Rosenbluh, and S. Feng, "Memory effects in propagation of optical waves through disordered media," *Phys. Rev. Letters*, **61**, No. 20, 1988.

[6] T. R. Michel and K. A. O'Donnell, "Angular correlation functions of amplitudes scattered from a one-dimensionally, perfectly conducting rough surface," *J. Opt. Soc. Am.*, **9**, No. 8, 1992.

[7] M. Nieto-Vesperinas and J. A. Sánchez-Gil, "Intensity angular correlations of light multiply scattered from random rough surfaces," *J. Opt. Soc. Am.*, **10**, No. 1, 1993.

[8] T-K Chan, Y. Kuga and A. Ishimaru, "Angular memory effect of MMW scattering from two-dimensional conducting rough surfaces," submitted to *Radio Science*, 1995.

[9] C. Le, A. Ishimaru and Y. Kuga, "Angular correlation function based on the second-order Kirchhoff approximation and comparison with experiments," to appear, *J. Opt. Soc. Am.*, May, 1996.

[10] P. Phu, A. Ishimaru and Y. Kuga, "Co-polarized and cross-polarized enhanced backscattering from two-dimensional very rough surfaces at millimeter wave frequencies," *Radio Science*, 29, pp. 1275–1291, 1994.

[11] Y. Kuga and P. Phu, "Experimental studies of MMW scattering in discrete random media and rough surfaces," *Progress in Electromagnetics Research*, Elsevier Science Publishers, Cambridge, MA, 1995.

Numerical Study of Detection of a Buried Object Under a Single Random Rough Surface with Angular Correlation Function

Leung Tsang, Guifu Zhang and Kyung Pak
Electromagnetics and Remote Sensing Laboratory
Department of Electrical Engineering
Box 352500
University of Washington, Seattle, WA 98195-2500
Telephone: (206)685-7537 Fax: (206)543-3842

Abstract

The detection of an object buried under a random rough surface has important applications. The bistatic scattering intensity of the rough surface can be comparable to that of the object making it difficult to detect the buried object. In this paper we study the angular correlation functions (ACF) of scattering. We first study ACF of rough surface scattering. It is shown that a memory line is still exhibited for a single random rough surface of moderate extent based on frequency average. If the incident and scattered angles are away from the memory line of rough surface scattering, then the ACF of rough surface scattering is small. For the problem of buried object under a rough surface, numerical simulations indicate that even when the ratio of scattered intensities with and without the buried object is close to unity, the corresponding ratio of ACF can be 15dB. Thus, using ACF is superior to using intensities in the detection of buried object.

1. Introduction

An important objective in the detection of buried objects is the ability to distinguish the scattering of electromagnetic waves of the buried object from the scattering by the random rough surface above it (Figure 1). The bistatic scattered intensity of the rough surface can be larger than or comparable to that of the buried object. Instead of using intensities, we study the use of an coherent averaging technique based on angular correlation functions.

The study of scattering by random rough surfaces has been carried out for many years [1,2]. Studies have been mostly restricted to the measurement and calculation of bistatic intensities. However, the study of angular correlation shows that disordered media can exhibit memory effect [3-6]. It has been shown that the values of the angular correlation function are small except along the memory line. In all these studies of angular correlation function and memory effect of rough surface, the memory line does not exhibit itself for a single random rough surface. Memory line are shown to exist only when averages are taken over many surfaces (realizations) of random rough surface. In real life, however, the buried object is always under a single random rough surface. Taking realization average over different surfaces as customarily done is meaningless. In this paper, we use frequency averaging instead of realization averaging to study the angular correlation function of wave scattering by a buried object under a single random rough surface.

2. Formulation

Consider a tapered wave $\psi^i(\overline{\rho})$ incident upon a random rough surface with an object buried under it (figure 1). The buried object is assumed to be a perfect conducting cylinder centered at $(x, z) = (0, -d)$. By using surface integral equation method and the boundary conditions at the rough surface and the surface of the object, the wave field ψ and its normal derivative $\frac{\partial \psi}{\partial n}$ are solved by the method of moments. Then, the far field scattered field in direction θ_s can be represented as

$$\psi_s(\overline{\rho}') = \frac{e^{ik\rho'}}{\sqrt{\rho'}} \psi_s^N(\theta_s, \theta_i) \qquad (1)$$

where

$$\psi_s^N(\theta_s, \theta_i) = \frac{i}{4}\sqrt{\frac{2}{\pi k}} e^{-i\pi/4} \int dx$$

0-7803-3068-4/96$5.00©1996 IEEE

$$\left[-\sqrt{1+\left(\frac{df}{dx}\right)^2}\frac{\partial\psi}{\partial n}+\psi ik\left(\frac{df}{dx}\sin\theta_s-\cos\theta_s\right)\right]$$
$$e^{-ik(x\sin\theta_s+f(x)\cos\theta_s)} \quad (2)$$

Consider incident waves at two incident directions θ_{i1} and θ_{i2} with corresponding scattered waves at θ_{s1} and θ_{s2} respectively, the angular correlation function (ACF) is defined as

$$\Gamma_r(\theta_{s1},\theta_{i1};\theta_{s2},\theta_{i2})=\frac{1}{N_r}\sum_{n=1}^{N_r}\psi_s^N(\theta_{s1},\theta_{i1},n)$$
$$\psi_s{}^{N*}(\theta_{s2},\theta_{i2},n)/\sqrt{W_1W_2} \quad (3)$$

where n is the realization index, N_r is the number of realizations. W_1 and W_2 are the energy flux through the surface at incident angles θ_{i1} and θ_{i2}, respectively.

In the present problem, however, the buried object is only under a single realization of rough surface. We use frequency averaging with the angular correlation function (ACF) defined by

$$\Gamma_f(\theta_{s1},\theta_{i1};\theta_{s2},\theta_{i2})=\frac{1}{N_f}\sum_{n=1}^{N_f}\psi_s^N(\theta_{s1},\theta_{i1},f_n)$$
$$\psi_s{}^{N*}(\theta_{s2},\theta_{i2},f_n)/\sqrt{W_1W_2} \quad (4)$$

where f_n is the frequency. The averaging is taken over the frequency range with center frequency f_o.

3. Numerical Results

In the numerical simulation, we use a circular cylinder as the buried object. We use a single random rough surface with the height profile plotted in figure 1. A rough surface of length $L = 40\lambda_o$ with rms height $h = 0.25\lambda_o$ and correlation length $l = 0.5\lambda_o$. The cylinder is placed at a depth $d = 2\lambda_o$. Unless specified otherwise, all distance units are based on wavelength λ_o. The tapering parameter is $g = L/4 = 10\lambda_o$. The relative permittivity of region 1 is $3.7 + i0.13$. The angular correlation functions are calculated by frequency averaging over a frequency band $0.5f_o$ to $1.5f_o$.

Figure 2 shows the 3-D plot of the angular correlation functions. The reference angles are $\theta_{i1} = 20^o$ and $\theta_{s1} = -20^o$. We can see a peak along the memory line, which is mainly due to the rough surface scattering. To demonstrate the usefulness of ACF, we compare angular correlation functions with scattered intensities. We calculate the ratios between with the buried object and without the buried object as plotted in figure 3. The comparisons of these two ratios indicate the advantage of using ACF over intensity for the detection of buried object. We make such a comparison in figure 6c. We note that generally the ratio of ACF is higher than that of the ratio of intensity. For example, for $-40^o < \theta_{i2} < 40^o$, the ratio of intensity is about 1 dB while the ratio of ACF is up to 15 dB.

4. Reference

1. A. Ishimaru, *Wave Propagation and Scattering in Random Media*, New York, Academic Press, 1978.

2. L. Tsang, J.A. Kong and R.T. Shin, *Theory of Microwave Remote Sensing,* New York, Wiley Interscience, 1985.

3. S. Feng, C. Kane, P. A. Lee, and A. D. Stone, "Correlations and fluctuations of coherent wave transmission through disordered media," *Phys. Rev. Lett.*, vol. 61, pp. 834-837, 1988.

4. L. Tsang, G. Zhang, and K. Pak, "Detection of a buried object under a single random rough surface with angular correlation function in EM wave scattering", *Microwave and Optical Technology Letters,* to appear in April 1996.

5. Y. Kuga, T.-K. Chan, and A. Ishimaru, "Detection of a target embedded in clutter using the angular memory effect," submitted for publication in *IEEE Transactions on Antennas and Propagation*, 1995.

6. G. Zhang, L. Tsang, and Y. Kuga, "Studies of angular correlation function of scattering by random rough surfaces with and without a buried object," to be submitted for publication in *IEEE Transactions on Geoscience and Remote Scening.*

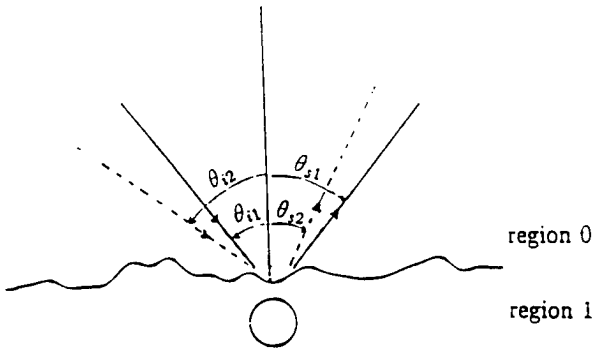


Figure 1: *Configuration of angular correlation of wave scattering by a buried object .*

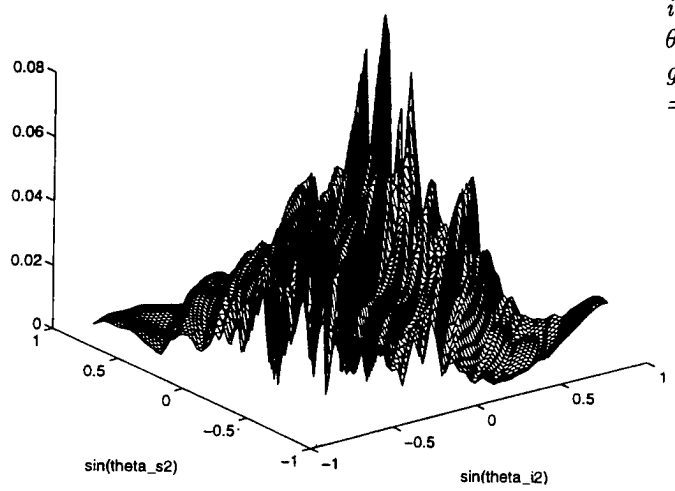


Figure 2: *3-D plot of angular correlation function by frequency averaging for wave scattering from a rough surface with a buried object. Averaging band is* $(0.5f_o - 1.5f_o)$. *Reference angles are* $\theta_{i1} = 20^o$, $\theta_{s1} = -20^o$. *Dielectric constant of region 1 is* $\epsilon_r = 3.7 + 0.13i$. $a = 1.5\lambda_o$, $L = 40\lambda_o$, $g = L/4$. $h = 0.25\lambda_o$, $l = 0.5\lambda_o$

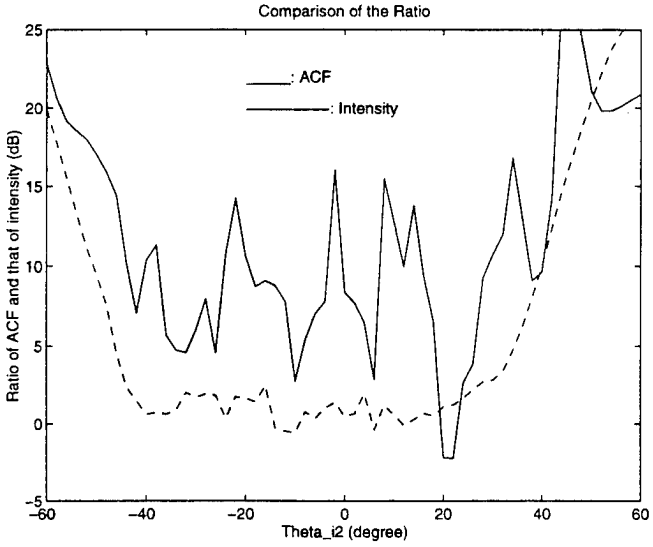


Figure 3: *Comparison between ACF and intensities for the ratios of wave scattering from a rough surface with and without a buried object. Averaging band is* $(0.5f_o - 1.5f_o)$. *Reference angles are* $\theta_{i1} = 30^o$, $\theta_{s1} = -50^o$. *Dielectric constant of region 1 is* $\epsilon_r = 3.7 + 0.13i$. $a = 1.5\lambda_o$, $L = 40\lambda_o$, $g = L/4$. $h = 0.25\lambda_o$, $l = 0.5\lambda_o$

Remote Sensing of Land Surface Temperature: The Directional Viewing Effect

James A. Smith
Code 920
NASA Goddard Space Flight Center
Greenbelt, MD 20771
Telephone: (301) 286-4950

Narinder S. Chauhan
The George Washington University
Washington, D.C. 20052

Jerry Ballard
USAE Waterways Experiment Station
Vicksburg, MS 39180

Abstract— **Land surface temperature is an important parameter in determining the earth radiation budget and heat and moisture flow between the surface and the atmosphere. Many vegetation, hydrologic and decomposition processes are strongly temperature dependent. Land surface temperature and emissivity products are currently being derived from satellite or aircraft remote sensing data using a variety of techniques to correct for atmospheric effects and land surface emissivity variations arising from simple, cover type differences. However, implicit in the commonly employed approaches is the assumption of isotropy in directional thermal infrared exitance. In reality, surface temperature observed from a satellite or aircraft platform is a function of both sun angle and sensor view angle. These variations, in turn, are a function of vegetation type and structure and the partitioning of radiative, sensible and latent heat exchanges between the vegetation and the atmosphere. While the Lambertian assumption may be taken as a first-order approximation, our analyses and observations indicate angular variations in apparent infrared temperature will typically yield land surface temperature errors ranging from 1 to 2 degrees Centigrade unless corrective measures are applied.**

Introduction

Land Surface Temperature (LST) is an important parameter in understanding global environmental change because it controls many of the underlying processes in the energy budget at the surface and heat and water transport between the surface and the atmosphere. Further, many biogeophysical or biogeochemical processes are strongly temperature dependent and accurate knowledge of LST is needed for evapotranspiration estimates, partitioning of sensible and latent heat, snow and ice-melting, monitoring water stress in crops and vegetation growth in general.

These applications require LST measurements at a variety of spatial and temporal scales and their extension to global coverage requires remote sensing means to achieve these goals. The data so acquired at multiple spatial and temporal scales can facilitate our understanding of local scale processes as they influence regional scale processes and eventually global assessments that are critical to our understanding of the coupling between the terrestrial landscape and the atmosphere. However, remotely sensed observations are obtained at fixed view and sun angles. This, coupled with atmospheric effects and the mixed pixel problem resulting from horizontal and vertical spatial heterogeneity, makes the accurate estimate of LST a formidable problem [1].

The measurement and interpretation of "Land Surface Temperature" for complex surfaces is not straightforward. Various terms have been employed to indicate its measurement and scaling properties [2]. For those cases where surface thermal infrared exitance varies with view angle, present LST algorithms will yield different land surface temperatures for the same cover type merely as a result of the sensor/sun view geometry at data acquisition. Further, none of these retrieved temperatures may be the correct one for computing surface energy balance components.

The directional viewing effect is well-documented in the experimental literature particularly for vegetation and vegetation mixtures and cannot be ignored. For example, Balick, et al. typically found 4 degrees variation with view angle for an Oak Hickory forest canopy [3] [4]. For snow, the effect is not as pronounced except at large zenith viewing angles [5]. Lagourde and Kerr [6] found variations in temperature as large as 8 degrees for corn and rough soil surfaces. Kimes [7] has reported even greater variations for a cotton row crop with 48 percent ground cover.

Sobrino and Caselles [8] proposed a two-dimensional radiance model to interpret the directional, remotely-sensed thermal infrared data obtained over vegetative surfaces. The model was validated for different view angles from the measurements made with a radiometer placed on board a helicopter in two different citrus regions. Their results show a temperature variation of 4-5 degrees C for an angular change of 0-50 degrees in zenith angle. Using this modeling approach, the authors subsequently interpreted AVHHR data from NOAA-9 and estimated the directional

0-7803-3068-4/96$5.00©1996 IEEE

effects to be between 0.2 to 2.8 degrees C [9].

Approach

We can formulate land surface temperature in terms of effective radiant temperature relationships which correctly scale the radiative flux for both homogeneous and complex heterogeneous surfaces using the definitions suggested by Price [10]. Surface hemispherical long-wave emittance can then be directly computed from satellite observations as well as large-scale sensible heat flux calculations, if additional surface resistances are included [11].

In our approach the canopy-soil system is abstracted as an n-layer canopy superimposed upon a simple soil surface layer [12]. Within each canopy layer the amount and mixture of components may vary, each possessing different optical, thermal and geometrical properties. The soil surface layer is characterized by a soil bulk density, water content, roughness height and soil composition. The energy balance equation of the coupled system in terms of net radiation, R_n, sensible heat, H, latent heat, LE, and ground conduction, G, is given by:

$$R_n = LE + H + G \tag{1}$$

Expanding the net radiation term into up welling and down welling longwave and absorbed shortwave radiation components for each system layer, i, yields:

$$\alpha_i \sum_j B_j S_{ij} - 2.0B_i + A_i - H_i - LE_i - G\delta_{i,s} = 0 \tag{2}$$

where B is the long-wave flux, A is the short-wave energy absorbed, α is the long wave absorption coefficient and $\delta_{i,s}$ is the Dirac delta function indicating that conduction must be included for the ground surface layer. The unknowns in this system of non-linear equations are the canopy layer temperatures and ground temperature. S_{ij} is the fraction of emitted flux from a source layer j that is intercepted by a foliage element within layer, i and can be approximated by:

$$S_{ij} = \int_0^{\pi/2} \int_0^{2\pi} F_{ijr} \ \sin\theta_r \cos\theta_r \ d\theta_r \ d\phi_r \tag{3}$$

The fraction of long-wave flux (F_{ijr}) is computed as a product of the fraction of vegetation in layer j, which is emitting along direction $\hat{r}$, times the probability of a gap for the emitted radiance through intermediate vegetation layers, k, before finally being intercepted in layer i. For emission and absorption within a given layer, a factor of 2 is required to account for both sides of the receiving elements. For vegetation layers, F_{ijr}, is given by

$$F_{ijr} = \begin{cases} [1 - P_0(j,r)] \prod_{k=i+1}^{j-1} P_0(k,r), & \text{if } i < j, \\ 2[P_0(i,r)], & \text{if } i = j, \\ [1 - P_0(j,r)] \prod_{k=j+1}^{i-1} P_0(k,r), & \text{if } i > j. \end{cases} \tag{4}$$

Many expressions may be used for the probability of gap for a layer in any arbitrary direction $\hat{r} = (\theta_r, \phi_r)$. A convenient one, including clumping, is given by:

$$P_o(\hat{r}) = e^{-LAI * \lambda * g(\hat{r})/cos(\theta_r)} \tag{5}$$

where LAI is leaf area index of the layer, g is the mean canopy projection in direction r and depends on the layer leaf slope distributions and λ is a clumping factor between 0 and 1 that accounts for clumping in vegetation

The S_{ij} have often been expressed as simple area proportions, but this is incorrect. In particular, $S_{ij}(\theta, \phi)$ varies with view angle resulting in an effective average emissivity which varies with view angle (θ, ϕ), and, thus, yielding directionally dependent brightness surface temperatures.

Preliminary Analysis and Predicted Error

We have performed initial model simulations using this approach for a forest canopy which we have previously studied [12]. A three-layer canopy with total LAI equal to 5.9 and a summer diurnal cycle under clear sky was simulated. We then applied the view factor matrices, S_{ij}, as described above, to predict directional thermal exitance. We also integrated the total, hourly outgoing hemispherical longwave emission from the canopy system to compute the effective radiant surface temperature (LST). Finally, the differences between this LST and the effective brightness temperature that would be inferred from measurements made at varying view angles were compared.

Fig. 1 below shows the resulting error to be expected in inferring LST from remote sensing measurements made at various observation times (sun angle) and at varying zenith view angle. In this plot zenith view angle ranges from 0 to 50 degrees corresponding to common satellite platforms (although assuming flat surfaces). The zenith view angle range is labeled between 0 (corresponding to 0 degrees) and 10 (corresponding to 50 degrees). The error in land surface temperature estimation can exceed 1-2 degrees K even for this fairly dense canopy.

Fig. 2 below shows a slice through this plot and extends the zenith view angle range to 90 degrees, as would be appropriate for topographically rough terrain. The zenith view angle range has been labeled from 0 (corresponding to 0 degrees) to 10 (corresponding to 90 degrees). The results for solar noon (1200) and for plus and minus two hours from solar noon are given. As has been noted by previous investigators [13], there appears to be a cross-over point in view angle where errors in LST estimation are minimized. However, at this large observation angle, path length through the atmosphere is significant and geometric and atmospheric corrections are thus more difficult. Atmospheric corrections at smaller angles are easier but, as our preliminary results indicate, the errors induced by surface interaction effects are greater and require additional correction.

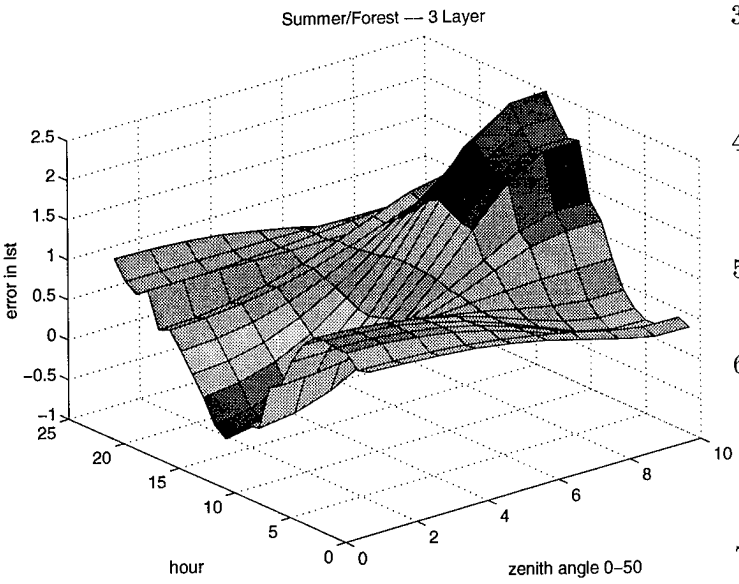


Fig. 1.

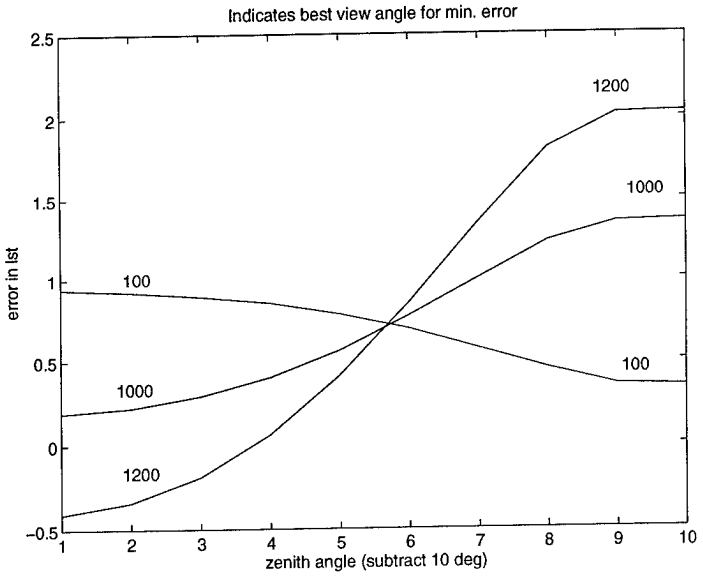


Fig. 2.

Acknowledgements

The research described in this paper was supported by the Remote Sensing Science component of the Ecological Processes and Modeling Program at NASA Headquarters and, in part, by U.S. Army Engineers Waterways Experiment Station.

References

1. A.J. Prata, V. Caselles, C. Coll, J. A. Sobrino, and C. Ottle, Thermal remote sensing of land surface temperature from satellites: current status and future prospects, Remote Sensing Reviews, 1995, vol. 12, pp. 175-224.
2. Francois Becker and Zhao-Liang Li, Surface temperature and emissivity at various scales: definition, measurement and related problems, Remote Sensing Reviews, 1995, vol 12. pp. 225-253.
3. L.K. Balick. B.A. Hutchison, J. A. Smith and M. J. McGuire, Directional thermal exitance distributions of a deciduous forest in summer, IEEE Trans. Geosc. Remote Sensing, 1987, vol. 25, pp. 410-412.
4. M. J. McGuire, J. A. Smith, L. K. Balick and B. A. Hutchison, Modeling directional thermal exitance from a forest canopy, Remote Sensing Environment, 1989, vol. 27, pp. 169-186.
5. J. Dozier and S. Warren, Effects of viewing angle on infrared brightness temperature of snow, Water resources, 1982, vol. 18, pp. 1424-11434.
6. J. P. Lagouarde and Y. Kerr, Experimental study of angular effects on brightness surface temperature for various types of surfaces, Proc. of the workshop on thermal remote sensing of the energy and water balance over vegetation in conjunction with other sensors, Sept. 20-23, 1993, La Londe Les Maures, France.
7. D. S. Kimes and J. A. Kirchner, Directional radiometric measurements of row-crop temperatures, Int. J. Remote Sensing, 1983, vol. 4, pp. 299-311.
8. J. A. Sobrino and V. Caselles, Thermal infrared radiance model for interpreting the directional radiometric temperature of a vegetative surface, Remote Sens. Environment, 1990, vol. 33, pp. 193-199.
9. J. A. Sobrino and V. Caselles, A methodology for obtaining the crop temperature from NOAA-0 AVHRR data, Int. J. Remote Sens., 1991, vol. 12, pp. 2461-2475.
10. John C. Price, On the use of satellite data to infer surface fluxes at meteorological scales, J. Appl. Meteorology, 1982,vol 21, pp. 1111-1122.
11. R. C. Vining and B. L. Blad, Estimation of sensible heat flux from remote sensed canopy temperature, J. Geophys. Res., 1992, vol 97, pp. 18951-18654.
12. J. A. Smith and S. M. Goltz, A thermal exitance and energy balance model for forest canopies, IEEE Trans. Geosci. Remote Sens., 1994, vol. 32, pp. 1060-1066.
13. J. Otterman, J. Susskind, T. Brakke, D. Kimes, R. Pielke and T. J. Lee, Inferring the thermal-infrared hemispheric emission from a sparsely vegetated surface by directional measurements, 1995, Boundary-Layer Meteorology, vol 74, pp. 163-180.

A Simulation of Topographic Solar Radiative Forcing Over A Mountainous Region Using Geostationary Satellite Data

S. Loechel[+], R. Dubayah[+], J. Barnett[+], C. Gautier[☆], M. Landsfeld[☆]

Phone: 301/504-6823; Email: sloechel@asrr.arsusda.gov

[+] Laboratory for Global Remote Sensing, Department of Geography, University of Maryland, College Park, Maryland

[☆] Institute for Computational Earth System Science , University of California, Santa Barbara

Abstract -- The radiative forcing effects of topography and clouds were examined for a mountainous region during the rainy season to further our understanding of the relative roles of each in modulating incoming solar energy at the Earth's surface. Solar radiation fields derived from hourly, 8 km GOES observations were used to drive a topographic solar radiation model at 60 m resolution during August 1988, for the Rio Grande River basin in Colorado. Monthly, basinwide mean solar radiative forcing as a percentage of average, clear-sky insolation was -37.3% for clouds and +10.2% for topography. The overall positive monthly topographic forcing (+10.2%) resulted from positive elevation effects (+18.6%); these outweighed the negative forcings (-8.4%) caused by terrain. These results suggested that topography must be considered for clear, cloudy, and partly cloudy conditions in mountainous regions, even at coarse temporal and spatial scales.

INTRODUCTION

This research examined the effect of topography on estimates of incoming solar radiation or insolation (SW↓) at the Earth's surface in a mountainous region under realistic atmospheric conditions simulated using satellite-derived insolation fields. Currently, radiative transfer models that estimate insolation ignore topography completely or partially in their calculations; many models assume the Earth's surface to be flat and at sea-level [4,5,11], while others include only a correction for elevation effects [2,6]. Therefore, we examined the amount of error incurred in insolation estimates as a result of the current treatments of topography. We employed solar radiative forcing, or the modulation of incoming solar radiation by physical conditions such as cloudiness or topography, to measure the effect of topography *per se* and relative to cloud effects at a range of temporal and spatial scales.

Solar radiation is the primary energy source fueling the global climate; fluctuations in solar radiation at the Earth's surface impact water, energy, and biophysical fluxes. Radiation is influenced by latitudinal gradients, atmospheric inhomogeneities, surface reflectance, and topography. Latitudinal gradients affect solar radiation at coarse scales through the changing orientation of the Earth relative to the Sun. The atmosphere affects solar radiation over a wide range of scales because of differences in the absorption and scattering properties of clouds and other atmospheric constituents relative to clear air. Surface reflectance impacts incoming solar radiation through multiple scattering. Topography leads to orographic cloud formation, while elevation, slope, exposure, and shadowing modulate insolation in various ways.

The definition of topography for the purposes of this research was considered to be only those factors that affected the insolation estimates directly. Therefore, topography was defined as those elevation and terrain formations that directly impacted the path length and direction of the incoming radiation through the geometrical relationship between a given point on the Earth's surface and the Sun. The indirect effects of topography through orographic cloud formation in mountainous terrain were beyond the scope of this research. Much research has been and continues to be performed on cloud properties relative to radiative transfer modeling; a thorough treatment of these topics is available in the literature [1].

METHODOLOGY

The methods applied in solving this problem, and ultimately in producing topographically corrected, broadband solar radiation fields and estimates of solar radiative forcing, can be divided into three conceptual groups: atmospheric corrections, geometric corrections, and statistical analysis. The atmospheric corrections included taking the Geostationary Operational Environmental Satellite (GOES) sensor's top-of-atmosphere (TOA) digital counts (DN) through the following four steps: (1) sensor calibration, (2) image navigation and reprojection, (3) initial radiative transfer calculations (assumed a sea-level, flat surface), and (4) elevation profiling to the true elevation. The geometric correction involved incorporating the fine-scale effects of slope, aspect, and sky obstruction. A more detailed explanation of our methods is given in [8].

Atmospheric Corrections. Estimates of sea-level insolation for August 1988, for Colorado were derived from hourly, 8 km GOES TOA digital counts obtained from the GOES Pathfinder Archive [14] which were then calibrated [13] and corrected for atmospheric effects using a physically based radiative transfer model [4,5]. A spatial cloud integration scheme was used to smooth the cloud fields by taking a distance-weighted average of the 8 km grid cells using a base resolution of 60 m [8] assuming a 3 km cloud base height, which is common to the region. Thereby, the nature of spatial

0-7803-3068-4/96$5.00©1996 IEEE

variability in the insolation fields was preserved. The vertical radiation profile was generated according to an elevation profiling method [3] that adapted an empirical approach [9]. The input to the profiling model was diffuse and direct radiation at a given elevation obtained from an empirical global-radiation partitioning algorithm [10].

Topographic-Geometric Corrections. In addition to elevation effects, topographic effects on insolation estimates include terrain formation. Mountainous topography results in terrain that modulates the incident radiation in various ways, such as the orientation of the surface, sky obstruction, and cast shadows. The topographic solar radiation model calculates incident radiation on a slope, which is illuminated from three possible sources: 1) direct irradiance, which includes shadows from nearby terrain and self-shadowing; 2) diffuse sky irradiance, where a portion of the sky overhead may be obstructed from view by nearby terrain; and 3) terrain irradiance, or direct and diffuse irradiance reflected onto the slope by nearby terrain. Given an exoatmospheric irradiance S_0, an optical depth τ_o, and a solar zenith angle θ_0, the topographic solar radiation model was initiated with elevation-adjusted estimates of diffuse ($F\downarrow(\tau_o)$) and direct ($\cos\theta_0 S_0\ e^{-\tau 0/\cos\theta 0}$) radiation. Then, total insolation on a slope is given by [3,8]:

$$R\downarrow_{slope} = [V_f F\downarrow(\tau_o) + C_t F\downarrow(\tau_o) + \cos i\ S_0\ e^{-\tau 0/\cos\theta 0}] \quad (1)$$

where V_f is a sky view factor that gives the percentage of the sky dome visible at a point and unobstructed by nearby terrain; $F\downarrow(\tau_0)$ is surface downwelling diffuse radiation; $C_tF\uparrow(\tau_0)$ combines a terrain configuration factor C_t to approximate the amount of diffuse and direct radiation reflected off surrounding terrain off a surface with $F\downarrow(\tau_0)$ downwelling radiation and an average reflectance of R_0; and cos(i), the cosine of the illumination angle, incorporates the effect of slope angle and azimuth relative to the solar position at the time of the observation. The terrain variables cos(i), V_f, and C_t were derived from digital elevation data.

Radiative Forcing. Radiative forcing is commonly used in analyses of cloud effects, and to characterize the effects of clouds [12]. In this research, however, radiative forcing was used as a measure of the effect of a given condition, such as the presence of cloud cover or mountainous topography, on an estimate of the incoming solar radiation on a surface.

The method that we employed for calculating each of the relevant radiative forcing (RF) effects, modified from [7], was as follows for a given effect:

$$RF_{effect} = R_{modeled\ with\ effect} - R_{modeled\ without\ effect} \quad (2)$$

so that any radiative forcing effect (Wm^{-2}) was equal to the difference between the insolation (R) modeled including the effect and insolation (R) modeled without the effect in question. Among the possible effects that we examined were cloud cover, full topography, elevation, and terrain.

Topographic Data and Study Area. The topographic data were a mosaicked data set of 39 individual U.S. Geological Survey (USGS) digital elevation models (DEM) at 30 m grid spacing covering the Rio Grande River basin. For computing purposes, the DEM was resampled to 60 m resolution.

The study area for this research was the Rio Grande River basin in the Rocky Mountains. The basin is located in southern Colorado at 37.7° N, 107° W. The dimensions of the basin are 110 km east-west by 79 km north-south, with a total area of 3419 km^2. The site is contained within the San Juan Mountain range, bound to the west by the Continental Divide and to the east by the San Luis Valley. Elevation ranges from 2432 to 4215 m, with a mean basin elevation of 3219 m. The basin has an average slope of 25 degrees.

RESULTS AND DISCUSSION

The following results demonstrate numerically and graphically the central tendencies of the basin scale simulation of insolation and radiative forcing by clouds and topography at a range of temporal scales. Prior to an analysis of forcing, the insolation estimates were examined throughout the day, and found to exhibit expected values and temporal patterns.

Table 1: Percent radiative forcing by clouds and topography

	Temporal scale		
Forcing Effect	Hourly (%)	Daily (%)	Monthly (%)
Clouds	-96.6 to -0.6	-81 to -3.5	-37.3
Topography	-5.8 to +15.8	+4.3 to +12.2	+10.2
Elevation	+11 to +26.5	+14.4 to +23	+18.6
Terrain	-28 to -5.2	-12.7 to -6.7	-8.4

A numerical representation of solar radiative forcing by clouds and topography is presented in Table 1, which gives the percent radiative forcing that was caused by clouds, topography, elevation, and terrain as a fraction of GOES clear-sky, unforced solar radiation such that the percentages are comparable. The percent radiative forcing caused by clouds exceeded topography at every temporal scale. Average monthly radiative forcing for August (in absolute and percentage terms) by clouds was -110 Wm^{-2} and -37.3%, while forcing by topography was +21 Wm^{-2} and +10.2%, respectively. Mean basinwide insolation load increased when elevation effects were included, and decreased when terrain effects were modeled. The basinwide forcing effect of topography on the monthly GOES insolation was positive (+10.2%), which resulted from the balance achieved between positive elevation effects (+18.6%) and negative terrain forcings (-8.4%). The negative effect that illumination angle and sky obstruction had on insolation was the result of a constant amount of solar energy impinging on a region with an increase in exposed surface area. This effect on the basinwide spatial

average occurred at every temporal scale.

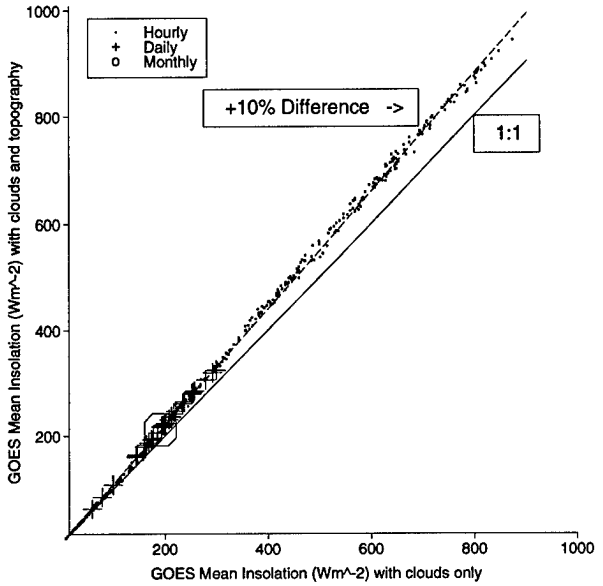


Figure 1: Basin mean insolation at different temporal scales: clouds vs. topography

A graphical representation of the effect of topography on basinwide mean insolation is given in Figure 1, which plots the spatial means of the GOES insolation fields at sea-level against the topographically corrected GOES insolation fields for each of the hourly, daily, and monthly observations. Note that topography consistently increased basin means in the range of 10% or more for daily and monthly estimates. The effect on hourly observations was often higher.

CONCLUSION

While topography is known to significantly impact insolation estimates at fine spatial scales, this research concluded that topographic effects can be significant in estimates of incoming solar radiation for coarse spatial and temporal scales. Using satellite insolation estimates and digital elevation data, estimates of incoming solar radiation were created for August 1988, in the Rio Grande River basin in the Colorado Rocky Mountains and corrected for the effects of topography. Topography caused mean radiative forcing of greater than 10% at all temporal scales examined for the study area (ranging from hourly to monthly). Our results implied the necessity to account for topography in global applications. Future research must improve the atmospheric correction methods, attempt to identify other concentrated regions where topography must be included in coarse-scale radiative transfer algorithms and where it can be ignored, and perhaps move to develop parameterizations of topographic variables for use at global scales.

Acknowledgments. Funding for this work was provided by NASA Grants NAGW-2928 and 940720-8010.

REFERENCES

[1] R.G. Barry, Mountain Weather and Climate, 2d ed. Routledge, New York, 1992.

[2] C. Bishop and W. Rossow, "Spatial and temporal variability of global surface solar irradiance," J. Geophys. Res., 98, 16,839-16,858, 1991.

[3] R. Dubayah and V. van Katwijk, "The topographic distribution of annual incoming solar radiation in the Rio Grande River basin," Geophys. Res. Letters, 19, 2231-2234, 1992.

[4] R. Frouin and C. Gautier, "Variability of photosynthetically available and total solar irradiance at the surface during FIFE," Proceedings 70th AMS Conference, Anaheim, CA. 98-104, 1990.

[5] C. Gautier, G. Diak, and S. Masse, "A simple physical model to estimate incident solar radiation at the surface from GOES satellite data," J. Appl. Meteor. 19: 1005-1012, 1980.

[6] J. Hansen, G. Russel, D. Rind, P. Stone, A. Lacis, S. Lebedeff, "Efficient three-dimensional global models for climate studies: Models I and II," Mon. Weather Rev., 111, 609-662, 1983.

[7] I. Laszlo and R. Pinker, "Shortwave cloud-radiative forcing at the top of the atmosphere at the surface and of the atmospheric column as determined from ISCCP C1 data," J. Geophys. Res., 98, 2703-2713, 1993.

[8] S. Loechel, "Solar radiative forcing by topography and clouds: a comparative analysis of topographic effects," 69 pp., M.A. thesis, Univ. of Maryland, College Park, 1995.

[9] W. Lowry, "Direct and diffuse solar radiation: variations with atmospheric turbidity and altitude," IES Research Report No. 6, UILU-IES 80 0006, p. 190, Urbana, 1980.

[10] G. Olyphant, "Insolation topoclimates and potential ablation in alpine snow accumulation basins: Front Range, Colorado," Water Resour. Res., 20, 491-498, 1984.

[11] R. Pinker and I. Laszlo, "Modeling surface solar irradiance for satellite applications on a global scale," J. Appl. Meteor., 31, 194-211, 1992.

[12] V. Ramanathan, R. Cess, E. Harrison, P. Minnis, "Cloud-radiative forcing and climate: results from the Earth Radiation Budget Experiment," Science, 243, 57-63, 1989.

[13] C. Whitlock, W. Staylor, G. Smith, R. Levin, R. Frouin, C. Gautier, "AVHRR and VISSR satellite instrument calibration results from both cirrus and marine stratocumulus IFO periods," Presented at the FIRE Science Team meeting, 9 Vail, CO, July 11-15, 1988.

[14] J. Young, J. Hagens, and D. Wade, "GOES Pathfinder product generation system," Conference on Appl. Climatology, 9th, Dallas, TX, 15-20 January, 1995. Boston, MA. American Meteorological Society.

Modeling Area-Averaged Fluxes Over Partially Vegetated Land Surfaces Using Aircraft and In-Situ Thermal Data

M. A. Friedl
Department of Geography and
Center for Remote Sensing
Boston University
Boston, MA 02215
friedl@crsa.bu.edu

Abstract – A surface energy balance model is used in association with remotely sensed and in-situ data to examine issues of measurement, scaling, and aggregation of high frequency spatial variation in land surface properties and fluxes over regional scales. Results from this analysis show that instantaneous land surface fluxes modeled from high spatial resolution remotely sensed data may be estimated only approximately. Comparisons between modeled versus observed fluxes averaged over regional scales (roughly 225 square km), on the other hand, exhibit excellent agreement. Based on these results it is concluded that the estimation of surface fluxes at high spatial resolution is problematic because the remotely sensed measurements reflect local land surface conditions, while land surface fluxes are produced by processes associated with surface-atmosphere interactions occurring over substantially larger areas. Because land surface-atmosphere interactions effectively integrate high frequency spatial variance in land surface properties, relatively coarse spatial resolution (100's of meters - 1 km), or random samples of high resolution data, may be used for surface energy balance modeling over regional scales.

INTRODUCTION

To properly account for the effects of land surface heterogeneity over regional scales, an improved understanding is required of how microscale surface properties and processes translate across spatial scales, and by extension, how to incorporate these effects within land surface climate models. Because of the complexity of these questions, several large scale field experiments have been conducted in recent years to specifically examine questions of scale in surface energy balance models, and to study the use of remote sensing as a tool for these purposes [1]. While results from these studies have demonstrated significant progress in remote sensing based models, significant questions remain unresolved particularly with respect to both the spatial aggregation of land surface fluxes over heterogeneous land surfaces and the use of thermal infrared (TIR) data [2]

In this paper, a land surface energy balance model is used in association with remotely sensed data to simulate land surface fluxes at both local and regional scales, and to study the interaction between data resolution and scaling of land surface fluxes. In this context, the specific objectives of this work are (1) to assess the accuracy with which land surface fluxes can be modeled using high spatial resolution remotely sensed data; (2) to assess the accuracy with which land surface fluxes may be estimated over regional scales using area-averaged input data; and (3) to consider the significance of sensor resolution in parameterizing land surface models using remotely sensed data.

To achieve these objectives, land surface fluxes of latent and sensible heat are estimated using remotely sensed data in association with a two-layer surface energy balance model at the FIFE site in northeastern Kansas for multiple dates during the growing season of 1987. Modeled fluxes estimated using both high spatial resolution remotely sensed data and area-averaged input data are then compared with in-situ measurements of both latent (LE) and sensible (H) heat. Results from these analyses are then used to consider questions related to the relationships among land surface heterogeneity, spatial variability in surface energy balance processes, scaling of surface energy balance models, and remotely sensed data.

MODELING APPROACH

For land surfaces composed of either dense vegetation or bare soils, remote sensing-based land surface energy balance models have been shown to estimate surface energy balance components with reasonable accuracy [3]. Over areas with incomplete canopy cover, however, more sophisticated modeling strategies are required due to the increased complexity of the upwelling radiance measured by TIR sensors over such areas [4]. Further, because soils and vegetation canopies possess coupled but distinct thermal and hydrologic properties, they act as separate sources and sinks for latent and sensible heat. Therefore, surface energy balance modeling over such areas is significantly more complicated than over areas with complete canopy cover [5]

0-7803-3068-4/96$5.00©1996 IEEE

To examine these issues a surface energy balance model (described below) was parameterized using a combination of ground and remotely sensed data. This model was then used to estimate land surface fluxes using surface temperature and LAI measurements estimated from high spatial resolution aircraft scanner data. Modeled fluxes were then compared to observed fluxes. Next, an approach to estimate area-integrated fluxes over the entire FIFE site using a big leaf modeling approach was tested. To this end, mean values for spatially variable input fields were calculated for the entire FIFE site and used as input to the surface energy balance model. The computed fluxes were then compared with observed site-wide mean fluxes calculated from in-situ data.

Data

The data employed for this work were compiled from three dates during each of three intensive field campaigns (IFCs) conducted during the growing season of 1987 (June 4,5,6: IFC 1; July 7,10,11: IFC 2; and August 15,16,17: IFC 3). These dates were identified as the optimal data collection periods during each of the IFCs. The data include surface energy balance measurements, surface meteorological parameters, and remotely sensed data.

Measurements of radiometric surface temperature (Ts) and NDVI were estimated from NS001 Thematic Mapper Simulator (TMS) data acquired from the NASA C-130 aircraft at approximately 4:05 pm on June 6, and 10:50 am and 3:35 pm on August 15 (local time). Atmospheric path radiances and transmissivities were calculated using LOWTRAN7 in association with radiosonde data (acquired concurrently with the NS001 data acquisition) at 11 scan angles ranging from -50 degrees to +50 degrees relative to nadir.

Surface Energy Balance Model

The model used for this work is based upon the formulation initially proposed by Choudhury [6] and is described in detail in [7]. The general formulation of the model employs a one-dimensional, two layer (soil and vegetation) potential resistance network for homogeneous surfaces under steady state conditions. The model partitions total net radiation at the land surface into the net radiation of the vegetation canopy and the net radiation at the soil surface.

Using this approach, the heat exchanges at the soil surface and within the vegetation canopy are modeled using a set of equations defined by two layer potential-resistence network. These equations describe distinct energy balance expressions for the soil surface and the vegetation canopy, and are coupled via the total energy balance for the surface and through the surface brightness temperature (Ts). A set of seven simultaneous equations are solved numerically for the unknown potentials in the system. Using input data regarding surface meteorological conditions, canopy LAI, and Ts, the model can then be used to estimate the net fluxes of latent and sensible heat from the land surface.

Canopy Reflectance Modeling

Because the microclimate regime of land surfaces characterized by partial canopy cover are highly dependent on the density of the vegetation canopy, LAI is a key input to this model. For this work, a relatively simple approach using the normalized difference vegetation index (NDVI) is employed to estimate LAI from the NS001 data. This index has been widely shown to be generally indicative of vegetation amount and fractional cover. To do this, simulated relationships between LAI and NDVI are estimated using a canopy reflectance model (SAIL; [8]). Using leaf and soil background optical properties measured at the FIFE site, NDVI data were simulated using SAIL for a range of LAIs from 0.1 to 3.0. The modeled relationship between NDVI and LAI was then inverted to predict green LAI from NDVI using a non-linear least squares procedure.

RESULTS

Aircraft DAta

The results from surface energy balance simulations using these data show relatively poor agreement between modeled versus observed fluxes (root mean squared errors were roughly 40 and 50 watts per square meter for LE and H, respectively). Figure 1 shows results from this comparison for LE. Overall, modeled values of LE show better correspondence between modeled and observed fluxes than do H, but this is partly an artefact caused by the larger range of LE values relative to the range in H values. More importantly, for any given date the correspondence between observed versus modeled fluxes is rather poor. In other words, most of the general agreement between modeled versus observed fluxes is produced by between-date differences in average fluxes, rather than the ability of the modeling procedure to accurately simulate land surface fluxes at high spatial resolution.

Area-Averaged Fluxes

Results from analyses of area-averaged fluxes show that modeled fluxes of LE and H compare well with observed fluxes, especially for IFCs 1 and 3. Results for LE in IFC1 are shown in Figure 2. H tends to be slightly overestimated in IFC1, and slightly underestimated in IFC3. LE, on the other hand, exhibits excellent agreement for both of these data sets. The cause of these relatively small biases may be attributed to several possible sources of error including the parameterization of soil heat flux (G) within the model, uncertainty in the value of emissivity used for the soil and vegetation canopies, and uncertainty in the canopy conductance model used to estimate vegetation transpiration.

DISCUSSION AND CONCLUSIONS

A modeling strategy was tested using a two-layer energy balance model in association with remotely sensed data to estimate fluxes of latent and sensible heat over an area characterized by fractional canopy cover. Model performance using the high resolution remote sensor data collected over individual surface flux sites was quite poor, especially with respect to H. At the same time, model simulations using area-averaged input data reproduced observed site-wide mean fluxes with excellent accuracy. On initial inspection, these results appear to be contradictory. However, examination of the scaling properties of the model, in combination with a mismatch in the resolution of the NS001 instrument relative to the length scales over which surface flux measurements are integrated by the atmosphere, suggest that this apparent contradiction is produced observational effects rather than by model mis-specification [9].

Results from this work support the use of radiometric surface temperature in association with two layer energy balance models to estimate land surface fluxes over areas characterized by incomplete canopy covers. Previous results from FIFE using less sophisticated single layer models have suggested that the use of Ts introduces substantial error to estimates of land surface fluxes in general, and H in particular [2]. The basis for this conclusion is mainly attributed to the fact that Ts is a poor surrogate for aerodynamic surface temperature over regions with sparse canopy cover, and also because of difficulties in estimating the aerodynamic resistance to heat transfer over such surfaces. For single layer models, both of these criticisms are valid. However, the results from this work and from previous tests of the model used here [7] suggest that both of these limitations are resolved by the use of a two layer model.

REFERENCES

[1] Kustas, W.P. (1995). Recent advances assocaited with large scale field experiments in hydrology, *Reviews of Geophysics*, supplement, 959-965.

[2] Hall.F.G., Huemmrich.K.F., Goetz.S.J., Sellers.P.J., Nickeson.J.E., (1992). Satellite remote sensing of surface energy balance: success, failures, and unresloved issues in FIFE, *Journal of Geophysical Research*, 97, D17, 19061-19089.

[3] Kustas.W.P., Jackson.R.D., Asrar.G. (1989). Estimating surface energy balance components from remotely sensed data, *Theory and Applications of Optical Remote Sensing*, G. Asrar (Ed), 604-627, John Wiley and Sons, New York.

[4] Friedl.M.A. and Davis.F.W. (1994). Sources of variation in radiometric surface temperature over a tallgrass prairie, *Remote Sensing of Environment*, 48, 1-17.

[5] Choudhury.B.J., and Monteith.J.L. (1988). A four-layer model for the heat budget of homogeneous land surfaces, *Quarterly Journal of the Royal Meteorological Society*, 114, 373-398.

[6] Choudhury.B.J. (1989). Estimating evaporation and carbon assimilation using infrared temperature data: vistas in modeling. *Theory and Applications of Remote Sensing*, G. Asrar (Ed), 628-690, John Wiley and Sons, New York.

[7] Friedl, M.A. (1995). Modeling land surface fluxes using a sparse canopy model, *Journal of Geophysical Research*, 100, D12, 25-435-25,446.

[8] Verhoef, W. (1984). Light scattering by leaf layers with application to canopy reflectance modeling: The Sail model, *Remote Sensing of Environment*, 16, 125-141.

[9] Friedl, M.A. (1996). Relationships among remotely sensed data, surface energy balance and area-averaged fluxes over partially vegetated land surfaces, accepted pending revisions *Journal of Applied Meteorology*.

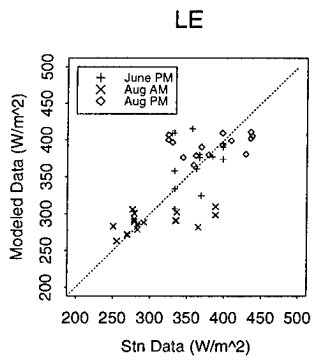


Figure 1: Modeled vs Observed LE from NS001 Data

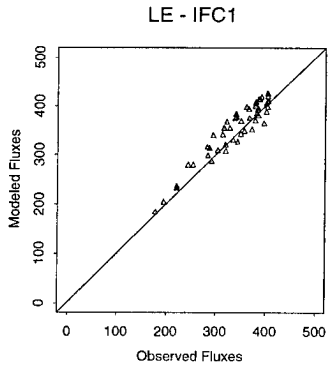


Figure 2: Site-Wide Average Modeled vs Observed LE

A ONE-DIMENSIONAL HYDROLOGY/RADIOBRIGHTNESS MODEL FOR FREEZING/THAWING SOILS

Yuei-An Liou and A. W. England

Department of Electrical Engineering and Computer Science,

and Department of Atmospheric, Oceanic and Space Sciences

The University of Michigan, Ann Arbor, Michigan 48109-2122, USA

Telephone: +1-313-763-8162, Facsimile: +1-313-747-2106

Email: yueian@eecs.umich.edu and england@eecs.umich.edu

ABSTRACT

Soil temperature and moisture profiles play a crucial role in governing energy and moisture fluxes between bare soils and the atmosphere. These profiles also co-determine radiobrightness so that the difference between model-predicted and observed radiobrightness becomes a measure of error in a model's estimate of temperature or moisture. In this paper, we present a physically based, coupled moisture and temperature, one-dimensional Hydrology/Radiobrightness (1dH/R) model for bare soil that is subject to freezing and thawing. We use this model to predict thermal, hydrologic, and radiobrightness signatures for a three-month simulation period in fall/winter on the northern Great Plains as part of an investigation of the influence of water transport on these signatures. Given a typical initial moisture content of 38%, we find that the difference in surface liquid water content between water transport and no water transport cases grows to 19% during the three-month period, and that the difference in surface ice content reaches 21% over the same period. The diurnal radiobrightness variation differs between the two cases by as much as 37 Kelvins.

INTRODUCTION

Surface temperature and moisture content/state are key parameters in partitioning observed radiant heat into sensible and latent heat transfer at the land-air interface, and they also govern the thermal microwave emission, or the radiobrightness, especially of bare or sparsely vegetated soil. The connection between radiobrightness and soil moisture is the basis of efforts to assimilate radiobrightness as a means for improving model estimates of stored water, i.e., the water that is available for evaporation or transpiration ([1]-[4]).

Mahfouf [5] has demonstrated that a surface transfer model can be used to estimate stored water from the history of screen-level temperature and humidity. This is further supported by Bouttier et al [6] using the sequential assimilation scheme, and implemented in a mesoscale model [7]. Therefore, it should be possible to predict stored soil moisture by forcing a one-dimensional Hydrologic model (1dH) with atmospheric model estimates of screen level temperature and humidity and by assimilating radiobrightness data. We first developed a one-dimensional Hydrology/Radiobrightness model (1dHu/R) with coupled heat and moisture transport for unfrozen soils [8]. This model demonstrated that water movement in unfrozen soils strongly modifies the radiobrightness signatures of bare soils. However, the 1dHu/R model could not be applied to freezing soils [9].

In this paper, we discuss the influence of water transport upon soil temperature, moisture, and radiobrightness during a 90-day simulation of dry-down in fall/winter at northern latitudes. For these simulations, we ignored hysteresis in soil processes and frost heaving.

MODEL DESCRIPTION

The 1dH model is based upon the Philip and de Vries theory ([10], [11]) except that we also account for ice in the soil. The initial profiles of temperature and moisture content/state within the soil and energy flux at depth are from our annual thermal model [12]. The Newton-Raphson method is used to match heat and moisture fluxes at the land-air interface for the unfrozen ground [13], while only the heat flux is matched for the frozen ground because unfrozen water content is defined by the temperature-suction relation. The liquid water content below the freezing depression point is found by iteratively solving the water-retention model of Rossi and Nimmo [14] and the temperature-suction relation by Williams [15].

Energy and moisture transport in soil are from conservation of heat and moisture, i.e.,

$$\frac{\partial X_{\mathrm{m}}}{\partial t} = -\nabla \cdot \vec{q_{\mathrm{m}}} \quad (1)$$

$$\frac{\partial X_{\mathrm{h}}}{\partial t} = -\nabla \cdot \vec{q_{\mathrm{h}}}, \quad (2)$$

where X_{m} is the total moisture per unit volume, kg/m^3, X_{h} is the total heat content per unit volume, J/m^3, t is the time, s, $\vec{q_{\mathrm{m}}}$ is the vector moisture (vapor and liquid) flux density, kg/m^2-s, $\vec{q_{\mathrm{h}}}$ is the vector heat flux density, J/m^2-s. The expressions for X_{m}, X_{h}, $\vec{q_{\mathrm{m}}}$, and $\vec{q_{\mathrm{h}}}$ are described by Liou and England [16].

0-7803-3068-4/96$5.00©1996 IEEE

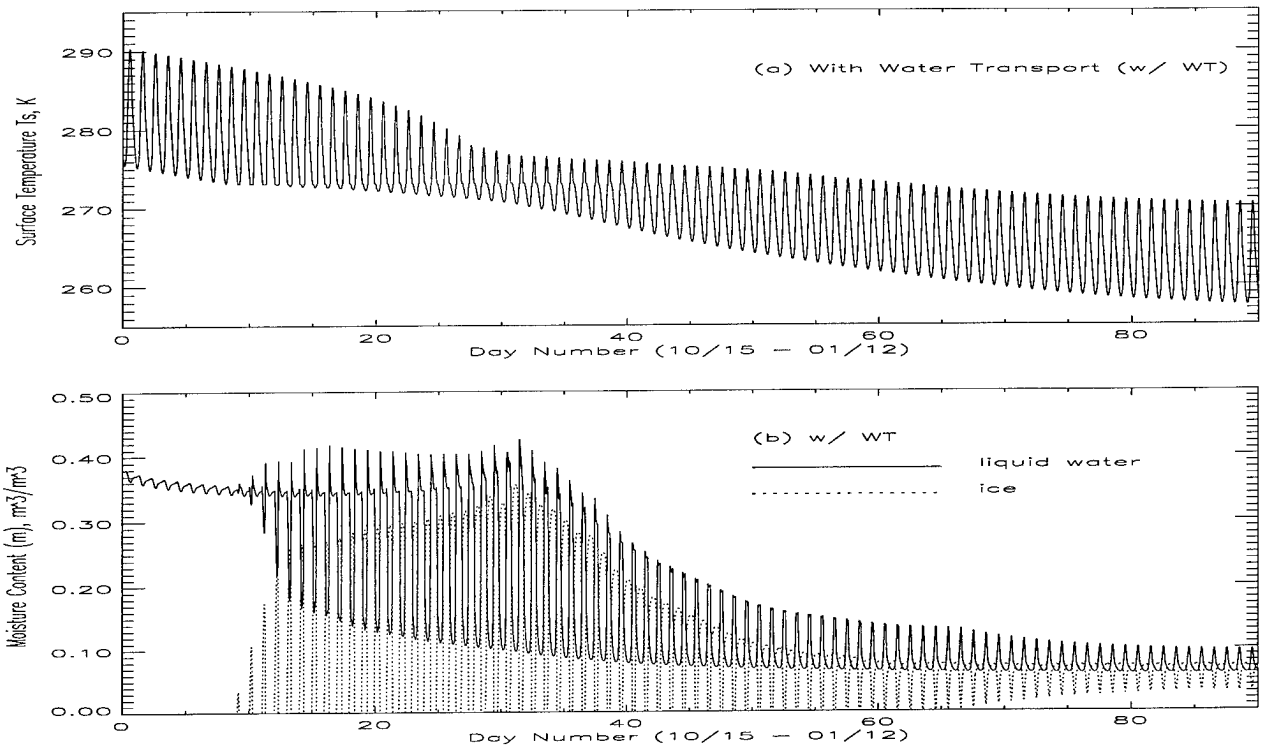


Figure 1: (a) Temperature and (b) liquid and ice contents at the surface for the water transport case. 10/15 is day 1.

Boundary conditions at the top of soil can be derived from weather and downwelling solar and long-wave radiation data, but, in this case, are provided by climatological data for the northern Great Plains during the 90 day period of interest. The lower boundary is assigned a soil depth that is significantly deeper than would be affected by typical surface forcing over a 90 day period. Below this depth, temperature and moisture are constant because the seasonal flux from the annual model is constant. Since soil properties (e.g., thermal conductivity, hydraulic conductivity, and water-retention) are strongly dependent upon temperature and moisture content/state, the governing equations are highly nonlinear. We use a finite difference scheme between soil layers that are thin at the surface but increase in thickness with depth to track temperature and moisture.

Estimates of radiobrightness are based upon a quasi-specular, microwave emission model ([17],[12],[8],[16]). This approximation is appropriate for 19.35 GHz over bare or sparsely vegetated soil, but increasingly less appropriate at 37.0 and 85.5 GHz where most soil surfaces appear increasingly rough.

RESULTS AND DISCUSSION

Figure 1 shows the surface temperature, liquid water content and ice content as a function of time for the water transport case. Temperature and moisture content/state at the surface are those of the first soil layer. Figure 1 (a) shows the 90-day dry-down simulation in fall. The diurnal temperature variation decreases with day number before day 30, but increases after that. The minimum occurs when freezing and thawing of soil moisture are most active and soil is wet (Figure 1 (b)). The amount of moisture and its transition between liquid and ice dominate apparent thermal inertia. Figure 1 (b) shows a dramatic decrease in surface liquid water as soils begin to freeze. Brief surges in daytime liquid water are associated with surface ice melting. These surges diminish with the downward penetration of the freezing front.

The 90-day, H-polarized, 19 GHz radiobrightness for the water transport case is shown in Figure 2 (a). The dependence upon liquid water is expressed as lower brightness temperatures during early, unfrozen-soil days. The difference over the 90 day period exceeds 50 Kelvins for some times-of-day. The decrease in liquid water content is about 20%. The difference in radiobrightnesses between daytime and nighttime is highly correlated with variations in the liquid water content over a diurnal cycle. The maximum diurnal variation of 57 Kelvins is seen near day 30 when surface liquid water content changes by 32% over a diurnal cycle (see Figure 1 (b)).

ACKNOWLEDGMENTS

This work has been supported by NASA grant NAGW 3430.

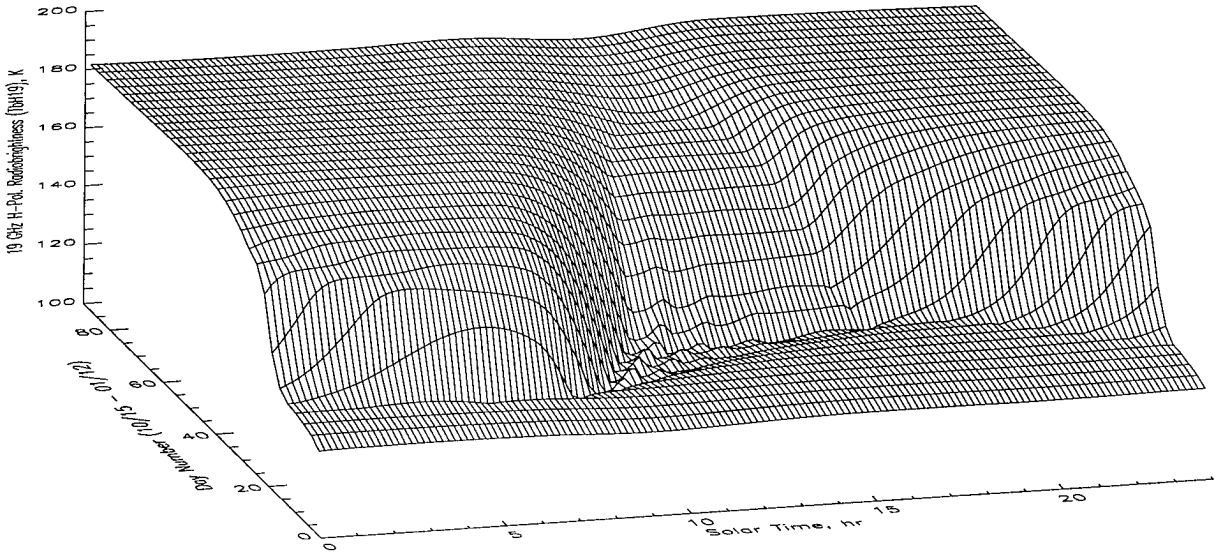


Figure 2: Radiobrightness signatures for 19 GHz horizontal polarization for the water transport case.

References

[1] Brutsaert, W., and M. Sugita, "Regional surface fluxes from satellite-derived surface temperatures (AVHRR) and radiosonde profiles," *Boundary-Layer Meteorol.*, **58**, 355–366, 1992.

[2] Huang, X., T. J. Lyons, R. C. G. Smith, J. M. Hacker, and P. Schwerdtfeger, "Estimation of surface energy balance from radiant surface temperature and NOAA AVHRR sensor reflectances over agricultural and native vegetation," *J. Appl. Meteor.*, **32**, 1441–1449, Aug. 1993.

[3] Kimura, F., and Y. Shimizu, "Estimation of sensible and latent heat fluxes from soil surface temperature using a linear air-land transfer model," *J. Appl. Meteor.*, **33**, 477–489, 1994.

[4] Gillies, R. R., and Carlson, T. N., "Thermal remote sensing of surface soil water content with partial vegetation cover for incorporation into climate models," *J. Appl. Meteor.*, **34**, 745–756, 1995.

[5] Mahfouf, J.-F., " Analysis of soil moisture from near-surface parameters: A feasibility study," *J. Appl. Meteor.*, **30**, 1534–1547, 1991.

[6] Bouttier, F., J.-F., Mahfouf, and J. Noilhan, "Sequential assimilation of soil moisture from atmospheric low–level parameters. Part I: Sensitivity and calibration studies," *J. Appl. Meteor.*, **32**, 1335–1351, Aug. 1993.

[7] Bouttier, F., J.-F., Mahfouf, and J. Noilhan, "Sequential assimilation of soil moisture from atmospheric low–level parameters. Part II: Implementation in a mesoscale model," *J. Appl. Meteor.*, **32**, 1352–1364, Aug. 1993.

[8] Liou, Y.-A., and A. W. England, "A land surface process/radiobrightness model with coupled heat and moisture transport in soil," Submitted to *IEEE Trans. Geosci. Remote Sensing*, January 1996.

[9] Galantowicz, J. F., *Microwave Radiometry of Snow-Covered Grasslands for the Estimation of Land-Atmosphere Energy and Moisture Fluxes*, Ph.D. dissertation, pp 196, 1995.

[10] Philip, J. R., and D. A. de Vries, "Moisture movement in porous materials under temperature gradients," *Trans. Am. Geophys. Union*, **38**, 222–232, Apr. 1957.

[11] de Vries, D. A., "Simultaneous transfer of heat and moisture in porous media," *Trans. Am. Geophys. Union*, **39**, 909–916, Oct. 1958.

[12] Liou, Y.-A., and A. W. England, "Annual temperature and radiobrightness signatures for bare soils," Submitted to *IEEE Trans. Geosci. Remote Sensing*, September 1995.

[13] Press, W. H., B. P. Flannery, S. A. Teukolsky, W. T. Vetterling, *Numerical Recipes (FORTRAN)*, pp. 702, Cambridge University Press, 1989.

[14] Rossi, C., and J. R. Nimmo, "Modeling of soil water retention from saturation to oven dryness," *Water Resour. Res.* , **30**, 701-708, Mar. 1994.

[15] Williams, P. J., "Experimental determination of apparent specific heats of frozen soils," *Geotechnique*, **14**, 133-142, 1964.

[16] Liou, Yuei-An, and A. W. England, "A land surface process/radiobrightness model with coupled heat and moisture transport for freezing soils," in preparation for *IEEE Trans. Geosci. Remote Sensing*, 1996.

[17] England, A. W., "Radiobrightness of diurnally heated, freezing soil," *IEEE Transactions on Geoscience and Remote Sensing*, vol. 28, pp. 464–476, July 1990.

On the Net Long-wave Radiation Determination from Satellite Data

Yong XUE, Sean P. Lawrence and David T. Llewellyn-Jones
University of Leicester

Earth Observation Science Group
Department of Physics and Astronomy
University of Leicester, Leicester, UK
Tel: +44-116-2523521, Fax: +44-116-2525262, Email: YX1@LE.AC.UK

Abstract -- This paper focuses on long-wave radiation of sea and land surfaces. SST data is from Rutherford Appleton Lab, Oxford. Land surface temperature (LST) and land surface emissivity retrieval by use of ATSR data was also discussed. In this paper two points on net longwave radiation will be addressed. The formulae used by Reed, Weare et al. and Wells and King-Hele are different from Berliant's formula, which Oberhuber used, in that surface temperature and air temperature are used differently. The surface temperature derived from satellite thermal band data is the skin temperature. Do we use skin temperature or bulk temperature as inputs to the empirical formula? One empirical formula has been proposed. Three empirical formulae were tested by using TOGA-TAO data and sea surface temperatures derived from ATSR thermal band data in Pacific ocean and by using LST from ATSR-2 thermal band data in UK.

INTRODUCTION

The Earth's surface, heated by absorbing solar radiation, is a source of emitted long-wave radiation, which heats the atmosphere. Water vapour in the atmosphere, dust, and various gases absorb long-wave radiation emitted from the Earth's surface. A great part of the emission from the Earth's surface is therefore compensated by the re-emission of counter-radiation from the atmosphere. The difference between the Earth's surface emission and the counter-radiation of the atmosphere is called the net long-wave radiation. The radiation balance (or budget) of the Earth's surface is equal to the difference between the absorbed solar radiation and the net long-wave radiation. The value of net long-wave radiation depends on air temperature, humidity, cloudiness, and the vertical gradients of temperature and moisture in the atmosphere. Since measurements of net long-wave radiation are very rare, this flux is usually computed with empirical formulas that use surface temperature and other meteorological parameters as inputs.

Berliant [1] established a theoretical dependence of clear sky net long-wave radiation upon the temperature and humidity of air using results obtained by Kondratyev [2]. Berliant's formula is corroborated well by the data of observations made at average and high humidities. Besides the temperature and humidity of the air, net long-wave radiation is considerably influenced by cloudiness and by the difference between temperatures of the surface and the air. The above formulae for calculation of net long-wave radiation relate to cases when the temperature of the Earth's surface is close to that of the lower layer of air. If these temperatures differ substantially, then the formulas must be modified to account for the effect of their difference on radiation.

EARTH SURFACE TEMPERATURE DERIVATION

As radiative heat transfer plays a significant and sometimes dominant role in the heat balance of the Earth's surface and of the lowest few metres of the atmosphere, surface radiative temperature is an important parameter in physical climatology.

The split-window technique [3,4,5,6] and the double viewing angle method [7] have been extensively studied to obtain LST. The effect of emissivity on the measurement of LST has been studied by Price [3], Becker and Li [4] and Prata [5]. Prata [8] focused on an experimental investigation aimed at establishing the validity and accuracy of the so-called split-window technique applied to the land surface by using AVHRR data.

For ATSR thermal band data, we can obtain two different channels, each with two viewing angles. The philosophy of simultaneous split-window method for Earth surface temperature determination is based on the fact that the actual Earth surface temperature are the same not only from multi-channel but also from multi-angle split-window method [9].

The formulae of multi-channel and multi-angle split-window should be chosen with caution. We used the formula from Becker and Li [4] for nadir-view ATSR data.

For two view angles at one wavelength Sobrino *et al.* [7] gave the equation which constitutes the single channel double viewing angle model for obtaining the surface temperature T_s from ATSR thermal band data, when the surface is viewed

0-7803-3068-4/96$5.00©1996 IEEE

both from nadir and at an angle (55°) close to 53° from the normal.

Based on above equations for 11μm channel and for 12μm channel, The solution of the simultaneous equations gives the surface temperature (T_s) and the surface emissivities for the 11μm channel (ε^{11}) and for the 12μm channel (ε^{12}).

PARAMETERIZATION OF LONGWAVE RADIATION

Parameterizations of longwave radiation based on surface observations have almost as long a history as the ones for shortwave radiation. Among the longwave irradiance or net irradiance formulae the following have been used frequently: Berliand M. E.[1]; Efimova N. A. (cited by Kondratyev [2] and Reed [10].

Watson [11] and Xue and Cracknell [12] used a Taylor series expansion and discarded quadratic and higher order terms to give (WXC formula)

$$R_{sky}-R_{earth} = -4\varepsilon\sigma\tau(T_s-T_{sky}), \quad (1)$$

where ε is the mean emissivity (spectral average) of the surface, T_{sky} and τ are function of T_a.

The O formula which Oberhuber [13] used is taken from Berliand [1]. For cloudless sky it is given by

$$Q_{Io}=\varepsilon\sigma T_A^4(0.39-0.05\sqrt{e(T_A)/100}) + 4\varepsilon\sigma T_A^3(T_s-T_A), \quad (2)$$

where ε is the emissivity of the sea surface, σ is the Stefan-Boltzman constant and $e(T_A)$ is the vapour pressure (mb) of the air at a height of 10 meter. $e(T_A)$ is obtained from the specification of T_A and relative humidity, r. Oberhuber [13] used another express for $e(T_A)$, which is

$$e(T_A)=611\times10^{7.5(T_A-273.16)/(T_A-35.86)}, \quad (3)$$

Following Reed [10], Wells and King-Hele [14] and Wear *et al.* [14] (RWWK formula), the net longwave radiation for clear skies, Q_{Io}, is parameterized by

$$Q_{Io}=\varepsilon\sigma T_s^4(0.39-0.05\sqrt{e(T_A)}) + \varepsilon\sigma T_s^3(T_s-T_A). \quad (4)$$

To take into account the effect of cloud on the net upward longwave radiation, Eq. (3) was modified following Wells and King-Hele [14] and Weare *et al.* [15]: $Q_I = Q_{Io}(1-B\cdot C)$, where C is the fractional cloud cover and B is a factor that depends on cloud type. Here a constant values of 0.53 was assumed from the product (B·C). This was obtained by averaging the cloud factor, from Weare *et al.* [15], over the tropical Pacific 20°N to 20°S.

TESTS AND RESULTS

The date and time of the ATSR data were 2nd August 1995 and 11:00 GMT. The gridded SST data are from RAL, Oxford. The emissivity of sea surface is assumed unity. Fig. 1 shows the LST calculated from simultaneous split-window methods. The 1995 is the hottest year since first global temperature recording in 1860 from the Meterological Office, UK. The sunny and exceptionally hot weather which began at the end of July lasted through the first three days of August with the temperature exceeding 33°C (306 degK) daily at several places [16]. The surface temperature determined from satellite data is the instantaneous effective surface temperature. The net longwave radiation calculated from the formulae of Oberhuber [13], Wells and King-Hele [14] and Wear *et al.* [15] and Watson [11] and Xue and Cracknell [12] were referred as O formula, RWWK formula and WXC formula. The results from O formula and WXC formula are agreement with each other in land. RWWK formula gives lower values in land areas but the values for sea agree with other two formulae. O formula gives lower values for sea areas than that from other formulae. Cloudy areas were not calculated.

Fig. 2 shows the monthly averaged net longwave radiation difference by using RWWK formula with ATSR SST and TOGA SST (1m depth) of April in 1993. We can see that the absolute differences are small, but the relative differences are

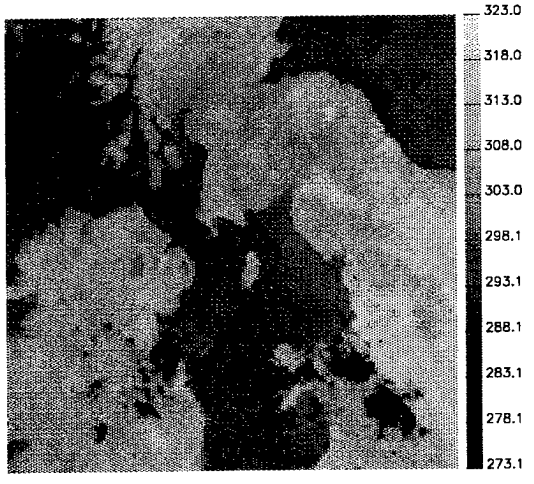


Fig. 1 The Earth surface temperature from ATSR thermal band data (Aug. 2, 1995). The unit is degK.

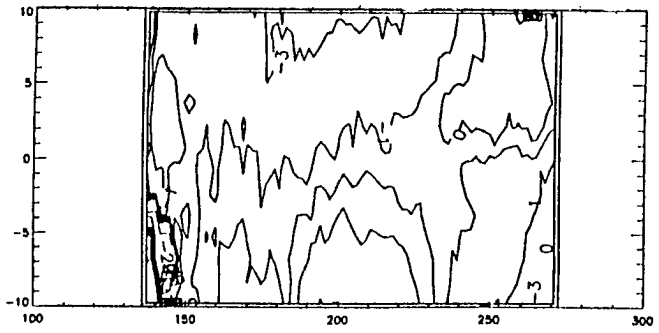


Fig. 2 Monthly aveaged net long-wave radiation by using ATSR SST and TOGA-TOA SST (04/1993). The unit is W/m^2.

up to 10% big because of the net longwave radiation is about 30 to 40 W/m^2 [15].

CONCLUSIONS

The exchange of energy and mass between the atmosphere and the biosphere has become a research topic of increasing importance in recent years. The important parameter, surface temperature (LST and SST), is presented in formulae to calculate the heat flux. ATSR thermal band data can be used to derive the LST and SST so that to calculate the net longwave radiation. The different of net longwave heat fluxes for use of TOGA-TAO SST and skin SST from ATSR can be used to develop a scheme, which will relate skin SST to ocean GCM. We have in hand some research work on this and expect to publish the results in due course.

ACKNOWLEDGEMENT

The authors thank the TOGA-TAO Project Office, Dr M. J. McPhaden, Director, for supplying the TOGA TAO data and the RAL, Oxford the ATSR data.

REFERENCES

[1] T. Berliand, "Methods of climatological computation of total incoming solar radiation," Meteorol. Gidrol., 5, 9-12. MGA 12:1486, 1960.

[2] K. Ya Kondratyev, Radiation in the Atmosphere, New York: Academic Press, 1969.

[3] J. C. Price, "Land surface temperature measurements from the split window channels of the NOAA-7 Advanced Very High Resolution Radiometer," J. Geophys. Res., Vol. 89, pp. 7231-7237, 1984.

[4] F. Becker, and Z. -L. Li, "Towards a local split window method over land surfaces," Inter. J. Remote Sensing, Vol. 11, pp. 369-393, 1990.

[5] J. A. Sobrino, C. Coll, and V. Caselles, "Atmospheric correction for land surface temperature using NOAA-11 AVHRR channel 4 and 5," Remote Sensing of Environment, Vol. 38, pp. 19-34, 1991.

[6] A. J. Prata, "Land surface temperatures derived from the advanced very high resolution radiometer and the along-track scanning radiometer 1. Theory," J. Geophys. Res., Vol. 98, pp. 16,689-16,702, 1993.

[7] J. A. Sobrino, Z. -L. Li, M. P. Stoll and F. Becker, "Determination of the surface temperature from ATSR data," In Proceedings of 25th International Symposium on Remote Sensing of Environment held in Graz, Austria, on 4th-8th April, 1993, pp II-19-II-109, ERIM, Ann Arbor, 1993.

[8] A. J. Prata, "Land surface temperatures derived from the advanced very high resolution radiameter and the along-track scanning radiometer 2. Experimental results and validation of AVHRR algorithms," J. Geophys. Res., Vol. 99, pp. 13,025-13,058, 1994.

[9] Y. Xue, and A. P. Cracknell, "The earth's surface temperature derivation from satellite data and its prediction by using a second-order approximation thermal inertia model (SoA-TI Model)," In The Determination of Geophysical Parameters from Space, Proceedings of the 43th Scottish Universities Summer School in Physics, N. E. Fancey, ed. 1996, In press.

[10] R. K. Eeed, "On Estimation of Net Long-Wave Radiation from the Oceans," J. Geophys. Res., Vol. 81, pp. 5793-5794, 1976.

[11] K. Watson, "Geological application of thermal infrared images," Proc. of the IEEE, Vol. 63, pp. 128-137, 1975.

[12] Y. Xue, and A. P. Cracknell, "Advanced Thermal Inertia Modelling," Inter. J. Remote Sensing, Vol. 16, pp. 431-446, 1995.

[13] J. M. Oberhuber, An atlas based on the COADS data set: the budgets of heat, buoyancy and turbulent kinetic energy at the surface of global ocean. Max-Planck-Institut für Meteorologie, Report No. 15, 1988.

[14] N. C. Wells and S. King-Hele, "Parameterization of tropical ocean heat flux," Quarterly Journal of Royal Meteorological Society, Vol. 116, pp. 1213-1224, 1990.

[15] B. C. Weare, P. T. Strub and M. D. Samuel, "Annual mean surface heat fluxes in the tropical pacific ocean," J. Phys. Ocenogr., Vol. 11, pp. 705-717, 1981.
[16] P. Eden, "Hot, dry, and sunny - a record-breaking month. Weather Log, August, 1995.

Landsat 7 System Design Overview

Jim Andary and Pete Spidaliere
NASA/Goddard Space Flight Center
Steve Jurczyk
NASA/Langley Research Center
Terry Arvidson
Lockheed Martin Corporation
NASA/GSFC, Code 430, Greenbelt, MD 20771
Telephone: (301) 286-7167/Facsimile: (301) 286-1744/
Email: steve _jurczyk@ccmail.gsfc.nasa.gov

Abstract -- This paper describes the overall Landsat 7 System design, the design of selected System segments, and nominal operation of the System. The Landsat 7 System consists of four segments, Satellite Segment, Flight Operations Segment, Ground Data Handling Segment, and Launch Segment. The discussion will focus on the design of the Satellite Segment which includes the spacecraft and instrument, and the Ground Data Handling Segment which includes the image processing and image assessment systems. Emphasis is given to design changes made to the spacecraft and instrument for the Landsat 7 mission to enhance performance and improve mission reliability. The Ground Data Handling System discussion provides a high level overview of the Landsat Processing System and Image Assessment System designs and their role in the overall system. This paper also describes the interfaces between the System elements and their interaction during nominal operations.

INTRODUCTION

In 1994 Landsat was made a part of NASA's Mission to Planet Earth, managed by the Goddard Space Flight Center in Greenbelt, MD. This is one of NASA's high priority programs to help further the understanding of the Earth system. The Landsat 7 satellite is planned to be launched in May 1998 on a Delta II launch vehicle into a 705 km, sun-synchronous orbit with a 10:00 am nodal crossing time. The primary objective of the Landsat 7 program is to maintain data continuity beyond Landsats 4 and 5, thereby providing users with data and data products sufficiently consistent with previous Landsat data to allow comparisons for global and regional change detection and characterization. It is a joint program among three government agencies: the National Aeronautics and Space Administration (NASA) for the development of the satellite and the Enhanced Thematic Mapper Plus (ETM+) instrument, launch and on-orbit checkout of the satellite; the National Oceanic and Atmospheric Administration (NOAA) for the operations of the satellite; and the U.S. Geological Survey (USGS) for data archive and distribution through the Earth Observing System Data and Information System (EOSDIS) Distributed Active Archive Center (DAAC) at the Earth Resources Observation System Data Center (EDC) in Sioux Falls, SD.

Another major program objective is to generate and periodically refresh the global archive with substantially cloud-free, sun-lit land mass scenes and to ensure that unenhanced data are available to all users at the cost of fulfilling user requests (COFUR). The Landsat 7 system is required to receive, capture, process to Level 0R, and archive the equivalent of 250 ETM+ scenes per day and generate up to 100 Level 0R ETM+ scenes per day for distribution to users. Level 0R data is reformatted but unrectified instrument data with appended spacecraft attitude and ephemeris data, radiometric calibration data and quality data.

SATELLITE SEGMENT

Spacecraft Design

The Landsat 7 spacecraft provides all of the necessary support for the ETM+ instrument. The spacecraft provides a stable pointing platform, electrical power, command and telemetry functions, wideband data storage and downlink, mechanical support, and limited thermal control. The Attitude Control Subsystem (ACS) provides 120 arcsec (3 sigma) attitude control and 135 arcsec (3 sigma) attitude knowledge in the precision pointing mode. The ACS design uses an Inertial Measurement Unit, a celestial Star Assembly, three-axis Magnetometers, and an uplinked ephemeris as sensor inputs and Reaction Wheel Assemblies and Magnetic Torque Rods as effectors. Thrusters are also available for momentum unloading if required. The Communications (COMM) subsystem supports S-Band uplink of commands and downlink of telemetry via ground stations and TDRSS. The Command and Data Handling (C&DH) subsystem accepts real-time, stored, and hardware commands from the S-band COMM subsystem. Hardware commands bypass software for immediate execution. The Landsat 7 Flight Software is written in JOVIAL and makes extensive reuse of Landsat 6 code. Telemetry is collected by the C&DH subsystem from the various sensors, effectors, and the ETM+ for downlink via the S-band COMM system. Wideband data from the ETM+ can be stored onboard in a 378 Gbit Solid State Recorder at a rate of 150 Mbps. The data can also be downlinked through any and all of the three X-band Antennas, which can be independently targeted to separate ground stations. Real-time wideband data and recorded data can be transmitted simultaneously. Thermal control support to the ETM+ is limited to keeping the Spacecraft and ETM+ thermally isolated.

0-7803-3068-4/96$5.00©1996 IEEE

Although Landsat 7 makes extensive use of the previous Landsat 6 design, some significant improvements have been made. One of these is the addition of a Sun Pointing Safe Hold (SPSH) mode, which uses Coarse Sun Sensors on the Solar Array and on the body to maintain the Sun roughly perpendicular to the Solar Array. This mode is implemented in software and is maintained in volatile and in non-volatile memory. Also, the Failure Detection and Correction (FDAC) system was significantly enhanced. The Failure Detection portion of the system monitors hardware that can place the satellite in an unsafe state and hardware that is required for maintaining a safe state, and identifies any failures. Given sufficient persistence of a detected failure, the system will take corrective actions, such as switching component sides or placing the satellite in a different state. A data or clock bus failure could result in many components appearing to fail which have not; a software monitor checks for such conditions and isolates the failure to higher level bus components. This avoids unnecessary and possibly unsafe switching to components that may no longer function.

Instrument Design

The Enhanced Thematic Mapper Plus (ETM+) is a derivative of the Thematic Mappers developed for Landsats 4 and 5 and the Enhanced Thematic Mapper for Landsat 6. The ETM+ is a nadir-viewing, multispectral, cross-track scanning radiometer capable of providing high resolution imagery of the Earth's surface. It is designed to collect, filter, and detect radiation from the Earth in a 185 km wide swath. Like previous Landsat instruments, the ETM+ employs a Scan Line Corrector to remove the underlap/overlap in scan lines resulting from the scanning and orbital motions.

The ETM+ has four spectral bands in the visible/very near infrared (VNIR) and one Panchromatic (PAN) band using a newly developed monolithic silicon detector array on the prime or warm focal plane. On the cold focal plane there are two short wave infrared (SWIR) bands using InSb detectors and a long wave infrared (LWIR) or thermal band using photoconductive HgCdTe detectors. The VNIR and SWIR bands employ staggered detector arrays of 16 elements mounted along track, each element having a "footprint" of 30m on the ground. The eight elements of the LWIR array each have a 60 m footprint which is a 2x improvement over previous Landsats. The PAN band which has not flown on previous missions consists of a staggered array of thirty two elements, each having a 15 m footprint.

Detected signals are passed through an analog amplifier chain, a multiplexer (which includes analog multiplexing, A/D conversion, and digital multiplexing), and finally to an output formatter. The output formatter generates an error detection and correction code, formats the data according to Consultative Committee on Space Data Systems (CCSDS) recommendations, and provides the data on two 75 Mbps channels. One channel contains format 1 data: bands 1-6; the other contains format 2 data: bands 6, 7 and 8 (Pan). All detector channels are available from one multiplexer on the two output channels. Band 6 is present in both formats.

The sensor will be calibrated on-orbit using the On-Board Calibrator assembly which presents a lamp and a blackbody source to the detector arrays to calibrate the reflective and thermal bands respectively at the end of each scan. The ETM+ also contains two new solar calibrators. A partial aperture calibrator relays an image of the Sun into the sensor aperture once per orbit approximately at spacecraft sunrise. A full aperture calibrator will be deployed approximately once per month to fill the entire sensor field-of-view with diffuse solar radiation. The ETM+ will also be calibrated through ground truth methods. The IAS will combine data from these four calibration methods to generate optimal calibration coefficients to meet a requirement for 5% overall radiometric accuracy, a 2-3 times improvement over previous Landsats.

GROUND DATA HANDLING SEGMENT

The Landsat 7 data throughput requirements are met by a ground data capture and processing system that is located at the EDC. The Landsat Ground Station (LGS), using a 10 meter antenna, receives the two 150 Mbps data streams from the satellite as it passes over the EDC site five or six times each day. This data is captured by the Landsat Processing System (LPS) and fed in a pipeline fashion through the LPS computers to produce the Level 0R data, the metadata and the browse data which is then sent to the DAAC for archiving and distribution to the users. Data quality checks and cloud cover assessments are also performed by the LPS.

Outside of the main data processing stream at EDC is a fourth element of the Landsat ground system, the Image Assessment System (IAS), responsible for processing selected scenes to Level 1 as a check on the quality of the image data archived in the DAAC. The IAS is also responsible for determining the radiometric calibration coefficients which are archived with the image data. Level 1 is geometrically and radiometrically corrected Level 0R data.

Landsat Processing System

The LPS receives wideband data, processes it to Level 0R, and makes it available to the EDC-DAAC for archive and distribution. The LPS front end captures and stores raw wideband data from the LGS at the real-time rate of 75 Mbps per channel, using a NASA I/O card with receive/playback capability of 82/80 Mbps and two Redundant Array of Inexpensive Devices (RAID) storage devices. There are five LPS processing strings, each processing a 75 Mbps channel. Four strings are nominally active, with the fifth used for test and maintenance. Each string ingests data from the front end at one-tenth real-time rate.

The first steps in Level 0R processing are CCSDS processing and error detection and correction, utilizing CRC, Reed-Solomon and Bose-Chaudhuri-Hocquenghem (BCH) codes. Next, ETM+ major frames are assembled and data subintervals are determined. A subinterval is a subset of data with continuous, contiguous timecode and becomes the data granule. Extraction of calibration and Mirror Scan Correction

Data (MSCD) from the major frames for each scan line and accumulation of Payload Correction Data (PCD) is performed. The bands are deinterleaved and reversed; forward and reverse scans are aligned, using integer pixel offsets provided by the IAS. The PCD data is assembled into cycles and scene identification is performed. The scene center location is determined, within an accuracy of 22 meters, and the corner points are calculated. These data, along with data quality statistics, are assembled into a metadata file that will accompany the Level 0R product.

The image data is aggregated into band files and a browse file is generated for format 1 data (bands 1-6). The format 1 data is copied and radiometrically corrected prior to cloud cover assessment. A new algorithm for automated cloud cover assessment has been developed for Landsat 7; it improves performance over previous algorithms for almost all cloud and land cover types. The final Level 0R product is assembled and made available for transfer to the EDC-DAAC. The product comprises: 9 band files (band 6 from both format 1 and 2); PCD, MSCD, and calibration data files for each format; browse image file (format 1 only); and a metadata file. The metadata references the calibration parameters file that is applicable to the product and will be sent out with all product orders by the EDC-DAAC.

Image Assessment System

The primary purpose of the IAS is to calibrate Landsat 7 radiometry and geometry. The IAS will develop and provide radiometric and geometric processing parameters to the LPS, to the International Ground Stations (IGSs) via the Mission Operations Center, and to customers via the EDC-DAAC. The IAS will also assess the quality of Level 0R data products on a sparse sample basis and evaluate/monitor image-related System performance.

To accomplish the above the IAS will request Level 0R data from the EDC-DAAC as would any user. Using the same processing parameters as those distributed to the customers, the IAS will process at least one scene per day to produce radiometrically and geometrically corrected, or Level 1G, data products. The IAS will perform System characterization using the Level 1G product. For example, as part of the radiometric characterization the IAS will establish instrument quality by determining key parameters such as correlated noise and modulation transfer function, and will determine image quality by analyzing signal-to-noise ratios and identifying image artifacts such as striping and banding, as well as other image quality factors.

The IAS will use this data to analyze and trend System performance. If the IAS detects a significant change in System performance, it will report its findings to other System elements and may update the processing parameters provided to users. During the 5 year Landsat 7 mission the IAS will periodically update these parameters to provide users with the best possible information to perform image processing.

SYSTEM INTERFACES AND OPERATIONAL CONCEPT

All of the wideband data handling facilities are located at the EDC. The timeline requirement, from data receipt at the LGS to product availability in the archive, is 32 hours. The Landsat 7 wideband data is downlinked on X-band, either in real-time or from the onboard solid state recorder, to the LGS. In the future additional X-band stations may be added to the program. The data is also downlinked in real-time to the IGSs, most of which participated in previous Landsat programs. Data downlinked to the LGS is sent bent-pipe to the LPS which processes the data as described above. Once the Level 0R product is available, the EDC-DAAC retrieves the data from the LPS, archives it and distributes it in response to user orders. Queries and requests for browse data are supported free of charge for any user; Level 0R product orders are accepted from any user and are billed at COFUR.

Scheduling of ETM+ acquisitions is based on a Long Term Plan developed prelaunch by the Science Office to maximize the global archive refresh mission while incorporating known science community requirements. Cloud cover forecasts are used during the scheduling process to prioritize acquisitions over substantially cloud-free land mass. Some special requests, primarily for environmental and national emergencies, will be incorporated into the scheduling as required. Plans are in process to define a mechanism for accepting individual user requests and incorporating them into the scheduling process as best we can. As the Long Term Plan includes continuous refresh of scenes over the 48 contiguous states and Alaska, these individual user requests are expected to be for non-U.S. land masses.

SUMMARY

The Landsat 7 program bridges the gap between the Landsat 4/5 system and the next generation of land imaging systems. Currently, the design of the Landsat 7 spacecraft and instrument is complete and both are in the manufacturing process. The ETM+ will be delivered in November 1996 for integration with the spacecraft. The Ground System goes to Critical Design Review in April 1996 and starts development and test after approval of the system detail designs. The Long Term Plan is in development and will be out for review in 1997.

ACKNOWLEDGMENTS

We credit the hard work of the Landsat Project and Science Office teams and their contractors in the successful design and implementation of the Landat 7 System.

REFERENCES

[1] National Aeronautics and Space Administration (NASA), Goddard Space Flight Center (GSFC), Landsat 7 System Specification, 430-11-06-011, Rev. F, October 1995.

Landsat 7 and Beyond

James R. Irons, Darrel L. Williams, and Brian L. Markham
Biospheric Sciences Branch
Code 923
NASA/Goddard Space Flight Center
Greenbelt, Maryland 20771
USA
Telephone: 301-286-8978, 301-286-8860, 301-286-5240
Facsimile: 301-286-0239
Email: jim_irons@gsfc.nasa.gov, darrel@ltpmail.gsfc.nasa.gov, markham@highwire.gsfc.nasa.gov,

Abstract -- NASA's Mission to Planet Earth program has recently adopted the Landsat program as an explicit component of the Earth Observing System. This official recognition of the Landsat role has led NASA to consider steps to more fully integrated Landsat 7 and follow-on Landsat instruments into the operational strategy and technical design of the Earth Observing System. These steps include plans to fly the Landsat 7 satellite in formation with the EOS AM1 platform and the development of concepts for an advanced technology Landsat instrument aboard the EOS AM2 platform. Also under review is the early flight of an Earth-observing instrument employing high-risk technologies aboard a NASA New Millennium spacecraft. This presentation will discuss Mission to Planet Earth requirements for future Landsat missions and the efforts to fully incorporate Landsat into the Earth Observing System. With these efforts, the May 1998 launch of Landsat 7 will lead to more comprehensive and insightful observations of global land surfaces.

INTRODUCTION

The Land Remote Sensing Policy Act of 1992 (P.L. 102-555) provided the U.S. Government with guidelines for the development of Landsat 7 and follow-on land remote sensing missions. Following this act, a 1994 Presidential Directive from the National Science and Technology Council (Landsat Remote Sensing Strategy; PDD/NSTC-3) established the current government management strategy for the Landsat program. The directive gave the National Aeronautic and Space Administration (NASA) responsibility for Landsat program development while assigning the National Oceanic and Atmospheric Administration (NOAA) the task of post-launch Landsat 7 operations and the U.S. Geological Survey (USGS) the job of Landsat 7 data archival and distribution. Given the responsibility for building and launching Landsat 7, the NASA Mission to Planet Earth Office explicitly adopted the Landsat program as an integral component of its Earth Observing System (EOS). This paper discusses recent efforts to more fully incorporate the Landsat program into the EOS while following the guidelines of P.L. 102-555 for the development of Landsat 7 and follow-on systems.

0-7803-3068-4/96$5.00©1996 IEEE

LANDSAT MISSION OBJECTIVES

The mission objectives for Landsat 7 and follow-on system concepts now derive from several sources. First, P.L. 102-555 mandates specific goals with guidelines for meeting the goals. In particular, the law states that "the fundamental goal of the Landsat Program Management is the continuity of unenhanced Landsat data." The law defines continuity as data that are "sufficiently consistent (in terms of acquisition geometry, coverage characteristics, and spectral characteristics) with previous Landsat data to allow comparisons for global and regional change detection and characterization." Second, as a component of the EOS, mission objectives must lead to a vital role for Landsat within the larger system. Finally, the 24-year heritage of the program has created a broad and diverse constituency of users applying Landsat data to a wide spectrum of tasks. This constituency encompasses the commercial, academic, government agency (federal, state, and local), national security and international communities. The future data needs of this established constituency also drive the mission objectives. Their needs are entirely consistent with the goals of the public law and the role of Landsat within the EOS.

Landsat 7 and follow-on systems must achieve the following mission objectives to satisfy the public law, to fulfill a vital role in the EOS, and to meet the data requirements of the user community.

1) The Landsat program must afford synoptic and repetitive coverage of the Earth's continental surfaces at a high spatial resolution. Many important land cover characteristics, changes, and processes originate and progress at scales requiring spatial resolution on the order of 30 m for detection and monitoring. Deforestation serves as just one prominent example of such land processes. People will continue to need Landsat data to detect and track seasonal and episodic changes in land cover, land use, and land processes. Other EOS sensors will afford more frequent, up to daily, global coverage but only at coarse spatial resolutions. Landsat sensors must complement the other EOS sensors by providing less frequent, seasonal, global coverage at a higher spatial resolution.

2) Landsat 7 and follow-on missions must provide spectral coverage of the visible, near infrared, and shortwave infrared regions. The heritage Thematic Mapper (TM) spectral bands cover this spectral range and each band has its important applications. The rationale for selecting these bands has proven sound over the last 12 years of TM data collection from Landsat 4 and 5. Landsat sensors must cover the spectral region to ensure continuity, meet current and future user requirements, and advance the applications of Landsat data.

3) Landsat 7 and follow-on missions must afford calibration of absolute radiometry and of image geometry. People now commonly use Landsat data together with other types of geographic data, including data from other spaceborne sensors, and compare current data with historic Landsat data. Geometry must be calibrated to register Landsat digital image data to cartographic bases and incorporate the data into geographic information systems. Radiometry must be calibrated to afford meaningful comparisons to data from other sensors, to allow more effective comparisons to historic data for change detection and characterization, and to permit atmospheric corrections.

4) Landsat 7 and follow-on missions must be integrated into the EOS. The design and operations of the Landsat sensors must complement the other EOS sensors and promote the synergistic use of data from all the sensors. The NASA Mission to Planet Earth program cannot afford or justify a Landsat system that is not fully incorporated into the broader EOS.

LANDSAT 7 AND THE EOS

NASA has recently taken or has under consideration several actions to more fully integrate Landsat 7 into the EOS. First, a recent NASA research announcement (NRA-95-MTPE-03) called, in part, for proposals for members of a Landsat Instrument Team. The intent is to form a team analogous to the instrument teams supporting the development of the other EOS sensors. The announcement solicited team-member proposals to "apply Landsat data to the understanding of the Earth as a complex, coupled, interactive system and to the understanding and monitoring of global change." Proposals were due on December 01, 1995, and following peer review, NASA hopes to announce team selections by May or June 1996. The team is expected to advance the scientific integration of Landsat 7 ETM+ data with data from the other EOS sensors.

A second action under consideration involves flying Landsat 7 in an orbit closely coupled to the EOS-AM1 orbit. Both satellites will carry sensors designed for land imaging and both satellites are on schedule for 1998 launches into similar orbits. Both orbits will be circular, sun-synchronous, and near-polar with altitudes of 705 km and inclination angles of 98°. The satellites will both fly over the sunlit portion of the Earth during the descending (north-to-south) nodes of their orbits and both satellites will cross the equator in mid-morning. The idea under study calls for the EOS-AM1 platform to follow the ground track of Landsat 7 with a delay of 15 to 30 min. Landsat 7 would pass over the equator at approximately 10:00 a.m. local solar time with EOS-AM1 crossing at the same point between 10:15 and 10:30 a.m. This coordination would allow near-coincident observations of land surfaces with the high resolution Landsat 7 Enhanced Thematic Mapper-Plus (ETM+) and the MODIS (Moderate Resolution Imaging Spectrometer), MISR (Multi-angle Imaging SpectroRadiometer), CERES (Clouds and Earth's Radiant Energy System), and ASTER (Advanced Spaceborne Thermal Emission and Reflection Radiometer) imaging sensors aboard EOS-AM1. These near-coincident observations would promote synergistic applications of data from the two satellites.

FOLLOW-ON LANDSAT SENSOR DESIGN CONCEPTS

The Landsat 7 ETM+ will be the last Landsat sensor based on the TM multispectral scanner design heritage. Although the TM's have proven reliable and long-lasting, the design results in an instrument that is too large, heavy, power-hungry, and expensive for a follow-on system. NASA is striving to reduce the cost and improve the performance of the next generation of EOS satellites by using advanced technologies to reduce the size, mass, power consumption, and cost of sensors and satellites. In addition, P.L. 102-555 directs NASA to demonstrate "advanced sensor capabilities suitable for use in the anticipated land remote sensing program" and to demonstrate "an advanced land remote sensing design that could be less expensive to procure and operate." Further, the EOS-AM2 platform could potentially accommodate a small, light, efficient Landsat sensor to simplify coincident observations with the other sensors.

These considerations prompted NASA to begin planning for the incorporation of a Landsat Advanced Technology Instrument (LATI) into the EOS-AM2 payload, scheduled for launch in 2004. Engineers and scientists at NASA/Goddard Space Flight Center (GSFC) have studied preliminary LATI designs as a guide to specifying instrument requirements for more detailed design efforts. The launch of an experimental instrument in 1999 is also under study to rapidly test and demonstrate high-risk technologies potentially applicable to LATI.

GSFC personnel have evaluated two preliminary LATI designs [1]. The designs employ either linear detector arrays or area detector arrays operated in the pushbroom mode to reduce sensor size, mass, and power consumption, to improve signal-to-noise radiometric performance, and to eliminate moving parts. Both designs lead to sensors that meet the

mission objectives given above. Each design is being used to estimate sensor cost, size, mass, and power consumption and to identify advanced technologies requiring development and demonstration.

The first design under study was developed in 1994 by a small team from GSFC and the Massachusetts Institute of Technology (MIT) Lincoln Laboratories [1]. The design involves two identical sensors operated side-by-side to provide a total 185 km swath from a 705 km altitude for synoptic coverage. Each sensor would use three-mirror-anastigmatic optics to provide a 93 km swath (7.5° field-of-view) with a 1 km overlap between swaths. Each sensor would employ multiple linear arrays overlaid by interference filters to acquire multispectral data. The spectral bands include the six reflective TM bands (TM1 through TM5 and TM7) with 30 m spatial resolution, an additional infrared band (1.2 - 1.3 μm) at 30 m, a 10 m panchromatic band, and 5 narrow bands (0.855 - 0.875, 0.925 - 0.955, 0.965 - 0.995, 1.02 - 1.055, and 1.350 - 1.400) acquired at a coarse resolution (240 m) for atmospheric characterization. The five coarse resolution bands are based on a recommendations by a panel of experts convened by the U.S. Air Force [2] to discuss atmospheric correction of Landsat data. The optical design of each sensor also incorporates a gimballed mirror for ±30° cross-track pointing. Radiometric calibration would be accomplished using a deployable solar diffuser plate.

The second preliminary LATI design was developed in 1995 by engineers within the EOS-AM2 Project at GSFC [1]. This second design uses two focal plane assemblies in a single sensor to acquire hyperspectral data. Spectral dispersion is achieved on each assembly with a multi-layer linear wedge filter. One focal plane assembly uses a backside illuminated, silicon, charge coupled device detector array to acquire 50 spectral bands between 0.4 and 0.9 μm with a spectral resolution of 0.01 μm and a spatial resolution of 20 m. The other assembly employs a InGaAs detector array to acquire 24 bands between 1.2 and 2..4 μm with a spectral resolution of 0.05 μm and a spatial resolution of 20 m. Both assemblies are cooled with multistage thermal electric coolers. This hyperspectral design uses three-mirror-anastigmatic optics to achieve a full 185 km swath (15° field-of-view) from a 705 km altitude. Spectral continuity with the TM could be accomplished by aggregating adjacent hyperspectral bands to synthesize the heritage bands.

Both of the LATI designs incorporate advanced technologies that have not been demonstrated extensively in space. NASA has recently initiated a New Millennium Program (NMP) to quickly validate in-flight such high-risk technologies. The goal of the NMP is to identify and validate key technologies leading to the development of small, autonomous spacecraft. These developments are expected to lower the cost and improve the performance of scientific missions. Six Integrated Product Development Teams (IPDT's) were formed by NASA, on a competitive basis, to identify breakthrough technologies applicable to NASA missions and ready for validation aboard NMP spacecraft. The IPDT's have identified a visible/infrared land-imaging sensor as a prime candidate for an early NMP mission. The goal is to launch a sensor that tests and demonstrates high-risk technologies applicable to LATI by 1999. Sensor design concepts and performance requirements are currently being reviewed.

FOLLOW-ON LANDSAT OPERATING CONCEPTS

P.L. 102-555 also directs NASA to assess different operating concepts for managing a follow-on Landsat system including private sector management, an international consortium, U.S. Government management, and a partnership between the private sector and the U.S. Government. The law gives a preference for private sector management. Consequently, NASA sponsored in September 1995 a conference on "Land Satellite Information in the Next Decade" in conjunction with the American Society for Photogrammetry and Remote Sensing, NOAA , and USGS. International and commercial operators of land remote sensing systems were invited to present their systems and future plans. NASA is using the information presented at this conference to help assess options. The challenge for future operations will be to meet the Landsat mission objectives and maintain the Landsat role within the EOS.

SUMMARY

The Landsat 7 system will maintain data continuity, satisfy mission objectives, and serve an essential role in the EOS when the satellite is launched in 1998. NASA is now evaluating advanced sensor designs and management options for a follow-on system. The goal is to develop a system that maintains and advances the functions of Landsat 7 while reducing the cost to the EOS Program. The follow-on system must deliver data well into the next century to those who observe, characterize, monitor, manage, and explore the land surfaces of the Earth over time.

REFERENCES

[1] D.L. Williams, J.R. Irons, D. Lencioni, S.P. Neek, P.J. Sellers, W.R. Stabnow, R.L. Taylor, and P.A. Westmeyer, "Landsat Advanced Technology Instrument (LATI) concepts, " Land Satellite Information in the Next Decade Conference Proceedings, pp. IV-66 - IV-75, September 25-28, 1995, Vienna, VA.

[2] P.N. Slater and L.D. Mendenhall, "Executive summary of the Workshop on Atmospheric Correction of Landsat Imagery," 29 June - 01 July, 1993, Geodynamics Corporation, Torrance, CA, 32 pp.

REDUCING THE EFFECTS OF SPACE-VARYING WAVELENGTH-DEPENDENT SCATTERING IN MULTISPECTRAL IMAGERY

Mark J. Carlotto, PSR Corp., 1400 Key Blvd. Suite 700, Arlington VA 22209 (mjcarlotto@ma.psrw.com)

Abstract -- A new method for reducing space-varying, wavelength-dependent scattering in multispectral imagery caused by smoke and haze is described. It is intended for use in situations where atmospheric scattering affects the shorter wavelengths and varies in space. The method converts an image in which space-varying scattering is present into an image where the scattering has been equalized over the entire image so that previously developed techniques for removing constant scattering effects can be used.

BACKGROUND

Assume that the atmosphere can be modeled as a horizontally homogeneous medium, the earth is a Lambertian reflector, and atmospheric properties which vary exponentially with altitude can be assumed to be constant over the scene [1]. When the contribution of the ambient illumination (skylight) can be neglected and the scattering is constant over the image, the brightness

$$z(i,j) = ar(i,j) + b. \quad (1)$$

r is the radiance of the surface, a represents the effects of atmospheric transmittance, sensor gain, and other multiplicative factors, and b represents the contribution of the path radiance. The brightness values at two or more pixels in the image together with measurements of the surface radiance at the corresponding locations on the ground can be used to solve for a and b. Alternatively, when ground truth is not available several methods have been developed to estimate the path radiance component [2-4]. When the scattering is not constant a technique developed by Lavreau [5] which subtracts a portion of the fourth tasseled cap feature [6] from each band can be used. The method effectively removes space-varying haze but causes the corrected bands to become more correlated thus altering the spectral balance of the data.

METHODOLOGY

When the effects of scattering are not constant over the image, the image formation model becomes

$$z(i,j) = a(i,j)r(i,j) + b(i,j). \quad (2)$$

Assume that it is possible to segment the image into disjoint regions within which the radiance of the surface can be assumed to be constant. Let S_k represent the set of pixels in the k - th region. Within the k - th region the brightness is

$$z_{k'} = a_{k'}r_k + b_{k'} \quad (3)$$

0-7803-3068-4/96$5.00©1996 IEEE

where r_k is the surface radiance. The terms $a_{k'}$ and $b_{k'}$, $k' \in S_k$ represent the effective variation in the atmospheric transmittance and path radiance for the pixels within the region. The mean value of the brightness in the k - th region is

$$\hat{z}_k = E[z_{k'}] = E[a_{k'}]r_k + E[b_{k'}]. \quad (4)$$

and is computed over the pixels $k' \in S_k$. We assume that the pixels within each of the K regions are randomly distributed throughout the image and that the variation in scattering within the image is such that the distribution of atmospheric transmittance and path radiance effects is the same in all regions. Thus $E[a_{k'}] = \mu_a = a$ and $E[b_{k'}] = \mu_b = b$ are the same for all of the regions and

$$\hat{z}_k = ar_k + b. \quad (5)$$

Assembling the K regions back into an image we have

$$\hat{z}(i,j) = ar(i,j) + b \quad (6)$$

thus reducing the space-varying case (Eq. 2) to a simpler one in which the scattering can be treated as a constant over the image (Eq. 1). A key requirement is that we are able to segment the image into regions of constant surface radiance.

The dependence of scattering on wavelength is a function of the size of the particles relative to the wavelength of the radiation [7]. In multispectral imagery, haze (and smoke) tends tend to affect the shorter wavelengths (i.e., the visible bands), often having negligible effect in the IR bands. Let the multispectral image be divided into two sets of bands $Z = \{X, Y\}$ where X are the bands that are affected by haze and Y are the bands that are not. To be specific we shall focus on Landsat TM (although the method is applicable to other multispectral sensors as well) and assume that in a given situation the visible bands (Landsat TM bands 1-3) are affected by haze while the infrared (IR) bands (Landsat TM bands 4,5 and 7) are not. Thus $x(i,j,m)$ is the brightness at pixel (i,j) in the m - th visible band and $y(i,j,n)$ is the brightness at pixel (i,j) in the n - th IR band.

Let X^M and Y^N denote the corresponding M - and N - dimensional visible and IR subspaces where $M = N = 3$. A point in the IR subspace corresponds to pixels that have the same values in the IR bands. It is conjectured that pixels with the same IR values are likely to be the same surface material with the same illumination and

topography. In the absence of scattering, each point in the IR subspace is assumed to correspond to a point in the visible subspace. This is an approximation because the visible bands provide information not contained in the IR. If we assume that the distribution of pixels with the same IR values are randomly distributed throughout the image, when scattering is present the visible band values of those pixels will be affected by varying amounts, i.e., will have higher or lower brightness values because of increased or decreased path radiance in different parts of the image. Thus in situations where space-varying scattering is present in the visible bands, points in the IR subspace will correspond to a set of points in the visible subspace.

The correspondence between the two subspaces is used to establish a functional relationship that is used, in turn, to predict the values of the visible bands (i.e., what their values would be without scattering) as a function of the IR bands. Let $\mathbf{y}_k = \{y_k(n)\}$ denote the vector corresponding to the k-th unique combination of values in the IR bands where $y_k(n)$ is the value of the n-th IR band for the k-th combination (region). Let $\{\mathbf{x}_{k'}, k' \in S_k\}$ denote the set of visible band values that occur within the k-th region where $x_{k'}(m)$ is the value of pixel k' in the m-th band. The joint distribution

$$P(x(m), \mathbf{y}) = P(x(m), y(1) \cdots y(N)) \tag{7}$$

is the probability of observing a particular combination of values in the m-th visible band and all N IR bands. For a given combination of values in the IR bands, the optimal estimate for the value of the m-th visible band is given by the conditional mean:

$$\hat{x}_k(m) = E[x_{k'}(m) \mid \mathbf{y}_k] = \frac{\sum_{k' \in S_k} x_{k'}(m) P(x(m) = x_{k'}(m), \mathbf{y} = \mathbf{y}_k)}{P(\mathbf{y} = \mathbf{y}_k)} \tag{8}$$

It can be shown that the conditional mean minimizes the mean-squared prediction error of $x(m)$ as a function of $\mathbf{y}$ [8]. In other words it provides the best single haze-free value to assign to the $x_{k'}(m)$ in each region.

EXPERIMENTAL RESULTS

The method has been evaluated on several images to date. We present results from one of these images over Bitterfeld, Germany in September 1986. Figure 1 shows the original and haze-equalized band 1 images. The results have been stretched for visual presentation. Like the de-hazing technique described by Lavreau [5], our method effectively removes the space-varying haze. Lavreau's de-hazing algorithm subtracts a portion of the fourth tasseled cap feature from the visible bands. As noted by Crist et al [9] the fourth tasseled cap feature responds to atmospheric haze as well as to senescent vegetation, man-made materials (e.g., roads), some soils and water. Thus by subtracting a portion of the fourth tasseled cap feature from the visible bands, information about the surface may be lost in the process of removing the haze. One such example is shown in Figure 2 in which road information lost by de-hazing has been retained by haze equalization.

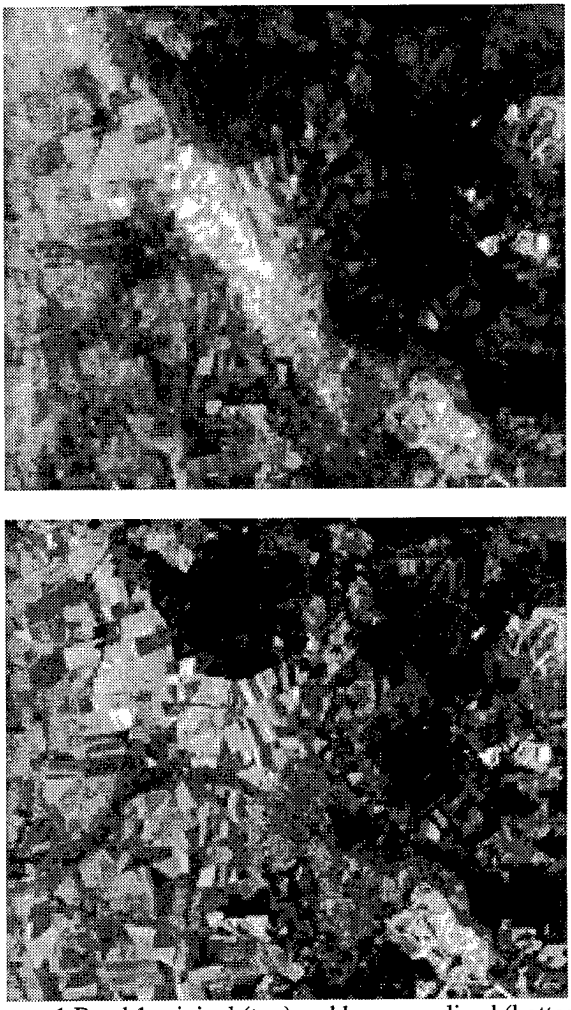
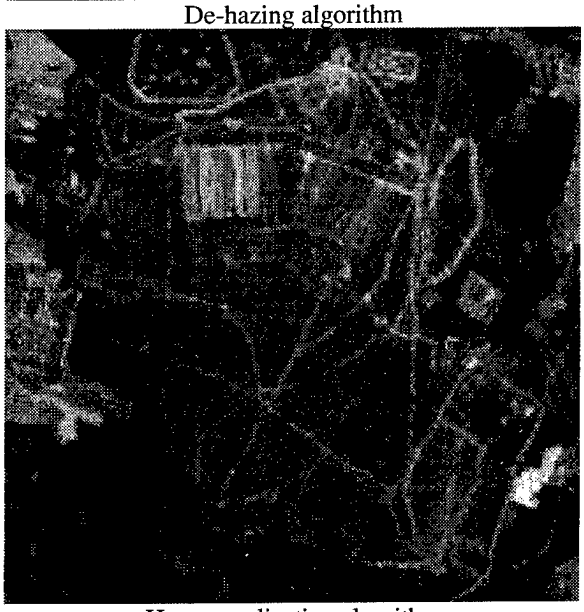


Figure 1 Band 1 original (top) and haze equalized (bottom)

As noted by Lavreau (1991), de-hazing can increase the correlation between bands. The eigenvalues summarize the spectral correlation structure of a multispectral image. Figure 3a compares the distribution of the eigenvalues corresponding to the three eigenvectors (principal components) computed from the visible bands before and after application of Lavreau's algorithm. A significant increase in the first eigenvalue indicates an increase in the correlation between the three visible bands. Figure 3b compares the distribution of the eigenvalues before and after application of our haze equalization algorithm. The correlation structure of the haze equalized bands is more similar to the original (uncorrected) bands thus spectral balance is better preserved.



De-hazing algorithm



Haze-equalization algorithm

Figure 2 Visual comparison of algorithms

CONCLUSION

A new method for reducing the effects of space-varying, wavelength-dependent scattering in multispectral imagery caused by smoke and haze was described. The method converts an image in which space-varying scattering is present into an image where the scattering has, in effect, been equalized over the entire image so that previously developed techniques for removing constant scattering effects can be used. The algorithm predicts the values of those bands that are affected by scattering from those that are not on a pixel-by-pixel basis. It was compared to an earlier algorithm for removing space-varying haze and found to better preserve subtle detail in the image and spectral balance between bands. Future work will concentrate on testing the algorithm as part of a land cover classification system in order to assess its effect on classification accuracy.

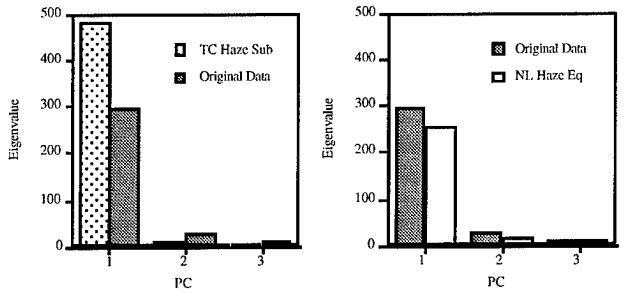


Figure 3 Eigenvalues before/after de-hazing (left) and haze-equalization (right)

References

[1] R.W. Sjoberg and B.K.P. Horn, "Atmospheric effects in satellite imaging of mountainous terrain," *Applied Optics*, Vol. 22, No. 11, pp 1702-1716, 1983.

[2] R.B. Crane, "Preprocessing techniques to reduce atmospheric and sensor variability in multispectral scanner data," *Proceedings 7-th International Symposium on Remote Sensing of Environment*, 1971.

[3] J.F. Potter and M.A. Mendlowitz, " On the determination of haze levels from Landsat data," *Proceedings 10-th International Symposium on Remote Sensing of Environment*, 1975.

[4] R.E. Crippen, "The regression intersection method of adjusting image data for band ratioing," *Int. J. Remote Sensing*, Vol. 8, No. 2, pp 137-155, 1987.

[5] J. Lavreau, "De-hazing Landsat Thematic Mapper images," *Photogrammetric Engineering and Remote Sensing*, Vol. 57, No. 10, pp 1297-1302, 1991.

[6] E.P. Crist and R.C. Cicone, "A physically-based transformation of thematic mapper data - The TM Tasseled Cap," *IEEE Trans. Geoscience and Remote Sensing*, Vol. 22, No. 3, May 1984.

[7] E. Schanda, *Physical Fundamentals of Remote Sensing*, Springer-Verlag, Berlin Heidelberg, 1986.

[8] A. Papoulis, *Probability, Random Variables and Stochastic Processes,* McGraw-Hill, 1965.

[9] E.P. Crist, R. Laurin and R.C.Cicone, "Vegetation and soils information contained in transformed Thematic Mapper data," Proceedings IGARSS, pp 1465-1470, 1986.

Fractal Analysis of Bidimensional Profiles and Application to Electromagnetic Scattering from Soils

S. Rouvier[1,2] , P. Borderies[1] , I. Chênerie[2] , J.C. Souyris[3] . T. Le Toan[3], N. Floury[3]

[1]CERT-ONERA/DERMO
2 Ave. E. Belin, BP 4025
31055 Toulouse Cedex, FRANCE
☎ : 33 62 25 27 18
fax : 33 62 25 25 77
Stephane.Rouvier@onecert.fr
Pierre.Borderies@onecert.fr

[2]AD2M - Université Paul Sabatier
118 Route de Narbonne
31062 Toulouse Cedex, FRANCE
☎ : 33 61 55 84 52
fax : 33 62 25 25 77

[3]CESBIO
18 Ave. E. Belin
31055 Toulouse Cedex, FRANCE
☎ : 33 61 55 85 84
fax : 33 61 55 85 00
souyris@cnes.cesbio.fr
thuy.letoan@cnes.cesbio.fr

ABSTRACT

This communication addresses relevancy of fractals as descriptors of bare soils and fractal dimension of the ultra wide band scattered field as a discriminating feature for them. The box counting method is described and applied to numerically generated profiles, experimental soil profiles and simulated scattered fields. The experimental soil profiles are found to exhibit a fractal behavior. It is shown that a monotonous relation links profile and scattered field fractal dimensions.

INTRODUCTION

Use of scattering models appears necessary for the interpretation of microwave remote sensing data acquired over bare soil surfaces as a function of soil properties (surface roughness, moisture content). Such scattering models require good descriptors of geometrical and electromagnetic properties of soil surface and volume. For surface scattering computation, statistical models based on the surface rms height and the correlation length have been extensively used. Nevertheless, this simple statistical description may be insufficient to account for complex media description, in particular in the case of multi-scale effects. To get a finer representation of the soil surface, one approach consists in using more sophisticated random models such as random fractals or statistical description involving several correlation lengths. Such approaches are expected to be very useful to interpret multi-frequency and/or multi-incidence/multi-resolution data, and are strictly necessary in the context of ground and foliage penetrating radar using ultra wide band signals.

Moreover, natural targets can be easily described by fractals : the fractal geometry of vegetation is frequently reported [1], whereas the fractal geometry of soils is less known, but also investigated [2] [3] [4].

Thus, we address here electromagnetic scattering of soils in relation with fractals. First, we present a method to extract the fractal dimension of a signal. To validate this method, we apply it on some fractals whose dimension is known.

Then the fractality of real soils is investigated through study of experimental data.

At last, the temporal field scattered by a perfectly conducting fractal profile is calculated and relationship between the fractal dimension of the profile and of the signal are then studied for several conditions of polarization, and incidence and observation directions.

FRACTAL DIMENSION EXTRACTION

To extract the fractal dimension of a signal, the well known box counting method is used : if A is the fractal set under study and B(x,r) is a bounded ball (in the algebraic sense) with radius r and center x, we can define N(A,r) as the smallest number of B(x,r) required to cover the set A.

N(A,r) is given by : $N(A,r) = c \cdot r^{-D}$ (1)

The box counting method is based on this definition.

$\ln N(A,r) = -D \cdot \ln(r) + c' \quad$ with $c' = \ln(c)$ (2)

By definition, D is the fractal dimension of the signal. Also, if the above linear relationship holds for a curve, then this curve is said to be fractal. The slope of the least squares straight line of the {-ln(r) ; ln N(A,r)} set is known to be a good estimate of the fractal dimension.

To apply this method to a sampled signal, this one is primarily normalized in both coordinates. A square grid is subsequently superimposed on the signal (Fig. 1)

The edges r_i of the cells are multiple of the sampling rate where i ranges from one to the number of samples. Then we count the number N_i of squares of dimension r_i, required to cover the entire signal, (in gray on Fig. 1). The curve {-ln r_i ; ln N_i} is plotted. The fractal dimension is given by the slope of the least squares line.

0-7803-3068-4/96$5.00©1996 IEEE

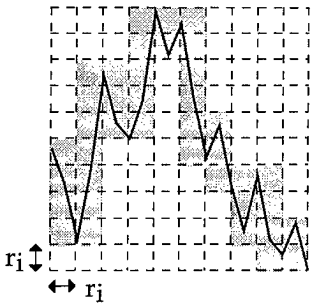


Fig. 1 : The box counting method

However, this method needs improvements to provide more reliable results. This basic method has been improved [5] [6]. Our own implementation is described in [7] by using an iterative process based on a correlation coefficient.

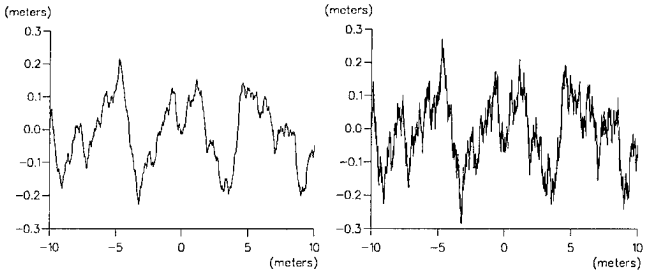
FRACTAL FUNCTION GENERATION

To generate a fractal function, the Weierstrass functions [8] is used :

$$W(x) = \eta \cdot \sum_{n=1}^{N_2} \left(\frac{1}{b^{(2-D)n}} \cdot \cos\left(2\pi b^n x + \theta_n\right) \right) \qquad (3)$$

D is the fractal dimension. b must be greater than one. η controls the amplitude of the signal. θ_n are a set of random phases, uniformly distributed on [0 ; 2π]. If N_2 is a finite number, a deterministic realization of the function is obtained.

Our improved method of fractal dimension calculation was validated with these functions. Results obtain with 50 simulations are shown in the following table.



D = 1.1 D = 1.5

Fig. 2 : Weierstrass Functions {$b=(\pi)^{1/2}$; $N_2=120$}

Theoretical Dimension	Calculated Dimension (Mean)	Standard deviation (%)
D = 1.3	1.30	0.48%
D = 1.5	1.50	0.34%
D = 1.7	1.66	0.22%

EXPERIMENTAL PROFILES

Experimental profiles acquired over agricultural soil surfaces presenting a rough structure have been analyzed. The length of these profiles ranges between 3 and 9 meters (200 samples and 600 samples). All the profiles are shown to have fractal properties, with fractal dimension ranging between 1.3 to 1.65 depending on soil roughness and observation direction, with respect to the rows. These results show that fractals are relevant to simulate the profiles for this type of soil surfaces. A work is in progress at this time to investigate the relationships between the traditional representation (correlation length, rms height) and the fractal dimension of the profile. To that extent, an extensive study will be based using larger profiles (45 m).

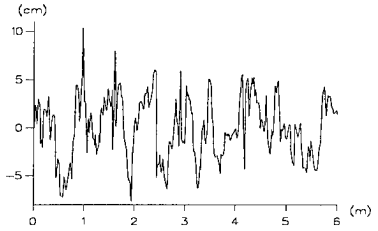


Fig. 3 : An example of an experimental profile

SCATTERED FIELD

Because the profile roughness involves multiscale effects, the method of moment is used. We have limited the calculation of the scattered field to a 2-D metallic profile for computational simplicity. So, both polarizations, different incidence and observations angles can be considered. End effects are neglected. The field is calculated in the frequency domain and transformed in the temporal domain using a Fast Fourier Transform. The incident pulse is defined from 100 MHz to 9 GHz by a Rayleigh function. The spectral window is centered at 3 GHz.

Profiles are generated by Weierstrass functions. Their fractal dimension D_p is known. The fractal dimension D_s of the field scattered by these profiles is then calculated and compared with D_p for both polarizations and different incident and observation angles.(Fig. 4)

For a given configuration, D_s is a monotonous increasing function of D_p. Moreover, D_s is nearly constant with regard to observation and incidence angles. Thus, D_s can be considered as an intrinsic parameter of the profile and so used as a discriminating parameter.

Noise influence was also studied in [9] and this parameter appears to be robust on this point.

CONCLUSION

Simulations show that the fractality of a profile leads to the fractality of the scattered field in the time domain. Even if some differences are observed between polarizations, this fractal dimension seems to be an intrinsic parameter of the profile, and consequently pertinent in characterization and classification applications. Experimentally measured soil profiles have exhibited fractal behavior and current work address scattered field measurement.

BIBLIOGRAPHY

[1] P. Prusinkiewicz, A. Lindenmayer, Fractal properties of plants, The algorithmic beauty of plants, Springer-Verlag, 1990

[2] J.A. Ogilvy, Theory of wave scattering from random rough surfaces, Adam Hilger, 1991

[3] A. Le Mehauté, Les géométries fractales, Hermès, 1990

[4] J.M. Keller, S. Chen, R.M. Crownover, Texture description and segmentation trough fractal geometry, Computer vision, graphics and image processing, vol 45, n°2, pp 150-166, February 1989

[5] S.S. Chen, J.M. Keller, R.M. Crownover, On the calculation of fractal features from images, IEEE Trans.-Pattern Anal.-Mach.-Intell., vol 15, n°10, pp 1087-90, 1993

[6] C. Tricot, J.F. Quiniou, D. Wehbi, C. Roques-Carmes, B. Dubuc, Evaluation de la dimension fractale d'un graphe, CRM-1465, Université de Montréal, May 1987

[7] S. Rouvier, P. Borderies, I. Chênerie, Electromagnetic scattering of a fractal profile: direct and inverse problems, International Symposium Retrieval Of Bio- And Geophysical Parameters From SAR Data For Land Applications, 10-13 October 1995

[8] D.L. Jaggard , On Fractal Electrodynamics, Recent advances in Electromagnetic Theory, Springer-Verlag, pp 183-222, 1990

[9] S. Rouvier, P. Borderies, I. Chênerie, Ultra Wide Band Electromagnetic Scattering of a Fractal Profile, unpublished

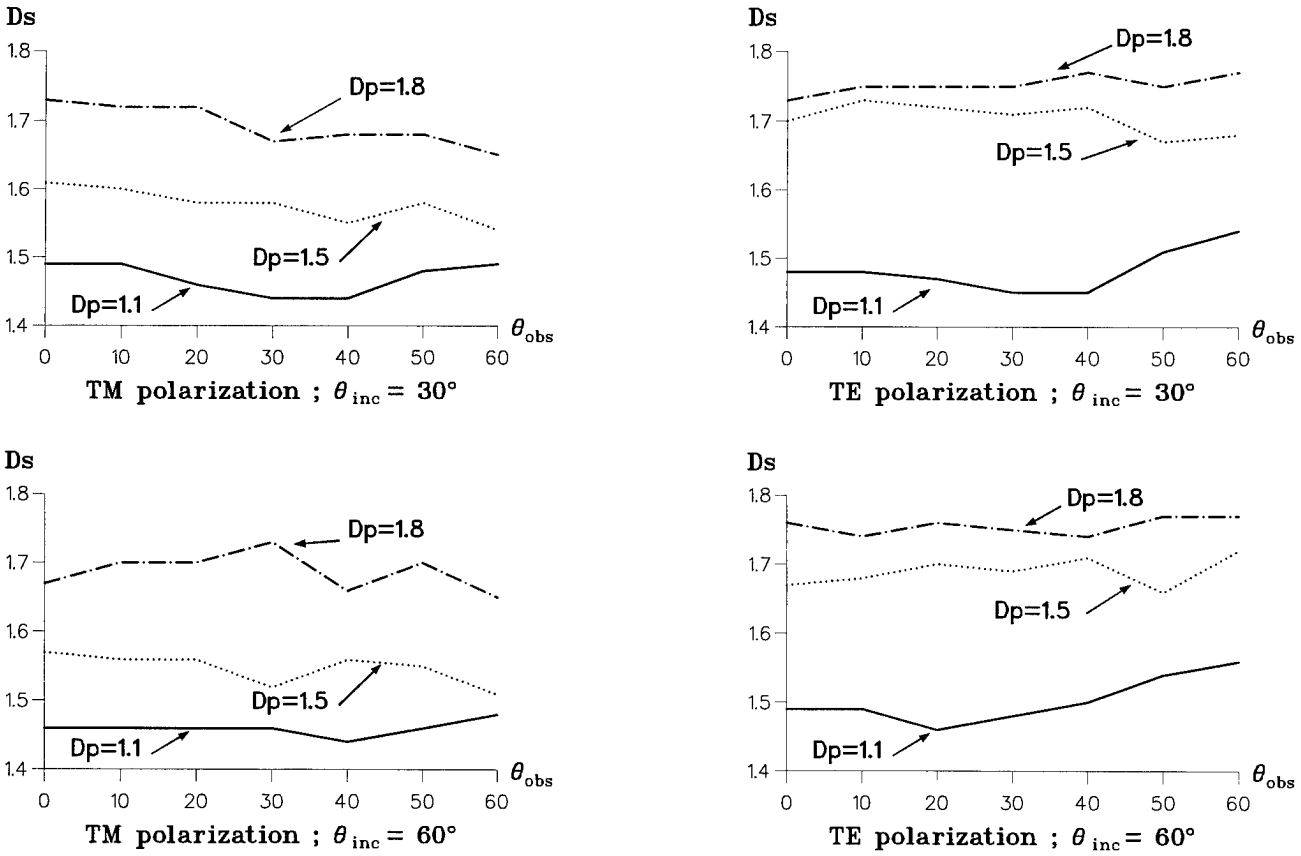


Fig. 4 : Fractal dimension of the scattered far field
Influence of observation and incidence angles for both polarizations

Like and Cross Polarized Cross Sections for Two Dimensional Random Rough Surfaces: Bistatic Single and Double Scatter

M. El-Shenawee* and E. Bahar
Department of Electrical Engineering — University of Nebraska-Lincoln — Lincoln, NE 68588–0511, USA
e.mail: bahar@dragon.unl.edu
* Electronics Research Institute — El-Tahrir St., Dokki, Cairo, Egypt
e.mail: magda@sgiris.unl.edu

Abstract — In this work, full wave solutions for the single and double scatter radar cross sections from two dimensional random rough surfaces are given. The solutions are expressed as multidimensional integrals. The high frequency approximations are used to reduce the double scatter integrals from twelve to four dimensional. The single scatter cross section is given in closed form. The large radius of curvature approximation is used. The incident waves are assumed to be plane waves. The effects of changing the rough surface parameters, such as mean square height and mean square slope, on the double scatter cross sections are studied. The level and width of the peak in the backscatter direction depend on the mean square height and slope of the rough surface. The numerical results show sharp enhancement in the backscatter directions. This sharp backscatter enhancement, which is observed for all polarizations and for both normal and oblique incident angles, is associated with the quasi antiparallel double scatter paths.

FORMULATION OF THE PROBLEM

Noting that the major contributions to the double and single scatter cross sections, in the high frequency limit, come from the neighborhood of the specular points of the rough surface, the statistical average of the radar cross section (with respect to the random heights and large-scale slopes of the surface) for the quasi parallel, double scatter path ($\bar{n}' \approx \bar{n}''$) is given by

$$\left\langle \sigma_{dp}^{PQ} \right\rangle = \frac{(2k_0 Lm)^2}{\pi} P_2(\bar{n}^i) P_2(\bar{n}^f) \sum_{R,S=V,H}$$

$$\left\{ \int \frac{[D_{2'}^{PS}(\bar{n}^f, \bar{n}') D_{1'}^{SQ}(\bar{n}', \bar{n}^i) D_{2''}^{*PR}(\bar{n}^f, \bar{n}'') D_{1''}^{*RQ}(\bar{n}'', \bar{n}^i)]}{(n_y^f - n_y')(n_y^f - n_y'')(-n_y^i + n_y')(-n_y^i + n_y'')} \right.$$

$$\cdot \frac{p(h_{xc1s}, h_{xc2s}, h_{zc1s}, h_{zc2s})}{(n_y^f - (n_y' + n_y'')/2)^2 (-n_y^i + (n_y' + n_y'')/2)^2}$$

$$\cdot [1 - P_2(|n_y'|)][1 - P_2(|n_y''|)]$$

$$\cdot \operatorname{sinc}[k_0 L_m (n_x' - n_x'')] \operatorname{sinc}[k_0 L_m (n_z' - n_z'')]$$

$$\cdot \exp\left(-\langle h^2 \rangle k_0^2 (n_y'' - n_y')^2\right)$$

$$\left. \cdot \sin\vartheta' \sin\vartheta'' d\vartheta' d\vartheta'' d\varphi' d\varphi'' \right\} \qquad (1)$$

0-7803-3068-4/96$5.00©1996 IEEE

where $\bar{n}^i \bar{n}^f$ are unit vectors in the directions of the incident waves and scattered waves to the receiver, $\bar{n}'$ and $\bar{n}''$ are unit vectors in the directions of the spectrum of scattered waves between two points on the rough surface $1'$, $2'$, and $1''$, $2''$ respectively (see Fig. 1) and ϑ', ϕ' and ϑ'', ϕ'' are the spherical coordinate variables for $\bar{n}'$ and $\bar{n}''$. The surface element scattering coefficients D^{PQ} are evaluated at the specular point slopes h_{xc1s}, h_{xc2s}, h_{zc1s} and h_{zc2s}. The probability density functions of the (large scale) slopes $p(h_{xc1}, h_{xc2}, h_{zc1}, h_{zc2})$ and heights are assumed to be Gaussian. The free space wave number and the mean square height are k_0 and $\langle h^2 \rangle$.

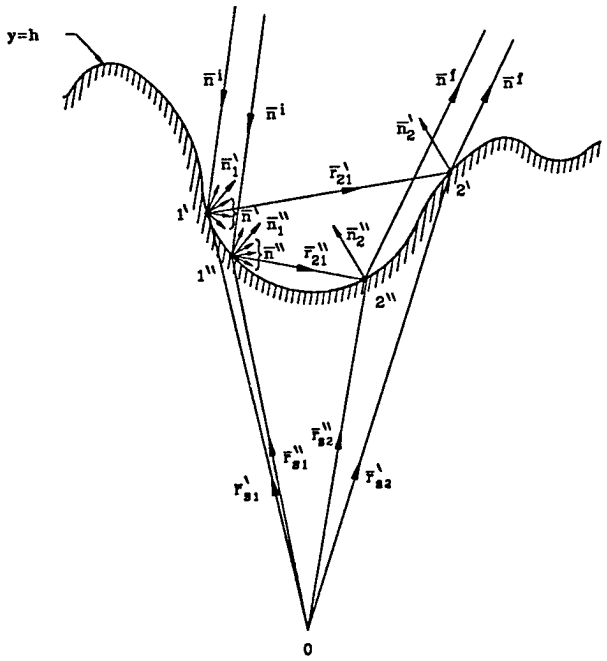


Fig. 1 Double scattered electromagnetic waves

Furthermore, L_m is the mean width of a typical depression on the rough surface [1], [2], [3]. The probabilities that the surface does not shadow the incident and scattered waves are given by $P_2(\bar{n}^i)$ and $P_2(\bar{n}^f)$, respectively [4], and $[1 - P_2]$ is associated with the probability of a double scatter event. The symbols V and H are for vertical and horizontal polarizations. For the quasi antiparallel double scatter paths, one gets the

following expression for the high frequency double scatter cross section

$$\left\langle \sigma_{dp}^{PQ} \right\rangle = \frac{(2k_0Lm)^2}{\pi} P_2(\bar{n}^i) P_2(\bar{n}^f) \sum_{R,S=V,H}$$

$$\left\{ \int \frac{[D_{2'}^{PS}(\bar{n}^f,\bar{n}') D_{1'}^{SQ}(\bar{n}',\bar{n}^i) D_{2''}^{*PR}(\bar{n}^f,\bar{n}'') D_{1''}^{*RQ}(\bar{n}'',\bar{n}^i)]}{(n_y^f - n_y')(n_y^f - n_y'')(-n_y^i + n_y')(-n_y^i + n_y'')} \right.$$

$$\cdot \frac{p(h_{xc1s}, h_{xc2s}, h_{zc1s}, h_{zc2s})}{\left((n_y^f + n_y' - n_y'' - n_y^i)/2\right)^2 \left((n_y^f - n_y' + n_y'' - n_y^i)/2\right)^2}$$

$$\cdot [1 - P_2(|n_y'|)][1 - P_2(|n_y''|)]$$

$$\cdot \operatorname{sinc}\left[k_0 L_m (n_x^f + n_x^i - n_x' - n_x'')\right]$$

$$\cdot \operatorname{sinc}\left[k_0 L_m (n_z^f + n_z^i - n_z' - n_z'')\right]$$

$$\cdot \exp\left(-\langle h^2 \rangle k_0^2 (n_y^f - n_y' - n_y'' + n_y^i)^2\right)$$

$$\left. \cdot \sin\vartheta' \sin\vartheta'' d\vartheta' d\vartheta'' d\varphi' d\varphi'' \right\} \qquad (2)$$

The slopes at the specular points for the quasi antiparallel case are given by h_{xc1s}, h_{xc2s}, h_{zc1s} and h_{zc2s}. Note that a stationary phase (quasi optics) integration over the wave vector variables $\bar{n}'$ and $\bar{n}''$ is not performed since the points 1 and 2 on the rough surface are not necessarily far apart ($k_0 r_{21}'$ and $k_0 r_{21}''$ are not large compared to one; see Fig. 1). The sharp enhancement in the backscatter direction $(-\bar{n}^i = \bar{n}^f)$ is associated with the quasi antiparallel $(\bar{n}' \approx -\bar{n}'')$ double scatter cross section (2). The expressions for the slopes at the specular points for the quasi parallel and the quasi antiparallel cases are not the same. For backscatter at normal incidence the major contributions to the double scatter cross sections come from quasi horizontal paths between points 1 and 2 (see Fig. 1) and the slopes at the stationary points are approximately $\pm 45^\circ$.

NUMERICAL EXAMPLES

The incoherent double scatter cross sections (quasi parallel + quasi antiparallel) for two dimensional rough surfaces are plotted in Figs. 2, 3 and 4 as functions of the scatter angle $\vartheta^f \cos\varphi^f$ (where $\varphi^i = 0$, $\varphi^f = 0, \pi$). The two dimensional rough surface is assumed to be coated with gold of permittivity $\varepsilon_r = -9.888312 - j1.051766$ at $\lambda = 0.633\mu m$. The incident angle is equal to 10^0. The Rayleigh roughness parameter $\beta = 4k_0^2\langle h^2 \rangle$ is assumed to equal 394.105 in Figs. 2 and 4. In Figs. 2 and 3, the VV polarized double scatter cross sections are shown. The effect of changing the mean square slope (m.s.s.) is shown in Fig. 2 where it is assumed to be 0.25, 0.4, 0.5, 0.65, 0.75, 0.85 and 1.0. The level of the peak enhanced backscatter cross section is highest for mean

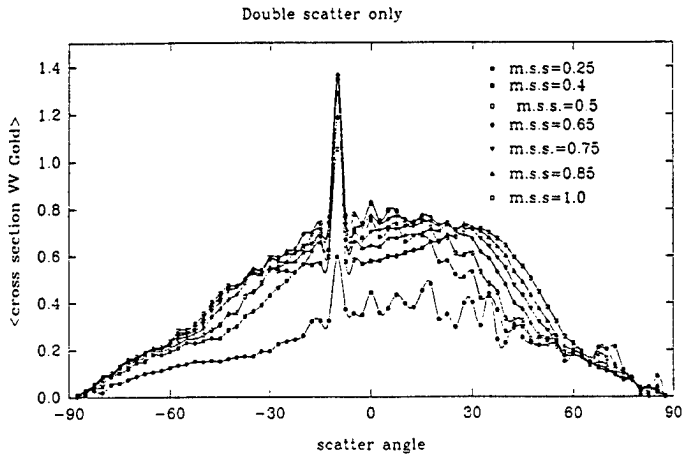


Fig. 2 $\vartheta^i = 10^\circ, \varepsilon_r = 9.888312 - j1.051766$, $\lambda = 0.633\mu m, \beta = 394.105$

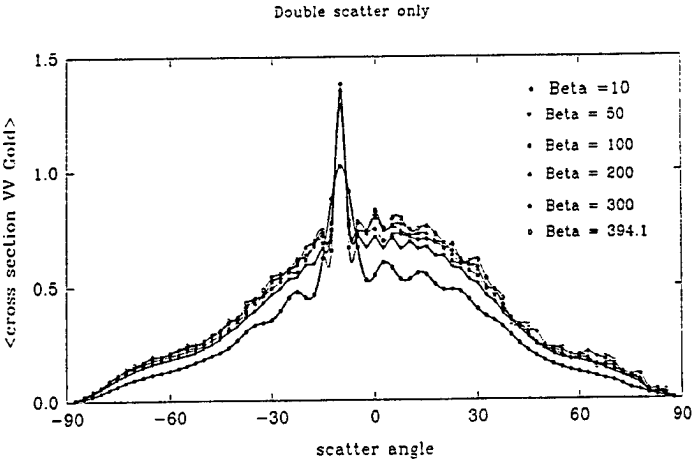


Fig. 3 $\vartheta^i = 10^\circ, \varepsilon_r = 9.888312 - j1.051766$, $\lambda = 0.633\mu m$, mean square slope=0.5

square slope equal to 1.0 and it decreases as the mean square slope decreases to 0.25. In Fig. 3, the mean square slope is assumed to be 0.5 and the Rayleigh roughness parameter is assumed to be 10, 50, 100, 200, 300, and 394.105. The level of the peak enhanced backscatter increases as the Rayleigh roughness parameter increases. The width of the enhanced backscatter peak increases as both the Rayleigh roughness parameter and the mean square slope decrease. The cross sections for different polarizations (VV, HH, VH, HV) are shown in Fig. 4 in which the mean square slope is assumed to be 0.5 and β is assumed to be 394.105. Enhanced backscatter is observed for the four polarizations considered. The levels of the peak double scatter cross sections (in the backward direction) are approximately the same for both the like and cross polarized cases. The sharp backscatter enhancement observed for all polarizations, is associated with the quasi antiparallel double scatter paths.

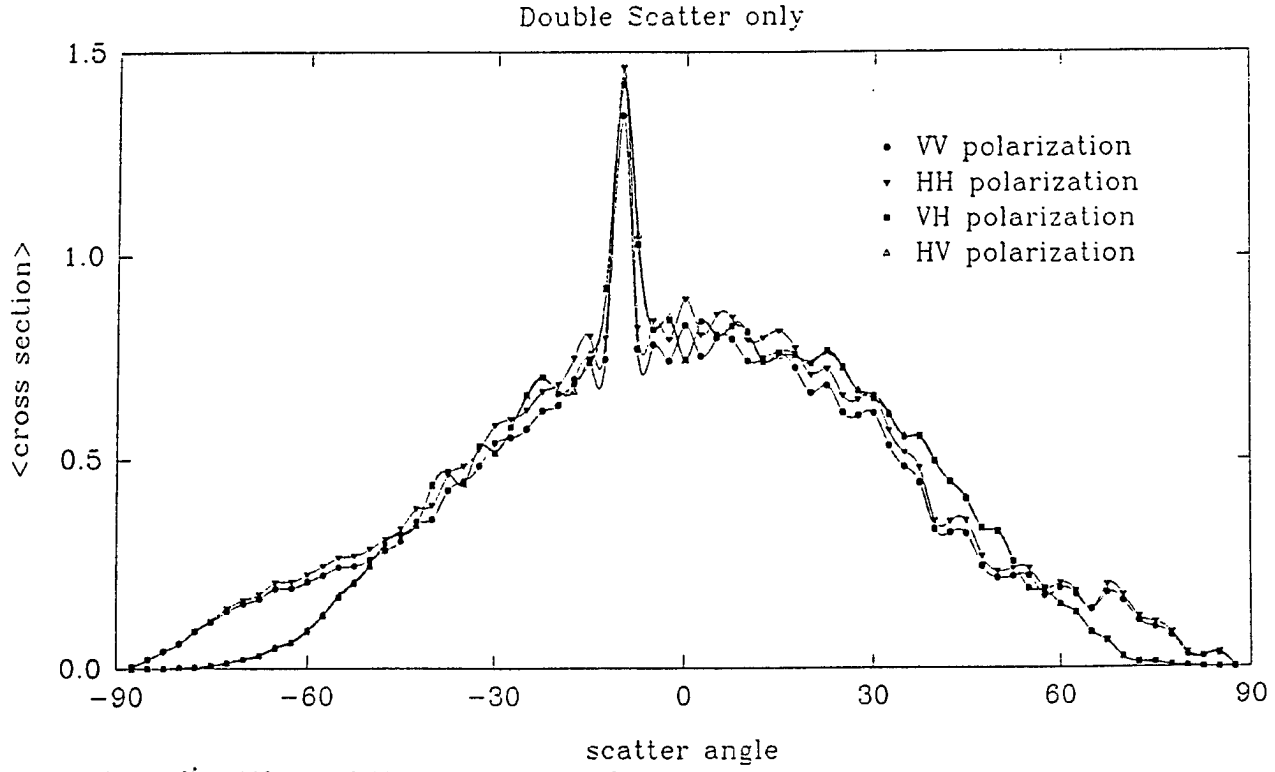


Fig. 4 $\vartheta^i = 10°, \varepsilon_r = 9.888312 - j1.051766$, $\lambda = 0.633\mu m$, mean square slope=0.5, β=394.105

ACKNOWLEDGMENT

This work is supported partially by the Department of Electrical Engineering and the Center for Electro-Optics at the University of Nebraska-Lincoln and the Supercomputer facility at Cornell University.

REFERENCES

[1] Bahar and M. El-Shenawee, "Enhanced Backscatter from One Dimensional Random Rough Surfaces — Stationary Phase Approximations to Full Wave Solutions," The Journal of the Optical Society of America A, Vol. 12, No. 1, pp. 151–161, January 1995.

[2] E. Bahar and M. El-Shenawee, "Vertically and Horizontally Polarized Diffuse Double Scatter Cross Sections of One Dimensional Random Rough Surfaces that Exhibit Enhanced Backscatter — Full Wave Solutions," Journal of the Optical Society of America A, pp. 2271–2285, August 1994.

[3] M. El-Shenawee and E. Bahar, "Double Scatter Radar Cross Sections for Two Dimensional Random Rough Surfaces — High Frequency Approximation," proceedings of the 1995 IEEE AP-S International Symposium and USNC/URSI Radio Meeting, Newport Beach, CA, June 18–23, 1995.

[4] M. I. Sancer, "Shadow-Corrected Electromagnetics Scattering from a Randomly Rough Surface," IEEE Trans. Antennas Propagat., Vol. AP-17, No. 5, pp. 577–585, September 1969.

A Knowledge-based Inversion of Physical BRDF Model and Three Examples

Xiaowen Li and Alan Strahler
Center for Remote Sensing and Department of Geography, Boston University, 725 Commonwealth Ave., Boston MA, 02215, USA Tel. +1-617-353-2088, Fax +1-617-353-3200, e-mail: lix/alan@crsa.bu.edu

Abstract – Three sets of directional observations with different sampling patterns and a gometric-optical model of forest BRDF are used to test our algorithm for physical BRDF model inversion. The results show that *stochatic programming* is the right mathematical tool for multiangular remote sensing. The experiments also indicated areas for further improvements of the algorithm and the BRDF model.

INTRODUCTION

The bidirectional reflectance distribution function (BRDF) of land surface contains invaluable information about surface characteristics, especially surface structure. Thus it is widely expected that the new generation of multiangular remote sensing instruments will provide great opportunities to extract such information through BRDF model inversion. However, physical BRDF models are usually very complex and difficult to invert.

The authors have developed a general framework to ease BRDF model inversion, originally for a BRDF/Albedo product of EOS (Earth Observing System of NASA). The inversion is based on accumulation of knowledge and frequent observations. The knowledge about the earth surface is expressed in forms of: 1) selection of the appropriate model and possible seasonal change; 2) physical bounds of parameters; 3) expected values of such parameters; 4) uncertainties of such expectations; and 5) different weighting factors for new observations according to their information content, determined by the directional sampling pattern, by the physical parameters to be extracted, and the noise level. With directional observations, the inversion gives the results in forms of 1) new expectations of parameters and associated uncertainties; and 2) detection of possible unusual changes which require new selection of models.

Three sets of directional observations with different sampling patterns and data qualities are used to test the algorithm. The results show that knowledge-based inversion, or stochastic programming [1], is the right mathematical tool for multiangular remote sensing. The experiments also indicated areas for further improvements of the algorithm and the BRDF model.

INVERSION ALGORITHM

The inversion requires a forward BRDF model and a set of directional observations, $\{R_j\}$, of earth surface reflectance. Each directional observation occupies a line of input data in order of solar zenith angle (SZN), solar azimuth angle (SAZ), viewing zenith angle (VZN), viewing azimuth angle (VAZ), reflectance of band 1, band 2, and so on.

The forward model picks up the 4 angles in each data line to calculate predicted reflectance, $\hat{R}_j$, according to model-specific parameters and equations.

The inversion algorithm tries to find a set of model-specific parameters, $\{f_i\}$, which produces the best-fit set of predicted values to observations. A Powell algorithm [1] is used to guide how to try the next parameter set according to the fitting error of previous tried parameter sets.

Prior knowledge is employed in defining the fitting error SSE (Note that we here use abridgement SSE of "sum of square error" for simplicity, which should be really called "weighted SSE with penalty", or WSSEWP [2]):

$$SSE = S_b \sum_j W_j (R_j - \hat{R}_j)^2 + P_{enalty} \qquad (1)$$

where the soft-bound S_b is:

$$S_b = \prod_i e^{(\frac{f_i - \overline{f_i}}{\sigma_i})^2}$$

where f_i is the i'th parameter used to calculate $\hat{R}_j$, $\overline{f_i}$ is the best guess value of this parameter and σ_i is its uncertainty. If one has no knowledge about the value of the parameter, a very large σ_i can be specified.

P_{enalty} is another way to express priori knowledge of the nature of parameters:

$$P_{enalty} = \sum_i |out - of - range : f_i| * 10^{20}$$

where the absolute value is the differece of the parameter f_i and the physical bound (either lower or upper) if violated; zero if not.

So for each parameter, four quantities should be specified: a pair of physical lower and upper (hard) bounds, and a soft bound expressed as expected value and its uncertainty.

W_j is the weighting factor of the the observation, which depends on its information content and noise level. Usually when we don't have such knowledge, all W_j are specified as one. But, for example, in the PARABOLA [3] data below we use for demonstrating the inversion, the nadir viewing observation is repeated for each viewing azimuth (13 in total), and thus we gave it a weighting factor 2/13. In addition, since the azimuth ranges from 0 to 360 degrees (at a step of 30), while SAZ is at 180 degrees, and the forward model we used in inversion is principal-plane symmetric, thus the azimuth backward to sun is under-represented. Therefore for this azimuth, a weighting factor of 2.0 is specified, in order to make all directions equally

0-7803-3068-4/96$5.00©1996 IEEE

Table 1: Inversion results for red channel in OJP site

SZN	NR^2	$\frac{B}{R}$	$\frac{H}{B}$	$\frac{\Delta H}{B}$	G	C	Z	SSE
35	.21	2.3	1.0	3.8	.17	.04	.001	.002
40	.18	2.7	1.0	3.5	.18	.05	.001	.002
45	.17	2.7	1.1	3.7	.18	.05	.001	.001
50	.13	3.3	1.0	3.2	.17	.06	.001	.002
55	.13	2.9	1.0	3.9	.17	.07	.001	.002
60	.10	3.2	1.0	3.8	.17	.08	.001	.002
65	.09	3.2	1.0	3.6	0.17	.08	.001	.003
69	.08	3.1	0.9	3.7	0.17	.10	.001	.004
74	.08	2.6	0.7	3.7	0.17	.11	.002	.006

Table 2: Mode 3 Inversion results, Yellowstone conifers

channel	NR^2	$\frac{B}{R}$	$\frac{H}{B}$	$\frac{\Delta H}{B}$	G	C	Z	SSE
red	.18	3.5	0.7	4.1	14.6	11.5	4.7	197
NIR	.10	3.9	1.0	4.4	24.4	19.1	7.2	462

Table 3: Mode 1 Inversion results, Yellowstone conifers

NR^2	$\frac{B}{R}$	$\frac{H}{B}$	$\frac{\Delta H}{B}$	SSE
0.183	2.563	0.795	3.555	462.56

weighted. Later we'll show some cases when observations should be weighted unequally.

The output of the inversion includes: a set of parameters which yields the best fit (i.e., the smallest SSE defined above, and the SSE as an evaluation of the quality of the fitting, the mean and standard deviation of each parameter which yields an SSE smaller than a certain threshold. These values can be used as a set of expected values and uncertainty of the parameters for next inversion using new observations.

THREE EXAMPLES

To demonstrate how knowledge is gained through observations and inversions, a GOMS model [4] and three sets of observations are used. The first set is associated with quite a lot of ground measurements and has a very good directional sampling [3], and the second is a record of three year's AVHRR data with no ground truth available except a landcover type [5]. The third is a set of ASAS images [6] of a BOREAS old black spruce forest. In all cases, uncertainties about ground truth are greatly reduced.

Don Deering's PARABOLA measurements used in this research were taken in an old jack pine in the BOREAS Southern Study Area on July 25, 1994. For the reasons we mentioned above, we have 72 equally weighted observations over the hemisphere for each SZN. The PARABOLA data set has three bands, and we used its red (662nm) and NIR (862nm) bands. The inversion has three modes: 1) knowing 6 spectral signatures to invert 4 structural parameters, 2) knowing 4 structural parameters to invert spectral signatures of both bands; and 3) knowing nothing to invert 4 parameters and 3 signatures for single band. Since the PARABOLA has good data quality (well sampled and no atmospheric blurring) and quantity, we decide to use Mode 3 for each SZN, with widest soft and hard bounds as if we knew almost nothing. Table 1 summarizes the inversion results of the red band for all SZN's. The physical meaning of the variables in the table can be found in [4].

From the inversion results, we can conclude:

1. The signature of sunlit crown increases with SZN, as we observed and modeled before [7].
2. The pattern of decrease of vertical crown coverage with increasing SZN is of special interest. It fits well with the gap probability increase with angle observed at the site by J. M. Chen [8] and Roujean [9]. This increase is thought to be explained by the horizontal whorl branch structure of this conifer species.
3. Rather small $\frac{H}{B}$ and large $\frac{\Delta H}{B}$ indicates the crown shape may deviate to cone from spheroid [4].

The second data set used in this research is an AVHRR collection provided by Joy Hood of EDC over a Yellowstone coniferous forest during three years from 1990 to 1992. After cloud screening [5], the data set has 95 directional observations over a wide range of solar zeniths. Because the signature of sunlit crown varies with solar zenith, we exclude those smaller than 35^o or greater than 75^o, and have 79 observations remained. Since we have no knowledge about ground truth, we specify a wide range of soft bound and use Mode 3 to invert. Results are shown in Table 2.

Now we use the inversion Mode 1, fixing the signatures as listed in Table 2, and obtain the structural parameters listed in Table 3. In order to verify how reliable these parameters are, we used them to calculate the proportions of sunlit/viewed ground K_g and its correlation with AVHRR Band 4 temperature. The correlation is 0.624. Though there are too many uncertain factors during this 3 years' record of AVHRR data, the inversion of GOMS model successfully extracts some structural information about the Yellowstone coniferous forest.

As the third experiment, we used J. Irons' ASAS images over an old black spruce forest (OBS) in the BOREAS SSA, taken on 4/19, 1994. The data consist of 9 viewing images in total, ranging from forward 60^0 to backward 55^0 on the principal plane. We registered the images and selected a forest site right near the center of the hotspot image (46^0 forward looking at solar zenith 47.8^0). Then the spatial average for each viewing direction is taken as a directional sample for inversion, 9 samples in total. Assuming we know nothing about the forest, Mode 3 gives the results shown in Table 4.

Though the results look reasonable, it is probably by chance – using 9 samples to invert for 7 parameters yields very little confidence even if the model were linear. Small fluctuations

Table 4: Inversion results, SOBS

channel	NR^2	$\frac{B}{R}$	$\frac{H}{B}$	$\frac{\Delta H}{B}$	G	C	Z	SSE
red	.20	3.2	3.1	9.6	.21	.10	.00	.0007
NIR	.15	3.0	3.3	7.8	.41	.30	.00	.0017

Table 5: Inversion results using hotspot ASAS only

channel	NR^2	G	SSE
red	0.142	0.287	0.00259
NIR	0.124	0.559	0.01133

or noise in the observations, or small discrepancies between the model and reality, may change the results in a large range with still very good fitting. This is especially true for the 46^0 forward looking image which has a very strong and sharp hotspot and contributes the most to SSE. It is sensitive to small errors in accuracies in viewing positions. Therefore we can no longer pretend of knowing nothing about the possible range of parameters.

In all seven parameters, we have the least prior knowledge of ground signature G and vertical coverage (function of NR^2). So we have to invert for these two parameters first at the hotspot. Because the pixels on each ASAS line have a slightly different azimuth angle, approximately 0.0525^0/pixel, in order to increase the reliability of inversion, we selected four more segments of forest stands near the original one of the same classification (airphoto and classification provided by R. Robb of the Phillips Laboratory), and grouped pixels of all segments by azimuth angle relative to solar position, and hence obtained more samples near the hotspot but crossing the principal plane, very closely parallel to the almucanter. Using these 48 samples, ranging from VAZ of 0.118^0 to -2.265^0, and by fixing all other parameters but NR^2 and G only, we obtained the results shown in Table 5.

On the other hand, the directional reflectance of ASAS shows a very flat and low bottom around the coldspot, ranging almost from nadir to the 55^0 opposite to sun. Note that Z is basically insensitive to inversion for hotspot and its nearby samples, while G and possibly C are still sensitive to the cold spot where the sensor sees mostly shadows only. Slight overestimation of gaps or G and C near the coldspot may bring Z down to a negative value if we do not specify a physical lower bound. Therefore for the inversion of shadow signature Z, we need to select a subset of samples where the proportions of sunlit and viewed surfaces are the minimum. We simply select the 5 samples opposite to the sun azimuth, fix NR^2 and the other three structural parameters, and use inversion mode 2 to invert G, C and Z with G and C soft bounded by an uncertainty half of their means. The results are shown in Table 6.

Table 6: Inversion results for Z using coldspot ASAS only

channel	G	C	Z	SSE
red	0.255	0.042	0.003	0.00008
NIR	0.578	0.210	0.021	0.00005

DISCUSSION AND CONCLUSION

Inversion of physical BRDF models is challenging. In [2], we have pointed out that the key difficulty in such inversions is the matching of information content in a given specific spectral/directional sampling with the uncertainty of structural and spectral parameters that is to be reduced through inversion, but we were not sure what was the right approach to solve the problem.

The main conclusion of this experiment is that stochastic programming, a branch of optimization which deals with minimization or maximization of functions of several variables usually subject to constraints, is the right mathematical tool for BRDF model inversion.

The difference between stochastic programming and other branches of optimization is well explained by R. Wets (1989):

"It is difficult to find examples of systems ... that do not include some level of uncertainty about the values to assign to some of the parameters ... of the system. In a rather larger number of cases not much is lost by assuming that these uncertain quantities are actually known, either because the level of uncertainty is low, or because these quantities play an insignificant role in the process that we want to analyze or control.

"... One rather general approach which has been successfully applied to a variety of problems is to assign explicitly or implicitly, a probability distribution to various unknown parameters. ... The stochastic model can be viewed as an extension of the linear or nonlinear programming models to decision models where the coefficients that are not known with certainty have been given a probabilistic representation. ... The solution must be found on the basis of *a priori* knowledge."

Our knowledge-based inversion aims at accumulation of knowledge of ground truth, and at using remote sensing observations to reduce uncertainty in such knowledge. The primary reason to develop this algorithm is based on the fact that some ground characteristics do not change much with time, while others do. Given that any set of remotely sensed observations has a limited information content, this information should be used to gain knowledge of the most uncertain and sensitive characteristics of ground, rather than to infer time-stable parameters repeatedly. And since different observations contain different amount of noise, different information, and have different sensitivities to the parameters, the correct weight should be given to observations according to what specific parameters are to be inverted. In our inversion experiment we accumulated knowledge through inversion, giving different weights to different bands or directional observations, through selecting the appropriate subset of bands/directions for specic parameters in the proper orders. In order to do the same globally, it's necessary to accumulate a global knowledge base of ground surface

structure gradually, and further develop the algorithm so that the weights of samples and order of inversion for different parameters can be automatically determined through sensitivity analysis for given sampling pattern and prior knowledge.

One of advantages of employing *a priori* knowledge in inversion is that expected values of parameters are the natural choices as their initial values in numberical inversion. But what if the expectations are wrong? Our initial analysis shows that wrong expectation values will yield large SSE and the result will be somewhere between wrong expectation and true value, depending on the speciafied range of uncertainty. Iteration using the same observation but renewed expectation may converge to the true value, but this needs more comprehensive investigation, though it is not that important a issue in our scheme of frequently repeated observations.

Our experiments also reveal some drawbacks of GOMS model – for example, all three cases show small $\frac{H}{B}$ and large $\frac{\Delta H}{B}$, indicating a slower drop-off in reflectance when deviating from hotspot, and more shadows on crown surfaces visible than what a spheroidal model predicts, i.e, the crown tops tend more toward a cone. Meanwhile, the decreasing NR^2 estimates with SZN requires modeling branch structure in more detail. A more thorough discussion can be found in [10].

ACKNOWLEDGEMENT

This work is supported in part by NASA under contract NAS5-31369, and in part by China's NSF under grant 49331020. We thank Drs. J. Irons, C. Russell, W. Kovalick, and F. Irani of NASA Goddard Space Flight Center for their discussion on navigation of the ASAS-taking flight and description of the BOREAS SSA. We also thank two graduate students, B. Hu and W. Ni, for their help in formatting the data and this manuscript.

References

[1] Wets, R. J.-B., "Stochastic Programming", in Optimization, Chapter 8, ed. by Nemhauser, G.L., A.H.G. Rinnoy Kan, and M.J. Todd, vol. 1 of Handbooks in Operations Research and management Science, Elsevier Science Pub., Amsterdam, 1989.

[2] Li, X., J. Wang, C. Zhu, "Inversion of remote sensing models", New Progress of Remote Sensing Science, Science Press, 1995, Beijing, pp135-141 (in Chinese).

[3] Deering, D. W., "Temporal attributes of the bidirectional reflectance for three boreal forest canopies", IGARSS95 Proceding, 1239-1241.

[4] Li, X. and A.H. Strahler, "Geometric-Optical Bidirectional Reflectance Modeling of Mutual Shadowing Effects of Crowns in a Forest Canopy", IEEE trans on Geoscience and Remote Sensing, 1992, Vol. 30, No. 2, p276-292.

[5] Wu, A., Z. Li, and J. Cihlar, "Effect of land cover types and greenness on AVHRR bidirectional reflectance: Analysis and removal", Journal Geophysical Research, 1995, Vol.100 No.5, p9179-9192.

[6] Irons, J. R., Ranson, K. J., Williams, D. L., Irish, R. R. and Huegel, F. G., "An off-nadir pointing imaging spectroradiometer for terrestrial ecosystem studies", IEEE Trans. Geosci. Remote Sens., 1991, Vol.29, p66-74.

[7] Schaaf, C. B. X. Li and A. H. Strahler, "Effects of solar zenith angle on forest canopy albedo calculated with a Geometric-Optical Model", IGARSS92 proceedings, p347-349.

[8] Chen J., "Optically-based methods for measuring seasonal variation of LAI in boreal forest stands", 1996, Ag. For. Met., in press.

[9] Ni, Li, Roujean, Woodcock, Davis and Strahler, "Modeling solar radiation transmission in boreal conifer forests", accepted by IGARSS'96.

[10] Li, Strahler, Hu, "Inversion of A Geometric-Optical BRDF Model Using Multiangular Observations Over the Black Spruce Forest in BOREAS SSA", submitted to Journal Geophysical Research, 1996.

Scattering Cross Sections of Composite Random Rough Surfaces New Unified Full Wave Solutions

E. Bahar and Yuzhi Zhang

Department of Electrical Engineering and Center for Electro-Optics
University of Nebraska, Lincoln, NE 68588-0511 USA
Tel: 402.472.1966 Fax: 402.472.4732
EMail: bahar@dragon.unl.edu zhang@sgiris.unl.edu

Abstract— A new unified approach, based on the original full wave solutions, is presented here to evaluate the like and cross polarized scattering cross sections of composite (multiple scale) random rough surfaces. The rough surfaces are assumed to be characterized by the Pierson-Moskowitz spectral density function. To account for the large scale surface undulations, the incoherent radar cross sections are obtained by regarding the composite rough surface as an ensemble of pixels of arbitrary orientation.

Introduction

A new unified full wave approach is developed to determine the radar scatter cross sections of composite (multiple scale) random rough surfaces such as the sea surface. The basis for the current analysis are the original full wave solutions [1]. These solutions are obtained from second order iterative solutions of the rigorous generalized telegraphists equations associated with scattering from irregular layered media. Thus, these single scatter solutions are restricted to surfaces with moderate slopes. While the surface element scattering coefficients are exactly the same as those of the small perturbation solutions [2], the original full wave solutions are not restricted by the small surface height assumption.

In order to increase the range of validity of the original full wave solutions and to account for the undulations of the large scale surface, extensive use is made here of the full wave scattering cross section modulation for arbitrarily oriented composite rough surfaces [3]. Thus, the incoherent diffuse radar cross sections of the composite (multiple scale) rough surface are obtained by regarding the composite rough surface as an ensemble of individual pixels (several pixel correlation lengths in the lateral dimension) of arbitrary orientation. The cross section per unit area of the composite rough surface is obtained by averaging (over slope) the cross sections of the arbitrarily oriented pixels. It is shown that the (unified full wave) cross section of the composite rough surface is relatively stationary over a broad range of pixel sizes. This stationary property was first realized in earlier work [4]. In this broad range of values of pixel size, the norm of the relative error is minimum. Thus, using the full wave approach the pixel size is not chosen in order to retrofit the experimental date. In a comprehensive study of the hybrid (perturbation-physical optics) approach based on a two scale rough surface model, it was shown that the results

0-7803-3068-4/96$5.00©1996 IEEE

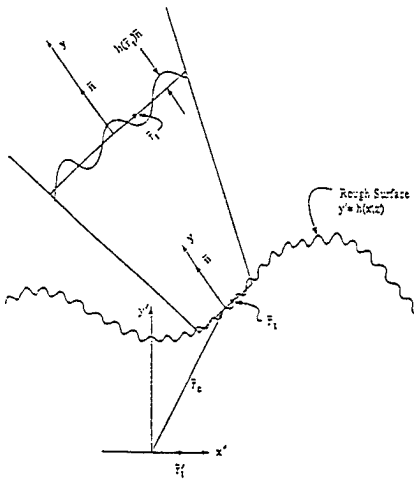


Fig. 1. Arbitrarily oriented pixel on a rough surface

for the scattering cross sections (expressed as a sum of two cross sections) critically depend on the choice of the wave number at which the spectral separation between the large and small scale surface is assumed to occur. Unlike the hybrid (perturbation-physical optics) solution, the uniform full wave solution contains only one term.

Full Wave Scatter Cross Sections

The starting point in this work is the radar cross section (per unit projected area A_y) obtained from the original full wave solution (see Fig. 1)

$$< \sigma_o^{PQ} > \; = \; |S^{PQ}(\bar{n}^f, \bar{n}^i)|^2 \; Q(\bar{n}^f, \bar{n}^i) \qquad (1)$$

in which $S^{PQ}(\bar{n}^f, \bar{n}^i)$ is the surface element scattering coefficient for incident waves in the direction $\bar{n}^i$ and polarization $Q = V$ (vertical), H (horizontal), and scattered waves in the direction $\bar{n}^f$ and polarization $P = V, H$. It should be noted that the scattering coeffiecients $S^{PQ}(\bar{n}^f, \bar{n}^i)$ are not functions of slope. In (1), $Q(\bar{n}^f, \bar{n}^i)$ is expressed in terms of the surface height joint characteristic function χ_2 and characteristic function χ as follows, for rough surfaces $y = h(x, z)$ that are homogenous and isotropic.

The y component of $\bar{v} = k_0(\bar{n}^f - \bar{n}^i)$ is v_y, $\langle h^2 \rangle$ is the mean square height and $R(r_d)$ is the surface height autocorrelation function

$$Q(\bar{n}^f, \bar{n}^i) \; = \; \frac{2k_o^4}{v_y^2} \int_0^\infty [\chi_2(v_y, -v_y) \; - \; |\chi(v_y)|^2] \qquad (2)$$
$$J_o(v_{xz} r_d) r_d dr_d$$

where J_o is the Bessel function of order zero. Furthermore, k_0 is the free space wave number

$$v_{xz} = (v_x^2 + v_z^2)^{\frac{1}{2}} = (v^2 - v_y^2)^{\frac{1}{2}}. \quad (3)$$

Note that $Q(\bar{n}^f, \bar{n}^i)$ remains finite as $v_y \to 0$.

A pixel is assumed to be oriented normal to the vector (see Fig. 1)

$$\begin{aligned} \bar{a}_y &= sin\Omega cos\tau \bar{a}'_x + cos\Omega cos\tau \bar{a}'_y + sin\tau \bar{a}'_z \quad (4) \\ &= (-h_x \bar{a}'_x + \bar{a}'_y - h_z \bar{a}'_z)/(1 + h_x^2 + h_z^2)^{\frac{1}{2}} \end{aligned}$$

where $\bar{a}'_x, \bar{a}'_y$, and $\bar{a}'_z$ are the unit vectors in the fixed (reference) coordinate system associated with the mean plane $y = h_o = 0$ and $h_x = \partial h/\partial x, h_z = \partial h/\partial z$. The unit vectors $\bar{a}_x$ and $\bar{a}_z$ are tangent to the mean plane of the pixel. The angles Ω and τ are the tilt angles in and perpendicular to the fixed plane of incidence (the x', y' plane).

The surface element scattering coefficient for the tilted pixel is expressed as follows [3]

$$D_p = T_p^f S_p T_p^i \quad (5)$$

in which S_p^{PQ} the elements of the 2×2 scattering matrix of S_p are obtained from S^{PQ} on expressing the incident and scatter wave vectors in the pixel (with respect to the pixel coordinate system, (see Fig. 1). The matrices T^f and T^i relate the vertically and horizontally polarized waves in the reference coordinate system to the vertically and horizontally polarized waves in the local (pixel) coordinate system [3].

The radar cross section (per unit area) for the tilted pixel can be expressed as follows

$$\sigma_p^{PQ} = |D_p^{PQ}|^2 Q_p(\bar{n}^f, \bar{n}^i) \quad (6)$$

and

$$\begin{aligned} Q_p(\bar{n}^f, \bar{n}^i) = \frac{k_o^4}{\pi(\bar{a}'_y \cdot \bar{a}_y)^2 v_y^2} \int_{-2L_p}^{2L_p} \int_{-2l_p}^{2l_p} \\ (1 - \frac{|x_z|}{2L})(1 - \frac{|z_d|}{2L})[\chi_{2p}(v_y, -v_y) - |\chi_p(v_y)|^2] \\ exp(i\bar{v} \cdot \bar{r}_{dt}) d\bar{r}_{dt} \quad (7) \end{aligned}$$

where $\bar{a}'_y \cdot \bar{a}_y = [1 + h_x^2 + h_z^2]^{-1/2}$

$$\bar{v} = \bar{k}_0^f - \bar{k}_0^i = v'_x \bar{a}'_x + v'_y \bar{a}'_y + v'_z \bar{a}'_z = v_x \bar{a}_x + v_y \bar{a}_u + v_z \bar{a}_z$$

and (8)

$$v_y = \bar{v} \cdot \bar{a}_y = v'_x \sin\Omega \cos\tau + v'_y \cos\Omega \cos\tau + v'_z \sin\tau,$$

$$v_t = (v^2 - v_y^2)^{\frac{1}{2}},$$

Thus, in (6) both $|D_p^{PQ}|^2$ and Q_p are functions of the large scale surface slopes h_x, h_z of the tilted pixel mean plane (see Fig. 1). If the composite rough surface height is random, the tilted pixel cross section (per unit area) (6) for the rough surface is also a random function of the pixel orientation. Thus, in order to determine the cross section per unit area of the composite random rough surface, it is necessary to evaluate the statistical average of σ_p^{PQ}. The cross section of the composite random rough surface is given by

$$< \sigma_p^{PQ} > = < |D_p^{PQ}|^2 \ Q_p(\bar{n}^f, \bar{n}^i) > \quad (9)$$

where $< \cdot >$ denotes the statistical average (over the slope probability density function $p(h_x, h_z)$ of the tilted pixel).

It is shown that the value of the cross section for the composite rough surface is relatively stationary over a broad range of values of pixel size L_p or $k_p = \frac{2\pi}{L_p}$ (the maximum wave number associated with the large scale surface slope). In this broad range of values of the pixel size (or k_p) the relative error ϵ_p^{PQ} is defined by the following norm

$$\epsilon_p^{PQ} = || \left[\langle \sigma_{p+1}^{PQ} \rangle - \langle \sigma_p^{PQ} \rangle \right] ||/|| \langle \sigma_p^{PQ} \rangle ||, \ p \geq 0 \quad (10)$$

where $\langle \sigma_p^{PQ} \rangle$ and $\langle \sigma_{p+1}^{PQ} \rangle$ are the values of $\langle \sigma_p^{PQ} \rangle$ (9) associated with k_p. Thus, using this full wave approach, k_p is not chosen in order to retrofit the experimental data, rather k_p is chosen in the range where $\langle \sigma_p^{PQ} \rangle$ is relatively stationary [4].

I. Illustrative Examples

Consider the Pierson-Moskowitz surface height spectral density function

$$W(k) = \begin{cases} \frac{2Bk^4}{\pi(k^2+\kappa^2)^4} & k < k_c \\ 0 & k \geq k_c \end{cases} \quad (11)$$

where $k^2 = k_x^2 + k_z^2 (cm^{-2})$, the cutoff wavenumber $k_c = 12 (cm^{-1})$, $B = 0.0046$, $\kappa = (335.2V^4)^{\frac{1}{2}} (cm^{-1})$. In the examples, the wind speed $V = 4.3$ m/sec, and $V = 5.6$m/s and $\lambda_0 = 2$ cm.

The pixel surface height correlation function is [5],

$$R_p = \left[1 + \frac{(\kappa_p r_d)^2}{8} \right] \kappa_p r_d K_1(\kappa_p r_d) - (\kappa_p r_d)^2 K_0(\kappa_p r_d) \quad (12)$$

where

$$\kappa_p = \sqrt{\frac{B}{6 < h_p^2 >}} \quad (13)$$

A smooth filtering of the pixel surface height spectral density function is assumed here [5]. In this section, the pixel lateral dimension is chosen to be

$$L_p = \frac{20 l_c}{(1.05)^p} \quad , \quad p = 1, 2, 3 \cdots \quad (14)$$

where l_c is the rough surface correlation length. The cross section for the composite rough surface is given by (9) for

$p \geq 1$. For $p = 0$, $\langle \sigma_0^{PQ} \rangle$ (1), is used since the slope of the mean plane is zero, $(\sigma_s \to 0), L_p \to \infty$, and $k_p \to 0$.

For the cases considered here, the complex relative permittivity is $\epsilon_r = 42 - j39$ (at $\lambda = 2cm$). The like and cross polarized backscatter cross sections are evaluated for all angles of incidence and different pixel sizes (denoted by p (4)). In Figs. 2a, b, c, d, $V = 5.6m/s$, $\langle h^2 \rangle = 254cm^2$ and $\sigma_s^2 = 0.098$. In Fig. 2d, the relative error ϵ_p (10) is plotted as a function of p. The above rough surface parameters are the same as those considered earlier using the two scale approach. Since $p = 0$ corresponds to the original full wave solution $(\sigma_s \to 0)$, there is a small discontinuity in $\langle \sigma_p^{PQ} \rangle$ between p=0 and p=1.

From Figs. 2, it is seen that the pixel size corresponding to p=1 (4) is sufficient to make $\epsilon_{p=1} < 10^{-5}$.

References

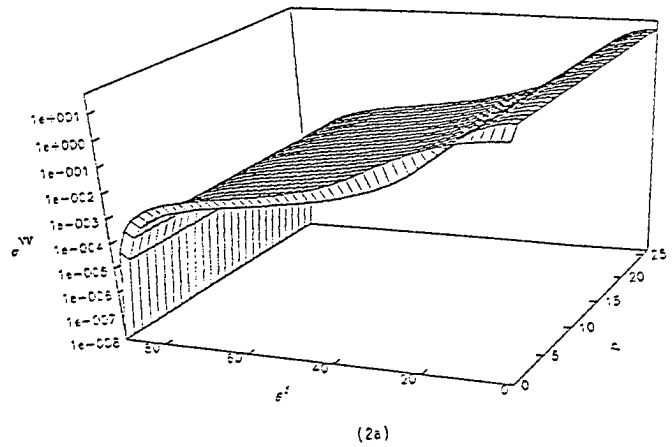
[1] Bahar, E., and R. Rajan (1979), "Depolarization and Scattering of Electromagnetic Waves by Irregular Boundaries for Arbitrary Incident and Scatter Angles - Full Wave Solutions," *IEEE Trans. on Antennas and Propagation*, Vol. AP-27, No. 2, pp. 214-225.

[2] Rice, S. O. (1951) "Reflection of Electromagnetic Waves from Slightly Rough Surfaces," *Communications of Pure and Applied Math*, Vol. 4, pp. 251-378.

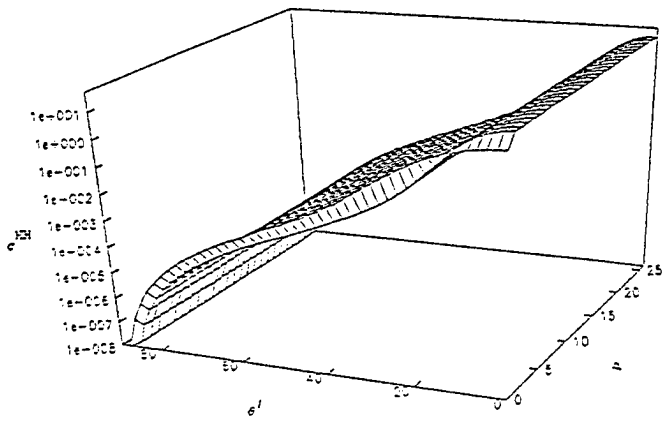
[3] Bahar, E., C. L. Rufenach, D. E. Barrick and M. A. Fitzwater (1983), "Scattering Cross Section Modulation for Arbitrarily Oriented Composite Rough Surfaces - Full Wave Solutions," *Radio Science*, Vol. 18, No. 5, pp. 675-690, September-October 1983.

[4] Bahar, E., D. E. Barrick and M. A. Fitzwater (1983), "Computations of Scattering Cross Sections for Composite Surfaces and the Specification of the Wavenumber Where Spectral Splitting Occurs," with *IEEE Trans. on Antennas and Propagation*, Vol. AP-31, No. 5, pp. 698-709, September 1983.

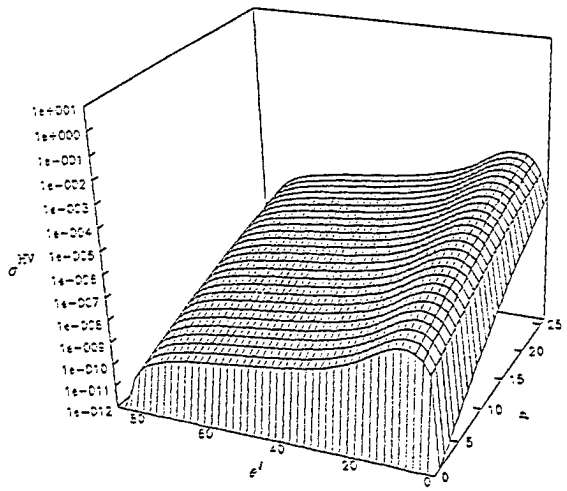
[5] Bahar, E. and R. D. Kubik (1993), "Tilt Modulation of High Resolution Radar Backscatter Cross Sections: Unified Full Wave Approach," *IEEE Transactions on Geoscience and Remote Sensing*, Vol. 31, No. 6, pp. 1229-1242.



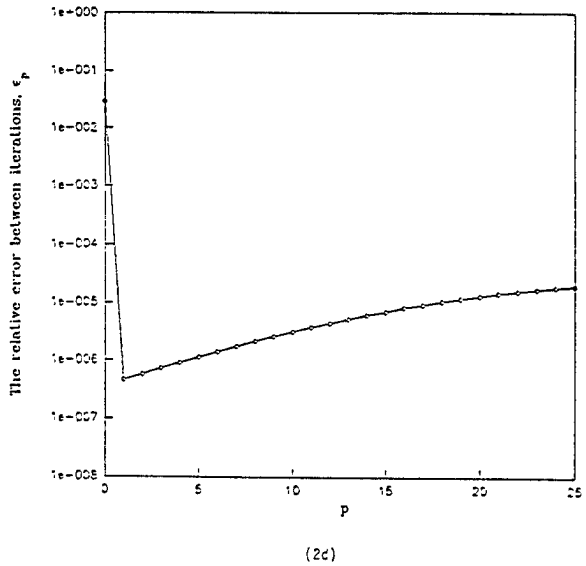
(2a)



(2b)



(2c)



(2d)

Fig. 2. Backscatter cross sections for rough surface with W(k) given by (10), $\langle h^2 \rangle = 254$ cm^2 $\sigma^2 = 0.098$ V = 5.6m/s (a) $< \sigma^{VV} >$ (b) $< \sigma^{HH} >$ (c) $< \sigma^{VH} > = < \sigma^{HV}$ (d) Relative error ϵ_p as function of p

Scatter Cross Sections for Two-Dimensional Random Rough Surfaces-Full Wave Analysis

E. Bahar and Bom Son Lee*

Department of Electrical Engineering and Center for Electro-Optics
University of Nebraska, Lincoln, NE 68588-0511, USA
T: 402.472.1966 F: 402.472.4732 EMail: bahar@dragon.unl.edu

* Department of Radio Science and Engineering, Kyung Hee University
1 Seocheon-ri, Kihung-eup, Yongin-gun, Kyungki-do, Korea

Abstract—The full wave solutions for the fields diffusely scattered from two-dimensional random rough surfaces are used to evaluate the scatter cross sections. Unlike the original full wave solution [4], this full wave solution accounts for rough surface height and slope correlations and can, therefore, be used for a wide range of surface roughness scales [2]. The computation time is relatively sort compared to the numerical results based on Monte Carlo simulations (even for one-dimensional random rough surfaces). The full wave scatter cross sections for the two-dimensional random rough surfaces are shown to reduce to the small perturbation and physical optics solutions in their appropriate regions of validity. It is also shown that there is good agreement between the full wave results and experimental data or numerical results based on Monte Carlo simulations [1], [3].

FORMULATION OF THE PROBLEM

For isotropic 2-dimensional random rough surfaces with Gaussian statistics, the full wave solutions for the bistatic radar scatter cross sections can be expressed as a 3-dimensional integral

$$\langle\sigma_1^{PQ}\rangle_{co} = \frac{k_o^4}{\pi v_y^2} 2\pi \iiint f^{PQ}(\bar{n}) \Big\{ |\chi(v_y)|^2 \cdot \Big[\exp\Big(\frac{\sigma_s^2}{2} v_y^2 r_d^2 \exp\Big(-\frac{2r_d^2}{l_c^2}\Big) + \langle h^2\rangle v_y^2 \exp\Big(-\frac{r_d^2}{l_c^2}\Big)\Big) \cdot J_o(v'_{xz} r_d) - J_o(v_{xz} r_d)\Big] - \chi(v_y)\Big[\exp\Big(\frac{\sigma_s^2}{2} v_y^2 r_d^2 \cdot \exp\Big(-\frac{2r_d^2}{l_c^2}\Big) J_o(v'_{xz} r_d) - J_o(v_{xz} r_d)\Big)\Big]\Big\} \cdot p(h_x, h_z) r_d dr_d dh_x dh_z \tag{1}$$

where

$$\bar{v} = \bar{k}_o^f - \bar{k}_o^i = v_x \bar{a}_y + v_y \bar{a}_y + v_z \bar{a}_z, \tag{2}$$

$$\bar{k}_o^f \equiv k_o \left(\sin\theta_o^f \cos\phi^f \bar{a}_x + \cos\theta_o^f \bar{a}_y + \sin\theta_o^f \sin\phi^f \bar{a}_z\right), \tag{3}$$

$$\bar{k}_o^i \equiv k_o \left(\sin\theta_o^i \cos\phi^i \bar{a}_x - \cos\theta_o^i \bar{a}_y + \sin\theta_o^i \sin\phi^i \bar{a}_z\right), \tag{4}$$

$$f^{PQ}(\bar{n}) = D^{PQ}(\bar{n}) D^{PQ*}(\bar{n}) P_2\left(\bar{n}^f, \bar{n}|\bar{n}\right), \tag{5}$$

$$\chi(v_y) = \exp\left[-(v^2 3_y \langle h^2\rangle)/2\right]. \tag{6}$$

$$v_{xz} = \sqrt{v_x^2 + v_z^2}, \tag{7}$$

$$v'_{xz} = \sqrt{(v'_x)^2 + (v'_z)^2}, \tag{8}$$

$$v'_x = v_x + v_y h_x \exp\left(-(r_d^2/4l_c^2)\right), \tag{9}$$

$$v'_z = v_z + v_y h_z \exp\left(-(r_d^2/4l_c^2)\right). \tag{10}$$

In (1), $p(h_x, h_z)$ is the probability density function for the large scale slopes in x and z directions (assumed here to be Gaussian), $\langle h^2\rangle$ is the mean square surface height, σ_s^2 is the mean square slope in x or z direction, l_c is the correlation length, and r_d is the distance variable. In (5), $\bar{n}$ is the unit vector normal to the large scale rough surface, P_2 is Sancer's shadow function [8], and $D^{PQ}(P, Q = V, H)$ is the surface element scattering coefficient which depends upon the incident and scatter angles, large scale slopes of the rough surface, and the electromagnetic parameters of the media above and below the surface [1], [3]. The full wave, incoherent diffuse scatter cross sections (1) account for surface height/slope correlations. They can be used for a wide range of surface roughness scales.

When the surface slopes are small $\left(\sigma_{sT}^2 < 0.15\right)$, it is shown that the surface height and slopes can be assumed to be uncorrelated and the full wave solution (1) reduces to the following product of a 2- and a 1-dimensional integral

$$\langle\sigma_I^{PQ}\rangle_{UC} = I^{PQ} Q \tag{11}$$

in which

$$I^{PQ} = \frac{1}{\pi} \iint f^{PQ}(\bar{n}) p(h_x, h_z) dh_x dh_z \tag{12}$$

and

$$Q = \frac{k_o^4}{v_y^2} \iint \left[\chi_2(v_y, -v_y) - |\chi(v_y)|^2\right] \cdot \exp\left(iv_x x_d + iv_z z_d\right) dx_d dz_d = 2\pi \frac{k_o^4}{v_y^2} \int \left[\chi_2(v_y, -v_y) - |\chi(v_y)|^2\right] J_o(v_{xz} r_d) r_d dr_d. \tag{13}$$

In (13), χ_2 is the surface height joint characteristic function of the 2-dimensional random rough surface [1]. When the surface slopes are small $\left(\langle h_x^2\rangle \ll 1, \langle h_z^2\rangle \ll 1\right)$ and the Rayleigh roughness parameter $\left(\beta = 4k_o^2\langle h^2\rangle\right)$ is of the same order of smallness (as the surface slopes), the

0-7803-3068-4/96$5.00©1996 IEEE

full wave expression ((2) or (11)) can be shown to reduce to the small perturbation solution of Rice [7]

$$\langle\sigma_I^{PQ}\rangle_{SP} = \pi k_o^4 \left|D^{PQ}(\bar{n}=0)\right|^2 W(v_x,v_z) \quad (14)$$
$$= \pi k_o^4 \left|D_0^{PQ}\right|^2 W(v_x,v_z)$$

where

$$W(v_x,v_z) = \frac{\langle h^2\rangle l_c^2}{\pi}\exp\left[-\left(v_x^2+v_z^2\right)l_c^2/4\right] \quad (15)$$

is the 2-dimensional rough surface height spectral density function. Unlike the small perturbation solution, the original full wave solution [4] given below is not restricted to surfaces with small Rayleigh parameters.

$$\langle\sigma_I^{PQ}\rangle_{zs} = I^{PQ}Q = \frac{1}{\pi}\left|D_0^{PQ}\right|^2 \frac{k_0^4}{v_y^2}2\pi \quad (16)$$
$$\cdot\int\left[\chi_2(v_y,-v_y)-|\chi(v_y)|^2\right]J_0(v_{xz}r_d)r_d dr_d$$

The small scale slopes are accounted for in the above original full wave solutions. If the most significant contributions to the scattered field come from the neighborhood of the stationary phase (specular) points on the rough surface, the full wave solution reduces to the physical optics solution [5]

$$\langle\sigma_I^{PQ}\rangle_{PO} = \frac{1}{\pi}f^{PQ}(\bar{n}_s,\bar{n}_s)\frac{k_0^4}{v_y^2}2\pi \quad (17)$$
$$\int\left[\chi_2(v_y,-v_y)-|\chi(v_y))|^2\right]J_o(v_{xz}r_d)r_d dr_d$$

where

$$\bar{n}_s = \bar{v}/|\bar{v}|. \quad (18)$$

In high frequency limit, it can be shown that the full wave solution reduces to the closed form geometrical optics solution

$$\langle\sigma_I^{PQ}\rangle_{GO} = \quad (19)$$
$$\frac{4\pi k_0^4}{v_y^4}\left|D^{PQ}(\bar{n}_s)\right|^2 P_2\left(\bar{n}^f,\bar{n}^i|\bar{n}_s\right)p(h_{xs},h_{zs})$$

where $p(h_{xs},h_{zs})$ is the large scale slope probability density function evaluated at the specular points where $\bar{n}=\bar{n}_s$ (18).

ILLUSTRATIVE EXAMPLES

For the illustrative examples, the incoherent scattering cross sections (obtained from the following solutions 1 to 6) are compared with each other. They are also compared with experimental data [6].

1. The full wave solution $\langle\sigma_I^{PQ}\rangle_{co}$ using equation (1) (Symbol Δ)
2. The full wave solution $\langle\sigma_I^{PQ}\rangle_{UC}$ using equation (11) (Symbol $\square$)

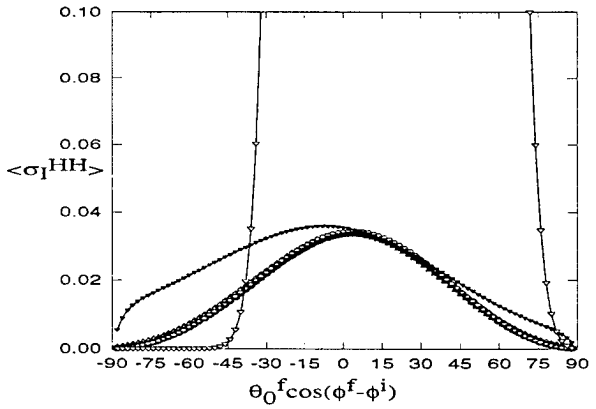


Fig. 1. Bistatic scatter cross section for $\theta_i^i = 20^o, k_o h = 0.1, k_o l_c = 1, \sigma_{sT}^2 = 0.04$

3. The original full wave solution $\langle\sigma_I^{PQ}\rangle_{zs}$ using equation (16)(Symbol $\bullet$)
4. The small perturbation solution $\langle\sigma_I^{PQ}\rangle_{SP}$ using equation (14) (Symbol $\circ$)
5. The physical optics solution $\langle\sigma_I^{PQ}\rangle_{PO}$ using equation (17)(Symbol $\blacktriangledown$)
6. The geometrical optics solution $\langle\sigma_I^{PQ}\rangle_{GO}$ using equation (19)(Symbol ∇)
7. The experimental data (Symbol —)

In Fig. 1 through 5, the bistatic scatter cross sections are plotted as a function of $\theta_0^f\cos(\phi^f-\phi^i)$ for perfectly conducting isotropic Gaussian rough surfaces. The scattering cross sections are computed for $\phi=\phi^f-\phi^i=0$ and π. In Fig. 1, the six solutions (1 to 6) are used to compute the scatter cross sections for $\theta_0^i = 20^o$, $k_o h = 0.1$, $k_o l_c = 1$, and $\sigma_{sT}^2 = 0.04(\sigma_{sT}^2 = 2\sigma_s^2$ is the total mean square slope). It is shown that for the rough surfaces with root mean square heights appriximately of the same order of smallness as the surface slopes, the full wave solutions (1 to 3) are all in good agreement with the small perturbation solution. The physical and geometrical optics solutions are not valid for these scales of surface roughness.

In Fig. 2 through 5, the full wave solutions $\langle\sigma_I^{PQ}\rangle_{co}$ and $\langle\sigma_I^{PQ}\rangle_{zs}$ are compared with the physical optics solution and the experimental data [6]. The results have been normalized to compare with the experimental data. The case in Fig. 2 is in the high frequency range. The full wave solutions are shown to be in good agreement with the physical optics solution and experimental data.

In Fig. 3, $\theta_o^i = 20^o$, $k_o h = 1.3456$, $k_o l_c = 12.3885$, $\sigma_{sT}^2 = 0.047$. The results here are also in good agreement with each other.

In Fig. 4, the surface parameters are exactly the same as in the case given in Fig. 2. The only difference is the incident angle ($\theta_o^i = 70^o$). In this case (large incident angles), the physical optics solution deviates considerably from the experimental data. The full wave solutions $\langle\sigma_I^{PQ}\rangle_{co}$ and $\langle\sigma_I^{PQ}\rangle_{zs}$ are in much better agreement with the experi-

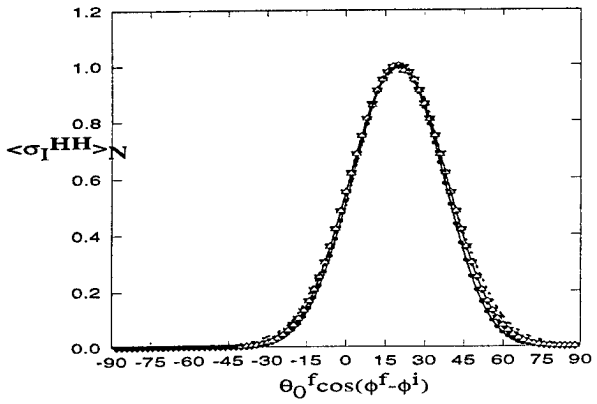


Fig. 2. Bistatic scatter cross section for $\theta_i^i = 20°, k_o h = 22.5321, k_o l_c = 207.4543, \sigma_{sT}^2 = 0.047$

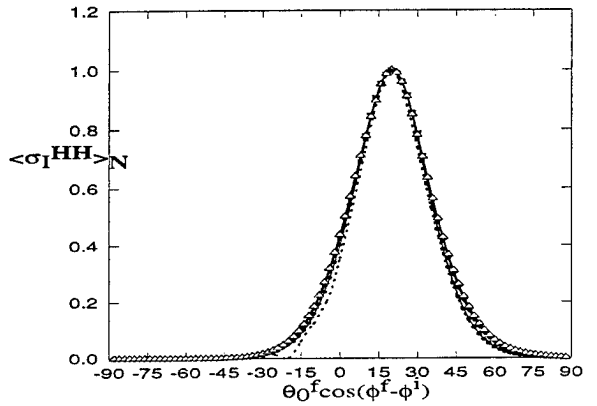


Fig. 3. Bistatic scatter cross section for $\theta_o^i = 20°, k_o h = 1.3456, k_o l_c = 12.3885, \sigma_{sT}^2 = 0.047$

mental data. At near grazing angles, the deviations between the full wave solutions and the experimental data are primarily due to the fact that it is a ssumed that the surface height autocorrelation function is Gaussian. (The impact of the oscillatory behavior of the true autocorrelation function is significant at near grazing angles.)

In Fig. 5, the surface parameters are exactly the same as the case given in Fig. 3. The only difference is the incident angle ($\theta_o^i = 70°$). As in the case given in Fig. 4, the physical optics solution deviates from the experimental data significantly. However, the full wave solutions $\langle \sigma_I^{PQ} \rangle_{co}$ and $\langle \sigma_I^{PQ} \rangle_{zs}$ are in good agreement with the experimental data for the near resonant region ($h/\lambda \approx 1$).

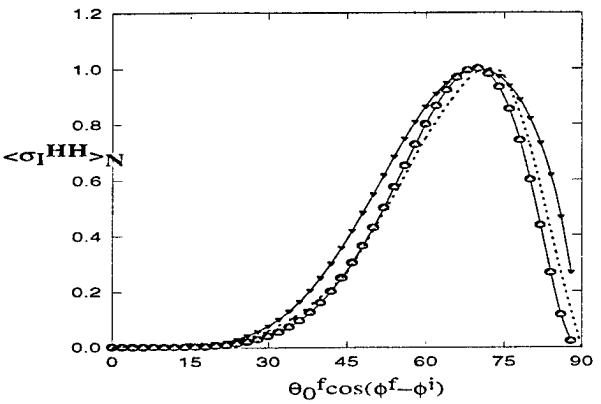


Fig. 4. Bistatic scatter cross section for $\theta_o^i = 70°, k_o h = 22.5321, k_o l_c = 207.4543, \sigma_{sT}^2 = 0.047$

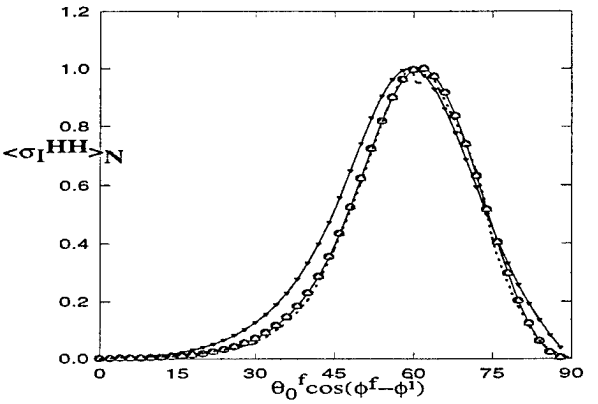


Fig. 5. Bistatic scatter cross section for $\theta_o^i = 70°, k_o h = 1.3456, k_o l_c = 12.3885, \sigma_{sT}^2 = 0.047$

References

[1] E. Bahar and B.S. Lee, "Full wave solutions for rough surface bistatic radar cross sections - Comparison with small perturbation, physical optics, numerical, and experimental results," Radio Science, vol. 29, pp. 407-429, 1994

[2] E. Bahar and B.S. Lee, "Full wave scatter cross sections for two-dimensional random rough surfaces using joint conditional surface height characteristic functions," Proceedings of International Geoscience and Remote Sensing Symposium, pp. 1638-1640, 1994.

[3] E. Bahar and B.S. Lee, "Full wave vertically polarized bistatic radar cross sections for random rough surfaces - Comparison with experimental and numerical results, IEEE Trans. Antennas Propag., Vol. 43, pp. 205-213, 1995.

[4] E. Bahar and G.G. Rajan, "Depolarization and scattering of electromagnetic waves by irregular boundaries for arbitrary incident and scatter angles full wave solutions," IEEE Trans. Antennas Propag., Vol. 27 pp. 225-232, 1979

[5] P. Beckmann and A. Spizzichino, The Scattering of Electromagnetic Waves from Rough Surfaces, Macmillan, New York, 1963

[6] K.A. O'Donnell and E.R. Mendez, "Experimental study of scattering from characterized random surfaces," J. Opt. Soc. Amer. A., vol. 4, pp. 1194-1205, 1987.

[7] S.O. Rice, Commun. Pure Appl. Math., vol. 4, pp. 251-378, 1951

[8] M.I. Sancer, "Shadow corrected electromagnetic scattering from randomly rough surface," IEEE Trans. Antennas Propag., vol. SP-17, pp. 577-585, 1969.

The Measured Polarized Bidirectional Reflectance Distribution Function of a Spectralon Calibration Target

C. L. Betty[1], A. K. Fung[1], and J. Irons[2]
[1]Wave Scattering Research Center
Department of Electrical Engineering
The University of Texas at Arlington
P.O. Box 19016 Arlington, Texas 76019
Phone: 817-794-5659 FAX: 817-273-3443
EMAIL: cbetty@omega.uta.edu
[2]NASA-GSFC
Code 923, Greenbelt, MD 20771

Abstract -- The polarized bidirectional reflectance distribution function is measured for a Spectralon calibration target using an automated, broadband, polarized, optical goniometer. Measurements are acquired for illumination angles of 0, -20 ,-30 ,-40 -50, and -60 degrees as a function of receiver view angle. Both like- and cross-polarized components are measured for horizontally polarized incident illumination. The Spectralon target exhibits stronger specular behavior than expected where the ratio of the cross-polarized to like-polarized component in the specular direction varies from 0.67 to 0.1 for 0 and -60 degrees incidence respectively.

INTRODUCTION

Bidirectional reflectance of terrestrial surfaces is a phenomenon which has received much attention in the past twenty years due to the increased number and sophistication of satellite, aircraft, and ground based remote sensors. Remotely sensed reflectance measurements, such as satellite measurements, are intrinsically bidirectional due to the variation in position of both the source (sun) and sensor (satellite) relative to the target (area on earth) and the small field of view of the sensor. Terrestrial surfaces such as soil, vegetation, snow, and ice have shown to exhibit a wide variety of directional reflectance behavior. For example, smooth ice reflects incident light sharply towards the specular direction while dark soils reflect light strongly towards the backscatter or antisolar direction. Additionally, snow, fine white powders, and Spectralon and $BaSO_4$ calibration targets have shown to approximately reflect light diffusely (i.e. equal reflected radiance in all directions regardless of incident angle). This type of reflector is said to be Lambertian.

Most terrestrial surfaces have shown to exhibit anisotropic directional reflectance meaning that the reflected intensity is dependent upon both the source incident and receiver view angle. This directional anisotropy is both good and bad. On one hand this directional behavior can be used to infer the fundamental properties of the reflecting medium based upon bidirectional reflectance measurements since the fundamental physical and electromagnetic properties of the medium govern the light scattering process. On the other hand this nonlinear reflectance behavior makes satellite observations dependent upon the relative positions of the sun, earth, and satellite [1] making it difficult to distinguish between fluctuations in the received signal due to orientation differences and those associated with a change in the targets properties (i.e different soil type, change in vegetation, change in soil moisture, etc.). Furthermore, measurements acquired at the same location by different instruments cannot be directly compared. Lastly, anisotropic soil reflectance interferes with NDVI [2] and atmospheric measurements and must be accounted for similar to the way LOTRAN accounts for atmospheric fluctuations. Thus, there is a need to better understand the soil-radiation interaction so that useful models can be developed for routine data correction.

However light scattering from complex media is a complicated process and not understood well enough to make possible such a model. Thus, it is necessary to document reflectance behavior, investigate phenomena, and quantify parameter variations.

These goals are best accomplished by conducting controlled experimental measurements in parallel with theoretical investigation. The remainder of this paper contains a description of a newly built polarized bidirectional reflectometer and the first set of measurements acquired by the system. The polarized BRDF (HH & VH) of Spectralon is plotted as a function of receiver view angle for incident angles ranging from 0 to -60 degrees.

0-7803-3068-4/96$5.00©1996 IEEE

EXPERIMENTAL SET-UP

The instrument is illustrated in Fig. 1 and utilizes a 150 W Xe arc lamp as the source. The light emitted from the source is spectrally filtered by an optical bandpass filter, spatially filtered by a lens arrangement and an iris diaphragm, and directed through the center hole of rotary table 1. The light is then directed by a mirror through a polarizer and a chopper after which two additional mirrors direct the quasi-collimated light beam towards the target located at the center of the goniometer. A lens is used to focus the beam to a diameter of 1 cm at the target. Rotary table 1 controls the angle of incidence, rotary table 2 controls the receiver view angle and is motorized, and rotary table 3 controls the receiver azimuth angle.

The receiver separates the received radiation into two orthogonally polarized components (i.e. like- and cross-polarized components) and the relative intensity of these two components is quantified via a photodetector. If horizontally polarized (H) illumination is used then, like-pol=HH and cross-pol=VH, else for vertically (V) polarized illumination, like-pol=VV and cross-pol=HV where the first letter represents the received polarization and the second represents the transmitted polarization. Two Si over InGaAs sandwich type detectors are used and provide coverage from 400 nm to 1700 nm. The receiver has a 0.66 degrees field-of-view which correspond to a 1 inch diameter area at the target.

The motorized rotary table and detector electronics are connected to a motor driver board and data acquisition board, respectively, and are controlled by a computer.

The system was designed more as a polarized reflectometer than a spectrometer because of the usefulness associated with polarization information (i.e. how it relates to single and multiple scattering). Secondly, the system is designed so that true backscatter, incident irradiance, and transmission measurements can be obtained. Thirdly, the orientation is designed so that measurements from all unique positions are possible, and lastly the system is made versatile by using standardized optical rails and mounts which facilitate quick and easy modifications

MEASUREMENTS

The two most common reflectance nomenclature are the bidirectional reflectance distribution function (BRDF) and the bidirectional reflectance factor (BRF). Both involve normalizing reflectance to Lambertian behavior but the BRDF requires measuring the incident irradiance while the BRF references media reflection to a Lambertian reflectance standard for normalization.

For constant incident and azimuth angle the BRDF can be approximated by

$$f_r = \frac{\Phi_r}{\Phi_i \cos\theta_r \omega_r} \quad [\mathrm{sr}^{-1}] \qquad (1)$$

where Φ_r is the reflected flux [W] within the solid angle of the receiver (ω_r) located at (θ_r) which is measured by the detector and Φ_i represents the incident flux.

Spectralon is a common calibration surface and was used in the past by the author as a reference for BRF measurements. Thus the first set of measurements from the new instrument are obtained for Spectralon. Furthermore, the same surface is used by Irons and its unpolarized behavior was documented and is listed in [3]. The curves listed by Irons show no significant specular peaks whereas the curves listed in this paper do show significant peaks in the specular direction.

All measurements were acquired in the principle plane and were obtained with horizontally polarized illumination in the red (650 nm +- 20 nm). Similar measurements were acquired using a Laser (632 nm) and for vertically polarized illumination and the results were similar but are not listed in this paper.

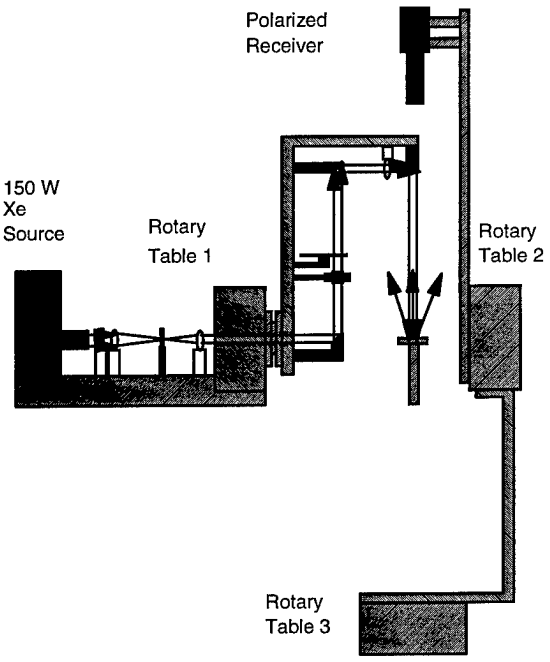


Figure 1 Polarized bidirectional reflectometer

The polarized BRDF as a function of receiver view angle for incident angles of 0, 20, 30, 40, 50, and 60 degrees are listed as Figure 1. Note the broad peak in the specular direction for the like-pol (HH) and the flat (i.e. Lambertian) cross-pol (VH). For normal incidence the depolarization ratio χ (VH/HH) is about 0.7 while for 60 degrees incidence it is about 0.1.

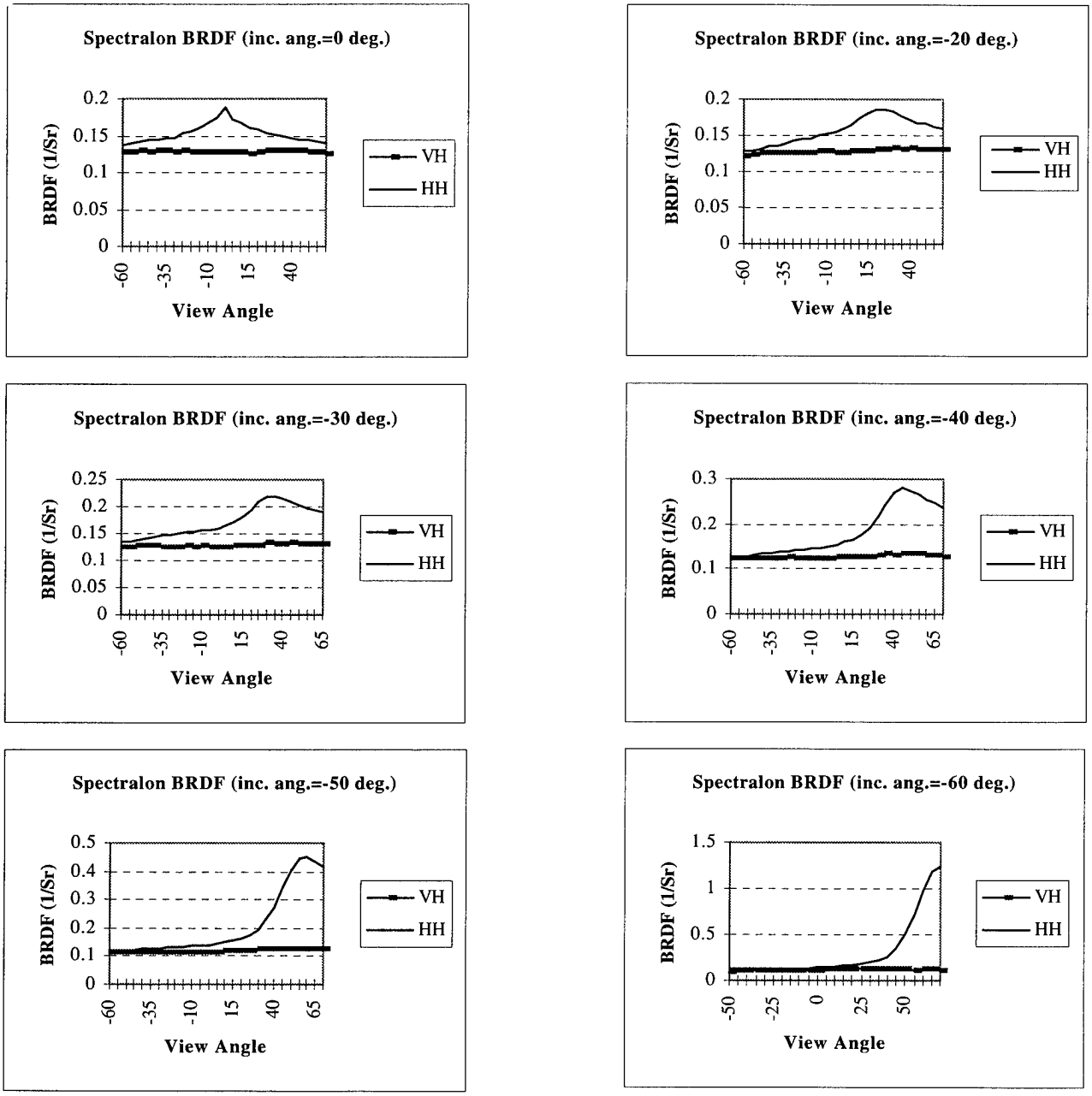


Figure 2 Spectralon polarized BRDF for various incident angles.

Conclusions

The Spectralon calibration target shows significant anisotropic scattering behavior for HH illumination and additional unpolarized measurements are planned. However, if unpolarized measurements indicate similar peaks then it is necessary to understand the discrepancy between the measurements listed in [3] and those obtained by the author. Possible causes for the discrepancy are differences between the two instruments fields-of-view and/or illumination area. If this is the case then future researchers must be careful about using Spectralon calibration curves obtained by one instrument to calibrate data acquired by another instrument.

References

[1] Roujean, I.J., Leroy, M., Deschamp, P.Y., and Podaire, A. (1990), A surface bidirectional reflectance model to be used for the correction of directional effects in remote sensing multitemporal data sets, In Remote Sensing Science for the Nineties, IGASS'90, College Park, MD., pp.1785-1789.

[2] Huete, A. R. (1988), A Soil-Adjusted Vegetation Index (SAVI), *Remote Sens. Enviro.* 25:295-309.

[3] Irons, James R. (1993), Solar Radiation Scattered by Soils, Ph. D. Dissertation, The University of Maryland.

Energy Conservation In Soil Surface Scattering In The Optical Region

Z. Li, A. K. Fung, S. Tjuatja and C. Betty
Wave Scattering Research Center
Department of Electrical Engineering
University of Texas at Arlington
Box 19016
Arlington, Texas 76019

J. R. Irons
Biospheric Sciences Branch, Code 923
Goddard Space Flight Center
National Aeronautics and Space Administration
Greenbelt, Maryland 20771

Abstract -- Most of the studies in the past used empirical phase functions that were not directly related to the physical and electromagnetic properties of the medium. These phase functions do not conserve energy. Although one can normalize these functions to realize conservation, no meaningful albedo or extinction properties can be derived from them, and energy transfer is not correctly represented. In fact, the albedo and extinction coefficient have to be determined separately and empirically. Furthermore, when these phase functions are incorporated into a scattering model, attempts to retrieve soil parameters from such models sometimes result in unstable conditions. The purpose of this study is to derive a phase function for soil based upon physical principles using a ray-tracing technique that allows the summation of multiply scattered rays. The final result is expressed in terms of the electromagnetic properties of soil. It is shown that such a phase function conserves energy and includes a proper amount of absorption. Then, by incorporating this phase function into a radiative transfer formulation, we arrive at a scattering model for the soil medium. The inputs to this model are particle and background permittivity, volume fraction, particle size relative to wavelength, and individual particle and soil surface roughness. The scattering model can be used for soil parameter retrieval without the problem of instability.

INTRODUCTION

In the radiative transfer theory, the energy transfer process is represented by the transfer equation based on correct representation of phase function, medium albedo, and extinction coefficient. A phase function used in the transfer equation is the normalized Stokes matrix that represents the spatial scattering energy distribution of a typical medium particle. As a result, it is not clear whether there is energy conservation in the derivation of a phase function. The energy conservation problem only occurs in the process to determine the medium albedo and extinction coefficient. Most of the phase functions used in the existing soil models are empirically chosen. For example, the widely used Greenstein function [1] is only a normalized empirical function with one parameter to adjust its shape, and Hapke [2] expands his phase function in series of Legendre polynomials. In those two cases, the scattered and absorbed energy can not be determined from the phase functions, and then parameters in the transfer equation are obtained separately and empirically. It is obvious that, as the phase functions vary, the parameters would not be able to change automatically and accordingly. Therefore, the energy transfer process in the medium is not correctly represented. Furthermore, the retrieval procedure turns out to be unstable [3].

To conserve the energy in the transfer process, it is essential that the phase function must be physically based, which normally is obtained by deriving Stokes matrix first and then normalizing it [4] [5]. In the present physical models, due to the approximations made to simplify Stokes matrix developments, the scattered and absorbed energy are either computed from the energy unconserved phase function [6] or obtained experimentally. Neither of them can accurately estimate the scattered and absorbed energy in the transfer process.

The purpose of this study is to derive a polarized phase function for soil based upon physical principles that conserves its energy. The final result is expressed in terms of the electromagnetic properties of soil. It is shown that such a phase function can accurately infer its scattered and absorbed energy. Then, by incorporating this phase function into a radiative transfer formulation, we arrive at a scattering model for the soil medium. The inputs to this model are particle and background permittivity, volume fraction, particle size relative to wavelength, and individual particle and soil surface roughness.

MODEL APPROACH

For an irregular soil particle whose size is much larger than a wavelength in the optical region, the conventional ray-tracing technique is impractical and the Mie theory is inefficient. The approach proposed in this paper is a ray-tracing like method. In this method, a light beam is

0-7803-3068-4/96$5.00©1996 IEEE

represented by a spatial distribution function and traced when the light beam encounters an interface. The interface of air and the soil particle viewed by the light beam is so rough and irregular that it can be modeled as an assembly of small facets that are uniformly oriented in the space. If for a one-direction incident light, the reflected and transmitted light beams distributed in the space are represented by $\boldsymbol{R}_{\mathrm{p}}$ and $\boldsymbol{T}_{\mathrm{pq}}$, which are called characteristic reflection and transmission matrix of the interface, then the response for a distributed incidence $\boldsymbol{G}_{in}$ will be

$$\boldsymbol{R}'_p = \iint_{4\pi} \boldsymbol{R}_p \cdot \boldsymbol{G}_{in} d\Omega \tag{1a}$$

$$\boldsymbol{T}'_{pq} = \iint_{4\pi} \boldsymbol{T}_{pq} \cdot \boldsymbol{G}_{in} d\Omega \tag{1b}$$

After these relations are established, each time the light encounters an interface between the air and the soil particle the reflected or transmitted light beam distribution can be calculated from the incident light beam and $\boldsymbol{R}_{\mathrm{p}}$ or $\boldsymbol{T}_{\mathrm{pq}}$. In the end we are able to trace out the incident light through the entire tracing process.

FORMULATION

Characteristic Matrices

To derive the characteristic reflection and transmission matrix $\boldsymbol{R}_{\mathrm{p}}$ and $\boldsymbol{T}_{\mathrm{pq}}$, first let (θ_i, ϕ_i) and (θ_s, ϕ_s) be incident and scattered direction, respectively. Note that the contribution to this scattered direction could be reflected or/and transmitted light. So $\boldsymbol{R}_{\mathrm{p}}$ and $\boldsymbol{T}_{\mathrm{pq}}$ are functions of the entire space, but they could be zero along some directions. In the case of reflection, since the facet is larger than the wavelength, law of reflection is employed to calculated the reflection. To do so, a local coordinate system is set up so that both the reflected and incident light are in the same plane. Applying the rotation conversion matrix [7] and considering the probability of the facet which is uniform [8], the reflection matrix is obtained as

$$\boldsymbol{R}_p(\Omega_s, \Omega_i) = \boldsymbol{C}' \cdot \frac{1}{4\pi} \boldsymbol{R}'_{\mathrm{p}} \cdot \boldsymbol{C} \tag{2}$$

In the case of transmission, we also need to set up a local coordinate system so that the incident and transmitted direction are in the same plane, go through the same procedure in the reflection case and finally arrive at

$$\boldsymbol{T}_{pq}(\Omega_s, \Omega_i) = \boldsymbol{C}' \cdot \frac{\sin\theta'_i}{\sin\theta'_s} \frac{n_2 \cos\theta'_t \cos\theta'_i}{\left| n_2 \cos\theta'_t - n_1 \cos\theta'_i \right|} \boldsymbol{T}'_{pq} \cdot \boldsymbol{C} \tag{3}$$

where $\boldsymbol{C}$ and $\boldsymbol{C}'$ are the rotation conversion and inverse conversion matrices defined in [7], $\boldsymbol{R}'_{\mathrm{p}}$ and $\boldsymbol{T}'_{pq}$ are reflectivity and transmissivity matrices defined in [7], and the prime in angles indicates those are local angles.

Tracing Process

The situation that the incident light penetrates into and bounces between interfaces inside the soil particle is conceptually depicted in Figure 1. Note that each time the light beam encounters an interface there is a light beam propagating away from the soil particle, which constitutes the Stokes matrix. In fact, our goal is to find out those light beam distributions. To this end, the light beams are categorized into three terms: direct reflection $\boldsymbol{S}_1$, direct transmission $\boldsymbol{S}_2$, and multiple reflection-transmission $\boldsymbol{S}_3$.

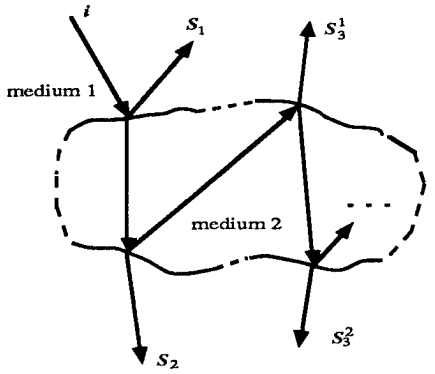


Figure 1 illustration of soil particle scattering

For $\boldsymbol{S}_1$, it is easy to show that

$$\boldsymbol{S}_1(\Omega_s, \Omega_i) = \boldsymbol{R}_1(\Omega_s, \Omega_i) \tag{4}$$

and for $\boldsymbol{S}_2$ it is also pretty straightforward to show that

$$\boldsymbol{S}_2(\Omega_s, \Omega_i) = \exp(-kn_{im}\bar{l}) \iint_{4\pi} \boldsymbol{T}_{12}(\Omega_s, \Omega') \cdot \boldsymbol{T}_{21}(\Omega', \Omega_i) d\Omega' \tag{5}$$

where k is the wavenumber in free space, n_{im} is the imaginary part of the index of refraction, and $\bar{l}$ is the average path of the light traveling inside the soil particle.

For $\boldsymbol{S}_3$, since it is a composite term, we need to figure out each subterm before summing them up. From equation (2), (3), and (5), it is seen that the interaction of the light and an interface is mathematically represented by an integration. Therefore, we have the following equations for those subterms.

$$\boldsymbol{S}_3^1(\Omega_s, \Omega_i) = \exp(-2kn_{im}\bar{l}) \int_{4\pi} \boldsymbol{T}_{12}(\Omega_s, \Omega'') \cdot \left[\int_{4\pi} \boldsymbol{R}_2(\Omega'', \Omega') \boldsymbol{T}_{21}(\Omega', \Omega_i) d\Omega' \right] d\Omega'' \tag{6}$$

and

$$\boldsymbol{S}_3^m(\Omega_s, \Omega_i) = \exp\{-(m+1)kn_{im}\tilde{l}\} \iint_{4\pi} \boldsymbol{T}_{12}(\Omega_s, \tilde{\Omega}''') \cdot \overbrace{\{\iint_{4\pi} \boldsymbol{R}_2(\tilde{\Omega}''', \tilde{\Omega}'') \cdots \iint_{4\pi} \boldsymbol{R}_2(\Omega''', \Omega'')}^{m-1} \cdot \left[\iint_{4\pi} \boldsymbol{R}_2(\Omega'', \Omega') \boldsymbol{T}_{21}(\Omega', \Omega_i) d\Omega' \right] d\Omega'' \cdots d\tilde{\Omega}'' \} d\tilde{\Omega}''' \tag{7}$$

Notice that the integration $\iint_{4\pi} \boldsymbol{R}_p(\Omega_s, \Omega_i) d\Omega_s$ and $\iint_{4\pi} \boldsymbol{T}_{pq}(\Omega_s, \Omega_i) d\Omega_s$, the energy of $\boldsymbol{R}_{\mathrm{p}}$ and $\boldsymbol{T}_{\mathrm{pq}}$, are independent of Ω_i. Thus, integrating $\boldsymbol{S}_3$ over scattered direction and

changing the integration orders, the total energy of S_3 is found to be

$$En(S_3) = \exp(-2kn_{im}\bar{l})En(T_{12})En(R_2)En(T_{21}) + \cdots + \exp\{-(m+1)kn_{im}\bar{l}\}En(T_{12})[En(R_2)]^m En(T_{21}) + \cdots = \frac{\exp(-2kn_{im}\bar{l})En(T_{12})En(R_2)En(T_{21})}{1-\exp(-kn_{im}\bar{l})En(R_2)} \quad (8)$$

From the above equation, S_3 is approximated by

$$S_3(\Omega_s,\Omega_i) = \frac{\exp(-2kn_{im}\bar{l})}{1-\exp(-kn_{im}\bar{l})En(R_2)} \iint_{4\pi} T_{12}(\Omega_s,\Omega'') \cdot \left[\iint_{4\pi} R_2(\Omega'',\Omega') \cdot T_{21}(\Omega',\Omega_i) d\Omega'\right] d\Omega'' \quad (9)$$

RESULTS AND CONCLUSION

To demonstrate the energy conservation property of the derived Stokes matrix, let us first examine the conservation property of the characteristic reflection and transmission matrix, $\boldsymbol{R}_p$ and $\boldsymbol{T}_{pq}$. Since the energy of an incident radiation splits into $\boldsymbol{R}_p$ and $\boldsymbol{T}_{pq}$ only, the sum of the energies of $\boldsymbol{R}_p$ and $\boldsymbol{T}_{pq}$ should be unity if energy is to conserve. Table 1 shows the calculated energies of $\boldsymbol{R}_p$ and $\boldsymbol{T}_{pq}$ and their sum for several indices of refraction and the cases that the incidence is in air and in soil particle. Note in the table, when the incidence is in soil particle, the energy of reflection increases dramatically as the index of refraction varies from 1.5 to 5.5. This phenomenon is caused by total reflection.

Table 1 The energy conservation of characteristic matrices

	incidence in air		
n	En($\boldsymbol{R}_1$)	En($\boldsymbol{T}_{21}$)	Sum
1.5	0.01283	0.98717	1.00000
2.5	0.05252	0.94747	0.99999
3.5	0.09304	0.90696	1.00000
4.5	0.13075	0.86925	1.00000
5.5	0.16532	0.83468	1.00000
	incidence in soil particle		
1.5	0.15104	0.84897	1.00000
2.5	0.55128	0.44872	1.00000
3.5	0.77010	0.22990	1.00000
4.5	0.87164	0.12836	1.00000
5.5	0.92187	0.07812	0.99999

The property of energy conservation of the Stokes matrix can only be illustrated under the condition that there is no loss inside the soil particle. Otherwise, it is difficult to tell if the unconserved energy is caused by loss or by its energy property. Table 2 shows the energies of three scattering terms and the total energy of the Stokes matrix for several indices of refraction and under condition where n_{im} is zero. Note in the table, the energy of S_3 increases rapidly as the index varies from 1.5 to 5.5, which indicates that the amount of energy trapped in the soil particle by total reflection and eventually escaping the particle increases dramatically with index of refraction. So S_3 is definitely not a small quantity that can be neglected in the derivation of the phase function.

Table 2 The energy conservation of the Stokes matrix

n	En(S_1)	En(S_2)	En(S_3)	Total
1.5	0.01283	0.83791	0.14911	0.99985
2.5	0.05252	0.42513	0.52249	1.00014
3.5	0.09304	0.20850	0.69861	1.00015
4.5	0.13075	0.11158	0.75745	0.99978
5.5	0.16532	0.06521	0.76948	1.00001

From this study, it is shown that the phase function so derived obeys energy conservation. Thus, by incorporating such a phase function into a radiative transfer equation, it is believed that the energy transfer process is more accurately represented and then renders a more accurate solution. Such a study lends more confidence to the model derived.

Acknowledgment: This work was supported by NASA grant, NAGW-3421.

REFERENCES

[1] Henyey, C. And Greenstein, J. (1941), Diffuse radiation in the galaxy. *Astrophys. J.*, 93:70-83.

[2] Hapke, Bruce (1981), Bidirectional Reflectance Spectroscopy 1. Theory, *Journal of Geophysical Research*, Vol. 86, No. B4, pp 3039-3054.

[3] Pinty, Bernard, Verstraete, Michel M., and Dickenson, Robert E. (1989), A Physical Model for Predicting Bidirectional Reflectances over Bare Soil, *Remote Sens. Enviro.* 27:273-288.

[4] Ishimaru, Akira (1978), Wave Propagation and Scattering in Random medium, Vol 1, *Academic Press*, New York.

[5] Fung, A.K. (1994), Microwave Scattering and Emission Models and Their Applications, *Artech House*, Boston.

[6] Aronson, J. and Emslie, A. (1975), Applications of infrared spectroscopy and radiative transfer to earth sciences. *In Infrared and Raman Spectroscopy of Lunar and Terrestrial Minerals*, ed. C. Karr (pp 143-64), New York: Academic Press.

[7] Li, Z., Fung, A.K., Tjuatja, S., Gibbs, D., Betty, C., and Irons, J.R. (1994), A Modeling Study Of Backscattering From Soil Surfaces, *IEEE Trans. On GeoSci. And Remote Sensing*, volume 34, pp 264-271, Jan.,1996.

[8] Li, Z., Fung, A.K., Tjuatja, S., Gibbs, D., Betty, C., and Irons, J.R. (1995), A Bidirectional Scattering Model for Soil Surfaces, *IGARSS*, 1995.

Optical versus Radar Roughness in Agricultural Tillage

Bruce G. Colpitts
Department of Electrical Engineering
University of New Brunswick, P.O. Box 4400
Fredericton, NB, Canada, E3B 5A3
Tel.(506)447-3139, Fax.(506)453-3589, email colpitts@unb.ca

ABSTRACT

The relationship between soil roughness as measured with an optical roughness meter and soil roughness causing microwave radar scatter is explored. Optically measured soil profiles and associated soil moisture measurements will be analyzed using the FDTD technique to solve for the electromagnetic fields within the soil. Through the volume equivalence theorem these fields can be shown to generate the radar backscatter. The microwave roughness can then be defined in terms of the shape of these equivalent currents in the soil. Changes in both the rms surface roughness and the surface autocorrelation between optical and microwave roughness are shown.

INTRODUCTION

Application of this work is in the analysis of radar backscatter from agricultural tillage with the objective of uncoupling roughness and moisture information using multi-incidence angle data as provided by RADARSAT. The major requirement for achieving this is an adequate model relating soil properties and incidence angles to backscatter. Conventional rough surface scattering models derived using ideal surfaces are limited in their applicability particularly when optically measured roughness is used as input. This work elucidates the scattering mechanism using FDTD and demonstrates the need for alternative roughness parameters for use in conventional scattering models.

The Integral Equation Model (IEM) [1] has been shown to reduce to the geometric optics and small perturbation "classic" models in the limiting cases [2] but is valid over a wide range of surface roughnesses. The inadequacy of these classical solutions is demonstrated in [3] even in cases where the surface statistics are valid. Yet it is shown in [1] that for ideal rough surfaces such as perfect conductors or high dielectric surfaces that the IEM is valid. This raises the question of the behaviour of the soil surface as compared to the ideal surface. An actual soil surface can take a multitude of forms in terms of both roughness and moisture. A rough surface can have undercutting of the large clods which do not appear in an optical observation from above and create havoc with surface roughness statistics. The geometry of the clods will cause air to be trapped in the near surface layer causing voids which can have dimensions comparable to the wavelength. Also the moisture is usually increasing with depth into the soil unless there has been recent rain or irrigation. Thus the soil is not a homogeneous dielectric that begins immediately below the optical profile and extends to infinity. Therefore until we are better able to analytically model the near soil surface the empirical models such as [3] are likely to yield superior results in the extraction of soil moisture and roughness information from radar observations.

The objective is to create an equivalent surface roughness that incorporates the microwave interaction with the soil but retains the concept of rms surface roughness and autocorrelation function for use in models such as the IEM. This will allow the computational benefits of a surface scattering model while retaining the accuracy of a full electromagnetic scattering analysis.

ROUGHNESS OF SURFACE CURRENTS

As the radar signal impinges on a rough soil surface it excites microwave currents in the soil throughout a layer near the surface. For a perfectly conducting surface the currents flow only on the surface. The far-field scatter can be found by integrating these currents throughout the volume illuminated by the antenna beam [4].

The equivalent roughness has been termed the microwave roughness [5] as is obtained in this two-dimensional simulation through evaluation of the soil currents. An optically measured soil profile, measured soil moisture and soil constituents are used in a FDTD simulation to produce the soil currents as a function of depth that are excited by a uniform plane wave with a zero degree incidence angle. Fig. 1 shows the currents within the soil. Conversion of the currents into roughness is achieved by translating all the currents in one soil column onto a plane above the soil. The process involves phase shifting each current element to the plane directly above the soil and summing all these current

NSERC support of this work is acknowledged.

0-7803-3068-4/96$5.00©1996 IEEE

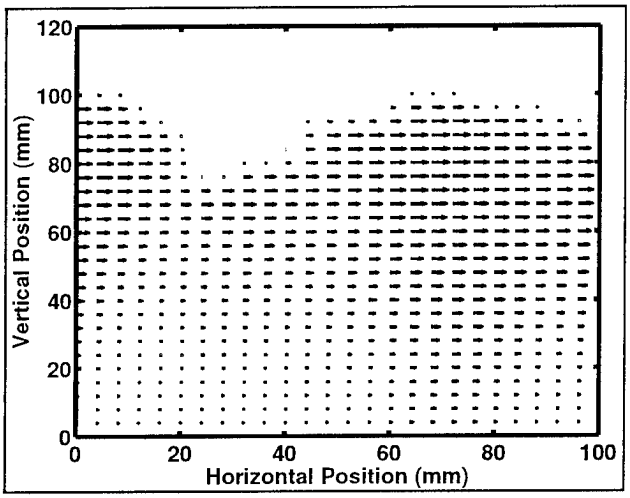


Fig. 1. Arrow plot of horizontal soil currents excited in a two-dimensional cross-section of moldboard tillage. Longer arrows indicate larger currents.

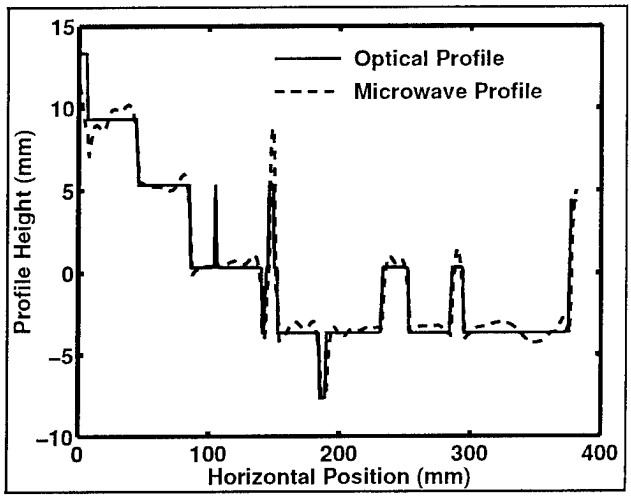


Fig. 3. Surface profile of seedbed tillage measured optically and the equivalent surface roughness associated with the microwave currents.

elements. The resulting phase of this near reflected field contains the roughness information but is double since propagation to and from the surface is included. The electrical phase is converted into distance based upon the wavelength in free space and divided by two in order to be consistent with surface effects. This soil profile is related to what the microwave radar sees in that the fine detail of the surface is lost as would be expected with a signal having a wavelength of 56 mm.

RESULTS

Figures 2 and 3 show optical and microwave surface profiles for moldboard and seedbed tillage respectively. From these one can see the basic profile shape is retained but sharp or rapidly changing features are rounded.

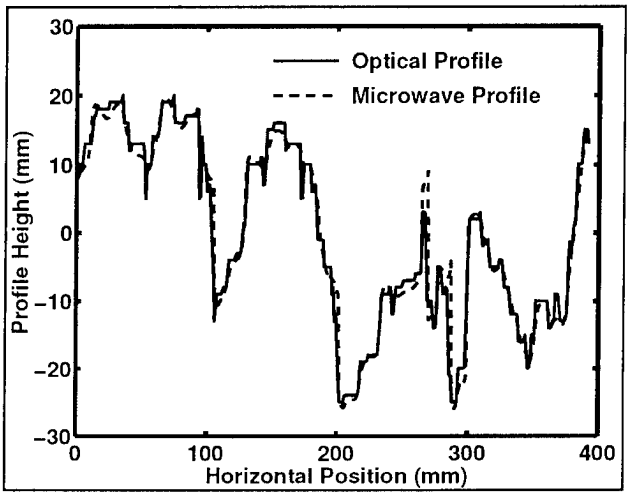


Fig. 2 Surface profile of moldboard plough tillage measured optically and the equivalent surface roughness associated with the microwave currents.

The net effect shows a very slight reduction in the rms surface roughness and change in the autocorrelation function in that the higher frequency surface roughness components are reduced. The surface roughness for the moldboard tillage is 13.3 mm when measured optically and 13.2 mm as determined from the microwave current. In the seedbed optical roughness is 4.8 mm and microwave roughness 4.6 mm. Consideration needs to be given in this two-dimensional simulation to the fact that the modeled profile is a corrugated surface in that these peaks and troughs extend to infinity and are not the simple peak expected in actual situations. Thus a three-dimensional model is expected to show a greater difference between optical and microwave results than this two-dimensional case.

The autocorrelation functions shown in Fig. 4 show little difference in the moldboard tillage between optical and microwave while in the seedbed case the optical roughness shows higher frequency components than the microwave profile.

The usual practice is that the correlation length of the surface roughness is determined and a Gaussian, exponential, modified-exponential, two-parameter or 1.5 power correlation function assumed. Each of these functions produces a change in the assumed surface spectral content and thus a change in backscatter. By selecting one of these functions the user is moving from the actual optical surface to some other surface. This choice may be made for computational reasons but often results in superior agreement with experimental results. That is, a surface closer to that seen by the microwave energy has been chosen rather than the optical surface.

An extensive three-dimensional study of soil currents is expected to yield the necessary parameters in order to predict microwave scattering using conventional models with

microwave roughness parameters.

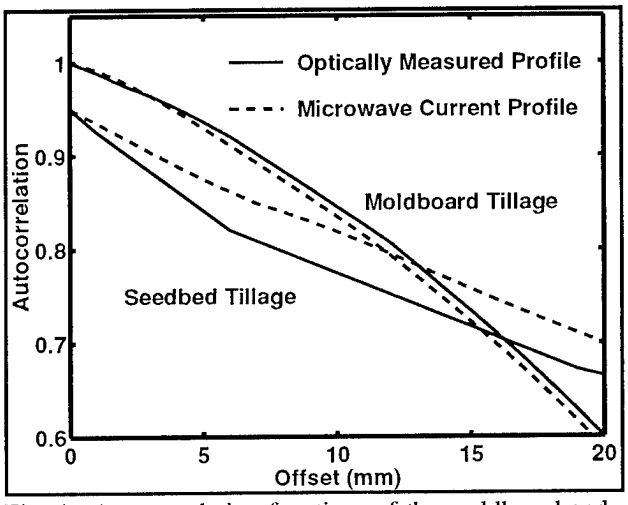


Fig. 4. Autocorrelation functions of the moldboard and seedbed profiles shown in Fig. 2 and Fig. 3. The seedbed autocorrelation functions are reduced by 0.05 for clarity.

CONCLUSIONS

A redefinition of roughness is important if rough surface scattering models such as the IEM are to be used in separating soil roughness and moisture information using multi-incidence angle measurements. Empirical scattering models such as [3] have been used to produce results superior to the analytical surface scattering models [3]. This work shows that the microwave signal is responding to a surface that is not the same as the optical surface and therefore the surface parameters need to be redefined in terms of what the microwave energy is responding to.

ACKNOWLEDGMENTS

Thank you to the Canada Centre for Remote Sensing for providing the surface roughness profiles used in this study.

REFERENCES

[1] Fung, A.K., Microwave Scattering and Emission Models and Their Applications, Artech house, Norwood, MA, 1994.

[2] Fung, A.K., Z. Li, and K.S. Chen, "Backscattering from a Randomly Rough Dielectric Surface," IEEE Trans. Geosci. Remote Sensing, vol. 30, no. 2, pp. 356-369, March 1992.

[3] Oh Y., K. Sarabandi, and F.T. Ulaby, "An Empirical model and an inversion Technique for Radar Scattering from Bare Soil Surfaces," IEEE Trans. Geosci. Remote Sensing, vol. 30, no. 2, pp. 370-381, March 1992.

[4] Balanis, C.A., Advanced Engineering Electromagnetics, John Wiley & Sons, Toronto, 1989.

[5] Colpitts, B.G., and J.B. Boisvert, "Application of the Integral Equation Model in Prediction of Radar Backscatter from Agricultural Land," 17th Canadian Symposium on Remote Sensing, June 13-15, 1995, Saskatoon, Saskatchewan, Canada, pp. 454-459.

The Soil Surface Reflectivity in the Partial Coherent Microwaves at the Frequencies 300 and 900 MHz

P.P.Bobrov, I.M.Schetkin

Omsk State Pedagogical University, 14, Tuckhachevsky Embankment, Omsk, 644099, Russia
Tel: 7 381-2-24-37-95 Fax: 7 381- 2-23-12-20 E-Mail: fis@lvt.ospi.omsk.su

Abstract —The results of soil reflection characteristics investigation are presented. Reflection coefficients of air-soil interface have been measured by the special wideband noise reflectometer for the waveguide loaded with quarter- wavelength flange in contact with tested media. The field measurement program was undertaken in Altai region and in Omsk Region. Most measurements were made with loamy soil . It was found that microwave reflectivity correlated with the soil moisture in the 100 cm depth at the 300 MHz and in the 40 cm depth at the 900 MHz. One purpose was to test the accuracy of numerical calculation derived from multilayer model of soil.

INTRODUCTION

It is known that the soil moisture sampling depth of the microwave sensors is only a few tenths of a wavelength [1]. As expected, the longer wavelengths showed a greater ability to penetrate a loss dielectric media and a deeper soil moisture sampling depth. Because of increasing the sky emission and interference from man-made sources the passive method is useless at these frequencies. We used the active method with noise generator as a source of radiation and open-ended rectangular waveguide as antenna. In this paper we present the results of soil reflectivity measurement. A relationship between soil water content in the layer up to 100 cm and the reflectivity at frequencies of 300 and 900 MHz are established. These results are evaluated numerically using multilayer model of a soil.

EXPERIMENT DESCRIPTION

The geometry of system performance are demonstrated in Fig.1. For reflectivity measurements the same antenna can be applied for both transmitting and receiving. As an antenna the open-ended rectangular waveguide was used. The waveguide was loaded with qarter-wavelength flange in contact with soil surface. The transmitter was a noise generator, whose signal was amplified, transmitted through circulator, modulator and the reflected from soil surface signal was received via a circulator. The reflectometer bandwidth is amounted to 50 percents at 300 MHz and 20 percents at 900 MHz. The wide bandwidth was used to minimize the multiply reflection effects from soil homogeneous and within the antenna feed system.

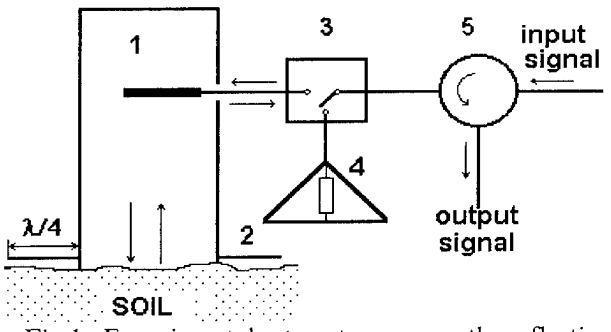


Fig.1. Experimental set-up to measure the reflection coeffisient of the soil. 1 - rectangular open-ended waveguide, 2 - quarter-wavelength flanger, 3 - modulator, 4 - matched load, 5 - circulator.

This experiment was conducted in Altai region and in Omsk Region. The objectives were 1) to determine the relationship between the reflection coefficient and soil moisture content, 2) to identify the soil layer measured sampling depth. The first series of measurement were made under the native soil moisture conditions. The plots were then irrigated for a few days. The soil reflectivity was measured by comparison with that of a water surface and a metal sheet. The soil reflectivity measurements have been accompanied by measurements of the soil characteristic. Gravimetric soil moisture and soil balk density were evaluated at depth intervals at 0-10, 10-20, ... 90-100 cm. The typical volumetric soil moisture vertical profiles are represented in Fig.2. The granulometric analysises for some samples was made.

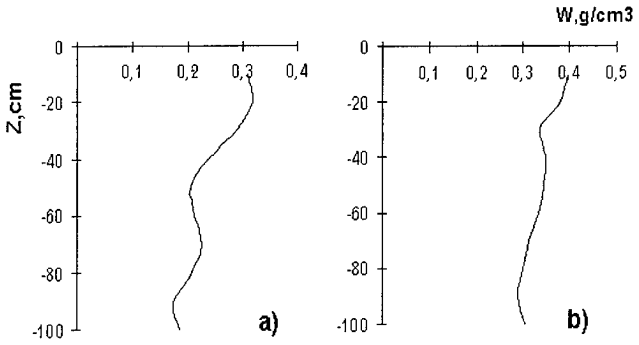


Fig. 2. The typical soil moisture vertical profile for (a) and after (b) irrigation.

0-7803-3068-4/96$5.00©1996 IEEE

DATA ANALYSIS

The reflection coefficients at the frequency of 300 and 900 MHz as a function of the average soil moisture in the layer of 0-80 cm and 0-10 cm, respectively, are displayed in Fig. 3. We can recognize two data groups: the one

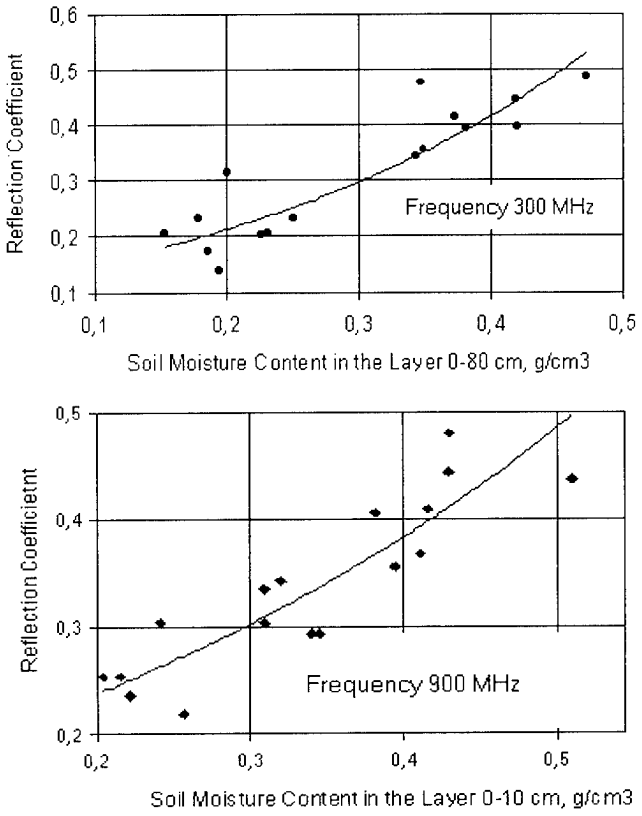


Fig.3. Relationship between average volumetric soil moisture and reflection coefficient.

corresponding to native condition of the soil moisture; the second data group has a greater reflectance caused by artificial irrigation. This difference of reflectivity of native and irrigated samples happened only at 300 MHz because the rise of the soil water content is more considerable in the lower layers (See Fig.2). The best overall linear correlation was between soil moisture and reflection coefficient R at a frequency 900 MHz. We arrived at this conclusion by analyzing plots, such as Fig.4 that shows the correlation coefficient as a function of the soil moisture in the 10-cm thickness layers at the different depth "d" (Fig.4,a) and a function of the soil moisture in the layer of increasing thickness from 0 to Z (Fig.4,b). We observed that the trend was for correlation to increase to a maximum at about 50 cm depth for 300 MHz and about 10 cm depth for 900 MHz. Volumetric soil moisture - R correlation decreased with increasing depth more

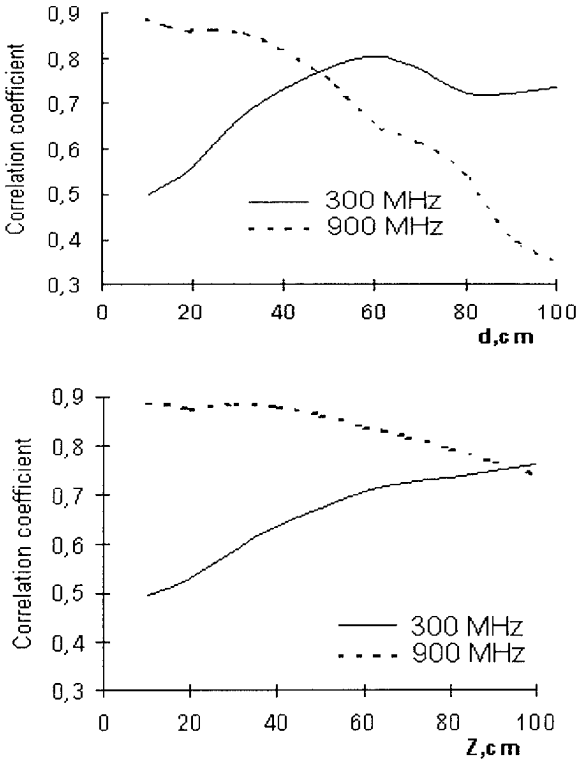


Fig.4. Volumetric soil moisture - reflectivity correlation as a fumction of the depth of 10 cm - thickness layer (a) and as a function of thickness of an upper layer (b).

significant at 900 MHz due to low wavelength and, consequently, low measured sampling depth.

A possible reason of low correlation at the frequency of 300 MHz is the errors of measurement because of the wave divergence and the diffraction effect which have the greatest influence at the high wavelength. Fig.4,b shows the improvement in the correlation at the frequency of 300 MHz when a deeper soil depth was used. The high correlation is also at the frequency 900 MHz up to 40 cm depth. To explain this behavior we take into account that the soil moisture in the surface layer is usually correlated with the soil moisture in lower layers.

COMPARISON OF MEASUREMENT WITH THEORY

If we consider a soil as a multilayer media then the air-soil reflectivity may be determined by using very known equation for two-layer media:

$$r'_{0,1} = \frac{r_{0,1} + r'_{1,2} exp(2jk_1\Delta Z)}{1 + r_{0,1} r'_{1,2} exp(2jk_1\Delta Z)} \qquad (1)$$

where - $r'_{0,1}$ is the reflectivity of a multilayer media at the air-first layer boundary, $r_{0,1}$ is Frenel's reflection coefficient at this boundary, $r'_{1,2}$ is reflectivity a multilayer media, living under the first layer, it can be found by using equation similar to (1), $k_1, \Delta Z$ is wave number and thickness of the first layer, respectively. It assumes that every layer consists of a homogeneous media. Reflectivity of the soil surface depends on the dielectric properties of the soil.

We used the model of dielectric properties developed by Wang and Schmugge [2] and supposed the real part of the dielectric permittivity at frequency of 300 MHz is to be fairly similar to that at 900 MHz. The results of computations of reflectivity of different soil class are presented in Fig.5. It is assumed that the soil moisture vertical profile is uniform. Comparison of these results with measured data (Fig.3) shows a good coincidence of the computed values and the empirical trend lines for the loamy soil which have a dielectric properties similar to that of the clay.

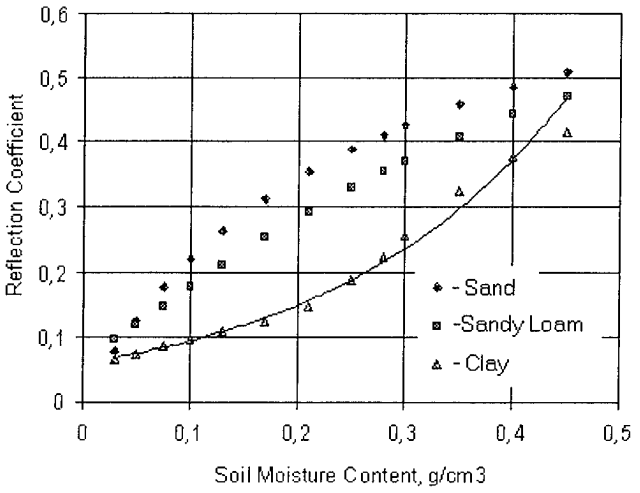


Fig.5. The calculated reflectivity of different soil class.

The calculation results derived from multilayer model are demonstrated in the scatter plot (Fig.6). The straight line corresponds to $R_C=R_M$, where subscript C and M refer to calculated and measured values, respectively. The considerable scattering of points takes place. It seems that variations in the measured reflectance are not associated with multiple reflections from an internal layer boundary. Bat the most likely reason of this point scattering could come from the significant variation in the vertical distribution of the soil moisture at the native conditions. This conclusion follows from the fact that the more considerable scattering take place at the low soil moisture content and at the highest wavelength . In the model only the average soil moisture in the 10-cm layers is taken into

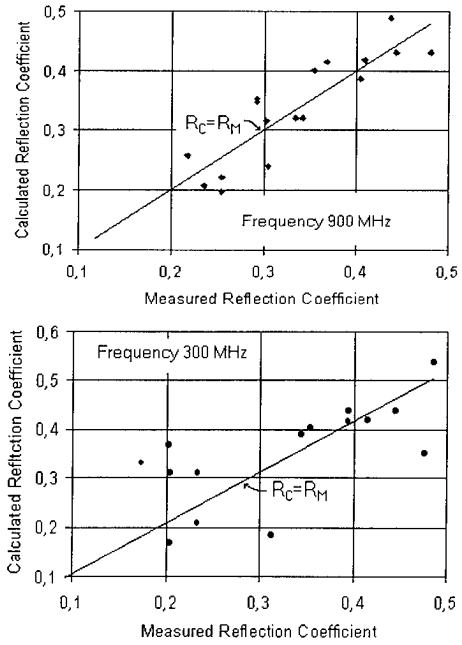


Fig. 6. Comparision of the measured and calculated data.

account and it assumed a uniform soil moisture distribution in the one layer. Probably, this point scattering occurred because the model did not consider the incoherent part of the probing signal.

When we analyzed data to determine if the measured - calculated reflectivity relationship could be improved by choosing of image part of the permittivity in the model calculating, we found that image part of the permittivity at frequency 300 MHz less then that at 900 Mhz.

CONCLUSION

Many experiments using active microwave system to determine the soil moisture- reflectance relationship have been conducted. Linear correlation analysises were performed to relate the reflection coefficient to the volumetric soil moisture. The results of experiments indicate that the maximum depth of measured soil layer is about 40 cm at 900 MHz and 1 m at 300 MHz.

REFERENCES

[1] J.R.Wang, T.J.Schmugge, "An Empirical Model for the Complex Dielectric Permittivity of Soil as a Function of Water Content", IEEE Trans. on Geosci. and Remote Sens., vol.GE-18, N 4, pp.288-295, 1980.

[2] T.J.Schmugge, P.E.O'Neil, J.R.Wang, "Passive Microwave Soil Moisture Research", IEEE Trans. on Geosci. and Remote Sens., vol.GE-24, N 1, pp.12-22, 1986.

Laboratory Investigations of the Hydrodynamics and Radar Backscattering Properties of Breaking Waves

Guy Meadows[1], Eric B. Dano[1], David R. Lyzenga[1], Hans VanSumeren[1], Robert Onstott[2] and Donald E. Lund[1]

[1]The University of Michigan
Department of Naval Architecture and Marine Engineering
Ann Arbor, MI. 48109-2145
PH: (313) 764-6470, FAX: (313) 936-8820;
EMAIL :gmeadows@engin.umich.edu, ebd@engin.umich.edu, lyzenga@umich.edu, vansumer@engin.umich.edu, dlund@engin.umich.edu

[2]The Environmental Research Institute of Michigan, Center For Earth Sciences
P.O. Box 134001 Ann Arbor, MI. 48113-4001
PH: (313) 994-1200 x2544, FAX: (313) 665-6559; EMAIL : onstott@erim.org

Abstract -- An experiment was conducted in a 110m x 7.6m x 4m deep Marine Hydrodynamics facility to study the hydrodynamics of intermediate scale breaking waves and how they effect radar backscatter. An energetic spilling breaking wave, characterized by considerable whitecapping, was chosen for analysis. To characterize the wave, an array of seven capacitance wave probes were placed throughout the test basin. The waveprobes observed the temporal evolution of the breaking waves at multiple spatial locations, and were used to determine the spectral content of the pre and post-breaking small scale roughness. Wave probe data showed that the breaking wave reached its greatest amplitude at breaking and then decreased rapidly thereafter. Spectral analysis of the waveprobe data showed that prior to wave breaking, the spectral wave energy was confined to the low frequency wave components of the generated wave group. After breaking, some energy was transferred to high frequency waves, and some energy was dissipated. The energy transferred to the high frequency waves appeared as small scale roughness and was found to influence the radar backscatter.

EXPERIMENTAL DESIGN

Capacitance waveprobes were used as the primary wave characterization sensors in this experiment. Wave probes determine the instantaneous wave height at a point by comparing the outputs of an internally mounted local oscillator and variable oscillator. The variable oscillator is connected to a wave probe element (acting as a variable capacitor) and changes its output frequency based upon the instantaneous water height on the probe. The outputs of the two oscillators are then mixed and converted to a voltage, linearly proportional to the wave height. The wave probes were sampled at 100 Hz., and were accurate to 0.5 mm. Waveprobe locations were referenced to the wavemaker, and are listed in Table 1.

The breaking waves were generated using a wedge shaped wave maker with a 30 degree face. The wavemaker was programmed to produce a sinusoidal output that was linearly decreasing over a small bandpass of frequencies. The frequency components were chosen, based upon linear wave theory, to create waves that would add constructively and break at a given location [1]. The spilling breaking waves were generated using frequencies from 0.75 Hz to 1.2 Hz.. Waves produced at these frequencies ranged from deep to intermediate depth gravity waves. Using linear wave theory and the deep water approximation, the maximum phase speed can be found to equal 2.08 m/s. [2].

To ensure the repeatability of each run, both intrusive (capacitance wave probes) and nonintrusive (laser sheet and video) techniques were used to monitor the waves. The water level was maintained at a constant level throughout the experiment and cleaned with several surface skimmers between each series of runs.

A comprehensive description of the radar and how it was positioned in this experiment is found in [3].

Table 1.

	Downrange Distance
Wavemaker	0 m
Waveprobe #1	7.6 m
Waveprobe #2	11.4 m
Point of Breaking	20.7m
Waveprobes #3,4	20.9 m
Waveprobes #5,6	21.0 m
Waveprobes #7	23.8 m

0-7803-3068-4/96$5.00©1996 IEEE

TEMPORAL DATA

The time series data from the waves probes was used for several purposes. Time plots of waveprobes nearest the wavemaker (#s 1 and 2), were used to monitor the consistency of the generated wave group and ensure the repeatability of all runs. The wave probes nearest wave breaking (#s 3, 4, 5 and 6), were used to analyze the shape of the of the wave at breaking. Fig. 1 shows a representative waveprobe measurement 20 cm past breaking (as defined by initial roughness on the wave face). This measurement was taken prior to the collapse of the wave crest. As can be seen, the breaking wave is highly peaked and has achieved the highest amplitude in the wave group (t=33.6 sec). Video analysis of the breaking wave found the wave crest collapsed 30 cm beyond breaking. At this point, the wave amplitude decayed rapidly to approximately one fifth of its peak amplitude. The wave then continued to propagate down the tow tank with a constant amplitude rounded crest (Fig. 2, t=35 sec).

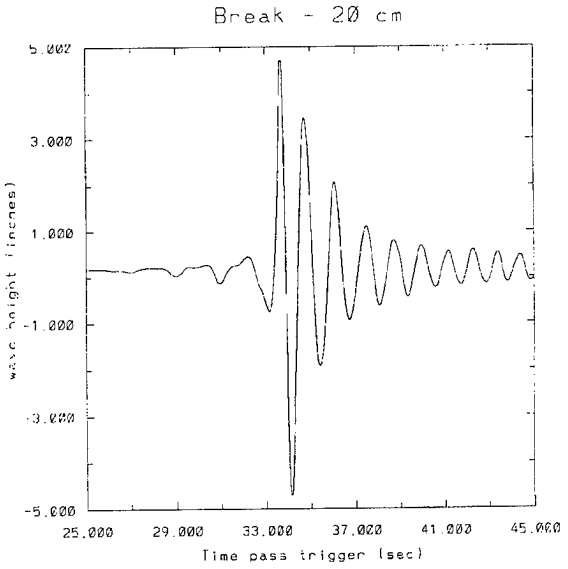


Fig. 1

SPECTRAL DATA

The temporal data from all the waveprobes were Fast Fourier Transformed (FFT) over 0.64 second intervals, and then averaged over 64 FFTs. This technique greatly reduced the speckle in the data and yielded resolutions of 1.56 Hz.. Representative plots of the waveprobes power spectral densities are shown for a pre-breaking case, and two post-breaking cases with increasing distances from the point of breaking (Fig. 2).

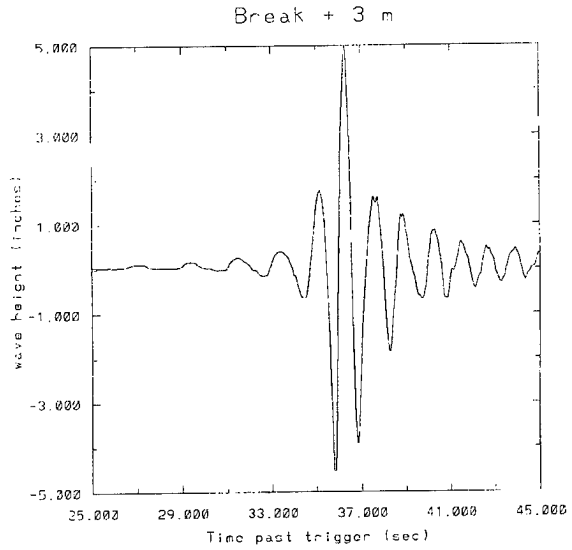


Fig. 2

The power in the pre-breaking spectrum is primarily confined to a frequency range of 0.75 to 1.2 Hz. This is the range of wave frequencies generated by the wavemaker, and could be expected. The power drops off rapidly beyond these frequencies and may be considered the high frequency noise floor for the waveprobe measurements. Integrating over the whole pre-break spectrum yields a total spectral power of 44.31 cm2 (6.87 in2). This power was constant in the waveprobes located prior to breaking (#s 1 and 2) and will act as a reference for total wave group power.

To analyze the evolution of the breaking waves, a two-scale approach will be utilized. Waves of frequency less than 2 Hz. will be considered "low" frequency, whereas waves with frequencies greater than 2 Hz. will be considered "high" frequency. This analysis yields a low frequency wave power of 44.25 cm2 (6.86 in2), and a high frequency wave power of 0.06 cm2 (.01 in2) for the pre-breaking case.

The first post-break spectrum was from a waveprobe located 30 cm past wave breaking. As discussed previously, the wave crest was collapsing and the amount of small scale roughness was observed to increase dramatically at this point. The spectral power attributed to the post-break roughness, is distributed from 4 to 15 Hz..

Integrating the spectral density over frequency yields a total spectral power of 33.23 cm2 (5.15 in2). This is a 25% reduction in total wave group power, and indicates that power is dissipated away very early in the wave breaking process. This case yields a low frequency wave power of 32.97 cm2 (5.11 in2), and a high frequency wave power of 0.26 cm2 (0.04 in2). This indicates that some power has been transferred from the low to high frequency waves.

The second post-break spectrum was from a waveprobe located 3 m from breaking. The total spectral power for this

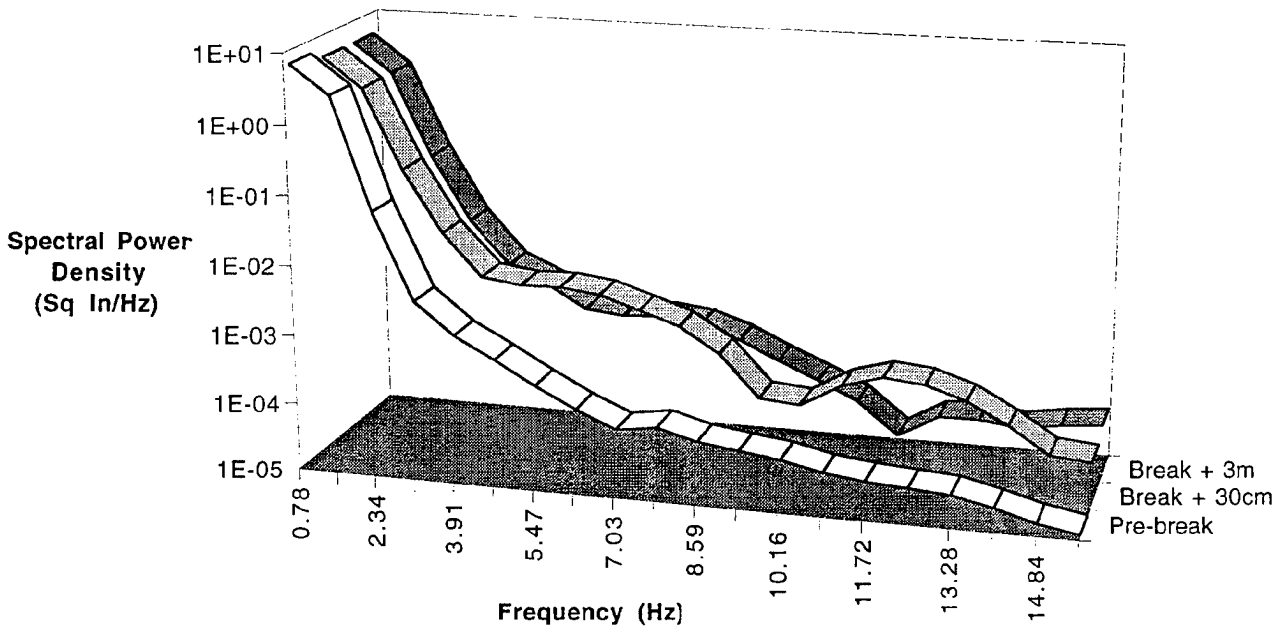


Fig. 3 Power Spectral Densities of the Spilling Breaking Wave.

case was found to be 32.77 cm2 (5.08 in2). This shows that an additional 1.0% of the initial wave group power dissipates between 30 cm and 3 m after breaking. The power in the low frequency waves was found to have increased 10% from the last waveprobe. This can be attributed to the growth of other waves in the wave group, and is evidenced in Fig. 2 (t=36.2 sec). The high frequency waves decreased in power from the last wave probe to a value of 0.13 cm2 (0.02 in2). This is due to the rapid decay of the high frequency waves generated by wave breaking.

The post-break roughness was shown to influence the radar backscatter at several azimuth angles [3], and may be correlated to high frequency wave spectral power.

CONCLUSIONS

Temporal and spectral data were presented from several wave probes used to characterize an energetic spilling breaking wave. The breaking wave was shown to have its maximum amplitude at breaking and to quickly collapse 30 cm past breaking. The total power of the wave decreased throughout breaking, dissipating 25% of the original wave group power within the first 30 cm of breaking, and an additional 1.0% in the next 3 m.

A two-scale approach was taken to analyze the waveprobe spectra, with 2 Hz. separating the low and high frequency wave regions The low frequency waves decreased in power after breaking, but then increased as other waves in the wave group steepened. The high frequency waves increased in power after breaking, but then decreased as the small amplitude waves decayed.

The amount of power in the high frequency waves appears to correlate with backscattered power from the post-break small scale roughness, and will be a subject of future research.

ACKNOWLEDGMENTS

This research was funded under the Office of Naval Research, Contract # N00014-92-5-1650. The authors would also like to thank Messon Gbah and Lorelle Meadows for their help in processing the wave probe data.

REFERENCES

[1] M. Davis and E. Zarnick, "Testing ship models in transient waves," Proceedings 5th Symp. Naval Hydro., p507, 1964.

[2] G. Crapper, "Introduction to Water Waves," John Wiley & Sons, New York, p. 35, 1984.

[3] E. Dano, D. Lyzenga and G. Meadows, "Doppler characteristics and angular dependence of radar backscatter from laboratory breaking waves," Proceedings 1996 IEEE IGARSS, in press.

Doppler Characteristics and Angular Dependence of Radar Backscatter From Laboratory Breaking Waves

Eric B. Dano, David R. Lyzenga and Guy Meadows

The University of Michigan
Department of Naval Architecture and Marine Engineering
Ann Arbor, MI. 48109-2145
PH: (313) 764-6470, FAX: (313) 936-8820;
EMAIL : ebd@engin.umich.edu, lyzenga@umich.edu, gmeadows@engin.umich.edu

Abstract -- Radar backscatter measurements were conducted on transient breaking waves in a 330 foot laboratory wave facility. The radar measurements were taken using a dual polarization K-Band (24.125GHz) CW Doppler radar positioned at various azimuth angles relative to the direction of wave propagation. Backscatter measurements were made for low energy (minimal whitecapping) and high energy (considerable whitecapping) spilling breaking waves. The peak radar cross section (RCS) was found to be the same for both breaking waves and occurred in the upwave look direction, just prior to whitecapping. Azimuthal radar measurements yielded variations on the order of 17dB with the lowest RCS values occurring in the crosswave direction. The Doppler spectra of the upwave radar returns contained a narrow peak corresponding to the phase speed of the underlying long waves. The downwave radar returns yielded broad Doppler spectra corresponding to a distribution of velocities.

EXPERIMENTAL DESIGN

Design of the K-band CW Doppler radar used in this experiment is described in detail in [1]. Both internal and external calibrations were performed on the radar [2] to ensure accurate RCS measurements and spectral information. The K-band CW Doppler radar was operated at an incidence angle of 40 degrees, and manually positioned to obtain azimuth angles of 0, 45, 90, 135 and 180 degrees relative to the direction of wave propagation. Radar absorbent material was used to restrict the radars energy to the water surface and prevent contamination from secondary reflections. The 10dB footprint was approximately 40cm by 50cm, and the radar was sampled at 512 Hz..

A comprehensive description of the wave generation techniques, frequencies used and surface characterization techniques can be found in [3].

TEMPORAL DATA

The radar was positioned so that wave breaking (as defined by visible whitecapping) occurred at the center of the radar footprint. A plot of the peak RCS per unit area (σ^o) for each azimuth run is plotted for the low (Fig. 1) and high (Fig. 2) energy spilling breaking waves.

The 180 degree (upwave) measurements produced the largest RCS values observed. The maximum returns corresponded temporally to the point at which the forward face of the wave was perpendicular to the radar boresight, approximately 0.15 seconds prior to breaking. The average peak RCS was 4.6dB for both breaking waves, and the horizontally and vertically polarized returns were approximately equal. This implies that the peak backscatter was most likely caused by specular facets on the steepening wave face.

The peak upwave returns were followed by approximately 0.2 seconds of strong returns, which correlated temporally to the initial whitecapping along the face of the waves. These returns can also be seen in the 90 and 135 degree measurements, and yielded averaged peak RCS values of -13 to 2dB.

The 0 and 45 degree measurements produced peak returns approximately 0.25 seconds after breaking. Averaged peak RCS values ranged from -10 to 0dB, with the high energy wave achieving values 1-2dB higher than the low energy wave. The polarization dependence expected for Bragg scattering was not observed, suggesting radar returns may be due to Rayleigh-like scattering from elements of the small scale roughness.

The strong azimuthal dependence of the backscatter appears to be due to a combination of the surface tilt effects and a possible anisotropy of the small scale roughness. The upwave measurements were presented with steeply sloped wave faces and were dominated by specular scattering. The 90 and 135 degree measurements were not presented with specular wave faces, and therefore, were dominated by backscatter from the initial roughness generated on the forward wave face. The downwave, and 45 degree measurements were initially shadowed from the scatterers just mentioned. These measurements were dominated by scattering from the post-break small scale roughness, after the breaking wave collapsed, and the roughness became visible in the radar footprint.

0-7803-3068-4/96$5.00©1996 IEEE

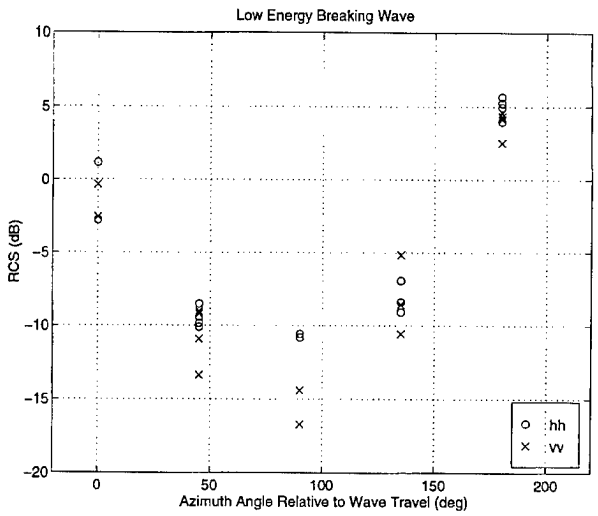


Fig. 1

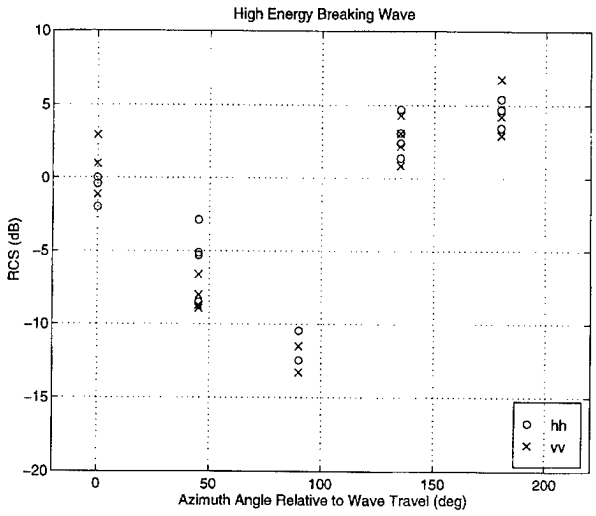


Fig. 2

SPECTRAL DATA

The temporal data from all the runs were Fast Fourier Transformed (FFT) over eighth of a second intervals, yielding Doppler resolutions of 8Hz. Plots of the Doppler spectra for 5 time intervals are displayed for the low (Figs. 3 and 4) and high energy (Figs. 5 and 6) breaking waves.

In the upwave measurements (Figs. 4 and 6), the spectra were dominated by a single narrow peak. These peaks correspond to Doppler shifts of 122.0 Hz and 208.0 Hz, for the low and high energy waves respectively. These Doppler shifts corresponded to the radial components (in the direction of the radar) of the long wave phase speeds of 1.18 m/s and 2.01 m/s. [4]. Recent particle tracking velocimetry (PTV) studies have shown that particles on the steepening wave face may have orbital velocities with approximately the same radial component [5], and thus produce the same spectra. This supports the hypothesis that the upwave returns were caused by specular scattering from the steepening wave face.

Some additional returns can be seen in the upwave spectra corresponding to slower scatterer velocities. This indicates that other scattering mechanisms were present in the upwave measurements, but were small when compared to specular backscatter components.

The spectra in the downwave measurements (Figs. 3 and 5) were broader than those in the upwave direction, and were split into two distinct groups of peaks. This implies that the primary scatterers had a distribution of velocities. With the amplitude of the wave decreasing after breaking, it can be assumed that the orbital velocities the surface particles will decrease. Further, it may be inferred that the decrease in velocity would occur at different rates, and therefore, a spread Doppler spectra could be expected. No explanations are offered as to why the spectra are split instead of uniformly distributed over a range of Doppler frequencies. The split Doppler spectra have also been observed in open ocean experiments [6].

CONCLUSIONS

Temporal and spectral data has been presented for spilling breaking waves of two different energies. The amount of backscatter obtained was shown to be directly related to the geometry of the breaking wave in relation to the radar.

The maximum RCS values were observed in the upwave direction, just prior to wave breaking. The maximum RCS was the same value for both breaking waves and was independent of polarization. This implies that the maximum backscatter was due to specular facets on the steepening wave face. This is consistent with the upwave Doppler spectra, whose dominant peaks most likely corresponded to the orbital velocities of the particles on the wave face.

The peak RCS values obtained in the 0, 45, and 90 degree measurements occurred after wave breaking, with the high energy breaking wave producing values 1-2dB higher than the low energy wave. Returns of both polarizations were approximately equal, which implies that Rayleigh-like scattering may have been present. The downwave measurements produced spectra that were broad and split into two distinct groups of peaks. While the split in the spectra can not be presently explained, the broad spectra are due to the distribution in orbital velocities of the post-break small scale roughness.

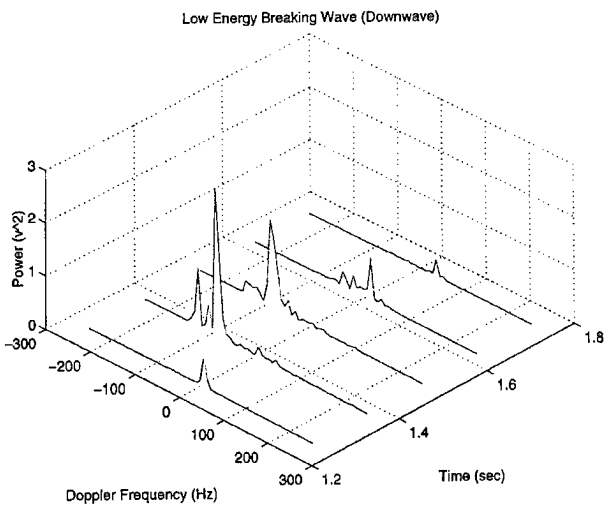


Fig. 3

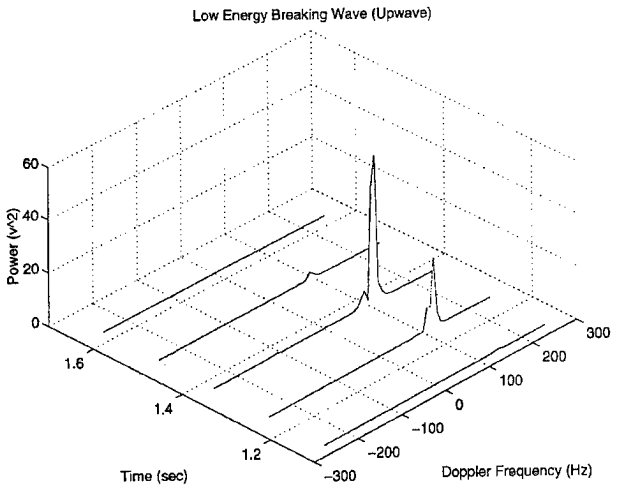


Fig. 4

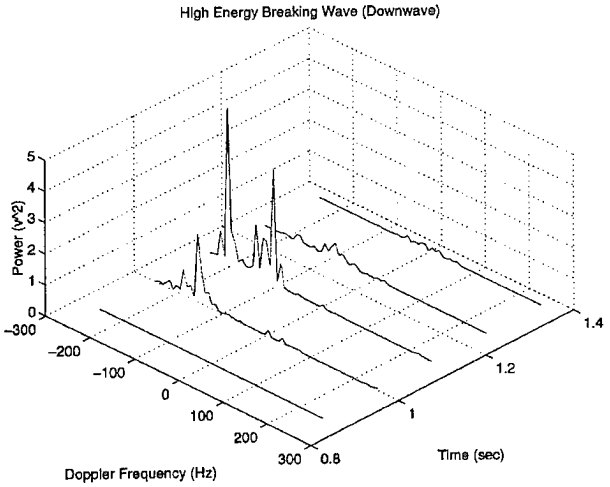


Fig. 5

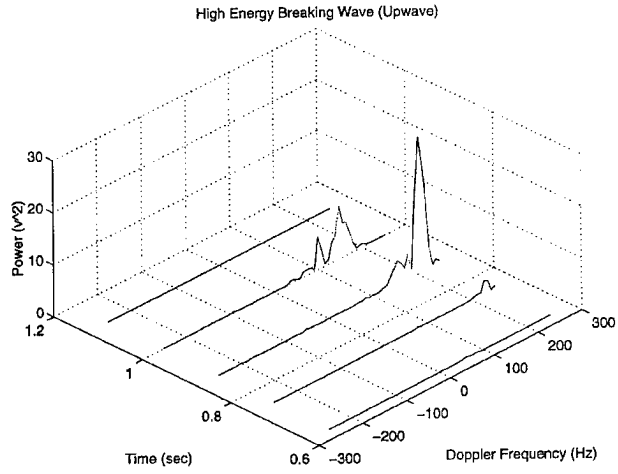


Fig. 6

ACKNOWLEDGMENTS

This research was funded under the Office of Naval Research, Contract # N00014-92-5-1650. Their support is greatly appreciated.

REFERENCES

[1] E. Dano and D. Kletzli Jr., "Low cost CW scatterometers for field and laboratory use," Procedings 1996 IEEE Natl. Radar Conf., in press.

[2] F. Ulaby, R. Moore and A. Fung , "Microwave Remote Sensing: Active and Passive, Volume II," Artech House, Norwood, MA, pp. 746-779, 1982.

[3] G. Meadows, et. al., "Laboratory investigations of the hydrodynamics and radar backscattering properties of breaking waves," Proceedings 1996 IEEE IGARSS, in press.

[4] W. Saunders, "CW and FM Radar," in Radar Handbook 2nd Ed., M. Skolnick, Ed., McGraw Hill, New York, p14.2, 1990.

[5] M. Perlin, et. al., "An experimental study of deep water plunging breakers," unpublished.

[6] P. Lee, et. al., "X-band microwave backscattering from ocean waves," JGR, 100, pp. 2591-2611, 1995.

Dependence of Polarimetric Doppler Spectra on Breaking-Wave Energy

P.H.Y. Lee, J.D. Barter, K.L Beach, B.M. Lake, H. Rungaldier,
J.C. Shelton, H.R. Thompson, Jr., R. Yee

TRW, R1-1008, 1 Space Park, Redondo Beach, CA 90278, USA
Tel: 310.814.9077 Fax: 310.814.2359 e-mail: peter_lee@atdmac.sp.trw.com

Abstract -- Breaking gravity waves are studied in a wave tank at small grazing angles (4.5° - 11°) where all four polarization elements (HH, VV, HV, VH) are simultaneously measured. Temporally averaged Doppler spectra are obtained for mechanically-generated 4 m breaking waves of various energies. We describe the dependence on breaking-wave energy of the parameters describing the backscatter. The results of grazing angle dependence of the backscatter are also shown and discussed.

INTRODUCTION

Microwave scattering experiments performed at the wind-wave tank facility of the Ocean Engineering Laboratory (OEL) of the University of California at Santa Barbara (UCSB) are reported. Breaking waves are studied at small grazing angles (4.5°-11°) using a fully polarimetric X-band pulse-chirped radar. Time-averaged Doppler spectra are obtained for 4 m breaking waves of various energies. The averaging time for each spectrum shown in this paper is 409 seconds. As the breaking-wave energy is increased, wave-breaking progresses from "incipiently" breaking to "fully" breaking. We observe a direct dependence on breaking wave energy of many of the parameters describing the backscatter including: power spectral densities (PSDs) of all polarization-matrix elements, polarization ratio (HH/VV), ratio of cross- to co-polarization cross section (HV/HH, VH/VV), and Doppler frequencies of the PSD maxima. We further study the grazing-angle dependence of the "fully" breaking wave and find that the PSDs of the HH, HV and VH components decrease monotonically with increasing grazing angle, whereas the VV component shows a minimum near 7° grazing angle. We note also that cross-polarization returns are present even at incipient breaking. The present results agree with earlier conjectured scattering mechanisms.[1,2] A direct verification of the existence of such scattering mechanisms using a new optical diagnostic (OSED) is reported in another session (J.D. Barter and P.H.Y. Lee, IGARSS '96 Paper No. 96-0087).

DEPENDENCE ON BREAKING-WAVE ENERGY

The degree of breaking of the 4.0 m wave is specified by the temporal profile of the vertical displacement of the mechanical wavemaker foot. The wave-breaking energy at the fetch at which radar measurements are taken is controlled by the choice of relative amplitude of the symmetrical, balanced side-bands to the fundamental gravity wave while holding the fundamental wave-amplitude and all frequencies fixed. The fundamental frequency is 0.624 Hz (4 m gravity wave) while the upper and lower sidebands are offset by ±0.008 Hz, respectively. The wave amplitude at R=10 m is measured to be ~20 cm. The breaking-wave energy is characterized by the ratio of the sideband amplitude to the amplitude of the fundamental wave (a_{SB}/a_{fund}) at the wavemaker. With increasing sideband amplitude, the wave breaking becomes more energetic. The descriptive terms of breaking corresponding to values of a_{SB}/a_{fund} = 0.26, 0.27, 0.28 and 0.30 are "incipient", "mild", "intermediate" and "full", respectively, and reflect the relative radar return amplitudes. All backscatter measurements were made at a radar boresight range of 10 m. Range resolution of the pulse-chirped radar system is 13.6 cm.

Figure 1 shows spectra of the *incipiently* breaking wave at 4.5° grazing angle. The spectrum of each polarization element is shown for four alternate successive range gates. First, note that both the HH and VV spectra are peaked at approximately the same frequency, ~120 Hz. The narrow peaks near ~35 Hz in two of the range gates are artifacts. These artifacts appear whenever the proper signal does not dominate in the vicinity of 35 Hz and should be disregarded for the consideration of physics. Super events (defined as HH>VV) are clearly evident. Figure 2 shows spectra of the *mildly* breaking wave. Note that both the HH and VV spectra are peaked near 120 Hz. The HH PSDs averaged over the four gates are greater than the corresponding averaged VV PSDs and the peaks are offset, with the HH PSD being at a slightly higher frequency. Figure 3 shows spectra of the *intermediate* breaking wave. Note that above ~120 Hz, the HH PSDs are clearly larger than the VV PSDs. The HH spectra peak at slightly higher frequency than the VV spectra. Figure 4 shows spectra of the *fully* breaking wave. Note that both the HH and VV PSD spectra exhibit a pronounced increase over the whole Doppler range shown as compared to the case shown in Figure 3. This points to the nonlinear nature of the wave breaking process since the breaking-wave energy has increased only slightly from the previous case. The HH and VV spectra are now clearly distinct. The VV spectra also have a low frequency component, presumably due to scattering from breaking-wave-generated free and bound gravity-capillary (Bragg) waves (which are also visible to the eye). The peak HH PSDs for all four gates are greater than the corresponding peak VV PSDs by about 7 dB. The HH spectra also peak at slightly higher frequency. Due to the large increase in PSD, the earlier mentioned artifacts near ~35 Hz of the two particular range gates are now buried in the signal. Space limitations prevent display of breaking-wave- energy dependent cross-polarized spectra in this paper.

0-7803-3068-4/96$5.00©1996 IEEE

The dependence of the backscattered power on breaking-wave energy is summarized as follows: At fully breaking, the sudden increase in polarization-ratio, and peak values of both HH and VV PSD is apparent. The HH and VV PSD peak Doppler frequencies are found to lie below the Doppler frequency corresponding to the phase speed of the 4.0 m gravity wave ($f_D \approx 166$ Hz). However the peak frequencies of the PSDs increase gradually with wave-breaking energy, from ~$0.7f_D$ for incipiently breaking to about ~$0.8f_D$, for fully breaking.

GRAZING ANGLE DEPENDENCE

Doppler spectra at grazing angles of 4.5°, 7° and 11° of *fully* breaking waves are examined. Space limitations prevent the inclusion of all spectral data in this paper, however a summary of the results is provided.

Co-polarized spectra: At 7° grazing angle, the HH and VV PSDs have decreased substantially in amplitude (compared to the 4.5° case) but the HH and VV spectra are still clearly distinct. The VV now has a pronounced low frequency component (-20 to ~70 Hz), extending to negative frequencies and presumably due to scattering from breaking-wave generated free and bound Bragg waves which are affected by the orbital motion in the trough of the fundamental gravity wave. The HH and VV spectra peak at approximately the same frequency, and super events are clearly evident. At 11°, the HH and VV PSDs have approximately the same amplitude as the 7° case and the HH and VV spectra are still distinct. The VV has a low frequency component (-30 to ~80 Hz) with a more prominent extension to negative frequencies. The negative components in the VV PSD could be due to the effect of negative orbital velocity on the free Bragg waves generated by wave breaking. The increase of the range in negative frequencies and the slight increase in PSD values in the negative frequency range could be due to the increased area of the trough and back side of the breaking (or broken) wave visible to the radar at increased grazing angle. The fact that VV sees this while HH does not indicates that Bragg scattering is the likely explanation. Super events are still clearly evident.

Cross-polarized spectra: The cross-polarized spectra are compared with the co-polarized spectra for the various grazing angles. Again, not all data can be shown due to space limitations. The HH and HV Doppler spectra at 4.5° have approximately the same shape and peak at approximately the same frequency. The resolved spectral lineshapes, however, reveal subtle differences. The peak value of the HV PSD is ~16 dB lower than the peak HH PSD value. At 7°, both the HH and HV spectra have reduced PSD values compared to the 4.5° case, but are still approximately the same shape and peak at approximately the same frequency. The peak PSD value of the HV is again ~16 dB lower than the peak HH PSD value. The HH and HV Doppler spectra at 11° are shown in Figure 5. Both the HH and HV spectra show little change in magnitude compared to the 7° case and have approximately the same shape and peak at approximately the same frequency. Unlike the HH and HV cases, the VV and VH spectra at 4.5° grazing angle have dissimilar shape, however the spectra both peak at approximately the same frequency. The range-gate resolved spectral lineshapes reveal interesting details of the components which constitute the spectral lineshape. The peak VH PSD value is ~7 dB less than the peak VV PSD value. As in the previous case, the VV and VH spectra at 7° have dissimilar shape but peak at approximately the same frequency. Since backscattering at 7° grazing angle occurs in the vicinity of maximum Brewster effect for X-band microwaves, a minimum is expected for the VV returns, thus the VH to VV ratio should be larger and, indeed, the VH/VV ratio peaks at ~ -5 dB. The VV and VH Doppler spectra at 11° are shown in Figure 6. As in the 7° case, the VV and VH spectra have dissimilar shape, however the spectra both peak at approximately the same frequency. Due to the increase in grazing angle, the radar sees still more of the trough and backside of the breaking wave, and the VV PSD extends still further into the negative frequency region. Since the difference between the Brewster angle and the complement to the nominal grazing angle is now ~4°, the VH/VV ratio drops again to approximately -7.5 dB.

The grazing-angle dependent results are summarized as follows: 1) Since HH/VV > 0 dB, double-bounce super events or similar mechanisms dominate single-bounce specular processes in providing the co-polarized returns; 2) The "dip" of the VV PSD at 7° grazing angle is further evidence that a Brewster reflection in double-bounce scattering is effective in attenuating the vertical return, and 3) the Doppler frequencies at the PSD maxima of all polarization-elements indicate that the average speed of the scatterers is smaller than the phase speed of the fundamental gravity wave.

SUMMARY

The power of each polarization element (at 4.5° grazing angle), integrated over the entire range of Doppler frequencies, and averaged over four range gates, is shown as a function of breaking-wave energy (characterized by a_{SB}/a_{fund}) in Fig. 7. At *fully* breaking, the backscattered power dependence on grazing angle is shown in Fig. 8. In another paper, (P.H.Y. Lee et al., IGARSS '96 Paper No. 96-0089) we will report on investigations of the depolarization effect caused by scattering from a breaking-wave surface.

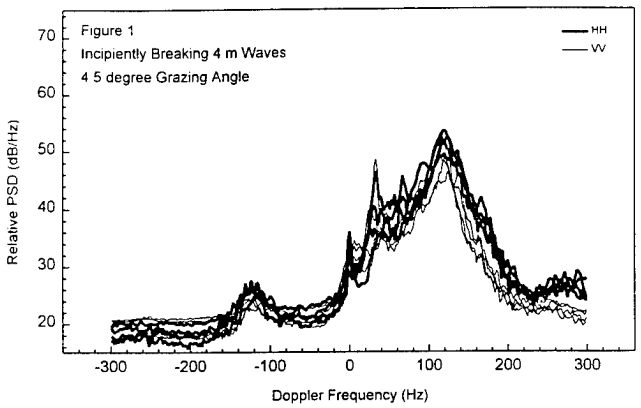
ACKNOWLEDGMENT

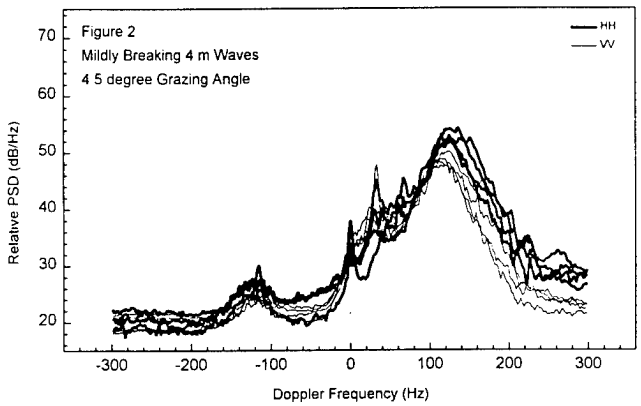
This work was supported by ASAP/ISSO, Department of Defense, Contract No. DMA 800-94-C-6008. The authors thank Prof. Marshall Tulin of UCSB/OEL and his staff for the use of the OEL wavetank facility.

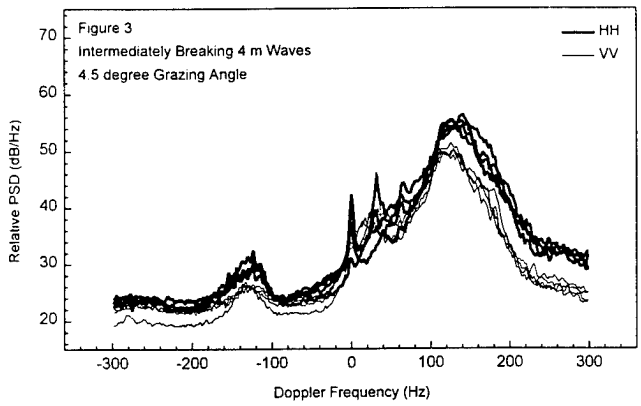
REFERENCES

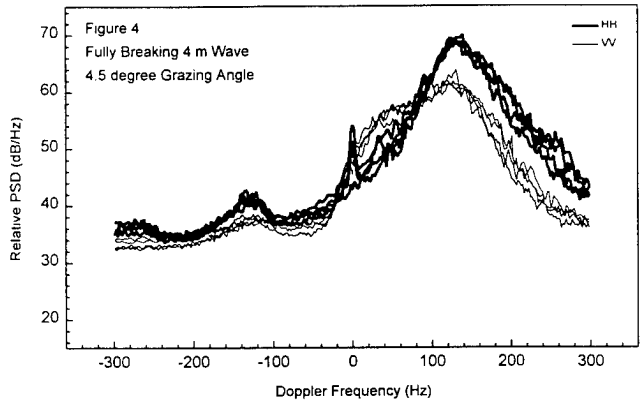
[1] P.H.Y. Lee et al., *J. Geophys. Res.* **100**, 2591-2611 (1995).

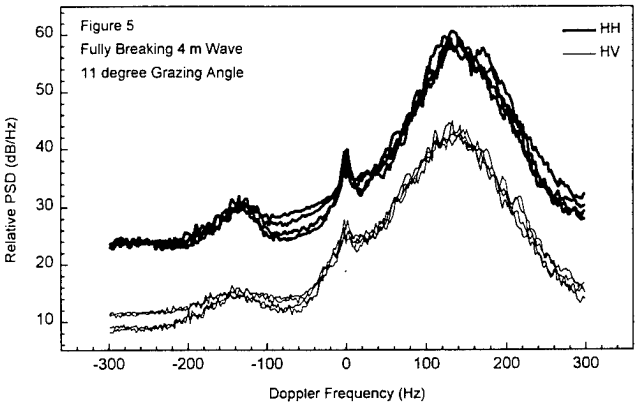
[2] P.H.Y. Lee et al., *IEEE Trans. Antennas & Propagation* **AP-44**, 333-340 (1996).

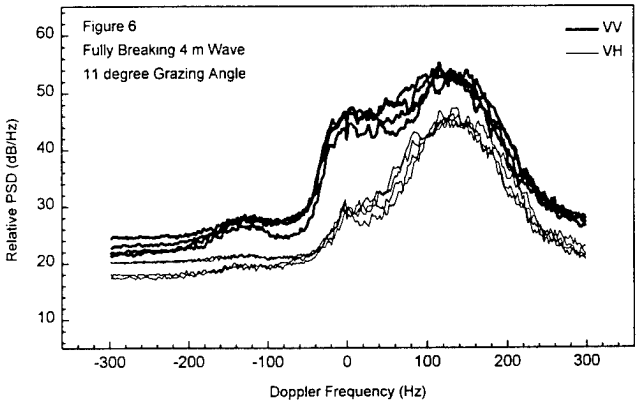

Figure 1
Incipiently Breaking 4 m Waves
4 5 degree Grazing Angle
HH
VV
Relative PSD (dB/Hz)
Doppler Frequency (Hz)

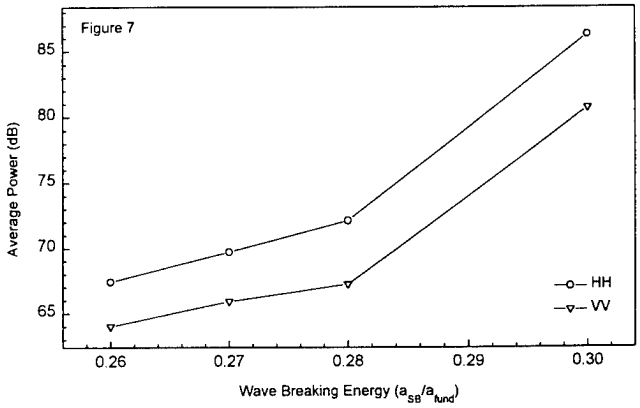

Figure 2
Mildly Breaking 4 m Waves
4 5 degree Grazing Angle
HH
VV
Relative PSD (dB/Hz)
Doppler Frequency (Hz)

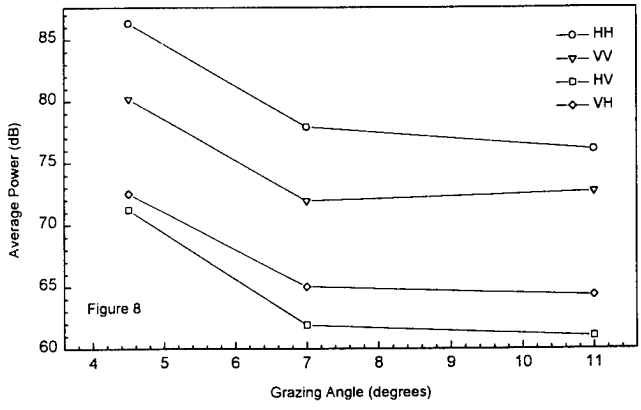

Figure 3
Intermediately Breaking 4 m Waves
4.5 degree Grazing Angle
HH
VV
Relative PSD (dB/Hz)
Doppler Frequency (Hz)


Figure 4
Fully Breaking 4 m Wave
4.5 degree Grazing Angle
HH
VV
Relative PSD (dB/Hz)
Doppler Frequency (Hz)


Figure 5
Fully Breaking 4 m Wave
11 degree Grazing Angle
HH
HV
Relative PSD (dB/Hz)
Doppler Frequency (Hz)


Figure 6
Fully Breaking 4 m Wave
11 degree Grazing Angle
VV
VH
Relative PSD (dB/Hz)
Doppler Frequency (Hz)


Figure 7
HH
VV
Average Power (dB)
Wave Breaking Energy (a_{SB}/a_{fund})


HH
VV
HV
VH
Average Power (dB)
Figure 8
Grazing Angle (degrees)

LABORATORY STUDY OF THE FINE STRUCTURE OF BREAKING WAVES FOR SCATTEROMETRY APPLICATIONS

A. Rozenberg, W. K. Melville, M. Ritter
Scripps Institution of Oceanography
University of California, San Diego, La Jolla, CA 92093-0238.
Ph. (619) 534-8035, Fax (619) 534-7641, email: anatol@mpl.ucsd.edu

Abstract Laboratory measurements of the fine space-time structure of short gravity-capillary waves, as well as Ku-band scattering at grazing and moderate incidence from spilling and plunging breaking waves in a wave channel are presented. Unsteady breaking waves are generated by focusing the waves in space and time. A scanning laser slope gauge was used for measuring short waves of wavelength 0.2-20cm, and frequencies up to 150Hz. A dual polarized (VV, HH) coherent pulsed Ku-band scatterometer with good temporal resolution (3ns) was used to simultaneously obtain Doppler spectra of the scattered signals from the breaking area. It was found that the breaking splash is the main source of small-scale surface-wave generation. The short surface wave slope field produced by the breaking could be separated into regular short (5-10mm wavelength), fast, bound waves, and free gravity-capillary waves. Both types of waves were found to co- and counter-propagate relative to the direction of the dominant wave propagation.

Measurements of the Doppler frequency of the scattered signal are consistent with this description of the slope gauge measurements.

INTRODUCTION

Microwave scattering from breaking surface waves is poorly understood. Breaking is a strongly non-linear phenomenon comprised of a number of different processes. The best way to separate these processes is to simultaneously measure both the scattered signal and the fine structure of the surface which is responsible for the scattering. Laboratory experiments using mechanically generated waves under computer control offer the simplest means of generating breaking in a repeatable (in the mean) way without the complicating factor of the wind. We anticipate that the direct effects of the wind are only of consequence for the shorter breaking waves which do not actively entrain air to form a whitecap. Rapp and Melville [1] have used these techniques in a study of unsteady deep-water breaking. They used laser-Doppler anemometry to measure horizontal and vertical fluid velocities, and wave gauges for surface displacement measurements. The structure of the breaking region was examined in detail. The present study is an extension of this experiment to include microwave scattering. A scanning laser slope gauge (SLSG) was used to measure the 2-D space-time structure of the surface slope, and a Ku-band, dual-polarized, coherent, pulsed scatterometer was used for the microwave measurements.

Kwoh and Lake [2] attempted to describe deterministically the scattering from "gently" breaking 2.5 Hz paddle-generated waves at grazing and moderate incidence using an X-band CW dual-polarized scatterometer and SLSG. The different contributions from slow and fast scatterers, as well as specular facets, was discussed. Our data are in qualitative agreement with their results, but the more comprehensive wave slope and velocity measurements in our study (2-component velocity field and 2-D slope field measurements) permit a more detailed examination of the source of the scatterers.

EXPERIMENTAL METHODS

The experiments were conducted in a glass-walled channel in the Hydraulics Laboratory at the Scripps Institution of Oceanography. The channel is 30 m long, 0.5m wide, and filled to a depth of 0.6m with fresh water. The SLSG was designed for measuring short waves with wavelength from 0.1 to 20 cm and frequencies up to 150Hz. The SLSG consists of an underwater laser and scanner assembly, and the position-sensor assembly above the water surface. The 60kHz sampling rate produced two 50x300 pixel space-time images every second.

A coherent, 14 GHz (λ=2.1cm), dual-polarized, pulsed (3ns pulsewidth) scatterometer was used for obtaining the amplitude and frequency of the scattered signal. The scatterometer is described in detail in Rozenberg et. al.[3]. The scatterometer's antennas were fixed 40 - 140 cm above the water surface, with the grazing angle varying from 6 to 45 degrees. The scatterometer was mounted looking in an upstream direction at a common footprint with the SLSG and resistance wire wave gauge. Unsteady single breaking waves were generated by focusing wave groups, with center frequencies in the range 0.9-1.3 Hz, in space and time [1]. Two-dimensional filtering in the wavenumber-frequency domain was used for separating the direction of propagation of the surface waves as they appeared within the breaking region.

0-7803-3068-4/96$5.00©1996 IEEE

RESULTS

Measurements of the slope-field fine structure for different strengths of breaking from gentle to plunging, as well as both VV and HH polarizations at grazing incidence angles from 6 to 45 degrees, were taken. Typical samples of simultaneous time series of the wire wave gauge and the SLSG for a single spilling wave are presented in Fig.1. From the top the figure shows surface displacement $\eta(t)$, wave slope s(t) from the SLSG without scanning, and the 2-D space-time slope field s(x,t) with the SLSG scanning in the direction of wave propagation. The last panel shows a sequence of interweaved patches with different frequencies and phase velocities depending on the wave profile. A burst of strongly nonlinear short waves can be seen both in the SLSG time series and in the space-time slope field. More detailed examination of these data show surprisingly regular sets of the short fast waves at the very moment of breaking and a lot of intermittent patches with smaller frequencies and phase velocities approximately 0.1-0.15s after breaking. Two-dimensional filtering to separate co- and counter-propagating waves shows approximately equal contributions from both fast and slow waves in both directions of propagation. Of particular interest are the characteristics of the wave field and scattered signal which could be associated with the same scatterers.

Fig.1 shows also spectrograms taken with a 0.25s window (0.1s overlap) for the slope and both VV and HH scatterometer signals for the same breaking wave parameters and 8 degree grazing angle looking towards the oncoming breaking wave. The similarity of all the spectrograms is readily apparent. Again, the moment of breaking is marked by the appearance of high frequencies in both the scattered signals and the slope field; while a short time after breaking all the local spectra rapidly shift to lower frequencies.

The large differences between the high-frequency patches of the scattered signals, as well as the high frequency slope features on the breaking crests of the dominant waves, versus the relatively slow waves following breaking may be characterized in terms of "fast" (or bound), and "slow" (or free) scatterers. The velocities of "fast" scatterers (150-170 cm/s) correspond to phase velocity of the dominant waves; their wavelengths at the moment of breaking are in the range 0.5-1.0cm, and they are surprisingly regular. All these features are consistent with parasitic (bound) capillary waves, generated by the steepening wave immediately prior to breaking. After breaking, the scatterers with smaller phase velocities are clearly associated with Bragg scattering from free surface capillary waves. A noteworthy difference between the VV and HH signals, especially in the post-breaking region, is that the local VV spectra have a more continuous tail, with the HH spectra more intermittent. The presence of the long-lived turbulent velocities following breaking were reported in [1]. This could be considered as a potential source of the observed differences in the polarized scattering. The possibility of scattering by turbulent wakes and their influence on the Doppler bandwidth was discussed in [2] and by Jessup et al.[4]. Measurements of the spatial and temporal decorrelation scales should clarify the source of these phenomena.

CONCLUSIONS

i. Laboratory measurements of Ku-band scattering at grazing incidence, as well as the fine space-time structure of mechanically-generated breaking waves are presented.

ii. Both VV and HH local Doppler spectra could be separated into two groups. The first group corresponds to scattering at the onset of breaking and shows large values of the Doppler frequency ("fast" scatterers). No significant difference between VV and HH signals in this area is found (HH spectra are slightly higher). The second corresponds to scattering following breaking and has much lower values of the Doppler frequencies ("slow" scatterers).

iii. Direct comparison of the measured fine space-time structure of short wave slopes and parameters of the scattered signals, demonstrates the differences between the fast and slow scatterers. The slow group is consistent with the Bragg scattering from the free capillary waves, while the fast group is associated with scattering from the bound capillary waves on the crests of the dominant breaking waves.

REFERENCES

[1] R. J.Rapp and W.K.Melville, Laboratory Study of Deep-Water Breaking Waves. 1990 Tr. R. Soc. London, A331, 735-800

[2] D.S.W.Kwoh and B.M.Lake, A Deterministic, Coherent, and Dual-Polarized Laboratory Study of Microwave Scattering From Water Waves, Part I. 1984 IEEE Jour. of Ocean. Eng., v. OE-9, No.5, 291-308

[3] A. D.Rozenberg, D. C. Quigley, and W. K. Melville, Laboratory Study of Polarized Scattering at Grazing Incidence, Part I. 1995 IEEE Tr. on Geoscience and Remote Sensing, v.33, No.4, 1037-1046

[4] A.T. Jessup, W.K. Melville, and Keller, W.C., Breaking waves affecting microwave backscatter. 1. Detection and verification. 1991 J. Geophys. Res., 96,20547-20559.

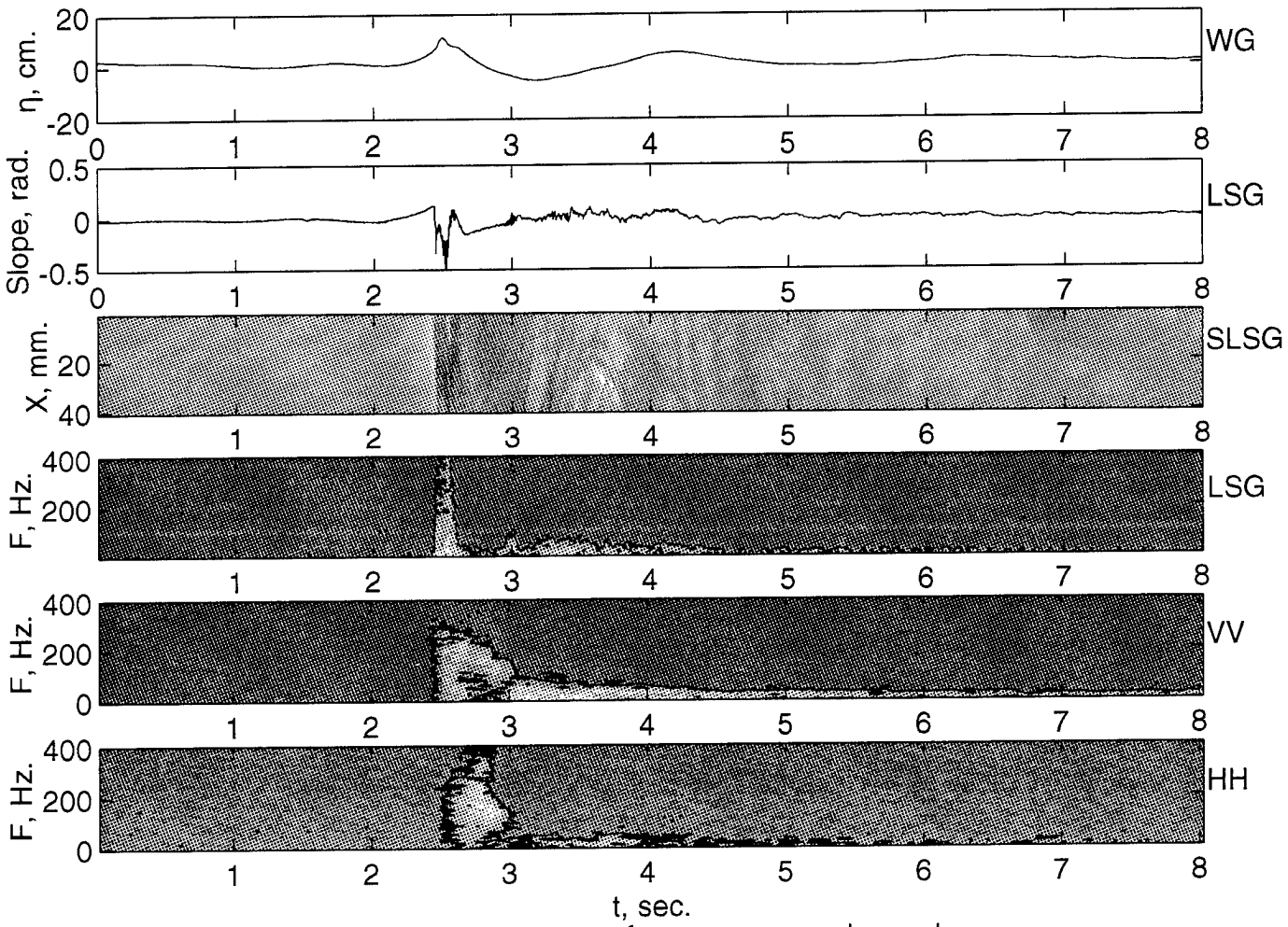


Fig.1. Time series and spectrograms for wave gauge, laser slope gauge, and scatterometer signals. Spilling breaking, 8 deg. grazing angle.

Small Grazing Angle Radar Scattering from a Breaking Water Wave: Demonstration of Brewster Angle Damping

James C. West, J. Michael Sturm
School of Electrical and Computer Engineering
Oklahoma State University, 202 ES
Stillwater, OK 74078
(405) 744-6096, FAX: (405)744-9198
jwest@master.ceat.okstate.edu

Mark Sletten
Naval Research Laboratory, Code 7255
4555 Overlook Ave, SW
Washington, DC 20375-5320
(202) 404-7971, FAX: (202) 767-3303
mslette@seascat.nrl.navy.mil

Abstract—**The small-grazing-angle backscattering from breaking water waves is examined using a hybrid MM/GTD numerical technique. The calculated scattering shows that Brewster angle damping strongly limits the multipath scattering from breaking plumes at vertical polarization, yielding HH/VV scattering ratios of up to 15 dB. Comparison with experimentally measured scattering from a small breaking wave demonstrates the validity of the numerical approach.**

INTRODUCTION

Radar returns from the sea surface at near-grazing illumination are characterized by short bursts of power that are significantly stronger than the random average scattering. These "sea spikes" can last up to a second, and often yield horizontal (HH) to vertical (VV) radar-cross-section ratios of 10 dB or more. Rapid fluctuations in sea-spike echos have also been observed, particularly at horizontal polarization. The characteristics of the sea spikes are not predicted by the distributed surface scattering theories that have proven effective at more moderate grazing angles.

Wetzel [1] suggested that sea spikes are due to multi-path scattering from the plumes of breaking waves. As shown in Figure 1, the plume introduces four ray paths that lead to backscatter: the direct back-reflection from the plume, the two reciprocal paths that include reflection from the plume and the front face, and the path that reflects from the front face, plume, and front face again. Sletten and Wu [2] found strong experimental evidence for this scattering mechanism in the ultrawideband radar backscatter from wavetank breakers. This multipath scatter model explains the large magnitude and rapid fluctuations of sea-spike returns, but does not predict the large HH/VV scattering ratios observed. Trizna [3] expanded this model to include the effects of the finite conductivity of sea water. He suggested that the VV multipath is strongly attenuated by the Brewster angle effect at the front-face reflection point, so the backscatter is almost entirely due to direct back-reflection from the plume. The HH multiple-reflection scattering is not strongly affected by the surface conductivity, and constructive interference of the multipaths leads to the large signals observed. Sletten *et al.* [4] have recently explored this model experimentally with an ultrawideband radar and have found it to be an accurate descripttion of the multipath process.

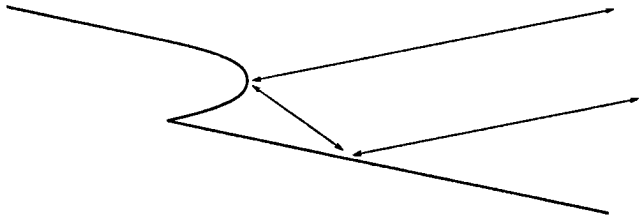


Figure 1. Multipath scattering from a breaking wave plume.

In this paper we use numerical calculation of the scattering from sea water surfaces that include breaking wave features to demonstrate the Brewster-angle-damping effect. Use of a hybrid numerical approach that combines the moment method (MM) and geometrical theory of diffraction (GTD) allows the scattering calculations to be applied at arbitrarily small grazing angles. Electromagnetically large plumes such as those considered by Trizna are first addressed, and we then show that Brewster angle damping can also affect the multipath scattering from much smaller breaking wave features.

NUMERICAL MODEL

A modified form of the hybrid MM/GTD numerical technique first used by West [5] to describe scattering from perfectly conducting surfaces was used for the calculations. In this approach the numerically modeled scattering surface is extended to infinity. Single MM basis functions derived from GTD, plus the known physical optics currents, are used the describe the surface current on the infinite surface extensions. Because there are no artificial edges in the modeled surface, no illumination weighting function is needed and the technique can

This work was supported in part by the Office of Naval Research under contract N00014-96-1-0075.

0-7803-3068-4/96$5.00©1996 IEEE

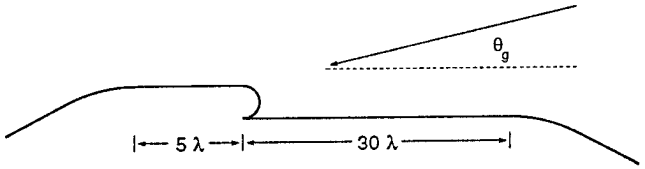


Figure 2. Scattering surface that approximates a large breaking-wave plume. (Not to scale.)

be applied at arbitrarily small grazing angles. The additional computational expense over the standard moment method is modest since only a few additional basis functions are needed to describe the infinitely extending current. The resistive-sheet boundary conditions described by Glisson [6] allowed the application of the technique to the sea-water dielectric interface.

RESULTS

Large-Plume Surface

The surface shown in Figure 2 was used to represent the scattering from an electromagnetically large-scale plume. The front and back tilted sections of the surface extend to infinity, and are required for application of the numerical technique. The plume radius was one electromagnetic wavelength (1 λ).

The scattering from this surface is shown in Figure 3. (Since one-dimensionally rough surfaces are modeled the scattering cross-section is given in dB relative to one wavelength.) In part a) of the figure, the surface was modeled as perfectly conducting. At grazing angles above 10° the backscattering is approximately equal at VV and HH. Only small multipath interference is evident at these grazing angles. As the grazing angle decreases to 0° the HH scattering smoothly decreases to a small value but the VV scattering remains strong, behavior that was predicted by Wetzel.

Part b of Figure 3 shows the scattering from the plume surface when the dielectric properies of sea water are used. The only effect of the reduction in conductivity on the HH backscattering is a small drop (ranging from 2 and 3.5 dB) at all grazing angles. At VV, however, the scattering drops at all grazing angles, with the largest drop (more than 15 dB) occurring at the smallest grazing angles. This behavior is consistent with the predictions of Trizna, demonstrating that Brewster angle damping is indeed reducing the multipath scattering to quite small levels at VV. Most importantly, the HH/VV scattering ratio exceeds 0 dB, reaching 15 dB at 10° grazing, consistent with experimental observations of actual sea spikes.

Small Breaking-Wave Surface

Figure 4 shows a surface used to represent a small breaking wave. The surface approximates the displacement of an actual water wave measured in a wavetank. The solid line shows the true water surface and the dashed line shows the artificial

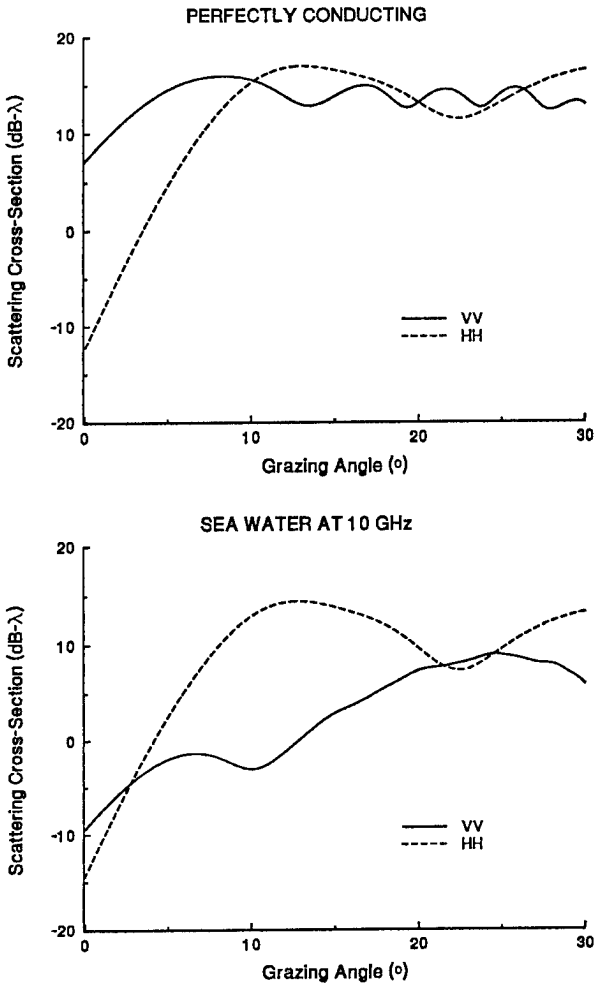


Figure 3. Numerically calculated scattering from the breaking-wave plume surface of Figure 2. a) The surface is perfectly conducting. b) The has the dielectric properties of sea water at 10 GHz.

extensions needed for the application of the numerical technique. The dotted line shows the multiple-bounce backscattering paths identified using geometrical optics.

The numerically calculated backscattering from the small breaking-wave surface at a grazing angle of 10° is shown in Figure 5. When the surface is perfectly conducting, strong interference is observed in the VV scattering, with much weaker interference at HH. When the scattering surface was replaced with sea water, the HH scattering is nearly unaffected other than an overall reduction of about 2 dB at all frequencies. At VV, however, the interference is dramatically reduced with the change in surface (down to the level observed at HH), showing that Brewster angle damping at the reflection point on the front face of the wave is greatly reducing the multipath scattering.

Figure 6 shows the experimentally measured backscattering from a small breaking wave generated in a wave tank at

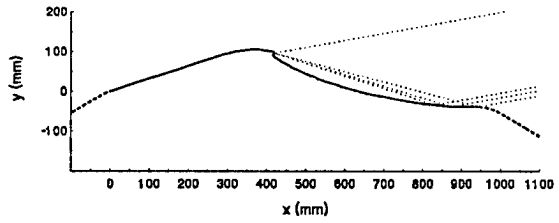


Figure 4. A breaking-wave surface that includes an electromagnetically small plume. The dashed line shows the artificial extensions needed for application of the numerical model. The dotted lines show the multiple backscattering paths.

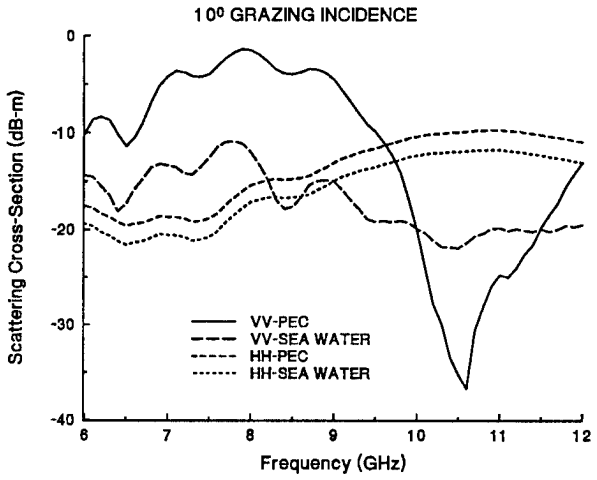


Figure 5. Numerically calculated scattering from the breaking-wave plume surface of Figure 4 when the surface is perfectly conducting and has the dielectric properties of sea water. The grazing incidence angle is 10°.

10° grazing. (Since absolute calibration was not available the cross-sections are presented as relative to the maximum at HH.) The wave was of approximately the same size and plume configuration of that in Figure 4 at the instant when the measurement was the taken. The average HH and VV scattering cross-sections are approximately the same, as are the interference levels, behavior that is similar to that in the numerical results of Figure 5b. Moreover, the frequencies of the relative maxima and minima in the experimental results also agree quite well with those in the numerical results (although the interference levels themselves are significantly stronger in the experiment). Considering the large uncertainties in the actual wave surface displacement, this is reasonably good agreement, supporting the validity of the numerical approach in examining the near-grazing scattering from a lossy dielectric interface.

CONCLUSIONS

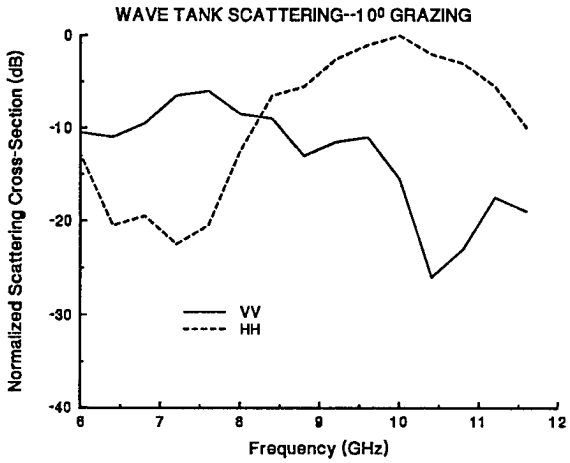


Figure 6. Experimental wavetank measurement of the scattering from a small breaking wave similar to that in Figure 4.

A numerical approach has been used to examine the multi-path backscattering from sea-water surfaces approximating breaking wave features. The results confirmed that Brewster-angle damping limits the multi-path scattering from electromagnetically large breaking plumes at VV, leading to HH/VV scattering ratios that can approach 15 dB. Comparison of the numerically-calculated scattering from a small breaking wave with experimental wave tank measurements demonstrated the validity of the numerical approach, and further showed that Brewster angle damping can be important in the scattering from these smaller waves.

REFERENCES

[1] L. B. Wetzel, "On microwave scattering by breaking ocean waves", in *Wave Dynamics and Radio Probing of the Ocean Surface*, O. M. Phillips and K. Hasselmann, Eds., pp. 273–284. Plenum Press, New York, 1986.

[2] M. A. Sletten and J. Wu, "Ultrawideband, polarimetric radar studies of breaking waves at low grazing angles", *Radio Science*, vol. 31, no. 1, pp. 181–192, Jan. 1996.

[3] D. B. Trizna, "A model for Brewster angle effects on sea surface illumination for sea scatter studies", *IEEE Transactions on Geoscience and Remote Sensing*, 1996, in press.

[4] M. A. Sletten, D. B. Trizna, and J. P. Hansen, "Ultrawideband radar observations of multipath propagation over the sea surface", *IEEE Transactions on Antennas and Propagation*, vol. 44, no. 5, May 1996, in press.

[5] J. C. West, "Effect of shadowing on electromagnetic scattering from rough ocean-wave-like surface at small grazing angles", *IEEE Transactions on Geoscience and Remote Sensing*, 1996, in press.

[6] A. W. Glisson, "Electromagnetic scattering by arbitrary shaped surfaces with impedance boundary conditions", *Radio Science*, vol. 27, no. 6, Nov. 1992.

Dominant Wave Effects in Wavetank Measurement of Microwave Doppler Spectra

W.J. Plant, V. Hesany, W.C. Keller
Applied Physics Laboratory
University of Washington
1013 NE 40th St
Seattle, Washington 98105-6698
plant@apl.washington.edu

M.A. Donelan
Canada Centre for Inland Waters
Burlington, Ontario, Canada L7R 4A6
U025@cs.cciw.ca

Abstract— Coherent microwave measurements of backscattering from a rough water surface were made in a wind wavetank at the Canada Centre for Inland Waters. Ku-band return was collected simultaneously at HH and VV polarizations at a 45 degree incidence angle looking upwind. Data were collected when the wind was steady and when it was suddenly started. We found that the Doppler spectra exhibited peak frequencies which correspond to those expected from a scatterer moving at the phase speed of the dominant wave in the tank. The ratio of VV and HH backscattering cross sections goes from about 6 dB at low wind speeds to about 2 dB at high. Finally, we find that when the wind is suddenly started, both HH and VV cross sections grow rapidly and that the polarization ratio is very nearly 8 dB during this growth. Shortly after the growth stops, however, the polarization ratio drops to a value corresponding to that in the steady wind state. We interpret these results to mean that the primary scatterers in this wind wavetank are not free Bragg waves but scatterers tied to the dominant waves in the tank. We suggest that a tilted Bragg wave bound to the dominant wave could explain these results.

1. INTRODUCTION

In April, 1993, we carried out a series of experiments in the wind-wave tank of the Canada Centre for Inland Waters (CCIW). Doppler spectra of calibrated Ku-band microwave backscatter were collected at a 45° incidence angle looking upwind. HH and VV polarized returns were measured simultaneously. Furthermore wire wave probes, hot film anemometers and a scanning laser slope gauge (belonging to Erik Bock and Tetsu Hara) were operated along with the microwave system. The tank was 76 cm wide, the water depth was 22 cm, and the air channel height was 63 cm. The fetch at the microwave footprint on the water was 11 m. We made measurements at a variety of steady wind speeds, at a variety of water temperatures, and for a series of sudden starts of the wind.

2. KU-BAND DOPPLER SPECTRA

We found that except at the lowest wind speeds, the peak of the Doppler spectrum was at frequencies much higher than that expected for the 1.51 cm Bragg wave. Figure 1 gives examples of HH and VV polarized spectra at a friction velocity, u_* of 0.41 m/s. Note that the spectral peaks in this figure are at 42.7 Hz while the expected Bragg wave frequency is 23 Hz. Some evidence of a secondary peak near the Bragg wave frequency is evident in the VV spectrum but not in the HH one. Such secondary peaks were only evident at higher wind speeds.

3. POLARIZATION RATIOS

Figure 2 shows HH and VV polarized normalized cross sections plotted versus the measured friction velocity for various air and water temperatures. Also shown in the figure is the polarization ratio as a function of u_*. Obviously not much variation of the cross section is observed at different water temperatures at a constant value of u_*. Furthermore, the polarization ratio never reaches the 8 dB level expected from Bragg scattering theory for these condition, probably because of noise contributions for $u_* < 0.1$ m/s. Above this wind speed, however, Figure 2 shows that the polarization ratio is well below 8 dB, decreasing to 2 dB at high wind speeds.

4. SUDDEN STARTS OF THE WIND

We examined the behavior of the polarization ratio, friction velocity, and mean-square wave height following a sudden start of the wind. Figure 3 gives an example of one such run. We note that before the waves have grown above the viscous boundary layer, the friction velocity levels off at about 0.2 m/s and the polarization ratio reaches the

0-7803-3068-4/96$5.00©1996 IEEE

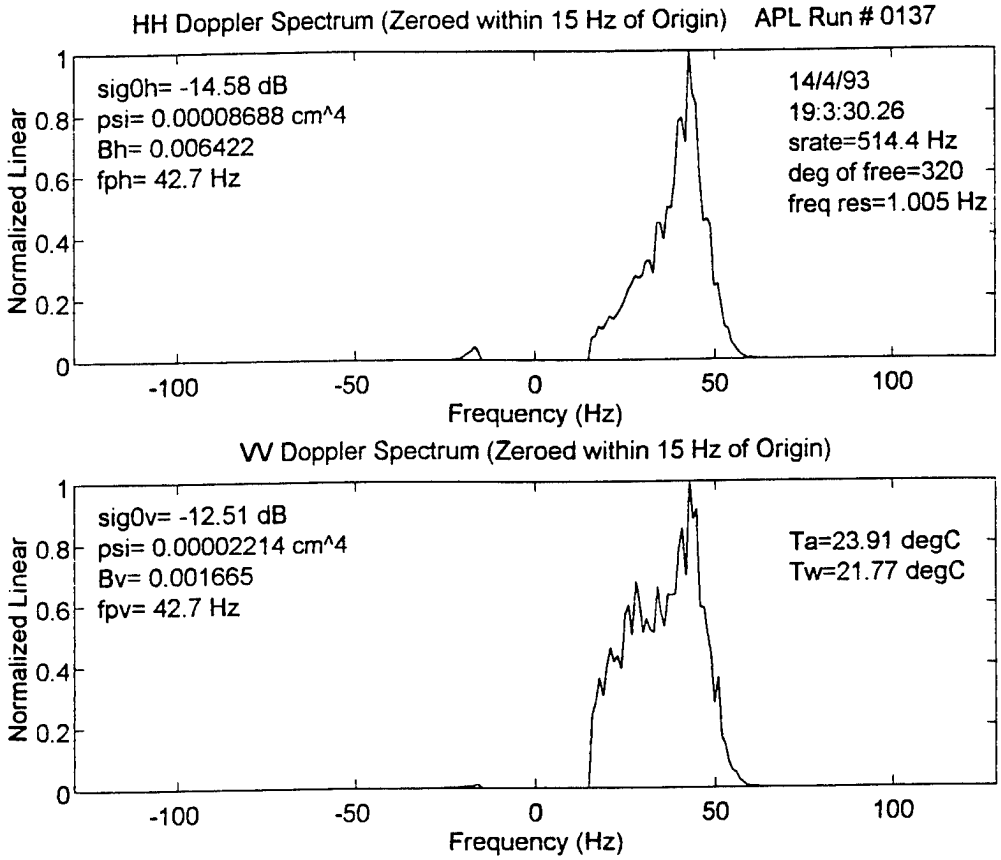


Figure 1: HH and VV polarized Ku-band Doppler spectra taken at a friction velocity of 0.41 m/s.

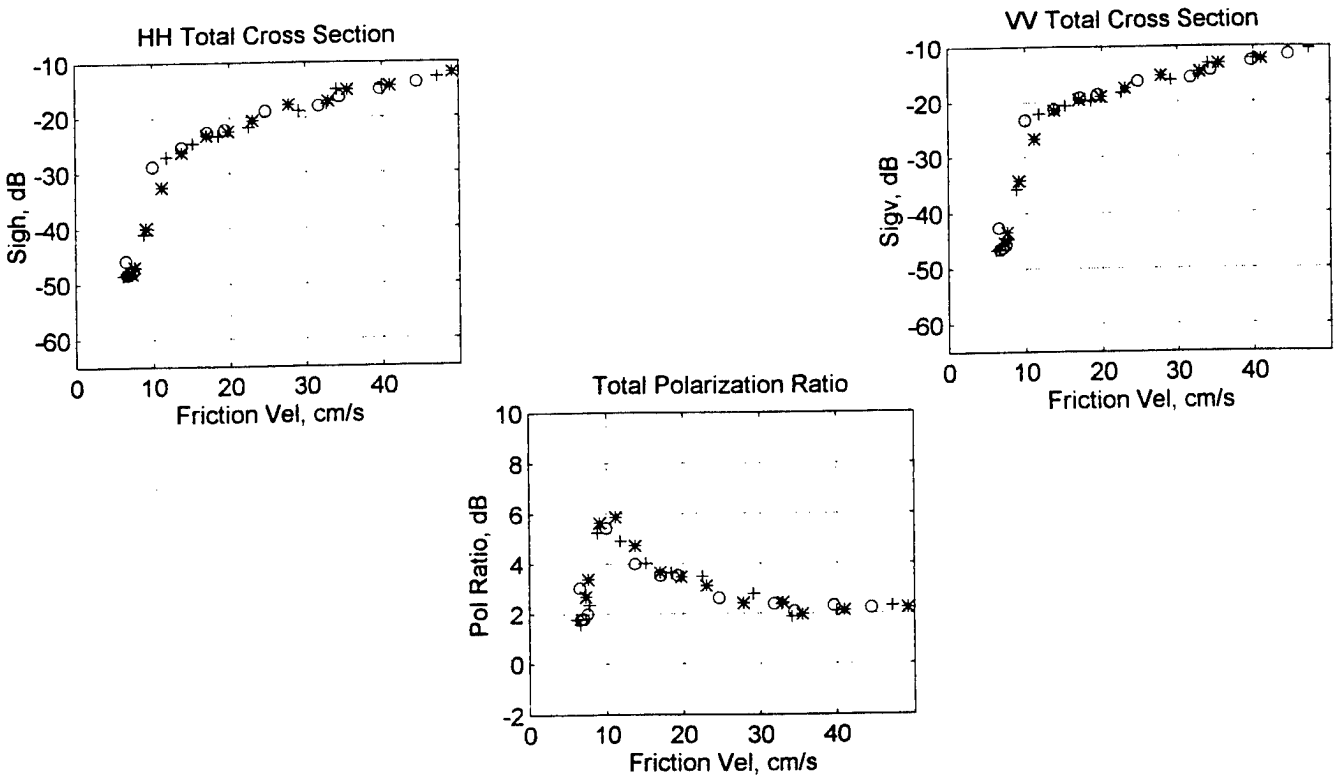


Figure 2: HH and VV polarized Ku-band normalized cross sections and the polarization ratio as a function of friction velocity. Open circles: Ta = 25.9°C, Tw = 10.2°C; Pluses: Ta = 24.6°C, Tw = 17.2°C; Stars: Ta = 24.9°C, Tw = 29.6°C.

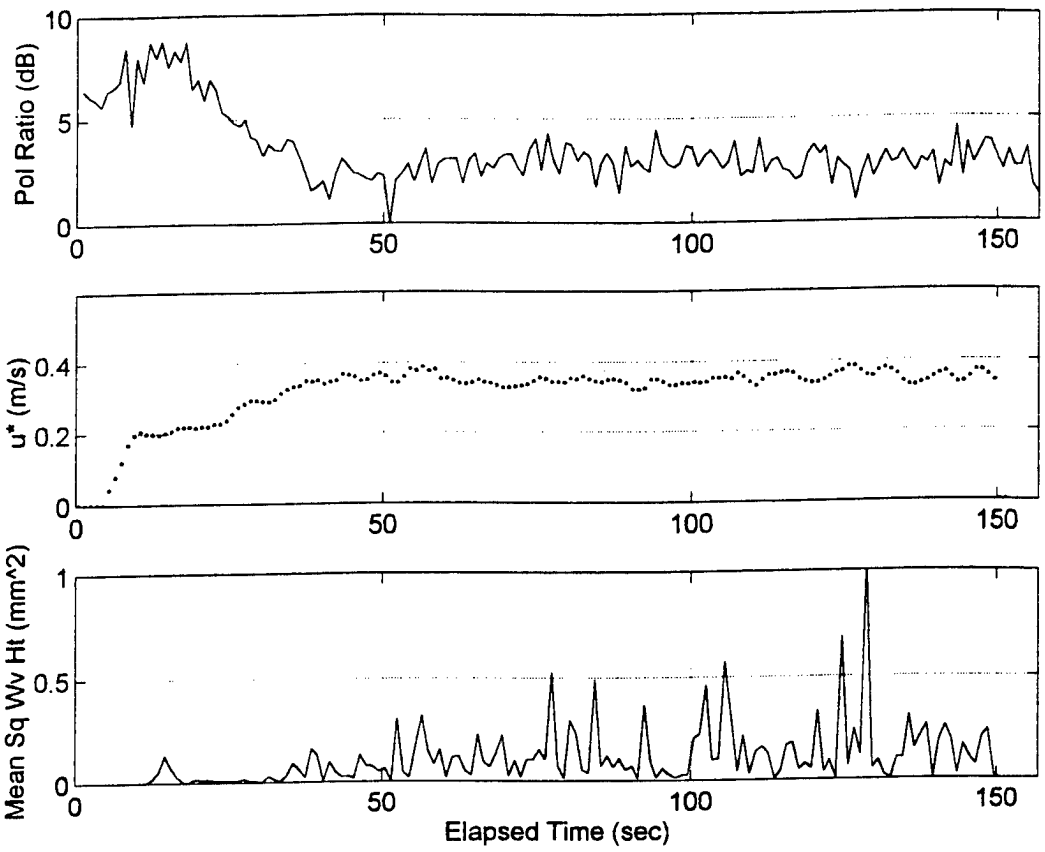


Figure 3: Polarization Ratio, friction velocity, and mean-square wave height observed following a sudden start of the wind.

level characteristic of slightly rough perturbation theory, ie, Bragg scattering. As the waves continue to grow, however, the friction velocity increases toward its final value and the polarization ratio drops toward its final value.

5. INTERPRETATION

We believe that these observations are indicative of the importance of bound waves in a wind-wavetank setting. The laser slope spectra made by Hara and Bock clearly showed that a significant amount of the wave energy propagated at the speed of the dominant wave in the tank. We have attempted to model our measured steady-state cross sections and Doppler offsets using both models in which specular points and tilted Bragg waves move along with the dominant wave. We find that both models are capable of reproducing our observations. The specular point model, however, requires that specular scattering exceed HH polarized Bragg scattering by 3 dB at a friction velocity of 0.25 m/s and an incidence angle of 45° in order to reproduce the data. Since we find this improbable, we suggest that scattering from Bragg waves which are riding on the front face of the dominant wave is the most likely explanation of our results. The importance of such a mechanism on the open ocean remains uncertain.

Depolarization in Microwave Scatterometry

P.H.Y. Lee, J.D. Barter, K.L. Beach, B.M. Lake, H. Rungaldier,
J.C, Shelton, H.R. Thompson, Jr., R. Yee

TRW, R1-1008, 1 Space Park, Redondo Beach, CA 90278, USA
Tel: 310.814.9077 Fax: 310.814.2359 e-mail: peter_lee@atdmac.sp.trw.com

Abstract -- Recent observations of microwave backscatter from breaking gravity waves indicate that the cross-polarized signals (HV and VH) are much larger than expected from theoretical predictions derived using perturbative methods. Experiments have been conducted to specifically examine the depolarization effects of scattering from breaking waves which give rise to such large cross-polarized signals. A simple model is constructed to provide the scattering mechanism which can explain the scattering results.

INTRODUCTION

From wave-tank scattering experiments, we noted that the time-resolved, backscattered, cross-polarized RCS signals peaked simultaneously with the co-polarized signals during a wave-breaking event,[1] and that the cross-polarized signal levels were much *larger* than anticipated from a theoretical point of view based on perturbative models or one-bounce backscatter models. This phenomenon was also seen in the PSD values of the polarimetric Doppler spectra.[2] These results strongly suggested that existing models of depolarized microwave backscatter from rough water surfaces are inadequate. We performed experiments to investigate the depolarization issue in detail. Microwave backscatter results are temporally correlated to polarimetric optical images of the scattering surface using a novel optical diagnostic (the OSED[1]). The OSED also independently verifies the depolarizing nature of a breaking-wave surface. A multiple-scattering model, based on some simple physics, is proposed.

A BRIEF COMMENT ON DEPOLARIZATION THEORIES

The approaches used in extant theories of depolarization in microwave ocean scattering comprise the following: application of the Kirchhoff equation in the tangent plane approximation,[3-5] one-bounce forward scattering from a plane tilted out of the plane of incidence,[3,6] scattering from a perfect conductor,[3,6] scattering in the optical limit,[7] and second-order small perturbation.[8] The physics contained in the above body of work fall into either one of two categories: i) in a specular, *forward reflection* from a tilted plane, the reflected wave's polarization can be rotated if the local surface is tilted such that the normal is not in the plane of incidence (which is defined with respect to the mean water level) and the reflector is not a perfect conductor, or ii) when an incident wave creates a surface current which radiates in all directions, including the backward direction, the backscattered wave's polarization may be rotated if the local surface tilt is out of the plane of incidence and the reflector is not a perfect conductor.

A PROPOSED SIMPLE MODEL

Allowing for multiple scattering, and taking into account that it is *monostatic backscatter* that we are considering, then the *simplest* multiple-scattering element to consider, from which two-bounce backscattering may occur, is a 90°-dihedral. We now construct a simple model which makes use of the 90°-dihedral as an elemental scattering unit by invoking the anholonomic transport of polarization.[9] Simply put, anholonomic transport refers to reflections from a series of reflectors which can result in rotation of the polarization of a given incident electromagnetic wave. Using Jones vectors, one can construct a tool to calculate the polarization of a final wave field for any given incident wave field which has experienced a series of reflections. Let an incident wave field be characterized by the vector $[p_i, s_i]$, where we use standard physics notation in which p- and s-polarizations of the incident and reflected wave fields correspond to the microwave vertical- and horizontal-polarization, respectively. In general, for a series of n successive reflections, the final reflected vector $[p_r, s_r]$, viewed in the direction of the wave propagation vector, is given by:

$$\begin{bmatrix} p_r \\ s_r \end{bmatrix} = R(\alpha_{n,n+1}) M_n(\theta_n) R(\alpha_{n-1,n}) \ldots R(\alpha_{1,2}) M_1(\theta_1) \begin{bmatrix} p_i \\ s_i \end{bmatrix}$$

where M is the reflection operator, R is the rotation operator, and the θ's are the *local incidence angles*. The operators are given by

$$R(\alpha_{j,j+1}) = \begin{bmatrix} \cos\alpha_{j,j+1} & \sin\alpha_{j,j+1} \\ -\sin\alpha_{j,j+1} & \cos\alpha_{j,j+1} \end{bmatrix} \quad \text{and}$$

$$M_j(\theta_j) = \begin{bmatrix} r_p(\theta_j) & 0 \\ 0 & r_s(\theta_j) \end{bmatrix},$$

where $\alpha_{j,j+1}$ is the angle between the normals to the successive planes of incidence, given by $\alpha_{j,j+1} = \cos^{-1}(\vec{a}_j \cdot \vec{a}_{j+1})$, where $\vec{a}_j = (\hat{n}_j \times \hat{k}_j)/\sin\theta_j$ is the unit vector normal to the plane of incidence. $\hat{n}$ and $\hat{k}$ are the local unit surface normal and the incident wavenumber unit vector, respectively. In the mirror operator, r_p and r_s are the reflectances (i.e., Fresnel formulae for reflection) of the p- and s-polarized waves, respectively, at the corresponding local incidence angles, given by:

0-7803-3068-4/96$5.00©1996 IEEE

$$r_p(\theta_j) = \frac{\varepsilon \cos\theta_j - \sqrt{\varepsilon - \sin^2\theta_j}}{\varepsilon \cos\theta_j + \sqrt{\varepsilon - \sin^2\theta_j}} \quad \text{and}$$

$$r_s(\theta_j) = \frac{\cos\theta_j - \sqrt{\varepsilon - \sin^2\theta_j}}{\cos\theta_j + \sqrt{\varepsilon - \sin^2\theta_j}},$$

where $\varepsilon = \varepsilon_r - i\varepsilon_i$ is the dielectric constant of the medium from which scattering (or reflection) occurs.

Consider now a 90°-dihedral shown in Figure 1 where the x-y plane is parallel to the mean water surface. Defining monostatic backscatter as $\hat{k}_3$ anti-parallel to $\hat{k}_1$ (where $\hat{k}_1$, the incident direction, is parallel to the boresight-axis $\hat{r}_b$), reflections from the 90°-dihedral will yield the following two-bounce backscattering results: i) if the dihedral is rotated about the y-axis, a two-bounce reflected wave will retain the same polarization as the incident wave, except that the reflected wave may have a retarded phase if the reflector is a lossy dielectric and p- and s-polarization components may be absorbed differently depending on incidence angle; ii) if the dihedral is rotated about the boresight-axis ($\hat{r}_b$), a rotation of the polarization (with respect to the polarization direction of the incident wave vector) occurs resulting in what is often called depolarization. In essence, vertically-polarized transmitted waves may have a portion (or all) of the incident wave energy returned as horizontally-polarized received waves, thus resulting in a signal in the VH channel, and similarly for the HV counterpart. For a *two-bounce* reflection, it can be shown that the rotation angle in the equation for the rotation operator is equivalent to a rotation of the dihedral with respect to the boresight-axis ($\vec{r}_b$), which we denote as α. Let the first and second reflections occur at *incidence* angles θ_i and θ_{i2}, respectively. For an elemental 90°-dihedral, clearly $\theta_{i2} = (\pi/2 - \theta_i)$.

Using the 90°-dihedral as a scattering element, specular and Brewster events become *special* cases of this model. For $\theta_i = 0°$ and arbitrary α, one-bounce specular reflection results. For $\theta_i = \theta_B$, or for $\theta_i = \pi/2 - \theta_B$, where θ_B is the Brewster angle, and arbitrary α, the first bounce (or the second bounce) is a reflection at Brewster angle and strong attenuation of the locally p-polarized wave results. For arbitrary $\theta_i > 0°$ and arbitrary α, "depolarization" (anholonomic transport of polarization) of the incident wave occurs.

MODEL DEMONSTRATIONS

Applying the anholonomic transport model (henceforth abbreviated to ATM) proposed above, simple demonstrations of effective rotation of polarization (i.e., depolarization in backscatter) using an aluminum 90°-dihedral were performed. The dihedral target is mounted on a loudspeaker cone which can be rotated about its symmetry axis. In operation, the vibrating target is apertured using microwave absorbing material so that only the dihedral portion is visible to the radar and the OSED. Assuming that aluminum is a perfect conductor, it is easily shown that if $\alpha = 22.5°$, an incident p-polarized wave will be returned with p- and s-polarized components of equal amplitude, and for $\alpha = 45°$, an incident p-polarized wave will be returned as an s-polarized wave, and *vice versa.*

Two symmetry properties exist for a two-bounce backscatter from a 90°-dihedral, if temporal phase shifts of $\pm\pi$ are equivalent to unshifted. They are: 1) A symmetry with respect to rotation about the boresight-axis. Thus, the backscatter will yield the same result with respect to rotation, i.e., whether the rotation angle is $+\alpha$ or $-\alpha$; and 2) A symmetry about $\alpha = 45°$, e.g., the result at $\alpha = 67.5°$ will be identical to the result obtained at $\alpha = 22.5°$, and the result at $\alpha = 90°$ will be identical to the result obtained at $\alpha = 0°$, and likewise for negative angles due to the first symmetry.

Data of microwave backscatter results from the dihedral at local incidence angle of $\theta_i = 45°$ and rotation angles (α) of 0°, 22.5°, 45°, 67.5° and 90° respectively, where the dihedral is vibrated at 21 Hz by the loudspeaker and Doppler spectra (PSD) are obtained (space limitations prevent the display of these data in this paper). At $\alpha = 0°$, no depolarization should occur; one observes that the co-polarized (HH and VV) PSDs are equal, and are much greater than the cross-polarized (HV and VH) PSDs. The existence of non-zero cross-polarized components are probably due to edge-effects of the dihedral, non-perfect conductivity of aluminum and imperfect orientation of the speaker cone upon which the dihedral is mounted. At $\alpha = 22.5°$, "partial" depolarization should occur in which the backscattered co- and cross-polarized PSDs should be equal, and one observes that the co-polarized PSDs are indeed equal to the cross-polarized PSDs. At $\alpha = 45°$, "full" depolarization should occur, the cross-polarized components (HV and VH) are much greater than the co-polarized components (HH and VV), which is observed. Symmetry dictates that the result at $\alpha = 67.5°$ should match the result at $\alpha = 22.5°$, and the result at $\alpha = 90°$, should match the result at $\alpha = 0°$; and indeed, both cases are verified by experiment.

Concurrent OSED[1] images of the dihedral at different rotation angles were also obtained in this experiment. The results, being visible, are more dramatic but essentially verify the results obtained using microwaves. Again, due to space limitations, these color images, which indicate the degree of polarization, are not displayed in this paper.

OSED EVIDENCE OF THE DEPOLARIZING NATURE OF BREAKING WAVE SURFACES

The OSED has also been used to independently verify that a breaking-wave surface is capable of significantly depolarizing incident electromagnetic radiation in backscatter. Examples of breaking wave surfaces illuminated by either s- or p-polarized light will be shown (space limitations prevent

the display of data in this paper). Illumination of the wave surface with s- or p-polarized light is achieved by placing appropriate polarizing filters in front of the OSED light source. The polarizing filters used have extinction ratios of $\sim 10^{-4}$. If the polarimetric image (obtained from backscattered light) is the color assigned to the incident polarization, then no depolarization has occurred; if, however, the image has different color, then depolarization has occurred.

A TEST OF THE SIMPLE *AT* MODEL

In order to test our simple model based on anholonomic transport, we examine the case of fully breaking waves as measured at 4.5° grazing angle. Results of the data on co-polarized and cross-polarized ratios of spectral *peak* values are given in the table below. Data of Experiment 1 were obtained using only coarse range gating (i.e., the footprint is several meters in the range direction). Data of Experiment 2 were obtained using range-resolving software where the range resolution is 13.6 cm. The result, calculated using the simple Anholonomic-Transport model (ATM), for parameters $\theta_i = 3.6°$ and $\alpha = \pm 13.3°$, is given in the last row.

	HH/VV	**HV/HH**	**VH/VV**	**HV/VH**
Exper. 1	8.5 dB	-14.5 dB	-8 dB	1.5 dB
Exper. 2	8 dB	-16 dB	-7.5 dB	-1 dB
ATM	*8.4 dB*	*-15.9 dB*	*-7.5 dB*	*0 dB*

The result calculated from the model is in remarkably good agreement with the experimental data, considering that all four polarization ratios have to be matched simultaneously with just one configuration of the dihedral as prescribed by the two angles θ_i and α. Geometrically, it is obvious that the breaking wave surface is not a single large dihedral. However, the result does suggest that multiple scattering is important and anholonomic transport of polarization is a very natural phenomenon. Consequently, one may think of the dihedral model as being representative of an ensemble of scattering elements of varying size, with appropriate orientations. In other words, the ensemble has a mean spread of dihedral orientations given by the corresponding θ_i and α. Thus, if the field backscattered by a rough breaking-wave surface may be considered to be due to scattering from an ensemble of 90°-dihedral elements oriented according to an appropriate random distribution, it may be depolarized in the same way as the field reflected by a single, large 90°-dihedral of the same electrical properties tilted and rotated in such a way that similar backscatter signals will be obtained. In any case, the result shown in the example is sufficiently convincing of the merit of the model that further investigations regarding the AT model will continue.

SUMMARY

We have introduced a simple model based on anholonomic transport of polarization to explain the physical mechanism which could provide the measured results of microwave backscatter data obtained from breaking waves at small grazing angle. Furthermore we have also independently demonstrated through OSED measurements, that breaking-wave surfaces are capable of returning depolarized (polarization rotated) backscatter. Finally, the results of model calculations are shown to be in good agreement with measured microwave data. It should be pointed out that a *complex model* could also be constructed if the matrix elements in the reflection operator were complex scattering coefficients instead of reflectances given by the Fresnel formulae, however, such a consideration requires a full treatment of multiple scattering which we will reserve for a future effort.

ACKNOWLEDGMENTS

This work was supported by ASAP/ISSO, Department of Defense, Contract No. DMA 800-94-C-6008. The authors are grateful to Professor Marshall Tulin and his staff of UCSB/OEL for the use of the OEL wavetank facility.

REFERENCES

[1] J.D. Barter and P.H.Y. Lee, *IGARSS '96*, Paper No. 96.0087.
[2] P.H.Y. Lee, et al, *IGARSS '96*, Paper No. 96.0088.
[3] P. Beckmann, *Proc. Symp. Electr. Theory and Antennas* (E.C. Jordan, Ed.), 717-726 Pergamon, NY (1963).
[4] T. Hagfors, *J. Geophys. Res.* **69**, 3378-3784 (1964).
[5] A.K. Fung, *Proc. IEEE* **54**, 395-396, (1966).
[6] K.M. Mitzner, *Radio Science* **1**, 27-29 (1966).
[7] R.D. Kodis, *IEEE Trans. Ant. and Propagation* **AP-14**, 77-82 (1996).
[8] G.R. Valenzuela, *IEEE Trans. Ant. and Propagation* **AP-15**, 552-557 (1997).
[9] M.V. Berry, *Nature* **326**, 277-278 (1987).

Figure 1

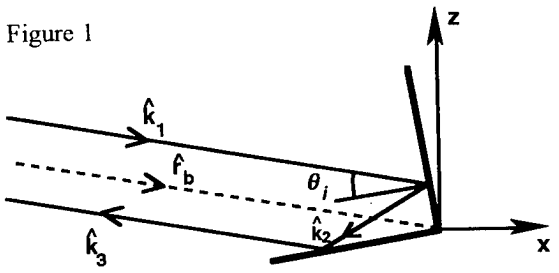


FIG. 1 Schematic of scattering from a 90°-dihedral. The incident wave has direction $\hat{k}_1$ and is parallel to the boresight direction $\hat{r}_b$. Successive ray paths have directions $\hat{k}_2$ and $\hat{k}_3$. The local incident angle θ_i need not be equal to the boresight grazing angle of the PCR if the dihedral is tilted (i.e., rotated with respect to the y-axis), as shown in the figure. The dihedral may rotate with respect to the boresight axis (but is not rotated in this figure), which then rotates the polarization.

Influences of Wind Bursting on Radar Return

Andrew Savtchenko, Shih Tang and Jin Wu

Air-Sea Interaction Laboratory
Graduate College of Marine Studies, University of Delaware
Lewes, Delaware 19958
(302) 645-4214 / FAX: (302) 645-4201 / andrey@udel.edu

Abstract -- Wind bursting events associated with intermittent and violent momentum transfers in the marine surface layer are identified with a three-axis sonic anemometer. Simultaneous measurements of X-band radar returns, airlows and sea-surface displacements are investigated during these events. Localizations of bursts, with respect to the underlying dominant waves, are estimated. Energies of surface elevations and radar returns during burstings are also estimated. The conditional sampling of the data during bursting events does not reveal any link among the enhanced air-sea momentum transfers, surface elevations and the radar returns.

INTRODUCTION

The existence of ordered motions in shear flows has been established in a number of experimental works. In [1] a sheared airflow above a wavy water surface was studied in a tank and evidences of ordered motions were presented. Using visualizing techniques, it was demonstrated that these motions had a horizontal length scale corresponding to the wavelength of the underlying wind waves. The detailed laboratory study in [2] demonstrated that the wave breaking induced a significant augmentation of the total wind stress. Apparently, water surface waves trigger instabilities in the airflow, which results in strongly enhanced intermittent wind stress (bursting) or momentum flux [3]. The local jump of the wind stress, shown in the wave crest region, may feed back to change the nature of the wave crest, resulting in wave breaking. The study [4] of the roughness structure in the breaking region showed that it was ordered and yielded Bragg-like return in their X-band radar. In this sense, the suggestion to incorporate in the radar modulation transfer function a term, describing wind stress modulation, deserves due attention [5]. However, the periods between burstings in the field showed no dependence on the surface wave field [6]. Still, the equilibrium spectrum of water waves and the intermittent wind turbulence were theoretically linked in [7]. The apparent contradiction between laboratory and field observations, as well as the scarce of synchronous radar return and turbulent flow records, motivated us to conduct a field study in which simultaneous observations of air flows, surface elevations and radar returns were performed.

EXPERIMENTAL SET-UP

The field station was located in the Delaware Bay, about 600 m offshore in 4-m deep water, as shown in Fig.1. A 6-m instrument boom was extended away from the tower with a three-axis sonic anemometer, wave gauge, and radar mounted at the end. The sonic measured three wind-velocity components, u, v, w, and temperature T at a rate of 10 Hz. The sea-surface displacements were measured with the wave gauge [8]. The radar used was a simple Gunnplexer transceiver with a transmitted power of 20 mW and a horn antenna to form a conical beam. It operated in the X-band (10.28 GHz) in continuous-wave regime and illuminated the surface underneath the sonic. The antenna beam width of 25° at -3 dB and the incidence angle θ_i of 45° gave an illumination spot of the order of 40 cm x 25 cm. The polarization of the transmitted and received radiation was vertical. Finally, the signals from all instruments were sampled at 300 Hz.

CALCULATIONS

The downwind and crosswind components of the airflow, denoted as u and v correspondingly, were retrieved from the sonic U and V channels using: $u = V\sin\theta + U\cos\theta$, $v = V\cos\theta - U\sin\theta$. Here $\theta = \tan^{-1}(\langle V\rangle/\langle U\rangle)$ and brackets indicate one-minute average. The wind fluctuations u', v' and w' were

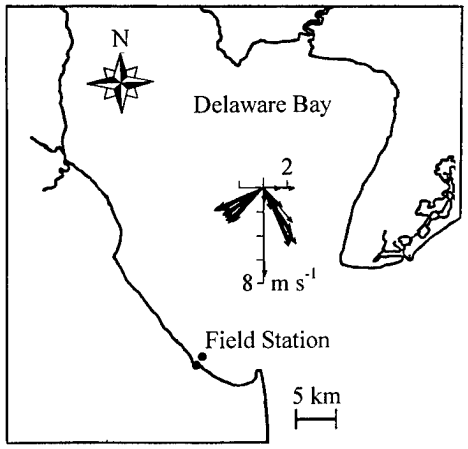


Figure 1. Location of the field station and derived U_{10} winds.

0-7803-3068-4/96$5.00©1996 IEEE

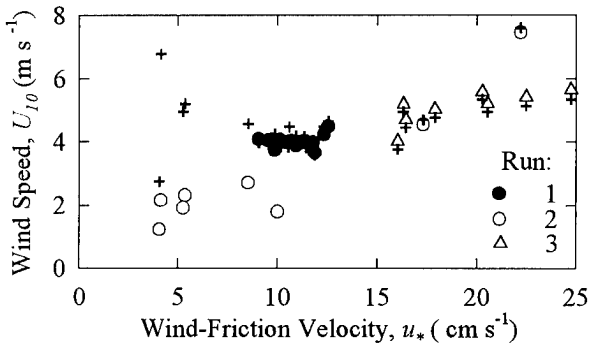


Figure 2. Derived U_{10N} (+) and U_{10} (all others)

derived by subtracting the corresponding averaged values, $<u>$, $<v>$, and $<w>$ from the instantaneous wind components u, v, and w. Every five of the averages were combined to form a five-minute average. Similarly, the five-minute averages of the wind-friction velocity, u_*, were derived using

$$u_*^4 = <u'w'>^2 + <v'w'>^2$$

The detection of bursting was accomplished using approaches similar to [1] and [6]. Whenever $(u'w')/(\sigma_u\sigma_w)<-1$ a bursting was detected, after which the event was classified as a burst ($w'>0$) or a sweep ($w'<0$). Here σ_u and σ_w are the root mean square values of u and w, respectively. We assume that the time scale T_b of every event is defined by the mean airflow $<u>$ and the dominant wavelength λ_p of the sea surface: $T_b = \lambda_p/<u>$ [1]. In terms of number of samples it is $N_b = T_b f_s$, where f_s is the sampling frequency. Now, we can accomplish conditional sampling of a property of interest P_i during jth event:

$$(P_i)_j = \sum_{k=k_j-N_b/2}^{k_j+N_b/2} P_{i,k} \qquad i = b \text{ or } s$$

where the summation is centered about k_j, the point of the first appearance of the jth event. We study properties ($u'w'$) and mean-square (MS) surface elevations and radar return. We define a five-minute estimate of contribution in moments of bursts and sweeps as

$$C_i = \left[\sum_{j=1}^{N} (P_i)_j\right] \Big/ \left(\sum_{k=1}^{N_5} P_k\right) \qquad i = b \text{ or } s$$

where N is the number of detected bursts or sweeps in a five-minute interval, N_5 is the total number of samples of the property in five-minute interval, and occurrence as $O_i = N{\cdot}N_b/N_5$, $i = b$ or s. O_i must be treated as the portion of a five minute period occupied by bursts or sweeps. The wavelet decomposition of the dominant surface waves is invoked to study the relation between the phase of the dominant waves and moments of the first appearance of burst and sweep events. Fourier spectra of the wavegauge signal are calculated (not shown here) to retrieve λ_p, H, and c_p, the last two being the mean wave height and the phase speed of the dominant waves. The observed winds are converted to U_{10} and neutral U_{10N} winds using procedures described in [3].

ENVIRONMENTAL CONDITIONS

The experiment was carried out in the summer of 1994. The conditions under study are grouped into three runs, 1, 2, and 3 conducted on August 11, 29, and 30, respectively. Low to moderate winds were prevailing during the experiment, Fig.2. Run 1 was during slightly stable , Run 2 very stable, and Run 3 slightly unstable conditions. The winds with the longest fetches are selected from all records, and the five-minute U_{10} averages are pictured as vectors in Fig.1. The basic parameters of the selected conditions are given in the table below:

Run	λ_p (m)	c_p/u_*	u_* (cm s^{-1})	H/λ_p
1	3.2	21	11	0.037
2	4.3	18	14	0.023
3	7.7	17	20	0.022

RESULTS AND DISCUSSION

Bursts and sweeps contribution to the along-wind component of the stress vector, $<u'w'>$, are presented in Fig.3a. The value C_i 110% is detected during stable conditions. In general, bursts contribute slightly more than sweeps, which is in agreement with [6]. The contributions to the MS surface elevations from the periods of bursts and sweeps is shown in Fig.3b. The frequency range here is from 0.017 to 12 Hz. This picture almost repeat occurrences (Fig.4), showing that there is no significant augmentation of the surface elevations over this frequency range during detected events. The contribution to the MS surface elevations is merely proportional to the time occupied by the events. The contribution to the MS radar return from bursts and sweeps has the same pattern, Fig.3c. The contribution does not depend on u_*. There is some increase in the sweeps contribution at low u_*. It is likely, however, that this increase is influenced by the very stable stratification, rather than u_*. During higher winds of Run 2 the stratification changes to neutral, Fig.2. The contribution of the radar signal during these higher winds is virtually the same as for the neutral lower-winds conditions of Run 1. Run 2 with its large range of winds and stratifications shows that all contributions, as well as occurences, decrease as u_* increases and stratification tends to neutral. On average, bursts and sweeps occupy only about 30% of the observation time, giving the dominant surface wavelength is involved as a length scale in the calculation of the time scale of the ordered motions, Fig.4. However, $u'w'$ overcome the threshold actually for a much shorter time. The probability that k_j appears over a certain phase of the dominant waves

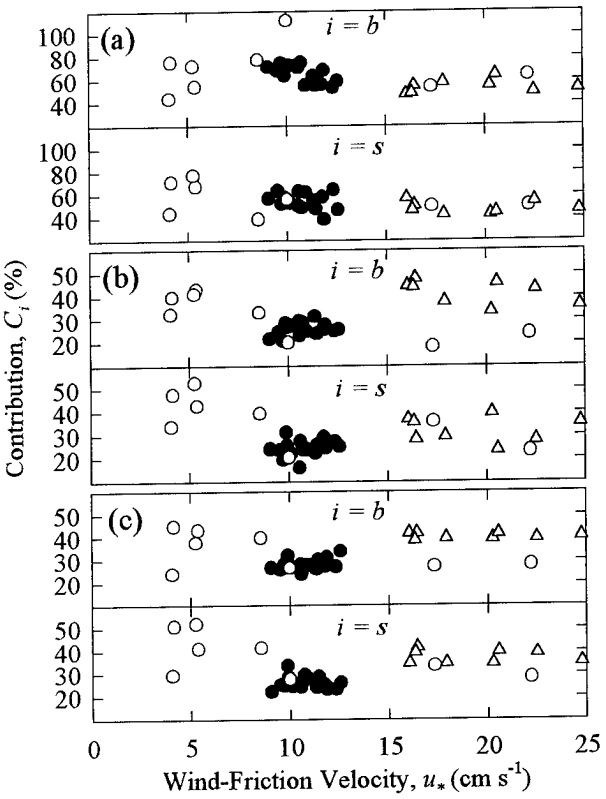


Figure 3. Burst and sweep contribution to (a) <u'w'>, (b) surface elevations, and (c) radar return.

is shown in Fig.5. Apparently, bursts and sweeps are distributed uniformly over the dominant wave profile.

CONCLUSIONS

Strong contributions of bursts and sweeps to the $<u'w'>$ component are identified at low to moderate winds. The instants of appearance of these events are not correlated with the phase of dominant waves. Most likely, only the most sharp-crested waves serve as a trigger. The mean square surface elevations and radar returns do not reveal enhancement during events. Apparently, the intermittent energy cascade in the airflow ends on the surface viscous scales which are quite fine and short-living. The contributions during events show a tendency to depend stronger on the atmospheric boundary layer stratification than on u_*.

REFERENCES

[1] H. Kawamura, and Y. Toba, "Ordered motion in the turbulent boundary layer over wind waves", J. Fluid Mech., vol.197, pp.105-138, 1988.

[2] M. L. Banner, "The influence of wave breaking on the surface pressure distribution in wind-wave interactions", J. Fluid Mech., vol.211, pp.463-495, 1990.

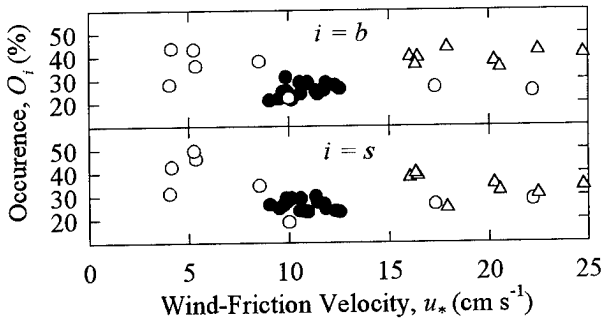


Figure 4. The occurences of bursts and sweeps.

[3] G. L. Geernaert, "Bulk parameterization for the wind stress and heat fluxes", in Surface Waves and Fluxes: Theory and Remote Sensing, vol.1, G. L. Geernaert and W. J. Plant, Eds. Norwell, Mass.: Kluwer Academic, 1990, pp.91-172.

[4] M. L. Banner and E. H. Fooks, "On the microwave reflectivity of small-scale breaking water waves", Proc. R. Soc. London, A399, pp.93-109, 1985.

[5] A. Schmidt, V. Wismann, R. Romeiser, and W. Alpers, "Simultaneous measurements of the ocean wave-radar modulation transfer function at L, C, and X bands from the research platform *Nordsee*", J. Geophys. Res., vol.100, pp.8815-8827, 1995.

[6] R. S. Boppe and W. L. Neu, "Quasi-coherent structures in the marine atmospheric surface layer", J. Geophys. Res, vol.100, pp.20635-20648, 1995.

[7] Z. Shen and L. Mei, "Equilibrium spectra of water waves forced by intermittent wind turbulence", J. Phys. Oceanogr., vol.23, pp.2019-2026, 1993.

[8] R. Chapman and F. M. Monaldo,"The APL wave gauge system", SIR-91-041, 1991, Applied Physics Lab., The Johns Hopkins Univ., Laurel, MD.

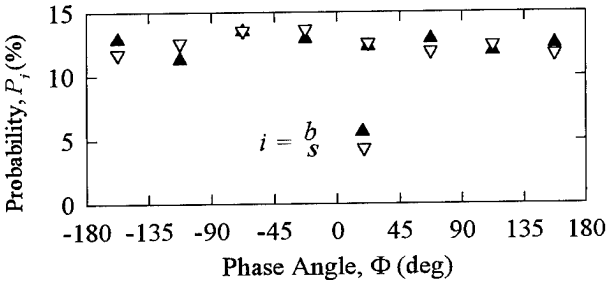


Figure 5. The phase of dominant waves at bursts and sweeps in 45° bins.

Measuring Small-Scale Water Surface Waves: Nonlinear Interpolation & Integration Techniques for Slope-Image Data

Jason M. Daida[1], Robert R. Bertram[1], David R. Lyzenga[2], Christian Wolf[2], David T. Walker[2], Stephen A. Stanhope[1], Guy A. Meadows[2], John F. Vesecky[3], and Donald E. Lund [2]

[1]The University of Michigan, Artificial Intelligence Laboratory
2455 Hayward Avenue, Ann Arbor, Michigan 48109-2143
(313) 747-4581 FAX (313) 764-5137 EMAIL: daida@eecs.umich.edu
[2]The University of Michigan, Department NAME, 2600 Draper Rd., Ann Arbor, MI 48109-2145
[3]The University of Michigan, Department AOSS, 2455 Hayward Ave., Ann Arbor, MI 48109-2143

1. INTRODUCTION

In observing oceans using synthetic aperture radar (SAR), researchers have shown that small-scale water surface waves can significantly affect the radar backscatter from an ocean surface. Furthermore, these small scale water surface waves are known to have a significant role in affecting the ocean's drag coefficients and gas-exchange rates. Unfortunately, the hydrodynamics of these small scale water waves are neither well understood nor easily measured.

Key innovations that have allowed measurement of small-scale water waves currently include Jähne's refraction-based technique [3]. Several instruments have now been built that have been based on Jähne's technique (including instruments at the Scripps Institute of Oceanography, the University of Heidelberg, and The University of Michigan). Unlike other techniques (like stereo imaging) that attempt to measure the topography of an ocean surface directly, Jähne's technique measures topography indirectly by imaging surface derivatives (i.e., slope-image data).

In many cases, deriving topography from slope-image data is a linear problem and is amenable to numerical integration. However, for cases involving breaking waves and turbulence, the derivation becomes nonlinear because of discontinuities caused either by air entrainment or by instrument physics that limit the dynamic range of wave-slope angles that can be measured. Both types of discontinuities can significantly affect analyses that depend on either slope or topographic data. (See Figures 1 and 2.)

Consequently, our investigation has focused on surface reconstruction methods using nonlinear interpolation and numerical integration techniques. This paper briefly describes our method and shows a few examples of reconstructed surfaces.

2.METHOD

In [1], we introduced a computational hybrid that has demonstrated to be capable of mitigating the types of nonlinearities present in slope-image data. (The hybrid uses both FFT integration and genetic algorithms to solve for Fourier series coefficients. The coefficients, in turn, are used for interpolation and for integration.) Since then, we have incorporated complementary methods that have increased the performance of our earlier solution. These methods have stemmed from our ongoing work in computational hybridization. (See [2].)

Many of the new enhancements involve the genetic algorithm portion of the hybrid. Genetic algorithms belong to the class of domain-independent algorithms (which includes neural nets) and represents one of the few probabilistic techniques that exploit combinatorial search for optimization. In our case, a genetic algorithm optimizes for a set of Fourier coefficients along a row (or column) vector from a slope image that describes a curve that contains those portions of the vector data that are unaffected by either bubbles or drop-outs. The search space is substantial, but can be highly constrained. For constraining, we have used bootstrapping and an index-mediated hybridization scheme that is described in [2]. We have implemented our system prototype on a parallel machine (i.e., an IBM SP-2).

3. RESULTS AND CONCLUSION

The data set featured in this paper is from a custom built, single-gradient direction Jähne-type instrument [4]. Measured were small-scale waves in the context of a steady spilling breaking wave, which were generated in a specialized wave tank facility at U-M. (This facility features a recirculating flow with an extremely low turbulence level across a wide cross section, so that breaking waves can be observed fairly undisturbed from the flow.) Over three gigabytes of data have been collected that represent various breaking and non-breaking conditions.

Figure 3 shows examples of our method for nonlinear interpolation and integration along the gradient direction imaged by the instrument. The results were obtained with our parallel system prototype on an IBM SP-2 and used four processing nodes.

The results indicate that the algorithm does correctly perform nonlinear interpolation and integration. Further refinements are indicated, however, to increase reconstruction accuracy and artifact suppression.

BIBLIOGRAPHY

[1] Daida, J.M., et al., "Measuring Topography of Small-Scale Water Surface Waves," Proc. IGARSS '95, pp. 1881–83.

[2] Daida, J.M., S.J. Ross, and B.C. Hannon, "Biological Symbiosis as a Metaphor for Computational Hybridization," *Proceedings of the Sixth Int. Conf. GA*, San Francisco: Morgan Kauffman, Inc., 1995. pp. 328–35.

[3] Jähne, B., *Spatio-Temporal Image Processing: Theory and Scientific Applications*, Berlin: Springer-Verlag, 1993.

[4] Wolf, C., *Surface Properties of Breaking Waves*, Diploma thesis, University of Heidelberg, Germany, 1994.

0-7803-3068-4/96$5.00©1996 IEEE

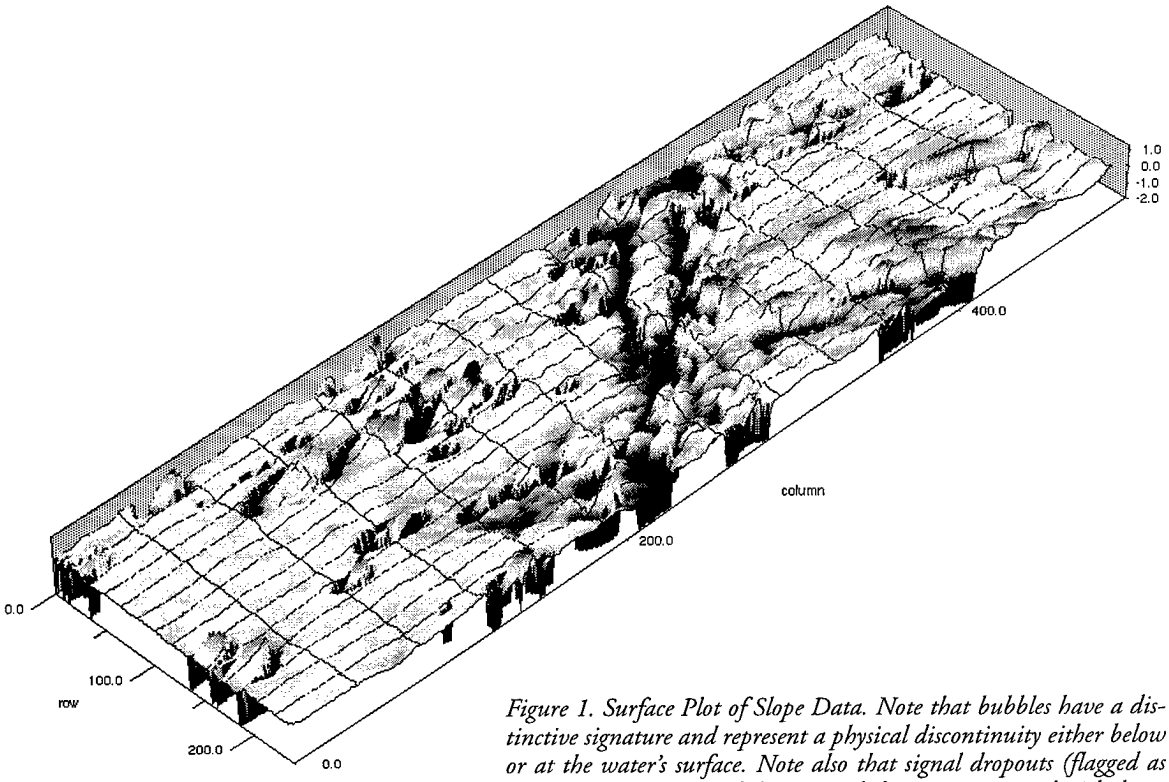


Figure 1. Surface Plot of Slope Data. Note that bubbles have a distinctive signature and represent a physical discontinuity either below or at the water's surface. Note also that signal dropouts (flagged as pixels with slope -2.0 rad) have rounded corners associated with them.

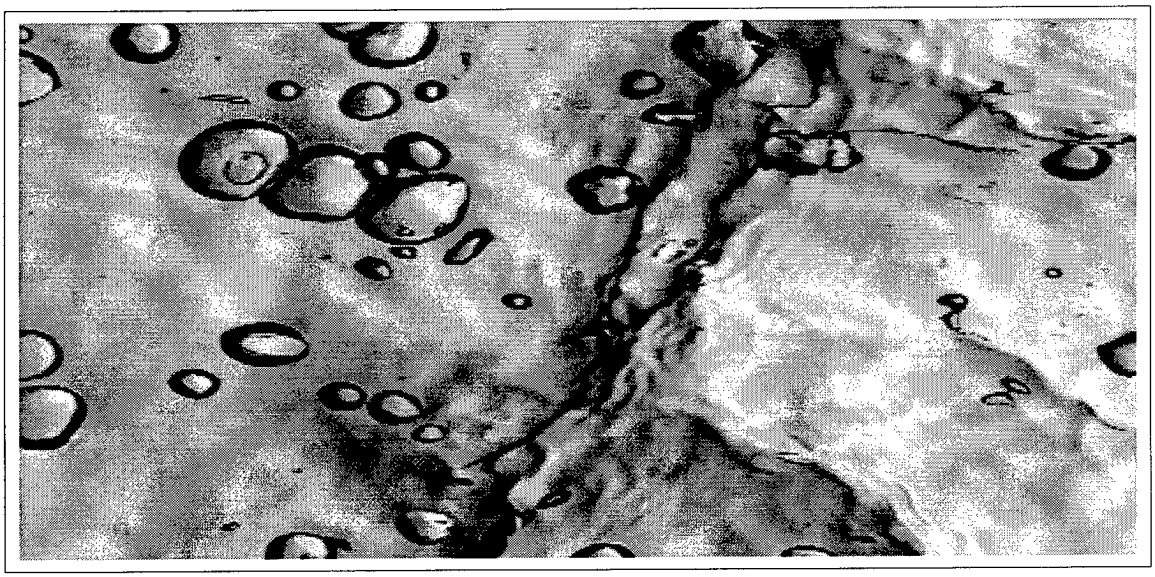


Figure 2. Density Plot of Slope Data: Breaking Wave Case. This slope image is associated with the data shown in Figure 1. The plot measures 500 × 240 pixels, which corresponds to an area of 80 mm × 62 mm of water surface. Black areas depict signal dropouts (i.e., slopes corresponding to such areas have exceeded instrument measurement capability). This data is typical of slope imagery of breaking waves.

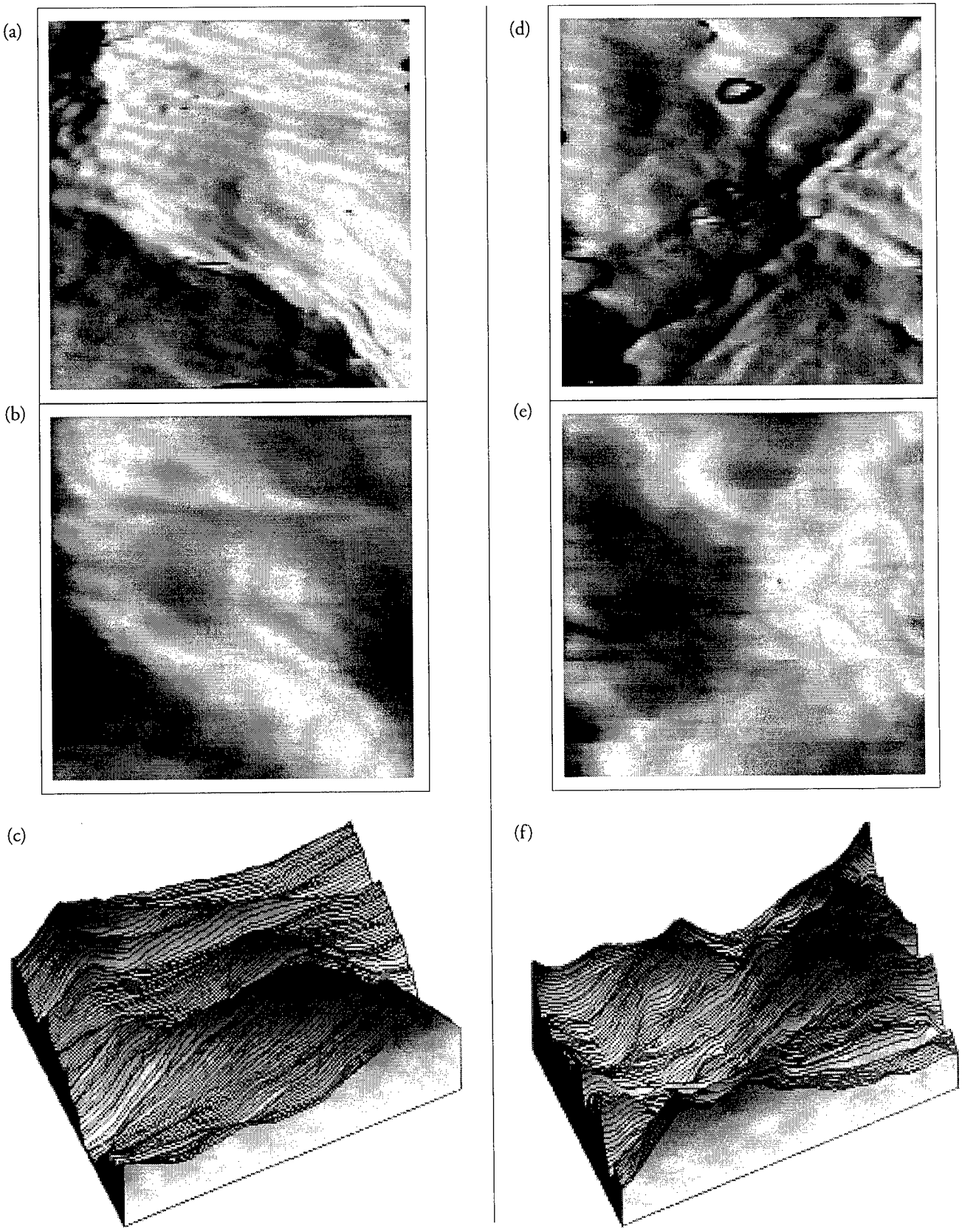


Figure 3. Results. (a) 128× 128 Pixel Slope Image. (b) Reconstructed Topography. (c) Surface Plot. (d) 128× 128 Pixel Slope Image. (e) Reconstructed Topography. (f) Surface Plot.

Remote Sensing: Economic Viability of Environmental Monitoring

Molly K. Macauley and Timothy J. Brennan
Resources for the Future, 1616 P Street, NW, Washington, DC 20036
tel. 202-328-5043, fax. 202-939-3460, email: macauley@rff.org

Abstract -- We assess the benefits of future higher spatial and spectral resolution space-based remote sensing for environmental regulation and enforcement. We draw from the economics literature on regulation, monitoring, and enforcement to frame our analysis of the technological attributes of the emerging remote sensing systems. We find that the systems are likely to have significant and highly beneficial implications for regulation and enforcement.

INTRODUCTION

The environmental benefits of future, higher spatial and spectral resolution remote sensing space systems (hereinafter, RSS) are significant. Higher resolution sensors will offer more information and in some cases, more accurate and timely information than existing systems. Their coverage will also enable a synoptic and geographic context generally unmatched by aerial or *in situ* data. The systems will not, however, supply continuous real-time monitoring information, although as future configurations of RSS systems include more spacecraft, permitting denser data collection, some approximations to continuous monitoring may become available.

The emerging systems have several implications for the way in which the Environmental Protection Agency and other decision makers regulate. For instance, new remote sensing technologies can improve understanding of, and in many cases, reduce the range of uncertainty regarding the extent of environmental degradation. The new technologies may also reduce the cost of compliance with and enforcement of both domestic regulations and international agreements concerning the environment (for general discussion of using RSS data for monitoring international agreements, see [1] and [2]). In addition, the data may permit closer monitoring of information that is self-reported by regulatees and play a key role in adjudicating environmental lawsuits and disputes.

RESULTS FROM THE LITERATURE

In this paper we focus on enforcement properties of RSS with respect to their implications for how regulatory policy is made and conducted. We base our analysis on the literature on monitoring and enforcement (for example, see [3] - [8]). From that literature, we know that

- The purpose of environmental regulation is to reduce the level of pollution or ecosystem degradation to the point where the benefits of any *additional* environmental improvements just equal the *additional* costs, in lost production or extra abatement, from achieving those improvements.
- The purpose of detecting and punishing those who violate such regulations is to lead potential polluters to take the costs of environmental degradation into account in making their production and abatement decisions.
- Achieving the benefits of enforcing environmental regulations itself involves a variety of costs associated with identifying and measuring potential violations, the accuracy of those measurements, the resolution of disputes regarding liability, and the imposition of specific punishments.

RSS, REGULATION, AND ENFORCEMENT

Several factors related to RSS affect the efficacy with which these principles can govern regulation and enforcement. These factors include:

-- the nature of the RSS information (quantity and quality). RSS offers to increase the information base with which to enforce regulation, by providing more information, more accurate information, and more information over time. While it is not clear the extent to which details of specific emissions in some media (such as air) will be available from space-based sensing, it can provide a context for understanding the damages that may be linked to such emissions. This information in turn can assist in more accurately assessing damages, in better targeting enforcement and remediation, and in providing better information for deciding whether to use quantity- or tax-based means of pollution control (that is, whether to regulate emissions *per se* or use taxes, fees, or other financially based approaches). In addition, more accurate information in enforcement can minimize punishment of those who do not violate regulations.

-- data access. RSS data may be more readily available to regulators, regulatees, and third parties than aerial or *in situ* information. This accessibility may be one of the most significant attributes of RSS for enforcement. RSS data availability may reduce transactions costs of

0-7803-3068-4/96$5.00©1996 IEEE

enforcement to the point where private bargaining may substitute for public policy. Regulatees may find that their own use of RSS data can improve their self-reporting efforts. Moreover, if the accessibility of RSS data encourages credible use (since other parties can acquire the data and check its veracity), then RSS may further reduce the need for inspections.

-- cost. Emerging RSS may be most cost-effective compared with other means of data collection when information is sought about processes or locales that are difficult to access, require a synoptic view, or require nonobtrusive (such as a pristine habitat) or concealed sensing (such as random, unannounced site inspections). The prices to be charged for data from emerging RSS are not yet certain, but the costs of using RSS have, in general, been declining for several reasons. One is the decreasing cost of small spacecraft and launch services; another is decreasing costs and increasing capability of software (such as geographic information systems) and hardware (such as computers and processing). Another important development is the availability of the global positioning spacecraft system (see [9] for excellent discussion). If the combined costs of data and its application indeed result in more cost-effective information, then several policy implications follow. One is that reductions in the cost of repeated measurements can improve accuracy and the likelihood of detection of violations of environmental regulations, or foster detection when polluting activities are subject to random variation from climate and other factors. Lower monitoring costs can also facilitate enforcement and in turn boost any deterrence effects of that enforcement.

-- sensor concealment. RSS has a rather unique attribute, namely some ability to observe without the awareness of the observed entity (although the orbital parameters of the spacecraft are on public record). The possible opportunity to conceal the act of observation can increase both the likelihood of detection and the costs of concealment of activities by the observed party, thus improving the effectiveness of enforcement activities.

Table 1 summarizes these policy implications. Taken together, they may significantly improve the effectiveness of environmental regulation and enforcement. They may even radically alter the way in which decision makers frame new environmental regulation in the future.

ACKNOWLEDGMENTS

This research is part of a larger research project on RSS and regulation, jointly funded by the U.S. Environmental Protection Agency, Office of Policy, Planning, and Evaluation, and Resources for the Future. Responsibility for errors and opinions rests with the authors.

REFERENCES

[1] B. Berkowitz, "Use of Intelligence Data for Environmental Monitoring: Summary of Meetings Held by the Council on Foreign Relations," unpublished.

[2] M. Macauley, "Collective Goods and National Sovereignty: Conflicting Values in Global Information Acquisition," Proc. of the Conf. on Space Monitoring of Global Change. San Diego: Univ. of California Inst. on Global Conflict and Cooperation, 1992, pp. 31-47.

[3] C. Russell, W. Harrington, and W. Vaughan, Enforcing Pollution Control Laws. Washington: Resources for the Future, 1986.

[4] W. Harrington and M. Macauley, "The Value of Information and th Cost of Advocacy, unpublished.

[5] C. Russell, "Monitoring and Enforcement," in Public Policies for Environmental Protection. P. Portney, Ed. Washington: Resources for the Future, 1990, pp. 243-274, esp. 248-253.

[6] J. Harford, "Self-Reporting of Pollution and the Firm's Behavior under Imperfectly Enforceable Regulations," J. of Environ. Econ. and Management, vol. 14, pp. 293-303, 1987.

[7] A. Malik, "Self-Reporting and the Design of Policies for Regulating Stochastic Pollution," J. of Environ. Econ. and Management, vol. 24, pp. 241-257, 1993.

[8] L. Kaplow and S. Shavell," Optimal Law Enforcement with Self-Reporting of Behavior," J. of Pol. Econ., vol. 102, pp. 583-606, 1994.

[9] S. Pace et al., The Global Positioning System. Washington: RAND Corporation, 1996.

Table 1. Implications of New RSS Technologies for Enforcing Environmental Regulations

Factors in regulation and enforcement	Is new RSS advantageous?	Implications for enforcement
Information (quantity, quality)		
geographic coverage	++	permits more accurate assessment of damages, including context
synoptic view	++	permits improved targeting of enforcement activity
accuracy	+	informs choice between quantity- and tax-based control
real-time coverage of some activities	+	helps minimize punishment of nonviolators
continuous monitoring	-	
Data access		
to regulators	++	facilitates private enforcement by regulatees
to regulatees	++	facilitates role of third parties in enforcement
to third parties	++	reduces need for inspections
in real time	+	
Cost		
of difficult-to-access processes/sites	++	likely to be cost effective compared with aerial or *in situ* observation
of nonobtrusive observation	++	permits some repeated measurements
of concealed sensing	++	lowers enforcement costs, boosts deterrence effects
Sensor concealment	++	increases cost of concealment by observed, increases likelihood of detection, improves effectiveness of enforcement

Key: ++ = significant benefit; + = some benefit; - = no particular advantage

Ecosystem Management: A Decision Support GIS Approach

Wayne (Wei) Ji, Ph.D.
Southern Science Center
National Biological Service
700 Cajundome Blvd.
Lafayette, LA 70506
(318)266-8587; jiw@nwrc.gov

ABSTRACT

This paper describes a new approach using decision support GIS for handling information in ecosystem management. Technical research efforts resulted in specialized spatial decision support systems for wetland restoration planning, wetland permit analysis, and wildlife research and management. These applications are briefly presented to illustrate the usage of the methodology. With its powerful capabilities in information synthesis, analytical visualization, and spatial simulation and modeling, the decision support GIS provided cost-effective technical tools and a conceptual framework for integrating natural resource management with an ecosystem approach.

INTRODUCTION

Ecosystem management is a new vision of environmental conservation in which information is the key. The following technical barriers have been identified by resource managers and researchers in information synthesis and analysis in ecosystem management: (1) A large volume of various spatial and non-spatial data are managed under various procedures and thus are not in a ready format to support interagency, multidisciplinary resource research and management at an ecosystem level. (2) When pursuing an ecosystem approach, scientists lack methods, models, and tools for information synthesis, environmental modeling, and ecological predictions at various spatial and temporal scales, and resource managers require new tools for management decision analysis and adaptation of resource management measures based on the most currently available scientific information. (3) Techniques are needed to combine spatial and temporal information in order to understand natural resource processes in relation to spatiotemporal dynamics of ecosystems.

0-7803-3068-4/96$5.00©1996 IEEE

To remove these technical barriers, the author conducted research to study spatial analysis methodologies with the following objectives: (1) compiling, synthesizing, and analyzing existing natural resource data for application issues in ecosystem management, mainly focusing on data sets derived from past and current resource programs at a regional level; (2) exploring the new methods for use of spatial data and models at a landscape scale; and (3) developing customized application tools that make data and information and analytical methods easily available for resource managers and scientists. Computerized GIS and remote sensing data were used as primary technical means to develop decision support capabilities that included information synthesis, analytical visualization, spatial simulation, and modeling. Based on these techniques, specialized GIS-based decision support systems have been developed (Ji and Johnston 1995) for use in wetland restoration planning (Ji and Mitchell 1995), wildlife analysis (Ji and Jeske 1996), and wetland permit analysis (Ji and Johnston 1994). The systems are based on ARC/INFO GIS, with customized interfaces created to facilitate system implementation.

INFORMATION SYNTHESIS

In ecosystem management, one natural resource issue is often considered in relation to others, decision making involves various aspects of natural resource processes, and modeling analysis can involve the integration of various components of ecosystems. All these are based on information synthesis, which includes two related components: designing appropriate information structure for specific management tasks and integrating related data sets in specific technical applications.

For the two aspects of information synthesis, "the ecosystem database" concept is devised to develop a functional structure for organizing data sets: Each ecosystem database has one or more "theme layer,"

possibly along with subtheme layers, and "ancillary layers" which are ecologically or geographically related to (sub) theme layers (Figure 1). Such a database structure can provide a framework to synthesize related information in the context of a specific management theme by using interrelated data layer interfaces (customized menus) with the decision support GIS. For example, in a study of the distribution of pintail ducks in the lower Mississippi valley (Ji and Jeske 1996), the ecosystem database consisted of pintail duck data sets (the theme layer) for multiple years, boundary coverages of the lower Mississippi valley region (the ecoboundary layer). satellite images (the landscape background layer), and various environmental resource data sets such as wildlife refuges, forests. and lakes (the ecofactor layer). These data sets are integrated by linking each data layer to a specific customized interface menu of the decision support GIS. Such information synthesis approaches and data integration techniques made it possible and efficient to simultaneously analyze the impacts of multiple environmental factors on pintail duck distribution.

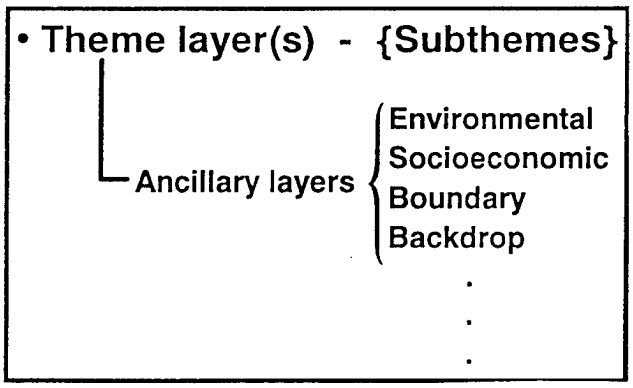


Figure 1. Ecosystem Database Structure.

ANALYTICAL VISUALIZATION

In ecosystem management, resource managers and scientists often need to understand the spatial domain of specific natural resources, identify the characteristics of the resources, and examine their spatial relations to other related resources or environmental processes. These implementations can be facilitated by analytical visualization with a decision support GIS. Examples of analytical visualization include: (1) interactively querying and displaying GIS data sets through customized interface operations; (2) graphically defining a spatial data search: (3) automatically retrieving, segmenting, and overlaying a large set of satellite imagery based on the areal extent of a displayed boundary of a vector data set; and (4) identifying rule-based attribute information.

Analytical visualization with the decision support GIS allowed viewing data with analytical rules or targets. For example, in a wildlife analysis with the decision support GIS, species data were interactively retrieved and visualized with user-specified criteria, such as species sex and age, specific spatial regions, and time ranges (year, month, or week). Species data sets were also visualized over specific landscape background such as satellite images of dry and wet seasons and over related environmental data sets. Associated attribute information was interactively queried. In this way, researchers and managers better understood the behavior of wildlife populations in relation to major landscape features, water resources, forests, and refuge boundaries in the study area.

For the wetland restoration application, wetland and upland habitat classifications (Ji and Mitchell 1995) were aggregated as part of the decision-support function to automatically identify wetland habitat features in categories such as "open water," "aquatic bed," "flats," "emergents," "shrub/scrub," "forested wetlands," or "uplands." As another example, to analyze the impact of a proposed permit activity on spatially related environmental resources, the decision support GIS for wetland permit analysis allowed the user to query and display the permit site with other criteria, such as activity type and the countyship. A graphical search radius could be specified to retrieve environmental data for an area-specified impact assessment (Ji and Johnston 1994).

SPATIAL SIMULATION AND MODELING

Simulation and modeling play an important role in resource analysis and management and are key components of a decision support GIS. In the GIS environment, simulation and modeling possess spatial properties and are often constrained by temporal variables. With a decision support GIS, spatial simulation and modeling are tightly coupled with the GIS database for input and output, and are usually implemented through a customized interface by selecting embedded algorithms and analytical criteria.

As shown below, in this study techniques were developed to simulate the spatial behavior of wildlife species and to model habitat changes in response to projected wetland restoration.

To understand how wildlife species behavior was affected by ecological conditions and how the distribution of species was related to other natural resources, analytical functions were developed to simulate the movement of selected groups of bird populations, such as eagles, pintail ducks, and various water birds, in respect to specific geographical areas, temporal duration, and environmental conditions. The spatial region for simulation was graphically delineated on the system screen. The simulated group of birds was selected based on birds' age, immature or adult, and sex. These variables and temporal constraints were evaluated interactively in the decision support GIS environment. The trajectory of the movement of an individual bird could also be simulated by identifying and tracking a specific bird using the assigned bird identification number. As a component of the simulation, bird data were overlaid with "target" ecofactors, and associated information such as habitat conditions in a specific location was identified. The simulation was also conducted along with spatial statistical analysis of species. Examples of spatial statistical analysis included calculating statistics about the maximum frequency of located birds, the number of locations of instrumented birds, the average number of times the specific groups of birds were contacted through the tracking period, and the number of instrumented birds killed each year.

To facilitate planning wetland ecosystem restoration, an analytical spatial model for Wetland Value Assessment (WVA) was integrated into ARC/INFO GIS, and ancillary functions were developed to support this spatial modeling. The model is a habitat-based resource assessment procedure primarily used as a planning tool in prioritizing coastal wetland restoration project proposals submitted for federal funding. The rule-based WVA model predicts changes in wetland quality and quantity that are expected as a result of a proposed project. The output of the model, measured in average annualized habitat units, can be combined with project costs to measure the effectiveness of a proposed project. The model contains different algorithms for various marshes and swamps that were programmed into the GIS environment. This analytical modeling was integrated with GIS-based spatial analysis through the system implementation in the following ways: (1) the projected modeling areas were displayed in a vector format of GIS coverages with satellite images as the backdrop; (2) habitat types were classified based on embedded decision rules; (3) the modeling boundaries were delineated interactively, and the corresponding statistics was calculated automatically as part of modeling inputs; and (4) the system provided capabilities to identify modeling scenarios (wetland types, project duration, etc.) based on model input parameters and to switch modeling procedures in response to projected wetland changes (Ji and Mitchell 1995). This decision support GIS technique has been used by decision makers in Louisiana to aid in selecting projects for coastal wetland ecosystem restoration.

CONCLUSIONS

The decision support GIS approach provided an integrated technical solution for a variety of information handling issues in ecosystem management. The developed decision support systems proved to be powerful tools for information synthesis, data visualization, and spatial simulation and modeling in the case applications in ecosystem management.

REFERENCES

Ji, W. and J. B. Johnston. 1994. A GIS-based decision support system for wetland permit analysis. In Proceedings of GIS/LIS '94, Phoenix, Arizona, October 22-28, 1994.

Ji, W. and L.C. Mitchell. 1995. An analytical model-based decision support GIS for wetland resource management. Page 31-47 in J. Lyon and J. McCarthy, eds. Wetland and Environmental Applications of Geographic Information Systems. Lewis Publishers, Boca Raton, Florida.

Ji, W. and J. B. Johnston. 1995. Coastal ecosystem decision support GIS: functions and methodology. Marine Geodesy 18(4): 229-241.

Ji, W. and C. Jeske. 1996. Ecosystem management decision support GIS: a new approach for wildlife studies and management. In Proceedings of the Southeast Regional Interagency Endangered Species Research and Development Workshop, April 23-25, Atlanta, Georgia (in press).

Dawn of a New Era: *THE IMAGE INFORMATION AGE*

Lawrie E. Jordan, III
ERDAS, Inc.
2801 Buford Highway, N. E.
Atlanta, Georgia, USA 30329

ABSTRACT

The explosion in commercially available high-resolution imagery in near-real-time will drive the new GIS marketplace and will leverage a fundamental shift in the way we create and use "maps." The map of the future will be an Intelligent Image with virtual resolution and which can be interactively navigated and queried in two, three, or four dimensions. High standards of precision and data integrity for these worldwide digital building blocks will be maintained through GPS and metadata "agents." Access to this vision will be at the mass-market level for non-technical individuals through the "Home Shopping Channel for Imagery."

Historical Perspective

> *"The want of accurate maps has been a grave disadvantage to me. I have in vain endeavored to procure them, and have been obliged to make shift with such sketches as I could trace out of my own observations and that of gentlemen around me. I think if persons of known character and probity could be employed in making maps (from actual surveys) it would be of the greatest advantage."*
>
> *General George Washington, 1777*

The need for timely and accurate geographic information has been with us since the beginning. From the earliest known maps, with their religious overtones depicting Adam and Eve at the center of the universe, to medieval versions of the globe emphasizing commercial trade (see Figure 1), we are constantly reinventing ways to visualize the world around us. About 100 years ago we began to see the early prototypes of Geographic Information Systems being applied by landscape architects and land planners such as Warren Manning for regional town planning in New England[1] . These early GIS "systems" used a series of natural resource overlays including soils, slope, vegetation, etc., to develop site design layouts that were not only visually pleasing, but also sensitive to the environment.

Since these early data bases preceded the invention of both computers and plastic transparencies, the overlays were created on linen or silk and manually combined. Analyses could quickly and easily be performed by using the overlays in different sequences to create alternative development scenarios. Specific "site models" for vulnerability to soil erosion or attractiveness for green space parkways were integrated with budget requirements and professional judgement into a composite master plan that was not only cost effective from a construction standpoint, but also in harmony with nature.

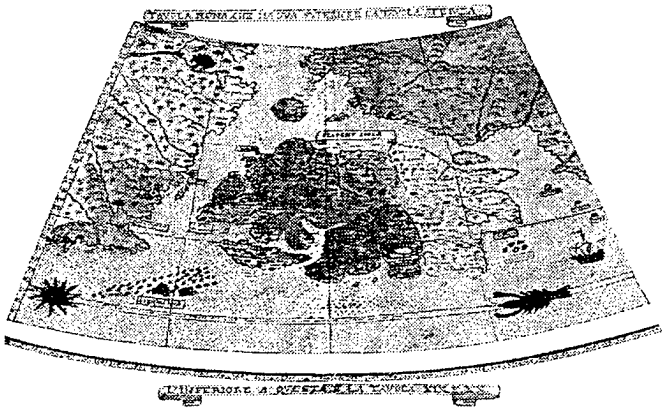


Figure 1. Section of Italian book from 1588 comprising largest known antique map of the world, for which map makers accepted Japanese traders' assertions that their country occupied most of the Pacific. From the Karpeles Museum.

One of the earliest issues confronting those involved with GIS analysis was the seemingly unlimited appetite of the "system" for better and more accurate data to feed upon. Historically, the single largest expense with any GIS has been the cost of building and maintaining the data base, rather than the cost of the techniques employed (silk or software) to exploit it. Today, it is not uncommon for data collection costs on large projects to exceed the costs of all other GIS system components combined, including computer hardware and multiple software licenses, by several orders of magnitude. This is especially true of traditional manually-digitized vector data bases which, when finally completed and edited, are not only expensive but also frequently out of

[1] Steinitz, C., P. Parker, L. Jordan, 1976. Hand- Drawn Overlays: Their History and Prospective Uses. *Landscape Architecture*. Sept., 1976

0-7803-3068-4/96$5.00©1996 IEEE

date or incorrectly positioned when compared to current orthorectified imagery of the same area.

The time and expense associated with traditional digitizing techniques for GIS data base development created a financial barrier to entry for many potential users of the technology. This is reflected in the market profile of early users, which were primarily dominated by government organizations or large corporate concerns. A breakthrough finally occurred in the Remote Sensing arena with the launch of the first Landsat Satellite (aka "ERTS") in 1972.

Enter Digital Remote Sensing

Digital multispectral imagery (MSI) from the Landsat program provided a highly cost-effective source of digital land cover information for large areas. Successful studies conducted over a period of 20 years on geologic, vegetation, and wetlands mapping, combined with software advances in geometric correction and temporal analyses, validated the contribution and savings that digital remote sensing could bring to GIS data base construction. Further advances in satellite sensor design, such as the SPOT system with 10 meter panchromatic stereo, enhanced the level of information obtainable to include digital elevation data (DEM) from photogrammetric techniques, as well as "pan-sharpened" multispectral products. Advanced applications software available in the commercial sector now allows us to orthorectify imagery for use in updating vector data bases, as well as automatically extract features from MSI and directly generate a topologic vector layer as shown in Figure 2.

The unique benefits of radar imagery, such as day/night/all-weather collection, bathymetric applications, plus interferometric SAR processing for DEM generation in persistently cloudy areas, further expands the opportunity for global GIS coverage and data base cost reductions.

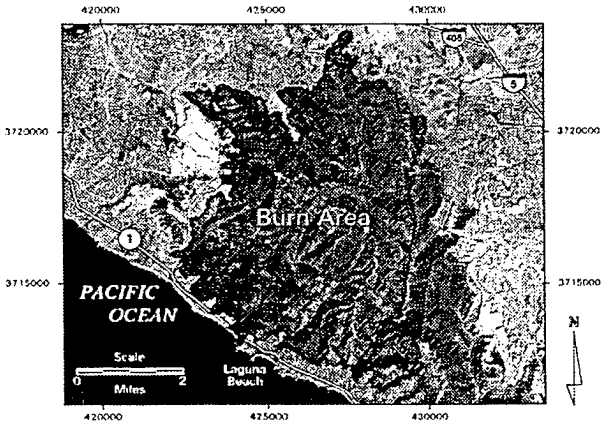


Figure 2. Automatic classification and feature extraction of burn area into ARC vector coverage. Multispectral satellite imagery courtesy of SPOT Image Corporation.

Over the next five years, commercial high resolution imagery from multiple sources including Space Imaging, Earthwatch, Almaz-1B, Orbimage, Positive Systems, and others will complement current commercial and government sources. These new systems will overcome the existing shortfalls in global digital imagery coverage and create new opportunities and challenges for the value-added community. Traditional pixel-by-pixel algorithms for multispectral classification, as an example, will need to be upgraded with rule-based spectral and spatial logic to handle the increased level of detail (e.g., individual trees versus "forest") in the new imagery. Exciting new products will emerge from the synthesis of electro-optical, multispectral, hyperspectral, radar and infrared imagery.

The unique contribution of each sensor will be enhanced and strengthened further through this synthesis, resulting in composite products that offer greater added value than the simple sum of their individual parts. The positive business impact of this will be a widening of the marketplace for new forms of geographic information that were previously too expensive to obtain or simply not available at all. In order to realize the full potential of this technology, however, a new vision for "maps" is required.

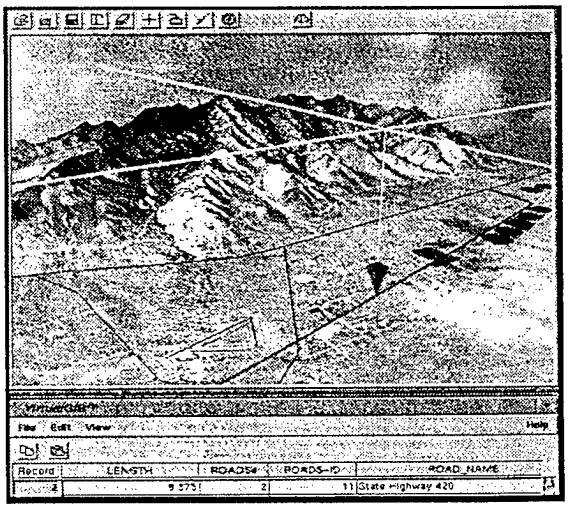


Figure 3. Virtual GIS ™ derived from stereo imagery, with real time fly-through and interactive GIS query using "Plumb-Bob" 3-D cursor. Satellite imagery courtesy of EOSAT and SPOT Image Corporation.

The Map of the Future

By taking advantage of high resolution near real-time collection, all-weather capabilities, stereo terrain generation, and precision GPS control, a new paradigm for mapping will drive the GIS marketplace. This Map of the Future will be an Intelligent Image (see Figure 3, above) which can be interactively navigated and queried in two, three, or four dimensions over time.

Data quality, integrity, and precision will be maintained in this softcopy environment through GPS control and software "agents" enforcing industry-adopted metadata standards. The cooperative and intelligent organization of these digital building blocks within the GIS industry will result in a Global Visualization System that will generate significant new applications and business revenues. Its appeal will extend greatly beyond the current borders of the traditional technical mapping community, reaching into new market areas such as vacation planning, entertainment, and nightly news events. Access to this information must be quick, simple, inexpensive, and oriented towards individuals without a technical background. This "Home Shopping Channel for Imagery" will use an Information Appliance (integrated personal computer, TV set, and telephone) to access the Map of the Future through a new multi-media interface such as the one shown in Figure 4, below.

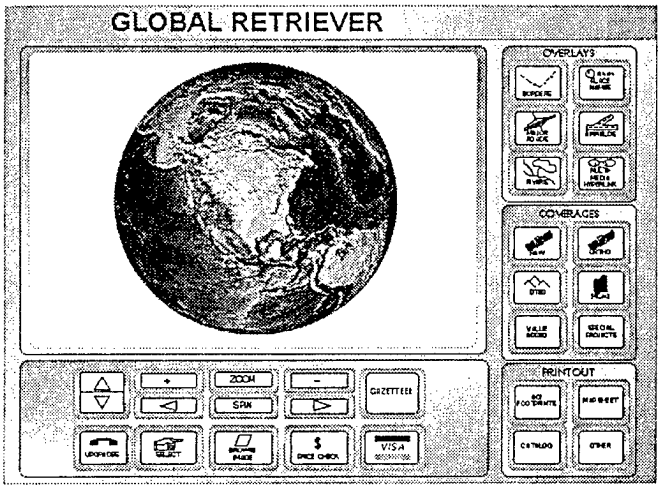


Figure 4. Global Retriever - interface to "The Home Shopping Channel for Imagery".

Visualization of coverages, thematic reference overlays, gazetteer index, browse images, electronic imagery ordering, tasking requests, and automatic credit card debiting combine to create a new user interface which gets the information into the hands of the user quickly, easily, and (with realistic imagery prices) affordably. This vision also serves the dual role as a business engine for the commercial providers of data and value-added services. A tailored version could allow the U. S. Government to efficiently implement a business plan in partnership with industry to supplement existing government imagery sources with commercial imagery. Deployed forces could use Global Retriever to electronically share imagery information through protocols such as the National Imagery Transmission Format (NITF).

Collectively, these ideas provide a pathway into the new **Image Information Age**, which promises to be the most interesting chapter yet in the rich history of Remote Sensing and GIS.

Non Point Source Pollution

Wilma Subra
Subra Company, Inc.
P. O. Box 9813
New Iberia, LA 70562
Phone: (318) 367-2216
Fax: (318) 367-2217
Email: SubraCom@aol.com

Jeff Waters
Lake Pontchartrain Basin Foundation
P. O. Box 6965
Metairie, LA 70009-6965
Phone: (504) 836-2215

INTRODUCTION

Non Point Source (NPS) pollution is a major contributor to the degradation of surface water quality. NPS pollution is caused by water movement over and through the surface of the land. The runoff picks up and transports natural and man-made pollutants. The pollutants are transported into rivers, streams, lakes, wetlands, coastal waters, and ground water. Federal and state governments have targeted the identification and control of non point source runoff as major pollution minimization goals. Location of NPS pollution runoff, types of areas drained, and drainage channels are data vital to leaders in agricultural, forestry, and urban planning industries. State and federal agencies can use these data for planning purposes and for prioritizing allocation of resources.

OBJECTIVE

The objective of this study was to identify areas of prime NPS pollution concern using remotely sensed imagery and GIS modeling techniques. A model was designed to identify, quantify and prioritize areas of NPS contribution potential within a water quality basin area.

STUDY AREA

A 20 by 20 mile section of the Calcasieu River Basin, located in southwest Louisiana, and draining 3,775 square miles was selected for the analysis. The boundaries of the study area were located to include known land cover of various types within the river basin. Habitats include fresh, intermediate, brackish and saline marshes, bottom land swamps, prairie terrace, and upland forest. The land cover types were urban, commercial, light industry, heavy petrochemical refining industry, agriculture, forest, pasture, swamp and marsh wetlands, rivers, streams, open bays, lakes and an estuary system.

0-7803-3068-4/96$5.00©1996 IEEE

LAND COVER

A recent Landsat Thematic Mapper (TM) scene was used to develop a land cover classification. The ERDAS 7.5 program CLUSTR was used with TM bands 2, 3, 4 and 5 and the number of class parameters set to 63 to develop a land cover classification. Mixed classes were further broken down using MASK followed by CLUSTR to identify specific components. The ERDAS 7.5 Program STITCH was employed to incorporate the new classes into the classification. The 103 resulting classes were then reduced to the 15 land cover types presented in Table 1. The land cover classifications were weighed on a scale of 1 to 20 ranging from low to high contribution potential for NPS (Table 1).

WATERSHEDS

Watershed boundaries were digitized from a Water Quality Management Basins map acquired from the Louisiana

TABLE 1. LANDCOVER CLASSIFICATIONS

Land Cover Type	Model Weight
Open Water	2
Shallow Water	2
Industrial/Commercial	17
Heavy Industrial	20
Agricultural	10
Wetland Vegetation	1
Residential	13
Agricultural/Residential/Wetland Mix	8
Bare Soil	10
Scrub/Shrub	4
Upper Wetland Grasses	1
Coniferous Forest	7
Deciduous Forest	5
Bottom Land Hardwoods	1
Coniferous/Deciduous Mix	6

Department of Environmental Quality, Office of Water Resources. The study area contained all or part of eight watersheds. The watershed boundaries were useful in creating a "distance to water" layer within each watershed and were useful in restricting statistics to individual watersheds.

HYDROGRAPHY

A hydrography layer was developed from 1:100,000 United States Geologic Survey (USGS) Digital Line Graph (DLG) data. The DLG provided better identification of small streams and canals than did the image classification but failed to delineate local wetland boundaries. Known wetlands from the land cover classification were added to provide more accurate delineation of open water bodies. The watershed and hydrography layers were then joined together to permit distance to water calculations by individual watershed.

DISTANCE TO WATER

A distance to water routine was used to measure the distance to water within each individual watershed. With the maximum distance to water set to 254 pixels, the distance layer extended beyond the boundaries of each Watershed. The distance layer was clipped to each watershed boundary by multiplying by the appropriate watershed set to 1 and all other Watersheds set to 0. The resulting eight distance layers were then put together into one layer. For input into the model, the distance to water layer was ranked based on how far from water a given location fell.

SLOPE

USGS Digital Elevation Model (DEM) data were not available at any scale for this study area. To obtain elevation data, the contours on 1:62,500 quad sheets were digitized. From the digitized contours, elevation and slope were derived using TOPO. For the model, the slope layer was ranked based on percent slope. The greater the slope, the more quickly water drains through the area, increasing its impact on NPS pollution.

SOIL PERMEABILITY

Soil types were digitized from 1:316,800 United States Department of Agriculture (USDA) General Soil Maps. The types were grouped into 4 categories: poorly to moderately well drained soils, poorly drained soils, very poorly drained soils, and open water.

POLLUTION POTENTIAL MODEL

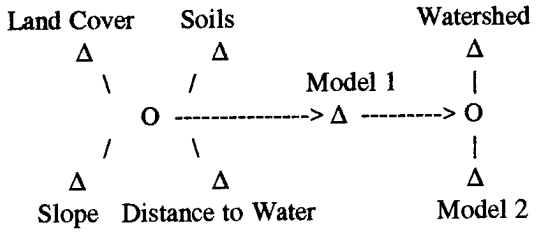
Using the ERDAS Imagine Spatial Modeler, the ranked land cover, soil type, slope and distance to water layers were input to the model, Figure 1. The layers were added together, producing a sensitivity layer ranging from 9 to 80. The higher numbers indicate the locations more likely to contribute to NPS pollution. The range of values was divided into 13 equal classes which were "painted" various colors using software in order to produce a visual display.

In order to evaluate the potential impacts of Non Point Source run off to existing water quality, the Watersheds were ranked from 1 through 20 based upon their compliance with designated water uses. The compliance is established every two years by the Louisiana Department of Environmental Quality as part of their requirements under the Clean Water Act, Section 305 (b). The watersheds were ranked on the basis of compliance: full compliance - 4, threatened to full - 10, threatened - 14, threatened to non compliance - 16 and non compliance - 18. The output of the NPS Pollution Potential Model was then combined with the weighted Watershed compliance of designated uses to produce the NPS Pollution Impact Layer. The addition of the ranked Watershed layer produced a sensitivity layer ranging from 13 through 98, the higher numbers indicated locations most likely to contribute to Non Point Source Pollution.

The majority of locations in Watersheds 2, 5 and 7 were shifted towards the low end of the sensitivity range, indicating less of a priority because the Non Point Source Pollution in these Watersheds will have less of an impact on surface water quality. Watersheds 1, 3, 4, 6 and 8 remained high in Non Point Source Pollution potential and therefore are a priority for the control of Non Point Source Pollution.

The land cover classification were subjected to statistical routines. The various land cover categories in each

FIGURE 1. NON POINT SOURCE POLLUTION MODEL



watershed were calculated (Table 2). The outputs from models 1 and 2 were compiled into data tables for each watershed to demonstrate the statistics of pollution potential (Table 3).

The watershed with the lowest potential for NPS pollution is known as the Calcasieu Lake area and consist of 53% open water, 22% wetlands, 9% agriculture and 4% shallow water. The designated water user are threatened by upstream sources and surface runoff.

The watershed with the highest NPS pollution potential and impact consist primarily of industrial and commercial facilities and agricultural land use. The watershed does not meet its designated uses and is being impacted by petro chemical industrial facilities, industrial and municipal storm sewers, surface runoff and non point sources.

CONCLUSION

The application of remote sensing and GIS technologies will enable federal and state agencies to identify land use classification provides up to date information at a land cover types that are major contributors to NPS pollution, level of detail far superior to off the shelf land use classification reports. The detail provided by remotely sensed imagery results in a beneficial cost savings. The process provides federal and state agencies the tools necessary to specific areas where these land cover types have the highest potential for polluted runoff, and areas where the non point source runoff has the highest potential impact to the receiving water body. The use of remotely sensed imagery to develop develop appropriate management measures for sources of non point pollution, estimate the cost of various management approaches, determine the effectiveness of implemented management approaches, prioritize spending and concentrate resources on implementing plans that will result in the significant reduction of pollution. Periodic updates of data enable evaluation over time as well as the effectiveness of projects. The techniques can also enable industries and businesses to determine the most appropriate locations on which to build facilities and develop appropriate management measures for existing and proposed facilities.

TABLE 2. LAND COVER CATEGORIES IN WATERSHED I
WATERBODY SEGMENT 0308
WEST FORK OF THE CALCASIEU RIVER
IN THE CALCASIEU RIVER BASIN

Land Cover Category #	Description	Acres	Watershed
1	Open Water	459.893	1.79%
2	Shallow Water	128.462	0.50%
3	Industrial/Commercial	483.016	1.88%
4	Heavy Industrial	0.000	0.00%
5	Agricultural	4,449.912	17.32%
6	Wetland Vegetation	1,610.909	6.27%
7	Residential	852.985	3.32%
8	Ag/Residential/Wetland Mix	4,103.066	15.97%
9	Bare Soil	154.154	0.60%
10	Scrub Shrub	5,580.375	21.72%
11	Upper Wetland Grasses	698.831	2.72%
12	Coniferous Forest	734.801	2.86%
13	Deciduous Forest	644.878	2.51%
14	Bottomland Hardwoods	115.616	0.45%
15	Coniferous/Deciduous Mix	5,675.437	22.09%

TABLE 3. POTENTIAL FOR CONTRIBUTION TO NON POINT SOURCE POLLUTION IN WATERSHED III
WATERBODY SEGMENT 0309

Potential for Contribution to Non Point Source Pollution		Model I Acres	Model I %	Model 2 Acres	Model 2 %
Low	1	118.985	0.58		
	2	115.204	0.57		
	3	306.915	1.51	73.393	0.36
	4	787.081	3.87	129.216	0.64
	5	2359.464	11.60	338.496	1.66
	6	3622.930	17.81	1159.160	5.70
	7	4549.680	22.36	3657.180	17.98
	8	2903.459	14.27	5373.012	26.41
	9	1939.569	9.53	4033.262	19.82
	10	2063.891	10.14	2455.319	12.07
	11	862.475	4.24	2041.206	10.03
	12	385.645	1.90	691.671	3.40
High	13	328.933	1.62	392.317	1.93

Cost-Effective Environmental Consulting Using Geographic Information Systems and Remote Sensing

Dawn R. Gibas-Tracy
Summit Envirosolutions, Inc.
10201 Wayzata Boulevard, Suite 100
Minneapolis, Minnesota 55305
612-595-8888
612-595-0888 (fax)

ABSTRACT

Summit Envirosolutions, Inc. is working in partnership with the National Aeronautics and Space Administration's Commercial Remote Sensing Program under the Earth Observations Commercial Applications Program to integrate the use of Geographic Information Systems and Remote Sensing technology into our environmental consulting business. A primary goal of our project is to develop a system, called RealFlow$_{SM}$, that enables us to better characterize and monitor study areas. The objectives of RealFlow$_{SM}$ include reducing client costs associated with environmental compliance, particularly with respect to preparation of Environmental Protection Agency mandated Wellhead Protection Plans. While the RealFlow$_{SM}$ system is aimed primarily at subsurface characterization and wellhead protection, we are also using the technology in other service areas within our company. This paper discusses the goals and objectives of the National Aeronautics and Space Administration partnership and project, as well as our experience with the cost-effective implementation of this technology in private-sector consulting.

INTRODUCTION

Summit Envirosolutions, Inc. (Summit) is working in partnership with the National Aeronautics and Space Administration (NASA) in the Earth Observations Commercial Applications Program (EOCAP). Our program began in 1994 and has an end date of 1999. The EOCAP program was developed to provide a basis for partnerships between NASA and the private sector and to encourage the commercialization of new technology through the private sector. Both parties provide funding and therefore have a "risk" associated with bringing a product or service to the marketplace. In Summit's case, the EOCAP program has allowed us to obtain the hardware and software necessary for remote sensing and geographic information system (RS/GIS) technology that would have been difficult for a small company, such as Summit, to purchase outright.

Investment in RS/GIS technology will not occur unless an organization's leaders believe that the benefits will exceed the cost of implementation (Antenucci, 1995). The nature and magnitude of benefits to different organizations varies, as do the costs. Benefits include increased productivity, integration of operations both internally and externally, integration of maps and attributes, quicker turn-around time, and a centralized spatial database that is easily updated. Costs include hardware, software, training, and database creation and management.

The initial decision to "risk" an investment in RS/GIS technology was made looking at several criteria within the marketplace for environmental consulting. The cost of the technology versus the benefits to Summit were studied. For the technical operations personnel, implementation of RS/GIS technology was an easy decision, primarily based on its ability to reduce time spent on many tasks that were currently being accomplished manually. The management, however, needed to assess cost-effectiveness prior to implementing new technologies both internal and external to the company.

OBJECTIVES

The major emphasis of Summit's EOCAP project is to provide a service, RealFlow$_{SM}$, which can reduce client costs associated with environmental compliance (in particular, preparation of EPA-mandated Wellhead Protection Plans), more accurately characterize aquifer parameters, and readily assess changes in well field operations and potential impacts of environmental stresses. The EOCAP project objectives are aimed at developing a system or product that enables both Summit and our clients to improve decision making capabilities and regulator confidence by providing scientifically sound data. Summit's objectives within the framework of a cost/benefit analysis of the EOCAP project are as follows:

- To provide a unique and cost-effective approach to the protection, assessment, and remediation of groundwater resources.

ACKNOWLEDGMENTS

The author and Summit would like to thank NASA and the EOCAP program personnel for the opportunity to participate in EOCAP '93 and for the support that has been provided by the Commercial Remote Sensing Program at Stennis Space Center, Mississippi. We would also like to thank the City of Osseo, Minnesota for allowing access to their property for the purposes of testing our systems.

0-7803-3068-4/96$5.00©1996 IEEE

- To integrate currently available technologies for the improvement of existing data acquisition, analysis, and presentation capabilities.
- To utilize telecommunication links that enable efficient access to remote data and provide real-time data to system users.
- To provide an integrated system that can be used to characterize sites with greater speed and accuracy; i.e. in an optimized manner and at lower cost.
- To decrease typical project costs to clients by 10 to 30 percent over conventional assessment and management techniques. Decreases in costs would be realized in less field and mobilization time, lower equipment costs, and less time spent in data conversion, data analysis, and graphical depiction of results.
- To obtain a significant portion of the industry market share for the product and realize a reasonable profit from net revenues.
- To develop a service that addresses surface environmental issues through the use of new technologies such as global positioning systems, GIS, and RS. This should decrease costs as well as provide a database that can be easily updated for future environmental issues to clients.

PLANNING FOR RS/GIS

Summit considered several items in its evaluation of the benefits of RS/GIS both internally and to our clients. The consulting business is highly competitive, and spending money on acquisition of software, hardware, and training needed to be offset by the type of service that our clients are willing to pay for, as well as the quality of service to our clients. Both quantifiable and intangible costs or benefits needed to be identified in terms of the environmental consulting business.

Summit initially worked closely with the University of Minnesota Remote Sensing Laboratory to plan a phased approach to integrating RS/GIS into the company. The concept used for this phased approach was the GIS life cycle (Queen and Blinn, 1993). The life cycle is a strategic process using a data-centered approach for designing and implementing this technology (Fig. 1). As the figure illustrates, this is an ongoing cycle that can be used both within Summit and with our clients.

Phase I involves a systematic review of the users, and their data and information needs. Education of decision makers regarding the cost and benefits of the technology was undertaken during this phase, as well as considering the needs of our clients. We found that education of our client was, and continues to be, an important aspect of planning. The items that were considered by Summit in Phase I are are listed below:

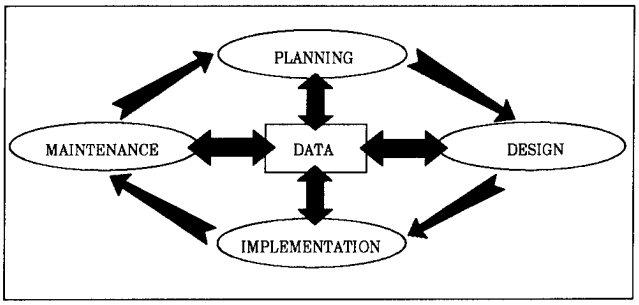


Fig. 1. RS/GIS life cycle approach (Queen and Blinn, 1993).

- The ability to offer new service areas to our clientele such as RS/GIS, Wellhead Protection, and Aquifer Resource Management.
- An ability to apply innovative approaches to our existing service areas.
- The availability of better data management tools.
- An ability to provide better decision making tools to both ourselves and our clients.

Phase II is the system design, when the user needs are matched to the functionality of the technology. With input from experts within the RS/GIS industry, Summit selected hardware and software that would be compatible with the majority of clients' needs. Hardware and software are purchased as needed, and usually only after we have used it for a period of time. Database design is project specific and is an ongoing process.

Phase III involves implementation of the technology along with training and education. For Summit this means continually updating and educating staff and clients on how this RS/GIS can be used for various tasks and projects.

Phase IV is maintenance of the system and the database. This includes updating the database, keeping the system functionality up to date, and keeping current with hardware and software. Many of our clientele see the advantages of having an accurate and current database of their operations, especially for regulatory requirements.

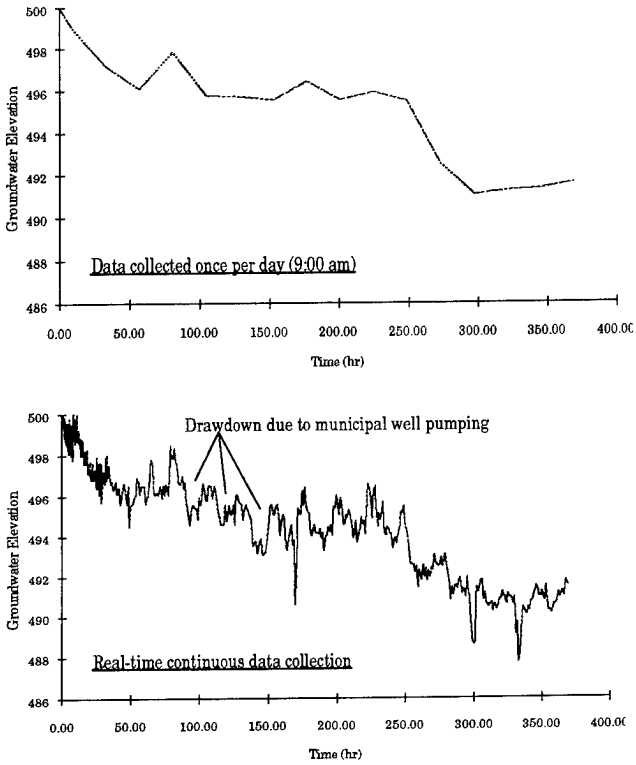
The process described above is one way of determining the cost/benefit of implementing RS/GIS. Antenucci (1995) describes another process that could be used, where various benefit and cost types are specifically listed for the reader to use as a guide. Other references can also be found regarding cost/benefit analyses for RS/GIS technology. The general structure for doing this analysis is the same, but each company (or industry) must decide on its own unique set of criteria in order to obtain an accurate cost/benefit analysis for their particular business.

DISCUSSION AND CONCLUSIONS

In Summit's case, the planning phase and a portion of the design phase were completed prior to becoming an EOCAP partner. The EOCAP contract was designed for a specific way to use RS/GIS in a market that we had researched and found to be in its early stages of development. For instance, the extent and scope of federal regulations has increased, which has set the stage for the rapid development of the environmental consulting industry. In addition, the symbiotic nature of telecommunications, knowledge-based algorithms, geographic technologies, and microcomputers is enabling a revolution in data acquisition and analysis. In looking at the wellhead protection market, we considered several items in developing this service area:

- The 1986 Amendments to the Safe Drinking Water Act require states to develop a wellhead protection program that provides safe, adequate, and long-term supplies of water through best management practices.
- Based on an extensive review of literature authored in the United States between the late 1960's and the present time, approximately 5,400 technical papers have been published relating to GIS technologies. Of these published papers, only approximately 100 address the application of GIS to groundwater resources or wellhead protection.
- Summit has expertise within the company to do this type of work, is in a position to identify areas where costs could be cut with the implementation of new technology, and has existing clientele who require this type of service area and are willing to be part of its development.
- In addition, Summit has other service areas that provide opportunities for integrating RS/GIS into the way we do business, allowing us to realize a reduction in overall costs for large projects.

The following is an example of a cost savings benefit to our client, as well as a way to provide better data for decision making. The labor involved in collecting, analyzing, and graphically depicting results of groundwater elevation data from monitoring or pumping wells usually constitutes the largest single cost associated with aquifer testing and modeling. Moreover, the data collected represent a relatively small "snapshot in time" view of the aquifer response to stress. As a result of this process, errors accumulate during the modeling phase due to anisotropy, heterogeneity, and boundary conditions not apparent during the short-term aquifer tests. These errors could be greatly reduced by providing a mechanism for collecting continuous, real-time data directly from remote locations and graphically depicting the data for analysis and interpretation. The differences in data collection are illustrated in Figs. 2 and 3.



Figs. 2 and 3. Data collection once per day versus continuous readings once per minute.

GIS/RS technology is just beginning to make its way into the private sector for use in environmental consulting. The use of the technology in applications such as wellhead protection and environmental assessments is changing the way environmental consulting is done. Due to the ability of these technologies to provide us with a clearer picture of complex systems, we are able to better understand these natural systems, we can provide better decision-making for our clients, and overall we can practice better science.

REFERENCES

[1] J.C. Antenucci, "Financial Justification of GIS," Tutorial 8, A/E/C Systems '95, June 5-8, 1995.

[2] L.P. Queen and C.R. Blinn, "The Basics of Geographic Information Systems," Minnesota Extension Service, University of Minnesota, Publication No. NR-FO-5926-S, 1993.

Land Surface Remote Sensing and Geographical Information Systems for Water Quality Modeling

Nandish M. Mattikalli, and Edwin T. Engman
NASA Goddard Space Flight Center, Laboratory for Hydrospheric Processes
Hydrological Sciences Branch, Code 974, Greenbelt, MD 20771, USA
Tel: (301) 286-7696 Fax: (301) 286-1758
E-mail: nandish@hydro5.gsfc.nasa.gov

Abstract -- Recent trends in surface water quality of various rivers in the USA and abroad clearly demonstrate an increasing pattern of solute concentrations. These changes in surface water quality are mainly attributed to human influences that both transform land-use/ land-cover from one type to another and that change or intensify the management regime on lands over regional and global scales. Space-borne satellite observations in the visible and near-infrared bands enable us to gather information on land-use/ land-cover on a frequent basis which can be used for real-time water quality modeling. Geographical information systems (GIS) provide an appropriate technology for efficient storage, handling, manipulation of large volumes of spatially referenced data derived from remote sensing. This paper demonstrates that both land surface remote sensing and GIS coupled with an empirical model (viz. the export coefficient model) can successfully be employed to estimate surface water quality. The approach has a potential for real time estimation of surface water quality on regional, continental and global scales.

INTRODUCTION

Recent trends in surface water quality of various rivers in the USA and abroad clearly demonstrate an increasing pattern of solutes (viz. nitrogen and phosphorous concentrations) often exceeding the World Health Organization (WHO) directives on drinking water quality [6,8]. A review of water quality of 298 rivers indicate a widespread increase in surface water nitrate concentrations throughout the USA, particularly in the drier eastern states, and in the Pacific coastal areas [8]. Another study of a fifty year trend of Passiac River concur with this trend indicating that increase in nitrate and ammonium concentrations related to land-use intensification [2].

Surface water quality as indexed by nitrogen and phosphorus is a function of several geophysical parameters and hydrological, atmospheric and ecological processes. Sources of nutrients fall into two categories: allogenic and authogenic. The former category comprises natural geological, pedological and atmospheric sources; and anthropogenic inputs from agricultural, domestic and industrial, and atmospheric sources. The latter sources largely derive from aquatic cycling processes, particularly from nutrient rich bed and bank sediments, and the decomposition of dead organic matter. A detailed review of the sources, processes and delivery mechanisms reveals that significant factors affecting surface water quality (which include agricultural practice, land drainage, fertilizer use etc.) can be expressed in terms of dynamic nature of watershed land-use/ land-cover, and other geomorphological parameters (such as soils, geology, topography) can be held static [7]. This clearly suggests that water quality is affected by human influences that both transform land-use/ land-cover from one type to another and that change or intensify the management regime on lands.

This paper demonstrates that land surface remote sensing and Geographical Information System (GIS) coupled with the export coefficient model can successfully be employed to estimate surface water quality as indexed by total oxydized nitrogen concentration.

REMOTE SENSING AND GIS

Land surface remote sensing in the visible and near-infrared regions of the electromagnetic spectrum offers viable tools for the characterization and quantification of land-use/ land-cover. Revisit capability of space borne sensors enables us to capture the dynamic nature of land-use/ land-cover. Methods are well established for derivation of accurate land-use/ land-cover information from remotely sensed data, and the present and future satellite systems assure availability of such data sets. Temporal resolution of the present day systems is about 30 days which can be reduced to 7-10 day resolution (subject to availability of cloud free days) if data from different platforms are integrated.

Remotely sensed land-use information constitute a large volume of data, and require powerful and sophisticated tools for easy manipulation and analysis. GIS provide an appropriate technology for this task. GIS are ideal tools to handle spatially heterogeneous nature of both land-use data and geophysical processes within a watershed, and to integrate data of different scales and resolution obtained from various satellite sensors. Although a variety of GIS are available, systems mainly designed on raster data structure and having some vector capabilities are ideal for handling remotely sensed data for water quality modeling [7].

WATER QUALITY MODELING

Remotely sensed land-use/ land-cover data can be employed in the export coefficient model within a GIS framework to

0-7803-3068-4/96$5.00©1996 IEEE

estimate nitrogen loading. Based on the areal extents of different types of land-use and their associated fertilizer application rates the model calculates total nitrogen load [1,3,4]. The model accounts for all possible sources of nitrogen by defining appropriate export coefficients. Since the study was focused on a predominantly rural watershed only losses from arable, grassland, and woodland were considered. Sediment losses were not addressed owing to the lack of data in the literature on sediment export rates.

The nitrogen loss, L (in kg/year), at the outlet of a watershed is given by:

$$L = \left(\sum_{i=1}^{n} \sum_{k=1}^{m} A_{ki} \cdot E_{ki} \right) + a$$

where

A = area of a discrete land-use patch (ha)
E = export coefficient for a specific land-use type (kg/ha)
m = number of discrete patches under one land-use class
n = number of land-use classes
a = artificial inputs (e.g. sewage, industrial etc.) (kg/year)

An export coefficient (E) indicates a proportion of the total nitrogen applied to a given land-use patch which is lost to surface water. Individual coefficient (such as $E_{woodland}$, $E_{grassland}$, E_{arable} etc.) is deemed to allow for biological, atmospheric and geological (weathering) contributions. The export coefficients were compiled from the literature (Table 1). Nitrogen input and loss from the human and livestock population were not considered because urban area constitutes a very small proportion in the River Glen watershed and emphasis of the study was on agricultural inputs. Results were validated by comparing model estimated annual loads with observed loads recorded at water quality sampling stations. Yearly observed loads were computed using rating relationships between daily discharge and nitrogen concentration.

STUDY SITE, DATA DESCRIPTION AND METHODOLOGY

The River Glen watershed is located between Grantham, Bourne and Stamford in eastern England. This region is characterized by major changes in agricultural activity with increased arable farming in the past few decades [5]. Crops such as wheat, barley and sugar beet dominate the watershed. In addition to arable farming, grassland cultivation is also dominant within the watershed although much of the grassland has changed to arable.

Land-use data are available for the watershed for 1931, 1963 and 1971 in the form of maps The first two are from the Land Utilization surveys, and third one is from interpretation of air photographs. An extensive search was carried out to acquire remotely sensed data, but it lead to only two cloud free scenes for 1984 (MSS) and 1987 (HRV). These remotely sensed Landsat and SPOT satellite images taken in visible and near-infrared bands were classified to derive land-use information. Land-use data for 1989 were extracted from a nationwide land-use map of the U. K. generated using Landsat TM multi-temporal images [5]. Daily average stream flow data were obtained from the National Rivers Authority (NRA) for eight stream gauging stations, out of which only three gauging stations (viz. Burton Coggles, Holywell Brook and Kates Bridge) contained data coinciding with land-use data.

Table 1. Export coefficients for nitrogen for land-use classes encountered in the River Glen watershed (from [8]).

	Land-use	N fixed (%)	N loss (kg/ha)
1.	Temporary grass	5	30
2.	Permanent grass	5	50
3.	Cereals	12	4
4.	Root crops	20	10
5.	Oilseed rape	30	4
6.	Woodland	13	20
7.	Rough grazing and Set-aside	2	10

A vector-based GIS was employed since majority of the land-use data were in hard-copy paper format. Data were input using semi-automatic digitization. Remotely sensed land-use classifications were geo-registered using the nearest neighbor algorithm. Since these three data layers were in raster format, a raster-to-vector conversion algorithm was used to integrate them with the vector-based GIS [5]. Analysis of land-use change revealed that the watershed experienced significant land-use change from grassland to arable [5]. Several special GIS routines were developed to automatically carry out the specific computations of the model.

RESULTS AND DISCUSSION

Model estimated and observed nitrogen loads for three water quality stations within the watershed are presented in Table 2 for 1984, 1987 and 1989. It can be observed that despite some errors, the export coefficient model predicts nitrogen loading with reasonable accuracy. This demonstrates a generally successful application of the model, and the export coefficients used, as a basis to estimate nitrogen loading. However, errors of estimation may be attributed to the use of rating relationships to calculate the observed loads in the validation process and the application of export coefficients selected from the literature [7].

Estimated loss of nitrogen for the entire watershed for all six years are presented in figure 1. It is clear that nitrogen loading increased from 67.8 tonnes/year in 1931 to 603.8 tonnes/year in 1989. This increase in solute loading in the surface water is due to combined effect of increased arable land and increased rate of nitrogen fertilizer application. Marked increase of nitrogen loading during 1971-1984, may be attributed to the increased rate of nitrogen fertilizer applicati-

Table 2. Comparison of nitrogen loading estimated by the export coefficient model with the observed loads (from [7]).

Sampling station	Year	Nitrogen loss (tonnes/year) Observed	Predicted	% Error
Burton Coggles	1984	106.35	128.33	+ 21
	1987	83.76	124.36	+ 48
Holywell Brook	1984	84.36	92.39	+ 10
	1987	91.61	84.87	- 7
Kates Bridge	1984	612.87	533.68	- 13
	1987	536.73	470.50	- 12
	1989	562.07	603.80	+ 7

on (i.e. 200 kg/ha) in 1984 as compared to the much smaller rate in 1971.

The model performance may be improved by using a set of refined export coefficients. Refinement of coefficients can be performed in a sensitivity analysis of land-use - water quality relationship using observed water quality records using a more sophisticated and physically based water quality model and GIS.

Availability of high temporal resolution data from the NASA Pathfinder data set and the future MODIS sensor onboard EOS satellites provide us with the capability of monitoring dynamic nature of land-use/ land-cover more closely. Satellite data need to be classified and geo-registered before using in modeling. Considering the number of images to be processed, classification and geometric registration of satellite images would form potential problems. However, with the availability of GIS systems which readily accept remotely sensed data, and new developments in classification techniques using artificial neural networks and automatic registration using wavelet transformation could provide viable alternatives.

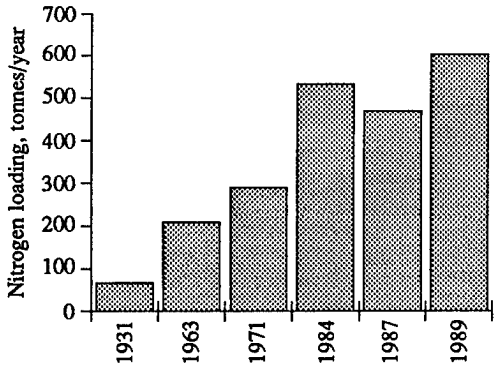


Figure 1. Predicted losses of nitrogen loading for the entire watershed: 1931-89 (from [7]).

CONCLUSIONS

Increasing nitrogen concentrations in the surface water have been mainly attributed to land-use change. Export coefficient model is an useful approach to predict nitrogen concentrations using land-use/ land-cover data derived from remote sensing. GIS enable us to efficiently store and manipulate remotely sensed land-use data, and to account for its spatial variability in water quality modeling. Results for a medium sized watershed suggest that the model predicts nitrogen loading reasonably satisfactorily. It is shown that land surface remote sensing and GIS could be employed to monitor, hindcast and forecast changes in surface water quality in response to land-use changes, and approach has potential for application over larger areas utilizing coarse resolution satellite data.

ACKNOWLEDGMENTS

This paper was prepared while Nandish M. Mattikalli held a National Research Council - NASA GSFC Post-doctoral Research Associateship. The support was provided by the Science Division of the Office of Mission to Planet Earth, NASA Headquarters.

REFERENCES

[1] M. N. Beaulac, and K. M. Reckhow, "An examination of land-use-nutrient export relationships," Wat. Resou. Bull., vol. 18, pp. 1013-1024, 1982.

[2] J. Cirello, R. A. Rapaport, P. F. Storm, V. A. Matulewich, M. Morris, S. Goetz, and M. S. Finstein, "The question of nitrification in the Passiac River, New Jersey: an analysis of historical data and experimental investigation," Water Research, vol. 13, pp. 525-537, 1979.

[3] P. J. Johnes, and P. E. O'Sullivan, "The natural history of Slapton Ley Nature Reserve XVIII: Nitrogen and phosphorus losses from the catchment- an export coefficient approach," Field Studies, vol. 7, pp. 285-309, 1989.

[4] S. E. Jorgensen, Lake management, Pergamon, 1980.

[5] N. M. Mattikalli, "Integration of remotely sensed raster data with a vector-based geographical information system for land-use change detection," Int. J. Rem. Sensing, vol. 16, no. 15, pp. 2813-2828, 1995.

[6] N. M. Mattikalli, "Time series analysis of historical surface water quality data of the River Glen catchment, U.K.," J. Environ. Managmt, vol. 46, no. 2, pp. 149-172, 1996.

[7] N. M. Mattikalli, B. J. Devereux, and K. S. Richards, "Prediction of river discharge and surface water quality using an integrated geographical information system's approach," Int. J. Rem. Sensing, vol. 17, no. 4, pp. 683-702, 1996.

[8] M. D. Meybeck, Chapman, and P. Helmen, (eds.) Global freshwater quality: a first assessment, Global Environment Monitoring System/UNEP/WHO, 1989.

Satellite Remote Sensing and Geographic Information System for Monitoring Morphodynamics of the Active Yellow River Delta, China

Xiaojun Yang [1], Michel C. J. Damen, Robert van Zuidam [2], Andre van Gelder, Jan H. van den Berg [3], and Guodong Cheng [4]

1) Department of Geography, The University of Georgia, Athens, GA 30602, USA
2) International Institute for Aerospace Survey and Earth Sciences, Enschede, The Netherlands
3) Department of Physical Geography, Utrecht University, The Netherlands
4) Institute of Marine Geology, MGMR, Qindao, China

Abstract -- An integrated approach of satellite remote sensing and geographic information systems techniques has been employed to survey and monitor the contemporary processes and the dynamics of the actual active delta lobe (Post 1976), i.e. the most rapidly changing portion of the Yellow River Delta, China. The main used sources for data analysis are the Landsat-MSS and -TM images (60 scenes or windows) spanning the last nineteen years. The research have been focused on the coastal and fluvial morphologic changes. This research demonstrates that satellite remote sensing in combination with GIS techniques is very useful for documenting the time-sequential dynamic morphologic changes and for analyzing the contemporary processes involved.

INTRODUCTION

Satellite sensors are valuable tools for surveying and monitoring the dynamic environmental system. Passive sensor systems, like Landsat-MSS and -TM, record and measure reflected energy in the visible and infrared portions of the electromagnetic spectrum, in which the majority of spectral information on landform features may be detected.

Present-day deltas, such as the active Yellow River Delta, belong to the most dynamic natural systems on earth. They are therefore ideal to apply remote sensing and GIS based monitoring. Using images with high resolution, landform features, such as the shifting-, geometry-, and patterns- of river channels can be distinguished and characterized.

The research work was performed during the past two years as a joint research project between Institutes of the People's Republic of China and the Netherlands. The main focus of the study is the integration of satellite remote sensing and GIS technologies for surveying and monitoring of contemporary processes and dynamics of the delta after 1976.

THE YELLOW RIVER DELTA

The Yellow River is unique for its morphodynamic processes. Since 1855, the Yellow River has shifted its main channel more than 10 times. Subsequently an actual delta consisting of at least ten sub-deltas or lobes has been formed in the north of Shandong Province. The sub-surface of the delta contains the second largest oil field in China: The Shengli Oilfield. Statistically, the formation of a sub-delta (lobe) has taken 10 - 12 years. For other large deltas, such as the Mississippi Delta, it generally has taken hundreds of years to develop a sub-delta.

The presently active delta is the tenth deltaic lobe of the Yellow River Delta since 1855, formed since May 27, 1976 when the Yellow River course was artificially dammed near Xihekou and subsequently forced to run through the Qinshuigou River into the Bohai Sea. It is an active flood plain environment with point bars, alternating bars and swales, active shifting zones, large crevasse splays, infilled channels, salt marsh, and rapidly prograding tidal flats.

The whole period of development of this deltaic lobe *synchronizes* with the operational age of the Landsat Satellites. Therefore the available images make it possible to monitor the entire period of geomorphological development of the sub-delta.

DATA AND METHODOLOGY

An integrated approach combining digital image

0-7803-3068-4/96$5.00©1996 IEEE

processing (DIP) and geographic information system (GIS) techniques has been applied for data collection, processing, analysis, and presentation. The main sources of data are 60 scenes or windows of Landsat-MSS (hardcopy of band 4 only) and -TM images (3 in digital form) spanning the last 19 years (1976-1994). A standard procedure of digital image processing has been carried out on about 17 digitally scanned images (hardcopies), and three (1/4 scenes) of digital Landsat-TM images from 1992, 1993 and 1994. A false colour composite of the Landsat-TM image of April 11, 1992, was geometrically corrected and used as the master map for image to image correction of the other scenes. Geographical point data were derived from GPS measurements and the topographical map. The software used was the Integrated Land and Water Information System (ILWIS), developed by the ITC, The Netherlands. After this, visual interpretation was performed using the on-screen ILWIS digitizing program. For adequate mapping, the screen image display was enlarged to scale 1:3,500.

INTERPRETATION AND ANALYSIS

The interpretation and analysis has been focused on the coastal fluvio-morphologic changes, including channel shifting change, channel geometric change, and channel pattern change.

Both banks have been examined separately as regards their shifting and erosion changes. The north bank showed an extremely unstable behaviour by shifting northward and southward alternately during the first 66 months of the actual delta environment, i.e. from May. 1976 until November, 1981. The maximum shifting distance amounted to more than 6,458 m (northward) within 17 months for a certain reference section Q4. It showed a declining shifting rate after 1981, ranging from -150 to -500 m per year. The south bank showed a similar change with the north bank during the first 66 months. The maximum shifting distance amounted to -3,728 m (southward) within six months for the reference section Q7. From 1982 till 1987, it tended to decrease its migration rate. It became increasingly unstable after 1987. The difference of the shifting change between both banks after 1987 possibly results from the differences in the embankments. The northern embankment seems to be stronger than the southern bank.

Some aspects of the channel geometric change are examined. The channel length increases with an average of 1,650 m per year, but tends to slow down. Also the channel width tends to decrease and is becoming approximately equally wide in the whole stretch.

The channel pattern is changing from braiding via straight to slightly meandering as has been well documented by earlier studies (Yang, 1995) and other authors. As a whole, the channel bifurcation index tends to decrease, while the channel sinuosity tends to increase. Two major stages can be well defined. The second stage can be further subdivided, based on the degree of artificial intervention.

1. *Braiding Stage (*1976 - 1980): During this period, the river channel system was extremely unstable, showing the most significant changes. The channel system changed from disorderly braiding via well-organized braiding to a generally straight pattern. The channel bifurcation index tends to reduce as well as the longitudinal profile gradient. The channel stability index indicates an obvious decreasing trend, since the channel tends to become more stable.

2. *Straight - Slightly Meandering Straight Stage I* (1981 -1987): During this period, the channel stability index tends to increase, and as a result the channel became less stable. The longitudinal river profile gradient became much more gentle due to the rapid seaward progradation. This diminishes the capacity of the flow to transport its suspended bed-load. It has resulted in severe silting which caused successive flooding (twice within 1987). The situation in late 1986 -1987 evidenced that the development of the channel is now entering the stage of *decay*.

3. *Straight - Slightly Meandering Straight Stage II* (after1987): As the channel sinuosity has been increased, the channel gradually changed from straight to slightly meandering straight. The channel as a whole tends to become more stable. Human intervention has been successful, especially during the first two years (1988-1989), by improving the capacity of the flow to transport its suspended bed-load. Although dredging and dike building may keep

the actual channel running for several decades, on the long run, a well-organized (artificial) diversion has to be carefully considered.

CONCLUSIONS

This study documents the morphodynamic evolution of the large and active Yellow River Delta, by integrating multi-temporal image data with field observations. The presently active delta lobe has displayed complicated morphological changes, since its initiation in May 1976. For 1986, after ten years of its existence, the present river channel has entered a stage of *decay* even under a natural condition. Human intervention maintains the actual running state of the river course. However, for the near future, an artificial diversion has to be carefully considered and probably to be carried out. The results of this study demonstrate that satellite remote sensing combined with GIS technology is very useful for documenting the time-sequential mophodynamic changes and for analyzing the contemporary processes involved.

Since the marine processes, like tides and waves, are relatively weak, the active delta can be classified as a fluvial-dominated delta. Linear fit analysis has demonstrated that the general trends of the changes of the length and deltaic area is highly synchronous. The change of position of the river outlet determined the configuration of the delta. As the yearly total amount of the sediment discharge decreases, the increment of the channel length tends to decrease, and also for the increment of the deltaic area. When the action of the fluvial processes decline, the prograding of the (front) sand bar and the coastline tend to slow down. Marine actions, however, are becoming more important when the river discharge becomes less and the channel runs dry. This tends to happen more and more frequently, because of the diversion of river water upstream for irrigation purposes. For example, in 1992 the riverbed was dry for 150 days (April - August). Hence, no sediment load was carried to the delta and consequently, the sand/silt bars in the river mouth suffered from severe marine erosion. Therefore the channel length as well as the deltaic area showed a noticeable loss in the 1992 images.

Human activities, in the form of building of embankments, artificial diversion, channelization, dredging, and pumping of ground fluids, have posed a very important effect on the development of the delta. A canal with a length of 8.75 km, together with approximately 95 km embankments, has been constructed for the artificial diversion project, and became effective in May 1976. These embankments played a significant role in limiting the channel shift and bank full flooding, and they guided the prograding orientation of the delta. Since 1988, an intensified dredging programme has been carried out around the river mouth. This event has effectively controlled the development of the mouth channel , especially during the first two years (1988 -1989).

Because most of the oil fields are located north of the actual channel, the embankments have been made stronger on the north than on the southern bank. As a result, the northward shifting of the north bank is less than the southward shifting, which may affect the overall shifting behaviour of the channel thalweg.

As mentioned before, there is a southward shifting of the river channel (thalweg as well as both banks), the river outlet, and the delta (silt bar). The reason seems to be very complex. Although this southward shifting can be logically explained by the principle of the *Coriolis Force*, the involvements of the marine hydraulic effect, the tectonic activities, and the differential embankments need to be studied in more detail.

ACKNOWLEDGMENTS

This work was supported by the Royal Dutch Academy of Sciences (KNAW), the International Institute for Aerospace Survey and Earth Sciences (ITC), and Utrecht University in the Netherlands, as well as the Institute of Marine Geology of the Ministry of Geology and Mineral Resources (MGMR) in Qingdao, China.

SELECTED REFERENCE

[1] X.Yang, *"Monitoring Morphodynamic Aspects of the present Huanghe River Delta, China. An Approach of the Integration of Remote Sensing and Geographic Information System "*, Enschede, The Netherlands, 1995, 192pp.

Remote Sensing & Core Data Needed to Support Planning and Policy Decision Making

Dr. Timothy W. Foresman
Department of Geography, University of Maryland Baltimore County, Baltimore, MD 21228
Phone: 410-455-3149; Fax: 410-455-1056; Email: foresman@umbc.edu

Dr. John E. Estes
Department of Geography, University of California, Santa Barbara, CA 93106
Phone: 805-893-3649; Fax: 805-893-3703; Email: estes@geog.ucsb.edu

Mr. Jerry J. Garegnani
NASA Headquarters, Code YD, 300 E Street, SW, Washington, DC 20546
Phone: 202-358-0770; Fax: 202-358-3098; Email: JGaregna@mtpe.hq.nasa.gov

Ms. Dana L. Porter
Department of Geography, University of Maryland Baltimore County, Baltimore, MD 21228
Phone: 410-455-3847; Fax: 410-455-1056; Email: dhinzm1@strabo.umbc.edu

Abstract -- A variety of sustainable development research efforts and related activities are attempting to reconcile the issues of conserving our natural resources without limiting economic motivation while also improving our social equity and quality of life. Land use/land cover change, occurring on a global scale, is an aggregate of local land use decisions and profoundly impacts our environment. It is therefore the local decision making process that should be the eventual target of many of the ongoing data collection and research efforts which strive toward supporting a sustainable future. Satellite imagery data is a primary source of data upon which to build a core data set for use by researchers in analyzing this global change. A process is necessary to link global change research, utilizing satellite imagery, to the local land use decision making process. One example of this is the NASA-sponsored Regional Data Center (RDC) prototype. The RDC approach is an attempt to integrate science and technology at the community level. The anticipated result of this complex interaction between research and the decision making communities will be realized in the form of long-term benefits to the public.

DISCUSSION

As human population increases, the earth's resources we consume in our pursuit of improved quality of life are stressed and depleted. Significant research in monitoring natural resource changes is currently underway within various scientific communities, specifically dealing with the topics of sustainability, sustainable development, and global change. Each of these areas have a broad research agenda of global scope to understand how Earth's natural and anthropogenic systems are changing in order that we can make necessary and timely adjustments to sustain a livable environment for our global population. Within the scope of these general areas are some common themes that deal with social, economic, and environmental measurements or indices dealing with such issues as urbanization and land use change. The interdisciplinary science to study these complex interactions between humans and nature at global, regional and local levels is still relatively young and often controversial. Currently there is no agreement on indices that can properly relate the overall health of the planet, or even the local area, and its inhabitants to the policy or decisions being made every day effecting that health.

Consensus on measurable sustainability parameters seems possible among various scientific disciplines, as well as between conservationists and commercial developers, if the scientific community can demonstrate the relationship sustaining naatural resource quality has with economic viability. The most common definition of sustainable development is "...development that meets the needs of the present generation without compromising the ability of future generations to meet their own needs [1]." The definition of sustainability must be accepted so that planning and decision making can operate towards a more widely accepted and focused goal. A widely accepted goal can then indicate what core data is necessary and how to distribute that data to various levels of decision makers and to the public. Within the remote sensing community this core data need can be met by harnessing the emerging data wave from government sponsored and commercial spacecraft into effective core data sets.

Many of us in the field of remote sensing believe that, the better data we can gather, the better we will be able to produce a more functional product. As a result, the users of these functional products will be able to make better decisions for the allocation of our natural resources. We will then have sped our pursuit towards an improved living condition. The

0-7803-3068-4/96$5.00©1996 IEEE

technology to produce gross resolution core data is generally available. Satellite sensors, global positioning systems, image processing, digital cartographic and geographic information systems are in place and are revolutionizing mapping. However, public policy decision makers do not recognize the need for this data nor understand how to apply it to their decision making process. Sufficient funding has not been committed to acquire the full set of data, from the available remote sensing technology, that is necessary to create functional products.

In spite of the various research agendas, satellite programs, and data distribution systems in development, the final application of these efforts is not linked to the land use decision making process. The scientific community needs to do more to publicize the lack of appropriate core data and how that data can be used to achieve defined policy goals. Additionally, the policy goals toward a sustainable future must be broken down into discreet land use decisions based upon the results of scientific research and available technology.

The President's Council on Sustainable Development and the Interagency Working Group on Sustainable Development Indicators (IWGSDI) and various regional, state and local sustainability efforts are attempting to implement this research at the grassroots level [2]. A critical part of these sustainability efforts relies on the access and availability of current, useable data sets. To address the question of the adequacy of data sets needed by environmental planners, resource managers and public policy decision makers, an international symposium was held in November 1994, in Bangkok, Thailand. Participants identified 10 high-priority "core" data sets central to the generation of sustainable development strategies. These ten priority core data sets are: Land Use/Land Cover, Topography, Demographics, Economy, Hydrology, Soils, Infrastructure, Air Quality, Climatology, and Water Quality [3].

NASA's Earth Observing System (EOS) and the associated Data Information System (EOSDIS) is an example of data collection and distribution system under development to support global science questions in cooperation with the interagency Global Change Research Program. The current Earth system monitoring efforts at NASA, and at several other agencies, are in response to global changes which have already become apparent [4]. Global changes are reflected in several ways such as increasing concentrations of carbon dioxide, an ozone hole over Antarctica and alterations in the global nitrogen cycle. Of the several global changes occurring, human induced land use/land cover change has the most profound effect on the integrity of ecosystem components that affect the quality of our lives [5]. The land use/land cover change, occurring on a global scale, is an aggregate of local land use decisions. It is therefore the local decision making process that should be the eventual target of many of the ongoing data collection and research efforts which strive toward supporting a sustainable future. There is a great need for the science community to pursue development of integrated data sets for realistic sustainability models as the ultimate target and land use decision makers (county supervisors, town planners, etc.) as the ultimate users of their results. This approach would focus results on a process of local zoning that is currently fragmented in approach [6] and allow the application of best science, best technology, and best practice to what is thought by many to be the most critical driver of global change.

The timely translation from scientific research to practical application requires a complex set of interactions depicted in Fig. 1. In order to base scientific research on real world issues, definition should be provided by local decision makers. Research results are then translated into proven indices and thresholds for well calibrated and proven models which, in turn, are used by decision makers to actually make decisions.

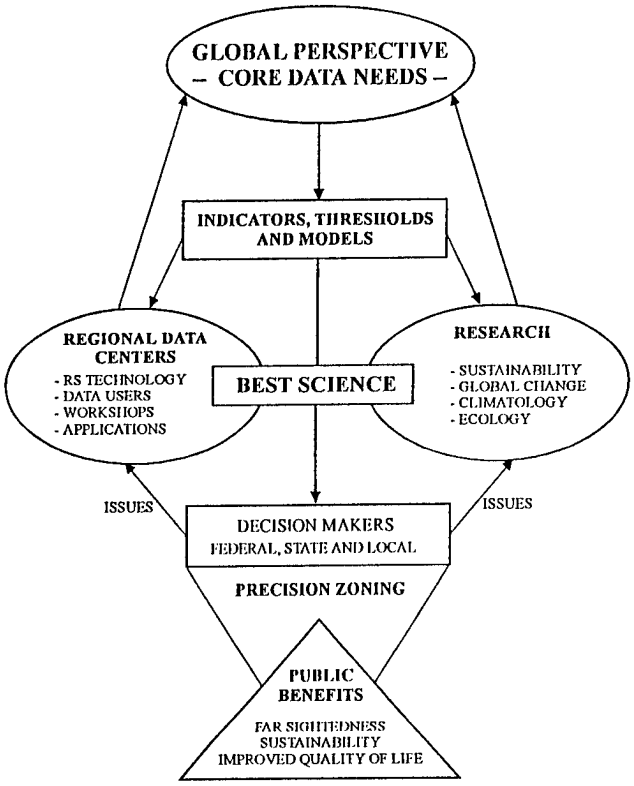
In order to relate developing technology, space imaging data and science results to regional land use issues, NASA has recently established prototype Regional Data Centers (RDCs). One of the prototype RDCs has been established at the University of Maryland at Baltimore County and is focused on the Baltimore and Washington DC area [7]. This RDC has established partnerships with state and local agencies that deal with land use issues and who can benefit from collaboration with research scientist. The RDC provides a testbed where interdisciplinary science can interact with planners and resource managers on specific land use issues utilizing developing spatial technologies. The Regional Data Center (RDC) approach is an attempt to integrate science and technology at the community level. Fig. 1 is a model of how the RDC approach can facilitate the exchange of issues, science results, data, and models between the different levels of the decision making community and the scientific community in order to produce beneficial land use decisions in a local area.

Of great significance in a decision influencing process is the definition of core data needs based upon the issues to be addressed, the technology available, and the ability of the research community to deal with the data. From these data are derived critical indices and thresholds that measure the state or condition of the environment. These measurements are necessary to monitor the effect of changes over time so that decision makers can take proper action. Models are also derived from scientific understanding and combined with these core data to provide insight to decision makers on the potential long-term consequences of their decisions and to define decision options.

The result of this overall process in Fig. 1 will be a new tool which the authors have coined as "Precision Zoning". This is a term borrowed from the precision agriculture concept [8]. Precision Zoning utilizes best science and best technology on which to base local land use decisions that will

provide the most beneficial long-term results. Precision Zoning is the culmination of scientific research manifest in the decision making process through the use of spatial technologies and is the conceptual vehicle to reaching sustainability.

FIGURE 1.



SUMMARY

The idea of sustainable development is still very theoretical and requires concrete steps for its realization. The RDC concept is a step in this direction, yet the actual implementation of carefully considered and has just begun. The concept of Precision Zoning as a tool will be further investigated by the authors. The potential for the application of a Precision Zoning tool will provide local benefits that eventually aggregate towards global benefits. Our goal is the broader use of satellite imagery data in the local land use decision making process.

REFERENCES

[1] G. H. Brundtland, M. Khalid, et. al. "Our common future." Oxford University Press, Oxford, 1987.

[2] W. Corson. "An inventory of local and regional programs using goals and indicators to define and measure quality of life, progress, and sustainability at the city, county and state level." Global Tomorrow Coalition, 1995, unpublished.

[3] J. Estes, J. Lawless, D. Mooneyhan, et. al. "Report of the international symposium on core data needs for environmental assessment and sustainable development strategies." UNEP, Bangkok, Thailand, 1994.

[4] G. Asrar and J. Dozier. "EOS: science strategy for the Earth Observing System," AIP Press. Woodbury, NY, 1994.

[5] P. Vitousek. "Beyond global warming: ecology and global change." Ecology. New York, 1994.

[6] W. Baker. "State must enact a real land-use growth plan." Letter to the Editor, Baltimore Sun, December 1995.

[7] T. Foresman, H. Wiggins, D. Porter, P. Masuoka, W. Acevedo. "Design and documentation of a Baltimore Washington regional spatial database testbed for environmental model calibration and verification." Proceedings: Third International Conference/Workshop on Integrating Geographic Information and Environmental Modeling, Santa Fe, NM, 1996.

[8] E. L. Usery, S. Pocknee, and B. Boydell. "Precision farming data management using geographic information systems." ASPRS Journal, Bethesda, MD, vol. 61, pp. 1383-1391, November 1995.

Analysis of Snow Cover in Alaska using Aircraft Microwave Data (April 1995)

D. K. Hall*
J. L. Foster*
A. T. C. Chang*
D. J. Cavalieri**
J. R. Wang***
*Hydrological Sciences Branch, Code 974
**Oceans and Ice Branch, Code 971
***Microwave Sensors Branch, Code 975
Laboratory for Hydrospheric Processes
NASA/Goddard Space Flight Center
Greenbelt, MD 20771
E-mail: dhall@glacier.gsfc.nasa.gov

and

C. S. Benson
Geophysical Institute
University of Alaska
Fairbanks, AK 99775-7320

ABSTRACT

During April of 1995, a field and aircraft experiment was conducted in central and northern Alaska. A Millimeter-wave Imaging Radiometer (MIR), and other sensors, were flown on-board a NASA ER-2 aircraft in a grid pattern centered over Fairbanks. Resulting MIR data show brightness temperature patterns that are related to land cover and snowmelt patterns.

INTRODUCTION

From 31 March to 25 April, 1995, a mission was conducted to study snow cover in northern and central Alaska, respectively. The utility of high frequency passive-microwave aircraft data is assessed as is the influence of a variety of surface cover types on the microwave brightness temperatures of dry and melting snow. The aircraft data included the Millimeter-wave Imaging Radiometer (MIR) and the Moderate Resolution Imaging Spectroradiometer (MODIS) Airborne Simulator (MAS). Analysis of MAS data will be discussed in a subsequent paper. In this paper, the MIR data are analyzed along with ground-truth and meteorological data that were acquired simultaneous with the aircraft overpasses in the series of aircraft flights flown over Fairbanks.

AIRCRAFT INSTRUMENTATION

The MIR is a mechanically-scanned imaging microwave radiometer that measures radiation at the following frequencies: 89, 150, 183.3±1, 183.3±3, 183.3±7 and 220 GHz. It has an angular resolution of about 3.5°. It is a cross-track scanner with an angular swath width of about 100°, centered at nadir. Its polarization vector is in the horizontal plane and perpendicular to the velocity vector of the aircraft so that the measured radiation is a mixture of vertical and horizontal polarizations depending on the viewing angles. The temperature sensitivity is < = 1 K for all channels. The 183.3-GHz channels are not used in this work due to its location in the water vapor absorption line. The MIR data in this study have a spatial resolution of approximately 1 km at nadir.

BACKGROUND

The ability to infer snowpack thickness using passive-microwave data has been recognized for many years. However, many factors have been found that complicate the relationship between passive microwave brightness temperature and snow depth [1]. For example, snow grain size differences [2], [3] and forest cover [4], [5] influence the brightness temperature of snowpacks, and there is a strong

0-7803-3068-4/96$5.00©1996 IEEE

dependence of microwave brightness temperature on topography and land cover [2].

Chang et al. [6] found that 92-GHz aircraft data, acquired over Alaska during a 1983 experiment, was more sensitive to snow-crystal scattering than was 37-GHz data, but was also more sensitive to atmospheric parameters. In cloud-free areas, 37- and 92-GHz brightness- temperature patterns over snow in Alaska were similar. However, at 92 GHz, the atmospheric brightness temperature contribution is much higher than it is at 37 GHz, 50 K in the subarctic winter and 100 K in the subarctic summer [6].

METHODOLOGY

Field measurements of snow depth, density, grain size and shape were made in Fairbanks (64°50'N, 147°48'W) and at Ester Dome which is about 5 km northwest of Fairbanks, as well as in other parts of Alaska. Aircraft flight lines were flown in a grid pattern in central Alaska, including Fairbanks, on 5, 6, 13 and 21 April. These data have been gridded to a polar stereographic equal area map. In addition, a vegetation map of Alaska [7] was registered to the MIR data to compare with the aircraft data.

RESULTS AND DISCUSSION

Field and air-temperature measurements showed that the snow in and near Fairbanks was melting during the daytime during the month of April. Except within the city, snow cover was nearly continuous. Table 1 shows snow depths from a location in Fairbanks and at Ester Dome. Table 2 shows air temperatures at the approximate time of the aircraft takeoff on the flight days over the 'Fairbanks grid.' Each flight over the Fairbanks grid lasted about 2 hours and 20 minutes.

Table 1. Snow depths in Fairbanks and at Ester Dome on selected dates in April.

Date	Fairbanks	Ester Dome
4/1/95	59 cm	---
4/2/95	54 cm	---
4/6/95	39 cm	---
4/7/95	35 cm	---
4/8/95	---	100 cm
4/11/95	23 cm	---

Table 2. Average air temperatures at approximate times of aircraft takeoffs, and time of flights over the 'Fairbanks grid.'

Date	°C	Fairbanks local time
4/5/95	8°	10:50 - 13:11
4/6/95	3°	8:42 - 11:01
4/13/95	10°	11:08 -13:36
4/21/95	-1°	6:59 - 9:29

Analysis of the MIR 89-, 150-and 220-GHz data shows that the brightness temperature increases with frequency, due to increased emission from the atmosphere as discussed by Chang et al. [6]. For example, on 5 April, the 89-, 150- and 220-GHz MIR brightness temperatures averaged 263, 264 K and 269 K, respectively, in the vicinity of Fairbanks.

Snow in Fairbanks was actively melting during the daytime during the month of April. As soon as snow becomes wet, scattering is reduced as the crystals become coated with liquid water. As a result, the snowpack behaves as a lossy medium, and the brightness temperature increases. In the vicinity of Fairbanks, the 89-GHz brightness temperatures averaged 263 K, while in the southern part of the study area (central Alaska Range) brightness temperatures were ≅210 K on 5 April. Deeper snow and lower temperatures caused the brightness temperatures to be lower there. Additionally, on lines flown north of Fairbanks, toward the Brooks Range and on the North Slope, also on 5 April, brightness temperatures are 10-40 K lower than in the Fairbanks area because the snow to the north was still dry in April (Figure 1). Also, in the Brooks Range and on the North Slope, there are no trees to increase the brightness temperatures there.

Comparison of the vegetation map with the MIR data shows that several land-cover types influence the microwave signal. On each of the 4 MIR images (at 89 GHz) for the Fairbanks grid, the boundary between the black spruce forest and the meadow dryas is evident at a latitude of approximately 64°N, just south of Fairbanks (Figure 1). Coniferous trees emit more microwave radiation than do tundra or dryas vegetation, and this is one explanation for the higher brightness temperatures in the black spruce forests.

In the central part of the Fairbanks grid, brightness temperatures are generally quite high due to the melting snow. The relatively high brightness temperatures there overwhelm the brightness-temperature differences that result from land-cover variability. This is especially true on April 13, when the air temperatures were the highest of the 4 flight days (Table 2), and presumably, when melting covered the largest extent of area.

On 6 April, note in Figure 1 that brightness temperatures are quite low over the Fairbanks grid as compared to the other days. The air temperature as recorded at Fairbanks was 3°C, but may have actually been below freezing over most of the Fairbanks grid. If this were the case, and the snowpack was dry, this would explain the much-lower brightness temperatures measured during the 6 April flight, and the closer match between brightness temperatures there and to the north..

Other regions of interest are where finger-like projections of the spruce-birch forest to the east of Fairbanks intersect dryas meadows and barren areas. Brightness temperatures are higher in the spruce-birch forest (≅261 K) than in the dryas meadows and barren areas (≅251 K) presumably due to the higher emissivity of the trees.

CONCLUSIONS AND FUTURE WORK

The land-cover type is shown to influence microwave brightness temperature under dry snow conditions. Snow-covered forests cause higher brightness temperatures than do snow-covered dryas meadows and tundra. However, when the snowpack is wet, the high emissivity of the snowpack overwhelms the contribution of the vegetation to the brightness temperature.

Work will continue on the current data set to investigate the influence of land cover particularly the influence of the dryas meadows and black spruce. Satellite data will be analyzed in conjunction with MIR data in order to modify snow depth retrieval algorithms so that they are more responsive to the snow and land surface conditions encountered in central and northern Alaska.

ACKNOWLEDGMENTS

The authors would like to thank Janet Chien for her expertise in preparing the MIR data for analysis, Penny Masuoka for digitizing Kuchler's vegetation map, and NASA Ames Research Center for the aircraft support. Work was supported by NASA's Mission to Planet Earth project office.

REFERENCES

1. A.T. C. Chang, J.L. Foster, D.K. Hall, B.E. Goodison, A.E. Walker, J.R. Metcalfe and A. Harby, "Snow parameters derived from microwave measurements during the BOREAS winter field campaign, submitted to *Journal of Geophysical Research,* in press.

2. D.K. Hall, C.S. Benson and J.Y.L. Chien, "Analysis of visible and microwave satellite data for snow mapping in Alaska," *Proceedings of the 50th Eastern Snow* Conference, Quebec City, pp. 129-137, 1993.

3. R. Armstrong, A.T.C. Chang, A. Rango and E.G. Josberger, "Snow depth and grain size relationships with relevance for passive microwave studies," *Annals of Glaciology*, vol. 17, pp.171-176, 1993.

4. M. Tiuri and M. Hallikainen, "Remote sensing of snow depth by passive microwave satellite observations," *Proceedings of the 11th European Microwave Conference,* Amsterdam, pp. 233-238, 1981.

5. D.K. Hall, J.L. Foster and A.T.C. Chang, "Measurement and modeling emission from forested snow fields in Michigan," *Nordic Hydrology*, vol. 13, pp. 129-138, 1982.

6. Chang, A.T.C., J.L. Foster and D.K. Hall, 1987: Microwave snow signatures (1.5 mm to 3 cm) over Alaska, Cold Regions Science and Technology, vol. 13, pp. 153-160.

7. Kuchler, A.W., 1985: Potential Natural Vegetation, USGS Map from National Atlas, sheet no. 89.

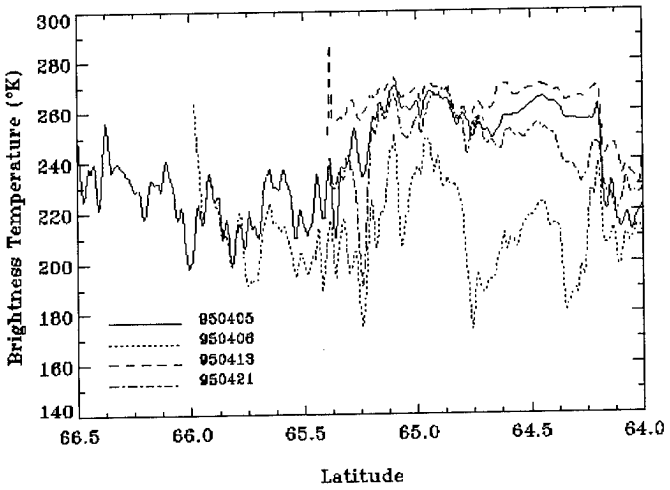


Figure 1. 89-GHz data from transects of MIR imagery showing brightness-temperature changes from northern Alaska to southern Alaska. Note that not all of the flights were flown of the same areas on each day.

Estimation of Snow Surface Albedo Using Landsat Thematic Mapper

*Jiancheng Shi, Thomas H. Painter and Jeff Dozier**

Institute For Computational Earth System Science (ICESS)
**School of Environmental Science and Management*
University of California, Santa Barbara, CA 93106, U.S.A
Tel:805-893-2309, Fax:805-893-2578, E-mail:shi@icess.ucsb.edu

ABSTRACT - Snow surface albedo is important to climatological and hydrological investigations. Using data acquired with the Landsat Thematic Mapper (TM) over Mammoth Mountain, California, we derived snow particle size from which surface albedo was estimated. Quantitative measurements of temporal and spatial variations in snow surface albedo will permit accurate parameterization for climatological and hydrological studies.

INTRODUCTION

Satellite remote sensing has become increasingly important to snow hydrologists, because the data provide information on the spatial and temporal distributions of parameters of hydrologic importance; snow-covered area, surface albedo, snow wetness and snow water equivalence. For the seasonal snow cover, remote sensing has been used to improve the monitoring of existing conditions and has been incorporated into forecasting snowmelt runoff [1][2][3].

We need to estimate the snow surface albedo from satellite in order to estimate the net solar radiation flux, given by the convolution of the spectral distribution of the incoming radiation and the spectral albedo. However, from satellite or aircraft we can measure only a part of the spectral BRDF (bidirectional reflectance distribution function), at a few wavelengths and usually only one solar-viewing orientation.

In this study, we show the physical principles and techniques to estimate snow particle size and snow surface spectral albedo, one of the important snow physical parameters, in an alpine region using Landsat Thematic Mapper. The data, acquired on April 14, 1994 over Mammoth Mt., California, were used to demonstrate the principles and techniques.

ESTIMATION OF SNOW PARTICLE SIZE

The spectral response to snow physical parameters in visible and near-infrared wavelengths has been studied for decades. In visible wavelengths ice is highly transparent, so that the albedo of snow is sensitive to both small amounts of absorbing impurities [4] and finite snow depth [5]. In the near-infrared wavelengths ice is more absorptive, so the albedo depends primarily on grain size [6].

0-7803-3068-4/96$5.00©1996 IEEE

Atmospheric and Topographic Corrections

Estimation of ice grain size in alpine regions from TM data requires that we compensate for the effects of the atmosphere and rugged terrain. In our examination of the atmospheric and terrain effects on TM measurements, the directional-hemispherical reflectance [7] was used, defined as the ratio of the reflected radiance integrated over all angles to the incoming direct irradiance. This is used because (1) the atmospheric effects are relatively small at the high altitude region, and (2) it is computationally time-consuming to calculate the angular distribution of the reflected radiation as a function of the local solar illumination, the satellite viewing angles, and the elevations of imaged pixel. Atmospheric parameters at different elevations were obtained using the LOWTRAN-7 model [8] for a typical mid-latitude summer atmospheric profile. Relationships between planetary reflectances from TM bands and the surface effective reflectances at the air-snow interface for each elevation were evaluated by a multi-scattering radiative transfer model - the two stream model. The values of simulated planetary reflectance, then, can be obtained from the mean values weighted by the TM band-pass filter within the wavelength range of the TM bands to account for the band width effect of TM measurements.

Figure 1 shows the simulated relations of TM band - 4 between planetary reflectance and surface effective reflectance at two elevations. The solid line indicates the one-to-one correspondence for no-atmospheric effect. The dotted and dashed lines are for elevations 2000 and 4000m, respectively. In the low surface reflection regions, the planetary reflectance is higher than the surface effective reflectance. This is because the amount of attenuated irradiance through the atmosphere from the low reflection surface is smaller than that from the scattering contribution of the atmosphere. The opposite is true for high surface reflectance so that the planetary reflectance is smaller than the surface effective reflectance. In addition, the slopes and intercepts of the relations between the planetary and the surface effective reflectances change with elevation due to atmospheric optical thickness change. It is then necessary to compensate for the elevation dependence during atmospheric correction.

In addition to the atmospheric effect, the variations in surface gradient (slope and aspect angles) in alpine regions

cause the great variations in local solar illumination and satellite viewing angles of the imaged pixels. The irradiance reflected from adjacent slopes toward imaged pixels must also be considered for quantitative estimation of snow particle size from TM measurements. In mountainous terrain, we consider that the irradiance at the air-snow interface consists of three components [5]:

1. direct solar irradiance, $\mu_s S_0 e^{-\tau_0/\mu_0}$,
2. diffuse irradiance from the sky, $V_d \overline{F_d}(\tau_0)$,
3. irradiance reflected from adjacent slopes toward imaged pixel, $C_t \overline{F_u}(\tau_0)$.

In the above, $\overline{F_d}(\tau_0)$ is average downward irradiance on an unobstructed horizontal surface. $\overline{F_u}(\tau_0)$ is mean flux density reflected from the surrounding terrain. V_d and C_t are the sky view factor and terrain view factor, respectively.

To incorporate topographic effects, we first need to convert the estimated the effective surface reflectance, R_{eff}, to the reflectance R_0 on the sloping surface. The effective reflectance is defined as the equivalent reflectance for a horizontal surface that would produce the same upwelling radiative flux as the sloping surface with reflectance R_0 and slope S [5]:

$$R_{eff} = R_0 \cos(S)\left[V_d + C_t R_0 + \frac{e^{\tau_0/\mu_0}}{T_s}\left(\frac{\mu_s}{\mu_0} - V_d\right)\right] \qquad (1)$$

where τ_0 and T_s are the optical thickness of the atmosphere and atmospheric transmittance, respectively. All of the above terrain-related parameters can be calculated by the method given in [9].

Effects of snow anisotropic reflectance

The satellite measurement of upwelling radiance from a snow surface is a value of the bidirectional reflectance at some particular combinations of incidence and reflection angles. For new fresh snow, the snow particle size is relatively small, the bidirectional reflectance is nearly isotropic. In this case, the relationship between snow particle size and the surface reflectance, R_0, may be evaluated by the integrated directional-hemispherical reflectance. In other word, R_0 is only a function of snow particle size and the local solar illumination angle. However, for moderate to large snow particles the R_0 depends also the satellite viewing angles in addition to snow particle size and the local solar illumination angle. Because of the strong forward reflection property of a natural snowpack, the calculation of the relationship between the satellite measurement and snow particle size requires a correction for anisotropic reflectance. Since TM is a nadir view sensor, the satellite viewing angle can be directly determined from the local slope angle and the difference between the solar and surface azimeth angles.

In order to take the snow anisotropic reflectance property into account, we simulated the relationship between the surface reflectance, R_0, and snow particle sizes by the discrete-ordinate model [10], the complex angular momentum approximation to the Mie equations [11]. A look-up table was built for the possible local solar illumination and satellite viewing angles using 2.5 degree increments based on the numerical simulation of the bidirectional reflectance for the range of snow particle radius from 0.05 *mm* to 4 *mm*. Then the estimated R_0 can be used to retrieve snow particle size.

ESTIMATION OF SNOW SURFACE ALBEDO

As mentioned above, in addition to snow particle size, we need information on the effects of snow impurities and shallow snow to calculate the spectral albedo. Whereas grain size determines the near-infrared signature, absorbing impurities and the water equivalent of the snowpack determine the visible signature. For a natural snowpack, observed snow albedo in the visible spectrum is always lower than the albedo calculated for pure snow. This is due to absorption by impurities such as soot and dust, which enter the snowpack as condensation nuclei and scavenged constituents during snowfall, and through atmospheric fallout and local dust wind-driven redistribution. This becomes particularly important in late spring when the infiltration of snowmelt leads to an agglomeration of impurities at the snow surface. Snow spectral albedo is strongly influenced by impurities in visible wavelengths because the imaginary part of the complex index of refraction for impurities can be several orders of magnitude larger than for ice. In near-infrared wavelengths though, ice is highly absorptive and swamps the impurity effect by virtue of its much larger volume fraction.

Thin snow likewise decreases the visible reflectance of a snowpack and not the near-infrared. Snow is most penetrable in visible wavelengths, so an incident photon has a far greater chance of encountering the darker substrate than a NIR photon. Figure 2 shows the effects of thin snow on the snow surface albedo. Where the solid, dotted and dashed lines are calculated for a pure and optically semi-infinite snow pack , 20 cm, and 10 cm snow depth (with snow density 0.3 and grain radius 0.5 mm), respectively. The boundary reflectances used in the numerical simulation were derived from AVIRIS measurements over a rock surface at the same study site.

To account for the effects of absorbing impurities and shallow snow depth on snow surface spectral albedo in the visible spectrum, we use the estimated snow particle size from TM band - 4 to calculate the surface reflectance of semi-infinite pure snow at band - 2. We selected band - 2 because it has less saturation problem than either band - 1 or band 3. A correction factor for each pixel can be derived from the ratio of the measured surface reflectance (after atmospheric and terrain corrections) to the calculated reflectance of the pure and semi-infinite snow. With this information, we now can estimate the snow surface albedo for either spectrally and hemispherically-

integrated albedo or spectrally dependent albedo for snow surface net radiation calculations.

CONCLUSION

This study shows recent results of our efforts to develop and verify the algorithms for snow particle size retrieval and estimation of the snow surface albedo from Landsat Thematic Mapper. TM band - 4 was used to estimate snow particle size because the reflectance in this spectral region is insensitive to snow impurities and shallow snow depth. Our method of snow particle size retrieval is based on the numerical simulation of the discrete-ordinate radiative transfer model. The effects of atmosphere with elevation dependence, topography and anisotropic reflection properties of a natural snowpack have been taken into account. In order to estimate the effects of the thin snow and impure snow on calculation of snow surface albedo at visible spectrum, we derived the correction factor from the ratio of TM band - 2 measured reflectance and that calculated for a pure, semi-infinite snow pack so that the snow surface albedo can be estimated. The spatial measurements of temporal and spatial variations in these snow properties will improve our understanding of the processes of natural snowpacks and provide the quantitative measurements with which to parameterize climatological and hydrological studies.

References

[1] A. Rango, An international perspective on large-scale snow studies, *Hydrological sciences bulletin*, vol. 50, no. 4, pp. 225--238, 1985.

[2] J. Dozier and D. Marks, Snow mapping and classification from Landsat Thematic Mapper data, *Annals of glaciology*, vol. 9, pp. 97--103, 1987.

[3] A. Rango and J. Martinec, Application of a snowmelt-runoff model using Landsat data, *Nordic Hydrology*, vol. 10, pp. 225--238, 1979.

[4] S. G. Warren and W. J. Wiscombe, A model for the spectral albedo of snow, II, Snow containing atmo spheric aerosols, *Journal of the Atmospheric Sciences*, vol. 37, no. 12, pp. 2734--2745, 1980.

[5] J. Dozier, Spectral signature of alpine snow cover from the Landsat Thematic Mapper, *Remote Sensing of Environment*, vol. 28, pp. 9--22, 1989.

[6] W. J. Wiscombe and S. G. Warren, A model for the spectral albedo of snow, I, pure snow, *Journal of the Atmospheric Sciences*, vol. 37, no. 12, pp. 2712--2733, 1980.

[7] K. Stamnes, S. Tsay, W. Wiscombe, and K. Jayaweera, Numerically stable algorithm for discrete-ordinate-method radiative transfer in multiple scattering and emitting layered media, *Applied Optics*, vol. 27, pp. 2502--2509, 1988.

[8] H. M. Nussenzveig and W. J. Wiscombe, Efficiency factors in Mie scattering, *Physical Review Letters*, vol. 45, no. 18, pp. 1490--1494, 1980.

[9] F. E. Nicodemus, J. C. Richmond, J. J. Hsia, I. W. Ginsberg and T. Limperis, Geometrical Considerations and Nomenclature for Reflectance, U.S. Department of Commerce, no. *National Bureau of Standards Monograph* 160, 1977.

[10] F. X. Kneizys, E. P. Shettle, L. W. Abreu, J. H. Chetwynd, G. P. Anderson, W. O. Gallery, J. E. A. Selby, and S. A. Clough, Users Guide to LOWTRAN7, *Air Force Geophysics Laboratory*, no. AFGL-TR-88-0177, 1988.

[11] J. Dozier and J. Frew, Rapid calculation of terrain parameters for radiation modeling from digital elevation data, *IEEE Trans. Geosci. Remote Sens.*, vol. 28, no. 5, pp. 963--969, 1990.

Figure 1. *The simulated relationships between planetary reflectance and surface effective reflectance at two elevations 2(dot) and 4 (dash) km.*

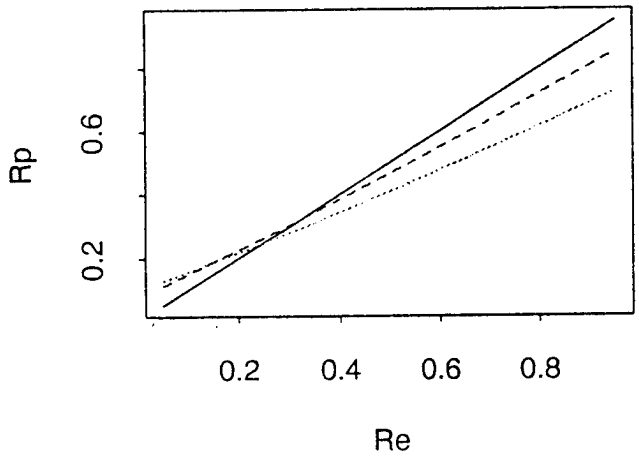
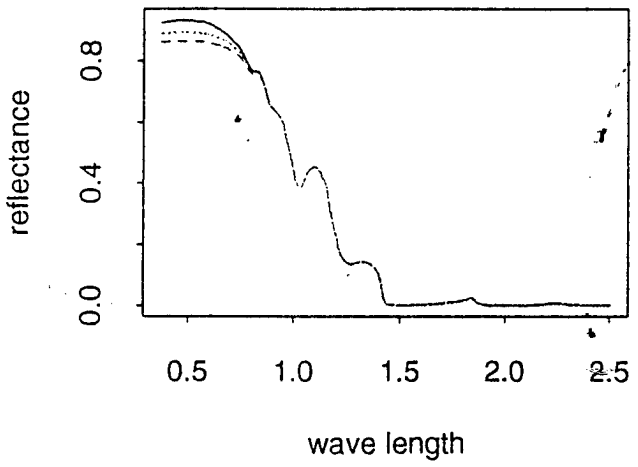


Figure 2. *Effect of thin snow depth on surface spectral albedo.*



Estimating Alpine Snow Cover With Unsupervised Spectral Unmixing

Walter Rosenthal
Institute for Computational Earth System Science
University of California, Santa Barbara
P.O. Box 7457, Mammoth Lakes, CA 93546
619-935-4464 walter @icess.ucsb.edu

Abstract – An unsupervised algorithm estimates snow-covered area at subpixel resolution from multispectral image data. Classification trees fragment the data set along boundaries of distinct land and cloud cover classes. The dimensionality and number of endmembers for each image fragment are determined from principal components analysis. Each fragment is unmixed with all endmember sets on its convex hull, and the best set is selected. Endmember spectra are converted to surface reflectance with an atmospheric radiative transfer code, and the endmembers are identified by automated search of a spectral library. The final snow cover estimate is a composite of the best mixture model per pixel, adjusted for endmember impurity. The algorithm is tested on Landsat Thematic Mapper data against high resolution aerial photographs.

INTRODUCTION AND BACKGROUND

Alpine snow and ice fields are major reservoirs of the Earth's fresh water, and may be sensitive indicators of the effects of climatic change on the hydrologic cycle. Snow-covered area (SCA) is a key variable for estimating snow-water equivalence over a watershed.

Researchers have attacked the problem of mapping alpine SCA from multispectral satellite data for two decades [1, 2, 3, 4]. Most schemes are binary: pixels are classified either "snow" or "not snow." Most pixels, however, are mixtures of snow, rock, vegetation, or water.

Decision trees have been used to generalize spectral mixture analyses of winter and spring Thematic Mapper (TM) data and accurately map snow cover in the Sierra Nevada at subpixel resolution [5]. The trees provide accurate estimates of SCA over the domain of the learning sample, but improved generalization requires retraining on additional cases supplied by further mixture modeling.

Supervised spectral unmixing is an iterative and subjective process. Possible endmember combinations typically number in the tens or hundreds of thousands; model evolution is influenced by the initial set of endmembers; there is no guarantee of convergence on a "best" solution; there are no stopping criteria; there is a strong tendency to overfit the data by adding endmembers until the average root mean squared error ($\overline{\mathrm{RMSE}}$) is acceptably low.

An unsupervised approach to mixture modeling can avoid these problems [6], but a new one arises when the target is snow. Sunlit snow has a unique spectral signature: it is among the brightest of all natural targets in the visible and near infrared part of the solar spectrum ($\sim 0.4-1.0\mu$m), but among the darkest in the short-wave infrared ($\sim 1.5-2.5\mu$m). Shadowed snow, in contrast, can be difficult to distinguish from materials such as shallow water or bright wet soils. Pure snow spectra occupy a continuum between these extremes, depending on grain size and illumination geometry. How are admixtures of snow in a pixel to be distinguished from those of other substances?

METHODS

A multispectral image, Earth-Sun geometric parameters, and an initial estimate of atmospheric path radiance are read by an unsupervised classification program. Machine speed, image size, and time constraints may force subsampling of the data, but this topic is omitted for clarity. The decision tree program from [5] masks clouds and isolates snow-free pixels from those probably containing snow. Snow pixels are further sorted into two sets: those suffering from detector saturation in at least one band, and those free of saturation problems. For each of these image fragments:

1. Its dimensionality, D, is estimated by principal components analysis (PCA).

2. The best set of image endmembers is assumed to lie on the convex hull of the data. Its size, k, is constrained to $D+1$. The n points on the D-dimensional convex hull are identified. All endmember sets of size k are compiled.

   The number of sets of size k that can be drawn from a set of n points (^nC_k) is

$$^nC_k = \frac{n!}{(n-k)!k!}. \quad (1)$$

0-7803-3068-4/96$5.00©1996 IEEE

3. All ${}^nC_k$ mixture models are computed by singular value decomposition. Endmember fractions are constrained to be non-negative and to sum to 1 or less.

4. The models are ranked by $\overline{\text{RMSE}}$; the model with the lowest value is chosen as the "best".

The endmembers for each image fragment must be identified. The 5S radiative transfer code [7] calculates downward and upward atmospheric transmittances, path radiance, and diffuse sky and direct irradiances at the surface. The conversion to surface reflectance is only approximate; terrain-dependent factors like substrate bidirectional reflectance, illumination from surrounding pixels, the fraction of the sky visible to the pixel, and local illumination geometry are not calculated at present.

The best matches to the corrected endmember reflectance spectra are found by automated search of a spectral library that has been adjusted for detector saturation. The library used in this study was restricted to 105 snow, rock, vegetation, and soil spectra drawn primarily from [8]. The search method computes the error sum of squares between endmember and library spectra [9].

The purity of the snow fragment endmembers is estimated by unmixing them as linear combinations of spectra from the convex hull of the entire data set. These "outer" endmembers are chosen by applying to the full data set the methods outlined above for the image fragments. There are now two error estimates for each snow endmember: one for the fit to the best match in the spectral library and the other for the fit to the outer endmembers. The endmember is considered pure if the library match produced the lower error, and is assigned a weight of 1 or 0 depending on whether the match was with snow. Otherwise, the endmember is weighted by the ratio of the outer snow fraction(s) to the sum of all outer endmember fractions.

The full scene is modeled with the best endmember set from each image fragment. The model with the smallest $\overline{\text{RMSE}}$ is chosen for each pixel, producing a snow fraction map that is a composite of best estimates. The raw snow fractions are weighted by the snow purity estimates. The ratio of the sum of all snow fractions to the sum of all fractions is then computed for each pixel to produce the final snow cover estimate.

The algorithm was tested with TM data against SCA estimates obtained from large format, color aerial photographs. The TM data comprised 6.2×10^6 pixels (about 5073 km^2) over the central Sierra Nevada of California, acquired on May 10, 1992. The program subsampled these to 97559 pixels. Decision trees masked 529 pixels because of clouds and sorted 25248 into the snow fragments. 9521 pixels suffered from band saturation problems. The snow-free, band-saturated snow, and unsaturated snow image fragments were found to be 3–, 2–, and 3–dimensional, respectively, with 34, 18, and 34 points on their convex hulls. As ordained by (1), 93568 mixture models were computed to determine the best fragment endmember sets. To estimate the purity of the snow fragment endmembers, an additional 148995 models were calculated for the 45 points on the convex hull of all 97559 points. Finally, the full data set was unmixed with each set of endmembers and the model with the lowest RMS error was selected for each pixel.

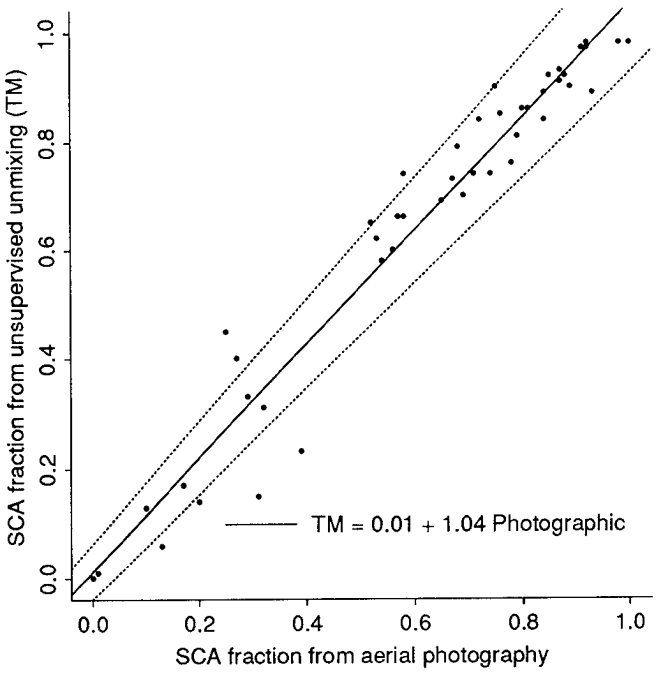


Figure 1: Snow cover fraction estimates, unsupervised unmixing of TM data v. aerial photography. The 95% confidence interval is plotted (dotted line).

The aerial photographs were acquired at the time of the satellite overpass along 3 flightlines within the scene. The nominal photographic scale was 1:8400 for the average surface elevation below the flightlines. The photos were digitized at 24 pixels per millimeter and the central portion ($\approx$ 10%) of each was registered to the TM data.

Field measurements of snow depth, density, and grain size along two of the flightlines at the time of the satellite and aircraft overpasses established that the snow pack was optically semi-infinite. The influence of the substrate on the snow spectra could therefore be ignored.

RESULTS

Fractional snow cover estimates from the unsupervised algorithm are plotted in Fig. 1 against the photographic estimates for 45 test sites. The coefficient of determination is 0.95. Except for 3 points, the distribution of the residuals is reasonably normal with constant variance.

The hypotheses that the regression line has a slope of 1 and an intercept of 0 cannot be rejected for the 95% confidence interval using student's t – statistic for 43 degrees of freedom.

Nearly 1.9×10^6 pixels were classified as containing snow. The $\overline{\text{RMSE}}$ was 5.6 DN for all pixels, 5.5 DN for snow pixels without band saturation problems, 6.7 DN for those with saturated bands, and 5.5 DN for pixels classified snow-free.

The library search matched two of the "unsaturated" snow endmember spectra not with snow, but with granite and basalt. The endmembers from the outer hull were matched with weathered granite, basalt, canyon live oak, and old snow with a grain radius of 1000 microns. All the matches were good except for basalt. The snow "basalt" endmember resembled open water (which was not in the library), while the outer hull endmember resembled dark vegetation. The fraction image abundances were congruent with the occurences of these substances.

DISCUSSION AND CONCLUSIONS

Although both TM and photographic estimates of SCA are random variables, the high quality of the photos suggests that the algorithm is the primary source of error. While the hypotheses of 0 intercept and unit slope in Fig. 1 cannot be rejected, the algorithm appears to produce a small but systematic overestimate of SCA for snow fractions greater than 0.5. The three points with the largest residuals are found among fractions smaller than 0.5.

Many simplifying assumptions were made to ease the development of the algorithm, and agreement between the estimates should improve as the assumptions are rectified. To give three examples: 1) $\overline{\text{RMSE}}$ is not the sole criterion for judging a model. The number of constraint violations and the condition number of the endmember matrix could influence the choice of best endmember sets. The outstanding problem is how to weight these measures in the selection process. 2) Estimates of the energy incident on a pixel and scattered to the sensor from all sources will improve with the use of digital elevation data and approximate substrate reflectance in the atmospheric correction. The substrate reflectance is not known a priori, but might be estimated using the general shape of the pixel spectrum or iterative atmospheric modeling. 3) Expansion of the spectral library to include all likely candidate spectra will improve endmember identifications and alter the final weighting of the snow fractions. The addition of a library search reliability measure [10] will provide a way to guage the value of an identification or detect the failure of a search.

This paper has presented an unsupervised spectral unmixing approach to mapping alpine SCA at subpixel resolution. Simplifying assumptions notwithstanding, the algorithm performed well with TM data against aerial photography in its first quantitative test. With refinement and further validation it should become a valuable tool for mapping snow with optical sensors other than TM, such as ASTER, MODIS, and NOAA-K/AVHRR.

REFERENCES

[1] Rango, A. and K. I. Itten, "Satellite potentials in snowcover monitoring and runoff prediction," *Nordic Hydrol.*, vol. 7, pp. 209–230, 1976.

[2] Martinec, J. and A. Rango, "Areal distribution of snow water equivalent evaluated by snow cover monitoring," *Water Resour. Res.*, vol. 17, no. 5, pp. 1480–1488, 1981.

[3] Dozier, J. and D. Marks, "Snow mapping and classification from Landsat Thematic Mapper data," *Ann. Glaciol.*, vol. 9, pp. 97–103, 1987.

[4] Dozier, J., "Spectral signature of alpine snow cover from the Landsat Thematic Mapper," *Remote Sens. Environ.*, vol. 28, pp. 9–22, 1989.

[5] Rosenthal, W. and J. Dozier, "Automated mapping of montane snow cover at subpixel resolution from the Landsat Thematic Mapper," *Water Resour. Res.*, vol. 32, no. 1, pp. 115–130, 1996.

[6] Boardman, J. W., "Automating spectral unmixing of AVIRIS data using convex geometry concepts," in *Summaries of the Fourth Annual JPL Airborne Geoscience Workshop*, vol. 1, pp. 11–14, 1993.

[7] Tanre, D., C. Deroo, P. Duhaut, M. Herman, et al., "Description of a computer code to simulate the satellite signal in the solar spectrum: the 5S code," *Intl. J. Remote Sens.*, vol. 11, no. 4, pp. 659–668, 1990.

[8] Satterwhite, M. B. and J. P. Henley, "Hyperspectral signatures (400 to 2500 nm) of vegetation, minerals, soils, rocks, and cultural features: laboratory and field measurements," Tech. Rep. ETL-0573, U.S. Army Corps of Engineers, Engineering Topographic Laboratories, Fort Belvoir, VA, 1990.

[9] Lowry, S. R. and D. A. Huppler, "Infrared spectral search system for gas chromatography/Fourier transform infrared spectrometry," *Analytical Chemistry*, vol. 53, no. 6, pp. 889–893, 1981.

[10] Harrington, P. B. and T. L. Isenhour, "A quantitative measure of the reliability of searches of spectral libraries," *Analytica Cimica Acta*, vol. 197, pp. 105–119, 1987.

Airborne and Spaceborne SAR Interferometry: Application to the Athabasca Glacier Area

P.W. Vachon, D. Geudtner, L. Gray, K. Mattar, M. Brugman[1], I. Cumming[2], J.-L. Valero[2]

Canada Centre for Remote Sensing, 588 Booth St., Ottawa, Ont. K1A 0Y7 CANADA
Phone: (613) 998-9060 Fax: (613) 993-5022 E-mail: vachon@ccrs.emr.ca

[1]National Hydrological Research Institute, Saskatoon, Sask. S7N 3H5 CANADA
[2]Dept. of Electrical Engineering, University of British Columbia, Vancouver, B.C. V6T 1Z4 CANADA

Abstract – ERS tandem mode differential synthetic aperture radar (SAR) interferometry (InSAR) is used to measure the surface flow field of a mid-latitude alpine glacier. The interferometric imaging geometry was reconstructed using accurate orbit data and a digital elevation model (DEM) derived from the CCRS CV-580 cross-track InSAR. The flow field is favorably validated against historical and nearly coincident displacement measurements made using surveying techniques.

INTRODUCTION

In this paper, InSAR measurements of the Athabasca and the nearby Saskatchewan and Dome Glaciers in the Canadian Rocky Mountains (N52.2° W117.25°) are considered. These typical mid-latitude alpine glaciers are tightly constrained by mountains, can move rather rapidly with significant vertical and horizontal velocity components, and may have significant summertime melt rates. It is important that long term monitoring of these glaciers be carried out in order to assess changes in glacier volume and mass transport rates. Such information is essential for validating and improving relevant hydrological models, and could have a role in assessing global climate change.

Differential InSAR offers the potential to provide the required monitoring and model validation capability and has already been studied in connection with polar ice sheets [1, 2]. We have considered three interferometry cases: first, CCRS CV-580 cross-track InSAR; second, ERS-1 interdisciplinary orbit repeat-pass InSAR with 35 days repeat cycle; and third, ERS-1/ERS-2 tandem mode repeat-pass InSAR with 1 day repeat cycle.

In the first case, two images with a known baseline are acquired simultaneously, allowing DEM generation from the interferogram phase [3]. In the second case, our experience has shown that the 35 day interval is too long to retain any useful scene coherence over the glaciers of interest. In the third case, we have found that useful interferograms (*i.e.* having significant scene coherence over the glaciers of interest) can be generated from the 1 day interval data, under certain weather conditions. In this case, the interferometric phase contains topographic as well as glacier displacement information.

DATA AND RESULTS

A field program to the area from 23 to 26 August, 1995 included the installation of survey markers on Athabasca and Saskatchewan Glaciers. The marker positions were measured in Aug., Sept., and Dec. 1995. CV-580 cross-track InSAR data were collected in March and August, 1995 for reference DEM generation. Only ascending ERS passes were considered, because the glaciers of interest are well-aligned with the radar line-of-sight. The descending passes provide only limited coverage of the glaciers due to significant layover. We have considered passes from two different relative orbits (ROs) of the ERS-1/2 tandem mode phase G operations, with passes at 05:53 UTC (23:53 local time). The tandem mode passes considered so far are summarized in Table 1.



Figure 1: Interferogram magnitude, 24/25 Aug. 1995. Azimuth: bottom-to-top. Ground range: left-to-right. The scene covers 16-by-12 km.

The interferometric processing was carried out as described in [4]. Fig. 1 is a representative interferogram magnitude image, while Figs. 2 and 3 are representative scene coherence maps for 24/25 Aug. 1995 and for 2/3 Nov. 1995. In each figure, Dome, Athabasca, and Saskatchewan Glaciers appear top-to-bottom, with the Columbia Ice Field to the left. The measured scene coherence γ on Athabasca Glacier is included in Table 1, along with temperature data measured by an automatic weather station located on the glacier. We require high scene coherence (say, $\gamma > 0.25$) to warrant proceeding with differential interferogram generation. High scene coherence is

0-7803-3068-4/96$5.00©1996 IEEE



Figure 2: Scene coherence, 24/25 Aug. 1995.

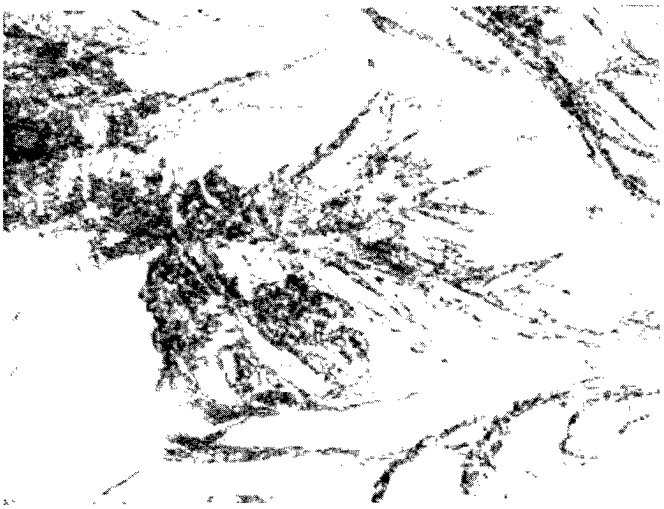


Figure 3: Scene coherence, 2/3 Nov. 1995.

usually associated with below freezing maximum temperatures, the absence of precipitation, and no blowing snow during the data collection interval.

The glacier flow field was derived from the ERS tandem mode image pairs having high scene coherence over the glaciers. The measured interfermetric phase due to topography was removed using the DEM derived from the airborne SAR data. This was accomplished by using accurate ERS orbit data and an algorithm to reconstruct the ERS imaging geometry [5] and to map the phase derived from the DEM into the slant-range, azimuth coordinate system. The actual interferogram was multiplied by the complex conjugate of the synthetic interferogram, leaving the differential phase due to glacier motion. The differential phase was unwrapped using a variant of the cut-line method [6] controlled by a mask made from the scene coherence and layover maps, and was mapped back into UTM coordinates. In Fig. 4, we show the unwrapped differential phase for 21/22 Nov. 1995.

Table 1: Summary of data and conditions.

dates 1995	RO	B_n [m]	γ	$T_{\max}$ [° C]	precip. [mm]
8/9 Aug.	220	55	0.22	+7	7
24/25 Aug.	449	78	0.17	+9	5
28/29 Sep.	449	248	0.21	+5	< 1
17/18 Oct.	220	203	0.36	−1	0
2/3 Nov.	449	94	0.77	−7	0
21/22 Nov.	220	17	0.67	−1	0
7/8 Dec.	449	205	0.28	−10	0

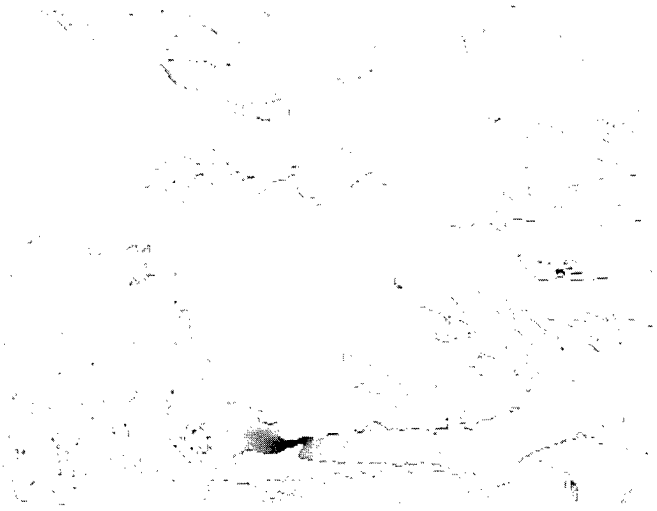


Figure 4: Unwrapped differential phase, 21/22 Nov. 1995.

If we ignore any residual phase due to uncorrected topography over the glacier, which is well-justified for the cases with small baseline B_n, we can interpret the residual phase as relating to the surface displacement field of the glacier over a 24 hour period. The residual fringes are not related to atmospheric heterogeneities since the differential phase was consistent for the high coherence cases examined so far.

The surface displacement field is measured as projected along the radar line-of-sight. We have only one displacement component to work with, so we must make an assumption in order to derive the 3-dimensional surface flow field. In our case, we have assumed a plastic flow model and that the flow vectors point downslope, in the direction of maximum basal slope. This assumption is suitable near the centreline of the glacier, but may be unsatisfactory near the glacier's margins. The downslope direction was determined from the airborne SAR DEM, as shown in Fig. 5. In Fig. 6, we show a validation of the measured displacement along the centreline of Saskatchewan Glacier. Two separate InSAR-measured glacier flow fields, based on tandem mode pairs collected 19 days apart, are compared with the *in situ* measured point velocities derived from the historical [7]

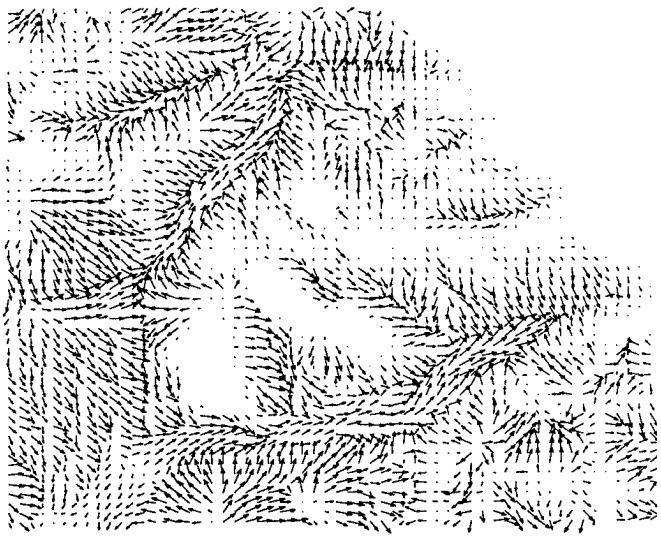


Figure 5: Airborne InSAR DEM flow directions. The arrow length is proportional to the surface slope.

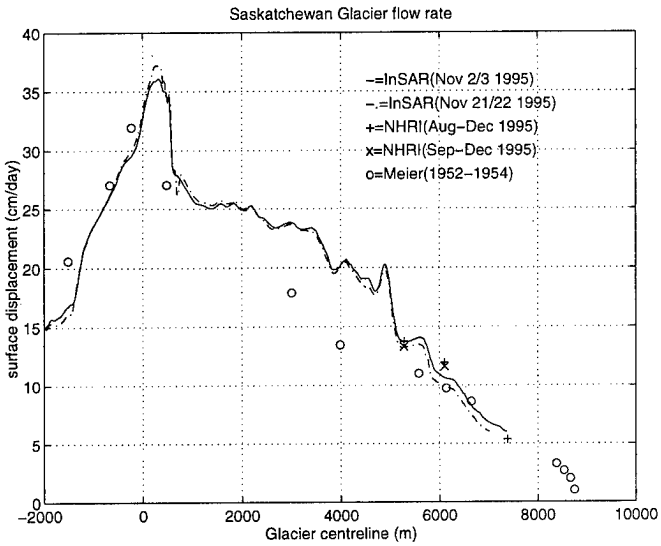


Figure 6: Displacement field validation.

and more recent point displacement measurements. The agreement between subsequent tandem mode image pairs is excellent and is consistent with both sets of surveying measurements.

CONCLUSIONS

It has been shown that spaceborne SAR interferometric image pairs collected with a 24 hour interval may be used to measure the surface displacement field of a typical mid-latitude alpine glacier. This result was validated against historical flow field measurements and more recent surveying measurements coincident with the image pair acquisition time frame. We measured peak flow rates close to 40 cm/day on the Saskatchewan Glacier and fine scale velocity structure with a repeatability on the order of 1 cm/day over a 19 day interval, suggesting that the measured small scale velocity structure is real. The principal limitation of this technique at our site was the loss of scene coherence, even over the 24 hour interval between subsequent passes. The technique appears to work best during winter when the potential of daytime melting is minimized.

ACKNOWLEDGMENTS

We thank ESA for providing the ERS data, and in particular Steve Coulson (ESA/ESRIN) for ensuring correct scheduling of our tandem mode data.

REFERENCES

[1] R.M. Goldstein, H. Englehardt, B. Kamb, and R.M. Frolich. Satellite radar interferometry for monitoring ice sheet motion: Application to an Antarctic ice stream. *Science*, 262:1525–1530, 1993.

[2] R. Kwok and M.A. Fahnestock. Ice sheet motion and topography from radar interferometry. *IEEE Trans. Geoscience Rem. Sens.*, 34(1):189–200, 1996.

[3] A.L. Gray, K.E. Mattar, and M.W.A. van der Kooij. Cross-track and along-track airborne inteferometric SAR at CCRS. In *Proc. 17th Canadian Symposium on Remote Sensing, 13–15 June 1995, Saskatoon, Saskatchewan, Canada*, pages 232–237, 1995.

[4] P.W. Vachon, D. Geudtner, A.L. Gray, and R. Touzi. ERS-1 synthetic aperture radar repeat-pass interferometry studies: Implications for RADARSAT. *Can. J. Rem. Sens.*, 21(4):441–454, 1995.

[5] D. Geudtner and M. Schwäbisch. An algorithm for precise reconstruction of InSAR imaging geometry: Application to "flat earth" phase removal, phase-to-height conversion, and geocoding of InSAR-derived DEMs. In *Proc. EUSAR'96, Königswinter, Germany*, 1996. In press.

[6] R.M. Goldstein, H.A. Zebker, and C.L. Werner. Satellite radar interferometry: Two-dimensional phase unwrapping. *Radio Science*, 23(4):713–720, 1988.

[7] M.F. Meier. Mode of flow of Saskatchewan Glacier Alberta, Canada. Professional Paper 351, 1960. U.S. Geological Survey, U.S. Government Printing Office, Washington, D.C.

Effects of System Errors on Combined MM/IR Neural Network Inversion of Surface Snow Properties

Sandy R. Jackson and Ram M. Narayanan

Department of Electrical Engineering and Center for Electro-Optics
University of Nebraska, Lincoln, NE 68588-0511, USA
T: 402.472.5141 F: 402.472.4732 EMail: eerdrmn@engvms.unl.edu

Abstract— The University of Nebraska has recently developed a neural network inversion algorithm for the estimation of surface snow properties, viz., surface roughness, wetness, and average grain size. The algorithm uses concurrent measurements of the near-infrared reflectance and millimeter-wave backscatter of the snow surface. The performance of the inversion algorithm was found to be satisfactory under noise-free conditions. However, under operational conditions, noise is invariably present in the data, and the addition of noise causes errors in estimation. The performance of the inversion algorithm was investigated under noise-added conditions. A parameter that was varied was the signal-to-noise ratio. Inversions of free-water content and the grain size were relatively robust, while the surface roughness estimation was very sensitive to added noise. The results of our study can be useful in setting bounds for system performance for accurate snow surface parameter inversion.

Introduction

We have recently developed a neural network inversion algorithm for the estimation of surface snow properties, viz., surface roughness, wetness, and average grain size, and tested the same using simulated data from existing models [1]. The algorithm uses concurrent measurements of the near-infrared reflectance and millimeter-wave backscatter of the snow surface. While near-infrared reflectance is strongly dependent on snow grain size and free-water content, millimeter-wave backscatter is primarily dependent on free-water content, and to some extent, on the surface roughness. By combining these measurements, the estimation of free-water content is improved considerably over a single sensor system, while simultaneously providing accurate estimates of grain size and surface roughness. Temporal and spatial monitoring of these surficial snow properties can shed light on the metamorphic state of the snow, and thereby provide clues to weathering and climatic processes.

ADDITION OF NOISE

The neural network inversion algorithm uses near-infrared reflectance at 1160 nm, 1260 nm, and 1360 nm wavelengths, as well as millimeter-wave co-polarized and cross-polarized backscatter at 95 GHz frequency. From these measurements, three ratios are formed, and these are used as inputs to the neural network. The ratios are designated as S_1, S_2, and D_R, and are given by:

$$S_1 = \frac{R(1160)}{R(1260)} \quad (1)$$

$$S_2 = \frac{R(1260)}{R(1360)} \quad (2)$$

$$D_R = \frac{\sigma_x^o}{\sigma_c^o} \quad (3)$$

In the above, $R(\lambda)$ is the near-infrared reflectance at a wavelength of λ nm, σ_c^o is the co-polarized backscatter at 95 GHz, and σ_x^o is the cross-polarized backscatter at 95 GHz. The use of reflectance or backscatter ratios is advantageous in remote sensing applications, since the need for absolute calibration can be avoided if one can assume the same atmospheric propagation characteristics at the two wavelengths or frequencies used in forming the ratio.

The outputs of the neural network are the snow wetness, snow surface roughness, and average snow grain size. The neural network was trained using the backpropagation algorithm, and tested using simulated data. Its performance under ideal, i.e., noise-free conditions, was found to be extremely satisfactory, and the RMS errors obtained were 0.2% for snow wetness, 0.86 mm for snow surface roughness, and 0.26 mm for average snow grain size. These values correspond to the case when the signal-to-noise ratio (SNR) is infinity. Full details of the neural network inversion algorithm and its performance in a noise-free environment are provided in [2].

Under operational conditions, an SNR value of infinity is seldom achieved. Noise is invariably present in the system, and its effect modifies the input to the network. It must be remembered that the weights and the bias values for the neural network are derived assuming noise-free conditions. In order to incorporate the effects of noise, we assume that each measurement (reflectance or backscatter) can be split into a noise-free component, and a component that includes the effects of noise. We write

$$v(n) = S(A + k) \quad (4)$$

where $v(n)$ is the n-th observation, S is the signal amplitude, A is the attenuation factor, and k is given by

$$k = \frac{\text{noise amplitude}}{\text{signal amplitude}} \quad (5)$$

The parameter k is determined according to the distribution of noise. We assume that the noise signal is a

0-7803-3068-4/96$5.00©1996 IEEE

zero-mean Gaussian distributed random variable whose variance can be related to the SNR.

The distribution of the noise signal v_n is given by

$$p(v_n) = \frac{1}{\sqrt{2\pi\psi^2}} \exp(-\frac{v_n^2}{2\psi^2}) \quad (6)$$

where ψ^2 is the noise variance. The relationship between SNR and ψ^2 is [3]

$$SNR = \frac{A^2}{2\psi^2} \quad (7)$$

Thus, for a given combination of A and ψ^2, the SNR can be computed. Alternately, for a given SNR, A or ψ^2 can be determined if the other is known.

RESULTS

The performance of the inversion algorithm was evaluated for values of SNR ranging from 0 dB (1) to 60 dB (1000), as well as under noise-free conditions, i.e, infinite SNR. A was kept constant at 1.0 and corresponding ψ^2 values were computed. From the known values of ψ^2, various realizations of the noise signal amplitude were obtained by sampling the normal distribution described in (6). After the noise-added data were generated for each measurement, appropriate ratios were formed to provide the inputs to the neural network.

For each output, the RMS error was computed between the assumed value of the parameter and the inverted (estimated) value of the same parameter, for different SNR values. These results are plotted in Figs. 1-3. Since large unacceptable errors occurred at SNR values between 0 and 20 dB, the RMS error is shown only for SNR values greater than 20 dB. As expected, the RMS errors are seen to decrease as SNR increases. The asymptotic straight line parallel to the X-axis in each plot shows the RMS error under infinite SNR.

Based on acceptable values of the RMS error for each snow parameter, one can deduce the minimum SNR required from the plots. Alternately, one can fix SNR and determine the maximum RMS error achieved for each snow parameter. We considered as acceptable, RMS errors of 0.3 mm for grain size, 2 mm for surface roughness, and 2% for snow wetness. From the plots, we determined that corresponding minimum SNR values were approximately 27 dB, 32 dB, and 29 dB respectively. Thus, an SNR value of greater than 32 dB provides acceptable errors in the surface snow parameter estimation using our neural network inversion algorithm.

CONCLUSIONS

Our study indicates that addition of noise degrades the neural network inversion of surface snow properties, and under low SNR conditions, these estimates may lose their utility. Such studies are useful in specifying sensor parameters for a meaningful estimation of geophysical properties. Further studies are required to determine the sensitivity of the inverted estimates to the SNR values of individual sensors. In the present study, it was assumed that all sensors possessed the same SNR value, which might not be a valid assumption in a multisensor system.

REFERENCES

[1] R.M.Narayanan, S.R.Jackson, and K.M.St.Germain, "Estimation of surface snow properties using combined near-infrared reflectance and millimeter-wave backscatter," Proc. CO-MEAS'95, Atlanta, GA, pp. 189-191, April 1995.

[2] S.R.Jackson, Inversion of Snow Parameters from Combined Millimeter-Wave Backscatter and Near-Infrared Reflectance Measurements, M.S. Thesis, University of Nebraska-Lincoln, Lincoln, NE, 1995.

[3] M.I.Skolnik, Introduction to Radar Systems, 2nd ed. New York: McGraw-Hill, 1980.

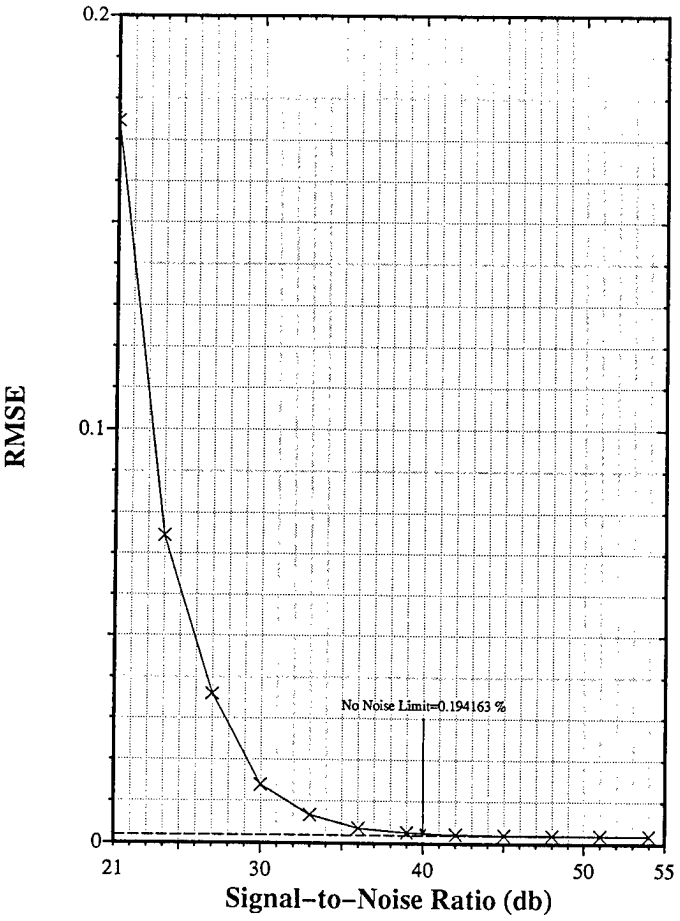


Figure 1: RMS error in snow wetness estimation vs. signal-to-noise ratio.

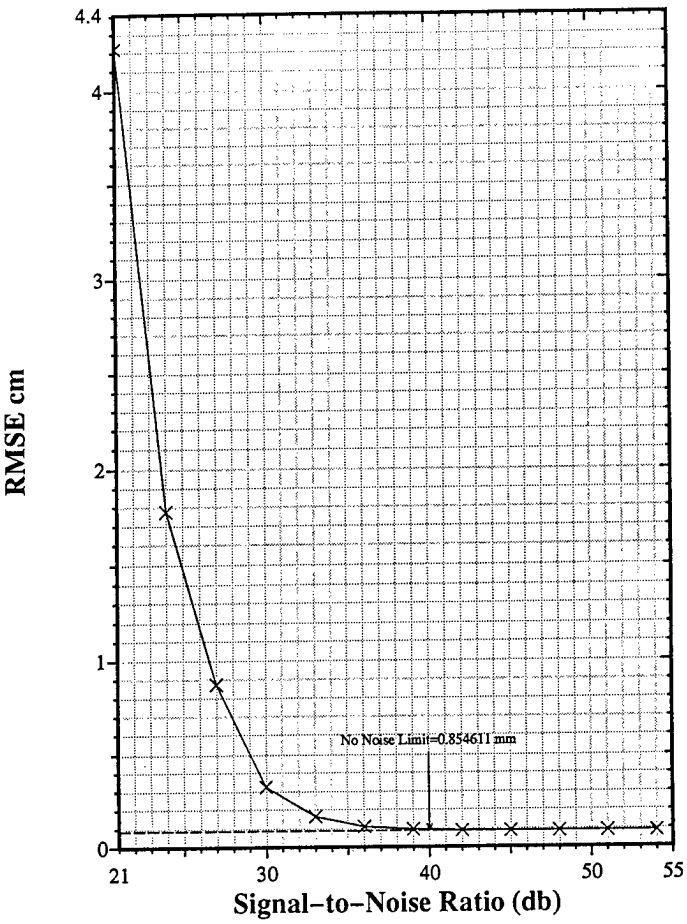


Figure 2: RMS error is snow surface roughness estimation vs. signal-to-noise ratio.

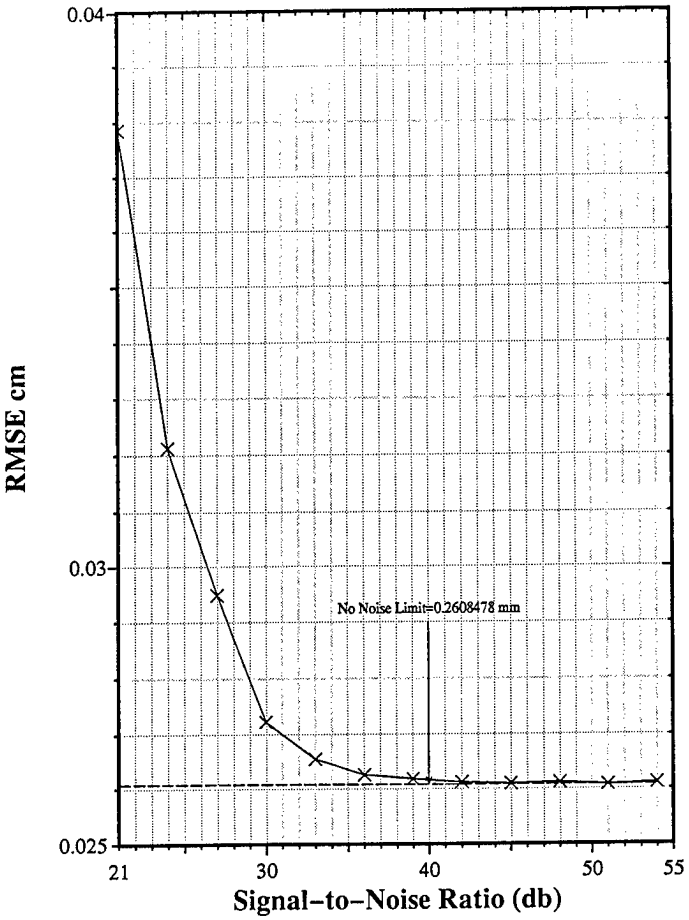


Figure 3: RMS error in snow grain size estimation vs. signal-to-noise ratio.

Machine-Based Snow Line Determination and the Identification of Ice Sheet Features in Visible and SAR Imagery

I-I Lin* (1) and W. G. Rees (2) *IEEE member
(1) Centre for Remote Imaging, Sensing and Processing, Block S6, Level 3, Faculty of Science, National University of Singapore, Lower Kent Ridge Road, SINGAPORE 119260 Tel: 65-7727908 Fax: 65-7757717 Email: crslinii@nus.sg
(2) Scott Polar Research Institute, University of Cambridge, Lensfield Road, Cambridge, CB2 1ER UK Tel: 44-1223-336559 Fax: 44-1223-336549 Email: wgr2@cam.ac.uk

0. ABSTRACT

This study contributes to the study of the glacier mass balance in two aspects. First, the possibility of automated (machine-based) determination of the snow line position in the visible imagery is assessed. A texture parameter, the fractal dimension, is found to be characteristic of snow/ice facies and will thus be especially useful in the development of automatic algorithms. Secondly, the identification of glaciological features in SAR imagery is validated against aerial photography.

Keywords: Mass balance, Automated snow line determination, Ice mass surface features.

1. INTRODUCTION

Monitoring of large terrestrial ice masses (ice sheets and ice caps) is crucial to the study of the global climate change. Regular, synoptic monitoring of these ice masses will provide a powerful tool for studying global climate change. The most important parameter to be monitored is the mass balance, which measures the difference between the annual input and output of ice. High resolution visible (e.g. LANDSAT MSS and TM) and radar (SAR) remote sensing images are most useful in identifying the glaciological features which are necessary for mass balance determination. These features include the position of the snow line and different snow/ice facies.

Currently, our understanding of visible imagery has reached a mature stage though the determination of the snow line position is still largely dependent on visual interpretation (Williams et al., 1991). The development of machine-based (automated or semi-automated) algorithms is highly desirable as human visual-manual interpretation is not efficient for routine monitoring over large areas. For example, the size of a remote sensing scene is typically 100km square. If the entire Antarctic ice sheet (1.39×10^7 km^2) is to be mapped, at least 1390 scenes are required. For terrestrial ice masses, this monitoring is required at least annually. Clearly the development of machine algorithms which can be substituted for human vision is highly desirable. This study investigates the possibility of developing the main image processing techniques, i.e. tone and texture analysis, into machine-based algorithms.

Due to the complex interaction between microwave radiation and ice surfaces, interpretation of SAR images is still at the research stage. We study one C band SAR scene taken by the JPL airSAR of the south-western part of the Greenland ice sheet. Different features are identified with the aid of aerial photographs and previous investigations of the same datasets by different researchers.

2. MACHINE BASED SNOW LINE DETERMINATION OF THE LANDSAT MSS IMAGERY

2.1 THE DEFINITION OF THE SNOW LINE

In general, a glacier can be divided into a number of zones on the basis of snow/ice density and wetness. From Paterson (1981), these zones include the dry snow zone, percolation zone, wet snow zone, superimposed ice zone, and ablation zone. The line between the wet snow and the superimposed ice zone is called the snow line. Its usual representation in visible imagery is the line which divides the high reflectance snow facies and the lower reflectance ice facies. By definition, the snow facies occurs only above the snow line while below the snow line, only the ice facies exits. However, due to the vast size of ice sheets and ice caps in comparison with glaciers, the idea of the snow line is more of a general threshold. Typically a 'melt zone', rather than a snow line, exits. Figure 1 gives a typical example of the situation. Visual observation of this LANDSAT MSS image of the Nordaustlandet ice cap, Svalbard, reveals three clearly distinguishable zones . Located at the central region, the first zone consists of areas of uniform snow facies (characteristic of its high reflectance and smooth visual texture). Towards the lower edge of this zone, a second zone which contains discontinuous patches of melt features (low reflectance) and wet snow (higher reflectance) is found. Below this second zone is a third zone, containing only continuous melt features (low reflectance features such as ice, water, lakes and streams) without any patches of wet snow. This observation is validated by aerial photographs (not presented) taken in the same season where discontinuous patches of wet snow and ice cover the edge of the ice cap. The determination of the snow line of a large ice mass can be subjective due to the occurrence of the second zone (i.e. the melt zone). For small glaciers, zone 2 does not exist and the snow line is a clear boundary between snow (zone 1) and ice (zone 3). For large ice masses, the position of the snow line can be at the upper or the lower boundary of the melt zone (e.g. Dowdeswell and Drewry, 1989) or anywhere within it.

0-7803-3068-4/96$5.00©1996 IEEE

2.2 DETERMINATION OF THE SNOW LINE POSITION

We select samples from all of the six possible classes that can occur in the three zones and assess the possibility of classifying them. These classes include firn, wet snow, small, medium, large degrees of melting, and ablation areas (figure 2). Firn samples are taken from the centre of the ice cap. Wet snow samples are located near the upper boundary of the melt zone; the three different degrees of melting classes are wtihin the melt zone, the degree of melting being determined from the proportion of the melt patterns within each sample. Ablation samples are from the region just below the lower boundary of the melt zone where no snow but only ice and water exist. Once the classes are classified, it is straightfoward to determine the snow line since it is the boundary between classes. If the snow line is chosen to be at the upper boundary of the melt zone, its location corresponds to the boundary between wet snow and small degree of melt classes. If it is located within the melt zone, differentiation between the three melt classes is required. The classification between large melt and ablation classes determines the snow line position at the lower boundary of the melt zone.

Tone and texture analyses are the two main approaches in image classification. We apply tone (mean value of the sample) and three different texture techniques, first order statistics (calculation of the normalised standard deviation), the Power Law Semi-Variogram (PSV) (Lin, unpublished 1995), and the Grey Level Coocurrence Matrix (GLCM) (Haralick et al, 1973). It is found that none of the techniques is able to discriminate between classes. An algorithm which combines all the techniques is proposed (figure 3). This algorithm can classify most of the classes except between medium and large degrees of melting. This algorithm is thus capable of automatically locating the snow line position at both boundaries of the melt zone. It can also partially locate the position within the melt zone.

2.3 THE CHARACTERISTIC FRACTAL DIMENSION

In the PSV analysis, we discovered that the parameter Fractal Dimension (FAD) is strongly characteristic of image classes. The FAD value of the firn and wet snow classes is found to be around 3.0; the value of the three melt classes is within the range of 2.3 and 2.6 while in the ablation class it has a value in the range between 2.6 and 2.8. Similar results are also found in other MSS images acquired at different times and with different calibrations (Lin, unpublished 1995). None of the other investigated techniques, however, possess this degree of invariance. Such invariance is especially important in automatic algorithms as the FAD is only dependent on the snow/ice properties (Rignot and Kwok, 1993). Different images can thus be processed together without any other preprocessing or supervision.

3. IDENTIFICATION OF ICE SHEET FEATURES IN THE SAR IMAGERY

The investigated SAR scene is shown in figure 4a. An overlapping aerial photograph (figures 4b) is used to identify the image features. The main features include residual wet snow collected in topographical depressions, ice facies, melt stream systems and lakes. The large, dark shapes such as the 'arrow' (figure 4a) are believed to be topographic patterns as they are also apparent in the SEASAT scene which was acquired more than 10 years earlier (Jezek et al., 1993). Residual wet snow and water are the two possible constituents of these areas because they appear to be dark in the SAR scene. Residual wet snow is a more likely possibility because these areas are found to have a bright tone in the L and P band scenes of the same area (Lin, unpublished 1995). If these areas contain water, a dark tone should also be found in the L and P band imagery. The 'arrow' shape is not clearly delineated in the aerial photograph (figure 4b) though patterns like ridges can be seen. The fact that it is so clearly apparent in the SAR scene may be because C band is very sensitive to the wet snow collected in this area which results in the clear dark arrow patch.

The bright patches in figure 4a are interpreted as ice. This response is believed to be due to scattering from the rough ice surface as the roughness scale of the ice is comparable to the C band wavelength. Jezek et al. (1993) find a high HH/VV co-polar ratio from this area which implies that surface scattering is dominant, which in turn implies that the surface cannot be drier snow. In addition, the bright tone eliminates the possibility of it being wet snow. Fahnestock et al. (1993) and Rees et al. (1995) report consistent findings that ice facies are bright in C band imagery as a result of roughness possibly associated with crevassing and melt water channels. Comparing with the overlapping aerial photograph, although the two images are taken in different years (July 1985 for the aerial photograph and end August 1989 for the airSAR scene), it is likely that the ice sheet underwent similar mass balance processes (Bindschadler and Vornberger, 1992). A large area containing ice and crevasses is observed just a few kilometres downslope in the aerial photograph (figure 5). It is reasonable to predict that this ice region will progress upslope from July to the end of August when the SAR flew over this region.

Figures 4a and 4b show that melt stream systems can be identified clearly in both the SAR scene and the aerial photograph. Many of the streams are linked to lakes and surrounded by ice and wet snow.

The small (kilometre scale), 'tear drop' features scattered in the field are identified as frozen lakes (figure 4). These features often link with melt systems. At least two of them (lake 1 and 2) can be identified in both the SAR image and the aerial photograph. The backscatter responses of these features are between those of wet snow and ice. These lakes often show a dark strip along their northern edges. From the size, shape and visual texture, these features are likely to be the 'blister lakes' reported by Echelmeyer et al. (1991). The blister lakes are found along the snow line in west Greenland at the Jakobshavn drainage basin (elevation between 600m and 1450m). These lakes range from a few tens of square metres up to 10km^2 and are formed when the ice on the lakes is not totally removed during the summer; areas of open water form at their up-glacier ends which push the remaining ice cover down glacier.

5. ACKNOWLEDGEMENTS

We gratefully acknowledge the assistance of Dr. J A Dowdeswell and Dr. M R Drinkwater for providing the aerial photographs and the SAR data set.

6. REFERENCES

Dowdeswell J. A., and Drewry D., 1989 'The dynamics of Austfonna, Nordaustlandet, Svalbard: surface velocity,mass balance and subglacial melt water', Annals of Glaciology, vol.12, 37-45.

Echelmeyer K. et al., 1991 'Surficial glaciology of Jakobshavns Isbrae, West Greenland: Part 1. Surface morphology', Journal of Glaciology, vol.37, no.127, 368-382.

Fahnestock M. et al., 1993 'Greenland ice sheet surface properties and ice dynamics from ERS-1 SAR imagery' Science, vol.262, 1530-1534.

Haralick R. M. et al., 1973, 'Textural features for image classification', IEEE transactions of Syst., Man, Cybern., vol. SMC-3, 610-621.

Jezek K.C. et al., 1993, 'Analysis of synthetic aperture radar data collected over the southwestern Greenland ice sheet', Journal of Glaciology, vol.39, no.131.

Lin I., 1995 'Spatial texture of visible and radar imagery of terrestrial ice masses', unpublished PhD thesis, University of Cambridge, UK

Paterson W. S. B., 1981 'The physics of glaciers, 2nd edition', Pregamon Press.

Rees W.G. et al., 1995 'Analysis of ERS-1 synthetic aperture radar data from Nordaustlandet, Svalbard', International Journal of Remote Sensing, vol.16, 905-924.

Rignot E., and Kwok R., 1993 'Characterization of spatial statistics of distributed targets in SAR data', International Journal of Remote Sensing, vol.14, no.2, 345-363.

Williams R.S. Jr et al., 1991 'Analysis of glacier facies using satellite techniques', Journal of Glaciology, vol.37, no.125 120-128.

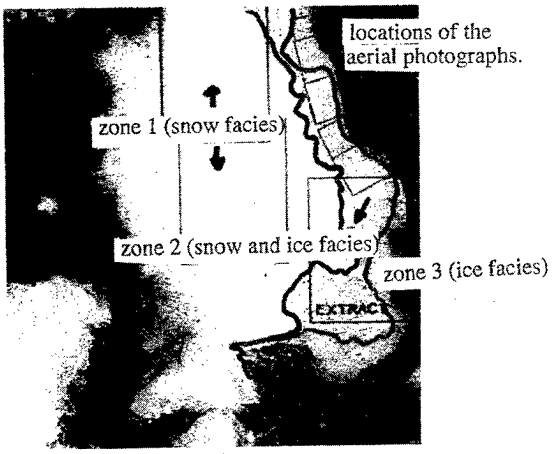


Figure 1: A LANDSAT MSS image of the Nordaustlandet ice cap, Svalbard taken on 1st August 1981. The locations of the aerial photographs used are also indicated. The samples studied are taken from extract 3.



Figure 2: Extract 3 of figure 1 where samples from six classe are taken.

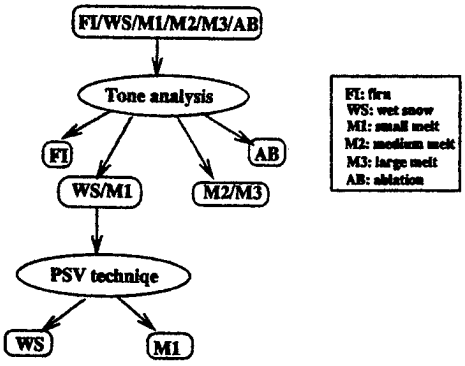


Figure 3: Proposed combined algorithm for classification.

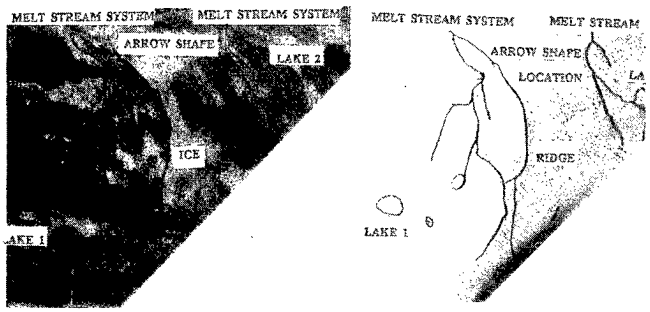


Figure 4: The studied airSAR scene (Left: 4a) and the overlapping aerial photograph (Right: 4b).

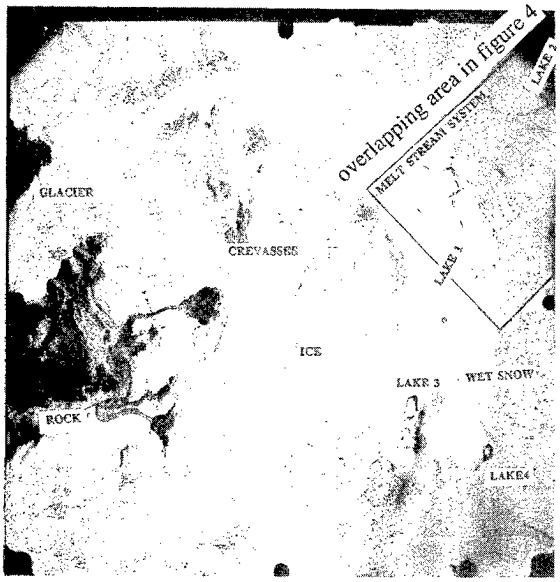


Figure 5: The full aerial photograph where figure 4b is taken from.

Thawing of Soils in Siberia Observed by the ERS-1 Scatterometer Between 1992 and 1995

Kai Boehnke and Volkmar R. Wismann

Institute for Applied Remote Sensing, Bahnhofstraße 54, 22880 Wedel, Germany
T: +49-4103-13922 F: +49-4103-7469 E: 100412.1731@compuserve.com

ABSTRACT

Based on multi-temporal radar backscatter measurements over Siberia, obtained from the ERS-1 scatterometer at various incidence angles, a method was developed for monitoring the state (frozen/thawed) of the upper layer of the soils. In spring and to some lesser extent in fall, the normalized radar cross section (NRCS) data show distinct variations which can be attributed to thawing and freezing soils.

In spring, during snow melt, the NRCS first decreases by up to 5 dB and shortly later, when the soils start thawing, increases dramatically. In autumn, the freezing of the soils is a more gradual process. Due to the huge extent of the Siberian test site, it takes more than three months for the entire region to be thawed. For the years 1992 to 1995, maps of the time period of thawing were constructed for the Siberian test site which reveal the geographical distribution and the interannual variability of the "onset of thawing". A first comparison with monthly SSM/I snow cover data and in situ air temperature data confirm the good behavior of the proposed technique.

INTRODUCTION

The C-band (5.3 GHz) scatterometer of the ERS-1 satellite operates at vertical polarization, both for transmission and reception (VV). Its incidence angle ranges from 18 to 57 degrees, the illuminated swath is 500 km wide, and the along-track and cross-track spatial resolution is 50 km [1]. The scatterometer measurements are independent of cloud coverage and illumination by the sun and, therefore, superior to measurements by optical systems. Compared to the synthetic aperture radar (SAR) aboard ERS-1, the scatterometer delivers a manageable amount of data albeit the global coverage within 3 to 4 days and a geometric resolution which is reasonable for many applications [2].

When the vegetation cover is sparse or absent, the normalized radar cross section (NRCS) at C-band, VV polarization, depends mainly on the moisture content of the soil, the dielectric constant, the penetration depth and the surface roughness. The radar backscatter increases with soil moisture and decreases with surface roughness. When liquid water in soil freezes, the dielectric constant of the soil falls dramatically. This process is reversed in spring when the soil thaws. Fig. 1 shows the dependence of the NRCS at 40°-57° incidence angle on the air temperature as measured at the weather station Kolpashevo. A step-like increase in NRCS of approx. 2 dB can be seen when the temperature exceeds 0°C.

Information on the state of the soils (frozen/thawed) is of great importance for climate modeling because evapo-transpiration and gas exchange processes change significantly when going from one state to the other. Also, practical applications (transportation, construction and oil/gas production) would benefit from near real-time estimates of the extent of frozen grounds.

SOIL STATE DETECTION

In this investigation, ERS-1 scatterometer data distributed on CD-ROM by CERSAT, the French Processing and Archiving Facility were used.

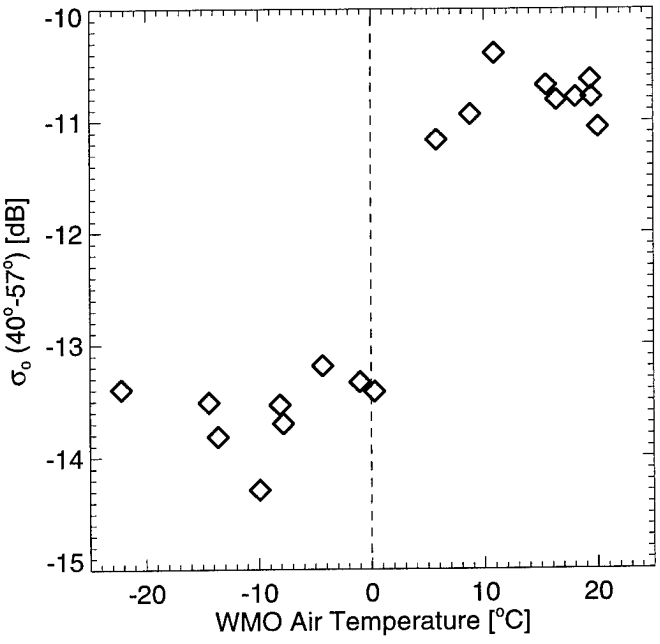


Fig. 1: NRCS(40°-57°) versus air temperature (monthly means) at the weather station Kolpashevo (58.2°N; 82.9°E).

This research was funded by the European Space Agency within the Earth Observation Preparatory Programme (EOPP) under ESTEC contract 11103/94/NL/CN.

0-7803-3068-4/96$5.00©1996 IEEE

Detecting the thawing of the soils requires two steps: First, the NRCS data are re-sampled to a grid with a resolution of 0.5° in latitude and 1° in longitude which corresponds roughly to the instrument resolution of 50 by 50 km. For three day intervals, an average radar cross section (NRCS-40) is computed for each grid point by linear regression between the measured NRCS and their respective incidence angles. NRCS-40 is the value of this regression line at an incidence angle of 40°. This procedure accounts for the incidence angle dependence of the NRCS which is highly variable in spring when the backscattering mechanism changes from volume to surface scattering depending on snow cover, snow wetness, soil moisture and penetration depth of the microwaves. Moreover, irregular distributions of NRCS measurements with respect to the incidence angle due to sampling and orbital characteristics have no influence on NRCS-40. Fig. 2 shows two typical time series of NRCS-40 for two grid points in Siberia (68.75° N; 79.5°E and 56.25°N; 62.5°E, respectively). Note the extreme stability of the signal in early spring and the large variations (>5 dB) associated with the onset of thawing.

The second step involves determining the monthly means for February and July of each year and finally, detecting the point of time of thawing. The latter is achieved by analyzing the NRCS-40 time series during the spring (for the time period March, 1 to July, 1) for the step-like increase seen in Fig. 1. A bin is marked as thawed when two consecutive NRCS-40 values exceed 50% of the difference between the monthly mean of NRCS-40 for July and February of the respective year. The constraint of requiring two values above the threshold eliminates spikes which are not removed when computing NRCS-40 and single events which are not connected to the thawing process.

In Fig. 2, for the grid point located in the North, the onset of thawing is detected at the beginning of June, whereas further South, the algorithm detects thawing at the beginning of April. During the melting of the snow cover and the thawing of the soil, the surface is covered by numerous shallow water ponds which are responsible for the drop in NRCS-40 seen in the time series of the northern grid point.

By applying the above described algorithm to the Siberian test site (50°-80°N; 42°-172°E) in 1994, a map of the temporal change of the state of the soils (frozen to thawed) has been constructed (Fig. 3). Each gray scale corresponds to a time step of 15 days. In general, thawing commences in the South and then progresses towards the North. Northern central Siberia is the last area to be thawed. On a regional scale, the onset of thawing follows orographic particulars. As expected, mountainous regions (e.g. Ural, Werchojansk, Stanowoi) thaw later than regions of lower elevation.

We are aware of the weakness of our definition of the point of time of thawing. The accuracy with which this point can be detected depends also on the temporal resolution of the in situ data and so far, only monthly mean values of air temperature have been available. Future evaluation of more detailed in situ data and SAR imagery will clarify this point. But as one can see from Fig. 2, any other definition of the point of time of thawing can only lead to a relative time shift of a few days.

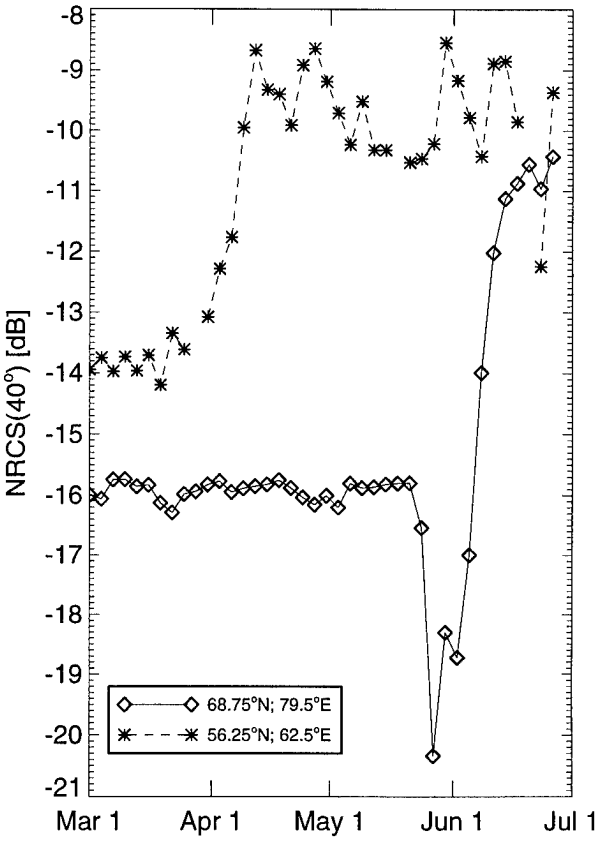


Fig. 2: Time series of NRCS-40 for two grid points in 1993.

INTERANNUAL VARIABILITY

For the years 1992 to 1995 maps of the point of time of thawing deduced from ERS-1 scatterometer data have been produced for a sub-region (55°-70°N; 50°-120°E) of the Siberian test site. For each time step, the area classified as thawed was calculated and is shown in Fig. 4(B). In 1993 and 1994, the area thawed gradually increases throughout the entire time period. Whereas in 1992, the onset of thawing is late, but then progresses much faster than in the other years. In 1995 thawing begins very early and by the end of April covers a large area. Then thawing slows down so that for all years, the entire region is thawed at approximately the same time. For comparison, a similar procedure is applied to SSM/I derived snow cover data (Fig. 4(A)). The curves show the area where the time-space averaged values (1° x 1°, 1 month) of snow cover [3] are below 50%. The interannual variations detected in the ERS-1 scatterometer data are recovered in the SSM/I data despite the coarse temporal resolution of 1 month.

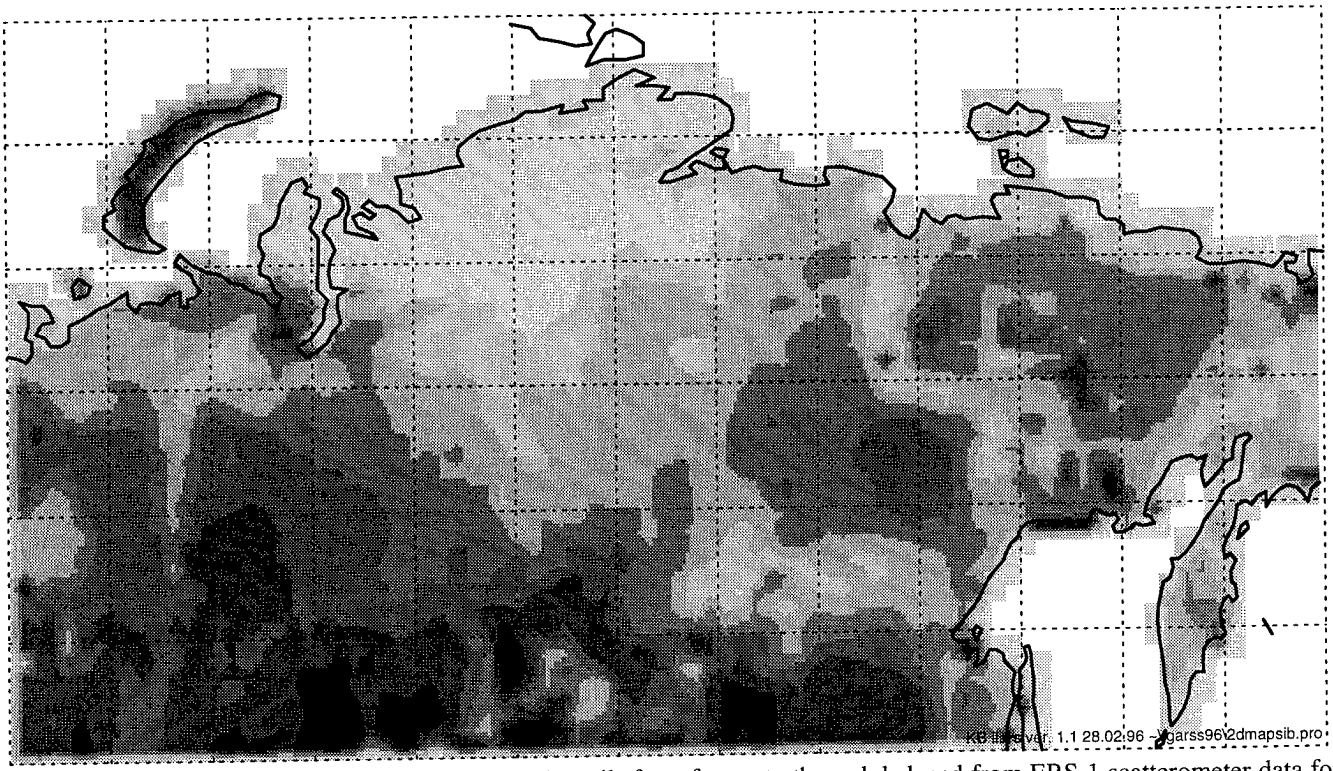


Fig. 3: Map of the temporal change of the state of the soils from frozen to thawed deduced from ERS-1 scatterometer data for the Siberian test site (50°-80°N; 42°-172°E) in 1994. The observation time period is March, 1 to July, 1. Each gray scale represents a time step of 15 days, i.e. regions in black have thawed before Mar., 15 and regions in the next lightest gray tone before Apr. 1 and so on. The spatial resolution is 0.5° in latitude and 1° in longitude.

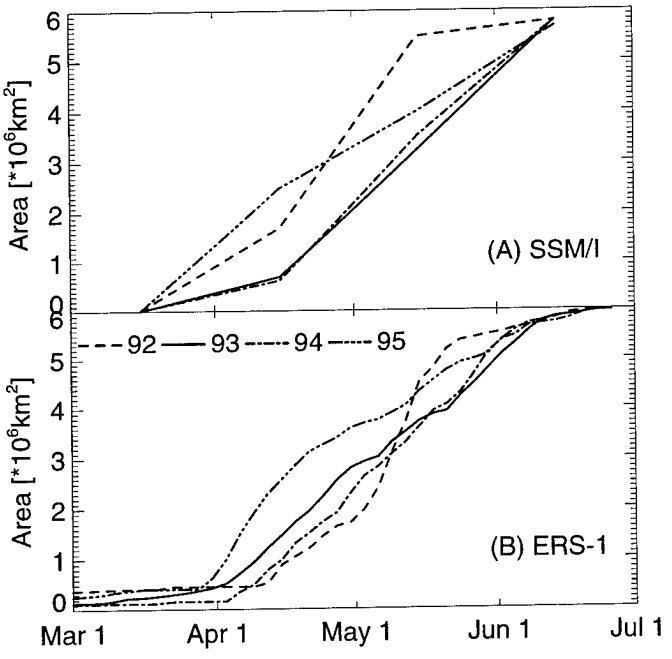


Fig. 4: Interannual variability of (A) the area with less than 50% snow cover deduced from SSM/I radiometer data [3] and (B) the area marked as thawed deduced from ERS-1 scatterometer data for the years 1992 to 1995.

CONCLUSION

A method has been developed for monitoring the state of the soils in arctic to temporate climate regions. It was demonstrated that the proposed algorithm reveals reasonable geographical distributions and temporal evolution of the thawing of the soils. The interannual variations detected in the scatterometer data agree well with those detected in SSM/I derived snow cover data and reported weather conditions.

An additional advantage of the proposed method is that with minor modifications, the algorithm detecting the time point of thawing is suitable for operational use and could make soil state information available in near real time. This would provide a good data basis for climate models which are very sensitive to changes in the evapotranspiration exchanges between the atmosphere and the ground which essentially depend on the soil state.

REFERENCES

[1] ESA, ERS-1 System, ESA Publications Division ESTEC Noordwijk, The Netherlands, ESA SP-1146, 87 pages, 1992.

[2] Wismann, V., A. Cavanie, D. Hoekman, I. Woodhouse, K. Boehnke and C. Schmullius, Land surface observations using the ERS-1 scatterometer, Report for the European Space Agency, 57 pages, Feb., 1996.

[3] Ferraro, R., Microwave Sensing Group, NOAA / Satellite Research Lab. Personal communication, 1995.

Passive Microwave Freeze/Thaw Classification For Wet Tundra Regions

E. J. Kim and A. W. England
University of Michigan
1301 Beal Ave., Ann Arbor, Michigan 48109-2122, USA
Telephone: 1-313-763-8162, Facsimile: 1-313-747-2106
email: ejk@eecs.umich.edu, england@eecs.umich.edu

Abstract -- Several climate change scenarios have predicted that the greatest changes would occur at high latitudes. In the arctic, long-term changes in temperature would be reflected, for example, in the growth or retreat of permafrost regions and in the response of the vegetation. Tundra-covered areas are a major terrestrial reservoir of carbon and changes in temperature and moisture will affect the storage and release of carbon by the tundra.

The most important annual hydrological events for tundra regions are the thaw in the spring and freeze-up in the fall. These regions are often cloud-covered for extended periods, especially during these key times of the year. A remote freeze/thaw classification technique based on microwave satellite measurements has the potential for providing more consistent observations compared with one based on visible observations. We begin by developing a classification technique from ground-based data (i.e., no intervening atmosphere) collected during our Radiobrightness Energy Balance Experiment 3 (REBEX 3) on the North Slope of Alaska from September, 1994 until September, 1995 [1].

Radiobrightness measurements were made at 19.35, 37.0, and 85.5 GHz using a tower-mounted Special Sensor Microwave/Imager (SSM/I) simulator. Co-located surface energy balance measurements included: thermal IR surface brightness, solar and net radiation, soil and snowpack temperatures, soil heat flux, sensible heat, latent heat, soil moisture, and other related meteorological variables. REBEX 3 was conducted in conjunction with other interdisciplinary experiments under the Arctic System Science (ARCSS) program of the U.S. National Science Foundation*.

Using the spectral gradient, changes in the spectral gradient on a diurnal time scale, polarization effects, and absolute radiobrightnesses, a technique for classifying tundra as snow-free frozen, snow-free thawed, or snow-covered will be described. Supporting measurements of subsurface temperature and moisture will be used to understand the physical basis for the differing radiobrightness signatures.

*Support was also provided by NASA and the U. S. Geological Survey.

0-7803-3068-4/96$5.00©1996 IEEE

INTRODUCTION

Satellite-based passive microwave detection of snow extent, snow parameter estimation, and freeze/thaw classification has been the subject of much previous research [2]-[4].

In this paper, we make use of "ideal" data from our Radiobrightness Energy Balance Experiment 3 (REBEX-3), that is, multi-frequency, multi-polarization, and multi-temporal passive microwave observations with no intervening atmosphere, in order to estimate data accuracy requirements for successful space-based classification algorithms for tundra regions. Tundra covers some 8 million square kilometers of the earth's land area, approximately equal to the area covered by temperate grasslands [5].

REBEX-3 FIELD DATA

Apparent ground brightness temperatures (T_B's), 19 GHz-to-37 GHz spectral gradients, the 37 GHz polarization difference, and surface physical temperatures for two portions of REBEX-3 are shown in fig. 1 (days 252-268) and fig. 2 (days 501-511). The period shown in fig. 1 includes three snow-free days (254-256) preceding the onset of winter snow accumulation on day 257. The period shown in fig. 2 includes several days with air temperatures below freezing (until day 508) which occurred after the disappearance of the winter snowpack at the site. A small amount of snow (< 5 cm) covered the site during days 505-507. Beginning with day 508, the tundra surface was snow-free and thawed except for nighttime refreezing between days 508 and 509.

The tussock tundra at the REBEX-3 site is representative of large areas of the North Slope of Alaska, and is comprised of sedges (grasses), mosses, and lichens overlying organic and mineral soil layers. Continuous permafrost underlies the entire region, and the active layer thickness (summertime thaw depth) is typically 40-80 cm. The uppermost portion of the active layer has a very low volume fill factor and is very dry unless heavy fog or rain is present or unless the pores are filled with wet snow. Thus, near-surface air temperature (Tair, in figs. 1d and 2d) is a good indicator of the snow-free tundra surface temperature.

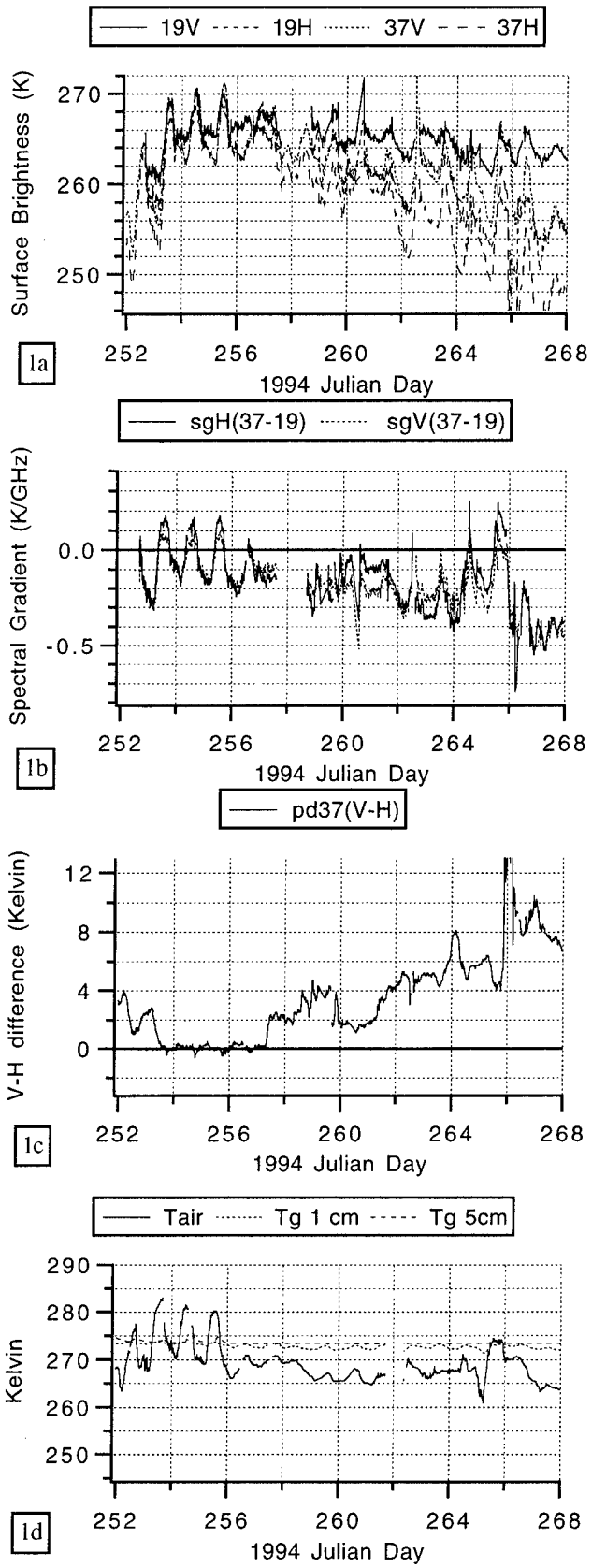


Fig. 1. Freeze-up and winter snow arrival.

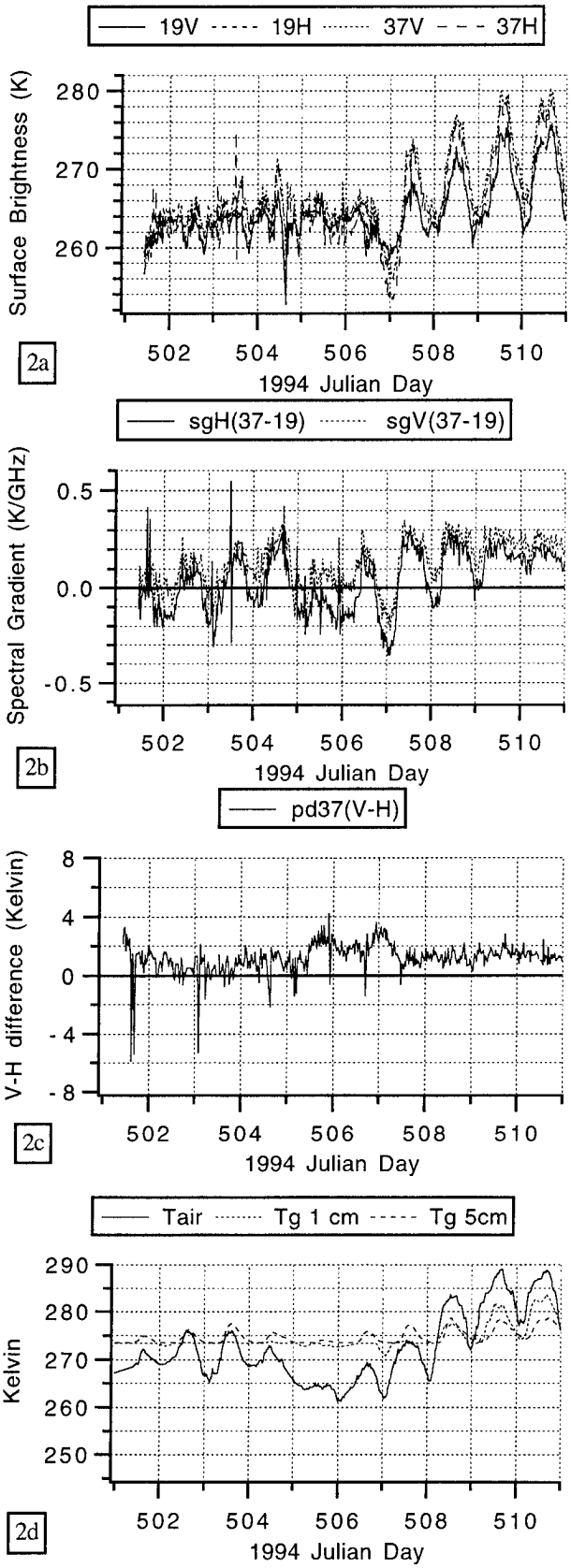


Fig. 2. Spring cold snap after thaw.

CLASSIFICATION

The 37 GHz V-H polarization difference (figs. 1c and 2c) clearly indicates the onset of winter snow accumulation at day 257.2, and the presence of snow on days 252-253 and from day 505.5 to 507.5. Snow-free periods are characterized by nearly constant low values near zero in the fall (fig. 1) and around 1 K in the spring (fig. 2). Increased values of 1.5 K or more above these indicate the presence of snow, with an increase of at least 2 K indicating the presence of at least 5 cm of snow.

The sensitivity of the 37 GHz polarization difference to the presence of snow can be explained as follows. Snow-free (frozen or thawed) tundra vegetation has an essentially unpolarized signature due to the isotropic geometry of tussocks and tussock vegetation. Snow, on the other hand, has been shown [6], [7] to have consistently greater V-polarized emission over a wide range of water equivalent values, snowpack thicknesses, and other parameters. Thus, the presence of even a few centimeters of snow is enough to polarize the signature from tundra.

Snow amounts are given here in terms of snow depth rather than water equivalent since the latter was not measured during REBEX-3. Tundra regions are generally classified as deserts based on total annual precipitation, and the non-melting snow is relatively dry.

Snow-free tundra which is thawed from the surface to a depth of at least 5 cm displays a positive spectral gradient of 0.2 K/GHz. Snow-free tundra which is frozen from the surface to a depth of at least 5 cm displays a near-zero or slightly negative spectral gradient of 0 to -0.2 K/GHz. When the upper 5 cm were partially thawed, an intermediate spectral gradient was observed. Snow-covered periods are characterized by negative spectral gradients in general, however, daytime warming can apparently increase the gradient to even positive values as seen on days 262, 264, and 265. These findings are consistent with those of [8] as reported in [3] with the possible exception of positive spectral gradient values when snow was present. If the polarization difference is used first to discriminate between snow-covered and snow-free periods, no ambiguities result.

As is the case for many space-based classification techniques, no correction of the apparent brightness temperatures was made for sky emission reflected from the surface.

CONCLUSIONS

Changes in the 37 GHz V-H polarization difference have been shown to indicate the presence or absence of snow in tussock tundra regions. To detect snow cover of 5 cm or less, a change in the polarization difference of 1.5 K must be detectable. If this level of precision is not available, then a classifier based on polarization difference can still be applied but the minimum detectable snowpack thickness increases. When used with polarization difference information, the 19.35 GHz-37 GHz spectral gradient can be used to further classify the snow-free tundra surface as frozen or thawed provided that a spectral gradient accuracy of at least 0.2 K/GHz (ΔT_B of 3.5 K) is available. A thawed tundra surface displays a positive spectral gradient of 0.2 K/GHz, and a snow-free frozen tundra surface displays a slightly negative spectral gradient of 0 to -0.2 K/GHz. A satellite-based classification must meet these accuracy requirements after any effects of spatial scaling and any atmospheric corrections.

The multi-temporal data make possible (1) the use of the 37 GHz polarization difference as a snow-detection discriminant by making a change from a constant "background" level visible, and (2) temporal averaging of the noisy observations (the data in figs. 1 and 2 are not averaged) in order to increase the percentage of correctly classified cases. The temporal coverage of major tundra-covered regions provided by polar-orbiting Special Sensor Microwave/Imager (SSM/I) instruments has good potential in this regard. Each makes typically four passes per day over points at the 68.8-degree latitude of the REBEX-3 site. The passes are clustered 12 hours apart, and there are currently three healthy SSM/I sensors in orbit with staggered overflight times.

REFERENCES

[1] E.J. Kim and A.W. England, "Field Data Report for Radiobrightness Energy Balance Experiment-3," Univ. of Michigan Radiation Lab. Report, RL-915, 1996.

[2] A.T.C. Chang, B.J. Choudhury, and P. Gloersen, "Microwave Brightness of Polar Firn as Measured by Nimbus 5 and 6 ESMR," J. Glaciol., vol. 25, pp. 85-91, 1980.

[3] F.T. Ulaby, R.K. Moore, and A.K. Fung, Microwave Remote Sensing: Active and Passive, vol. 3. Norwood: Artech House, 1986, pp. 1603-1634.

[4] B. Zuerndorfer, A.W. England, and F.T. Ulaby, "An Optimized Approach to Mapping Freezing Terrain with SMMR Data, " Proc. of IGARSS '90, May, 1990.

[5] W.H. Schlesinger, Biogeochemistry: an Analysis of Global Change, p. 135, Academic Press, 1991.

[6] A.K. Fung and H.J. Eom, "Emission from a Rayleigh Layer with Irregular Boundaries," J. Quant. Spectrosc. Radiat. Transfer, vol. 26, pp. 397-409, 1981.

[7] E. Schanda, C. Matzler, and K. Kunzi, "Microwave Remote Sensing of Snow Cover, Int. J. Remote Sensing," vol. 4, pp. 149-158, 1983.

[8] K. Kunzi, S. Patil, and H. Rott, "Snow-Cover Parameters Retrieved from Nimbus-7 Scanning Multichannel Microwave Radiometer (SMMR) Data," IEEE Trans. Geosci. Remote Sensing, GE-20, pp. 452-467, 1982.

Freeze/Thaw Classification for Prairie Soils Using SSM/I Radiobrightnesses

Jasmeet Judge, J.F. Galantowicz, A.W. England, and P. Dahl
Radiation Laboratory
3236, EECS Bldg., 1301, Beal Ave
Ann Arbor, MI 48109-2122, USA
T: (313) 763-8162 F: (313) 747-2106
Email: jasmeet@eecs.umich.edu

ABSTRACT

The state of soil moisture is an important variable in land surface processes. Moist soils can be classified as frozen or thawed using SSM/I radiobrightness signatures. Though the lowest frequency of SSM/I, 19.35 GHz, is above the Debye relaxation frequency of liquid water, the spectral gradient remains sensitive to the state of soil moisture. Frozen soil was classified as such by a negative 19.35 to 37 GHz or 19.35 to 85 GHz spectral gradient and a low 37 GHz radiobrightness.

INTRODUCTION

Weather and climate are affected by energy fluxes at the land-atmosphere interface. A significant fraction of these fluxes is the latent energy transfer through evaporation and transpiration, which is greatly diminished when moist soils freeze. Radiobrightness can be used to classify moist soils as frozen or thawed. Wegmüller et. al [5] have reported brightness signatures of freezing and thawing bare soils. Zuerndorfer et. al [7] have developed a freeze/thaw classification algorithm based upon radiobrightness data from the Nimbus 7 Scanning Multi-channel Microwave Radiometer (SMMR). Their discriminants were the 10.7 to 37 GHz spectral gradient and the 37 GHz radiobrightness. The spectral gradients of wet soils are positive because the SMMR frequencies lie just above the Debye relaxation frequency of liquid water, while the spectral gradients of frozen soils are negative because of volume scatter darkening in the more transparent frozen soils [6].

SMMR stopped collecting data in 1987. The current near-equivalent is the Defense Meteorological Satellite's Special Sensor Microwave Imager (SSM/I) [3], which has 19.35, 22.235, 37.0 and 85.5 GHz radiometers with dual polarizations at all frequencies except the 22.235 GHz water vapor channel. Though the SSM/I frequencies are well above the Debye relaxation frequency of liquid water, our models suggest that 19 to 37 GHz and 19 to 85 GHz spectral gradients should be sensitive to the state of moisture in the soil. In this paper, we demonstrate an SSM/I based classification of moist prairie soil and examine the sensitivity of this classification to atmospheric emission and absorption at the higher SSM/I frequencies.

Atmospheric oxygen and water vapor exhibit significant absorption and emission at SSM/I frequencies. Correcting for their effects require estimates of the temperature and water vapor profiles. We evaluated three potential correction techniques. The first was based upon rawinsonde data from the National Weather Service (NWS); the second was based upon the difference between 19 & 22 GHz V-polarized channels of SSM/I; and the third was a partial correction that included only the effects of oxygen.

For this study, we chose a 10^4 km^2 region near Sioux Falls, South Dakota (SD) as representative of northern prairie and selected resampled SSM/I data at 0100 UTC (7:00 pm CST) for four clear, snow-free days during October 1988 through January 1989.

FREEZE/THAW CLASSIFICATION

Figure 1 shows the freeze/thaw decision criteria for SMMR data [6]. We found that SSM/I derived 19 to 37 and 19 to 85 GHz spectral gradients are nearly as sensitive to the state of moisture as were the SMMR gradients (figures 2a and 2b). The spectral gradients between 19 & 37 GHz (figure 2b) form a tighter cluster than those between 19 & 85 GHz spectral gradients (figure 2a), because at 85 GHz very rough absorbing surfaces such as wet grass appear black or bright, and scattering surfaces such as dry and frozen canopies and soil are likely to be scatter-darkened. The result is greater variability in radiobrightnesses at 85 GHz.

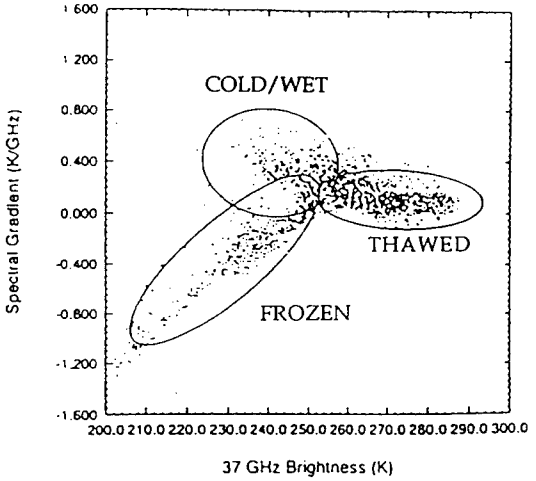


Figure 1: 10-37 GHz SMMR Spectral gradients for N. Dakota and the surrounding region. Cluster data at noon collected from August 1984 through December 1984 [6].

0-7803-3068-4/96$5.00©1996 IEEE

Using classification discriminants analogous to those used by Zuerndorfer et. al, we found that frozen soil is characterized by negative spectral gradients ($\partial T/\partial f<0$) and low 37 GHz brightnesses (<255K). Wet surfaces are characterized by positive spectral gradient and low 37 GHz brightness, while nearly neutral spectral gradients and high 37 GHz brightness correlate with warm, dry surfaces.

ATMOSPHERIC ABSORPTION AND EMISSION

SSM/I measures the apparent radiometric temperature, T_{ap} from above the atmosphere, where

$$T_{ap} = \frac{T_{terrain}}{L_a} + T_{up} . \quad (1)$$

This equation ignores the second order effects of reflected downwelling sky brightness. $T_{terrain}$ is the radiobrightness of the surface (the quantity we seek), L_a is the loss factor caused by absorption in the atmosphere, and T_{up} is the upwelling brightness from the atmosphere. The atmospheric gas absorption coefficient, κ_g, from which L_a and T_{up} are calculated [4], is

$$\kappa_g = \kappa_{O_2} + \kappa_{H_2O} \quad (2)$$

where κ_{H_2O} and κ_{O_2} are the absorption coefficients for water vapor and oxygen, respectively. Semi-empirical formulae for

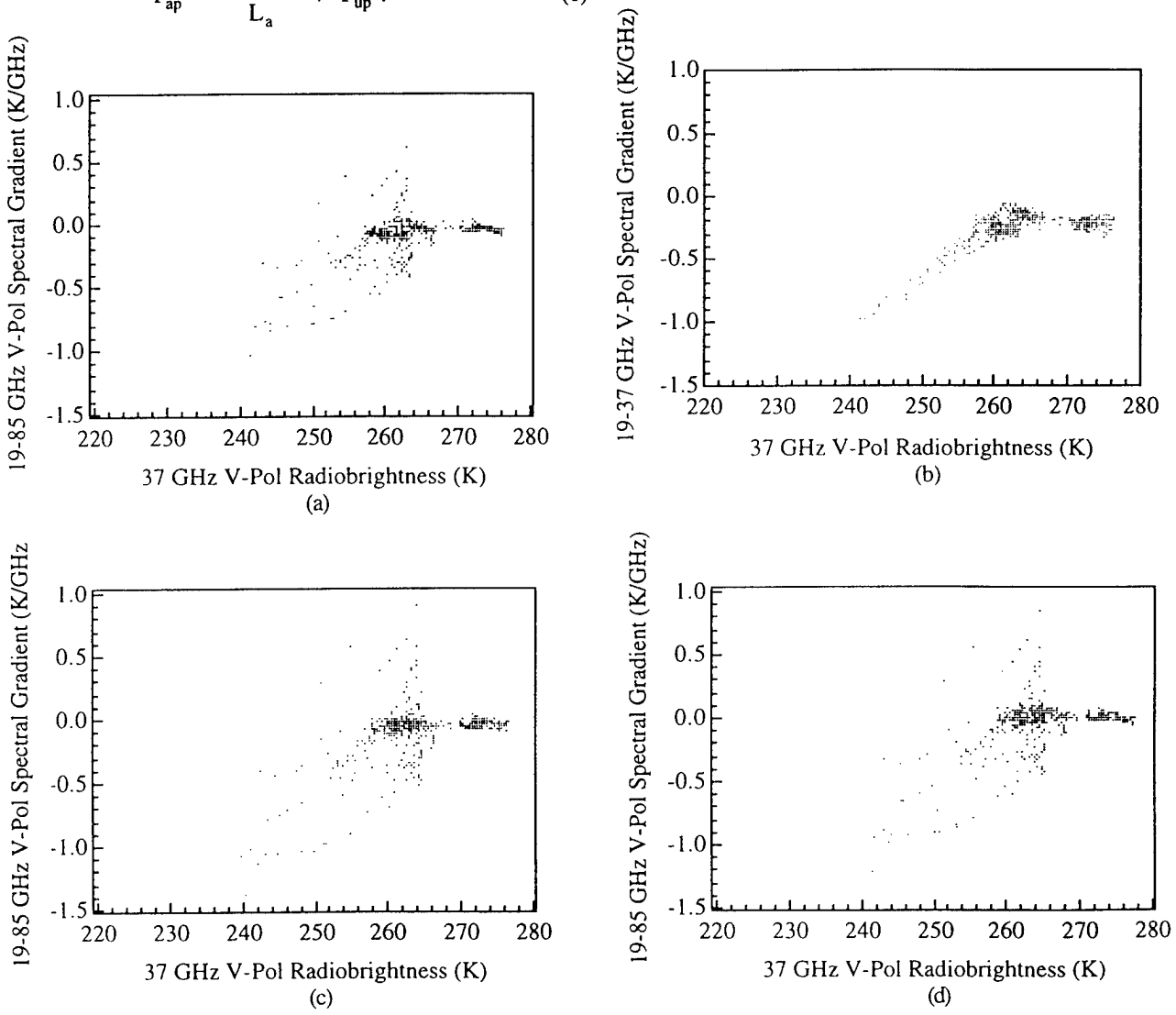


Figure 2: Cluster data from 14 October, 6 and 21 December 1988, and 27 January 1989 at 0100 UTC. (a) 19-85 GHz V-Pol Spectral gradients, and (b) 19-37 GHz V-Pol spectral gradients without atmospheric correction, (c) With atmospheric correction using rawinsonde profiles, and (d) With oxygen correction

the coefficients as functions of frequency, air temperature, pressure, and water vapor are given by Ulaby et. al [4].

Atmospheric corrections with rawinsonde data:

NWS measures atmospheric temperature, pressure and humidity profiles with rawinsondes near selected cities in the US. Huron, SD, one of the NWS cities, lies within our study area. Figure 2c shows the cluster data for spectral gradients derived from SSM/I brightnesses that have been corrected with Huron rawinsonde data. Though rawinsonde data promise the most reliable atmospheric correction, they are available only for a few cities in each state and only twice per day.

Atmospheric corrections using 19V and 22V GHz brightness:

Without a direct atmospheric measurement like those provided by rawinsondes, we must assume some attributes of the atmosphere, e.g., that it exhibits some characteristics of a US Standard Atmosphere (SA) [4]. We used the SA values for temperature lapse rate, surface pressure, and pressure & density scale heights. Surface temperatures were derived from local climatological data for the period of the study. With these assumption, only ρ_0, the surface water vapor density, is needed to compute an atmospheric correction. Since 22 GHz, the water vapor absorption line, is close to 19 GHz, we assume that terrain brightness is the same for both. Using equation (1), we obtain

$$\left[T_a(22V) - T_{up}(22V)\right] \times L_a(22V) - \left[T_a(19V) - T_{up}(19V)\right] \times L_a(19V) = \Delta_{22,19} \quad (3)$$

We seek a ρ_0 that minimizes $\Delta_{22,19}$. However, a simulation study [2] shows that the difference, $\Delta_{22,19}$, becomes insensitive to ρ_0 when $T_{terrain}$ is around 235K, i.e., when $T_{terrain}$ lies near the effective thermal temperature of the atmosphere. This second correction technique is the least effective among the three that we evaluated and its results were thought not worth showing.

Atmospheric corrections for oxygen:

Here we assume that $\rho_0 = 0$, so that the model becomes a dry Standard Atmosphere. While this is a partial correction, it is a reliable correction for the oxygen. Figure 2d shows the resulting spectral gradients.

The relative magnitudes of the oxygen corrections were about 0.25%, 2.5% and 4% of un-corrected SSM/I radiobrightness for 19.35, 37 and 85 GHz respectively, and the magnitudes of corrections using the rawinsonde data were approximately double the oxygen corrections. These values were too small to cause any significant changes in the freeze/thaw classification. The results might be different for times other than the 7:00 pm overflight times of these data, or for days with heavy clouds.

CONCLUSION

We demonstrate that SSM/I data can be used for freeze/thaw classification in northern prairie. The classification is not significantly sensitive to atmospheric absorption and emission for clear skies at the 7:00 pm, local overflight times.

ACKNOWLEDGMENT

This work has been supported by NASA Hydrology Program grant NAGW-3430.

REFERENCES

[1] A.W. England, "Radiobrightness of Diurnally heated, Freezing Soil," IEEE Trans. Geosc. Remote Sensing, GE-28, pp. 464-476, 1990.

[2] J. Galantowicz,, " Microwave Radiometry of Snow-covered Grasslands for the Estimation of Land-Atmosphere Energy and Moisture Fluxes," Ph.D. Dissertation, University of Michigan, September 1995.

[3] J. Hollinger, "DMSP Special Sensor Microwave/Imager Calibration/Validation ", Final Report Volume I, Naval Research Laboratory, 1989.

[4] F. T. Ulaby, R. K. Moore, and A. K. Fung, "Microwave Remote Sensing: Active and Passive," Vol. I, Addison Wesley, 1981.

[5] U. Wegmüller," The Effect of a Frozen Soil Layer on the Microwave Signatures of Bare Soil," Remote Sensing Environ., Vol. 33, pp. 123-135, 1990.

[6] B. Zuerndorfer, and A. W. England," Radiobrightness Decision Criteria for Freeze/Thaw Boundaries," IEEE Trans. Geosc. Remote Sensing, Vol. 30, No. 1, January 1992.

[7] B. W. Zuerndorfer, A. W. England, C. M. Dobson, and F. T. Ulaby," Mapping Freeze/Thaw Boundaries with SMMR data," Jour. of Agr. and Forest Meteor., Vol. 52, pp. 199-225, 1990.

Integrating Global Positioning Systems with Satellite Remote Sensing: Avoiding Major Pitfalls

Bryan C. Leavitt and Steven L. Payton
Center for Advanced Land Management and Information Technologies (CALMIT) University of Nebraska at Lincoln
113 Nebraska Hall, Lincoln, NE 68588-0517
Phone (402) 472-2565 Fax (402) 472-2410 Email: leavitt@tan.unl.edu payton@tan.unl.edu

Abstract -- Global positioning systems (GPS) have high potential for use with satellite remote sensing. However, there are a number of factors that may limit the suitability of GPS data for remote sensing purposes. Consideration must be given to hardware limitations, site characteristics, GPS operation parameters, satellite sensors used, and the user's needs.

Hardware considerations include power requirements, equipment specifications, the need for shelter, safety concerns, and various accessories that may be required. Site considerations are also important. It may be difficult to find or access a benchmark; trees and other tall objects will affect the quality of the GPS signals; equipment located at the site may be susceptible to damage or theft, and weather conditions such as snow or lightening may prevent or impede the acquisition of data. Major factors affecting GPS data include selective availability (SA), position dilution of precision (PDOP), signal to noise ratio (S/N), differential correction, accuracy of benchmarks, map accuracy standards, and techniques used in collecting the data. Satellite sensors determine the spatial resolution of the acquired image and this in turn defines the minimum acceptable accuracy of the GPS system. User's needs define data requirements, and usually require conversions between geodetic datums, and map projections.

Successful integration of these two technologies requires careful planning and attention to detail. It can result in better ground truth, faster acquisition of field data, and an improved final product. In this paper we have attempted to cover areas that can be major hurdles to the use of GPS in satellite remote sensing. It is based on our use of GPS data with Landsat and ERS-1 images.

INTRODUCTION

Global positioning systems (GPS) can be very useful for accurately determining the location of ground control points (GCPs) used in satellite remote sensing. GPS, if it is used correctly, can rapidly and accurately determine a location almost anywhere on earth and at most times of the day. For satellite remote sensing purposes the maximum allowable error for a positional fix is generally one-half the spatial resolution of the acquired image. For example, when working with an image that has a spatial resolution of 30 meters, the maximum error in locating a position should be no greater than 15 meters. In this paper we assume that the maximum acceptable error in the position of a given location will be in the range of 1 to 10 meters.

GPS systems vary in their accuracy from 100 meters to millimeters [4]. For most satellite remote sensing purposes a GPS system with an accuracy of 1 to 2 meters is sufficient. There is no guarantee that you will be able to attain this level of accuracy, to do so requires a thorough understanding of basic GPS principles and their proper application.

GPS PARAMETERS

The GPS satellite system consists of 21 satellites with three spares. In order to determine a position on the surface of the earth GPS receivers must monitor a number of satellites simultaneously. Two monitoring modes are available; 2-D and 3-D. In 2-D mode a minimum of three satellites are needed to obtain a positional fix, however this mode can be very inaccurate and is not recommended for most uses. Obtaining a positional fix in 3-D mode requires a minimum of four satellites but is much more accurate than the 2-D mode and should always be used.

The United States GPS satellites are operated by the Department of Defense. For security purposes the signal from these satellites is degraded by a process called selective availability (SA) [5]. SA limits the accuracy of a single GPS receiver to be within 100 meters of the actual location 95% of the time. Without SA a single GPS receiver will have an accuracy of approximately 20 meters. Obtaining a GPS position with an accuracy of less than 100 meters requires a process called differential correction. Differential correction is done using two GPS receivers. One receiver, called the base, is placed on a known location. A second receiver, called the rover, is then used to obtain fixes at the desired locations. It is extremely important to understand that the best differential corrections can only be done if both the base and the rover see the same satellites at the same time. In practice this limits the distance between the base and the rover, and means that the base station has a wider view of the sky and acquires data at a rate equal to or faster than the rover. For example if the rover is acquiring positional fixes at the rate of one every 5 seconds and the base station is acquiring fixes every 30 seconds then only 1 in 6 of the rover fixes can be corrected. Two types of differential processing can be done; real time and postprocessed. Real time differential processing requires a radio link between the base station and the rover. It allows the rover to compute a

0-7803-3068-4/96$5.00©1996 IEEE

corrected position immediately. Real time processing is necessary for navigating to a predetermined location. Postprocessing of GPS data means that correction of the data occurs later.

Advantages of real time correction include immediate corrected readings, assurance that the system is working, and little or no data storage requirements. Disadvantages include higher cost, more complex setup, and the rover and the base must remain with in sight of each other.

Advantages of postprocessed correction include simpler setup, lower cost, and no line of sight requirement between the base and rover. Disadvantages include large data storage requirement for the base, no assurance that the system is working properly, and corrected data is not immediately available.

The location of the base station must be very accurately known as any error in the base station coordinates will be incorporated into all differentially processed data. Coordinates obtained from a topographic map are generally not accurate enough to use for most satellite remote sensing purposes. One millimeter on a 1:24,000 United States Geological Survey (USGS) map equates to 24 meters of ground distance. National map accuracy standards require that objects be within 1/40 of an inch or 0.635 millimeters of their actual location on the map. This is greater than 15 meters of ground distance. We recommend that the base station be placed at a location whose position is known to within 1 meter. An index of such locations, many accurate to a few millimeters, is available from the National Geodetic Survey [1]. The fastest and least expensive to way to access this information is through the Internet at http://www.ngs.noaa.gov. The Internet site has a search engine that will enable you to find benchmarks by name, number, or location.

The location of the satellites across the sky forms a constellation and the design of this constellation affects GPS accuracy. Constellations where the satellites are spread throughout the sky allow higher accuracy than constellations where the satellites are close to each other. A unitless number, position dilution of precision (PDOP), describes the accuracy obtainable from the current constellation. A high PDOP indicates a poor constellation while a low PDOP indicates a good constellation. Readings should be 6 or less for most GPS work. Since the GPS satellites are constantly moving the PDOP changes during the day and will at times be higher than 6. High quality GPS receivers and software will allow the downloading of an almanac from the GPS satellite data stream. By using the almanac it is possible to predict in advance what the PDOP will be throughout the day at a given location. Use of this tool will enable you to better plan your field schedule and enable you to avoid using the GPS receiver when the PDOP is too high.

Several other factors can affect the accuracy of GPS signals [2]. Signal to noise ratio (S/N) is simply a measure of the strength of the radio signal from a satellite compared to the background noise. A (S/N) of 6 or higher is preferred. Most GPS receivers can be programmed to ignore a satellite whose (S/N) is below the minimum acceptable level.

Determination of a position on the surface involves taking multiple GPS fixes then differentially correcting the data and finally averaging the corrected points. The number of data points necessary to attain the defined level of system accuracy varies by system but 300 or more readings may be required. Such a high number of readings is usually not difficult as many GPS receivers can log data points as fast as once a second. New equipment and software can provide 1 meter accuracy in less than 5 minutes [3]. GPS rovers have a finite amount of memory for storing data points and there is usually a tradeoff between the number of data points taken and the amount of available storage space.

Accuracy should be checked during each field session. This can be done by taking the rover to one or more precision benchmarks and acquiring their position. For best results these benchmarks should be different from the one used by the base station. Accuracy is checked after differentially processing the data. The position of the benchmark as determined by GPS is compared to its actual position. Errors in the east/west and north/south directions as well as a root mean squared (RMS) value of the overall error should be determined. Error that is greater than the acceptable limit and higher than system specifications indicates a need to adjust procedures, GPS parameters, or both. Good procedures combined with correct GPS settings should yield accuracy close to system specifications.

HARDWARE REQUIREMENTS

Base stations generally require a computer which is used to run base station software and store received data. A laptop model is usually the best as it is lightweight, can take rough handling, and has low power requirements. The computer should be fast enough to log data every second and have adequate storage capacity to hold the received data. Base station files can easily consume megabytes of data storage each day.

GPS base stations and accessory equipment usually require 120 volt ac power. A small generator (1000 watts) is generally sufficient for this purpose. A number of factors dealing with the generator should be considered. Is the rated power of the generator adequate for the task? Is there any fire hazard associated with operating the generator at the site? Will rain or inclement weather damage the generator or create a hazardous condition? How long will the generator run before it needs to be refueled? The base station may be difficult to access and could be some distance from where the rover is being used. Refueling can significantly reduce the time available for data collection. The generator should not be allowed to run out of fuel.

Equipment may be damaged by power surges and data files can become corrupted by both surges and an abrupt loss of power. If power fails while the system is logging data into an open file, the file will almost certainly become unusable.

Shelter should be provided for the base station and associated equipment. The shelter will provide protection from the sun, moisture, wind, dirt, etc. as well as furnishing a convenient surface for the setup of equipment. A small enclosed trailer makes a good shelter. It can be used to help transport equipment to the desired site and is useful as a storage facility while in the field. For security purposes valuable items can be locked in or chained to the trailer.

Security is an issue that should not be overlooked. It is expensive to replace a GPS base station and support equipment. Large investments in planning, time, and resources could be lost due to theft or damage. High risk items can be chained together, and access to the inside of the trailer or other storage facility can be limited. Sites with a high theft potential should be avoided and it may be necessary for someone to stay at the base location.

SITE CONSIDERATIONS

Sites for GPS data acquisition should allow an unobstructed view of the sky. Locations with trees, buildings, or tall objects can cause multi-path reflections of the GPS signals degrading accuracy. Tree canopies can completely block GPS signals. Tall objects hide portions of the sky from the view of the receiving antenna increasing the PDOP and limiting the number of satellites that can be seen by the receiving system. Objects with a smooth surface such as lakes and roadways can cause ground-plane reflectances that also degrade accuracy.

For surveying purposes highly accurate benchmarks tend to be on points elevated above the surrounding terrain. These sites can provide a clear view of the sky but access may be difficult requiring a four-wheel drive vehicle. Setup of a GPS antenna on top of the benchmark means that the antenna is the tallest object in the immediate area making it a prime target for lightening. Since even a close lightening strike can damage or destroy the GPS receiver and associated equipment they should not be left out in a thunderstorm. To be completely safe from lightening equipment must be totally enclosed in a metal trailer or vehicle and have absolutely no connections to anything on the outside. A GPS receiver and its accessory equipment are not safe if they are inside a metal trailer but are connected to an antenna or generator that is on the outside.

OTHER CONSIDERATIONS

Rectification of satellite remotely sensed data requires the use of accurate maps. In the United States USGS 7.5 minute quadrangle maps are commonly used. Many, if not most, of these maps are based on the North American Datum of 1927 (NAD27). Data output from a GPS receiver normally uses a more recent datum such as the North American Datum of 1983 (NAD83). Conversion between datums is necessary. The authors have noted differences exceeding 200 meters between NAD27 and NAD83 coordinates. Software which comes with your GPS equipment must be capable of converting between any datums that are used.

A number of problems may be encountered by GPS users outside the United States. Many areas of the world lack an accurate spatial reference system making it difficult or impossible to pinpoint base station locations. High quality maps may be nonexistent or difficult to acquire. Equipment performance may be affected by environmental conditions especially in extreme climates.

SUMMARY

GPS can be an invaluable tool in remote sensing, however users should not expect this tool to perform adequately unless they are familiar with the equipment and throughly understand its use and function. We strongly recommend that users attempt several "dry runs" with the GPS before using it in a critical application. Practice runs can be done in the local area but should simulate actual field sessions as closely as possible. Postprocessing of data, if required, and accuracy checking should be included as part of the practice sessions as well as the actual GPS missions. Appropriate preparation cannot be over emphasized it will result in the saving of time, frustration, and expense.

REFERENCES

[1] B. Acharya, and R. Poop, "Project Planning for a GPS Geodetic Control Network," Surveying and Land Information Systems, vol. 54, pp. 69-75, 1994.

[2] C. Gilbert, "Sources of GPS Error What Can Be Fixed and What Cannot," Earth Observation Magazine, pp. 44-45, May 1995.

[3] R. Shrestha, M. Campbell, and A. Piazza, "A Global Positioning System Base Station and Session Length for 1-m Accuracy," Surveying and Land Information Systems, vol. 54, pp. 51-57, 1994.

[4] R. Shrestha, B. Dewitt, and M. Wilson, "Consideration and Effect of a Local Base Station Range in Horizontal Position Determination by GPS Techniques," Surveying and Land Information Systems, vol. 55, pp.39-49, 1995.

[5] T. Herring, "The Global Positioning System," Scientific American, pp. 44-50, February 1996.

Remote Sensing with Hyperspectral Imagery using DASI - An Imaging Interferometer

Philip D. Hammer
NASA Ames Research Center
Earth Science Div., m/s 242-4, Moffett Field CA 94035-1000
415-604-5897, Fax: 415-604-4680, hammer@gaia.arc.nasa.gov

David L. Peterson
NASA Ames Research Center
Earth Science Div., m/s 242-4, Moffett Field CA 94035-1000
415-604-5899, Fax: 415-604-4680, dpeterson@gaia.arc.nasa.gov

William H. Smith
Washington University
Dept. of Earth & Planetary Sciences, St. Louis MO 63130
314-935-5638, Fax: 314-935-7361, whsmith@dasi.wustl.edu

Stephen E. Dunagan
NASA Ames Research Center
Earth Science Div., m/s 242-4, Moffett Field CA 94035-1000
415-604-4560, Fax: 415-604-4680, Stephen_Dunagan@qmgate.arc.nasa.gov

Lee F. Johnson
Johnson Controls World Services Inc.
NASA Ames, m/s 242-4, Moffett Field CA 94035-1000
415-604-3331, Fax: 415-604-4680, Lee_Johnson@sggate.arc.nasa.gov

Anthony W. Strawa
NASA Ames Research Center
Earth Science Div., m/s 245-4, Moffett Field CA 94035-1000
415-604-3437, Fax: 415-604-3625, strawa@ames.arc.nasa.gov

Joe Zott and Gary Langford
Skywatch Information Systems Inc.
155 Moffett Park Dr., Sunnyvale CA 94089
408-541-7606, Fax: 415-328-6828, skywatch@crl.com

Abstract -- We describe an approach to terrestrial remote sensing using a novel technique, imaging interferometry. A practical implementation of the instrument, the Digital Array Scanned Interferometer (DASI), has been under development at our laboratories. An overview of recent terrestrial scenes measured using an airborne DASI sensor is presented.

INTRODUCTION

Hyperspectral imagery (spatial imagery with many contiguous spectral bands over an extended spectral range) is a promising yet underdeveloped remote sensing technique. Although the motivation for obtaining such high spectral resolution images to study the terrestrial environment has been high, imaging spectrometry is a relatively new field [1]. Progress on instrumentation and analysis techniques has occurred only recently with the advent of instruments such as AVIRIS (Airborne Visible/Infrared Imaging Spectrometer) [2]. These developments have been spurred by recent advances in solid state detector array technology, particularly for infrared detection.

The established imaging spectrometers to date have been based on spectral dispersion, using a grating or prism to achieve spectral resolution. They have tended to be large, complex, and expensive relative to standard imaging instruments and non-imaging spectrometers. These undesirable characteristics have stemmed from fundamental optical design constraints when consideration was made of performance requirements for spectral and spatial resolution and coverage,

Acknowledgments -- The airborne measurements were made possible by flight time granted to us by NASA's Office of Mission to Planet Earth. DASI instrument development was made possible with support from the NASA Ames Director's Discretionary Fund.

0-7803-3068-4/96$5.00©1996 IEEE

signal sensitivity, signal-to-noise, and calibration accuracy.

Because of the limitations of conventional sensor technologies there has been considerable motivation to develop new technologies to improve imaging spectrometer remote sensing capabilities and adaptability to surface, aircraft, and spacecraft platforms. NASA Ames and Washington University have been developing and applying a new instrument concept, the digital array scanned interferometer (DASI), for ground and airborne-based spectral imaging. The DASI achieves spectral discrimination using two-beam interference rather than dispersion. DASIs have many of the positive characteristics associated with Fourier transform spectrometers and also the capability for spatial imaging. Perhaps one of the most notable features of DASIs is their ability to acquire an entire interferogram simultaneously without any moving optical elements, enabling the observation of rapidly changing signals within the instrument's field-of-view. (This feature is analogous to push-broom type dispersion spectrometers that acquire all spectral components simultaneously). The compactness, simplicity of design and operation, and low cost of DASIs make them particularly suitable candidates for airborne and spaceborne platform based remote sensing instruments.

References [3] and [4] describe he basic concept of digital array scanned interferometry (DASI). The principle of DASI operation is similar to that of scanned interferometers. Detected signals result from two-beam interference. Spectra are obtained by Fourier transforming these recorded interferograms. Unlike conventional interferometers, the DASI operates with its optics fixed in position. Interferograms are resolved spatially in one dimension at the detector plane by a detector array. Spatial information is available in the orthogonal dimension. Two-dimensional spatial images are obtained by scanning over a scene in a push-broom manner.

RESULTS

During 1994 and 1995, observations were made using a nadir viewing DASI prototype sensor flown aboard the NASA C-130 aircraft. The characteristics of this sensor are given in Table 1. This sensor utilized a two-dimensional short-

Table 1 - DASI imaging spectrometer specifications

A. March 1994 C-130 flights

Instrument configuration	
Principle of operation	Imaging spectrometer based on interferometry: fringes are resolved spatially
Image acquisition	Push-broom (line-by-line)
Type of data	Spectral images (2 dimensional spatial with a spectrum associated with each pixel)
Detector	NICMOS short wavelength MCT 256 × 256 array, 4 Hz maximum frame rate
Size	Core optics: 30 cm length × 10 cm height × 10 cm width; Collector lens ϕ = 1 cm
Spectral characteristics	
Range	4550 - 9090 cm^{-1} (1.1 - 2.2 μm)
Resolution	266 cm^{-1} (60 nm at 6670 cm^{-1} or 1.5 μm (mid-band))
Bands	17 contiguous resolution elements (sampling interval is selected numerically)
Spatial characteristics	
Full field of view (FOV) cross track	7.7 degrees, 256 pixels
Single pixel IFOV cross track	0.03 degrees or 0.53 mrad
Cross track coverage / resolution	0.61 km / 2.4 m for typical flight altitude of 4.6 km
Long track coverage / resolution	3.1 km / 31 m for typical flight velocity of 124 m/s
Signal-to Noise	80:1 at peak spectral intensity

B. March 1995 C-130 flights

Instrument configuration - same as above	
Spectral characteristics	
Range	4550 - 12500 cm^{-1} (0.8 - 2.2 μm)
Resolution	250 cm^{-1} (36 nm at 8330 cm^{-1} or 1.2 μm (mid-band)) - double sided interferograms
	150 cm^{-1} (22 nm at 8330 cm^{-1} or 1.2 μm (mid-band)) - single sided interferograms
Bands	32 contiguous resolution elements (double sided), 53 (single sided)
Spatial characteristics	
Full field of view (FOV) cross track	25 degrees, 256 pixels
Single pixel IFOV cross track	0.1 degrees or 1.7 mrad
Cross track coverage / resolution	2 km / 8 m for typical flight altitude of 4.6 km
Long track coverage / resolution	5 km / 25 m for typical flight velocity of 100 m/s, 200 lines acquired
Signal-to Noise	Estimated 100:1 at peak spectral intensity

Table 2
Regions studied using DASI sensor from the NASA C-130 aircraft

Scene date and descriptions	scene size: cross track	along track
3/94		
Crow's Landing Airfield, San Joaquin Valley, CA	0.6 km	3.1 km
Miscellaneous agricultural fields, San Joaquin Valley, CA	0.6 km	3.1 km
Elkhorn Slough, (Pacific Ocean coastal area North of Monterey Bay, CA)	0.6 km	3.1 km
San Francisco Bay, Southern coastal regions	0.6 km, 0.2 km	3.1 km
9/95		
Mono Lake shoreline , East central CA	1.5 km	5 km
Stanislaus Forest, Western Sierra foothills, East central CA	2 km	5 km
Crow's Landing airfield, San Joaquin Valley, CA	2 km	5 km
Salinas Valley, East of Monterey Bay, CA	2 km	5 km
Moss Landing, (Pacific Ocean coastal area North of Monterey Bay, CA)	2 km	5 km
Fort Ord, (Pacific Ocean coastal area North of Monterey Bay, CA)	2 km	5 km
Jasper Ridge, East of Palo Alto, CA	2 km	5 km

wavelength infrared detector array and birefringent interferometer optics [5]. The images acquired were over selected coastal and inland regions of central California. Information about the specific sites that were studied are given in Table 2. Analysis of these images is underway for the study of land and coastal zone conditions and processes. The Mono Lake images are being used to assess the feasibility of a Mars orbiter mission to search for aqueous mineral deposits that may indicate past climate conditions supportive of life.

FUTURE PLANS

Currently, we have several DASI instruments under development that will have improved performance characteristics under a variety of observing objectives. Over the next year, several observation projects are planned. A compact near-IR DASI (0.8 - 2.5 μm) is being designed for use in small aircraft. A DASI using a CCD (Charge Coupled Device) detector array (0.4 - 1.0 μm) is under design for use with a UAV (Unpiloted Air Vehicle) as part of NASA's ERAST (Environmental Research Aircraft and Sensor Technology) program. Spectral images of aircraft contrails and surrounding atmosphere using ground-based DASI sensors are planned as part of NASA's SUCCESS (Subsonic Aircraft:Contrail and Cloud Effects Special Study) field experiment. The contrail studies will be analogous to a previous cirrus cloud study [6]. Development of Algorithms for processing and interpreting interferometric image data is also underway, including the implementation of an unusual noise isolation algorithm [7]. Reference [8] describes other considerations for the development of future DASI type sensors.

REFERENCES

[1] A. F. H. Goetz, G. Vane, J. E. Solomon, and B. N. Rock, "Imaging spectrometry for Earth remote sensing", Science, vol. 228, pp. 1147-1153, 1985.

[2] G. Vane, Editor, Imaging Spectroscopy II, Proc. SPIE, vol. 834, pp. 2-43, 1987.

[3] W. H. Smith, U. S. Pat. 4,976,542, 1990.

[4] W. H. Smith and W. V. Schempp, "Digital Array Scanned Interferometers", Exp. Astron.,vol. 1, pp. 389-405, 1991.

[5] P. D. Hammer, F.P.J. Valero, D. L. Peterson, and W. H. Smith, "An imaging interferometer for terrestrial remote sensing". In: Gregg Vane, Ed., Imaging Spectrometry of the Terrestrial Environment, Proc. SPIE vol. 1937, pp. 244-255, 1993.

[6] P. D. Hammer, F. P. J. Valero, and W. H. Smith, "Spectral imaging of clouds using a digital array scanned interferometer", Atmos. Res., vol. 34, pp. 347-366, 1994.

[7] P. D. Hammer, D. L. Peterson, and W. H. Smith. "Imaging interferometry for terrestrial remote sensing - digital array scanned interferometer instrument developments". In: M. R. Descour, J. M. Mooney, D. L. Perry, L. Illing (Eds.), Imaging Spectrometry. Proc., Society of Photo-Optical Instrumentation Engineers (SPIE), vol. 2480, pp. 153-164, 1995.

[8] W. H. Smith and P. D. Hammer, "Digital array scanned interferometer: sensors and results", Appl. Opt., in press.

Multi-Mission Radar Altimeter: Concept and Performance

J. Robert Jensen and R. Keith Raney
The Johns Hopkins University
Applied Physics Laboratory
Laurel, MD 20723-6099
Tel: (301) 953-5384 E-mail: Keith_Raney@jhuapl.edu Fax: (301) 953-5384

Abstract -- Satellite radar altimeters have proven to be a reliable source of data on sea surface elevation to the precision of several centimeters. Conventional instruments are limited to open ocean applications. This paper describes a new approach to radar altimetry that circumvents most of those limitations. The concept exploits unfocused SAR processing in the along-track direction, and monopulse techniques in the cross-track direction. The result is an instrument that is insensitive (to first order) to small angles of surface slope, is not confused by hill tops or other prominent terrain features, and has a sharper flat surface impulse response than conventional radar altimeters. Full Doppler integration and range curvature correction allow more independent looks than TOPEX, for example, while achieving a resolved footprint of about 250 meters, and requiring less radiated power. An instrument including real-rate on-board processing is described, suitable for a small satellite.

INTRODUCTION

The flat surface impulse response of the multi-mission radar altimeter has spatial characteristics that depart substantially from those of a conventional radar altimeter. The new instrument extends radar altimetry to applications in ice sheet monitoring and coastal studies while maintaining the height precision necessary for open oceans.

The Old Way

A conventional altimeter is essentially a "what-you-see-*first*-is-what-you-get" device. Only the minimum range reflections contribute to useful height estimation. At all other relative positions, the distance between a reflecting facet and the radar is larger, so that the observed round-trip pulse delay is larger. The later reflections combine to form a step-function response waveform [1]. Sea surface height, significant wave height, and mean wind speed are deduced from the measured range delay, the slope of the leading edge, and the mean power of the waveform. All space-borne radar altimeters to date are of this class [2,3].

Instruments that have been optimized for open ocean observations have several shortcomings when used over surfaces with less benign characteristics. Effective pulse-limited footprints, which may be on the order of 1-2 km in diameter over calm water, expand to several kilometers over rougher surfaces, and exhibit unwanted (and generally undetermined) sensitivity to terrain slope and topography if such features are illuminated anywhere within the antenna pattern. A prominent feature lying away from the sub-satellite point by several kilometers can dominate the return and corrupt the altimeter's response; in effect the measurement footprint hops from hilltop to hilltop. Even more troublesome, altimeter tracking usually is lost near coasts, either when approaching land from the open ocean, or conversely.

The New Way

The new APL concept combines delay/Doppler processing [4] in the along-track direction and phase-monopulse processing [5] in the cross-track direction to arrive at a radar altimeter that circumvents most of the disadvantages of existing radar altimeters.

Delay/Doppler processing converts the one-dimensional (time-delay) observation space of a conventional altimeter into a two-dimensional (time-delay/along-track) image space. The relative along-track viewing angle between the altimeter and each reflecting facet can be estimated through Doppler analysis of the reflections. The extra round-trip delay caused by viewing angle (Figure 1) can be calculated in Doppler space, and all delay estimates corrected accordingly. The altimeter along-track footprint size and position are determined by the radar timing and Doppler signal processing [6], not by the surface slope, roughness or height characteristics. The time-delay responses from all Doppler bins are detected and summed to form the output waveforms (Figure 2) accumulated for each along-track position as the spacecraft passes.

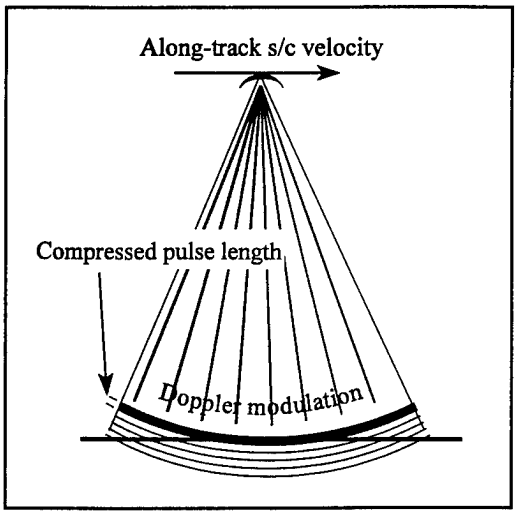


Figure 1. Doppler (along-track) geometry

0-7803-3068-4/96$5.00©1996 IEEE

Across-track, there is no Doppler or analogous modulation that might be exploited to constrain footprint location. However, lateral footprint displacement can be estimated if two separated receiving antennas are used, forming a monopulse configuration in the cross-track direction (Figure 3). The output of each receiver channel is processed as discussed above, and coherently compared. The observed phase difference is a direct measure of the cross-track displacement of the dominant scatterer. Thus, subject to angular constraints imposed by the radar antenna pattern, the altimeter's footprint location may be determined through combination of the Doppler along-track and monopulse cross-track observations, regardless of surface slope or topographic influence.

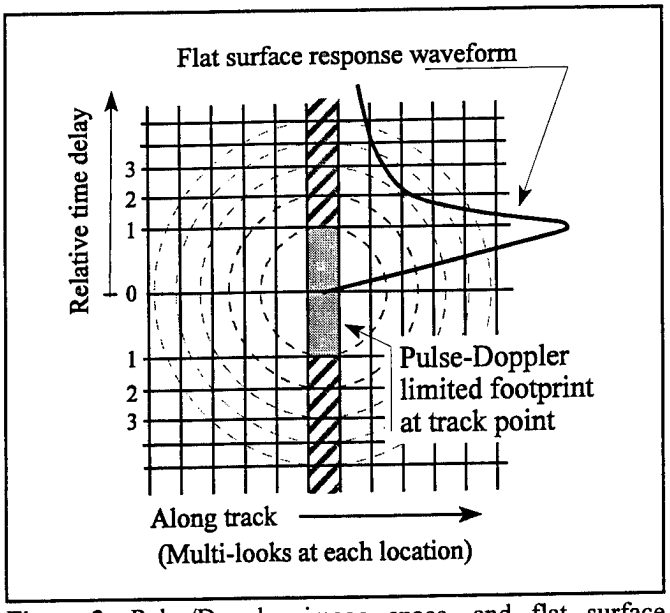


Figure 2. Pulse/Doppler image space, and flat surface response waveform footprint and power envelope

EXPECTED PERFORMANCE

Each of the altimeter waveforms derive from a narrow strip limited in along-track extent by the width of the Doppler frequency bin. After the initial response, at each delay time the waveform power is proportional to the area of the range-resolved cells that lie at progressively greater distance from the satellite. Over a quasi-flat surface the resolved range cells for the new altimeter have areas that decrease as the square root of time, unlike a conventional altimeter for which the range cells are equal-area annuli. Thus, the response waveform is a relatively sharp impulse in contrast to the flat step-function of a conventional instrument.

A typical number for along-track footprint size would be ~250 meters, with averaging of about 264 looks per 50 ms. (TOPEX [3] gets about 215 looks per 50 ms.) Along-track location of the zero-Doppler bin is determined by knowledge of spacecraft position along its orbit (the tolerance of which is smaller than the footprint size), and by knowledge of the vertical velocity component of the spacecraft.

Across-track footprint location depends on the monopulse phase angle measurement. The precision of this measurement will be limited by thermal noise, speckle noise, and knowledge of the spacecraft roll attitude. Thermal noise is independent in the two receiver channels. Speckle noise is largely correlated between the two channels but contains a small uncorrelated component. If the two antennas are about 1 meter apart and the wavelength is 2.2cm, angle precision of 0.01° is achievable with single-pulse signal-to-noise ratios in excess of 13 dB and coherent averaging of at least 14 pulses. These requirements are practical for a small satellite instrument. From an altitude of 800 km, an error of 0.01° in knowledge of roll angle would result in a height error of only 1.2 cm. Spacecraft attitude knowledge and the limitations imposed by thermal and speckle noise are consistent with a system capable of height measurements at the 1-2 cm level, and therefore are well suited to the multi-mission altimeter described in this paper.

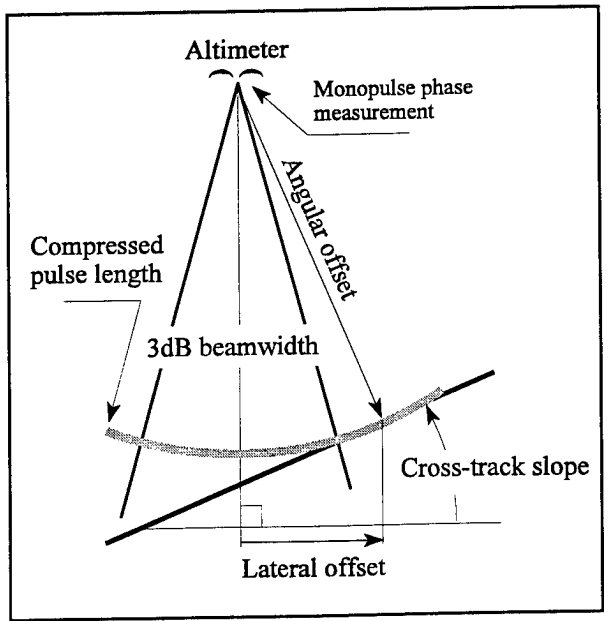


Figure 3. Cross-track monopulse phase measurement to deduce the lateral offset of the track point

It has been shown by simulation that the advantages of a pulse-limited range measurement are maintained over a wider range of surface slopes than is the case for a conventional altimeter. In the old way, the level plateau of the waveform and the distinct leading edge are lost as the surface slope exceeds half of the antenna beamwidth. For the new multi-mission altimeter, however, the sharp leading edge of the waveform is maintained. This contrast is illustrated in Figure 4, in which the surface slope equals three-quarters of the antenna beamwidth, but the sharp

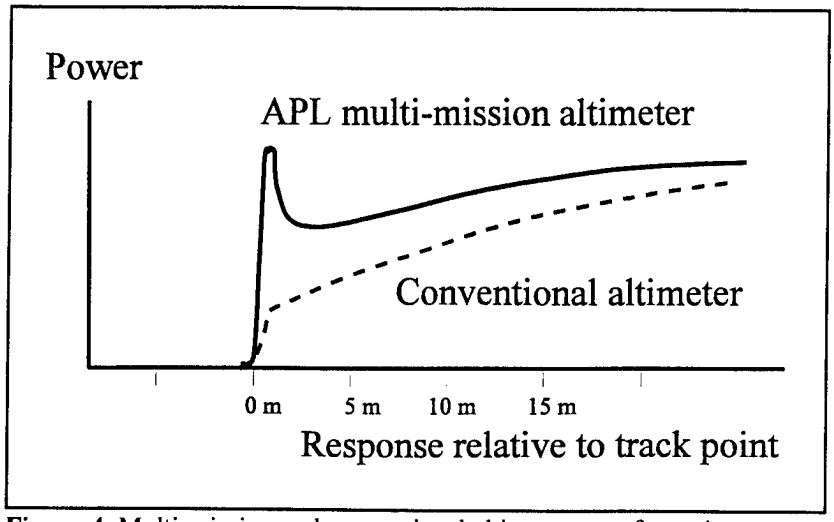


Figure 4. Multi-mission and conventional altimeter waveforms in response to a flat surface with cross track slope

leading edge of the waveform is preserved and accurate height tracking is still possible. Only when the surface slope approaches the full beamwidth does the distinctness of the measurement point become lost.

The delay/Doppler altimeter is able to isolate signals from the leading edge of the antenna pattern, since those signals occupy the highest observed Doppler frequencies. The delay of these returns indicates the relative elevation of the terrain over which the altimeter is to pass. The information would allow the range gate tracker to anticipate terrain elevation changes. Thus, this system is well suited to track terrain elevation variations that are substantially larger than those which have baffled conventional radar altimeters. For example, there is at present no satisfactory altimetric data record for the margins of the Greenland ice cap [6,7]. The advantage of predictive range gate tracking, combined with its narrow impulse response, suggests that a delay/Doppler radar altimeter should provide useful science data even over ice sheet margins.

CONCLUSION

The delay/Doppler and monopulse configurations were conceived in response to the need for better altimetric techniques for ice sheet monitoring [4,5]. The resulting altimeter has several new and appealing characteristics. It will support the same open ocean precision as TOPEX, if comparable orbit determination and path length corrections are available [3]. There are further advantages. Its small footprint would allow exploration of small gravity field anomalies (frontier oil exploration and sub-surface topographic studies). The unique delay/Doppler sharp response function reduces wave height estimation errors in the presence of propagation anomolies, such as attenuation from tropical rain cells. The waveform width and weight should have a first order dependence on significant wave height and wind-driven surface roughness, respectively, with better responsiveness than conventional altimetry.

Instrument reponse is only part of the challenge. Requirements on orbit choice, maintenance, and knowledge depend on the intended application. Path length delay estimation and compensation may require radiometers, and/or the use of two altimeter frequencies. Nevertheless, the instrument outlined in this paper opens new possibilities for a true multi-mission altimeter that could be responsive to needs of marine science and climatology as well as ice sheet monitoring.

REFERENCES

[1] Moore, R. K., and C. S. Williams, Jr., Radar Terrain Return at Near-Vertical Incidence, *Proceedings of the IRE*, Vol. 45, Feb 1957, pp. 228-238.

[2] McArthur, J. L., C. C. Kilgus, C. A. Twigg, and P. V. K. Brown, Evolution of the Satellite Radar Altimeter, *The Johns Hopkins APL Technical Digest*, Vol. 10, No. 4, 1989, pp. 405-413.

[3] Marth, P. C., J. R. Jensen, C. C. Kilgus, J. A. Perschy, J. L. MacArthur, D. W. Hancock III, G. S. Hayne, C. L. Purdy, L. C. Rossi, and C. J. Koblinsky, Prelaunch Performance of the NASA TOPEX/POSEIDON Altimeter, *IEEE Transactions on Geoscience and Remote Sensing*, Vol. 31, March 1993, pp. 315-332.

[4] Raney, R. K., A Delay/Doppler Radar Altimeter for Ice Sheet Monitoring, Proceedings IEEE Geoscience and Remote Sensig Symposium IGARSS'95, Florence, Italy, July 1995, pp. 862-864.

[5] Jensen, J. R., Design and Performance Analysis of a Phase-Monopulse Radar Altimeter for Continental Ice-Sheet Measurement, *Ibid.* , pp. 865-867.

[6] Thomas, R. H., B. A. Bindschadler, R. L. Cameron, F. D. Carsey, B. Holt, T. J. Hughes, C. W. M. Swithinbauk, I. M. Whillans, and H. J. Zwally, *Satellite Remote Sensing for Ice Sheet Research*, NASA Tech. Memo 86233, 1985.

[7] Zwally, H. J., J. A. Major, A. C. Brenner, and R. A. Bindschadler, Ice Measurements by Geosat Radar Altimetry, *Johns Hopkins APL Technical Digest*, Vol. 8, No. 2, 1987, pp 251-254.

[8] Brown, G. S., The Average Impulse Response of a Rough Surface and its Applications, *IEEE Trans. on Antennas and Propagation*, AP-25, No. 1, 1977, pp. 67-74.

Backscatter Characteristics of Buried Targets Measured Using an Ultrawideband Polarimetric Random Noise Radar

Paul D. Hoffmeyer, Yi Xu, Ram M. Narayanan, and John O. Curtis*

Department of Electrical Engineering and Center for Electro-Optics
University of Nebraska, Lincoln, NE 68588-0511, USA
T: 402.472.5141 F: 402.472.4732 EMail: eerdrmn@engvms.unl.edu

*U. S. Army Corps of Engineers, Waterways Experiment Station
Environmental Engineering Division
3909 Halls Ferry Road, Vicksburg, MS 39180-6199, USA
T: 601.634.2855 F: 601.634.2732 EMail: curtisj@ex1.wes.army.mil

Abstract—The University of Nebraska has developed a unique ultrawideband polarimetric random noise radar for subsurface probing applications. The radar system was used to measure the backscatter characteristics of buried metallic as well as non-metallic objects which primarily mimicked the sizes and shapes of land mines. These objects were buried in a specially designed sand box at different depths and relative orientations. The data collected on a variety of targets are expected to be useful in developing target detection and discrimination algorithms using this novel radar system.

INTRODUCTION

The need for non-destructive ground probing systems is increasing [1]. These systems must have high image resolution in order to determine exactly what lies below the surface. One way to accomplish this is to use a Ground Penetrating Radar (GPR) system. There are several modulation techniques used in GPR systems. A Short Pulse radar gives extremely high depth resolution through the use of a narrow transmit pulse. This is accomplished at the expense of high peak power requirements and wide bandwidth antennas. Another method is Frequency-Modulated Continuous Wave (FM/CW). This system does not have the peak power requirements of the Short Pulse radar but there is a stringent requirement on the linearity of the sweep signal to prevent resolution degradation. The noise modulation technique is promising due to the ease with which the correlation operation can be performed and its immunity from hostile detection. This is the basis for the design described in the next section.

SYSTEM DESCRIPTION AND TEST SETUP

A block diagram of the system is shown in Fig. 1 [2]. The noise source produces a signal having a Gaussian amplitude distribution and a constant power spectral density in the 1-2 GHz frequency range. The average output power of the noise source is 0 dBm. This signal is divided into two in-phase components by a 3 dB power divider with a 1 dB insertion loss. One component is fed to an amplifier with a gain of 34 dB. This amplifier has a power output of greater than +40 dBm at its 1-dB gain compression point. The average power output of the amplifier is +30 dBm (1 W), and can amplify noise spikes that are as high as 10 dB above the mean noise power. The output of this amplifier is connected to either the V or H polarization input on the dual-polarized broad band log-periodic transmit antenna. This antenna has a constant gain of 7.5 dB over the frequency range, and a cross-polar isolation of greater than 20 dB.

The second component is connected to a combination of a fixed and a digitally controlled variable delay line. The fixed delay line serves to ensure that the correlation operation is performed such as to avoid antenna-to-antenna direct coupling. The variable delay provides the delay of the transmit signal in order to correlate it with the received signal from objects or interfaces at that depth corresponding to that delay. The delay line can be programmed for delays from 0 to 19.968 nsec in 0.156 nsec steps. This step size will ensure the vertical resolution required of the system. The output of the delay line is then mixed with a 160 MHz signal from a phase lock oscillator. This is done in order to perform coherent processing of the received noise signals. The output from this mixer is the lower sideband in the 0.84-1.84 GHz range. The coherent noise signal is amplified by a 19 dB amplifier and then this signal is divided by a 3 dB power divider into the co-polarized and cross-polarized receive channels. The co-polarized and cross-polarized receive channels are constructed with identical components. The co-polarized channel corresponds to the channel connected to the same antenna polarization as the transmit antenna. The cross-polarized channel is orthogonal to the transmit antenna polarization. The received noise signal is amplified by a 20 dB low noise amplifier and then mixed with the coherent noise signal. The output of the mixer is passed through a bandpass filter with a center frequency of 160 MHz and a bandwidth of 5 MHz. This signal is divided by a 3 dB power divider. One output goes to a logarithmic amplifier with a 70 dB dynamic range. This ensures that a wide range of scattered power levels can be processed. The sec-

The partial support of this work by the U.S. Army Corps of Engineers, Waterways Experiment Station under Contract #DACA39-93-K-0031 is gratefully acknowledged.

0-7803-3068-4/96$5.00©1996 IEEE

The original 160 MHz phase lock oscillator signal is the second input to the I/Q detector. Since frequency translation preserves phase differences, the I and Q outputs can be related to the polarimetric co-polarized or cross-polarized scattering characteristics of the buried object or interface.

The system was used to gather data from an assortment of different buried objects in a specially designed sand box. The dimensions of the sand box are 3.5 m long, 1.5 m wide and 1 m deep. Metallic as well as non-metallic objects were buried at different depths and orientations. The radar antennas were scanned over the surface as data was collected continuously.

TEST RESULTS

The following images where obtained using the polarimetric random noise radar. Each figure contains four images from one radar scan over various buried objects. The top image is the co-polarized received power output. The second image is the cross-polarized received power output. The third image is the depolarization ratio, and the fourth image is the absolute phase difference between the co-polarized and the cross-polarized received channels.

Fig. 2 shows the image pertaining to two metal plates, each 23 cm in diameter and 2 cm in thickness, buried 23 cm below the surface with a 15-cm separation between the two. The co-polarized and depolarization ratio images clearly show and resolve these two objects.

Fig. 3 is the image obtained from the same metal plates (as in Fig. 2) but each plate buried at different depths. The first was buried 23 cm below the surface and the second was buried at 8 cm depth. Spacing between the plates was retained at 15 cm. Again the co-polarized and depolarization ratio images not only clearly show these objects, but are also able to resolve them.

Fig. 4 shows the image pertaining to a metal plate (same size and shape as above) and an identical wooden plate. Both plates were buried at a depth of 23 cm below the surface. In this image, it is easy to detect the metal plate, but the wooden plate becomes obscured by the high surface reflection. Further data processing using the phase information may make this object more visible, and one such technique based on Stokes matrix processing is discussed in [3]

Fig. 5 shows the image of a 6-cm diameter metal pipe which was buried 29 cm below the surface. The transmit polarization was parallel to the pipe's axis, while the scan direction was perpendicular to the pipe's axis. Under these conditions, the pipe acts as a point target with low interaction time with the radar during its scan. Again the co-polarized and depolarization ratio images clearly show the pipe, and the familiar hyperbolic curve shape is observed.

CONCLUSIONS

From the images shown, it is easy to conclude that the metallic objects are fairly easy to locate with the polarimetric random noise radar. Objects other than metal, such as the wooden plate are much harder to discern from the raw data, and additional processing may be required in order to enhance detection. The initial large reflection from the surface also obscures objects just below the surface. Further signal processing may also be used to overcome this drawback. More study into the processing techniques is needed to improve the performance of this unique radar system.

REFERENCES

[1] D.J. Daniels, D.J. Gunton, and H.F. Scott, "Introduction to subsurface radar," IEE Proceedings Part F, vol. 135, pp. 278-320, August 1988.

[2] R.M. Narayanan, Y.Xu, P.D. Hoffmeyer, and J.O.Curtis, "Design and performance of a polarimetric random noise radar for detection of shallow buried targets," Proc. SPIE Conf. on Detection Technologies for Mines and Minelike Targets, Orlando, FL, pp. 20-30, April 1995.

[3] Y.Xu, P.D.Hoffmeyer, R.M.Narayanan, and J.O.Curtis, "Signal processing aspects of polarimetric random noise radar data for shallow subsurface imaging," Proc. IGARSS'96, Lincoln, NE, May 1996.

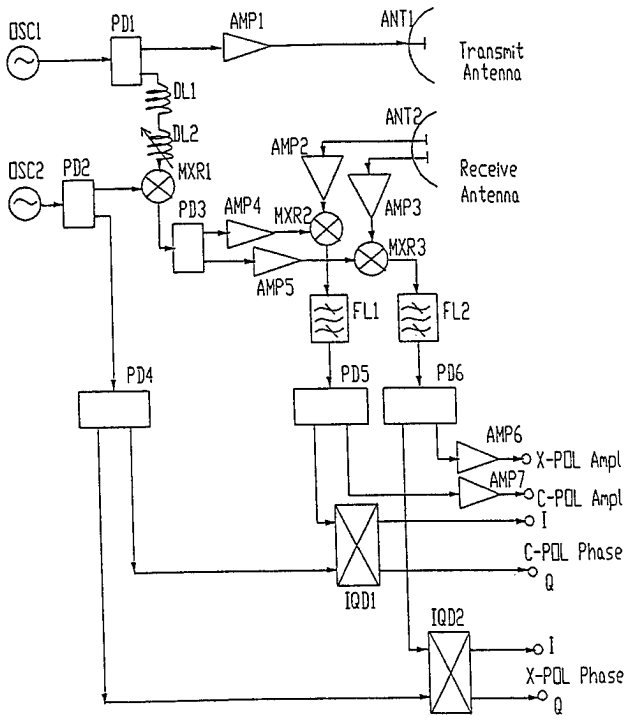


Figure 1: Block diagram of the polarimetric random noise radar.

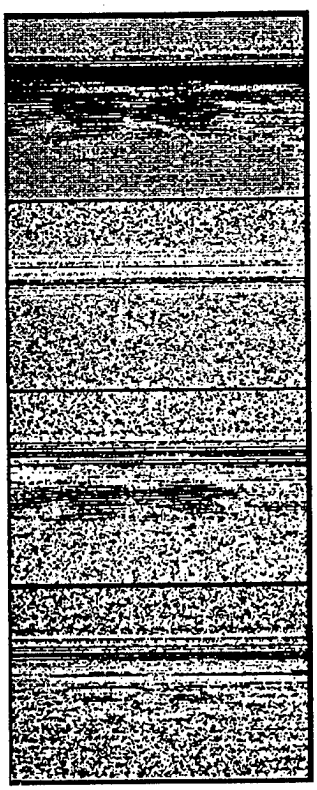


Figure 2: Radar image of two metal plate buried at the same depth.

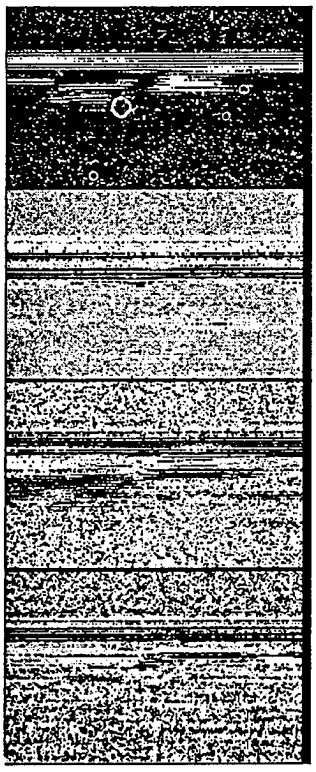


Figure 3: Radar image of two metal plates buried at different depths.

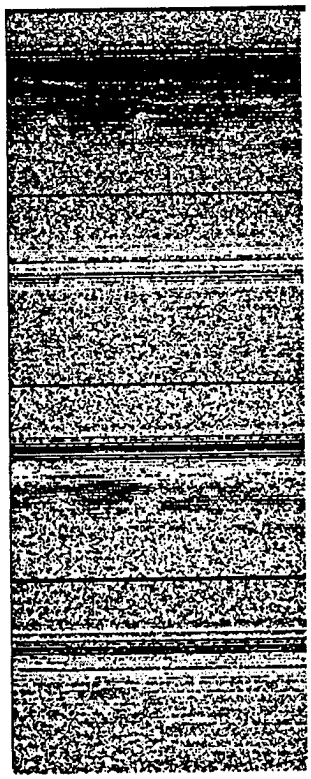


Figure 4: Radar image of a metal plate and a wooden plate buried at the same depth.

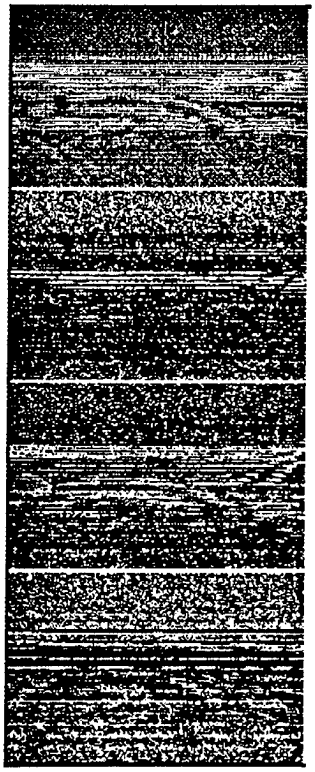


Figure 5: Radar image of a metal pipe with axis parallel to transmit polarization and perpendicular to scan axis.

Airborne 14-Channel Microwave Radiometer HUTRAD

Martti Hallikainen, Martti Kemppinen, Kimmo Rautiainen, Jörgen Pihlflyckt,
Janne Lahtinen, Tomi Tirri, Ilkka Mononen, Tuomo Auer
Laboratory of Space Technology, Helsinki University of Technology
Otakaari 5 A, 02150 Espoo, Finland
Telephone +358-0-451 2371, Fax +358-0-451 2898, E-mail Hallikainen@ava.hut.fi

Abstract -- Our airborne multifrequency microwave radiometer system HUTRAD (**H**elsinki **U**niversity of **T**echnology **RAD**iometer) is described. The system consists of a non-imaging subsystem and an imaging subsystem. The non-imaging subsystem operates at six frequencies between 6.8 and 94 GHz, with vertically and horizontally polarized channels at each frequency. Its main technical characteristics are close to those of the ESA MIMR (Multi-frequency Imaging Microwave Radiometer) instrument. The imaging subsystem operates at 93 GHz and is dual-polarized. HUTRAD is accommodated onboard the Helsinki University of Technology research aircraft Shorts Skyvan.

INTRODUCTION

The ESA near-future radiometer system MIMR will operate at 6.8, 10.65, 18.7, 23.8, 36.5, and 89 GHz. All receivers are dual-polarized.

In order to fully utilize satellite data, the geophysical algorithms have to be available before the launch of the satellite. Most algorithms developed so far for microwave radiometer applications are empirical or semi-empirical: they rely on experimental data sets collected under controlled conditions. Consequently, dual-polarized data in the range of 6.8 to 89 GHz is needed for MIMR algorithm development. HUT Laboratory of Space Technology acquired in 1994 a Shorts Skyvan aircraft and modified it into a research aircraft that allows several sensors to be flown simultaneously [1]. The main sensor is our multifrequency microwave radiometer system that has been gradually expanded into a MIMR-simulator.

DESIGN GOALS

The HUTRAD system was designed to meet the following requirements (motivation given in brackets):

- The main technical parameters, including frequency, polarization, and incidence angle, are identical to those of the ESA near-future MIMR instrument (algorithm development for MIMR)
- The main measurement parameters, including integration time, can be programmatically changed (flexible use of radiometer)
- The receivers are modular (easy service)
- Temperature stabilization of the radiometer is good (eliminates output drift)
- The receivers tolerate external interference (airborne measurements in populated areas)
- A reliable calibration method is used (correct brightness temperatures)
- The data storage system is flexible (good storage capacity and easy data handling)
- A data localization system is included (airborne and surface data can be reliably combined)
- For imaging channels, the platform's angular motion is compensated for (nondistorted image)
- Upgrading of suitable channels into polarimetric ones is possible.

SENSOR PLATFORM

HUT acquired in 1994 a Short Skyvan twin-engine turboprop aircraft. It is equipped with a relatively large (1.5 m by 1.9 m) rear cargo door and a large cabin (cross-section 2 m by 2 m), which make it ideal for remote sensing instrument installation. The aircraft is certified to operate under FAR 23 airworthiness regulations, making the operation cost reasonable.

The HUTRAD radiometer system is accommodated in the rear section of the aircraft, separated by a wall from the passenger cabin where the operating panels are located. HUTRAD looks backwards along the flight track from the open rear cargo door.

The nominal speed during data collection is 110 knots.

HUTRAD SUBSYSTEMS

HUTRAD consists of two main subsystems:

- Non-imaging subsystem for frequencies 6.8, 10.65, 18.7, 23.8, 36.5, and 94 GHz
- Imaging subsystem for 93 GHz.

0-7803-3068-4/96$5.00©1996 IEEE

Each receiver measures both vertically and horizontally polarized emission. The block diagram of the non-imaging subsystem is illustrated in Figure 1.

The imaging subsystem is discussed in detail in another IGARSS'96 paper [2].

Additional information on the target is provided by a video camera, providing a line scanned video image.

Position information is provided by a differential GPS receiver (DGPS). In future, platform attitude data from an attitude GPS is used for radiometric data correction.

TECHNICAL CHARACTERISTICS

The receivers for the 6.8 to 36.5 GHz range are Dicke-type radiometers, whereas the 93 and 94 GHz receivers are total power radiometers. A small deviation from the MIMR 89 GHz channel frequency is negligible in algorithm development. The temperature control is based on Peltier elements that provide rapid heating/cooling, thus reducing receiver output drift. The inside temperature stability is better than ±0.2 K.

The main characteristics of the non-imaging subsystem are depicted in Table 1 and those of the imaging subsystem in Table 2.

Presently, the incidence angle is 50°; it will be changed to the final value of MIMR in due time. The antenna 3 dB beamwidth varies with frequency from 5° to 3° for imaging channels and is 1.6° for the imaging channels . The integration time is programmable and the calculated sensitivity is better than 0.6 K for all non-imaging channels and 0.35 K for the imaging channels. The data storage capacity is 4 hours, providing data over a distance of 720 km with the Skyvan.

Figure 2 shows the accommodation of HUTRAD in our Skyvan aircraft. Grey color denotes the cargo door frame.

CALIBRATION

The receivers are calibrated on ground both before and after a measurement flight by using two calibration targets that consist of absorbing material. One of the targets is at ambient temperature (temperature measured before and after calibration) and the other is cooled to 77 K using liquid nitrogen.

In addition, the imaging subsystem employs an in-flight calibration system that provides both cold (liquid nitrogen) and hot (ambient temperature) references.

SYSTEM STATUS

The low-frequency channels (6.8 to 18.7 GHz) of the non-imaging subsystem and the imaging subsystem were completed in 1995 and they were used in the EMAC-95 airborne campaign. The high-frequency non-imaging channels will be tested in the spring of 1996.

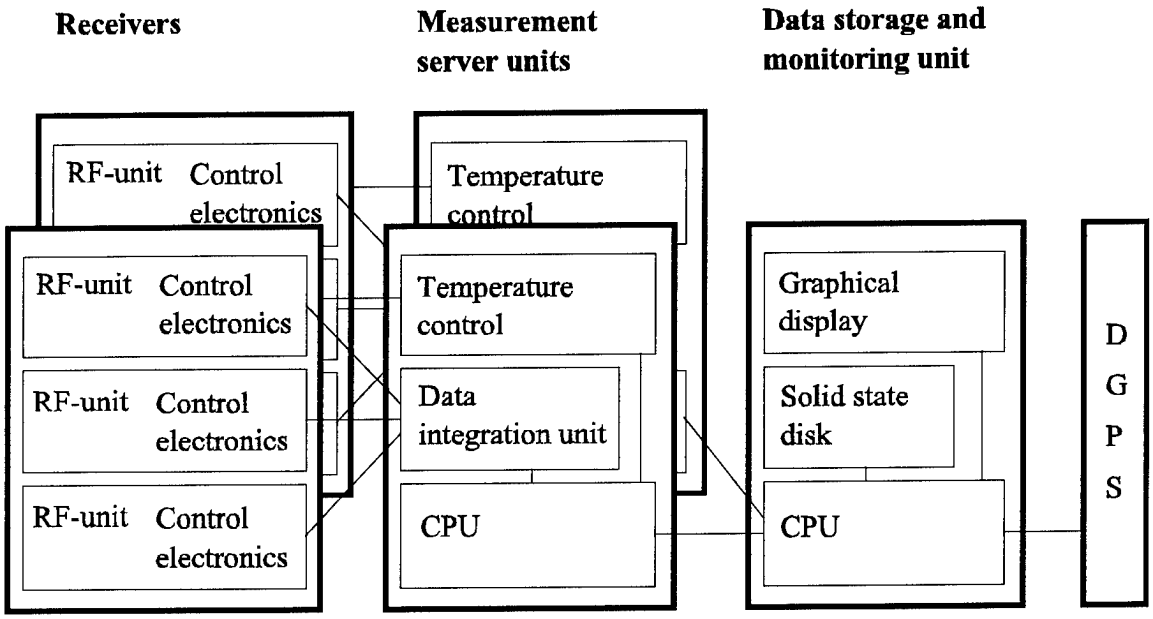


Figure 1. Block diagram of HUTRAD non-imaging subsystem.

Table 1. Technical characteristics of HUTRAD non-imaging subsystem. Nominal altitude is 500 m.

Parameter / Receiver	**1**	**2**	**3**	**4**	**5**	**6**
Center frequency (GHz)	6.8	10.65	18.7	23.8	36.5	94
Polarization	V and H	V and H	V and H	V and H	V and H	V and H
RF bandwidth (MHz)	680	110	750	750	400	2000
Antenna 3 dB beamwidth (deg)	5.0	3.2	3.7	3.8	3.8	3.0
Integration time τ (s)	≥ 0.2	≥ 0.2	≥ 0.2	≥ 0.2	≥ 0.2	≥ 0.2
Sensitivity (K) ($\tau = 0.5$ s)	< 0.25	< 0.60	< 0.35	< 0.30	< 0.40	< 0.50
Footprint size (m)	70 x 105	45 x 67	50 x 78	33 x 73	33 x 73	25 x 57
Incidence angle (deg)	50					
Data storage capacity (h)	4					

V = vertical polarization, H = horizontal polarization

Table 2. Technical characteristics of HUTRAD imaging subsystem. Nominal altitude is 500 m.

Parameter	Value
Center frequency	93 GHz
Incidence angle	50 deg
Polarization	Horizontal and vertical
Intergration time	0.01 s
Sensitivity	0.35 K
Scan method	Adjustable conical scan
Look direction	Backward along track
Scan angle	Adjustable, up to 70 deg
Swath width	662 m
Ant. 3 dB beamwidth	1.6 degrees
Footprint size	22 m x 34 m
Sampling overlap	Adjustable
In-flight calibration	Hot and cold load
Data storage	Hard disk
In-flight display	V and H polarization Video image

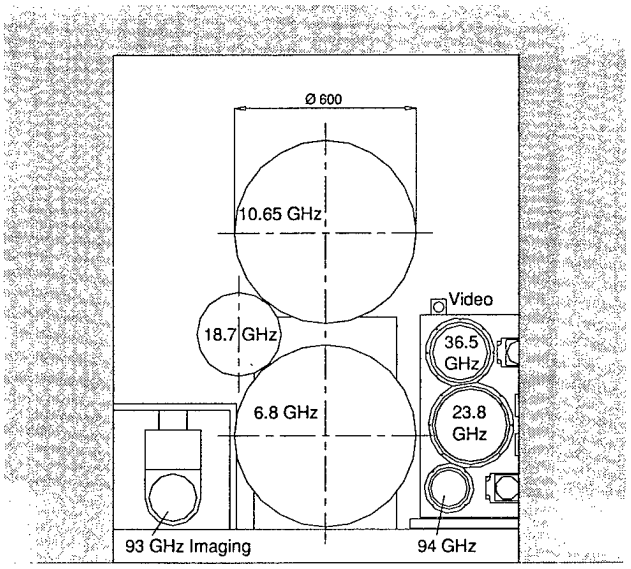


Figure 2. Accommodation of HUTRAD onboard Skyvan.

REFERENCES

[1] M. Hallikainen, M. Nikulainen, H. Taskinen, E. Panula-Ontto, L. Kurvonen, M. Kemppinen, "The Helsinki University of Technology remote sensing aircraft". Proc. First International Airborne Remote Sensing Conference, pp. 637-644, 11-15 September 1994, Strasbourg, France.

[2] M. Kemppinen, T. Auer, I. Mononen, M. Hallikainen, "Advanced airplane version of the HUT 93 GHz imaging radiometer". IGARSS'96, 27-31 May 1996, Lincoln, Nebraska, USA

Experimental Investigation of Diffraction Gratings for Millimeter/Submillimeter-Wave Instruments

Nadimi S. A., Bredow J. W., May G. C.
University of Texas at Arlington-Wave Scattering Research Center
Department of Electrical Engineering, Box 19016, Arlington, Texas 76019
PH:817-273-3522/Fax:817-273-3443/Email:nadimi@uta.edu

Abstract -- To better understand the behavior of frequency-selective waveguide gratings at microwave frequencies, measurements have been performed on two periodic arrays of dielectric gratings in the frequency range of 8-12 GHz. This paper briefly describes the measurement results from the electromagnetic wave diffracting from the gratings into the forward and backward waves. The results presented in this paper are compared with the theoretical results of a plane wave case, indicating a strong agreement between the measured data and the theory in the case of the transmission. However, the spherical nature of the incident wave on the gratings exhibits some effects on the results. These effects could be due to the phase differences between the successive periods away from the center of the grating, introducing additional diffraction orders.

INTRODUCTION

Periodic arrays of planar dielectric waveguide gratings have been studied by many researchers in microwave, millimeter, and optical regions [1]-[4]. Such structures, consisting of periodically varying dielectric strips, can totally transmit or reflect energy at selected frequencies by small variations in the incident angles or the operating frequencies. These waveguide gratings can be used as an alternative to dichroic filters in the millimeter/submillimeter region, offering low absorption loss as compared to metallic filters. In the microwave and optical regions, they can be used as notch filters and switches, providing an alternative to those common devices.

A single-layer waveguide grating consisting of alternating arrays of dielectric strips having dielectric constants of ε_1 and ε_2, with surrounding media having a dielectric constant of ε_3, is illustrated in Fig.1. The incident, reflected and transmitted waves are θ_i, θ_r, and θ_t respectively. d is the thickness of the grating and T is the grating period. The far-field diffraction orders of a plane-wave incidence are given by the grating equation,

$$\sin\theta_m - \sin\theta_0 = m\frac{\lambda}{T}, \qquad (1)$$

where m (m = 0, ±1, ±2, ...) is the diffraction order, and θ_0 is the angle of incidence. For λ=T=10 mm, the zeroth order will be at 0° and the first orders will be at ±90° [2].

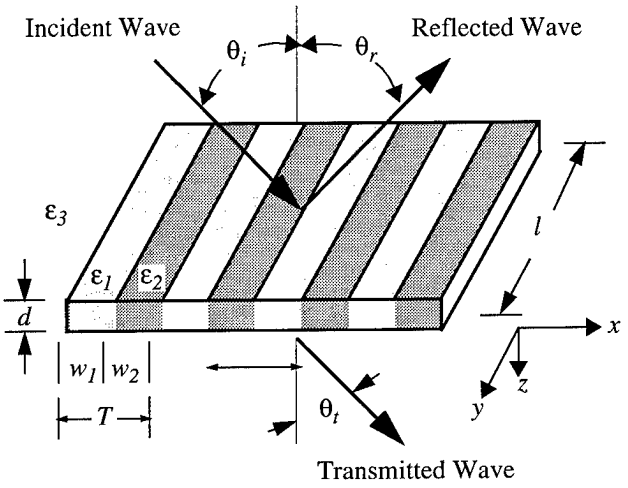


Fig.1 Waveguide grating model composed of dielectric strips.

SYSTEM DESCRIPTION

The measurements were performed using the anechoic chamber of the Wave Scattering Research Center at the University of Texas at Arlington. A simplified configuration of the measurement system used for this study is shown in Fig.2. The main component of this system is the HP 8510A network analyzer.

The other components of this system consist of a frequency synthesized source, variable attenuator, directional coupler, frequency convertor, microwave amplifier, circulator, and a pair of transmit/receive antennas. The antennas are dual-polarized conical horns with frequency range of 2 to 18 GHz. The overall operating bandwidth of the system is from 2 to 18 GHz as well. The circulator was used for the purpose of reflection measurements to allow one antenna to be used for both the transmitter and receiver. The beamwidths of the antennas were measured to be 29° and 16°, at 8 and 12 GHz, respectively.

The antennas were mounted on two tripods and were positioned inside the anechoic chamber at 1.4 meters above the ground, and 4.4 meters apart. A target stand with height of 1.1 meters was made of styrofoam with a dielectric constant of 1.03 and was placed at the center in between the two antennas.

0-7803-3068-4/96$5.00©1996 IEEE

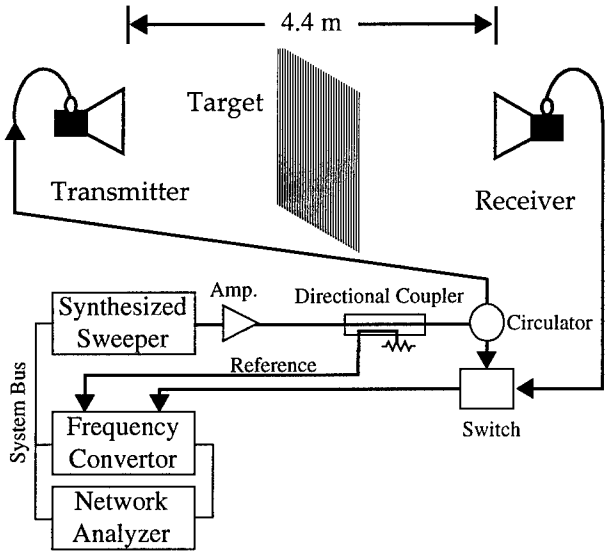


Fig.2 Simplified configuration of the measurement setup.

TARGET DESCRIPTION

For this experiment two sets of gratings, using plexiglas as the higher dielectric material and styrofoam and air as the lower dielectric material, were constructed: the first grating consisted of plexiglas and air having dielectric constants (ε_1) and (ε_2) of 1.67 and 1.0 respectively, with grating period (T) of 29 mm and thickness (d) of 6.4 mm; and the second grating consisted of plexiglas and styrofoam having dielectric constants (ε_1, and ε_2) of 1.67 and 1.03 respectively, with grating period (T) of 30 mm, and thickness (d) of 8.7 mm. In the case of the first grating, the surrounding medium was air (ε_3=1.0), and for the second target the surrounding medium was styrofoam (ε_3=1.03.) The dielectric constants of the materials at the frequency range of interest, were obtained using a dielectric probe. For each grating, the width of the dielectric strips were cut to one half of the grating period.

MEASUREMENT TECHNIQUES

The behavior of the target stand and the media holding the gratings were studied to ensure that they had no significant effects on the measurement. Once this was achieved, measurements of each grating were done using the following procedure: (1) to ensure that the antennas were at normal with respect to the grating, the scattering from a flat conducting plate placed on the target stand was used for alignment purposes; (2) the empty chamber including the target stand and the media holding the grating were measured and the data was saved to be used later for data processing purposes; and (3) the grating was measured for several incident angles and frequency bands.

DISCUSSION

The transmission and reflection from frequency-selective waveguide gratings at microwave frequencies has been studied experimentally. For both gratings, VV and HH polarizations were studied, however, due to the inconsistent behavior of the HH polarization, only the VV polarization is presented. The results show a good agreement with theory in the case of transmission.

The results are shown in term of power ratio, the transmitted, or reflected power over the input power, in dB. Experimental and theoretical diffraction patterns for the gratings with T=29 mm and T=30 mm are given in Fig.3 and 4. For comparison purposes, transmission results for both of the gratings are shown in Fig.5. For the case of T=29 mm, two angle of incidences, 0° and 1°, are considered in Fig.3(a) and 3(b). Notice that in addition to the first null at 9.6 GHz, there is also a second null at 9.2 GHz in Fig.3(b), which appears in the measured results as well. The sensitivity to the incident angle is noticeable in both the transmission and the reflection in Fig.4. Observe that the pick and the null at 9.1 GHz of Fig.4(b) agree with those of Fig.4(a.)

The incident wave at the surface of the gratings is not truly planar but is spherical. While the incident angle is 0° at the center of the grating, it is greater than 5° at the far ends of the grating, especially at higher frequencies. In the case of the metallic gratings, earlier researchers contribute the existence of extra diffraction orders and the broadening of the angular width of all diffraction orders to the incident spherical waves [2].

ACKNOWLEDGMENT

We thank Dr. R. Magnusson of the Electrical Engineering department for the use of their program for generating the theoretical curves.

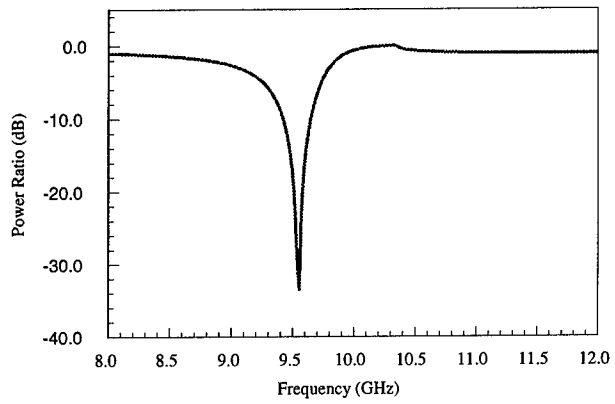
REFERENCES

[1] H. L. Bertoni, L. S. Cheo, and T. Tamir, "Frequency-selective reflection and transmission by a periodic dielectric layer," IEEE Trans. Antennas Propagat., vol. 37, pp. 78-83, 1989.

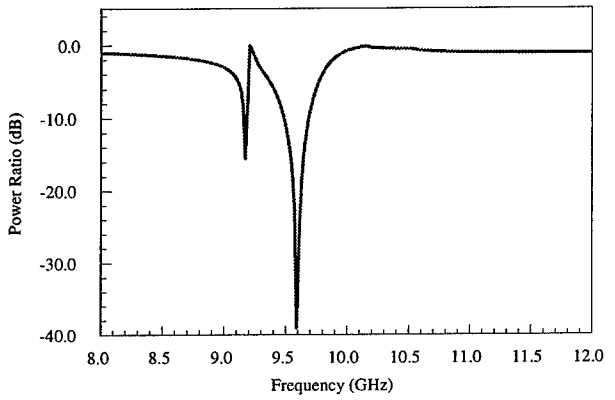
[2] S. A. Khan, D. N. Qu, and R. E. Burge, "Experimental analysis of diffraction by wavelength-sized metallic gratings in the microwave region," Opt. Eng., vol. 32, pp. 3249-3253.

[3] R. Magnusson and S. S. Wang, "Theory and applications of guided-mode resonance filters," Appl. Opt., vol. 32, pp. 2606-2613, 1993.

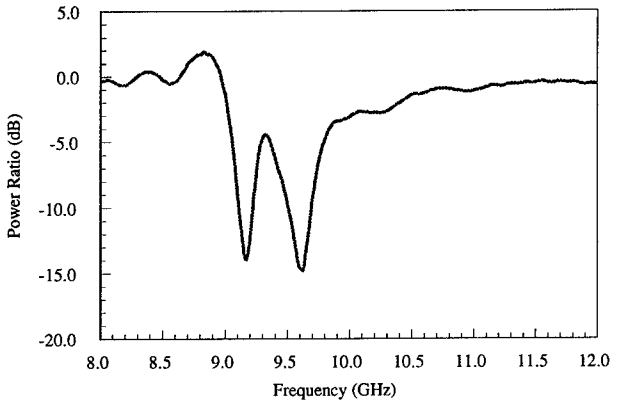
[4] M. G. Moharam and T. K. Gaylord, "Rigorous coupled-wave analysis of planar-grating diffraction," J. Opt. Soc. Amer., vol 71, pp.811-818, 1981.



(a)

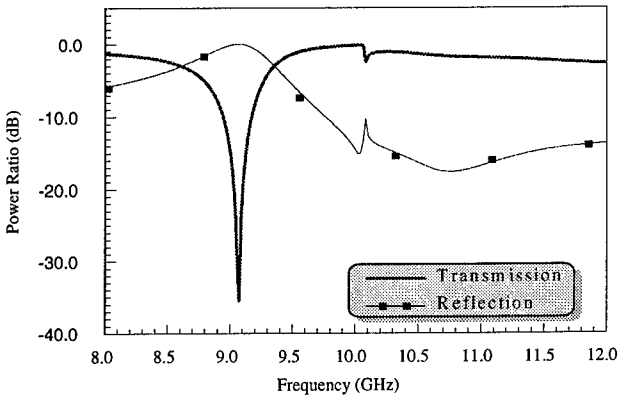


(b)

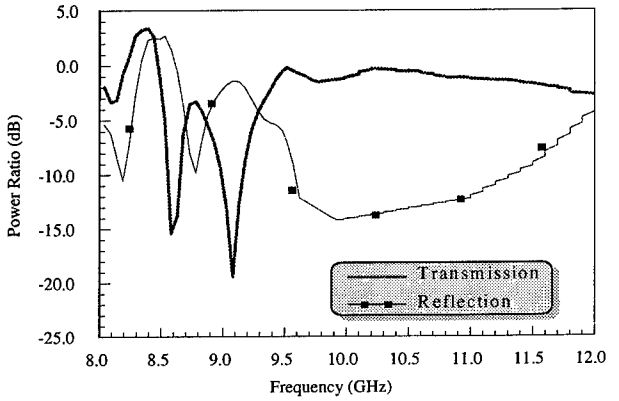


(c)

Fig.3 Transmission results for grating having T=29 mm, ε_1=1.67, ε_2=ε_3=1.0, and d=6.4 mm; (a) theoretical results with incident angle=0°, (b) theoretical results with incident angle=1°, and (c) experimental results.



(a)



(b)

Fig.4 Results for both transmission and reflection for grating with T=30 mm, ε_1=1.67, ε_2=ε_3=1.03, and d=8.7 mm. (a) theoretical results, and (b) experimental results.

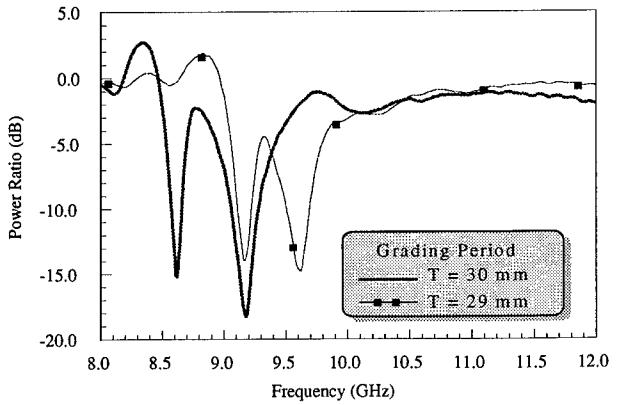


Fig.5 Comparison of the transmission results for both gratings:
T=30 mm: ε_1=1.67, ε_2=ε_3=1.03, and d=7.8 mm,
T=29 mm: ε_1=1.67, ε_2=ε_3=1.0, and d=6.4 mm.

Ground Segment for ERS–2/GOME Sensor at the German D–PAF

Wolfgang Balzer
Dipl.–Ing.
DFD, Münchener Str. 20, D–82234 Weßling
Tel: +49 8153 28–1187, FAX: –1443, E–mail: balzer@dfd.dlr.de

INTRODUCTION

On April 21st 1995 the second European Remote Sensing Satellite (ERS–2) was launched. This new satellite, is intended to provide data continuity between ERS–1 and the European polar platforms. In addition to the mission objectives of ERS–1, ERS–2 makes a significant contribution to atmospheric chemistry. Thus, in addition to the instruments on ERS–1, it also carries the Global Ozone Monitoring Experiment (GOME). This new instrument is able to measure a range of atmospheric trace constituents both in the troposphere and in the stratosphere.

GOME is a nadir–viewing spectrometer which in its normal mode scans across–track in three steps. The field of view may be varied in size from 120 km x 40 km to 960 km x 40 km – a total of five options. The mode with the largest footprint will provide global coverage at the equator within 3 days. The incoming radiation is dispersed and sensed by four individual detector arrays with 1024 detector pixels. The spectral range and resolution is given by the following table:

Detector	*Wavelength range (nm)*	*Resolution (nm)*
1	240 – 316	0.20
2	311 – 405	0.17
3	405 – 611	0.29
4	595 – 793	0.33

In most instances the GOME instrument measures the concentrations of trace gases as total column densities. The notable exception is ozone for which, in addition, vertical profiles can be obtained. Ozone distributions are derived using the Differential Optical Absorption Spectroscopy (DOAS) technique which yields total ozone column values. GOME demonstrates the feasibility of using this differential absorption technique which was used successfully for ground–based and balloon instruments. Existing nadir–viewing space instruments such as SBUV exploit the fact that the height at which solar radiation is backscattered by the atmosphere varies with wavelength. However, in contradiction to DOAS this approach depends on an accurate radiometric calibration.

Besides the on–line components being of ESA responsibility the GOME Data Processor (GDP) system is the only operational off–line ground segment of the GOME sensor. It incorporates a level 0 to 1 processing chain, the complete GOME data archive, a DOAS ozone total column retrieval process (level 1 to 2), and an image processing chain for the generation of higher–level products. The implementation of GDP was funded by the Deutsche Agentur für Raumfahrtangelegenheiten (DARA) in Bonn.

GOME DATA PROCESSOR

From an operational point of view level 0 to 1 processing is very straightforward. It takes one complete orbit of level 0 data and generates a level 1 data product, as described later.

An operational processor has to keep track with the sensors data rate. Therefore, the performance requirement for the level 1 to 2 processing of one ground pixel is very tight. The DOAS retrieval scheme runs much longer (>20 sec) than the value stated in the performance requirement (0.6 sec) but it may run independently for pieces of level 1 data consisting of just one ground scene. Therefore, it is possible to use parallel processors to perform the level 1 to 2 processing. To control these different processors, to supply them with level 1 data inputs and to gather the level 2 data results a corresponding network function is required.

All higher–level processing, e.g. the generation of different ozone maps, is not part of the generic GDP and is described in the section about image processing.

Level 0 to 1 Processing

Raw GOME data (level 0) is converted into "calibrated radiance" (level 1) by applying calibration algorithms and calibration parameters. The calibration parameters are determined regularly using in–flight data when the GOME operates during darkness or takes lamp, internal LED or sun calibration measurements. In addition, data from pre–flight instrument calibration is required. The extracted calibration parameters are collected to a complete "calibration data base" over the whole lifetime of the GOME sensor.

The main algorithms of the GOME level 0 to 1 processing are:

- Leakage current correction
- Pixel–to–pixel gain correction
- Straylight correction
- Spectral calibration
- Radiometric calibration
- Polarization correction
- Geolocation of the ground pixels
- Assessment of the scanning data quality
- Calculation of measurement errors

0-7803-3068-4/96$5.00©1996 IEEE

The most important algorithms of this list are described with a little bit more detail hereafter.

Spectral Calibration: The objective of the spectral calibration is to assign a wavelength to each individual array detector pixel during the flight of the sensor. For the spectral calibration no pre–flight calibration data is really needed. The necessary auxiliary information required, are the estimated pixel positions and their precise wavelength values of the PtCrNe–lamp lines in the wavelength range of GOME. It is possible to determine this information even after launch from the corresponding literature available on this subject. Two steps are required:

1. calculation of the spectral calibration parameters from the calibration lamp measurements. This task is again separated into two steps:
   a. determination of the precise pixel number center of the selected spectral lamp lines and
   b. fitting of a 4th order polynomial through these pixel number/wavelength pairs which yields a set of coefficients
2. application of these parameters to scanning and calibration data packets by calculation of the polynomial using the fitted coefficients.

Radiometric Calibration: The objective of the radiometric calibration is to transform the 16–bit binary units (BU) of the array detector readouts into calibrated radiances (photons s^{-1} m^{-2} nm^{-1} sr^{-1}). There are two calibration steps necessary to accomplished this task:

1. A radiometric calibration using the radiance sensitivity of GOME which was measured during pre–flight calibration and
2. the application of a polarization correction to the scanning data signals.

The first step is a simple multiplication with the corresponding radiance sensitivity values. The determination of the correction factor for the second step is much more complicated and is therefore counted as an algorithm of its own.

Polarization Correction: For the GOME spectral range, there are three wavelength regions which are covered by two detectors having different polarisation sensitivities. These are the three Polarisation Measurement Devices (PMDs) which overlap the wavelength ranges of detector 2, 3 and 4. The chief purpose of the Polarisation Correction Algorithm (PCA) is to calculate 3 values of fractional polarisation for the 3 PMD wavelength regions. An extra point may be supplied from a model calculation below 300 nm which just depends on viewing geometry.

As the fractional polarisation must be specified at all GOME wavelengths the application of the PCA is concerned with (a) the interpolation of the fractional polarization from the four determinable values, and (b) the subsequent generation of correction factors to convert the polarised signals to unpolarised values.

LEVEL 1 TO 2 PROCESSING

One of the advantages of the DOAS approach to total column retrieval is that the spectral fitting and the radiative transfer parts of the retrieval process are almost completely separate. The two main retrieval algorithms, namely the DOAS Fitting Routine and the Air Mass Factor (AMF) calculation produce separate results and diagnostics.

The results from these two algorithms are combined in the process which calculates the vertical columns, while the diagnostics from the two algorithms are examined in a quality control function.

The cloud preprocessing function is a fitting routine designed to produce two important variables to be used in the above mentioned algorithms – cloud top height and fractional cloud cover. This third algorithm is self–contained in the sense that the diagnostic analysis and quality control involved in cloud pre–processing will not affect the main quality control procedure adopted for the final level 2 output.

An important input function is the setup of the climatological and spectroscopic data bases, in which information is extracted (and sometimes interpolated) from a fixed bank of corresponding data bases, according to the requirements of the three processing algorithms.

DOAS Fitting

The Differential Optical Absorption Spectroscopy (DOAS) technique is used for the retrieval of atmospheric trace gas effective slant column (ESC) amounts from moderately high–resolution spectral data in the UV and visible regions of the spectrum. GOME represents the first application of the technique to passive remote sensing instruments in space. The first operational algorithm will focus on the retrieval of atmospheric columns of ozone.

DOAS involves the least–squares fitting of ratioed measurement spectra to a set of reference spectra (absorption cross–sections or instrument–specific reference measurements). The fitted ESCs are converted to geometry–independent vertical columns by division with an appropriate Air Mass Factor.

The differential absorption of trace gases is based on Beer's law – the incremental increase of radiation intensity at a certain wavelength through a slant path distance is proportional to the coefficient of absorption times the incident intensity and the absorber column amount. When there are several absorbers, the contributions are additive.

In the real atmosphere, incident solar light will be further attenuated by molecular (Rayleigh) scattering, and by absorption and scattering due to other particles (aerosols, clouds); there is also the surface reflecting property of the earth's surface to be accounted for. These effects contribute broad–scale spectral features to the back–scattered spectra; in the DOAS approach, such effects are filtered out from the highly structured and more

finely resolved differential trace gas spectral signatures. The broad–scale features are approximated by a low order polynomial in wavelength.

The simulated optical density is linear in the fitting parameters – the number of such parameters equals the number of reference spectra used in the fit plus the degree of the filtering polynomial. If no further adjustment of the reference spectra is assumed, then the fitting is linear least squares (linear multiple regression). The fitting can be improved when the reference spectra are adjusted to allow for uncertainties in the wavelength calibration of the instrumental measurements. An entire spectrum can be translated in wavelength by a single value (shift); it can also be stretched or compressed by a single value (squeeze) about some reference point. This non–linear fitting approach is much slower than linear fitting, but forgives wavelength errors.

Air Mass Factor Calculation

The Air Mass Factor (AMF) algorithm is the second major algorithm in the level 1 to 2 processing of GOME spectral data. AMFs are required for the conversion of effective slant column densities of trace gas absorbers (as produced by the DOAS spectral fitting algorithm) to vertical column densities, which are independent of viewing geometry (solar and line–of–sight). The AMF represents the enhancement of the absorption of a given trace gas due to slant paths of incident light in the atmosphere.

As stated before, the two major algorithms are essentially separated in the DOAS retrieval scheme. AMFs require the calculation of absorption paths in the atmosphere – there is no instrumental input other than viewing geometry extracted from the geolocation information, and the AMF computation is therefore a pure radiative transfer simulation.

Due to historical reasons the generic AMF module which is used within GDP calculates an AMF which considers a plan–parallel atmosphere and single scattering of the incident light only. A prototype of this module was made available to DFD by the University of Heidelberg. This AMF is multiplied with a correction factor which yields an AMF which considers a spherical atmosphere and multiple scattering. The correction factors are taken from a large table which was calculated with the radiative transfer model GOMETRAN of the Institute of Remote Sensing of the University of Bremen.

Cloud Fitting Algorithm

In order to determine ozone amounts more accurately, it is clear that a correction is required in the level 1 to 2 processing for cloudy and partially cloudy scenes. In its first operational version, the Initial Cloud Fitting Algorithm (ICFA) will be confined to stand–alone GOME measurements; synergy with ATSR measurements from ERS–2 was not considered at this stage.

Information about clouds will be extracted from GOME measurements both outside and within the well–known O_2 A–band (around 760 nm). The average transmittance through this band defines a relationship between cloud–top height and fractional cloud cover. If a canonical cloud–top height is specified, then the fractional cover is determined (this will be the method employed here).

The fitting algorithm is based on the least squares comparison of GOME–measured atmospheric reflection functions and their simulated equivalents. Simulated atmospheric reflectance is generated using a simple radiative transfer model. O_2 band absorption is the dominant feature, and templates of high–resolution atmospheric transmittances in the A–band are pre–calculated using suitable line–by–line code.

No information about the scattering properties of the clouds is assumed; instead, the algorithm approximates clouds as (bi–directionally) reflecting lower boundaries. This algorithm is only valid for optically thick water–droplet clouds, and cloud–top heights are therefore restricted to the troposphere. Bi–directional cloud–top reflectance depends on the optical depth of the underlying cloud; this is an external parameter to the algorithm (it cannot be inferred from GOME data in the present retrieval scheme). In the operational algorithm, clouds will be assumed semi–infinitely optically thick.

IMAGE PROCESSING

The generation of higher–level products includes the re–sampling of level 2 data into uniform grids in space and time. At present the generation of three ozone maps is planned which serve different aspects and requirements: a daily global map, a daily map of Europe and a polar map of the north or south pole corresponding to the season.

Provided that the largest swath width of 960 km is switched on the global product represents the smallest global unit showing the ozone distribution of three consecutive days. This product will be generated daily with the middle day being the reference given in a rectangular projection.

The daily map of Europe uses the data of just one day. Therefore, depending on the orbital status of the satellite no complete coverage of the earth surface will be obtained. The product is given in stereographic projection.

The polar maps will also use the data of just one day. The maps of the south and north pole which are given in an orthographic projection will be given daily starting from September and February, respectively. From the poles until 60° N or S latitude the ground coverage will be completely; to the equator the coverage is getting incomplete.

All of the above mentioned products will be generated from the ozone total column products (level 2) which are available in fragments of one orbit. They will be combined, transferred into the corresponding projection and mean values of overlapping data points will be calculated if necessary.

Dual Polarized L-Band Microstrip Patch Array for the AIRSAR/TOPSAR System

F. Rostan*, W. Wiesbeck*, J. J. van Zyl**
*Institut für Höchstfrequenztechnik und Elektronik, University of Karlsruhe
Kaiserstr.12, 76128 Karlsruhe, Germany
Telephone: +49 721/608-2522 Telefax: +49 721/691865 E-mail: rostan@ihewap.etec.uni-karlsruhe.de
**Jet Propulsion Laboratory
California Institute of Technology, 4800 Oak Grove Drive, Pasadena, CA 91109
E-mail: jacobv@blacks.jpl.nasa.gov

ABSTRACT

The paper describes the design and initial results of an advanced dual polarized 8x2 element microstrip patch array for the new NASA/JPL dual frequency C- and L-band interferometric SAR. The new dual polarized L-band antenna for the AIRSAR/TOPSAR system consists of aperture-coupled microstrip patch elements on a foam substrate, yielding a high polarization purity, low losses, a good port-to-port isolation and a large bandwidth.

INTRODUCTION

The TOPSAR instrument is a special mode of the AIRSAR system. This system consists of three radar transmitters (C-, L- and P-band) operated simultaneously and six receivers (two at each frequency), which receive data simultaneously from six different antennas. In the normal TOPSAR mode, the two antennas forming the interferometer at C-band are physically separated by 2.4 meters, while the L- and P-band antennas are the horizontally and vertically polarized feeds of the AIRSAR antennas, respectively.

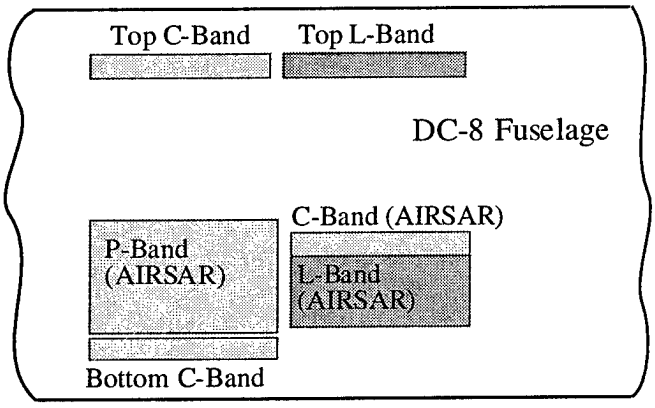


Fig. 1 Schematic of the AIRSAR/TOPSAR system antennas on the DC-8 fuselage

To implement a new dual frequency (C- and L-band) interferometric mode a vertically polarized aperture-coupled 10x1 element L-band antenna was added to the AIRSAR/TOPSAR system [1]. The L-band interferometer is formed by this vertically polarized Top L-band antenna and the vertical feed of the current L-band AIRSAR antenna. Both antennas are mounted on the fuselage of the NASA DC-8 behind the C-band top interferometric antenna and the P-band AIRSAR antenna (Fig. 1). The L-band baseline is limited by the physical size of the airplane to about 2 meters.
Flight tests of the upgraded instrument allowing simultanous acquisition of C-band and L-band interferometric data for topographic mapping showed excellent results [1]. Especially the new 10x1 element aperture-coupled L-band array showed an excellent performance. The flight tests proved that the gain of the tapered multilayer 10x1 element array is within a few percent of the current AIRSAR 8x2 element L-band array - a single layer corporate feed microstrip antenna.
Due to these results it was decided to replace the current single layer L-band AIRSAR antenna by an aperture-coupled dual polarized 8x2 element microstrip patch array.

RADIATOR DESIGN AND MODELING

The layout of the basic dual polarized antenna element is shown in Fig. 2. Due to the multilayer aperture-coupled design an independent optimization of the feeding and the radiating structure can be made. A 1 cm thick Rohacell foam substrate for the microstrip patches results in a large bandwidth as well as a low weight and low costs. Due to the low permittivity of the foam the mutual coupling between array elements can be kept to a minimum.

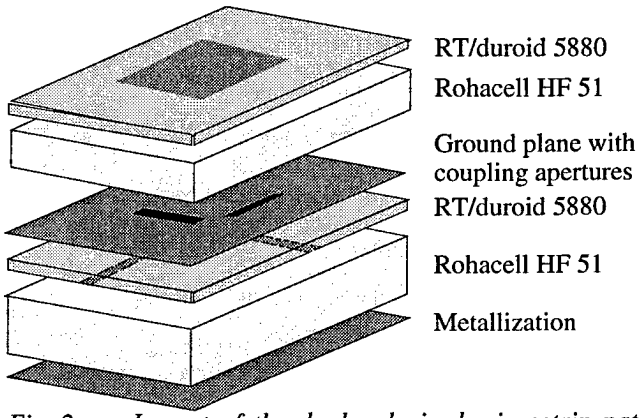


Fig. 2 Layout of the dual polarized microstrip patch antenna element

A 3.17 mm thick RT/duroid 5880 substrate is used as a support layer as well as a radome for the patches. To suppress the backradiation of the coupling slots a feed network in shielded microstrip technique is used. The shielding metallization is placed in a distance of a quarter wavelength from the ground plane to act as a reflector for the backradiation of the slots. The separation between shield and ground plane is performed by a Rohacell foam with a low dielectric constant. Since the feed network on the 3.17 mm thick RT/duroid 5880 substrate is entirely shielded by the metallization layer excellent polarization properties are achieved.
The mathematical modeling of the aperture-coupled antenna element is performed by a Galerkin solution of the electric field integral equation under consideration of spectral domain Green's functions for multilayered media [2]. The calculations

0-7803-3068-4/96$5.00©1996 IEEE

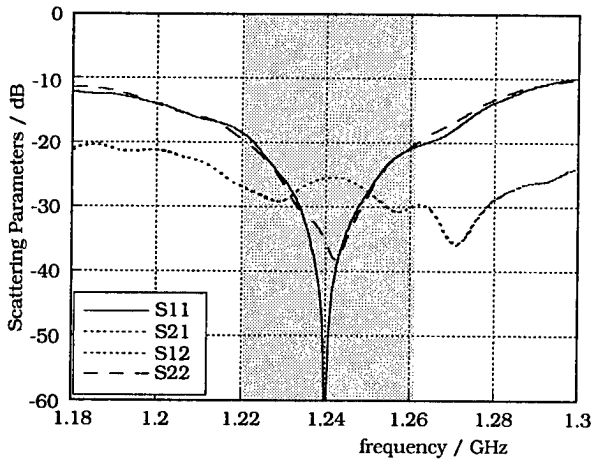


Fig. 3 Measured scattering parameters of the dual polarized antenna element

allow an accurate design of the single antenna elements as well as the complete 8x2 element array under consideration of the mutual coupling between the antenna elements.
In first step a dual polarized antenna element has been designed with the method of moments approach, manufactured and tested. Fig. 3 shows the measured scattering parameters. The input reflection coefficients remain below -18 dB within the required bandwidth of 40 MHz. Within the same bandwidth the coupling between both polarizations is lower than -25 dB.

8x2 ELEMENT ARRAY

The achieved polarization isolation of the single dual polarized antenna element can be further improved for the 8x2 element array by the use of a sequential feeding technique [3]. Fig. 4 shows a transparent top view of the 8x2 element array applying this technique. The array consists of two 8x1 element subarrays. Both are fed by corporate feed networks to preserve the wide bandwidth of the antenna elements. Always four neighboring patches within the 8x2 element array work together to cancel the cross-polarization and to improve the polarization purity of the whole antenna. In the case where the horizontal apertures of these four patches are fed by the corporate feed networks with equal amplitudes and phases, the corresponding vertical apertures are fed parasitically with equal amplitudes. However, the parasitically excited fields in neighboring apertures are 180° out of phase. This means, that the cross-polarized radiation of the single antenna elements cancels out in boresight and in the principal planes, whereas the co-polarized radiation can add in phase. Besides the improvement of the cross-polarization level also the port-to-port-isolation between the subarray ports, which is directly related to the cross-polarized radiation, is significantly reduced.
The original 8x2 element L-band antenna is currently under construction according to the described design. The measured antenna performance will be presented at the conference. However, in order to study the described feeding concept in advance, a scaled 8x2 element C-band array according to the layout in Fig. 4 was built and tested. The measured radiation patterns of this dual polarized 8x2 element array are shown in Fig. 5 to Fig. 10 for both polarizations in azimuth, elevation as well as in the diagonal plane. Excellent radiation properties are achieved. The polarization purity in azimuth (Fig. 5 and 6) is better than 35 dB for any aspect angle and even better 40 dB in the main lobe region. In elevation (Fig. 7 and 8) a cross-polarization level of better -40 dB for any aspect angle is achieved. Even in the diagonal plane (Fig. 9 and 10), which is the worst case, a polarization purity of better -40 dB is achieved in the main lobe region. The measured polarization isolation between the ports of the 8x1 element subarrays is also better -40 dB.

CONCLUSION

The design and initial results of an advanced dual polarized aperture-coupled 8x2 element microstrip patch array for the dual frequency NASA/JPL interferometric SAR has been presented. The used aperture-coupled antenna elements with a center frequency of 1.24 GHz show a bandwidth of 40 MHz. Within this bandwidth an input reflection coefficient of less than -18 dB is achieved. The used sequential feeding concept for the 8x2 element array proved to yield a polarization isolation of typically -40 dB.

REFERENCES

1. J. J. van Zyl, H. A. Zebker, S. Henley, D. Haub, W. Wiesbeck : "The New Dual Frequency (C- and L-Band) Topsar Airborne Interferometric SAR," *Proc. IEEE Int. Geoscience and Remote Sensing Symposium IGARSS'95,* July 1995, Florence, pp. 2270-2272
2. F. Rostan, E. Heidrich, W. Wiesbeck : "Design of Aperture-Coupled Patch Antenna Arrays with Multiple Dielectric Layers", *Proc. of the 23rd European Microwave Conference,* Sept. 1993, Madrid, pp. 917-919
3. F. Rostan, W. Wiesbeck : "Design Considerations for Dual Polarized Aperture-Coupled Microstrip Patch Antennas," *Proc. IEEE Int. Antennas and Propagation Symposium,* June 1995, Newport Beach, pp. 2086-2089

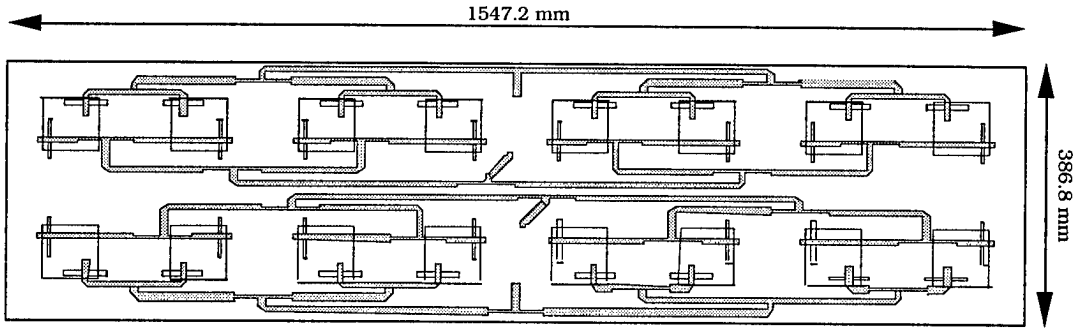


Fig. 4 Layout of the dual polarized 8x2 element L-band microstrip patch array

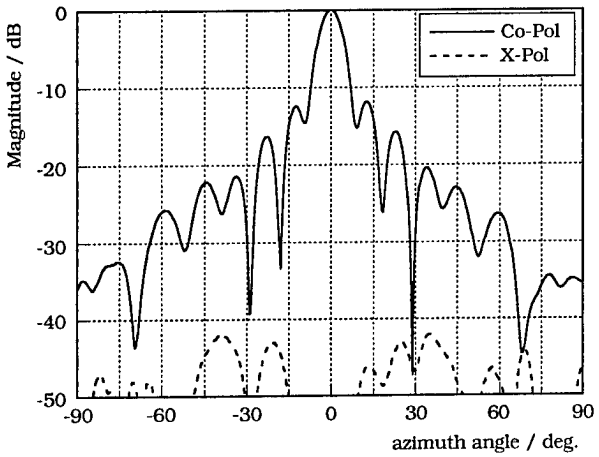


Fig. 5 *Measured radiation pattern of the 8x2 element array in azimuth for vertical polarization*

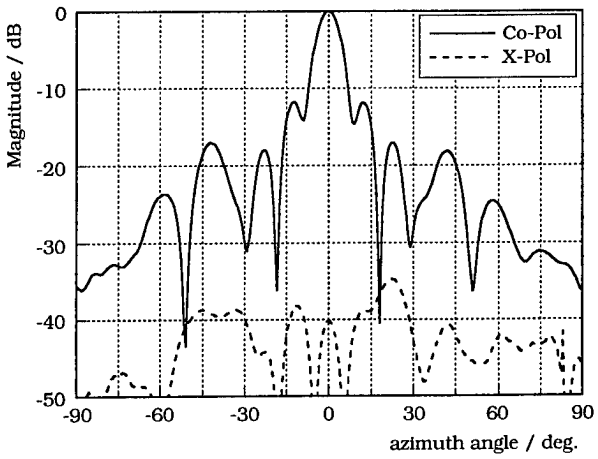


Fig. 6 *Measured radiation pattern of the 8x2 element array in azimuth for horizontal polarization*

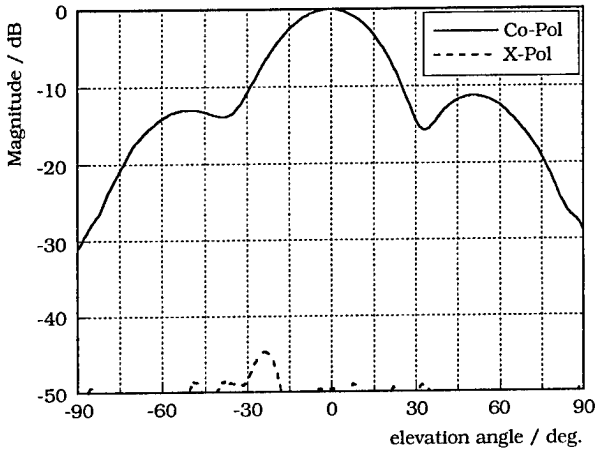


Fig. 7 *Measured radiation pattern of the 8x2 element array in elevation for vertical polarization*

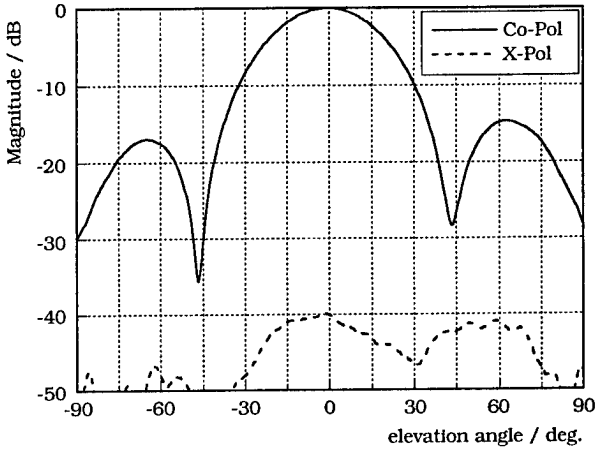


Fig. 8 *Measured radiation pattern of the 8x2 element array in elevation for horizontal polarization*

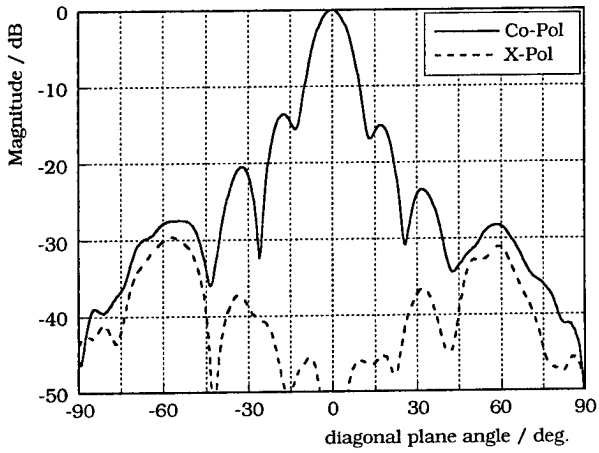


Fig. 9 *Measured radiation pattern of the 8x2 element array in the diagonal plane for vertical polarization*

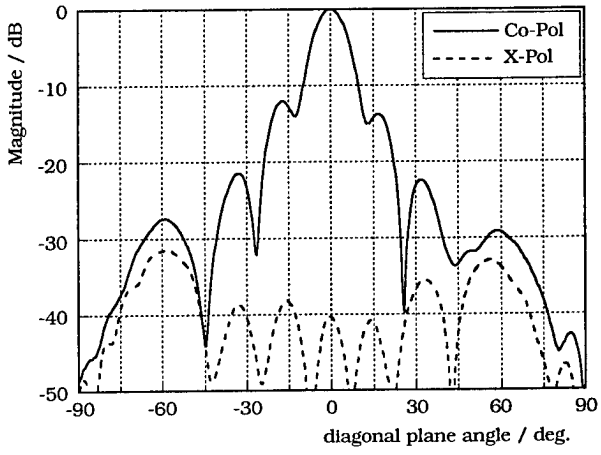


Fig. 10 *Measured radiation pattern of the 8x2 element array in the diagonal plane for horizontal polarization*

Self-adapting Sensor for Atmospheric Electricity Measuring

Felix J. Yanovsky
Kiev International University of Civil Aviation
1, Cosmonavta Komarova Prospect, Kiev, 252180, Ukraine
Telephone: 38 (044) 484-9445, Facsimile: 38 (044) 488-3027
e-mail: yanovsky@kmuga.freenet.kiev.ua

Abstract -- In this work, application of a new way of adaptive measuring of physical quantities is considered to creation of the self-calibrated adaptive sensor of the strength of an electrical field. The sensor is intended for work in free atmosphere, in conditions of external interference influence and destabilizing factors, for example, onboard an aircraft.

INTRODUCTION

Electric field strength (EFS) sensors in the atmosphere are applied for the study of atmospheric electricity and processes of thunderstorms' formation, ecological monitoring, detection of increased electrical activity zones for good aircraft flight safety, forecasting of seismic danger, and in other cases.

The technique for measuring atmospheric EFS requires the use of no less than four EFS sensors, located at various points of aircraft surface. The working head of such EFS sensor is practically out of the aircraft board, that is the severity of EFS sensors functioning conditions is close to extreme from point of sight of effect of temperature, humidity, wind and mechanical loads, differences in pressure, radiation (electro-magnetic, electronic, ionic).

Parameters of sensor's WorkingCharacteristic (WC), including the non-linearity of WC, can uncontrollably vary due to continuously and unpredictably varying disturbing effects and destabilizing factors.

Under such conditions, the problems of accuracy, noise stability, reliability and authenticity of measurements arise acutely.

Accuracy of indications of devices that use EFS sensors determines the possibility of good lightning safety of flight. Thus, the problem of developing primary converter (sensor), which is self-adaptive to a wide range of varying conditions and self-calibrates at unstable initial WC has arisen.

The purpose of this paper is to present a short description of the EFS sensor developed, which is based on new method of physical quantities measuring, and propose it for a further investigation and use.

ADAPTIVE MEASURING METHOD

The essence of the new method of measurement of physical quantities proposed [1] consists in periodically interlacing action onto the input of measurement means (on sensitive working head of sensor) by standard and stimulating signals (stimuli).

The stimulating signal's magnitude is determined with the help of special procedure. Calibrating steps are repeated periodically in the process of measurements with a frequency that exceeds the characteristic frequencies of changes of measuring, handicaps and destabilising factors.

Result of measurement is provided with the given accuracy from the moment of fulfilment of a condition

$$\left|\tilde{A}_{n+1} - A^{*}_{n+1}\right| \le A_0 \qquad (1)$$

where A^{*}_{n+1} and $\tilde{A}_{n+1}$ are meanings of two stimuli at (n+1)th step, A_0 is a given threshold. This condition, as it is shown below, will be achieved without fail during adaptation.

The real WC of the adaptive calibrated sensor is replaced by linear characteristic. Therefore it is important to ensure, that the linear approximation of the WC was tangent to the real nonlinear WC in a point, appropriate to the meaning of physical quantity that is measured. It is reached by that way, that stimuli get out in a vicinity of a current meaning of the physical quantity A_n that is measured. The algorithm of definition of the first A^{*}_{n+1} and the second $\tilde{A}_{n+1}$ stimuli at the (n+1)th step of calibration consists in following.

At first, we find a calculated physical quantity according to current meaning of a signal at an output of a means of measurement, equal X_n, i.e.

$$A^{*}_{n+1} = \frac{1}{K_n}\left(X_n - b_n\right) \qquad (2)$$

where K_n and b_n – are, accordingly, steepness and displacement of a linear representation of the WC of the sensor, which are received during previous (n)th step of calibration. Then we generate physical quantity, which is of the same nature as a measured quantity is, and is equal to A^{*}_{n+1}. This physical quantity is being submitted to the input of sensor, therefore at an output of a means of measurement, a signal

0-7803-3068-4/96$5.00©1996 IEEE

X^*_{n+1} is being received. So, the quantity of the second stimulus is defined by expression

$$\tilde{A}_{n+1} = \frac{1}{K_n}\left(2X - X^*_{n+1} - b_n\right). \quad (3)$$

If $\left|\tilde{A}_{n+1} - A^*_{n+1}\right| > A_0$, then stimulus $\tilde{X}_{n+1}$ is being carried out, and a signal X is being received at an output of a means of measurement. As a result, new meanings K_{n+1} and b_{n+1} is being defined:

$$K_{n+1} = \frac{X^*_{n+1} - \tilde{X}_{n+1}}{A^*_{n+1} - \tilde{A}_{n+1}}; \; b_{n+1} = \frac{\tilde{X}_{n+1}A^*_{n+1} - X^*_{n+1}\tilde{A}_{n+1}}{A^*_{n+1} - \tilde{A}_{n+1}}. \quad (4)$$

The proposed algorithm of the definition of the meanings of stimuli provides the self-co-ordination of the method. In other words, if the parameters of linear representation of the WC at the given step of calibration come nearer to its parameters at the previous step, then the difference between values of two stimuli aspires to zero. This fact provides the tangency of direct linear representation of the WC of the sensor to the curve real nonlinear WC in a point, which corresponds to meaning of physical quantity that is measured: i.e. there is no necessity to use expressions (4) for calibration.

It can be shown as follows. At $K_{n+1} \to K_n$ and $b_{n+1} \to b_n$, we shall receive that $A^*_{n+1} \to A_n$. Hence, $X^*_n \to X_n$ and from the formulas (2) and (3) it follows, that $\tilde{A}_{n+1} \to A^*_{n+1}$, i.e. condition (1) is carried out.

Proposed method of adaptive measuring of physical quantities provides an opportunity of use of the sensors without preliminary calibration. It is the important peculiarity of the method.

In this case, on the initial stage of a work of measuring device, a sequence of received linear representations of the WC (φ_1, φ_2, ... ,φ_i, ...) converges to the linear representation φ_s of this WC in a vicinity of acting meaning of a quantity A, that is being measured.

Let us prove such convergence. Directly after closing of a means of measurement, an initial linear representations φ_i of the WC comes true by realization of two standart actions A^*_1 and $\tilde{A}_1$ that according to the WC φ_w results in signals X^*_1 and $\tilde{X}_1$ on an output of a sensor accordingly.

Thus always meaning Kn > 0, and besides

$$\tilde{X}_n < X_1 < X^*_n, \text{ for } n \geq 2. \quad (5)$$

Let for definiteness

$$\varphi_w(A_1) \geq \varphi_n(A_1). \quad (6)$$

Then from (1) and (6) we receive

$$A^*_{n+1} = \frac{1}{K_n}(X_1 - b_n) =$$

$$= \frac{1}{K_n}\left[\varphi_w(A_1) - b_n\right] \geq \frac{1}{K_n}\left[\varphi_n(A_1) - b_n\right] = A_1, \text{ i.e.,}$$

$$A^*_{n+1} > A_1. \quad (7)$$

It means,

$$X^*_{n+1} > X_1. \quad (8)$$

On the other hand in view of the right inequality (5) we receive

$$A^*_{n+1} = \frac{1}{K_n}(X_1 - b_n) < \frac{1}{K_n}\left(\tilde{X}^*_n - b_n\right) = A^*_n. \quad (9)$$

The right equality in (9) follows from that condition, that the parameters of the n-th linear representation of the WC of a means of measurement at n-th calibration step are set by the stimuli A^*_n and $\tilde{A}_n$. They result in signals at the output, equal X^*_n and $\tilde{X}^*_n$ accordingly.

From here

$$X^*_{n+1} < X^*_n. \quad (10)$$

Uniting (8) and (10), we receive

$$X_1 < X^*_{n+1} < X^*_n. \quad (11)$$

Received inequalities show, that if n is being increased, the first border of an interval of calibration X^*_{n+1} is being displaced in the direction of X_1. Taking into account (2), it is possible to reach a conclusion, that in a considered case the proposed procedure of calibration is converging.

In the other cases, for example, at $\varphi_w(A_1) \leq \varphi_n(A_1)$, i.e. at monotonously decreasing φ_w, the proof of the convergence of the proposed procedure of calibration is made similarly carried out, with only difference, that the meaning $\tilde{X}_{n+1}$ acts as the right border of the (n+1)-th interval of calibration, instead of X^*_{n+1} as it is in the inequality (8).

Thus, the procedure of a determination of stimulating actions provides fulfilment of two conditions: first, the meaning of

measured quality is always inside the interval $(A^*, \tilde{A})$, and secondly, repeated determination of the meanings A^* and $\tilde{A}$ always brings to reduction of the interval $(A^*, \tilde{A})$. It excludes an opportunity of oscillatory process, which can be a source of instability of a system (and appropriate error of instability) at realization other algorithms of gradual approach of some parameter to reference, for example, in the case of a differential signal approaches to zero.

Computer simulation confirmed that measuring process is being converged quite quickly.

ADAPTIVE EFS SENSOR

The proposed way is realised in adaptive EFS sensor.

The device consists of the purely sensor EFS, stimulant (metal electrode), and screen of external influence, which all are incorporated in common Block of Adaptive Sensor (BAS).

Besides BAS, the Digital-to-Analog Converter (DAC) of stimulating actions, Relay of the Displacement of the Stimulant (RDSt), Relay of the Displacement of the Screen (RDSc), analog-digital converter (ADC) of the output signal of the sensor , Block of Measurement and Calibration Control (BMCC) are entered into the structure of the device.

The control block BMCC forms signals of switching on the relays RDSt and RDSc during calibration of the adaptive sensor. The relay RDSt enters a stimulating element in a working zone of the sensor, and the relay RDSc isolates the sensor from external influence with the help of the mobile screen, connected to zero-potential bus.

Thus, the procedure of calibration is being executed in comfortable conditions of functioning. It means that there are not enough disturbance influence from environment during calibration.

Codes of stimulating actions move from the output of the control block onto the bus of DAC. Appropriate to the code, voltage from an output of DAC acts onto stimulant, which forms the input stimulation signals for the sensor. The strobing signals fix the temporal intervals of the DAC and ADC functioning.

The purely sensor is carried out on the basis of one, which is described in [2], however, use of other sensors is quite possible.

The structure of the sensor is entered by the following elements: the metal measuring plate, covered with a ferroelectric plate, electrodes, imposed on the ferroelectric, amplifier, and generator of a variable voltage, which serves to control of the capacity of the ferroelectric.

Control block is in essence the controller of calibration, and it is carried out on the basis of microcomputer. The algorithm of control block's functioning realizes the adaptive way of physical quantities measuring, which is described above.

It is essential, that one controller of calibration can be used for management of work simultaneously of several adaptive gauges of intensity of an electrical field.

CONCLUSIONS

The new method of adaptive physical quantities measuring is developed and used for creation the adaptive sensor of electric field strength.

Algorithm of determination of stimulating action values is synthesized. This algorithm provides the self-coordination of the method.

Otherwise, if the parameters of linear representation of WC on given calibration step come nearer to parameters on previous step, then the difference between the values of two stimulating actions tends to zero, providing tangency of direct linear representation of sensor WC to the curve of real non-linear WC at a point that corresponds to the magnitude of physical quantity.

An important feature of the proposed adaptive sensor is the opportunity of use a sensor without preliminary calibration. Then at the initial stage of operating of measuring device, the sequence of received linear representations of WC converges to linear representation of this WC near acting magnitude of physical quantity. The proof of such convergence is made in this paper.

Requirements for the choice of the magnitudes of standard actions and features of the developed procedure of finding stimulating action magnitudes are also developed.

Aforementioned procedure excludes the opportunity of oscillatory process, which can be source of instability of system as it has place at realisation of other algorithms of gradual approach of a parameter to standard magnitude.

The use of self-calibration and self-checking sensor permits to apply sensors with comparatively low metrological characteristics and, hence, more simple and cheap ones.

REFERENCES

[1] F.J.Yanovsky, B.E.Fishman, and V.Y.Golubchik, "Physical quantities adaptive measuring method", Patent N1631449 (USSR).

[2] I.M.Imianitov, "Devices and Methods for Studying of Atmospheric Electricity," Moscow: Gostechizdat, 1957, 483 pp. [И.М.Имянитов. Приборы и методы для изучения электричества атмосферы. Москва, Гостехиздат, 1957, 483 с., in Russian]

Integration of Multispectral and Ecological Data for Characterizing Montane Meadow Communities in the Greater Yellowstone Ecosystem

Mark E. Jakubauskas
Department of Geography, 634 Energy Center
University of Oklahoma, Norman, OK 73019
(405) 325-5325 FAX:(405) 325-3148 email: jakubaus@uoknor.edu

Diane Debinski
Department of Animal Ecology, 124 Science II
Iowa State University, Ames, IA 50011
(515) 294-2460 FAX:(515) 294-7874 email: debinski@iastate.edu

Kelly Kindscher
Kansas Biological Survey
University of Kansas, Lawrence, KS 66045
(913) 864-7698 FAX:(913) 864-5093 email: k-kindscher@ukans.edu

ABSTRACT

Six spectrally and ecologically distinct montane meadow community types were identified and mapped within the Gallatin National Forest of the Greater Yellowstone Ecosystem by analysis of Landsat Thematic Mapper data. A distinct xeric-to-hydric gradient among the meadow types was predicted by analysis of the satellite data. Thirty sites (six meadow types x five occurrences of each) were selected for intensive field sampling of plant, bird, and butterfly species. Species richness was highest for all taxa (including forbs, grasses, and shrubs) in mesic meadows. Spectral response curves indicate a progression from strongly photosynthetically active vegetation to a composite vegetation/soil response.

INTRODUCTION

Montane, or subalpine meadows, are defined as nonforested habitat types occurring below timberline, but ecologically and geographically distinct from nonforested intermontane parklands. Montane meadows may exist as a result of patch disturbances (fire, windthrow, mass movement, or snow), natural geomorphic processes (underlying geology or soils), or animal disturbances (e.g., beaver meadows). The species composition and vegetation condition of montane meadow communities are closely linked to environmental conditions. Different meadow communities occupy specific sites based on narrowly defined adaptations to gradients of temperature and moisture.

Within the Greater Yellowstone Ecosystem, montane meadows represent important habitat for numerous species, including the grizzly bear (*Ursus arctos horribilis*), bison (*Bison bison*), and the Yellowstone checkerspot butterfly (*Euphydryas gillettii*). Because the montane meadows are relatively small and dispersed across the landscape, high spatial resolution satellite data are ideal for characterization, mapping, and monitoring of these critical habitat types. Remotely sensed multispectral data imagery provides a systematic means by which vegetation condition can be assessed over large areas on a regular basis. In recent years, there has been increasing interest in utilizing remotely sensed data for extracting biophysically important variables, relating observed spectral reflectance to leaf area index, biomass, net primary productivity, and vegetation moisture content [3, 6]. Our research objectives were to 1), use Landsat Thematic Mapper data to identify spectrally distinct meadow communities within the Gallatin National Forest; 2), link spectral differences to plant and animal species assemblages, and 3), develop an ecospectral classification system for montane meadow communities within the Greater Yellowstone Ecosystem.

STUDY AREA

Our study region was the Gallatin National Forest northwest of Yellowstone National Park. Yellowstone and Grand Teton National Parks, and the surrounding national forests form what has come to be known as the Greater Yellowstone Ecosystem (GYE). Geographically, Marston

0-7803-3068-4/96$5.00©1996 IEEE

and Anderson [5] roughly define the Greater Yellowstone Ecosystem as the Yellowstone Plateau and elevations above 2130 m in the surrounding region. At a local scale, the region includes a wide range of elevation and moisture gradients. Nonforest cover types within the ecosystem range from hydric willow and sedge meadows to high-altitude tundra and rock meadows [4]. Plant species distinctive to specific meadow types include *Artemesia spp., Festuca spp., Aster integrifolius, Trifolium longipes, Salix wolfii, Potentilla spp., Salix bebbiana, Agrostis scabra, Frageria virginiana, Equisetum hyemale, Bromus spp., and Geum trifolium.* The study area extends north-south from Porcupine Creek to Bacon Rind Creek and east-west from the crest of the Madison Range to the Gallatin Range.

METHODS

Satellite image analysis:

The methodology for this study was directed toward producing a map of spectrally distinct meadow communities within the Gallatin River watershed. Landsat 5 Thematic Mapper (TM) data from 31 July 1991 were resampled to a Universal Transverse Mercator coordinate system and transformed to radiance values ($mW/cm^2/sr/\mu m$). The thermal band (Band 6) was not used in the analysis. To reduce topographic effects upon spectral response and vegetation composition, cliffs and extremely steep slopes were identified by calculating slope values from 1:24,000 digital elevation model (DEM) data for the watershed. Topographically extreme areas (slope > 30 degrees) were eliminated (masked out) on the TM imagery. An unsupervised classification procedure was used to cluster radiance values for the six TM bands into 50 preliminary spectral classes.

Class means produced by the cluster analysis were then used as input to a second cluster analysis to determine the spectral similarity of the 50 classes. Cluster classes were evaluated using U.S. Forest Service (USFS) stand survey maps, aerial photography, and personal field knowledge of the study area. Based on statistical similarity and image interpretation, the 50 classes were combined to form eleven spectrally distinct cover type classes: six meadow types, representing an apparent continuum of moisture availability; three forest classes, representing high, medium, and low density coniferous forest; and two nonvegetation classes (talus slope and exposed rock). To facilitate location of study sites during fieldwork, the map was converted to vector format and plotted on translucent Mylar, allowing overlay onto the six 1:24,000 scale USGS topographic maps comprising the study region.

Field data collection:

Mapwork and field surveys were used to identify five spatially distinct examples of each meadow type (six habitat types, total sites = 30). Grasses, forbs, and shrubs were surveyed for total vegetation coverage on a per species basis in twenty-five 1 m^2 plots established at 4 m intervals along 100 m transects. Each plot was surveyed for total coverage on a per species basis for grasses/sedges, forbs, and shrubs. The species cover was determined by two observers visually estimating the sum of the greatest spread of foliage for each species in each plot [1].

Presence/absence data were collected for butterflies and birds during 1993 and 1994, employing previously developed methods [2]. Birds were surveyed from 0530-1000 hrs in thirty-five sites comprising three forest types (F1-F3) and five meadow types (M2 - M6). Auditory and visual surveys were conducted using four observers (two groups of two) moving systematically through the 100m x 100m plots for 45 minutes. Bird surveys were repeated three times at each site during the course of a summer. Butterflies were surveyed from 1000-1630 hrs in 30 meadows of type M1-M6. Butterflies were censused by netting and releasing for 20 minutes in three randomly selected 50 x 50 meter subplots within each larger 100 x 100 m plot. Sites of this scale were chosen to minimize habitat heterogeneity. Sampling was repeated three times during the course of the two field seasons.

RESULTS AND DISCUSSION

Field investigations in 1993 and 1994 confirmed the moisture gradient predicted for the meadows. M1 and M2 meadows were sedge marshes with some standing water. M3 meadows were characterized by willow thickets and were located near streams. M4 meadows were of medium moisture with cinquefoil (*Potentilla spp.*) and mixed herbaceous vegetation, while M5 meadows had a mixture of sagebrush (*Artemesia tridentata*) and herbaceous vegetation. M6 meadows were characteristically xeric, rocky, and dominated by sagebrush.

Six meadow types (M1 to M6) representing a distinct xeric-to-hydric gradient were identified by analysis of the satellite data. Fig. 1 shows the TM mean spectral response curves for the six meadow types. Meadow types M1 and M2 exhibit spectral response curves characteristic of strongly photosynthetically active vegetation, with strong absorption in TM 3 (red) and strong reflectance in TM 4 (NIR). As meadow types grade from M1 to M6 (hydric to xeric), the spectral reflectance in the visible and middle-infrared bands increases and progressively shifts from a classic vegetation response curve to one more closely resembling exposed soil and rock. Differences in spectral response between meadow types are most pronounced in TM 5.

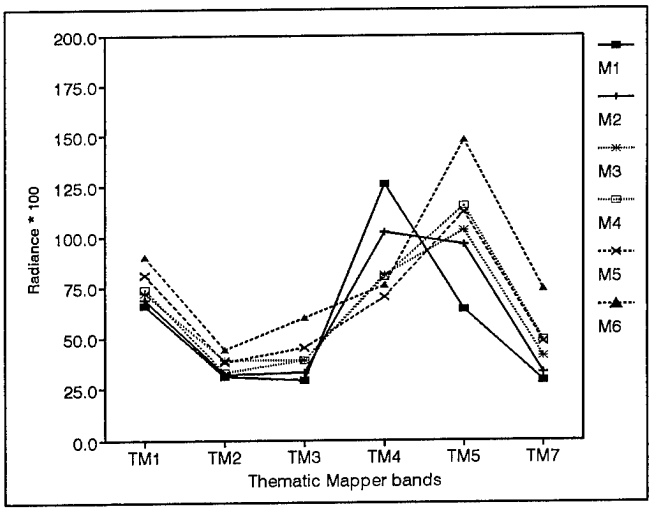


Fig.1. Landsat TM mean spectral response curves for six montane meadow types.

A total of one hundred and forty-one species (or species groups) of plants were observed on the 30 meadow sites. Species richness was highest for forbs, grasses, and shrubs in M3 meadows (Table 1). Twenty-five of the plant species were identified as significant in distinguishing among remotely sensed meadow habitat types.

Table 1

Species Richness in Remotely Sensed Meadows of the Greater Yellowstone Ecosystem

	M1	M2	M3	M4	M5	M6
Plant species	83	79	95	82	72	61
Butterflies	22	25	28	21	27	24
Birds	2	17	41	17	10	18

CONCLUSIONS

Landsat Thematic Mapper data can be used to identify spectrally and ecologically distinct meadow communities within the Greater Yellowstone Ecosystem. Because vegetation composition and structure governs the spectral reflectance of meadows, spectral response characteristics can be linked to distinct plant species assemblages to identify areas of high potential plant and animal species diversity. Data on vegetation composition and structure can be spatially extrapolated across a landscape by calibrating remotely sensed imagery with field-collected point data.

ACKNOWLEDGMENTS

This research was supported by a grant from the University of Wyoming/National Park Service (UW/NPS) Research Center, the University of Kansas General Research Fund and Panorama Society (DD). Additional support was contributed by the Kansas Applied Remote Sensing Program at the University of Kansas and an Oklahoma NASA Space Grant Consortium Fellowship (MJ). We owe our thanks to E. Merrill, A. Vandiver, and R. Krager for providing baseline data. We would also like to thank and A. Fraser for providing botanical expertise, and C. King, L. Kelly, K. Horst, R. Hurst, A. Trainer, P. Rich, M. Wieland, and J. Pritchard for their help in the fieldwork. Finally, we are indebted to N. Hallstrom of the Gallatin National Forest and K. Alt of Montana Fish, Wildlife, and Parks for providing us with housing during our field seasons.

REFERENCES

[1] Daubenmire, R.F. 1959. A canopy coverage method of vegetation analysis. *Northwest Science* 33:43-64.

[2] Debinski, D.M. 1991. *Inventory and Monitoring of Biodiversity: An assessment of methods and a case study of Glacier National Park, MT.* Ph.D. dissertation, Montana State University.

[3] Jensen, J.R. 1983. Biophysical remote sensing. *Annals of the Association of American Geographers*, 73(1):111-132.

[4] Knight, D.H. 1994. *Mountains and Plains: The Ecology of Wyoming Landscapes*. Yale University Press. 338 p.

[5] Marston, R.A., and J.E. Anderson. 1991. Watersheds and vegetation of the Greater Yellowstone Ecosystem. *Conservation Biology*, 5(3):338-346.

[6] Waring, R.H., J.D. Aber, J.M. Melillo, and B. Moore. 1986. Precursors of change in terrestrial ecosystems. *BioScience*, 36(7):433-438.

Case-Based Reasoning and Software Agents for Intelligent Forest Information Management

Daniel Charlebois, David G. Goodenough, A.S. (Pal) Bhogal and Stan Matwin[1]

Pacific Forestry Centre, Victoria, BC, Canada
[1]University of Ottawa, Ottawa, ON, Canada

Abstract - **To perform forest information management, SEIDAM integrates forest cover descriptions, topographic maps and remote sensing imagery. SEIDAM relies on an on-line robotic data storage device, image and GIS metadata databases, software agents and a case-based reasoning system to deliver information to decision makers in a timely fashion. The image and GIS metadata databases contain information about the sources of data, where the data are stored, where they have been delivered and the processing they have undergone. The software agents perform the actual processing by running image analysis, GIS, database and other software to accomplish specific tasks. The case-based reasoning system relies on the software agents, past experience from domain experts and information from the metadata databases to determine what processing is required to deliver products satisfying user goals. This paper describes the intelligent inventory update function in SEIDAM and its AI methodology.**

I. INTRODUCTION

As part of NASA's Applied Information Systems Research Program, a project is being conducted to create an intelligent system (SEIDAM [1-3]) which manages and fuses remote sensing data from aircraft and satellites with multiple geographic information systems (GIS) in order to respond to queries about forests and the environment. SEIDAM (System of Experts for Intelligent Data Management) was begun in 1991 under the Applied Information Systems Research Program of NASA. SEIDAM partners include NASA, the Government of British Columbia (Forests and Environment, Lands and Parks), the Joint Research Centre at Ispra, the Royal Institute of Technology in Stockholm Sweden (KTH), MacDonald Dettwiler, and the universities of BC, Victoria, and Ottawa. SEIDAM integrates several key technologies: image analysis for remote sensing data, geographical information systems (both vector and raster based), artificial intelligence (AI), modeling (growth and yield) and visualization. User queries range from simple relational database queries to complex queries such as the update of digital forest cover maps. This second type of query may require SEIDAM to automatically perform image analysis tasks to extract surface features necessary to update the digital maps.

The focus of this paper is on the design of the AI components of the system, their integration into SEIDAM and how they successfully process remote sensing data and GIS data.

A brief overview of the SEIDAM components is presented in the next section. The following section gives a detailed description of an example of SEIDAM at work on a forest cover update problem. The flexibility of SEIDAM is discussed in the fourth section followed by some conclusions.

II. SEIDAM: THE SYSTEM

The components of SEIDAM are shown in figure 1. They are: the main expert system, the reasoning system (PALERMO - Planning and LEarning for Resource Management and Organization [4]), the Smart Access software agents (software agents [5-7] are systems that unobtrusively observe the manner in which they are used, adapt to the tasks for which they are used, as well as learn from the circumstances of their use), the remote sensing software agents, the GIS software agents, the image and GIS metadata databases, the image and GIS data recorded on a robotic mass data storage device, the SEIDAM knowledge base and the reasoning system's case-base.

The SEIDAM expert system provides a graphical user interface (GUI) through which users can enter simple queries that trigger a range of simple to complex processing tasks. It also controls the activation of the Smart Access software agents and the case-based reasoning system. The Smart Access software agents provide an intelligent interface between SEIDAM's knowledge base and an image metadata database and a GIS metadata database.

0-7803-3068-4/96$5.00©1996 IEEE

The case-based reasoning system [8-10] uses three sources of information to determine how user queries can be satisfied. The first source is its case-base where generalized solutions to previous problems are stored. The second source is the SEIDAM knowledge base where the Smart Access software agents place all metadata relevant to the current problem. The final source is a set of remote sensing and GIS software agents. Each agent creates a STRIPS-like [11] planning operator describing the task it performs.

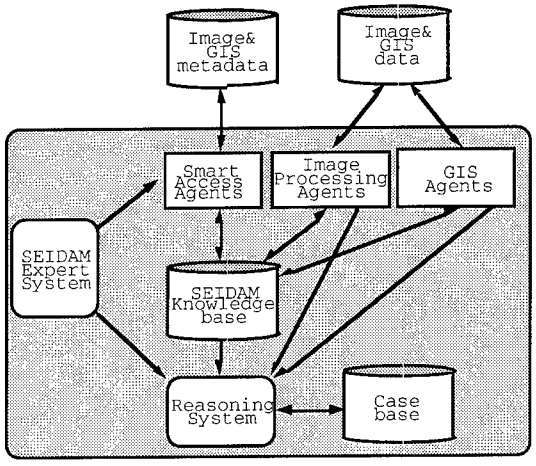


Figure 1 - SEIDAM

There are approximately 40 remote sensing and GIS software agents. They are implemented as expert systems that use third party software such as the PCI image analysis package and the Arc/Info GIS package, plus our own image analysis software, RIASSA. Each agent performs a specialized task such as copying files from their long term storage location to working directories; translating data between image file formats and GIS file formats; creating digital elevation models from point elevation data; applying topographic relief correction algorithms to remote sensing imagery, and performing analysis, segmentation and classification.

The image and GIS metadata databases provide information describing the owner, source, location, distribution privileges, processing history and other ancillary information relating to the remote sensing and GIS data available for SEIDAM. The GIS metadata database complies with the US' Federal Geographic Data Committee's Content Standards for Digital Geospatial Metadata. The image and GIS data are stored in a robotic mass storage device capable of containing over 1.1 terabytes of data. The robotic store is managed by a hierarchical management system that allows user's to treat the device as a large disk. The prime contractor for this robotic device was Digidyne Corporation in Vancouver, BC.

III. SEIDAM: THE SYSTEM AT WORK

One of the more complex problems SEIDAM must solve is the update of a digital forest cover map by using remote sensing images to detect forest depletion due to logging or other phenomena. This task can be carried out by overlaying a GIS digital forest cover map on an LANDSAT-TM image and allowing a user to digitize the lines around new clearcuts, thus creating updated polygons that can be added to the GIS. A geocoded TM image must also be corrected for topographic relief before it can be used for this purpose. Digital elevation models (DEMs) are used as the basis to correct the image for topographic relief. The example below describes how a TM image is prepared by using a DEM created from 1:20000 TRIM irregularly spaced elevation data.

The process is initiated by the user selecting from a list of functions the forest inventory update function in the SEIDAM forestry products window. Subsequently, the user specifies the spatial selection in the Spatial Specifications window. The administrative mapping structure for two provincial ministries guides the user to selecting digital GIS files either symbolically or by map sheet number. Once the map set selection is complete, SEIDAM activates the Smart Access software agents. Their task is to start the relational DBMS where the image and GIS metadata reside and submit SQL queries that will identify all of the GIS data available, as well as all of the TM imagery covering the selected maps. The metadata returned by the SQL queries will include the processing the data have undergone. The Smart Access agents then place this information in the SEIDAM knowledge base and shut down the DBMS.

SEIDAM then activates the case-based reasoning system to which it submits the user goal "update the forest GIS file using TM imagery over the selected map set". The reasoning system poles each of the remote sensing and GIS agents for their planning operator descriptions. It then attempts to find a case that solved a similar problem. Similarity is measured in terms of the user goal and sub-goals and the sub-goals of the case as described in SEIDAM's knowledge base. If a case is found, it is modified to account for the differences between the new user goal and

the previous update problem. If a case is not found, the reasoning system will use goal regression to find a solution. The solution will consist of an ordered list of processing tasks that must be executed to update the forest cover. Each processing task corresponds to one remote sensing or GIS software agent. The reasoning system assesses the processing states of the remote sensing and GIS data and only includes in the solution agents for which processing is required.

The reasoning system activates each of the processing agents listed in the solution. As each agent executes, it modifies the contents of SEIDAM's knowledge base by adding and deleting information and performing the necessary processing. Upon successful execution, the information added and deleted from the knowledge base should agree with the add and delete lists described by the planning operator provided by each agent. This allows the reasoning system to insure that the processing carried out by each agent is successful before activating the next one.

The solution for the forest update problem, after Smart Access execution is:

```
copy_files_to_working_dir,
trim_to_dlg,
import_hydrology,
erdascp_lakes,
sieve_lakes,
lakes_to_bitmap,
trim_to_dem,
create_tin,
erdascp_dem,
copy_bitmap,
set_georeference_tm_large,
create_tm_small,
dem_to_pix_image_match,
set_georeference_tm_small,
tercom,
export_clear_cuts_to_pci,
digitize_clear_cuts,
export_clear_cuts_to_arc,
```

- `copy_files_to_working_dir`: this agent will copy the TM image and GIS files from the robotic mass storage device to a working directory on disk.
- `trim_to_dlg`: this agent translates TRIM GIS data into the digital line graph standard readable by Arc/Info.
- `import_hydrology`: this agent creates an Arc/Info hydrology coverage.
- `erdascp_lakes`: this agent translates the hydrology coverage into a PCI image file.
- `sieve_lakes`: since the hydrology data contains many small lakes, a smoothing filter is used to remove any lake smaller than nine pixels or 5500 m^2.
- `lakes_to_bitmap`: convert the smoothed hydrology image into a bit map.
- `trim_to_dem`: creates a point elevation file readable by Arc/Info from TRIM data.
- `create_tin`: create a DEM from a triangulated irregular network constructed with the point elevation file and place the result in an Erdas file format for input to PCI.
- `erdascp_dem`: create a PCI image file from the Erdas DEM file.
- `copy_bitmap`: copy the hydrology bit map into the DEM image file.
- `set_georeference_tm_large`: get geo-reference information from the TM image file and DEM image file and place it in SEIDAM's knowledge base,
- `create_tm_small`: create a small TM file that fits over the current map and copy a subset image from the original TM image file.
- `dem_to_pix_image_match`: copy DEM into small TM file.
- `set_georeference_tm_small`: add geo-reference information to small TM file.
- `tercom`: apply topographic relief to small TM file.
- `export_clear_cuts_to_pci`: export old clear cut vectors from Arc/Info to PCI.
- `digitize_clear_cuts`: allow user to digitize new clear cuts.
- `export_clear_cuts_to_arc`: export the new clear cut vectors from PCI to Arc/Info.
- `generate_products`: create any paper maps or tabular summaries of forest cover changes.

After the agents have all executed, SEIDAM, once again, activates the Smart Access software agents. Their task now is to start the relational DBMS and submit Data Manipulation Language (DML) commands to update the image and GIS metadata databases to reflect the processing that has been carried out on the image and GIS files. Once this has been completed, the Smart Access agents will move the image and GIS data into the appropriate locations on the robotic data storage device.

IV. DISCUSSION

The procedure described above can be expanded to cover other sensors, automated segmentation and labeling of clear-cuts, or the use of other GIS software. For example, suppose the Smart

Access agents do not find TM data corresponding to a particular map sheet, but do find airborne optical AVIRIS data. The AVIRIS data would be copied to the working directory, and additional agents invoked to select the appropriate bands, perform atmospheric correction with MODTRAN 3, and to geocode the imagery. The topographic correction of AVIRIS data to the same accuracy as TM is difficult and it would likely be necessary to relax the geocoding standards of the GIS products.

The imagery would be segmented by creating an edge image based on edges in any band, inverting this edge image, finding the valleys in the inverted edge image, and building homogeneous segments. The domain expert would have specified in training the agents which filters to use for each sensor, the noise smoothing to apply, and the minimum mapping unit for segment size. The user would still need to validate the automated clear-cut labeling, but the automated process would dramatically reduce user efforts. Intelligent agents for such segmentation have been created and implemented in SEIDAM. They replace the "`digitize_clear_cuts`" agent in the automated solution.

SEIDAM connects to two other GIS packages, GRASS and PAMAP. Both are raster-oriented GIS packages. GRASS is free, but lacks an effective connection to a relational DBMS. It would not be able to support the many attributes of forest polygons. PAMAP can connect to Oracle and achieve functionality for the forest update similar to Arc/Info.

Finally, the update procedure has been modified to support the creation of forest fire fuel maps for planning responses to fire outbreaks.

V. CONCLUSION

The SEIDAM sequencing of intelligent agents for forest inventory update has been described. SEIDAM allows the rapid creation of processing chains which enhance software reuse, which are flexible, and which can operate over an ATM optical fibre network. Metadata databases are used to ensure easy access to a terabyte of remote sensing and GIS data held in a robotic data store. Future work includes the expansion of the update function to incorporate automated segmentation, use of airborne sensors, and the integration of a second DBMS, Oracle.

VI. REFERENCES

[1] S. Matwin, D. Charlebois, D. G. Goodenough, and P. Bhogal, "Machine Learning and Planning for Data Management in Forestry," *IEEE Expert Systems*, vol. 10, pp. 35-41, 1995.

[2] D. G. Goodenough, D. Charlebois, and S. Matwin, "Automating Reuse of Software for Expert Systems Analysis of Remote Sensing Data," *IEEE Trans on GRS*, vol. 32, pp. 525-533, 1994.

[3] D. G. Goodenough, P. Bhogal, D. Charlebois, S. Matwin, and O. Niemann, "Intelligent Data Fusion for Environmental Monitoring," presented at IGARSS'95, Florence Italy, 1995, pp. 2157-2160.

[4] D. Charlebois, D. G. Goodenough, S. Matwin, A. S. P. Bhogal, and H. Barclay, "Planning and Learning in a Natural Resource Information System," presented at Canadian AI, Toronto ON Canada, 1996, pp. (in press).

[5] T. Mitchell, S. Mahadevan, and L. Steinberg, "LEAP: A learning apprentice for VLSI design," presented at Ninth IJCAI, LA, 1985, pp. 573-580.

[6] T. Mitchell, R. Caruana, D. Freitag, J. McDermott, and D. Zabowski, "Experience with a learning personal assistant," *Communications of the ACM*, vol. 37, pp. 80-91, 1994.

[7] O. Etzioni and D. Weld, "A Softbot-Based Interface to the Internet," *Communications of the ACM*, vol. 37, pp. 72-79, 1994.

[8] J. G. Carbonell, "Derivational analogy: A theory of reconstructive problem solving and expertise acquisition," in *Machine Learning: An Artificial Intelligence Approach*, vol. II, R. S. Michalski, J. G. Carbonell, and T. M. Mitchell, Eds.: Morgan Kaufman, 1986.

[9] K. J. Hammond, *Case-Based Planning: Viewing Planning as a Memory Task.* Boston MA: Academic Press, 1989.

[10] M. Veloso, "Learning by Analogical Reasoning in General Problem Solving," : Carnegie Mellon University, 1992.

[11] R. E. Fikes, P. E. Hart, and N. J. Nilsson, "STRIPS: A New Approach to the Application of Theorem Proving to Problem Solving," *Artificial Intelligence*, vol. 2, pp. 189-208, 1971.

The Suitability of Future High-Resolution Satellite Imagery for Forest Inventory

Rune Solberg, Anne H. Schistad Solberg, Hans Koren and Kjersti Aas
Norwegian Computing Center
P.O. Box 114 Blindern N-0314 Oslo, Norway
Telephone: +47 2285 2500/Facsimile: +47 2269 7660/E-mail: rune.solberg@nr.no

Abstract Within a year or two, the first non-military high-resolution imaging satellites will be in orbit. Data from such satellites looks very promising for forest mapping in heterogeneous forests with small stands, like the Norwegian forests. The experiment presented here has tested how suitable such data may be for forest mapping. Aerial imagery has been digitized and converted to panchromatic and three-band multispectral data. Such data sets have been generated for five configurations of panchromatic and multispectral resolutions. Spectral and textural features have been extracted from each data set and classified into a selected subset of classes of interest in forestry. The results show that high-resolution data increases the performance of the classification significantly. There was a 16% reduction in the total error rate when the resolution was increased from 15 m panchromatic/30 m multispectral to 1 m panchromatic/4 m multispectral.

INTRODUCTION

Remote sensing has for several years been used as the main data source for forest mapping in some areas with large and homogeneous forests. Canada has been in the forefront of using satellite imagery for this purpose. As an example, the Inventory Branch in the Ministry of Forests in British Columbia has the mandate to annually update the provincial forest inventory database which consists of more than 6,600 1:20,000 scale mapsheets (Pilon & Wiart 1990). Visual interpretation is here combined with computer assisted mapping and a geographic information system. Such a small revision cycle would not be possible with traditional aerial photography. This is illustrated by the fact that the revision cycle was 10 years in 1978.

Traditional satellite-borne remote sensing sensors have been established as not to be very suitable for forest mapping in heterogeneous forests, like the Norwegian forests (see e.g. Strand, 1989). The spatial resolution is too low, and not all important parts of the electromagnetic spectrum may be covered. However, the fast development of civil high-resolution remote sensing sensors may soon make the most fundamental information available to the forest manager.

The commercial race towards high-resolution satellites started a few years ago when the government of the United States started to seriously consider allowing commercial sale of imagery with a spatial resolution as high as 1 meter. There are currently four private programs for the development of a series of high-resolution satellites: Earlybird, Quickbird, SIS and Orbview. It is expected that more companies and countries will follow in the same direction soon.

The typical high-resolution satellite will provide panchromatic data with highest resolution (e.g. 1 m) and multispectral data with somewhat lower resolution (e.g. 4 bands with 4 meters resolution). Such data is expected to compete strongly with data from aerial photography companies.

The work presented here has been carried out to investigate whether high-resolution satellite data may be a suitable data source for forest map updating. Spectral and textural features derived from multispectral and panchromatic imagery of various spaitial resolutions have been investigated for discrimination of tree species and cutting-class prediction. Further work is required to determine the suitability for derivation of other important parameters.

THE DATA SET

The test area is located to Grue county, west of the river Glomma in south-east Norway (60° 24' N, 11° 57' E). The area is nearly completely covered with coniferous forest, mostly spruce. There are some stands containing pine only, but in most cases pine grow together with spruce. Larger groups of deciduous trees are found only at the border of some of the marshes.

The image data applied in the experiments is derived from aerial photographic film. The photos were taken on August 16, 1994 at about 11 AM flying in a direction approximately west to east. The exposures were taken with a Leica 30/4 camera equiped with a lens of 55 degrees aperture angle. The approximate flying altitude was 700 m above the terrain (950 meters a.s.l). The photographic film used was 23 × 23 cm Kodak Aerochrome Infrared Film Type 2443. The images have been scanned with a resolution of 30 × 30 micrometers per pixel giving a ground resolution of approximately 0.5 meter per pixel. The combination of a short wavelength filter and the film's spectral sensitivity gave a spectral coverage from 525 nm to 900 nm. The combination of the emolusion layers colours and filters gave three effective wavelength bands, 525-580, 580-680 and 680-900 nm. For comparison, the corresponding bands for the SPOT HRV sensor is 500-590, 610-680 and 790-890 nm. Panchromatic data was derived by combining the first two bands, hence, the data covers the range 525-680 nm.

Five image data sets were derived from the original 0.5 meter resolution data. The data sets cover various combinati-

0-7803-3068-4/96$5.00©1996 IEEE

Table 1: The "natural classes" defined

Class	Comment
Shadow	Mainly tree shadows
Soil	Mainly bare soil in clear cuttings
Shrub	
Dry grassland	Very sparse green vegetation
Deciduous forest	
Impediment	Mostly rock, often with lichen
Peat	
Overexposed	Bright areas overexposed
Conifer	

ons of panchromatic and multispectral data: 0.5/0.5 (meters panchromatic/meters multispectral), 1/4, 5/10, 10/20 and 15/30. The first combination was included as a reference with for both panchromatic and multispectral. The last two, included for comparison, represent SPOT HRV and Landsat ETM.

Digital forest map data and three aerial images cover the study area. The most intensive parts of the studies have been limited to an area within one aerial image centered at the nadir point with a radius of about 1,2 km only to minimize the imaging effects in low-altitude data.

The forest map database for the area was revised in 1994. A set of about 100 different data types may be registered for a stand. The data cover topographical and vegetational properties of the stand, properties of the trees in the stand, transport, planned activities, economy, etc. Ground truth masks covering the parameters subject to the investigation, were derived from the data base. The parameres were stand border, tree type and cutting class.

In addition, "natural classes" were derived directly from an manual interpretation of the stereo imagery. The natural classes are a combination of vegetation and other ground cover classes. The applied classes are shown in Table. 1.

METHODS

Spectral features

The following procedure was followed to extract spectral featuers:

1. A few samples of each natural class was extracted (seed samples).
2. The image data was clustered based on the seed samples.
3. The local frequency of each class was computed.

Table 2: Error rates of classification result (%)

Class	15/30	10/20	5/10	1/4	.5/.5
S2	17	25	17	10	1
S3	40	49	58	38	70
S4	53	57	30	23	19
P	49	42	44	44	24
D	0	11	23	20	6
Total	46	46	37	30	24

The K-means algorithm was used for clustering (Jain & Dubes 1988). The clustering refines the means in an iterative process. The local natural class frequency was computed for each pixel for a wndow of size $w \times w$. The fraction of each class within the window was computed and was later used as spectral features.

Textural features

In a related study (Aas et al. 1996), extensive tests have been performed to test various textural features. These were features derived from:

- Grey-Level Cooccurence Matrix (GLCM) (Haralick et al. 1973),
- Local statistics (e.g. Ulaby et al. 1986),
- A random field model (Kashyap & Chellappa 1983), and
- A Grey-Level Run-length Matrix (GLRM) (Chu et al. 1990).

The study identifyed the following features as the most promising for forest applications: the GLCM features Angular Second Moment (ASM) and Inverse Difference Moment (IDM), the GLRM features Long Run Emphasis (LRE) and High Gray Level Run Emphasis (HGRE), and the local statistics method Power-to-Mean Ratio (PMR). These textural features were applied in the current study.

Classification

The textural and spectral features were combined into one feature vector for each pixel, and then analysed with a discrimination rule classifier.

A linear discrimination rule (Friedman and Rubin 1967) was used for dimensionality reduction and to test the performance of the spectral and textural featuers. The input features were projected into a space having fewer dimensions. The within class scatter was minimized while the between class scatter was maximized.

RESULTS

Preliminary experiments determined that there was almost no separation ability between cutting class 4 and 5 for spruce, thus these were merged to one class. For spruce, this resulted in the classes S2 (cutting class 2), S3 (cutting class 3) and S4 (cutting class 4+5). Very few pine stands were present, and only from cutting class 3 and 4. As one could expect, the discrimination ability between these two cutting classes was low. This resulted in only one class for pine, P3. The data material for deciduous trees was also limited, so only one class was used, D.

Table 2 shows the error rates for each spatial resolution configuration for each class and for each data set in total. As we can see for the total error rates, there was actually no error reduction from the 15/30 m resolution configuration to 10/20. However, from 10/20 to 5/10 there was a reduction of 9%. The error rate was further reduced 7% from the 5/10 configuration to 1/4. The reference configuration of 0.5/0.5 m resolution gave a further reduction of 6% compared to 1/4.

The most significant reduction of error rate by increasing the spatial resolution from the lowest to the highest, 30%, was obtained for class S4 (34% if we include 0.5/0.5). The reduction was typically about 5% for other classes. For deciduous trees, an increase in the error rate was observed when going from low to medium resolution. This may be explaned by effects from a very small data set for this class.

DISCUSSION AND CONCLUSIONS

First of all, a few comments are required about the absolute error rates. Most of them are high, even for the high-resolution cases. One explanation to some of the errors is attributed to a far from optimal image acquisition time with very small natural differences between spruce and pine. A much better time would be in the spring with fresh annual shoots on spruce, or in the early autumn. Some of the error must also be attributed to the viewing geometry. Even within the 1.2 km radius area centered about the nadir point, there are significant textural variations due to varying radial distortion of the trees. This makes textural discrimination difficult when one use position independent features. The radial distortion effect will be very little for satellite observations.

The results from the experiment must be interpreted with the small data set in mind. However, the main trends are very clear. The relative changes of the error rates by increasing the spatial resolution show very interesting and promising results. First, it is interesting to note that there was almost no difference between the 15/30 and 10/20 cases. This indicates, at least for this type of forest, that SPOT HRV should not do much better than Landsat TM (however, Landsat TM probably performs better due to better spectral coverage). A large reduction in the error rate is observed when going from 10/20 to 5/10. This looks promising for the SPOT 5 satellite. The tendency was similar when increasing the resolution further on. The results from the reference data set shows that even an increase of the resolution below the 1 meter level could be well worth (at least if one neglect the demands for computer processing).

The experiment has given strong evidence to the expectation of a significant better forest mapping ability when using high-resolution satellite data for forest applications in heterogeneous forests. If the price level of such data will be reasonable compared to aerial photography, high resolution satellite data may soon find an application in the Norwegian forestry.

ACKNOWLEDGMENTS

The authors are grateful for forest map data and valuable assistance from Glommen Skogeierforening (a Norwegian forest owner organization). The study was performed as a part of a contract for the Norwegian Research Council.

REFERENCES

A. Chu, C.M. Sehgal and J.F. Greenleaf. "Use of gray value distribution of run lengths for texture analysis." *Pattern Recognition Letters*, vol. 11, pp. 415-420, 1990.

H.P. Friedman and J. Rubin. "On some invariant criteria for grouping data." *J. American Statistical Association*, vol. 62, pp. 1159-1178, 1967.

R.M. Haralick, K. Shanmugam and I. Dinstein. "Textural features for image classification". *IEEE Tans. Syst. Man Cyber.*, vol. 3, pp. 610-621, 1973.

A.K. Jain and R.C. Dubes. *Algorithms for Clustering Data.* Prentice Hall, Englewood Cliffs, New Jersey, 1988.

R.A. Johnson and D.W. Wichern. *Applied Multivariate Statistical Analysis.* Prentice-Hall International, 1988.

R.L. Kashyap and R. Chellappa. "Estimation and choice of neighbourhoods in spatial-interaction models of images." *IEEE Trans. Inform. Theory*, vol. IT-29, pp. 60-72, 1983.

F.T. Ulaby, F. Kouyate, B. Brisco and T.H. Lee Williams. "Textural information in SAR images." *IEEE Trans. Geosc. Remote Sens.*, vol. 24, pp. 235-245, 1986.

K. Aas, A.H. Schistad Solberg, H. Koren and R. Solberg, *Semi-automatic revision of forest maps combining spectral, textural, laser altimeter and GIS data.* Tech. Report, Norwegian Computing Center, Oslo, Norway, 1996, in press.

Applications of Multi-Frequency, Multi-Polarization and Multi-Incident Angle SAR Systems in Urban Land Use and Land Cover Mapping

Zong-Guo Xia
Department of Geography
University of Massachusetts at Boston
100 Morrissey Boulevard, Boston, MA 02125-3393
Phone: (617) 287 - 5285, FAX: (617) 265 - 7173, E-mail: zgx@earth.geog.umb.edu

Abstract -- This paper provides a review of the current status of radar applications in urban land use mapping, identifies the problems that have prevented the operational use of radar remote sensing in urban studies, and gives a preliminary assessment of the potential of multi-frequency, multi-polarization, and multi-incident angle SAR systems for urban applications.

INTRODUCTION

About 70% of the population in North America, Europe, CIS, Latin America, and Oceania is located in urbanized areas. In the less developed countries, more than 20 million people migrate from rural areas to cities each year to seek employment opportunities and to escape from rural poverty. Urbanized areas are also centers of political, cultural, and economic activities. As a result, they represent the most dynamic living environment. The extent of most urbanized areas is rapidly expanding and the land use patterns within the urbanized areas are constantly changing. Accurate and timely information of urbanized areas is of tremendous importance for planners, economists, environmentalists, and resource managers.

Optical remote sensing has been routinely used for mapping urban land use and land cover patterns and for detecting land use changes. Comparatively, the potential of imaging radar systems for urban land use mapping has not been adequately explored although radar remote sensing is gradually emerging as an operational technology for applications in geology, soil science, agronomy, forestry, hydrology, oceanography, and studies of ice, snow and vegetation. Some of the reasons for this are: (1) the human landscape is highly variable and the interaction mechanisms between man-made features and radar signals are more complex; (2) the strong emphasis on environmental issues in the political arena as well as the scientific community during the last thirty years has influenced radar research to focus on water and vegetation related surface features; (3) the interactions between radar signals and ground surface features are not as well understood as the interacting mechanisms functioning in the optical region and the radar remote sensing technology is not as well developed as optical systems (operational, calibrated, multi-frequency imaging radar systems are still not available today); and (4) until very recently the geographic coverage of radar data was relatively limited and radar imagery was not readily available, particularly in digital form.

On the other hand, radar systems offer many distinctive advantages over optical sensors: (1) radar systems are capable of acquiring clear images independent of weather conditions; (2) they can operate at any time of day or night and in low light conditions such as the polar regions; (3) the ground surface can be illuminated in the optimum direction and at a selected incident angle to enhance features of special interest; (4) the use of radar systems adds additional discriminating power for identifying ground objects and mapping surface materials because the intensity of radar backscatter is largely determined by different properties of ground targets such as moisture content, surface roughness, and meso- and macro-scale geometry; (5) the radar signal polarization can be varied to allow an examination of the ability and manner of different objects to depolarize radar signals, providing information that is not available in other spectral regions; and (6) long wavelength radar signals have the ability to penetrate vegetation canopy, snow cover, sand layer, and the terrain surface under certain conditions so that subsurface characteristics can be studied. For these reasons, it is imperative that we focus our research on the identification of variables affecting the radar response patterns of natural and man-made features, the understanding of the manners of their influence, the quantification of the extent of their effects, and the development of suitable techniques for improving the quality of radar images and automated extraction of information from radar imagery with higher classification accuracy.

Single frequency, dual polarization airborne RAR system for civilian applications became available in 1964, dual frequency and dual polarization airborne SAR system appeared in 1973, and multi-frequency, multi-polarization, multi-incident angle digital airborne SAR systems were developed in the 1980s. However, these systems were largely designed for theoretical research and developing sensors for spaceborne systems. Geographic coverage of images acquired by these systems was very limited and the images were not readily available. The most significant development of radar remote sensing during the last thirty years is the design and successful testing of the SIR-C/X SAR system in 1994. The system can acquire images simultaneously in three frequencies

0-7803-3068-4/96$5.00©1996 IEEE

(X, C, L) with quad-polarization for C- and L-bands. The data acquired by this system is made available to the entire world through the internet, which has stimulated numerous research projects and will undoubtedly accelerate our theoretical understanding of the interacting mechanisms in the microwave region and lead to widespread, innovative applications in a large number of disciplines.

This paper provides a review of the current status of radar applications in urban land use mapping, identifies the problems that have prevented the operational use of radar remote sensing in urban studies, and gives a preliminary assessment of the potential of multi-frequency, multi-polarization, and multi-incident angle SAR systems for urban applications.

URBAN LAND USE MAPPING FROM RADAR DATA

Radar research with a clear focus on urbanized areas was begun in the late 1960s [1, 2, 3]. Bryan [4, 5, 6] and Henderson [7, 8, 9] have carried out most extensive research on issues related to urban land use mapping from radar data. A comprehensive review of radar applications in urban studies is given in Henderson and Xia [10].

Land use mapping from radar data involves converting radar response patterns into information classes that are useful for the purposes of economic development planning, resource allocation, and environmental management. The most commonly used land use and land cover classification system was developed by Anderson et al. [11]. It is a hierarchical system in which categories at Level I represent the most generalized classes. The Level I "Urban or Built-up Land" category is further divided into the following classes at Level II: Residential; Commercial and Services; Industrial; Transportation, Communications, and Utilities; Industrial and Commercial Complexes; Mixed Urban or Built-up Land; and Other Urban or Built-up Land.

Although the use of multidate radar images (HH-polarized X-band RAR) in crop type classification has achieved a correct classification accuracy of 88% [12], urban land use mapping from radar data has, in most cases, proven to be less successful. For Lawrence, Kansas, which is a small city with relatively simple urban structure, Peterson [3] was able to identify approximately 81% of the land use classes correctly on the Ka-band HH- and HV-polarized images acquired by the APQ-97 RAR system. However, the Level II land use mapping by Bryan [4] using the airborne X- and L-band HH- and HV-polarized imagery of Detroit and Royal Oak, Michigan, only achieved a total accuracy of 61% with individual class accuracies of 63% for Industrial, 59% for Commercial and Services, 60% for Transportation, Communications and Utilities, 72% for Residential, 13% for Institutional; and 62% for Open and Other.

One of the reasons for the low accuracy of urban land use mapping is the complexity of the urban environment. The meso- and macro-scale geometry of ground surface features plays an extremely important role in determining the radar response patterns of urban areas. Corner reflection is pervasive in urbanized areas. The effect of street orientation can far outweigh the influence of dielectric constant and surface roughness of urban features [13]. There is currently no easy way of removing the effect of corner reflection caused by the building walls.

Furthermore, the reflectivities in urbanized areas composed of man-made and natural surfaces vary within a wide range from one to a million (60 dB). When input signal dynamic range is commonly compressed for film recording or digital representation, images of urban areas display very low contrast. Man-made features that cause corner reflection become extremely saturated. This not only makes separation of different types of buildings such as industrial, commercial, and institutional facilities very difficult, but also hinders the interpretation of adjacent land use categories such as transportation networks.

Another important reason for the low level of classification accuracy of urban features is that the classification system of the U. S. Geological Survey (USGS) [11] was developed on the basis of optical remote sensors and does not suit for use with radar data [5, 14]. By forcing radar image interpretation to fit an unsuitable classification, the potential of radar remote sensing in urban land use mapping has been inevitably underestimated. For example, by using a modified, more detailed classification system, Henderson [9] was able to achieve an average accuracy of 83.6% in mapping the land use of Denver, Colorado, from Seasat SAR imagery.

In addition, the choice of Level I classes of the USGS system shows a clear bias towards the natural environments. The separation of various categories at Level II was largely limited by the capabilities of remote sensing systems that were operational in the middle 1970s. With the availability of operational high resolution spaceborne SAR systems such as the Radarsat, multi-frequency, multi-polarization, and multi-incident angle SAR systems such as the SIR-C/X SAR and EOS SAR, and the forthcoming 1-meter resolution spaceborne optical systems, the time has come for us to revise the USGS system so that we can make the most effective use of the state of the art capabilities of remote sensing today and give due consideration to the unique characteristics, advantages, and limitations of radar systems.

POTENTIAL OF MULTI-FREQUENCY SYSTEMS

The wavelength of a radar system may affect the signal return from urban features in a number of ways. Shorter wavelength SAR systems give better azimuth resolution and are more sensitive to surface roughness. On the other hand, short wavelength systems suffer from atmospheric attenuation

and dispersion of energy, which makes them unsuitable for spaceborne systems. Furthermore, due to their relatively low penetration capability, they tend to produce more volume scattering from vegetation canopy which can conceal or obscure signals from cultural features.

The most commonly used radar imagery for detecting cultural features in the 1960s was acquired by airborne Ka-band RAR systems (APQ-56, APQ-97). For the past thirty years, most radar images have been acquired by airborne SAR systems operating in the X-band (APQ-102/GEMS 101 SAR, ERIM SAR, CCRS CV-580 SAR, CCRS Airborne C/X SAR, STAR-1, STAR-2), C-band (CCRS CV-580 SAR, CCRS Airborne C/X SAR, NASA/JPL DC-8 SAR), L-band (ERIM SAR, CCRS CV-580 SAR, NASA/JPL CV-990 and DC-8 SAR), and P-band (NASA/JPL DC-8 SAR), and spaceborne experimental systems operating in the X-, C- and L-bands (SIR-A, SIR-B, SIR-C/X SAR). The operational spaceborne systems include C-band (ERS-1, ERS-2, Radarsat), S-band (Kosmos 1870, Almaz-1), and L-band (Seasat, JERS-1) SAR systems. Because most of these systems acquire images in a single band, relatively few studies have been done to examine the effect of wavelength on the interpretation of urban land use patterns.

Bryan [5] found that the X-band imagery was slightly better than the L-band imagery for overall interpretation of urban features. Haack [15] also reached the same conclusion in his study designed to assess the usefulness of L- and X-band like- and cross-polarized images for urban land cover delineations. Several other studies worked with single band images and achieved good results in urban feature identification from Ka-band [1, 2, 3], X-band [16], and L-band [9, 17, 18] imagery. Most importantly, Bryan [5] and Haack [15] demonstrated the importance of multi-frequency systems for urban studies. Bryan [5] reported that 100% of his land use sample areas could be identified at the 5% level of confidence and 84% could be identified at the 1% level of confidence when all four (X- and L-band HH- and HV-polarized) images were used, while only 52% could be identified at the 1% level of confidence when these images were interpreted separately.

BENEFITS OF MULTI-POLARIZATION SYSTEMS

Theoretical and empirical studies in the 1960s [19] confirmed the occurrence of terrain depolarization. It is believed that the differences between like-polarized and cross-polarized images are a result of different physical processes responsible for the two types of returns. Signal return of like-polarized imagery is dominated by quasi-specular surface reflection and surface or volume scattering, while cross-polarized returns are produced by (1) quasi-specular reflection as a result of the difference between the Fresnel reflection coefficients for a homogeneous, two-dimensional, smoothly undulating surface, (2) multiple scattering as a result of target surface roughness, (3) multiple volume scattering due to inhomogeneities of the target surface, and (4) anisotropic properties of the targets [20].

A number of researchers have studied the effect of polarization on the interpretation of cultural features and have reached quite different conclusions. Peterson [3] preferred to use the HH-polarized image in her land use study of Lawrence, Kansas and the HV-polarized image was only used for cross checking. Dowman and Morris [16] found that a higher percentage of urban buildings of various types in an area to the west of the City of Ottawa, Canada, could be mapped from the HH-polarized X-band images than the HV-polarized images. Similarly, Haack [15] rated the X-HH data of the Los Angeles basin in California as the most useful for urban land cover delineations, which was followed by the L-HH and then X-HV imagery with the L-HV data to be the least useful.

On the other hand, Moore [2] found the HV-polarized Ka-band image of Chicago more useful for defining the linear elements of the transportation network. Wu and Sader [21] also showed that cross polarization (VH) and cross polarization ratioed data (VH/HH, VH/VV) were better for delineating urban and surrounding surface features that were difficult to separate by like polarization data. Henderson [22] obtained higher accuracy in urban land use interpretation from the HV-polarized X-band imagery of Los Angeles, California.

Lewis [1] documented the value of both like-polarized and cross-polarized images. He stated that the HH polarization proved better for delineating vegetated areas within an urban complex, delimiting the Central Business Districts, detecting transportation and communication arteries traversing water bodies, and communication lines oriented parallel to the flight line, while the HV polarization was better for detecting buildings and transportation arteries in rural environments, large shopping centers, institutional complexes, industrial facilities, and communication lines oriented at an angle to the flight line. Variations between VV and VH imagery were only tested in the detection of buildings where it was found that VH imagery was better than VV imagery. Wu [23] reported that the simultaneous use of multi-polarization (HH, HV, VV) data of Kershow County, South Carolina, helped delineate several land cover types that were difficult to delineate by the single HH polarization data.

It is obvious that images of different polarization are best suited for interpretation of different urban features. The reason for the general preference of cross-polarized images in urban applications is because the cross-polarized imagery is less susceptible to the specular return from dihedral and trihedral reflectors that is apparent on the like-polarized imagery. However, the cross-polarized return is usually weaker than the like-polarized return and the receiver channel for the cross-polarized return is usually set higher to compensate for the weaker return signal. Unfortunately, this also raises the noise level of cross-polarized imagery, making image interpretation

more difficult. When corner reflection is not common, HH-polarized imagery should produce equally accurate results.

VALUE OF MULTI-INCIDENT ANGLE SYSTEMS

Multi-incident angle radar systems only became available about ten years ago. Most of the previous studies using images acquired by different systems aimed at defining the optimum incident angle for a particular application. Lichtenegger et al. [24] found that the SIR-A imagery was better for land use mapping than the Seasat imagery because of its larger incident angle. Henderson [25] examined three SIR-B images of southern Germany and northeastern France acquired at three different incident angles and reported that incident angles of less than 20-23 degrees were of minimum utility for settlement detection and urban analysis and the amount of information and accuracy of interpretation increased on the image acquired at 41 degrees but decreased on the image acquired at 51 degrees. Hussin [26] also indicated that an incident angle around 40 degrees produced the best results for urban area analysis.

The benefits of multi-incident angle systems are many. It is known that radar incidence angle affects feature identification in an urban environment through its control of range resolution, image layover, and radar shadows. Large incident angles give higher range resolution which is useful for mapping small, complex land cover units. On the other hand, large incident angles generate longer radar shadows which can conceal or obfuscate land cover. Multi-incident angle systems provide the best opportunity for defining the optimum balance between range resolution and radar shadows for urban land use mapping. In addition, the choice of optimum incident angle varies with applications. For example, geological applications generally prefer images acquired with large incident angles. On the other hand, for accurate settlement detection and urban land cover mapping, a moderate incident angle is required. With multi-incident angle systems, the needs of a wide variety of applications can be met. Furthermore, multi-incident angle systems allow the acquisition of stereo radar images which will undoubtedly aid the interpretation of urban features. Images acquired at different incident angles should also prove to be useful for separating certain man-made features from natural features and separating the effect of surface roughness from that of meso- and macro-scale geometry or urban morphology.

CONCLUSION

Radar systems offer many distinctive advantages over optical sensors. With the launch of Seasat, Almaz-1, ERS-1 and ERS-2, JERS-1, and Radarsat, radar remote sensing has become an operational technology for mapping natural resources, monitoring the dynamics of the cultural landscape, and studying the changing conditions of our living environment.

Previous studies indicate that for overall interpretation of urban features X-band images are better than L-band images, HV-polarized images are better than HH-polarized images with VV polarization least desirable, and images acquired at an incident angle around 40 degrees are better than images acquired at low or high incident angles. On the other hand, it has also become clear that radar systems of different frequencies and polarizations are best suited to interpretation of different urban features and the simultaneous use of multi-frequency and multi-polarization images produce better results than single frequency and single polarization images. However, these observations were based on studies of limited data sets which were often acquired by single frequency, single polarization, and single incident angle airborne systems. Conflicting results are not uncommon in the literature. Much research is needed to confirm, improve or refute these early findings and to clarify many existing confusions.

The availability of multi-frequency, multi-polarization, and multi-incident angle systems such as the SIR-C/X SAR system provides a wonderful opportunity for us to (1) define the intrinsic separability of urban features in the microwave region, (2) evaluate the types of urban features that can be identified and the level of accuracy that can be achieved in urban land use mapping from radar images of different wavelengths and polarizations, (3) assess the effects of system, target and extraneous variables on radar response patterns of urban features, and (4) determine the optimum system parameters for urban applications.

REFERENCES

[1] A.J. Lewis, Evaluation of Multiple Polarized Radar Imagery for the Detection of Selected Cultural Features, The U. S. National Aeronautics and Space Administration Technical Letter, NASA-130, October 1968, 56 pp.

[2] E.G. Moore, Side Looking Radar in Urban Research, The U. S. Geological Survey Interagency Report, NASA-138, January 1969, 24 pp.

[3] F. Peterson, "An urban land use study of Lawrence, Kansas using K-Band radar," in The Utility of Radar and Other Remote Sensors in Thematic Land Use Mapping from Spacecraft: Annual Report, The U. S. Geological Survey Interagency Report, NASA-140, January 1969, pp. 38-45.

[4] M.L. Bryan, "Extraction of urban land cover data from multiplexed synthetic aperture radar imagery," Proceedings of the Ninth International Symposium on Remote Sensing of Environment, pp. 271-288, 1974.

[5] M.L. Bryan, "Interpretation of an urban scene using multi-channel radar imagery," Remote Sensing of Environment, vol. 4, pp.49-66, 1975.

[6] M.L. Bryan and J. Clark, "Potentials for change detection using Seasat synthetic aperture radar data," Remote Sensing of Environment, vol. 16, pp. 107-124, 1984.

[7] F.M. Henderson and S.W. Wharton, "Seasat SAR identification of dry climate urban land cover," International Journal of Remote Sensing, vol. 1, pp. 293-304, 1980.

[8] F.M. Henderson, "Interpretation of digitally processed Seasat SAR imagery for urban analysis," Photo Interpretation, no. 2, pp. 3.1-3.6, 1981.

[9] F.M. Henderson, "An evaluation of Seasat SAR imagery for urban analysis," Remote Sensing of Environment, vol. 12, pp. 439-461, 1982.

[10] F.M. Henderson and Z.G. Xia, "Radar Applications in Urban Analysis, Settlement Detection and Population Estimation," in The Manual of Remote Sensing, 3rd edition, vol. 2 -- Principles & Applications of Imaging Radars in the Geosciences, F.M. Henderson and A.J. Lewis, Editors, Bethesda, Maryland: American Society for Photogrammetry and Remote Sensing, in press.

[11] J.R. Anderson, E.E. Hardy, J.T. Roach, and R.E. Witmer, A Land Use and Land Cover Classification System for Use with Remote Sensor Data, The U. S. Geological Survey Professional Paper 964, 28 pp.

[12] P. Hoogeboom, "Classification of agricultural crops in radar images," IEEE Transactions on Geoscience and Remote Sensing, vol. GE-21, pp. 329-336, 1983.

[13] M.L. Bryan, "The effects of radar azimuth angle on cultural data," Photogrammetric Engineering and Remote Sensing, vol. 45, no. 8, pp. 1097-1107, 1979.

[14] B. Drake, "Necessity to adapt land use and land cover classification systems to readily accept radar data," Proceedings of the Eleventh International Symposium on Remote Sensing of Environment, vol. II, pp. 993-1000, 1977.

[15] B.N. Haack, "L- and X-band like- and cross-polarized synthetic aperture radar for investigating urban environments," Photogrammetric Engineering and Remote Sensing, vol. 50, no. 3, pp. 331-340, 1984.

[16] I.J. Dowman and A.H. Morris, "The use of synthetic aperture radar for mapping," Photogrammetric Record, vol. 10, pp. 687-696, 1982.

[17] F.M. Henderson, "Interpretation of digitally processed Seasat SAR imagery for urban analysis," Photo Interpretation, no.2, pp. 3.1-3.6, 1981.

[18] R.C. Kozak, G.L. Berlin, and P. Chavez, "Seasat radar image of the Phoenix, Arizona region," International Journal of Remote Sensing, vol. 2, no. 3, pp. 295-298, 1981.

[19] R.D. Ellermeier, A.K. Fung, and D.S. Simonett, "Some empirical and theoretical interpretations of multiple polarization radar data," Proceedings of the Fourth Symposium on Remote Sensing of Environment, pp. 657-670, April 1966.

[20] A.K. Fung and F.T. Ulaby, "Matter-energy interaction in the microwave region," in Manual of Remote Sensing, 2nd edition, vol. I, D.S. Simonett and F.T. Ulaby, Editors, Falls Church, Virginia: American Society of Photogrammetry, pp.115-164, 1983.

[21] S.T. Wu and S.A. Sader, "Multipolarization SAR data for surface delineation and forest vegetation characterization," IEEE Transactions on Geoscience and Remote Sensing, vol. GE-25, no. 1, pp. 67-76, 1987.

[22] F.M. Henderson, "Polarization, land use type and intraurban location as variables in SAR mapping accuracy," Geocarto International, vol. 1, no. 4, pp. 27-37, 1986.

[23] S.T. Wu, "Analysis of synthetic aperture radar data acquired over a variety of land cover," IEEE Transactions on Geoscience and Remote Sensing, vol. GE-22, no. 6, pp. 550-557, 1984.

[24] J. Lichtenegger, J.F. Dallemand, P. Reichart, P. Rebillard, and M. Buchroithner, "Multi-sensor analysis for land use mapping in Tunisia, Earth Observation Quarterly, no. 33, pp. 1-6, 1991.

[25] F.M. Henderson, "An analysis of settlement detectability in central Europe using SIR-B radar imagery," International Archives of Photogrammetry and Remote Sensing, vol. 28, part 7-1, pp. 202-214, 1990.

[26] Y.A. Hussin, "Effect of polarization and incidence angle on radar return from urban features using L-band aircraft radar data," Proceedings of IGARSS'95 Symposium, 1995.

Variations In Land Cover Area Estimated From Remotely Sensed Data

Wenli Yang and James W. Merchant
Center for Advanced Land Management Information Technologies, University of Nebraska-Lincoln
113 Nebraska Hall, University of Nebraska-Lincoln, Lincoln, NE 68588-0517, USA
Phone: (402) 472-2565 Fax: (402) 472-2410 Email: yang@fish.unl.edu jm1000@tan.unl.edu

Abstract -- Land use and land cover (LULC) information is required for a host of environmental applications. Such information is needed at a variety of spatial resolutions ranging from meters to, on a global scale, hundreds of kilometers. This research explored impacts of selected upscaling procedures and landscape structure on LULC representation at multiple spatial resolutions. A LULC dataset having various spatial resolutions was derived from a Landsat Thematic Mapper image. Comparisons of class areas among different resolutions and between maps obtained from two different upscaling procedures were conducted. Effects of landscape structure on class area estimation were also examined. Results indicated that class areas changed substantially through resolutions, but that patterns of change were different for different classes and upscaling procedures. While class areas at coarse resolutions were predominantly determined by initial areas on the full resolution map, they were also significantly related to several metrics that characterize landscape structure (e.g., patch size, shape and interspersion indices). Considerable differences were found between coarse resolution LULC maps aggregated from the full resolution map and those classified from degraded images, indicating the difficulty of comparing a LULC map classified from coarse resolution images with one aggregated from a fine resolution classification.

INTRODUCTION

Information on land use and land cover (LULC) is required for a broad spectrum of environmental analyses including climate modeling and hydrological studies [1] [2]. Differing models and applications require LULC information over a range of spatial resolutions from meters to, on a global scale, hundreds of kilometers. Remote sensing is particularly effective for mapping and monitoring LULC; however, remotely sensed data are obtained at only a limited number of spatial resolutions. It may, therefore, be necessary to change the spatial resolution, either of the remotely sensed data themselves or of LULC maps derived from such data, to meet requirements of specific applications [1] [2] [3]. Several studies have shown that transformations in resolution may cause changes in representation of class areas [4][5][6]. Additional research is needed to define inter-relationships among LULC types, landscape structure, spatial resolution, and upscaling procedures over ecological regions with different landscape structures. The purposes of this research were: 1) to investigate relationships among LULC classes at multiple spatial resolutions obtained using different approaches; and 2) to identify and evaluate factors that influence LULC area estimation across various resolutions.

METHODS

Initial Classification

The study area, about 100x100 km^2 in size, was located in eastern Nebraska, USA. The area is predominately cropland, but includes two of Nebraska's largest cities, Lincoln and Omaha. A Landsat Thematic Mapper (TM) image acquired on August 26, 1991 (resolution = 30m) was used to identify and map land use and land cover over the study area. Unsupervised maximum likelihood classification was performed using bands 1-5 and band 7. Because of great differences in LULC between urban and rural areas, separate labeling procedures were carried out for the two strata. In urban areas, labeling of spectral classes was based on aerial photo interpretation and field investigation. The labeling of rural LULC classes was based on historical crop maps and acreage reports. Nineteen LULC classes were identified in the study area. Overall classification accuracy was over 75%.

Coarse Resolution Maps By Aggregation

Coarse resolution LULC maps were developed from the TM classification ba sed on a majority rule. Non-overlapping square windows, each representing one pixel in an output image, were overlaid on the 30 meter TM-derived LULC map. Each pixel in the output image was assigned to the class that comprised the majority in a window. When two or more classes occurred with the same frequency, the window was randomly assigned to one of the candidate classes. This condition occurred more frequently when the difference between coarse and fine resolutions was small. A total of ten LULC maps were created using this method. These had resolutions of 60, 90, 120, 240, 360, 480, 600, 720, 840, and 960 meters, respectively. Included in this series are images having resolutions approximately equivalent to currently operated or proposed sensors such as the Moderate Resolution Imaging Spectroradiometer

0-7803-3068-4/96$5.00©1996 IEEE

(MODIS) and the Advanced Very High Resolution Radiometer (AVHRR).

Coarse Resolution Maps By Re-Classification

The aggregation procedure described above is similar to map generalization, but quite different from direct classification of coarse resolution images. Initially ten coarse resolution images were generated through an averaging process. For example, digital number (DN) values at 60m resolution were averaged from 4 pixels in the 30m resolution TM data, and those at 90m resolution were derived from averaging 9 pixels in the 30m image. The resultant multi-resolution images are not directly comparable to those obtained from different sensors/satellites because they do not account for differing sensor characteristics, viewing/illumination geometries, and atmospheric conditions. Nevertheless, they are considered a good approximation. Maximum likelihood classifications were performed on all the coarse resolution images. To make classifications of coarse resolution images consistent, the same statistics used to determine class number and class covariances in the 30m image classification were adopted. Identical labeling procedures were used to assign spectral classes to LULC classes.

Landscape Structure Indices

Indices of landscape structure were calculated using *Fragstats,* a spatial pattern analysis software package [7]. Metrics used in this study included: largest patch index, number of patches, mean shape index, patch size standard deviation, mean shape index, area weighted mean shape index, double log fractal, and patch interspersion.

Statistical Analyses

Class areas obtained from the 30m resolution LULC map were considered as the base areas (A_0) and those from the coarse resolution maps as estimations of corresponding base areas (A_e). Relative estimation error was defined as the ratio of the difference between estimated and base areas to the base area, i.e., $e=(A_e-A_0)/A_0$. Forward stepwise multi-linear regression was used to explore relationships among estimated and base areas, relative errors, and landscape structure indices. The dependent variable was either the coarse resolution area or relative estimation error. The independent variables were base area, eight landscape indices and spatial resolution. Nineteen LULC classes at ten coarse resolutions resulted in a sample size of 190.

RESULTS AND DISCUSSIONS

Aggregation

As resolution became more coarse, the percentage of pixels that retained the original (30m) class labels declined as expected. There was a 25% difference between the full resolution map and the map at 60m resolution. From 60m to 960m, the percent of pixels retaining original labels decreased logarithmically. However, the results varied by class. Classes with large areas and mean patch size (MPS) were more like to be retained. In rural areas, sorghum and corn, the two classes with the largest base areas (22% and 26%) and MPS (5.77 and 2.26), showed a monotonic increase in area as the resolution became more coarse. Grasses, on the other hand, decreased in area as resolution coarsened. This appears to stem from the fact that grass occurs in scattered, rather small patches (MPS=0.51) as compared with large-grain crops like corn. In urban areas, the two largest classes, grass and trees, displayed a monotonic increase in area as resolution became coarser. Bright pavement, the class with the largest MPS (but small percentage area), remained relatively stable in area when resolution size was smaller than 360m, but decreased as resolution became more coarse.

Forward stepwise regression showed that six independent variables significantly contributed to the prediction of coarse resolution class area. They were, in descending order of R-square increment: original area, number of patches, double log fractal, largest patch index, mean shape index, and area weighted mean shape index. Among these variables, original area alone contributed 0.897 to R-square value, suggesting that the area of LULC at a coarse resolution was mainly determined by its initial area in the full resolution map. The final R-square was 0.974 when all six variables were included. On the other hand, the forward regression model with relative estimation error (e) as dependent variable showed that the original area only contributed 0.004 to the R-square value. The largest contributor to the R-square was mean shape index (0.622), followed by number of patches (0.046), resolution (0.037), and interspersion (0.033). The final R-square of the model was 0.834, with eight variables included. This suggests that landscape structure was the dominant factor controlling the consistent rate of class area over the range of spatial resolutions.

Re-Classification

Comparisons between LULC maps classified from coarse resolution data and the original map showed that less than 70% of pixels at the 60m level were classified to the same class as at the 30m level. The percentage decreased logrithmatically as the resolution became more coarse. At the 240m level, more than half of the pixels were assigned to classes different from their original assignments. Examination of class mixtures at coarse resolutions showed that the area of a class was related to the spectral purity of

the class. From 30m to 60m, the only class having over 90% consistency was water. Soybeans, forest, and bright pavement had over 80% consistency in area. All these classes possessed distinctive spectral characteristics. At coarse resolutions some classes tended to be confused with other classes having similar spectral characteristics. For example, a large number of pixels that were labeled corn or soybeans initially were classified as sorghum at coarse resolutions. Classes having unique spectral patterns such as forest, water (low DN) and barren (high DN), showed areas decreasing monotonically as the resolution became increasingly coarse.

Forward stepwise regression showed that initial class area contributed 0.929 R-square increment to the prediction of coarse resolution class area. Two other variables that significantly influenced the regression were double log fractal and mean shape index, which together increased 0.023 R-square. The results indicated that, with the degrading/classification method, coarse resolution class area was more dependent on initial area as compared to the aggregation procedure. In the regression with relative estimation error as the dependent variable, a moderate R-square value, 0.483, was obtained. About 0.042 was contributed by the initial class area and the rest by four landscape indices: double log fractal, mean shape index, area weighted mean shape index, and interspersion. Comparing the R-square value with that obtained in the aggregation procedure, it is obvious that the ability of landscape indices to predict relative estimation error decreased significantly in the degrading/classification procedure.

Pixel to pixel comparisons were made between coarse resolution LULC maps obtained by the two methods. About 76% of the pixels were labeled as the same class at the 60m level. This value dropped to about 63% at 240m level, 56% at the 480m level, and 52% at 960m level. Again, the change in consistent rate between the two as resolution became coarser was logarithmic. After resolution reached 480m, the decrease in consistent rate was little. As the degrading/classification procedure simulates LULC mapping using coarse resolution remote sensing data while the aggregation method simulates map generalization, the great discrepancy between the results obtained by the two methods indicated that it might be problematic to assess the accuracy of a coarse resolution LULC map using maps aggregated from fine resolution classification.

SUMMARY AND CONCLUSIONS

LULC areas estimated from coarse resolution maps were predominantly determined by their original areas in the full resolution maps, no matter which procedure was used to derive the coarse maps. However, the patterns of area changes in LULC classes over resolutions were determined by different rules when different upscaling procedures were used. When coarse LULC maps were produced using the aggregation method, the spatial configuration of patches (size, shape, and interspersion) played an important role in the behavior of area change. Relative errors of area estimation at coarse resolutions were also closely associated with landscape structure indices. Classes with large patch sizes, simple shapes and large initial areas tended to increase their areas as the resolution cell size increased. On the other hand, coarse resolution LULC areas were more dependent on their spectral properties than on spatial properties if the coarse maps were derived from data degraded from the original fine resolution images. Areas of classes with moderate DN values tended to increase as resolution became coarser. The different patterns of class area change with coarsening resolution resulted in significant differences in coarse resolution LULC maps developed from the two procedures. This suggests difficulty in using LULC maps derived from fine resolution images (e.g., TM) to validate those obtained from coarse data (e.g., AVHRR).

REFERENCES

[1] J. R. G. Townshend, ed., "Improving global data for land applications," IGBP Report No. 20, International Geosphere-Biosphere Programme, Stockholm, Sweden, 1993.

[2] D. L. Skole, "Data on Global Land-Cover Change: Acquisition, Assessment and Analysis", in: "Changes in Land Use and Land Cover: A Global Perspective". W.B. Meyer and B.L Turner II, Eds. New York, Cambridge University Press, 1994, pp. 437-471.

[3] B. L. Turner, R. Moss and D. Skole, eds. Relating Land Use and Land Cover Change, Report No. 24, International Geosphere - Biosphere Programme, Stockholm, Sweden, 1993.

[4] J. R. G. Townshend and C. O. Justice, "Selecting the spatial resolution of satellite sensors required for global monitoring of land transformations," International Journal of Remote Sensing, Vol. 2, 1988, pp.187-236.

[5] A. Moody and C. E. Woodcock, "Scale-dependent errors in the estimation of land-cover proportions: implications for global land-cover database," Photogrammetric Engineering & Remote Sensing, Vol. 60, 1994, pp. 585-594.

[6] A. Moody and C. E. Woodcock, "The influence of scale and the spatial characteristics of landscapes on land-cover mapping using remote sensing," Landscape Ecology, Vol. 10, 1995, pp.363-379.

[7] K. McGarigal and B. J. Marks, "FRAGSTATS report: spatial pattern analysis program for quantifying landscape structure," Forest Science Department, Oregon State University, 1993.

Recent experiences in mapping land cover from AVHRR data: People's Republic of China test sites

Zhicheng Qiu
National Bureau of Surveying and Mapping, Beijing, People's Republic of China
Limin Yang[1]
Center for Advanced Land Management Information Technologies
Conservation and Survey Division, Institute of Agriculture and Natural Resources
University of Nebraska-Lincoln, Lincoln, NE 68588-0517 USA
Thomas R. Loveland
U.S. Geological Survey, EROS Data Center
Sioux Falls, SD 57198 USA

Abstract -- Land cover types of two test sites in the north central and south east China were mapped using NOAA AVHRR 1-km NDVI data. For major land cover types, the results from this study compared favorably with the existing land use/cover maps of China. However, identification of detailed land cover types in certain study areas was difficult due to extremely complex and fragmented land use/cover patterns and the effect of cloud contamination on NDVI data. Use of ancillary data such as DEM and soil types was effective in post-classification and improved the quality of results.

INTRODUCTION

There are well-documented needs for small-scale (1-km) land cover data for use in national to global environment assessments [1]. While there is general acceptance that 1-km data from the Advanced Very High Resolution Radiometer (AVHRR) are the most appropriate imagery for mapping land cover over large areas, the practical understanding of the consistency of results in different landscapes is limited. For AVHRR to be used effectively throughout the globe, it is necessary to understand the environmental and technical factors that influence the quality of results. To better understand these factors, researchers from the People's Republic of China (PRC) National Bureau of Surveying and Mapping (NBSM), the U.S. Geological Survey (USGS), and the University of Nebraska-Lincoln mapped land cover for two test sites in China. This collaboration was conducted as part of a formal protocol between the NBSM and USGS.

STUDY SITES CHARACTERISTICS

The two sites, in the north central and south east regions of the country, differ in climate, vegetation, and land use intensity. The north central site encompasses an area from 31°N to 41°N and 101°E to 115°E. It includes all or portions of Shanxi, Shannxi, Hubei, Henan, Gansu, Sichuan provinces and the autonomous region of Inner-Mongolian. Three physiographic regions can be identified in the area: a temperate desert and semi-desert environment in the north west, a mosaic encompassing the Loess Plateau, a series of mountains and inter-mountainous basins, and several fluvial plains in the east, and the Tibetan Plateau in western Sichuan province. The south east site lies between 24°N to 28°N and 108°E to 114°E, including portions of Hunan, Guangxi, Guangdong, Guizhou, and Jiangxi provinces in southeastern China. This region is in the subtropical monsoon climate zone, and is an area heavily influenced by cultivation and socio-economic development.

DATA

Primary data used in this study are the NOAA AVHRR 1 km Normalized Difference Vegetation Index (NDVI) composites for the 1992 growing season. The NDVI composites were compiled by the USGS EROS Data Center [2]. Seven monthly composites (from April through October) were acquired initially for the two study areas. Because of excessive cloud-contamination in some monthly composites, a decision was made to combine six monthly composites into three bi-monthly composites for the north central site (i.e. April-May, July-August, and September-October). For the same reason, two monthly composites (July and October) for the south central site were not included in this study. Besides NDVI data, a digital elevation model (1:4,000,000) of the study area was provided by NBSM, and a digital soil database was acquired from the Remote Sensing Center, Beijing Agricultural University, China. An atlas of China land use (1:1,000,000), compiled by the Institute of Geography, Chinese Academy of Sciences in 1980, was referenced to aid land cover interpretation [3].

[1] Limin Yang's work was supported through U.S. National Aeronautics and Space Administration Grant (NAGW-3940).

0-7803-3068-4/96$5.00©1996 IEEE

LAND COVER CLASSIFICATION PROCEDURE

The land cover classification procedure utilized in this experiment drew from experience by land cover characterization research conducted by the USGS EROS Data Center and the University of Nebraska-Lincoln [4]. Several steps were taken to derive seasonally-distinct land cover regions from the NDVI time series and other ancillary data. The initial classification using NDVI composites was accomplished with an unsupervised clustering algorithm and minimum-to-mean-distance classifier implemented in the Land Analysis System (LAS) image processing package. More than eighty clusters were generated for two test sites and their statistics were computed for further analysis.

RESULTS AND ANALYSIS

Class labeling and refinement using ancillary data

Temporal NDVI profiles were examined for initial class labeling in relating some clusters to major land cover types (e.g., desert and semi-desert steppe, cropland, grassland, and forest). However, some clusters could not be readily labeled based on NDVI profile alone due to spectral-spatial confusions among land cover types. The confusion was primarily related to variations in vegetation phenology and topographic feature. Among the mixed classes, two types of clusters were distinguished: 1) clusters composed of two or more cover types coexisting within a similar environment, and 2) clusters corresponding to two or more cover types with each type occurring at different locations. Clusters of the second type were refined using ancillary data. For instance, cluster 9 in the north central site occurred in two geographic regions: the east section with predominant lowland agricultural land use, and the southwestern section located in the Tibetan Plateau. Accordingly, the cluster was split into dryland cropland and subalpine meadow based on elevation and geographic location. Cluster 25 covered both paddy fields and forest. The cluster was split by intercepting the class with paddy soil categories. Cluster 28 contained plain irrigated cropland, terraced paddy and slope grassland. Based on documentation of local environment [3], most plain cropland is located below 600 meters, the terraced paddy in between 600 to 1500 meters, and slope grassland above 1500 meters. Thus, digital elevation data were used in this case to split cluster 28 into three classes. A similar process was also applied to the south east site in post-classification.

The final classification yielded 26 distinct land cover types for the north central area and 16 classes for the south east site. Table 1 lists 18 major land cover categories identified from this study.

Table 1. Land Cover Classes

Class ID	Class Label
1	irrigated cropland (paddy)
2	irrigated dryland cropland
3	non-irrigated cropland
4	coniferous forest
5	deciduous forest
6	mixed forest
7	sparse woodland
8	firewood and bush
9	meadow
10	steppe
11	alpine and sub-alpine meadow
12	slope grassland
13	sandy desert
14	bare ground/sparsely vegetated land
15	woodland/grassland
16	woodland/cropland
17	woodland/bamboo/grassland
18	tree crop/woodland

Effect of cloud on classification

The presence of cloud and atmospheric haze caused some problem for the classification. Approximately one third of the total clusters (15 out of 46) in the south east site were affected by clouds. Low NDVI values (<0.15) were recorded for some forest area during the mid-growing season. For instance, class 25 is coniferous forest which is the same cover type as class 26 and 29; yet its NDVI of August is significantly different from the latter two classes (0.46 versus 0.15, 0.10). The severe cloud-contamination on the NDVI is related to the monsoon rainy season of the area, which can last for long period during growing season. This problem is a recurring issue for large area land cover mapping using AVHRR data and needs to be further addressed.

Heterogeneity of land cover

In general, broad land cover patterns were adequately defined in both test sites. However, identification of detailed land cover types was uneven, especially for the south east test site. The classification of this area was comprised of a significant number of mosaic categories that often included disparate land cover types. This was the result of extremely complex and fragmented land cover patterns resulting from topographic influences and intense human activity. The heterogeneity of land cover in this area necessitates the inclusion of several mixed (or mosaic) cover categories in the final classification (Table 1). For the northern site, the mixed land cover types include cropland/grassland, cropland/woodland, cropland/woodland/grassland. The south east site identified several unique mixed cover

types (grassland/tree-crop, forest/bamboo/grassland), in addition to those found in the northern site.

Special land cover classes

The identification of small paddy fields and bamboo forest in the south east site was a challenge. These cover types are often spectrally and spatially mixed with others, and therefore, are difficult to separate. In some area, the difficulties can be eased by using ancillary data. In eastern Hunan province, for instance, paddy fields were satisfactorily extracted using slope and soil data (slope < 1 degree, and soil type). One extensive bamboo forest area in this site was separated from other mixed grassland/woodland using elevation data. In contrast, other bamboo mixed classes were not separable due to a mixture with forest and grasslands. The inconsistency in occurrence of location and highly interspersion of those cover types make them difficult to identify.

Smoothing process

Because of the complex land cover patterns of the south east test site, the final land cover classification was further processed using a smoothing procedure developed by NBSM scientists. The smoothing process was based on mathematical morphology, noise cleaning, and region/neighborhood analysis. This method effectively generalizes the classification and allows the dominant regional land cover to be expressed. This procedure also facilitates the inclusion of the results into geographic information systems.

DISCUSSION AND SUMMARY

This experiment has demonstrated that large area land cover mapping in north central and south east China using NOAA AVHRR 1-km NDVI composite data is feasible. Qualitative comparison of the results with the 1:1,000,000 China land use/cover maps [3] suggested that major land cover types can be adequately mapped with AVHRR NDVI data aided by digital elevation model, soil database and other ancillary data. Several observations were made with regard to what has learned from this experiment.

The characteristics of the physical environment and land use practices of the two test areas had significant impact on the classification outcome and on post-classification strategy. For the north central site, distinct spatial differentiation in local climate, soil properties, and topography allows major land cover types to be readily identified on the classified image. In contrast, the extremely complex and fragmented land cover/land use patterns of the south east site imposed considerable difficulties in identifying certain land cover classes. In some cases, the same land cover types with different temporal NDVI were classified into several groups due to variation in plant phenology, geographic location, and local topography. Conversely, some different land cover types had similar NDVI temporal profiles and were classified into a single cluster. Under such circumstances, availability of ancillary data and information on the local environment become essential in formulating post-classification strategy in order to refine class labeling. In this study, the digital elevation model and soil data base were particularly useful in post-classification stage.

The effects of cloud-contamination on land cover classification has been an issue addressed by researchers. In the present study this problem was particularly noted in the south east test site, a region with subtropical monsoon climate. Because the growing season of the area corresponds to the rainy season, even the monthly NDVI composites are not adequate to generate usable data for some months. Research on development of robust cloud screening methods and techniques for mitigation of cloud-contamination for AVHRR data are warranted. Until such methods are available, the quality of the land cover mapping in the extreme cloud-prone regions may be necessarily compromised.

This study also suggests a need for developing an appropriate hierarchy for describing highly mixed land cove types. The mosaic and extreme fragmented land cover patterns in southeastern China is the rule rather than exception. The diverse land use patterns and frequent changes in spatial composition of cover types demand careful considerations in class labeling and post-classification as well as presentation of the results.

REFERENCE

[1] Townshend, J.R.G., 1994, Global data sets for land applications from the Advanced Very High Resolution Radiometer: an introduction. *International Journal of Remote Sensing*, **15**, 3319-3332.

[2] Eidenshink, J.C., and J.L. Faundeen, 1994, The 1-km AVHRR global land data set: first stages in implementation. *International Journal of Remote Sensing*, **15**, 3443-3462.

[3] Wu, C.J., 1989, *Atlas of China Land Use*, China Science Press, Beijing, P.R. China.

[4] Loveland, T.R., J.W. Merchant, D.O. Ohlen, and J.F. Brown, 1991, Development of a land-Cover characteristics database for the conterminous United States, *Photogrammetric Engineering and Remote Sensing*, **57**, 1453-1463.

ACKNOWLEDGMENTS

Jesslyn F. Brown and Bradley C. Reed of the USGS EROS Data Center and Kaiyu Lin and Yutong Liu of CHINA NBSM participated in the project.

This manuscript is currently undergoing formal approval by the United States Geological Survey.

Validating Global Landcover Classification Pattern Using Spatial Resolution-Independent Landscape Metrics.

Robert C. Frohn
and John E. Estes

Remote Sensing Research Unit
Department of Geography
University of California
Santa Barbara, CA 93106
805-893-3845
805-893-3703 fax
frohn@geog.ucsb.edu

INTRODUCTION

The EROS Data Center is in the process of completing a global land-cover classification using 1 km data by mid 1997 and has completed a global landcover classification for 1990 [1]. Although 1 km data is very coarse for land-cover classification, it is the only means by which landcover can be classified at a global scale. A number of validation schemes have been devised and proposed for use in evaluating global landcover classification. These validation schemes are primarily concerned with assessing thematic accuracy. In addition, to the importance of evaluating thematic global classification accuracy, we have recognized the importance of evaluating changes in landscape pattern at coarser scales. Thus, we have developed landscape metrics that are capable of quantifying landscape pattern while being independent of spatial resolution. These metrics include measures of patch shape complexity and landscape fragmentation. The metrics are similar in concept to those proposed for landscape monitoring and assessment by the United States Environmental Protection Agency's Environmental Monitoring and Assessment Program (EMAP). However, the metrics proposed by EMAP are dependent upon a number of factors with respect to remote sensing data, particularly, spatial resolution, level of classification, and sampling geometry, unlike our metrics which are independent of these factors. Following each level of classification the pattern metrics could be calculated to determine if coarser resolution data are capturing the same type of changes in pattern in landcover categories as finer resolution data. Such information would allow researchers and decision makers to establish an error estimate on the use of 1 km data for capturing landscape patterns. It is important to determine if landscape pattern is detected because pattern has many implications on regional and global environmental processes such as biodiversity, animal migration, vegetation dispersal, predator-prey interactions, plant succession, nutrient cycling, and climate [2]. By validating the 1 km data we will be able to better assess the effects of pattern on global processes.

NEEDS FOR GLOBAL VALIDATION TECHNIQUES

Ecological causes of regional and global landcover change and their consequences can occur at a variety of spatial scales. Unfortunately, the ability to monitor, assess, and model these cause and effects is restricted to the scale and resolution at which data are captured. Global and regional assessment requires the use of satellite remote sensing data. There is great need for the quantitative validation of large-scale, coarse-resolution land-cover databases derived from satellite remote sensing [1]. There is also need for development of ecological assessment techniques that operate independently of spatial resolution. Existing metrics [3] for indicators of watershed integrity, biotic integrity and diversity, and landscape sustainability and resilience have shown to be spatial resolution dependent [4] [5]. Their capability is limited in monitoring and assessment with data of different spatial resolutions (e.g. Landsat TM 30m, Landsat MSS 79m, AVHRR 1.1 km). This also limits comparison of results among different studies of varying spatial resolutions. We maintain that many of these needs are caused by a lack of collaboration and sharing of knowledge between the remote sensing and landscape ecology community. Landscape ecology offers remote sensing quantitative approaches to landscape monitoring and assessment. Remote Sensing, on the other hand, offers knowledge of sensor characteristics, sensor/environment relationships, sampling geometry, spatial resolution issues, and data structures that landscape ecologists are often unaware. If properly implemented, satellite remote sensing and landscape ecology metrics can be used to monitor and

0-7803-3068-4/96$5.00©1996 IEEE

assess regional and global landscape/landcover management techniques.

THEMATIC VALIDATION

There are several ways in which finer resolution classifications can be used to assess AVHRR classifications. In the past, comparisons have been made between proportion of landcover between finer resolution data and coarse resolution data [6] [7] [1]. Often these methods have resulted in high accuracies for AVHRR data [1]. Some reports have even gone on to maintain that accuracy increases with coarser resolution data. The reason for such counterintuitive conclusions is that accuracy is evaluated at the resolution level of the coarse data rather than the finer resolution data. Accuracy is often evaluated based on an areal approach as opposed to a site specific approach [7].

We have developed an approach that evaluates accuracy at the level of the finer resolution data. This approach can lead to different interpretations of accuracy. Rather than to aggregate finer resolution data such as Landsat TM 30 m data to a resolution that approximates AVHRR we do the opposite. We subsample the AVHRR data to a nominal resolution of 30m, co-register it to the Landsat data using accurate ground control points collected in the field, and overlay the two images. Subsampling the AVHRR data involves replicating pixels until a nominal resolution of 30 m is reached. Thus, we do not change the proportion nor pattern of landcover in the AVHRR data, but simply the number of pixels. The overlay results in a contingency matrix of correctly versus incorrectly classified pixels. Summary statistics such as percent correctly classified (PCC) and the Kappa statistic [8] [9] can be calculated from each contingency matrix. PCC provides a traditional intuitive overall measure of accuracy. Kappa statistic incorporates the probability that a pixel may be correctly classified randomly and thus is a more rigorous test of accuracy.

VALIDATION OF LANDSCAPE PATTERN

We maintain that validating the pattern of the landscape may be just as important, if not more important, than thematic accuracy. For example, one could have a classification accuracy of 90% for forest between AVHRR and Landsat TM. Yet the forest may be fragmented at the spatial resolution of TM and appear unfragmented at the resolution of AVHRR. The same is true for comparing landscape change. Thus, it is important to make comparisons using landscape pattern metrics.

Two such metrics measure the degree of fragmentation and landcover patch shape complexity and can be used for such comparisons. In comparing landscape patterns at different spatial resolutions it is important that the metrics employed be spatial-resolution independent. Otherwise, one would not know if the changes in metric values were due to changes in spatial resolution or actual pattern or both. In the past, the most popular metrics for fragmentation and complexity in landscape ecology were contagion and fractal dimension [10]. However, Frohn [5] has shown these metrics are very sensitive to spatial resolution, and has developed two improved metrics for fragmentation and patch shape complexity. These are called the patch-per-unit area metric (PPU) and the square-pixel metric (SqP). These are explained in detail in the next section and can be used for validating AVHRR landcover patterns.

IMPROVED LANDSCAPE METRICS

Landscape metrics are important for the assessment and monitoring of changes in landscape pattern. Many ecological processes such as vegetation dispersal, animal movements, plant succession, predator-prey interactions, foraging patterns, nutrient cycling, hydrological regimes, and global biodiversity are affected by changes in spatial patterns of the landscape [2]. Two of the most popular metrics developed have been contagion (a measure of fragmentation) and fractal dimension (a measure of patch complexity). The metrics of contagion and fractal dimension have also been recommended for implementation in EPAs EMAP program [3] [11]. These indices need to be critically evaluated with respect to the sampling geometry of remote sensing data and raster data structures before they are implemented. An initial analysis of these metrics indicates that improved metrics for contagion and fractal dimension can be used that are more sensitive to landscape pattern and insensitive to sampling variability associated with remote sensing data especially, spatial resolution [4] [5] [12] [13].

Fractal dimension does not consider the basic perimeter area relationship of a raster data structure, it has inherent problems with its regression estimation, and does not give consistent results for landscapes with predictable topological shapes. The contagion metric is based on pixel adjacency proportions, and thus very dependent on spatial resolution. The contagion equation itself measures not only clumping but also diversity and thus can give biased estimates depending on the diversity of the landscape. The development of the improved metrics have taken such factors into account such as eliminating the diversity factor in the contagion equation, and considering the perimeter to area relationship of raster data structures for an improved complexity index over that of fractal dimension.

For quantifying landscape fragmentation we contrast contagion with an alternative metric called patch per unit area (PPU) [4]. This being:

$$PPU = m/n * \lambda \qquad (1)$$

where m is the number of patches, n is the number of pixels and λ is a scaling constant equal to the area of a pixel (note that this area could be expressed in any convenient units, i.e. m^2 or ha). PPU is low when the landscape is not fragmented. As the landscape becomes more fragmented PPU increases. Because it is scaled to actual area PPU is not sensitive to measurement resolution in the way that contagion is. As the landscape becomes more generalized due to resampling, PPU decreases in the expected manner. Thus, we believe that being less sensitive to spatial

resolution and more sensitive to landscape pattern, PPU gives a better and more predictable quantification of landscape fragmentation or clumping than contagion.

As an alternative to fractal dimension for quantifying patch shape complexity, we have developed the square pixel metric (SqP) [4]. The square pixel metric considers the perimeter area relationship for raster data structures and normalizes the ratio of perimeter and area to a value between 0 (for squares) and 1 (maximum perimeter (edge) deviation from that of a perfect square). It is given as:

$$SqP = 1 - (4 * A^{1/2} / P) \qquad (2)$$

where A is area and P is perimeter .

The square pixel metric (SqP) is unit-less and insensitive to measurement resolution. SqP also provides an important alternative to fractal dimension because it does not assume a power law relationship between perimeter and area, and thus provides a more effective metric for landscapes which do not exhibit statistical fractal geometry.

CONCLUSION

These metrics by being insensitive to characteristic variation in remote sensing data especially spatial resolution will change predictably as pattern changes. Thus pattern values at different spatial resolutions (e.g. AVHRR 1.1 km and Landsat 30 m) can be extrapolated. Therefore, they are prime candidates for validation of pattern of global landcover classifications by AVHRR 1 km data with finer resolution data such as Landsat TM 30m classifications and verifications. If metric values behaved in an unpredictable sensitive manner, such as contagion and fractal dimension do then their utility as a pattern measure is greatly reduced because one would not know if the metrics were detecting spatial patterns or quantifying characteristic variation in remote sensing data or both. An example for the Sierra Nevada area follows.

The results of changing spatial resolution on the landscape metric PPU in the Sierra Nevada are presented in Fig. 1.

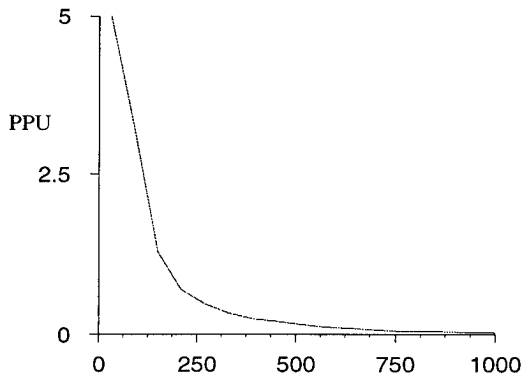


Fig 1 The effects of changing spatial resolution on PPU

PPU decreases at a predictable logistic rate as spatial resolution increases.

ACKNOWLEDGMENTS

Research was funded under NASA Grant NAGW-1754.

REFERENCES

[1] Loveland, T., J. Merchant, J. Brown, D. Ohlen, B. Reed, P. Olson, and J. Hutchinson, 1995, "Seasonal Land-Cover Regions of the United States", Annals of the Association of American Geographers, Vol. 85, No. 2, pp. 339-355.

[2] Turner, M.G., and Gardner, R.H. (editors). 1991. Quantitative Methods in Landscape Ecology, Springer-Verlag, New York NY.

[3] Environmental Protection Agency (EPA). 1994. Landscape monitoring and assessment research plan. EPA 620/R-94/009, Office of Research and Development, Washington D.C.

[4]Frohn, R.C. 1996. Improved Landscape Metrics for Environmental Monitoring and Assessment (in press) Proceedings of ASPRS/ACSM April 22-24 1996 , Baltimore, MD.

[5] Frohn, R.C., McGwire, K.C, Dale, V.H., and Estes, J.E. 1996. Using satellite remote sensing analysis to evaluate a socioeconomic and ecological model of deforestation in Rondonia, Brazil. *International Journal of Remote Sensing.*

[6] Turner, B.L., Koerper, G, Gucinski, H., Peterson, C., and Dixon, R.K. 1993 . Monitoring global change: comparison of forest cover estimates using remote sensing and inventory approaches. Environmental Monitoring and Assessment 26:295-305.

[7] Merchant, J.W., Yand, L., and Yang, W. 1994. Validation of continental-scale landcover databases developed from AVHRR. In Proceedings of the Pecora 12 Symposium, pp. 63-72.

[8] Congalton, R., Oderwald, R., and Mead, R. 1983. Assessing landsat classification accuracy using discrete multivariate statistical techniques. Photogrammetric Engineering and Remote Sensing 54: 593-600.

[9] Rosenfeld, G., and Fitzpatrick-Lins., K. 1986. A coefficient of agreement as a measure of thematic classification accuracy. Photogrammetric Engineering and Remote Sensing 52:223.

[10] O'Neill, R.V., Krummel, J.R., R.H. Gardner, G.Sugihara, Jackson, B., DeAngelis, D.L., Milne, B.T., Turner, M.G., Zygmut, B., Christensen, S.W., Dale, V.H., and Graham, R.L. 1988. Indices of landscape pattern. Landscape Ecology, 1:153-162.

[11 Environmental Protection Agency (EPA). 1996. Mid-Atlantic landscape indicators project plan. EPA 620/R-95/003, Office of Research and Development, Washington

[12] Frohn, R.C. and Estes, J.E. 1996. The assessment and monitoring of landcover change in the Amazon using improved landscape metrics and satellite remote sensing (in press). *Geoinformatic's 1996.*

[13 Frohn, R.C. and G.Menz. 1996. Spatial separability of landcover classes along a vertical transect in the Sierra Nevada using landscape pattern metrics and remote sensing (in press) Proceedings of ASPRS/ACSM April 22-24 1996 , Baltimore, MD.

Using Geoinformation System and Space Imagery to Monitore Environmental Changes in the Aral Sea Ecological Disaster Area

Elena V.Glushko, Andrej V.Ptichnikov, Vladimir S.Tikunov
Geographical Faculty, Moscow State University
Institute of Geography, Russian Academy of Sciences
Moscow, 119899,Russia
Telephone: 7-095-936-14-98; FAX: 7-095-932-88-36
E-mail: tikunov@env.geogr.msu.su

There is a currently considerable interest concerning ecological and environmental problems of the Aral sea disaster zone in the Central Asia. The introduction of a GIS provides a new set of analytical tools and this enabled previously accumulated data to be viewed both as a problem in spatial statistical analysis, and via GIS technology.

The Aral sea GIS is developing in the frame of corresponding UNESCO project. The aim of this project is to provide scientific background for ecological restoration of the most damaged areas in the Aral sea arid region - Amudarya and Syrdarya river deltas.

The Aral sea GIS uses tiered mapping structure that complements the sampling design and Remote sensing land and landscape characterization. Due to the very high rate of environmental changes last 30 years the studied area presents excellent terrain for dynamic analysis and modeling. To do this the GIS incorporates several layers of dynamic maps for the period between 1960 and nowadays, including dynamics of desertification processes, deltaic wetlands and solonnchaks, surface and ground water, soils and vegetation. On this basis, using regression, correlation and factor analysis we are trying to calculate trends of development of certain ecosystems and predict some negative effects of desertification in future.

In the Aral sea GIS project we use ARC/INFO software to input and process vector data, as well as IDRISI to handle space imagery and provide some analytical operations, available only in raster format, and FOX-PRO for data base compilation.

Complex investigations of the Aral Sea region were based on the small-scale black-and-white satellite photos at the scale of 1:2,400,000 taken from the "Salyut" orbital station in 1975-1980 which provide the full coverage of the territory. The use was also made of multiband black-and-white synthesized multispectral images from the "Resurs-F" satellite at the scale of 1:1,000,000 with several times coverage of the study area and at the scale of 1:200,000 for some parts of the area, taken in 1980-1989. Apart from space images numerous publications and cartographic works were analyzed as well as the results of selected land-based studies conducted by the authors. Complex geographical studies of the Aral Sea region within the frame of space monitoring included basic, special and operational mapping of the territory using the space images. The main objective was the interpretation and mapping of present-day landscapes at scales of 1:2,400,000 and 1:1,000,000.

The landscape maps served as a basis for mapping desertification processes, long-term dynamics of geoecological setting, natural decease foci, desertification control measures, at the same scales mainly. Besides, large-scale maps of the present-day landscapes and their dynamics were compiled for key sites using the materials of space and aerial surveys for different time periods at the scale of 1: 200,000 and more as well as the author's land-based observation data.

For computerized processing and thematic mapping survey data were digitized and stored in special databases. Thus the operational compilation of various thematical maps by means of computer plotting devices became possible. First of all basic maps of the present-day landscapes were compiled to be used as a reference for future special mapping. The present-day landscape maps reflect the actual landscape differentiation of the territory with the account of their anthropogenic transformation. Natural landscapes of the Central Kyzyl-Kum are distinguished at the 1:2,400,000 map together with their anthropogenic modifications formed under the influence of long-practised irrigation in the Amu-Darya and Syr-Darya river deltas and valleys, cattle grazing in sandy, solonchak and clay deserts. The landscapes of the Aral Sea dried-off bottom are also distinguished at this map. The maps of desertification processes compiled on the landscape basis characterize the spatial distribution of detrimental processes which occur in different components of landscapes and cause the destructive changes of the environment. The maps show about 30 processes leading to changes of relief, surface and ground water, soil and vegetation cover. The processes are grouped according to their association with drying of sea bottom and deltaic-alluvial plains, pasture overgrazing, irrigation and post-irrigation desertification. A distinct connection between a particular set of processes and certain landscapes and types of land use has been revealed.

Maps of long-term landscape dynamics for the last 30 years reflect the nature and degree of environmental changes under increasing anthropogenic influence. Long-term changes of landscape state and structure have been revealed with the help of dynamic and retro indicators while interpreting many -year series of space images and comparing them with geographical maps of study areas compiled in the early 60-yes of this century. The maps show territories where primary landscapes were formed; where one variant of landscape was replaced by another; where landscape structure has changed within the limits of the same variant of landscape; where properties and certain features of landscape structure have changed;

0-7803-3068-4/96$5.00©1996 IEEE

where no signs of change were identified.

Maps of geoecological setting were compiled on the basis of previously plotted maps. Geoecological assessment was carried within the limits of distinguished landscape units. For each of them the prevailing type of changes has been determined (natural, natural-anthropogenic, anthropogenic) and the main groups of natural-anthropogenic processes were indicated. The degree of changes of the main landscape components was evaluated by 10-points scale using various classifications. The actual trends of landscape changes - restorative, optimizational, digressional - were revealed.

On the basis of above-listed data and with the use of original geoecological classification of present-day landscapes five main categories of landscapes were distinguished: natural, optimized, compensated, depressed and disturbed, as well as their various combinations.

The results of mapping show the existence of a large ecological disaster zone which embraces most of the Aral Sea region including the dried-off sections of the sea bottom, peripheral parts of the Amu-Darya and Syr-Darya river valleys and ancient alluvial plains that divide them. In the Kyzyl-Kum desert three ecological disaster regions are identified: eolian plains in the northern part of the desert, ancient alluvial and eolian plains in the peripheral parts of the Bukhara oasis, and eolian and clayey plains in the south-eastern part of the Kyzyl-Kum desert.

Within the framework of the complex landscape-based mapping the schematic map showing the distribution and dynamics of plague epizooties among rodents was compiled at the scale 1:4,000,000. The use was made of space survey data obtained in different periods and the evidence of the Uzbek plague-prevention station for 1948-1982. The mapping has revealed the regional features of landscape differentiation and dynamics of natural decease foci under increasing desertification. Statistical processing of long-term observation data permitted to determine the typical dynamic series of epizooties in different landscapes. The joint analysis of the results of statistical and cartographical studies allowed to specify the natural and anthropogenic factors of long-term migrations of plague epizooties within the territory of the Kyzyl-Kum desert.

The map of desertification control measures was compiled on the basis of the above-discussed maps at the scale of 1:2,400,000. The recommendations on the implementation of complex measures are based on the existing proposals and regional experience with account of the actual geoecological situation. Within the landscape limits different sets of hydro-, phyto-, land and chemical ameliorations, restoration, socio-economic and research measures are presented. The experience of local implementation of effective measures can thus be taken into account and extended on the whole study area by distinguishing the analogous landscapes.

Multipurpose geoecological studies including mapping and conceptual modeling of landscape functioning and development represent an integrated series of experimental research works on space monitoring with the aim of environmental control and optimization in Middle Asia.

LIMITATIONS FOR MULTISPECTRAL CLASSIFICATION OF TEMPERATE FORESTS - SCALING PROBLEMS OF GROUNDTRUTH AND SATELLITE DATA -

Tobias W. Kellenberger and Klaus I. Itten

Remote Sensing Laboratories (RSL), Department of Geography
University of Zurich, CH-8057 Zurich, Switzerland
Phones: +41 1 257 5162, +41 1 257 5160, Fax: +41 1 362 5227
E-mails: knelle@geo.unizh.ch, kitten@geo.unizh.ch

Abstract -- This paper contributes to the development of a semi-operational forestcover classification method for monitoring the temperate european forest belt, using SPOT-XS or Landsat-TM on an example in Switzerland. Special emphasis is put on spatial resolution and scaling problems. Preprocessing of continuous binary groundtruth data, e.g. forest boundaries is examined. Digital forest cover classifications of SPOT-XS and Landsat-TM data were performed using an automatic parallel-epiped algorithm. All data were geometrically corrected considering terrain induced errors, and radiometrically corrected considering variations of illumination. Both data sets were classified with varying pixel size between 20m (HRV), 25m (TM) and 100m (both). For large scale applications where a 100m cell size is preferred the effects of upscaling on classification accuracy is discussed.

INTRODUCTION

Achieving actual forest coverages over Europe is a main topic in environmental monitoring. At a local scale, experts regularly use forest maps based primarily on ground and airborne surveys. At a continental scale international organizations, dealing with large conservation programs, usually base their decisions on updated forest maps at kilometer resolution and more, derived often from NOAA/AVHRR data. Regional foresters, environment and planning officials have an increasing need for forest maps at scales 1:50'000 to 1:200'000, which are often based on high-resolution satellite imagery.

In relatively flat areas with large and homogeneous patches of forests, such as in the boreal region, successful inventoring was done, using data from operational high-resolution satellite systems such as SPOT-XS and Landsat-TM. In mid latitude rugged alpine terrain however, with its very mixed and splitted forest coverage, varying regionally and in altitude in homogeneity and boundary shape, mapping with the systems mentioned above is severely affected.

The aim of this study is to develop a methodology, which allows an easy, econonomic and semi-operational detection of the forested area in Switzerland and its neighbouring area by means of multispectral, optical satellite data. This method should allow for the production of national and international forest databases with actual forested areas at raster sizes of about 100m.

BASE OF THE STUDY

Testsite

For the development of the method, the test area 'Beckenried', which is situated in the mountainous pre-alps of the Canton 'Nidwalden' in Central Switzerland, was selected. The site nearly covers the area of the Swiss topographic map sheet 1771 'Beckenried' at a scale of 1:25'000. To facilitate the processing and comparison of classifications at different cell resolutions, a smaller section was selected, which can be described completely with pixel sizes 20m (HRV), 25m (TM) and 100m (both). The testsite is dominated by parts of the Lake of Lucerne (25% of the area), a heterogeneous mixture of conifers and deciduous forest trees (30%), and mixed rural meadows with small villages on the border of the lake (45%). Terrain elevations range from 434m to 2404m above sea level with pronounced steep slopes.

Satellite Data

Due to the fact, that the foliage of the various forest types is only fully developed in summer time and due to the negative sun angle influence on cast shadows and illumination during the remaining seasons, satellite data of midsummer was selected. A Landsat-Thematic Mapper scene, dated July 11 1991, and a SPOT-HRV scene, dated June 30 1991 (in multispectral as well as in panchromatic mode) were used.

The Landsat-TM scene is affected by some cumulus clouds in the southern part of the testsite. The data set was preprocessed by the receiving facility of the European Space Agency (ESA) in Frascati, Italy, to level 05 using a 'nearest neighbor' resampling algorithm, which produced up to 3.5% of redundant information in the investigated area due to doubled lines and columns. The doubled lines were eliminated for further processing. Some banding was reduced by means of histogram modification on affected image lines.

The SPOT data set suffers from striping, induced by detec-

0-7803-3068-4/96$5.00©1996 IEEE

tor intercalibration problems. These effects have been corrected using a modified morphological filtering by Bannon and Barrera [1]. The scene is nearly cloudfree, apart from a jet contrail, crossing the investigated area in the southern part from east to west.

Digital Elevation Model

A digital elevation model (DHM25)[1] from the Swiss Federal Office of Topography with a resolution of 25m horizontally and 0.1m vertically was available for the whole testsite. The model was resampled according to the SPOT data resolution to 20m and additionally to 100m cell size, using a 'bilinear' interpolation method. Cast shadow masks as well as illumination data sets were calculated from the elevation model for the time frames of both satellite data sets. The illumination, defined as the cosine of the solar incidence angle, represents the direct solar radiation, hitting a pixel on the ground. It is basic to any radiometric terrain correction and depends directly on the relative orientation of the pixel towards the sun's actual position.

Area Groundtruth

For inventoring the forested area in the testsite groundtruth data by means of a spectral classifier, samples of forests, nonforested and water areas must be available. A continuous area groundtruth is needed to evaluate the pixel-by-pixel accuracies of the classification results. Therefore the green layer of the Swiss Topographic map sheets, at a scale of 1:25'000, was digitized and used as forest groundtruth. This layer represents the dense forest areas but lacks of open forests and regions affected by cartographic generalization (roads crossing the forests, forest patches with a diameter smaller than 25m). The water boundaries were digitized manually from the topographic map sheet.

PREPROCESSING

Groundtruth Preprocessing

The forest and water area groundtruth was converted from vector representation into various raster resolutions and then scaled to different pixel sizes using an area based scaling algorithm. The scaling of the forest area groundtruth from a 10m raster size to 100m resulted in a increasing of forested area of more than 2% (nonforest decreased by 2%, water had no change) [3], [4]. Best forest area groundtruth, with regard to the area and shape in vector representation, can be achieved by converting the vector data into a raster grid, with cell sizes appropriate to the natural main forest boundary variations (e.g. 10m to 15m) and by adding an area based scaling to the final raster resolution.

The forest area groundtruth in raster representation, derived from the topographic map sheets, has been compared visually to the satellite data. Small forest patches were missing in the groundtruth due to cartographic generalization and in the open forest regions at the upper natural tree limit. Therefore a new forest area groundtruth was derived by means of a pixel-by-pixel visual interpretation of the 10m panchromatic SPOT data, visualized on a computer monitor. This new 'visual' groundtruth shows 7.7% more forested areas than the groundtruth based on the topographic map sheets, and is better suited for the comparison with the forest in the satellite data [4].

Geometric Correction of Satellite Data

The satellite data sets used in this study, were geocoded to the rectangular and orthogonal coordinate system of the Swiss topographic maps. The rectification also included geometric correction of relief displacement due to variations in terrain elevation [2]. Landsat-TM data have been geocoded to 25m resolution, SPOT-XS data to 20m and panchromatic data to 10m. Two different resampling methods, 'nearest neighbor' and 'bilinear', have been applied and tested individually for classification accuracy performance. Geocoding the 30m Landsat-TM data into a 25m reference grid, using the 'nearest neighbor' resampling method, does produce up to 32% of redundant pixel information (raw pixel considered twice or more) in the output data. All geocoded satellite data sets were additionally scaled to 100m resolution using an area based scaling algorithm.

Radiometric Correction of Satellite Data

Besides the clouds in the Landsat data and the contrail in the SPOT data, the atmosphere in the testsite was clear without an obvious slicing into different atmospheric layers. Therefore no atmospheric correction was applied, neglecting thus atmospheric influence or adjacency effects. Variations in illumination have been considered by means of a semi-empirical slope-aspect C-correction [5], optimized for forested areas.

FOREST AREA CLASSIFICATION

Classification Algorithm

A modified 'parallel-epiped' method was used in this study. The separation of object classes is based on the signature of object samples. Setting the separation values in different image channels is usually done manually and individually by the operator and therefore not suited for operational use. The modified 'parallel-epiped' algorithm separates the object classes automatically on the base of the maximum difference of cumulative percentage histogram values between two classes in each image band. Separation values and image bands were selected automatically and reproducible [4].

Classification Scheme

The SPOT data has been classified at a size of 20m and 100m pixels, using the multispectral bands as well as multi-

1. Digital terrain model and map data courtesy:
Swiss Federal Office of Topography, 16 February 1996

spectral bands with the added and scaled panchromatic band. Landsat-TM data have been treated at the 25m and 100m level. For all data sets the influence of the two resampling methods (geocoding) and the slope-aspect correction have been treated separately. The forest groundtruth data sets (derived from topographic map and the analog interpretation of satellite data) were used as training sites as well as reference for classification accuracy assessments. The cloud mask, the contrail mask and the cast shadow masks have been applied in all possible combinations to the satellite and groundtruth data. On each separate data set, a one-step classification of forested, non-forested and water area was done. All combinations led to over 2000 classifications or accuracy evaluations, respectively.

Results on High Resolution Level

On a high resolution level (20m SPOT, 25m Landsat-TM) the accuracy of the best classification achieved over 0.81 kappa (Table 1). Using SPOT data with the panchromatic band added, resulted in 7% (mean over all classifications) better kappa accuracy, than using only the multispectral bands. With regard to the Landsat-TM data set an increasing kappa accuracy of 6% was achieved. The fact, that the water boundaries were classified with constant high accuracy (water specific user- and producer accuracy around 98%) in all classifications, shows very clearly, that the kappa coefficient is only influenced by the separation accuracy of the forested and the non-forested areas.

The forest area groundtruth derived from the satellite data by analogous interpretation, suited better than the groundtruth from the topographic map sheet. Kappa accuracy increased by up to 4% and the forest specific user accuracy up to 10% (using the SPOT panchromatic band). Most influence was detected due to open forest areas and small forest patches.

Correction of illumination influenced the classification positively too (+2% increased kappa). The 'bilinear' resampling method in the geocoding process performed always better than the 'nearest neighbor' method (+2% kappa). Treating redundant information in Landsat-TM data separately did not show any significant changes in classification performance.

Table 1: Best classification results of forested areas

Data set	producer accuracy for forest	user accuracy for forest	overall accuracy	kappa coeffi-cient
SPOT-XS (20m)	84.26%	81.61%	88.17%	0.8190
SPOT-XS & -Pan (20m)	91.16%	89.72%	92.99%	0.8942
Landsat-TM (25m)	88.96%	84.19%	90.62%	0.8581
SPOT-XS (100m)	87.27%	83.12%	89.90%	0.8451
SPOT-XS & -Pan (100m)	88.02%	89.71%	92.43%	0.8854
Landsat-TM (100m)	89.41%	87.29%	91.86%	0.8769

Results on Low Resolution Level

About the same classification performance on 100m resolution could be achieved compared to the results on the high resolution level. Using SPOT's multispectral bands with the panchromatic channel added shows again best kappa accuracy (0.885). But using Landsat-TM data, almost the same result is achieved. Due to the fact, that the price for 1 km^2 of SPOT data is four times the price of Landsat-TM data, TM data are the better choice for an operational forest area inventoring on a pixel size of about 100m.

Comparing both forest area groundtruths shows, that the classification results coincide better to the analogous groundtruth (+3% kappa, +5% forest user accuracy). Correction of illumination effects should be done specially on Landsat-TM data (+5% kappa) whereas in SPOT data only little changes were detected. The accuracies achieved proofed, that forest cover classification can be done successfully on a 100m resolution level. Big data sets and computing time on the high resolution level can thus be avoided.

CONCLUSIONS AND OUTLOOK

A compilation of all results, paired with economic considerations, results in a method to detect the forested area of the whole of Switzerland on a 100m raster size by means of illumination corrected Landsat-TM data [4]. The method was recently tested successfully in the large region of the Canton of Zurich in northeastern Switzerland. The accuracy achieved, with regard to the disputable and incorrect forest boundaries on the topographic map, amounted to 0.78 kappa. Summarizing the experience with the proposed method, we believe that this tool will help us to survey and monitor our precious forest resources in Switzerland for the next decade. In the next step, a forest cover classification of the whole of Switzerland is planned.

REFERENCES

[1] G.J.F. Banon and J.Barrera, "Morphological Filtering for Striping Correction of Spot Images", Photogrammetria 43, Amsterdam, 1989, pp. 195-205.

[2] K.I. Itten and P. Meyer, "Geometric and Radiometric Correction of TM-Data of Mountainous Forested Areas", IEEE Transaction of Geoscience and Remote Sensing, Vol. 31, No. 4, 1993, pp. 764-770.

[3] T.W. Kellenberger, St. Sandmeier, and K.I. Itten, "Comparison of forest / non-forest classification in raw and geometrically corrected images of an illumination corrected SPOT data set", Proc. of 6th International ISPRS Symposium on Physical Measurements and Signatures in Remote Sensing, Val d'Isère, France, 1994, pp. 85-92.

[4] T.W. Kellenberger, "Erfassung der Waldfläche in der Schweiz mit multispektralen Satellitenbilddaten - Grundlagen, Methodenentwicklung und Anwendungen", Ph.D. Thesis, Univ. of Zurich, 1996, in press.

[5] P. Meyer, K.I. Itten, T.W. Kellenberger, St. Sandmeier and R. Leu, "Radiometric Corrections of Topographically Induced Effects on Landsat-TM Data in Alpine Terrain", ISPRS Journal of Photogrammetry and Remote Sensing, Vol. 48, No. 4, 1993, pp. 17-28.

Practical SAR Orthorectification

Leland Pierce, Josef Kellndorfer, Fawwaz Ulaby

The University of Michigan, Radiation Lab
Ann Arbor, MI 48109-2122 USA
FAX: +1-313-747-2106 email: lep@eecs.umich.edu

Lynne Norikane

Vexcel Corp.
Boulder, CO 80301 USA
FAX: +1-303-444-0470 email: lynne@vexcel.com

ABSTRACT

SAR orthorectification procedures have been implemented at major processing facilities for several years, but only recently has workstation computer speed increased to a level where it is now practical for the SAR researcher to have their own orthorectification capability in-house. The present article presents our efforts to implement such a program and the practical lessons learned in doing so.

Orthorectification encompasses all the corrections needed to precisely align a SAR image with a map, accounting for actual topography. However, there are several other operations that are required in order to produce radiometrically corrected data during the orthorectification process: calculating layover and shadow masks, local incidence angle, and calibration to σ^0. Without calibration the image is far less useful in further processing, such as in land-cover classification and biophysical parameter estimation.

Specifics of our effort to apply this to ERS PRI data, and to JERS level2.1 data are presented, including an assessment of how well it performed.

1. INTRODUCTION

This paper is not intended to add any theoretical insight into the SAR orthorectification process. The best reference to the general theory is in Curlander and McDonough [1]. Instead, its goal is to present a practical strategy for implementing a computer program to accurately and efficiently carry out the orthorectification process. There are many parts to the process and each will be treated with the needs of accuracy, efficiency, and practicality in mind. The two main steps in the whole process are: (1) Pre-processing, including DEM (Digital Elevation Model, or raster elevation map) acquisition, parameter transformations, and tie-point collection; (2) Orthorectification, including updating the geocoding using the tie points, generation of local incidence angle and layover and shadow masks, and image generation, including calibration to σ^0. Each of these steps will be discussed in sections 2 and 3, with section 4 presenting some numerical results and summarizing a few very important points.

2. PRE-PROCESSING

This step is a basic requirement. It would be nice if it could be avoided, but it can't, yet. The three major steps are outlined below. Involved are: (1) Acquire DEM, (2) Parameter transformations, and (3) Tie point collection.

2.1. DEM Acquisition

Acquiring a DEM is basic for orthorectification to succeed since the terrain effects is what it corrects for. However, there is no universal method to obtain one for an area of interest. Eventually SAR interferometry holds the promise of generating a DEM and supplying the SAR data too, but not yet. The DEM data used in this study was generated from USGS (U.S. Geological Survey) DLG (Digital Line Graph) hypsography data, digitized at a 1:100,00 scale. This was not an easy process, but the details are beyond the scope of this paper. When finished, the DEM was a raster image in the UTM (Universal Transverse Mercator) projection using the NAD27 ellipsoid (as a model for the earth), with a 25 meter pixel size. Every user will have to devise their own procedure to acquire a DEM.

0-7803-3068-4/96$5.00©1996 IEEE

2.2. Parameter transformations

Parameter transformations is the next important, but user-specific, problem. The orthorectification procedure requires certain inputs that may not be specified in the input SAR data file. An algorithm must be devised for each, different, SAR format that transforms the given parameters into the required parameters. Sometimes the geometry of the image itself must transformed as well. As an example, the georeferencing information in the ERS-1 PRI product from the German processing facility (DLR) contains the geographic coordinates of the four corners of the image, and five samples from the sensor orbit. The JERS-1 data provides geographic coordinates of the first, mid, and last pixel on every line of the image. When writing the orthorectification program a choice between these two must be made and a translation from the other must be programmed. The image geometry may need to be rotated so that the azimuth and range directions are the same as another format. The image may need to be transformed from slant to ground-range. This parameter transformation step can be very time-consuming, but the alternative is to completely re-write the orthorectification program for each format, which would be even more work.

2.3. Tie point collection

Tie point collection is the process where a user finds points in the raster image whose geographic coordinates are known. For example, road intersections, or places where rivers and roads intersect, are common tie points. This is facilitated by using USGS DLG data from the site that gives roads, rivers, pipelines, and other features. This process is required for the end-product to be accurately transformed, although it need not be a manual procedure, as is assumed here. It can be very slow and painstaking work to collect a set of 5 – 10 points that are discernable in both the SAR image and in the DLG data, and a small error in just one point can effect the entire image. It is usually possible to perform this step successfully in one or two full-time days for a single SAR image.

Now the orthorectification procedure can be performed.

3. ORTHORECTIFICATION

At this stage, a few general comments are in order concerning the sequence of events in the ortrhorectificaion procedure that is described in the following subsections. One of the most critical decisions to make is what direction to warp: from DEM to SAR or SAR to DEM. For image generation the result is to be a raster image of the same size as the DEM, and so sweeping through the DEM pixel-by-pixel to fill in values for each one is the best way to go. For layover and shadow determination it makes more sense to stay in the geometry of the sensor and to determine where in the DEM one is looking. This involves warping in *both* directions. Warping in only one direction would be more efficient, but it would make one of the preceding operations extremely difficult to code, which is not worth it. So the strategy used here is to use the most appropriate direction for each operation.

3.1. Inputs:

The SAR image must be ground-range with early-time at the top and near-range at the right, with each line georeferenced at its start, middle, and end, using a particular ellipsoid that is specified. The DEM is georeferenced using a certain, specified, ellipsoid and the elvations are specified, in general, relative to a different ellipsoid. The slant range to the first and last pixels in each line are required in order to determine the orbital position of the sensor. There are several other parameters needed, but these are the most critical and often the ones that are missing or specified differently between the data sets in different formats and from different sensors.

3.2. Step 1: Refine georeferencing with tie points

Using the original geocoding, first calculate the sensor position for each line in the SAR image. Transform each DEM tie point to a SAR pixel using: (1) geocoding, (2) azimuth correction, (3) range correction. Calculate the offset of this result from the SAR tie point. Use the average offset from all the tie points to update the georeferencing with a simple translation.

3.3. Step 2: Determine Arbitrary Warp

Re-calculate the sensor positions based on the new georeferencing information. Warp each tie point again, and use resulting offsets to calculate a low-order warp (polynomial in x and y) to apply as a last step in the orthorectification procedure for each point. This is a way of accounting for residual errors in the sensor positioning. Other methods are possible, but this is simple and it works well.

3.4. Step 3: Warp from SAR to DEM

In order to determine the local incidence angle and the layover and shadow masks the best route is start with a pixel in the SAR image and warp to the DEM. This procedure is applied as the inverse to that used in step 1 to determine which DEM pixel is being imaged, and then the calculations are done for the three parameters of interest. Calculating layover and shadow are very simple with this algorithm and quite complex were one to start with a DEM pixel and solve for the SAR image pixel. Another paper [2] goes into more detail on this subject. Without the local incidence angle calibration is impossible and so it is calculated at this stage. It is also saved as an image channel, using the first 6 of the 8 bits in a byte, along with 2 bits specifying whether this pixel has experienced layover or shadowing during the imaging process. [3]

3.5. Step 4: Warp from DEM to SAR

For each pixel in the DEM the geocoding information is used to make a first guess as to the SAR data that belongs there. Then the azimuth correction is applied, followed by the range correction, resulting in a very good estimate of the correct SAR pixel. Lastly, the warp is applied to get a few more pixels of accuracy. The resulting image data is then interpolated and calibrated to σ^0.

4. RESULTS AND CONCLUSIONS

The algorithm presented here has achieved an accuracy better than 50 meters across an entire image, with most errors usually less than this. Even when applied to images containing high relief (see point #6 below for the example used here) this accuracy still holds. Important factors are:

1. Accurate geocoding: original geocoding by data provider plus tie points.

2. Precise geocoding within the image: This involves the use of a sixth-order polynomial fit of the provided geocoding information to allow accurate determination of the coordinates of SAR image points between the geocoding locations. Using a simple linear or bi-linear fit is not sufficient.

3. Slant Range: calculate via differences in coordinates of sensor and ground point. Other methods don't require sensor location, but are more complicated and less accurate.

4. Coordinate Conversions: converting between the different ellipsoids is accomplished using the Earth-Centered System (ECS) which can be used as an intermediary between geographic coordinates referenced to different ellipsoids. Algorithms exist for going both directions and do not require any iteration.[4]

5. Range Correction, of course.

6. Azimuth Correction: While it may be quite small, less than a pixel even, for sites with low relief, this correction is critical in mountainous areas. Just how critical? In one experiment, this correction was turned off and the resulting tie points were 650 meters off in azimuth, as compared to less than 30 meters when using the correction. This was in area with height variation from 1420 meters to 3050 meters.

One other consideration in the practicality of any computer program is speed. This algorithm can orthorectify an entire ERS-1 image to a 25 meter resolution DEM in less than 12 hours. That's overnight. So one can collect tie points in the day and orthorectify at night. An important part of making this program fast enough is reading the data files efficiently. Since this program often reads from relatively random spots in the data files, a special routine is used to read by blocks and deletes those blocks only when they are no longer needed. This makes the program more complex, but the program runs significantly faster using this strategy. How much faster? In an experiment regular reads were used instead, and the program took 120 hours or so to finish. Hence the block-reading strategy gives a speed-up of ten times. Without a strategy like this the program would be prohibitively slow.

Anyone interested in obtaining software of this kind, or wanting more information about these programs should contact Vexcel Corp. (info@vexcel.com, or http://www.vexcel.com). The authors have developed specialized codes for ERS-1 data from Gatineau, Canada in MLD format, ERS-1 data from DLR in PRI format, and JERS-1 data from the Japanese in Level 2.1 format. There are also programs for SIR-C/X-SAR data that supports all the formats, but does not yet calculate the local incidence angle or layover/shadow masks.

5. REFERENCES

[1] Curlander, John C., and Robert N. McDonough, Synthetic Aperture Radar: Systems and Signal Processing, Wiley: New York, 1991.

[2] Kellndorfer, Josef, M. Craig Dobson, and Fawwaz Ulaby, "Geocoding and Classification of ERS-1/JERS-1 Composites," *Proc. 1996 Intl. Geosci. and Rem. Sens. Symp. (IGARSS'96)*, Lincoln, Nebraska, May, 1996.

[3] Meier, Erich, Urs Frei, Daniel Nüesch, "Precise Terrain Corrected Geocoded Images," p. 184, in: Schreier, Gunter, editor, SAR Geocoding: Data and Systems, Wichmann: Karlsruhe, 1993.

[4] Frei, Urs, K. Christoph Graf, and Erich Meier, "Cartographic Reference Systems," p. 219, in: Schreier, Gunter, editor, SAR Geocoding: Data and Systems, Wichmann: Karlsruhe, 1993.

OPTIMIZATION OF THE TIE–POINTING PROCEDURE FOR THE TERRAIN CORRECTION OF SAR DATA

A. Roth, W. Knöpfle, M. Matschke

German Remote Sensing Data Centre (DFD)
German Aerospace Research Establishment (DLR)
D–82230 Oberpfaffenhofen, GER
Tel: +8153–28–2706 Fax: +8153–28–1445
email: roth@dfd.dlr.de

1. Abstract

Usually tie–points are manually derived from map sheets. This time consuming process requires a significant part of the overall terrain correction process. Additionally it hampers the automation of the SAR–orthorectification. Therefore an autocorrelation method was implemented for DFD's operational SAR geocoding system GEOS. It considers tie–point chips as reference. Further improvements can be achieved by considering a bundle block adjustment. The advantages are the reduction of tie–points required per scene and the ability to span areas without any reference for geolocation information. GEOS is currently supplemented by such a technique.

2. Introduction

Geocoding including terrain correction is a key processing of SAR data to enable their ingestion into global and regional information systems. Therefore terrain correction is offered as a service by value adding industry and within some missions like ERS and SIR–C/X–SAR it is even a standard product delivered by central processing and archiving facilities.

A parametric approach also known as radargrammetic model is well established and already allows a high degree of automation. But the limited determination accuracy of the imaging parameters orbit, range and azimuth timing requires an adjustment. This procedure is similar to the conventional photogrammetric approach, replacing the angular measurements by the "orientation" parameters azimuth, range and Doppler frequency. Up to now the interactive improvement of the imaging parameters and the product resampling are separate subtasks of the total process. But the regularity of the SAR imaging technique and the precision of the prior information indicate further automation capability.

Image matching can be applied to substitute the manual tie–point determination. Several techniques mainly developed for optical data are explained in the literature. The procedure implemented at the German Remote Sensing Data Centre is described in the following chapter.

Bundle block adjustment is today an accepted photogrammetric technique for determining the orientation resp. imaging parameters as well as coordinates of distinct points. Recent developments aim at it's adaptation to SAR data which will be presented in section 4.

3. Automated Tie–Pointing

A completely automated orthorectifaction system would allow a high precision bulk processing of SAR data. Precondition is beside the digital elevation model the availability of tie–points. In general their ground location is derived from maps. This leads to the following criteria being applied for suitable tie–points (see also in [1]) :

1. points must be identifiable in the SAR imagery,
2. points must be identifiable in the map,
3. the position of the points should be accurate enough for the adjustment,
4. points should cover the image as well as possible.

Assuming that the ground position can be delivered by other sources this list can be enlarged by

5. points should be distinct for supporting efficient image matching,
6. points should possibly be suited for multi–image–matching,
7. points should lie in as many overlapping images as possible.

3.1. Conceptual Aspects

The goal is to replace the time consuming manual tie–point measurement by an automatic image matching. The actual data set (in the following named as slave image) which shall be orthorectified is correlated with a set of reference points. These ground control points are determined in a "training phase", meaning that at least one master image needs to be treated manually. Based on the operator defined features tie–point chips are extracted and stored in a ground control point data base.

0-7803-3068-4/96$5.00©1996 IEEE

Fig. 1 shows the module flow of GEOS for a SAR terrain correction process. The shaded functions are relevant to this paper. Part of the process initialization is a search for tie–point candidates. The coverage of the slave image with ground control points is plotted. The operator decides whether additional manually tie–pointing is required. In any case after the image matching the adjustment is performed interactively. After the terrain correction the correlation and adjustment results are entered into the data base annotation records. New ground control points are stored in the data base as well.

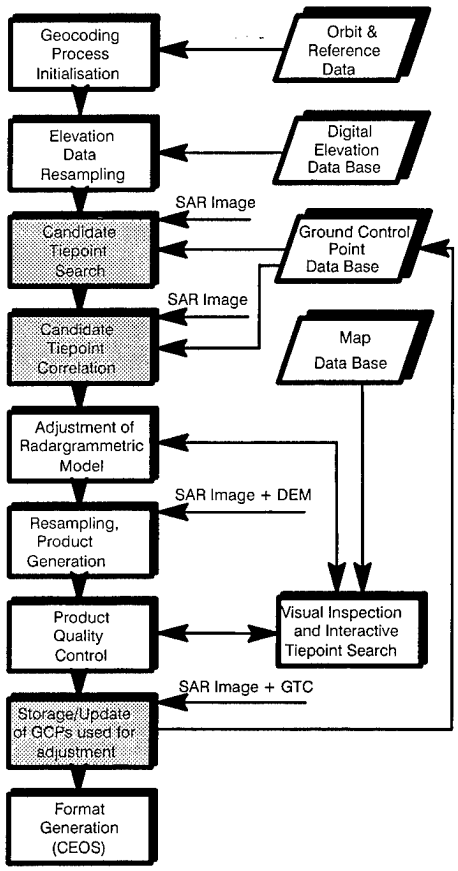


Fig. 1: GEOS Module flow for SAR terrain correction

3.2. Ground Control Point Data Base

Heart of this automation is the Ground Control Point Data base (GCP–DB). Approx. 6000 points covering Central Europe have been registered so far. Each location corresponds to a raster of 99 x 99 x 16 bit pixel values located around the point. Together with the image chip the geographic location, height and annotations are stored. The annotation contains information such as mission id, slant/ground range source product id, ascending / descending orbit mode, location within the master SAR scene, tie–point classifier and counters for successful usage and re–usage. A detailed description of the data base is given in [2].

3.3. Tie–Pointing Procedure

By means of a grid raster item 4 of the point criteria is achieved. For each data base derived ground control point the position in the slave image is calculated by the geolocation algorithm as described in [3]. The precision of the initial parameters determines whether a coarse registration must be performed. The accuracy of ERS, the main data source for GEOS, allows to ignore this additional step [6].

Due to the SAR inherent effects, such as speckle, simple cross correlation approaches fail in most cases. Therefore a phase correlation is performed in the frequency domain [7]. Prior to the Fourier transformation the tie–point chips are filtered to reduce noise. After the inverse Fourier transformation the position of the correlation maximum defines the shift vector. The whole correlation process is repeated with varying window sizes to automatically check the stability of the correlation result.

3.4. Discussion

The main achievement of the automation procedure becomes evident when studying the production of terrain corrected products (GTCs) at the German Processing and Archiving Facility. The average time for tie–pointing dropped by a factor of 4. Today approx. 40% of all ERS–GTCs are produced automatically. 55% require additional and 5% completely new manual tie–pointing.

Nevertheless discussing the presented procedure one should keep in mind that it is based on tie–points ingested during a training phase. This means they were measured manually. An operator automatically follows the criteria 1,2 and 3 of chapter 3. Mainly man made features are precisely mapped and clearly to identify in the SAR image. For a human operator the surrounding of the point is only a secondary information, but it significantly affects on the autocorrelation result; e.g. season and weather might change the appearance of a point in the slave image drastically. Therefore the availability of a sufficient number of tie–point candidates is required.

4. Bundle Block Procedure

The procedure described in the previous chapter processes each product separately. Bundle block adjustment techniques developed and applied for conventional aerotriangulation purposes are able to handle several images simultaneously. The precondition is that overlapping areas exist between adjacent data sets. The benefit of bundle block adjustment is that the required number of tie–points per individual image is significantly reduced.

For an absolute orientation the tie–points distributed over the entire area of the block are used. The combining between the individual scenes is performed based on so called homologue points. These homologue points fulfill all criteria of chapter 3, except item 2. Only their image

coordinates are required. Output of the bundle block adjustment are the improved imaging parameters and as a by-product the coordinates of the homologue points. After a successful geocoding these points can be entered into the GCP-DB as further ground control points.

4.1. Processing Scheme

Ref. [5] adapted the bundle block technique for SAR stereoscopy. Recent developments aim at it's integration into DFD's operational SAR geocoding system GEOS. Fig. 2 shows the module flow diagram. At first the queued products are inspected concerning their coverage. Also a combining with already geocoded products is possible. The inspection results in a overview plot which is used for the final bundle block definition. In a loop each data set is prepared separately. Then tie- and homologue points are prepared. An automatic procedure for homologue point determination is currently developed [4]. Afterwards the imaging parameters as well as the coordinates of the homologue points are adjusted simultaneously. The final products again are processed separately in a loop.

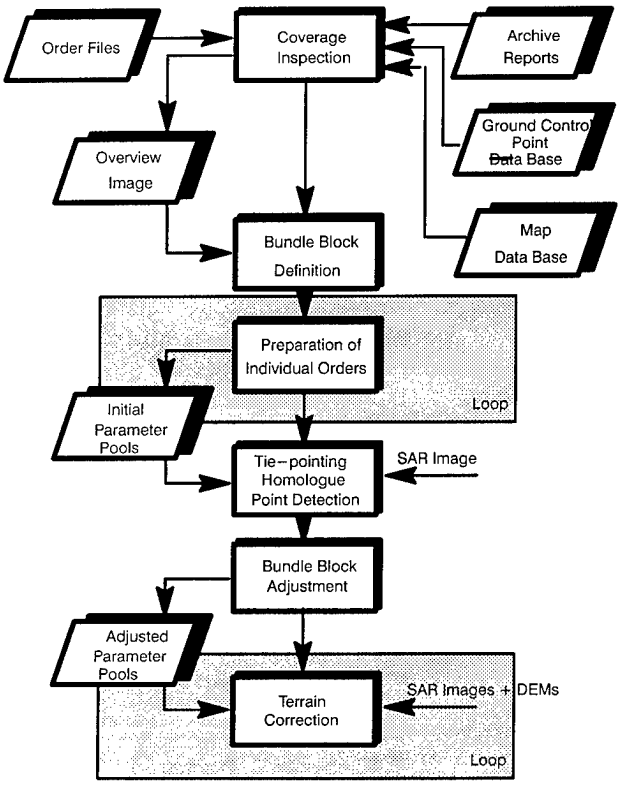


Fig. 2: Module flow for bundle block adjustment

4.2. Results

The bundle block procedure is tested in two steps. The first concentrates on the handling of relatively small blocks (max. 3 x 3 adjacent ERS scenes). The second phase will deal with the large area aspects.
The first results confirm the bundle block adjustment capability with SAR data on principle. Comparable results to individual scene processing concerning the product quality could be achieved. The tests also demonstrate that bundling the processing of adjacent scenes significantly improves the throughput. The interactive identification of homologue points is appr. 8 times faster then a manual tie-pointing and holds further automation abilities. Additionally the overall number of ground control points can be reduced equivalent to the number of scenes.

5. Conclusions

An autocorrelation of SAR-data based on tie-point chips leads to comparable results to a manual treating regarding the image quality. However a significant throughput enhancement could be achieved. Precondition is the availability of a sufficient number of points due to seasonal changes of their surrounding.

Bundle block adjustment improves the SAR-orthorectification further. This is valid for speeding up the entire process, but also to enlarge the area for terrain correction capability.

6. References

[1] W. Förstner: "Matching strategies for point transfer", Photogrammetric Week'95, Fritsch/Hobbie (Eds.), Wichmann Verlag, Karlsruhe, pp. 173-183, 1995

[2] W. Knöpfle, G. Schreier, H. Schumacher, "Image processing and geographic data bases for SAR geocoding", SAR Geocoding: Data and Systems, Schreier (Ed.), Karlsruhe, Wichmann Verlag, 1993, ch. 6, pp. 235-254

[3] E. Meier, U. Frei, D. Nüesch, "Precise terrain corrected geocoded images", SAR Geocoding: Data and Systems, Schreier (Ed.), Karlsruhe, Wichmann Verlag, 1993, ch. 6, pp. 173-186

[4] J. Raggam, A. Bauer, W. Hummelbrunner, "Applicability of automatic tie-pointing for geocoding and mosaicking of overlapping SAR images", to be published in Proc. of IGARSS'96, Lincoln, USA

[5] J. Raggam, D. Strobl, W. Hummelbrunner, A. Almer, "ERS-1 SAR Stereoscopy", Technical Note ERS-D-TN-A/06/93, Graz, 1993

[6] A. Roth, T. Hügel, D. Kosmann, M. Matschke, G. Schreier, "Experiences with ERS-1 SAR geopositional accuracy", Proc. of IGARSS'93, Tokyo, Japan, pp. 1450-1452, 1993

[7] G. Strunz, W. Knöpfle, A. Roth: "Automation of the tie-pointing procedure for the geocoding of satellite images", International Archives of Photogrammetry and Remote Sensing, vol 30, part 3, pp. 793-800, 1994

Geocoding for Classification of ERS/JERS-1 SAR Composites

Josef M. Kellndorfer, M. Craig Dobson, Fawwaz T. Ulaby

The University of Michigan, Radiation Lab, EECS Dept.
Ann Arbor, MI 48109-2122 USA
FAX: +1-313-747-2106 email: josefk@eecs.umich.edu

ABSTRACT

Using combined SAR image data acquired by the Japanese JERS-1 (L-band, hh-polarization) and the European ERS-1 (C-band, vv-polarization) yields excellent classification results. An important preprocessing step prior to classification is the geometric and radiometric calibration of the image data from each instrument. In order to match and radiometrically calibrate JERS-1 and ERS-1 radar images the geocoding of the scenes using terrain height information is indispensible. Therefore the generation of digital elevation models (DEM) and vector/point data for the search of ground control points is necessary. An invaluable data resource is made available on-line on the Internet through the US Geological Survey (USGS). Using DEM data, the sensor/target geometries are analyzed to derive the local incidence angle and determine layover and shadow regions from the DEM data. Layover and shadow regions need to be determined for both JERS-1 and ERS-1 scenes, and than excluded from the classification procedure. The radiometric information in both scenes needs to be calibrated using area correction terms derived from the local angle of incidence.

This paper discusses the generation of DEM's from USGS data, the generation of layover/shadow mask and local incidence angle maps, as well as the radiometric correction for ERS-1/ JERS-1 SAR data at the University of Michigan.

1. INTRODUCTION

Combining image data acquired by the European ERS-1 and Japanese JERS-1 satellites enables satellite data based land cover classification in a promising new way. If SAR data are accurately calibrated, than a physically based classifier is applicable globally and single scene training should no longer be necessary [1, 2, 3].

To create multi-sensor datasets for different test sites, which should enable studies to compare radar backscatter in equal and various ecological regions and for multi-temporal studies, precise geometric and radiometric calibration of the SAR data is an important preprocessing step. In recent years programs have been developed to allow accurate geocoding of SAR images [4, 5] and research has been conducted by several groups to radiometrically correct radar images for terrain induced distortions of the backscattering coefficient [6, 7]. Terrain height information is indispensible to achieve high geometrical and radiometrical accuracy from the calibration process.

This paper describes the efforts at the University of Michigan to geocode and calibrate JERS-1 Level 2.1 and ERS-1 PRI SAR data using available USGS data and a software package which has been developed in cooperation with the Vexcel Corp. [8].

2. DEM AND DLG DATA FROM THE USGS

Through the US Geological Survey (USGS) a valuable datapool of thematic vector and raster data is available for the continental US and parts of Alaska at different scales. Recently a hypsography layer was added to the 1:100,000 Digital Line Graph (DLG) data. As of today, for the entire US a complete coverage of roadlayers, hydrology layers and miscellaneous thematic layers is available, whereas the coverage of the hypsography data is almost complete.

From the 1:100,000 hypsography DLG data a raster DEM can be produced through vector/raster gridding with subsequent interpolation techniques. The algorithm we used in the PCI software package is described in [9]. For the collection of ground control points the road and hydrology vector data are another useful dataset. Both datasets are available on-line via anonymous-ftp *edcftp.cr.usgs.gov* or at the Internet adress: *http://edcwww.cr.usgs.gov/doc/edchome/ndcdb/ ndcdb.html.*

A comparison of geocoding results using DEMs generated from the 1:100,000 DLG hypsography data instead of 1:250,000 DEM data (nominal resolution 3 Arcsec.), both resampled to 25m resolution showed great improvement of the orthorectification, of the detection of layover and shadow regions as well as in smaller errors in absolute location.

3. LAYOVER, SHADOW MASKS AND LOCAL INCIDENCE ANGLE MAPS

When analyzing SAR image data, layover and shadow regions need to be determined and excluded from land cover classification. Different algorithms for the generation of layover and shadow maps from a DEM are described in [10] and [11].

The algorithm implemented in the Vexcel/University of Michigan geocoding package, differs from these algorithms and works in two steps:

0-7803-3068-4/96$5.00©1996 IEEE

Step 1: Layover and shadow masks are generated in the image geometry. This is done by determining for a complete iso-azimuth line the slant ranges and local look angles to each range bin as calculated using DEM data transformed to the image domain. Once all values for one iso-azimuth line are calculated, all layover regions are determined by looping twice thru the line from near to far range. In the first loop, for each layover region the slant ranges for the begining and end of the layover region are recorded. The beginning of a single layover region is marked by a decrease of the slant range. The end of a layover region is marked by the next occuring slant range which is higher than the slant range found before the beginning of the decrease. This marking of begin and end is necessary, since within the layover region multiple increases or decreases can occur. During the second loop all range bins falling within these begin and end marks are determined as layover. The two loop procedure is necessary to detect passive layover regions which are actually laid–over from active regions, as well.

Shadow regions are marked during the second loop, as regions where the local look angle is smaller than the constantly updated highest look angle found.

During Step 1 the local incidence angle (LIA) is calculated as described in [12] and stored in a LIA-map in the image domain.

Step 2: During the actual procedure of geocoding, the radar image is mapped from the image domain to the DEM geometry. For each image pixel found to be mapped to a DEM cell, the layover and shadow masks as well as the LIA are looked up and a new byte for each DEM pixel is coded as proposed in [11] and written to a "Layover, Shadow, LIA"-output channel.

Figure 1 shows layover and shadow maps generated during the geocoding procedure for the Monzano Mountains, New Mexico for JERS-1 (C) and ERS-1 (D). They were generated from a DEM (A), which was produced from the 1:100,000 hypsography vectors. The elevation in the area ranges from 1600m (dark left part) to 3000m (white). It can be seen, that almost no shadow is found in the ERS-1 image, whereas the effect of layover is much stronger in the ERS-1 image than in the JERS-1 scene. This can be explained through the different look angles of JERS-1 (35°) and ERS-1 (20°). Figure 1(B) shows the combined Layover/Shadow mask, which determines the final area to be excluded from classification.

4. RADIOMETRIC CALIBRATION OF JERS-1 AND ERS-1 DATA

During the geocoding procedure the JERS-1 and ERS-1 data will be calibrated adding an correction term for the local incidence angle to the calibration equations.

The delivered ERS-1 PRI scenes are corrected for antenna pattern and range spreading loss by the processing facility. Therefore the correction for local incidence angle and image replica power adjustment needs to be done using the following equation [13]:

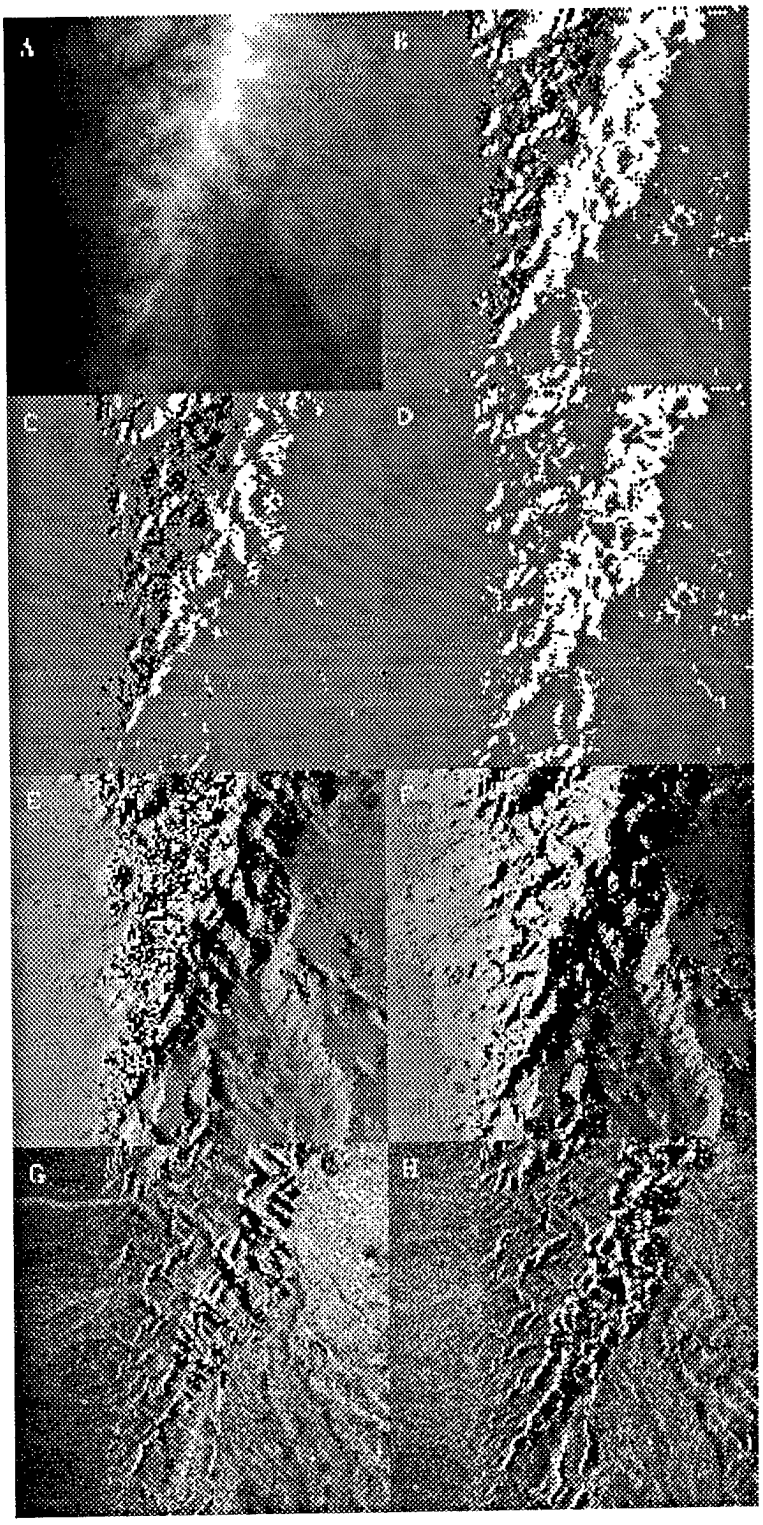


Figure 1: Monzano Moutains, New Mexico: (A) DEM, generated from USGS 1:100,000 DLG hypsography vector data. Layover(white)/ shadow(black) mask for (B) JERS-1 and ERS-1 combined, (C) JERS-1 alone and (D) ERS-1 alone. Local incidence angle maps for JERS-1 (E) and ERS-1 (F). Geocoded, calibrated JERS-1 (G) and ERS-1 (H) SAR images, both acquired during a descending pass, look direction to the west. The area covered is 12.8km × 12.8km.

$$\sigma^0 = \frac{< \mathrm{I} >}{\mathrm{K}} \frac{\sin(\alpha_{DEM})}{\sin(\alpha_{ref})} \frac{\mathrm{IRP}}{\mathrm{RRP}}$$

where: I = Intensity ((Digital Number)^2), K = Calibration constant, α_{DEM} = local incidence angle calculated from the DEM, α_{ref} = reference incidence angle, (23°), IRP is the Image Replica Power, RRP is the Reference Replica Power (205229).

For JERS-1 no replica power adjustment is necessary, since JERS-1 has an automatic gain control (AGC) aboard. Unlike the ERS-1 PRI data, the JERS-1 Level 2.1 SAR images are already corrected for the local incidence angle. However, this is done only for an ellipsoidal surface and not for the "true" local angle of incidence as derived from a DEM. Hence, calibration of JERS-1 SAR data is performed as follows: Assuming, the local incidence angle correction for the ellipsoid was done using the term $\sin(\alpha_{ELL})/\sin(\alpha_{ref})$, following equation can be applied to calibrate the JERS-1 data:

$$\sigma^0 = \frac{< \mathrm{I} >}{\mathrm{K}} \frac{\sin(\alpha_{DEM})}{\sin(\alpha_{ELL})}$$

where α_{ELL} = local incidence angle calculated from the Ellipsoid.

Figure 1 E,F show the local incidence angle maps for JERS-1 and ERS-1. The local incidence angles outside the layover and shadow areas ranged from 30° to 57° for JERS-1, and from 7° to 40° for ERS-1. This results in correction terms from -1.1dB to +1.2dB for JERS-1, and from -5.0dB to +2.2dB for ERS-1.

The final geocoded and calibrated JERS-1 and ERS-1 images are shown in Figure 1 G,H. Layover and shadow regions are not masked in these images.

5. CONCLUSIONS

It was pointed out that DEM data at a scale of 1:100,000 can be generated for almost the entire US from USGS on-line vector data. The generation of layover and shadow masks as well as the calculation of the local incidence angle for radiometric calibration as performed at the University of Michigan was described. Differences in the occurence of JERS-1 and ERS-1 layover and shadow regions were explained through the different look angles of the sensors. The combined layover and shadow regions need to be excluded from classification using radar signatures from both sensors.

6. REFERENCES

[1] Dobson, M.C., L.E. Pierce, F.T. Ulaby, "Konwledge-Based Land-Cover Classification Using ERS-1/JERS-1 SAR composites" *IEEE Trans. Geosci. and Remote Sensing*, Vol. 34, No. 1, Jan. 1996, 83–99.

[2] Kellndorfer, J.M., M.C. Dobson, F.T. Ulaby, "Regional Stability of an ERS/JERS-1 Classifier," *1996 Int. Geosc. and Remote Sensing Symp. (IGARSS'96)*, May 1996, Lincoln, Nebraska, USA.

[3] Kellndorfer, J.M., L.E. Pierce, M.C. Dobson, F.T. Ulaby, "Temporal Stability of an ERS-1/JERS-1 SAR Classifier," *1995 Int. Geosc. and Remote Sensing Symp. (IGARSS'95)*, pp 910–912, July 1995, Florence, Italy.

[4] Curlander, J.C., R.N. McDonough, *Synthetic Aperture Radar - Systems and Signal Processing*. John Wiley and Sons, Inc., New York, 1991.

[5] Schreier, G., editor, *SAR Geocoding: Data and Systems*. Wichmann, Karlsruhe, 1993.

[6] Bayer, T., R. Winter, G. Schreier, "Terrain Influences in SAR Backscatter and Attempts to Their Correction," *IEEE Trans. Geosci. and Remote Sensing*, Vol. 29, No. 3, May 1991, 451–462.

[7] Holecz, F., E. Maier, D. Nüesch, "Postprocessing of Relief Induced Radiometric Distorted Spaceborn SAR Imagery," pp.299–352, in: Schreier, G., editor: SAR Geocoding: Data and Systems, Wichmann, Karlsruhe, 1993.

[8] Pierce, L.E., J.M. Kellndorfer, F.T. Ulaby, "Practical SAR Orthorectification" *1996 Int. Geosc. and Remote Sensing Symp. (IGARSS'96)*, May 1996, Lincoln, Nebraska, USA.

[9] Carrara, A., "Drainage and Divide Networks Derived from High-fidelity Digital Terrain Models," *Proc. of the NATO Advanced Study Inst. on Statistical Treatments for Estimation of Mineral and Energy Resources, II Ciocco (Lucca)*, Italy, June, 1986, D. Reidel Publishing Company, Dordrecht, Holland (1988), 581–597.

[10] Kropatsch, W.G., D. Strobl, "The Generation of SAR Layover and Shadow Maps from Digital Elevation Models," *IEEE Trans. Geosci. and Remote Sensing*, Vol. 28, No. 1, Jan. 1990, 98–107.

[11] Maier, E., U. Frei, D. Nüesch, "Precise Terrain Corrected Geocoded Images," pp.173–185, in: Schreier, G., editor: SAR Geocoding: Data and Systems, Wichmann, Karlsruhe, 1993.

[12] Johnsen, H., L. Lauknes, T. Guneriussen, "Geocoding of Fast Delivery ERS-1 SAR Image Mode Product Using DEM Data," *Int. J. of Remote Sensing*, Vol. 16, No. 11, Nov 1995, 1957–1968

[13] Laur, H., P. Meadows, J.I. Sanchez, E. Dwyer, "ERS-1 SAR Radiometric Calibration" *Proc. of the CEOS SAR Calibration Workshop*, pp 257-281,Nordwijk. (ESA WPP-048).

[14] Shimada, M., "User's Guide to NASDA's SAR Products" Earth Observation Center, NASDA, March 1993. (NASDA HE93014)

EXPERIENCES IN MULTI–SENSORAL SAR GEOCODING

A. Roth, D. Kosmann, M. Matschke, B. Müschen, H. John

German Remote Sensing Data Centre (DFD)
German Aerospace Research Establishment (DLR)
D–82230 Oberpfaffenhofen, GER
Tel: +8153–28–2706 Fax: +8153–28–1445
email: roth@dfd.dlr.de

1. Abstract

Working with SAR data acquired by different sensors one has to keep in mind that they vary in wavelength, polarization and imaging geometry. This means that they are stored in incomparable ways after the SAR processing. To allow a combination of data delivered by different sources the images must be converted into a uniform system. In general the data are rectified and transformed in a map projection. This procedure is called geocoding.

The starting point is the goal to utilize multi–mission SAR data for monitoring purposes. The correction process, namely the parametric geocoding approach will be explained. The main problems like the SAR inherent distortions and their variations due to the different imaging conditions are described.

The accuracies achieved will be presented as well to allow an estimation of remaining distortions.

2. Introduction

Since 1991 the earth is continuously observed by a series of satellites carrying SAR sensors. Also for the coming years this surveillance capability will be saved due to further spaceborne SAR missions. The benefits of microwave remote sensing are the abilities of cloud penetration and day and night observation. This enables a monitoring of almost the entire earth's surface.

The SAR signal interaction with the ground is mainly influenced by the physical and electric characteristics of the surface [1]. But also the system design parameters polarization, frequency and incidence angle affect on the backscattered signal. This is important to estimate the information content of a SAR data set regarding the planed application. This paper intends to support this valuation in therms of the SAR geometry aspects.

3. SAR Geocoding

The SAR images the earth's surface by an oblique slanted view to a time grid. It is established by the satellite's orbit (azimuth) and the signal travel time from the sensor to the ground target (range). During the geocoding process the image pixels are transferred from this sensor specific imaging geometry into a map projection. Ref. [2] describes in detail the SAR geocoding system GEOS implemented at DLR for the ERS and X–SAR ground segments.

3.1. Parameteric Approach

To perform an operational geocoding in an efficient manner the traditional approach of visual tie–pointing and polynomial recitification is not acceptable. Especially the terrain correction requires a parametric solution precisely modelling the imaging conditions.
The parametric approach, also known as radargrammetric model, aims to the simultaneous determination of the SAR Doppler (1) and range (2) behavior. The simultaneous solution is performed by an iterativ method. The orbit position is iterated until both equations are fulfilled. The azimuth time defines the row in the input image while the range indicates the column.

$$F_1(i,j) = f_{DC} - \frac{2 \cdot (\vec{p} - \vec{s}) \cdot (\dot{\vec{p}} - \dot{\vec{s}})}{\lambda \cdot |\vec{p} - \vec{s}|} = 0 \qquad (1)$$

f_{DC} = Doppler reference function
λ = wavelength of the system
$\vec{p}$ = earth surface point vector
$\dot{\vec{p}}$ = velocity of earth surface point
$\vec{s}$ = sensor position
$\dot{\vec{s}}$ = sensor velocity

$$F_2(i,j) = r_0 - m_r \cdot j - |\vec{p} - \vec{s}| \qquad (2)$$

r_0 = range to the fist image pixel
m_r = pixel spacing in range of the input image
j = column number

3.2. GEC Product

During the ellipsoid correction (Geocoded Ellipsoid Corrected product) the flat surface of a reference ellipsoid is considered during the reconstruction of the imaging process. It is the bulk product and can be generated fully automatically based on the initial geometry. Terrain induced effects are not corrected. Fig. 1 shows a sub–image of

0-7803-3068-4/96$5.00©1996 IEEE

an alpine region. Clearly visible are the layover areas, appearing as bright fringes.

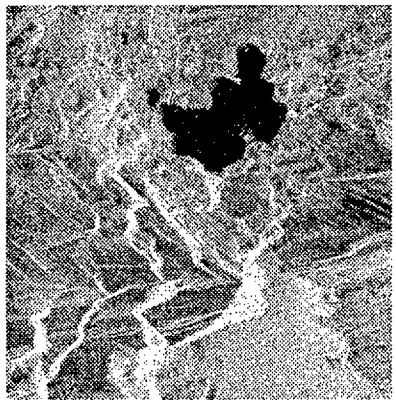


Fig. 1: ERS–SAR image, ellipsoid corrected

3.3. GTC Product

Due to the side–looking geometry of the SAR sensors the earth's relief causes distortions in the recorded data set. Therefore a high precision geocoding requires the consideration of a digital elevation model. The initial geometric parameters are improved by an adjustment. The main factors determining the precision of the terrain corrected data set is the DEM itself and the availability of suitable tie–points. Fig. 2 shows the same area as fig. 1 but terrain corrected. This time the layover and foreshortening areas are geometrically corrected. The layover regions appear as bright striped areas in the GTC.

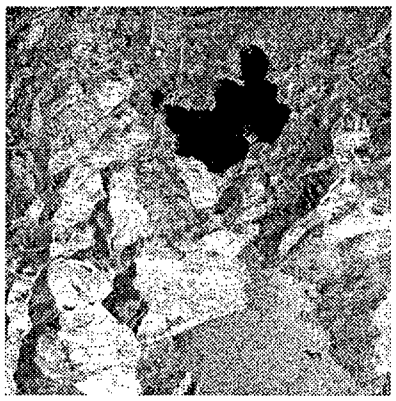


Fig. 2: ERS–SAR image, terrain corrected

A useful by–product is the layover shadow and incidence angle mask. It indicates layover and shadow areas and contains the incidence angle between the incoming radiation and the local surface normal. Fig 3 is the corresponding sub–image to the GTC of fig. 2.

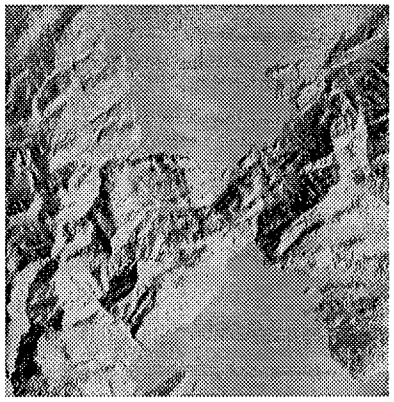


Fig. 3: layover shadow and incidence angle map

4. Geometric Distortions

Flat areas are mapped quite good with small distortions by the standard ground range product delivered by the SAR processor. The SAR geometry becomes more difficult when undulated terrain is imaged.

4.1. Foreshortening, Layover and Shadow

Three important SAR specific local distortions are known having their effects in range direction. Active microwave systems measure the signal travel time. The time delay between the received signals reflected by two targets on ground determine the size of the imaged region in the unrecitified radar image. Consequently mountain slopes bending towards the satellite are imaged much shorter than their real extension. This effect is called foreshortening.

An extreme case of foreshortening is layover. Here the top of a mountain is closer to the antenna than the bottom. So the top is imaged earlier. Subsequently the local mountain geometry is inverted. Comparing figures 1 and 2 foreshortening and layover areas can clearly be identified. Within the GEC they appear as bright fringes while terrain correction implies the smearing of the signal over the entire area of the slope.

Shadow in SAR images occurs on hill tops bending away from the sensor. If the slope is steeper then the incidence angle the backside of the mountain simply cannot be seen by the radar.

Obviously foreshortening, layover and shadow depend on the incidence angle of the SAR sensor. Unfortunately changing the incidence angle affects contrary on foreshortening and shadow. In other words a gentle incidence angle leads to layover only for very steep slopes, but causes shadow on the backside. Steep incidence angles avoid shadow but generate layover on the front of the mountain.

4.2. Range Displacement

SAR imaging causes elevated terrain to be mapped to close to the near range. This effect is known as range off-

set or range displacement. Table 1 lists the expected displacements for several incidence angles. The first rows specify the distortions in the precision–range of conventional DEMs. A height error of 10 m will result in a displacement of more then one resolution cell.

Table 1: Range offset effect on terrain height

Θ / cot Θ / Δh	16° / 3.49	20° / 2.75	23° / 2.36	30° / 1.73	40° / 1.19	50° / 0.83	60° / 0.58	67° / 0.42
5 m	17 m	14 m	12 m	9 m	6 m	4 m	3 m	2 m
10 m	35 m	28 m	24 m	17 m	12 m	8 m	6 m	4 m
50 m	175 m	138 m	118m	87 m	60 m	42 m	29 m	21 m
100 m	349 m	275 m	236 m	173 m	119 m	83 m	58 m	42 m
250 m	873 m	688 m	590m	433 m	298 m	208 m	145m	105m
500 m	1745 m	1375 m	1180 m	865 m	595 m	415 m	290 m	210 m
1000 m	3490 m	2750 m	2360 m	1730 m	1190 m	830 m	580 m	420 m
2000 m	6980 m	5500 m	4720 m	3460 m	2380 m	1660 m	1160 m	840 m

4.3. System Parameters

Also the precision of the overall system parameters cause distortions. The main parameters influencing the accuracy of the SAR data set are the orbit and the time measurements in azimuth and range. Obviously errors in the orbit determination are correlated with the timing in range and azimuth.

5. Results

A multi–sensoral approach requires a terrain correction for two reasons:
1. The SAR inherent geometric distortions are mainly induced by the topography.
2. The GTC production comprises a tie–pointing and an adjustment. System specific inaccuracies like the orbit determination are then corrected.
The main factors causing different geometric distortions are the incidence angle and the look direction.
Figures 4 and 5 show the mean location accuracies for ERS and X–SAR GTCs. It can be seen that the remaining overall errors are within the resolution of the SAR systems. This means that an accurate superposition can be achieved. Nevertheless a subpixel precision is impossible. Important to the precision of the terrain corrected product is the accuracy of the DEM. In this case the results are based on a DEM given in approx. 25 m horizontal and 1 m vertical resolution.

6. References

[1] C. Elachi: "Spaceborne radar remote sensing: Applications and techniques", IEEE Press, New York, 1988

[2] G.Schreier (Ed.): "SAR geocoding: data and systems", Wichmann Verlag, Karlsruhe, 1993

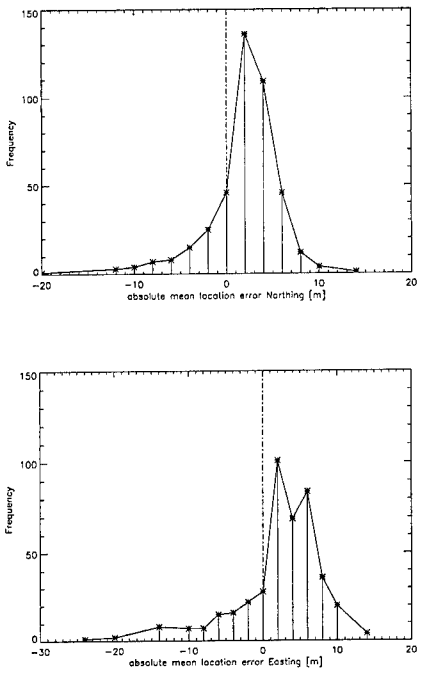


Fig. 4: mean location accuracies for ERS

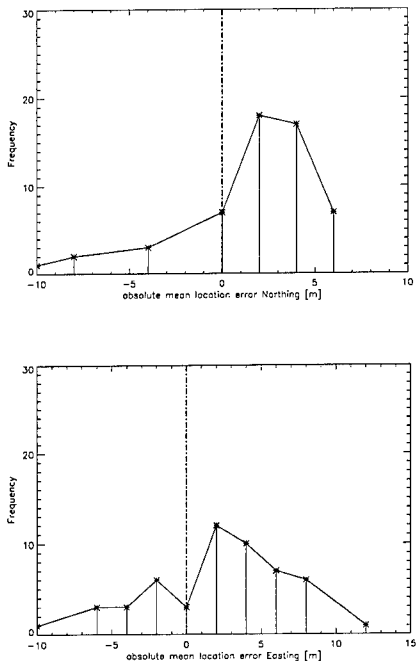


Fig. 5: mean location accuracies for X–SAR

Design, Performance and Technology Aspects in Relation to a Next Generation High Resolution Spaceborne SAR Instrument.

H.Böttger, C.Heer and J.J.W.Wilson*
Dornier Satellitensysteme 88039 Friedrichshafen Germany
Telephone 49 7545 84792 / Fax 49 7545 8 4177
and
* ESTEC 2200 AG Noordwijk The Netherlands
Telephone 31 1719 8 3326 / Fax 31 1719 8 4596

INTRODUCTION

A future synthetic aperture radar (SAR) System is currently being studied by the European Space Agency. The instrument is a high resolution / flexible swath SAR capable of providing detailed images of selected scenes. The related study to the instrument is entitled 'Next Generation SAR Instrument' where the main aim of the study is the identification of critical sub-systems and technologies which will require bread boarding. The study is being performed by Daimler-Benz Aerospace / Dornier (Germany) together with Alenia Spazio (Italy), Saab Ericson (Sweden), System Engineering & Assessment Ltd (United Kingdom), DLR (Germany) and Dassault Electronique (France).

The purpose of this paper is to consider design, performance and technology aspects in relation to the next generation SAR instrument.

This instrument is considered as a follow on instrument to the ERS-1/2 AMI SAR and the ENVISAT-1 ASAR providing advanced performance. The ERS-1/2 AMI SAR was the first satellite based C-band SAR System operating with a fixed swath, VV polarisation and a primary single look spatial resolution of approximately 30 m in ground range by 5 m in azimuth. The ENVISAT-1 ASAR provides extended spatial and temporal coverage by using seven different image mode swaths created by the ScanSAR technique. Although the ASAR is only able to operate at C-band, it will provide images with either VV or HH polarisation in Image Mode and with VV and HH or VV and VH or HH and HV polarisation in Alternating Polarisation Mode. The spatial resolution in image mode is similar to that provided by the ERS AMI SAR.

In the future it is expected that multiple parameter SAR instruments will be needed for commercial and governmental use. The provision of a dual or multiple frequency capability, which allows simultaneous imaging at least two frequencies is envisaged. Suitable frequencies for a high resolution SAR instrument are located in the L, S, C, and X bands, taking into consideration the power limitations, antenna accommodation limitations and bandwidth constraints which must be respected. The selection of frequencies must take into account the scientific needs. Fully polarimetric operation may be foreseen in order to allow the Stokes scattering operator to be determined. A future SAR instrument would also be expected to maintain or improve upon the radiometric accuracy and stability provided by the AMI SAR and ASAR instruments. In addition a primary single look spatial resolution of approximately 5m in ground range by 5 m in azimuth would be foreseen to provide enhanced SAR interferometric capabilities and a radiometric resolution more suitable for land use applications including crop identification and monitoring.

DESIGN ASPECTS

A number of key considerations must be taken into account in relation to the design of future high resolution SAR instruments. The following aspects in particular are deemed to merit special consideration:

(1) RF power amplification concept.

(2) Internal calibration.

(3) Data handling, storage and down linking.

(4) Appropriateness of antenna design with respect to polarimetric and multiple frequency capability.

(5) Structural efficiency of design.

These and other design aspects are briefly discussed below.

The selection of RF power amplification concept is fundamental. The possible options are essentially centralised (TWTA), partially distributed (solid state or TWT-based Microwave Power Modules (MPM)) or fully distributed (T/R Modules) however for the case of distributed concepts many realisations are possible. For example, the total number of distributed RF amplifiers is driven by the required scan angle range of the antenna beam and the transmit pulse bandwidth and impacts the efficiency and the reliability of the instrument. In general, the choice of concept must be traded-off for each frequency especially with respect to power requirements, losses, mass, performance and calibration complexity.

0-7803-3068-4/96$5.00©1996 IEEE

The data handling, storage and transmission sub-system of a future high resolution multiple frequency polarimetric SAR instrument is likely to necessitate a substantial increase in complexity. This arises as a consequence of the increased data rates resulting from the increase in spatial resolution, the increase in the number of channels associated with multiple frequency and polarimetric capabilities and the high number of operational modes. Data may be transmitted to ground directly or via data relay satellite. For direct down linking both X-band omnidirectional and Ka-band steerable pencil beam down links may be useful. Microwave or perhaps optical inter-orbit data links will also be required to permit down linking via data relay satellites. The use of high capacity on-board solid state mass memories is also foreseen to both store data in the normal fashion and to buffer data in order to allow down link data rates reduction. A 500 Gbit solid state mass memory is presently under development at (DASA / Dornier).

As regards the antenna design, special importance will be attached to achieving fully polarimetric capability and at the same time sufficient bandwidth to achieve the required ground range resolution; this will impose strict requirement on polarimetric channel mixing both within the instrument and via the ambiguities.

In relation to structural efficiency, in future a more integrated approach to mechanical design must be taken in order to reduce unnecessary mass. This is particularly the case for active antennae where mass reduction is expected to be achieved via utilisation of structural radiating elements where possible and by making unit containments play a structural role. Special importance should be given to materials selection in this context. For example an all CFRP structure can be made much less sensitive to thermally induced bowing than a similar aluminium structure.

Some other aspects of interest in relation to the design of a future SAR system are the following.

(A) Advanced data compression and data rate reduction techniques, both for raw and image data, including the use of on-board processing and averaging.

(B) Flexibility available to the SAR from a platform with multiple attitude modes, for example, to allow the SAR to look either side of the nadir track or to operate in squinted modes.

(C) Provision of fully flexible coded pulse generation and receive chain digital filtering hardware.

(D) Mode selection and justification in terms of applications including possible spotlight modes, normal and polarimetric image modes, squinted modes, stereo modes, scan SAR modes, wave modes and both along track and across track interferometry modes.

(E) Common hardware for multiple frequency SAR instruments and use of Rubidium masers for frequency generation.

PERFORMANCE ASPECTS

The existing engineering performance parameter employed for the ERS AMI SAR, the ENVISAT-1 ASAR and the SIR-C/X-SAR are being revisited and refined for future SAR instruments in the light of experience gained from these programs. In particular, new engineering performance parameters are required to characterise and control polarimetric and interferometric performance and new algorithms are required to compute these parameters. For fully polarimetric imaging, in principle, the ten independence components of the Stokes scattering operator may be measured and it is important to know and control the errors on each component, resulting from polarimetric channel mixing inside the instrument and via corruption from the ambiguities and from phase errors.
For example, using a crude model the error caused by the antenna cross-talk may be modelled as:

$$Z'_{HH} = Z_{HH} + 2\varepsilon Z_{HV} + \varepsilon^2 Z_{VV} \quad (1)$$
$$Z'_{VV} = Z_{VV} + 2\varepsilon Z_{HV} + \varepsilon^2 Z_{HH} \quad (2)$$
$$Z'_{HV} = Z_{HV} + \varepsilon Z_{HH} + \varepsilon Z_{VV} + \varepsilon^2 Z_{HV} \quad (3)$$

where the $Z'_{ab's}$ form the Matrix elements of the Stokes Matrix and $\varepsilon = 10^{-XI/20}$. XI is the antenna polarisation cross- talk.
The error mechanism for channel mismatch and ambiguities might be modelled as follows:

$$Z'_{ab} = (1 + \delta A_{ab})\, Z_{ab} \exp(j\, \delta\phi_{ab}) \quad (4)$$
$$Z'_{ab} = Z_{ab} + \Sigma\, Z_{ab}\,|_{\text{ambiguity}} \quad (5)$$

where δA_{ab} and $\delta\phi_{ab}$ are amplitude and phase channel mismatch.
A more general look to the distributed and point target ambiguity ratios can be done by the inverse impulse response function (IIRF) which describes the expected contribution from all points in a uniform target field to a point in the detected ground range image.

Also improvements may be required in relation to the definitions and algorithms characterising various instrument dynamic ranges and in relation to radiometric stability and accuracy definitions and algorithms . For example the radiometric stability can be considered as the standard deviation of the integral under the IIRF divided by the mean value of the integral under the IIRF.

Furthermore, for quadpol measurements the range ambiguity model has to account for co- and cross-polar components caused by nominal and corrupted contributions. In case of pulse alternating polarisation measurements where two receive chains account for the co- and cross-polar echo, the main ambiguous contributions to a HV measurement can be considered as:

$$E_{HV}^{amb} = f\,(E_{VV}\,\sigma_{VV}\,,\ E_{HV}\,\sigma_{HV}\,,\ E_{HV}\,\sigma_{HH}\,XI_{HV}^{rx}\,,\ E_{HV}\,\sigma_{VV}\,XI_{HV}^{tx}\,) \qquad (7)$$

where XI_{HV}^{rx} and XI_{HV}^{tx} respectively denotes the receiver and transmitter cross-talk.

Improved design and performance modelling tools incorporating the new engineering performance parameter algorithms will be developed to allow both optimisation and parametric analysis to explore appropriate regions of the design space.

TECHNOLOGY ASPECTS

Compared to existing SAR instruments, the requirements to the Next Generation SAR are more demanding. In order to accommodate a high resolution multifrequency, multipolarisation instrument to a satellite, significant reduction in mass and power must be achieved. As an alternative to a wave guide radiator, a micro strip patch array will be considered also for the higher frequency bands. The expected mass reduction is in the order of 30% including the radiator supporting structure. The following table compares briefly the performance of a patch array to a wave guide radiator.

Tab.1: Wave guide radiator vs. micro strip patch radiator

	wave guide radiator	micro strip patch radiator
Mass	-	++
Antenna polarisation cross-talk	+	++
Bandwidth	+	++
Ohmic loss	++	-
Space Qualification(X, C-band)	++	tbd
Temperature stability	++	-
Reproducibility	-	++
Production cost	-	++

Both, the micro strip patch technology and a dual polarised X-band wave guide radiator are presently under development.

A possible lay-out of a micro strip patch antenna is given below:

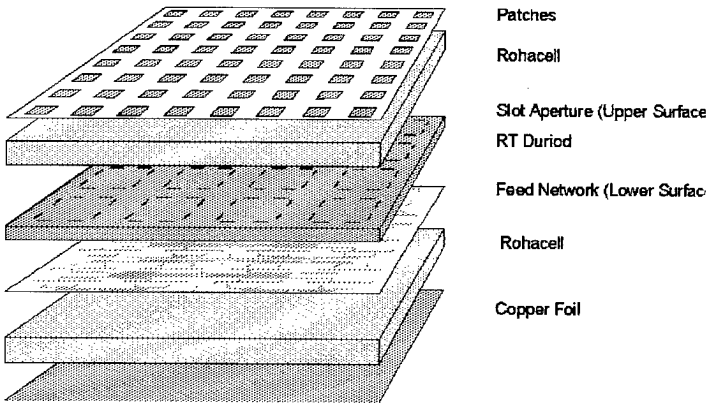


Fig.1: X-band micro strip patch radiator lay out

The DC to RF power efficiency is mainly driven by the efficiency of the RF Power Amplifier. In case of fully distributed T/R modules, the power added efficiency may be increased to over 23 % by using Heterojunction Bipolar Transistor (HBT) technology for the final output power amplifier in X-band. A Reduction in size and mass is expected to be achieved by use of core-chips in the low power electronic of the T/R module.

As regards the MPM concept, the following table summarises the expected MPM performance within the various frequency bands for a duty cycle of 10%.

Tab. 2: Performance of DASA/AEG Microwave Power Modules (MPM).

Frequency	X-band	C-band	S-band	L-band
Peak RF Output Power	300 W	200 W	200 W	100 W
DC Input Power	57 W	39W	41 W	21 W
Efficiency (total)	53 %	51 %	49 %	48 %
TWT	60 %	58 %	56 %	56 %
EPC	88 %	88 %	88 %	86 %
Mass	2.2 kg	2.21 kg	2.42 kg	2.54 kg

CONCLUSION

Some of the main issues, concerning design performance and technology which require consideration in relation to future SAR instruments have been outlined above. The results from the Next Generation SAR Instrument Study are expected to become available in November 1996. These results will include recommendations concerning the bread boarding of critical technology for future high resolution, multiple frequency, polarimetric SAR instruments.

Development of a High-Resolution Ground-Based Synthetic Aperture Radar

Keith Morrison & John C Bennett
Department of Electronic & Electrical Engineering
University of Sheffield
Mappin Street
Sheffield S1 3JD
UK
K.Morrison@Sheffield.ac.uk, Tel:+44 (0)114-282-5585, Fax:+44 (0) 114 272 2097
J.C.Bennett@Sheffield.ac.uk, Tel +44 (0)114-282-5359, Fax:+44 (0) 114 272 2097

Abstract--A description of an indoor SAR measurement facility is presented. The aim of the work is primarily to better understand the microwave backscatter characteristics of vegetation and soils. Based around a vector network analyser, the system utilises synthetic pulse techniques to obtain high resolution images. The principles of the technique are presented, together with a series of images of vegetation and artificial targets. Calibration procedures are implemented successfully and the images provide useful quantitative reflectivity information. The polarimetric capability of the system and its sensitivity to target structure is also demonstrated.

INTRODUCTION

Spaceborne and airborne synthetic aperture radar (SAR) systems provide a unique technology for investigating and monitoring biophysical and geophysical features on the Earth. However, our use of this data is limited in many ways because of a lack of understanding of the processes involved in radar imagery. The interaction between the radar wave and the target can be very complicated depending on the dielectric and geometric properties of the target, and parameters such as incidence angle, polarisation, frequency and revisit period. It is in order to enhance our understanding of these processes that a programme of ground-based SAR research is currently under way at the University of Sheffield. Synthetic pulse techniques and processing based on a vector network analyser provide great flexibility in the type of radar observations which can be made, with the realisation of variable range and cross-range resolutions far superior to those of conventional SAR. This paper discusses the principles and techniques of the SAR system under development. Images of both metallic and vegetation targets are shown.

PRINCIPLES OF THE TECHNIQUE

The facility is housed in a 10m by 3.5m by 3m microwave anechoic chamber. The mechanical sub-system utilises a high precision 2m by 2m vertically-aligned two-axis scanner on which is mounted a polarimetric cluster of four pyramidal horn antennas. An HP8408 network analyser in conjunction with an HP8672A synthesised source provide an output of +10dBm, with an HP8349B microwave amplifier providing approximately 16dB of gain in the transmit path. The PC data logger also controls the operation of the network analyser and the movement of the scanner. The synthetic aperture is produced by the translation of bi-static transmit-receive horn antennas across the scanner. The horns are suitably elevated to interrogate the target over the desired range of incidence angles. At each position, x, along the scan, phase and amplitude are measured at equal frequency intervals over the desired bandwidth. The imaging process uses the plane-to-plane technique [1,2], which involves the decomposition of the measured field into its angular spectrum of plane waves. This spectrum is then multiplied by a linear filter, which backward propagates each plane-wave component through a distance z from the SAR aperture to the plane of interest. The spectrum is then inverse-transformed into a spatial distribution.

RESULTS

This section presents a series of images which demonstrate the system performance and capabilities. The first image is of three freshly cut stem sections of the plant *Rubus Fruticosus Aggregate* (*aka*.bramble).Each was an approximately straight 80mm section with an average diameter of 2mm. They were arranged as shown in Fig.2, located at x=-0.3, 0, 0.3m, and at distances of z=1.26, 1.28, 1.27m, respectively.

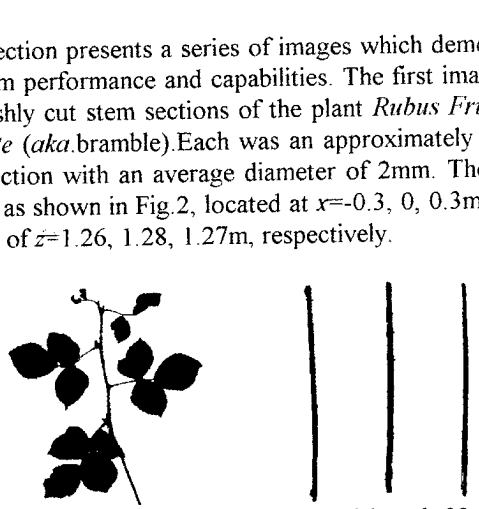


Fig.1 *Rubus Fruticosus Aggregate* (actual length 23cm), and the three stem sections used in Fig.2.

0-7803-3068-4/96$5.00©1996 IEEE

All the SAR images presented in this paper were created by scanning over a horizontal distance of 1m, providing 51 sample positions at each 0.02m interval. At each position, the network analyser was stepped in frequency intervals of 0.04GHz over the range 8-12GHz, producing data at 101 frequencies.

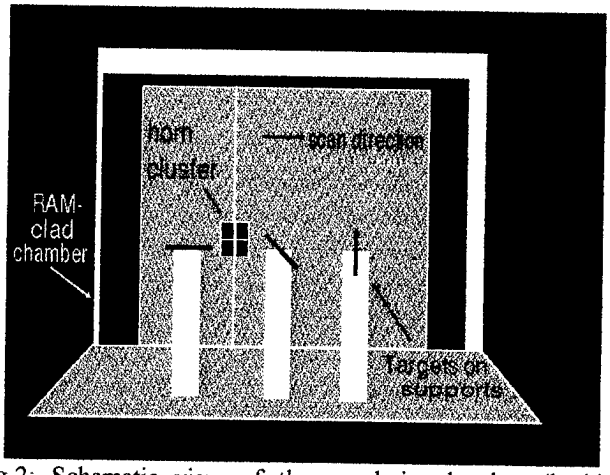


Fig.2: Schematic view of the anechoic chamber (looking towards the SAR) showing the positioning of the three stems.

In order to account for unwanted signals that arise from returns off objects other than the desired target, and from signal coupling within the measurement system, it is necessary to perform an empty room calibration. The empty room calibration is an identical repeat scan to that used in imaging the target, but with no target present [3]. The result is shown at top left in Fig.3. Top right shows the image of the target prior to the removal of the empty room contributions. A complex subtraction of the two data sets has produced the corrected image shown at bottom left. Whilst the unwanted signals have largely been removed, the target images are still not ideal and display a trailing down-range in the z dimension. This is due to degradation of the image convolving function by the non-ideal nature of the frequency response of the measurement system. This can be corrected for by measuring the frequency response of a reference target with a known frequency response, in this case a trihedral [3]. The corrected image is shown at bottom right. An improvement is now seen as a result of the removal of much of the trailing present earlier.

The image also demonstrates the polarimetric discrimination of the system to vegetation structure. As might be expected, the HH polarisation has responded most strongly to the horizontally-aligned stem (left), with reduced responses for the 45° (centre) and vertical (right) stems. To obtain quantitative reflectivity measurements from Fig.3 a spatial correction function was applied across the image to correct for space loss and antenna radiation pattern.

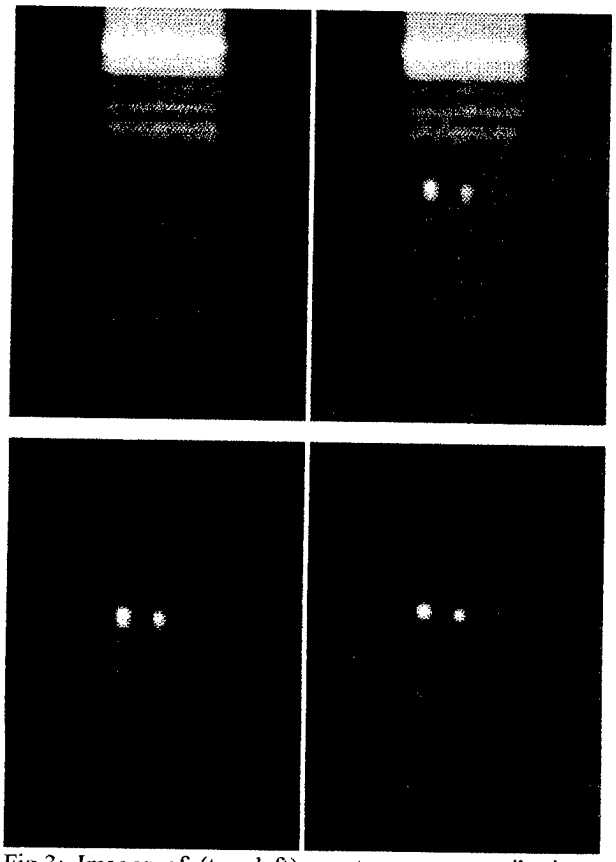


Fig.3: Images of (top left) empty room contributions; (top right) target and empty room contributions; (bottom left) image corrected for empty room contributions; (bottom right) and corrected for frequency response of system. The images are 2.56x3m, and displayed with a dynamic range of 25dB.

After correction, the reflectivity of the 45° and vertical stems were found to be reduced in amplitude by -5.2dB and -17.5dB, respectively, relative to the horizontal stem. Whilst these differ from the expected ideals of -6dB and -∞, given the sight-of-eye alignments of the stems and their deviation from ideal cylinders, the results are not unexpected.

To better understand the sensitivity of polarised signals to plant structure, single-position reflectivity measurements were made of the specimen of *Rubus Fruticosus Aggregate* displayed in Fig.1 (left). Its main stem was aligned vertically, and measurements of the angular dependence of the backscatter made as the plant was rotated through 360° about the vertical axis. Using VV polarisation no easy-characterisable angular variation in amplitude was observed. With the plant facing to the horns, removal of the leaves produced an amplitude change of -2.2dB. Further removal of the small stalks connecting between the main stem and leaves produced an additional reduction of -0.5dB. With HH polarisation, whereas there was a clear return with the leaves turned towards the horns, at 90° the specimen was not

detectable. This behaviour suggests that the HH radiation was backscattering primarily from the leaves, whilst the VV radiation was sensitive principally to the central vertical stem. In order to test the ability of the system to detect the backscatter from individual leaves, single leaves of *Prunus Lusticana* (*aka.* portugal laurel), *Hedera helix* (*aka.* ivy), and *Ligustrum Ovalifolium* (*aka.* garden privet) were placed at x=-0.25, 0, 0.25m, and z=1.26m. The relative sizes of the leaves and the resulting image are shown in Fig.4. Clearly, it has succeeded in detecting each of the leaves. Note that the down-range trailing is because no reference target measurement was available to correct for the frequency response of the system. The returns from *Hedera helix* and *Ligustrum Ovalifolium* were measured to be -13dB and -21dB compared with that from *Prunus Lusticana*.

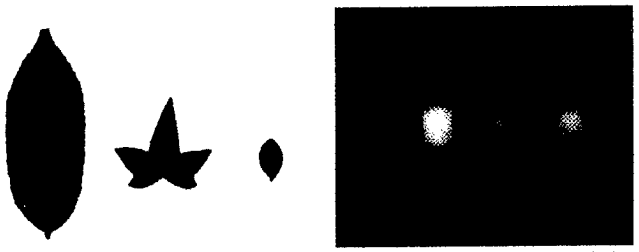


Fig.4: ***Left:*** Relative sizes of the leaves of (left to right) *Prunus Lusticana*, *Hedera helix*, and *Ligustrum Ovalifolium*. The actual length of the largest leaf is 11.5cm. ***Right:*** The resulting image (note the positions of the middle and right specimens are reversed in the image). The image is 1.28x1m, and displayed with a dynamic range of 30dB.

The type of measurements presented above will serve to enhance our understanding of microwave backscatter from vegetation. This is necessary to allow the development of more realistic scattering models.

REFERENCES

[1] Goodman, J W: "Introduction to Fourier Optics", McGraw-Hill, 1968.

[2] Shewell, J R and Wolf, E: "Inverse diffraction and a new reciprocity theorem", J. Opt. Soc. Am., 58, No.12, 1596-1603, 1968.

[3] Smith, F C, Chambers, B and Bennett, J C: "Calibration Techniques for Free Space Reflection Coefficient Measurements", IEE Proc-A, 139, Sept 1992, 247-253.

ACKNOWLEDGMENTS

The authors gratefully acknowledge the financial support of the University of Sheffield and the Sheffield Centre for Earth Observation Science, which enabled this work to be carried out.

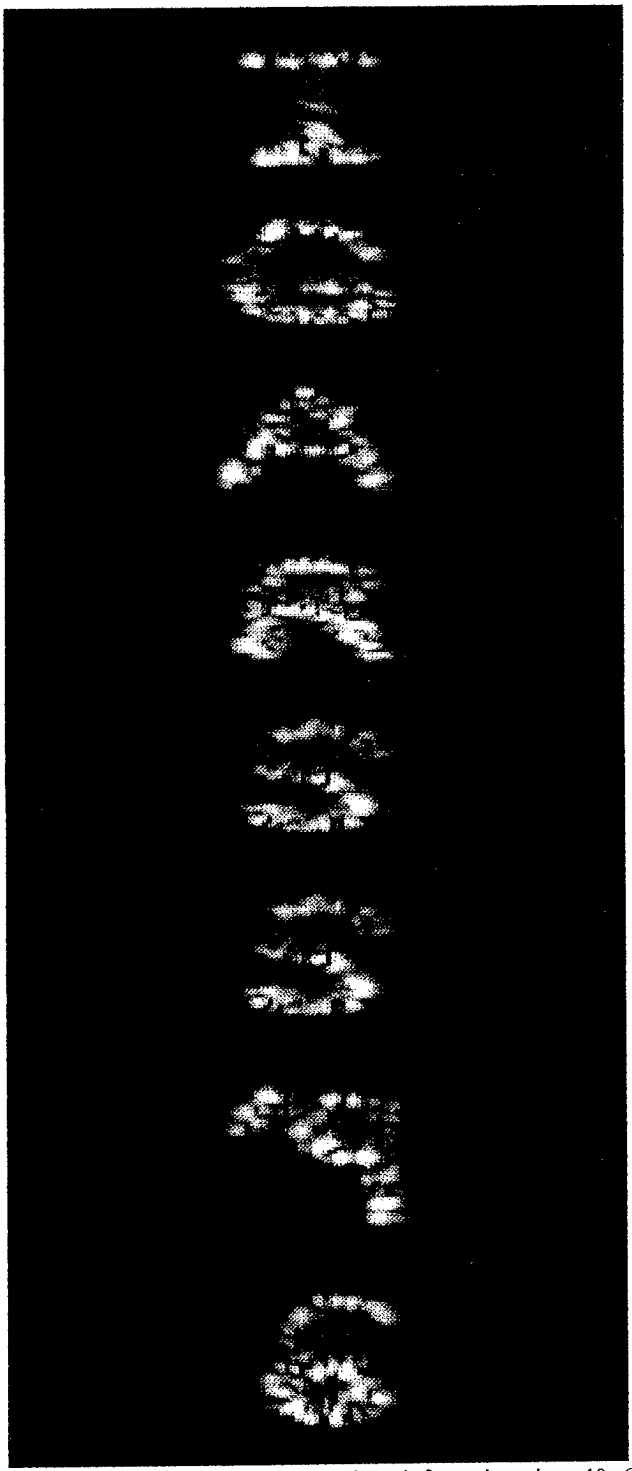


Fig.5: Montage of images produced from imaging 40 6cm steel bolts arranged in the shape of ~0.7 by ~0.7m letters and numbers. The images are 2.56x1m, and have been empty room corrected. They are shown with a dynamic range of 20dB.

Integrated Design of Synthetic Aperture Radars for Unmanned Aircraft

Professors John F. Vesecky* and John M. Cornwall**

***Atmospheric, Oceanic and Space Science Dept.**
The University of Michigan, Ann Arbor MI 48109-2143
Tel: 313-764-5151, FAX: 313-764-5137, jfv@umich.edu

**** Physics Dept.**
The University of California, Los Angeles CA 90024
Tel: 310-825-3162, FAX: 310-206-5668, cornwall@physics.ucla.edu

The use of synthetic aperture radar (SAR) on unmanned aircraft (UAV's) is often contemplated for aerial observation of regions where unmanned, long duration (tens of hours) observations are advantageous. Some current applications are severe weather, military surveillance and environmental observations. However, in most cases the initial SAR and aircraft designs are done independently and one is either trying to design a SAR to fit a particular UAV or a UAV to fit a particular SAR. For example, Schwartz et al. (1990) designed and built a SAR to fit the Amber UAV (Cassidy, 1991). This process is likely to lead to a restricted range of choices to accomplish a given objective and fails to provide the system designer with a complete range of possible choices and trade offs. Here we develop a first order, integrated approach to design in which the SAR and aircraft designs are coupled. This approach allows a broader exploration of the options available in SAR's for UAV's. There are a number of ways in which the SAR and aircraft interact. For example, radar echo power is influenced by antenna size, but aircraft size constrains the antenna size -- as does azimuth resolution. The aircraft velocity V impacts virtually all aircraft relationships as well as SAR azimuth resolution. For applications that push the limits of small UAV SAR's it is important to note that the aircraft power plant will need to power both the aircraft and the SAR.

ANALYSIS

We begin with basic design parameters for SAR, e.g. range, swath width, resolution, noise floor, system noise temperature, etc. as well as aircraft design parameters, such as mass, wing area, power, propulsion efficiency, etc. Important SAR equations are those for azimuth resolution, range resolution and radar echo power. For aircraft important equations are those for lift, drag and power.

The basic SAR equations used can be summarized as follows:

SAR azimuth (along track) resolution, $dy = \lambda R/(2\ V\ T)$

SAR range resolution, $dr = c/(2\ B)$

SAR average transmit power required:

$$P_{av} = (2\pi\ k\ T_{sys}\ \theta_v^2\ R^3\ V\ SNR)/[\lambda\ \sigma^\circ(\alpha)\ \rho_a^2\ dx\ (dy)^2]$$

where θ_v is antenna vertical beam width, R is radar range, V is aircraft velocity, T is SAR integration time, B is SAR bandwidth, c is the speed of light, k is Boltzmann's constant, T_{sys} is radar system noise temperature, SNR is signal to noise ratio, λ is radar wavelength, σ° is normalized radar cross section, α is elevation angle, ρ_a is antenna efficiency and dx is ground range resolution. SI units are used throughout and the radar equations are developed in Levanon (1988) for a single look case. Using a flat Earth geometry P_{av} can be reformulated to show parameters convenient for SAR design,

$$P_{av} = [2\pi\ k\ T_{sys}/(\lambda\ \rho_a^2)]\ [SNR/\sigma^\circ_{floor}]\ [W^2\ \sin\alpha/(dx\ dy^2)]\ [V\ h]$$

where σ°_{floor} is the minimum that is to be observed at a given SNR, W is swath width and h is aircraft altitude.

For an aircraft the basic equations are as follows, viz. Ashley (1992):

Lift: $M\ g = \rho\ V^2\ S\ C_L/2$

Drag: $D = \rho\ V^2\ S\ C_D/2$

Power: $P = \rho\ V^3\ S\ C_D/(2\ e)$

where M is aircraft mass, g is acceleration of gravity, ρ is air density, S is wing area, C_L is lift coefficient (≈ 1), D is drag force, C_D is drag coefficient (≈ 0.05), P is engine power and $e \approx 0.5$.

Combining these basic SAR and aircraft equations we can derive a variety of useful relationships that help define the range of choices for SAR-carrying UAV's. Solving the aircraft equations above for V we find that $V = [2\ M\ g/(\rho\ S\ C_L)]^{0.5}$ and similarly $P = V\ C_D\ M\ g/(C_L\ e)$. For long duration one wants low power to reduce fuel consumption, but this means a low V and hence a low search rate. A low V also means that T must be long in order to achieve a desired synthetic aperture and hence a desired dy. However, a long T requires platform stability and/or motion compensation over a longer time span. These relationships illustrate some trade offs and constraints on SAR and UAV design for a particular purpose.

RESULTS

To illustrate the interplay between the aircraft and radar requirements we consider radar and aircraft parameters that

0-7803-3068-4/96$5.00©1996 IEEE

are fixed for a typical case and then show how the choice of aircraft mass and SAR search rate and resolution impact aircraft velocity and aircraft and radar power requirements. As our typical case, we take an X-band SAR The minimum observable σ° is 3 x 10^{-4} at 15 dB SNR, T_{sys} = 500° K and antenna efficiency is 0.9. The radar observes a swath width W of 10 km from a mean radar range of 12.5 km and height of 7.5 km. This means an antenna with a height of ≈ 7 cm and a width of twice the along track resolution (2 dy). Thus, for resolutions of the order of a meter or less, the antenna easily fits along the fuselage of a small UAV, such as the GNAT-750 (Cassidy, 1991). For the observational geometry above prf's of 10 kHz are possible. For large compression ratios, e.g. 10^4, duty factors of about 10% would be typical.

Search (or areal coverage) rate, SR = VW is an important factor in designing SAR's as is resolution. For fixed W, V is determined by SR and if we fix dx = dy = 1 ft., the average power of the radar P_{av} is a function of SR only. The aircraft power required is a function of M and V with the wing area varying according to the equations above. We take the total radar power requirement to be a fixed 500 W plus 3 times the power required for a 4 look case (4 P_{av}). Fig. 1 shows how the aircraft velocity, radar power and total power vary with search rate SR. The ordinate is in horsepower to make comparison between radar and aircraft engine power easy.

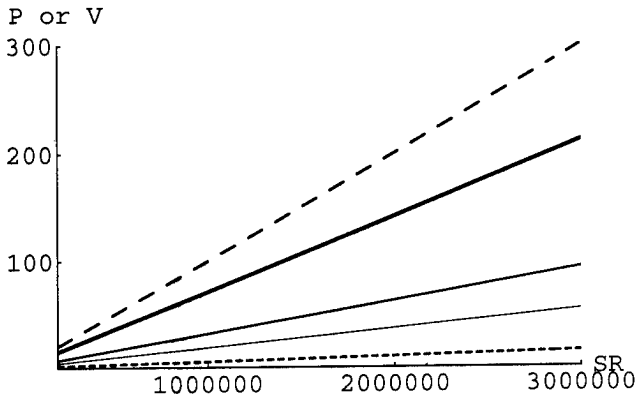


Fig. 1. Aircraft velocity V in m/s (long dashed line), Radar power (short dashed line) and Total power required (solid lines) vs. search rate SR. The progressively thicker lines are for total masses of 100, 200 and 500 kg. Ordinate is in horsepower (1 W = 746 hp).

The GNAT-750 has M ≈ 500 kg. and flies at V_{max} ≈ 70 m/s; hence, the search rate for this radar would be ≈ 7 x 10^5 m^2/s or ≈ 1000 square miles per hour with a resolution of 1 foot. It is clear that the radar power is a small fraction of the required engine power and the design is likely to be viable. In fact Schwartz et al. (1990) built a SAR and integrated it into the predecessor of the GNAT-750, called the Amber.

Another important SAR parameter is resolution. It is evident from P_{av} equation that resolution has a strong impact. To illustrate this we consider a case in which the UAV mass and search rate are fixed at 500 kg and 3 x 10^5 m^2/s. This is appropriate to the GNAT-750 flying at a slow speed to conserve fuel and enable a long endurance flight (≈ 30 hours). In Fig. 2 we show the radar power required PR, i.e. the power required from the prime power source, and the total aircraft power PT.

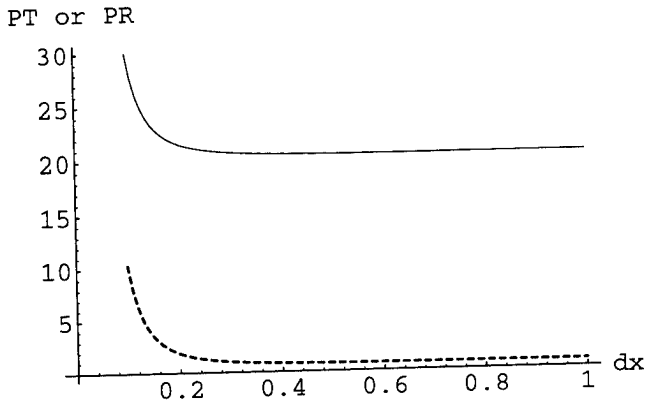


Fig. 2. Radar power required PR (dashed line) and Total power required PT (solid line) for ground resolution of from 10 cm to 1 meter. Power is in horsepower.

We see that at very fine resolution the radar power begins to seriously impact the total power required for the aircraft. This points up the fact that as the size of UAV is decreased and the total power available decreases SAR capabilities have to be reduced in order that there be enough power available to run both the radar and the aircraft.

CONCLUSIONS

We conclude that coupling the equations governing SAR performance with those governing aircraft flight enables a more complete exploration of the options for UAV SAR systems. In particular we note that the radar and total power requirements increase linearly with search rate and the rate of increase for the total power increases with aircraft mass. For small UAV SAR's the SAR power requirements impact the total power required and thus the coupling between SAR and UAV is stronger.

REFERENCES

Ashley, H., Engineering Analysis of Flight Vehicles, Dover NY, 1992.

Cassidy, T. J., "Long-endurance tactical surveillance & support systems," General Atomics, San Diego CA, 1991.

Levanon, N., Radar Principles, Wiley NY, 1988.

Schwartz, C. E., T. G. Bryant, J. H. Cosgrave, G. B. Morse & J. K. Noonan, "A Radar for unmanned air vehicles," Lincoln Lab. J., vol. 3, pp. 119-143, 1990.

ER-2 IFSAR Digital Terrain Matrix Collection System

Harold A. Malliot
Lockheed Martin Missiles & Space
Org. 92-20 B/255
3251 Hanover Street
Palo Alto, CA 94304
Tel. 415-424-2619 Fax: 415-424-2662

Abstract—A digital terrain matrix (DTM) with sub-meter precision and at least three meter posting is needed to support a variety environmental, geophysical, economic and resource management tasks. Repeated measurements of DTM changes with five centimeters to one meter vertical resolutions and at least ten meter posting are needed for detection and measurement of a variety of geophysical processes. The Lockheed Martin Missiles & Space Digital Terrain Elevation Mapping System (DTEMS) which will be capable of providing data to satisfy these needs. DTEMS will use a NASA/Lockheed ER-2 aircraft with an X-band interferometric synthetic aperture radar (IFSAR) for collection, processing and archive of DTM with thirty centimeter average precision and one to three meter posting. DTEMS is expected to become operational by April 1997.

INTRODUCTION

Lockheed Martin Missiles & Space is planning an airborne sensor campaign that will use an interferometric synthetic aperture radar (IFSAR) in an ER-2 aircraft to develop a comprehensive, high precision, high resolution digital terrain matrix (DTM) of the USA and other countries [1,2]. The initial DTM collection campaign will be followed by a DTM change detection and measurement campaign. The data will be available to the public and research personnel from a digital archive at a cost substantially less than the present cost to obtain equivalent data by stereo photogrammetry. The system will also provide cartographic, terrain perspective viewing, GIS, and topographic engineering products. The system will have an area coverage rate exceeding 700 km^2/minute and, for terrain with 45 degree slope, it will deliver a DTM with average relative one σ elevation precision of 0.3 meter and average absolute one σ elevation precision less than 0.6 meter. The DTM will satisfy National Map Accuracy Standards (NMAS) contour intervals of 0.7 to 1.7 meters

SCIENTIFIC APPLICATIONS OF DTM CHANGE

0-7803-3068-4/96$5.00©1996 IEEE

A variety of geological, hydraulic and glacial processes cause singular, periodic or continuous changes in the earth's topography[3]. The magnitude, spatial distribution and rates of topographic change depend on underlying physical processes (e.g., seismic movement, volcano bulging,, ground subsidence, erosion, and glacial melting). A high precision, high resolution DTM combined with a periodic remote sensing campaign to detect and measure topographic changes will provide data for development of phenomenological models of the processes. The ultimate benefits of such a remote sensing campaign would be better understanding of geophysical processes, means for prediction of dangerous catastrophic geophysical events and quantification of the lethality and economic and cultural impacts of catastrophic such events on nature and the human populace.

It was determined in the 1994 workshop on synthetic aperture radar (SAR) interferometry change detection [3] that surface topography changes produced by geophysical processes can be detected and measured. Large topography changes (e.g., >0.5 m) can be measured by differencing DTM's collected at different times. Smaller topography changes (and other phenomena that alter the phase of the signal) can be sensed by a process called coherent change detection (CCD) which extracts changes in phase from radar signals recorded at different times.

To establish initial conditions, a complete DTM is required prior to the inception of a topographic change measurement campaign. The largest data sets presently in existence are the USGS Digital Raster Graphics (DRG) data of the United States and the world digital terrain elevation data (DTED) archive maintained by the Department of Defense (DoD). Neither of these archives are complete and, with five to thirty meter elevation precision and thirty to 100 meter posting, have little utility for most geophysical, engineering, and economic applications. Further, the DoD DTED data is not available for general public use.

The required elevation resolution and period between topographic measurements depends on the magnitude and frequency of the physical events that cause the changes. Table 1, which was developed from data in [3], provides a

Table 1. This table summarizes topographic change sensing requirements for various geophysical applications.

Application	Elevation Resolution	Posting (m)	Revisit Interval
Earthquakes:			
Co-seismic	1cm–10m	10–30	1–3 days
Post-seismic	1cm–1m	10–30	3days–1yr.
Volcanism:			
Active	1cm–1m	10–30	1day–1mo.
Inactive	1cm–1m	10–30	1mo.–1yr.
Hydrology:			
Shore/Estuarine	5–30cm	10–30	5days–1yr.
Drainage Systems	5cm–5m	10–100	5days–1yr.
Streams	5cm–1m	10–100	1day–1yr.
Soil Moisture	2–10cm	10–30	5days–1yr.
Permafrost	2–10cm	10–30	1mo.–1yr.
Forests:	10cm–5m	10–100	1week–1yr.
Crust Movement:			
Tide/Atm Loads	10–30cm	10–100	1week–4mo.
Subsidence	2cm–2m	10–50	1mo.–1yr
Glaciers:	20cm–1m	10–50	1week–1yr.

summary of the sensing requirements for various geophysical applications. The most stringent requirements are daily measurements with one centimeter vertical resolution and ten meter posting.

ER-2 IFSAR DTM COLLECTION SYSTEM

An analysis of alternative techniques for DTM collection found that a wide swath interferometric synthetic aperture radar (IFSAR) carried in a NASA/Lockheed ER-2 aircraft would provide highest data quality at the lowest cost [1]. The ER-2, which is the NASA version of the Air Force U2-R, offers a number of advantages over other aircraft:

1. low operational cost ($6500 per flight hour as compared to $10,000 or more for other jet aircraft);
2. operations between 60,000 and 70,000 feet provide the capability for large area coverage rate, avoids the impacts of weather and air traffic control on flight operations, and subjects operations to minimal turbulence and jet stream;
3. the 8.5 meter center to center separation of the wing pods provides an 8.5 meter SAR interferometer geometric baseline (SIGB) and the rigid attachment of the wing pods to the wing eliminates excessive pod movement;
4. payload capacity of 4000 pounds and 25 kilowatts of power availability; and
5. mission durations up to eight hours with more than six hours of data collection time.

The major disadvantages of the ER-2 are special ground handling operations and use of an unusual fuel type. These eliminate ER-2 operations from most commercial airports. Also the single engine limits the off shore range of ER-2 operations to a few hundred miles.

Alternative techniques for sensing the terrain elevation include IFSAR [1], stereo photogrammetry, and laser ranging. IFSAR was selected for DTEMS for the following reasons:

1. IFSAR can provide a DTM with the desired data accuracy and posting;
2. IFSAR provides the maximum achievable area coverage consistent with the desired data quality;
3. data can be collected through cloud cover and day or night;
4. the data can be processed at relatively low cost on digital computers with minimum manual intervention;
5. topographic maps derived from IFSAR data are superior in many respects to topographic maps derived from stereo photographs [4]; and
6. production of marketable products and services that are presently not available (e.g., high resolution digital polarimetric SAR imagery, periodic measurements of terrain elevation changes, and detection of human activities).

The DTEMS system configuration, illustrated in Fig. 1, will use SAR receivers placed in the ER-2 wing pods to collect simultaneous images of the swath illuminated by the transmitter. At these locations, with zero roll, the horizontal baseline distance between the receivers will be 8.5 meters and the vertical baseline distance will be zero.

The radar transmitter will be located in an instrument bay in the fuselage behind the pilot. Four GPS antennas and receivers will be used, in the differential GPS (DGPS) mode, to collect aircraft position and velocity data which will be used for SAR image forming and DTM extraction. A GPS aided inertial navigation system will also be used to collect motion data that will be needed for motion compensation during SAR image formation. GPS interferometry (GPSI) will be used to measure the SAR interferometer geometric baseline attitude at one second intervals. An on-board clock, synchronized to the GPS 1 pulse per second time signals, will provide system time.

To realize the maximum area coverage per flight, DTEMS will collect data in swaths on both sides of the aircraft. The coverage, illustrated in Fig. 2, will extend from swath inner

edges at eight kilometers ground range to swath outer edges at 36 kilometers ground range. (Ground range is measured from the aircraft ground track.) The distance to the inner edges of swaths was selected to limit the smallest angle of incidence to 22 degrees to avoid excessive fold-over in the SAR images. The distance to the outer edges was selected to limit the largest angle of incidence to 61 degrees to limit shadowing in the SAR images. This geometry will produce 28 kilometers of coverage in each swath and, at an effective ground speed of 210 m/s, the area coverage rate will be 706 km^2/minute.

The 16 km gap in coverage (between the inner edges of the two 28 km swaths) will be covered by two-pass operations as illustrated in Fig. 3. A typical 6.5 hour mission will have 5.1 hours of cruise time during which radar operation is conducted. Radar operations will begin after ascent to 65,000 feet and will continue for about 153 minutes for 1937 km of flight distance. The pilot will then make a U turn and fly a reverse pass parallel to and 22 kilometers offset from the first pass. On the reverse pass, the swath on one side will cover the 16 km gap left on the first pass and the gap on the reverse pass will be over one of the first pass swaths. There will be six kilometers of adjacent track overlap. The total coverage is 1937 km by 94 km (182,078 km^2).

Mission data includes I&Q samples of the received radar signals, mission time, and samples of the aircraft position, velocity, and attitude. These data will be combined and transmitted via the Satellite Transmission and Relay Link (STARLink) through a NASA TDRSS satellite to the TDRS ground station at White Sands Missile Range, New Mexico. In the event that STARLink or TDRS is not available, on-board data recording will be used. Data will be transmitted or data tapes will be transported to the DTEMS data processing facility.

As illustrated in Fig. 4, the GPS receiver, GPS aided INS, and time clock outputs are input to the navigation and attitude sensing computer (NASC). The inputs are time tagged and processed to obtain the aircraft position, velocity, and attitude vectors at each time interval. The NASC output is combined in a multiplexer with radar data for either on-board recording or transmission via STARLink.

The data processing system, shown in Fig. 5, will use an array processing architecture. The mission data will be input to the array processor via a work station or PC. The resulting DTM and SAR images will be added to the DTM and image archives. Processing will include SAR image formation with motion compensation, SAR interferometry, extraction of the DTM, and coordinate transformations. The DTM will be used to geometrically correct and ortho-rectify the SAR images.

TERRAIN ELEVATION ACCURACY

The major source of terrain elevation error is the indeterminate error in the SIGB tilt [1]. Reference [1] also shows that the total phase error, from a combination of sources, is the second largest contribution to terrain elevation error. Approximately 230 micro-radian indeterminate SIGB tilt knowledge will be obtained by GPSI. A recursive processing technique that will reduce the indeterminate SIGB tilt error to ten micro-radians is described in [2]. The predicted RSS terrain elevation error distribution over the 94 kilometer two-pass swath is presented in Fig. 6. The average terrain elevation error is 0.3 meter. This error distribution will be repeated for adjacent flight coverage on each side. On repeated coverage of same areas, changes in the DTM will be measurable with an elevation resolution of five to ten centimeters.

CONCLUSIONS

The Digital Terrain Elevation Mapping System (DTEMS) will provide ortho rectified digital polarimetric SAR images with three meter resolution and a DTM of the covered area with three meter posting and, for areas with 45 degree or less slope, 0.21 to 0.53 one sigma elevation precision at each post. The horizontal precision at each post will be 0.5 meter and will support production of topographic maps with (NMAS) contour intervals of 0.7 to 1.7 meter. In 1997 DTEMS will create radar image and DTM archives of the USA. Data archives for other countries will follow. DTEMS will also conduct periodic operations for measurement of DTM changes with three meter horizontal and five to ten centimeter elevation resolution.

REFERENCES

[1] H. A. Malliot, "Digital Terrain Elevation Mapping System," *Proc. 1996 IEEE Aerospace Applications Conference* (IEEE 96CH35904), Vol. 4, pp. 91–105, Snowmass at Aspen, CO, Feb. 3–10, 1996.

[2] H. A. Malliot, "DTEMS Interferometric SAR Design and Method of Baseline Tilt Determination, *Proc. 1996 IEEE Aerospace Applications Conference* (IEEE 96CH35904), Vol. 4, pp. 107–127, Snowmass at Aspen, CO, Feb. 3–10, 1996.

[3] T. H. Dixon, Editor, "SAR Interferometry and Surface Change Detection," Report of the Workshop Held in Boulder CO, Feb. 3–4, 1994, Univ. of Miami Rosensteil School of Marine & Atmospheric Science.

[4] R. Ledner, "IFSAR earns high marks in mapping applications," Vexel Inc., Vexel Visions, Vol. 1, No. 3, Oct. 1994.

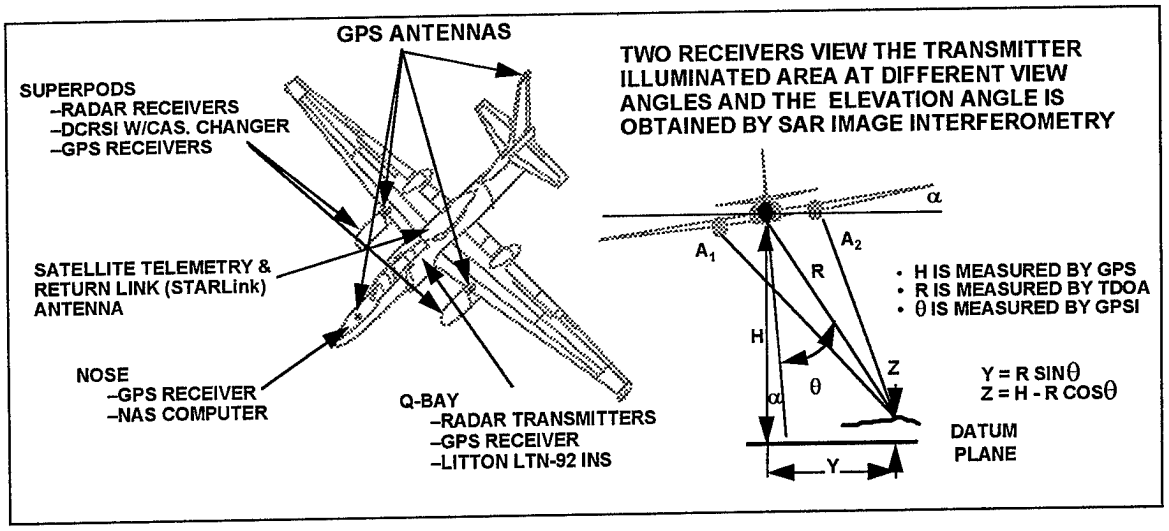


Figure 1. DTEMS incorporates SAR interferometry, differential GPS, GPS interferometry, and satellite data transmission.

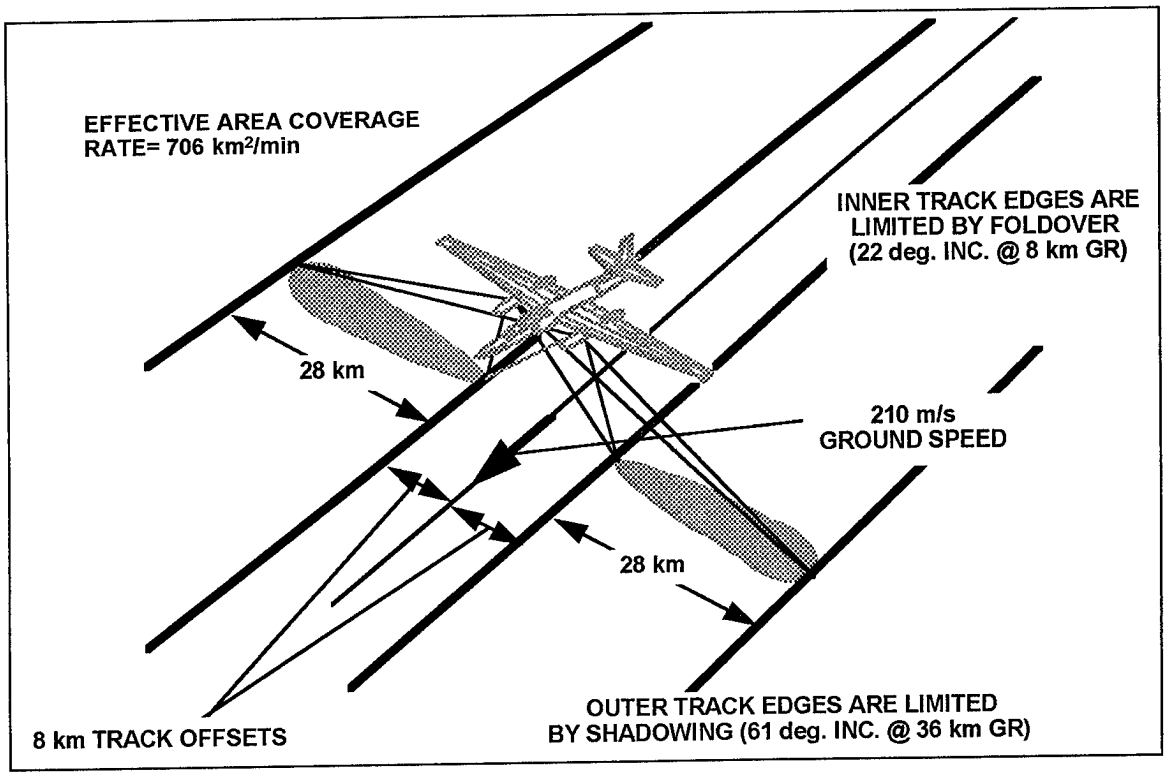


Figure 2. DTEMS will maximize area coverage rate by collecting SAR images in 28 kilometer swaths, simultaniously, on both sides of the aircraft.

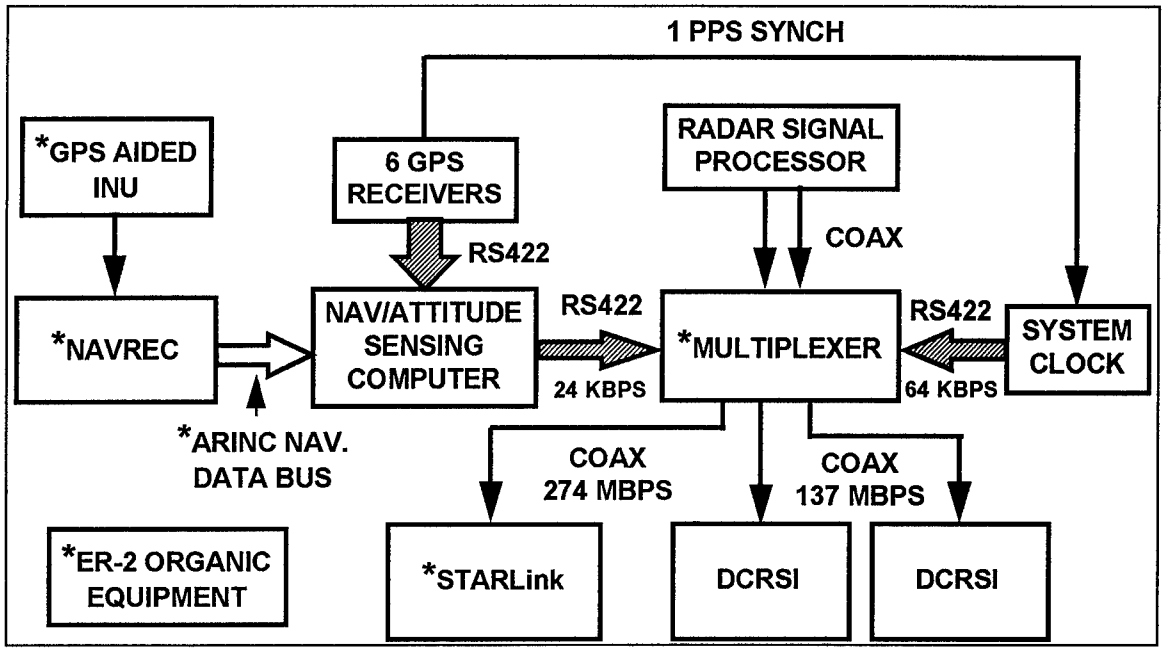


Figure 3. The on-board data processing and handling system.

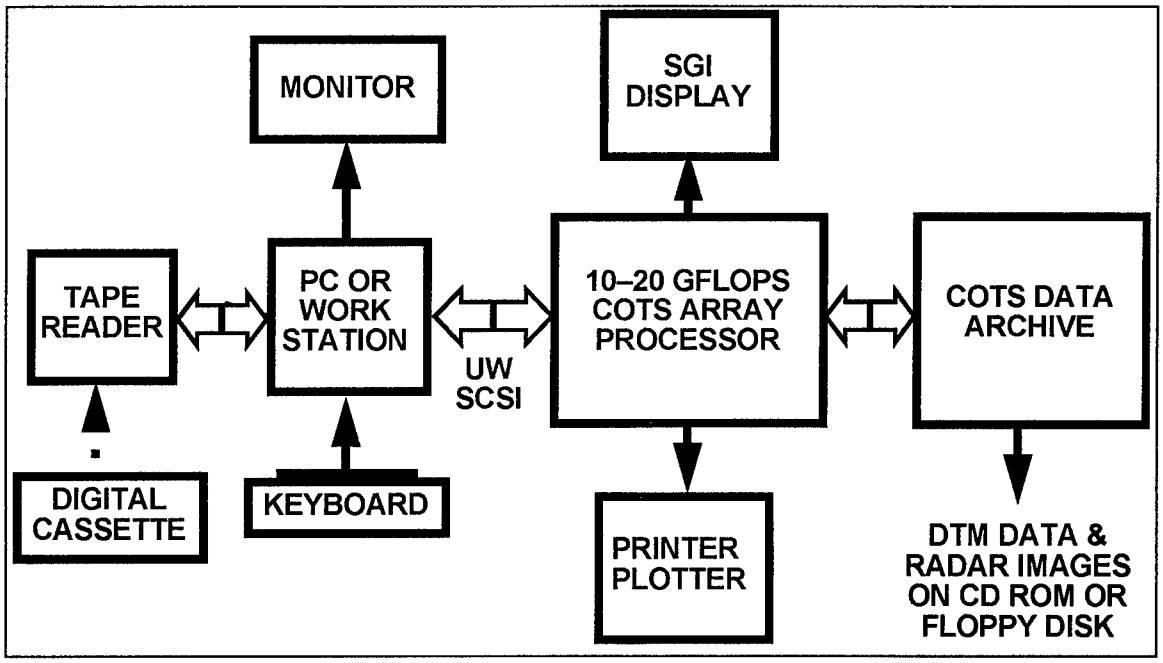


Figure 4. The data processing system will use an array processor to reduce the recorded raw data to produce DTM and SAR images which will be stored in an archive.

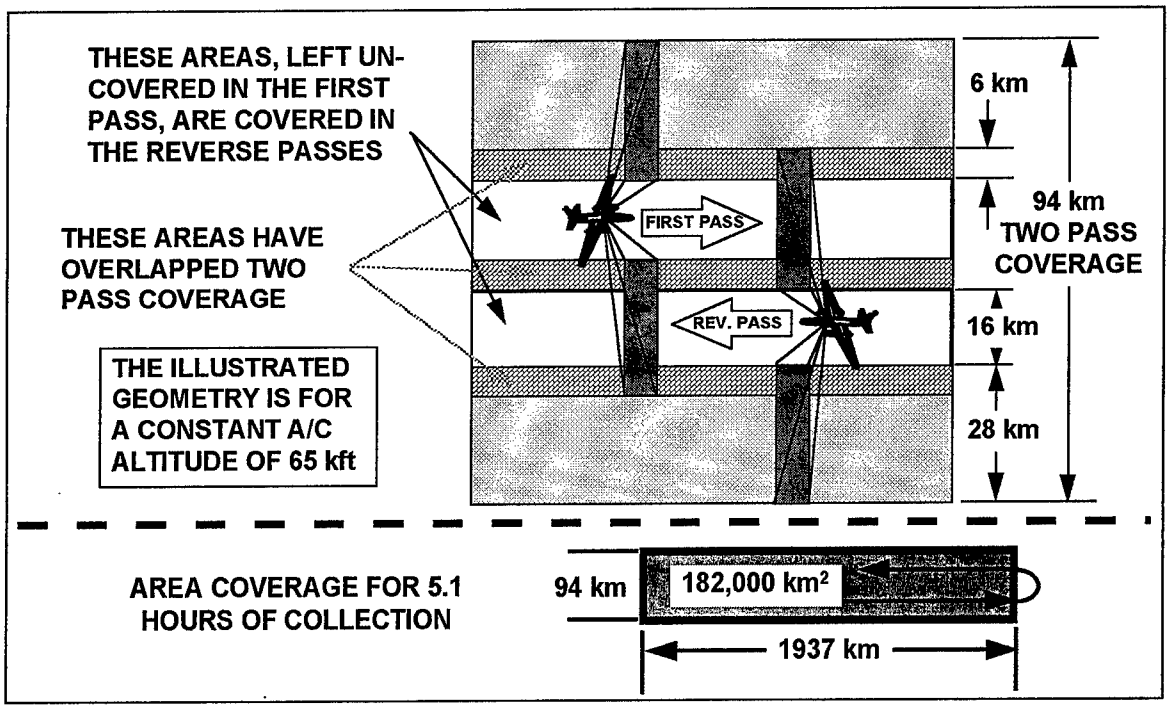


Figure 5. In two passes, DTEMS will fill in the uncovered swaths and cover a total width of 94 kilometers.

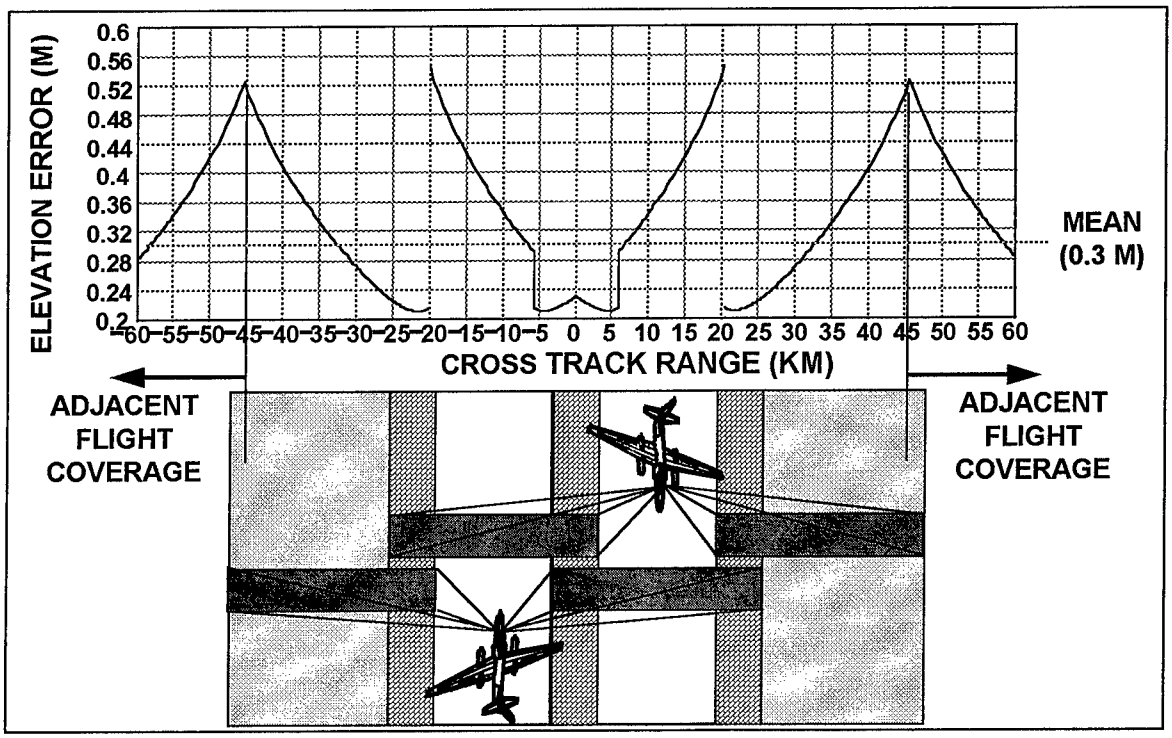


Figure 6. After recursive SAR IGB tilt correction, the terrain elevation error distribution ranges from 0.21 to 0.52 m and has a mean of 0.3 m.

Novel algorithms for remote sensing of chlorophyll content in higher plant leaves

Anatoly A. Gitelson[1], Mark N. Merzlyak[2] and Yuri Grits[1]

[1]Remote Sensing Laboratory, J. Blaustein Institute for Desert Research, Ben-Gurion University of the Negev, Sede-Boker Campus 84993, Israel. Phone: (972)-7-557 219; Fax: (972)-7-557 042; E-mail: gitelson@bgumail.bgu.ac.il

[2]Department of Cell Physiology and Immunology, Faculty of Biology, Moscow State University, 19899 GSP Moscow W-234, Russia. Phone: (007) 095-9392587; Fax: (007) 095-9393807; E-mail: merzlyak@biophys.bio.msu.su

ABSTRACT

The general features of reflectance spectra of higher plant leaves are considered with special reference to remote sensing of chlorophyll. Wavelengths with maximum sensitivity to chlorophyll content were found in the wide spectral range from 550 to 630 nm and near 700 nm. The wavelength of the red edge position of the reflectance spectrum correlated very closely with the reflectance at 550 and 700 nm. The ratios of reflectances in the near infra-red range of the spectrum (above 750 nm) to that at 700 nm R_{NIR}/R_{700} and R_{NIR}/R_{550} were directly proportional to the leaves' chlorophyll content. Newly introduced algorithms make it possible precise chlorophyll estimation (with an error of less than 5 nmol/cm^2) and probably could be applied to a number of plant species. They exhibit more than 6 times wider dynamic range than the widely used Normalized Difference Vegetation Index.

INTRODUCTION

The content of chlorophyll (Chl) in higher plant leaves changes throughout different stages of plant development and is affected when terrestrial vegetation is exposed to various kinds of natural and anthropogenic stresses. Remote determination of Chl content from near and far distance by non-invasive methods is therefore a good mean to detect physiological states and stress conditions in plants. Recently as a result of signature analysis of reflectance spectra of two deciduous species maple and chestnut [2-4] and tobacco plants growing under controlled conditions [7], several indexes were developed. It allowed precise Chl determination in the leaves in a wide range of pigment variation (from dark green to yellow). On the basis of these findings, a novel atmospheric resistant index for remote sensing of Chl was developed [5]. In addition, it was found that reflectance at 700 nm is strongly related to the red edge position in leaf reflectance spectra that can be also used in remote leaf pigment analysis [6,7].

The aim of this study was to examine whether the newly established indices are accurate in quantifying of Chl content in several other plant species growing in a different climatic environments.

METHODS

Maple and chestnut leaves were collected in Moscow from spring to late autumn and the data set covered all stages of leaf development and senescence [2, 3]. Cotoneatser leaves were collected during autumn. Pigment analysis was carried out as described previously [2, 3]. Spectral and Chl data for tobacco plants (both green and aurea mutant) were published in [7]. The leaves of fig, oleander, hibiscus, vine and rose plants were collected during winter 1995/96 in Sede-Boker Campus of Ben-Gurion University of the Negev (Israel).

Reflectance spectra for maple, chestnut and cotoneatser leaves were measured with a Hitachi 150-20 spectrophotometer equipped with an integrating sphere as described in details previously [2]. In experiments carried out in Israel a LICOR-1800 spectral radiometer with integrating sphere attachment LI-1800-12S with spectral resolution of 2 nm was used.

RESULTS AND DISCUSSION

The spectra of standard deviation of reflectance for dark green to yellowish-green leaves of different and non-related species and from different climatic regions revealed common spectral features (Fig. 1). In all cases (see also [2]) a minimum sensitivity to pigment variation was found between 400 and 500 nm and near 676 nm. Two distinct maxima of standard deviation were localized in a broad spectral band from 550 to 600 nm and in a relatively narrow band near 700 nm.

Consistent and diagnostic behavior of reflectance spectra in the red edge range (680 to 750 nm) was observed for leaves of maple, chestnut and tobacco plants [6, 7]. These included the wavelength position of the red edge and the reflectance in the range from 690 to 710 nm. Both characteristics were found to be dependent on chlorophyll concentration. The wavelength of the red edge position of the reflectance spectrum (inflection point) correlated very closely with the leaves' chlorophyll content in a curvilinear manner. The data in Fig. 2 indicate that the reflectance near 700 nm is a sensitive indicator of the red edge position and can be used for Chl determination in higher plant leaves.

0-7803-3068-4/96$5.00©1996 IEEE

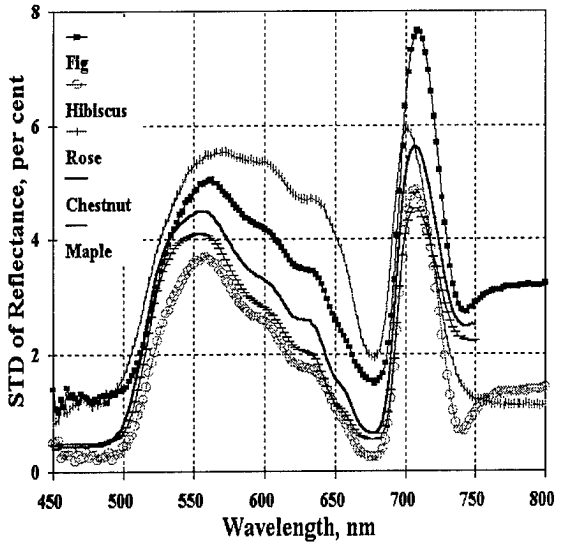


Fig. 1. Standard deviation of reflectance of the leaves with chlorophyll content > 5 nmol/cm^2.

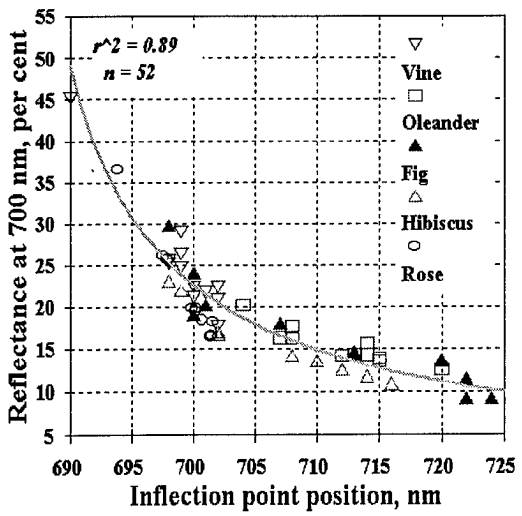


Fig. 2. Wavelength of the inflection point position (the peak at the 1st derivative of reflectance) versus the reflectance at 700 nm for five unrelated plant species. Solid line represents hyperbolic relationship with the coefficient of determination r^2 > 0.89.

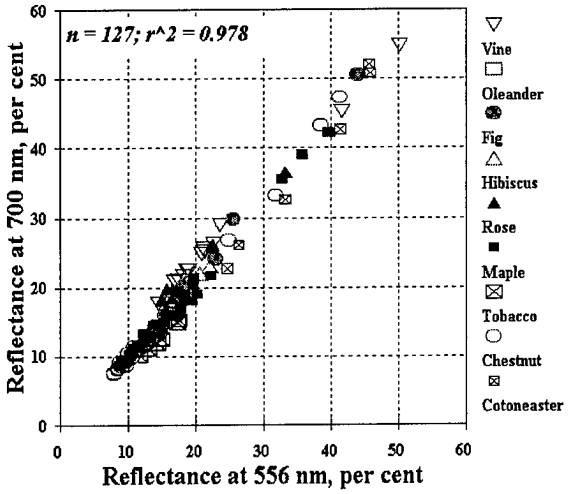


Fig. 3. Relationship of reflectances at 700 and 556 nm for the leaves of different plant species with chlorophyll *a* content from 0.3 to 45 nmol/cm^2. The square of the correlation coefficient was r^2=0.978 for all 127 leaves studied.

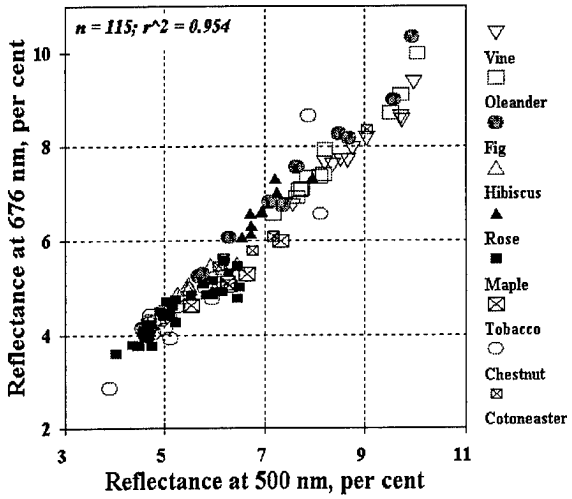


Fig. 4. Relationship of the reflectance at 500 nm with that at 670 nm for 115 studied leaves with chlorophyll *a* content from 5 to 45 nmol/cm^2. The solid line presents a linear relationship with the square of correlation coefficient r^2=0.954.

Maximum sensitivity to variation in Chl content was found in the green and red (near 700 nm) ranges of the spectrum (Fig. 1). As for soybean [1], maple, chestnut [4] and tobacco [7] leaves, reflectances at 700 and 550 nm correlated very closely for other species studied (Fig. 3). This phenomenon at 550 nm is due to an equilibrium of two strong non-linear absorption processes of plant pigments in the red and blue regions [2-4]. Near 700 nm the processes of Chl absorption and scattering by a leaf are also in an equilibrium.

Table. The algorithms for total Chl determination in leaves, having the form Chl = a+ b*R_{750}/R_x. Est. err., is estimation error of Chl, r is the correlation coefficient and n is number of samples measured. Est.err. and a are given in nmol/cm^2.

Leaves	n	R_{750}/R_{550}				R_{750}/R_{700}			
		r^2	a	b	Est.err.	r^2	a	b	Est.err.
tobacco [7]	13	0.95	-12.36	15.79	2.59	0.95	-11.31	12.91	2.54
chestnut	25	0.90	-11.72	12.74	5.97	0.92	- 9.39	1.82	5.38
maple	31	0.89	-11.62	13.75	4.53	0.92	-11.72	13.65	3.89
cotoneatser	8	0.98	-24.73	21.11	3.21	0.98	-20.36	18.48	3.14

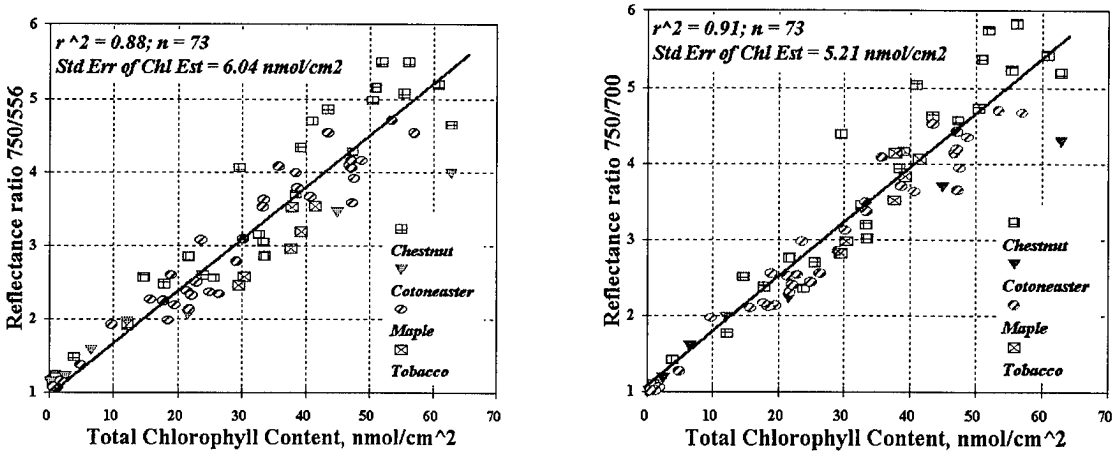


Fig. 5. Reflectance ratios R_{750}/R_{550} and R_{750}/R_{700} versus analytically measured chlorophyll content Data for tobacco leaves were taken from Lichtenthaller et al., 1996 [7].

Similar behavior of reflectances near 500 nm and 670 nm (with very small variation and sensitivity to changing in Chl content) was observed for yellowish-green to dark green leaves (Chl > 5 nmol/cm^2). The correlation was very high with determination coefficient $r^2 = 0.954$ (Fig. 4).

Several functions of reflectance directly proportional to Chl content have been found and novel and effective algorithms for estimation of pigment contents in leaves were introduced. These algorithms provide precise estimation of Chl in the leaves with a wide range of the pigment variation (total Chl from 0.6 to more than 56 nmol/cm^2). The results of application of two algorithms (R_{750}/R_{556} and R_{750}/R_{700}) utilizing spectral regions with maximal (reflectances near 550 and 700 nm) and minimal (reflectance at 750 nm was used as a reference) sensitivity to chlorophyll variations in the leaves are shown in Figs. 5 and in Table.

REFERENCES

[1] E.W. Chappelle, M. S. Kim, and J. E. McMurtrey, III, "Ratio analysis of reflectance spectra (RARS): An algorithm for the remote estimation of the concentrations of chlorophyll *a*, chlorophyll *b*, and carotenoids in soybean leaves," Remote Sens. Environ., vol. 39, pp. 239-247, 1992.

[2] A.Gitelson and M.N. Merzlyak, "Spectral reflectance changes associated with autumn senescence of *Aesculus hippocastanum* L. and *Acer platanoides* L. leaves. Spectral features and relation to chlorophyll estimation," J. Plant Physiol., vol. 143, pp. 286-292, 1994.

[3] A. Gitelson and M.N. Merzlyak, "Quantitative estimation of chlorophyll-*a* using reflectance spectra: Experiments with autumn chestnut and maple leaves," J. Photochem. Photobiol.(B), vol. 22, pp. 247-252, 1994.

[4] A. Gitelson and M. Merzlyak, Signature analysis of leaf reflectance spectra: algorithm development for remote sensing of chlorophyll. J.Plant Physiol.,1996, in press.

[5] A. Gitelson, Y.J. Kaufman and M.N. Merzlyak, "Green atmospherically resistant vegetation index for EOS-MODIS," Remote Sens. Environ., 1996, in press.

[6] A. Gitelson, M.N. Merzlyak, and H.K., Lichtenthaler, "Detection of red edge position and chlorophyll content by reflectance measurements near 700 nm," J. Plant Physiol., 1996, in press.

[7] H.K. Lichtenthaler, A.A. Gitelson and M. Lang, "Non-destructive determination of chlorophyll content of leaves of a green and an aurea mutant of tobacco by reflectance measurements," J. Plant Physiol.,1996, in press.

An Approach For Mapping Light-Use Efficiency On Regional Scales Using Satellite Observations

J M. Norman, M C. Anderson and G.R. Diak

1525 Observatory Drive, University of Wisconsin
Madison, WI 53706 USA
Tel: (608)262-4576 Fax: (608)265-2595
email: norman@calshp.cals.wisc.edu

ABSTRACT

Light-Use-Efficiency (LUE), which is the ratio of carbon dioxide uptake to intercepted photosynthetically active radiation (IPAR) for a plant canopy, is a simple way to characterize plant productivity. By combining the concept of LUE with a stomatal-response model for leaves that is adapted to canopies, we have derived a simple analytical biophysical (SAB) model of canopy assimilation and conductance that agrees with a detailed soil-plant-atmosphere model named Cupid under a range of conditions. Assimilation predictions from this SAB model include effects of IPAR, carbon dioxide concentration, atmospheric humidity, temperature and available soil water. This SAB model has been integrated into a two-source model for estimating surface energy balance components from satellite observations (vegetation index, albedo, surface radiometric temperature) along with plant type and ground measurements of wind speed and atmospheric lapse rates. By obtaining an estimate of vapor pressure near the surface, which is possible from a combination of surface synoptic network measurements and sunrise surface temperature measurements from a satellite like GOES, the LUE can be estimated. Predictions from the SAB model compare reasonably with measurements from FIFE.

INTRODUCTION

The assimilation of carbon dioxide by vegetation is dependent on many factors, including light, temperature, atmospheric humidity, and soil water available to the plant. Models of leaf assimilation are available for various kinds of plants [1], and these leaf models have been integrated into canopy models to predict the dependence of canopy assimilation on various factors [2,3]. These leaf and canopy models show a close relationship between transpiration and assimilation. This relationship between transpired water and assimilated carbon dioxide suggests that a method capable of estimating components of the surface energy budget may be useful for estimating canopy assimilation of carbon dioxide. Recently a new method (Two-Source Time Integrated Model -- TSTIM) has been proposed [4] for estimating the components of the surface energy budget from a combination of satellite observations, radiosonde measurements and surface synoptic data. The TSTIM requires two satellite observations of thermal and visible radiance (GOES) to estimate surface temperature along with solar and net radiation, satellite observations of vegetation cover and albedo (AVHRR or LandSat), an interpolated lapse rate in the lower kilometer of the atmosphere from radiosonde observations, general information on vegetation type, and surface wind speed. Estimates of sensible and latent heat fluxes for soil and vegetation separately can be derived from the TSTIM so that transpiration is available to potentially estimate assimilation. The only additional observational input required for estimating LUE is vapor pressure near the surface.

This paper describes a method for estimating canopy assimilation and canopy light-use-efficiency (LUE) from an extension of the TSTIM [4]. The LUE ($\beta(C_i)$) is defined as the assimilation rate (A) divided by the intercepted photosynthetically active radiation (IPAR). The TSTIM provides estimates of transpiration and the other energy balance components of the soil-vegetation layer, and it assumes that transpiration is proportional to the net radiation divergence of the canopy. The approach described here replaces the transpiration estimated from net radiation divergence with a simple analytical biophysical model that links transpiration and assimilation.

MODEL DEVELOPMENT

The simple analytical-biophysical (SAB) model we propose is a simplified adaptation of a physiologically-based leaf model [1] that is applied to the entire canopy as a unit. Canopy transpiration (T) can be estimated from

$$T = \frac{e_s - e_a}{P\,(r_s + r_x + r_a)} \qquad (1)$$

where e_s is the saturation vapor pressure at the vegetation temperature, e_a is the vapor pressure at a height several meters above the canopy, r_s is the effective stomatal resistance of the vegetation (canopy resistance), r_x is the effective boundary layer resistance of all the leaves in the canopy or might be

0-7803-3068-4/96$5.00©1996 IEEE

considered an approximation to the excess resistance, and r_a is the momentum aerodynamic resistance of the air layer above the canopy based on log-profile theory. From inputs and outputs of the TSTIM plus observed vapor pressure, the only unknown on the right hand side of (1) is r_s. Canopy resistance (r_s) also affects assimilation and that can be expressed as

$$A = \frac{C_a - C_i}{1.6r_s + 1.3r_x + r_a} \tag{2}$$

where C_a is the CO_2 concentration of the ambient air and C_i is the effective internal CO_2 concentration of the leaves in the canopy. Both r_s and C_i are unknowns in (2). Another equation relating stomatal conductance and assimilation is given by [1] as

$$\frac{1}{r_s} = a + b\frac{AH_s}{C_s} \tag{3}$$

where H_s and C_s are relative humidity and CO_2 concentration at the surface of the representative leaf in the canopy. The surface relative humidity is given by

$$H_s = 1 - \frac{T P r_s}{e_s} \tag{4}$$

and the surface CO_2 concentration given by

$$C_s = C_a - (1.3 r_x + r_a) A \tag{5}$$

Only one more relation is required to relate A to C_i for the canopy. The canopy assimilation (A) has been long known to be nearly linearly related to IPAR [5] so that

$$A = \beta(C_i)\, IPAR \tag{6}$$

where $\beta(C_i)$ is the light-use-efficiency. However in [5] the dependence on C_i was not considered. The LUE, $\beta(C_i)$, is dependent on C_i because as the stomata close in response to a desiccating atmosphere or a shortage of water in the soil, the assimilation rate will be reduced. Although the functional dependence of $\beta(C_i)$ or A on C_i is curvilinear for individual leaves, to solve the necessary canopy equations analytically we assume that $\beta(C_i)$ and A are linear functions of C_i according to

$$\begin{aligned} \beta(C_i) &= \beta_{max}\frac{C_i}{0.4C_a} & C_i <= 0.4C_a \\ \beta(C_i) &= \beta_{max} & C_i > 0.4C_a \end{aligned} \tag{7}$$

for C_4 species and

$$\beta(C_i) = \beta_{max}\frac{C_i}{0.8C_a} \tag{8}$$

for C_3 species. This truncated linear approximation is reasonable for C_4 species, but is most appropriate between C_i values of 150 and 350 μmol $(mol)^{-1}$ for C_3 species. This linear approximation overestimates A under moderate-to-severe stress at very low C_i until complete stomatal closure occurs and also overestimates A at very high C_i such as might occur under elevated ambient CO_2 concentration conditions. The overestimates of A under severe stress conditions are likely to cause small errors because most plants go from moderate to severe stress relatively quickly and then adjust green leaf area to alleviate this condition if possible.

Equations (2) - (8) can be solved for r_s, which is substituted into (1) to provide an estimate of T to be used in the TSTIM. Further, (2) can be solved for C_i using (6) for A and $\beta(C_i)$ given by (7) or (8). With C_i known, A can be obtained from (6) with either (7) or (8) as appropriate.

RESULTS

The SAB model is compared with predictions from the Cupid model [3] to determine whether its characteristics are suitable for estimating transpiration and assimilation. Weather, vegetation and soil input data for this comparison were taken from observations collected during the First ISLSCP Field Experiment (FIFE), conducted in and around the Konza Prairie near Manhattan, Kansas in May-October, 1987 [6]. Fig. 1 contains a comparison of transpiration rate from the Cupid model with the TSTIM using the SAB model for vegetation; Fig. 2 contains the same comparison for assimilation. In these comparisons for both C_3 and C_4 species, $\beta_{max} = 0.025$ for the SAB model. A comparison between the assimilation predicted from the SAB model and surface flux measurements from FIFE is included in Fig. 3. The data for this comparison come from site 4439 for selected days between May and October, 1987, and from sites 2133 and 4439 for selected days in July-August, 1989.

CONCLUSIONS

A simple model for relating transpiration and assimilation of carbon dioxide has been presented here and compared to a detailed soil-plant-atmosphere model as well as

measurements from FIFE. The model performs reasonably well and suggests that the Two-Source Time-Integrated model [4] may provide estimates of carbon fluxes as well as evapotranspiration.

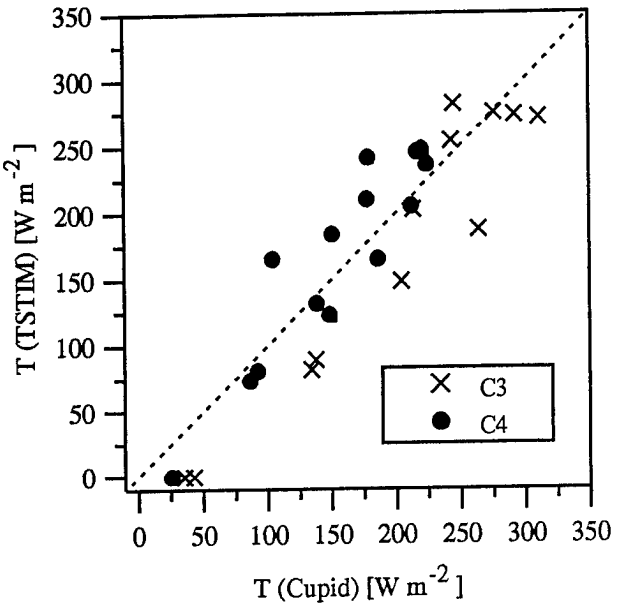


Figure 1. Comparison of transpiration predictions from SAB model with the Cupid model using input data from FIFE.

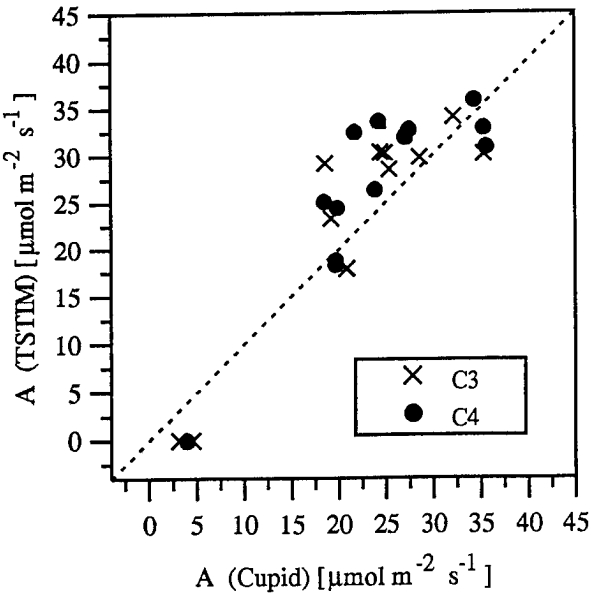


Figure 2. Comparison of assimilation predictions from SAB model with the Cupid model using input data from FIFE

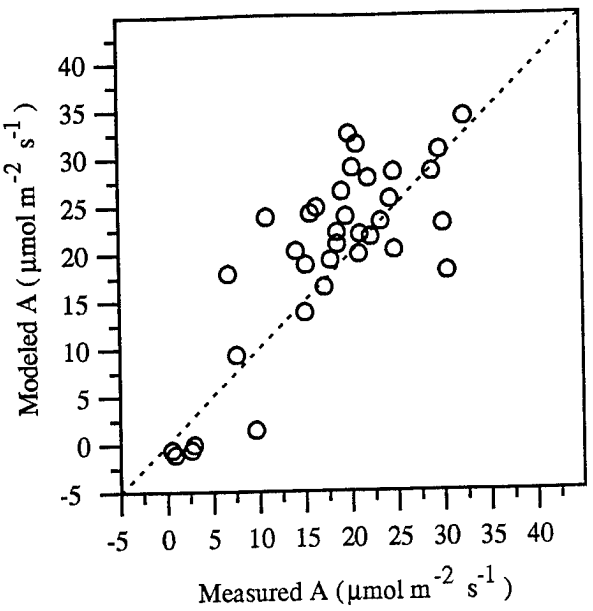


Figure 3. Comparison of assimilation predictions from the SAB model with measurements from FIFE for selected days in 1987 and 1989.

ACKNOWLEDGMENTS

This research was supported by NASA Grant NAGW-4138, with the assistance of the University of Wisconsin Agricultural Experiment Station.

REFERENCES

[1] G.J. Collatz, M. Ribas-Carbo, and J.A. Berry. "Coupled photosynthesis-stomatal conductance model of C_4 leaves", Aust. J. Plant Physiol., vol 19, pp. 519-538, 1992.

[2] J.M. Norman and T.J. Arkebauer, "Predicting canopy light-use efficiency from leaf characteristics", in Modeling Plant and Soil Systems, J.T. Ritchie and R.J. Hanks, ed. ASA: Madison, WI.,1991, pp. 125-143.

[3] J.M. Norman and W. Polley, "Canopy photosynthesis", in Photosynthesis, W.R. Briggs ed. Alan R. Liss, Inc.: New York, 1989, pp.227-241.

[4] M.C. Anderson, J.M. Norman, G. R. Diak, W.P. Kustas and J.R. Mecikalski, "A two-source time-integrated model for estimating surface fluxes from thermal satellite observations", Remote Sensing Environ. 1996. (Submitted)

[5] J.L. Monteith, Climate and the efficiency of crop production in britain. Philos. Trans. R. Soc. London B. vol. 281, pp. 277-294, 1977.

[6] P.J. Sellers, F.G. Hall, G. Asrar, D.E. Strebel, and R.E. Murphy, "An overfiew of the First International Satellite Land Surface Climatology Project (ISLSCP) Field Experiment (FIFE)", J. Geophys. Res., vol. 97, pp.18,345-18,371, 1992.

Detecting Spatial and Temporal Patterns of Aboveground Production in a Tallgrass Prairie Using Remotely Sensed Data

Haiping Su[1], John M. Briggs[2], Alan K. Knapp[2], John M. Blair[2], and John R. Krummel[1]
[1] Argonne National Laboratory, 9700 South Cass Ave., Argonne, IL 60439, U.S.A.
Tel: (708) 252-4091, Fax: (708) 252-6413, Email: hsu@spatail.ead.anl.gov
[2] Kansas State University, Division of Biology, Manhattan, KS 66506, U.S.A.

Abstract -- Spatial and temporal patterns of aboveground production in a tallgrass prairie ecosystem constitute one of the important spatial components associated with ecological processes and biophysical resources (e.g., water and nutrients). This study addresses the effects of disturbance, topography, and climate on the spatial and temporal patterns of North American tallgrass prairie at a landscape level by using high resolution satellite data. Spatial heterogeneity (SH) derived from the satellite data was related to the impacts of the disturbance of fire and grazing, topographical gradient, and amount of precipitation during the growing season. The result suggests that ecological processes and biophysical resources can be quantified with high resolution satellite data for tallgrass prairie management.

INTRODUCTION

Climatic change, disturbance (e.g., fire and grazing), and topography are three important factors influencing tallgrass prairie production and ecosystem function. Spatial variability in net primary production (NPP) is often associated with topographic gradients [1,2]. Topography is also related to soil moisture [3,4] and available soil nitrogen [5] gradients. The impacts of climate, disturbance, and topography on tallgrass production patterns and dynamics result in complete interactions among components with strong negative and positive feedbacks. Previous research on this issue focused on field-scale surveying and sampling, which make it difficult to extend the results to a spatially heterogeneous landscape if the number of field samples is limited. However, remote sensing techniques have provided the capability of detecting aboveground vegetation production for decades. As high resolution satellite images become available, detecting changes in vegetation patterns and dynamics within a watershed or landscape becomes possible.

Numerous studies have been reported on detecting and evaluating soil information [6], biophysical parameters [7], and primary production [8] in the tallgrass prairie ecosystem by using remotely sensed data. A few studies have addressed the spatial and temporal aspects of the landscape between the aboveground production patterns, derived from remotely sensed data, and the impacts of disturbance, topography, and environmental conditions. In an early study, Nellis and Briggs [9] suggested that Landsat TM and aerial photography are sufficient for conducting the landscape classification of burned and unburned watersheds in the tallgrass prairie. Later, Briggs and Nellis [10] examined the intraseasonal variability of the spatial structure derived from SPOT satellite images. To link remote sensing data with ecological processes in the tallgrass prairie, Davis et al. [11] and Henebry [12] used spatial dependence measures to detect changes in the tallgrass prairie with Landsat TM data. In our study, we used a spatial heterogeneity (SH) measure, calculated from the normalized difference vegetation index (NDVI) images that were derived from Landsat TM images, as a texture measure, to determine the spatial and temporal patterns of the grassland production and its relation to topography, disturbance, and climate.

In this paper, we (1) evaluate relationships between tallgrass prairie production and topographic gradient from ground and satellite-based data and (2) link the changes in spatial and temporal patterns of the tallgrass prairie production with the effects of precipitation, disturbance (fire and grazing), and topography.

MATERIALS AND METHODS

Study Area

This study was conducted in the Konza Prairie Research Natural Area (KPRNA), a 3,786-ha native tallgrass prairie about 10 km south of Manhattan, Kansas, U.S.A. Vegetation in the study area was dominated by warm season grasses, *Andropogon gerardii* Vit., *Sorghastrum nutans* (Michx.) Nash, and *Panicum virgatum* L. Soils were developed from the Permian limestones and shales with alternating layers of strata. Occasional loess deposits are found on ridge tops at the KPRNA. Limestones in the study area contain cherty components, which prevent soils from being converted into cropland. Average annual precipitation is 835 mm/yr with a variable seasonal distribution resulting in many wet-dry cycles in soils during a typical growing season (April to September). Soil depth varies from uplands (< 0.4 m) to lowlands (< 1 m).

On the basis of fire (prescribed burning) frequency treatment and water catchment basins, KPRNA is divided into about 66 watersheds. In the fall of 1987, bison (*Bison bison*) were introduced into a fenced area with five contiguous watersheds (N1A, N2A, N2B, N4C, and N20A, where the number in the watershed code is years of burning intervals) with different burning frequencies on KPRNA. Bison can move freely within this area. The bison-grazing area was

0-7803-3068-4/96$5.00©1996 IEEE

expanded in 1992 to include an additional five watersheds (N1B, N2B, N4B, N4D, and N20B, where the number is burning interval years). A total of 145 animals were present in 1992.

Plant Sampling

Plant biomass data were collected at the time of maximum seasonal biomass (early August) at eleven sites along an annually burned (1D) and long-term unburned (20B) transect since 1989. Four 0.1 m^2 quadrants were harvested at each of the eleven sites within each ungrazed watershed. The sampled vegetation was sorted into live graminoids, forbs and woody plants, current year's dead, and previous year's dead vegetation. All data except previous year's dead were combined to provide an estimate of aboveground production or NPP. NPP data from 1989 to 1993, except for 1992, were included in this study.

Satellite Image Analysis

A series of nine Landsat TM images acquired during July through August from 1983 to 1991 were used to calculate the normalized difference vegetation index (NDVI) from red (TM band 3) and infrared (TM band 4) bands. All nine Landsat TM images of KPRNA were registered to Universal Transverse Mercator (UTM) coordinates with a 30-m pixel-resolution. A radiometric rectification procedure [13,14] was used to normalize all images onto the 1987 image (as a reference image) on the basis of pseudoinvariant features in real space. This procedure has the advantage of not requiring ancillary information or a complex atmospheric correction model. The suitability of using the 1987 image as the reference has been demonstrated elsewhere [14].

SH was calculated using the intrawindow range, a max-min texture measure [10], for all nine NDVI images. Median values of SH for each watershed and the whole area were also calculated to better represent the spatial structure and minimize the skewness effect. Window sizes, ranging from 3 × 3 to 11 × 11, were used to examine the possible effects of spatial scales. Watersheds (N1A, N20A, N1B, and N20B) were selected for individual spatial pattern comparison. N1A and N20A are both in the riparian area, including a small portion of forest cover; N1B and N20B are in the upper land areas.

Digital elevation model (DEM) data of the study area, with a 30-m resolution, were also available from the Konza geographical information system (GIS) database and were integrated with satellite images to extract elevation information in each transect and watershed on the KPRNA. The SH measure was also applied to the DEM data for the topographical effect analysis. Weather information (e.g., precipitation) from 1983 to 1991 was available for the analysis from the Konza Headquarters Weather station.

RESULTS

Table 1 shows the relationships between NPP and elevation for the annually burned (1D) and long-term unburned (20B) transect from 1989 to 1993 (1992 data were unavailable). A significant linear correlation ($p < 0.05$) was found between NPP and topographic position for the annually burned transect with r^2 from 0.42 to 0.72. No clear trends were evident for the long-term unburned transect, for which no statistical correlation was found in 1990 and 1993 data. Relationships between NDVI and elevation from 1987 to 1991, as shown in Table 2, also suggest that higher correlation occurs for the annually burned transect than for the long-term unburned transect, except for 1991, in which case the correlation is enhanced by a wildfire.

Table 3 shows the Spearman correlation coefficient for the relationships between SH for NDVI and SH for elevation. There was a statistically significant relationship for most of the nine NDVI images and elevation data, except for the images in 1983, 1986, and 1988. No clear trends were seen as window sizes increase from 3 × 3 to 11 × 11.

Table 1. Coefficient of determination between net primary production (NPP) and elevation for the annually burned (1D) and long-term unburned (20B) transect.

	1D		20B	
Year[1]	r^2(n = 11)	p	r^2(n = 11)	p
1989	0.42	0.03	0.00	0.98
1990	0.51	0.02	0.41	0.03
1991	0.42	0.03	0.33	0.06
1993	0.72	0.03	0.01	0.88

[1] 1992 NPP data were not available.

Table 2. Coefficient of determination between NDVI and elevation for the annually burned (1D) and long-term unburned (20B) transect from 1987 to 1991.

	1D		20B	
Year	r^2(n = 10)	p	r^2(n = 9)	p
1987	0.71	0.00	0.53	0.03
1988	0.65	0.00	0.66	0.01
1989	0.51	0.02	0.35	0.09
1990	0.63	0.01	0.46	0.04
1991	0.41	0.04	0.69	0.01

Fig. 1 shows a negative correlation between SH and total growing season (April through August) precipitation. SH increases as the precipitation decreases. Fig. 2 shows the fire and grazing effects of SH for watersheds N1A, N20A, N1B, and N20B. It appears that there is no clear trend of variation in SH between two adjacent watersheds (N1A -- burned annually; N20B -- long-term unburned) from 1983 to 1987. SH of the annually burned watershed (N1A) is higher than that of the long-term unburned watershed from 1988 to 1991. Watersheds N1B and N20B, which did not have bison grazing from 1983 to 1991, also show very little difference in SH with the different burning frequency treatments.

DISCUSSION

At a landscape level, topography plays an important role in soil moisture distribution [3,4], soil nutrient cycling and availability [5], plant and water relation [15], and microclimate [2]. All those factors influenced by topography finally contribute to spatial variability of primary production in the tallgrass prairie ecosystem. The correlation between NPP and elevation for the annually burned transect agreed with the findings of Barnes et al. [1] and Knapp [2]. However, this relationship may vary in a long-term unburned watershed because of increasing SH or patchiness with invasion of woody species [16] and variation in soil moisture and other biophysical resources [3]. The topographic effect interacted strongly with seasonal and intraseasonal climatic change (e.g., precipitation variation). For example, in the relative dry (1983 or 1988) and wet (1986) years, the variation of the NDVI patterns was not significantly related to the topography (Table 3).

Table 3. Spearman correlation coefficient for the relationships between SH for NDVI and SH for elevation for 49 selected watersheds from 1983 to 1991.

	Window Size (pixels)				
Year	3 × 3	5 × 5	7 × 7	9 × 9	11 × 11
1983	0.14	0.13	0.14	0.24	0.24
1984	0.37**	0.38**	0.37**	0.43**	0.41**
1985	0.55**	0.55**	0.57**	0.49**	0.38**
1986	0.24	0.19	0.12	0.16	0.19
1987	0.26	0.31*	0.29*	0.32*	0.37**
1988	0.20	0.20	0.06	0.13	0.33*
1989	0.41**	0.50**	0.52**	0.57**	0.56**
1990	0.53**	0.53**	0.52**	0.57**	0.50**
1991	0.54**	0.47**	0.46**	0.50**	0.47**

* Statistically significant at a level of 5%.
** Statistically significant at a level of 1%.

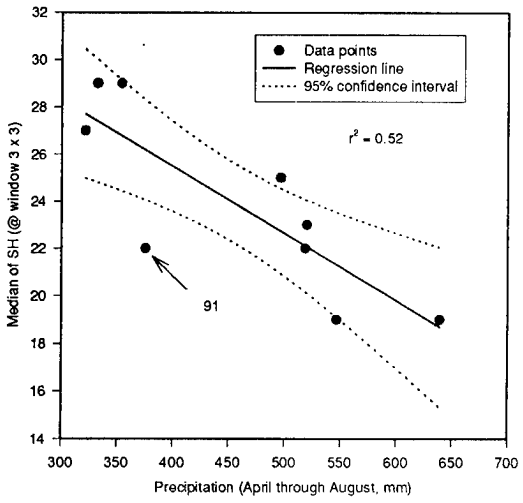


Fig. 1. Relationship between median of SH and total growing season precipitation for the nine Landsat TM images (1983-1991).

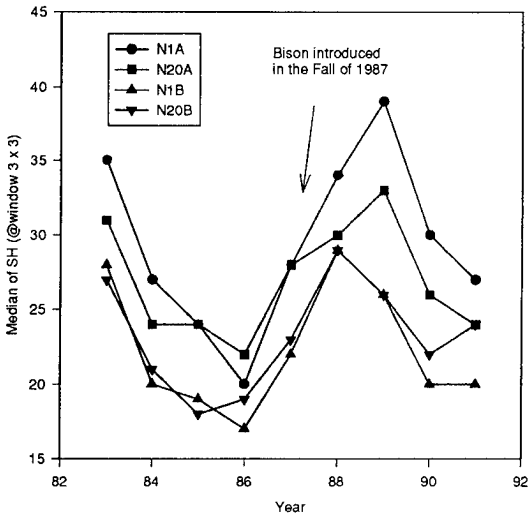


Fig. 2. Seasonal changes in SH values from 1983 to 1991 as affected by bison and fire. N1A is burned and grazed; N20A is unburned and grazed; N1B is burned and ungrazed; and N20B is unburned and ungrazed.

Total growing season precipitation, an important climatic variable, is a key parameter in vegetation production and is strongly correlated with the spatial structure of the NDVI patterns measured by the intrawindow range technique. Although Fig. 1 does not show the correlations for larger window sizes (> 3 × 3), the relation exhibits a similar trend.

Seasonal precipitation is responsible for increases or decreases in SH. However, the effect of precipitation could confound the topographic effect that causes the spatial variability in soil moisture [4], nutrients [5], and production [1]. It is not clear that the short-term drought from 1988 to 1989 caused plant species and community changes. Introduction of bison in the fall of 1987 may also have impacted the spatial structure.

Grazing not only removes vegetation but also increases compaction of soil by trampling and wallowing. Landscapes grazed by large herbivores can undergo changes in surface hydrology [17], plant community [18], and plant water relations [19], thereby creating SH (local patchiness) at the subpixel scale of the Landsat images. Grazing, coupled with the 1988-1989 drought, in the annually burned watershed (N1A) may be responsible for the increase of SH values after 1987. Selective grazing [19] on the annually burned watershed could be the major factor that results in higher SH values for the annually burned watershed compared to the long-term unburned watershed (N20A), even though the drought in 1988-1989 may have interacted with the grazing.

Nellis and Briggs [9] used a similar approach to assessing the effect of spatial scales on the impact of burning and grazing on the KPRNA. They suggested that finer scale remote sensing data, such as aerial photographs and Landsat TM, were sufficient for examining the SH of the burned and unburned areas (watersheds). However, on the basis of the results of our study, it is uncertain whether the burning effect can be assessed by the SH values derived from the Landsat TM images. Comparing the annually burned, ungrazed watershed (N1B) with the long-term unburned, ungrazed watershed (N20B), no clear trend suggested that the long-term unburned watershed exhibited higher SH. The interpretation by Nellis and Briggs [9] was based on a single Landsat TM image (1987) and different watersheds, which may not be comparable. We believe that the fire effect is scale dependent and may intermingle with other factors such as grazing, precipitation, and topography. However, further investigation is required to assess the spatial pattern and its relation to the ecological processes in the tallgrass prairie ecosystem.

CONCLUSIONS

Detecting spatial and temporal patterns in aboveground production is important for long-term monitoring of ecological and environmental conditions in the tallgrass prairie ecosystem. High resolution Landsat TM image data provide the capability of detecting landscape patterns in this ecosystem as affected by topography, disturbance (fire and grazing), and climatic change. We concluded that topographic effect in aboveground production was characterized by the SH measure derived from the Landsat TM images and intermingled with seasonal precipitation and possibly with fire and grazing. Landsat TM data are useful in detecting the spatial structure of the tallgrass prairie. However, the SH measure needs to be further investigated as a metric to monitor and assess the changes in ecological and environmental conditions as affected by natural and/or human impacts.

ACKNOWLEDGMENT

Research supported by the U.S. National Science Foundation under the Long-Term Ecological Research (LTER) program and the U.S. Department of Energy, Office of Policy, under contract W-31-109-Eng-38. Konza Prairie Research Natural Area (KPRNA), a preserve of the Nature Conservancy, is operated by the Division of Biology, Kansas State University. A special thanks to Dr. Kirk LaGory, Argonne National Laboratory, for providing valuable comments on this manuscript.

REFERENCES

[1] P.W. Barnes, L.L. Tieszen, and D.J. Ode, "Distribution, production, and diversity of C_3 and C_4 dominated communities in a mixed prairie," Can. J. Botany, vol. 61, pp. 741-751, 1983.

[2] A.K. Knapp, "Early season production and microclimate associated with topography in a C_4 dominated grassland," Ecol. Plant., vol. 6(20), pp. 337-346, 1985.

[3] D.S. Schimel, T.G.F. Kittel, A.K. Knapp, T.R. Seastedt, W.J. Parton, and V.B. Brown, "Physiological interaction along resource gradients in a tallgrass prairie," Ecol., vol. 72(2), pp. 672-684, 1991.

[4] H. Su, A.K. Knapp, and J.M. Briggs, "Effects of topography and fire on spatial and temporal distribution of soil moisture in a tallgrass prairie," Proceedings of Time Domain Reflectometry, Bureau of Mines, U.S. Department of Interior, Special Publication SP 19-94, pp. 154-162, 1994.

[5] P.G. Risser and W.J. Parton, "Ecosystem analysis of the tallgrass prairie: nitrogen cycle," Ecol., vol. 63, pp. 1342-1351, 1982.

[6] H. Su, E.T. Kanemasu, M.D. Ransom, S.S. Yang, "Separability of soils in a tallgrass prairie using SPOT and DEM data," Remote Sens. Environ., vol. 33, pp. 157-163, 1990.

[7] P.J. Sellers, F.G. Hall, G. Asrar, D.E. Strebel, and R.E. Murphy, "The First ISLSCP Field Experiment (FIFE)," Bull. Am. Meteorol. Soc., vol. 69, pp. 22-27, 1988.

[8] J.M. Briggs and M.D. Nellis, "Thematic Mapper digital data for predicting aboveground tallgrass prairie biomass," Proceedings of the Eleventh North American Prairie Conference, pp. 53-55, 1989.

[9] M.D. Nellis and J.M. Briggs, "The effect of spatial scale on Konza Landscape classification using textural analysis," Landscape Ecol., vol. 2, pp. 93-100, 1989.

[10] J.M. Briggs and M.D. Nellis, "Seasonal variation of heterogeneity in the tallgrass prairie: a quantitative

measure using remote sensing," Photogram. Eng. Remote Sens., vol. 57, pp. 407-411, 1991.

[11] F. Davis, R. Dubayah, J. Dozier, and F.G. Hall, "Covariance of greenness and terrain variables over the Konza Prairie," in Quantitative Remote Sensing: An Economic Tool for the Nineties Digest - International Geoscience and Remote Sensing Symposium (IGARSS), IEEE, Piscataway, NJ, Vol. 3, pp. 1322-1325, 1989.

[12] G.M. Henebry, "Detecting change in grasslands using measures of spatial dependence with Landsat TM data," Remote Sens. Environ., vol. 46, pp. 223-234, 1993.

[13] J.R. Schott, C. Salvaggio, and W.K. Volchok, "Radiometric scene normalization using pseudoinvariant features," Remote Sens. Environ., vol. 26, pp. 1-16, 1988.

[14] G.M. Henebry and H. Su, "Using landscape trajectories to access the effects of radiometric rectification," Int. J. Remote Sens., vol. 14(12), pp. 2417-2423, 1993.

[15] A.K. Knapp, "Water relations and growth of three grasses during wet and drought years in a tallgrass prairie," Oecologia, vol. 65, pp. 35-43, 1984.

[16] G. Towne and C.E. Owensby, "Long-term effects of annual burning at different dates in ungrazed Kansas tallgrass prairie," J. Range Manage., vol. 37, pp. 392-397, 1984.

[17] W.H. Blackburn, "Impacts of grazing intensity and specialized grazing systems on watershed characteristics and responses," in Developing Strategies for Rangeland Management, National Research Council/National Academy of Sciences, Ed., Boulder, Co., pp. 927-983, 1984.

[18] S.L. Collins, "Interaction of disturbances in tallgrass prairie: a field experiment," Ecol., vol. 68, pp. 1243-1250, 1987.

[19] R.L. Senft, M.B. Coughenour, D.W. Bailey, L.R. Rittenhouse, O.E. Sala, and D.E. Swift, "Large herbivore foraging and ecological hierarchies," BioSci., vol. 37, pp. 789-799, 1987.

Assimilation of shortwave remote sensing observations within an agrometeorological model - Crop production estimation.

S. Moulin, A. Fischer and G. Dedieu
CESBIO, Unité mixte CNES-CNRS-UPS
bpi 2801 - 18, avenue E. Belin - 31055 Toulouse Cedex - France
Tel : (33) 61 55 85 19 - Fax : (33) 61 55 85 00 - e-mail : sophie.moulin@cesbio.cnes.fr

Abstract -- The time profile of high spatial resolution satellite signal (SPOT HRV, 20x20m2) was predicted at field scale through the link between a crop model (AFRCWHEAT2, Porter, 1993) and a reflectance model (SAIL, Verhoef, 1984). Both net primary productivity (NPP) and yield were predicted by the crop model. Then satellite observations were used to constrain the crop model, using the 'assimilation' technique. The assimilation of synthetic observations showed that the most pertinent acquisition dates are the ones which occur during the growth period.

INTRODUCTION

The link between an agrometeorological model and shortwave satellite data allows the consistency of the modelling of some remotely observable variables' time profiles to be controlled. Mechanistic crop models provide a good description of matter and energy exchanges between vegetation, soil and atmosphere. This study deals with the modelling of the time profile of satellite reflectances, and then the use of remotely sensed observations in order to constrain the modelling. Over agricultural countries, an important issue is the assessment of the crop production. The possible use of satellite measurements according to this technique is very interesting. Using assimilation technique of remotely sensed data in short wavelengths, we expect to retrieve parameters which drive vegetation seasonal behaviour. Through assimilation technique, we adjust pertinent parameters i.e. parameters which (i) influence the temporal course of radiometric signal, and (ii) have an impact on biophysical processes. In the frame of this study, as a prerequisite step, we focus on one parameter: the sowing date.

In the first section we compared simulated seasonal profile of reflectances to high resolution data for a field. The second section displays the results of the assimilation of 4 satellite observations, by adjusting the sowing date. The retrieved sowing date was then introduced in growth model to estimate primary production and crop yield. The third section concerns a feasibility study performed using synthetic observations. We discuss the number and dates of acquisitions.

MATERIALS AND METHODS

The study site is a 40km by 40km winter wheat region near Chartres (48.5°N, 1.5°E) during 1991/1992 growing season.

High spatial resolution satellite data

SPOT HRV data were available for 4 clear days during the growing period. Data were calibrated (Dinguirard and Henry, 1993) and corrected for atmospheric effects (Rahman and Dedieu, 1994). The error on measured reflectances due to calibration and atmospheric effects was estimated to 0.02.

Field ground survey

Ground surveys (Sharman and Boissezon, 1992) performed for 1992 by agricultural services on 16 randomly distributed areas (test-sites, 700m x 700m) provided field size, crop species, cultivar name and sowing date.

The AFRCWHEAT2 crop growth model

This winter wheat model (Porter, 1993) predicts daily net CO2 assimilation, respiration, assimilate distribution to different plant organs, phenological development, grain yield, and organic matter net production. Input parameters are: meteorological data, environmental data, farming practices and some plant characteristics. A water budget submodel and a nitrogen submodel are included. The model predicts the leaf area index (LAI) of the canopy which is the link with the canopy radiative transfer model.

The SAIL canopy reflectance model

The SAIL (Scattering by Arbitrarily Inclined Leaves) model (Verhoef, 1984) is a generalization of the Suits model (Suits, 1972) which calculates reflectance in the sensor direction as a function of canopy parameters and the acquisition and solar angles. Leaf orientation is described by an elliptical distribution represented by a discrete function of leaf inclination angle distribution (Leaf Inclination Density Function or LIDF). The model accounts for canopy hot-spot as described by Kuusk (1991). LAI is provided by AFRCWHEAT2.

0-7803-3068-4/96$5.00©1996 IEEE

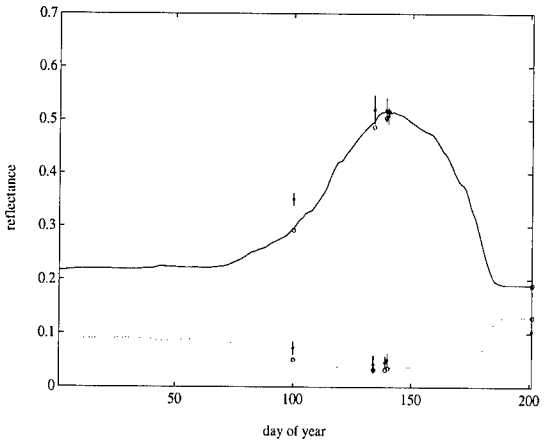
Simulation and assimilation of satellite data

AFRCWHEAT2 crop growth model and SAIL radiative transfer model were jointly used to predict reflectances in the SPOT/HRV spectral bands (Moulin *et al.*, 1995). The linkage of crop model with radiative model, using a 'first guess' sowing date, provided a temporal profile of reflectances. Synthetic or real observations represented the reference set of reflectances. We assumed that the first guess sowing date was uncertain. We selected the sowing date that minimized the merit function, and thus the difference between modelling and observation.

RESULTS AND DISCUSSION

Simulation of seasonal variations of reflectances

We plotted (Fig. 1) the seasonal profile of modelled reflectances for a surveyed field ('Soissons' cultivar sown on October 15, doy 288), with superimposed SPOT measurements plus or minus standard deviation (*). Simulations were performed in Nadir view conditions, except for SPOT acquisition dates where SPOT acquisition angles were used. Upper curves concern nir wavelength, the lower concern visible. Simulations were obtained by coupling the AFRCWHEAT2 crop production model (Porter, 1993) and the SAIL radiative transfer model (Verhoef, 1984).

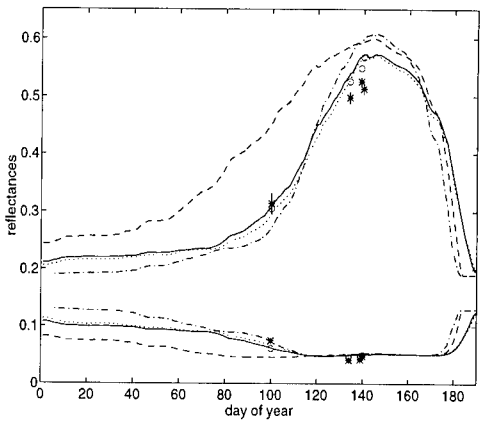


The crop model predicts a yield of 88 qx/ha and a NPP of 2775 gCO2/m2/year.

Real data assimilation

We used the 4 SPOT-HRV scenes to adjust the sowing date for a surveyed field. The real sowing date is October 23 (doy 296). The adjustment performed with 7 first-guess dates converges towards the same sowing date (doy 299), 3 days latter than the real one.

The retrieved value was introduced into the growth model to compute reflectance time profile (Fig. 2). In April, the reflectances simulation (-) agrees well with observations (*) whereas there is a shift in May, for both reference and adjusted time profiles. The adjusted profile (..), obtained using a 2 months range of sowing date around the reference (--, -.), is close to the reference one.



Using the first guess dates, we estimated the NPP and the yield with the crop model. We notice a variation of the seasonal NPP and of the yield with the sowing date used. The estimations of NPP and yield were compared with values obtained for the real sowing date.
The estimated NPP with real sowing date is 2820 gCO2.m-2.y-1. The relative error between NPP estimated with first guess and real dates reaches 17.6% if the error on sowing date is 30 days, whereas the relative error between the adjusted NPP (2740 gCO2.m-2.y-1) and the reference NPP is -2.8%. The estimated yield with real sowing date is 85.6 qx.ha-1. The relative error between yield estimated with first guess and real dates reaches 13.6% if the error on sowing date is 30 days, whereas the relative error between the adjusted yield (87.7qx.ha-1) and the reference yield is 2.4%. The yield provided by ground survey is 79 qx.ha-1 .
In both cases of NPP and yield estimations, the relative error between adjusted and reference values is less than 3%.

Synthetic data assimilation

The synthetic observations were obtained using LAI time profile from a reference simulation (cultivar Soissons sown on 15 October, doy 288) in Nadir view conditions. Tests were performed using first-guess dates varying from doy 258 to doy 318 (i.e. one month more or less the reference date) with a time step of 1 day.
Number of acquisitions: We shared the reference reflectances time profiles in 4 periods: (1) quasi constant reflectances, (2) and (3) increase of nir and decrease of visible reflectances and (4) decrease of nir and increase of visible reflectances. We distinguished periods (2) and (3)

because they correspond to a large variation of reflectances, in particular in nir. In most cases, the more data we have, the more the curvature of the merit function is marked. However, there is no improvement if we add one observation at the end of the cycle. If we have only one observation, the best period is the second one. If we have 2 observations, the best configuration is one acquisition in period 2, the other in period 3.

Dates of acquisition: We performed assimilation tests using successively acquisition dates from the beginning to the end of the cycle with a 10-day time step. In case of one acquisition, the best result (pronounced curvature of the merit function) was obtained with acquisitions on the beginning of the nir signal increase. A couple of acquisitions during period 2 leads to a merit function shape which allows to easily deduce the reference date (provided that observations are perfect). When the sooner acquisition date occurs during end of period 3, the merit function does not allow to retrieve the sowing date.

CONCLUSION AND PERSPECTIVES

First, this study allows to check our ability to reproduce the temporal profile of radiometric signal that can be observed from satellite. SAIL radiative transfer model was linked to AFRCWHEAT2 crop growth model with the leaf area index to predict reflectances. The linked crop/reflectance models are able to predict SPOT HRV high spatial resolution radiometric signal with given initial conditions.

The second part displays the assimilation of real satellite observations into a canopy model. We assume that correction of the initial state can be obtained by the minimization of the differences between observed and simulated reflectances. We assimilated 4 SPOT HRV observations (nir and visible reflectances) into the coupled AFRCWHEAT2/SAIL model for a surveyed wheat field. When satellite observations are used to constrain the crop model, the adjusted parameter is retrieved with a satisfactory accuracy. The yield and Net Primary Productivity estimated with the adjusted date correspond to values obtained with the real sowing date with an error of plus or minus 3%.

In the last part, we used synthetic observations to optimize the number and dates of acquisition. The tests have shown the best adjustments are obtained when at least one observation is acquired at the beginning of nir reflectance increase.

ACKNOWLEDGEMENTS

This work was carried out at the LERTS/CESBIO and supported by CNES, CNRS, "Région Midi_Pyrénées", and the "Programme National de Télédétection spatiale". We thank the JRC of Ispra, SOTEMA, and J. R. Porter.

REFERENCES

Dinguirard, M., Henry, P., (1993), Calibration of SPOT HRV cameras, Remote Sens. Environ., forthcoming.

Kuusk, A., 1991, Determination of vegetation canopy parameters from optical measurements, *Remote Sensing of Environment*, **37**:207-218.

Moulin, S., Fischer, A. , Dedieu, G., and Delécolle, R., 1995, Temporal variations in satellite reflectances at field and regional scales compared with values simulated by linking crop growth and SAIL models, *Remote Sens. Environ.*, 54:261-272.

Porter, J.R., (1993), AFRCWHEAT2 : A model of the growth and development of wheat incorporating responses to water and nitrogen. *Eur. J. Agron.*, **2**,69-92.

Rahman, H., and Dedieu, G., (1994), SMAC : a simplified method for atmospheric correction of satellite measurements in the solar spectrum, *Int. J. Remote Sensing*, vol **15**, no 1, 123-143.

Sharman, M. and Boissezon, H., 1992. Action IV, de l'image aux statistiques : Bilan opérationnel après deux années d'estimations rapides des superficies et des rendements potentiels au niveau européen, *Proceedings of the Conference on the Application of Remote Sensing to Agricultural Statistics*, 26-27 November 1991, Belgirate, Italy, pp 177-186.

Suits, G.H., 1972. The calculation of the directional reflectance of a vegetative canopy. *Remote Sens. Environ.*, 2, 117-125.

Verhoef, W., (1984). Light scattering by leaf layers with application to canopy reflectance modeling : the SAIL model. *Remote Sens. Environ.*, 16, 125-141.

Mapping Field Crop Evapotranspiration Using Airborne Multispectral Imagery

Rashid H. Ahmed and Christopher M.U. Neale
Biological & Irrigation Engineering, Utah State University, Logan, UT 84322-4105
Tel:(801)797-1041 Fax:(801)797-1248 email:rashid@indigo.ecob.usu.edu

ABSTRACT -- Multispectral video images were collected over a wheat field in Smithfield, Utah. The data included digital images in the green, red, near-infrared and thermal-infrared portion of the spectrum. The images were registered to each other. Three layers of reflectance and a surface temperature layer were computed from the images. Spatially distributed net radiation, soil heat flux and sensible heat were estimated using the layers along with meteorological data from the USU drainage farm weather station. The estimated fluxes were compared to independent measurement from a bowen ratio energy balance system setup in the field.

INTRODUCTION

Some of the methods commonly used for determining evapotranspiration (ET) (e.g., lysimeters) give the value of a point in field that may not represent the entire field. Other methods (e.g., bowen ratio, eddy correlation) give integrated ET value for an upwind footprint. Determining the distribution of ET as well as crop stress and biomass is important for irrigation management. Airborne remotely sensed spectral imagery offers a practical method for mapping surface dependent parameters such as canopy temperature and biophysical properties at frequent intervals over large agricultural areas.

The energy balance method used with remotely sensed data has been used for estimating ET [1,2,3]. Evapotranspiration can be estimated as residual from the energy balance equation if the other terms of equation such as net radiation, sensible heat flux and soil heat flux are determined with remotely sensed data inputs. Reference [3] estimated net radiation and soil heat flux from spectral data. Reference [1] estimated the surface energy balance fluxes from airborne radiometric data. Reference [2] used satellite image with ground data to map the energy fluxes. The objective of this study was to investigate the feasibility of mapping evapotranspiration using high resolution airborne multispectral video/radiometer data.

METHODOLOGY

Multispectral imagery was acquired over the study area using the USU airborne video/radiometer remote sensing system [4]. Thermal imagery was acquired using an Inframetrics 760 scanner. The single video image frames containing the experimental wheat field were digitized and registered to each other forming a four band image (green, red, near-infrared and thermal infrared). The images were digitized such that the wheat field was near the center of the frame. This positioned the field in the near-nadir area minimizing bidirectional reflectance effects. The shortwave bands were converted into reflectance through calibration curves developed for the site using measurements of reflectance over different surfaces attained with the airborne Exotech radiometer which is part of the USU system and a calibrated standard reflectance panel. The thermal band was calibrated to yield surface temperatures.

The energy balance equation can be written as:

$$LE = R_n - G - H \tag{1}$$

where LE is latent heat flux, Rn is net radiation, G is soil heat flux and H is sensible heat flux (all in W/m^2). The three right hand side components were estimated and LE was obtained as residual.

Net radiation was estimated as:

$$R_n = (1-\alpha)R_s + \sigma(\epsilon_a T_a^4 - \epsilon_s T_s^4) \tag{2}$$

where α is surface albedo, R_s is incoming short wave radiation, σ is the Stefan-Boltzmann constant, ϵ and T are emmisivity and temperature with subscripts a and s representing air and surface respectively. Surface albedo for the vegetated area was estimated using the [5] equation and the videographic based red band (VIS) and near-infrared (NIR) reflectance. For non vegetated areas the NIR multiplier in (3) would become 0.478. The emmisivity was estimated with the [6] equation. Air temperature and vapor pressure were obtained from bowen ratio setup in the field while solar radiation was obtained from the USU drainage farm meteorological station located about 13 km from the field.

$$\alpha = 0.525VIS + .418NIR \tag{3}$$

$$\epsilon = 1.24\,(e_0/T_a)^{(1/7)} \tag{4}$$

Several expressions relating G to R_n and vegetation indices were evaluated [7,2]. Other expressions estimate G as percentage of R_n.

The sensible heat flux was estimated as:

$$H = \rho_a c_p (T_s - T_a)/r_a \tag{5}$$

0-7803-3068-4/96$5.00©1996 IEEE

where ρ_a is air density [kg/m^3], c_p is air specific heat capacity [J/^{0}C/kg] and r_a, the bulk aerodynamic resistance, was estimated as:

$$r_a = ln[(z-d)/z_0]^2/[uk^2] \quad (6)$$

where z is wind measurement height, d is zero plane displacement [m], z_0 is roughness height [m], u is wind speed [m/s] and k is the von Karman constant. Corrections due to non neutral atmospheric conditions are generally required. The data presented in this study were collected in near neutral conditions and required no correction. The roughness coefficient and zero pane displacement can be estimated from NDVI and NIR/RED respectively [2]. If NDVI exceeds 0.6, z_0 would be fixed as 0.1 meter.

$$d = -0.015 + 0.029 NIR/RED \quad (7)$$

$$z_0 = -0.173 + 1.168 NDVI - 1.125 NDVI^2 \quad (8)$$

RESULTS AND DISCUSSION

Multispectral video data were collected on July1, 1994 and registered to each other. The registered video bands were converted into reflectance using the curves presented in Table 1. The curves were developed using video images taken on July 20, 1994 with reflectance values from the on board Exotech radiometer with field of view centered in the video frames [5]. Reflectance values from the video images were found to be in agreement with independent ground measurements taken with a hand held Exotech radiometer on July 3, 1994.

Several GIS layers were developed from the four band image. First a surface of albedo was obtained using (3) with bands one and two as inputs. As expected albedo values were lower in densely vegetated areas of the field. The albedo layer was used along with the canopy temperature layer "Fig.1" to yield a net radiation map "Fig.2". This layer shows higher values (brighter values) at densely vegetated areas. A sensible heat flux map "Fig.3" was produced using (5) with band 4 (thermal). The distribution of sensible heat followed the surface temperature because the other parameters in (5) were almost constant throughout the field. NDVI exceeded 0.6 most of the areas, therefore z_0, ρ and c_p were assumed constant and d had small variation.

A number of expressions for estimating soil heat flux were considered. The closest to the bowen ratio data was used by [2] for alfalfa.

$$G = 0.583 EXP(-2.13 NDVI) R_n \quad (9)$$

where NDVI is the normalized difference vegetation index.

Table 1.Reflectance vs Videographic Brightness Values.

Band	Slope	Intercept	Rsquare
Green	0.0019	-0.0237	0.99
Red	0.0154	0.0151	0.94
Near Infrared	0.0028	-0.0079	0.96

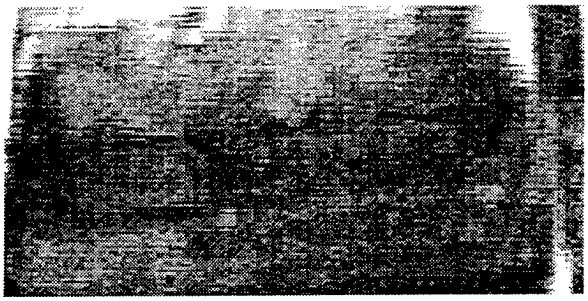


Figure 1. Surface temperature from thermal camera.

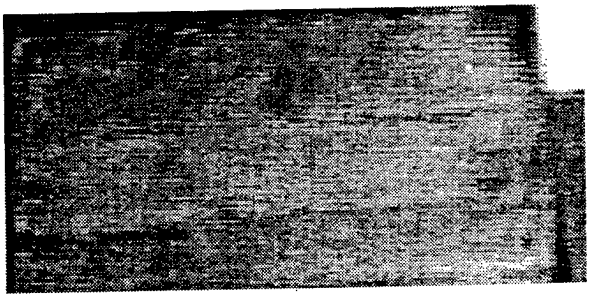


Figure 2. Net radiation map of the wheat field

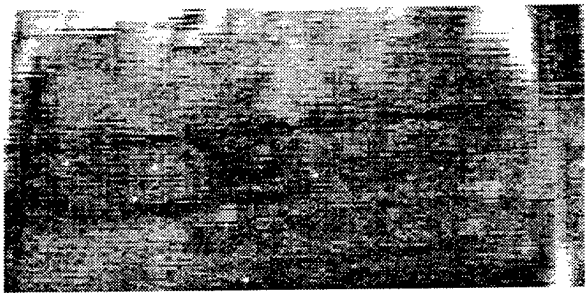


Figure 3. Sensible heat flux map of the wheat field

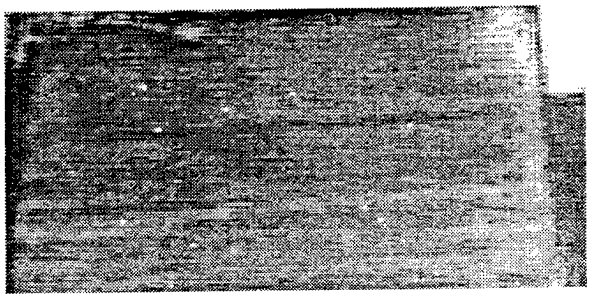


Figure 4. Soil heat flux map of the wheat field

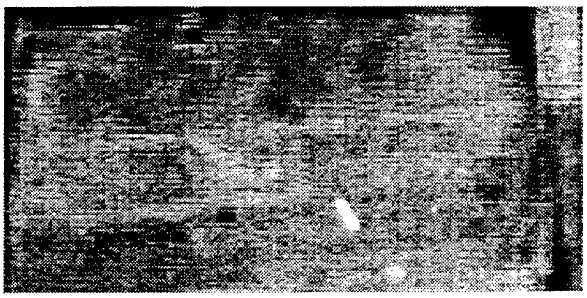


Figure 5. Latent heat flux map of the wheat field

Using the NDVI layer developed from the reflectance image with the R_n layer, a map soil heat flux "Fig.4" was obtained through (9). Areas with lower biomass show higher soil heat flux. Finally, a layer of latent heat flux was created using (1) with the flux layers as input. "Fig.5" showed the LE layer with lower values in less vegetated values and increasing as biomass increased.

Average values of the fluxes were obtained from an upwind footprint of the field. These instantaneous average values were compared to twenty minute average fluxes from a bowen ratio set up in the north end of the field at the top of the image. The predominant wind direction was from south-southwest. Table 2 shows the results from the Bowen ratio and digitized multispectral video as well as the standard deviation (STD) of the videographic data, the difference between the two methods and error as percentage.

The videographic estimates of net radiation, soil heat and latent heat fluxes were sufficiently accurate. However, the sensible heat flux estimate was not satisfactory. The Bowen ratio measurement shows positive sensible heat flux indicating the crop was warmer than air. The multispectral imagery however indicated the crop canopy was cooler than the air resulting in a negative H. A possible source of error could be the calibration of the thermal band. Earlier calibrations of the thermal band from the same instrument with lake water and a desert environment gave accurate results. For this study, however, no independent measurements of canopy temperature were available to confirm accuracy of the instrument calibration. Also, no atmospheric corrections were carried outon the thermal imagery.

Table 2. Comparison of Near Instantaneous Surface Fluxes from Video Imagery and Bowen Ratio [W/m^2].

Fluxes	Rn	G	H	LE
Bowen Ratio	652.0	66.7	12.7	573.2
Multispectral Video	613.8	71.1	-51.9	594.7
STD Video	6.4	2.3	24.6	29.5
Difference	-38.2	4.4	-64.1	-30.5
% Err	-5.9	6.6	-525.4	-5.3

The reported bowen ratio values were twenty minute averages (13:40-14:00), while the instantaneous multispectral video imagery corresponded to 13:45. The temperature difference between the upper and lower arm of the bowen ratio was very small during the period encompassing the flight time so that sensor measurement errors may have contributed.

The latent heat flux was estimated within 6% of the actual. Because most of the net radiation was used for evaporation, the error contribution from H and G was small. This was not unexpected for clear sky day, with wind speed over 4 m/s and plenty of water for evaporation. However, with higher values of H or G, LE estimates would not be as accurate.

CONCLUSIONS

A method of estimating the energy balance fluxes from multispectral video images was described. Net radiation and soil heat flux were estimated with good accuracy (within 7% of actual). This agrees with earlier studies that used radiometric data and satellite images. The advantage of this method is that distribution of the energy balance fluxes can be obtained with high spatial resolution. The method could not adequately estimate the sensible heat flux. Latent heat flux, estimated as residual, was within 6% of the actual. Improvement of sensible heat estimation is necessary for successful application of the method. More work is needed to confirm the suitability of multispectral video to this application.

REFERENCES

[1] W.P.Kustas et al.,"Surface energy balance estimates at local and reg. scales using opt. remote sens. from aircraft platform and atmospheric data collected over semiarid rangelands,"Wat.ResourRes.vol.30,No.5,pp1241-1259,1994

[2] M.S.Moran, "A satellite based approach for evaluation of the spatial distribution of evapotranspiration from agricultural lands," unpublished.

[3] C.S.T. Daughtry et al.,"Spectral estimates of net radiation and soil heat flux," Remote Sens. of Environ., vol.32,pp.111-124, 1990.

[4] C.M.U.Neale and B.Crowther,"An airborne multispectral video/raiometer remote sensing system:development and calibration,"RemoteSens.Environ.,vol.49,No.3,pp.187-194.

[5] C.L.Brest and S.N.Goward, "Driving surface albedo measurements from narrow band satellite data," Int.J. Remote Sens., vol.8,pp.351-367, 1987.

[6] W.Brutsaert,"On a drivable formula for long-wave radiation from clear skies," Water Resour. Res.,vol.11, pp.742-744, 1975.

[7] B.E. Clothier et al., "Estimation of soil heat flux from net radiation during growth of alfalfa," Agric. For. Meteorol.,vol.37, pp.319-329, 1986.

Effects of Shadows on Vegetation Indices

Karl Fred Huemmrich
Hughes STX
NASA/Goddard Space Flight Center
Code 923
Greenbelt MD 20771 USA
Phone: (301) 286-4862
Fax: (301) 286-0239
Email: fred@ltpmail.gsfc.nasa.gov

INTRODUCTION

An important methodology in the remote sensing of biophysical variables is the use of Spectral Vegetation Indices (SVI). A SVI is an algebraic combination of reflectance values from different wavelength bands to produce a single value. Two SVI are evaluated for their usefulness in determining the Fraction of Absorbed Photosynthetically Active Radiation (FAPAR). Evaluating a SVI requires a comparison to a perfect metric for the desired variable. For remote sensing that means the SVI being tested should be sensitive to the variable to be measured, and should provide consistent results for different vegetation types, minimizing the effect of varying canopy characteristics, such as soil background reflectance.

The SVI evaluated in this study are the Normalized Difference Vegetation Index (NDVI) and the Soil Adjusted Vegetation Index (SAVI).

Most work on the remote sensing of biophysical variables has been performed on crop and grassland canopies. This study broadens the landscape types to include forest and woodland canopies. Forest canopy spectral reflectance is simulated using the GeoSail model [1]. The GeoSail model combines a geometric model, which calculates the amount of shadows, with the Scattering from Arbitrarily Inclined Leaves (SAIL) model, which calculates the reflectance of the trees. Scene reflectance is modeled by calculating an area weighted average of three landscape components: illuminated canopy, illuminated background, and shadowed background. The reflectance of these components are obtained from the SAIL model. Illuminated canopy reflectance is the SAIL reflectance with LAI set at the value for the LAI of a single tree. The illuminated background reflectance is the same background reflectance used in the SAIL model. The shadow reflectance is the product of the transmittance through the canopy, calculated from SAIL, and the background reflectance. The geometric part of GeoSail uses the model developed by Jasinski for the limiting case where the shadows cast by clumps of vegetation are very small relative to the size of the area observed [2]. The Jasinski model describes a scene made up of identical geometric solids, in this case cylinders, scattered over a plane with a Possion distribution. In these model runs canopy cover is varied from 0 to 100 percent to produce the SVI - FAPAR relationships.

GeoSail model inputs come from the Superior National Forest (SNF) Study, the Oregon Transect Terrestrial Ecosystem Research (OTTER) Study, and the First International Satellite Land Surface Climatology Project Field Experiment (FIFE) [1]. The model is used to describe the spectral reflectance and FPAR for six different vegetation types: red alder (Alnus rubra), Douglas fir (Pseudotsuga menzeisii), ponderosa pine (Pinus ponderosa), western juniper (Juniperus occidentalis), black spruce (Picea mariana), big bluestem (Andropogon gerardi). Background reflectances are from the materials found below each canopy. For alder and Douglas fir the background is leaf litter, for juniper and big bluestem the backgrounds are soils. Some canopies have vegetation in their backgrounds, black spruce has sphagnum moss and ponderosa pine has rabbit bush as the background.

SVI and FAPAR

NDVI is one of the most often used SVI in biophysical remote sensing. NDVI is defined as:

$$NDVI = (N - R) / (N + R) \quad (1)$$

where N and R are the near infrared and red reflectances, respectively. Figure 1a shows FAPAR and NDVI. All of the relationships shown are curves. For the forest stands, the NDVI - FAPAR curve begins with a steep slope and flattens out as NDVI increases. The prairie NDVI - FAPAR relationship curves in the opposite direction. There is a wide range in the background NDVI values, with background NDVI ranging between approximately 0.1 for the bright soil of the juniper site to 0.6 for sphagnum. The NDVI - FAPAR curves for most stands tend to clump together. Although the closed canopy reflectance endmembers for these species are not the same, the NDVI values of the endmembers are close in value.

Two of the forest types stand out as being different from the others in these plots: black spruce and juniper. The black spruce curve shows very little change in NDVI over the range of FAPAR values, due to sphagnum background having a high NDVI value and the closed canopy NDVI being lower than most of the other stands. The closed canopy NDVI for juniper is much lower than any of the other stands.

Significant errors in FAPAR can occur when trying to estimate it using NDVI. Differences in possible FAPAR values for a given NDVI may be as great as 90 percent FAPAR when considering the range between the ponderosa pine background and the closed canopy juniper. The maximum FAPAR difference between the litter background forests and the prairie is about 35 percent. A relationship

0-7803-3068-4/96$5.00©1996 IEEE

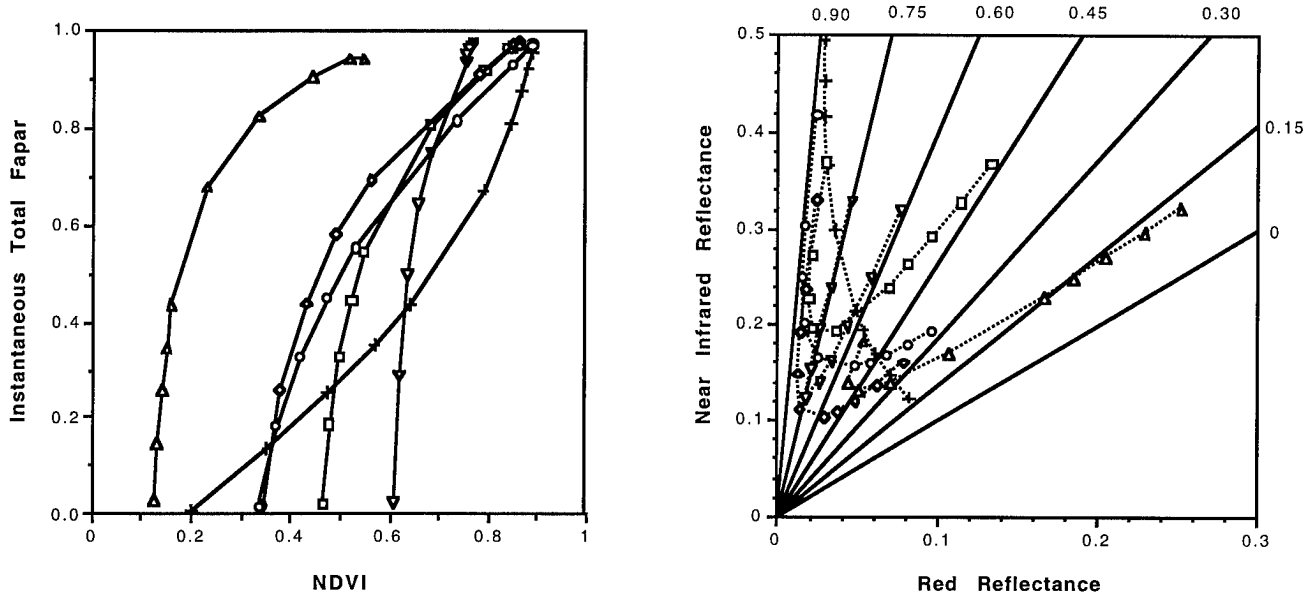


Figure 1 a) FAPAR and NDVI from GeoSail model simulations. b) Near infrared and red reflectance, solid lines are lines of equal NDVI with the value for each line labeled at the right or top of plot, dotted lines are reflectances from GeoSail model simulations. In both plots the following symbols are used to denote the different landscape types simulated: circle for alder, diamond for Douglas fir, square for ponderosa pine, triangle for juniper, inverted triangle for black spruce, and cross for prairie.

developed from prairie data and used in forests would consistently underestimate FAPAR.

SAVI was developed as an index that would minimize soil brightness effects [3]. SAVI is basically NDVI moved into a different coordinate system. SAVI is defined as:

$$SAVI = \{(N - R) / (N + R + L)\} (1 + L) \quad (2)$$

where N and R are the near infrared and red reflectances respectively, and L is a constant offset factor. L shifts the origin of the coordinate system for the NDVI. The value of L may be varied, in this analysis L is set at 0.5.

In figure 2a SAVI is plotted with FAPAR. SAVI shows little sensitivity to FAPAR when it is less than 80 percent. In this region of the curves, both positive and negative relationships can be found between SAVI and FAPAR. When FAPAR is greater than 80 percent, SAVI has a large range of values, while FAPAR varies little. The relationship between SAVI and FAPAR for the prairie shows SAVI's strength in these continuous canopies. The prairie curve is nearly a straight line, nearly an ideal linear relationship. SAVI adjusts for variations in soil brightness, and this is seen in the closeness of the two soil endpoints, juniper and prairie, despite their differences in brightness. SAVI did not adjust as well for the litter or vegetated backgrounds.

As with NDVI, if a relationship between FAPAR and SAVI were developed using prairie data and then used in forests, it would almost always underestimate FAPAR. The underestimation of FAPAR could be as great as 60 percent.

HOW DO SVI WORK?

The calculation of a SVI reduces the information from multiple variables, in these cases the red and near infrared reflectances, to a single value. Ideally, these values are highly correlated with the biophysical variable to be measured. In the case of two band SVI this transform can be displayed graphically. Lines of equal SVI are plotted over graphs of canopy reflectance in red and near infrared reflectance space in figures 1b and 2b. The solid lines in these figures are lines of equal SVI. In these plots note the difference in the reflectance curves between the continuous prairie canopy and the forest canopies. The forest canopy reflectance trajectories have greater curvature due to the presence of shadows in the scene. Each set of SVI lines represent equal changes in the values of the SVI over the range of that SVI. This allows an examination of two important functional characteristics of SVIs: how a SVI divides up the reflectance space to simplify the data, and the sensitivity of a SVI to changes in reflectance.

NDVI is a measure of the slope of the line from the origin to a given reflectance point. In the GeoSail model, the scene reflectance was the weighted sum of three components: illuminated background, illuminated canopy, and shadow. If shadows are dark, that is shadow reflectances are low, then the shadow spectral endmember is near the origin. Thus varying amounts of shadow in a scene, if the proportions of the other two components stay the same, will move the scene reflectance along a line toward the origin. That line is a line of equal NDVI. This indicates one of the properties of NDVI, to minimize the effects of brightness variations in scene.

The separation of the NDVI lines is fairly uniform over the range of NDVI value. For the forest stands most of the change in FAPAR occurs before the canopy coverage reaches the point of maximum shadow cover. In the reflectance space this is the part of the curve where both red and near infrared

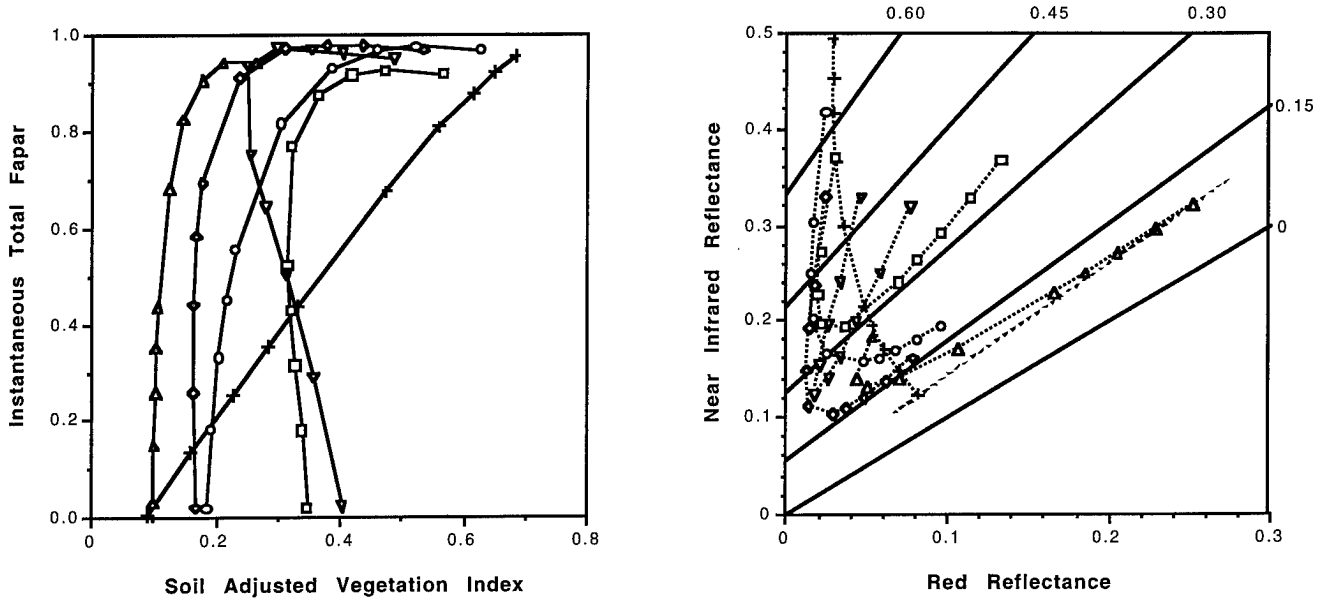


Figure 2 a) FAPAR and SAVI from GeoSail model simulations. b) Near infrared and red reflectance, solid lines are lines of equal SAVI with the value for each line labeled at the right or top of plot, dotted lines are reflectances from GeoSail model simulations, dashed line is the soil line. Plot symbols as in figure 1.

reflectances are decreasing.

SAVI is NDVI with the position of the origin moved to another coordinate. Like NDVI, lines of equal SAVI are straight lines radiating from a single point. The origin for the SAVI lines is outside of the displayed area in figure 2b, having negative reflectance values. Separation of the SAVI lines produces uniform sectors from its origin, as does NDVI. However since the origin is displaced the lines of equal SAVI over the range of reflectances in the examples appear to be only slightly non-parallel. In these examples the soil line should connect the endpoints of the juniper and prairie curves and is shown as a dashed line in figure 2b. The soil line is close to being a line of equal SAVI. Because of this, variations in background soil brightness should have little effect on the value of SAVI. The sections of the reflectance curves with canopy cover less than that of the point of maximum shadow coverage run nearly along the lines of equal SAVI or are crossing the lines such that SAVI is decreasing. SAVI has little sensitivity to these sections of the reflectance curve, where FAPAR is changing the most in forests.

Most of the remote sensing studies of the estimation of FAPAR have been done on crops and grasses. Both of the SVI shown here produced results for the estimation of FAPAR in the prairie which, although curved, could be approximated by a straight line without introducing large errors. However, for the forests, the relationship between the SVI and FAPAR were far from linear, and most would be difficult to use to estimate FAPAR, even if the curves were well defined. In nearly all cases the use of the relationship between SVI and FAPAR developed for the prairie on forest stands would result in an underestimation of FAPAR, sometimes by large amounts.

A critical factor introducing errors in the estimation of a biophysical variable from remote sensing in crop and grass canopies is variation in the background reflectance. Since most of the remote sensing studies have been done with crops and grasses, it is natural that SVIs that have come out of these studies reduce the effect of soil background reflectance variations in some way. With SAVI an attempt is made to have a line of equal SVI go through the soil line, making any soil reflectance have the same value of SVI.

There are two problems with this type of adjustment in the SVI. The lesser of the problems is that not all backgrounds are bare soil. In the data presented here, litter and sphagnum had reflectances well off the soil line. The major problem with these SVIs is that attempts to minimize the effects of variations in soil brightness also minimizes the sensitivity to shadows in the scene in open forest stands. This lack of sensitivity to shadows in forests, with canopy coverage less than that of the point of maximum shadow cover, makes these SVIs vary little in value over the stands where FAPAR is changing the most.

REFERENCES

[1] K. Huemmrich, "An analysis of remote sensing of the fraction of absorbed photosynthetically active radiation in forest canopies," Ph.D. Diss., Univeristy of Maryland, 1995.

[2] M. Jasinski and P. Eagleson, "The structure of red-infrared scattergrams of semivegetated landscapes," IEEE Trans. Geos. Rem. Sens., vol. 27, pp. 441-451, 1989.

[3] A. Huete, "A soil-adjusted vegetation index (SAVI)," Remote Sens. Environ., vol. 25, pp. 295-309, 1988.

Multisensor Estimation of Vegetation Characteristics

J. Zhang*, R. M. Narayanan*, B. T. Tracy**, B. L. Gwilliam**, R. L. Bolus**, T. Pangburn**, H. L. McKim**
* Dept. of Elec. Engr. and Center for Electro-Optics, Univ. of Nebraska-Lincoln, Lincoln, NE 68588-0511,
Tel: 402-472-5141, Fax: 402-472-4732, Email: rnarayanan@unl.edu
** RS/GIS Center, U.S.Army CRREL, 72 Lyme Road, Hanover, NH 03755-1290

Abstract— The case for a multisensor approach to estimate and monitor vegetation characteristics has been well-established. SAR sensors have shown promise in not only classifying vegetation types but also in estimating parameters such as biomass, canopy height, and diameter at breast height (dbh). The accuracy with which vegetation types can be classified and the above parameters estimated can be significantly improved by using data from other optical sensor systems such as color-infrared (IR) imagery and satellite photography.

We have obtained contemporaneous and coregistered SIR-C SAR and airborne color-IR images as well as satellite photographs of a forested area in New Hampshire. Bayesian classification technique is being investigated in order to classify vegetation into broad classes. Inversion algorithms are also being developed for estimating specific vegetation parameters once broad classes have been delineated. The added benefit of integrating optical sensor data with the SAR imagery is being studied in terms of classification and estimation accuracy.

INTRODUCTION

Vegetation on the earth's surface has a great effect on the global ecosystem. It plays an important role in impacting the global carbon cycle, water cycle and climate change. Remote sensing methods to investigate and delineate the extent of land-cover have been proven to be successful in the past. In the 1980's, researchers studied the use of SPOT imagery to classify land-cover. Both manual and computer-assisted image interpretation techniques were studied, and the manual interpretation was also aided with color-IR visual analysis. However, singular use of optical imagery is unreliable under conditions of continued cloud cover that can persist over large areas of the earth's surface. In recent years, researchers are investigating the use of imagery radar data to obtain additional data, that is both complementary as well as reliable under adverse weather conditions, in analyzing land-cover characteristics. Several single-frequency synthetic aperture radar (SAR) systems such as those aboard ERS-1 (C-band, VV polarization), JERS-1 (L-band, HH polarization) have been launched to obtain useful images. The study results clearly demonstrate the potential of SAR in land-cover analysis. For more detailed studies, researchers have found that multi-frequency SAR has the potential to yield more complete information about land-cover characteristics[1]. In 1994, SIR-C/X-SAR was launched to provide multi-frequency polarimetric radar images of the earth. SIR-C/X-SAR is operated at three frequencies in L-band, C-band and X-band. For L-band and C-band, there are four polarization combinations availables: HH, HV,VH and VV. The X-band system operates on VV polarization alone.

In this paper, we will discuss the combined use of SAR data with SPOT as well as color-IR images to classify land-cover, and further estimate the biophysical characteristics of vegetation. Emphasis is placed on SAR data utilization. The potential of optical imagery to improve the classification accuracy is being investigated. The ultimate goal of this project is to estimate the biophysical properties of classified trees.

RESEARCH APPROACH

There are two popular methods that use SAR data to perform land-cover classification. One is a statistical method, called the Bayesian classification approach [2][3][4], while the other is the neutral network approach. In this paper, we will develop the use of the Bayesian classification approach, and evaluate its performance over a test site when compared to the ground truth data.

First, one needs obtain the characteristic matrix for each land-cover class. First, the ground truth maps are digitized and co-registered with the SAR image. Next, a suitable training area is chosen from the SAR image in order to develop the algorithm. The training area could not be too large since anly one SAR image was available, although it is recognized that a large training area reduces the effects of noise. Measures of central tendency, such as the mean and the median are used to construct the characteristic matrix for each class. According to the Bayesian classification method, a pixel is classified into a class with the smallest distance measure. In order to improve the accuracy, the classification is done in an iterative manner. The adaptive a priori probability for each pixel is calculated after every classification, and this information is used in the next iteration. The number of iterations is controlled by the percentage of reclassified pixels.

The classification is done at several levels, as follows:
Level one : man-made vs. natural cover
Level two : water vs. non-water cover
Level three: vegetation vs. bare soil cover
Level four: vegetation types , i.e., brush, trees, meadows
Level five : tree types

The accuracy at each level is determined by comparing the classified pixels with the ground truth data. For pixels which are classified as trees, further analysis is performed

* The above work was partially supported by Contract DACA89-95-K-0020 awarded by the U.S. Army CRREL.

0-7803-3068-4/96$5.00©1996 IEEE

to estimate its biophysical characteristics, such as height, dbh and stand density. The biophysical parameters are estimated on the basis of empirical equations whose parameter constants are derived using regression analysis. The estimated parameters are compared with the ground truth data available from forest inventory.

CLASSIFICATION RESULTS

The study site is located in New Hampshire, near Suncook City, in Bear Brook State Park (43.47N, 71.12W). The site is bounded by the Suncook River. Most of site is covered with different types of vegetation. There are several ponds as well as wetland areas on the site. Some man-made objects such as buildings, roads, and parking areas are distributed throughout the park. The SIR-C/X-SAR data were collected on October 2, 1994. The data obtained from CRREL have been calibrated. The L-band and C-band data cover part of the park, while the X-band image covers the entire park. The ground truth data are available at 1:1500 scale.

Initial studies have focussed on performing level one and level two classification using appropriate training areas. L-band and C-band radar backscatter coefficients, both co-polarized and cross-polarized, were used in these studies.The mean backscatter coefficients for different classes are shown in Table I. These results are shown in Table II and Table III. From the tables, it appears that the for natural object and water cover, classifications appear satisfactory, but a large number of man-made pixels are misclassified as natural areas. The algorithm is expected to be improved in the next stage of our study.

TABLE I

SIGMA0 VALUES FOR DIFFERENT CLASSES

class	LHH	LVV	LHV	CHH	CVV	CHV
A	5.3	8.8	-12.0	16.0	12.8	-2.3
B	-8.2	-8.4	-12.3	-9.6	-11.2	-13.3
C	-23.7	-26.0	-32.6	-21.6	-19.4	-27.2

A -MANMADE B -NATURAL C -WATER

TABLE II

CLASSIFICATION CONFUSION MATRIX

class	manmade	natural
manmade	60%	40%
natural	13%	87%

CONCLUSION

Our preliminary study indicates that SAR imagery is useful in broadly classifying gross terrain types. However, it is felt that the classification can be improved if supporting data are available from alternate optical sensors [5]. This aspect forms the basis of continuing study on this topic.

TABLE III

CLASSIFICATION CONFUSION MATRIX

class	water	nonwater
water	89%	11%
nonwater	27%	73%

REFERENCES

[1] K. J. Ranson, S. Saatchi, and G. Sun, "Boreal forest ecosystem characterization with SIR-C/XSAR", IEEE Trans. Geosci Remote sensing, vol.33, pp867-876,1995.

[2] H. H. Lim, A. A. Swartz, H. A. Yueh, J. A. Kong ,and R. T. Shin, "Classification of earth terrain using polarimetric systhetic aperture radar images" Journal of Geophysical Research, vol.94, pp7049-7057,1989.

[3] J. J. Van zyl and C. F. Burnette, "Bayesian classification of polarimetric SAR images using adaptive *a priori* probabilities", Int.J.Remote Sensing, vol.13, pp835-840,1992.

[4] M. C. Dobson and F. T. Ulaby, "Knowledge-based land-cover classification using ERS-1/JERS-1 SAR composites", IEEE Trans. Geosci. Remote sensing, vol.34, pp83-99,1996.

[5] E. Nezry, E. Mougin, A. Lopes, J. P. Gastellu-Etchegorry and Y. Laumonier, "Tropical Vegetation Mapping with Combined Visible and SAR Spaceborne Data", Int. J. Remote Sensing, vol. 14, pp2165-2184, 1993.

SUBPIXEL SPATIOTEMPORAL PATTERN ANALYSIS OF REMOTE SENSING OBSERVATIONS FOR PREDICTING GRASSLAND ECOLOGICAL AND BIOPHYSICAL PARAMETERS

Ferko Csillag, Andrew Davidson, Scott Mitchell
Department of Geography, University of Toronto
Erindale College, Mississauga, Ontario, L5L 1C6, Canada
tel: 905-828-3862; fax: 905-828-5273; e-mail: fcs@geog.utoronto.ca

Bruce Wylie
Hughes/STX, EROS Data Center, Sioux Falls, SD, USA

David Wedin, Heather Peat
Department of Botany, University of Toronto

Miklós Kertész
Hungarian Academy of Sciences, Budapest

Abstract -- One of the most important limiting factors in reliable estimation of grassland ecosystem parameters from remotely sensed data is "too coarse" resolution. Areal averages obtained from readily available imagery do not match well with ecological field data. To address this discrepancy we have collected simultaneous spectral, other biophysical and ecological data with similar ground resolution between May and August 1995 in the Grassland National Park, Saskatchewan, Canada. Beyond calibration for a wide variety of conditions, the applied nested sampling design facilitates scaling of measured and estimated properties from 0.5 m to 100 m by partitioning overall variability, and by hierarchical scene simulation. Analysis of the spatiotemporal pattern reveals potential probelms with using areal averages in long-term monitoring and assessment of ecological status of grasslands.

INTRODUCTION

There are wide ranging arguments for the advantages of remote sensing observations in studying the spatiotemporal pattern of vegetation, particularly in investigations about the effects of scale [1]. In "everyday practice" it is frequently convenient to neglect some or all of the complications related to the statistical [2], biophysical [3] and ecological [4] aspects and assumptions "behind" changing resolution. It is particularly interesting that inferences are frequently drawn based on biophysical (e.g., reflectance, NDVI) and ecological (e.g., species, or functional groups) observations when their respective spatial resolutions are different with several orders of magnitude.

MEASUREMENT PLAN

To investigate directly this discrepancy, the impact of changing spatial resolution on the potential of remote sensing to detect patch and/or landscape level pattern, we have collected simultaneous spectral reflectance, leaf-area, biomass, Chlorphyll and species composition data with similar ground resolution between May and August 1995 in the Grassland National Park, Saskatchewan, Canada. Around 49:15 N, 107 W, the sites are in the northernmost portion of the Great Plains where cool and warm season (C3 and C4) grasses are mixed. There were 30 plots where phenological data were collected regularly. Three "hectare-plots" were located on various parts of the park (their centre coinciding with the phenology plots) according to species dominance and patchiness and spectral measurements were carried out according to an unbalanced nested sampling design (Fig.1.).

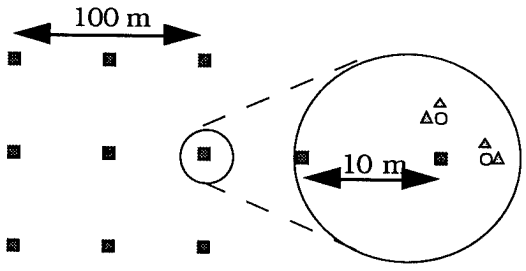


FIGURE 1.
The unbalanced nested sampling desing for spectral and coenological observations. The 72 samples (with 50 cm nominal ground resolution) are distributed over five distinct distance ranges between 0.5 m and 50 m.

0-7803-3068-4/96$5.00©1996 IEEE

Each sample had a nominal ground resolution of 50 cm. Several calibration measurements were completed during the measurement period (e.g., ceptometer readings, clipping and sorting, repeated EXOTECH measurements from a ladder) and in mid-June all plots were surveyed with an array of instruments (Fig.2.).

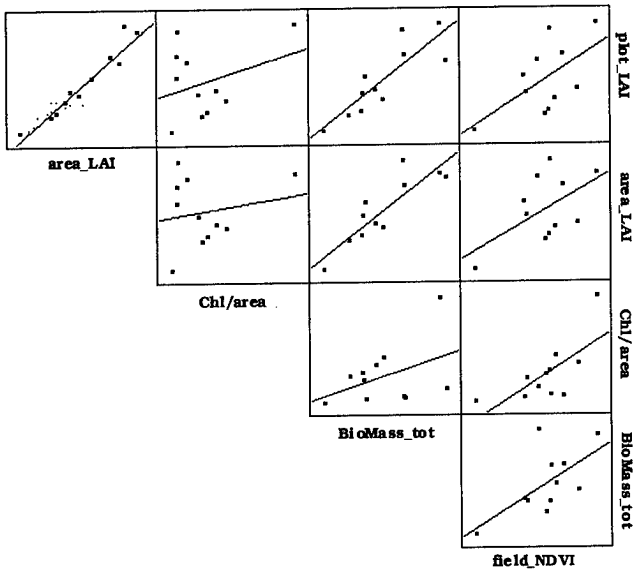


FIGURE 2.
Some calibration relationships for mid-June. BioMass_tot [g/m^2] and Chl/area [g/ m^2] were determined from clipped 50 cm-by-50 cm quadrats, field_NDVI is based on EXOTECH spectra, plot_LAI is based on LICORR-2000, while area_LAI is an average of 36 plot_LAI observations on a 5 m grid around the plot.

MULTIRESOLUTION PATTERN CHARACTERIZATION

There is ample evidence in ecology that most pattern/process relationships are scale dependent [5]. Therefore, our goal was not to determine "a" best resolution to estimate ecological parameters from spectral observations, rather to characterize their relationship across scales (Fig.3.]. The nested design not only requires less samples than geostatistical methods, but allows for testing the significance of differences among variance components and is not resticted to stationary cases [6].

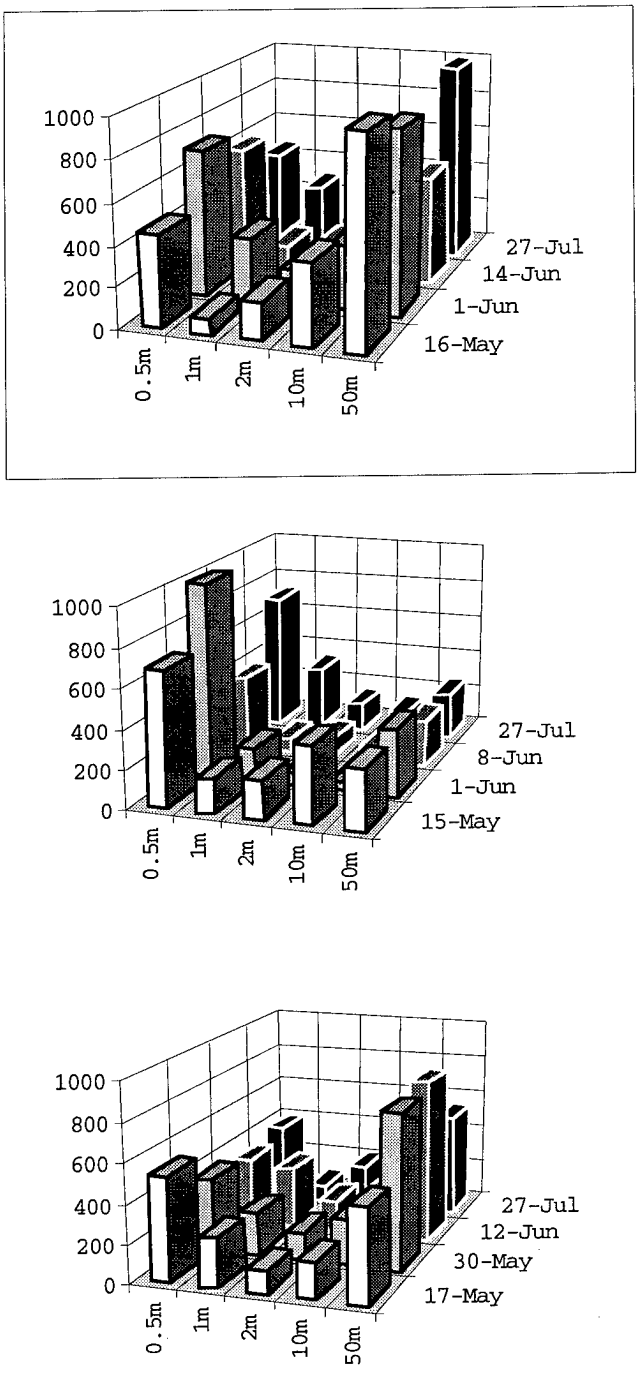


FIGURE 3.
Spatiotemporal pattern of field-observed NDVI at three hectare-plots. The vertical axis represents variability (measured by the total sum-of-squares); spatial partitioning from 0.5 to 50 m is shown left-to-right (not to scale) at given dates during the growing season.

The three hectare-plots exhibit dramatically different patterns. The high variance components at coarse resolutions reveal patch formation, while high variance components at fine resolutions indicate local heterogeneity. The relatively high weight of the finest resolution component warnes that calibrations using typical botanical samples can be noisy. The changing temporal pattern corresponds to the different "green-up" periods of C3/C4 grasses. It also indicates that neglecting spatial heterogeneity can locally bias productivity estimates, particularly if, for example, fine resolution NDVI/LAI relationships are extrapolated to coarser scales.

TOWARD SIMULATING FINE RESOLUTION LANDSCAPES

The partitioned overall variability can be used for simulating fine resolution realizations with given (measured) characteristics [6]. The pattern of these images (Fig. 4.) can be compared to theoretical models (e.g., uniform variance distribution), or to actual satellite images [7]. When only a coarse resolution data set is available, but the distribution of variability is known across scales (e.g., from coenological studies), it can serve as a scene model.

REFERENCES

[1] J. R. Ehleringer and C. B. Field (eds.), "Scaling physiological processes: Leaf to globe," San Diego: Academic Press, 1993, p.387.

[2] G. Arbia, "Spatial data configuration in statistical analysis," Doordrecht: Kluwer Academic Publsihers, p. 256.

[3] A. H. Strahler, C. E. Woodcock and J. A. Smith, "On the nature of models in remote serising," Remote Sensing of Environment Vol. 20., pp. 121-139. 1986.

[4] R. J. Hobbs, "Remote sensing of spatial and temporal dynamics of vegetation," In:Remote sensing of biosphere functioning, R. J. Hobbs and H. A. Mooney (eds.), New York: Springer Verlag, pp. 203-220.

[5] E. D. Schulze and H. A. Mooney (eds.), "Biodiversity and ecosystem function," New York: Springer Verlag, 1993, p. 520.

[6] F. Csillag and S. Kabos, "Hierarchical decomposition of variance with applications in environmental mapping based on satellite images," Mathematical Geology Vol. 28 (in press), 1996.

[7] M. Kertész, F. Csillag and Á. Kummert, "Optimal tiling of heterogeneous images," Int. J. Remote Sensing, Vol. 16, pp. 1397-1415.

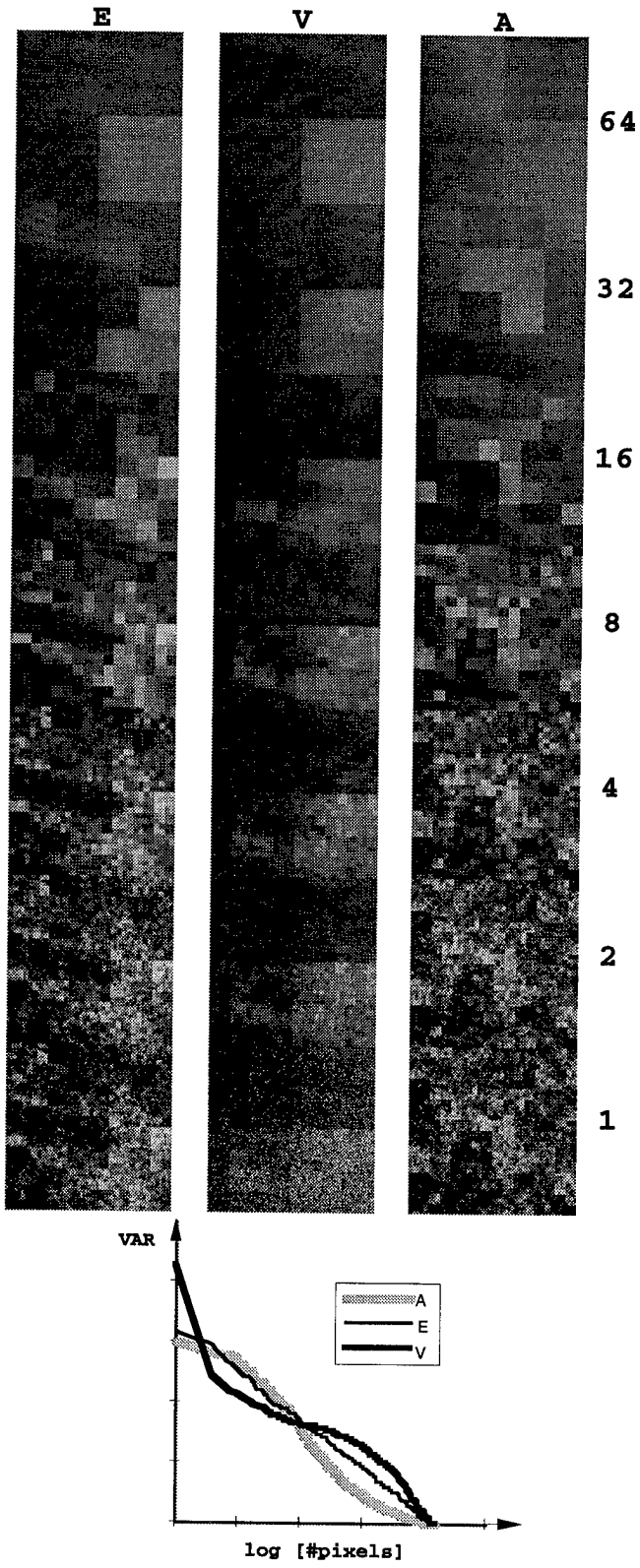


FIGURE 4.
Hierarchical-quadtree (HQ) simulations for different types of patterns and their corresponding variance distribution during decomposition.

RETRIEVAL OF CROP BIOMASS IN 1989 BY USING ANN MODEL OF 1988

Ya-Qiu Jin
Department of Electronic Engineering
Wave scattering and Remote sensing Centre
Fudan University, Shanghai, China 200433

ABSTRACT

By using the observation data of microwave active/passive remote sensing and measurements of crop biomass parameters during the days of 1988, the artificial neural network (ANN) is trained. This ANN model is then used to retrieve the temporal variation of crop biomass parameters from active and passive observation during the days of 1989. The retrieval results are good comparing with the ground truth measurements in 1989.

INTRODUCTION

An important objective of remote sensing over the terrain surfaces is how to quantitatively derive the biomass variations from the remote sensing observation, collected from observations by multi-frequency, dual-polarized, multi-day, multi-angle, active and passive sensors. Scattering and thermal emission from vegetation canopies take account for multiple scattering of vegetation scatterers, and complex coupling with scattering from the underlying surfaces. It is a highly non-linear process. How to derive the characteristic biophysical parameters from the radiometer/radar observations is an non-linear inverse problem. However, some available retrieval approaches such as regularization smoothing method, Backus-Gilebert method, D-matrix method etc. do not seem to be simply tractable to access the inversion for highly non-linear relationships between biomass parameters and remote sensing measurements (Ishimaru 1978). In most recent years, the artificial neural network (ANN) has become of interest (Rogers and Kabrisky 1991). The principle and algorithm of ANN is applicable to the inversion of characteristic parameters of the terrain surfaces from high-dimensional remote sensing data. By using the ANN techniques, the pairs of the known parameters/observations are used to train ANN. This is a self-study process by multi-feed and iterations. Once the ANN training is complete, a set of new observation data is then input to the ANN to retrieve the corresponding parameters. In recent years, Tsang et al. (1992) used ANN to restructure the snow parameters based on radiative transfer simulations. Yoshitomi et al.(1993) used ANN to retrieve the correlation lengths and variance from scattering calculations from rough surface. Smith (1993) used the ANN to obtain LAI evaluation. Further study on the ANN technique for retrieval process from real data might be able to demonstrate great potential of the ANN applications. Jin et al.(1995) have presented a method of the ANN technique to retrieve the crop biomass parameters from real data (Wegmullera and Maetzker 1993).

In this paper we report an application of the ANN model to retrieval of temporal variations of crop biomass parameters from observation of microwave passive/active remote sensing (i.e. horizontal and vertical emissivities e_h, e_v , and co-horizontally and co-vertically polarized back-scattering coefficients σ_{hh}, σ_{vv}). The active/passive observations compose the data vector $\vec{d}=(e_h,e_v,\sigma_{hh},\sigma_{vv})$. The ground truth of biomass parameters include: canopy hight h(cm), water content of canopy d_w (mm or kg/m^2), dry matter fraction m_d , and the volumetric wetness of the underlying

0-7803-3068-4/96$5.00©1996 IEEE

land m_v . These four parameters compose the parameter vector $\vec{p}=(h,d_w,m_d,m_v)$. The dry biomass and wet biomass are usually defined by d_w, m_d . Our ANN is a three-layer perceptrons (MLP) which consists of one input layer, one hidden layer and one output layer. The ANN is first trained by a pair set of the multi-day data $\vec{d}_{1988}$ and the ground truth parameters $\vec{p}_{1988}$ for wheat canopy during days of the year 1988 as available from experiments by Wegmullera and Maetzler (1993). Here the subindex 1988 denotes that the data were collected in measurements of the year 1988 as a training class. Once the ANN model-training is complete, a new set of multi-day data $\vec{d}_{1989}(e_h,e_v,\sigma_{hh},\sigma_{vv})$ of wheat canopy is input to the ANN model to retrieve the corresponding parameters $\vec{p}'_{1989}(h,d_w,m_d,m_v)$, where the subindex 1989 indicates that the data were collected during days of the year 1989 as the inversion class. These retrieved parameters $\vec{p}'_{1989}$ are then compared with the real parameters $\vec{p}_{1989}$ as available from the ground truth measurements during the same days of the year 1989. Comparison can show that the ANN technique is well applicable to the retrieval of biomass parameters.

BIOMASS RETRIEVAL FOR WHEAT CANOPIES

Wegmullera and Maetzker (1993) made extensive active and passive observations on various crop canopies. We choose two independent sets of the data $(e_h,e_v,\sigma_{hh},\sigma_{vv})$ of wheat canopy at 10.2 GHz and observation angle 50° for 26 days of 1988 (from December 21, 1987 to July 18, 1988) and for 6 days of 1989 (from Feb.8 to July 21, 1989) and the correspondingly ground truth measurements (h,d_w,m_d,m_v) . The observation data $(e_h,e_v,\sigma_{hh},\sigma_{vv})$ versus the day of year (DoY) are shown by the solid points for 1988 and the hollow points for 1989 in Figs.1a-d, respectively.

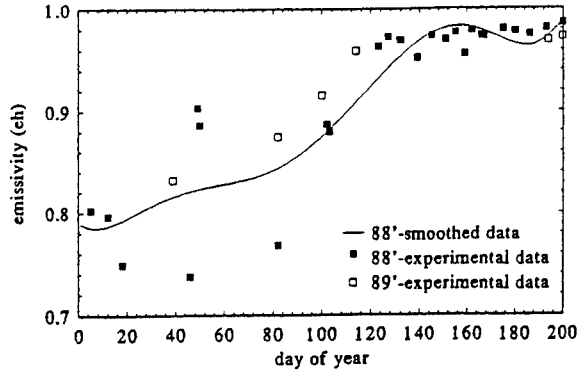


Fig.1a Observations of horizontally polarized emissivity vs DoY for wheat

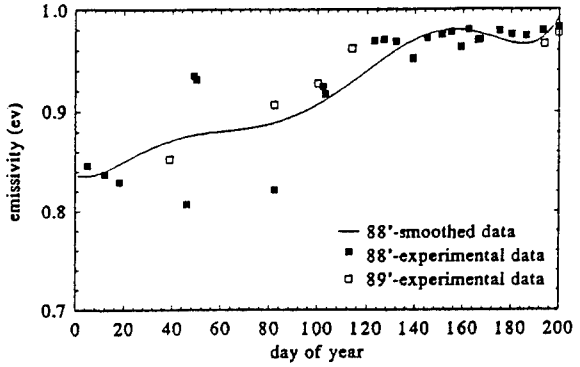


Fig.1b Observations of vertically polarized emissivity vs DoY for wheat

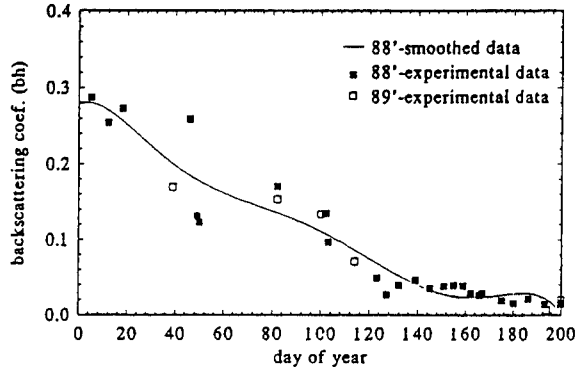


Fig.1c Observations of co-horizontally polarized back-scattering vs DoY for wheat

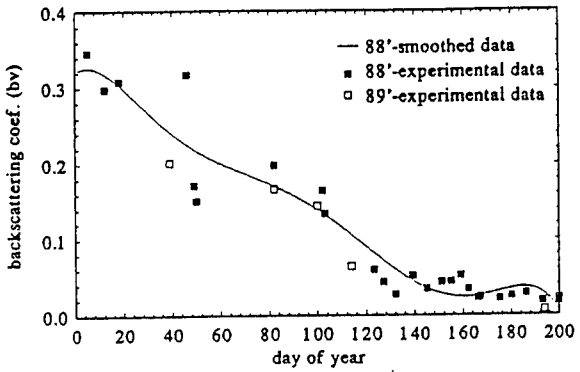


Fig.1d Observations of co-vertically polarized back-scattering vs DoY for wheat

The ground truth parameters vs DoY are given by the solid points for 1988 and the hollow points for 1989 in Figs.2a-d, respectively. To have more samples for training, we smooth the discrete data of 1988 in Figs.1,2a-d and obtain a set of the simulated data and parameters of 200 days. These simulation data and parameters are shown by the solid lines in Figs.1a-d and Figs.2a-d, respectively. Thus some sampling randomness and trivial perturbation are eliminated. We use these simulations to train ANN, where the perceptron numbers of each layer $N_1=N_3=4$, $N_2=27$. The initial guess is important for a good retrieval. We choose the initial guess simply as a linear function. Some constraints are also imposed. For example, the height change should not be larger than a certain number between a day and the next day. After the ANN model-training is complete, the set of observations of the year 1989, as shown by the hollow points in Figs.1a-d, are input to the ANN model to retrieve the corresponding parameter vector.

The retrieval results are shown by the hollow points in Figs.3a-d, and the real parameters by ground truth measurements are given by the solid points on the same figures. Comparison can show that the retrievals are agree well with the desired results.

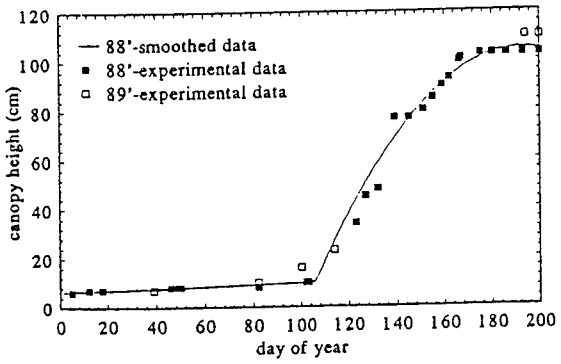


Fig.2a Ground truth of wheat hight h

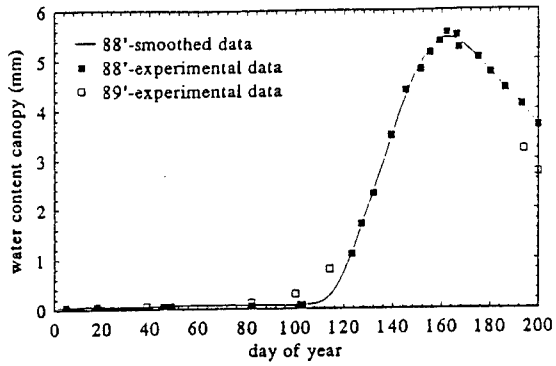


Fig.2b Ground truth of wheat water content

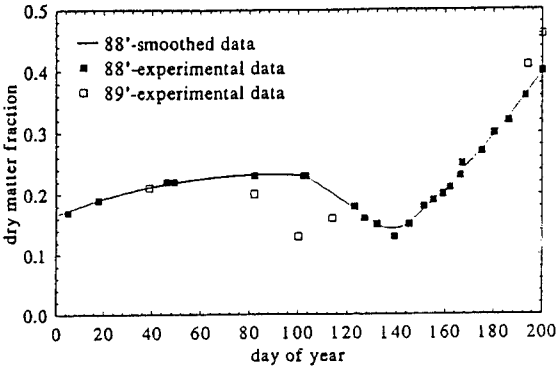


Fig.2c Ground truth of wheat dry matter fraction

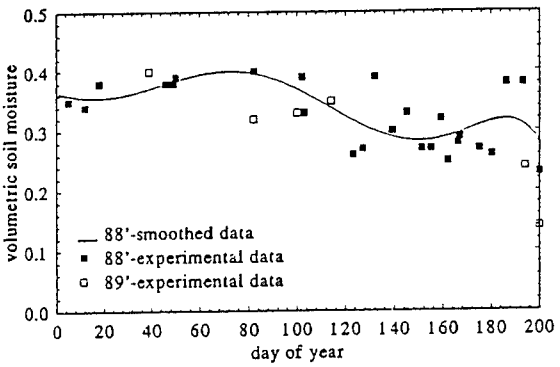


Fig.2d Ground truth of volumetric wetness of soil

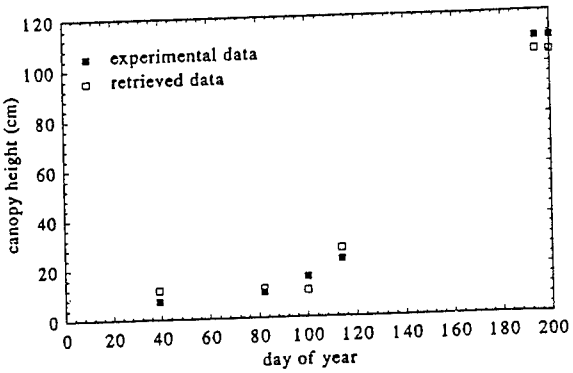


Fig.3a Comparison of Ground truth and retrieval for wheat hight in 1989

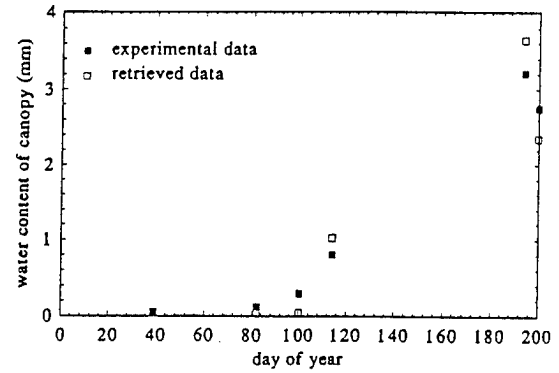


Fig.3b Comparison of Ground truth and retrieval for wheat water content in 1989

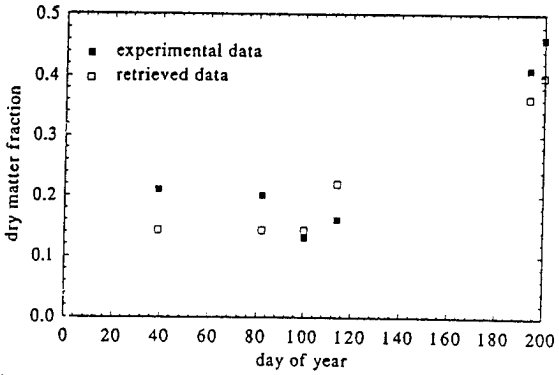


Fig.3c Comparison of Ground truth and retrieval for wheat dry matter fraction in 1989

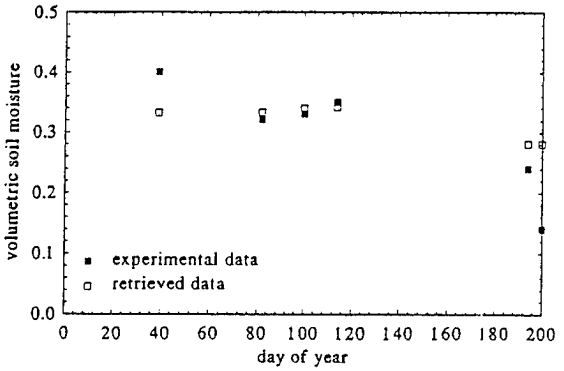


Fig.3d Comparison of Ground truth and retrieval of volumetric wetness of soil in 1989

CONCLUSIONS

We present an application of the ANN model to retrieve the biomass parameters from multi-day, dual-polarization, active and passive remote sensing data. By using the observation data of microwave active/passive observation of wheat and ground truth of biomass parameters in 1988, the ANN model is trained. This ANN model is then used to retrieve the temporal variation of wheat biomass parameters from active /passive observation in 1989. The retrieval results are good comparing with the real ground truth. Numerical results proved the retrieval capability of the ANN model trained by the active and passive data for applications to high-dimensional data such as multi-day, multi-frequency, multi-angle, etc. The priori knowledge and constraints about variation limit of inverted parameters can greatly promote the retrieval convergence and improve the retrieval results.

ACKNOWLEDGEMENT

This work was supported by the National Science Foundation of China, the Shanghai Research Centre for Applied Physics, and the Changchun Jing Yue Tang Remote Sensing Site of Chinese Academy of Sciences. The authors are very grateful to Dr. Maetzker for providing the experimental data.

REFERENCES

Ishimaru A. (1978), *Wave Propagation and Scattering in Random Media*, Academic Press, NY, Vol.1,2.

Jin Y.Q. and Liu C. (1996),*International Journal of Remote Sensing* (to be in press).

Rogers S.K. and Kabrisky M. (1991), *SPIE Optical Engineering Press, WA.*

Smith J.A. (1993), *IEEE Transaction on Geoscience and Remote Sensing*, **GR-31**(5): 1102-1106.

Tsang L., Chen Z., Oh S., Marks R.J.II, and Chang A.T.C. (1992), *IEEE Transaction on Geoscience and Remote Sensing*, **GR-30**(5):1015-1024.

Wegmullera U. and Maetzker C. (1993), *Active and Passive Microwave Signature Catalog (2-12GHz)*, University of Berne, Switzland.

Yoshitomi K., Ishimaru A., Hwang J.N. and Chen J.S. (1993), *IEEE Transaction on Antenna and Propagation*, **AP-41**(4): 498-502.

Conference Author Index

A

Aarholt, E. 1736
Aas, K. 2307
Abel, P. 1816
Abshire, J. B. 1538
Abuelgasim, A. A. 1426
Adah, T. 700
Advokatov, V. R. 1947
Ahamad, A. 1266
Ahmed, R. H. 2369
Ahola, P. 1998
Ahuja, L. R. 1058
Aiazzi, B. 411, 460, 1042
Akpa, S. *
Alba, P. S. 460, 1042
Alberta, T. A. 1911
Alexander, D. R. 857
Alfoldi, T. T. 324
Alfultis, M. A. 1165, 1504
Alhumaidi, S. M. 1526
Allan, N. 905, 1745
Allen, C. 1932, 2033, 2036
Alparone, L. 411, 460, 1042
Alpers, W. 860, 1370, 1478, 1487
Alumbaugh, D. L. 1941
Alves, M. 830
Amalric, J. *
Amar, F. *
Amodeo, G. 736
Amsbury, D. L. 929
Andary, J. 2160
Anderson, L. E. 1877
Anderson, M. C. 2104, 2358
Anderson, M. R. 959
Anderson, R. *
Andreadis, A. 377
Andres, P. *
Angarkhaeva, L. H. 1945, 1947
Anterrieu, E. 869
Antoniou, A. 990
Arakelian, A. K. 625, 811, 885
Arakelian, K. A. 885
Arbelo, M. *
Arca, G. 520, 854
Armour, B. 339
Arnason, K. 414
Arnaud, A. *
Arnavut, Z. 463
Arnold, D. V. 1475, 1892
Arnon, I. *
Arst, H. 76
Arvidson, T. 2160
Asae, M. 1666
Askari, F. 1141
Asner, G. P. 1663
Atakturk, S. S. 805
Attema, E. 1995
Auer, T. 484
Austin, A. *
Awaya, Y. *
Axelsson, S. R. J. *
Aydin, K. 560, 563
Azimi-Sadjadi, M. R. 1105, 1108

B

Bachem, A. 282
Bachmann, C. M. 356
Baggeroer, P. A. 145
Bahar, E. 1794, 2170, 2177, 2180
Baikalova, T. V. *
Baker, J. *
Bakhanov, V. P. *
Bakhanov, V. V. 609
Baldini, L. 7, 1367
Ballard, J. 2146
Balsiger, F. 1826
Balzer, W. 2291
Bambha, R. 1553
Bamler, R. 1217, 2050
Band, L. E. 212, 420
Banik, R. 1290
Bao, M. 860, 1370
Bara, J. 315, 869
Baraldi, A. 709
Barber, D. G. 953, 1187, 1552, 1992
Barbier, C. 251
Barbosa da Silva, V. 374
Barclay, H. 1873
Barker, J. L. *, 1270, 1276, 1600
Barkerm, J. L. 1273
Barnett, J. 2149
Baronti, S. 411, 460, 1042
Barstow, D. 631, 925
Bartel, L. C. 1935
Barter, J. D. 618, 2201, 2213
Bartoloni, A. *
Barwell, B. R. 1438
Bashkuev, Yu. B. 1945, 1947
Bates, J. J. 1710
Bateson, C. A. 1663
Batista, G. *
Batz, O. 872
Bauer, A. *
Bayma, R. W. 1615
Beach, K. L. 2201, 2213
Beal, R. C. *, 896, 1143
Bearman, G. H. *
Beaven, S. G. *, 115
Becchi, I. 1312
Beh, B. 996, 1266
Belchansky, G. I. 642
Belisle, W. R. 1315
Bellemain, P. *
Belliss, S. 1839
Belongie, M. 1035
Belova, N. I. *
Belward, A. *
Belyaev, B. I. 19, 366
Belyaeva, T. A. 1323
Bencherif, H. 10
Benediktsson, J. A. 63, 414, 1848
Benelli, G. 377
Bennardo, A. *
Bennett, J. C. 2344
Benson, C. S. 2246
Bentamy, A. 805
Bergen, K. M. 580, 1092, 1568
Bergen, Z. D. *
Bergen, Z. 659
Berizzi, F. 1230
Bersano-Begey, T. F. 1520, 2077
Berthod, M. *, 25, 345
Bertram, R. R. 2219
Bertrand, J. 2080
Bertrand, P. 2080
Bessafi, M. 10
Betty, C. L. 2183
Betty, C. 2186
Beus, S. E. 1263
Bhogal, A. S. 1873, 2303
Bianchi, R. *
Bicheron, P. 1901
Bickel, D. L. 2063
Bickel, D. 659
Bidwell, S. W. 402, 1550
Bird, P. 493
Bisson, S. E. 691
Bixler, P. *, 631
Bjerkelund, C. 1155
Bjorgo, E. 932
Blair, J. M. 2361
Blanchard, A. J. *
Blanco, A. 76
Blankenship, C. B. *
Blari, J. B. 1806
Blonda, P. *
Blurton, C. 917
Boback, J. P. 1692
Bobrov, P. P. 2192
Bock, E. J. *
Boehnke, K. *, 839, 2014, 2264
Bogaturov, A. N. 369
Boller, B. D. 269
Bolus, R. L. 1073, 2375
Boncyk, W. C. 1270, 1273
Boncyk, W. 1276
Borak, J. S. 243
Borak, J. 233
Borderies, P. 2167
Borel, C. C. *
Borocz, S. 697
Bosdogianni, P. 1379
Bostater, C. *
Botman, A. M. 324
Bottger, H. 2341
Botti, J. A. 1506
Boucher, D. J. 1704
Bourbigot, K. *
Bourdeau, M. 833
Boutry, J. M. *
Boyarskii, D. A. *
Brakke, T. W. 1657
Brammer, C. *
Brandt, P. 1487

*Author's paper not available at the time of printing.

Braswell, B. H. *
Breaker, L. C. 1712
Bredow, J. W. 863, 947, 2288
Brennan, T. J. 2222
Bresci, E. 1312
Briggs, J. M. 2361
Brisco, B. G. *
Brisco, B. *
Brodley, C. E. 532, 1382
Brown de Colstoun, E. C. 1904
Brown de Coulston, E. 586
Brown, G. S. 2119
Brown, R. A. 805
Brown, R. J. *
Brownsword, C. 1141
Bruegge, C. 1279
Brugman, M. 2255
Bruniquel, J. 387, 662
Bruzzone, L. *
Buckley, J. R. 808
Buckley, J. 1155
Budge, A. *
Bufton, J. L. 423
Bugden, P. *
Bulatov, M. G. 1490
Bulgarelli, B. 1584
Bullock, P. R. 1992
Bundschuh, B. O. 999
Bur, M. C. *
Burgess, M. P. 1618
Burkhart, G. R. 659
Burns, B. E. 2020
Burns, B. 1881
Byrd, M. *

C

Caffey, T. W. H. 2023
Callaghan, G. 796
Cames, A. 869
Campbell, J. W. M. 1146
Campbell, J. W. 1621
Campbell, J. 1155
Capms, A. 315
Capolino, F. 13
Carande, R. E. *, 665, 1211
Carande, R. 659
Carayon, G. 273
Carello, R. 1953
Carlotto, M. J. 34, 2089, 2164
Carpenter, G. A. 529
Carsey, F. 634, 1181, 1775
Carswell, A. I. *
Carswell, J. 1385, 1466
Casar Corredera, J. R. *
Caselles, V. *
Cavalier, D. J. 2246
Cavalieri, D. J. *, 956, 1523, 1529
Cavalli, R. M. *
Cavallo, A. *
Cavayas, F. 236
Caylor, I. J. 1550
Cazaban, F. 387
Cazzaniga, G. 1845
Celani, C. *
Cespedes, E. R. *, 857
Chabert, M. 1842
Chadwick, D. J. 2134
Chadwick, R. B. *
Chagnon, R. *
Chakrabarti, S. 1867
Chan, S. S. 1005
Chan, T. K. 2137, 2140
Chandrasekar, V. 566, 574
Chang, A. T. C. 2011, 2246
Chang, P. *, 1123, 1707
Chang, S. Y. S. 85
Chapman, B. 823, 830
Chapman, R. D. 1736
Chappelle, E. W. 1812
Chapron, B. 600, 606, 612, 621, 1385, 1389
Charlebois, D. 1873, 2303
Chauhan, N. 2146
Che, C. Y. *
Che, X. *
Chen, C. 551
Chen, G. 2240
Chen, H. *
Chen, J. M. 586, 1651
Chen, J. *
Chen, K. S. *, 1297
Chen, L. 1908
Chen, M. *, 43
Chenebault, J. 279
Chenerie, I. 2167
Cheng, H. D. 133
Cheng, S. Y. S. 380
Cherny, I. V. 360, 1968
Cheshire, H. 1609
Cheung, K. 1035
Chiaradia, M. T. 2060
Chinchilla, N. 891
Chiu, T. C. 1070
Chiu, T. 2122
Cho, J. Y. N. 1926
Cho, S. 1977
Choi, J. 469
Choi, M. Y, 628
Choi, S. K. *
Chong, C. C. 180
Choudhury, B. J. 106
Chrien, T. G. *
Chu, A. *, 43
Chubb, S . R. 902, 911
Chugurin, V. V. *
Chun, C. 396
Churilov, V. P. *
Churnside, J. H. 1328
Cialella, A. T. 1904
Cihlar, J. *
Cipollini, P. 91, 1398
Ciucci, A. 520, 854
Clabau, P. 70
Clark, J. H. 1146
Clark, S. 881
Claude, J. 869
Clifford, S. F. 1739
Clift, S. 1293
Clothiaux, E. E. 356
Cloutier, C. *, 1290
Coan, S. M. *
Cohn, S. A. 1914
Coleman, T. L. 1315
Collins, J. D. *
Collins, M. J. 2068
Collins, M. 1141, 2027
Colpitts, B. G. 2189
Coltelli, M. 350
Comiso, J. C. 2008
Compton, M. 1211
Console, E. 1376
Cooper, A. L. 902, 911
Cooper, D. I. *
Cooper, D. *
Coppo, P. 2131
Corbella, I. 315, 869
Corner, B. R. 1920
Cornwall, J. M. 2347
Corp, L. A. 1812
Corsini, G. 290, 1230, 1398
Cowen, R. *
Coyle, D. B. 1806
Crawford, J. P. 1775
Crawford, M. M. *, 263, 1870
Cremers, D. A. *
Cress, D. H. 1935
Crevier, Y. *
Croft, S. K. *
Cromwell, D. 91
Crowley, R. D. 269
Cruz Pol, S. L. 1435
Csillag, F. 2377
Csiszar, I. 1114
Cubero-Castan, E. 457
Cuddy, D. 1358
Cui, T. J. 763, 766, 1340
Cumming, I. 336, 2044, 2255
Cuomo, S. 817
Curlander, J. 1775
Curtis, J. O. 2030, 2282

D

Dabney, P. W. *
Dahl, P. 2270
Dai, X. 1609
Daida, J. M. 891, 1520, 2077, 2219
Dall, J. 276, 1629
D'Amelio, C. *
Damen, M. C. J. 2240
Damiao, D. P. *
Dano, E. B. 2195, 2198
Dano, E. 1158
Daout, F. 615, 746
Das, J. *
Datcu, M. *, 310, 2054
Daughtry, C. S. T. 224, 1803, 1812
Daum, D. R. 1606
Davidson, A. 2377
Davidson, G. W. 2050
Davidson, G. 1217
Davidson, K. L. 1260
Davidson, K. 1158
Davidson, M. W. J. 1980
Davis, C. H. 1783
Davis, F. W. 1077, 1083
Davis, R. E. 254, 754, 757
Davis, R. 591
Davis, S. *
Dawn, D. R. 848
Dawson, M. S. *, 1297
Day, J. L. 1083
De Abreu, R. A. 639
Debinski, D. 2300
De Carolis, G. 1306

Dechambre, M. 833
Dedieu, G. 2366
Deering, D. W. 1654, 1897
DeFries, R. 535
De Grandi, G. 1574, 2086
Dekker, A. G. *
Delaney, P. A. 987
Delignon, Y. 70, 706
Dellepiane, S. 714
Demarest, K. 778
Demarez, V. 1002, 1660
de Matthaeis, P. 736
de Miguel-Vela, G. *
Derksen, C. P. 127
Desachy, J. 2074
Deschaux-Beaume, M. 387
Desjardins, R. 236
Desnos, Y. L. 1217, 1355
De Troch, F. P. 1303
Diak, G. R. 2104, 2358
Diani, M. 1230
Diaz, J. P. *
Di Bisceglie, M. 1580
Dickinson, S. 805
Dietrich, S. *
Diffendal, R. F., Jr. 1017
Dimaio, S. P. 2020
Diner, D. 1279
Ding, K. H. 757, 1208
Dionisio, C. 28
Dmitriev, W. V. 1950
Dobson, F. W. 1155
Dobson, M. C. 580, 1092, 1093, 1568, 2335
Dolash, T. 697
Domanov, M. M. *
Donato, T. 1141
Donelan, M. A. 2210
Donelan, M. *
Dong, Y. 1556
Donnelly, W. 1385, 1466
Douglas, D. C. 642
Doviak, R. J. 1914
Dozier, J. 2002, 2249
Driese, K. L. 186
Drobot, S. D. 1187
Drucker, R. 1190
Du, L. J. 439
Dubayah, R. O. 2149
Dubbert, D. 1881
Dubina, I. N. *
Dufrene, E. 1002
Dugan, J. *
Dunagan, S. E. 2276
Dupont, S. 25, 345
Dutra, L. *
Dwyer, J. L. 547

E

Early, D. S. 124
Eastwood, M. L. *
Ebel, R. *
Echavarria, F. R. *
Eck, T. F. 1897
Edelsohn, C. R. *
Ediriwickrema, D. J. 793
Edson, J. B. *
Ehrismann, J. 339
Eichinger, W. *
Eis, K. E. 1105, 1108
El-Khattib, H. M. 1756
El-Mowilhi, N. M. 1756
El-Shenawee, M. 2170
Elachi, C. *
Elfouhaily, T. 600, 606, 621, 1389
Eloranta, E. *
Emblanch, C. 1067
Emery, W. J. 186, 1138
Emery, W. 192
Ender, J. H. C. *
England, A. W. 2155, 2267, 2270
Engman, E. T. 1058, 1064, 1297, 2237
Entekhabi, D. 1076
Erasmi, S. *
Erbie, E. 2011
Eriksson, M. *
Ersoy, O. K. *
Erxleben, W. H. 1014
Espedal, H. A. 1158
Estes, J. E. 198, 820, 2242, 2321
Etling, D. 1478
Evans, K. *
Exposito, F. J. *

F

Facheris, L. 7, 13
Falls, M. J. 1681
Fang, Y. 496, 1266
Fedele, G. 383
Federici, G. 817
Fedor, L. S. 1450, 1681
Fedoseev, Y. G. *
Fellerhoff, J. R. 659
Fellerhoff, R. 1881
Ferguson, S. 1526
Fernandes, D. 1227
Fernandes, R. 212, 420
Fernandez, D. M. *, 1749
Fernandez, D. *
Ferrare, R. A. 1685
Ferrare, R. *
Ferrazzoli, P. 736
Ferris, M. J. *
Field, C. T. 1800
Filho, O. R. 1986
Firda, J. M. 1
Fischer, A. 2366
Fischer, K. W. 648, 694
Fischer, M. 787
Fiset, R. 236
Fisher, B. 631
Fitzgerald, R. W. *
Fjortoft, R. 457
Flamant, P. H. 4
Floury, N. 836, 842, 975, 1306, 2167
Flynn, T. J. 2057
Fochesatto, G. J. 4
Ford, R. E. 1501
Foresman, T. W. 2242
Foresman, T. 820
Fornaro, G. *, 350, 2047
Forster, B. 1080, 1556
Fortner, R. W. *, 1166
Fortuny, J. *
Foster, J. L. 2011, 2246
Fotedar, L. K. 239
Fowler, C. 73
Franceschetti, G. 51, 350, 680, 2047
Frasier, S. 984, 1730
Frattura, F. 7
Freeman, A. 823, 830
Freemantle, J. *
Frei, M. 1833
Freilikher, V. *
French, N. B. *
Freylikher, V. D. 369
Friedl, M. A. 532, 1382, 2152
Frison, P. L. *
Fritsch, B. *
Frohn, R. C. 2321
Frolind, P. O. 668, 1877
Fromard, F. 733
Frost, E. 925
Frulla, L. A. *
Frulla, L. *
Fuglistaler, S. 342
Fukao, S. 1929
Fung, A. K. *, 772, 947, 1202, 1297, 2008, 2116, 2183, 2186
Furger, M. 399

G

Gade, M. 860
Gagliardini, D. A. *
Gaikovich, K. P. 369
Gaiserl, P. W. *, 1123
Galantowicz, J. F. 1076, 2270
Galbraith, A. E. 683, 1244
Galdi, C. 1580
Galloway, J. 743
Gamba, P. 266, 2071
Garegnani, J. J. 2242
Garello, M. 1584
Garello, R. 612, 621, 1956
Garzelli, A. 377
Gasiewski, A. J. 1120, 1129, 1688
Gasparini, O. 315
Gastellu-Etchegorry, J. P. 1002, 1660
Gatelli, F. 671
Gault, K. A. *, 1221
Gautier, C. 2149
Gazdag, L. 697
Gelautz, M. 31
Gemmill, W. H. 1712
German, M. L. 1441
Gerstl, S. A. W. *, 1642
Geudtner, D. 966, 2255
Giarrusso, J. M. *
Gibas-Tracy, D. R. 2234
Gibbs, D. P. 1541
Gibeaut, J. C. *, 263
Gimond, M. *
Ginzburg, A. I. *
Gird, R. *
Girou, D. *
Gitelson, A. A. *, 2355
Gitelson, A. 209
Giuli, D. 7, 13, 817, 1367
Givri, J. R. *
Gjaja, M. N. 529
Glushko, E. V. 2324
Goblirsch, W. 656

Goel, N. S. 526, 1645
Gogineni, P. 1867
Gogineni, S. P. 115, 1196
Gogineni, S. 1932
Golden, K. M. *
Goldsmith, J. E. M. 691
Golovachev, S. 175
Gomarasca, M. A. *
Gong, P. 2068
Gonzalez, K. D. 1506
Goodberlet, M. A. *
Goodenough, D. G. 1873, 2303
Goodin, D. G. 215
Goodman, N. 2033, 2036
Gopal, S. 529, 538, 787, 1426
Goto, A. 920
Gottfried, J. 1178
Gotwols, B. L. *, 1736
Gouinaud, C. 257, 474
Gourrion, J. 1389
Goutoule, J. M. 869
Gow, A. J. 1184, 1190
Goward, S. N. 1803
Gowda, K. C. 1858
Gower, J. 1146
Graber, W. K. 399
Graf, G. 1355
Grandell, J. *, 583, 1998, 2110
Granhohm, J. 674, 1629
Grankov, A. 175
Grassin, S. 1956
Gray, A. L. 1146, 1155, 1621
Gray, L. 2255
Gray, R. B. 1290
Gray, R. 1352
Green, R. O. *
Greidanus, H. 1633
Grenfell, T. C. 1199
Grindel, M. 999
Grits, Y. 2355
Grodsky, S. A. 1971
Gromov, V. D. 442
Gross, G. 1478
Grunes, M. R. 1574
Guarnieri, A. M. *
Guarnieri, P. 460
Guenther, B. D. 445
Guerra, J. C. *
Guerriero, L. 2060
Guijarro, J. 1355
Guindon, B. *
Guneriussen, T. *
Gurvich, A. S. 369
Gustafson-Bold, C. L. 1283
Gustavsson, A. 1877
Gutierrez, R. O. *, 263
Gutman, S. I. *
Gwilliam, B. L. 1073, 2375

H

Haake, K. 1597
Haas, A. 1080
Haese-Coat, V. 717
Hahn, T. 842
Hall, D. K. 139, 956, 2011, 2246
Hall, F. G. 230, 1657
Hall, K. 254
Hall, S. E. 1498
Hallidin, S. *
Hallikainen, M. *, 484, 583, 1089, 1759, 1998, 2110, 2285
Halthore, R. N. 1904
Haltrin, V. I. 285, 305
Hambaryan, A. K. 625, 811
Hammer, P. D. 2276
Han, L. 1395
Han, Y. 1685
Hanado, H. 487, 512
Hansen, M. 535
Happ, L. 2027
Haptanov, V. B. 1945
Hara, T. *
Hardin, P. J. 827, 848, 1606
Harding, D. J. 1806
Harris, R. 1826
Hart, D. G. 145
Hartnett, J. 1111
Hashimoto, S. 1695
Hassol, S. 1169
Haugen, H. *
Haung, Z. 778
Hautecoeur, O. 204, 1901
Haverkamp, D. 109, 1532
Hawela, F. 1756
Hawkins, R. K. *, 1290, 1621
Hayes, K. *, 1733
Hazen, D. A. 1432
Heer, C. 2341
Hehr, L. H. *
Hein, A. *
Heinrichs, J. 950
Helder, D. L. 1270, 1273
Helder, D. 1276
Hellsten, H. 1877
Hellwich, O. 330, 1836
Henebry, G. M. 166, 195, 215, 448
Henry, J. C. *
Henschel, M. *
Hensley, S. 31
Hensley, W. H. 2063
Hensley, W. 659
Henson, J. M. 254
Herland, E. A. *
Hernandez, P. A. *
Herrera, F. *
Herry, P. *
Hesany, V. *, 888, 1733, 2210
Hesany, *
Hess, L. L. *
Hevizi, L. G. *
Heygster, G. C. 1788
Heymsfield, G. M. 1550
Hicks, M. R. 1504
Hillion, A. 523
Hines, D. 1257, 1385
Hipple, J. 1501
Hirsave, P. P. 1073
Hjartarson, A. 414
Ho, L. L. *
Hochheim, K. P. 1992
Hochschild, G. 436
Hoekman, D. H. 260, 845
Hoffmeyer, P. D. 2030, 2282
Holden, H. M. 427
Holden, H. 88
Holecz, F. 248
Holloway, C. L. 1914
Holt, B. *
Holzworth, R. H. 569
Homer, J. 796
Hood, R. E. 1460
Hoogeboom, P. 1633
Hoogenboom, H. J. *
Hopcraft, G. 1923
Horie, H. 512, 1364
Horn, R. 1624
Hosomura, T. *
Hou, S. 1032
Houzelle, S. *
Howard, S. 246
Howarth, P. J. 1986
Howell, P. B. 1926
Hoyt, P. *
Hsieh, C. Y. 2116
Hsieh, P. 1855
Hsu, A. Y. 1061, 1297
Hsu, A. 1064
Hsu, C. C. 836, 1208
Hu, B. 1587, 1669
Huan, S. 60
Huang, S. *, 1571
Huddleston, J. N. 1718
Huehnerfuss, H. 860
Huemmrich, K. F. 2372
Huete, A. R. *, 157, 1423
Hug, J. F. *
Hughes, W. *, 1221
Huguenin, G. R. 1544
Hummelbrunner, W. *
Hunt, J. 631
Hurlemann, P. *
Hurtaud, Y. 615
Hussein, Z. A. 515
Hwang, J. N. 130
Hyyppa, J. 1089

I

Iacozza, J. 1187
Ignatov, A. *
Iguchi, T. *, 512, 554, 1364
Iisaka, J. *
Inggs, M. R. 454, 2020
Inggs, M. 1889
Iodice, A. 680
Irisov, V. G. 1126, 1450, 1457, 1672
Irons, J. R. *, 1657, 1904, 2161
Irons, J. 2183, 2186
Isernia, T. 1241, 2083
Ishimaru, A. 2128, 2137, 2140
Itten, K. I. 2326
Ivanov, A. Y. 1971
Ivanov, A. Yu. *
Ivanov, V. K. 369
Ivlev, O. V. *
Iwata, Y. 781

J

Jaaskelainen, V. *
Jackson, S. R. 2258
Jackson, T. J. 1058, 1061, 1064
Jacobson, M. D. 1138, 1678

Jain, A. K. 1851
Jakob, G. 31
Jakubauskas, M. E. 2300
Jameson, A. R. 402
Jamsa, S. 2092
Jansen, R. W. 902
Jayaprakash, P. 408
Jayaram Hebbr, K. 784
Jeffries, W. 1352
Jelinski, D. E. *
Jen, L. *
Jenkins, A. D. 1158
Jensen, J. R. 2279
Jenserud, T. 1141
Jessup, A. T. *
Jeyarani, K. 784
Jezek, K. C. 142, 145, 148, 1775
Jezek, K. 118, 1196, 1772
Ji, J. 1300
Ji, W. 2225
Jia, J. C. 180
Jia, S. *, 1423
Jiang, J. 739
Jiang, W. W. *
Jiao, J. *
Jin, M. *
Jin, Y. Q. 2380
Jingli, W. 466
Jingshan, J. 466
Johannessen, J. A. 1158
Johannessen, O. M. 932, 1158
Johansen, B. *
John, H. 2338
Johnsen, H. 1155
Johnson, D. R. *, 1175
Johnson, J. T. *, 1401
Johnson, L. F. 2276
Johnson, P. E. 1721
Johnson, R. S. 808
Jones, M. A. *, 631
Jones, W. L. 1526
Jonsson, T. 1877
Jordan, A. K. 1208
Jordan, L. E., III 2228
Jordan, M. S. 1260
Josberger, E. G. 648
Judge, J. 2270
Jung, M. 1870
Jurczyk, S. 2160
Juying, J. 947

K

Kabashnikov, V. P. 19
Kadygrov, E. N. *
Kaiser, D. *
Kaiser, J. A. C. *, 911
Kaita, E. 1273
Kalb, M. 1175
Kalshoven, J. E. 1797, 1809
Kambhammettu, N. 1392
Kanagaratnam, P. 115, 1196, 1867
Kandus, P. *
Kane, T. J. 993
Kanevsky, M. B. 1493
Kanzieper, E. *
Karaev, V. Y. 1493
Karam, M. A. 154, 594
Karlinsey, T. 1892
Karszenbaum, H. *
Kashkarov, S. S. 369
Kasilingam, D. *
Kassebaum, R. *, 631
Katehi, L. P. B. 1346
Katkovsky, L. V. 19, 366
Kato, Y. 875
Katou, K. *
Katsaros, K. B. 805
Katsaros, K. 1389
Katsev, I. L. *
Katzenberger, J. 1509
Kaupp, V. H. *
Kawata, Y. *, 1250, 1666
Kazandjiev, V. *
Kazmin, A. S. *
Keane, A. N. 603
Keck, C. L. *
Keeler, M. *
Keeler, R. J. 574
Keihm, S. J. 1435
Keithley, C. *, 227
Kellenberger, T. W. 2326
Keller, M. R. *
Keller, M. *, 248
Keller, W. C. *, 888, 1733, 2210
Kellndorfer, J. M. 1093, 2335
Kellndorfer, J. 2329
Kelly, R. E. 1938
Kemarskaya, O. N. 609
Kemppinen, M. 484, 499, 1998, 2285
Kenyi, L. W. 353
Kerbaol, V. 621, 1389
Kerenyi, J. 1114
Kerr, R. B. 686
Kertesz, M. 2377
Kerzner, M. G. 451
Kess, B. L. 1048
Key, J. R. 636
Key, J. 73
Keyte, G. 493
Kheeroug, S. S. 189
Khenchaf, A. 615, 746
Khire, M. V. 430
Khlif, M. S. 857
Khorram, S. 793, 1609
Kiang, R. K. 1864
Kietzmann, H. 1086
Kilic, O. 760
Kim, C. 1977
Kim, E. J. 2267
Kim, H. J. 405
Kim, H. S. 405
Kim, M. S. 1812
Kim, Y. *, 1612
Kimbreau, G. 891
Kimura, I. 775, 1361
Kindscher, K. 2300
Kirchner, C. *
Kirscht, M. 333
Kiselev, S. S. 442
Kishi, A. M. 1704
Kittler, J. 1379
Knapp, A. K. 166, 2361
Knight, A. 869
Knoepfle, W. 2332
Knopfle, W. 802
Knowles, D. S. *
Knudson, C. 296
Knulst, J. 1158
Kobjakova, N. *
Kogan, F. 209
Koh, G. *
Kokhanovsky, A. A. *
Komarov, S. A. *
Komiyama, K. 875
Kong, J. A. *, 757, 836, 1190, 1208, 1401
Kontar, E. A. *
Kooi, P. S. *
Koomen, P. 1633
Koren, H. 2307
Kosmann, D. 2338
Kosov, A. S. 442
Kostina, V. L. 172, 178
Kovalick, W. M. *
Kowk, R. 935
Kozlov, A. I. 299
Kozu, T. *, 512
Kraemer, R. *
Kraft, U. R. 866
Kraft, U. 872
Krasnopolsky, V. M. 1712
Kravtsov, Y. A. 103
Kravtsov, Yu. A. 1454
Krenek, B. *, 1541
Krishen, K. 239
Krishna, A. P. 221
Krivonozhkin, S. N. 369
Kropfli, R. A. 1739
Krueger, D. A. *
Krummell, J. R. 2361
Krupa, R. 436
Kudryavtsev, V. N. 1971
Kuga, Y. 2128, 2137, 2140
Kuhbauch, W. 1980
Kumagai, H. 487, 512
Kumar, S. R. 1858
Kummerow, C. 1429
Kunkee, D. B. 1129
Kuntz, M. 433
Kurtz, J. 2027
Kurvonen, L. 1759
Kusaka, T. *, 1250
Kusneirkeiwicz, D. Y. 1143
Kustas, W. P. 2104
Kutser, T. 76
Kux, H. J. H. *, 195, 374
Kuzmenko, Yu. A. *
Kuzmin, A. V. *, 1454
Kwok, R. *, 1190

L

Labrousse, D. *, 345
la Forgia, V. *
Lahtinen, J. 1998
Lai, S. J. *
Lake, B. M. 2201, 2213
Lalbeharry, R. 1155
Lalonde, M. 1621
Lamont-Smith, T. 1742
Lanari, R. *, 350, 2047
Landgrebe, D. A. 790, 1855
Landgrebe, D. 414
Landry, R. 726

Landsfeld, M. 2149
Lane, J. *
Lang, R. H. 577, 726, 760
Langford, A. O. *
Langford, G. 2276
Langham, C. W. 324
Langlois, P. M. 1917
Langman, A. 2020
Lannes, A. 869
Laroussinie, O. *
Larsen, M. F. 1926
Larsson, B. 1877
Lataitis, R. J. 1914
Lauknes, I. *
Laur, H. 477
Laursen, V. 869
Lavorato, M. B. 4
Lavrenov, I. 1495
Lawrence, S. P. 417, 2158
Lawson, J. *
Lay, W. L. 57
Le, C. T. C. 2128, 2137
Leach, A. *
Leavitt, B. C. 2273
Lebed, L. 209
Leberl, F. 31
Le Ber, J. *
Leblanc, E. 224
Leblanc, S. G. 1651
Lebon, F. 457
Le Caillec, J. M. 612
Le Dantec, V. 1002
LeDrew, E. F. 127, 230, 639, 645, 938
LeDrew, E. P. 427
LeDrew, E. 88
Lee, B. S. 1794, 2180
Lee, J. S. 439, 1162, 1574, 2086
Lee, L. *
Lee, M. E. *
Lee, P. H. Y. 618, 2201, 2213
Lee, R. 118
Le Hegarat-Mascle, S. 1067
Lehmann, F. 2107
Lemaire, P. 251
Leone, A. 1584
Leonelli, J. 697
Leong, M. S. *
Leroy, M. 204, 1654, 1901
Lesht, B. M. 1675
Le Toan, T. 836, 842, 975, 1306, 1983, 2167
Leu, C. H. 160
Leung, K. *, 43, 1358
Leuschen, C. 2033, 2036
Leuskiy, V. Ye. 1672
Leveau, J. 10
Le Vine, D. M. *, 878, 1547
Lewis, J. E. *
Lewis, M. R. *
Lewis, P. 1405, 1408
Lewis, T. B. *
Li, F. K. 1132, 1469, 1959
Li, J. *
Li, L. W. *
Li, L. 1123, 1707
Li, T. L. 1064
Li, X. 293, 591, 1587, 1669, 2173
Li, Z. J. 772
Li, Z. *, 136, 2186
Liang, S. 1648
Liao, L. 16, 554
Liberman, B. 175, 1320
Lieberman, S. H. *
Lightstone, L. *
Liljegren, J. C. 1675
Lim, I. 57, 67
Lin, I. I. 2261
Lin, L. 509
Lin, Y. C. 1334
Lindemer, W. 872
Lindgren, P. D. 1172
Lintz Christensen, E. 1629
Liou, Y. A. 2155
Litovechenko, K. 251
Liu, A. K. 85, 380
Liu, G. *, 1571
Liu, H. 1535
Liu, W. 1515
Livingstone, C. E. 1515, 1621
Llewellyn-Jones, D. T. 417, 2158
Loechel, S. E. 586
Loechel, S. 2149
Loffeld, O. *
Logvin, A. I. 299
Lohi, A. *
Loizzo, R. *
Lombardo, P. 347
Long, D. G. 124, 218, 827, 848, 1463, 1475, 1606, 1715, 1721, 1724, 1892
Longstaff, D. 796
Lopes, A. 387, 457, 662
Lord, R. T. 454
Lou, S. H. 935, 1959
Lou, Y. *, 1612
Loumagne, C. 1067
Loutin, E. A. 299
Loveberg, J. 881
Loveland, T. R. *, 2318
Lu, Y. H. 57, 67
Ludwig, F. L. 891
Lukin, V. P. 1830
Lukin, V. 22
Lukowski, T. I. *, 1290, 1621
Lund, D. E. 2195, 2219
Luong, D. Q. 356
Luscombe, A. P. 1290, 1352
Luvall, J. 1286
Lyzenga, D. R. *, 899, 908, 1158, 2195, 2198, 2219
Lyzenga, D. 1141

M

Ma, W. *
MacArthur, J. L. 1143
Macauley, M. K. 2222
MacDonald, H. C. *
MacDonald, M. C. *, 183
Macelloni, G. 2131
MacGregor, D. *
Mack, J. M. 1938
Madisetti, V. K. 1592
Madsen, S. N. 276, 674, 677, 972, 1629
Magotra, N. 1029
Mahlke, J. 1769
Mahootian, F. *
Maitre, H. 474, 503
Makisara, K. 1010
Makkonen, P. 1998
Makynen, M. 1998
Malaret, E. 1141
Maldonado, L. 1612
Maleev, S. N. 442
Malinovski, V. *
Malliot, H. A. 2349
Manara, G. 290
Mancini, P. L. 279
Mancini, P. 1355
Mandyam, G. 1029
Manninen, T. 583
Manning, W. *
Manohar, M. 1023
Manry, M. T. *
Maotang, L. 466
Marazzi, A. 266, 2071
Marchand, R. 2119
Marechal, N. *, 1233
Marenco, A. L. 1592
Mariani, A. *
Markham, B. L. 586, 1270, 1273, 1276, 1797, 2121
Markina, N. N. 1698
Markus, T. 1247, 1529, 1791
Marmorino, G. O. *
Marra, J. 100, 296
Marthon, P. 457
Martin, S. *, 1190
Martin-Neira, M. 315, 869
Martinez, P. 37
Martinez-Madrid, J. J. *
Marty, G. 1002
Martynov, O. V. *
Marzano, F. S. *
Marzouki, A. 706
Maslanik, J. A. 186
Maslanik, J. 73, 192, 950
Matschke, M. 802, 2332, 2338
Mattar, K. E. 1146
Mattar, K. 1621, 2255
Mattia, F. 1306
Mattikalli, N. M. 1058, 2237
Matwin, S. 1873, 2303
Maupin, P. 1373
Mauser, W. 1974
Mavrocordatos, C. 490
May, G. C. 947, 2288
Mayer, T. S. 993
Mayer, V. J. 1166
Mayor, S. 1911
Mazetti, P. 1367
McBride, W. E., III 285
McCalmont, J. F. 1535
McCleese, D. *
McColl, K. C. 1710
McCoy, W. 1029
McDonald, K. *
McDonnell, J. J. 133
McGee, S. 917
McGuire, J. 631
McIntosh R. E. 1, 984, 1553, 1917, 1923
McIntosh, R. 743, 1466, 1730
McKim, H. A. 1073
McKim, H. L. 2375
McLaughlin, C. D. 929
McLaughlin, D. J. 905, 1745
McLauglin, D. J. *
McMurtrey, J. E. 1812

McNally, T. *
McNeill, S. 1839
Mead, J. B. 1553, 1917, 1923
Meadows, G. A. 2219
Meadows, G. 2195, 2198
Mecocci, A. 2071
Meier, D. 1352
Meier, W. 73
Melack, J. M. *
Melfi, S. H. *, 1257
Melnikov, V. M. *
Melsheimer, C. 1370
Melville, W. K. 2204
Memon, N. D. 1039
Menegasssi Menchik, M. T. *
Meneghini, R. *, 16, 554, 1364
Menon, A. K. 408
Merchant, J. W. 541, 2315
Merzlyak, M. N. 2355
Mesarch, M. A. 1005, 1908
Mesnager, G. 1842
Meyers, R. J. 1506
Michel, T. R. 248
Middleton, E. E. 1005
Miewald, T. 929
Migliaccio, M. *, 680
Migliacio, M. 350
Mikami, T. 1695
Mikheev, P. V. 189
Mikkela, P. 1759
Mikulin, L. *
Miles, M. W. 932
Milillo, G. *
Millar, P. S. 1800
Miller, J. R. *, 212, 1411
Miller, J. 420
Miller, T. 1612
Miller, W. H. 1032
Milovich, J. *
Milshin, A. 175, 1320
Miner, G. F. 1892
Minino, M. *
Minnis, P. 1911
Mironov, V. L. *
Mitchell, S. 2377
Mittermayer, J. 1214, 1217
Mityagina, M. I. *, 103
Miyawaki, M. 1639
Miyazaki, T. 781
Mochi, M. *
Moens, J. B. *
Moghaddam, M. *, 730, 978
Mogili, A. 1266
Mohling, W. *
Mohr, J. J. 677, 972
Moldenhauer, O. 94
Molinaro, F. 10
Moller, D. 984
Monaldo, F. M. 1143, 1149
Mononen, I. 484
Monorchio, A. 290
Montgomery, B. 577
Monti Guarnieri, A. 671, 1845
Moody, A. 544
Moon, C. J. *
Moon, W. M. *
Moore, J. D. 922
Moore, R. K. 496, 996, 1266, 1392
Moore, S. L. *
Mora, F. 541
Morain, S. *
Moran, M. S. 157, 1420
Mordvintsev, I. N. 642
Moreau, L. *, 70
Moreira, A. 1214, 1217
Moreira, J. R. *, 350, 799, 1227
Moreira, J. *
Moreno, J. F. 1823, 1861
Morrison, K. 2344
Moses, R. W. 1938
Mouchot, M. C. 236, 523, 1376, 1753
Mougin, E. *, 733, 1002
Moulin, S. 2366
Mourad, P. D. *
Mozley, E. C. *
Muchoney, D. 233
Mudukutore, A. 574
Mueller, H. J *
Mueshen, B. 2338
Mugnai, A. *
Mukherjee, D. P. *
Mulchi, C. L. 224
Muller, J. 1775
Muller, M. R. 1618
Murata, M. 1639
Murni, A. 1851
Murphy, T. J. *
Myers, R. J. *
Myneni, R. *

N

Nadimi, S. A. 863, 947, 2288
Naeije, M. C. 97
Nagabhushan, P. 1045, 1858
Nagata, H. 1639
Nagatani, G. 628
Nagler, P. L. 1803
Naka, M. 781
Nakajima, M. 390
Nakajima, T. Y. 390
Nakajima, T. 390
Nakamura, K. 512
Nakamura, S. *
Nakamura, T. 1929
Nakonechny, V. P. 1968
Narayanan, R. M. 445, 506, 1017, 1073, 1920, 1926, 2030, 2258, 2282, 2375
Narumalani, S. *, 463
Nash, G. G. *
Nassar, E. 118
Nativi, S. 1367
Naumov, A. P. 1698
Neale, C. M. U. 133, 2369
Nekrasov, V. P. 19, 366, 1441
Nelson, B. *
Nelson, D. H. 393
Nelson, R. F. 1797
Nemani, R. *
Nervi, A. 1603
Neuenschwander, A. 1512
Neumann, G. 1469, 1959
Newman, G. A. 1941
Nezry, E. 1574
Ng, W. E. 57, 67
Ngai, F. M. 665
Nghiem, S. V. 1190, 1208, 1469, 1959
Nguyen, L. 1911
Ni, W. 293, 591
Nichol, J. 2113
Nicolas, J. M. 503
Nielsen, F. 1766
Nielsen, N. B. 686
Niemann, O. 1873
Nikulainen, M. 1998
Nirchio, F. *
Nithack, J. *
Njoku, E. G. 1054
Nocera, L. 25
Nogotov, E. F. 1441
Nohmi, H. 1639
Noll, J. *, 1995
Noltimier, K. F. 142
Norikane, L. 1772, 1775, 2329
Norman, J. M. 2104, 2358
Normand, M. 1067
North, P. R. 1654
Noto, J. 686
Nuesch, D. *
Nunez, M. 1417
Nunnelee, W. M. 1678

O

Oaku, H. 1636
Oden, S. F. 1143
Oertel, D. 2107
Ogor, B. 717
Ohura, Y. 1639
Ojima, D. *
Okamoto, K. *
Okomel'kova, J. A. 609
O'Leary, E. 823
Oleson, K. W. 186
Oleson, K. 192
Oliphant, T. E. 1715, 1721, 1724
Olsen, R. B. *
Olson, W. 1429
O'Neill, P. E. 1061, 1064
O'Neill, P. O. 1297
Onstott, R. G. 944, 1193, 1202, 1520
Onstott, R. 2195
Osharin, A. M. *
Otterman, J. 1657
Oudart, P. 273

P

Paar, G. 31
Paduan, J. D. 1749
Pahl, U. 1478
Painter, T. H. 2249
Pairman, D. 1839
Pak, K. *, 1401, 2125, 2137, 2143
Pal, P. *
Palleschi, V. 520, 854
Palm, S. P. 1257
Palmer, R. D. 1920, 1926, 1929
Paloscia, S. 736, 2131
Pampaloni, P. 736, 2131
Panah, A. A. *
Panegrossi, G. *
Pangburn, T. 1073, 2375
Pankin, A. A. 360

Pantzov, S. Y. 360
Papathanassiou, K. P. *, 350, 799
Paquerault, S. 503
Parishikov, S. V. *
Park, J. D. 1526
Park, S. H. 560
Parkin, S. H. 1102
Parmiggiani, F. 709
Parra, G. A. 1753
Pasaribu, D. P. 372, 1590
Pascazio, V. 1241, 1577, 2083
Pasquali, P. *, 342, 656
Pasquariello, G. *, 1306, 1562, 2060
Payne, B. 321
Payton, S. L. 2273
Pazmany, A. L. 1553
Pazmany, A. 743
Peat, H. 2377
Peczeli, I. 697
Peddle, D. R. 212, 230, 427, 938
Peddle, D. 88
Pellegrini, P. F. 1603
Peltoniemi, J. I. *
Peng, C. Y. 380
Pepin, M. P. 54
Pereira, J. *
Perfiliev, Y. P. 1701
Perona, G. 1584
Perov, A. O. *
Perovich, D. K. 1184, 1190
Peterson, D. L. 2276
Peterson, J. R. *
Petrenko, B. Z. 481
Petrin, R. R. 393
Petrou, M. 1379
Pham, K. 37
Philbrick, C. R. 1253, 1826
Piazza, E. 1603
Picardi, G. 383
Pieczynski, W. 706
Piepmeier, J. R. 1120
Pierce, L. E. 580, 1092, 1568
Pierce, L. 40, 2329
Pierri, R. 1241, 2083
Pignatti, S. *
Pihlflyckt, J. 1998, 2285
Piironen, A. *
Pilant, D. *, 121
Pillai, S. R. 990
Pinel, V. 1660
Piwowar, J. M. 127, 645, 938
Planes, J. G. 387
Plant, W. J. *, 888, 1733, 2210
Plotnizky, S. *
Plumb, R. 778, 2033, 2036
Plummer, S. E. 1654
Plutchak, J. 1498
Poggio, L. 399
Pollard, B. 1923
Pons, I. 257
Porter, D. L. 1152, 2242
Posa, F. 1306
Pospelov, M. N. 1135, 1454
Poulain, D. E. 857
Poulton, M. M. *
Pouwels, H. 1633
Pozdnyakova, V. P. 609
Prakash, H. N. S. 1858
Prati, C. *, 671
Prevosto, M. 1956
Prietzsch, C. 282
Prikhach, A. S. *
Princz, J. *, 1221
Privette, J. L. *, 1663
Proffitt, M. H. *
Proisy, C. 733
Ptichnokov, A. V. 2324
Puglisi, G. 350
Pulliainen, J. 1759
Pullianinen, J. 583, 2110
Pultz, T. J. *
Pungin, V. G. 103
Pyhalahti, T. *

Q

Qi, J. 1420
Qin, P. 1989
Qin, W. 526, 1645
Qiu, Z. 2318
Quagliano, J. R. 393
Quartly, G. D. 91
Quel, E. J. 4
Quick, C. R. 393
Quilfen, Y. 805
Quintanilha, J. A. *

R

Rabine, D. L. 423
Racette, P. 1429
Rackley, K. *, 631
Raev, M. D. 1490
Raggam, H. *, 353
Rague, B. W. 1054
Rahmat-Samii, Y. 515
Rais, J. 1851
Raizer, V. Yu. *
Rall, J. A. R. 1538
Ramamurthy, M. K. 1498
Ramirez, A. *
Rampa, V. 2038
Raney, R. K. 2279
Rango, A. 2011
Ranson, K. J. 577, 1096
Ranzi, R. 266
Rao, C. R. N. *
Rao, K. S. 163, 201, 430
Rao, P. V. N. 163, 201
Rao, Y. S. 163, 201, 430
Rapoport, V. O. *
Rastelli, S. 520, 854
Rautiainen, K. 1998, 2285
Reagan, J. A. 683, 987, 1014, 1244, 1535
Reagan, J. T. 1020
Reed, B. *
Reed, R. 1475
Rees, W. G. 2261
Refice, A. 2060
Refling, J. P. 1102
Reichel, H. 872
Reichenbach, S. E. 1048, 1597
Reiners, W. A. 186
Reinke, D. 1105
Reistad, M. 1158
Remund, Q. P. 827, 848
Ren, Y. 1929
Ressler, M. A. 1886
Rey, L. 273
Reynaud, J. *
Ribbes, F. 842, 1983
Ricci, D. N. 1704
Riccio, D. *, 350, 680
Richard, J. 490
Richter, P. I. 697
Ride, S. *
Rieck, D. R. 448
Riggs, G. 139
Rignot, E. *
Rijkeboer, M. *
Rincon, R. F. 402
Ritter, M. 2204
Roberts, D. A. *
Roberts, M. 227
Rocca, F. *, 671
Rodenas, J. A. 1953
Roeder, R. S. 269
Roenko, A. N. 172, 178
Roli, F. *
Romeiser, R. 597, 981, 1962
Romig P. R., III 1048
Ronsin, J. 717
Roschier, M. 1998
Rosello, J. 1224
Rosenkranz, P. W. *
Rosenthal, W. 2252
Rosich Tell, B. 477
Ross, S. J. 1520, 2077
Rossi, M. *
Rostan, F. 2294
Rosten, D. P. 1809
Roth, A. 802, 2332, 2338
Roth, L. *
Rothrock, D. A. *
Rothrock, D. *
Rott, H. 2125
Rougean, J. L. 1408
Roujean, R. J. 591
Rouvier, S. 2167
Roux, C. 1753
Rozenberg, A. 2204
Rubertone, F. 1571
Rubino, A. 1487
Ruddick, K. G. *
Ruf, C. S. *, 1263, 1435, 1692
Rufenach, C. L. 814
Rungaldier, H. 2201, 2213
Running, S. *
Russell, C. A. *, 648
Russell, M. 1417
Ruzek, M. 1175
Ruzhentsev, N. V. *
Ryzhkov, A. V. *, 557

S

Saatchi, S. S. *, 1861
Saatchi, S. *, 730
Sabet, K. F. 1346
Sabinin, K. D. 103
Sacchini, J. J. 54
Sadjadi, F. 396
Sado, S. *
Saghri, J. A. 1020

Sahr, J. D. 569
Saillard, J. 615, 746
Saint-Joan, D. 2074
Sakurai-Amano, T. *
Salomonson, V. V. 139
Samal, A. 1048
Samuel, P. 1158
Sand, K. *
Sandberg, D. 1181
Sander, G. 1881
Sander, R. K. 393
Sano, E. E. 157
Sansosti, E. 2047
Sarabandi, K. 720, 723, 969, 978, 1070, 1334, 1337, 1346, 2122
Sarita, S. 1045
Sarture, C. M. *
Satalino, G. 1562
Sato, K. 487
Sato, S. 339
Sato, T. 775, 1361, 1612
Sausa, R. C. 851
Savazzi, P. 2071
Savtchenko, A. 2216
Sayler, K. L. 547
Sayood, K. 1026
Sazonov, Y. A. *
Scepan, J. 198
Scharroo, R. 97
Scheiber, R. 1214
Schertzer, D. 37
Schetkin, I. M. 2192
Schiavon, G. 736
Schiller, S. 1286
Schimel, D. S. *
Schirinzi, G. 1241, 1577
Schistad Solberg, A. H. 1484, 2307
Schloss, A. L. 106
Schlueter, N. 1247
Schmidt, G. M. 2101
Schmitt, M. J. 393
Schmugge, T. J. 2101
Schmugge, T. 1051
Schmullius, C. *
Schneider, D. 999
Schoening, V. L. 987
Schuler, D. L. 1162, 2086
Schulze, E. D. *
Schuster, G. L. 1911
Schwabisch, M. *, 350, 802
Schweiger, A. J. 636
Schwemmer, G. *, 1257
Schwichow, H. 339
Seifert, F. M. 1086
Seiferth, J. C. 1600
Sekelsky, S. M. 1, 1553
Seliga, T. A. 551, 569
Sergi, R. *, 1562
Serpico, S. B. *, 714
Servomaa, H. 1998
Sery, F. 457
Sessenrath, G. *
Seu, R. 383
Shaikh, M. A. 1105, 1108
Sharma, A. 1315
Shaw, J. A. 1328
Sheen, D. R. *
Shelton, J. C. 2201, 2213
Shen, C. Y 902
Sheng, Y. 48, 1559
Shepherd, N. W. 1290
Shepherd, N. 1352
Shepherd, P. R. *
Shereshevsky, I. A. 609
Shevtcov, B. M. 369
Shi, J. C. 2125
Shi, J. 136, 754, 2022, 2249
Shih, S. E. 757, 1208
Shimada, J. 43
Shimada, M. 1636
Shin, R. T. *, 1401
Shinme, H. 1639
Shinohara, H. 1639
Shippert, M. M. 169
Shire, H. N. 896
Shirer, H. N. *
Showman, G. A. 1688
Shuchman, R. A. 648
Shuchman, R. 1158
Siddiqui, K. J. 1099
Sieber, A. J. *
Sigismondi, S. 736, 2131
Sikora, T. D. *, 893, 896
Singh, R. *
Siqueira, P. 1337
Skirta, E. A. 603
Skoelv, A. 1141
Skofronick, G. M. 1688
Skotnicki, W. 1612
Skou, N. 674, 749, 869, 1629
Skriver, H. 1300, 1766
Skulachev, D. P. 442
Skvortsov, E. I. 1490
Slatton, K. C. *, 263
Sletten, M. A. 2017, 2207
Small, D. 342
Smirnov, A. I. 1454
Smirnov, A. V. 1481
Smith, G. L. 1414
Smith, J. A. 2146
Smith, M. C. 269
Smith, N. 1414
Smith, R. 1618
Smith, W. H. 2276
Smith, W. L., Jr. 1911
Smits, P. C. 714
Smokty, O. *
Snider, J. B. 1432
Snoeij, P. 1633
Snuttjer, B. R. J. 506
Snyder, W. 2095
So, C. S. *
Soffer, R. 1411
Soh, L. K. 112, 1532, 1565
Sohl, T. 246
Sohn, H. G. 148
Sohus, A. 321
Solaiman, B. 236, 523, 1373, 1562
Solberg, R. *, 1484, 2307
Solimini, D. 736
Solov'ev, D. M. *, 1971
Song, S. 996, 1392
Sosnovsky, Yu. M. 1323
Sottili, F. 13
Souffez, S. H. *
Souffez, S. S. *
Soulis, E. D. 1986
Souyris, J. C. 975, 1306, 2167
Soyris, J. C. 836
Spagnolini, U. 2038
Spencer, M. W. 82, 1463
Spencer, R. W. 1460
Spidaliere, P. 2160
Spinhirne, J. D. 683, 1244
Spring, F. 1515
Sridhar, M. 1498
Srivastava, S. K. 1290
Srivastava, S. 1352
St. Germain, K. M. 1026, 1523
Stacey, N. J. S. 1618
Stacy, N. J. S. *
Stalino, G. *
Stanhope, S. A. 2219
Stanichny, S. V. *
Staples, G. C. *
Starmer, W. J. 198
Steffen, K. 950
Steinauer, R. *
Steingieer, R. 1980
Stenstrom, G. 1877
Stern, H. *
Sternberg, B. K. *
Sterner R. E., II 1736
Stevens, D. 493
Stevens, T. D. 1253
Steyn-Ross, D. A. 94, 1293, 2098
Steyn-Ross, M. L. 94, 1293, 2098
Stiles, J. M. 720, 723
Stogryn, A. 154
Stolz, R. 1974
Stone, R. S. 636
Stork, E. J. 628
Stowe, L. *
Strahler, A. H. 243, 532, 538, 1405, 1426, 1587, 1669
Strahler, A. 233, 293, 591, 2173
Strawa, A. W. 2276
Streck, C. 330, 1836
Stretch, L. *
Strobl, P. 2107
Strukov, I. A. 442
Stuopis, P. A. 254
Sturgess, K. 2027
Sturm, J. M. 2207
Su, H. 2361
Su, Z. *, 1303
Subra, W. 2231
Subramanya, B. 1816
Suchall, J. L. 1355
Sud'bin, A. I. 100
Suga, Y. 1763
Sugawara, M. 1639
Sugimura, T. 79
Suinot, N. 273, 279, 490
Sukhatme, J. S. 430
Sun, C. 133
Sun, G. 577, 1096
Susini, C. 411
Sveinsson, J. R. 63, 1848
Swain, P. H. 1848
Swift, C. T. *, 1547
Sylvester, J. 1205
Syvertson, M. *

T

Taconet, O. 1067
Tadjudin, S. 790
Tait, A. 2005
Takasaki, K. 79
Takemata, K. 1666
Takemura, K. 775
Takeuchi, S. 1763
Talitsky, V. G. *
Tamlourrino, A. 2083
Tamoikin, V. V. *
Tan, S. Y. 67
Tanaka, S. 79
Tang, S. 2216
Tano, F. 1980
Tarchi, D. *
Taskinen, H. 1998
Tauriainen, S. 1998
Teany, L. D. *, 1290
Teraoka, T. 1361
Terre, C. 772
Tesauro, M. 51
Tescher, A. G. 1020
Thames, P. 192
Thayer, J. P. 686
Thiele, O. W. 402
Thomas, A. 953
Thomas, B. H. 1704
Thomas, C. H. 1788
Thomasson, L. 836
Thome, K. J. 1283
Thompson, D. G. 1892
Thompson, D. R. *, 893, 896, 981, 1152
Thompson, H. R., Jr. 2201, 2213
Thompson, L. L. *
Thompson, M. 1881
Thomsen, A. 1300, 1766
Thursby, M. H. 1526
Tian, B. 1105, 1108
Ticehurst, C. 1556
Tiee, J. J. 393
Tierney, M. R. *
Tighe, L. *
Tikhonov, V. V. *
Tikunov, V. S. 2324
Tilton, J. C. 703, 1023
Timchenko, A. I. *
Ting, C. M. *
Tirri, T. 1998
Titov, V. I. 1331
Tjuatja, S. 772, 2008, 2186
Todhunter, J. S. 189
Tognoni, E. 520, 854
Tommervik, H. *
Tomppo, E. 1010
Tong, K. 1035
Torre, A. *, 60, 1571
Torres, F. 315, 869
Torres, R. 1355
Totuka, H. 1639
Tournadre, J. 1389
Tourneret, J. Y. 1842
Touzi, R. 662
Townshend, J. 535
Tracy, B. T. 1073, 2375
Treitz, P. M. 1986
Treuhaft, R. 978
Trimble, J. 823
Trizna, D. B. 905, 2017
Troch, P. A. *, 1303
Trofimov, V. T. *
Troisi, V. J. 651
Troitsky, A. V. *
Trokhimovski, Yu. G. 1126, 1450, 1457, 1672
Troufleau, D. 157
Trump, C. L. *
Tsai, W. Y. 935, 1718
Tsang, L. *, 130, 728, 754, 1401, 2125, 2143
Tsatsoulis, C. 109, 112, 1532, 1565
Tseng, W. Y. 85
Tsu, H. 1763
Tucker, C. J. 1169
Tupin, F. 474
Twarog, E. M. 1745

U

Ueda, K. 1250
Ulaby, F. T. 723, 1070, 1092, 1093, 1568, 2335
Ulaby, F. 2329
Ulander, L. M. H. 668, 1877
Ungar, S. G. *
Usha, P. V. 408

V

Vachon, P. W. 966, 1155, 1621, 2255
Vachon, P. W. 966
Vachon, P. 662
Vadkovsky, V. N. *
Vadon, H. *
Valero, J. L. 336, 2255
Vandemark, D. 1257, 1385, 1389
van den Berg, J. H. 2240
van der Keur, P. 1300
van der Kooij, M. W. A. 339, 963
Vandersteene, F. *
van Gelder, A. 2240
van Halsema, D. 963
van Leeuwen, W. J. D. *, 1423
VanSumeren, H. 2195
Van Woert, M. L. 1117
van Zuidam, R. 2240
van Zyl, J. J. 2294
van Zyl, J. 978, 1612
Vasilevsky, A. F. *
Vasilyev, Yu. F. 172, 178
Vaugh, C. R. 423
Vedel, S. *
Velipasaoglu, E. O. *
Veltroni, M. 1230
Veneziani, N. 2060
Venkataraman, G. 430
Venkataratnam, L. 163, 201
Vermotel, E. R. 1904
Vescoui, F. 1980
Vesecky, J. F. 891, 1520, 2077, 2219, 2347
Vidal, A. 157, 1224
Vidal-Madjar, D. 1067
Vierling, L. A. 1897
Viggian, R. *
Vincent, N. 279, 490
Vishniakov, V. 175
Vogelmann, J. E. 246
Vogelzang, J. *
Volynsky, V. A. *, 100, 296
Von Ahn, J. *
Vorosmarty, C. L. 106

W

Waite, W. P. *
Wakayama, T. 775
Walavalkar, V. 430
Wales, C. 634, 1775, 1777
Walker, B. 1881
Walker, D. T. 2219
Walker, N. 583
Wall, S. *, 51
Wallace, B. 881
Waller, G. 1227
Walsh, T. M. 563
Walter-Shea, E. A. 1005, 1908
Walthall, C. L. 586, 1423, 1797, 1904
Wan, Z. 2095
Wang, B. 1645
Wang, J. R. 956, 1429, 2134, 2246
Wang, J. 1297
Wang, M. X. *
Wang, N. 1989
Wang, Y. *, 1077, 1083
Wanner, W. 1405, 1408, 1411, 1669
Ward, E. 914
Warner, K. K. 1017
Wash, C. H. 1260
Wasrin, U. R. 842
Waters, J. 2231
Way, J. B. *, 628
Weaver, R. L. 651
Wedin, D. 2377
Weeks, R. 2125
Weidemann, A. D. 285, 305
Weinman, J. A. *
Weissman, D. E. 878, 888, 1472
Wergin, W. 2011
Wersinger, J. M. 914
Wessel, G. R. I. 645
Wessman, C. A. 1663
West, J. C. 2207
West, R. D. 1718, 1727
Westwater, E. R. 1138, 1450, 1672, 1681, 1685
Wever, T. 1833
Weydahl, D. J. 151
Weydal, D. *
White, H. P. 212, 1411
White, M. A. *
Whitehead, M. 393
Whiteman, D. *
Whitlock, C. H. 1911
Wick, G. A. *
Wiesbeck, W. 763, 766, 1340, 2294
Wilheit, T. T. *
Wilhelmson, R. B. 1498
Wilkner, D. 881
Williams, D. L. 1797, 2161
Williams, J. 1780
Williams, R. N. 1111
Willis, K. J. 929
Willmott, C. J. 106
Wilson, B. 1772
Wilson, C. J., III 218

Wilson, J. J. 2341
Wilson, L. L. 130
Wilson, W. J. *, 1132
Winebrenner, D. P. 941, 1205
Winokur, R. S. *
Winstead, N. S. *, 893
Winter, R. 966
Wismann, V. R. 839, 2014, 2264
Wismann, V. *
Woelders, K. 276, 674, 1629
Wojtowicz, D. 1498
Wolf, C. 2219
Wolfe, D. E. *
Wolhletz, B. P. 1932
Wood, E. F. 1061, 1064
Woodcock, C. E. 529, 538, 591
Woodcock, C. 293
Woodhouse, I. H. 260, 845
Woodhouse, R. 1279
Wooding, M. 1995
Wu, J. 509, 739, 1965, 2216
Wu, S. T. S. 1309
Wylie, B. 2377

X

Xia, Z. G. 48, 1559, 2310
Xiao, R. 566
Xiong, H. *
Xu, W. 2044
Xu, Y. 2030, 2282
Xuan, J. 700
Xue, Y. 417, 2158

Y

Yacobi, Y. Z. *
Yakin, G. Y. 189
Yakovlev, V. V. *, 103
Yamaguchi, Y. *
Yamanashi, M. 1636, 1929
Yamashita, N. 1695
Yamazaki, A. 1250
Yang, G. 2068
Yang, J. *
Yang, L. 2318
Yang, W. 2315
Yang, X. 1989, 2240
Yang, Y. E. 757
Yankielun, N. E. *
Yanovsky, F. J. 2297
Yanow, G. 321
Yarwood, M. 490
Yea, J. H. 2137
Yee, R. 2201, 2213
Yeh, P. S. 1032
Yeo, T. S. *, 57, 67
Yevtyushkin, A. V. *
Yildirim, O. 1343, 1444
Yonekura, T. 1666
Yook, J. G. 1346
Young, G. S. *, 893, 896
Young, J. 118
Yu, Y. 60
Yueh, S. H. *, 935, 1132, 1190, 1718, 1727
Yueh, S. Y. *
Yushakov, V. N. *
Yutsis, V. V. *

Z

Zagolski, F. 1002
Zaitsev, V. A. 1971
Zaitsev, V. V. *, 363
Zakarin, E. 209
Zakharov, A. I. *
Zamaraev, B. D. 172, 178
Zege, E. P. *
Zeng, Q. *
Zhan, J. 1429
Zhang, B. 1405
Zhang, C. B. 57, 67
Zhang, G. 728, 2143
Zhang, J. 2375
Zhang, N. *
Zhang, Y. 2095, 2177
Zheng, X. *
Zhiqiang, Y. 466
Zhu, K. 2041
Zhukov, B. 2107
Zimmermann, R. *
Zinichev, V. A. *
Zink, M. 1086
Zion, M. 1061
Zlystra, G. J. 547
Zott, J. 2276
Zribi, M. 1067
Zrnic, D. S. 557
Zurk, L. M. 754
Zuykova, E. M. 1331